BIOMARKERS FROM MULTI-TRACER AND MULTI-MODAL NEUROIMAGING IN AGE-RELATED NEURODEGENERATIVE DISEASES

EDITED BY: Ping Wu, Behrooz Hooshyar Yousefi, Wei Cheng and Binbin Nie

PUBLISHED IN: Frontiers in Aging Neuroscience

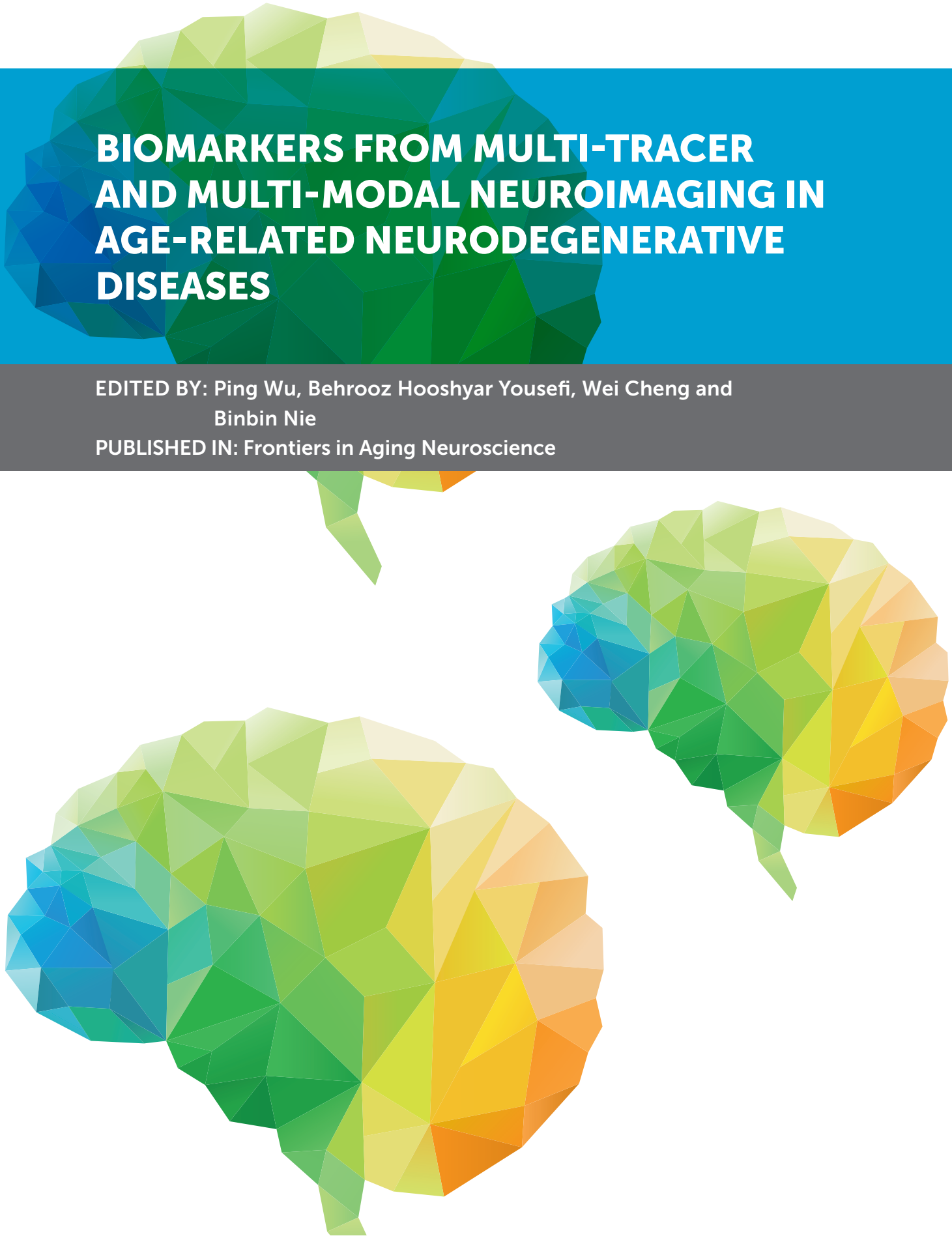

frontiers Research Topics

frontiers

ISSN 1664-8714
ISBN 978-2-88976-956-8
DOI 10.3389/978-2-88976-956-8

About Frontiers

Frontiers is more than just an open-access publisher of scholarly articles: it is a pioneering approach to the world of academia, radically improving the way scholarly research is managed. The grand vision of Frontiers is a world where all people have an equal opportunity to seek, share and generate knowledge. Frontiers provides immediate and permanent online open access to all its publications, but this alone is not enough to realize our grand goals.

Frontiers Journal Series

The Frontiers Journal Series is a multi-tier and interdisciplinary set of open-access, online journals, promising a paradigm shift from the current review, selection and dissemination processes in academic publishing. All Frontiers journals are driven by researchers for researchers; therefore, they constitute a service to the scholarly community. At the same time, the Frontiers Journal Series operates on a revolutionary invention, the tiered publishing system, initially addressing specific communities of scholars, and gradually climbing up to broader public understanding, thus serving the interests of the lay society, too.

Dedication to Quality

Each Frontiers article is a landmark of the highest quality, thanks to genuinely collaborative interactions between authors and review editors, who include some of the world's best academicians. Research must be certified by peers before entering a stream of knowledge that may eventually reach the public - and shape society; therefore, Frontiers only applies the most rigorous and unbiased reviews.
Frontiers revolutionizes research publishing by freely delivering the most outstanding research, evaluated with no bias from both the academic and social point of view. By applying the most advanced information technologies, Frontiers is catapulting scholarly publishing into a new generation.

What are Frontiers Research Topics?

Frontiers Research Topics are very popular trademarks of the Frontiers Journals Series: they are collections of at least ten articles, all centered on a particular subject. With their unique mix of varied contributions from Original Research to Review Articles, Frontiers Research Topics unify the most influential researchers, the latest key findings and historical advances in a hot research area! Find out more on how to host your own Frontiers Research Topic or contribute to one as an author by contacting the Frontiers Editorial Office: frontiersin.org/about/contact

BIOMARKERS FROM MULTI-TRACER AND MULTI-MODAL NEUROIMAGING IN AGE-RELATED NEURODEGENERATIVE DISEASES

Topic Editors:
Ping Wu, Fudan University, China
Behrooz Hooshyar Yousefi, University of Marburg, Germany
Wei Cheng, Fudan University, China
Binbin Nie, Institute of High Energy Physics, Chinese Academy of Sciences (CAS), China

Citation: Wu, P., Yousefi, B. H., Cheng, W., Nie, B., eds. (2022). Biomarkers from Multi-tracer and Multi-modal Neuroimaging in Age-related Neurodegenerative Diseases. Lausanne: Frontiers Media SA. doi: 10.3389/978-2-88976-956-8

Table of Contents

frontiers | Frontiers in Aging Neuroscience

TYPE Editorial
PUBLISHED 03 August 2022
DOI 10.3389/fnagi.2022.961718

OPEN ACCESS

EDITED AND REVIEWED BY
Allison B. Reiss,
New York University, United States

*CORRESPONDENCE
Binbin Nie
niebb@ihep.ac.cn

SPECIALTY SECTION
This article was submitted to Alzheimer's Disease and Related Dementias, a section of the journal Frontiers in Aging Neuroscience

RECEIVED 05 June 2022
ACCEPTED 14 June 2022
PUBLISHED 03 August 2022

CITATION
Nie B (2022) Editorial: Biomarkers from multi-tracer and multi-modal neuroimaging in age-related neurodegenerative diseases. *Front. Aging Neurosci.* 14:961718. doi: 10.3389/fnagi.2022.961718

Editorial: Biomarkers from multi-tracer and multi-modal neuroimaging in age-related neurodegenerative diseases

Binbin Nie[1,2]*

[1]Beijing Engineering Research Center of Radiographic Techniques and Equipment, Institute of High Energy Physics, Chinese Academy of Sciences, Beijing, China, [2]School of Nuclear Science and Technology, University of Chinese Academy of Sciences, Beijing, China

KEYWORDS

deep learning, neurodegenerative diseases, heterogeneous, magnetic resonance imaging, positron emission tomography

Editorial on the Research Topic
Biomarkers from multi-tracer and multi-modal neuroimaging in age-related neurodegenerative diseases

With the progress of neuroimaging methods, more neurodegenerative diseases have been revealed to have heterogeneous phenotypes and stages (Leyton et al., 2011; Thenganatt and Jankovic, 2014; Graff-Radford et al., 2021). This underlying heterogeneity influences the precision of diagnosis and subsequent medical treatment. In this Research Topic on "*Biomarkers from Multi-tracer and Multi-modal Neuroimaging in Age-related Neurodegenerative Diseases*," researchers have contributed unique opinions and solutions for this issue. For example, using blood oxygen level-dependent (BOLD) functional magnetic resonance imaging (fMRI), Sheng et al. studied the heterogeneous stages of Parkinson's disease by exploring the altered cortical cholinergic network, while Li et al. investigated the alterations of regional homogeneity. Chiu et al. designed a composite scale to improve the diagnostic accuracy of heterogeneous dementia, differentiating Lewy body dementia (DLB) from Alzheimer's Disease (AD).

Apart from traditional statistical methods, as a state-of-the-art method, deep learning (DL) methods have the leading advantage of exploiting hierarchical feature representations, instead of human-designed features by the expert's understanding of the domain (LeCun et al., 2015; Litjens et al., 2017). The DL might therefore be a better method to discover the more heterogeneous patterns of different neurodegenerative diseases.

DL methods can help to improve diagnosis and predictive accuracy. Qu et al. reviewed the performance of the generative adversarial network (GAN) in the diagnosis of AD. Zhou et al. evaluated the deep-learning radiomics (DLR) method for predicting the conversion of mild cognitive impairment (MCI) to AD. The performance of pattern recognition of these models could both exploit the mutual information among different modalities and detect the heterogeneous disease patterns in neuroimaging.

DL methods can also be inspired by other algorithms for their unique characteristics. Some unsupervised methods in machine learning have also shown promising effects. (Díaz-Álvarez et al., 2022) used a machine learning algorithm with genetic algorithms, K-nearest neighbor, and BayesNet Naives to distinguish AD and frontotemporal dementia (FTD). The application of graph theory can lead to the combination of graph neural networks. Wei et al. and Zhang T. et al. have addressed graph characteristics among the regional neuroimaging biomarkers of MCI and AD.

Apart from MCI and AD dementia, Zhang et al. (2021) focused on uncertain cases of memory impairment. The use of the DL method based on ^{18}F-fluorodeoxyglucose (FDG) positron emission tomography (PET) can help to distinguish real AD-related pathology from fake memory impairment caused by a depressed mental state. This classification between heterogeneous causes could lead to less misdiagnosis and inappropriate treatment.

Although studies have made much progress in the application of DL among heterogeneous neurodegenerative diseases, some questions are still waiting to be addressed in the future. First, reliable statistical results should also be presented along with the DL results of the disease heterogeneity. Second, after detecting the heterogeneity by innovative methods, more non-imaging information like neuropsychological tests, genetics, and demography can be combined to detect more related features. Finally, the explanation of the DL models should be addressed further through the purposive design of model structures or experiments.

Author contributions

BN were responsible for the study concept and wrote the manuscript.

Funding

This work was financially supported by the National Natural Science Foundation of China (12175268 and 11975249).

Conflict of interest

The author declares that the research was conducted in the absence of any commercial or financial relationships that could be construed as a potential conflict of interest.

Publisher's note

All claims expressed in this article are solely those of the authors and do not necessarily represent those of their affiliated organizations, or those of the publisher, the editors and the reviewers. Any product that may be evaluated in this article, or claim that may be made by its manufacturer, is not guaranteed or endorsed by the publisher.

References

Díaz-Álvarez, J., Matias-Guiu, J. A., Cabrera-Martín, M. N., V., Segovia-Ríos, I., García-Gutiérrez, F., et al. (2022). Genetic algorithms for optimized diagnosis of Alzheimer's disease and frontotemporal dementia using fluorodeoxyglucose positron emission tomography imaging. *Front. Aging Neurosci.* 13:708932. doi: 10.3389/fnagi.2021.708932

Graff-Radford, J., Yong, K., Apostolova, L. G., Bouwman, F. H., Carrillo, M., Dickerson, B. C., et al. (2021). New insights into atypical Alzheimer's disease in the era of biomarkers. *Lancet Neurol.* 20, 222–234. doi: 10.1016/S1474-4422(20)30440-3

LeCun, Y., Bengio, Y., and Hinton, G. (2015). Deep learning. *Nature* 521, 436–444. doi: 10.1038/nature14539

Leyton, C. E., Villemagne, V. L., Savage, S., Pike, K. E., Ballard, K. J., Piguet, O., et al. (2011). Subtypes of progressive aphasia: application of the international consensus criteria and validation using beta-amyloid imaging. *Brain* 134, 3030–3043. doi: 10.1093/brain/awr216

Litjens, G., Kooi, T., Bejnordi, B. E., Setio, A. A. A., Ciompi, F., Ghafoorian, M., et al. (2017). A survey on deep learning in medical image analysis. *Med. Image Anal.* 42, 60–88. doi: 10.1016/j.media.2017.07.005

Thenganatt, M. A., and Jankovic, J. (2014). Parkinson disease subtypes. *JAMA Neurol.* 71, 499–504. doi: 10.1001/jamaneurol.2013.6233

Zhang, W., Zhang, T., Pan, T., Zhao, S., Nie, B., Liu, H., et al. (2021). Deep learning with 18F-fluorodeoxyglucose-pet gives valid diagnoses for the uncertain cases in memory impairment of alzheimer's disease. *Front. Aging Neurosci.* 13, 764272. doi: 10.3389/fnagi.2021.764272

frontiers in Aging Neuroscience

ORIGINAL RESEARCH
published: 21 July 2021
doi: 10.3389/fnagi.2021.676899

Alterations of Regional Homogeneity in the Mild and Moderate Stages of Parkinson's Disease

*Junli Li, Haiyan Liao, Tianyu Wang, Yuheng Zi, Lin Zhang, Min Wang, Zhenni Mao, ChenDie Song, Fan Zhou, Qin Shen, Sainan Cai and Changlian Tan**

Department of Radiology, The Second Xiangya Hospital, Central South University, Changsha, China

Objectives: This study aimed to investigate alterations in regional homogeneity (ReHo) in early Parkinson's disease (PD) at different Hoehn and Yahr (HY) stages and to demonstrate the relationships between altered brain regions and clinical scale scores.

Methods: We recruited 75 PD patients, including 43 with mild PD (PD-mild; HY stage: 1.0–1.5) and 32 with moderate PD (PD-moderate; HY stage: 2.0–2.5). We also recruited 37 age- and sex-matched healthy subjects as healthy controls (HC). All subjects underwent neuropsychological assessments and a 3.0 Tesla magnetic resonance scanning. Regional homogeneity of blood oxygen level-dependent (BOLD) signals was used to characterize regional cerebral function. Correlative relationships between mean ReHo values and clinical data were then explored.

Results: Compared to the HC group, the PD-mild group exhibited increased ReHo values in the right cerebellum, while the PD-moderate group exhibited increased ReHo values in the bilateral cerebellum, and decreased ReHo values in the right superior temporal gyrus, the right Rolandic operculum, the right postcentral gyrus, and the right precentral gyrus. Reho value of right Pre/Postcentral was negatively correlated with HY stage. Compared to the PD-moderate group, the PD-mild group showed reduced ReHo values in the right superior orbital gyrus and the right rectus, in which the ReHo value was negatively correlated with cognition.

Conclusion: The right superior orbital gyrus and right rectus may serve as a differential indicator for mild and moderate PD. Subjects with moderate PD had a greater scope for ReHo alterations in the cortex and compensation in the cerebellum than those with mild PD. PD at HY stages of 2.0–2.5 may already be classified as Braak stages 5 and 6 in terms of pathology. Our study revealed the different patterns of brain function in a resting state in PD at different HY stages and may help to elucidate the neural function and early diagnosis of patients with PD.

Keywords: Parkinson's disease, resting-state functional MRI, regional homogeneity (ReHo), Hoehn and Yahr stage, early diagnosis

OPEN ACCESS

Edited by:
Binbin Nie,
Institute of High Energy Physics, Chinese Academy of Sciences, China

Reviewed by:
Sachchida Nand Rai,
University of Allahabad, India
Fuchun Lin,
Innovation Academy for Precision Measurement Science and Technology (CAS), China

****Correspondence:***
Changlian Tan
tanchanglian@csu.edu.cn

Received: *06 March 2021*
Accepted: *23 June 2021*
Published: *21 July 2021*

Citation:
Li J, Liao H, Wang T, Zi Y, Zhang L, Wang M, Mao Z, Song C, Zhou F, Shen Q, Cai S and Tan C (2021) Alterations of Regional Homogeneity in the Mild and Moderate Stages of Parkinson's Disease. Front. Aging Neurosci. 13:676899. doi: 10.3389/fnagi.2021.676899

INTRODUCTION

Parkinson's disease (PD) was first described by James Parkinson in 1817 (Hurwitz, 2017) and is now the second most common neurodegenerative disease after Alzheimer's disease (Khan et al., 2019). The worldwide prevalence of PD is approximately 0.3% in the general population above 40 years of age (Pringsheim et al., 2014). It is estimated that the number of people suffering from PD in China will rise from 1.99 million in 2005 to 5 million in 2030, accounting for almost half of the total global population of PD patients (Li G. et al., 2019). PD is a multi-system disorder that is manifested by a range of motor symptoms, including rest tremor, stiffness, bradykinesia, and postural instability, as well as concomitant non-motor symptoms, such as hyposmia, depression, anxiety, cognitive dysfunction, and sleep disorders (Shrestha et al., 2017; Reich and Savitt, 2019; Singh et al., 2020a; Zahra et al., 2020). With an aging population, the prevalence of PD will undoubtedly reduce the quality of life for the elderly and create a significant medical burden on human society.

The core pathology of PD is considered to involve the deposition of Lewy bodies and the destruction of dopamine neurons in the substantia nigra pars compacta of the midbrain, thus leading to disruption of the basal ganglia and the initiation of motor symptoms (Rai et al., 2016, 2017, 2019; Singh et al., 2020b). In Braak's staging system, the pathology of PD can be divided into six stages according to the presence of Lewy bodies; the deposition of Lewy bodies begins in the dorsal IX/X motor nucleus or intermediate reticular zone and reaches the lower brain stem nuclei and eventually extends upwards to the neocortex (Kon et al., 2020). However, when motor symptoms appear, the loss of dopaminergic neurons in the substantia nigra has already reached at least 60% (Hornykiewicz, 2006), thus corresponding to Braak stage 3 or 4. At Braak stages 1 or 2, patients with PD often have only motor symptoms with no typical characteristics on conventional imaging. Consequently, these patients tend to be diagnosed with other neurological diseases, such as depression, anxiety disorders, Alzheimer's disease, and sleep disorders. Hence, identifying PD patients at an early stage is critical for the clinical management and treatment of this disease.

Resting-state functional magnetic resonance imaging (rs-fMRI) can measure continuous cerebral activity by recording blood oxygen level-dependent (BOLD) signals and is one of the main major imaging methods used to study the neurobiological mechanisms of PD. rs-fMRI can be divided into functional separation and functional integration. Functional separation predominantly investigates the characteristics of regional neural spontaneous activity, such as the amplitude of low frequency fluctuation analysis (ALFF) and regional homogeneity analysis (ReHo). In contrast, functional integration emphasizes the correlations and interactions between remote brain regions by functional connectivity (FC) or network analysis, such as independent component analysis (ICA), FC density analysis (FCD), seed-based FC analysis, and graph analysis (Zuo and Xing, 2014; Lv et al., 2018).

Functional integration is the primary method used to explore the activity of the human brain. However, functional separation can potentially influence the global network dynamics. For example, changes in the ReHo value are thought to cause alterations of remote FC (Jiang and Zuo, 2016). ReHo values are determined by the Kendall coefficient of concordance (KCC) in between the BOLD time-series, and describes the homogeneity of a given voxel and the most adjacent 26 voxels (Yang et al., 2020). ReHo values can be regarded as indicators of network centrality to represent the significance of nodes in functional connectomes within the cerebrum (Jiang and Zuo, 2016; Lv et al., 2018).

A multitude of researchers has attempted to use magnetic resonance to study the early phases of PD. For example, Claassen et al. (2016) identified asymmetric cortical atrophy in the left cerebrum, particularly in the left insula and olfactory sulcus. In a series of rs-fMRI studies, a number of cerebral areas were proposed to be related to early PD (Long et al., 2012; Yang et al., 2013; Fioravanti et al., 2015; Xu et al., 2019). These studies made a significant contribution to the possible cerebral structural or functional changes in early PD. Nevertheless, these results were inconsistent. We hypothesize that this inconsistency is because PD patients at different stages correspond to different cerebral alteration patterns.

Based upon the Hoehn and Yahr (HY) scale, created in 1967, the "modified HY scale" features 0.5 increments and has been widely used to evaluate the clinical progression of PD (Hoehn and Yahr, 1967; Goetz et al., 2004). Guan et al. (2019) coupled various oscillation frequencies in PD and observed progressive oscillation-specific nodal alterations from the early to middle stages of PD. Further research based on the ALFF and FC of PD patients with different HY stages indicated a higher function default mode network(DMN) in stage II (Luo et al., 2015). More recent research has focused on the use of structural MRI to investigate PD patients at different HY stages. Compared to a mild PD group, a group of patients with moderate PD showed an increased cortical thickness in a number of brain areas, including the temporal pole, isthmus cingulate cortex, superior frontal cortex, fusiform gyrus, insula lobe, and the inferior temporal cortex (Gao et al., 2018). Therefore, we hypothesized that ReHo values will vary as PD progresses. In this study, we used ReHo analysis to compare changes in cerebral function at various HY stages of Parkinson's disease (PD). We also investigated how the pathogenesis of PD changed with different stages.

MATERIALS AND METHODS

Subjects

All PD patients and healthy subjects were recruited between December 2015 and October 2020. This research was authorized by the Ethics Committee of the 2nd Xiangya Hospital. All patients were diagnosed by two neurologists according to the Movement Disorder Society (MDS) PD criteria (Postuma et al., 2015). For both PD patients and normal controls, we obtained a range of demographic and clinical information, including age, gender, education, the 17-item Hamilton Depression

Scale (HAMD-17) score, and the Mini-Mental State Exam (MMSE) score. For PD patients, we recorded disease duration, the Unified Parkinson's Disease Rating Scale score (UPDRS, featuring a motor component named UPDRS-III), and the HY Scale score. Patients who met the following criteria were included: (1) patients satisfied the MDS PD criteria for clinically established PD; (2) patients were right-handed; (3) patients had stopped taking anti-PD drugs for 12 h; and (4) patients had motor signs and symptoms at an HY stage of 1.0–2.5. Subjects were excluded if they: (1) had other diseases that could potentially affect brain function, such as atypical Parkinsonism, depression, cerebral trauma, stroke, and other diseases of the neurological system, $n = 3$; (2) had contraindications to MRI or were unable to cooperate with an MRI scan and clinical scales, $n = 6$; or (3) had an MMSE score less than the corresponding education degree, $n = 3$. MMSE scores of >17 for illiterate subjects, >20 for 1–6 years of education, and >23 for 7 or more years of education, were defined as normal MMSE scores (Li et al., 2016); (4) had excessive head motion (greater than 0.5 mm in transformation and 0.5 degrees in rotation), $n = 4$; and (5) had not withdrawn from anti-Parkinson drugs, $n = 6$. In total, 75 PD patients (with HY stages of 1.0–2.5) were included in this research. PD patients with an HY stage of 1.0–1.5, corresponding to unilateral motor symptoms, were defined as having mild PD (PD-mild, $n = 43$). Patients with an HY stage of 2.0–2.5, corresponding to bilateral motor symptoms, were defined as having moderate PD (PD-moderate, $n = 32$). Thirty-seven right-handed healthy subjects that were matched for age, sex, and education, were recruited as healthy controls (HC, $n = 37$).

Image Acquisition

Imaging data were acquired by a Siemens 3.0T MRI scanner by a radiologist at the Radiology Department of the 2nd Xiangya Hospital, Central South University. During MRI scanning, each individual was asked to lie in a supine position wearing earmuffs to reduce the sound of the MRI system. The patients also had foam pads around their heads to minimize head movement. All subjects were then informed to remain relaxed during rs-fMRI acquisition, with their eyes closed but avoiding sleep and active thought. Rs-fMRI images were acquired by an Echo Planar Imaging (EPI) sequence with the following parameters: echo time (TE) = 25 ms; repetition time (TR) = 2,500 ms; voxel size = 3.75 × 3.75 × 3.5 mm; flip angle (FA) = 90°; field of view (FOV) = 240 × 240 mm^2, data matrix = 64 × 64; slice gap = 0 mm; slice thickness = 3.5 mm; 39 interleaved slices and 200 volumes. T1WI three-dimensional magnetization- prepared rapid acquisition gradient echo (T1WI-3D-MP RAGE) images were acquired with the following parameters: TE = 2.01 ms; TR = 1900 ms; voxel size = 1 × 1 × 1 mm; slice thickness = 1 mm; FA = 9°; FOV = 256 mm × 256 mm; 176 continuous sagittal slices.

MRI Data Pre-processing

The rs-fMRI data were preprocessed by the Resting State fMRI Data Analysis Toolkit (RESTplus) software version 1.21 (Xi-Ze et al., 2019)[1]; this is a software package that is based on Statistical Parametric Mapping 8 (SPM8) on the MATLAB R2014b platform (The MathWorks Inc., Natick, MA, USA). Pre-processing involved seven steps, as follows: (1) converting data from digital imaging and communications in medicine(DICOM) to neuroimaging informatics technology initiative(NIFTI); (2) eliminating the initial 10 volumes; (3) slice timing; (4) realignment and the evaluation of head movement (exclusion criteria: >0.5 mm in transformation and >0.5 degrees of rotation); (5) spatial normalization (this was divided into three steps: setting the origin to anterior commissure for each patient's T1WI-3D-MP RAGE; registration of high resolution T1WI to mean functional MRI, division of the T1WI with Diffeomorphic Anatomical Registration *via* the Exponentiated Lie Algebra (DARTEL; Ashburner, 2007) toolkit, the generation of a group template; transformation and normalization of the resulting aligned data to the Montreal Neurological Institute (MNI) space with the segmented gray matter from DARTEL); (6) removal of the linear trend generated from MRI or other factors; (7) nuisance covariate regression with six head motion parameters, white matter, and cerebrospinal fluid signal (Yan et al., 2013); and (8) filtering with a bandpass of 0.01−0.08 Hz.

Regional Homogeneity

Next, we used RESTplus software to calculate a voxel-wise ReHo map for each patient. A z-transformation was then performed by deducting the mean value of the entire brain from the resulting ReHo map and dividing by the global standard deviation. In addition, we smoothened the ReHo map with a full width at a half maximum (FWHM) Gaussian kernel of 6 mm. The standardized ReHo Z-maps were then used for correlative analysis while the smoothened ReHo maps were used for statistical analysis to investigate regional homogeneity.

Statistical Analysis for Demographic and Clinical Information

First, we tested data for normality with the Shapiro–Wilk Test; Levene's Test was used to evaluate the homogeneity of variance. Patient age and the number of years of education were distributed normally and showed homogeneity of variance; the other clinical data did not comply with these stipulations ($p < 0.05$). Differences in age and education degree across the PD-mild, PD-moderate, and HC groups were compared by analysis of variance (ANOVA), while the independent *t*-test was used to identify differences between the entire PD group and the HC or PD groups. Due to the qualitative nature of the data, gender distribution among/between groups was tested by the Pearson Chi-squared test. Due to the non-normal distribution of data, differences in UPDRS, UPDRS-III, and disease duration, between the PD groups were compared with the Mann–Whitney Wilcoxon test. Differences in the MMSE and HAMD-17 scores across the three groups, and between the PD groups, were compared with the Kruskal–Wallis test and the Mann–Whitney Wilcoxon test, respectively. We also attempted

[1] http://www.restfmri.net

TABLE 1 | Demographic information and clinical characteristics of the three groups.

Item	PD	PD-mild	PD-moderate	HC	$p_{(PD\ vs.\ NC)}$	$p_{(PD\text{-}mild\ vs.\ NC)}$	$p_{(PD\text{-}moderate\ vs.\ NC)}$	$p_{(PD\text{-}mild\ vs.\ PD\text{-}moderate)}$
Number (M/F)	75(42/33)	43(27/16)	32(15/17)	37(17/20)	0.316	0.131	0.938	0.170
Age (years)	58.95 ± 9.55	57.30 ± 8.58	61.16 ± 10.46	58.05 ± 8.78	0.634	0.717	0.166	0.076
Duration (month)	23.69 ± 20.74	18.00 ± 16.61	31.34 ± 23.39	–	–	–	–	0.005
Education (years)	7.03 ± 3.71	7.35 ± 3.92	6.59 ± 3.42	7.64 ± 3.46	0.406	0.726	0.238	0.375
HY stages	1.63 ± 0.60	1.15 ± 0.23	2.27 ± 0.25	–	–	–	–	0.000
UDPRS	25.12 ± 15.10	19.84 ± 11.90	32.22 ± 16.17	–	–	–	–	0.001
UDPRS-III	15.3 ± 10.42	11.12 ± 7.09	20.94 ± 11.58	–	–	–	–	0.000
MMSE	26.08 ± 3.73	26.35 ± 2.98	26.53 ± 2.64	25.38 ± 5.07	0.748	0.846	0.703	0.996
HAMD-17	5.82 ± 6.11	6.30 ± 6.30	8.78 ± 6.90	2.70 ± 3.13	0.000	0.002	0.000	0.060

Data are shown as means ± SD. PD, Parkinson's disease; PD-mild, Parkinson's disease at 1.0–1.5 stage; PD-moderate, Parkinson's disease at 2.0–2.5 stage; HC, Healthy controls; M, male; F, female; HY, Hoehn and Yahr; UPDRS, Unified Parkinson's Disease Rating Scale; UDPRS-III, the motor part of UPDRS; MMSE, Mini-Mental State Examination; HAMD-17, 17-item Hamilton Depression Scale; –, Data not available.

to identify correlations among the clinical data. These analyses were conducted by IBM SPSS statistical analysis software (version 25.0; SPSS Inc. Chicago, IL, USA).

Statistical Analysis for Regional Homogeneity and Correlative Analysis

One-way analysis of covariance (ANCOVA) was used to compare differences between the smoothened ReHo maps created for the PD-mild, PD-moderate, and HC groups, with age, gender, and education, serving as covariates. Significant differences were generated among the three groups (voxel-level $p < 0.005$; minimal cluster size >24 voxels; corresponding to $p < 0.05$ for a two-tail test as corrected by the AlphaSim program). In order to investigate the significant brain regions, we used a *post hoc* two-sample *t*-test to compare differences between each pair of the three groups (corrected by the AlphaSim program with a voxel-level $p < 0.005$; cluster-level $p < 0.05$ for a two-tail test and a cluster size >24 voxels). Brain regions that showed significant differences in the ANCOVA were extracted as masks so that we could investigate the correlative relationships between mean ReHo values and clinical data in the PD groups. Spearman's correlation coefficient was calculated and the threshold of significance was set to $p < 0.05$ (corrected by Bonferroni's correction). Correlation analysis was performed by SPSS version 25.0.

RESULTS

Demographics and Clinical Characteristics

Table 1 summarizes the demographic information and clinical characteristics of the three groups. There were no significant differences between the three groups in terms of age, gender, years of education, and MMSE scores ($p > 0.05$). In our study, we excluded subjects with depression. However, we observed a significant difference in the HAMD-17 scores when compared between the PD and HC groups ($p < 0.001$); there was no significant difference when comparing between the PD-mild and PD-moderate groups ($p = 0.060$). The PD-moderate group had significantly higher UPDRS scores and a significantly longer disease duration than the PD-mild group ($p = 0.001$ and $p = 0.012$, respectively). Correlation analysis revealed a positive correlation between the following clinical parameters in the PD groups: MMSE scores with years of education ($r = 0.621$, $p < 0.001$); disease duration with UPDRS scores ($r = 0.396$, $p < 0.001$) and UPDRS-III scores ($r = 0.382$, $p = 0.001$); HAMD scores with UPDRS scores ($r = 0.579$, $p < 0.001$) and UPDRS-III scores ($r = 0.444$, $p < 0.001$); HY stages with disease duration ($r = 0.323$, $p = 0.005$), UPDRS scores ($r = 0.576$, $p < 0.001$), UPDRS-III scores ($r = 0.609$, $p < 0.001$), and HAMD scores ($r = 0.295$, $p = 0.010$).

Group Differences of Regional Homogeneity

Statistical analyses were observed using an automated anatomical atlas (AAL) template[2]. ANCOVA revealed the significant differences between the PD-mild, PD-moderate, and HC groups in the following brain regions: the bilateral cerebellum (Cerebellum_8/9_R, Cerebellum_8_L, Cerebellum_Crus2_L), the right superior orbital gyrus (Frontal_Sup_Orb_R), the right rectus (Rectus_R), the right superior temporal gyrus (Temporal_Sup_R), the right Rolandic operculum (Rolandic_Oper_R), the right postcentral gyrus (Postcentral_R), and the right precentral gyrus (Precentral_R; **Figure 1**).

In the *post hoc* analysis (**Table 2** and **Figure 2**), only one cluster survived when comparing the PD-mild group to the PD-moderate group, with the cluster extending from the Frontal_Sup_Orb_R to the Rectus_R (**Figure 2A**). When compared to the HC group, the PD-mild group presented with increased ReHo values in the Cerebellum_8_R (**Figure 2B**). The PD-moderate group presented with increased ReHo values in the bilateral cerebellum (Cerebellum_8_R, Cerebellum_8_L), and reduced ReHo values in the Temporal_Sup_R, Rolandic_Oper_R, Superior Temporal Gyrus, Postcentral_R, and Precentral_R (**Figure 2C**). The results were corrected by the AlphaSim program with a voxel-level $p < 0.005$, cluster-level $p < 0.05$ for a two-tail test and cluster size >24 voxels.

Correlative Analysis

Using the two PD groups, we calculated Spearman correlation coefficients between the ReHo values of the clusters showing significant differences and clinical scale scores, including disease duration, UPDRS, UPDRS-III, HY, MMSE, and HAMD-17

[2]http://www.gin.cnrs.fr/tools/aal

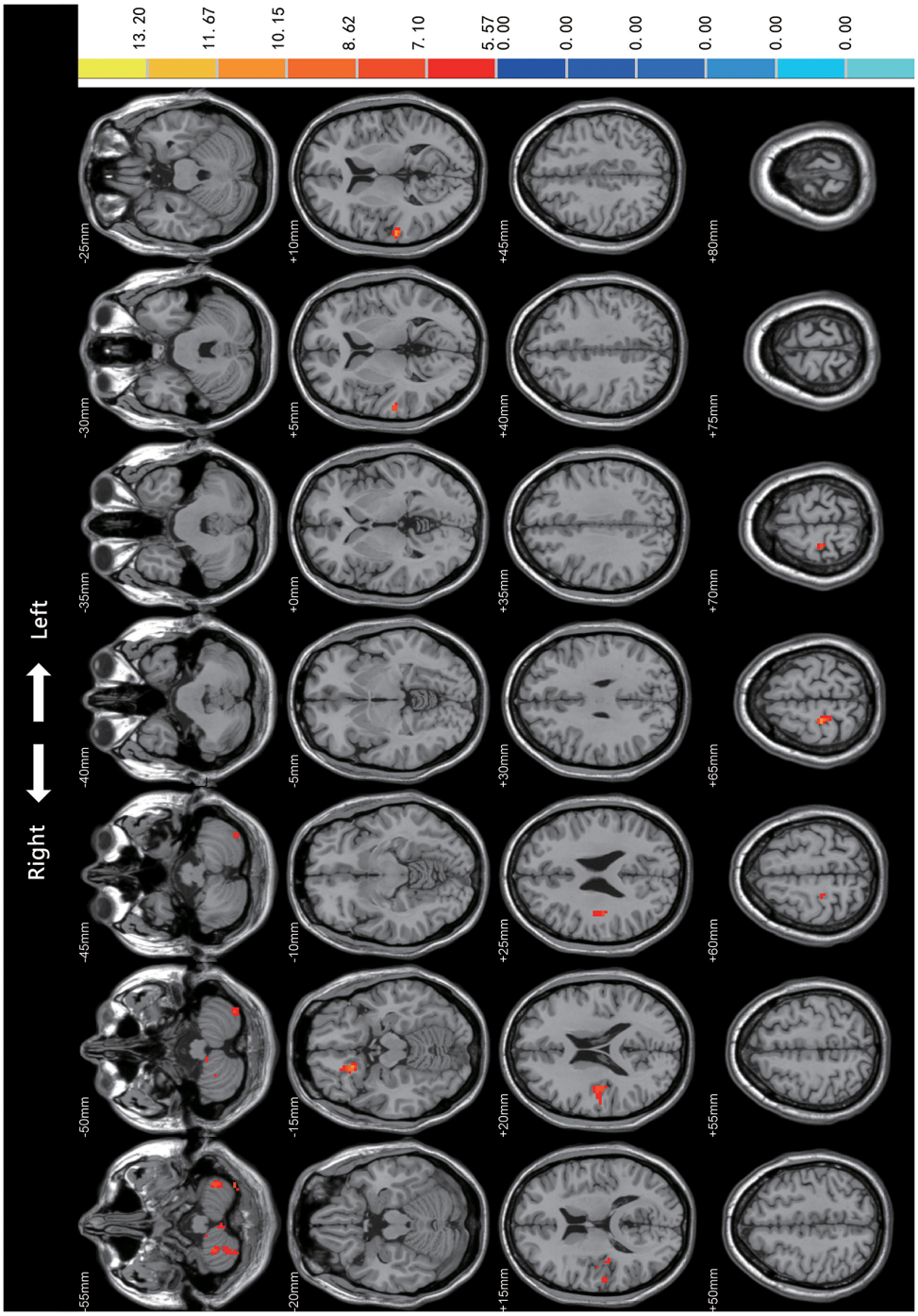

FIGURE 1 | Comparison of Regional Homogeneity (ReHo) among PD-mild, PD-moderate, and HC groups. Significant differences were revealed in the following brain regions: bilateral cerebellum (Cerebellum_8/9_R, Cerebellum_8_L, Cerebellum_Crus2_L), right superior orbital gyrus, right rectus, right superior temporal gyrus, right Rolandic operculum, right postcentral gyrus, and the right precentral gyrus ($p < 0.05$).

scores. The brain regions related to the above clinical data have been marked in **Figures 3A** and **3B**. Negative correlations were identified between the following pairs: ReHo values of the Frontal_Sup_Orb_R and MMSE scores (**Figure 3C**, $r = -0.378$, $p = 0.001$), ReHo values of the Pre/Postcentral_R and HY stages (**Figure 3D**, $r = -0.308$, $p = 0.007$). The results were corrected by Bonferroni's correction (0.05/6).

Correlations were also identified between the following pairs: ReHo values of the Cerebellum_8/9_R and HY stages (**Figure 3E**, $r = 0.230$, $p = 0.047$), ReHo values of the Pre/Postcentral_R and

TABLE 2 | Brain regions showing significant ReHo differences between paired groups from the PD-mild, PD-moderate, and HC groupings.

Groups	Brain region (AAL template)	Cluster size	Peak MNI coordinates (x y z)	*t*-value
PD-mild<PD-moderate	Frontal_Sup_Orb_R	24	18 21 −12	−3.8828
	Rectus_R			
PD-mild > HC	Cerebellum_8_R	57	9 −63 −63	3.5775
PD-moderate > HC	Cerebellum_8_R	143	9 −51 −63	4.3226
	Cerebellum_9_R			
	Cerebellum_8_L	24	−42 −51 −57	3.8637
PD-moderate< HC	Temporal_Sup_R	56	60 −24 9	−4.3039
	Rolandic_Oper_R			
	Precentral_R	30	21 −30 66	−4.8632
	Postcentral_R			

L, left hemisphere; R, right hemisphere; AAL, automated anatomical atlas; MNI, Montreal neurological institute; sup, superior; t-value, t statistic of post hoc analysis in two sample t-test.

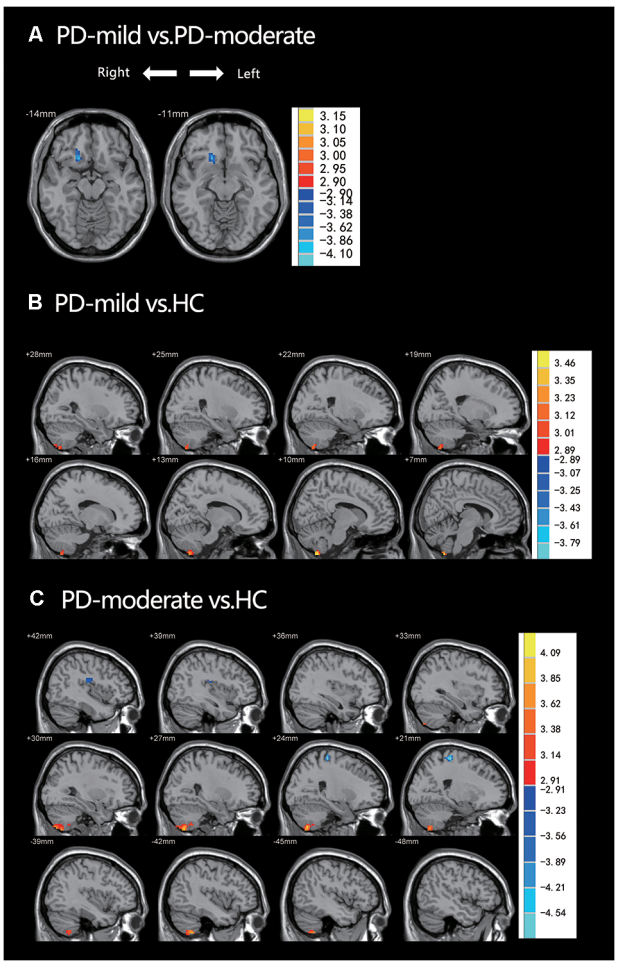

FIGURE 2 | **(A)** PD-mild vs. PD-moderate groups; ReHo had decreased in the Frontal_Sup_Orb_R and the Rectus_R. **(B)** PD-mild vs. HC; ReHo had increased in the Cerebellum_8_R. **(C)** PD-moderate vs. HC; ReHo had increased in the bilateral cerebellum and decreased in the Temporal_Sup_R, Rolandic_Oper_R, Superior Temporal Gyrus, Postcentral_R, and Precentral_R. **Table 2** shows more specific information relating to the significant brain regions.

UPDRS-III ($r = -0.252$, $p = 0.029$). However, both of them were not significant under the Bonferroni's correction.

DISCUSSION

In this study, we used the ReHo value as an indicator to investigate differences in local synchronization among HC, PD-mild, and PD-moderate groups. We also analyzed correlations between different brain regions and clinical scale scores. We attempted to investigate the imaging and functional features of PD within HY 2.5 stages in order to assist with the early diagnosis and treatment of PD patients.

In comparison with the PD-moderate group, we observed reduced ReHo values in the PD-mild group in the Frontal_Sup_Orb_R extending to the Rectus_R. Previous structural and functional MRI studies have revealed that frontal regions, such as the insula, orbitofrontal, olfactory sulcus, and dorsolateral frontal, are more apt to change than posterior regions in the early stage of PD (Yang et al., 2013; Claassen et al., 2016; Chaudhary et al., 2020). The Frontal_Sup_Orb, located in the ventral surface of the prefrontal lobe, is part of the orbitofrontal cortex (OFC); the Rectus is sometimes incorporated into the OFC. It has become clear that the OFC is related to the production of emotions, sensory integration, and hedonic experiences. These are complex neural mechanisms in which information flows from the OFC and other brain regions, especially the anterior cingulate cortex (ACC) and the amygdala (Kringelbach, 2005; Deng et al., 2016). When the OFC malfunctions, subjects may experience a number of mental or behavioral disorders, such as cognition dysfunction, emotion disorder, a failure to make decisions, social dysfunction, and impulse-control disorders (Damasio et al., 1994; Rudebeck and Rich, 2018). For patients with PD, these disorders are frequently associated with non-motor symptoms and tend to occur during the early stages of the disease (Pfeiffer et al., 2014; Bhattacharjee, 2018). In the present study, we observed differences in the ReHo values in the Frontal_Sup_Orb and the Rectus between the PD-mild and PD-moderate groups; correlation analysis suggested that this brain region was associated with cognition (**Figure 3C**). Collectively, our data indicate that changes in the Frontal_Sup_Orb and the Rectus may serve as a differential indicator for mild and moderate PD.

Compared with the HC group, the PD-mild and PD-moderate group showed increased ReHo values in cerebellum_8/9_R and cerebellum_8_L region. Over recent years, the role of

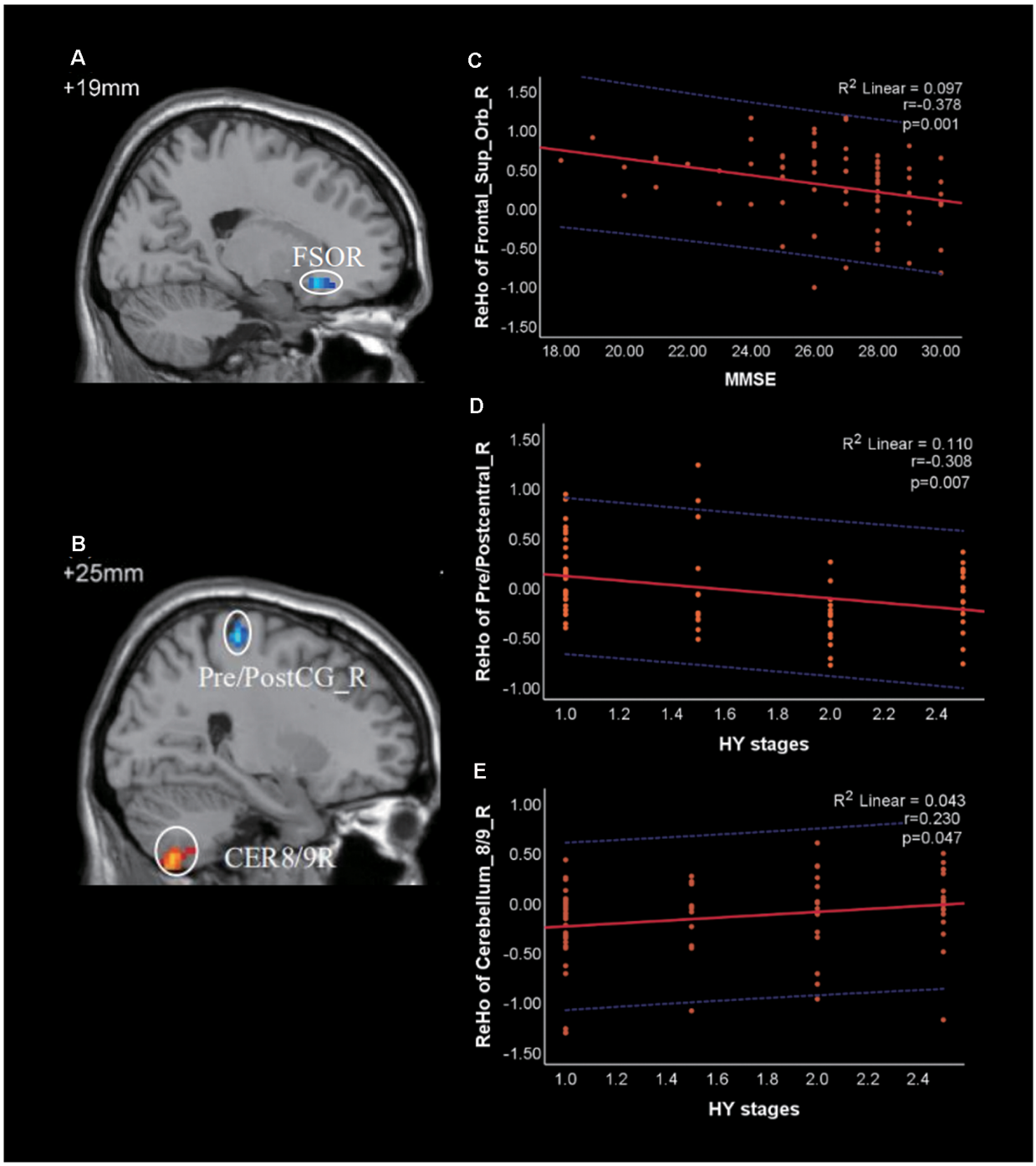

FIGURE 3 | Correlation of Regional Homogeneity (ReHo) between brain regions and clinical scale scores in patients with PD. **(A)** FSOR, Frontal_Sup_Orb_R; **(B)** CER8/9R, Cerebellum_8/9_R; Pre/PostC_R, Pre/postcentral_R. **(C)** The ReHo value of Frontal_Sup_Orb_R was negatively correlated with Mini-Mental State Exam (MMSE). **(D,E)** The ReHo value of Pre/Postcentral_R and Cerebellum_8/9_R were negatively and positively correlated with HY stages, respectively. The red solid line shows the existence of a significant correlation, while the blue dotted line depicts the 95% prediction interval for the red solid line.

the cerebellum in PD has received increasing amounts of research attention. A number of pathological, morphological, and functional, studies have revealed that the cerebellum plays an important role in the pathological and compensatory effects of PD with regards to both motor and non-motor symptoms (Wu and Hallett, 2013; Stöger et al., 2017; Li M. et al., 2019; Miterko et al., 2019). Deep brain stimulation (DBS) of the basal ganglia or the pedunculopontine nucleus may work well on

PD patients if there is a connection to the cerebellum, thus indicating the compensatory role of the cerebellum in PD, at least indirectly (Miterko et al., 2019). In addition, it is now widely accepted that the cerebellum plays a role in perceptual and connective processing (Baumann et al., 2015; Adamaszek et al., 2017; Kansal et al., 2017). The posterior cerebellar lobes, particularly lobules VI and VII, are known to be involved in a range of cognitive tasks, including memory and execution (Stoodley et al., 2012; Li M.-G. et al., 2019). Collectively, these lines of evidence indicate that the cerebellum may contribute to both motor and non-motor symptoms in PD patients. In our study, the increased ReHo values observed in the cerebellum may form part of the compensatory mechanism in PD.

When compared with the HC group, patients in the PD-moderate group showed a more extensive increased ReHo value in the cerebellum than the PD-mild group; furthermore, this increase was noted in both the right and left cerebellum. Correlation analysis indicated that the ReHo value in the Pre/Postcentral_R decreased as disease deteriorated, while the ReHo value in the cerebellum increased (not significant under the strict Bonferroni's correction). Consistent with previous findings, our study suggested that the increase in ReHo value in the cerebellum forms part of a compensatory effect for abnormalities in the cerebral cortex. We believe that larger increases in ReHo value in the cerebellum of the PD-moderate group referred to a wider form of compensation. It appears that the compensation for cortical changes moved from right to the left in the cerebellum; however, whether this direction was inherent or related to the left- and right-onset of PD, remains unclear and requires further investigation.

In comparison with the HC group, subjects in the PD-moderate group exhibited reduced ReHo values in the cerebral cortex while subjects in the PD-mild group did not, including the Rolandic_Oper_R, Temporal_Sup_R, Postcentral_R, and Precentral_R regions. Some previous studies have reported structural or functional alterations in the Rolandic Operculum in PD patients (New et al., 2015; Xu et al., 2018; Liu et al., 2019; Wang T. et al., 2020). One previous study focused on the voice network of PD patients with vocalization impairment; this work identified alterations in the Rolandic Operculum (New et al., 2015). In the current study, we observed reduced ReHo values in the PD-moderate group when compared to the HC group, thus providing further support to the growing number of studies that have revealed the importance of the Rolandic Operculum in PD. Lesions or gray matter atrophy in the Rolandic Operculum have been related to movement disorders or tonic contractions of the perioral muscle; these changes can induce swallowing dysfunction or dysarthria (Tonkonogy and Goodglass, 1981; Biesbroek et al., 2016; Shen et al., 2016; Wang Y. et al., 2020). In addition, an fMRI study concluded that the Rolandic Operculum was involved in speech production and motor control (Behroozmand et al., 2015). Swallowing dysfunction has been frequently observed in PD patients and is evident in up to 100% of patients with advanced stages (Simons, 2017). However, this form of dysfunction is not just observed in the late stages of PD; mild oropharyngeal symptoms and esophageal dysfunction are quite common events in the early stages of PD (Potulska et al., 2003; Simons, 2017). Dysphagia or speech disturbances are frequently observed in patients with different stages of PD. The most common speech impairment is hypokinetic dysarthria, a disorder that is characterized by articulatory deficits and phonetic monotony (Jankovic, 2008; Ricciardi et al., 2016; Melchionda et al., 2020). Combined with previous findings, our current analyses indicate that the reduced ReHo values in the Rolandic Operculum of patients in the PD-moderate group were most likely related to the swallowing and speech disorders observed in PD patients. The neocortex has been shown to be involved in Braak stages 5 and 6 of PD; this relates to the progressive deposition of Lewy bodies in the brain (Kon et al., 2020). Previous functional and *in vivo* metabolic studies have also suggested that abnormal cortical activity can be observed in the early stages of PD (Brooks, 2010; Choe et al., 2013). Combined with these earlier findings, our data suggest that cases of early PD in HY stages 2.0–2.5 may already have reached Braak stages 5 and 6 in terms of pathology.

There were some limitations to the present study that need to be considered. Firstly, we compared different HY stages of PD using a cross-sectional study instead of a longitudinal study. Secondly, although we identified a functional change in the Rolandic Operculum in patients in the PD-moderate group, we were unable to perform further correlation analysis due to the lack of clinical assessment data relating to swallowing function or speech disorders. Thirdly, we did not include PD patients with HY stages 3.0–5.0; this was because of the small number of patients in these stages and due to the risk of dopamine against withdrawal syndrome (Rabinak and Nirenberg, 2010) in these patients.

CONCLUSION

In conclusion, our current findings suggest that the HC, PD-mild, and PD-moderate, groups exhibited different ReHo alterations in the bilateral cerebellum, right superior orbital gyrus, right rectus, right superior temporal gyrus, right Rolandic operculum, right postcentral gyrus, and right precentral gyrus. The superior orbital gyrus and rectus may serve as differential indicators for mild and moderate PD. Patients with moderate PD had greater scope for ReHo alterations in the cortex and compensation in the cerebellum than those with mild PD. PD patients in HY stages 2.0–2.5 may already be at Braak stages 5 and 6 in terms of pathology. Our findings revealed differences in the resting-state brain functional pattern in PD patients at different HY stages and may help us to elucidate the neural function and the early diagnosis of PD.

DATA AVAILABILITY STATEMENT

The raw data supporting the conclusions of this article will be made available by the authors, without undue reservation.

ETHICS STATEMENT

The studies involving human participants were reviewed and approved by Ethics Committee of the 2nd Xiangya Hospital,

Central South University. The patients/participants provided their written informed consent to participate in this study.

AUTHOR CONTRIBUTIONS

JL, YZ, LZ, MW, ZM, CS, and FZ: data collection. JL, HL, QS, and SC: data analysis. JL, HL, and TW: manuscript writing. CT: project development and manuscript revision. All authors contributed to the article and approved the submitted version.

FUNDING

This study was supported by the National Natural Science Foundation of China (Grant No. 81471646).

ACKNOWLEDGMENTS

We thank all the study participants.

REFERENCES

Adamaszek, M., D'Agata, F., Ferrucci, R., Habas, C., Keulen, S., Kirkby, K. C., et al. (2017). Consensus paper: cerebellum and emotion. *Cerebellum* 16, 552–576. doi: 10.1007/s12311-016-0815-8

Ashburner, J. (2007). A fast diffeomorphic image registration algorithm. *NeuroImage* 38, 95–113. doi: 10.1016/j.neuroimage.2007.07.007

Baumann, O., Borra, R. J., Bower, J. M., Cullen, K. E., Habas, C., Ivry, R. B., et al. (2015). Consensus paper: the role of the cerebellum in perceptual processes. *Cerebellum* 14, 197–220. doi: 10.1007/s12311-014-0627-7

Behroozmand, R., Shebek, R., Hansen, D. R., Oya, H., Robin, D. A., Howard, M. A., et al. (2015). Sensory-motor networks involved in speech production and motor control: an fMRI study. *Neuroimage* 109, 418–428. doi: 10.1016/j.neuroimage.2015.01.040

Bhattacharjee, S. (2018). Impulse control disorders in Parkinson's disease: review of pathophysiology, epidemiology, clinical features, management and future challenges. *Neurol. India* 66, 967–975. doi: 10.4103/0028-3886.237019

Biesbroek, J. M., van Zandvoort, M. J. E., Kappelle, L. J., Velthuis, B. K., Biessels, G. J., and Postma, A. (2016). Shared and distinct anatomical correlates of semantic and phonemic fluency revealed by lesion-symptom mapping in patients with ischemic stroke. *Brain Struct. Funct.* 221, 2123–2134. doi: 10.1007/s00429-015-1033-8

Brooks, D. J. (2010). Examining Braak's hypothesis by imaging Parkinson's disease. *Mov. Disord.* 25, S83–S88. doi: 10.1002/mds.22720

Chaudhary, S., Kumaran, S. S., Goyal, V., Kaloiya, G. S., Kalaivani, M., Jagannathan, N. R., et al. (2020). Cortical thickness and gyrification index measuring cognition in Parkinson's disease. *Int. J. Neurosci.* 18, 1–10. doi: 10.1080/00207454.2020.1766459

Choe, I.-H., Yeo, S., Chung, K.-C., Kim, S.-H., and Lim, S. (2013). Decreased and increased cerebral regional homogeneity in early Parkinson's disease. *Brain Res.* 1527, 230–237. doi: 10.1016/j.brainres.2013.06.027

Claassen, D. O., McDonell, K. E., Donahue, M., Rawal, S., Wylie, S. A., Neimat, J. S., et al. (2016). Cortical asymmetry in Parkinson's disease: early susceptibility of the left hemisphere. *Brain Behav.* 6:e00573. doi: 10.1002/brb3.573

Damasio, H., Grabowski, T., Frank, R., Galaburda, A. M., and Damasio, A. R. (1994). The return of phineas gage: clues about the brain from the skull of a famous patient. *Science* 264, 1102–1105. doi: 10.1126/science.8178168

Deng, X., Li, F.-J., Tang, C.-Y., Zhang, J., Zhu, L., Zhou, M.-H., et al. (2016). The cortical surface correlates of clinical manifestations in the mid-stage sporadic Parkinson's disease. *Neurosci. Lett.* 633, 125–133. doi: 10.1016/j.neulet.2016.09.024

Fioravanti, V., Benuzzi, F., Codeluppi, L., Contardi, S., Cavallieri, F., Nichelli, P., et al. (2015). MRI correlates of Parkinson's disease progression: a voxel based morphometry study. *Parkinsons Dis.* 2015:378032. doi: 10.1155/2015/378032

Gao, Y., Nie, K., Mei, M., Guo, M., Huang, Z., Wang, L., et al. (2018). Changes in cortical thickness in patients with early Parkinson's disease at different hoehn and yahr stages. *Front. Hum. Neurosci.* 12:469. doi: 10.3389/fnhum.2018.00469

Goetz, C. G., Poewe, W., Rascol, O., Sampaio, C., Stebbins, G. T., Counsell, C., et al. (2004). Movement disorder society task force report on the hoehn and yahr staging scale: status and recommendations. *Mov. Dis.* 19, 1020–1028. doi: 10.1002/mds.20213

Guan, X., Guo, T., Zeng, Q., Wang, J., Zhou, C., Liu, C., et al. (2019). Oscillation-specific nodal alterations in early to middle stages Parkinson's disease. *Transl. Neurodegener.* 8:36. doi: 10.1186/s40035-019-0177-5

Hoehn, M. M., and Yahr, M. D. (1967). Parkinsonism: onset, progression and mortality. *Neurology* 17, 427–442. doi: 10.1212/wnl.17.5.427

Hornykiewicz, O. (2006). The discovery of dopamine deficiency in the parkinsonian brain. *J. Neural Transm. Suppl.* 70, 9–15. doi: 10.1007/978-3-211-45295-0_3

Hurwitz, B. (2017). The Status of "Nonmotor" features of the malady in an essay on the shaking palsy 1817. *Int. Rev. Neurobiol.* 133, 3–12. doi: 10.1016/bs.irn.2017.04.008

Jankovic, J. (2008). Parkinson's disease: Clinical features and diagnosis. *J. Neurol. Neurosurg. Psychiatry* 79, 368–376. doi: 10.1136/jnnp.2007.131045

Jiang, L., and Zuo, X.-N. (2016). Regional homogeneity: a multimodal, multiscale neuroimaging marker of the human connectome. *Neuroscientist* 22, 486–505. doi: 10.1177/1073858415595004

Kansal, K., Yang, Z., Fishman, A. M., Sair, H. I., Ying, S. H., Jedynak, B. M., et al. (2017). Structural cerebellar correlates of cognitive and motor dysfunctions in cerebellar degeneration. *Brain* 140, 707–720. doi: 10.1093/brain/aww327

Khan, A. U., Akram, M., Daniyal, M., and Zainab, R. (2019). Awareness and current knowledge of Parkinson's disease: a neurodegenerative disorder. *Int. J. Neurosci.* 129, 55–93. doi: 10.1080/00207454.2018.1486837

Kon, T., Tomiyama, M., and Wakabayashi, K. (2020). Neuropathology of Lewy body disease: clinicopathological crosstalk between typical and atypical cases. *Neuropathology* 40, 30–39. doi: 10.1111/neup.12597

Kringelbach, M. L. (2005). The human orbitofrontal cortex: linking reward to hedonic experience. *Nat. Rev. Neurosci.* 6, 691–702. doi: 10.1038/nrn1747

Li, G., Ma, J., Cui, S., He, Y., Xiao, Q., Liu, J., et al. (2019). Parkinson's disease in china: a forty-year growing track of bedside work. *Transl. Neurodegener.* 8:22. doi: 10.1186/s40035-019-0162-z

Li, H., Jia, J., and Yang, Z. (2016). Mini-Mental State examination in elderly chinese: a population-based normative study. *J. Alzheimer's Dis.* 53, 487–496. doi: 10.3233/JAD-160119

Li, M., Liu, Y., Chen, H., Hu, G., Yu, S., Ruan, X., et al. (2019). Altered global synchronizations in patients with Parkinson's disease: a resting-state fMRI study. *Front. Aging Neurosci.* 11:139. doi: 10.3389/fnagi.2019.00139

Li, M.-G., Chen, Y.-Y., Chen, Z.-Y., Feng, J., Liu, M.-Y., Lou, X., et al. (2019). Altered functional connectivity of the marginal division in Parkinson's disease with mild cognitive impairment: a pilot resting-state fMRI study. *J. Magn. Reson. Imaging* 50, 183–192. doi: 10.1002/jmri.26548

Liu, Y., Li, M., Chen, H., Wei, X., Hu, G., Yu, S., et al. (2019). Alterations of regional homogeneity in Parkinson's disease patients with freezing of gait: a resting-state fMRI study. *Front. Aging Neurosci.* 11:276. doi: 10.3389/fnagi.2019.00276

Long, D., Wang, J., Xuan, M., Gu, Q., Xu, X., Kong, D., et al. (2012). Automatic classification of early Parkinson's disease with multi-modal MR imaging. *PLoS One* 7:e47714. doi: 10.1371/journal.pone.0047714

Luo, C., Guo, X., Song, W., Chen, Q., Yang, J., Gong, Q., et al. (2015). The trajectory of disturbed resting-state cerebral function in Parkinson's disease at different Hoehn and Yahr stages. *Hum. Brain Mapp.* 36, 3104–3116. doi: 10.1002/hbm.22831

Lv, H., Wang, Z., Tong, E., Williams, L. M., Zaharchuk, G., Zeineh, M., et al. (2018). Resting-State Functional MRI: everything that nonexperts have always wanted to know. *Am. J. Neuroradiol.* 39, 1390–1399. doi: 10.3174/ajnr.A5527

Melchionda, D., Varvara, G., Perfetto, D., Mascolo, B., and Avolio, C. (2020). Perceptive and subjective evaluation of speech disorders in Parkinson's disease. *J. Biol. Regul. Homeost. Agents* 34, 683–686. doi: 10.23812/19-412-L-2

Miterko, L. N., Baker, K. B., Beckinghausen, J., Bradnam, L. V., Cheng, M. Y., Cooperrider, J., et al. (2019). Consensus paper: experimental neurostimulation of the cerebellum. *Cerebellum* 18, 1064–1097. doi: 10.1007/s12311-019-01041-5

New, A. B., Robin, D. A., Parkinson, A. L., Eickhoff, C. R., Reetz, K., Hoffstaedter, F., et al. (2015). The intrinsic resting state voice network in Parkinson's disease. *Hum. Brain Mapp.* 36, 1951–1962. doi: 10.1002/hbm.22748

Pfeiffer, H. C. V., Løkkegaard, A., Zoetmulder, M., Friberg, L., and Werdelin, L. (2014). Cognitive impairment in early-stage non-demented Parkinson's disease patients. *Acta Neurol. Scand.* 129, 307–318. doi: 10.1111/ane.12189

Postuma, R. B., Berg, D., Stern, M., Poewe, W., Olanow, C. W., Oertel, W., et al. (2015). MDS clinical diagnostic criteria for Parkinson's disease. *Mov. Disord.* 30, 1591–1601. doi: 10.1002/mds.26424

Potulska, A., Friedman, A., Królicki, L., and Spychala, A. (2003). Swallowing disorders in Parkinson's disease. *Parkinsonism Relat. Dis* 9, 349–353. doi: 10.1016/s1353-8020(03)00045-2

Pringsheim, T., Jette, N., Frolkis, A., and Steeves, T. D. L. (2014). The prevalence of Parkinson's disease: a systematic review and meta-analysis. *Mov. Disord.* 29, 1583–1590. doi: 10.1002/mds.25945

Rabinak, C. A., and Nirenberg, M. J. (2010). Dopamine agonist withdrawal syndrome in Parkinson disease. *Arch. Neurol.* 67, 58–63. doi: 10.1001/archneurol.2009.294

Rai, S. N., Birla, H., Singh, S. S., Zahra, W., Patil, R. R., Jadhav, J. P., et al. (2017). Mucuna pruriens protects against MPTP intoxicated neuroinflammation in Parkinson's disease through NF-κB/pAKT signaling pathways. *Front. Aging Neurosci.* 9:421. doi: 10.3389/fnagi.2017.00421

Rai, S. N., Yadav, S. K., Singh, D., and Singh, S. P. (2016). Ursolic acid attenuates oxidative stress in nigrostriatal tissue and improves neurobehavioral activity in MPTP-induced Parkinsonian mouse model. *J. Chem. Neuroanat.* 71, 41–49. doi: 10.1016/j.jchemneu.2015.12.002

Rai, S. N., Zahra, W., Singh, S. S., Birla, H., Keswani, C., Dilnashin, H., et al. (2019). Anti-inflammatory activity of ursolic acid in mptp-induced Parkinsonian mouse model. *Neurotox. Res.* 36, 452–462. doi: 10.1007/s12640-019-00038-6

Reich, S. G., and Savitt, J. M. (2019). Parkinson's disease. *Med. Clin. North Am.* 103, 337–350. doi: 10.1016/j.mcna.2018.10.014

Ricciardi, L., Ebreo, M., Graziosi, A., Barbuto, M., Sorbera, C., Morgante, L., et al. (2016). Speech and gait in Parkinson's disease: When rhythm matters. *Parkinsonism. Relat. Disord.* 32, 42–47. doi: 10.1016/j.parkreldis.2016.08.013

Rudebeck, P. H., and Rich, E. L. (2018). Orbitofrontal cortex. *Curr. Biol.* 28, R1083–R1088. doi: 10.1016/j.cub.2018.07.018

Shen, D., Cui, L., Fang, J., Cui, B., Li, D., and Tai, H. (2016). Voxel-wise meta-analysis of gray matter changes in amyotrophic lateral sclerosis. *Front. Aging Neurosci.* 8:64. doi: 10.3389/fnagi.2016.00064

Shrestha, S., Kamel, F., Umbach, D. M., Beane Freeman, L. E., Koutros, S., Alavanja, M., et al. (2017). Nonmotor symptoms and Parkinson disease in united states farmers and spouses. *PLoS One* 12:e0185510. doi: 10.1371/journal.pone.0185510

Simons, J. A. (2017). Swallowing dysfunctions in Parkinson's disease. *Int. Rev. Neurobiol.* 134, 1207–1238. doi: 10.1016/bs.irn.2017.05.026

Singh, S. S., Rai, S. N., Birla, H., Zahra, W., Rathore, A. S., and Singh, S. P. (2020a). NF-κB-Mediated neuroinflammation in Parkinson's disease and potential therapeutic effect of polyphenols. *Neurotox. Res.* 37, 491–507. doi: 10.1007/s12640-019-00147-2

Singh, S. S., Rai, S. N., Birla, H., Zahra, W., Rathore, A. S., Dilnashin, H., et al. (2020b). Neuroprotective effect of chlorogenic acid on mitochondrial dysfunction-mediated apoptotic death of DA neurons in a Parkinsonian mouse model. *Oxid. Med. Cell Longev.* 2020:6571484. doi: 10.1155/2020/6571484

Stöger, R., Scaife, P. J., Shephard, F., and Chakrabarti, L. (2017). Elevated 5hmC levels characterize DNA of the cerebellum in Parkinson's disease. *NPJ Parkinson's Dis.* 3:6. doi: 10.1038/s41531-017-0007-3

Stoodley, C. J., Valera, E. M., and Schmahmann, J. D. (2012). Functional topography of the cerebellum for motor and cognitive tasks: an fMRI study. *Neuroimage* 59, 1560–1570. doi: 10.1016/j.neuroimage.2011.08.065

Tonkonogy, J., and Goodglass, H. (1981). Language function, foot of the third frontal gyrus and rolandic operculum. *Arch. Neurol.* 38, 486–490. doi: 10.1001/archneur.1981.00510080048005

Wang, T., Liao, H., Zi, Y., Wang, M., Mao, Z., Xiang, Y., et al. (2020). Distinct changes in global brain synchronization in early-onset vs. late-onset Parkinson disease. *Front. Aging Neurosci.* 12:604995. doi: 10.3389/fnagi.2020.604995

Wang, Y., Wang, X., Zhao, B.-T., Sang, L., Zhang, C., Hu, W.-H., et al. (2020). The Rolandic operculum generates different semiologies in insulo-opercular and temporal lobe epilepsies. *Epilepsy Behav.* 114:107614. doi: 10.1016/j.yebeh.2020.107614

Wu, T., and Hallett, M. (2013). The cerebellum in Parkinson's disease. *Brain* 136, 696–709. doi: 10.1093/brain/aws360

Xi-Ze, J., Jue, W., Hai-Yang, S., and Han, Z. (2019). RESTplus: an improved toolkit for resting-state functional magnetic resonance imaging data processing. *Sci. Bull.* 64, 953–954. doi: 10.1016/j.scib.2019.05.008

Xu, S., He, X.-W., Zhao, R., Chen, W., Qin, Z., Zhang, J., et al. (2019). Cerebellar functional abnormalities in early stage drug-naïve and medicated Parkinson's disease. *J. Neurol.* 266, 1578–1587. doi: 10.1007/s00415-019-09294-0

Xu, X., Guan, X., Guo, T., Zeng, Q., Ye, R., Wang, J., et al. (2018). Brain atrophy and reorganization of structural network in Parkinson's Disease with hemiparkinsonism. *Front. Hum. Neurosci.* 12:117. doi: 10.3389/fnhum.2018.00117

Yan, C.-G., Craddock, R. C., Zuo, X.-N., Zang, Y.-F., and Milham, M. P. (2013). Standardizing the intrinsic brain: towards robust measurement of inter-individual variation in 1000 functional connectomes. *Neuroimage* 80, 246–262. doi: 10.1016/j.neuroimage.2013.04.081

Yang, H., Zhou, X. J., Zhang, M.-M., Zheng, X.-N., Zhao, Y.-L., and Wang, J. (2013). Changes in spontaneous brain activity in early Parkinson's disease. *Neurosci. Lett.* 549, 24–28. doi: 10.1016/j.neulet.2013.05.080

Yang, J., Gohel, S., and Vachha, B. (2020). Current methods and new directions in resting state fMRI. *Clin. Imaging* 65, 47–53. doi: 10.1016/j.clinimag.2020.04.004

Zahra, W., Rai, S. N., Birla, H., Singh, S. S., Rathore, A. S., Dilnashin, H., et al. (2020). Neuroprotection of rotenone-induced Parkinsonism by ursolic acid in PD mouse model. *CNS Neurol. Dis. Drug Targets* 19, 527–540. doi: 10.2174/1871527319666200812224457

Zuo, X.-N., and Xing, X.-X. (2014). Test-retest reliabilities of resting-state FMRI measurements in human brain functional connectomics: a systems neuroscience perspective. *Neurosci. Biobehav. Rev.* 45, 100–118. doi: 10.1016/j.neubiorev.2014.05.009

Conflict of Interest: The authors declare that the research was conducted in the absence of any commercial or financial relationships that could be construed as a potential conflict of interest.

frontiers in Aging Neuroscience

ORIGINAL RESEARCH
published: 30 July 2021
doi: 10.3389/fnagi.2021.688926

Predicting MCI to AD Conversation Using Integrated sMRI and rs-fMRI: Machine Learning and Graph Theory Approach

Tingting Zhang, Qian Liao, Danmei Zhang, Chao Zhang, Jing Yan, Ronald Ngetich, Junjun Zhang, Zhenlan Jin and Ling Li* for the Alzheimer's Disease Neuroimaging Initiative†*

Key Laboratory for NeuroInformation of Ministry of Education, High-Field Magnetic Resonance Brain Imaging Key Laboratory of Sichuan Province, Center for Information in Medicine, School of Life Sciences and Technology, University of Electronic Science and Technology of China, Chengdu, China

Background: Graph theory and machine learning have been shown to be effective ways of classifying different stages of Alzheimer's disease (AD). Most previous studies have only focused on inter-subject classification with single-mode neuroimaging data. However, whether this classification can truly reflect the changes in the structure and function of the brain region in disease progression remains unverified. In the current study, we aimed to evaluate the classification framework, which combines structural Magnetic Resonance Imaging (sMRI) and resting-state functional Magnetic Resonance Imaging (rs-fMRI) metrics, to distinguish mild cognitive impairment non-converters (MCInc)/AD from MCI converters (MCIc) by using graph theory and machine learning.

Methods: With the intra-subject (MCInc vs. MCIc) and inter-subject (MCIc vs. AD) design, we employed cortical thickness features, structural brain network features, and sub-frequency (full-band, slow-4, slow-5) functional brain network features for classification. Three feature selection methods [random subset feature selection algorithm (RSFS), minimal redundancy maximal relevance (mRMR), and sparse linear regression feature selection algorithm based on stationary selection (SS-LR)] were used respectively to select discriminative features in the iterative combinations of MRI and network measures. Then support vector machine (SVM) classifier with nested cross-validation was employed for classification. We also compared the performance of multiple classifiers (Random Forest, K-nearest neighbor, Adaboost, SVM) and verified the reliability of our results by upsampling.

Results: We found that in the classifications of MCIc vs. MCInc, and MCIc vs. AD, the proposed RSFS algorithm achieved the best accuracies (84.71, 89.80%) than the other algorithms. And the high-sensitivity brain regions found with the two classification groups were inconsistent. Specifically, in MCIc vs. MCInc, the high-sensitivity brain regions associated with both structural and functional features included frontal, temporal, caudate, entorhinal, parahippocampal, and calcarine fissure and surrounding cortex.

OPEN ACCESS

Edited by:
Binbin Nie,
Institute of High Energy Physics, Chinese Academy of Sciences, China

Reviewed by:
Xiaowei Zhang,
Lanzhou University, China
Seyed Hani Hojjati,
Cornell University, United States

****Correspondence:***
Zhenlan Jin
jinzl@uestc.edu.cn
Ling Li
liling@uestc.edu.cn

†Data used in the preparation of this article were obtained from the Alzheimer's Disease Neuroimaging Initiative (ADNI) database (adni.loni.usc.edu)

Received: *31 March 2021*
Accepted: *23 June 2021*
Published: *30 July 2021*

Citation:
Zhang T, Liao Q, Zhang D, Zhang C, Yan J, Ngetich R, Zhang J, Jin Z and Li L (2021) Predicting MCI to AD Conversation Using Integrated sMRI and rs-fMRI: Machine Learning and Graph Theory Approach. Front. Aging Neurosci. 13:688926. doi: 10.3389/fnagi.2021.688926

While in MCIc vs. AD, the high-sensitivity brain regions associated only with functional features included frontal, temporal, thalamus, olfactory, and angular.

Conclusions: These results suggest that our proposed method could effectively predict the conversion of MCI to AD, and the inconsistency of specific brain regions provides a novel insight for clinical AD diagnosis.

Keywords: resting-state fMRI, structural MRI, mild cognitive impairment, graph theoretical analysis, machine learning, classification

INTRODUCTION

Mild cognitive impairment (MCI) is considered a transitional state between normal aging and early Alzheimer's disease (AD) (Lee et al., 2012). Studies have shown that individuals with MCI tend to develop AD at a rate of about 10–15% per year (Allison et al., 2014), but the probability of a healthy elderly to be diagnosed with AD is only 1∼2% (Bischkopf et al., 2002). If MCI is diagnosed at an early stage, through rehabilitation exercise and medication, the incidence of AD can be reduced by nearly one-third (Golob et al., 2007). Thus, early detection of MCI individuals makes it possible to potentially delay or prevent the transition from MCI to AD. The following are MCI clinical conversion criteria: MCI patients can be divided into MCIc and MCInc, depending on whether they become converted into AD patients within a certain period (for instance, the conversion time could be 36 months, 48 months, etc.). Interestingly, the two types of patients have similar clinical manifestations in the early stage, and the morphological differences of their brain lesions are small. To intervene in the diagnosis and treatment of AD disease earlier, the diagnosis and prediction of MCI disease have been studied from multiple perspectives such as genetics, pathology, and medical imaging. Currently, there are different opinions on biomarkers that can accurately reflect the timeliness of preclinical disease progression. However, no research has established the versatility of such markers using prediction/validation study designs. Furthermore, there are defects and difficulties in the diagnosis and classification of MCI disease development. Therefore, finding high discriminative features and establishing a robust classification mechanism is of clinical significance for the diagnosis and timely treatment of MCI diseases, especially the provision of early warning signs for high-risk MCI patients. This may guide the patients to make rational treatment decisions, and thus, even prevent them from developing AD.

Neuroimaging studies of AD patients have found atrophy of structural tissues, and abnormal connections between brain regions in structure and function (Liu et al., 2012; Dai et al., 2019; Zhang et al., 2019). Especially, neuroanatomical abnormalities have been found to spread from one brain area to another based on distinctive network patterns in neurodegenerative diseases (Yates, 2012; Pandya et al., 2017; Cauda et al., 2018). Eskildsen and his colleagues (Eskildsen et al., 2013) classified MCI and AD using cortical thickness features from structural MRI and achieved accuracies ranging from 70 to 76% depending on the conversion time. Taking advantage of the difference in the time dimension of disease, Li and his colleagues (Li et al., 2012) proposed a 4-D disease classification algorithm based on the thickness of the cerebral cortex. The classification of MCIc and MCInc achieved the highest classification accuracy (81.7%). Since most studies have reported abnormal and inconsistent brain connections, many recent studies have used the construction of a classification framework combining brain networks and machine learning to classify MCI\AD. Raamana and colleagues (Raamana et al., 2015) constructed a brain network based on the difference in cortical thickness, by taking the average clustering coefficient, boundary number, and node degree as features, and using a multi-core Bayes classifier to classify MCIc and MCInc with a classification accuracy of 64%. Our previous study (Wei et al., 2016) proposed a classification framework to distinguish MCIc from MCInc by using MRI and network features and attained the best accuracies of 76.39%.

To improve the classification effect, many studies have been dedicated to fusing different types of data, such as MRI, fMRI, positron emission tomography (PET), cerebrospinal fluid (CSF), and cognitive scoring scales. Liu et al. (2014) proposed a new multi-modal classification method combining PET and MRI with an accuracy of 67.83% for the classification of MCInc and MCIc. While Wee et al. (2012b) used multi-core SVM to integrate diffusion tensor image (DTI) and rs-fMRI functional network features to classify MCI and normal elderly people and obtained a higher classification accuracy of 96.3%, which was 7.4% higher than that of single-mode data. Besides, appropriate feature selection (Zuo et al., 2010; Chu et al., 2012) and frequency division (Wee et al., 2012a; Mascali et al., 2015) have also been proven to effectively improve classification accuracy. One of our recent studies (Zhang et al., 2019) supports this view. Essentially, our earlier study distinguished individuals with EMCI and LMCI using a functional brain network of three frequency bands and three feature selection algorithms, during the Resting States, and obtained 83.87% accuracy using the mRMR algorithm in a slow-5 band. Although most previous studies have investigated the utility of the structural MRI or rs-fMRI for classification of MCIc from MCInc, few studies have used cortical and subcortical measurements extracted from DTI/MRI, and graph measures extracted from rs-fMRI, to classify MCIc and MCInc (Mascali et al., 2015; Hojjati et al., 2018). Besides, previous studies only focused on the classification of the different groups of patients, but whether this kind of classification can truly reflect the changes in the structure and function of the brain regions in disease progression remains unverified.

To address these issues, this study aims to: (i) incorporate multiple structural and functional metrics into a combined graph theoretical and machine learning analysis, to evaluate the efficacy of a classification framework to distinguish MCInc/ AD from MCIc. (ii) predict the highly sensitive brain regions of AD conversion, by comparing the difference of the brain regions between MCIc and MCInc, with that between MCIc and AD. Firstly, we proposed structural features including MRI features by FreeSurfer and nodal parameters from thickness network, and functional features derived from constructed functional brain network among time series of the brain regions with three frequency bands (full-band, slow-4, slow-5) at Resting State. Subsequently, we established a weighted network by using a kernel function, and then thresholded it to a binary network at a high discriminative range of sparsity from 8 to 44%. In the current study, the SS-LR and mRMR feature selection algorithms build upon our previous work (Wei et al., 2016; Zhang et al., 2019). We employed novel feature selection algorithms (RSFS) to find effective features, and then trained and tested the SVM classifier for classification. We also tested the reliability and stability of the best classification results by applying multiple classifiers (Random Forest, K-nearest neighbor (KNN), AdaBoost, SVM) by upsampling. Finally, we compared the selected top 10 features from the classification of MCInc vs. MCIc and those from the MCIc vs. AD group. Meanwhile, we also investigated the contribution of each modal to the multi-modal classification to explore the conversion of MCI. We hypothesized that the proposed method will improve the accuracy and the sensitivity of identifying prodromal AD, and that the high-sensitivity brain regions of the two classification groups may be inconsistent. To the best of our knowledge, this is the first study that has used cortical thickness, structural brain network, and sub-frequency functional brain network for this classification (MCInc vs. MCIc, MCIc vs. AD). Besides, another innovation of this study is the employment of the intra-subject and inter-subject design to classify the two groups of patients.

MATERIALS AND METHODS

Participants

Data used in this study were obtained from the Alzheimer's Disease Neuroimaging Initiative (ADNI) database.[1] The ADNI was launched in 2003 as a public-private partnership, led by Principal Investigator Michael W. Weiner, MD. The primary goal of ADNI was to test whether serial magnetic resonance imaging (MRI), positron emission tomography (PET), some biological markers, and clinical and neuropsychological assessment can be combined to measure the progression of mild cognitive impairment (MCI) and early Alzheimer's disease (AD). The demographic data of the datasets are listed in **Table 1**. A total of 108 participants with full structural and resting-state functional data were collected, but 4 of them failed to pass the data quality control. In the ADNI project, the diagnostic criteria of MCI were as follows: (1) Mini-Mental State Examination (MMSE) scores between 24 and 30. (2) Clinical Dementia Rating (CDR) is 0.5. (3) Memory complaint, objective memory loss measured by education adjusted scores on the Wechsler Memory Scale Logical Memory II. (4) No observable impairment in other cognitive fields, and able to remember the activities of daily life (no dementia).

The present study included 55 MCI non-converters (MCInc), 30 MCI converters (MCIc), and 19 AD. We divided the MCI patients according to Wolz's study (Wolz et al., 2011), into MCInc and MCIc, in which MCIc were defined as patients whose diagnosis changed within 36 months and the complementary MCInc patients defined as MCInc group (up to the time of data screening, MCI had not been converted in the database). Also, 19 out of 30 former MCIc developed AD within 36 months (Other 11 subjects were excluded because of the absence of data and data quality control). In the first instance, we took a baseline for all MCI patients. Thereafter, we continued to take scans until the first reported conversion to AD or up to a period of 36 months. As illustrated in **Table 1**, gender, age, education and CDR had no significant difference for MCInc and AD, compared to the MCIc.

Data Acquisition and Preprocessing

According to the ADNI acquisition protocol, participants underwent sMRI and rs-fMRI scanning on 3T Philips scanner (Jack et al., 2008). Scan parameters were as follows: sMRI data were acquired with T1-weighted magnetization prepared rapid acquisition gradient echo (MPRAGE) sequences [repetition time (TR) = 3,000 ms; echo time (TE) = 30 ms; matrix = 256 × 256; flip angle = 9°; voxel size = 1.2 mm^3 × 1.0 mm^3 × 1.0 mm^3; 170 slices]. rs-fMRI data were acquired with a gradient echo planar imaging (EPI) sequence (TR = 3,000 ms; TE = 30 ms; matrix = 64 × 64; flip angle = 80°; voxel size = 3.313 mm^3 × 3.313 mm^3 × 3.313 mm^3; 48 slices).

These methods are similar to those used in our previous studies (Wei et al., 2016; Zhang et al., 2019). sMRI data were preprocessed using software FreeSurfer 6.00 (FreeSurfer v6.00)[2], which contained: automatic Talairach space transformation, correction of the non-uniformity of image intensity, removal of non-brain tissue, intensity normalization, tissue segmentation (Fischl et al., 2002), automatic topology correction, surface deformation to generate gray/white matter boundaries, fragmentation of the gray matter/cerebrospinal fluid boundary, and cerebral cortex. We used the Desikan-Killiany atlas (34 areas in each hemisphere) for parcellation (Desikan Rahul et al., 2006). rs-fMRI data preprocessing was performed using Basic Edition of Data Processing Assistant for Resting-State Functional MR Imaging (DPARSF) (Yan and Zang, 2010), Statistical Parametric Mapping software (Friston et al., 2007) (SPM8)[3], and Resting-State fMRI Data Analysis Toolkit (Song et al., 2011) (REST)[4], based on MATLAB 2013a (MathWorks, Inc)[5] platform, which involved: (1) Discarding of the first 10 time points for signal stabilization. (2) Slice timing. (3) Realigning and limiting head

[1] http://adni.loni.usc.edu

[2] http://surfer.nmr.mgh.harvard.edu/fswiki

[3] http://www.fil.ion.ucl.ac.uk/spm

[4] http://restfmri.net

[5] https://www.mathworks.com

TABLE 1 | Characteristics of the participants.

Variable	MCInc (n = 55)	MCIc (n = 30)	AD (n = 19)	p-value MCInc vs. MCIc	p-value MCIc vs. AD
Gender (M/F)	25/30	16/14	10/9	0.487	0.962
Age	72.01 ± 8.21	74.40 ± 7.19	75.08 ± 6.33	0.186	0.734
MMSE	28.16 ± 1.78[a]	27.00 ± 1.88	25.00 ± 2.79[a]	0.006	0.004
CDR	0.47 ± 0.12	0.55 ± 0.20	0.84 ± 0.24[a]	0.060	< 0.001
Education	15.85 ± 2.71	15.80 ± 2.59	16.37 ± 2.36	0.928	0.443

MMSE, Mini Mental State Examination scores; CDR, Clinical Dementia Rating.A Chi-square test was used for gender comparison. A two-tailed student's t-test was used to compare age, neuropsychological tests, and education level.[a]Indicates significance compared to the MCIc. $p > 0.05$, not significant.

motion to less than 2 mm or 2°. (4) Spatial normalization. (5) Spatial smoothing with FWHM [6 6 6] Gaussian kernel and linear detrending. (6) Regressing out nuisance covariates: white matter (WM), cerebrospinal fluid (CSF) signals, and six head motion parameters (Ciric et al., 2017). (7) The filtering process, here, the low-frequency signal was divided into 0.01–0.08 Hz, 0.027–0.08 Hz and 0.01–0.027 Hz.

Feature Extraction

As illustrated in **Figures 1A,B**, we selected 1150 structural and functional features of each subject for subsequent feature selection. (1) In the structural section, there were 68*3 = 204 MRI features [cortical thickness (CT), cortical volume (CV), and cortical surface area (CS)], 68*2 = 136 nodal features [nodal path length (NL) and nodal degree (ND)]. (2) In the functional section, there were 810 nodal features [NL, ND, and betweenness centrality (BC)]. For a given node i, V is the size of a graph. NL, ND, and BC were defined as follows:

$$L_i = \frac{\sum_{j \neq i \in V} L_{ij}}{(V-1)} \tag{1}$$

where L_{ij} represents the minimum number of edges between node i and j,

$$K_i = \sum\nolimits_{j \in V} b_{ij} \tag{2}$$

and b_{ij} is the connection between node i and j.

$$B_i = \sum\nolimits_{i \neq j \neq m \in V} \frac{S_{jm}(i)}{S_{jm}} \tag{3}$$

S_{jm} represents the number of shortest path lengths between node m and j, $S_{jm}(i)$ represents the number of shortest paths through node i between node m and j.

MRI Features

As indicated in **Figure 1A**, the atlas used in Desikan-Killiany template included 68 cortical regions. For each cortical region, CT, CV, and CS were calculated as MRI features. CT at each vertex of the cortex was defined as the average shortest length between white and pale surfaces. While CV at each vertex was defined as the product of the CS and CT at each surface vertex. On the other hand, CS was defined as a computation of the area of every triangle in a standardized spherical surface tessellation. This section yielded 204 MRI features for each participant.

Thickness Network Features

The thickness network matrix w_{ij} (i, j = 1,2,…,68) was defined by calculating the difference of CT between each pair of regions, as follows:

$$w_k(i,j) = exp\left(\frac{-\left[CT_k(i) - CT_k(j)\right]^2}{\alpha}\right) \tag{4}$$

Where $CT_k(i)$ represents the cortical thickness of i ROI of k participants, and the kernel width α is 0.01. To eliminate the influence of false connections and noise, we thresholded the thickness network matrix of each participant into a binary matrix $B_{ij} = \left[b_{ij}\right]$. The threshold represents the cost of network connection, defined as the ratio of over-threshold connections to the total number of possible connections in the network (Sanz-Arigita et al., 2010). If the weight of the two ROIs was greater than the given threshold, then b_{ij} was 1, or otherwise 0. Notably, there is no golden rule for the definition of a single sparsity threshold, and different sparsity will lead to different results (He et al., 2009; Hojjati et al., 2018). Therefore, we analyzed the range of costs from 8 to 44%, at 1% intervals. Finally, 136 nodal features were employed for subsequent analysis (**Figure 1A**).

Functional Network Features

The nodes of the functional brain network were defined by dividing the brain into 90 regions using the automatic anatomical labeling (AAL) template (Tzourio-Mazoyer et al., 2002). The brain network of each participant was a 90*90 connection matrix. Each element of the matrix was the Pearson correlation coefficient between brain regions. Then, we applied Fisher's r-to-z transformation on the raw undirected connectivity matrix (Wee et al., 2012b). The connection of the brain area itself is meaningless, so the diagonal of the connection matrix was set to zero (Zhan et al., 2013). Consistent with the structural network, we set the threshold 8–44%, at 1% intervals. In this part, 810 nodal features (NL, ND, and BC) were obtained for subsequent feature selection (**Figure 1B**).

Feature Selection

In the feature selection section, three feature selection algorithms were applied to classification (**Figure 1C**).

Random Subset Feature Selection Algorithm (RSFS)

The RSFS is an algorithm that can find a set of features whose performance is better than the average feature performance of the available feature set (Pohjalainen et al., 2015). The RSFS process

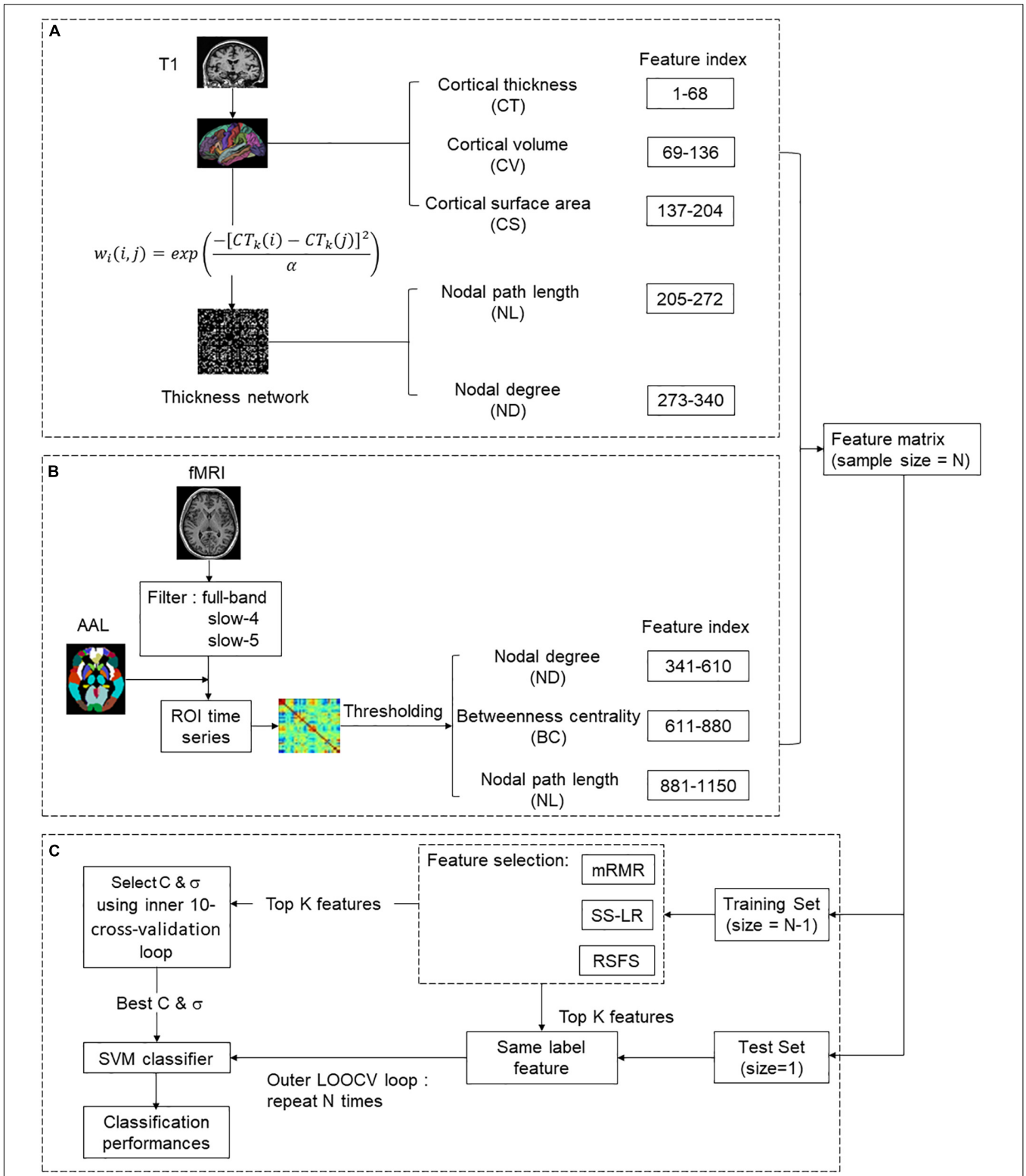

FIGURE 1 | The overall classification framework for predicting the conversion of MCI. **(A)** Structural feature extraction: preprocessing T1 data, extract MRI features and thickness network features. **(B)** Functional feature extraction: preprocessing rs-fMRI data, constructing resting-state functional brain network and extracting features. **(C)** Feature selection and Classification.

includes the main ideas of the random forest (Breiman, 2001) and random K-Nearest neighbor (KNN) (Li et al., 2011). It repeatedly selects a random feature subset from the set of all possible features and then classifies it by KNN.

In RSFS, F represents a full feature set with j true features, each true feature f_j from a full set of features F has a relevance value $r_j \in (-\infty, \infty)$ associated with it. In addition, a set of dummy features $z_j \in Z$ with related relevances q_j is also defined.

During each iteration i, the RSFS algorithm mainly executes the following steps:

(1) Randomly select a subset S_i of n features ($|S_i| = n$) from the full set F by sampling from a uniform distribution.

(2) For the given data set, uses S_i to perform KNN classification and calculates the value of the criterion function c_i to measure the performance of classification.

(3) Update r_j of all used f_j by replacing them according to the formula (5):

$$r_j^{'} = r_j + c_i - E\{c\} \tag{5}$$

Where r_j is current relevance value, $r_j^{'}$ is the updated relevance value, c_i is the current function value and $E\{c\}$ is the expectation of the criterion function value (corresponding to the average of all previous iterations of c_i). Specifically, relevance (feature indices) = relevance (feature indices) + performance criterion – expected criterion value.

(4) Repeats step (1) with a new random subset.

In parallel to updating the feature relevance, similar processing was performed on virtual features by always selecting a random subset of m virtual features and then updating the relevance values of these features according to formula (5) but using the criterion function value of the true features from the same iteration.

Finally, a statistical test was performed to find the feature set $S \subset F$, that truly surpasses the relevance ratings of virtual features. The selection condition formula is as follows:

$$p\left(r_j > r_{rand}\right) \geq \delta, \quad \forall f_j \in B, F, \tag{6}$$

In formula (6), r_{rand} is the baseline level and δ is the probability threshold. The r_{rand} is modeled as the normal distribution of the virtual correlation q_j. Then obtain the probability that the feature is more relevant than a virtual feature from the cumulative normal distribution.

$$p\left(r_j > r_{rand}\right) = \frac{1}{\sigma_g\sqrt{2\pi}} \int_{-\infty}^{r_j} \exp\left(\frac{-(x-\mu_g)^2}{2\sigma_g^2}\right) dx \tag{7}$$

Verification was performed in each repeated process of RSFS. If the feature that exceeds the random feature classification performance was no longer selected, the screening was stopped or the feature selection ended by setting a fixed number of program repetitions (Li et al., 2011; Pohjalainen et al., 2015).

Minimal Redundancy Maximal Relevance Feature Selection Algorithm (mRMR)

We used mRMR proposed by Ding and Peng for feature selection (Peng et al., 2005). mRMR can use mutual information as a measure to solve the trade-off between feature redundancy and relevance (Morgado and Silveira, 2015).

Max-Relevance is defined as:

$$\max D(S, c), D = \frac{1}{|S|} \sum\nolimits_{x_i \in S} I(x_i; c) \tag{8}$$

S represents a feature set with m features $\{x_i\}$, D is the mutual information value between the attribute subset, and the label and c is the class.

Min-Redundancy is defined as:

$$\min R(S), R = \frac{1}{|S|^2} \sum\nolimits_{x_i, x_j \in S} I(x_i, x_j) \tag{9}$$

R represents the mutual information value between feature attributes.

The combination of formula (8) and formula (9) is the criterion for selecting feature subsets with minimum redundancy and maximum relevance. Therefore, mRMR was defined as:

$$mRMR = \max_S \left\{ \frac{1}{|S|} \sum\nolimits_{x_i \in S} I(x_i; c) - \frac{1}{|S|^2} \sum\nolimits_{x_i, x_j \in S} I(x_i, x_j) \right\} \tag{10}$$

Sparse Linear Regression Feature Selection Algorithm Based on Stationary Selection (SS-LR)

The SLEP package (Liu et al., 2009) was used to solve sparse linear regression. Given a data set $T = (X, Y)$, where $X = (x_1, x_2, \ldots, x_n)^T \in R^{n \times m}$ is the sample, $Y = (y_1, y_2, \ldots, y_n)^T \in R^{n \times 1}$ is a true label, n is the number of samples, and m is the number of features for each sample. The linear regression model can be defined as:

$$f(X) = Xw \tag{11}$$

Where the coefficient of the linear regression is defined as $w = (w_1, w_2, \ldots, w_n) \in R^{m \times 1}$, $f(X)$ is the predicted label vector obtained by distinguishing the unknown samples. Let $L(w)$ be the loss function of linear regression, the function is defined as a formula (12):

$$L(w) = \min_w \frac{1}{n} ||f(X) - Y||_2^2 \tag{12}$$

Add an L_1 regularization term after the loss function to control the complexity of the model, and add the regularized expression:

$$L(w) = \min_w \frac{1}{n} ||f(X) - Y||_2^2 + \lambda ||w||_1 \tag{13}$$

Where $||w||_1 = \sum_{i=1}^m |w_i|$, $\lambda > 0$ is the regularization parameter of the model control. As λ increases, the sparseness of the function becomes larger. The range is $0.05 < \lambda < 0.3$ and the step size is 0.005. Sub-sampling or bootstrapping from the original sample for stability selection to solve the problem of proper regularization (Meinshausen and Bühlmann, 2010).

SVM Classifier

The SVM classifier adopted here comes from the LIBSVM software package, which was developed by Lin's team

(Chang and Lin, 2011). The kernel function in the SVM classifier uses the radial basis kernel function (RBF), where the penalty parameter $\mathcal{C}$ and the kernel bandwidth σ in the kernel function range from $[4^{-4}, 4^4]$. The RBF kernel was defined as follows:

$$K(X_1, X_2) = exp\left(-\frac{||X_1 - X_2||}{2\sigma^2}\right) \quad (14)$$

where X_1, X_2 are two eigenvectors, σ is the width parameter of the REF kernel. Both internal and external cross-validation methods were used in **Figure 1C**. Internal cross-validation was used to find the best classifier parameters, and external cross-validation was used to verify the performance of the classifier. A nested cross-validation was used to obtain unbiased estimates. After normalization and feature screening of the training data set, an internal cross-validation (10-fold cross-validation and grid search method) was performed on the training set (inner loop). In the outer loop, leave-one-out cross-validation (LOOCV) was repeated for N (N = 85 or 49) times. Finally, the held-out sample was used to evaluate the training classifier. These parameters were defined as follows (Fawcett, 2006; Wee et al., 2012b):

$$Accurary = \frac{TP + TN}{TP + TN + FP + FN},$$

$$Sensitivity = \frac{TP}{TP + FN}, \quad Specificity = \frac{TN}{TN + FP}, \quad (15)$$

$$Balanced\ Accuracy(BAC) = \frac{Sensitivity + specificity}{2} \quad (16)$$

where TP is true positive; TN, true negative; FP, false positive and FN, false negative respectively. Area Under Curve (AUC) was defined as the area under the ROC curve and the coordinate axis.

Statistical Analysis

All statistical calculations were performed in the matlab2016b platform (MathWorks, Inc, see text footnote 5). The exact Clopper–Pearson method was used to calculate the 95% confidence intervals (CIs) of sensitivity, specificity, and accuracy (Agresti and Coull, 1998). The CIs of AUC was calculated by the DeLong methods (DeLong et al., 1988; Mercaldo et al., 2007; Mei et al., 2020). McNemar's test (Bates and McNemar, 1964) was used to calculate the two-sided *P*-value for AUC between MCInc vs. MCIc, AD vs. MCIc.

RESULTS

Classification Results

To reduce feature redundancy for each threshold containing 1150 features, the features of the two classification groups (MCInc vs. MCIc, MCIc vs. AD) were selected by the RSFS, SS-LR, and mRMR in the cost range of 8–44%. The classification results showed that the AUC and ACC obtained by the RSFS algorithm were significantly higher than the other algorithms (**Supplementary Figures 1A,B**). By comparison, it was found that the classification result obtained by the MCInc vs. MCIc group at cost = 39%, was the best and the most stable, and the classification result obtained by the MCIc vs. AD group at cost = 19%, was the best and the most stable. Therefore, the subsequent results were analyzed and discussed in cost = 39 and 19%. The receiver operating characteristic (ROC) curves and classification results are depicted in **Figure 2** and **Table 2**.

In MCInc vs. MCIc group, the RSFS algorithm achieved an 84.71% accuracy (95% CI 75.3%, 91.6%), an 66.67% sensitivity (95% CI 47.2%, 82.7%), a 94.55% specificity (95% CI 84.9%, 98.9%) and 0.888 AUC (95% CI 0.814, 0.962). The SS-LR algorithm had an 65.88% accuracy (95% CI 54.80%, 75.82%), 50.0% sensitivity (95% CI 31.30%, 68.70%), 74.55% specificity (95% CI 61.00%, 85.33%), and 0.738 AUC (95% CI 0.629, 0.847). The mRMR algorithm had 61.18% accuracy (95% CI 49.99%, 71.56%), 33.33% sensitivity (95% CI 17.29%, 52.81%), 76.36% specificity (95% CI 62.98%, 86.77%), and 0.605 AUC (95% CI 0.478, 0.733).

In MCIc vs. AD group, the RSFS algorithm achieved an 89.80% accuracy (95% CI 77.77%, 96.60%), 78.95% sensitivity (95% CI 54.43%, 93.95%), 96.67% specificity (95% CI 82.78%, 99.92%), 0.854 AUC (95% CI 0.709, 1.000). The SS-LR algorithm had 51.02% accuracy (95% CI 36.34, 65.58), 36.84% sensitivity (95% CI 16.29, 61.64), 60.00% specificity (95% CI 40.60, 77.34) and 0.451 AUC (95% CI 0.281, 0.620). The mRMR algorithm had 40.82% accuracy (95% CI 27.00, 55.79), 5.26% sensitivity (95% CI 0.13, 26.03), 63.33% specificity (95% CI 43.86, 80.07), and 0.297 AUC (95% CI 0.151, 0.444).

Comparing Classification Results Based on Different Feature Selection Methods

In **Figure 3**, the top K features (K = 1, 2,…, 30) were used for classification to prove the effect of the number of selected features on the classification performance respectively. After the top 8 features, the AUC curves appeared stable in the two groups. In MCIc vs. AD group, the AUC curves of the mRMR algorithm and SS-LR algorithm go downward and can hardly be classified correctly. We compared the classification performance of the three feature selection algorithms, and the results are shown in **Table 3** and **Figure 3**. As shown in **Table 3**, the classification performance obtained by the RSFS algorithm showed significant differences compared to those obtained by the mRMR algorithm and the FS algorithm in the two classification groups. But we found no significant difference between the mRMR algorithm and the FS algorithm.

As illustrated in **Figure 3A**, the AUC scores of the RSFS algorithm were significantly higher than those of the SS-LR algorithm (K = 1, 2, 9–14, 16–30) and mRMR algorithm (K = 10–30) in MCInc vs. MCIc group. At K = 14, the AUC scores of the three algorithms showed significant differences. As shown in **Figure 3B**, the AUC scores of the RSFS algorithm were significantly higher than those of the SS-LR algorithm (K = 2–4, 8–30) and mRMR algorithm (K = 2–30) in MCIc vs. AD group. At K = 5, 15–18, 21, 24–30, the AUC scores obtained by the SS-LR algorithm were significantly higher than those obtained by mRMR. We found that the AUC scores of the three algorithms have significant differences (K = 15–18, 21, 24–30).

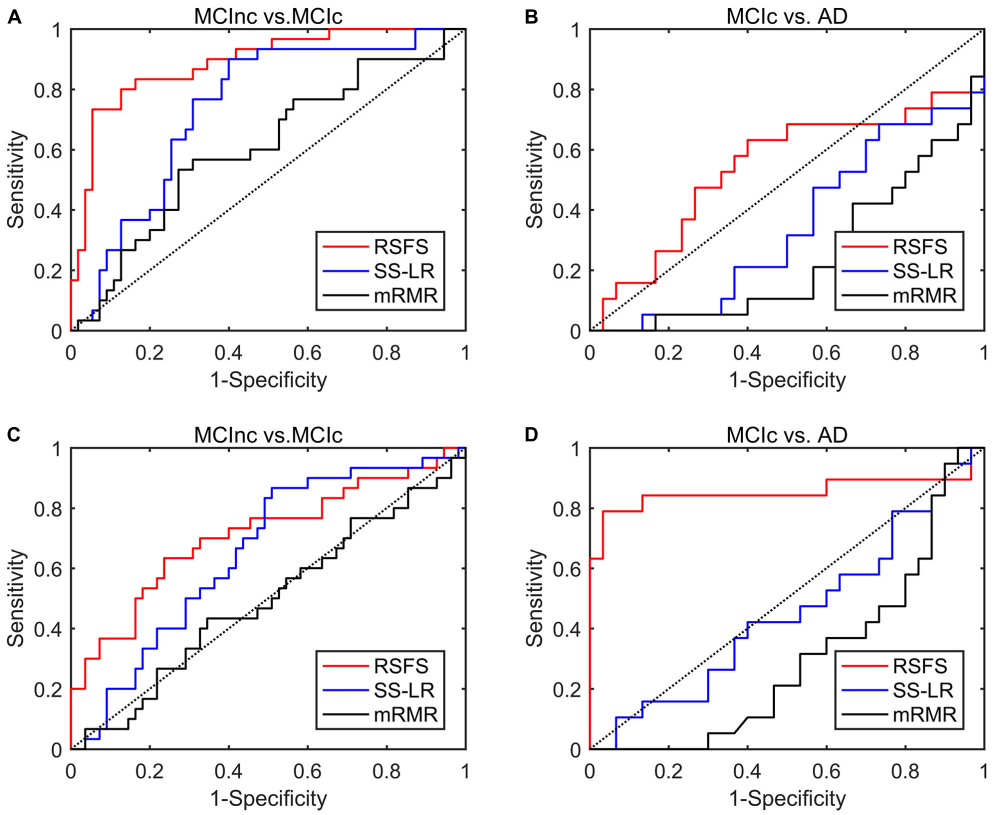

FIGURE 2 | ROC curves of the three algorithms performed SVM classifier using the top 10 features. **(A)** MCInc vs. MCIc group at cost = 39%, **(B)** MCIc vs. AD group at cost = 39%. **(C)** MCInc vs. MCIc group at cost = 19%, **(D)** MCIc vs. AD group at cost = 19%.

TABLE 2 | Classification results performance of different methods using the top 10 features.

GROUP	RSFS				SS-LR				mRMR			
	ACC (%)	SEN (%)	SPE (%)	AUC	ACC (%)	SEN (%)	SPE (%)	AUC	ACC (%)	SEN (%)	SPE (%)	AUC
MCInc vs. MCIc	84.71 [75.27, 91.60]	66.67 [47.19, 82.71]	94.55 [84.88, 98.86]	0.888 [0.814, 0.962]	65.88 [54.80, 75.82]	50.00 [31.30, 68.70]	74.55 [61.00, 85.33]	0.738 [0.629, 0.847]	61.18 [49.99, 71.56]	33.33 [17.29, 52.81]	76.36 [62.98, 86.77]	0.605 [0.478, 0.733]
MCIc vs. AD	89.80 [77.77, 96.60]	78.95 [54.43, 93.95]	96.67 [82.78, 99.92]	0.854 [0.709, 1.000]	51.02 [36.34, 65.58]	36.84 [16.29, 61.64]	60.00 [40.60, 77.34]	0.451 [0.281, 0.620]	40.82 [27.00, 55.79]	5.26 [0.13, 26.03]	63.33 [43.86, 80.07]	0.297 [0.151, 0.444]

ACC, accuracy; SEN, sensitivity; SPE, specificity; AUC, area under the curve.AUC comparisons were evaluated by the DeLong test to compute the 95% CI; accuracy, sensitivity and specificity comparisons were calculated by using the exact Clopper–Pearson method to compute the 95% CI; all CIs shown in parentheses.

TABLE 3 | Comparison of classification results between different feature selection methods.

GROUP	Sig.(RSFS vs. SS-LR)	Sig.(RSFS vs. mRMR)	Sig.(mRMR vs. SS-LR)
MCInc vs. MCIc	0.001383	0.000329	0.479500
MCIc vs. AD	0.000085	0.000006	0.358795

The "Sig." column gives the p-value. McNemar's test to calculate the p-value.

In summary, the classification results of the RSFS algorithm in the MCInc vs. MCIc group was the best, followed by that of the SS-LR algorithm, and then the mRMR algorithm. For the MCIc vs. AD group, the classification results of the RSFS algorithm was also the best, while the classification results obtained by using the other algorithms were relatively poor. Hence, only the two classification groups of results obtained by applying the RSFS algorithm are discussed below.

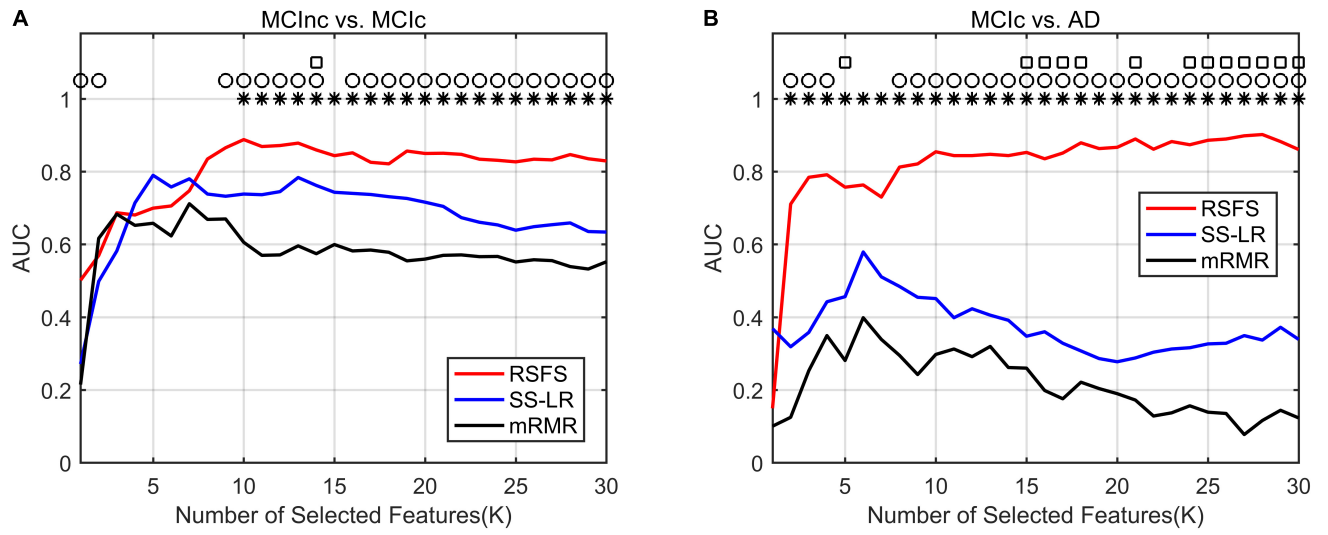

FIGURE 3 | Comparison of AUC scores of three algorithms performed SVM classifier. Subgraphs **(A)** and **(B)** represent AUC scores with the number of features K of MCInc vs. MCIc, and MCIc vs. AD.

○ Indicate the classification performance of the RSFS algorithm and SS-LR algorithm is significantly different.

✱ Indicate the classification performance of the RSFS algorithm and mRMR algorithm is significantly different.

□ Indicate the classification performance of the mRMR algorithm and SS-LR algorithm is significantly different.

Confirmatory Analyses – Further Resampling Results

With the higher AUC and ACC, the classification effect obtained by the RSFS algorithm outperformed the SS-LR algorithm and mRMR algorithm (**Figure 2** and **Table 2**). In **Table 2**, it is observable that the imbalanced data caused a gap between sensitivities and specificities. Therefore, we compared the performance of multiple classifiers and verified the reliability of our results through upsampling. As shown in **Table 4** and **Supplementary Figure 2**, the upsampled data were trained and tested by four classifiers (Random Forest (Breiman, 2001), KNN (Yang et al., 2007), AdaBoost (Hastie et al., 2009), SVM). The results showed that the classification accuracy obtained by SVM was the highest and equally matched the results before upsampling.

The reported results of this study were based on only a limited number of iterations (based on the number of subjects) which may be the main reason for the high classification performances. To address this issue and considering the impact of single sampling on classification performance, we upsampling and downsampling the data (Dubey et al., 2013; Hojjati et al., 2017). In general, we performed 500 iterations of the outer loop in the resampling part, and performed the leave-one-out method in the inner loop (For upsampling, based on the number of samples in MCIc vs. AD group is 60 or the number of samples in MCInc vs. MCIc group is 110) for classification prediction, and finally reported the average of those performances average ((60 or 110) × 500 iterations) as the classification result. As illustrated in **Supplementary Figures 3**, **4**, these results show that the result classification performance of the original nosampling data is between upsampling and downsampling when the number of features is 1–30. We compared the classification performance of resample data based on RSFS algorithm and SVM classifier using the top 10 features, and the results are shown in **Table 5**. In MCInc vs. MCIc group, compare with classification performance of the downsampling (80.20% accuracy, 76.37% sensitivity, 84.03% specificity, 0.853 AUC), nosampling classification performance were slightly higher. However, upsampling classification performance were greater than 90%. In MCIc vs. AD group, compare with classification performance of the downsampling (80.80% accuracy, 71.87% sensitivity, 89.73% specificity, 0.827 AUC), nosampling classification performance were slightly higher, upsampling1 classification performance were greater than those of nosampling. But the accuracy of upsampling2 was lower than that of nosampling. Based on the above results, this study analyzed and compared the nosampling data in the following analysis.

Highly Sensitive Characteristic

In order to investigate which features are highly sensitive brain regions related to MCI disease, we accumulate the number of selected features used for classification, and finally obtain the frequency of occurrence of all selected features. **Tables 6, 7** and **Figure 4** summarize the details of the top 10 features that can be used to distinguish MCInc and MCIc, MCIc and AD. As shown in **Table 6**, there was 30% structural features, 20% structural connectivity network features, and 50% functional connectivity network features. Consistent with the previous studies, the brain regions selected by our method to identify MCInc subjects from MCI included the left banks superior temporal sulcus (Khazaee et al., 2017), left entorhinal cortex (Zhang et al., 2011; Nickl-Jockschat et al., 2012; Suk et al., 2015; Rasero et al., 2017), right caudate nucleus (Khazaee et al., 2015; Suk et al., 2015), left calcarine fissure and surrounding cortex (Khazaee et al., 2015; Wang et al., 2015; Pusil et al., 2019), left frontal

TABLE 4 | Classification performance of multiple classifiers based on RSFS algorithm using the top 10 features.

	MCInc vs. MCIc				MCIc vs. AD			
	ACC(%)	SEN(%)	SPE(%)	AUC	ACC(%)	SEN(%)	SPE(%)	AUC
RF[a]	67.06	46.67	78.18	0.742	67.35	57.89	73.33	0.716
KNN[a]	69.41	93.33	56.36	0.887	63.27	84.21	50.00	0.884
Adaboost[a]	69.41	60.00	74.55	0.725	71.43	52.63	83.33	0.763
SVM[a]	84.71	83.33	85.45	0.886	87.76	73.68	96.67	0.849
SVM[b]	84.71	66.67	94.55	0.888	89.80	78.95	96.67	0.854

ACC, accuracy; SEN, sensitivity; SPE, specificity. RF, Random Forest; KNN, k-nearest neighbor classification. [a]Represents the use of upsampling balanced data for classification. [b]Represents the use of original data for classification.

TABLE 5 | Classification performance of resample data based on RSFS algorithm and SVM classifier using the top 10 features.

	MCInc vs. MCIc				MCIc vs. AD			
	ACC(%)	SEN(%)	SPE(%)	AUC	ACC(%)	SEN(%)	SPE(%)	AUC
nosampling	84.71	66.67	94.55	0.888	89.80	78.95	96.67	0.854
downsampling	80.20	76.37	84.03	0.853	80.80	71.87	89.73	0.827
upsampling1	91.59	90.00	93.18	0.953	91.57	85.65	97.49	0.947
upsampling2	92.70	91.74	93.66	0.962	88.90	80.59	97.21	0.934

Downsampling and upsampling1 are defined as random resampling. Upsampling2 is defined as ensuring that each original sample is included, and then randomly resampling the remaining data.

pole (Wee et al., 2014), right parahippocampal gyrus (Suk et al., 2015; Hojjati et al., 2017; Pusil et al., 2019), right lenticular nucleus, pallidum (Zhang et al., 2011), right cuneus cortex (Nickl-Jockschat et al., 2012; Suk et al., 2015), right posterior cingulate gyrus (Khazaee et al., 2015).

As demonstrated in **Table 7**, all features came from the functional network and the proportion of the three frequency bands is 3(full-band):3(slow-5):4(slow-4). Moreover, it should be noted that 70% of features came from betweenness centrality. The selected brain regions included the right middle frontal gyrus orbital part (Khazaee et al., 2015), right thalamus (Nickl-Jockschat et al., 2012; Khazaee et al., 2015), right superior frontal gyrus, orbital part (Suk and Shen, 2014), right olfactory cortex (Khazaee et al., 2015), right angular gyrus (Suk et al., 2015; Wang et al., 2015),right paracentral lobule (Suk and Shen, 2014), right inferior temporal gyrus (Wee et al., 2014), right temporal pole: superior temporal gyrus (Wee et al., 2014; Khazaee et al., 2015), left superior frontal gyrus, and medial orbital (Khazaee et al., 2015; Wang et al., 2015; Pusil et al., 2019).

DISCUSSION

In the present study, we used structure-functional MRI and the combined graph theory with multiple machine learning methods to accurately classify patients with MCIc and MCInc/AD. Our findings demonstrated that, by including the cortical thickness features, structural brain network features, and sub-frequency (full-band, slow-4, slow-5) functional brain network features, the proposed method performed effectively in identifying MCIc subjects from MCInc/ AD. In the classifications of MCIc vs. MCInc and MCIc vs. AD, the proposed RSFS algorithm achieved the best accuracies (84.71%, 89.80%) compared to other algorithms (**Table 2** and **Figure 3**).

In **Table 2**, there is a gap between specificities and sensitivities due to the imbalanced data. However, our proposed method obtained the best BAC of 80.61 and 87.81% with the RSFS algorithm. We also compared the performance of multiple classifiers and verified the reliability of our results through upsampling (**Supplementary Figure 2**). The results indicated that the SVM classifier obtained the best accuracy, and was consistent with the results before upsampling. The balance of sensitivities and specificities has also been appropriately improved. In addition, we observed that the mRMR algorithm achieved 5.26% sensitivity in MCIc vs. AD group compared to other methods as described in **Table 2**. Actually, as shown in **Supplementary Figures 1A,B**, the SS-LR algorithm and the mRMR algorithm achieved best performance (84.71% ACC, 73.33% SEN, 90.91% SPE, 83.45% AUC at cost = 27%, K = 4 and 77.65% ACC, 53.33% SEN, 90.91% SPE, 74.45% AUC at cost = 8%, K = 20, respectively) in MCInc vs. MCIc group. The SS-LR algorithm and the mRMR algorithm achieved the best performance (71.43% ACC, 42.11% SEN, 90.00% SPE, 70.53% AUC at cost = 36%, K = 2 and 71.43% ACC, 52.63% SEN, 83.33% SPE, 70.35% AUC at cost = 33%, K = 12, respectively) in MCIc vs. AD group.

As illustrated in **Tables 8**, **9**, the classification results obtained by the combination of sMRI and rs-fMRI in the present study are better than those of the unimodal (sMRI\rs-fMRI) approach, including those of our previous studies (Wei et al., 2016; Zhang et al., 2019). Meanwhile, we also compared the classification performances with other studies. Most previous methods that constructed brain networks only considered structural or functional features (Suk and Shen, 2014;

TABLE 6 | Selected feature distributions in the MCInc vs. MCIc group using the RSFS algorithm.

Feature index	Modality	Frequency band	Networks attribution	Region	Frequency (%)
1	Structural		Thickness	BSTS.L	100
39	Structural		Thickness	ENT.L	100
862	FCN	Slow-4	BC	CAU.R	100
1013	FCN	Slow-5	ND	CAL.L	100
337	SCN		NL	FP.L	98.82
830	FCN	Slow-4	BC	PHG.R	98.82
506	FCN	Full band	ND	PAL.R	97.65
208	SCN		ND	CUN.R	94.12
69	Structural		Volume	BSTS.L	92.94
826	FCN	Slow-4	BC	PCG.R	36.47

FCN, functional connectivity network; SCN, structural connectivity network; BSTS.L, Left Banks superior temporal sulcus; ENT.L, Left Entorhinal cortex; CAU.R, Right Caudate nucleus; CAL.L, Left Calcarine fissure and surrounding cortex; FP.L, Left Frontal pole; PHG.R, Right Parahippocampal gyrus; PAL.R, Right Lenticular nucleus, pallidum; CUN.R, Right Cuneus cortex; PCG.R, Right Posterior cingulate gyrus.

TABLE 7 | Selected feature distributions in the MCIc vs. AD group using the RSFS algorithm.

Feature index	Modality	Frequency band	Networks attribution	Region	Frequency (%)
440	FCN	Full band	ND	ORBmid.R	100
778	FCN	Slow-4	ND	THA.R	100
1066	FCN	Slow-5	BC	ORBsup.R	100
1082	FCN	Slow-5	BC	OLF.R	100
688	FCN	Slow-4	NL	THA.R	87.76
1126	FCN	Slow-5	BC	ANG.R	85.71
590	FCN	Full band	BC	PCL.R	73.47
880	FCN	slow-4	BC	ITG.R	71.43
874	FCN	Slow-4	BC	TPOsup.R	46.94
545	FCN	Full band	BC	ORBsupmed.L	44.90

FCN, functional connectivity network; ORBmid.R, Right Middle frontal gyrus orbital part; THA.R, Right Thalamus; ORBsup.R, Right Superior frontal gyrus, orbital part; OLF.R, Right Olfactory cortex; ANG.R, Right Angular gyrus; PCL.R, Right Paracentral lobule; ITG.R, Right Inferior temporal gyrus; TPOsup.R, Right Temporal pole, superior temporal gyrus; ORBsupmed.L, Left Superior frontal gyrus, medial orbital.

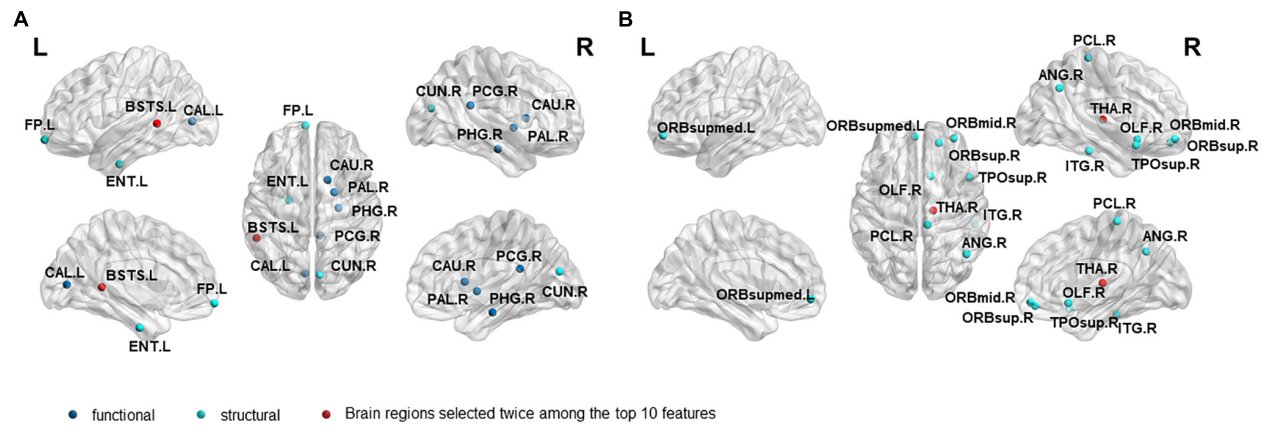

FIGURE 4 | The location and networks attribution of top 10 brain regions, listed in Tables 6 **(A)**, 7 **(B)**, which might be affected in early stage of MCI.

Hu et al., 2015; Moradi et al., 2015; Raamana et al., 2015; Ardekani et al., 2016; Suk et al., 2016; Beheshti et al., 2017; Hojjati et al., 2017, 2018; Zheng et al., 2019; Gupta et al., 2020; Zhu et al., 2021), and obtained an accuracy lower than that of the present study. Only Hojjatia's study (Hojjati et al., 2017) used graph theory and machine learning approach (mRMR, FS) to

TABLE 8 | Classification performance of different methods to distinguish different stages of MCI.

Article	Method	Cohort	ACC (%)	SEN (%)	SPE (%)	AUC
Proposed	rs-fMRI, sMRI, graph theory, machine learning approach (RSFS)	MCIc/MCInc(30/55)	84.71	66.67	94.55	0.888
	sMRI, graph theory, RSFS	MCIc/MCInc	68.24	80.00	46.67	0.673
	rs-fMRI, graph theory, RSFS	MCIc/MCInc	64.71	78.18	40.00	0.670
Wei et al., 2016	Combination of MRI and thickness network (SS-LR)	MCIc/MCInc(61/83)	76.40	65.60	84.30	0.813
Hojjati et al., 2017	rs-fMRI, graph theory, machine learning approach (mRMR, FS)	MCIc/MCInc(18/62)	91.40	83.24	90.10	N/A
Hojjati et al., 2018	rs-fMRI, sMRI, 6 features, graph theory, machine learning approach (mRMR)	MCIc/MCInc(18/62)	97.00	95.00	100	0.980
Suk and Shen, 2014	93 features from a MR image and the same dimensional features from a FDG-PET image.	MCIc/MCInc(43/56)	74.04	58.00	82.67	0.696
Suk et al., 2016	MRI, DW-S^2MTL	pMCI/sMCI(43/56)	69.84	44.00	89.00	N/A
Moradi et al., 2015	MRI, age and cognitive measures 10-fold cross-validation	pMCI/sMCI(164/100)	81.72	86.65	73.64	0.902
Raamana et al., 2015	Thickness network fusion	MCIc/MCInc(56/130)	64.00	65.00	64.00	0.680
Hu et al., 2015	sMRI, tight wavelet frame, SVM	MCIc/MCInc(71/62)	76.69	71.83	82.26	0.790
Ardekani et al., 2016	hippocampal volumetric integrity (HVI) from structural MRI scans RF with 5,000 trees	pMCI/sMCI(86/78)	82.30	86.00	78.20	N/A
Beheshti et al., 2017	sMRI, t-test scores and a genetic algorithm, SVM	pMCI/sMCI(71/65)	75.00	76.92	73.23	0.751
Zheng et al., 2019	MRI and FDG-PET, PCA, SVM	pMCI/sMCI(51/75)	79.37	74.51	82.67	0.892
Gupta et al., 2020	sMRI, FDG-PET, AV45-PET, rs-fMRI, DTI and APOE genotype, MKL	MCIc/MCInc(31/30)	95.08	100	93.93	0.969
Zhu et al., 2021	sMRI, patch-level features, DA-MIDL	pMCI/sMCI(172/232)	80.20	77.10	82.60	0.851

The best multivariate predictors of MCI conversion are shown for each study.ACC, accuracy; SEN, sensitivity; SPE, specificity; AUC, area under the curve; pMCI, progressive MCI; sMCI, stable MCI; FDG-PET, fluorideoxyglucose positron emission tomography; RF, Random forest; DW-S^2MTL, deep weighted subclass-based sparse multi-task learning; PCA, principal component analysis. MKL, multiple kernel learning. DA-MIDL, dual attention multi-instance deep learning network.

classify rs-fMRI and obtained a classification accuracy of 91.4%. However, the sample size was too small (<20), and the effect was not widely representative. Besides, the studies in **Table 8**, Zhang and Shen (2012) used a multi-modal multi-task learning algorithm to fuse MRI, FDG-PET, and CSF data and regressed the MMSE and ADAS-Cog scores to classify MCInc and MCIc with a classification accuracy of 73.9%. Similarly, Cui et al. (2011) combined MRI, CSF, and cognitive scoring scale features to classify MCInc and MCIc with a classification accuracy of 67.13%. Ye et al. (2012) used sMRI, ApoE, and cognitive scores to classify MCIc and MCInc using a smooth selection method based on sparse logistic regression, and obtained good classification results of 0.859 AUC. Therefore, these results may suggest that the method we have proposed could effectively help predict the conversion to Alzheimer's disease.

Different from the previous studies, our research not only focused on the brain regions' conversion sensitivity of the two groups of patients (MCIc vs. MCInc), but also studied the conversion sensitivity of the brain regions of the same group of patients (MCIc vs. AD). **Tables 6, 7** and **Figure 4** list the highly sensitive brain regions selected from the two groups. These results proved the inconsistency of the selected brain regions in the two classification groups. As shown in **Table 6**, there were 30% structural features, 20% structural connectivity network features, 50% functional connectivity network features. The proportion of functional connectivity network features in each frequency band is listed as follows: 1(full-band):1(slow-5):3(slow-4). In **Table 7**, all features came from the functional network and the proportion of the three frequency bands was 3(full-band):3(slow-5):4(slow-4). Moreover, it is worth noting that 70% of features came from betweenness centrality. Our results suggest that the betweenness centrality in a functional network carries more disease information and the top 10 selected features are more sensitive to more efficient classification for MCIc and AD. According to **Tables 6**, **7**, it can be seen that the network parameter characteristics of all frequency bands from rs-fMRI have been selected. However, the cortical surface area (CS) was not selected for the top 10 features in two classification

TABLE 9 | Classification of MCIc and AD.

Article	Method	Cohort	ACC (%)	SEN (%)	SPE (%)	AUC
Proposed	rs-fMRI, sMRI, graph theory, machine learning approach (RSFS)	MCIc/AD(30/19)	89.80	78.95	96.67	0.854
	sMRI, graph theory, RSFS		57.14	15.79	83.33	0.428
	rs-fMRI, graph theory, RSFS		77.55	63.16	86.67	0.812

groups by three algorithms. More importantly, in Wei's work (Wei et al., 2016), the selected top 10 combined structure features did not include CS. Based on the above results, we consider that CS is not an effective marker for AD disease. In future work, we will assess whether it can be excluded from the feature set. Different from our previous work on EMCI and LMCI classification (Zhang et al., 2019) the characteristics of the slow-5 band did not show high sensitivity in MCInc and MCIc classification. The reason may be that the former is mainly based on the degree of memory impairment of MCI disease, and the latter is based on the longitudinal time diagnosis status to classify whether MCI develops into AD. Therefore, we suggest that the difference in their brain activity may be reflected in different frequency bands.

Our findings converge nicely with what has been suggested by the previous studies (see Results Section), and these selected brain regions have been shown to be related to MCI conversion. The important roles of several brain regions in MCI disease have been widely recognized. Braak and Braak (1991) used structural magnetic resonance imaging (sMRI) to study AD patients. They first discovered a large number of neurofibrillary tangles in the medial temporal lobe, and the brain areas involved mainly included the olfactory cortex, hippocampus, and parahippocampal gyrus, amygdala, and cingulate cortex area, which is consistent with the conclusion that the brain atrophy of AD or MCI patients are mainly located in the medial temporal lobe (Fan et al., 2008; Das et al., 2015). In line with the previous studies (Khazaee et al., 2015; Wang et al., 2015; Pusil et al., 2019), we also found that the left calcarine fissure and the surrounding cortex are associated with MCI conversion to AD. Damage to this brain area may cause central visual diseases (such as macular avoidance and hallucinations). Studies have reported that visual impairment can affect patients' cognition, thereby increasing the risk of dementia (Uhlmann et al., 1991; Naël et al., 2019). Besides, the top 10 highly sensitive features provided by the other two algorithms are also listed in the **Supplementary Material** (**Supplementary Tables 3.1–3.4**). Although the sensitivity was lower than that of the RSFS algorithm, the selected top 10 highly sensitive features are also important to brain areas related to AD disease. It shows that the classification framework of graph theory and machine learning methods considering structural and functional MRI provides a new view for improving MCI clinical prediction and diagnosis. Moreover, our findings suggest that the inconsistency of the selected brain regions between the two classification groups requires more attention. The transformation of MCI disease may imply that the structure of the brain area changed in the early stage of AD, and the function of the brain area later began to degenerate. Inconsistency of the brain regions obtained by the two classification groups indicates that the conversion sensitivity brain regions of the two group patients (MCInc vs. MCIc) and the same group patients (MCIc vs. AD) may be different, which further suggests that the classification between the different groups of patients provides limited information. For the follow-up within a group, it may be more meaningful for the study of diseases.

In the current study, the best performances achieved with costs of 39 and 19% based on MCInc vs MCIc group MCIc vs. AD group, respectively. The cost was defined as the ratio of the number of above-threshold edges to the total number of edges in a network. Cost range can be defined from 0 to 1, but the upper limit is generally less than 50% (Tan et al., 2019). Compared to cost = 19%, cost = 39% is the low threshold. Compared to the MCIc vs. AD group, the MCInc vs. MCIc group can be distinguished when the cost is large and there are more edges in the network. Refer to the study of Jie et al. (2014), as the threshold increases, weak connections and unimportant connections are removed, and significant differences are found between different groups of patients. Therefore, we suggested that the best classification performance of the two classification groups at different costs is due to the different topological properties of the brain network. Specifically, the larger the cost, the higher the global and local efficiency, the higher the clustering coefficient, the lower the characteristic path length, and the lower the small-world attributes (Zhang et al., 2019). The difference between brain network parameters is significant, and the topological characteristics of brain regions can be better distinguished. In the future, we will investigate the specific differences in the brain network characteristics of different groups of patients, and combine their clinical scales for predictive analysis.

However, this study has several limitations. One major limitation is the small sample size. Another limitation is the imbalanced data. Despite the promising results of using the RSFS algorithm and the SVM to screen patients with MCIc, further data collection is required to test the generalizability of the method to other patient populations. In future studies, a larger sample should be collected, and the number of subjects balanced as the scale of the ADNI database is expanding (Aisen et al., 2010). Furthermore, future studies should attempt to explore different methods of classification in different stages of AD, including the interpretability of structural and functional brain abnormalities (Ibrahim et al., 2021). The versatility in multiple data sets will be necessary to validate the robustness of the models. For the study of

the topological properties of the brain, Power-264 brain regions might be considered as a template for constructing brain networks. In addition, other well-known prognostic information (DTI, ApoE status, Tau/Amyloid/FDG-PET) will be considered for classification (Gupta et al., 2020; Fan et al., 2021). In terms of subject design, we believe that the follow-up data within the subject can better reveal the brain area where the sensitive characteristics of the transformed biomarker are located. The limitation is that the data sample size is too small. If there are subjects who can collect follow-up data through cognitive training (Hernes et al., 2021) and set a baseline control at the same time, more meaningful and reliable results may be obtained.

CONCLUSION

The present study investigated the predictive power of cortical thickness features and brain connectivity network features derived from the sMRI and rs-fMRI to identify individuals with MCI from MCInc/AD for the first time. For the selection of subjects, we proposed a mixed-subject method with an inter- (horizontal) and intra-subject design (longitudinal, follow up), which is rarely used in AD classification. In this classification framework, multiple modalities integration was achieved by using graph theory and machine learning algorithms. We found that this framework improves the classification performance of identifying precursor AD (MCIc), and the high-sensitivity features derived with two classification groups are inconsistent. These findings indicate that the converted sensitivity brain regions of the two groups of patients (MCInc vs. MCIc) and the same group of patients (MCIc vs. AD) may be different, which further indicates that the former way of classifying two different groups of patients may provide limited information. Ultimately, such a classification framework integrating information from sMRI and fMRI can effectively predict the conversion of MCI, and different brain regions obtained in this framework from inter-subject and intra-subject design are probably diagnostic markers for AD.

DATA AVAILABILITY STATEMENT

Publicly available datasets were analyzed in this study. This data can be found here: adni.loni.usc.edu.

ETHICS STATEMENT

The studies involving human participants were reviewed and approved by Ethics approval and informed consents were obtained from the Alzheimer's Disease Neuroimaging Initiative (ADNI). The patients/participants provided their written informed consent to participate in this study.

AUTHOR CONTRIBUTIONS

TZ: roles/writing – original draft, conceptualization, investigation, methodology, writing – review and editing. QL: resources. DZ: investigation. CZ: software. JY and RN: writing – review and editing. JZ and ZJ: funding acquisition and writing – review and editing. LL: conceptualization, supervision, funding acquisition, project administration, and writing – review and editing. All authors reviewed the manuscript.

FUNDING

This work was supported by grants from Sichuan Science and Technology Program (2020YFS0230), NSFC (61773092, 61673087, and 61773096), 111 project (B12027), and the Fundamental Research Funds for the Central Universities.

ACKNOWLEDGMENTS

Data collection and sharing for this project was funded by the Alzheimer's Disease Neuroimaging Initiative (ADNI) (National Institutes of Health Grant U01 AG024904) and DOD ADNI (Department of Defense award number W81XWH-12-2-0012). ADNI is funded by the National Institute on Aging, the National Institute of Biomedical Imaging and Bioengineering, and through generous contributions from the following: AbbVie, Alzheimer's Association; Alzheimer's Drug Discovery Foundation; Araclon Biotech; BioClinica, Inc.; Biogen; Bristol-Myers Squibb Company; CereSpir, Inc.; Cogstate; Eisai Inc.; Elan Pharmaceuticals, Inc.; Eli Lilly and Company; EuroImmun; F. Hoffmann-La Roche Ltd and its affiliated company Genentech, Inc.; Fujirebio; GE Healthcare; IXICO Ltd.; Janssen Alzheimer Immunotherapy Research & Development, LLC.; Johnson & Johnson Pharmaceutical Research & Development LLC.; Lumosity; Lundbeck; Merck & Co., Inc.; Meso Scale Diagnostics, LLC.; NeuroRx Research; Neurotrack Technologies; Novartis Pharmaceuticals Corporation; Pfizer Inc.; Piramal Imaging; Servier; Takeda Pharmaceutical Company; and Transition Therapeutics. The Canadian Institutes of Health Research is providing funds to support ADNI clinical sites in Canada. Private sector contributions are facilitated by the Foundation for the National Institutes of Health (www.fnih.org). The grantee organization is the Northern California Institute for Research and Education, and the study is coordinated by the Alzheimer's Therapeutic Research Institute at the University of Southern California. ADNI data are disseminated by the Laboratory for Neuro Imaging at the University of Southern California.

SUPPLEMENTARY MATERIAL

The Supplementary Material for this article can be found online at: https://www.frontiersin.org/articles/10.3389/fnagi.2021.688926/full#supplementary-material

REFERENCES

Agresti, A., and Coull, B. A. (1998). Approximate is better than "Exact" for interval estimation of binomial proportions. *Am. Stat.* 52, 119–126. doi: 10.1080/00031305.1998.10480550

Aisen, P. S., Petersen, R. C., Donohue, M. C., Gamst, A., Raman, R., Thomas, R. G., et al. (2010). Clinical core of the Alzheimer's disease neuroimaging initiative: progress and plans. *Alzheimers Dement.* 6, 239–246. doi: 10.1016/j.jalz.2010.03.006

Allison, J. R., Rivers, R. C., Christodoulou, J. C., Vendruscolo, M., and Dobson, C. M. (2014). A relationship between the transient structure in the monomeric state and the aggregation propensities of α-synuclein and β-synuclein. *Biochemistry* 53, 7170–7183. doi: 10.1021/bi5009326

Ardekani, B. A., Bermudez, E., Mubeen, A. M., and Bachman, A. H. (2016). Prediction of incipient Alzheimer's disease dementia in patients with mild cognitive impairment. *J. Alzheimers Dis.* 55, 269–281. doi: 10.3233/JAD-160594

Bates, G. E., and McNemar, Q. (1964). Psychological statistics. *Am. Math. Mon.* 71:812. doi: 10.2307/2310937

Beheshti, I., Demirel, H., and Matsuda, H. (2017). Classification of Alzheimer's disease and prediction of mild cognitive impairment-to-Alzheimer's conversion from structural magnetic resource imaging using feature ranking and a genetic algorithm. *Comput. Biol. Med.* 83, 109–119. doi: 10.1016/j.compbiomed.2017.02.011

Bischkopf, J., Busse, A., and Angermeyer, M. C. (2002). Mild cognitive impairment – a review of prevalence, incidence and outcome according to current approaches. *Acta Psychiatr. Scand.* 106, 403–414. doi: 10.1034/j.1600-0447.2002.01417.x

Braak, H., and Braak, E. (1991). Neuropathological stageing of Alzheimer-related changes. *Acta Neuropathol.* 82, 239–259. doi: 10.1007/bf00308809

Breiman, L. (2001). Random forests. *Mach. Learn.* 45, 5–32. doi: 10.1023/A:1010933404324

Cauda, F., Nani, A., Manuello, J., Premi, E., Palermo, S., Tatu, K., et al. (2018). Brain structural alterations are distributed following functional, anatomic and genetic connectivity. *Brain* 141, 3211–3232. doi: 10.1093/brain/awy252

Chang, C.-C., and Lin, C.-J. (2011). LIBSVM. *ACM Trans. Intell. Syst. Technol.* 2, 1–27. doi: 10.1145/1961189.1961199

Chu, C., Hsu, A. L., Chou, K. H., Bandettini, P., and Lin, C. P. (2012). Does feature selection improve classification accuracy? Impact of sample size and feature selection on classification using anatomical magnetic resonance images. *Neuroimage* 60, 59–70. doi: 10.1016/j.neuroimage.2011.11.066

Ciric, R., Wolf, D. H., Power, J. D., Roalf, D. R., Baum, G. L., Ruparel, K., et al. (2017). Benchmarking of participant-level confound regression strategies for the control of motion artifact in studies of functional connectivity. *Neuroimage* 154, 174–187. doi: 10.1016/j.neuroimage.2017.03.020

Cui, Y., Liu, B., Luo, S., Zhen, X., Fan, M., Liu, T., et al. (2011). Identification of conversion from mild cognitive impairment to alzheimer's disease using multivariate predictors. *PLoS One* 6:e21896. doi: 10.1371/journal.pone.0021896

Dai, Z., Lin, Q., Li, T., Wang, X., Yuan, H., Yu, X., et al. (2019). Disrupted structural and functional brain networks in Alzheimer's disease. *Neurobiol. Aging* 75, 71–82. doi: 10.1016/j.neurobiolaging.2018.11.005

Das, S. R., Pluta, J., Mancuso, L., Kliot, D., Yushkevich, P. A., and Wolk, D. A. (2015). Anterior and posterior MTL networks in aging and MCI. *Neurobiol. Aging* 36, S141–S150. doi: 10.1016/j.neurobiolaging.2014.03.041

DeLong, E. R., DeLong, D. M., and Clarke-Pearson, D. L. (1988). Comparing the areas under two or more correlated receiver operating characteristic curves: a nonparametric approach. *Biometrics* 44:837. doi: 10.2307/2531595

Desikan Rahul, S., Florent, S., Bruce, F., Quinn Brian, T., Dickerson Bradford, C., Deborah, B., et al. (2006). An automated labeling system for subdividing the human cerebral cortex on MRI scans into gyral based regions of interest. *Neuroimage* 31, 968–980. doi: 10.1016/j.neuroimage.2006.01.021

Dubey, R., Zhou, J., Wang, Y., Thompson, P. M., Ye, J., Alzheimer's Disease, et al. (2013). Analysis of sampling techniques for imbalanced data: an n=648 ADNI study. *Neuroimage* 87, 220–241. doi: 10.1016/j.neuroimage.2013.10.005

Eskildsen, S. F., Coupé, P., García-Lorenzo, D., Fonov, V., Pruessner, J. C., and Collins, D. L. (2013). Prediction of Alzheimer's disease in subjects with mild cognitive impairment from the ADNI cohort using patterns of cortical thinning. *Neuroimage* 65, 511–521. doi: 10.1016/j.neuroimage.2012.09.058

Fan, Y., Batmanghelich, N., Clark, C. M., and Davatzikos, C. (2008). Spatial patterns of brain atrophy in MCI patients, identified via high-dimensional pattern classification, predict subsequent cognitive decline. *Neuroimage* 39, 1731–1743. doi: 10.1016/j.neuroimage.2007.10.031

Fan, Y., Gao, Y., Therriault, J., Luo, J., Ba, M., and Zhang, H. (2021). The effects of CSF neurogranin and APOE ε 4 on cognition and neuropathology in mild cognitive impairment and Alzheimer's Disease. *Front. Aging Neurosci.* 13:667899. doi: 10.3389/fnagi.2021.667899

Fawcett, T. (2006). An introduction to ROC analysis. *Pattern Recognit. Lett.* 27, 861–874. doi: 10.1016/j.patrec.2005.10.010

Fischl, B., Salat, D. H., Busa, E., Albert, M., Dieterich, M., Haselgrove, C., et al. (2002). Whole brain segmentation: automated labeling of neuroanatomical structures in the human brain. *Neuron* 33, 341–355. doi: 10.1016/S0896-6273(02)00569-X

Friston, K. J., Ashburner, J. T., Kiebel, S. J., Nichols, T. E., and Penny, W. D. (2007). *Statistical Parametric Mapping*. Elsevier, AcademicPress, USA. doi: 10.1016/B978-012372560-Q218/50002-4

Golob, E. J., Irimajiri, R., and Starr, A. (2007). Auditory cortical activity in amnestic mild cognitive impairment: relationship to subtype and conversion to dementia. *Brain* 130, 740–752. doi: 10.1093/brain/awl375

Gupta, Y., Kim, J., Kim, B. C., and Kwon, G. (2020). Classification and graphical analysis of Alzheimer ' s disease and its prodromal stage using multimodal features from structural, diffusion, and functional neuroimaging data and the APOE genotype. *Front. Aging Neurosci.* 12:238. doi: 10.3389/fnagi.2020.00238

Hastie, T., Rosset, S., Zhu, J., and Zou, H. (2009). Multi-class AdaBoost. *Stat. Interface* 2, 349–360. doi: 10.4310/sii.2009.v2.n3.a8

He, Y., Chen, Z., Gong, G., and Evans, A. (2009). Neuronal networks in Alzheimer's disease. *Neuroscientist* 15, 333–350. doi: 10.1177/1073858409334423

Hernes, S. S., Flak, M. M., Løhaugen, G. C. C., Skranes, J., Hol, H. R., Madsen, B., et al. (2021). Working memory training in amnestic and non-amnestic patients with mild cognitive impairment: preliminary findings from genotype variants on training effects. *Front. Aging Neurosci.* 13:624253. doi: 10.3389/fnagi.2021.624253

Hojjati, S. H., Ebrahimzadeh, A., Khazaee, A., and Babajani-Feremi, A. (2017). Predicting conversion from MCI to AD using resting-state fMRI, graph theoretical approach and SVM. *J. Neurosci. Methods* 282, 69–80. doi: 10.1016/j.jneumeth.2017.03.006

Hojjati, S. H., Ebrahimzadeh, A., Khazaee, A., and Babajani-Feremi, A. (2018). Predicting conversion from MCI to AD by integrating rs-fMRI and structural MRI. *Comput. Biol. Med.* 102, 30–39. doi: 10.1016/j.compbiomed.2018.09.004

Hu, K., Wang, Y., Chen, K., Hou, L., and Zhang, X. (2015). Multi-scale features extraction from baseline structure MRI for MCI patient classification and AD early diagnosis. *Neurocomputing* 175, 132–145. doi: 10.1016/j.neucom.2015.10.043

Ibrahim, B., Suppiah, S., and Ibrahim, N. (2021). Diagnostic power of resting-state fMRI for detection of network connectivity in Alzheimer' s disease and mild cognitive impairment: a systematic review. *Hum. Brain Mapp.* 42, 2941–2968. doi: 10.1002/hbm.25369

Jack, C. R., Bernstein, M. A., Fox, N. C., Thompson, P., Alexander, G., Harvey, D., et al. (2008). The Alzheimer's Disease Neuroimaging Initiative (ADNI): MRI methods. *J. Magn. Reson. Imaging* 27, 685–691. doi: 10.1002/jmri.21049

Jie, B., Zhang, D., Gao, W., Wang, Q., Wee, C., Shen, D., et al. (2014). Integration of network topological and connectivity properties for neuroimaging classification. *IEEE Trans. Biomed. Eng.* 61, 576–589. doi: 10.1109/tbme.2013.2284195

Khazaee, A., Ebrahimzadeh, A., and Babajani-Feremi, A. (2015). Identifying patients with Alzheimer's disease using resting-state fMRI and graph theory. *Clin. Neurophysiol.* 126, 2132–2141. doi: 10.1016/j.clinph.2015.02.060

Khazaee, A., Ebrahimzadeh, A., and Babajani-Feremi, A. (2017). Classification of patients with MCI and AD from healthy controls using directed graph measures of resting-state fMRI. *Behav. Brain Res.* 322(Pt B), 339–350. doi: 10.1016/j.bbr.2016.06.043

Lee, G. J., Lu, P. H., Hua, X., Lee, S., Wu, S., Nguyen, K., et al. (2012). Depressive symptoms in mild cognitive impairment predict greater atrophy in alzheimer's disease-related regions. *Biol. Psychiatry* 71, 814–821. doi: 10.1016/j.biopsych.2011.12.024

Li, S., Harner, E. J., and Adjeroh, D. A. (2011). Random KNN feature selection – a fast and stable alternative to random forests. *BMC Bioinformatics* 12:450. doi: 10.1186/1471-2105-12-450

Li, Y., Wang, Y., Wu, G., Shi, F., Zhou, L., Lin, W., et al. (2012). Discriminant analysis of longitudinal cortical thickness changes in Alzheimer's disease using dynamic and network features. *Neurobiol. Aging* 33, e15–e427. doi: 10.1016/j.neurobiolaging.2010.11.008

Liu, F., Wee, C. Y., Chen, H., and Shen, D. (2014). Inter-modality relationship constrained multi-modality multi-task feature selection for Alzheimer's disease and mild cognitive impairment identification. *Neuroimage* 84, 466–475. doi: 10.1016/j.neuroimage.2013.09.015

Liu, J., Ji, S., and Ye, J. (2009). {SLEP}: sparse learning with efficient projections. *Arizona State Univ. Note* 6:491. Retrieved from http://www.public.asu.edu/~jye02/Software/SLEP,

Liu, Z., Zhang, Y., Yan, H., Bai, L., Dai, R., Wei, W., et al. (2012). Altered topological patterns of brain networks in mild cognitive impairment and Alzheimer's disease: a resting-state fMRI study. *Psychiatry Res.* 202, 118–125. doi: 10.1016/j.pscychresns.2012.03.002

Mascali, D., Dinuzzo, M., Gili, T., Moraschi, M., Fratini, M., Maraviglia, B., et al. (2015). Intrinsic patterns of coupling between correlation and amplitude of low-frequency fMRI fluctuations are disrupted in degenerative dementia mainly due to functional disconnection. *PLoS One* 10:e0120988. doi: 10.1371/journal.pone.0120988

Mei, X., Lee, H. C., Diao, K. Y., Huang, M., Lin, B., Liu, C., et al. (2020). Artificial intelligence–enabled rapid diagnosis of patients with COVID-19. *Nat. Med.* 26, 1224–1228. doi: 10.1038/s41591-020-0931-3

Meinshausen, N., and Bühlmann, P. (2010). Stability selection. *J R Stat. Soc. Ser. B Stat. Methodol.* 72, 417–473. doi: 10.1111/j.1467-9868.2010.00740.x

Mercaldo, N. D., Lau, K. F., and Zhou, X. H. (2007). Confidence intervals for predictive values with an emphasis to case-control studies. *Stat. Med.* 26, 2170–2183. doi: 10.1002/sim.2677

Moradi, E., Pepe, A., Gaser, C., Huttunen, H., and Tohka, J. (2015). Machine learning framework for early MRI-based Alzheimer's conversion prediction in MCI subjects. *Neuroimage* 104, 398–412. doi: 10.1016/j.neuroimage.2014.10.002

Morgado, P. M., and Silveira, M. (2015). Minimal neighborhood redundancy maximal relevance: application to the diagnosis of Alzheimer's disease. *Neurocomputing* 155, 295–308. doi: 10.1016/j.neucom.2014.12.070

Naël, V., Pérès, K., Dartigues, J. F., Letenneur, L., Amieva, H., Arleo, A., et al. (2019). Vision loss and 12-year risk of dementia in older adults: the 3C cohort study. *Eur. J. Epidemiol.* 34, 141–152. doi: 10.1007/s10654-018-00478-y

Nickl-Jockschat, T., Kleiman, A., Schulz, J. B., Schneider, F., Laird, A. R., Fox, P. T., et al. (2012). Neuroanatomic changes and their association with cognitive decline in mild cognitive impairment: a meta-analysis. *Brain Struct. Funct.* 217, 115–125. doi: 10.1007/s00429-011-0333-x

Pandya, S., Mezias, C., and Raj, A. (2017). Predictive model of spread of progressive supranuclear palsy using directional network diffusion. *Front. Neurol.* 8:692. doi: 10.3389/fneur.2017.00692

Peng, H., Long, F., and Ding, C. (2005). Feature selection based on mutual information: criteria of max-dependency, max-relevance, and min-redundancy. *IEEE Trans. Pattern Anal. Mach. Intell.* 27, 1226–1238. doi: 10.1109/TPAMI.2005.159

Pohjalainen, J., Räsänen, O., and Kadioglu, S. (2015). Feature selection methods and their combinations in high-dimensional classification of speaker likability, intelligibility and personality traits. *Comput. Speech Lang.* 29, 145–171. doi: 10.1016/j.csl.2013.11.004

Pusil, S., López, M. E., Cuesta, P., Bruña, R., Pereda, E., and Maestú, F. (2019). Hypersynchronization in mild cognitive impairment: the 'X' model. *Brain* 142, 3936–3950. doi: 10.1093/brain/awz320

Raamana, P. R., Weiner, M. W., Wang, L., and Beg, M. F. (2015). Thickness network features for prognostic applications in dementia. *Neurobiol. Aging* 36, S91–S102. doi: 10.1016/j.neurobiolaging.2014.05.040

Rasero, J., Alonso-Montes, C., Diez, I., Olabarrieta-Landa, L., Remaki, L., Escudero, I., et al. (2017). Group-level progressive alterations in brain connectivity patterns revealed by diffusion-tensor brain networks across severity stages in Alzheimer's disease. *Front. Aging Neurosci.* 9:215. doi: 10.3389/fnagi.2017.00215

Sanz-Arigita, E. J., Schoonheim, M. M., Damoiseaux, J. S., Rombouts, S. A. R. B., Maris, E., Barkhof, F., et al. (2010). Loss of "Small-World" networks in Alzheimer's disease: graph analysis of fMRI resting-state functional connectivity. *PLoS One* 5:e13788. doi: 10.1371/journal.pone.0013788

Song, X. W., Dong, Z. Y., Long, X. Y., Li, S. F., Zuo, X. N., Zhu, C. Z., et al. (2011). REST: a toolkit for resting-state functional magnetic resonance imaging data processing. *PLoS One* 6:e25031. doi: 10.1371/journal.pone.0025031

Suk, H. l., Lee, S. W., and Shen, D. (2015). Latent feature representation with stacked auto-encoder for AD/MCI diagnosis. *Brain Struct. Funct.* 220, 841–859. doi: 10.1007/s00429-013-0687-3

Suk, H. l., Lee, S. W., and Shen, D. (2016). Deep sparse multi-task learning for feature selection in Alzheimer's disease diagnosis. *Brain Struct. Funct.* 221, 2569–2587. doi: 10.1007/s00429-015-1059-y

Suk, H. l., and Shen, D. (2014). Subclass-based multi-task learning for Alzheimer's disease diagnosis. *Front. Aging Neurosci.* 6:168. doi: 10.3389/fnagi.2014.00168

Tan, B., Liu, Q., Wan, C., Jin, Z., Yang, Y., and Li, L. (2019). Altered functional connectivity of alpha rhythm in obsessive-compulsive disorder during rest. *Clin. EEG Neurosci.* 50, 88–99. doi: 10.1177/1550059418804378

Tzourio-Mazoyer, N., Landeau, B., Papathanassiou, D., Crivello, F., Etard, O., Delcroix, N., et al. (2002). Automated anatomical labeling of activations in SPM using a macroscopic anatomical parcellation of the MNI MRI single-subject brain. *Neuroimage* 15, 273–289. doi: 10.1006/nimg.2001.0978

Uhlmann, R. F., Larson, E. B., Koepsell, T. D., Rees, T. S., and Duckert, L. G. (1991). Visual impairment and cognitive dysfunction in Alzheimer's disease. *J. Gen. Intern. Med.* 6, 126–132. doi: 10.1007/BF02598307

Wang, Z., Xia, M., Dai, Z., Liang, X., Song, H., He, Y., et al. (2015). Differentially disrupted functional connectivity of the subregions of the inferior parietal lobule in Alzheimer's disease. *Brain Struct. Funct.* 220, 745–762. doi: 10.1007/s00429-013-0681-9

Wee, C. Y., Yap, P. T., Denny, K., Browndyke, J. N., Potter, G. G., Welsh-Bohmer, K. A., et al. (2012a). Resting-state multi-spectrum functional connectivity networks for identification of MCI patients. *PLoS One* 7:e37828. doi: 10.1371/journal.pone.0037828

Wee, C. Y., Yap, P. T., Zhang, D., Denny, K., Browndyke, J. N., Potter, G. G., et al. (2012b). Identification of MCI individuals using structural and functional connectivity networks. *Neuroimage* 59, 2045–2056. doi: 10.1016/j.neuroimage.2011.10.015

Wee, C. Y., Yap, P. T., Zhang, D., Wang, L., and Shen, D. (2014). Group-constrained sparse fMRI connectivity modeling for mild cognitive impairment identification. *Brain Struct. Funct.* 219, 641–656. doi: 10.1007/s00429-013-0524-8

Wei, R., Li, C., Fogelson, N., and Li, L. (2016). Prediction of conversion from mild cognitive impairment to Alzheimer's disease using MRI and structural network features. *Front. Aging Neurosci.* 8:76. doi: 10.3389/fnagi.2016.00076

Wolz, R., Julkunen, V., Koikkalainen, J., Niskanen, E., Zhang, D. P., Rueckert, D., et al. (2011). Multi-method analysis of MRI images in early diagnostics of Alzheimer's disease. *PLoS One* 6:e25446. doi: 10.1371/journal.pone.0025446

Yan, C., and Zang, Y. (2010). DPARSF: a MATLAB toolbox for "pipeline" data analysis of resting-state fMRI. *Front. Syst. Neurosci.* 4:13. doi: 10.3389/fnsys.2010.00013

Yang, S., Jian, H., Ding, Z., Hongyuan, Z., and Giles, C. L. (2007). "IKNN: informative K-nearest neighbor pattern classification," in *Lecture Notes in Computer Science (Including Subseries Lecture Notes in Artificial Intelligence and Lecture Notes in Bioinformatics)* Vol. 4702, eds J.N. Kok, J. Koronacki, R. Lopez de Mantaras, S. Matwin, D. Mladenič, A. Skowron (Berlin: Springer), 248–264. doi: 10.1007/978-3-540-74976-9_25

Yates, D. (2012). Neurodegenerative networking. *Nat. Rev. Neurosci.* 13:289. doi: 10.1038/nrn3248

Ye, J., Farnum, M., Yang, E., Verbeeck, R., Lobanov, V., Raghavan, N., et al. (2012). Sparse learning and stability selection for predicting MCI to AD conversion using baseline ADNI data. *BMC Neurol.* 12:46. doi: 10.1186/1471-2377-12-46

Zhan, L., Jahanshad, N., Jin, Y., Toga, A. W., McMahon, K. L., De Zubicaray, G. I., et al. (2013). "Brain network efficiency and topology depend on the fiber tracking method: 11 tractography algorithms compared in 536 subjects," in *Proceedings of the International Symposium on Biomedical Imaging* (San Francisco, CA: IEEE), 1134–1137. doi: 10.1109/ISBI.2013.6556679

Zhang, D., and Shen, D. (2012). Multi-modal multi-task learning for joint prediction of multiple regression and classification variables in Alzheimer's disease. *Neuroimage* 59, 895–907. doi: 10.1016/j.neuroimage.2011.09.069

Zhang, D., Wang, Y., Zhou, L., Yuan, H., and Shen, D. (2011). Multimodal classification of Alzheimer's disease and mild cognitive impairment. *Neuroimage* 55, 856–867. doi: 10.1016/j.neuroimage.2011.01.008

Zhang, T., Zhao, Z., Zhang, C., Zhang, J., Jin, Z., and Li, L. (2019). Classification of early and late mild cognitive impairment using functional brain network of resting-state fMRI. *Front. Psychiatry* 10:572. doi: 10.3389/fpsyt.2019.00572

Zhang, Y., Qiu, T., Yuan, X., Zhang, J., Wang, Y., Zhang, N., et al. (2019). Abnormal topological organization of structural covariance networks in amyotrophic lateral sclerosis. *Neuroimage Clin.* 21:101619. doi: 10.1016/j.nicl.2018.101619

Zheng, W., Yao, Z., Li, Y., Zhang, Y., Hu, B., and Wu, D. (2019). Brain connectivity based prediction of Alzheimer's disease in patients with mild cognitive impairment based on multi-modal images. *Front. Hum. Neurosci.* 13:399. doi: 10.3389/fnhum.2019.00399

Zhu, W., Sun, L., Huang, J., Han, L., and Zhang, D. (2021). Dual attention multi-instance deep learning for Alzheimer's disease diagnosis with structural MRI. *IEEE Trans. Med. Imaging*, 1–13. [Epub ahead of print]. doi: 10.1109/TMI.2021.3077079

Zuo, X. N., Di Martino, A., Kelly, C., Shehzad, Z. E., Gee, D. G., Klein, D. F., et al. (2010). The oscillating brain: complex and reliable. *Neuroimage* 49, 1432–1445. doi: 10.1016/j.neuroimage.2009.09.037

Conflict of Interest: The authors declare that the research was conducted in the absence of any commercial or financial relationships that could be construed as a potential conflict of interest.

frontiers in Aging Neuroscience

ORIGINAL RESEARCH
published: 06 August 2021
doi: 10.3389/fnagi.2021.687001

The Contribution of White Matter Diffusion and Cortical Perfusion Pathology to Vascular Cognitive Impairment: A Multimode Imaging-Based Machine Learning Study

Yao Wang[1†], Peiwen Lu[2†], Yafeng Zhan[3†], Xiaowei Wu[1], Yage Qiu[1], Zheng Wang[3], Qun Xu[2] and Yan Zhou[1*]*

[1] Department of Radiology, RenJi Hospital, School of Medicine, Shanghai Jiao Tong University, Shanghai, China, [2] Department of Neurology, RenJi Hospital, School of Medicine, Shanghai Jiao Tong University, Shanghai, China, [3] Center for Excellence in Brain Science and Intelligence Technology, State Key Laboratory of Neuroscience, Key Laboratory of Primate Neurobiology, Institute of Neuroscience, Chinese Academy of Sciences, Shanghai, China

OPEN ACCESS

Edited by:
Behrooz Hooshyar Yousefi, University of Marburg, Germany

Reviewed by:
Kuangyu Shi, University of Bern, Switzerland
Mustapha Bouhrara, National Institutes of Health (NIH), United States
Masafumi Ihara, National Cerebral and Cardiovascular Center, Japan

***Correspondence:**
Qun Xu
xuqun628@hotmail.com
Yan Zhou
clare1475@hotmail.com

[†] These authors have contributed equally to this work

Received: *28 March 2021*
Accepted: *02 July 2021*
Published: *06 August 2021*

Citation:
Wang Y, Lu P, Zhan Y, Wu X, Qiu Y, Wang Z, Xu Q and Zhou Y (2021) The Contribution of White Matter Diffusion and Cortical Perfusion Pathology to Vascular Cognitive Impairment: A Multimode Imaging-Based Machine Learning Study. Front. Aging Neurosci. 13:687001. doi: 10.3389/fnagi.2021.687001

Widespread impairments in white matter and cerebrovascular integrity have been consistently implicated in the pathophysiology of patients with small vessel disease (SVD). However, the neural circuit mechanisms that underlie the developing progress of clinical cognitive symptoms remain largely elusive. Here, we conducted cross-modal MRI scanning including diffusion tensor imaging and arterial spin labeling in a cohort of 113 patients with SVD, which included 74 patients with vascular mild cognitive impairment (vMCI) and 39 patients without vMCI symptoms, and hence developed multimode imaging-based machine learning models to identify markers that discriminated SVD subtypes. Diffusion and perfusion features, respectively, extracted from individual white matter and gray matter regions were used to train three sets of classifiers in a nested 10-fold fashion: diffusion-based, perfusion-based, and combined diffusion-perfusion-based classifiers. We found that the diffusion-perfusion combined classifier achieved the highest accuracy of 72.57% with leave-one-out cross-validation, with the diffusion features largely spanning the capsular lateral pathway of the cholinergic tracts, and the perfusion features mainly distributed in the frontal-subcortical-limbic areas. Furthermore, diffusion-based features within vMCI group were associated with performance on executive function tests. We demonstrated the superior accuracy of using diffusion-perfusion combined multimode imaging features for classifying vMCI subtype out of a cohort of patients with SVD. Disruption of white matter integrity might play a critical role in the progression of cognitive impairment in patients with SVD, while malregulation of coritcal perfusion needs further study.

Keywords: small vessel disease, multimode imaging, machine learning, diffusion tensor imaging, arterial spin labeling

INTRODUCTION

Vascular dysfunction and associated cerebral damage have been identified as critical components of the pathophysiology of late-life dementia, and may constitute the predominant pathological cause of cognitive impairment in East Asia (Iadecola et al., 2019). Patients with small vessel disease (SVD) have recently been receiving increasing attention because of its high prevalence (Rosenberg et al., 2016; Wardlaw et al., 2019). SVD is generally referred to as a disorder of cerebral microvessels causing widespread physiological and structural abnormalities including subcortical lacunar infarcts, white matter hyperintensities (WMH), and microbleeds (Pantoni, 2010; Rosenberg et al., 2016). The pathogenesis of SVD has been attributed to a wide variety of pathological events including vessel occlusion, leakage of toxins, impaired vascular reactivity, decreased clearance of waste products, oligodendrocyte dysfunction, increased oxidation, and inflammation. These pathological events give rise to diverse brain lesions that are able to be detected by using different imaging modalities (Schuff et al., 2009; Duering et al., 2015; Sun et al., 2016; Duncombe et al., 2017; Muñoz Maniega et al., 2017), although the relationships between the imaged lesions and clinical symptoms remain poorly understood (Wardlaw et al., 2013, 2019). As the management of risk factors and symptom-specific treatment could help prevent the evolution of small vascular mild cognitive impairment (vMCI, the prodromal stage of vascular dementia) to vascular dementia (Seo et al., 2010), there is an urgent need to identify imaging-based biomarkers for early diagnosis and monitoring disease progression.

Aggregated evidence obtained from case-control designs has demonstrated associations between cognitive decline in patients with SVD and widespread cerebral impairments of various kinds such as cerebral perfusion and WM integrity (O'Sullivan et al., 2001, 2004; Tuladhar et al., 2015; Shi et al., 2016; Malojcic et al., 2017; Li et al., 2018; Liu et al., 2020; Yu et al., 2020). For instance, with the developed three dimensional arterial spin labeling (3D-ASL) technique, Sun and colleagues found (Sun et al., 2016) widespread lower cerebral blood flow (CBF) in patients with symptomatic SVD in comparison to patients with non-symptomatic SVD, particularly where deficits in brain perfusion in the temporal and frontal lobe, hippocampus, thalamus, and insula were related to the degree of cognitive impairment. Reduced CBF, impaired cerebral autoregulation, and increased blood–brain barrier permeability were also manifested in subcortical areas of patients with SVD (Li et al., 2018). Region-specific malregulation of CBF has been suggested as a critical factor in SVD-related dementia, which may be linked to the progression of cognitive decline and hence used to track the course of disease progression (Shi et al., 2016; Malojcic et al., 2017). Moreover, in addition to lower perfusion-related cortical atrophy often reported in SVD, Schuff et al. (2009) observed a volumetric increase in subcortical WMH associated with reduced CBF in the frontal cortex. Meanwhile, Yu et al. (2020) reported a tight correlation of total SVD burden score (composed of lacunes, cerebral microbleeds, and enlarged perivascular spaces) with both global and regional CBF. Diffusion tensor imaging (DTI) is a sensitive technique to detect subtle changes of WM microstructural integrity, researchers have found that cognitive disturbances in subjects with SVD were related to abnormalities of multiple WM fibers connecting different cortical and subcortical regions (Tuladhar et al., 2015; Liu et al., 2020). It has been postulated that long-term hypoperfusion contributes to impairment of WM integrity, thereby leading to subcortical–cortical and cortical–cortical dysconnectivity, which is linked to diverse cognitive domains, namely "disconnection syndrome" (O'Sullivan et al., 2004). The disconnection of frontal–subcortical circuits is believed to be the underlying mechanism of cognitive impairment in SVD (O'Sullivan et al., 2001; Pantoni, 2010). However, whether and how cortical perfusion and WM damage jointly contribute to the early stage of cognitive impairment in patients with SVD remains unclear, which holds great implication for disease prevention and treatment.

To this end, we developed a cross-modal multimode imaging-based machine learning approach to investigate both diffusion and perfusion disturbances in a cohort of 113 patients with SVD, of which 74 were SVD patients with vMCI. We conducted a comprehensive battery of neuropsychological tests including attention, executive function, language, and working memory tests, and collected both DTI and ASL data from all subjects. From the imaging data, we extracted WM diffusion and cortical perfusion features including mean fractional anisotropy (FA), mean diffusivity (MD), axial diffusivity (AD), radial diffusivity (RD), and CBF within multiple regions of interest (ROIs) defined according to widely used gray and WM templates. Using diffusion-based, perfusion-based, and combined diffusion-perfusion features, we trained three sets of sparse logistic regression (SLR) classifiers to distinguish patients with vMCI from patients with normal cognition (control patients). Classification accuracy was evaluated using leave-one-out cross validation (LOOCV) and statistical comparisons were made between the three classifiers. Furthermore, we used the partial correlations to examine associations between the identified discriminative features and cognitive functions. Our research objective was to characterize abnormalities in gray matter perfusion and WM integrity, and enhance the understanding of the pathological evolution of cognitive decline in patients with SVD.

MATERIALS AND METHODS

Participants

One hundred and thirteen patients with SVD were recruited from the Department of Neurology at RenJi Hospital between August 2017 and January 2020. SVD can be defined as subcortical WM hyperintensity on T2-weighted images with at least one lacunar infarct, following the criteria suggested by Galluzzi et al. (2005). Each subject underwent a standard evaluation, including neurological examination, complete sociodemographic and clinical data, and MRI examination. The inclusion criteria were as follows: (1) at least 6 years for education; (2) age 50–85 years; (3) informed consent form signed by the participant (Galluzzi et al., 2005). The following exclusion criteria were applied: (1) cortical and/or cortico-subcortical non-lacunar territorial infarcts and watershed infarcts; (2) neurodegenerative

diseases (including Parkinson's disease and Alzheimer's disease); (3) signs of normal pressure hydrocephalus; (4) specific causes of WMH (e.g., metabolic, toxic, infectious, multiple sclerosis, brain irradiation); (5) alcoholic encephalopathy or illicit drug use; (6) major depression [Hamilton Depression Rating Scale (HDRS) $\geq$ 18]; (7) severe cognitive impairment (inability to perform the neuropsychological test or undergo the whole MRI scan); (8) MRI safety contraindications and claustrophobia (Galluzzi et al., 2005). All patients underwent laboratory examinations to exclude systemic or other neurological diseases.

Neuropsychological Assessment

Neuropsychological assessments were performed within 1 week of the MRI examination. No patients suffered any transient ischemic attacks or strokes between the MRI examination and the evaluation. The Montreal Cognitive Assessment (MoCA) and Mini-Mental State Examination (MMSE) were used to assess overall cognitive performance. Moreover, a comprehensive battery of neuropsychological tests was designed to evaluate four key cognitive domains as described in previous studies (Hachinski et al., 2006; Xu et al., 2014). These tests were as follows: (1) attention and executive function: Trail-Making Tests A and B (TMT-A and TMT-B), Stroop color-word test (Stroop C-T), and verbal fluency test (VFT); (2) visuospatial function: Rey-Osterrieth Complex Figure Test (copy); (3) language function: Boston Naming Test (30 items); (4) memory function: auditory verbal learning test (short and long delayed free recall). Functional ability was assessed using the Katz basic activities of daily living (BADL) and Lawton and Brody instrumental activities of daily living (IADL) scales. The norms used here were based on mean scores of each measurement from a sample of typical elderly community members in Shanghai, China (Guo et al., 2007). Cognitive impairment was defined as 1.5 standard deviations below the normative mean on any neuropsychological test. The diagnostic criteria of vMCI included: (1) subjective cognitive difficulty reported by the patient or caregiver; (2) quantifiable cognitive decline within one or more cognitive domains (e.g., attention-executive function, memory, language, or visuospatial function); (3) normal instrumental activity of daily living. Controls were defined as SVD with no cognitive impairment, which means the scores of patients in all neuropsychological tests were within the normal range. After checking for the high quality of clinical and imaging data of enrolled participants, 74 vMCI participants and 39 age-, sex-, and education- matched controls were finally included in this study.

MRI Acquisition

All MRI data were obtained using a 3.0 T MRI scanner (Signa HDxt; GE HealthCare, Milwaukee, WI, USA) equipped with an eight-channel phased array head coil. The following whole-brain sequences were obtained: (1) The sagittal T1-weighted images covering the whole brain were acquired by the 3D-fast spoiled gradient recalled echo (SPGR) sequence [repetition time (TR) = 5.6 ms, echo time (TE) = 1.8 ms, inversion time (TI) = 450 ms, flip angle = 15°, slice thickness = 1.0 mm, number of slices = 156, gap = 0, field of view (FOV) = 256 × 256 mm, and matrix = 256 × 256, scanning time=3′53″]; (2) T2-fluid attenuated inversion recovery (FLAIR) sequences (TR = 9,075 ms, TE = 150 ms, TI = 2,250 ms, FOV = 256 × 256 mm, matrix = 256 × 256, slice thickness = 2 mm, and number of slices = 66, scanning time=7′18″); (3) DTI (TR = 17,000 ms, TE = 89.8 ms, slice thickness = 2 mm, gap = 0, FOV = 256 × 256 mm, number of slices = 66, matrix = 128 × 128, and 20 diffusion-weighted directions with b-value = 1,000 s/mm^2, scanning time = 6′14″); (4) Pseudocontinuous ASL (pCASL) images were acquired using 3D fast spin-echo acquisition with background suppression and with a labeling duration of 1,500 ms and a post labeling delay of 2,000 ms, one control and one labeled images were acquired (TR = 4,337 ms, TE = 9.8 ms, FOV = 240 × 240 mm, slice thickness = 4 mm, flip angle = 155°, NEX = 3, and number of slices = 34 scanning time = 4′12″). The total scanning time is 21′39″.

MRI Data Preprocessing

Processing of the diffusion MRI dataset was implemented using a pipeline toolbox, PANDA v1.3.1 (https://www.nitrc.org/ projects/panda), which is based on FMRIB's Software Library (FSL) tools. In the pipeline, skull-stripping with the brain extraction tool (BET) was done to extract brain tissue for b0 image in each subject. Eddy current-induced distortion and head motion artifacts were corrected by registering each raw diffusion-weighted image to the b0 image with an affine transformation. Diffusion metrics including FA, MD, AD, and RD were calculated within a mask created from b0 image. ASL images were post-processed at a General Electric Company (GE) workstation, version 4.4. ASL images of each subject were inspected for the excessive head movement ($\geq$2 mm or 2°), and the area outside of the brain was excluded, then the quantitative CBF map of each subject was calculated.

The image registration was performed using Advanced Normalization Tools (ANTs) (http://stnava.github.io/ANTs/). The Johns Hopkins University International Consortium for Brain Mapping (ICBM)-DTI-81 FA template (Mori et al., 2008) was registered to the FA map of each individual using ANTs deformable registration. This transformation was inversed to warp the labels of WM regions in Johns Hopkins University ICBM atlas to individual FA space through General Label interpolation (WM regions listed in **Supplementary Table 1**). Quality control was performed through visual inspection of the FA map of each subject and the wrapped atlas in individual space. The CBF maps were skull-stripped by FSL with manual correction and then registered to 3D-T1WI structure imaging, the 3D-T1WI images were used for image registration and normalization into a standardized space that is consistent with the AAL template, with a reslicing resolution of 2 × 2 × 2 mm^3. Mean values of diffusion parameter maps for each WM label were extracted. Moreover, the mean CBF value of GM labels in the AAL template was obtained. A total of 308 features, including 192 diffusion features and 116 CBF features, were extracted for each individual.

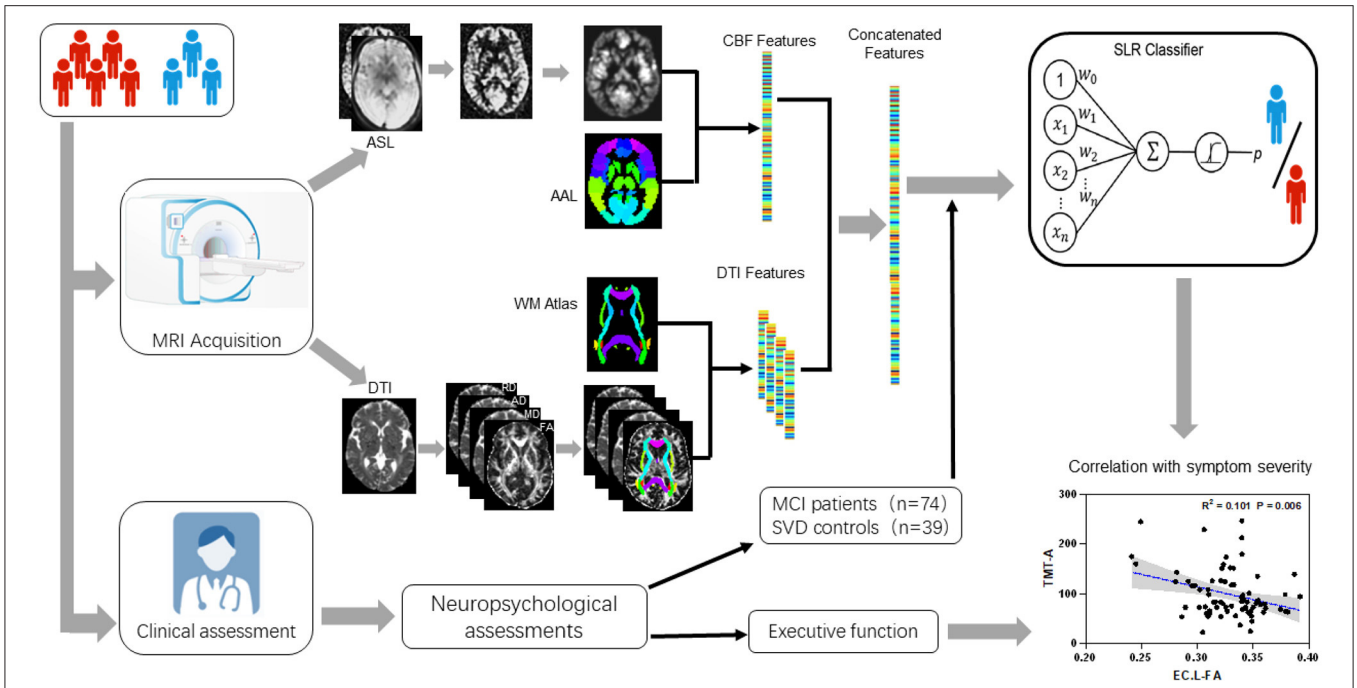

FIGURE 1 | Research flow chart including: MRI procedures from DTI and ASL data collecting to features extracting, multimode imaging features including mean FA/MD/AD/RD and CBF within multiple ROIs defined by widely used ICBM templates for white matter diffusion features and AAL templates for gray matter perfusion features; A comprehensive battery of neuropsychological tests including general cognitive function, attention-executive function, visuospatial function, language and working memory, functional ability; Three sets of sparse logistic regression (SLR) classifiers were trained using diffusion-based, perfusion-based, and diffusion-perfusion combined features; Correlation of the final selected features with executive function.

TABLE 1 | Demographic and executive function characteristics.

	vMCI	Controls	*p*-value
Number	74	39	
Age (y)	65.97 ± 6.84 (50–80)	63.44 ± 7.04 (52–81)	0.066
Male (%)	57 (77.03%)	30 (76.9%)	0.610
Education (y)	10.51 ± 2.69	10.54 ± 2.47	0.962
MoCA	21.72 ± 3.43	26.33 ± 1.23	<0.001
MMSE	27.17 ± 1.98	28.49 ± 1.23	<0.001
TMT-A	99.18 ± 50.60	59.46 ± 15.10	<0.001
TMT-B	225.38 ± 87.38	150.83 ± 38.41	<0.001
Stroop C-T	126.40 ± 56.94	79.26 ± 15.36	<0.001
VFT	13.01 ± 4.00	16.12 ± 3.63	<0.001

Data represent means ± standard deviation, with the range in parentheses, if applicable. vMCI, subcortical vascular mild cognitive impairment; TMT-A, trail-making tests A; TMT-B, trail-making tests B; Stroop C-T, stroop color-word test; VFT, verbal fluency test.

Feature Selection

A sparse logistic regression classifier (Yamashita et al., 2008) with LOOCV was implemented to distinguish patients with vMCI from patients with SVD with normal cognition (control) using the combined features from the CBF and diffusion metrics. The workflow for the SLR-based classification framework is shown in **Supplementary Figure R1**. Before constructing the SLR classification model, it is necessary to determine a subset of discriminative features and elimination of the non-informative features for use in classification, which was widely employed to boost classification performance (Yahata et al., 2016; Drysdale et al., 2017). The standard lasso (Tibshirani, 1996) with a 10 × 10 nested feature selection (FS) method was employed to achieve a sparse model by excluding the majority of features from the model. Then, the SLR classifier was implemented on the basis of the optimal features. Concretely, the whole data set was split into 10-folds using a stratified approach, to keep an equal amount of (diagnosis and gender) combinations per fold. In each LOOCV fold, all-but-one subjects were used to train a SLR classifier, while the remaining subject was used for evaluation. Prior to

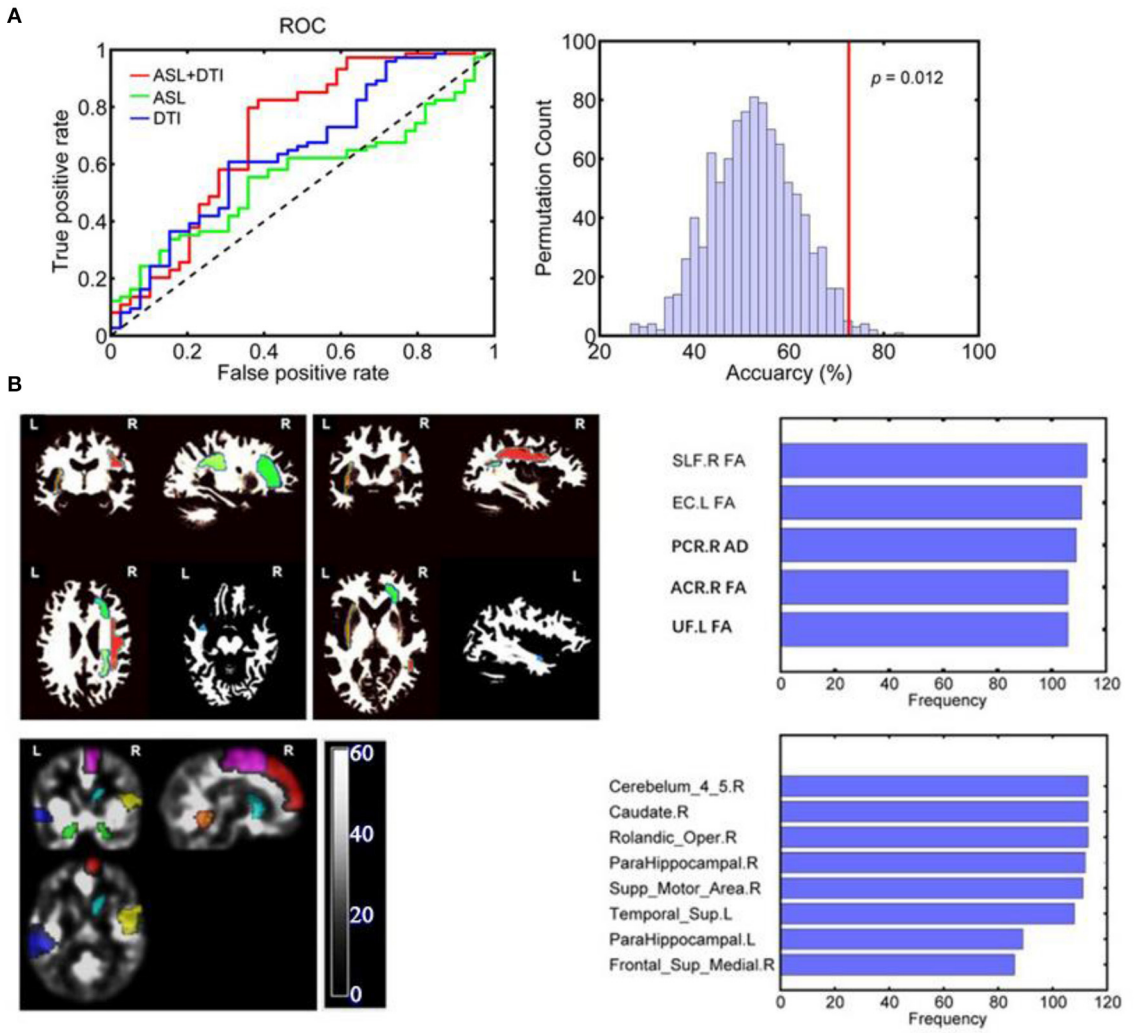

FIGURE 2 | (A) ROC curves of each SLR classifier for discriminating vMCI and controls: The AUC for the combined model, a single ASL model, and a single DTI model were 0.708, 0.559, and 0.647, respectively. **(B)** The discriminative gray and white matter regions for SLR classifier based on combined features. The combined CBF areas included Rolandic_oper, Supp_Motor_Area, Frontal_Sup_Medial, ParaHippocampal and Caudate of the right hemisphere as well as ParaHippocampal and Temporal_ Sup in the left hemisphere. The combined DTI features included ACR_FA, PCR_AD, and SLF_FA of the right hemisphere as well as EC_FA and UF_FA in the left hemisphere. SLF, superior longitudinal fasciculus; EC, external capsule; ACR, anterior corona radiata; PCR, posterior corona radiata; UF, uncinate fasciculus; L, left; R, right.

LOOCV, the 10 × 10 nested FS was performed using lasso. In this way, the lasso was trained on different subsamples of the data set, to increase the stability of the selected features. The "test set" of the outer loop FS process was kept as a testing pool for LOOCV, whereas the 10-folds of the inner loop FS were used to select features. Consequently, the LOOCV folds that belonged to the same testing pool of the outer loop FS shared the same reduced features. In the inner loop FS, the FS was completed using *Statistics and regression Toolbox* of MATLAB (Mathworks Inc. version 2014a). Features were selected using the default setting of the lasso function. The hyperparameter λ was estimated default by lasso. The features selected at each inner fold and λ were combined by the union operation, to include features that are important for any possible subsample (inner 10 folds) of the training data set. Once the inner loop FS was executed, one participant was taken from the testing pool of the outer loop FS, and used as the test set of the LOOCV. The remaining samples were used to train SLR on the features retained during the inner loop FS.

Feature selection in each fold of the outer LOOCV was implemented using a slightly different sample subset, which led to a different set of selected features across folds. The "consensus" features that were selected on 75% folds of the outer LOOCV were defined as the discriminative features.

Sparse Logistic Regression Classification

To predict the diagnostic label from the optimal features, we employed logistic regression as the classifier. In logistic

TABLE 2 | Classification performance of SLR classifiers using diffusion features, CBF features, and their combined features.

Model	Accuracy (%)	Sensitivity (%)	Specificity (%)	AUC	*p*
CBF+DTI	72.57	77.03	64.10	0.708	–
CBF	57.52	62.16	48.72	0.559	0.003
DTI	61.06	64.86	53.85	0.647	0.039

AUC, area under curve. Compared to single model with diffusion/perfusion features (p = 0.003/p = 0.039), the SLR classifier achieved the highest accuracy using combined diffusion and perfusion features (accuracy 72.57%, sensitivity 77.03%).

TABLE 3 | Identified combined diffusion/perfusion features for discriminating vMCI and Controls.

Frequency	Type	Region	vMCI	Controls	*p*-values
1.000	CBF	Rolandic_Oper_R	49.215	55.617	0.020*
0.982	CBF	Supp_Motor_Area_R	41.087	48.511	0.003*
0.761	CBF	Frontal_Sup_Medial_R	37.611	40.417	0.162
0.788	CBF	ParaHippocampal_L	45.680	50.681	0.020*
0.991	CBF	ParaHippocampal_R	44.219	50.527	0.003*
1.000	CBF	Caudate_R	34.338	35.348	0.342
0.956	CBF	Temporal_Sup_L	51.629	56.769	0.094
1.000	CBF	Cerebelum_4_5_R	41.420	43.792	0.342
0.938	FA	Right anterior corona radiata	0.316	0.346	0.002*
0.965	AD#	Right posterior corona radiata	13.612	13.125	0.142
0.982	FA	Left external capsule	0.328	0.350	0.002*
1.000	FA	Right superior longitudinal fasciculus	0.369	0.380	0.162
0.938	FA	Left uncinate fasciculus	0.336	0.357	0.039*

*#Unit is 10-4; *p < 0.05 corrected by FDR. CBF, cerebral blood flow; FA, fractional anisotropy; AD, axial diffusivity; Rolandic_Oper, rolandic operculum; Supp_Motor_Area, supplementary motor area; Frontal_Sup_Medial, medial superior frontal gyrus; ParaHippocampal, parahippocampal; Temporal_Sup, superior temporal gyrus; FDR, false discovery rate; vMCI, subcortical vascular mild cognitive impairment.*

regression, a logistic function is used to define the probability of a participant belonging to the vMCI class as follows:

$$P(y = 1\hat{z}; w) = \frac{1}{1 + \exp\left(-w^T \hat{z}\right)}$$

where y represents the diagnosis class label, that is $y = 1$ indicates patients with vMCI and $y = 0$ indicates patients with SVD with normal cognition (control), respectively. $\hat{z} = \left[z^T,\ 1\right]^T \in \mathbb{R}^{k+1}$ is a feature vector with an augmented input. $w \in \mathbb{R}^{k+1}$ is the weight vector of the logistic function. A receiver operating characteristic (ROC) curve was plotted to illustrate the classification ability of the model at varying discrimination thresholds. The predictive accuracy means the proportion of subjects who were correctly classified as a vMCI or a control label. To compare the ability of these classifiers to identify patients with vMCI, we applied the McNemar's test for comparing the area under the curve (AUC) of paired ROC curves (McNemar, 1947). The research flow chart is illustrated as **Figure 1**.

Statistical Analysis

All data analyses and statistics were performed using R-3.6.0 (https://www.r-project.org). The Kolmogorov-Smirnov test was used to test the distribution of age, education, and identified features. Standard distribution data were compared using the *t*-test, and non-normally distributed data were analyzed using the Wilcoxon rank-sum test. A Chi-square test was used to compare the gender between the training set and the validation set. Partial correlations of Pearson were used to assess the associations between the identified imaging features and the scores of attention-executive function tests independently in vMCI and control groups, with sex, age, and education controlled as covariates. False discovery rate (FDR) was used for multiple comparison corrections.

RESULTS

Demographic and Cognitive Characteristics

The demographic and cognitive characteristics of the participants are presented in **Table 1**. No significant differences in age, sex, and education were observed between the vMCI and the control patient groups. The mean MoCA score of the vMCI group was significantly lower than that of the control group ($p < 0.01$), with 85.14% of the patients with vMCI exhibiting executive dysfunction. The completion time for the TMT-A and TMT-B and the reaction time in the Stroop C-T test were significantly longer in the vMCI group than in the control group (all $p < 0.01$). The VFT performance was markedly worse in the vMCI group than in the control group ($p < 0.01$).

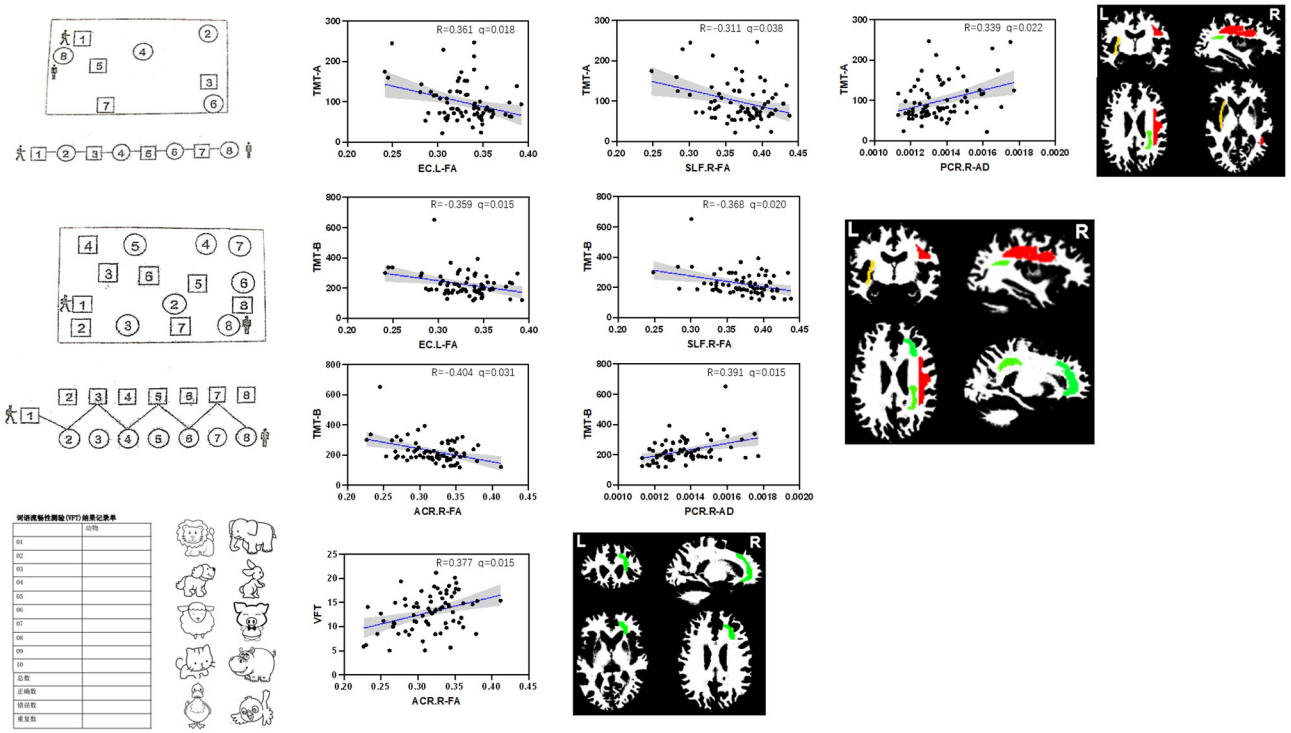

FIGURE 3 | Correlations between discriminative features and executive function tests within vMCI group, controlled for gender, age, and education. All results were corrected by FDR. The mean AD value of right PCR ($r = 0.339$, $P < 0.037$) and the mean FA values of the left EC ($r = -0.361$, $P < 0.026$) were significantly associated with TMT-A; the mean FA values of the right ACR ($r = -0.404$, $P < 0.026$), left EC ($r = -0.359$, $P < 0.026$) and right SLF ($r = -0.368$, $P < 0.026$), and the mean AD value of right PCR ($r = 0.391$, $P < 0.026$) were significantly associated with TMT-B; the mean FA values of the right ACR (r =0.377, $P < 0.026$) were significantly associated with VFT.

Diffusion and Perfusion Features Predicted Vascular Mild Cognitive Impairment Patients

Distinct features with a frequency of ≥75% for distinguishing patients with vMCI from control patients were selected and used to construct SLR classifiers. The performance results of the SLR classifiers, including both single-mode models and a combined model with both diffusion and perfusion features, are shown in **Figure 2A** and **Tables 2**, **3**. Compared with the single-mode models, the SLR classifier with both diffusion and perfusion features achieved the highest accuracy of 72.57%, with sensitivity of 77.03%.

The classification results are shown as an ROC curve using each classification score of subject as a threshold in **Figure 2A**. The AUCs for the combined model, single ASL model, and single DTI model were 0.708, 0.559, and 0.647, respectively.

The CBF areas in the combined model included the right Rolandic operculum, supplementary motor area (SMA), medial superior frontal gyrus (mSFG), parahippocampal gyrus and caudate, and the left parahippocampal and superior temporal gyrus (STG). The DTI features in the combined model included the FA of the right anterior corona (ACR) radiata, right superior longitudinal fasciculus (SLF), left external capsule and left uncinate fasciculus, and the AD of the right posterior corona radiata (PCR). The combined CBF and DTI features are shown in **Figure 2B**.

Associations Between Executive Function and Diffusion and Perfusion Features

In the vMCI group, correlation analysis showed that the mean AD of the right PCR ($r = 0.339$, $p < 0.037$) and the mean FA of the left external capsule ($r = -0.361$, $p < 0.026$) were significantly associated with TMT-A time. The mean FA of the right ACR ($r = -0.404$, $p < 0.026$), left external capsule ($r = -0.359$, $p < 0.026$), and right SLF ($r = -0.368$, $p < 0.026$), and the mean AD of the right PCR ($r = 0.391$, $p < 0.026$), were significantly associated with the TMT-B time. The mean FA of the right ACR (r =0.377, $p < 0.026$) was significantly associated with VFT, as shown in **Figure 3** and **Table 4**. No discriminative perfusion feature showed a significant association with attention-executive performance, as shown in **Table 4**. None of the discriminative perfusion and diffusion features were significantly associated with attention-executive performance within control group, as shown in **Supplementary Table 2**.

TABLE 4 | Correlations between discriminative combined diffusion/perfusion features and executive function tests in vMCI group.

Type	Region	TMT-A		TMT-B		Stroop C-T		VFT	
		R	*p*	R	*p*	R	*p*	R	*p*
CBF	Rolandic_Oper_R	0.003	0.592	0.103	0.407	−0.043	0.534	0.058	0.522
CBF	Supp_Motor_Area_R	−0.183	0.242	0.037	0.547	0.052	0.522	0.144	0.293
CBF	Frontal_Sup_Medial_R	0.066	0.510	0.007	0.587	−0.002	0.582	0.140	0.289
CBF	ParaHippocampal_L	−0.190	0.228	−0.049	0.519	0.014	0.582	0.163	0.268
CBF	ParaHippocampal_R	−0.161	0.263	−0.024	0.580	0.100	0.394	0.139	0.282
CBF	Caudate_R	0.055	0.522	0.237	0.187	−0.084	0.456	−0.009	0.593
CBF	Temporal_Sup_L	−0.102	0.398	0.016	0.588	−0.031	0.560	0.146	0.300
CBF	Cerebelum_4_5_R	−0.160	0.256	−0.169	0.269	0.017	0.595	0.233	0.184
FA	Right anterior corona radiata	−0.216	0.166	−0.404	0.031*	−0.181	0.238	0.377	0.015*
AD#	Right posterior corona radiata	0.339	0.022*	0.391	0.015*	0.209	0.177	−0.219	0.184
FA	Left external capsule	−0.361	0.018*	−0.359	0.015*	−0.168	0.260	0.313	0.173
FA	Right superior longitudinal fasciculus	−0.311	0.042*	−0.368	0.020*	−0.219	0.200	0.221	0.207
FA	Left uncinate fasciculus	−0.061	0.522	−0.141	0.295	−0.137	0.280	0.070	0.504

*#Unit is 10^{-4}; *$p < 0.05$, corrected by FDR. The selected white matter diffusion features were significantly associated with TMT-A/TMT-B/VFT. No discriminative perfusion feature was detected associated with attention-executive performance significantly.*

DISCUSSION

Associations between cognitive decline and impairments to anterior thalamic radiation (ACR) have been broadly reported in SVD. Voxel-based lesion-symptom mapping studies (Duering et al., 2011, 2014; Biesbroek et al., 2013) found that strategic locations of WM damage within ACR were associated with processing speed performance or executive function in SVD. Tract-based spatial statistics study also found that diffusion metrics along the forceps minor and ACR were discriminative for cognitive impairments in patients with SVD (Chen et al., 2018), which is consistent with the present finding that ACR diffusion abnormalities not only contributed to the classification accuracy of patients with SVD with-/without- cognitive symptoms, but also were significantly correlated with executive function. This indicates the involvement of the ACR in the early stage of cognitive decline in SVD. Furthermore, other discriminative WM fibers revealed in our study constituted the lateral pathway of the cholinergic system (external capsule, uncinate fasciculus, CR, and SLF), which radiates to the dorsal frontoparietal neocortex, the temporal cortex, and the parahippocampal gyrus (Caruso et al., 2019; Nolze-Charron et al., 2020). Specifically, fiber bundles that radiated to the dorsal frontoparietal cortex were associated with performance in the executive function tests in the vMCI group. As a matter of a fact, cholinergic dysregulation in SVD has been discussed extensively, including cholinergic neuronal deficits and cholinergic denervation (Mesulam et al., 2003; Keverne et al., 2007), decreased cerebrospinal fluid acetylcholine concentrations (Wallin et al., 2003), and the promising effects of cholinergic therapies (Caruso et al., 2019). In particular, a tractography study (Liu et al., 2017) identified significantly lower FA within cholinergic pathways (including the external capsule, cingulum, and claustrum) in patients with vascular cognitive impairment no dementia group. The disrupted pathways could fully explain the executive dysfunction and partly explain the memory and global cognitive impairments. Another tractography study isolated the external capsule as the lateral cholinergic tract and found that diffusion metrics of both the external capsule and the overlying SLF were correlated with executive dysfunction (Nolze-Charron et al., 2020). Our findings are consistent with these reports, with a broad range of lateral cholinergic tracts up and down the external capsule being significantly related to executive dysfunction in the early stage of cognitive decline in SVD but not the non-symptomatic stage. Collectively, results that showed frontal fiber dysconnectivity and potential cholinergic dysregulation shed light on the clinical characteristics of attention and executive dysfunction in vMCI, thereby supporting a physically active lifestyle and cholinergic therapy as a potential effective treatment option for vMCI (Dey et al., 2016; Strömmer et al., 2020).

Cortical perfusion abnormalities in frontal (mSFG, SMA, Rolandic operculum), subcortical (caudate nucleus), and limbic (parahippocampal gyrus) areas also contributed to the accuracy of subtype classification in the present machine learning model, although no associations with performance of cognitive tests in these patients were found. Previous ASL studies showed widespread significant reductions in cortical CBF in patients with SVD with cognitive impairment (Schuff et al., 2009; Gao et al., 2013; Sun et al., 2016), although the spatial profiles of CBF abnormalities reported among these studies were rather divergent. Cortical perfusion is regulated by neurovascular coupling and a complex autoregulation system, and may not therefore be simply related to cognitive impairment (Caruso et al., 2019). Recent studies suggested an important role for the autonomic nervous system in the maintenance of CBF (Hamner et al., 2012). It was suggested that cholinesterase inhibitors modulate cerebral vascular functions because of the possible role of cholinergic fibers in cerebral flow regulation (Brown and Thore, 2011). Considering the WM diffusion abnormalities in our classification model, CBF disturbance of the frontal–subcortical–limbic system may partly result from dysfunction

of the lateral capsular pathway of cholinergic tracts which needs further study. Moreover, recent study showed that cortical perfusion abnormalities may also affect cognition through secondary changes in subcortical myelin content (Chen et al., 2013; Bouhrara et al., 2020). The diffusion-perfusion combined classifier with the highest cognitive classification accuracy in this study might suggest the interaction of gray matter perfusion and WM integrity, which explained the cognitive outcomes.

This study had several limitations. First, because of inherent limitations of the atlas used for WM parcellation, only the main WM tracts were evaluated, and fibers in superficial regions were not included in our study. Future studies of the fibers in superficial regions may provide additional information on vMCI. Second, the low spatial resolution of the CBF images may have resulted in partial volume effects causing bias in the CBF features. Third, the results were not validated on an external dataset. Further studies using multicenter validation datasets are needed to acquire high-level evidence. Fourth, resting CBF only provides information for a cut-off time point, at which CBF might still be relatively preserved or compensated. Fifth, although detailed clinical history, imaging analysis, and neuropsychological evaluation were used to avoid the interference of AD, the influence of mixed dementia on this study could not be completely excluded. Finally, compared with the dimensionality of the features, the sample size was relatively small. In addition, there were more males in both groups, which may lead to biasness in results.

CONCLUSIONS

We demonstrated the superior accuracy of using diffusion-perfusion combined multimode imaging features for classifying vMCI subtype out of a cohort of patients with SVD. Importantly, these findings highlight that disrupted WM integrity might play a critical role in the progression of cognitive impairment in patients with SVD, while malregulation of coritcal perfusion needs further study.

DATA AVAILABILITY STATEMENT

The raw data supporting the conclusions of this article will be made available by the authors, without undue reservation.

ETHICS STATEMENT

The studies involving human participants were reviewed and approved by Research Ethics Committee of Renji Hospital, School of Medicine, Shanghai Jiao Tong University. The patients/participants provided their written informed consent to participate in this study.

AUTHOR CONTRIBUTIONS

YW: data collection, image registration, statistical analysis, data interpretation, and manuscript preparation. PL: data collection and neuropsychological assessment. YZha: statistical analysis, data interpretation, and manuscript preparation. XW: data collection and image registration. YQ: data collection. ZW: data interpretation and manuscript preparation. QX: study design. YZho: study design and commenting on drafts. All authors contributed to the article and approved the submitted version.

FUNDING

This work was supported by the Shanghai Science and Technology Committee Project (Natural Science Funding; grant nos. 20ZR1433200 and 19ZR1430500), National Natural Science Foundation of China (grant nos. 81901693 and 82001457), Shanghai Municipal Education Commission-Gaofeng Clinical Medicine Grant Support (grant no. 20172013), the Project of Collaborative Innovation Center of Translational Medicine (TM201808), Incubating Program for Clinical Research and Innovation of Ren Ji Hospital, School of Medicine, Shanghai Jiao Tong University (grant nos. PYIV-17-003, PYIII-17-027, and PY2018-III-03), and Shanghai Rising Stars of Medical Talent Youth Development Program, Youth Medical Talents-Medical Imaging Practitioner Program [grant no. SHWRS (2020)_087].

SUPPLEMENTARY MATERIAL

The Supplementary Material for this article can be found online at: https://www.frontiersin.org/articles/10.3389/fnagi.2021.687001/full#supplementary-material

REFERENCES

Biesbroek, J. M., Kuijf, H. J., van der Graaf, Y., Vincken, K. L., Postma, A., Mali, W. P. T. M., et al. (2013). Association between subcortical vascular lesion location and cognition: a voxel-based and tract-based lesion-symptom mapping study. The SMART-MR study. *PLoS ONE* 8:e60541. doi: 10.1371/journal.pone.0060541

Bouhrara, M., Alisch, J. S. R., Khattar, N., Kim, R. W., Rejimon, A. C., Cortina, L. E., et al. (2020). Association of cerebral blood flow with myelin content in cognitively unimpaired adults. *BMJ Neurol Open* 2:e000053. doi: 10.1136/bmjno-2020-000053

Brown, W. R., and Thore, C. R. (2011). Review: cerebral microvascular pathology in ageing and neurodegeneration. *Neuropathol. Appl. Neurobiol.* 37, 56–74. doi: 10.1111/j.1365-2990.2010.01139.x

Caruso, P., Signori, R., and Moretti, R. (2019). Small vessel disease to subcortical dementia: a dynamic model, which interfaces aging, cholinergic dysregulation and the neurovascular unit. *Vasc. Health Risk Manag.* 15, 259–281. doi: 10.2147/VHRM.S190470

Chen, H.-J., Gao, Y.-Q., Che, C.-H., Lin, H., and Ruan, X.-L. (2018). Diffusion tensor imaging with tract-based spatial statistics reveals white matter abnormalities in patients with vascular cognitive impairment. *Front. Neuroanat.* 12:53. doi: 10.3389/fnana.2018.00053

Chen, J. J., Rosas, H. D., and Salat, D. H. (2013). The relationship between cortical blood flow and sub-cortical white-matter health across the adult age span. *PLoS ONE* 8:e56733. doi: 10.1371/journal.pone.0056733

Dey, A. K., Stamenova, V., Turner, G., Black, S. E., and Levine, B. (2016). Pathoconnectomics of cognitive impairment in small vessel disease: a systematic review. *Alzheimer's Dement.* 12, 831–845. doi: 10.1016/j.jalz.2016.01.007

Drysdale, A. T., Grosenick, L., Downar, J., Dunlop, K., Mansouri, F., Meng, Y., et al. (2017). Resting-state connectivity biomarkers define neurophysiological subtypes of depression. *Nat. Med.* 23, 28–38. doi: 10.1038/nm.4246

Duering, M., Gesierich, B., Seiler, S., Pirpamer, L., Gonik, M., Hofer, E., et al. (2014). Strategic white matter tracts for processing speed deficits in age-related small vessel disease. *Neurology* 82, 1946–1950. doi: 10.1212/WNL.0000000000000475

Duering, M., Righart, R., Wollenweber, F. A., Zietemann, V., Gesierich, B., and Dichgans, M. (2015). Acute infarcts cause focal thinning in remote cortex via degeneration of connecting fiber tracts. *Neurology* 84, 1685–1692. doi: 10.1212/WNL.0000000000001502

Duering, M., Zieren, N., Hervé, D., Jouvent, E., Reyes, S., Peters, N., et al. (2011). Strategic role of frontal white matter tracts in vascular cognitive impairment: a voxel-based lesion-symptom mapping study in CADASIL. *Brain* 134, 2366–2375. doi: 10.1093/brain/awr169

Duncombe, J., Kitamura, A., Hase, Y., Ihara, M., Kalaria, R. N., and Horsburgh, K. (2017). Chronic cerebral hypoperfusion: a key mechanism leading to vascular cognitive impairment and dementia. Closing the translational gap between rodent models and human vascular cognitive impairment and dementia. *Clin. Sci.* 131, 2451–2468. doi: 10.1042/CS20160727

Galluzzi, S., Sheu, C.-F., Zanetti, O., and Frisoni, G. B. (2005). Distinctive clinical features of mild cognitive impairment with subcortical cerebrovascular disease. *Dement. Geriatr. Cogn. Disord.* 19, 196–203. doi: 10.1159/000083499

Gao, Y.-Z., Zhang, J.-J., Liu, H., Wu, G.-Y., Xiong, L., and Shu, M. (2013). Regional cerebral blood flow and cerebrovascular reactivity in Alzheimer's disease and vascular dementia assessed by arterial spinlabeling magnetic resonance imaging. *Curr. Neurovasc. Res.* 10, 49–53. doi: 10.2174/15672021380486016

Guo, Q.-H., Sun, Y. M., Yu, P. M., Hong, Z., and Lv, C.-Z. (2007). Norm of auditory verbal learning test in the normal aged in China community. *Chinese J. Clin. Psychol.* 2, 132–134. doi: 10.3969/j.issn.1005-3611.2007.02.007

Hachinski, V., Iadecola, C., Petersen, R. C., Breteler, M. M., Nyenhuis, D. L., Black, S. E., et al. (2006). National Institute of Neurological Disorders and Stroke-Canadian Stroke Network vascular cognitive impairment harmonization standards. *Stroke* 37, 2220–2241. doi: 10.1161/01.STR.0000237236.88823.47

Hamner, J. W., Tan, C. O., Tzeng, Y.-C., and Taylor, J. A. (2012). Cholinergic control of the cerebral vasculature in humans. *J. Physiol.* 590, 6343–6352. doi: 10.1113/jphysiol.2012.245100

Iadecola, C., Duering, M., Hachinski, V., Joutel, A., Pendlebury, S. T., Schneider, J. A., et al. (2019). Vascular cognitive impairment and dementia: JACC scientific expert panel. *J. Am. Coll. Cardiol.* 73, 3326–3344. doi: 10.1016/j.jacc.2019.04.034

Keverne, J. S., Low, W. C. R., Ziabreva, I., Court, J. A., Oakley, A. E., and Kalaria, R. N. (2007). Cholinergic neuronal deficits in CADASIL. *Stroke* 38, 188–191. doi: 10.1161/01.STR.0000251787.90695.05

Li, Q., Yang, Y., Reis, C., Tao, T., Li, W., Li, X., et al. (2018). Cerebral small vessel disease. *Cell Transplant.* 27, 1711–1722. doi: 10.1177/0963689718795148

Liu, C., Zou, L., Tang, X., Zhu, W., Zhang, G., Qin, Y., et al. (2020). Changes of white matter integrity and structural network connectivity in nondemented cerebral small-vessel disease. *J. Magn. Reson. Imaging.* 51, 1162–1169. doi: 10.1002/jmri.26906

Liu, Q., Zhu, Z., Teipel, S. J., Yang, J., Xing, Y., Tang, Y., et al. (2017). White matter damage in the cholinergic system contributes to cognitive impairment in subcortical vascular cognitive impairment, no dementia. *Front. Aging Neurosci.* 9:47. doi: 10.3389/fnagi.2017.00047

Malojcic, B., Giannakopoulos, P., Sorond, F. A., Azevedo, E., Diomedi, M., Oblak, J. P., et al. (2017). Ultrasound and dynamic functional imaging in vascular cognitive impairment and Alzheimer's disease. *BMC Med.* 15:27. doi: 10.1186/s12916-017-0799-3

McNemar, Q. (1947). Note on the sampling error of the difference between correlated proportions or percentages. *Psychometrika* 12, 153–157. doi: 10.1007/BF02295996

Mesulam, M., Siddique, T., and Cohen, B. (2003). Cholinergic denervation in a pure multi-infarct state: observations on CADASIL. *Neurology* 60, 1183–1185. doi: 10.1212/01.WNL.0000055927.22611.EB

Mori, S., Oishi, K., Jiang, H., Jiang, L., Li, X., Akhter, K., et al. (2008). Stereotaxic white matter atlas based on diffusion tensor imaging in an ICBM template. *Neuroimage* 40, 570–582. doi: 10.1016/j.neuroimage.2007.12.035

Muñoz Maniega, S., Chappell, F. M., Valdés Hernández, M. C., Armitage, P. A., Makin, S. D., Heye, A. K., et al. (2017). Integrity of normal-appearing white matter: influence of age, visible lesion burden and hypertension in patients with small-vessel disease. *J. Cereb. Blood Flow Metab.* 37, 644–656. doi: 10.1177/0271678X16635657

Nolze-Charron, G., Dufort-Rouleau, R., Houde, J.-C., Dumont, M., Castellano, C.-A., Cunnane, S., et al. (2020). Tractography of the external capsule and cognition: a diffusion MRI study of cholinergic fibers. *Exp. Gerontol.* 130:110792. doi: 10.1016/j.exger.2019.110792

O'Sullivan, M., Jones, D. K., Summers, P. E., Morris, R. G., Williams, S. C., and Markus, H. S. (2001). Evidence for cortical "disconnection" as a mechanism of age-related cognitive decline. *Neurology* 57, 632–638. doi: 10.1212/WNL.57.4.632

O'Sullivan, M., Morris, R. G., Huckstep, B., Jones, D. K., Williams, S. C. R., and Markus, H. S. (2004). Diffusion tensor MRI correlates with executive dysfunction in patients with ischaemic leukoaraiosis. *J. Neurol. Neurosurg. Psychiatr.* 75, 441–447. doi: 10.1136/jnnp.2003.014910

Pantoni, L. (2010). Cerebral small vessel disease: from pathogenesis and clinical characteristics to therapeutic challenges. *Lancet Neurol.* 9, 689–701. doi: 10.1016/S1474-4422(10)70104-6

Rosenberg, G. A., Wallin, A., Wardlaw, J. M., Markus, H. S., Montaner, J., Wolfson, L., et al. (2016). Consensus statement for diagnosis of subcortical small vessel disease. *J. Cereb. Blood Flow Metab.* 36, 6–25. doi: 10.1038/jcbfm.2015.172

Schuff, N., Matsumoto, S., Kmiecik, J., Studholme, C., Du, A., Ezekiel, F., et al. (2009). Cerebral blood flow in ischemic vascular dementia and Alzheimer's disease, measured by arterial spin-labeling magnetic resonance imaging. *Alzheimer's Dement.* 5, 454–462. doi: 10.1016/j.jalz.2009.04.1233

Seo, S. W., Ahn, J., Yoon, U., Im, K., Lee, J.-M., Tae Kim, S., et al. (2010). Cortical thinning in vascular mild cognitive impairment and vascular dementia of subcortical type. *J. Neuroimag.* 20, 37–45. doi: 10.1111/j.1552-6569.2008.00293.x

Shi, Y., Thrippleton, M. J., Makin, S. D., Marshall, I., Geerlings, M. I., de Craen, A. J. M., et al. (2016). Cerebral blood flow in small vessel disease: a systematic review and meta-analysis. *J. Cereb. Blood Flow Metab.* 36, 1653–1667. doi: 10.1177/0271678X16662891

Strömmer, J. M., Davis, S. W., Henson, R. N., Tyler, L. K., and Campbell, K. L. (2020). Physical activity predicts population-level age-related differences in frontal white matter. *J. Gerontol. Ser. A Biol. Sci. Med. Sci.* 75, 236–243. doi: 10.1093/gerona/gly220

Sun, Y., Cao, W., Ding, W., Wang, Y., Han, X., Zhou, Y., et al. (2016). Cerebral blood flow alterations as assessed by 3D ASL in cognitive impairment in patients with subcortical vascular cognitive impairment: a marker for disease severity. *Front. Aging Neurosci.* 8:211. doi: 10.3389/fnagi.2016.00211

Tibshirani, R. (1996). Regression shrinkage and selection via the Lasso. *J. R. Stat. Soc. Ser. B Methodol.* 58, 267–288. doi: 10.1111/j.2517-6161.1996.tb02080.x

Tuladhar, A. M., van Norden, A. G. W., de Laat, K. F., Zwiers, M. P., van Dijk, E. J., Norris, D. G., et al. (2015). White matter integrity in small vessel disease is related to cognition. *NeuroImage Clin.* 7, 518–524. doi: 10.1016/j.nicl.2015.02.003

Wallin, A., Sjögren, M., Blennow, K., and Davidsson, P. (2003). Decreased cerebrospinal fluid acetylcholinesterase in patients with subcortical ischemic vascular dementia. *Dement. Geriatr. Cogn. Disord.* 16, 200–207. doi: 10.1159/000072803

Wardlaw, J. M., Smith, C., and Dichgans, M. (2013). Mechanisms of sporadic cerebral small vessel disease: insights from neuroimaging. *Lancet Neurol.* 12, 483–497. doi: 10.1016/S1474-4422(13)70060-7

Wardlaw, J. M., Smith, C., and Dichgans, M. (2019). Small vessel disease: mechanisms and clinical implications. *Lancet Neurol.* 18, 684–696. doi: 10.1016/S1474-4422(19)30079-1

Xu, Q., Cao, W.-W., Mi, J.-H., Yu, L., Lin, Y., and Li, Y.-S. (2014). Brief screening for mild cognitive impairment in subcortical ischemic vascular disease: a comparison study of the Montreal Cognitive Assessment with the Mini-Mental State Examination. *Eur. Neurol.* 71, 106–114. doi: 10.1159/000353988

Yahata, N., Morimoto, J., Hashimoto, R., Lisi, G., Shibata, K., Kawakubo, Y., et al. (2016). A small number of abnormal brain connections predicts adult autism spectrum disorder. *Nat. Commun*. 7:11254. doi: 10.1038/ncomms11254

Yamashita, O., Sato, M. A., Yoshioka, T., Tong, F., and Kamitani, Y. (2008). Sparse estimation automatically selects voxels relevant for the decoding of fMRI activity patterns. *Neuroimage* 42, 1414–1429. doi: 10.1016/j.neuroimage.2008.05.050

Yu, C., Lu, W., Qiu, J., Wang, F., Li, J., and Wang, L. (2020). Alterations of the whole cerebral blood flow in patients with different total cerebral small vessel disease burden. *Front. Aging Neurosci*. 12:175. doi: 10.3389/fnagi.2020.00175

Conflict of Interest: The authors declare that the research was conducted in the absence of any commercial or financial relationships that could be construed as a potential conflict of interest.

Publisher's Note: All claims expressed in this article are solely those of the authors and do not necessarily represent those of their affiliated organizations, or those of the publisher, the editors and the reviewers. Any product that may be evaluated in this article, or claim that may be made by its manufacturer, is not guaranteed or endorsed by the publisher.

frontiers in Aging Neuroscience

ORIGINAL RESEARCH
published: 11 August 2021
doi: 10.3389/fnagi.2021.709215

Motor Dysfunction Questionnaire and Dopamine Transporter Imaging Composite Scale Improve Differentiating Dementia With Lewy Bodies From Alzheimer's Disease With Motor Dysfunction

Pai-Yi Chiu[1,2], *Cheng-Yu Wei*[3], *Guang-Uei Hung*[4]* and *Shey-Lin Wu*[5,6]*

[1] Department of Neurology, Show Chwan Memorial Hospital, Changhua, Taiwan, [2] Department of Nursing, College of Nursing and Health Sciences, Da-Yeh University, Changhua, Taiwan, [3] Department of Neurology, Chang Bing Show Chwan Memorial Hospital, Changhua, Taiwan, [4] Department of Nuclear Medicine, Chang Bing Show Chwan Memorial Hospital, Changhua, Taiwan, [5] Department of Neurology, Changhua Christian Hospital, Changhua, Taiwan, [6] Department of Biomedical Sciences, Da-Yeh University, Changhua, Taiwan

OPEN ACCESS

Edited by:
Behrooz Hooshyar Yousefi,
University of Marburg, Germany

Reviewed by:
Francesco Iodice,
San Raffaele Pisana (IRCCS), Italy
Richard Camicioli,
University of Alberta, Canada

***Correspondence:**
Shey-Lin Wu
sheylin@cch.org.tw
Guang-Uei Hung
106143@gmail.com

Received: 13 May 2021
Accepted: 13 July 2021
Published: 11 August 2021

Citation:
Chiu P-Y, Wei C-Y, Hung G-U and Wu S-L (2021) Motor Dysfunction Questionnaire and Dopamine Transporter Imaging Composite Scale Improve Differentiating Dementia With Lewy Bodies From Alzheimer's Disease With Motor Dysfunction. Front. Aging Neurosci. 13:709215. doi: 10.3389/fnagi.2021.709215

Objective: Characteristic parkinsonism is the major comorbidity of dementia with Lewy bodies (DLB). We aimed to differentiate DLB from Alzheimer's disease (AD) with motor dysfunction using a composite scale with a characteristic motor dysfunction questionnaire (MDQ) and dopamine transporter (DAT) imaging. It could help detect DLB easily in healthcare settings without movement disorder specialists.

Methods: This is a two-phase study. In the design phase, seven questions were selected and composed of a novel MDQ. In the test phase, all participants with DLB, AD, or non-dementia (ND) control completed dementia and parkinsonism survey, the novel designed questionnaire, DAT imaging, and composite scales of MDQ and DAT. The cutoff scores of the MDQ, semiquantitative analysis of the striatal–background ratio (SBR) and visual rating of DAT, and the composite scale of MDQ and DAT for discriminating DLB from AD or ND were derived and compared.

Results: A total of 277 participants were included in this study (126 with DLB, 86 with AD, and 65 with ND). Compared with the AD or ND groups, the DLB group showed a significantly higher frequency in all seven items in the MDQ and a significantly lower SBR. For discrimination of DLB from non-DLB with MDQ, SBR, and composite scale, the cutoff scores of 3/2, 1.37/1.38, and 6/5 were suggested for the diagnosis of DLB with the sensitivities/specificities of 0.91/0.72, 0.91/0.80, and 0.87/0.93, respectively. The composite scale significantly improved the accuracy of discrimination compared with either the MDQ or SBR.

Conclusion: This study showed that the novel designed simple questionnaire was a practical screening tool and had similar power to DAT scanning to detect DLB. The questionnaire can be applied in clinical practice and population studies for screening DLB. In addition, the composite scale of MDQ and DAT imaging further improved the diagnostic accuracy, indicating the superiority of the dual-model diagnostic tool.

Keywords: Alzheimer's disease, dementia with Lewy bodies, non-dementia, motor dysfunction, striatal–background ratio

INTRODUCTION

Dopamine transporter (DAT) imaging is an indicative biomarker for diagnosing dementia with Lewy bodies (DLB). A recent systematic analysis showed that the sensitivity and specificity for the differentiation of DLB from other brain disorders were 0.86 and 0.81 and 0.93 and 0.75 for visual and semiquantitative assessments of DAT-Single Photon Emission Computed Tomography (DAT-SPECT), respectively (Nihashi et al., 2020). However, there is still a lack of tracers that target α-synuclein, and DAT has become the most important biomarker for the diagnosis of DLB.

Clinical diagnosis of DLB is mainly based on consensus criteria, and the core clinical features help detect and differentiate DLB from other dementia syndromes. Core clinical features include fluctuations of cognition, characteristic visual hallucinations (VH), rapid eye movement (REM) sleep behavior disorder (RBD), and spontaneous parkinsonism. For the clinical detection of DLB, Galvin (2015) provided a simple risk score composed of 10 questions associated with core/supportive clinical features.

Parkinsonism is a cardinal feature for the diagnosis of Parkinson's disease (PD) (Emre et al., 2007; Postuma et al., 2015) and a core clinical feature for the diagnosis of DLB (McKeith et al., 2017). However, PD is also comorbid with many other neurological and systemic disorders. The prevalence rate of the coexistence of parkinsonism and AD may be higher than previously recognized (Lopez et al., 1997; Sasaki, 2018). Clinical and differential diagnosis of DLB can only be made accurately by acquiring a detailed clinical history and performing neurological examinations, neuroimaging, or other laboratory studies. The characteristics of parkinsonism associated with DLB are different from motor dysfunction due to other common disease entities, such as essential tremor (ET), skeletal disorders, cardiovascular diseases, cerebrovascular diseases, and frailty in older adults. In particular, the characteristics of parkinsonism associated with DLB are unfamiliar and difficult for researchers or clinicians without well-trained skills in taking neurological history and/or performing the neurological examination. Therefore, several clinical and community-based screening questionnaires for PD were designed and studied with a sensitivity of 48–100% and a specificity of 22–100% (Tanner et al., 1990; Mutch et al., 1991; Chang et al., 1996; The Italian Longitudinal Study on Aging Working Group, 1997; Chan et al., 2000; Dahodwala et al., 2012). The screening efficacies of these scales on clinical or community populations vary (Dahodwala et al., 2012). However, none of these scales addressed the discrimination of motor dysfunction between DLB and other dementia disorders, although DLB is the second most common degenerative dementia (McKeith et al., 2005, 2017; Zaccai et al., 2005), and the clinical presentations of DLB and Alzheimer's disease (AD) dementia are easily confused.

Based on clinical experience and the previous study on the diagnosis of parkinsonism, we also found some discrepancies between the characteristic motor symptoms described by caregivers and the performance of patients examined by physicians (Lin et al., 2018). To narrow down the differences, this study aims to compare the different presentations of parkinsonism to those with AD as observed by the caregivers of patients with DLB, and therefore, to design a simple motor dysfunction questionnaire (MDQ). The questionnaire was constructed with clinically frequent questions or usual complaints of characteristic motor symptoms obtained from caregivers or patients in the clinics or bedsides and modified according to the clinical diagnostic criteria for PD dementia (PDD) or DLB. In addition, we intended to validate the newly designed informant-based motor dysfunction screening tool by testing it among a registered-based population with a diagnosis objectively proven by DAT imaging. Furthermore, during the consecutive data collection, the embedded auto-judgment program in the questionnaire will continue to revise the weighting of each question using machine learning techniques to improve the diagnostic ability.

METHODS

Participants

This was a two-phase study to design and test the MDQ embedded in the History-based Artificial Intelligence Clinical Dementia Diagnostic System (HAICDDS), which is currently used to register patients with dementia or motor dysfunction in the Show Chwan Healthcare System (Lin et al., 2018; Chiu et al., 2019a,b; Wang et al., 2020; Zhu et al., 2020). Before beginning the project, 30 patients with their caregivers were tested by neuropsychologists from three centers, and the reproducibility was studied using the interrater reliability analysis. Then, the coefficient was calculated to estimate the reliability of the newly developed questionnaire. After that, the baseline and follow-up data of participants were continuously collected, and the embedded diagnostic system was modified with machine learning techniques to improve the diagnostic accuracy and efficiency.

In the design phase (2014–2016), we retrospectively analyzed 13 motor-associated questions, including resting tremor, action tremor, bradykinesia, rigidity, postural instability, monotonic and hypotonic speech, jerk, impaired fine motor movement, restlessness, gait or truncal deviation, dystonic movement, asymmetric onset, and repeated falls in the early stage. These questions were selected based on the characteristic PD/DLB motor symptoms suggested by the criteria (Emre et al., 2007). Along with other common motor symptoms observed in patients with brain disorders, the original 13 questions were compared between the PD/DLB and AD groups. The first seven questions with the highest odds ratios (ORs) for the discrimination of PD/DLB from non-PD/DLB were selected to compose the MDQ (HAI-MDQ) (**Supplementary Table 1**).

In the test phase (2017–2020), the participants with DLB or AD who registered in the HAICDDS database with at least one DAT imaging were analyzed and compared for their HAI-MDQ, DAT imaging, and demographic, clinical, neuropsychological, and neuroimaging characteristics. The cutoff scores for HAI-MDQ and the striatal–background ratio (SBR) of DAT were derived. Composite scores of HAI-MDQ and SBR were calculated using the total HAI-MDQ score plus abnormal DAT (DATabN) by either visual rating (VR) or SBR. The weighting of DATabN by either VR or SBR was given as the same as the cutoff score for diagnosing DLB in HAI-MDQ based on a presumed equal diagnostic power of clinical and imaging tools.

Diagnostic Procedures

The diagnosis of DLB was made according to the revised consensus criteria for probable DLB developed by the fourth report of the DLB consortium in 2017 (McKeith et al., 2017). Patients with AD were diagnosed according to the criteria for probable AD with dementia developed by the National Institute on Aging and Alzheimer's Association (NIA-AA) 2011 criteria (McKhann et al., 2011).

Neuropsychological tests, including cognitive and daily function, were assessed using the Montreal Cognitive Assessment (MoCA) (Chen et al., 2016) and instrumental activities of daily living (IADL) scales (Lawton and Brody, 1969). The tests for all patients were performed by trained neuropsychologists. The clinical features of DLB, including REM, RBD, VH, and cognitive fluctuations, were assessed by neurologists using a structured interview. Motor signs of all participants were assessed by neurologists using the motor subscale of the Unified Parkinson's Disease Rating Scale (UPDRS-m) (Ballard et al., 1997). The motor symptoms of each participant were assessed using the HAI-MDQ. In performing HAI-MDQ, the caregivers of the participants were interviewed by a well-trained neuropsychologist. They were requested to complete the whole HAICDDS questionnaire, including the 13-item motor questionnaire (the original Chinese version of the questionnaire with a tentative English translation is shown in **Supplementary Table 1**). DATabN derived from Tc99m TRODAT-1 imaging by VR was assessed by two nuclear medicine physicians using interrater reliability tests. Only participants with at least one cerebral structure imaging (CT or MRI) and Tc99m TRODAT-1 imaging were analyzed.

Statistics

The Chinese version of SPSS 22.0 software for Windows (IBM, SPSS Inc., Chicago) was used for statistical analyses. For the composition of the MDQ, the chi-square test for each question in the HAI-MDQ was compared between the DLB and non-DLB groups. Demographic data, including sex, RBD, VH, cognitive fluctuation, DATabN, SBR, UPDRS-m, levodopa equivalent dose (LED), and neuropsychological tests, including Clinical Dementia Rating (CDR), IADL, MoCA, HAI-MDQ, and the sum of scores of the Neuropsychiatric Inventory (NPI-sum) (Ballard et al., 1997), were summarized. The cutoff scores of the HAI-MDQ and SBR to differentiate DLB from non-DLB were derived. To determine the cutoff scores and maximize both sensitivity and specificity, Youden's index was applied. A composite score of the HAI-MDQ and positive SBR were summed with a total score of 7.0, and the cutoff score was also derived and compared. ORs for each variable adjusted for age and disease severity (sum of boxes of the Clinical Dementia Rating scale, CDR-SB) were compared between the DLB and non-dementia (ND) groups, the DLB and AD groups, or HAI-MDQ+ and the HAI-MDQ–groups.

RESULTS

In the design phase, 253 participants with PD/DLB and 491 with non-PD/DLB were analyzed and compared for the 13 candidate symptoms for the composition of the HAI-MDQ. All 13 symptoms were much higher in the PD/DLB group than those in the non-PD/DLB group (all $p < 0.001$). Therefore, seven questions (i.e., MD01, MD02, MD03, MD04, MD05, MD07, and MD08) with the highest ORs were selected to compose the HAI-MDQ (**Supplementary Table 1**).

In the test phase, a total of 277 participants with complaints of motor dysfunction were referred for this study, including 65 participants with ND, 86 participants with AD, and 126 participants with DLB. The duration of motor dysfunction among patients with ND (2.0 ± 4.3), AD (1.0 ± 1.7), and DLB (2.3 ± 2.7) was significantly different ($p = 0.010$). The duration of dementia in patients with AD (2.8 ± 1.0) and DLB (2.5 ± 2.8) was not different. The frequencies of DATabN determined using VR by nuclear medicine physicians were significantly higher in the DLB group (92.1%) than those in the AD (30.2%) or ND (9.2%) groups. The prevalence of each item among the different diagnostic groups in the test phase is shown in **Figure 1**.

The selected items were equally weighed; therefore, the total HAI-MDQ score was 7.0. The comparison of the demographic data among the DLB, ND, and AD groups revealed significantly higher HAI-MDQ total score, UPDRS-m, LED, and lower SBR (all $p < 0.001$). The DLB non-motor features, including DATabN, RBD, cognitive fluctuations, and VH (all $p < 0.005$), were also significantly higher in the DLB group than those in the other groups (**Table 1**).

Among the participants with DLB, at least three symptoms of HAI-MDQ were reported in 91.2% of the DLB group. These symptoms were reported to be much lower in the non-DLB groups (30.8% for ND and 23.3% for AD). Therefore, a cutoff score of 3/2 for the total HAI-MDQ score was suggested for

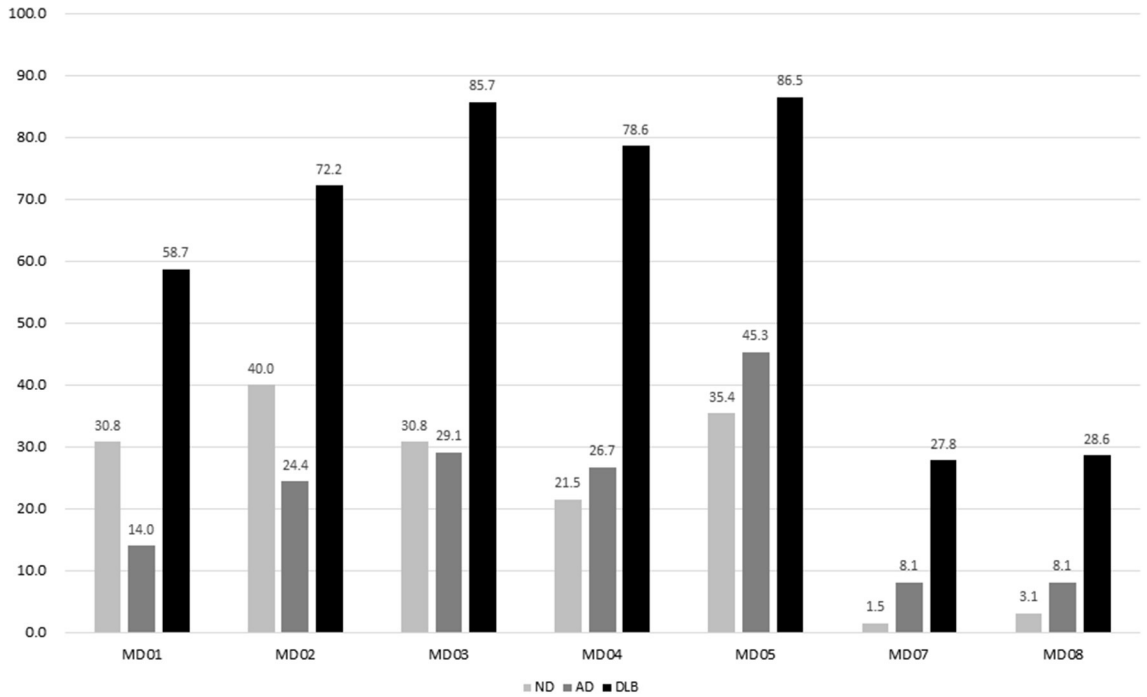

FIGURE 1 | Prevalence of each item in MDQ among different diagnostic groups. MDQ, motor dysfunction questionnaire.

TABLE 1 | Comparison of demographic data among the ND ($N = 65$), AD ($N = 86$), and DLB ($N = 126$) groups.

	ND, mean (SD)	AD, mean (SD)	DLB, mean (SD)	*p*	*Post-hoc*/paired comparison
Age, year	75.1 (6.3)	75.3 (10.5)	76.9 (7.6)	NS	ND = AD = DLB
Female, N (%)	40 (61.5)	53 (61.6)	71 (56.3)	0.12	
Education, year	6.4 (4.4)	4.5 (4.4)	4.9 (9.7)	NS	ND = AD = DLB
Disease duration					
Dementia, year	-	2.8 (2.5)	2.5 (2.8)	NS	AD = DLB
Motor, year	2.0 (4.3)	1.0 (1.7)	2.3 (2.7)	0.010	ND = AD; ND = DLB; AD < DLB
CDR-SB	1.8 (0.8)	5.5 (3.9)	7.7 (4.4)	<0.001	ND < AD < DLB
CASI	76.4 (11.6)	50.1 (22.7)	47.3 (22.7)	<0.001	ND > AD = DLB
MoCA	17.5 (5.8)	9.9 (6.4)	8.4 (5.9)	<0.001	ND > AD = DLB
NPI-sum	5.5 (8.8)	9.8 (11.9)	13.7 (11.0)	<0.001	ND < AD < DLB
UPDRS-m	14.9 (9.9)	17.1 (14.3)	35.4 (19.3)	<0.001	ND = AD < DLB
LED	98.7 (136.9)	52.2 (117.3)	205.4 (202.3)	<0.001	ND = AD < DLB
MDQ	1.6 (1.6)	1.6 (1.5)	4.4 (1.5)	<0.001	ND = AD < DLB
DATabN, N (%)	6 (9.2)	26 (30.2)	116 (92.1)	<0.001	ND < AD < DLB
RBD, N (%)	10 (15.4)	10 (11.6)	67 (53.2)	<0.001	ND < AD < DLB
Fluctuation, N (%)	2 (3.1)	14 (16.3)	87 (69.0)	<0.001	ND < AD < DLB
VH, N (%)	0 (0.0)	11 (12.8)	52 (41.3)	<0.001	ND < AD < DLB

ND, non-dementia control; AD, Alzheimer's disease; N, number of participants; DLB, dementia with Lewy bodies; NS, non-significance; CDR-SB, Sum of Boxes of the Clinical Dementia Rating scale; CASI, Cognitive Abilities Screening Instrument; MoCA, Montreal Cognitive Assessment; NPI-sum, sum score of neuropsychiatric inventory; UPDRS-m, the motor score of the Unified Parkinson's Disease Rating Scale; LED, levodopa equivalent dose; SBR, striatal–background ratio of dopamine transporter imaging; MDQ, motor dysfunction questionnaire in the History-based Artificial Intelligence Clinical Dementia Diagnostic System; DATabN, abnormal dopamine transporter imaging by VR; RBD, REM sleep behavior disorder; Fluctuation, fluctuation of cognition; VH, visual hallucinations.

the screening of motor dysfunction due to DLB vs. non-DLB with a sensitivity of 0.91, a specificity of 0.72, and an area under the curve (AUC) of 0.89. A cutoff score of 1.37/1.38 for SBR in DAT imaging was derived with a sensitivity of 0.91, a specificity of 0.80, and an AUC of 0.90. Two types of composite scores were derived from a further combination of the questionnaire

TABLE 2 | Comparison of SEN, SPEC, PPV, NPV, and AUC with 95% CI among the DLB vs. ND, DLB vs. AD, and DLB vs. non-DLB groups using a cutoff score of 3/2 for the HAI-MDQ, a cutoff score of 1.37/1.38 for the SBR, and a cutoff score of 6/5 for the combination of the MDQVR or MDQSBR.

	SEN	SPEC	PPV	NPV	AUC (95% CI)
HAI-MDQ					
DLB vs. ND	0.91	0.68	0.85	0.80	0.87 (0.84–0.94)
DLB vs. AD	0.91	0.76	0.85	0.86	0.89 (0.84–0.94)
DLB vs. Non-DLB	0.91	0.72	0.73	0.91	0.89 (0.85–0.93)
SBR					
DLB vs. ND	0.91	0.89	0.97	0.84	0.93 (0.89–0.97)
DLB vs. AD	0.91	0.72	0.83	0.85	0.93 (0.89–0.97)
DLB vs. Non-DLB	0.91	0.80	0.79	0.92	0.90 (0.86–0.94)
MDQVR					
DLB vs. ND	0.87	0.97	0.98	0.79	0.98 (0.96–1.00)
DLB vs. AD	0.87	0.91	0.93	0.82	0.95 (0.93–0.98)
DLB vs. Non-DLB	0.87	0.93	0.92	0.89	0.96 (0.94–0.98)
MDQSBR					
DLB vs. ND	0.86	0.97	0.98	0.78	0.98 (0.96–1.00)
DLB vs. AD	0.86	0.90	0.92	0.81	0.95 (0.92–0.98)
DLB vs. Non-DLB	0.86	0.93	0.91	0.89	0.96 (0.94–0.98)

SEN, sensitivity; SPEC, specificity; PPV, positive predictive value; NPV, negative predictive value; AUC, area under the curve; DLB, Lewy body dementia; ND, non-dementia control; AD, Alzheimer's disease; SBR, striatal–background ratio of dopamine transporter imaging; HAI-MDQ, motor dysfunction questionnaire in the History-based Artificial Intelligence Clinical Dementia Diagnostic System; MDQVR, the composite scale of MDQ and DAT VR scale; MDQSBR, the composite scale of MDQ and SBR.

and DAT imaging. First, the composite score was combined with a total HAI-MDQ plus SBR (MDQSBR); if SBR $<$ 1.38, the weighing of SBR was scored as 3, which is the same as the cutoff score for DLB in HAI-MDQ; on the contrary, if SBR $\geq$ 1.38, the weighing of SBR was scored as 0. Second, the composite score was combined with the total HAI-MDQ plus VR of DAT (MDQVR) by a nuclear medicine physician. If the rating was abnormal, the weighing of VR was 3, which is the same as the weighing of SBR and the cutoff score of the abnormal MDQ. In contrast, if VR is negative, the score is 0. A cutoff score of 6/5 of the composite score of MDQSBR was derived for discriminating DLB from non-DLB with a satisfactory sensitivity, specificity, positive predictive value, negative predictive value, and AUC. The AUCs discriminating DLB from non-DLB in HAI-MDQ, SBR, and composite scores were 0.94, 0.89, and 0.96, respectively (**Table 2**).

A comparison of the total scores of the four diagnostic tools among the DLB, ND, and AD groups is shown in **Figure 2**, which shows significantly higher MDQ, MDQVR, and MDQSBR and a significantly lower SBR in the DLB group (all $p < 0.001$).

The comparison of receiver operating characteristic (ROC) curves of MDQ, SBR, MDQSBR composite scale, and MDQVR composite scale among the ND, AD, and DLB groups are shown in **Figure 3**.

To investigate the clinical significance of positive HAI-MDQ among all participants, multivariate risk estimates for all participants in the positive MDQ (HAI-MDQ+) group were compared with the negative (HAI-MDQ–) group with adjustment for age and disease severity (CDR). The HAI-MDQ+ group had a higher diagnosis of PD/DLB (OR = 38.72, $p <$ 0.001), lower MoCA (OR = 0.95, $p = 0.014$), lower IADL (OR = 0.69, $p < 0.001$), higher LED (OR = 1.01, $p = 0.004$), higher UPDRS-m (OR = 1.12, $p < 0.001$), lower SBR (OR = 0.07, $p <$ 0.001), and higher frequency of all PD/DLB non-motor features, including DATabN (OR = 11.27, $p < 0.001$), RBD (OR = 4.31, $p < 0.001$), cognitive fluctuation (OR = 4.11, $p < 0.001$), and VH (OR = 2.47, $p = 0.020$) (**Table 3**).

DISCUSSION

We retrospectively analyzed the data from a relatively large population with a DAT imaging study along with a complete dementia/motor function survey and obtained some important results. First, after adjustment for age and disease severity by CDR, the participants with DLB in this study revealed significantly more motor dysfunction and higher non-motor features, including fluctuations of cognition, VH, RBD, and DATabN. These findings of the participants with DLB were consistent with the clinical criteria for the diagnosis of DLB (Galvin, 2015; McKeith et al., 2017). A higher frequency of DATabN than that in the non-DLB group (9.2% in ND and 30.2% in AD) was probably because the patients who received DAT imaging in the non-DLB group were clinically considered to have motor dysfunction that needed to be ruled out of the possibility of PD/PDD or DLB. In this study, 25 participants with ET were enrolled and classified into the NC group (28.1%). According to previous findings, DATabN was found in some cases of ET (Isaias et al., 2008; Waln et al., 2015) or AD (Costa et al., 2003; McKeith et al., 2007). Studies on ET showed that patients with ET had higher uptake values compared with those in patients with PD but lower than those in healthy subjects (Isaias et al., 2008; Waln et al., 2015). Studies comparing DLB and AD have also found that DATabN appears in some patients with AD (Costa et al., 2003; McKeith et al., 2007).

Second, instead of the neurological examination by physicians, from the point of view of caregivers, high rates of different manifestations of characteristic motor dysfunction in patients with DLB are noticeable and significantly higher in different stages or subtypes of the disease. In this study, three or more symptoms of HAI-MDQ were reported in 91.2% of patients with DLB, and these were reported to be much lower in NC (32.2%) or AD (24.4%) with motor dysfunction. These results demonstrated much higher characteristic motor symptoms in DLB than those in non-DLB using the HAI-MDQ, which indicated the practical use of the HAI-MDQ for the screening of parkinsonism due to DLB.

In addition, to differentiate DLB from non-DLB using either the HAI-MDQ (sensitivity: 0.91, specificity: 0.72, and AUC: 0.89) or SBR (sensitivity: 0.91, specificity: 0.80, and AUC: 0.90) was satisfied, whereas a combination of both tools (MDQVR) further increased the power of differentiation with a sensitivity of 0.87, a specificity of 0.93, and an AUC of 0.96. Therefore, we are looking forward to combining complex clinical data

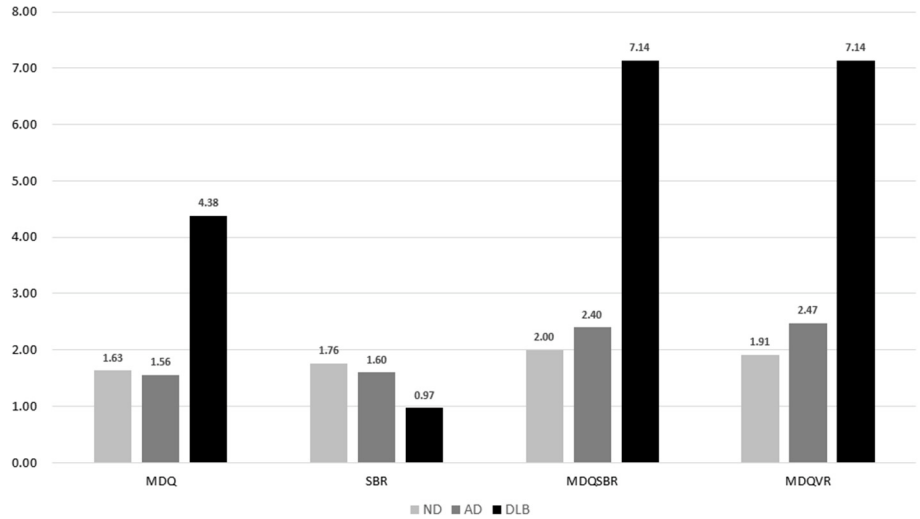

FIGURE 2 | Comparison of MDQ, SBR, MDQSBR, and MDQVR among the ND, AD, and DLB groups. MDQ, motor dysfunction questionnaire in the history-based artificial intelligence clinical dementia diagnostic system; SBR, striatal–background ratio of dopamine transporter imaging; MDQSBR, the composite scale of MDQ and SBR; MDQVR, the composite scale of MDQ and DAT VR scale; ND, non-dementia control; AD, Alzheimer's disease; DLB, dementia with Lewy bodies.

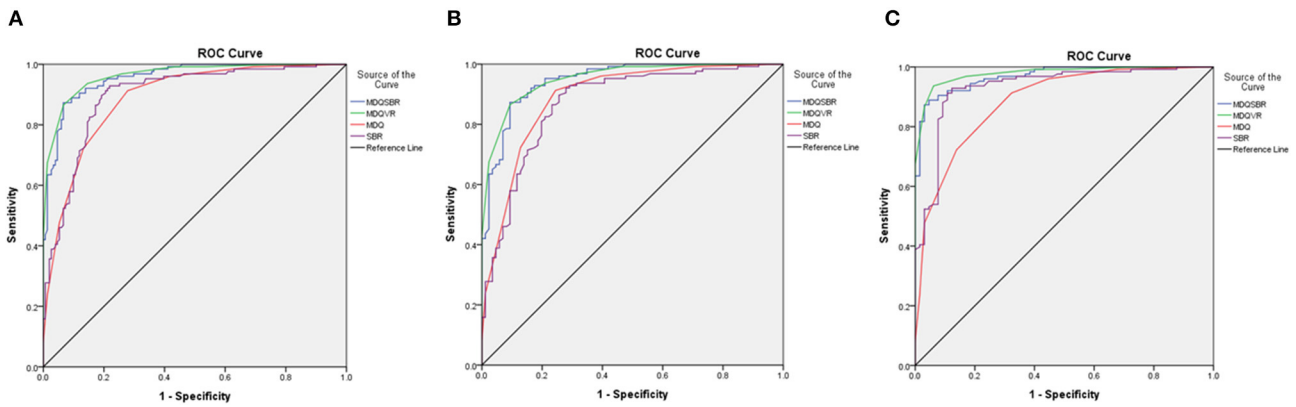

FIGURE 3 | Comparison of ROC curves of MDQ, SBR, MDQSBR composite scale, and MDQVR composite scale among ND, AD, and DLB groups. **(A)** DLB vs. non-DLB (ND+AD). **(B)** DLB vs. AD. **(C)** DLB vs. ND. ROC, receiver operating characteristic; MDQ, motor dysfunction questionnaire in the history-based artificial intelligence clinical dementia diagnostic system; SBR, striatal–background ratio of dopamine transporter imaging; MDQSBR, the composite scale of MDQ and SBR; MDQVR, the composite scale of MDQ and DAT VR scale; ND, non-dementia control; AD, Alzheimer's disease dementia; DLB, dementia with Lewy bodies.

and biomarkers supplemented with artificial intelligence and deep learning procedures to provide an even better diagnostic tool for the clinical diagnosis of dementia with and without movement disorders.

Third, the factors associated with positive MDQVR in all participants in this study provided clinical evidence of the value of the questionnaire for clinical screening of DLB in non-DLB. Findings of much higher MDQVR total score in the MDQVR+ group (7.5 ± 1.3) than that in the MDQVR– group (2.2 ± 1.8) and higher UPDRS-m subscores in the MDQVR+ group (34.4 ± 19.4) than those in the MDQVR– group (17.6 ± 14.3) indicated a positive correlation of motor dysfunction between the two tools. The correlation coefficient of MDQVR with UPDRS-m is 0.56 in the later analysis. In other words, the DLB motor features can be well-detected and differentiated from non-DLB using a combined scale of both tools. A significantly lower SBR in the MDQVR+ group (1.1 ± 0.5) than that in the MDQVR– group (1.7 ± 0.4) and a high correlation coefficient of MDQVR with SBR (−0.65) indicated a good correlation of the questionnaire with reducing DAT uptake in striatal areas, which is currently the hallmark of brain imaging study for the diagnosis of DLB. Higher rates of non-motor DLB features, including DATabN, RBD, VH, and cognitive fluctuations, were found in the HAI-MDQ+ group, revealing that the MDQ and the composite questionnaire MDQVR for the clinical detection of DLB were simple, practical, and reliable.

This study has several limitations. First, the original HAICDDS questionnaire was written in Chinese. Although

TABLE 3 | Multivariate risk estimates (ORs) for all participants in the positive MDQVR composite scale (MDQVR+) group compared with the negative (MDQVR–) group adjusted for age, sex, and CDR-SB.

	MDQVR+, mean (SD)	MDQVR–, mean (SD)	ORs	*p*
N	119	158		
Age, year	76.2 (7.2)	75.8 (9.1)	NA	
CDR-SB	7.5 (4.4)	4.2 (3.8)	NA	
Female, N (%)	90 (54.2)	69 (50.0)	NA	
CASI	48.8 (22.8)	61.3 (22.9)	1.01	NS
MoCA	8.9 (5.9)	12.5 (7.4)	1.01	NS
NPI-sum	14.1 (12.1)	7.9 (9.9)	1.03	0.048
NPI-burden	6.6 (6.0)	3.5 (5.1)	1.06	0.037
UPDRS-m	34.4 (19.4)	17.6 (14.3)	1.06	<0.001
Fluctuation, N (%)	74 (62.2)	29 (18.4)	4.56	<0.001
VH, N (%)	42 (35.3)	21 (13.3)	2.12	0.024
RBD, N (%)	56 (47.1)	31 (19.6)	3.41	<0.001
Parkinsonism	112 (94.1)	68 (43.0)	23.3	<0.001
SBR	0.96 (0.38)	1.64 (0.45)	1.06	<0.001
LED	208.7 (204.5)	69.9 (125.3)	1.01	0.001

ORs, odds ratio; MDQVR, the composite scale of MDQ and DAT VR scale; CDR-SB, Sum of Boxes of the Clinical Dementia Rating scale; N, number of participants; NA, not applicable; NS, non-significance; CASI, Cognitive Abilities Screening Instrument; MoCA, Montreal Cognitive Assessment; NPI-sum, sum score of Neuropsychiatric Inventory; NPI-burden, caregiver burden score of neuropsychiatric inventory; UPDRS-m, the motor score of the Unified Parkinson's Disease Rating Scale; Fluctuation, fluctuation of cognition; VH, visual hallucinations; RBD, REM sleep behavior disorder; SBR, striatal–background ratio of dopamine transporter imaging; LED, levodopa equivalent dose.

we tentatively translated the questionnaire to English, more colloquial and precise translations are required. Second, this study was conducted in only three regional hospitals in Taiwan. Therefore, the findings of different presentations of motor dysfunction might not be generalizable to all patients. Third, the diagnoses of ND, AD, and DLB were based only on clinical criteria. Therefore, the diagnosis of AD was not based on the newest research framework that emphasizes some important biomarkers, including amyloid PET, tau PET, or CSF studies for the diagnosis of AD with or without dementia (Jack et al., 2018). However, detailed clinical information and DAT imaging may help to differentiate DLB from non-DLB, which was supported by robust clinicopathological evidence (Rizzo et al., 2018).

CONCLUSION

This study showed that an informant-based motor questionnaire is a practical tool for the screening of characteristic motor symptoms related to DLB, and this should be the first simple clinical questionnaire for the screening of motor dysfunction characteristic of DLB. The diagnostic value of the questionnaire was further confirmed by positive correlations with the DAT imaging study and motor subscores of the UPDRS. Both questionnaires and DAT imaging were effective in differentiating DLB from AD or ND. A combination of both tools can further improve diagnostic accuracy. This simple screening tool can be applied at the bedside and in clinics for the screening of motor dysfunction related to DLB, and it can help non-specialists to detect DLB easily in healthcare settings without neurologists. Embedded in the HAICDDS project, the MDQ diagnosis requires further machine learning techniques using artificial intelligence and is expected to improve the accuracy and efficiency of the clinical diagnosis of DLB and the differential diagnosis of AD from DLB. Further study of the HAI-MDQ on the discrimination or detection of parkinsonism due to PD and PDD is warranted and is currently in progress.

DATA AVAILABILITY STATEMENT

The original contributions presented in the study are included in the article/**Supplementary Material**, further inquiries can be directed to the corresponding authors.

ETHICS STATEMENT

The studies involving human participants were reviewed and approved by the institutional review board of Show Chwan Memorial Hospital. Written informed consent for participation was not required for this study in accordance with the national legislation and the institutional requirements.

AUTHOR CONTRIBUTIONS

P-YC undertook the literature search and data analysis and was mainly responsible for revisions and drafts of the manuscript. S-LW contributed to revisions and the final draft of the manuscript. G-UH undertook the literature search and contributed to revisions. C-YW contributed to revisions of the manuscript. All authors contributed to the article and approved the submitted version.

FUNDING

This study was funded by Show Chwan Memorial Hospital (Grant No. RD-105032).

ACKNOWLEDGMENTS

We would like to thank Dr. Hsing-Ju Wu at the Research Assistant Center of Show Chwan Memorial Hospital for helping edit this manuscript.

SUPPLEMENTARY MATERIAL

The Supplementary Material for this article can be found online at: https://www.frontiersin.org/articles/10.3389/fnagi.2021.709215/full#supplementary-material

REFERENCES

Ballard, C., McKeith, I., Burn, D., Harrison, R., O'Brien, J., Lowery, K., et al. (1997). The UPDRS scale as a means of identifying extrapyramidal signs in patients suffering from dementia with Lewy bodies. *Acta Neurol. Scand.* 96, 366–371. doi: 10.1111/j.1600-0404.1997.tb00299.x

Chan, D. K., Hung, W. T., Wong, A., Hu, E., and Beran, R. G. (2000). Validating a screening questionnaire for parkinsonism in Australia. *J. Neurol. Neurosurg. Psychiatry* 69, 117–120. doi: 10.1136/jnnp.69.1.117

Chang, S. F., Su, C. L., Chen, Z. Y., Lee, C. S., and Chen, R. C. (1996). Neuroepidemiological survey in Ilan, Taiwan (NESIT)(1): validation of screening instrument in an out-patient department population. *Acta Neurol. Taiwan* 5, 105–110.

Chen, K. L., Xu, Y., Chu, A. Q., Ding, D., Liang, X. N., Nasreddine, Z. S., et al. (2016). Validation of the Chinese version of montreal cognitive assessment basic for screening mild cognitive impairment. *J. Am. Geriatr. Soc.* 64, e285–e290. doi: 10.1111/jgs.14530

Chiu, P. Y., Tang, H., Wei, C. Y., Zhang, C., Hung, G. U., and Zhou, W. (2019a). NMD-12: a new machine-learning derived screening instrument to detect mild cognitive impairment and dementia. *PLoS ONE* 14:e0213430. doi: 10.1371/journal.pone.0213430

Chiu, P. Y., Wei, C. Y., and Hung, G. U. (2019b). Preliminary study of the history-based artificial intelligent clinical dementia diagnostic system. *Show Chwan Med. J.* 18, 18–27. doi: 10.3966/156104972019061801003

Costa, D. C., Walker, Z., Walker, R. W., and Fontes, F. R. (2003). Dementia with Lewy bodies versus Alzheimer's disease: role of dopamine transporter imaging. *Mov. Disord.* 18(Suppl. 7), S34–S38. doi: 10.1002/mds.10576

Dahodwala, N., Siderowf, A., Baumgarten, M., Abrams, A., and Karlawish, J. (2012). Screening questionnaires for parkinsonism: a systematic review. *Parkinsonism Relat. Disord.* 18, 216–224. doi: 10.1016/j.parkreldis.2011.09.003

Emre, M., Aarsland, D., Brown, R., Burn, D. J., Duyckaerts, C., Mizuno, Y., et al. (2007). Clinical diagnostic criteria for dementia associated with Parkinson's disease. *Mov. Disord.* 22, 1689–1707. doi: 10.1002/mds.21507

Galvin, J. E. (2015). Improving the clinical detection of Lewy body dementia with the Lewy body composite risk score. *Alzheimers Dement. (Amst)* 1, 316–324. doi: 10.1016/j.dadm.2015.05.004

Isaias, I. U., Canesi, M., Benti, R., Gerundini, P., Cilia, R., Pezzoli, G., et al. (2008). Striatal dopamine transporter abnormalities in patients with essential tremor. *Nucl. Med. Commun.* 29, 349–353. doi: 10.1097/MNM.0b013e3282f4d307

Jack Jr., C. R., Bennett, D. A., Blennow, K., Carrillo, M. C., Dunn, B., Haeberlein, S. B., et al. (2018). NIA-AA Research Framework: Toward a biological definition of Alzheimer's disease. *Alzheimers Dement.* 14, 535–562. doi: 10.1016/j.jalz.2018.02.018

Lawton, M. P., and Brody, E. M. (1969). Assessment of older people: self-maintaining and instrumental activities of daily living. *Gerontologist* 9, 179–186. doi: 10.1093/geront/9.3_Part_1.179

Lin, C. M., Hung, G. U., Wei, C. Y., Tzeng, R. C., and Chiu, P. Y. (2018). An informant-based simple questionnaire for language assessment in neurodegenerative disorders. *Dement. Geriatr. Cogn. Disord.* 46, 207–216. doi: 10.1159/000493540

Lopez, O. L., Wisnieski, S. R., Becker, J. T., Boller, F., and DeKosky, S. T. (1997). Extrapyramidal signs in patients with probable Alzheimer disease. *Arch. Neurol.* 54, 969–975. doi: 10.1001/archneur.1997.00550200033007

McKeith, I., O'Brien, J., Walker, Z., Tatsch, K., Booij, J., Darcourt, J., et al. (2007). Sensitivity and specificity of dopamine transporter imaging with 123I-FP-CIT SPECT in dementia with Lewy bodies: a phase III, multicentre study. *Lancet Neurol.* 6, 305–313. doi: 10.1016/S1474-4422(07)70057-1

McKeith, I. G., Boeve, B. F., Dickson, D. W., Halliday, G., Taylor, J. P., Weintraub, D., et al. (2017). Diagnosis and management of dementia with Lewy bodies: fourth consensus report of the DLB Consortium. *Neurology* 89, 88–100. doi: 10.1212/WNL.0000000000004058

McKeith, I. G., Dickson, D. W., Lowe, J., Emre, M., O'Brien, J. T., Feldman, H., et al. (2005). Diagnosis and management of dementia with Lewy bodies: third report of the DLB Consortium. *Neurology* 65, 1863–1872. doi: 10.1212/01.wnl.0000187889.17253.b1

McKhann, G. M., Knopman, D. S., Chertkow, H., Hyman, B. T., Jack, C. R. Jr., Kawas, C. H., et al. (2011). The diagnosis of dementia due to Alzheimer's disease: recommendations from the National Institute on Aging-Alzheimer's Association workgroups on diagnostic guidelines for Alzheimer's disease. *Alzheimers Dement.* 7, 263–269. doi: 10.1016/j.jalz.2011.03.005

Mutch, W. J., Smith, W. C., and Scott, R. F. (1991). A screening and alerting questionnaire for parkinsonism. *Neuroepidemiology* 10, 150–156. doi: 10.1159/000110261

Nihashi, T., Ito, K., and Terasawa, T. (2020). Diagnostic accuracy of DAT-SPECT and MIBG scintigraphy for dementia with Lewy bodies: an updated systematic review and Bayesian latent class model meta-analysis. *Eur. J. Nucl. Med. Mol. Imaging.* 47, 1984–1997. doi: 10.1007/s00259-019-04480-8

Postuma, R. B., Berg, D., Stern, M., Poewe, W., Olanow, C. W., Oertel, W., et al. (2015). MDS clinical diagnostic criteria for Parkinson's disease. *Mov. Disord.* 30, 1591–1601. doi: 10.1002/mds.26424

Rizzo, G., Arcuti, S., Copetti, M., Alessandria, M., Savica, R., Fontana, A., et al. (2018). Accuracy of clinical diagnosis of dementia with Lewy bodies: a systematic review and meta-analysis. *J. Neurol. Neurosurg. Psychiatry* 89, 358–366. doi: 10.1136/jnnp-2017-316844

Sasaki, S. (2018). High prevalence of parkinsonism in patients with MCI or mild Alzheimer's disease. *Alzheimers Dement.* 14, 1615–1622. doi: 10.1016/j.jalz.2018.06.3054

Tanner, C. M., Gilley, D. W., and Goetz, C. G. (1990). A brief screening questionnaire for parkinsonism. *Ann. Neurol.* 28, 267–268.

The Italian Longitudinal Study on Aging Working Group. (1997). Prevalence of chronic diseases in older Italians: comparing self-reported and clinical diagnoses. The Italian longitudinal study on aging working group. *Int. J. Epidemiol.* 26, 995–1002. doi: 10.1093/ije/26.5.995

Waln, O., Wu, Y., Perlman, R., Wendt, J., Van, A. K., and Jankovic, J. (2015). Dopamine transporter imaging in essential tremor with and without parkinsonian features. *J. Neural Transm. (Vienna)* 122, 1515–1521. doi: 10.1007/s00702-015-1419-z

Wang, C. T., Hung, G. U., Wei, C. Y., Tzeng, R. C., and Chiu, P. Y. (2020). An informant-based simple questionnaire for visuospatial dysfunction assessment in dementia. *Front. Neurosci.* 14:44. doi: 10.3389/fnins.2020.00044

Zaccai, J., McCracken, C., and Brayne, C. (2005). A systematic review of prevalence and incidence studies of dementia with Lewy bodies. *Age Ageing* 34, 561–566. doi: 10.1093/ageing/afi190

Zhu, F., Li, X., McGonigle, D., Tang, H., He, Z., Zhang, C., et al. (2020). Analyze informant-based questionnaire for the early diagnosis of senile dementia using deep learning. *IEEE J. Transl. Eng. Health Med.* 8:2200106. doi: 10.1109/JTEHM.2019.2959331

Conflict of Interest: The authors declare that the research was conducted in the absence of any commercial or financial relationships that could be construed as a potential conflict of interest.

frontiers in Aging Neuroscience

REVIEW
published: 18 August 2021
doi: 10.3389/fnagi.2021.704661

Cognitive Decline Assessment: A Review From Medical Imaging Perspective

Caroline Machado Dartora[1]*, *Wyllians Vendramini Borelli*[2,3], *Michel Koole*[4] and *Ana Maria Marques da Silva*[1,3,5]

[1] School of Medicine, Pontifical Catholic University of Rio Grande do Sul, PUCRS, Porto Alegre, Brazil, [2] Neurology Department, Hospital de Clínicas de Porto Alegre, Porto Alegre, Brazil, [3] Brain Institute of Rio Grande do Sul, Bralns, Porto Alegre, Brazil, [4] Nuclear Medicine and Molecular Imaging, Department of Imaging and Pathology, KU Leuven, Leuven, Belgium, [5] Medical Image Computing Laboratory, School of Technology, Pontifical Catholic University of Rio Grande do Sul, PUCRS, Porto Alegre, Brazil

Aging is a complex process that involves changes at both molecular and morphological levels. However, our understanding of how aging affects brain anatomy and function is still poor. In addition, numerous biomarkers and imaging markers, usually associated with neurodegenerative diseases such as Alzheimer's disease (AD), have been clinically used to study cognitive decline. However, the path of cognitive decline from healthy aging to a mild cognitive impairment (MCI) stage has been studied only marginally. This review presents aspects of cognitive decline assessment based on the imaging differences between individuals cognitively unimpaired and in the decline spectrum. Furthermore, we discuss the relationship between imaging markers and the change in their patterns with aging by using neuropsychological tests. Our goal is to delineate how aging has been studied by using medical imaging tools and further explore the aging brain and cognitive decline. We find no consensus among the biomarkers to assess the cognitive decline and its relationship with the cognitive decline trajectory. Brain glucose hypometabolism was found to be directly related to aging and indirectly to cognitive decline. We still need to understand how to quantify an expected hypometabolism during cognitive decline during aging. The Aβ burden should be longitudinally studied to achieve a better consensus on its association with changes in the brain and cognition decline with aging. There exists a lack of standardization of imaging markers that highlight the need for their further improvement. In conclusion, we argue that there is a lot to investigate and understand cognitive decline better and seek a window for a suitable and effective treatment strategy.

Keywords: brain imaging, aging brain, cognitive aging, Alzheimer's disease, PET, MRI

OPEN ACCESS

Edited by:
Binbin Nie,
Institute of High Energy Physics, Chinese Academy of Sciences, China

Reviewed by:
Tengfei Guo,
Shenzhen Bay Laboratory, China
Giovanni Bellomo,
University of Perugia, Italy

***Correspondence:**
Caroline Machado Dartora
caroline.dartora@acad.pucrs.br

Received: *03 May 2021*
Accepted: *19 July 2021*
Published: *18 August 2021*

Citation:
Dartora CM, Borelli WV, Koole M and Marques da Silva AM (2021) Cognitive Decline Assessment: A Review From Medical Imaging Perspective. Front. Aging Neurosci. 13:704661. doi: 10.3389/fnagi.2021.704661

INTRODUCTION

Aging is associated with several transformations in our body, including the brain. The aging process causes modifications from molecular to morphological levels, thereby altering the brain size, vasculature, and, more often, cognition (Peters, 2006). However, biological and chronological aging is not completely linked. By 2050, the global life expectancy is expected to increase 6 years (the average global life expectancy is 72 years) (World Health Organization, 2017). Thus, it is necessary to understand how it will affect health, memory, and cognition of people. Aging influences

both brain anatomy and function, but these phenomena are not well-understood. Oschwald et al. (2019) has emphasized the need to study the relationship between neuroanatomy and specific cognitive abilities in the aging brain.

Since the 1960s, cognitive decline has been diagnosed by using clinical signs (measured by tests and scores) and post-mortem evaluation of neurodegeneration and protein accumulation in the brain. In 1985, the *Archives of Neurology* published the first recommended use of neuroimaging, biomarkers, genetics, longitudinal studies, brain banks, and the establishment of family registries and animal models to study the phenomenon of normal brain aging (Khachaturian, 2005). New technologies have emerged in the field of diagnosis, treatment, care, and knowledge related to the causes of normal cognitive decline and Alzheimer's disease (AD). For example, diagnosis of AD involves conducting genetic tests for alleles of apolipoprotein ε (APOE ε), blood/spinal fluid test, amyloid-β (Aβ), and tau protein quantification and aggregation distribution by using positron emission tomography (PET). In the past decade, imaging biomarkers, including hippocampal volume in structural magnetic resonance images (MRI), temporoparietal glucose hypometabolism, neocortical Aβ, and medial temporal and neocortical tau deposition in PET images have been used to stage AD and understand the associated cognitive decline (Besson et al., 2015; Jack et al., 2018). However, which characteristics in PET and MRI indicate a prospective cognitive decline in the elderly population still need to be discerned.

Alzheimer's disease is a progressive, irreversible, and neurodegenerative disease that affects several regions of the brain, including the brain cortex and hippocampus (Citron, 2010; Masters et al., 2015). AD is associated with a dysfunction of the amyloid precursor protein (APP), leading to an accumulation of insoluble Aβ and generating plaques in extracellular spaces. The patients with AD present an inherent failure of the cerebral system to remove Aβ peptides (Masters et al., 2015). The amyloid cascade hypothesis suggests that Aβ super-production and failure in peptide clearance lead to amyloid deposition, triggering the production of neurofibrillary tangles (NFTs), cell death, synaptic loss, and symptoms of memory loss and cognitive decline (Cohen et al., 2012). In addition, AD is related to NFTs formed by the abnormal accumulation of hyperphosphorylated tau protein filaments (Masters et al., 2015). AD is associated with a significant loss of neurons and a deficit in the neuronal transmission system in brain areas related to memory and cognition, prominent inflammatory pathways, and innate immune response (Citron, 2010; Cohen et al., 2012).

Diagnosis of AD by using only clinical factors is often challenging; it can be misdiagnosed due to similarities in symptoms and biomarkers with other conditions, such as cerebrovascular diseases, dementia with Lewy bodies, frontotemporal dementia, and hippocampal sclerosis (Masters et al., 2015). In 2011, the National Institute on Aging–Alzheimer's Association (NIA–AA) workgroup revised the 1984 criteria for AD dementia by implementing guidelines and diagnostic criteria for neuropsychological testing, advanced imaging, and cerebrospinal fluid (CSF) measures, which could be used by both specialists with these tools available and general healthcare providers with no access to these tools (FDA-NIH Biomarker Working Group, 2016). The imaging biomarkers defined by NIA–AA include a decrease in the uptake of ^{18}F-FDG in the temporoparietal cortex, a positive PET Aβ imaging, and atrophy in medial, basal, and lateral temporal lobes and medial parietal cortex detected by structural MRI.

In 2018, Jack et al. (2018) presented a research framework of NIA–AA with a biological definition of AD as an aggregate of neuropathological changes determined by *in vivo* biomarkers and post-mortem evaluation without considering clinical symptoms. It has proved beneficial in approximately 10– 30% of individuals who are clinically diagnosed with AD (demented individuals) but do not present neuropathological changes at autopsy and 30–40% of cognitively unimpaired (CU) elderly individuals who present with neuropathological changes in autopsy (Jack et al., 2018). Subjects who present amyloid and tau markers are defined as AD, and when only amyloids are present, individuals are known to have so-called Alzheimer's pathological change. This classification is based on pathological examinations and not clinical symptoms or the presence of neurodegeneration. Clinical symptoms without any biomarker evaluation are categorized as "Alzheimer's clinical syndrome" (ACS) and AD biomarker confirmation is used for staging the progression of the disease. Because the NIA–AA research framework was published in 2018 and is still being implemented, individuals denominated as "AD" or "probable AD" in this review are renamed ACS.

A few studies have analyzed the cognitive-decline images with the so-called AD-signature regions of interest (ROIs) that are brain regions that show remarkable changes in ACS. They comprise hippocampus in MRI and temporoparietal cortex and posterior cingulate cortex in ^{18}F-FDG studies. However, with the new NIA–AA research framework proposed by Jack et al. (2018), these AD-signature ROIs have become invalid, because AD is pathologically defined as a proteinopathy that is characterized by the presence of amyloid and tau aggregates, not by hippocampus shrinkage or brain hypometabolism. The major limitation of this signature is that it cannot be used when a subject already has the imaging marker, and cognitive decline usually occurs in a stage where the pharmacological treatment for symptom retardation is unsuccessful. Consequently, it is essential to find early or set markers and their thresholds for healthy brain aging and the development of cognitive decline.

The present study addresses the following questions: Which biomarkers are used in cognitive decline assessment? How do dementia imaging patterns correlate with cognitive decline trajectories? How do brain glucose metabolism and amyloid and tau burden change with aging? How are cutoff values for classifying cognitive decline trajectories defined? How can joint evaluation of imaging biomarkers add value to the cognitive decline assessment? What are the trends and open questions in the assessment of cognitive decline that use medical images?

This review presents different views and aspects of cognitive decline evaluation by using medical images, primarily based on the differences between studies on CU individuals and those with cognitive declines, such as mild cognitive impairment (MCI) and AD. Biomarkers, including imaging markers, patterns based on ROIs, and their relationship with aging markers and

neuropsychological tests have been discussed. Our goal is to delineate how aging has been studied with medical imaging and find answers to the above questions in the context of the aging brain and its cognitive decline.

BIOMARKERS IN THE COGNITIVE DECLINE ASSESSMENT

A biomarker is an indicator of normal biological or pathogenic processes or responses to an exposure or intervention, including therapeutic interventions. Biomarkers can have molecular, histologic, radiographic, and physiologic characteristics with a direct effect, for example, measurement of amyloid, or indirect effect such as ^{18}F-FDG imaging to measure neuronal activity. Furthermore, biomarkers are divided into different categories such as predictive, prognostic, diagnostic, response seeking, monitoring, safety, and risk (FDA-NIH Biomarker Working Group, 2016).

Aging biomarkers are the indicators of the functional state of a person and the risk factors for specific age-related pathologies; these include specific proteins in the CSF, brain structural images, and pathological proteins (Moskalev, 2019). Prognostic biomarkers can be used in clinical trials to screen patients with a high risk of having a disease-related endpoint event or a substantial worsening. Several markers have been used to study the decline in human brain activity, with cognitive tests being the gold standard. Both direct and indirect imaging markers have shown promising results in differentiating brain patterns in the early stages of decline.

A strict relationship exists between physiological biomarkers and imaging markers. Physiological biomarkers are measurable physical aspects such as a clinical symptom or blood glucose, which are evaluated by their values in normal biological or pathogenic processes (Strimbu and Tavel, 2010). Imaging (bio)markers are characteristics visualized by analyzing a medical image.

Amyloid PET image detects amyloid plaques and is based on the staining agents used in post-mortem studies. In 2004, the first-generation Aβ tracer, the Pittsburg compound B (^{11}C) or ^{11}C-PiB, was developed for *in vivo* evaluation of Aβ plaque accumulation as it was only possible in a post-mortem examination. The compound is derived from a staining agent called thioflavin-T and is similar to ^{18}F-NAV4694, a third-generation agent. Another PET Aβ tracer is florbetapir (^{18}F) or ^{18}F-AV45 that is derived from Congo red and Chrysamine-G. All PET Aβ tracers bind to fibrillary forms of Aβ, mostly Aβ42 fibrils. The differences among different PET Aβ radiotracers are attributed to the specific binding on Aβ plaques, uptake time, and clearance (Bao et al., 2017).

Recently, several tau PET tracers, such as ^{18}F-AV1451, ^{18}F-T808, ^{18}F-THK5351, and ^{11}C-PBB3, have been developed. However, each one of these has different binding properties with tau isoforms. For example, ^{18}F-AV1451 shows a high affinity with classical, paired helical filament–tau tangles in its six isoforms and low affinity with tangles of the 4R isoforms. ^{18}F-THK5351 exhibits a high signal-to-background ratio and binding affinity for hippocampal damaged tissue but off-target binding for MAO-B. Similarly, ^{11}C-PBB3 has a high specificity for tau deposition; however, its sulfate conjugate crosses the blood–brain barrier, hindering the quantitative evaluation of the tau tracer (Bao et al., 2017). The tau PET brain pattern distribution at different disease stages can be explained by six different Braak stages (Braak and Braak, 1991) that are based on post-mortem evaluation of NFTs and neuropil threads (NTs). Stage I is represented by the modest involvement of the transentorhinal region, a few isolated NFTs in the regions of the basal forebrain and thalamus. Stage II is an aggravation of stage I with hippocampal involvement and isolated NFTs in isocortical regions. Stage III consists of a severe attachment of NFTs in entorhinal and transentorhinal regions; mild involvement of the hippocampus and isocortex, forebrain nuclei, thalamus, and amygdala, scattered NFTs and NTs in the basal portions of frontal, temporal, and occipital areas and subiculum. Stage IV is characterized by a thalamic nucleus densely filled with NFTs and NTs. In stage V, the isocortex is severely affected and the thalamus, claustrum, and amygdala are more consistently involved. In stage VI, all stage IV changes are more pronounced with a considerable loss of nerve cells and all isocortical regions, such as severely affected subcortical nuclei (Braak and Braak, 1991).

In summary, relevant regions for different Braak stages are as follows (Braak and Braak, 1991; Alafuzoff et al., 2008):

- Braak I: transentorhinal region.
- Braak II: entorhinal region.
- Braak III: temporo-occipital gyrus.
- Braak IV: temporal cortex.
- Braak V: peristriatal cortex.
- Braak VI: isocortical areas, subcortical nuclei, and extrapyramidal system (striatal cortex).

Analyzing different image markers together can be challenging. A voxel-wise analysis (Besson et al., 2015) found that the brain patterns of healthy elders selected independently as positive or negative for biomarkers (metabolism, degeneration, or amyloid burden) did not match with the patterns found in a group with positive or negative subjects for another biomarker of the same list. Healthy elders with higher hypometabolism showed a global distribution of hypometabolic areas, especially in the frontal cortex. The prevalence of amyloid positivity increased from 10 to 44% in CU subjects aged from 50 to 90 years (Ewers et al., 2012; Besson et al., 2015; Jansen et al., 2015).

In a study by Jack et al. (2019), the Aβ/tau/neurodegeneration, AT(N), system showed a significant improvement in predicting memory decline in non-demented elders. The AT(N) system was proposed in the NIA–AA research framework (Jack et al., 2018) to categorize elder individuals by pathology. The AT(N) system was defined by several biomarkers, where A represented amyloid markers, T represented tau, and N represented the presence of neurodegeneration (or neuronal injury, atrophy on MRI, FDG hypometabolism, and CSF total tau). The presence of A and T positives are neuropathological indicators of AD, whereas (N) is not a disease specific (Jack et al., 2018, 2019) enabling the use of different measures with similar but not completely redundant information (Jack et al., 2015). In non-demented

elders, Jack et al. (2019) showed that individuals with A+T–(N)+ showed cognitive decline at all ages, independent of APOE $\varepsilon 4$ presence, whereas the cognitive decline in A+T–(N)– individuals was slower than in other evaluated groups with a positive amyloid biomarker.

Memory scores and amyloid burden have been extensively studied. Chételat et al. (2011) Click or tap here to enter text. assessed the correlation between Aβ deposition and episodic memory scores. After reviewing the literature, they found that pooling the subjects in groups with different decline patterns (CU elders, MCI, and ACS) could drive erroneous correlations. For example, ACS and non-demented individuals, when pooled together in an Aβ deposition analysis and memory test, showed a high correlation due to a higher level of Aβ deposition in ACS and not due to the whole group representation. However, subjects in predementia stages had lower episodic memory performances due to the Aβ deposition, especially in the temporal neocortex, and independently because of hippocampal atrophy. Ewers et al. (2012) suggested that the first step in predicting cognitive decline is assessing the combination of structural and functional brain decline associated with Aβ deposition. Although amyloid accumulation has been repeatedly associated with further memory decline in longitudinal studies (Lim et al., 2014; Farrell et al., 2017; Landau et al., 2018), high amyloid accumulation, including intermediate "gray zone" burden (Ebenau et al., 2020), is associated with further memory decline (Landau et al., 2018), but not baseline amyloid levels. Amyloid accumulation across multiple posterior regions predicted memory decline (Farrell et al., 2018), but a specific region within the superior temporal sulcus of CU individuals was associated with memory decline (Guo et al., 2020).

The problem of wrong correlation between the instrumental activities of daily living (IADL) and tau and Aβ burden occurs during pooling the groups with different decline patterns. MCI and ACS groups, when pooled, showed higher tau and Aβ uptake than CU individuals, making the correlation with IADL stronger. When analyzed individually, the association between tau and amyloid burden and IADL impairment was weak (Halawa et al., 2019). Although the evidence suggested an emerging heterogeneity of biomarker expression in ACS subjects (Osorio et al., 2014) as the AT(N) system, still there are no standard cutoff values for evaluating the biomarkers.

High Aβ accelerates atrophy in CU elders in the medial temporal lobe and precuneus compared with subjects with low Aβ levels (Ewers et al., 2012). Chételat et al. (2011) studied the effects of temporal Aβ deposition and found that it had no relation with memory and hippocampal atrophy. Recent studies have shown that disentangling the effects of Aβ and tau on cognitive decline is not an easy task. The accumulation of both proteins has a relationship with age in cognitively impaired and unimpaired individuals (Lowe et al., 2018). An increase in tau abnormality was associated with age in Aβ+ and Aβ− CU individuals and was not confined to the medial temporal lobe, being widespread through the brain, mostly corresponding to early Braak stages I–IV (Lowe et al., 2018; Pascoal et al., 2020). These isolated cases of tau pathology, without amyloid and neurodegeneration abnormal markers, occurred in the absence of cognitive impairment (Altomare et al., 2019). Cognitive decline has shown to be associated with abnormal tau levels, independent of Aβ levels; however, it was associated with increased worsening of memory when associated with abnormal Aβ (Sperling et al., 2019; Guo et al., 2021). The contrary was not confirmed: abnormal Aβ levels without abnormal tau are not related to cognitive decline in CU individuals (Sperling et al., 2019; Guo et al., 2021; Pereira et al., 2021). There is no consensus on which biomarkers can be used to assess cognitive decline and how they are associated. It is hard to find an agreement within the studies in evaluating the cognitively healthy older adult population.

IMAGING BIOMARKERS IN COGNITIVE DECLINE TRAJECTORIES

Neurodegeneration, glucose hypometabolism patterns, amyloid, or tau burden are the primary characteristics of brain-imaging analysis. Clinical studies usually focus on analyzing (AD–) signature ROIs. It is used as a differential diagnosis for ACS. However, specific regions for analysis in Aβ and tau studies are not well-understood. In this section, we will present findings of each imaging biomarker (MRI and FDG, amyloid or tau PET) in cognitive-decline trajectory.

MRI have been widely used to evaluate the decline and differential diagnosis of ACS due to its high spatial resolution and structural characteristics. The most clinically used ROI in MRI is the hippocampus for shrinkage compared to CU elders. However, studies showed different structures with neuroanatomical changes in healthy aging. Ewers et al. (2012) measured the gray matter (GM) volume in regions such as the hippocampus, middle temporal gyrus, superior temporal gyrus, amygdala, parahippocampus, entorhinal cortex, inferior parietal lobe, precuneus, and thalamus. A meta-analysis (Schroeter et al., 2009) showed that these regions are more predictive of ACS than the hippocampus and associated MRI measures with the Aβ scale (Ewers et al., 2012). In addition, he found that MCI individuals had a more significant effect of Aβ on the annual rate of volume decline in the inferior parietal lobe, entorhinal cortex, parahippocampus, middle temporal gyrus, inferior parietal lobe, and a trend for the precuneus.

Besson et al. (2015) performed a voxel-wise analysis of CU individuals with positive and negative MRI biomarkers. He used the hippocampal volume as the ROI and found that CU individuals with a positive marker for atrophy showed lower executive-function performance than its counterpart (MRI-negative individuals). In addition, positive subjects showed a significantly lower volume in the hippocampus, frontoinsular, ventromedial, prefrontal, and lateral temporal cortex bilaterally. Rizk-Jackson et al. (2013) conducted a longitudinal 48-month study and found that the volume loss in the hippocampus, temporal lobe, and the overall brain was higher in elder subjects who experienced cognitive decline relative to those who remained stable.

Chételat et al. (2011) assessed the brain regions with a higher difference between ACS and CU individuals in the GM and white matter (WM) of T1-weighted MRI in a different voxel-wise

approach. The regions were turned to a mask and assessed for a correlation between regions and episodic memory scores in healthy elders and MCI. They found that GM atrophy was mainly located in the hippocampus and temporal neocortex, extending to the temporoparietal, temporo-occipital, anterior cingulate cortex, and precuneus regions. WM atrophy involved the cingulum bundle, perforant path, and corpus callosum. The relationship with episodic memory scores and GM volume was confined bilaterally to the hippocampi, with no relation with the WM volume in family-wise error corrected threshold of $p < 0.05$. However, when the $p_{\text{uncorrected}} < 0.001$ was applied, a significant correlation was found in the perforant path bilaterally. The mean cortical thickness of entorhinal, inferior temporal, middle temporal, and fusiform regions was used to find cutoff values for GM degeneration for a marker to differentiate cognitively impaired individuals from unimpaired individuals (Jack et al., 2017a). MRI is a fundamental imaging modality in clinical practice, which provides useful information about the progression of cognitive decline in healthy older adults. When associated with amyloid positivity, MRI can strongly predict further decline (Jack et al., 2018). However, MRI findings presented mixed patterns in patients with consistent memory complaints, the theoretical first symptom of AD, which makes the utility of MRI in early AD neurobiology unclear (Wang et al., 2020).

Jie et al. (2015) used a selection feature method to find the most important brain regions in differentiating between MCI subjects and healthy elders. Volume (based on MRI) and the ^{18}F-FDG average intensity of 93 brains ROIs were used. A manifold regularized multitask selection feature between MCI and healthy elders was applied. The selected brain regions were localized mostly on the left (L) brain side: L. cuneus, L. and right (R) precuneus, L. temporal pole, L. entorhinal cortex, L. and R. hippocampal formation, L. angular gyrus, L. and R. occipital pole, R. amygdala, L. parahippocampal gyrus.

Rizk-Jackson et al. (2013) used ^{18}F-FDG images to determine which clinical measure could classify healthy elders who remained stable and those whose condition progressed to MCI. An ROI-based analysis calculated the average glucose metabolism in the right and left angular gyri, right and left temporal gyri, and bilateral posterior cingulate gyrus. An analysis of the differences between healthy elders and those who progressed to MCI revealed that only posterior cingulate cortex hypometabolism showed statistical significance, bringing back the idea of a signature ROI.

An ROI-based study on associations between Aβ levels and ^{18}F-FDG uptake (Ewers et al., 2012) used a meta-analysis of regions typically affected in ACS, based on previous studies (Jagust et al., 2009; Landau et al., 2011). The selected areas for ^{18}F-FDG analysis were the angular gyrus, posterior cingulate/precuneus, and inferior temporal cortex.

Besson et al. (2015) defined the ^{18}F-FDG analysis regions by using the most remarkable changes in ACS areas in an independent sample. These regions were the posterior cingulate and temporoparietal, the AD-signature ROIs. In addition, he used a binary mask corresponding to the entire GM, except for the cerebellum, occipital, and sensory-motor cortices, hippocampi, amygdala, and basal nuclei to study an Aβ signature in a healthy elder (between 50 and 84 years of age) group.

By using the group of healthy elders (Besson et al., 2015), Oh et al. (2014) examined the regional patterns of Aβ deposition, glucose metabolism, and GM volume and their correlation with cognition using composite scores from neuropsychological tests. He calculated a global PIB index based on the mean distribution volume ratio values of large cortical ROIs that spanned through the frontal, temporal, and parietal cortices and anterior/posterior cingulate gyri. A correlation with Aβ topography using the scaled subprofile modeling analysis was found. In addition, reduced amyloid deposition in the hippocampus bilaterally and the visual and motor cortex was found. However, positive amyloid deposition was found in the medial frontal, temporoparietal, lateral cortices, and precuneus. A negative correlation was present between GM volume and global PIB index in the medial frontal, lateral temporal, and posterior cingulate cortices and hippocampus and positive loadings in the superior frontal, primary sensory/motor, and visual cortices. The relationship of global PIB index increased with a relative decrease in glucose metabolism in the inferior medial frontal cortex, lateral and medial temporal cortex, anterior cingulate, and visual cortex, and relative increase in the lateral prefrontal cortex, lateral parietal cortex, and precuneus.

Chételat et al. (2011) performed a voxel-wise analysis of Aβ images between ACS and CU individuals. Regions with higher differences between the groups were the posterior cingulate-precuneus area, anterior cingulate and medial frontal cortex, and lateral temporal and temporoparietal regions. They found a significant correlation between Aβ deposition and episodic memory scores in the inferior and middle temporal neocortex regions, anterior and posterior cingulate, and prefrontal cortex. Ewers et al. (2012) used ROIs for Aβ evaluation, comprising the prefrontal, lateral temporal, anterior cingulate gyrus, parietal, and posterior cingulate/precuneus area, the same regions as in a previous study (Halawa et al., 2019).

A pathological study comparing Aβ burden by immunohistochemistry and ^{18}F-florbetapir uptake in ACS elders showed a good correlation with the frontal, temporal, parietal, anterior and posterior cingulate, and precuneus regions (Clark et al., 2011). These regions were used to analyze longitudinal changes in unimpaired older individuals and progression of the Aβ burden. However, the rate of Aβ accumulation was dependent on the reference region used to calculate the standardized uptake value (SUV) ratio (Landau et al., 2015). Moreover, these regions were not related to age, baseline memory, or executive function in longitudinal (Landau et al., 2018) and cross-sectional studies (Jansen et al., 2018), but they were associated with higher Aβ in baseline, poorer longitudinal memory performance (Landau et al., 2018), and CDR changes (Mormino et al., 2017) and contributed to the individual estimates of cognitive level in the transversal approach (Jansen et al., 2018). Furthermore, for MCI and dementia of uncertain etiology, the use of amyloid PET images has proved to be useful in challenging clinical diagnosis (Rabinovici et al., 2019). In contrast, cortical Aβ deposition did not affect cognitive and behavioral domains within 2 years in CU

older individuals (70 years old or more) with subjective cognitive decline (Dubois et al., 2018).

Increased tau uptake in the meta-ROI can accurately distinguish AD dementia from other dementias (Ossenkoppele et al., 2018) with a variety of tau tracers (Leuzy et al., 2021). In addition, it can predict memory decline in cognitively healthy older adults (Jack et al., 2019). Despite its high accuracy for AD-related brain alterations, the potential use of tau PET in clinical practice remains to be thoroughly discussed. Interesting patterns were found in a voxel-wise analysis using Aβ and tau images (Shimada et al., 2017). Tau pathology showed a gradual expansion with age within a restricted region around the medial temporal cortex. A recent study suggested that brain amyloid accumulation may occur earlier than tau-related axonal damage (Pereira et al., 2021). Thus, in the presence of Aβ, tau progression occurred in the entire neocortex via the collateral sulcus. Medial temporal atrophy was a normal finding in healthy aging that was probably caused by tau pathology even without a significant association between tau burden and brain volume in the hippocampus.

Halawa et al. (2019) used the regions related to the IADL scores from previous studies (bilateral entorhinal cortex, inferior temporal cortex, rostral anterior cingulate cortex, posterior cingulate cortex, supramarginal gyrus, orbitofrontal cortex, precuneus, and dorsolateral prefrontal cortex) for tau imaging to investigate the association between IADL impairment and regional cerebral tau deposition in healthy elders, MCI, and ACS subjects. He performed the same analysis for Aβ images but used the frontal, cingulate, and lateral parietal and lateral temporal cortices. He found more significant medial and inferior temporal tau and cortical Aβ burden associated with greater IADL impairment.

The brain regions for analyzing the initial cognitive decline are not well-defined. Even the AD-signature ROIs are not the best alternative for the analysis because their characteristics are better represented when transitioning between MCI and ACS. The brain regions to be analyzed are still miscellaneous for MR, ^{18}F-FDG, amyloid, or tau PET images and are usually related to the marker. **Figure 1** shows an example of a tag cloud built with the most commonly diagnosed brain regions in amyloid PET studies, extracted from seven papers (Chételat et al., 2011; Ewers et al., 2012; Oh et al., 2014; Besson et al., 2015; Mattsson et al., 2015; Hanseeuw et al., 2017; Halawa et al., 2019).

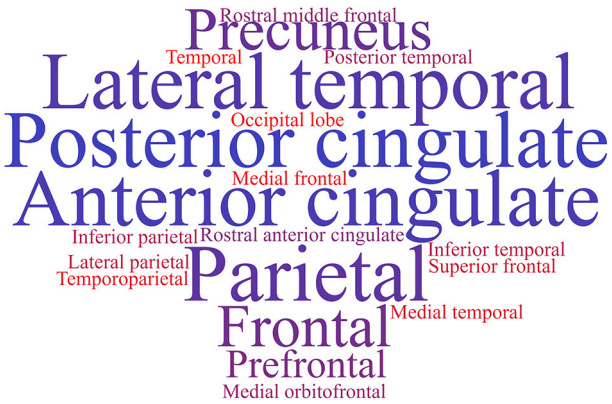

FIGURE 1 | Tag cloud of the most used brain regions in amyloid studies based on the information retrieved from seven papers (Chételat et al., 2011; Ewers et al., 2012; Oh et al., 2014; Besson et al., 2015; Mattsson et al., 2015; Hanseeuw et al., 2017; Halawa et al., 2019).

AGING AND BRAIN GLUCOSE HYPOMETABOLISM

Like brain atrophy, hypometabolism is a neurodegeneration signal detected with structural MRI. Hypometabolism, being common in aging, could predict cognitive decline. However, metabolism patterns are not always related to all aging image markers.

Besson et al. (2015) found that the ^{18}F-FDG positive (FDG+) vs. negative (FDG–) group (with positive cutoff values defined in the AD-signature ROIs as the 90th percentile of the biomarker residuals estimated in an independent group of ACS subjects) did not reveal a typical AD-like pattern of decreased volume in MRI and an increased Aβ burden. However, they detected a mixed hypometabolic pattern, including AD-signature ROIs and the prefrontal cortex. The involvement of the prefrontal cortex may be related to the non-ACS process, but with healthy aging or frontotemporal dementia, because it is expected to appear in the later stages of ACS. Hypometabolism in the prefrontal cortex can be age related, and Aβ deposition may not be associated with degeneration. In their findings, no statistical differences were found in age, sex, education level, or APOE ε4 between FDG+ and FDG– subjects (Besson et al., 2015).

Ishibashi et al. (2018) studied the effect of aging on brain glucose metabolism and analyzed CU elderly individuals longitudinally (67.9 and 75.7, mean age at baseline and second scan, respectively). The analysis was voxel-based and showed a decrease in the ^{18}F-FDG uptake in the anterior cingulate, posterior cingulate/precuneus, and lateral parietal cortices in healthy aging. However, the Mini-Mental State Examination of these subjects remained CU (29.2 ± 1.1, ranging from 25 to 30) in the time point of the second scan showing that it is not directly related to cognitive decline even with the glucose metabolism decrease.

Oh et al. (2014) found that ^{18}F-FDG patterns did not account for individual differences in cognition to the spectrum of healthy control aging. Healthy elders presented a relative increase in glucose metabolism and Aβ deposition in the posterior cingulate/precuneus and lateral parietal and prefrontal cortices. Hypometabolic regions in brain glucose metabolism images did not show a direct relation to aging. Although the brain hypometabolism in temporoparietal regions of the brain was commonly used as a marker of cognitive decline, it was not related to cognitive decline but to a normal hypometabolism due to age.

AGING AND AMYLOID BURDEN

Neurodegeneration biomarkers include morphological and metabolic measures, such as hippocampal atrophy and posterior

cortical glucose metabolism (Wirth et al., 2013). The relationship between brain hypometabolism and the amyloid burden was interpreted as evidence of disruption of neuronal functions and synaptic activity (Oh et al., 2014). However, Oh et al. (2014) showed that both higher levels of Aβ and relative increase in glucose metabolism were present in a population of healthy elders. Besson et al. (2015) found similar results, with subjects with reduced brain glucose metabolism in (AD–)signature ROIs without a high Aβ deposition. Conversely, Wirth et al. (2013) did not find significant associations between amyloid tracer uptake, cortical hypometabolism, and hippocampal atrophy. Brain hypometabolism and Aβ burden are unrelated. The two markers showed that Aβ might induce neurodegeneration with a temporal delay, with a relation of additivity instead of sequentially in the decline process.

Oh et al. (2014) hypothesized that no correlation between brain hypometabolism and Aβ burden could be attributed to several factors. One of them was related to the microglia surrounding the Aβ plaques, producing an inflammatory reaction that may increase the glucose metabolism in these regions. Other hypotheses are based on the possibility of an increase in abnormally hyperactive neurons in cortical circuits, alterations in brain homeostasis, and increased neural activity due to Aβ production. The cognitive reserve and its involvement in brain aging are also other hypotheses for maintaining cognition even with deposits of Aβ.

Cognitive reserve was proposed due to the differences between brain damage and pathology (observed in imaging markers) and its clinical manifestations (Stern, 2009). It is postulated that individual differences in cognitive processing and task performance allow certain individuals to cope better with brain damage (Stern, 2009). Due to this coping mechanism, some subjects could have elevated brain metabolism even with amyloid deposition (Ewers et al., 2012). However, it is unclear how to measure cognitive reserve from a neurobiological view (Stern, 2009). An increase in brain glucose metabolism in Aβ-accumulated regions could be a natural compensatory mechanism, permitting elders to remain CU even with Aβ plaques. Thus, a longitudinal analysis of the behavior of brain metabolism and Aβ features needs to be jointly evaluated (Oh et al., 2014). Other features that need to be assessed extensively are the relationship between cognitive domains and Aβ burden.

Episodic memory and executive functions are two cognitive domains that decline with advancing age (Oh et al., 2012). However, there is an unclear relationship between episodic memory, executive domains, and imaging biomarkers. Wirth et al. (2013) found that the Aβ burden was related to longitudinal decline instead of cross-sectional cognitive decline. A similar study (Jang et al., 2019) showed that Aβ+ MCI individuals who showed cognitive decline within 3 years to ACS had a higher Aβ burden than those with a slow decline (after 3 years). In addition, Aβ- MCI has a considerably lower chance of dementia conversion in 3 years than Aβ+ MCI. Moreover, Wirth et al. (2013) found that hippocampal neurodegeneration biomarkers do not significantly interact with Aβ uptake status on the longitudinal executive function decline. Jang et al. (2019) showed that additional abnormal neurodegeneration markers worsened the prognosis in Aβ+ MCI individuals within 3 years.

Mattsson et al. (2015) evaluated the amyloid tracer ^{11}C-AZD2184 binding in elder subjects (between 58 and 71 years old) with and without a decline in episodic memory. They hypothesized that the Aβ burden was more common in subjects with decline. On the contrary, the amyloid binding was higher in healthy elders than in those with a decline. Wang et al. (2020) reported no agreement between amyloid load and cognitive decline in the characterization of subjective cognitive decline.

Nebes et al. (2013) evaluated healthy elders using amyloid PET scans and cognitive tests and divided the subjects into Aβ-positive and Aβ-negative individuals. No differences were found between the groups and a set of cognitive scores (including tests for information processing speed, working memory, and inhibitory control). The only difference was that Aβ-positive subjects had a higher frequency of APOE $\varepsilon 4$ carriers than Aβ-negative subjects. Wirth et al. (2013) found a correlation between Aβ positivity and a decline in semantic and visual memory and visuospatial abilities. The amyloid burden did not affect logical memory and executive functions. Jessen et al. (2020) showed that CU individuals with subjective cognitive decline and Alzheimer's disease biomarkers without objective cognitive impairment presented a 40–62% increased chance to progress to MCI or AD within 3 years.

Oh et al. (2012) found that although limited to visual domains in cognitively healthy elders, visual episodic memory is negatively associated with Aβ deposition and the degree of covariance pattern of Aβ deposition. According to Oh et al. (2012), the difference could be related to cognitive reserve, because elders with higher cognitive reserves showed no correlation between Aβ burden and decline in cognitive performance, obscuring an Aβ effect. However, Oh et al. (2014) found that the GM volume Aβ-dependent patterns did not account for individual differences in cognition in the spectrum of healthy aging.

Longitudinal studies revealed the fastest decline in Aβ deposition. Healthy elders with a high amyloid burden have a higher tendency to progress to MCI within 3 years (Rizk-Jackson et al., 2013), and the interaction of Aβ pathology with neurodegenerative biomarkers could exacerbate cognitive worsening (Wirth et al., 2013). The relationship between brain hypometabolism, atrophy, and Aβ burden is not well-defined. These processes appear to be more additive than sequential in aging and cognitive decline and can be associated with other brain changes, such as microglia activation or alterations in brain homeostasis. In addition, the relationship between cognitive domain performance and the Aβ burden is not well-understood. More longitudinal studies are required for a better panorama on the changes in the brain and cognition with aging in both cases.

AGING AND TAU BURDEN

Recently, new phospho-tau radiotracers have allowed the study of cognitive aging trajectories. The deposition of phospho-tau (p-tau) in the brain of CU individuals is an inevitable consequence of the aging process (Braak et al., 2011), following a specific

neuropathological sequence (Braak's stages). Braak's stages are closely related to memory dysfunction, also reflecting the disease progression (Bao et al., 2021). The increased p-tau burden in cognitively healthy older adults must be carefully interpreted (Castellani, 2020).

Although primary age-related tauopathy (PART) has been described in both pathological and imaging studies, it is poorly related to clinical symptoms (Crary et al., 2014; Harrison et al., 2019). The accumulation of tau in healthy older adults spreads to the bilateral temporal lobe and retrosplenial regions (Harrison et al., 2019) and increases with age. In CU older adults, medial temporal tau deposition is related to memory decline, associated with decreased volume in these regions (Ziontz et al., 2019). A temporal meta-ROI accumulation was proposed to be highly specific for AD tau brain pathology and is uncommon in CU older adults (Ossenkoppele et al., 2021a). Furthermore, the temporal meta-ROI has been used with different tau-PET tracers (Leuzy et al., 2019) and in different cognitive aging trajectories, reflecting Braak stages I to IV (bilateral entorhinal, amygdala, fusiform, inferior and middle temporal cortices, respectively) (Ossenkoppele et al., 2018; Pereira et al., 2021).

The accumulation of tau was higher in CU individuals with imaging and clinical variables consistent with AD, such as amyloid positivity and baseline cognitive performance (Jack et al., 2020). Amyloid positivity is a strong predictor of temporal tau accumulation in CU individuals (Jack et al., 2020). Tau accumulation is magnified by amyloid deposition, especially in individuals with MCI or AD dementia (Smith et al., 2020). However, young, amyloid-positive individuals show an accelerated rate of tau deposition. Lower baseline cognitive performance is associated with higher tau deposition in the temporal lobe (Pontecorvo et al., 2017) and neocortical regions (Maass et al., 2017; Ziontz et al., 2019). Compared to amyloid PET and MRI, tau PET has emerged as the most promising tool for predicting cognitive change in Aβ+ individuals (Ossenkoppele et al., 2021b).

CLASSIFYING COGNITIVE DECLINE TRAJECTORIES USING IMAGING BIOMARKERS

For each biomarker, a different cutoff value was used for defining its positive or negative presence. According to Mckhann et al. (2011), biomarker results are normal or abnormal, positive or negative in several cases, and a qualitative interpretation is enough. However, the problem of ambiguous or indeterminate results exists because biomarkers have a continuous measure, and cutoff values are applied to continuous biological phenomena. Furthermore, quantitative and objective image analysis may not completely resolve the issue of the lack of standard values to differentiate normal and abnormal biomarkers.

Ewers et al. (2012) studied the association of Aβ PET and CSF ($A\beta_{1-42}$) in healthy elders and MCI subjects in a 2-year rate of cognition change based on memory and cognitive scores, regional GM volume (hippocampus, middle temporal gyrus, superior temporal gyrus, amygdala, parahippocampus, entorhinal cortex, inferior parietal lobe, precuneus, and thalamus), and brain metabolism assessed with ^{18}F-FDG (in the bilateral angular gyrus, posterior cingulate/precuneus, and inferior temporal cortex). He used a cutoff value of 1.6 to define an amyloid group dichotomization. When 1.5 and 1.41 cutoff values were applied to other studies, different results were found in Aβ patterns, with no difference in the cognition change rate. Previous studies showed different cutoff values depending on the parameters used for Aβ evaluation and discrimination on its presence (positive) or absence (negative). **Table 1** shows certain cutoff values and parameters used in the literature.

The Centiloid project aims to produce comparable methods across imaging centers to analyze amyloid PET images and solve the problem of applying a universal cutoff value between normal and abnormal ranges of amyloid deposits. It uses a linear scale for data of any amyloid PET image to an ^{11}C-PiB-based scale. The scale has an average value of zero for "high-certainty" amyloid-negative subjects and a value of 100 for typical AD subjects. Images in Centiloid units are interpretable longitudinally and across several imaging centers by using ^{11}C-and ^{18}F-amyloid tracers (Klunk et al., 2015).

In 2017, Jack et al. (2017b) developed and defined cutoffs for amyloid PET, FDG PET, tau PET, and MRI using five methods. For ^{11}C-PIB (an amyloid PET radiotracer), a cutoff of 1.42 was defined based on a reliable worsening method, equivalent to 19 on the Centiloid scale. For FDG PET, tau PET, and MRI, different methods were applied with accuracy based on young clinically CU or age-matched clinically CU vs. cognitively impaired Aβ+ individuals. However, the cognitively unpaired Aβ+ group was selected based on the cutoff value of ^{11}C-PIB (1.42).

The image-based cutoff values of Aβ biomarkers are diverse. The use of regional rather than global cutoff values could explain the variability in the results when evaluated with significant cognitive effects. It is attributed to certain subjects in the positive or negative groups with extremely focal Aβ deposition that may not be clinically meaningful in a group evaluation (Nebes et al., 2013). Recent studies (Landau et al., 2015; Farrell et al., 2018; Guo et al., 2020) have been focusing on the longitudinal evaluation of Aβ-CU individuals in specific brain regions, searching for regions of first Aβ accumulation and more indicative of a higher risk of cognitive decline. The use of regional cutoff values has enhanced the predicted memory decline, mainly when the most Aβ affected regions are used. The magnitude of Aβ change, not dichotomization, is a better predictor of risk for cognitive decline in Aβ-CU individuals (Farrell et al., 2017, 2018; Guo et al., 2020). The Centiloid method of scaling the Aβ burden is a better alternative for cutoff value variations on brain Aβ burden and staging of subjects. However, the cutoff values on the Centiloid scale to differentiate between normal loads of amyloid burden due to aging and disease are not yet completely known and require further studies.

BIOMARKERS JOINT EVALUATION

According to Besson et al. (2015), the amyloid cascade consists of three stages for the preclinical phase of AD: (Peters, 2006)

TABLE 1 | Cutoff values for Aβ tracers from the literature.

References	Cutoff value	Additional information	Cohort data	Diagnostic performance
Besson et al., 2015	1.005	90th percentile of estimated values in a group of 26 CU individuals aged 31 ± 8.4 years from the IMAP project.	54 CU elders between 50 to 84 years old (mean age 65.8 ± 8.3) recruited from the community	15% of CU individuals were Aβ+.
Ewers et al., 2012	1.6	Minimum density value of ^{11}C-PiB PET scores between the 2 modes of the probability density function of mean ^{11}C-PIB scores of 19 CU, 65 MCI, and 19 ACS individuals*.	124 CU, 229 amnestic MCI, and 112 ACS individuals from ADNI that have ^{11}C-PiB or CSF $A\beta_{42}$ data.	iPIB+ was present in 92.0% of the ACS, 72.5% of the MCI, and 41.1% of the CU subjects.
Halawa et al., 2019	1.4	SUV ratio determined based on the distribution across the entire sample.	51 CU, 39 MCI/AD individuals from ADNI with a mean age of 76.3 ± 6.9 years;	22.9% of CU, 40% of MCI, and 100% of ACS individuals were Aβ+.
Hanseeuw et al., 2017	1.34	Gaussian mixture model of the DVR of 277 CU individuals from the HABS.	Two samples of CU individuals from HABS according to the availability of tau imaging (90 CU) or memory follow-up (277 CU).	First sample: 36.6% of CU were Aβ+. Second sample: 28.5% of CU were Aβ+.
Jack et al., 2017b	1.42	SUV ratio based on the reliable worsening cutoff method. It is equivalent to a Centiloid value of 19.	CU, MCI, and ACS individuals between 30 to 95 years old of the Mayo Clinic Study of Aging (MCSA).	71% of autopsied individuals with Thal phase < 2 were Aβ-; 92% with Thal phase > 2 were Aβ+.
Maass et al., 2018	1.065	Calculated using the DVR of previous literature.	83 CU from the BACS with a mean age of 77 ± 6 years.	56.6% CU were classified as Aβ-, and 43.4% CU as Aβ+.
Nebes et al., 2013	1.50 to 1.78	Calculated on the anterior cingulate, anterior-ventral striatum, precuneus, frontal, lateral temporal, and parietal cortex, of 62 CU individuals.	71 CU between 65 and 88 years, and 37 younger individuals between 18 and 30 years, recruited from the community.	25% of CU individuals were Aβ+, 75% were Aβ-.
Oh et al., 2011	1.08	Mean DVR of young (±25 years) and elders (+65 years) + 2 standard deviations of young adults within the frontal, temporal, parietal, and anterior/posterior cingulate regions.	52 CU with a mean age of 74.1 ± 6.0 years recruited from the community.	36.5% of CU elders individuals were classified as Aβ+, and 63.5% as Aβ-.
Shimada et al., 2017	1.34	Mean cortical SUV ratio which maximizes the sum of sensitivity and specificity for discrimination between CU and AD individuals.	10 young CU (38.2 ± 4.7 years) and 18 older CU (67.3 ± 6.4 years), volunteers from the National Institute of Radiological Sciences, and 9 MCI (74.2 ± 4.4) and 17 ACS (71.6 ± 9.6) individuals from the Chiba University Hospital.	Young CU were considered Aβ. Study design excluded older CU individuals that were Aβ+. All MCI and ACS individuals were Aβ+.
Wirth et al., 2013	1.08	Mean Aβ uptake + 2 standard deviations of the frontal, temporal, parietal, and anterior/posterior cingulate regions derived from an independent group of healthy young adults.	38 CU individuals recruited from the BACS between 61 and 87 years.	65.8% of individuals were Aβ-, and 34.2% were Aβ+.

**iPIB model was created for these subjects that did not have ^{11}C-PIB scans and was calculated using least square regressions to estimate PIB score based on the correlation of CSF $A\beta_{1-42}$ and Apolipoprotein E ε4 genotype with ^{11}C-PIB. BACS, Barkeley Aging Cohort Study; DVR, distribution volume ratio; HABS, Harvard Aging Brain Study; SUV, standardized uptake value.*

Aβ deposition alone, (2) Aβ deposition and neurodegeneration, and (3) Aβ deposition, neurodegeneration, and subtle decline. However, studies showed that neurodegeneration is not followed in this sequence or related to each other in a decline paradigm. In the NIA–AA research framework (Jack et al., 2018), the use of the AT(N) system is implemented to define the biomarker profile of amyloid and tau deposition and neurodegeneration and divided into categories. This system is classified on the basis of biomarkers, stages of normal AD biomarker, AD pathological change, AD and non-AD pathological changes, and independence of cognitive (clinical) status.

Tau pathology was found to be related to neurodegeneration as much as Aβ pathology, and NFTs can be observed in the aged brain even without the presence of Aβ plaques. NFTs are usually present around the medial temporal cortex, and Aβ presence expands these fibrillated taus to the entire cortex (Hanseeuw et al., 2017; Shimada et al., 2017; Maass et al., 2018). The anatomy of glucose hypometabolism correlated with

the interaction between Aβ and neocortical tau distribution. Thus, hypometabolism in tau-associated regions may be an early imaging marker of memory decline in healthy elders with different levels of Aβ load (Hanseeuw et al., 2017). Imaging markers and the Aβ/tau ratio showed a predictive potential to decline in the Clinical Dementia Rating scale in healthy elders (Rizk-Jackson et al., 2013).

A combination of findings correlating with the presence of Aβ and tau showed that one potentiates physiological consequences of the other (Hanseeuw et al., 2017). It is still unclear whether Aβ pathology itself shows neurotoxicity *in vivo* and influences the clinical features (Shimada et al., 2017) or the mechanism or anatomic link that mediates Aβ and tau interaction (Hanseeuw et al., 2017). What has been reported is that the accumulation of Aβ and tau is associated with synaptic dysfunction and axonal degeneration and is correlated with changes in memory, global cognition, and axonal degeneration, which are useful for diseases prognosis (Pereira et al., 2021). The use of both amyloid and tau PET showed high potential as imaging markers of aging and cognitive decline. As tau radiotracers are still in development, more studies are required to evaluate the relationship between tau burden, neurodegeneration, and cognitive status.

OPEN QUESTIONS

The review revealed that biomarkers are more complementary than the determinants. MRI, FDG PET, amyloid PET, and even tau PET show only one imaging marker above the normality threshold in healthy elders.

The majority of the reviewed studies comprised cross-sectional (and not longitudinal) data or only limited longitudinal information about the subjects. There still exists a lack of longitudinal studies exploring the relationship between images and aging markers. Moreover, the studies did not clarify the relationship between cognition, brain metabolism, and Aβ and/or tau accumulation in understanding dimensionality of the biomarkers in memory and cognitive decline.

Another issue identified is the lack of standardization of imaging markers. The Centiloid project has been trying to develop a standardized scale for the Aβ burden, using a well-delineated methodology for imaging analysis. The scale ranges from 0 for no Aβ burden in young, healthy adults to 100 for AD subjects with a high Aβ burden (Klunk et al., 2015). However, standardized methods for brain ^{18}F-FDG PET, tau PET, and brain atrophy in MRI are still lacking. The cutoff values for positive and negative Aβ are still under discussion even with the Centiloid standardization. A composite biomarker is used to generate a new analysis approach, such as a combined ^{18}F-FDG and MR biomarker for neurodegeneration or a composite score to determine the cognition spectrum.

The review showed the requirement for brain image patterns to identify the first signs of cognitive decline, enabling the implementation of new approaches for early therapeutic intervention. In addition, it emphasized the need for understanding the used biomarkers to detect the first changes leading to permanent cognitive decline and the possibility to intervene and differentiate dementia from other neurological diseases. In conclusion, we argue that in-depth studies on cognitive decline are required to understand it better and find the proper therapeutic intervention and its optimal windows for a suitable and effective treatment strategy.

AUTHOR CONTRIBUTIONS

CD contributed to study design, search, revision, writing, and discussion. WB critically reviewed and discussed the manuscript. MK critically reviewed the manuscript. AM contributed to study design and writing, and critically reviewed the manuscript. All authors approved the submitted version of the manuscript.

FUNDING

This study was financed in part by the Coordenação de Aperfeiçoamento de Pessoal de Nível Superior–Brasil (CAPES)–Finance Code 001.

REFERENCES

Alafuzoff, I., Arzberger, T., Al-Sarraj, S., Bodi, I., Bogdanovic, N., Braak, H., et al. (2008). Staging of neurofibrillary pathology in Alzheimer's disease: a study of the BrainNet Europe consortium. *Brain Pathol.* 18, 484–496. doi: 10.1111/j.1750-3639.2008.00147.x

Altomare, D., de Wilde, A., Ossenkoppele, R., Pelkmans, W., Bouwman, F., Groot, C., et al. (2019). Applying the ATN scheme in a memory clinic population: the ABIDE project. *Neurology* 93, e1635–e1646. doi: 10.1212/WNL.0000000000008361

Bao, W., Jia, H., Finnema, S., Cai, Z., Carson, R. E., and Huang, Y. H. (2017). PET imaging for early detection of Alzheimer's disease: from pathologic to physiologic biomarkers. *PET Clin.* 12, 329–350. doi: 10.1016/j.cpet.2017.03.001

Bao, W., Xie, F., Zuo, C., Guan, Y., and Huang, Y. H. (2021). PET neuroimaging of Alzheimer's disease: radiotracers and their utility in clinical research. *Front. Aging Neurosci.* 13:624330. doi: 10.3389/fnagi.2021.624330

Besson, F. L., Joie, R., Doeuvre, L., Gaubert, M., Mézenge, F., Egret, S., et al. (2015). Cognitive and brain profiles associated with current neuroimaging biomarkers of preclinical Alzheimer's disease. *J. Neurosci.* 35:10402–10411. doi: 10.1523/JNEUROSCI.0150-15.2015

Braak, H., and Braak, E. (1991). Neuropathological stageing of Alzheimer-related changes. *Acta Neuropathol.* 82, 239–259. doi: 10.1007/BF00308809

Braak, H., Thal, D. R., Ghebremedhin, E., and del Tredici, K. (2011). Stages of the pathologic process in alzheimer disease: age categories from 1 to 100 years. *J. Neuropathol. Exp. Neurol.* 70, 960–969. doi: 10.1097/NEN.0b013e318232a379

Castellani, R. J. (2020). The significance of tau aggregates in the human brain. *Brain Sci.* 10, 1–14. doi: 10.3390/brainsci10120972

Chételat, G., Villemagne, V. L., Pike, K. E., Ellis, K. A., Bourgeat, P., Jones, G., et al. (2011). Independent contribution of temporal β-amyloid deposition to memory decline in the pre-dementia phase of Alzheimer's disease. *Brain* 134, 798–807. doi: 10.1093/brain/awq383

Citron, M. (2010). Alzheimer's disease: strategies for disease modification. *Nat. Rev. Drug Discov.* 9, 387–398. doi: 10.1038/nrd2896

Clark, C. M., Schneider, J. A., Bedell, B. J., Beach, T. G., Bilker, W. B., Mintun, M. A., et al. (2011). Use of florbetapir-PET for imaging β-amyloid pathology. *JAMA* 305, 275–283. doi: 10.1001/jama.2010.2008

Cohen, A. D., Rabinovici, G. D., Mathis, C. A., Jagust, W. J., Klunk, W. E., and Ikonomovic, M. D. (2012). Using Pittsburgh compound B for *in vivo* PET imaging of fibrillar amyloid-beta. *Adv. Pharmacol.* 64, 27–81. doi: 10.1016/B.978-0-12-394816-8.00002-7

Crary, J. F., Trojanowski, J. Q., Schneider, J. A., Abisambra, J. F., Abner, E. L., Alafuzoff, I., et al. (2014). Primary age-related tauopathy (PART): a common pathology associated with human aging. *Acta Neuropathol.* 128, 755–766. doi: 10.1007/s00401-014-1349-0

Dubois, B., Epelbaum, S., Nyasse, F., Bakardjian, H., Gagliardi, G., Uspenskaya, O., et al. (2018). Cognitive and neuroimaging features and brain β-amyloidosis in individuals at risk of Alzheimer's disease (INSIGHT-preAD): a longitudinal observational study. *Lancet Neurol.* 17, 335–346. doi: 10.1016/S1474-4422(18)30029-2

Ebenau, J. L., Verfaillie, S. C. J., Bosch, K. A., van den, Timmers, T., Wesselman, L. M. P., Leeuwenstijn, M., et al. (2020). Grey zone amyloid burden affects memory function: the SCIENCe project. *Eur. J. Nuclear Med. Mol. Imaging.* 48, 747–756. doi: 10.1007/s00259-020-05012-5

Ewers, M., Insel, P., Jagust, W. J., Shaw, L., Trojanowski, Q. T., Aisen, P., et al. (2012). CSF biomarker and PIB-PET-derived beta-amyloid signature predicts metabolic, gray matter, and cognitive changes in nondemented subjects. *Cereb. Cortex* 22:1993. doi: 10.1093/cercor/bhr271

Farrell, M. E., Chen, X., Rundle, M. M., Chan, M. Y., Wig, G. S., and Park, D. C. (2018). Regional amyloid accumulation and cognitive decline in initially amyloid-negative adults. *Neurology* 91, E1809–E1821. doi: 10.1212/WNL.0000000000006469

Farrell, M. E., Kennedy, K. M., Rodrigue, K. M., Wig, G., Bischof, G. N., Rieck, J. R., et al. (2017). Association of longitudinal cognitive decline with amyloid burden in middle-aged and older adults: evidence for a dose-response relationship. *JAMA Neurol.* 74, 830–838. doi: 10.1001/jamaneurol.2017.0892

FDA-NIH Biomarker Working Group (2016). *BEST (Biomarkers, EndpointS, and other Tools) Resource*. Food and Drug Administration (US). Co-published by National Institutes of Health (US), Bethesda, MD.

Guo, T., Korman, D., Baker, S. L., Landau, S. M., and Jagust, W. J. (2021). Longitudinal cognitive and biomarker measurements support a unidirectional pathway in Alzheimer's disease pathophysiology. *Biol. Psychiatry* 89, 786–794. doi: 10.1016/j.biopsych.2020.06.029

Guo, T., Landau, S. M., and Jagust, W. J. (2020). Detecting earlier stages of amyloid deposition using PET in cognitively normal elderly adults. *Neurology* 94, E1512–E1524. doi: 10.1212/WNL.0000000000009216

Halawa, O. A., Gatchel, J. R., Amariglio, R. E., Rentz, D. M., Sperling, R. A., Johnson, K. A., et al. (2019). Inferior and medial temporal tau and cortical amyloid are associated with daily functional impairment in Alzheimer's disease. *Alzheimers Res. Therapy* 11:14. doi: 10.1186/s13195-019-0471-6

Hanseeuw, B. J., Betensky, R. A., Schultz, A. P., Papp, K. V., Mormino, E. C., Sepulcre, J., et al. (2017). Fluorodeoxyglucose metabolism associated with tau-amyloid interaction predicts memory decline. *Ann. Neurol.* 81, 583–596. doi: 10.1002/ana.24910

Harrison, T. M., la Joie, R., Maass, A., Baker, S. L., Swinnerton, K., Fenton, L., et al. (2019). Longitudinal tau accumulation and atrophy in aging and Alzheimer disease. *Ann. Neurol.* 85, 229–240. doi: 10.1002/ana.25406

Ishibashi, K., Onishi, A., Fujiwara, Y., Oda, K., Ishiwata, K., and Ishii, K. (2018). Longitudinal effects of aging on 18F-FDG distribution in cognitively normal elderly individuals. *Sci. Rep.* 8:11557. doi: 10.1038/s41598-018-29937-y

Jack, C. R., Wiste, H. J., Weigand, S. D., Knopman, D. S., Mielke, M. M., Vemuri, P., et al. (2015). Different definitions of neurodegeneration produce similar amyloid/neurodegeneration biomarker group findings. *Brain* 138, 3747–3759. doi: 10.1093/brain/awv283

Jack, C. R., Wiste, H. J., Weigand, S. D., Therneau, T. M., Knopman, D. S., Lowe, V., et al. (2017a). Age-specific and sex-specific prevalence of cerebral β-amyloidosis, tauopathy, and neurodegeneration in cognitively unimpaired individuals aged 50-95 years: a cross-sectional study. *Lancet Neurol.* 16, 435–444. doi: 10.1016/S1474-4422(17)30077-7

Jack, C. R., Wiste, H. J., Weigand, S. D., Therneau, T. M., Lowe, V. J., Knopman, D. S., et al. (2017b). Defining imaging biomarker cut points for brain aging and Alzheimer's disease. *Alzheimers Dement.* 13, 205–216. doi: 10.1016/j.jalz.2016.08.005

Jack, C. R., Wiste, H. J., Weigand, S. D., Therneau, T. M., Lowe, V. J., Knopman, D. S., et al. (2020). Predicting future rates of tau accumulation on PET. *Brain* 143, 3136–3150. doi: 10.1093/brain/awaa248

Jack, C. R. Jr., Bennett, D. A., Blennow, K., Carrillo, M. C., Dunn, B., Budd Haeberlein, S., et al. (2018). NIA-AA research framework: toward a biological definition of Alzheimer's disease HHS Public Access Author manuscript. *Alzheimers Dement.* 14, 535–562. doi: 10.1016/j.jalz.2018.02.018

Jack, C. R. Jr., Wiste, H. J., Therneau, T. M., Weigand, S. D., Knopman, D. S., Mielke, M. M., et al. (2019). Associations of amyloid, tau, and neurodegeneration biomarker profiles with rates of memory decline among individuals without dementia. *JAMA* 321, 2316–2325. doi: 10.1001/jama.2019.7437

Jagust, W. J., Landau, S. M., Shaw, L. M., Trojanowski, J. Q., Koeppe, R. A., Reiman, E. M., et al. (2009). Relationships between biomarkers in aging and dementia. *Neurology* 73, 1193–1199. doi: 10.1212/WNL.0b013e3181bc010c

Jang, H., Park, J., Woo, S., Kim, S., Jin Kim, H., Na, D. L., et al. (2019). Prediction of fast decline in amyloid positive mild cognitive impairment patients using multimodal biomarkers. *Neuroimage. Clin.* 24:101941. doi: 10.1016/j.nicl.2019.101941

Jansen, W. J., Ossenkoppele, R., Knol, D. L., Tijms, B. M., Scheltens, P., Verhey, F. R. J., et al. (2015). Prevalence of cerebral amyloid pathology in persons without dementia: a meta-analysis. *JAMA* 313, 1924–1938. doi: 10.1001/jama.2015.4668

Jansen, W. J., Ossenkoppele, R., Tijms, B. M., Fagan, A. M., Hansson, O., Klunk, W. E., et al. (2018). Association of cerebral amyloid-β Aggregation with cognitive functioning in persons without dementia. *JAMA Psychiatry* 75, 84–95. doi: 10.1001/jamapsychiatry.2017.3391

Jessen, F., Amariglio, R. E., Buckley, R. F., van der Flier, W. M., Han, Y., Molinuevo, J. L., et al. (2020). The characterisation of subjective cognitive decline. *Lancet Neurol.* 19, 271–278. doi: 10.1016/S1474-4422(19)30368-0

Jie, B., Zhang, D., Cheng, B., and Shen, D. (2015). Manifold regularized multitask feature learning for multimodality disease classification. *Hum. Brain Mapp.* 36, 489–507. doi: 10.1002/hbm.22642

Khachaturian, Z. S. (2005). Diagnosis of Alzheimer's disease: Two decades of progress. *J. Alzheimers Dis.* 9(3 Suppl), 409–415. doi: 10.3233/JAD-2006-9S346

Klunk, W. E., Koeppe, R. A., Price, J. C., Benzinger, T. L., Devous, M. D., Jagust, W. J., et al. (2015). The Centiloid project: standardizing quantitative amyloid plaque estimation by PET. *Alzheimers Dement.* 11, 1.e4–15.e4. doi: 10.1016/j.jalz.2014.07.003

Landau, S. M., Fero, A., Baker, S. L., Koeppe, R., Mintun, M., Chen, K., et al. (2015). Measurement of longitudinal β-amyloid change with 18F-florbetapir PET and standardized uptake value ratios. *J. Nuclear Med.* 56, 567–574. doi: 10.2967/jnumed.114.148981

Landau, S. M., Harvey, D., Madison, C. M., Koeppe, R. A., Reiman, E. M., Foster, N. L., et al. (2011). Associations between cognitive, functional, and FDG-PET measures of decline in AD and MCI. *Neurobiol. Aging* 32, 1207–1218. doi: 10.1016/j.neurobiolaging.2009.07.002

Landau, S. M., Horng, A., and Jagust, W. J. (2018). Memory decline accompanies subthreshold amyloid accumulation. *Neurology* 90, e1452–e1460. doi: 10.1212/WNL.0000000000005354

Leuzy, A., Chiotis, K., Lemoine, L., Gillberg, P. G., Almkvist, O., Rodriguez-Vieitez, E., et al. (2019). Tau PET imaging in neurodegenerative tauopathies-still a challenge. *Mol. Psychiatry* 24, 1112–1134. doi: 10.1038/s41380-018-0342-8

Leuzy, A., Pascoal, T. A., Strandberg, O., Insel, P., Smith, R., Mattsson-carlgren, N., et al. (2021). A multicenter comparison of [18F]flortaucipir, [18F]RO948, and [18F]MK6240 tau PET tracers to detect a common target ROI for differential diagnosis. *Eur. J. Nuclear Med. Mol. Imaging* 48, 2295–2305. doi: 10.1007/s00259-021-05401-4

Lim, Y. Y., Maruff, P., Pietrzak, R. H., Ames, D., Ellis, K. A., Harrington, K., et al. (2014). Effect of amyloid on memory and non-memory decline from preclinical to clinical Alzheimer's disease. *Brain* 137, 221–231. doi: 10.1093/brain/awt286

Lowe, V. J., Wiste, H. J., Senjem, M. L., Weigand, S. D., Therneau, T. M., Boeve, B. F., et al. (2018). Widespread brain tau and its association with ageing, Braak stage and Alzheimer's dementia. *Brain* 141, 271–287. doi: 10.1093/brain/awx320

Maass, A., Landau, S., Horng, A., Lockhart, S. N., Rabinovici, G. D., Jagust, W. J., et al. (2017). Comparison of multiple tau-PET measures as biomarkers in aging and Alzheimer's disease. *Neuroimage* 157, 448–463. doi: 10.1016/j.neuroimage.2017.05.058

Maass, A., Lockhart, S. N., Harrison, T. M., Bell, R. K., Mellinger, T., Swinnerton, K., et al. (2018). Entorhinal tau pathology, episodic memory decline, and neurodegeneration in aging. *J. Neurosci.* 38, 530–543. doi: 10.1523/JNEUROSCI.2028-17.2017

Masters, C. L., Bateman, R., Blennow, K., Rowe, C. C., Sperling, R. A., and Cummings, J. L. (2015). Alzheimer's disease. *Nat. Rev. Dis. Primers* 1:15056. doi: 10.1038/nrdp.2015.56

Mattsson, P., Forsberg, A., Persson, J., Nyberg, L., Nilsson, L. G., Halldin, C., et al. (2015). β-Amyloid binding in elderly subjects with declining or stable episodic memory function measured with PET and [11C]AZD2184. *Eur. J. Nuclear Med. Mol. Imaging* 42, 1507–1511. doi: 10.1007/s00259-015-3103-9

Mckhann, G. M., Knopman, D. S., Chertkow, H., Hyman, B. T., Jack, C. R. G., Kawas, C. H., et al. (2011). The diagnosis of dementia due to Alzheimer's disease: recommendations from the National Institute on Aging-Alzheimer's Association workgroups on diagnostic guidelines for Alzheimer's disease NIH Public Access. *Alzheimers Dement.* 7, 263–269. doi: 10.1016/j.jalz.2011.03.005

Mormino, E. C., Papp, K. V., Rentz, D. M., Donohue, M. C., Amariglio, R., Quiroz, Y. T., et al. (2017). Early and late change on the preclinical Alzheimer's cognitive composite in clinically normal older individuals with elevated amyloid β. *Alzheimers Dement.* 13, 1004–1012. doi: 10.1016/j.jalz.2017.01.018

Moskalev, A. (ed.). (2019). *Biomarkers of Human Aging*, Vol. 10. Cham: Springer International Publishing. doi: 10.1007/978-3-030-24970-0

Nebes, R. D., Snitz, B. E., Cohen, A. D., Aizenstein, H. J., Saxton, J. A., Halligan, E. M., et al. (2013). Cognitive aging in persons with minimal amyloid-β and white matter hyperintensities. *Neuropsychologia* 51, 2202–2209. doi: 10.1016/j.neuropsychologia.2013.07.017

Oh, H., Habeck, C., Madison, C., and Jagust, W. (2014). Covarying alterations in Aβ deposition, glucose metabolism, and gray matter volume in cognitively normal elderly. *Hum. Brain Mapp.* 35, 297–308. doi: 10.1002/hbm.22173

Oh, H., Madison, C., Haight, T. J., Markley, C., and Jagust, W. J. (2012). Effects of age and β-amyloid on cognitive changes in normal elderly people. *Neurobiol. Aging* 33, 2746–2755. doi: 10.1016/j.neurobiolaging.2012.02.008

Oh, H., Mormino, E. C., Madison, C., Hayenga, A., Smiljic, A., and Jagust, W. J. (2011). β-Amyloid affects frontal and posterior brain networks in normal aging. *Neuroimage* 54, 1887–1895. doi: 10.1016/j.neuroimage.2010.10.027

Oschwald, J., Guye, S., Liem, F., Rast, P., Willis, S., Röcke, C., et al. (2019). Brain structure and cognitive ability in healthy aging: a review on longitudinal correlated change. *Rev. Neurosci.* 31, 1–57. doi: 10.1515/revneuro-2018-0096

Osorio, R. S., Pirraglia, E., Gumb, T., Mantua, J., Ayappa, I., Williams, S., et al. (2014). Imaging and cerebrospinal fluid biomarkers in the search for alzheimer's disease mechanisms. *Neurodegener. Dis.* 13, 163–165. doi: 10.1159/000355063

Ossenkoppele, R., Leuzy, A., Cho, H., Sudre, C. H., Strandberg, O., Smith, R., et al. (2021a). The impact of demographic, clinical, genetic, and imaging variables on tau PET status. *Eur. J. Nuclear Med. Mol. Imaging* 48, 2245–2258. doi: 10.1007/s00259-020-05099-w

Ossenkoppele, R., Rabinovici, G. D., Smith, R., Cho, H., Scholl, M., Strandberg, O., et al. (2018). Discriminative accuracy of [18F]flortaucipir positron emission tomography for Alzheimer disease vs other neurodegenerative disorders. *JAMA* 320, 1151–1162. doi: 10.1001/jama.2018.12917

Ossenkoppele, R., Smith, R., Mattsson-Carlgren, N., Groot, C., Leuzy, A., Strandberg, O., et al. (2021b). Accuracy of tau positron emission tomography as a prognostic marker in preclinical and prodromal Alzheimer disease. *JAMA Neurol.* 28:e211858. doi: 10.1001/jamaneurol.2021.1858

Pascoal, T. A., Therriault, J., Benedet, A. L., Savard, M., Lussier, F. Z., Chamoun, M., et al. (2020). 18F-MK-6240 PET for early and late detection of neurofibrillary tangles. *Brain* 143, 2818–2830. doi: 10.1093/brain/awaa180

Pereira, J. B., Janelidze, S., Ossenkoppele, R., Kvartsberg, H., Brinkmalm, A., Mattsson-Carlgren, N., et al. (2021). Untangling the association of amyloid-β and tau with synaptic and axonal loss in Alzheimer's disease. *Brain* 144, 310–324. doi: 10.1093/brain/awaa395

Peters, R. (2006). Ageing and the brain. *Postgrad. Med. J.* 82, 84–88. doi: 10.1136/pgmj.2005.036665

Pontecorvo, M. J., Devous, M. D., Navitsky, M., Lu, M., Salloway, S., Schaerf, F. W., et al. (2017). Relationships between flortaucipir PET tau binding and amyloid burden, clinical diagnosis, age and cognition. *Brain* 140, 748–763. doi: 10.1093/brain/aww334

Rabinovici, G. D., Gatsonis, C., Apgar, C., Chaudhary, K., Gareen, I., Hanna, L., et al. (2019). Association of amyloid positron emission tomography with subsequent change in clinical management among medicare beneficiaries with mild cognitive impairment or dementia. *JAMA* 321, 1286–1294. doi: 10.1001/jama.2019.2000

Rizk-Jackson, A., Insel, P., Petersen, R., Aisen, P., Jack, C., and Weiner, M. (2013). Early indications of future cognitive decline: stable versus declining controls. *PLoS ONE* 8:e74062. doi: 10.1371/journal.pone.0074062

Schroeter, M. L., Stein, T., Maslowski, N., and Neumann, J. (2009). Neural correlates of Alzheimer's disease and mild cognitive impairment: a systematic and quantitative meta-analysis involving 1351 patients. *Neuroimage* 47, 1196–1206. doi: 10.1016/j.neuroimage.2009.05.037

Shimada, H., Kitamura, S., Shinotoh, H., Endo, H., Niwa, F., Hirano, S., et al. (2017). Association between Aβ and tau accumulations and their influence on clinical features in aging and Alzheimer's disease spectrum brains: a [11C]PBB3-PET study. *Alzheimers Dement Diagn. Assess. Dis. Monitor.* 6, 11–20. doi: 10.1016/j.dadm.2016.12.009

Smith, R., Strandberg, O., Mattsson-Carlgren, N., Leuzy, A., Palmqvist, S., Pontecorvo, M. J., et al. (2020). The accumulation rate of tau aggregates is higher in females and younger amyloid-positive subjects. *Brain* 143, 3805–3815. doi: 10.1093/brain/awaa327

Sperling, R. A., Mormino, E. C., Schultz, A. P., Betensky, R. A., Papp, K., V., Amariglio, R. E., et al. (2019). The impact of amyloid-beta and tau on prospective cognitive decline in older individuals. *Ann. Neurol.* 85, 181–193. doi: 10.1002/ana.25395

Stern, Y. (2009). Cognitive reserve. *Neuropsychologia* 47, 2015–2028. doi: 10.1016/j.neuropsychologia.2009.03.004

Strimbu, K., and Tavel, J. A. (2010). What are biomarkers? *Curr. Opin. HIV AIDS* 5, 463–466. doi: 10.1097/COH.0b013e32833ed177

Wang, X., Huang, W., Su, L., Xing, Y., Jessen, F., Sun, Y., et al. (2020). Neuroimaging advances regarding subjective cognitive decline in preclinical Alzheimer's disease. *Mol. Neurodegen.* 15:55. doi: 10.1186/s13024-020-00395-3

Wirth, M., Oh, H., Mormino, E. C., Markley, C., Landau, S. M., and Jagust, W. J. (2013). The effect of amyloid β on cognitive decline is modulated by neural integrity in cognitively normal elderly. *Alzheimers Dement.* 9, 687.e1–698.e1. doi: 10.1016/j.jalz.2012.10.012

World Health Organization (2017). *Life Expectancy at Birth*. Available online at: https://www.who.int/data/gho/data/indicators/indicator-details/GHO/life-expectancy-at-birth-(years)

Ziontz, J., Bilgel, M., Shafer, A. T., Moghekar, A., Elkins, W., Helphrey, J., et al. (2019). Tau pathology in cognitively normal older adults. *Alzheimers Dement. Diagn. Assess. Dis. Monitor.* 11, 637–645. doi: 10.1016/j.dadm.2019.07.007

Conflict of Interest: The authors declare that the research was conducted in the absence of any commercial or financial relationships that could be construed as a potential conflict of interest.

frontiers in Aging Neuroscience

ORIGINAL RESEARCH
published: 10 September 2021
doi: 10.3389/fnagi.2021.723948

Altered Cortical Cholinergic Network in Parkinson's Disease at Different Stage: A Resting-State fMRI Study

Wenshuang Sheng[1†], Tao Guo[2†], Cheng Zhou[2], Jingjing Wu[2], Ting Gao[3], Jiali Pu[3], Baorong Zhang[3], Minming Zhang[2], Yunjun Yang[1*], Xiaojun Guan[2*] and Xiaojun Xu[1,2*]*

[1] Department of Radiology, The First Affiliated Hospital of Wenzhou Medical University, Wenzhou, China, [2] Department of Radiology, The Second Affiliated Hospital, Zhejiang University School of Medicine, Hangzhou, China, [3] Department of Neurology, The Second Affiliated Hospital, Zhejiang University School of Medicine, Hangzhou, China

OPEN ACCESS

Edited by:
Wei Cheng,
Fudan University, China

Reviewed by:
Zaixu Cui,
University of Pennsylvania, United States
Feng-Tao Liu,
Fudan University, China
Zhang Jinbo,
Chinese Institute for Brain Research, Beijing, China, in collaboration with reviewer ZC

***Correspondence:**
Minming Zhang
zhangminming@zju.edu.cn
Yunjun Yang
yyjunjim@163.com
Xiaojun Guan
xiaojunguan1102@zju.edu.cn
Xiaojun Xu
xxjmailbox@zju.edu.cn

[†] These authors have contributed equally to this work and share first authorship

Received: 11 June 2021
Accepted: 09 August 2021
Published: 10 September 2021

Citation:
Sheng W, Guo T, Zhou C, Wu J, Gao T, Pu J, Zhang B, Zhang M, Yang Y, Guan X and Xu X (2021) Altered Cortical Cholinergic Network in Parkinson's Disease at Different Stage: A Resting-State fMRI Study. Front. Aging Neurosci. 13:723948. doi: 10.3389/fnagi.2021.723948

The cholinergic system is critical in Parkinson's disease (PD) pathology, which accounts for various clinical symptoms in PD patients. The substantia innominata (SI) provides the main source of cortical cholinergic innervation. Previous studies revealed cholinergic-related dysfunction in PD pathology at early stage. Since PD is a progressive disorder, alterations of cholinergic system function along with the PD progression have yet to be elucidated. Seventy-nine PD patients, including thirty-five early-stage PD patients (PD-E) and forty-four middle-to-late stage PD patients (PD-M), and sixty-four healthy controls (HC) underwent brain magnetic resonance imaging and clinical assessments. We employed seed-based resting-state functional connectivity analysis to explore the cholinergic-related functional alterations. Correlation analysis was used to investigate the relationship between altered functional connectivity and the severity of motor symptoms in PD patients. Results showed that both PD-E and PD-M groups exhibited decreased functional connectivity between left SI and left frontal inferior opercularis areas and increased functional connectivity between left SI and left cingulum middle area as well as right primary motor and sensory areas when comparing with HC. At advanced stages of PD, functional connectivity in the right primary motor and sensory areas was further increased. These altered functional connectivity were also significantly correlated with the Unified Parkinson's Disease Rating Scale motor scores. In conclusion, this study illustrated that altered cholinergic function plays an important role in the motor disruptions in PD patients both in early stage as well as during the progression of the disease.

Keywords: Parkinson's disease, substantia innominata, cholinergic network, motor, functional connectivity

INTRODUCTION

Parkinson's disease (PD), a chronic and progressive movement disorder, has been recognized as a heterogeneous syndrome (Zhang et al., 2005; Reich and Savitt, 2019). The pathological and neurotransmitter basis of PD is not all dopaminergic, other non-dopaminergic neurotransmitter systems are involved (Sethi, 2008), which leads to the heterogeneous clinical manifestations, not only including classic motor symptoms but involving differed extents of non-motor symptoms.

Over the past decades, a major pathological emphasis has been placed on the disruption of dopaminergic system; however, it was found that the damage of non-dopaminergic system precedes the development of dopaminergic pathology (Braak et al., 2003), and has a profound influence on disease progression (Langston, 2006). Therefore, the investigation of the non-dopaminergic neurotransmitter system could provide a better understanding of the mechanism of PD.

Cholinergic system is a kind of major non-dopaminergic neurotransmitter system. Previous studies revealed that the abnormal function of cholinergic system is critical in the PD pathology (Mallet et al., 2019), which could account for various clinical symptoms in PD, including both motor symptoms (e.g., gait impairment, balance dysfunction and falls) (Bohnen et al., 2009; Bohnen and Albin, 2011; Lord et al., 2011; Yarnall et al., 2011; Rochester et al., 2012; Dalrymple et al., 2021) and non-motor symptoms (e.g., cognition impairment and visual hallucinations) (Yarnall et al., 2011; Kim et al., 2017; Lee et al., 2018). The substantia innominata (SI) in the basal forebrain is the major sources of cholinergic projections in the brain (Mesulam and Geula, 1988; Li et al., 2014). The loss of SI neurons represents cortical cholinergic deficits (Perry et al., 1985). According to the classic PD pathology model, basal forebrain is a main target of the α-synuclein accumulation (Braak et al., 2003), and the α-synuclein accumulation in which area simultaneously occurs with the accumulation in the substantia nigra at the early stage of PD (Lee et al., 2018). A positron emission tomography (PET) study of cerebral acetylcholinesterase demonstrated that cholinergic dysfunction occurs in the early course of PD (Hughes et al., 1992; Latt et al., 2009). This evidence suggests that the pathology of early PD involves the cholinergic-related dysfunction. Given that PD is a progressive disorder, patients at advanced stages seem to have a significantly faster disease progression (Zhao et al., 2010) and show a high incidence of balance dysfunction (Latt et al., 2009). These heterogeneous clinical symptoms indicate that the degenerative mechanisms of the cholinergic system may be different during PD progression, which have yet to be elucidated.

Advanced magnetic resonance imaging (MRI) technology provides an avenue to explore the cholinergic function in PD patients. Currently, MRI studies have found a piece of evidence indicating the abnormal cholinergic function in PD patients. A whole brain voxel-based morphometry study has found that the gray matter density of SI was reduced in PD patients and it was associated with gait impairment (specially reduced gait speed) as well as balance dysfunction (Dalrymple et al., 2021). Other studies using resting-state functional MRI (rs-fMRI) revealed that in PD patients, altered cholinergic network of SI was significantly correlated with cognitive performance (Kim et al., 2017; Lee et al., 2018). However, these studies mainly focused on the specific PD population, such as PD patients at early stage or patients before the surgical stage. Researchers argue that functional alterations likely precede structural atrophy and examination of cerebral functional connectivity may be essential to understanding the etiologies of many neuropsychiatric disease (Liang et al., 2011; Guan et al., 2019). Low-frequency fluctuations of resting-state blood oxygenation level-dependent (BOLD) signal reflect connectivity between functionally related brain regions (Fox and Raichle, 2007). So resting-state functional connectivity (rsFC) can be used to evaluate altered relationships between the SI and particular areas of the whole brain thus defining brain regions related to the severity of motor symptoms. Earlier studies of rsFC have mainly focused on the role of cholinergic function in cognition (Kim et al., 2017; Lee et al., 2018). Taken together, considering the progressive characteristics of PD as we mentioned above, exploring the cholinergic function of PD patients at different stages would help us understand the pathophysiological mechanism with PD progression better.

On the basis of a previous study (George et al., 2011), we firstly segmented bilateral SI in the individual high-resolution structural images and defined them as seeds in the following rsFC calculation. We aimed to explore the altered cholinergic function in different stages of PD patients via the measure of functional connectivity of SI and investigate the relationships between aberrant SI connectivity and the disease severity. We hypothesized that with the progression of disease, PD patients' SI-FC would be disrupted and associated with the disease severity.

MATERIALS AND METHODS

Participants

All participants were recruited from the Department of Neurology, Second Affiliated Hospital of Zhejiang University and this study was approved by the Medical Ethics Committee of The Second Affiliated Hospital of Zhejiang University School of Medicine and the ethical approval number was (2017) Ethical Approval Study No. 008. Written informed consent was obtained from all participants before enrollment in the study. We excluded participants with a history of anticholinergic drugs, a history of neurologic or psychiatric disorders, brain trauma, or general exclusion criteria for MR scanning and analyzing. Specifically, seven normal controls and eight patients with PD were excluded for the following reasons: (1) with significant motion artifact during scanning, $n = 6$; (2) with severe brain atrophy or enlarged ventricles, $n = 4$; (3) with poor coregistration results, $n = 2$; (4) with incomplete demographic information, $n = 3$. After exclusion, 79 patients with PD and 64 healthy controls (HC) were included in this study. PD was diagnosed by a senior neurologist (BZ) according to the United Kingdom PD Society Brain Bank criteria (Hughes et al., 1992). For PD patients who were under antiparkinsonian treatment, MRI scanning and clinical assessments were performed in the morning after withdrawing all antiparkinsonian drugs overnight (at least 12 h) (on "drug-off status"). Basic demographic information, including age, gender, education duration, drug state and neurologic, and psychiatric scales including Hoehn-Yahr stage, Unified Parkinson's Disease Rating Scale (UPDRS) and Montreal Cognitive Assessment (MoCA) score were obtained from all PD patients. UPDRS motor scores were divided into subscores of axial symptoms (items 27–30). According to Hoehn-Yahr stage, PD patients were divided into two groups: 35 patients with Hoehn-Yahr stage ≤ 1.5 were grouped into early-stage PD group (PD-E) and 44 patients with Hoehn-Yahr stage ≥ 2 were grouped into middle-to-late stage

PD group (PD-M) (Li et al., 2020). For HC, basic demographic information and MoCA score were recorded.

MRI Data Acquisition

All participants were scanned on a 3.0-Tesla MRI scanner (GE Discovery 750) equipped with an 8-channel head coil. During MRI scanning, the head was stabilized using restraining foam pads, and earplugs were provided to reduce the noise during scanning. Structural T1 images were acquired using a fast spoiled gradient recalled sequence: repetition time = 7.336 ms; echo time = 3.036 ms; inversion time = 450 ms; flip angle = 11°; field of view = 260 × 260 mm^2; matrix = 256 × 256; slice thickness = 1.2 mm; 196 continuous sagittal slices. Rs-fMRI images were acquired using gradient recalled echo-echo planar imaging sequence: repetition time = 2,000 ms; echo time = 30 ms; flip angle = 77°; field of view = 240 × 240 mm^2; matrix = 64 × 64; slice thickness = 4 mm; slice gap = 0 mm; 38 interleaved axial slices. During MRI scanning, subjects were instructed to remain awake with their eyes closed and not to move or focus on a specific thought.

Seed Definition and Normalization

The bilateral SI were manually drawn on the coronal T1-weighted MRI images by a radiologist who was blinded to the participants' identity according to the method provided by George et al. (2011). Specifically, the SI was drawn at three consecutive gapless 1.2 mm-thick slices on T1-weighted coronal images reformatted to be perpendicular to the anterior commissure (AC)-posterior commissure (PC) line. The three consecutive sections analyzed were located at the level of the crossing of the AC, the level where the AC might be uncrossed, and the level of the emergence of the AC from the temporal lobe. The boundaries of the SI were as follows: the dorsal border was the ventral aspect of the globus pallidus, the ventral border was the base of the brain containing the anterior perforated space, the medial border was operationally defined by a vertical line extending from the ventrolateral border of the bed nucleus of the stria terminalis to the base of the brain, and the lateral border extended to the medial aspect of the putamen. The SI delineation of each section was shown in **Figure 1**.

The bilateral SI normalization was conducted using the VBM8 toolbox[1] implemented in SPM8.[2] All native T1-weighted images were normalized to the standard Montreal Neurological Institute (MNI) space. The corresponding normalization parameters were then applied to the bilateral SI, and therefore native SI was transformed into standard MNI space. After the SI normalization, a group-based probability map of bilateral SI was generated, and a threshold of 0.4 was used to obtain the binary SI mask (de Flores et al., 2017).

MRI Data Preprocessing and Functional Connectivity Analysis

The rs-fMRI data preprocessing was performed using the standard pipeline in the Data Processing and Analysis for (Resting-State) Brain Imaging suite (see text footnote 2) (Yan et al., 2016), which included first 10 volumes removing, slice timing, realignment, the nuisance covariates regression (Friston 24 head motion parameters, white matter, and cerebrospinal fluid signal), spatial normalization through structure images, smoothing with a gaussian kernel of 6 × 6 × 6 mm^3 full width at half maximum, temporal band-pass filtering (0.01–0.1 Hz), linear detrending, and scrubbing. No subject showed apparent head motion over 2 mm (transformation) and/or 2°(rotation). The bilateral SI mask in MNI space was used as seed, respectively, and a seed-based functional connectivity in whole brain was performed. Fisher's r-to-z transformation was applied to improve data's normality for parametric statistical analysis.

[1]http://dbm.neuro.uni-jena.de/vbm

[2]http://www.fil.ion.ucl.ac.uk/spm/

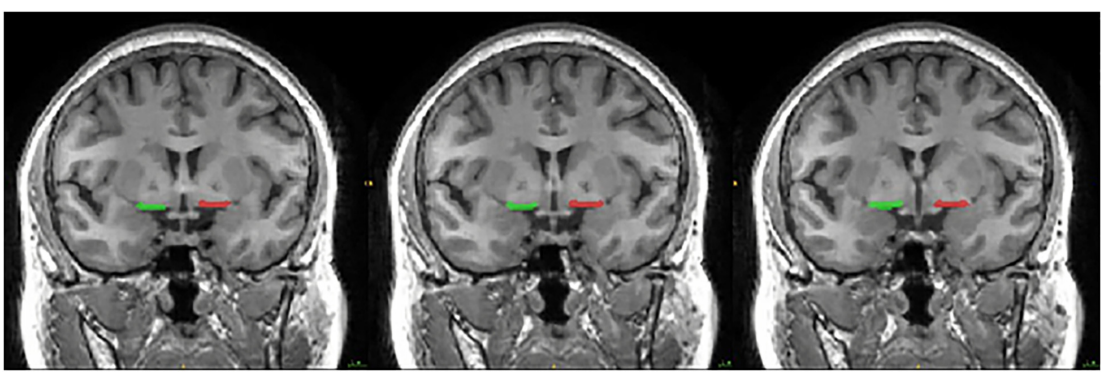

FIGURE 1 | Coronal slice of the MRI image showing the location of the substantia innominate (SI) used in the seed-based resting-state functional connectivity (rsFC) analysis. The SI was drawn at three consecutive gapless 1.2 mm-thick slices on T1-weighted coronal images reformatted to be perpendicular to the anterior commissure (AC)-posterior commissure (PC) line. The three consecutive sections analyzed were located at the level of the crossing of the AC, the level where the AC might be uncrossed, and the level of the emergence of the AC from the temporal lobe. The boundaries of the SI were as follows: the dorsal border was the ventral aspect of the globus pallidus, the ventral border was the base of the brain containing the anterior perforated space, the medial border was operationally defined by a vertical line extending from the ventrolateral border of the bed nucleus of the stria terminalis to the base of the brain, and the lateral border extended to the medial aspect of the putamen.

Statistical Analysis

Statistical analyses of demographic and clinical data were performed using SPSS 20.0 statistical software. Categorical variables were assessed using chi-square tests. The one-sample Kolmogorov-Smirnov test was used to check the data's normality. Normally distributed continuous variables were assessed using independent sample *t* test or analysis of variance (ANOVA). Non-parametric data were assessed using Wilcoxon rank-sum test and Kruskal-Wallis test. LSD correction was performed for the multiple comparisons in *post hoc* analyses. Two-tailed $p < 0.05$ was regarded as significant.

To locate the brain regions with significant difference in functional connectivity with SI among the three groups, one-way analysis of covariance (ANCOVA) was performed by using the statistical analysis tool of DPABI (Yan et al., 2016). Age, sex, and education duration were incorporated as covariates. Gaussian Random Field (GRF) correction (voxel $p = 0.001$, cluster $p = 0.05$, two-tailed) was used for multivoxel comparisons. Then, the mean FC of each individual in these significantly differed regions was extracted to perform the group comparisons as well as *post hoc* analyses. Least-Significant Difference (LSD) correction was used to correct the multiple comparisons in *post hoc* analyses. Two-tailed $p < 0.05$ was regarded as significant.

To test whether functional connectivity in brain regions showing significant group difference was correlated with the disease severity indicated by motor symptoms, partial correlation analysis was then conducted to evaluate the relationship between the FC and raw scores of UPDRS III, controlling age, gender and education duration as covariates. Bonferroni correction was performed for the multiple comparisons in *post hoc* analyses. Statistical significance was set at $p < 0.05$.

RESULTS

Demographic and Clinical Characteristics

Demographic and clinical characteristics of all participants were shown in **Table 1**. No significant differences in gender ($p = 0.140$), education duration ($p = 0.359$) and MoCA score ($p = 0.555$) were observed between PD-E, PD-M and HC. No significant differences in disease duration ($p = 0.275$) and drug state ($p = 0.813$) were observed between PD-E and PD-M. And the details of drug state of each PD patient were shown in **Supplementary Table 1**, none of them have a history of anticholinergic drugs. The age ($p = 0.027$) of PD-M is older than PD-E. Hoehn-Yahr stage ($p < 0.001$) and UPDRS III scores ($p < 0.001$) of PD-M were significantly higher than PD-E.

Comparative Analysis of Functional Connectivity Between SI and the Rest of Brain Regions

Brain regions showing significant difference of functional connectivity between left SI and the rest of brain among three groups were shown in **Figure 2A**, and the comparisons of functional connectivity between groups were shown in **Figure 2B**. Anatomical location and *post hoc* comparison results of altered functional connectivity in significant brain regions were shown in **Table 2**. Compared with HC, both PD-E and PD-M groups showed decreased functional connectivity in left frontal inferior opercularis areas, partly extending to the left insula (cluster 1), and increased functional connectivity in the left cingulum middle area (cluster 2) and right primary motor and sensory areas (cluster 3). Interestingly, functional connectivity in the right primary motor and sensory areas (cluster 3) continued to increase in PD-M group when compared with PD-E group. These results indicated that even in the early stages of PD, cortical cholinergic denervation has occurred in left frontal inferior opercularis areas (cluster 1), and cholinergic hyperactivity has occurred in the left cingulum middle area (cluster 2) and right primary motor and sensory areas (cluster 3). And at advanced stages of PD, cholinergic hyperactivity in the right primary motor and sensory areas would develop further. There was no difference of functional connectivity between right SI and the rest of brain among three groups.

Correlation Analysis of UPDRS III Scores and Resting State Functional Connectivity

The results of correlation analyses were shown in **Figure 3**. Partial correlation analysis showed that decreased functional connectivity in left frontal inferior opercularis and insula area (cluster 1) was negatively correlated with UPDRS III scores ($r = -0.336$, $p < 0.001$) and subscores of axial symptoms ($r = -0.261$, $p = 0.002$). Increased functional connectivity in left cingulum middle area (cluster 2) and right primary motor and sensory areas (cluster 3) was positively correlated with UPDRS III scores ($r = 0.315$, $p < 0.001$, and $r = 0.325$, $p < 0.001$, respectively) and subscores of axial symptoms ($r = 0.342$, $p < 0.001$, and $r = 0.355$, $p < 0.001$, respectively).

DISCUSSION

The main findings of the present study were as follows: (1) The decreased functional connectivity in left frontal inferior opercularis areas, partly extending to the left insula (cluster 1), and increased functional connectivity in the left cingulum middle area (cluster 2) and right primary motor and sensory areas (cluster 3) were both shown in PD-E and PD-M groups when compared with HC; (2) at advanced stages of PD, functional connectivity in the right primary motor and sensory areas (cluster 3) was further increased; (3) decreased functional connectivity in left frontal inferior opercularis and insula area (cluster 1) was negatively correlated with UPDRS III scores and subscores of axial symptoms. And increased functional connectivity in left cingulum middle area (cluster 2) and right primary motor and sensory areas (cluster 3) was positively correlated with UPDRS III scores and subscores of axial symptoms.

Compared with the HC, we found that PD patients showed decreased functional connectivity between left SI and left frontal inferior opercularis, indicating the cholinergic denervation in the frontal inferior opercularis. A PET study found the

TABLE 1 | Demographic and clinical information for the participants.

	PD-E(*n* = 35)	PD-M(*n* = 44)	HC(*n* = 64)	*P* value	*Post hoc* analysis		
					PD-E vs PD-M	PD-E vs HC	PD-M vs HC
Age, years	58.64 (6.66)	60.38 (6.60)	59.49 (8.25)	0.072	0.027	0.070	0.538
Sex, F/M	16/19	18/26	38/26	0.140	–	–	–
Education, years	9.25 (4.02)	8.84 (3.24)	9.78 (3.15)	0.359	0.591	0.459	0.158
Disease duration, years	3.59 (3.71)	4.59 (4.24)	–	–	0.275	–	–
Drug-naïve, yes/no	6/29	8/36	–	–	0.813	–	–
H-Y	1.10 (0.20)	2.35 (0.45)	–	–	0	–	–
UPDRS-III	14.20 (5.00)	28.32 (12.21)	–	–	0	–	–
Axial symptoms	2.37 (1.21)	3.82 (1.96)	–	–	0	–	–
MoCA	24.28 (3.57)	23.48 (4.32)	24.13 (3.15)	0.555	0.329	0.834	0.366

H-Y, Hoehn-Yahr stage; UPDRS-III, part III of the Unified Parkinson's Disease Rating Scale; MoCA, Montreal Cognitive Assessment.

neuroinflammation of SI in patients with REM sleep behavior disorder, which would lead to cortical cholinergic dysfunction in the frontal inferior opercularis (Staer et al., 2020). Frontal inferior opercularis plays a key role in postural and gait control, and an impairment of this area might lead to abnormal postural and gait control. Previous studies showed that the disruption of the projection from the SI to frontal inferior opercularis may result to the deficiency in the information processing from the temporoparietal cortex to the frontal cortex, which may cause errors in anticipatory postural adjustment and gait difficulties (Takakusaki, 2017; Vastik et al., 2017). And a MRI study showed that the decreased cortical thickness in frontal inferior opercularis was associated with motor symptoms (e.g., gait impairment) in PD (Herman et al., 2014; Vastik et al., 2017). This evidence indicated that the disrupted function of frontal inferior opercularis driving by the cholinergic degeneration was related to the motor difficulties. In this study, we found that the cortical cholinergic denervation in left frontal inferior opercularis was negatively associated with UPDRS motor scores and subscores of axial symptoms, which further supported that the cholinergic dysfunction in frontal inferior opercularis was associated with the severity of motor symptoms in PD patients.

In this study, we found increased functional connectivity between SI and cingulum middle areas both in PD-E and PD-M patients, which indicated the cholinergic hyperactivity in cingulum middle areas in PD patients. The cingulate gyrus is an important component of the limbic system which has rich distribution and intensity of acetylcholinesterase containing fiber (Mesulam et al., 1984). Previous study found the functional connectivity increases in the cingulate gyrus in PD patients with mild cognitive impairment (Zhan et al., 2018), which was in line with our findings. Former studies revealed that the generation and release of acetylcholine (ACh) and dopamine (DA) are both reduced in PD, however, overall acetylcholine was in a dominant position, resulting to a relatively cholinergic hyperactivity; further, the preponderance of ACh over DA contributes to the motor deficit (McKinley et al., 2019). An animal study showed that the parkinsonian motor dysfunction could be relieved by locally injecting the botulinum neurotoxin A in order to reduce the release of ACh (Wree et al., 2011). These studies indicated that cholinergic hyperactivity was related to the motor deficits in PD. In this study, we found the cholinergic functional connectivity in cingulum middle areas was positively correlated with UPDRS III scores and subscores of axial symptoms, suggesting that the more cholinergic hyperconnectivity in cingulum middle areas, the more severe of motor symptoms, which were similar to the previous studies. Taken together, we proposed that cholinergic hyperactivity in cingulum middle area may cause severe motor symptoms in PD patients.

An interesting finding in this study was the progressively increment of the cholinergic functional connectivity in primary motor and sensory areas at advanced stages of PD. A previous PET study found that specific populations (e.g., patients with movement disorders) exhibited decreased acetylcholinesterase activity in paracentral lobule, precentral gyrus, and postcentral gyrus (Hirano et al., 2010), pointing to the increased activity of cholinergic function in these brain regions. Intriguingly, some studies found the functional connectivity in primary motor and sensory areas was increased (Onu et al., 2015) and a greater improvement in UPDRS-III scores following L-dopa administration was characterized by lower functional connectivity in primary motor and sensory area, which were in agreement with our findings (Akram et al., 2017). Additionally, we found that the hyperactivity in primary motor and sensory areas was positively correlated with UPDRS III score and subscores of axial symptoms, suggesting a disease severity relevant role of cholinergic hyperactivity of these regions. Considering the progressive characteristic of PD evolution, we supposed that the cholinergic hyperconnectivity in primary motor and sensory areas may be a crucial mechanism for the disease progression.

There are some limitations of this study. First, selecting seed of seed-based rsFC analysis must be based on previous literature, which is subjective and cannot fully explore altered functional connectivity of the whole brain. Second, the sample size of this study was moderate. Third, in this study, we did not find any correlation between general cognition function (MoCa) and cholinergic network. Because most of the patients did not have multiple-domain cognition assessment, current finding should be cautiously translated to other relevant studies.

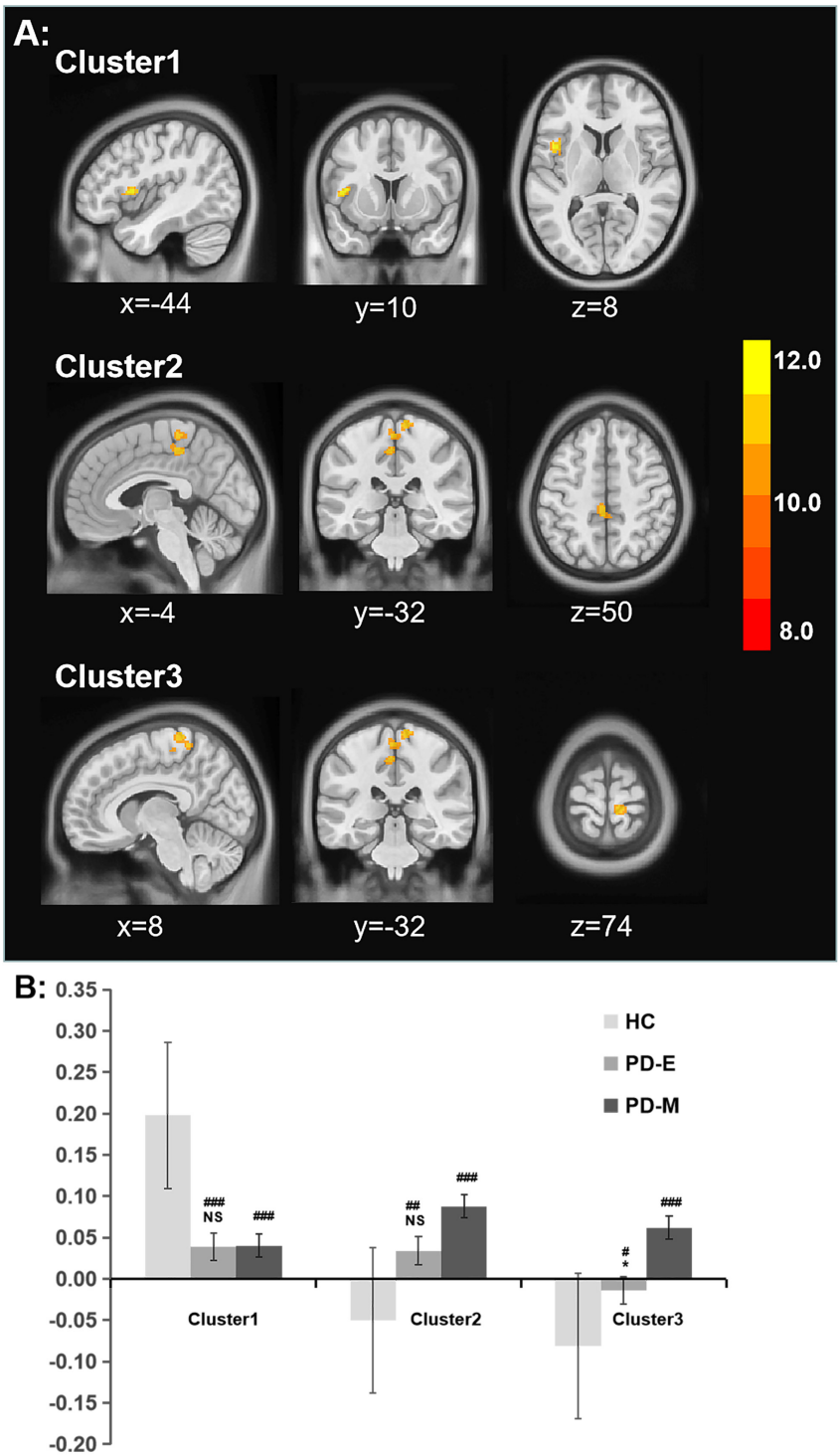

FIGURE 2 | (A) Significant alterations of rsFC between the left SI and whole brain among all groups. **(B)** The bar plot of comparisons of functional connectivity between groups. $^{*}p < 0.05$ vs the PD-M group, $^{\#}p < 0.05$; $^{\#\#}p < 0.01$; and $^{\#\#\#}p < 0.001$ vs the HC group. rsFC, resting-state functional connectivity; SI, substantia innominate.

And future studies are warranted to further disclose this interesting topic. Finally, this study is retrospective and cross-sectional. Further prospective and longitudinal studies with a larger sample size are expected to validate these finds and, importantly, to explore the longitudinal alterations of cholinergic-related functional connectivity along the disease

TABLE 2 | Anatomical location and *post hoc* comparison results of altered functional connectivity in significant brain regions.

Brain region	Number of voxels	Side	Peak MNI coordinate			F	The Mean FC of Each Cluster			*Post hoc* analysis			MD		
			X	Y	Z		PD-E	PD-M	HC	PD-E vs PD-M	PD-E vs HC	PD-M vs HC	PD-E vs PD-M	PD-E vs HC	PD-M vs HC
Cluster 1	98		–44	10	8	14.12	0.039 (0.127)	0.040 (0.202)	0.198 (0.183)	0.979	<0.001	<0.001	–0.011	–0.159	–0.158
Frontal Inferior Opercularis	66	L													
Insula	27	L													
Cluster 2	91		–4	–32	50	11.45	0.034 (0.133)	0.088 (0.162)	–0.050 (0.151)	0.114	0.009	<0.001	–0.054	0.084	0.138
Paracentral Lobule	47	L													
Cingulum Middle	40	L													
Cluster 3	317		8	–32	74	13.27	–0.014 (0.153)	0.062 (0.148)	–0.081 (0.130)	0.02	0.026	<0.001	–0.076	0.067	0.142
Paracentral Lobule	142	R													
Paracentral Lobule	70	L													
Precentral gyrus	24	R													
Postcentral gyrus	12	R													

FC, functional connectivity; MD, mean difference; L, left; R, right.

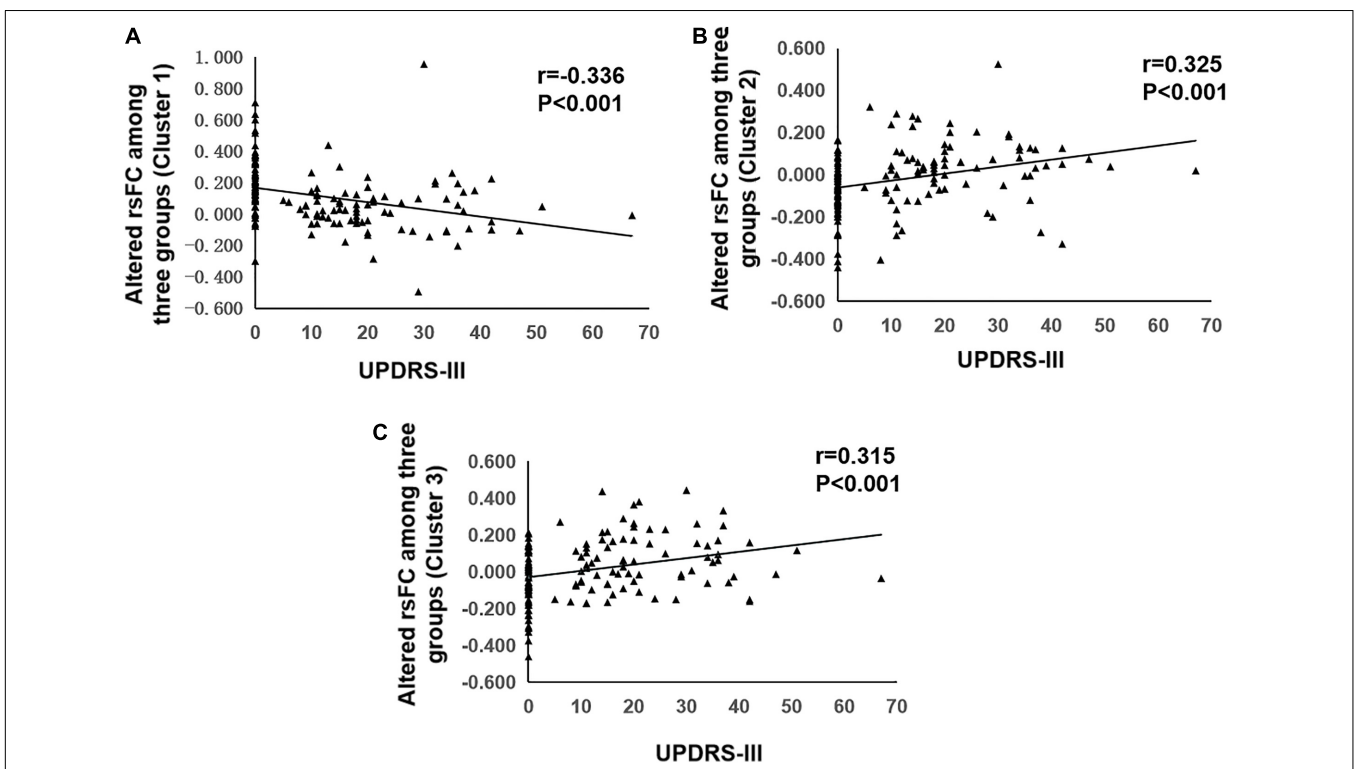

FIGURE 3 | Correlation analysis of UPDRS-III and resting state functional connectivity. **(A)** Correlation analysis of UPDRS-III and altered rsFC of Cluster 1. **(B)** Correlation analysis of UPDRS-III and altered rsFC of Cluster 2. **(C)** Correlation analysis of UPDRS-III and altered rsFC of Cluster 3. rsFC, resting-state functional connectivity; UPDRS-III, part III of the Unified Parkinson's Disease Rating Scale.

progression, which could provide greater insight into the cholinergic neuromechanism of PD progression.

In conclusion, this study revealed altered cholinergic functional connectivity in PD patients, which were associated with the severity of motor symptoms. Specifically, cholinergic functional connectivity in primary motor and sensory cortex was progressively increased at advanced stages of PD. These findings illustrated that altered cholinergic function plays an important role in the motor disruptions in PD patients both in early stage as well as during the progression of the disease.

DATA AVAILABILITY STATEMENT

The original contributions presented in the study are included in the article/**Supplementary Material**, further inquiries can be directed to the corresponding authors.

ETHICS STATEMENT

The studies involving human participants were reviewed and approved by the Medical Ethics Committee of The Second Affiliated Hospital of Zhejiang University School of Medicine. The patients/participants provided their written informed consent to participate in this study.

AUTHOR CONTRIBUTIONS

XX, XG, YY, and MZ were responsible for the study concept and design. WS wrote the main manuscript text. TGu revised the main manuscript text. WS, TGa, CZ, JW, TGu, JP, and BZ contributed to the acquisition of imaging data. WS, TGu, CZ, and JW performed data analysis and interpreted the findings. All authors contributed to the article and approved the submitted version.

FUNDING

This work was supported by the 13th Five-year Plan for National Key Research and Development Program of China (Grant No. 2016YFC1306600); the National Natural Science Foundation of China (Grant Nos. 82001767, 81971577, 82001767, 81701647, and 81771820); the Zhejiang Provincial Natural Science Foundation (Nos. LQ21H180008 and LQ20H180012); China Postdoctoral Science Foundation (Grant Nos. 2021T140599 and 2019M662082); the Health Foundation for Creative Talents in Zhejiang Province, China (Grant No. 2016), and Scientific Research Incubation Project of The First Affiliated Hospital of Wenzhou Medical University (FHY2019091).

ACKNOWLEDGMENTS

The authors sincerely thank all the volunteers and PD patients recruited in this project.

SUPPLEMENTARY MATERIAL

The Supplementary Material for this article can be found online at: https://www.frontiersin.org/articles/10.3389/fnagi.2021.723948/full#supplementary-material

REFERENCES

Akram, H., Wu, C., Hyam, J., Foltynie, T., Limousin, P., De Vita, E., et al. (2017). l-Dopa responsiveness is associated with distinctive connectivity patterns in advanced Parkinson's disease. *Mov. Disord.* 32, 874–883. doi: 10.1002/mds.27017

Bohnen, N. I., and Albin, R. L. (2011). The cholinergic system and Parkinson disease. *Behav. Brain Res.* 221, 564–573. doi: 10.1016/j.bbr.2009.12.048

Bohnen, N. I., Müller, M. L., Koeppe, R. A., Studenski, S. A., Kilbourn, M. A., Frey, K. A., et al. (2009). History of falls in Parkinson disease is associated with reduced cholinergic activity. *Neurology* 73, 1670–1676. doi: 10.1212/WNL.0b013e3181c1ded6

Braak, H., Del Tredici, K., Rüb, U., de Vos, R. A., Jansen Steur, E. N., and Braak, E. (2003). Staging of brain pathology related to sporadic Parkinson's disease. *Neurobiol. Aging* 24, 197–211. doi: 10.1016/s0197-4580(02)00065-9

Dalrymple, W. A., Huss, D. S., Blair, J., Flanigan, J. L., Patrie, J., Sperling, S. A., et al. (2021). Cholinergic nucleus 4 atrophy and gait impairment in Parkinson's disease. *J. Neurol.* 268, 95–101. doi: 10.1007/s00415-020-10111-2

de Flores, R., Mutlu, J., Bejanin, A., Gonneaud, J., Landeau, B., Tomadesso, C., et al. (2017). Intrinsic connectivity of hippocampal subfields in normal elderly and mild cognitive impairment patients. *Hum. Brain Mapp.* 38, 4922–4932. doi: 10.1002/hbm.23704

Fox, M. D., and Raichle, M. E. (2007). Spontaneous fluctuations in brain activity observed with functional magnetic resonance imaging. *Nat. Rev. Neurosci.* 8, 700–711. doi: 10.1038/nrn2201

George, S., Mufson, E. J., Leurgans, S., Shah, R. C., Ferrari, C., and deToledo-Morrell, L. (2011). MRI-based volumetric measurement of the substantia innominata in amnestic MCI and mild AD. *Neurobiol. Aging* 32, 1756–1764. doi: 10.1016/j.neurobiolaging.2009.11.006

Guan, X., Zhang, Y., Wei, H., Guo, T., Zeng, Q., Zhou, C., et al. (2019). Iron-related nigral degeneration influences functional topology mediated by striatal dysfunction in Parkinson's disease. *Neurobiol. Aging* 75, 83–97. doi: 10.1016/j.neurobiolaging.2018.11.013

Herman, T., Rosenberg-Katz, K., Jacob, Y., Giladi, N., and Hausdorff, J. M. (2014). Gray matter atrophy and freezing of gait in Parkinson's disease: is the evidence black-on-white? *Mov. Disord.* 29, 134–139. doi: 10.1002/mds.25697

Hirano, S., Shinotoh, H., Shimada, H., Aotsuka, A., Tanaka, N., Ota, T., et al. (2010). Cholinergic imaging in corticobasal syndrome, progressive supranuclear palsy and frontotemporal dementia. *Brain* 133, 2058–2068. doi: 10.1093/brain/awq120

Hughes, A. J., Daniel, S. E., Kilford, L., and Lees, A. J. (1992). Accuracy of clinical diagnosis of idiopathic Parkinson's disease: a clinico-pathological study of 100 cases. *J. Neurol. Neurosurg. Psychiatry* 55, 181–184. doi: 10.1136/jnnp.55.3.181

Kim, I., Shin, N. Y., Yunjin, B., Hyu Lee, P., Lee, S. K., and Mee Lim, S. (2017). Early-onset mild cognitive impairment in Parkinson's disease: altered corticopetal cholinergic network. *Sci. Rep.* 7:2381. doi: 10.1038/s41598-017-02420-w

Langston, J. W. (2006). The Parkinson's complex: parkinsonism is just the tip of the iceberg. *Ann. Neurol.* 59, 591–596. doi: 10.1002/ana.20834

Latt, M. D., Lord, S. R., Morris, J. G., and Fung, V. S. (2009). Clinical and physiological assessments for elucidating falls risk in Parkinson's disease. *Mov. Disord.* 24, 1280–1289. doi: 10.1002/mds.22561

Lee, Y., Ham, J. H., Cha, J., Park, Y. H., Lee, J. J., Sunwoo, M. K., et al. (2018). The cholinergic contribution to the resting-state functional network in

non-demented Parkinson's disease. *Sci. Rep.* 8:7683. doi: 10.1038/s41598-018-26075-3

Li, C. S., Ide, J. S., Zhang, S., Hu, S., Chao, H. H., and Zaborszky, L. (2014). Resting state functional connectivity of the basal nucleus of Meynert in humans: in comparison to the ventral striatum and the effects of age. *Neuroimage* 97, 321–332. doi: 10.1016/j.neuroimage.2014.04.019

Li, Y., Huang, P., Guo, T., Guan, X., Gao, T., Sheng, W., et al. (2020). Brain structural correlates of depressive symptoms in Parkinson's disease patients at different disease stage. *Psychiatry Res. Neuroimaging* 296:111029. doi: 10.1016/j.pscychresns.2019.111029

Liang, P., Wang, Z., Yang, Y., Jia, X., and Li, K. (2011). Functional disconnection and compensation in mild cognitive impairment: evidence from DLPFC connectivity using resting-state fMRI. *PLoS One* 6:e22153. doi: 10.1371/journal.pone.0022153

Lord, S., Baker, K., Nieuwboer, A., Burn, D., and Rochester, L. (2011). Gait variability in Parkinson's disease: an indicator of non-dopaminergic contributors to gait dysfunction? *J. Neurol.* 258, 566–572. doi: 10.1007/s00415-010-5789-8

Mallet, N., Leblois, A., Maurice, N., Beurrier, C., et al. (2019). Striatal cholinergic interneurons: how to elucidate their function in health and disease. *Front. Pharmacol.* 10:1488. doi: 10.3389/fphar.2019.01488

McKinley, J. W., Shi, Z., Kawikova, I., Hur, M., Bamford, I. J., Sudarsana Devi, S. P., et al. (2019). Dopamine deficiency reduces striatal cholinergic interneuron function in models of parkinson's disease. *Neuron* 103, 1056–1072.e6. doi: 10.1016/j.neuron.2019.06.013

Mesulam, M. M., and Geula, C. (1988). Nucleus basalis (Ch4) and cortical cholinergic innervation in the human brain: observations based on the distribution of acetylcholinesterase and choline acetyltransferase. *J. Comp. Neurol.* 275, 216–240. doi: 10.1002/cne.902750205

Mesulam, M. M., Rosen, A. D., and Mufson, E. J. (1984). Regional variations in cortical cholinergic innervation: chemoarchitectonics of acetylcholinesterase-containing fibers in the macaque brain. *Brain Res.* 311, 245–258. doi: 10.1016/0006-8993(84)90087-8

Onu, M., Badea, L., Roceanu, A., Tivarus, M., and Bajenaru, O. (2015). Increased connectivity between sensorimotor and attentional areas in Parkinson's disease. *Neuroradiology* 57, 957–968. doi: 10.1007/s00234-015-1556-y

Perry, E. K., Curtis, M., Dick, D. J., Candy, J. M., Atack, J. R., Bloxham, C. A., et al. (1985). Cholinergic correlates of cognitive impairment in Parkinson's disease: comparisons with Alzheimer's disease. *J. Neurol. Neurosurg. Psychiatry* 48, 413–421. doi: 10.1136/jnnp.48.5.413

Reich, S. G., and Savitt, J. M. (2019). Parkinson's Disease. *Med. Clin. North Am.* 103, 337–350. doi: 10.1016/j.mcna.2018.10.014

Rochester, L., Yarnall, A. J., Baker, M. R., David, R. V., Lord, S., Galna, B., et al. (2012). Cholinergic dysfunction contributes to gait disturbance in early Parkinson's disease. *Brain* 135, 2779–2788. doi: 10.1093/brain/aws207

Sethi, K. (2008). Levodopa unresponsive symptoms in Parkinson disease. *Mov. Disord.* 23, S521–S533. doi: 10.1002/mds.22049

Staer, K., Iranzo, A., Stokholm, M. G., Østergaard, K., Serradell, M., Otto, M., et al. (2020). Cortical cholinergic dysfunction correlates with microglial activation in the substantia innominata in REM sleep behavior disorder. *Parkinsonism Relat. Disord.* 81, 89–93. doi: 10.1016/j.parkreldis.2020.10.014

Takakusaki, K. (2017). Functional neuroanatomy for posture and gait control. *J. Mov. Disord.* 10, 1–17. doi: 10.14802/jmd.16062

Vastik, M., Hok, P., Valosek, J., Hlustik, P., Mensikova, K., and Kanovsky, P. (2017). Freezing of gait is associated with cortical thinning in mesial frontal cortex. *Biomed. Pap. Med. Fac. Univ. Palacky Olomouc Czech Repub.* 161, 389–396. doi: 10.5507/bp.2017.035

Wree, A., Mix, E., Hawlitschka, A., Antipova, V., Witt, M., Schmitt, O., et al. (2011). Intrastriatal botulinum toxin abolishes pathologic rotational behaviour and induces axonal varicosities in the 6-OHDA rat model of Parkinson's disease. *Neurobiol. Dis.* 41, 291–298. doi: 10.1016/j.nbd.2010.09.017

Yan, C. G., Wang, X. D., Zuo, X. N., and Zang, Y. F. (2016). DPABI: Data Processing & Analysis for (Resting-State) Brain Imaging. *Neuroinformatics* 14, 339–351. doi: 10.1007/s12021-016-9299-4

Yarnall, A., Rochester, L., and Burn, D. J. (2011). The interplay of cholinergic function, attention, and falls in Parkinson's disease. *Mov. Disord.* 26, 2496–2503. doi: 10.1002/mds.23932

Zhan, Z. W., Lin, L. Z., Yu, E. H., Xin, J. W., Lin, L., Lin, H. L., et al. (2018). Abnormal resting-state functional connectivity in posterior cingulate cortex of Parkinson's disease with mild cognitive impairment and dementia. *CNS Neurosci. Ther.* 24, 897–905. doi: 10.1111/cns.12838

Zhang, Z. X., Roman, G. C., Hong, Z., Wu, C. B., Qu, Q. M., Huang, J. B., et al. (2005). Parkinson's disease in China: prevalence in Beijing, Xian, and Shanghai. *Lancet* 365, 595–597. doi: 10.1016/s0140-6736(05)17909-4

Zhao, Y. J., Wee, H. L., Chan, Y. H., Seah, S. H., Au, W. L., Lau, P. N., et al. (2010). Progression of Parkinson's disease as evaluated by Hoehn and Yahr stage transition times. *Mov. Disord.* 25, 710–716. doi: 10.1002/mds.22875

Conflict of Interest: The authors declare that the research was conducted in the absence of any commercial or financial relationships that could be construed as a potential conflict of interest.

Publisher's Note: All claims expressed in this article are solely those of the authors and do not necessarily represent those of their affiliated organizations, or those of the publisher, the editors and the reviewers. Any product that may be evaluated in this article, or claim that may be made by its manufacturer, is not guaranteed or endorsed by the publisher.

frontiers in Aging Neuroscience

ORIGINAL RESEARCH
published: 15 September 2021
doi: 10.3389/fnagi.2021.732159

Prominent Striatum Amyloid Retention in Early-Onset Familial Alzheimer's Disease With PSEN1 Mutations: A Pilot PET/MR Study

Qi Qin[1,2,3,4†], *Liping Fu*[5,6†], *Ruimin Wang*[6], *Jihui Lyu*[7], *Huixuan Ma*[1,2,3,4], *Minmin Zhan*[1,2,3,4], *Aihong Zhou*[1,2,3,4], *Fen Wang*[1,2,3,4], *Xiumei Zuo*[1,2,3,4] *and Cuibai Wei*[1,2,3,4*]

[1] *Innovation Center for Neurological Disorders and Department of Neurology, Xuanwu Hospital, National Clinical Research Center for Geriatric Diseases, Capital Medical University, Beijing, China,* [2] *Center of Alzheimer's Disease, Beijing Institute for Brain Disorders, Beijing, China,* [3] *Beijing Key Laboratory of Geriatric Cognitive Disorders, Beijing, China,* [4] *Neurodegenerative Laboratory of Ministry of Education of the People's Republic of China, Beijing, China,* [5] *Department of Nuclear Medicine, China-Japan Friendship Hospital, Beijing, China,* [6] *Department of Nuclear Medicine, The First Medical Center, Chinese People's Liberation Army General Hospital, Beijing, China,* [7] *Center for Cognitive Disorders, Beijing Geriatric Hospital, Beijing, China*

Background: With the advancements of amyloid imaging in recent years, this new imaging diagnostic method has aroused great interest from researchers. Till now, little is known regarding amyloid deposition specialty in patients with early-onset familial Alzheimer's disease (EOFAD), and even less is known about its role in cognitive impairments.

Objectives: Our study aimed to evaluate the amyloid deposition in five patients with EOFAD, 15 patients with late-onset sporadic AD, and 12 healthy subjects utilizing ^{11}C-labeled Pittsburgh compound-B (^{11}C-PiB) amyloid PET imaging. Moreover, we figured out the correlation between striatal and cortical standardized uptake value ratios (SUVRs). We also investigated the correlation between ^{11}C-PiB retention and cognitive presentation.

Results: All patients with EOFAD showed high amyloid deposition in the striatum, a pattern that is not usually seen in patients with late-onset sporadic AD. The SUVR in the striatum, especially in the amygdala, showed significant correlations with cortex SUVR in EOFAD. However, neither striatal nor cortical ^{11}C-PiB retention was related to cognitive decline.

Conclusions: The amyloid distribution in patients with EOFAD differs from late-onset sporadic AD, with higher amyloid deposits in the striatum. Our study also demonstrated positive correlations in ^{11}C-PiB retention between the striatum and other cortical areas. We revealed that the distribution of amyloid in the brain is not random but diffuses following the functional and anatomical connections. However, the degree and pattern of amyloid deposition were not correlated with cognitive deficits.

Keywords: early-onset familial Alzheimer's disease, PET/MR hybrid neuroimaging, amyloid deposition, striatum, Pittsburgh compound-B PET, cognitive performance

OPEN ACCESS

Edited by:
Binbin Nie,
Chinese Academy of Sciences (CAS), China

Reviewed by:
Yating Lv,
Hangzhou Normal University, China
Jigang Yang,
Capital Medical University, China

***Correspondence:**
Cuibai Wei
chuibainews@126.com

[†] These authors have contributed equally to this work

Received: *28 June 2021*
Accepted: *13 August 2021*
Published: *15 September 2021*

Citation:
Qin Q, Fu L, Wang R, Lyu J, Ma H, Zhan M, Zhou A, Wang F, Zuo X and Wei C (2021) Prominent Striatum Amyloid Retention in Early-Onset Familial Alzheimer's Disease With PSEN1 Mutations: A Pilot PET/MR Study. Front. Aging Neurosci. 13:732159. doi: 10.3389/fnagi.2021.732159

INTRODUCTION

Alzheimer's disease (AD) is the leading cause of dementia and a severe public health problem worldwide (Jia et al., 2019). AD clinical manifestations begin with memory loss and then progress to cognitive dysfunction (Barnett, 2019). Several genetic mutations contribute to AD (Lane et al., 2018). AD is divided into early-onset AD (EOAD) and late-onset AD (LOAD) according to the age of onset (Bird, 2008). LOAD, also known as sporadic AD, is the most common AD with onset age over 65 years (Bateman et al., 2012). The EOAD onset age is earlier than 65 years. Approximately 10% of patients with EOAD are autosomal-dominant inheritance. PSEN1 (HGNC: 9508, OMIM: 104311), PSEN2 (HGNC: 9509, OMIM: 600759), and APP (HGNC: 620, OMIM: 104760) are three primary genes involved in familial EOAD (EOFAD). These genes encode amyloid precursor protein, presenilin-1, and presenilin-2, respectively (Bateman et al., 2011). The PSEN1 mutations are the most prevalent mutations, accounting for 75% of all EOFAD (Qin et al., 2020). The presenilin-1 protein is an essential component of the "y-secretase" enzyme complex, which is responsible for the cleavage of amyloid-β (Aβ) from its precursor APP (Brunkan and Goate, 2005). Therefore, mutations in PSEN1 could result in enhanced amyloid deposition.

The amyloid deposition has been considered as a pathognomonic marker of AD and regarded as an important target of intervention (Hanseeuw et al., 2018). In addition, the National Institute on Aging Alzheimer's Association (NIA-AA) workgroup proposed biomarkers of amyloid levels detected by cerebrospinal fluid assays and PET, which provide feasible tools to diagnose AD (McKhann et al., 2011; Louie, 2019). Moreover, plenty of research studies have indicated that amyloid deposition precedes clinical symptoms. In this regard, early detection of amyloid deposition has emerged as a goal of AD diagnosis and intervention. Thus, the clinical and research utility of amyloid PET imaging has become an effective diagnostic tool for patients with AD and an interesting topic among clinicians and researchers over the years.

The ^{11}C-labeled Pittsburgh compound-B (^{11}C-PiB) has a high affinity for fibrillar Aβ. This compound was the first ligand used to detect amyloid distribution in AD (Ikonomovic et al., 2008). Typically, the Aβ deposition initiates from the temporal lobe and orbitofrontal cortex and then spreads to the frontal lobe, parietal lobe, precuneus lobe, anterior cortex, and posterior cingulate cortex (Gordon et al., 2018). Over time, not only cortical structures but also subcortical structures can be strongly affected. However, different uptake patterns of early-onset familial carriers deserve special clinical attention. These autosomal-dominant EOFAD gene carriers initiated amyloid deposition in the striatum (Klunk et al., 2007).

In the past few years, hybrid imaging models have been widely accepted in clinical practice. The PET/MRI, a new hybrid model performed better in AD diagnosis. PET imaging can provide metabolic information of the brain, and MRI can provide structural information of the brain. PET/MR can also make up for the deficiency of PET/CT with no ionizing radiation (Arabi and Zaidi, 2016). Thus, the combination of functional imaging (PET) and structural imaging (MRI) has emerged as an accurate technique for AD diagnosis.

Till now, little is known regarding amyloid deposition specialty in patients with EOFAD and even less is known about its role in cognitive dysfunction (Klunk et al., 2007; Villemagne et al., 2009; Cohen et al., 2018). Therefore, our study aimed to use ^{11}C-PiB PET/MRI to compare amyloid burden in 5 patients with EOFAD, 15 patients with late-onset sporadic AD, and 12 healthy subjects. Moreover, we investigated the correlation between striatal and cortical standardized uptake value ratios (SUVRs). We also investigated the correlation between ^{11}C-PiB retention and clinical and cognitive presentation.

Utilizing amyloid imaging, we aimed to find the difference in amyloid deposition between patients with EOFAD and late-onset sporadic AD. In addition, we intended to reveal the correlation between striatum amyloid and cortex accumulation and the association between amyloid deposition and cognitive presentation.

METHODS

Subjects

The Institutional Review Board of Xuanwu Hospital approved the study. The methods were in accordance with the Declaration of Helsinki, and each participant signed an informed written consent form.

Five patients with EOFAD and 15 patients with LOAD were recruited from the memory clinic of Xuanwu Hospital, and three senior neurologists diagnosed all patients. The diagnosis met the criteria of the 2018 NIA-AA research framework (Louie, 2019). All participants underwent clinical evaluation, neuropsychological testing, genetic testing, and ^{11}C-PiB PET/MRI.

Twelve healthy participants were recruited from the community. They are free from a history of any neurological or psychiatric illness history and served as a normal control (NC) group. Clinical evaluation, neuropsychological testing, genetic testing, and ^{11}C-PiB PET/MRI revealed no apparent abnormal findings.

Neuropsychological Assessment

Neuropsychological evaluations included the Mini-Mental State Examination (MMSE), the Montreal Cognitive Assessment (MoCA), Clock Drawing Test (CDT), the Boston Naming Test (BNT), the Trail Making Test (TMT) A and B, and the Clinical Dementia Rating (CDR) scale assessment.

Genetic Testing

Genetic testing was performed on DNA obtained from a peripheral blood sample. DNA isolation was extracted from peripheral blood. Exonic regions of early-onset AD genes were captured (MyGenostics GenCap Enrichment Technologies, MyGenostics, Baltimore, MD, USA). The capture experiment was conducted according to the protocol of the manufacturer.

PET/MRI Procedure

All participants received an ^{11}C-PiB PET/MR scan. ^{11}C-PiB was synthesized with a radiochemical purity of over 95% and specific activity over 50 GBq/μmol (1.48 Ci/μmol). An initial 40-min intravenous tracer injection (range 333–518 MBq, 0.13–0.15 mCi/kg) was carried out prior to the ^{11}C-PiB data acquisition using the Siemens PET/MR systems (Biograph mMR, Siemens Medical Solutions, Grünwald, Germany). The built-in ultrashort echo-time sequence was used for the PET attenuation correction. The PET data were acquired within 20 min. The MRI scanning was performed with the following sequence protocol: sagittal 3D T1WI magnetization-prepared rapid gradient echo (T1WI 3D-MPRAGE): TR = 1,600 ms, TE = 2.15 ms, THK = 1.0 mm, FOV = 256 × 256 mm, matrix = 256 × 256; transverse T2WI fluid-attenuated inversion recovery (T2WI-FLAIR): TR = 8,000 ms, TE = 94 ms, THK = 5 mm, FOV = 192 × 220 mm, flip angle:150°; transverse diffusion-weighted images: with diffusion gradient encoding of $b = 0$, 1,000 s/mm^2. PET imaging and MRI were performed simultaneously.

Post-processing

All T1 scans were segmented into the gray matter (GM), white matter (WM), and cerebrospinal fluid (CSF) tissue classes and used the DARTEL group image registration algorithm to build a custom template. Statistical parametric mapping (SPM8) was used to co-register T1 scans with ^{11}C-PiB PET scans (http://www.fil.ion.ucl.ac.uk/spm). Co-registered T1 scans were spatially standardized to the custom template and generated the deformation fields for the ^{11}C-PiB PET scans, respectively. The cerebellar gray matter (CGM) region mask was created from the automated anatomic labeling (AAL) atlas and the GM mask. In order to obtain the individual CGM region, the AAL atlas was first transformed to the custom template space and then inverse transformed to the individual ^{11}C-PiB space using the inverse transformation of the deformation field obtained. The same normalization procedure was applied to the other 90 region of interests (ROIs) derived from the AAL atlas to obtain the individual ROIs. The CGM was selected as the reference region for SUVR measurement.

Statistical Analysis

Statistical data analysis was performed using the SPSS software (Version 20, SPSS Inc., Chicago, IL, USA). The assessment criterion of demographic information and neuropsychological tests between the EOFAD, LOAD, and NC were performed with one-way ANOVA. The SUVR of ROIs between groups was compared with one-way ANOVA at $p < 0.05$. Partial correlation analyses controlling for age and sex were used to study the relationship between SUVR value and neuropsychological test scores ($p < 0.05$, Bonferroni corrected, N = the statistical subject numbers).

RESULTS

Demographics and Clinical Characterization for EOFAD

Table 1 displays demographic, neuropsychological, genetic, and leading clinical symptoms for EOFAD. Among all these five patients, four of them are female. The average age of onset is 38.6 years old. All patients display progressive memory decline as the first symptom, especially working memory impairment. Besides memory loss, four patients exhibit decreased executive function. In addition, all patients with EOFAD showed significantly decreased cognitive scores on calculation and visuospatial function. None of the patients showed aphasia. Except for cognitive decline, the neurological examination reveals a positive Babinski sign and slightly increased muscular tension in Case 3. Case 4 has a positive family history. Notably, four patients suffered behavioral and psychological symptoms, such as depression and anxiety. The results of MMSE, MoCA, CDT, TMT A and B, BNT CDR, and the neuropsychiatric inventory (NPI) assessment were listed in **Table 1**. Initial blood chemistry and cerebral spinal fluid (CSF) analyses are negative. Five patients with early-onset AD undertook genetic testing, and all of them carry mutations in PSEN1.

Pattern of ^{11}C-PiB PET/MR Distribution in EOFAD, LOAD, and NC Groups

The ^{11}C-PiB PET/MR images of five patients with FAD, 15 patients with late-onset sporadic AD, and 12 NC subjects with the definite clinical diagnoses were analyzed. As expected, all the patients with EOFAD and late-onset sporadic AD performed significantly worse on MMSE compared with NC subjects (**Supplementary Table 1**). The maximum intensity projection images of ^{11}C-PiB PET in five patients with EOFAD were shown in **Figure 1**, in which increased ^{11}C-PiB retention was detected in both neocortex and striatum. From the ROI analysis, there were significant SUVR differences among the three groups in the frontal cortex, precuneus, anterior cingulated cortex, and parietal lobe (**Figures 2**, **3** and **Supplementary Table 2**). When compared to patients with EOFAD than that of patients with LOAD, the ^{11}C-PiB retention rate was found with no significant increase in 29 ROIs, but both two AD groups showed higher SUVR retention than the NC group. Regarding the three ROIs of the striatum, including caudate ($p = 0.014$, $p = 0.015$), putamen ($p = 0.012$, $p = 0.008$), and amygdala ($p = 0.016$, $p = 0.02$), the ^{11}C-PiB retention of EOFAD was found significantly higher than LOAD and NC (**Supplementary Tables 3, 4**).

Correlations of ^{11}C-PiB Accumulations Between Striatum and Cortex in EOFAD

Comparisons of ^{11}C-PiB distribution revealed differences among three groups, with higher striatal uptake in patients with EOFAD. Then, we detected correlations of ^{11}C-PiB accumulations between striatum and cortex in EOFAD. The strongest correlation with striatal uptake was seen in the amygdala. The amygdala ^{11}C-PiB accumulations significantly correlated with majority cortex ROIs including precentral area, frontal lobe, rolandic operculum, supplementary motor area, olfactory, rectus, insula, cingulate gyrus, hippocampus, parahippocampal area, calcaneus, cuneus, lingual area, occipital area, fusiform area, postcentral area, parietal area, supralimbic area, angular, precuneus area, paracentral lobule, globus pallidus, Heschl's gyrus, and temporal lobe. The correlation between the amygdala and frontal lobe ^{11}C-PiB accumulations is the most significant ($F = 15.659$, $p = 0.001$). The ^{11}C-PiB uptake

TABLE 1 | Demographics and clinical symptoms of five patients with early-onset familial Alzheimer's disease (EOFAD).

Case		1	2	3	4	5
Sex		Female	Female	Male	Female	Female
Onset age (years)		36	39	40	43	35
Education (years)		9	9	16	15	12
Cognitive impartment	Memory impairment	+	+	+	+	+
	Executive impairment	+	+	−	+	+
	Calculation impairment	+	+	+	+	+
	Visuospatial impairment	+	+	+	+	+
	Aphasia	−	−	−	−	−
Other neurological presentation		−	−	Positive Babinski sign Increased muscular tension	−	−
Depression or anxiety		+	−	+	+	+
Family history		−	+	−	+	−
Neuro-psychological test	MMSE	13	19	10	21	15
	MoCA	8	13	6	18	13
	CDT	1	2	0	2	1
	BNT	13	18	8	22	17
	TMT A	135	73.8	97.6	63.2	150
	TMT B	300	106	175	94	204
	CDR	2	1	2	1	2
	NPI	46	17	36	22	35
Genetic mutation		PSEN1 C410Y	PSEN1 L173F	PSEN1 G206S	PSEN1 L219P	PSEN1 F177L

BHT, Boston Naming Test; CDR, Clinical Dementia Rating; CDT, Clock Drawing Test; MMSE, Mini-Mental State Examination; MoCA, Montreal Cognitive Assessment; NPI, neuropsychiatric inventory; TMT, Trail Making Test.

of caudate also correlated significantly with several cortex areas such as rolandic operculum, insula, calcarine, cuneus, lingual, occipital lobe, posterior central lobe, parietal lobe, marginal superior horn lobe, paracentral lobule, and thalamus pallidus (**Supplementary Table 5**). These results revealed strong correlations of ^{11}C-PiB accumulations between striatum and cortex in EOFAD. They indicated that the ^{11}C-PIB accumulations in the striatum in patients with EOFAD are associated with amyloid accumulations in the cortex.

Correlations Between ^{11}C-PiB Accumulations and Neuropsychological Test in EOFAD

Besides ^{11}C-PiB accumulations of ROIs in EOFAD, we also detected the correlation of ^{11}C-PiB accumulations and neuropsychological tests in EOFAD. There was no significant difference between ^{11}C-PiB retention and neuropsychological test. Therefore, amyloid distribution in patients with EOFAD was not associated with cognitive impairment (**Supplementary Table 6**).

DISCUSSION

The ^{11}C-PiB amyloid PET/MRI provides a new perspective on Aβ deposition in the brain, and this auxiliary examination method facilitates research into the etiology, diagnosis, and treatment of AD (Linazasoro, 2008). Our study examined the pattern and degree of ^{11}C-PiB retention in five familial AD cases with PSEN1 mutations. All PSEN1 mutation carriers showed increased ^{11}C-PiB retention. Although the degree of cortical retention was lower than patients with late-onset sporadic AD, the striatal retention was remarkably higher. Furthermore, the high degree of striatum ^{11}C-PiB retention in patients with EOFAD is difficult to coincide than with patients with late-onset sporadic AD with the same clinical symptoms, and this pattern is coincident in previously reported patients with EOFAD (Klunk et al., 2007; Villemagne et al., 2009; Blautzik et al., 2017). Postmortem studies of patients with PSEN1 mutation also showed Aβ deposition in the striatum (Villemagne et al., 2009). These EOFAD studies suggested that amyloid deposition may follow a specific order, beginning in the striatum and then spreading diffusely throughout the neocortex (Klunk et al., 2007; Villemagne et al., 2009). There are four possible underlying mechanisms on the relatively early involvement of the striatum. First, the cortical predominantly amyloid deposition in patients with late-onset sporadic AD may be influenced by synaptic processes, whereas in EOFAD, amyloid deposition in subcortical areas, such as the striatum, may be mediated by amyloid precursor protein and its processing (Koivunen et al., 2008; Ishibashi et al., 2014). Second, the APP processing patterns differed between patients with EOFAD and sporadic AD. The PSEN1 gene mutation could induce axonal mis-trafficking, which was suggested as a potential culprit for striatal amyloid deposition. Such axonal mis-trafficking is considered to stem from a disruption in the APP processing (Maeda et al., 2007). Moreover, the striatum is vulnerable to tau protein accumulation in familial AD in the early stage (Jack et al.,

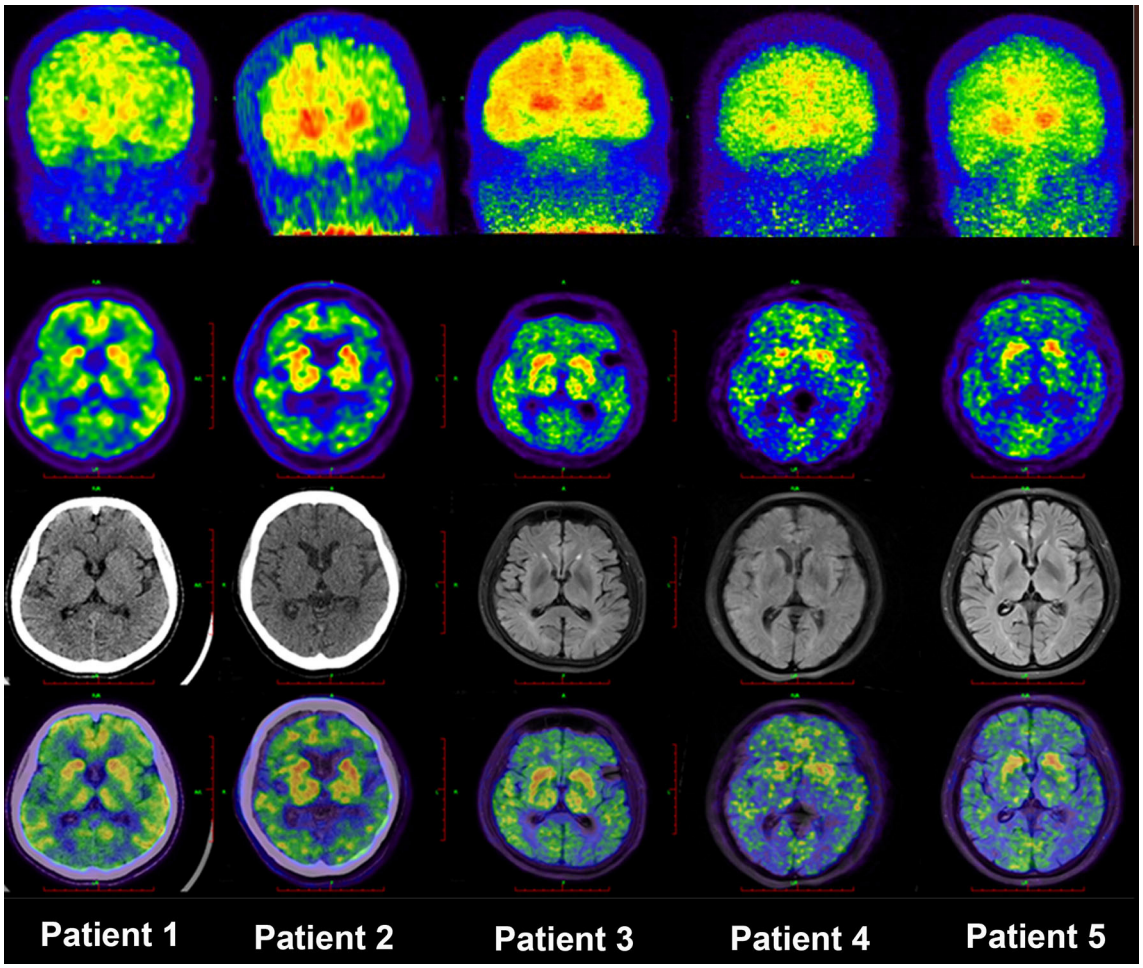

FIGURE 1 | MIP images of PIB-PET in five patients with EOFAD. The maximum intensity projection images of ^{11}C-PIB PET in five patients with EOFAD were shown, and increased PIB retention was detected in both the neocortex and striatum. ^{11}C-PiB, ^{11}C-labeled Pittsburgh compound-B; EOFAD, early-onset familial Alzheimer's disease.

2013a). Tau accumulation is considered more toxic to induce significant striatal neuronal injury. In addition, other studies concluded that different amyloid deposition could be due to different susceptibility to amyloidosis (Blautzik et al., 2017). The striatum exhibits amyloid deposition only in a more advanced phase of amyloidosis (Teipel et al., 2020). Patients with EOFAD showed more advanced amyloidosis in the striatum.

Given this background, our study also set out to investigate the connections between striatal and cortical regions. We detected that the ^{11}C-PiB accumulation in the striatum is correlated with cortex ^{11}C-PiB accumulation, especially in the amygdala. A similar study by Ishibashi et al. (2014) also found the highest ^{11}C-PiB distribution in the ventral striatum, and the SUVR value strongly correlated with ^{11}C-PiB retention in the frontal area (Koivunen et al., 2008). Our study also found that the correlations occurred between the amygdala and frontal lobe accumulation are the most significant. However, the connections between the frontal cortex and striatum are still not fully understood. Several studies have shown an anterograde distribution of input neurons in areas affected by amyloid deposition (Ikonomovic et al., 2008; Jung et al., 2010). In contrast to this finding, the striatum receives inputs from the frontal cortex, as revealed by a previous rat study (Mehlman et al., 2019). According to this study, the frontal cortex plays a vital role in determining the biological significance of associative information, and the input of the hippocampus may not be filtered. Moreover, several studies pointed out that the frontal lobe and the striatum are essential for executive function and decision-making (Seok et al., 2015; Orr et al., 2019). Therefore, the significant correlation between the striatum and cortical areas may explain the decision-making dysfunction in patients with EOFAD. There was also a high correlation between the cingulate cortex and striatum in our study. A previous study found significant functional connections between the cingulate cortex and striatum in patients with depression. The cingulate cortex showed reduced glucose metabolism in patients with depression, so it is assumed to be susceptible to depression (Clery-Melin et al., 2019). In our study, patients with EOFAD always presented with depression (four of five patients

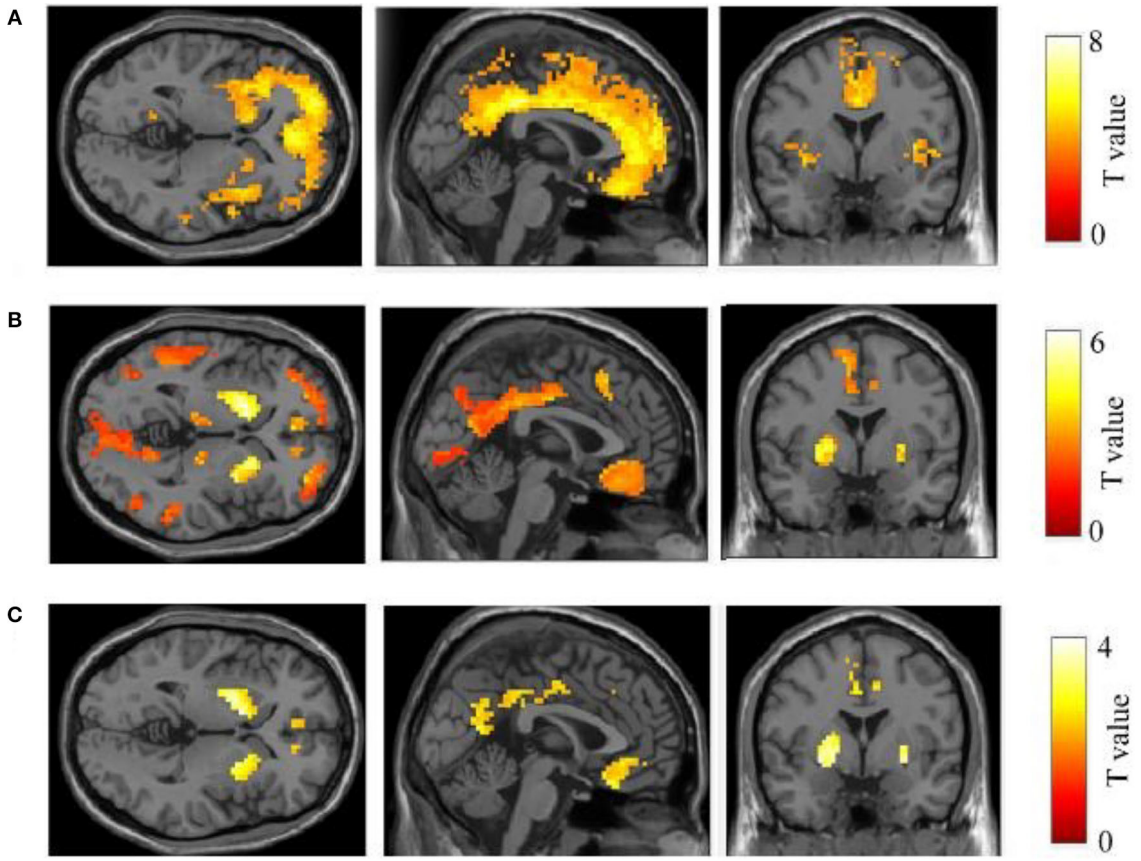

FIGURE 2 | Comparison of ^{11}C-PIB retention between three groups. In the comparison between LOAD–NC **(A)** and EOFAD–NC **(B)**, both AD groups were observed greater ^{11}C-PIB retention in the cortical and striatal regions. But the caudate, putamen, and amygdala were shown greater ^{11}C-PIB accumulation in patients with EOFAD than that in patients with LOAD **(C)**. ^{11}C-PiB, ^{11}C-labeled Pittsburgh compound-B; EOFAD, early-onset familial Alzheimer's disease; LOAD, late-onset Alzheimer's disease.

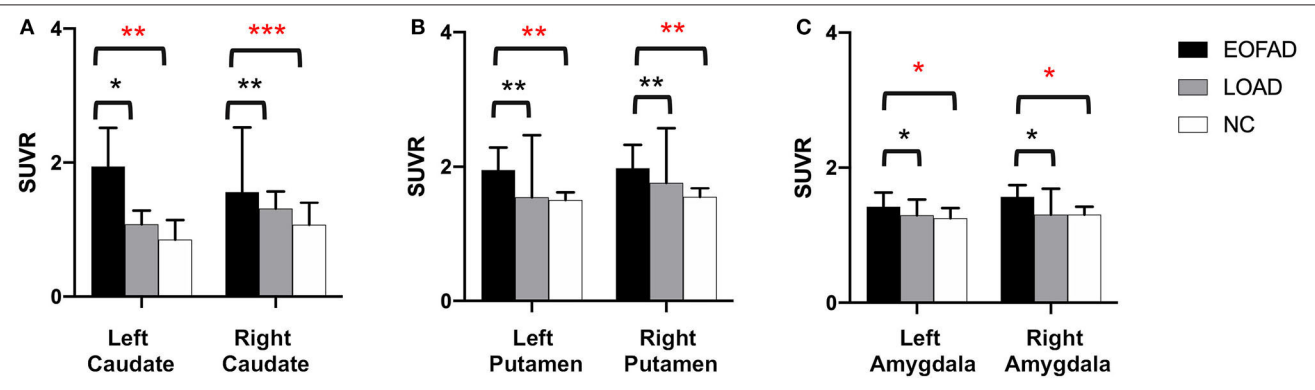

FIGURE 3 | ^{11}C-PIB retention among patients with EOFAD, patients with LOAD, and NC group in the striatum. There were significant SUVR differences among the three groups in caudate **(A)**, putamen **(B)**, and amygdala **(C)**. ^{11}C-PiB, ^{11}C-labeled Pittsburgh compound-B; EOFAD, early-onset familial Alzheimer's disease; LOAD, late-onset Alzheimer's disease; NC, normal control; SUVR, standardized uptake value ratio. *means $P < 0.05$, **means $P < 0.01$, and ***p < 0.001.

had depression or anxiety as shown in **Figure 1**). This further reinforces our reasoning that the strong correlation between cortical amyloid deposition and striatal amyloid accumulation is not random but reflects the functional connections.

Moreover, we found a significant negative correlation between cognitive performance and amyloid accumulation. This may be due to the progress of a biomarker, such as ^{11}C-PiB PET showed no linear increase in amyloid protein and cognitive decline

(Tentolouris-Piperas et al., 2017). The ^{11}C-PiB positive cases in our study may have already presented amyloid accumulation, so the neuropsychological test showed no further correlation between amyloid disposition and cognitive decline. Moreover, epidemiologic evidence suggests that cognitive decline in AD is also affected by other protective factors, such as cognitive training, high IQ, and high levels of education (Vemuri et al., 2011). Furthermore, we detect that the intense and focal striatal amyloid deposition in EOFAD did not lead to any movement disorder. This phenomenon indicated that striatum is not essential for the movement but is involved in decision-making in EOFAD.

Our study detected higher striatal ^{11}C-PiB retention in patients with EOFAD with PSEN1 mutations, unlike in patients with late-onset sporadic AD. The pattern and extent of Aβ accumulation were not associated with cognitive decline. Nevertheless, the distribution of amyloid deposits in the striatum correlated with the accumulation of cortical ^{11}C-PiB, particularly in the amygdala.

There are also some limitations of our study. First of all, our study is a cross-sectional study. Longitudinal and therapeutic studies are needed to compare striatal and neocortical ^{11}C-PiB measurements to track Aβ plaque deposition, evaluate AD treatments, and prognoses in patients with EOFAD. Then, there are only five cases included in our study; additional cases are needed to draw the conclusion. In addition, studies are needed to clarify the species and range of Aβ species merge to Aβ-tracer. ^{11}C-PiB shows higher affinity to N-terminal-truncated Aβ42 species in senile plaques and is less sensitive to diffuse Aβ plaques (Jack et al., 2013b). Cotton wool plaques are composed mainly of Aβ42 species and can be observed in the striatum of PSEN1 mutation carriers (Miki et al., 2019). More extensive studies should be conducted on cotton wool plaques to explain their etiological mechanisms and how they lead to different patterns of ^{11}C-PiB retention among patients with EOFAD and late-onset sporadic AD, and normal controls.

CONCLUSIONS

The amyloid deposition in EOFAD differs from that in late-onset sporadic AD; in that, the striatal ^{11}C-PiB retention is higher in EOFAD. Our study also found that amyloid deposition in the striatum correlated with the accumulation of cortical ^{11}C-PiB, particularly in the amygdala. The significant correlation between striatal and cortical areas is not random but reflects a functional link. Furthermore, the pattern and extent of amyloid distribution did not correlate with cognitive status.

DATA AVAILABILITY STATEMENT

The raw data supporting the conclusions of this article will be made available by the authors, without undue reservation.

ETHICS STATEMENT

The studies involving human participants were reviewed and approved by Xuanwu Hospital affiliated to Capital Medical University. The patients/participants provided their written informed consent to participate in this study. Written informed consent was obtained from the individual(s) for the publication of any potentially identifiable images or data included in this article.

AUTHOR CONTRIBUTIONS

CW, HM, and MZ collected the clinical data of patients and conducted neuropsychological tests. LF, RW, and QQ acquired the PET/MRI and executed post-processing. JL analyzed genetic reports. QQ performed the statics analysis. AZ, FW, and XZ participated in the literature review and helped to draft the manuscript. QQ drafted the manuscript. LF and CW revised the article. All authors read and approved the final manuscript.

FUNDING

This study was supported by the National Key R&D Program of China (No. 2017YFC1310103), Capital's Funds for Health Improvement and Research (CFH2020-4-1033), Beijing Municipal Administration of Hospitals Clinical Medicine Development of Special Funding Support (No. ZYLX201837), National Key R&D Program (2016YFC1306305), and Beijing Municipal Natural Science Foundation (No. 7192192).

SUPPLEMENTARY MATERIAL

The Supplementary Material for this article can be found online at: https://www.frontiersin.org/articles/10.3389/fnagi.2021.732159/full#supplementary-material

REFERENCES

Arabi, H., and Zaidi, H. (2016). Magnetic resonance imaging-guided attenuation correction in whole-body PET/MRI using a sorted atlas approach. *Med. Image. Anal.* 31, 1–15. doi: 10.1016/j.media.2016.02.002

Barnett, R. (2019). Alzheimer's disease. *Lancet* 393:1589. doi: 10.1016/S0140-6736(19)30851-7

Bateman, R. J., Aisen, P. S., De Strooper, B., Fox, N. C., Lemere, C. A., Ringman, J. M., et al. (2011). Autosomal-dominant Alzheimer's disease: a review and proposal for the prevention of Alzheimer's disease. *Alzheimers Res. Ther.* 3:1. doi: 10.1186/alzrt59

Bateman, R. J., Xiong, C., Benzinger, T. L., Fagan, A. M., Goate, A., Fox, N. C., et al. (2012). Clinical and biomarker changes in dominantly inherited Alzheimer's disease. *N. Engl. J. Med.* 367, 795–804. doi: 10.1056/NEJMoa1202753

Bird, T. D. (2008). Genetic aspects of Alzheimer disease. *Genet. Med.* 10, 231–239. doi: 10.1097/GIM.0b013e31816b64dc

Blautzik, J., Brendel, M., Sauerbeck, J., Kotz, S., Scheiwein, F., Bartenstein, P., et al. (2017). Reference region selection and the association between the rate of amyloid accumulation over time and the baseline amyloid burden. *Eur. J. Nucl. Med. Mol. Imaging.* 44, 1364–1374. doi: 10.1007/s00259-017-3666-8

Brunkan, A. L., and Goate, A. M. (2005). Presenilin function and gamma-secretase activity. *J. Neurochem.* 93, 769–792. doi: 10.1111/j.1471-4159.2005.03099.x

Clery-Melin, M. L., Jollant, F., and Gorwood, P. (2019). Reward systems and cognitions in major depressive disorder. *CNS Spectr*. 24, 64–77. doi: 10.1017/S1092852918001335

Cohen, A. D., McDade, E., Christian, B., Price, J., Mathis, C., Klunk, W., et al. (2018). Early striatal amyloid deposition distinguishes down syndrome and autosomal dominant Alzheimer's disease from late-onset amyloid deposition. *Alzheimers Dement*. 14, 743–750. doi: 10.1016/j.jalz.2018.01.002

Gordon, B. A., Blazey, T. M., Su, Y., Hari-Raj, A., Dincer, A., Flores, S., et al. (2018). Spatial patterns of neuroimaging biomarker change in individuals from families with autosomal dominant Alzheimer's disease: a longitudinal study. *Lancet Neurol*. 17, 241–250. doi: 10.1016/S1474-4422(18)30028-0

Hanseeuw, B. J., Betensky, R. A., Mormino, E. C., Schultz, A. P., Sepulcre, J., Becker, J. A., et al. (2018). PET staging of amyloidosis using striatum. *Alzheimers Dement*. 14, 1281–1292. doi: 10.1016/j.jalz.2018.04.011

Ikonomovic, M. D., Klunk, W. E., Abrahamson, E. E., Mathis, C. A., Price, J. C., Tsopelas, N. D., et al. (2008). Post-mortem correlates of *in vivo* PiB-PET amyloid imaging in a typical case of Alzheimer's disease. *Brain* 131, 1630–1645. doi: 10.1093/brain/awn016

Ishibashi, K., Ishiwata, K., Toyohara, J., Murayama, S., and Ishii, K. (2014). Regional analysis of striatal and cortical amyloid deposition in patients with Alzheimer's disease. *Eur. J. Neurosci*. 40, 2701–2706. doi: 10.1111/ejn.12633

Jack, C. R. Jr., Knopman, D. S., Jagust, W. J., Petersen, R. C., Weiner, M. W., Aisen, P. S., et al. (2013a). Tracking pathophysiological processes in Alzheimer's disease: an updated hypothetical model of dynamic biomarkers. *Lancet Neurol*. 12, 207–216. doi: 10.1016/S1474-4422(12)70291-0

Jack, C. R. Jr., Wiste, H. J., Lesnick, T. G., Weigand, S. D., Knopman, D. S., Vemuri, P., et al. (2013b). Brain beta-amyloid load approaches a plateau. *Neurology* 80, 890–896. doi: 10.1212/WNL.0b013e3182840bbe

Jia, L., Quan, M., Fu, Y., Zhao, T., Li, Y., Wei, C., et al. (2019). Dementia in China: epidemiology, clinical management, and research advances. *Lancet Neurol*. 19, 81–92. doi: 10.1016/S1474-4422(19)30290-X

Jung, Y. C., Ku, J., Namkoong, K., Lee, W., Kim, S. I., and Kim, J. J. (2010). Human orbitofrontal-striatum functional connectivity modulates behavioral persistence. *Neuroreport* 21, 502–506. doi: 10.1097/WNR.0b013e3283383482

Klunk, W. E., Price, J. C., Mathis, C. A., Tsopelas, N. D., Lopresti, B. J., Ziolko, S. K., et al. (2007). Amyloid deposition begins in the striatum of presenilin-1 mutation carriers from two unrelated pedigrees. *J. Neurosci*. 27, 6174–6184. doi: 10.1523/JNEUROSCI.0730-07.2007

Koivunen, J., Verkkoniemi, A., Aalto, S., Paetau, A., Ahonen, J. P., Viitanen, M., et al. (2008). PET amyloid ligand [11C]PIB uptake shows predominantly striatal increase in variant Alzheimer's disease. *Brain* 131, 1845–1853. doi: 10.1093/brain/awn107

Lane, C. A., Hardy, J., and Schott, J. M. (2018). Alzheimer's disease. *Eur. J. Neurol*. 25, 59–70. doi: 10.1111/ene.13439

Linazasoro, G. (2008). Imaging beta-amyloid burden in aging and dementia. *Neurology*. 70:1649; author reply 1650. doi: 10.1212/01.wnl.0000318046.06992.24

Louie, R. (2019). The 2018 NIA-AA research framework: Recommendation and comments. *Alzheimers Dement*. 15, 182–183. doi: 10.1016/j.jalz.2018.06.3062

Maeda, J., Ji, B., Irie, T., Tomiyama, T., Maruyama, M., Okauchi, T., et al. (2007). Longitudinal, quantitative assessment of amyloid, neuroinflammation, and anti-amyloid treatment in a living mouse model of Alzheimer's disease enabled by positron emission tomography. *J. Neurosci*. 27, 10957–10968. doi: 10.1523/JNEUROSCI.0673-07.2007

McKhann, G. M., Knopman, D. S., Chertkow, H., Hyman, B. T., Jack, C. R. Jr., Kawas, C. H., et al. (2011). The diagnosis of dementia due to Alzheimer's disease: recommendations from the National Institute on Aging-Alzheimer's Association workgroups on diagnostic guidelines for Alzheimer's disease. *Alzheimers Dement*. 7, 263–269. doi: 10.1016/j.jalz.2011.03.005

Mehlman, M. L., Winter, S. S., Valerio, S., and Taube, J. S. (2019). Functional and anatomical relationships between the medial precentral cortex, dorsal striatum, and head direction cell circuitry. I. Recording studies. *J. Neurophysiol*. 121, 350–370. doi: 10.1152/jn.00143.2018

Miki, T., Yokota, O., Haraguchi, T., Ikeuchi, T., Zhu, B., Takenoshita, S., et al. (2019). Young adult-onset, very slowly progressive cognitive decline with spastic paraparesis in Alzheimer's disease with cotton wool plaques due to a novel presenilin1 G417S mutation. *Acta Neuropathol. Commun*. 7:19. doi: 10.1186/s40478-019-0672-z

Orr, J. M., Imburgio, M. J., Bernard, J. A., and Banich, M. T. (2019). Striatal-frontal network activation during voluntary task selection under conditions of monetary reward. *Cogn. Affect. Behav. Neurosci*. 19, 568–585. doi: 10.3758/s13415-019-00689-0

Qin, Q., Yin, Y., Wang, Y., Lu, Y., Tang, Y., Jia, J., (2020). Gene mutations associated with early onset familial Alzheimer's disease in China: an overview and current status. *Mol. Genet. Genomic Med*. 8:e1443. doi: 10.1002/mgg3.1443

Seok, J. W., Lee, K. H., Sohn, S., and Sohn, J. H. (2015). Neural substrates of risky decision making in individuals with Internet addiction. *Aust. N. Z. J. Psychiatry*. 49, 923–932. doi: 10.1177/0004867415598009

Teipel, S. J., Dyrba, M., Chiesa, P. A., Sakr, F., Jelistratova, I., Lista, S., et al. (2020). In vivo staging of regional amyloid deposition predicts functional conversion in the preclinical and prodromal phases of Alzheimer's disease. *Neurobiol. Aging* 93, 98–108. doi: 10.1016/j.neurobiolaging.2020.03.011

Tentolouris-Piperas, V., Ryan, N. S., Thomas, D. L., and Kinnunen, K. M. (2017). Brain imaging evidence of early involvement of subcortical regions in familial and sporadic Alzheimer's disease. *Brain Res*. 1655, 23–32. doi: 10.1016/j.brainres.2016.11.011

Vemuri, P., Weigand, S. D., Przybelski, S. A., Knopman, D. S., Smith, G. E., Trojanowski, J. Q., et al. (2011). Cognitive reserve and Alzheimer's disease biomarkers are independent determinants of cognition. *Brain* 134, 1479–1492. doi: 10.1093/brain/awr049

Villemagne, V. L., Ataka, S., Mizuno, T., Brooks, W. S., Wada, Y., Kondo, M., et al. (2009). High striatal amyloid beta-peptide deposition across different autosomal Alzheimer disease mutation types. *Arch. Neurol*. 66, 1537–1544. doi: 10.1001/archneurol.2009.285

Conflict of Interest: The authors declare that the research was conducted in the absence of any commercial or financial relationships that could be construed as a potential conflict of interest.

The reviewer JY declared a shared affiliation, though no other collaboration, with several of the authors QQ, HM, MZ, AZ, FW, XZ, and CW to the handling editor.

Publisher's Note: All claims expressed in this article are solely those of the authors and do not necessarily represent those of their affiliated organizations, or those of the publisher, the editors and the reviewers. Any product that may be evaluated in this article, or claim that may be made by its manufacturer, is not guaranteed or endorsed by the publisher.

frontiers in Aging Neuroscience

ORIGINAL RESEARCH
published: 24 September 2021
doi: 10.3389/fnagi.2021.737002

Simultaneous PET/fMRI Detects Distinctive Alterations in Functional Connectivity and Glucose Metabolism of Precuneus Subregions in Alzheimer's Disease

Miao Zhang[1†], Wanqing Sun[2†], Ziyun Guan[2], Jialin Hu[2], Binyin Li[3], Guanyu Ye[3], Hongping Meng[1], Xinyun Huang[1], Xiaozhu Lin[1], Jin Wang[1], Jun Liu[3], Biao Li[1,4], Yaoyu Zhang[2]* and Yao Li[2]*

[1]Department of Nuclear Medicine, Ruijin Hospital, Shanghai Jiao Tong University School of Medicine, Shanghai, China, [2]School of Biomedical Engineering, Shanghai Jiao Tong University, Shanghai, China, [3]Department of Neurology & Institute of Neurology, Ruijin Hospital, Shanghai Jiao Tong University School of Medicine, Shanghai, China, [4]Collaborative Innovation Center for Molecular Imaging of Precision Medicine, Ruijin Center, Shanghai, China

OPEN ACCESS

Edited by:
Behrooz Hooshyar Yousefi, University of Marburg, Germany

Reviewed by:
Gabriel Gonzalez-Escamilla, Johannes Gutenberg University Mainz, Germany
Kuangyu Shi, University of Bern, Switzerland

***Correspondence:**
Yaoyu Zhang
yaoyu_zhang@sjtu.edu.cn
Biao Li
lb10363@rjh.com.cn

[†]These authors have contributed equally to this work

Received: *06 July 2021*
Accepted: *30 August 2021*
Published: *24 September 2021*

Citation:
Zhang M, Sun W, Guan Z, Hu J, Li B, Ye G, Meng H, Huang X, Lin X, Wang J, Liu J, Li B, Zhang Y and Li Y (2021) Simultaneous PET/fMRI Detects Distinctive Alterations in Functional Connectivity and Glucose Metabolism of Precuneus Subregions in Alzheimer's Disease. Front. Aging Neurosci. 13:737002. doi: 10.3389/fnagi.2021.737002

As a central hub in the interconnected brain network, the precuneus has been reported showing disrupted functional connectivity and hypometabolism in Alzheimer's disease (AD). However, as a highly heterogeneous cortical structure, little is known whether individual subregion of the precuneus is uniformly or differentially involved in the progression of AD. To this end, using a hybrid PET/fMRI technique, we compared resting-state functional connectivity strength (FCS) and glucose metabolism in dorsal anterior (DA_pcu), dorsal posterior (DP_pcu) and ventral (V_pcu) subregions of the precuneus among 20 AD patients, 23 mild cognitive impairment (MCI) patients, and 27 matched cognitively normal (CN) subjects. The sub-parcellation of precuneus was performed using a K-means clustering algorithm based on its intra-regional functional connectivity. For the whole precuneus, decreased FCS (p = 0.047) and glucose hypometabolism (p = 0.006) were observed in AD patients compared to CN subjects. For the subregions of the precuneus, decreased FCS was found in DP_pcu of AD patients compared to MCI patients (p = 0.011) and in V_pcu for both MCI (p = 0.006) and AD (p = 0.008) patients compared to CN subjects. Reduced glucose metabolism was found in DP_pcu of AD patients compared to CN subjects (p = 0.038) and in V_pcu of AD patients compared to both MCI patients (p = 0.045) and CN subjects (p < 0.001). For both FCS and glucose metabolism, DA_pcu remained relatively unaffected by AD. Moreover, only in V_pcu, disruptions in FCS (r = 0.498, p = 0.042) and hypometabolism (r = 0.566, p = 0.018) were significantly correlated with the cognitive decline of AD patients. Our results demonstrated a distinctively disrupted functional and metabolic pattern from ventral to dorsal precuneus affected by AD, with V_pcu and DA_pcu being the most vulnerable and conservative subregion, respectively. Findings of this study extend our knowledge on the differential roles of precuneus subregions in AD.

Keywords: Alzheimer's disease, mild cognitive impairment, hybrid PET/MRI, glucose metabolism, functional connectivity, precuneus, subregions

INTRODUCTION

The precuneus plays a critical role in fundamental cognitive functions including self-processing, memory, visual-spatial imagery, etc. (Cavanna and Trimble, 2006). In addition, it has been identified as a cortical hub for integrative processing of segregated systems in the brain (Buckner et al., 2009; Tomasi and Volkow, 2011). Likely due to its continuous high baseline activity and/or metabolism (Shokri-Kojori et al., 2019), the precuneus is susceptible to amyloid β (Aβ) deposition (Buckner et al., 2009), a pathophysiological biomarker of Alzheimer's Disease (AD). Increasing evidence has shown that the precuneus suffered disrupted functional connectivity (FC; Greicius et al., 2004; Damoiseaux et al., 2012) and glucose hypometabolism (Kapogiannis and Mattson, 2011; Pascoal et al., 2019), which might have a significant impact on the network degeneration of AD (Drzezga et al., 2011; Drzezga, 2018).

Despite its important role in the pathogenesis of AD as a whole cortical structure, the precuneus has been recognized as an anatomically and functionally heterogeneous brain region. Based on its cytoarchitecture as well as anatomical and functional connectivities, the precuneus has been broadly subdivided, or hieratically classified, into three clusters, namely the dorsal-anterior, dorsal-posterior, and ventral/central subregions (Margulies et al., 2009; Zhang and Li, 2012; Wang et al., 2019; Luo et al., 2020; Ye et al., 2021). Among them, the dorsal anterior and posterior subregions are majorly involved in sensorimotor and visual-related functions, and the ventral/central subregion mostly participates in higher-order cognitive and self-related functions (Cauda et al., 2010). Previous studies have demonstrated selective vulnerability of these subregions affected by AD. Specifically, while the ventral/central subregion of the precuneus showed significantly reduced resting-state FC with other brain regions in AD patients, the dorsal subregion was unchanged or slightly disturbed (Xia et al., 2014; Wu et al., 2016; Khan et al., 2020). Nevertheless, how the internal functional integrity of each subregion is affected by AD remains to be elucidated.

Besides functional disruptions, glucose metabolism, as a surrogate for neuronal activity, has been shown to reduce in the precuneus and suggested to predict the progression of AD (Kato et al., 2016; Mutlu et al., 2017). Previous studies further suggested that the disruptions in neuronal activity and FC are causally linked and may both be consequences of neurotoxic amyloid aggregation (Drzezga et al., 2011; Marchitelli et al., 2018). However, whether the glucose metabolism of each subregion is uniformly or differentially involved in the progression of AD and their associations with the functional disruption are not well understood.

The aim of this study is to investigate the functional and metabolic activities in the subregions of the precuneus across different stages over the spectrum of AD. A hybrid PET/fMRI technique was employed to measure the FC strength (FCS) with the blood oxygen-level dependent (BOLD) signal (Liang et al., 2013) and glucose metabolism with fluorine-18 (^{18}F) fluorodeoxyglucose (FDG) in AD patients, mild cognitive impairment (MCI) patients and age- and education-matched cognitively normal (CN) subjects. The functional and metabolic signals are known to change with head motions, different physiological states or moods of the participants (Waites et al., 2005), which are particularly susceptible to patients with MCI and AD in sequential and long acquisitions. The use of hybrid PET/MRI technique minimizes these fluctuations in a time-efficient manner, provides better temporal and spatial registrations between the two modalities, and enables a more accurate evaluation of the interrelated functional and metabolic changes due to AD (Cecchin et al., 2017). In addition, an FC-based K-means clustering algorithm (Ye et al., 2021) was adopted to subdivide the precuneus into the dorsal-anterior, dorsal-posterior and ventral subregions. Results of this study may pave the way for further understanding of selective disruptions in subregions of the precuneus in AD.

MATERIALS AND METHODS

Study Design

A total of 70 participants were included in the study [27 CN: 15 females and 12 males, mean age: 67.48 years (range: 52–83 years); 23 mild cognitive impairment (MCI) patients: 15 females and eight males, mean age: 70.56 years (range: 49–82 years); and 20 AD patients: 15 females and five males, mean age: 66.00 years (range: 46–83 years)]. Demographics of each group are listed in **Table 1**. The participants were recruited from ongoing studies of aging at Memory Clinic of Ruijin Hospital, Shanghai, China. All participants underwent cognitive assessments with the clinical dementia rate (CDR) scale. Those with CDR = 0.5 and CDR $\geq$ 1 were clinically diagnosed as MCI and AD, respectively. All subjects in the CN group had CDR = 0. Participants also completed the Mini-Mental State Examination (MMSE) as part of their evaluations. Exclusion criteria included: (1) psychiatric or other neurological diseases; (2) pregnancy or renal failure (critical for PET imaging); (3) major systemic disease; (4) history of traumatic brain injury; and (5) drug or alcohol addiction. All participants or their designees provided written informed consent to the study as part of the Institutional Review Board-approved protocol by Ruijin Hospital, which is in accordance with the Helsinki Declaration and its later revised ethical standards.

Image Acquisitions

All imaging data were acquired on a Biograph mMR scanner (Siemens Healthcare, Erlangen, Germany) in a single session. Each subject was required to fast for at least 6 h before receiving a bolus injection of the ^{18}F-FDG using a mean dose of 207.8 $\pm$ 35.5 MBq (range 140.6–329.3 MBq). Simultaneous PET/MR images were obtained at 40–60 min post injection. Structural MR images were acquired using T1-weighted magnetization-prepared rapid gradient echo (MPRAGE) sequence: repetition time (TR) = 1,900 ms, echo time (TE) = 2.44 ms, flip angle (FA) = 9°, field of view (FOV) = 256 × 256 mm^2, voxel size = 0.5 × 0.5 × 1.0 mm^3, number of slices = 192. Resting-state functional MRI (fMRI) images were acquired using a gradient-echo echo planar imaging sequence: TR = 2,000 ms, TE = 22 ms, FA = 90°, FOV = 192 × 192 mm^2, voxel size = 3.0 × 3.0 × 3.0 mm^3,

TABLE 1 | Demographic and clinical information.

	CN	MCI	AD	p-value
N	27	23	20	
Gender (F/M)	15/12	15/8	15/5	0.386
Age, year	67.48 (7.44)	70.56 (8.30)	66.00 (9.44)	0.188
Education, year	13.52 (2.82)	12.78 (3.72)	11.65 (3.70)	0.183
MMSE	29.37 (0.79)	27.26 (1.86)[a]	21.50 (4.65)[b,c]	<0.001
CDR 0/0.5/≥1	0	0.5	≥1	

Values are mean (SD). Chi-square was used for gender comparisons, one-way ANOVA with post hoc Bonferroni comparisons was used for comparisons of age, education and MMSE scores among all groups. [a]CN ≠ MCI ($p < 0.05$); [b]MCI ≠ AD ($p < 0.05$); [c]CN ≠ AD ($p < 0.05$). Abbreviations: CN, cognitively normal; MCI, mild cognitive impairment; AD, Alzheimer's Disease; MMSE, Mini-Mental State Examination; CDR, clinical dementia rating.

spacing between slices = 3.75 mm, number of slices = 36, number of volumes = 240. During the scan, the participants were instructed to lay supine with eyes closed but remain awake and avoid systematic thinking. The PET images were acquired in sinogram mode for 15 min. A matrix size of 344 × 344 × 127 was used, resulting in a voxel size of 2.1 × 2.1 × 2.0 mm^3. In order to improve the accuracy of the standardized uptake value, we applied an additional model-based bone compartment on the basis of Dixon method for attenuation correction. After corrections of random coincidences, dead-time, scatter and photon attenuation, the PET images were reconstructed using ordered subset expectation maximization algorithm (four iterations, 21 subsets). Post-filtering was performed using a 2 mm full width half-maximum (FWHM) Gaussian filter.

PET Data Processing

The PET data were processed using the statistical parametric mapping software (SPM12). All PET images of each subject were registered to their own T1-weighted images using affine transformation and corrected for partial volume effects using the Müller-Gärtner method (Müller-Gärtner et al., 1992) in the PETPVE12 toolbox (Gonzalez-Escamilla et al., 2017). The T1-weighted images were spatially normalized to the Montreal Neurological Institute (MNI)-152 template and the transformation parameters were subsequently applied to warp the PET images to the MNI space. Afterwards, the PET data were quantified using the standard uptake value ratio (SUVR) referenced by the mean uptake in the cerebellar gray matter and smoothed with a 6 mm FWHM Gaussian kernel.

fMRI Data Preprocessing

All fMRI images were processed using the Analysis of Functional Neuroimaging (AFNI 21.0.06) software (Cox, 1996). The first four volumes of each subject were discarded to avoid noises due to instable adaption to the scanning. The remaining volumes underwent slice timing and head motion corrections. All subjects had a mean framewise displacement ≤0.5 mm and a percentage of missing data points ≤40%. Nonlinear spatial normalization to MNI space were applied to all the images. Then, temporal band-pass filtering with bandwidth of 0.01–0.1 Hz was performed to reduce the effect of low-frequency drifts and high-frequency noises. Several nuisance signals, including estimated motion parameters, their first derivatives, as well as the averaged signals from white matter, cerebral spinal fluid and the global signal were regressed out. Finally, spatial smoothing was carried out with a 6 mm FWHM Gaussian kernel.

Functional Parcellation and FCS Analysis of the Precuneus

The precuneus was defined based on the anatomical automatic label (AAL-90) template (Tzourio-Mazoyer et al., 2002). For each subject, an FC matrix was generated by performing the Pearson's correlation (**r**) between the time series of each voxel and those of other voxels within the precuneus. This FC matrix was then subjected to Fisher's Z transformation.

Next, the z-transformed FC matrix of each subject in the CN group was averaged to obtain a mean FC matrix. Functional parcellation (Kahnt et al., 2012; Kahnt and Tobler, 2017) was performed to this mean FC matrix using the K-means clustering algorithm (Tou and Gonzalez, 1974) with customized MATLAB (R2018a, The MathWorks Inc., Natick, MA, USA) scripts. By this means, voxels with similar intrinsic connectivity properties tend to be clustered together. $K = 3$ was specifically selected for this study based on consistent evidences demonstrating the tripartite anatomical and functional features of the precuneus (Margulies et al., 2009; Wang et al., 2019). Finally, the optimized three clusters were mapped to the precuneus of each subject.

To compute FCS, weak correlations less than 0.2 (Dai et al., 2015) that might arise from noises were set to zero (Dai et al., 2015). Then, the FCS for a given voxel **i** was calculated by averaging its FC to all other voxels (Liang et al., 2013):

$$\mathbf{FCS\,(i)} = \frac{1}{\mathbf{n}-1}\sum_{\mathbf{j}=1,\mathbf{j}\neq\mathbf{i}}^{\mathbf{n}} \mathbf{z_{ij}}, \mathbf{r_{ij}} > \mathbf{r}_0$$

where $\mathbf{z_{ij}}$ represents the z-value between voxel **i** and voxel **j**, and **n** represents the number of voxels in the precuneus.

Statistical Analysis

All the statistical analyses were performed using the SPSS software (version 25.0, IBM Corporation, Armonk, NY, USA). Data normality was tested using the Kolmogorov-Smirnov test. Demographic and clinical characteristics were compared among the CN, MCI and AD groups using chi-square tests for categorical variables and one-way analysis of variance (ANOVA) with *post hoc* Bonferroni comparisons for continuous variables. For the whole precuneus and its subregions, the mean FCS and FDG-SUVR were obtained for each subject and compared among the three groups using analysis of covariance (ANCOVA) with *post hoc* least significant difference tests. Within each group, the

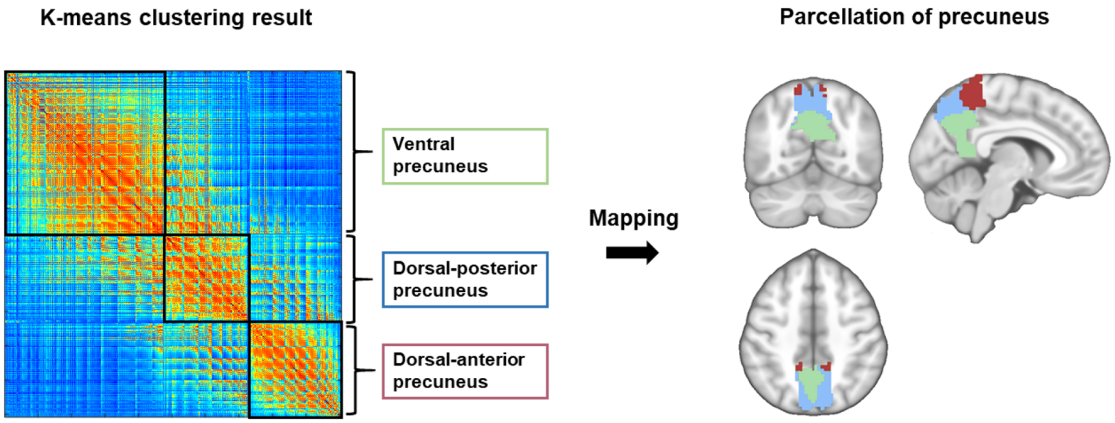

FIGURE 1 | Functional parcellation of the precuneus. Using the K-means clustering algorithm, the precuneus was subdivided into the dorsal anterior (red), dorsal posterior (blue) and ventral (green) subregions based on its intra-regional functional connectivity.

mean FCS and FDG-SUVR were compared among the three subregions using repeated measures ANOVA with *post hoc* least significant difference tests. The three-sigma rule (three standard deviations) was applied to detect outliers. Multiple comparisons were corrected using Bonferroni corrections with an alpha threshold of 0.008 (i.e., 0.05/6, two imaging markers in three subregions) as statistically significant. Standardized z-scores of both FCS and FDG-SUVR were calculated so that they can be averaged across subjects. Spearman's correlation analyses were then performed across voxels to explore the correlations between FCS and FDG-SUVR in the whole precuneus and its subregions. Finally, partial Pearson's correlation analyses were performed to explore associations the FCS and FDG-SUVR of the whole precuneus and its subregions with MMSE scores in all three subject groups. Age, gender, and education level of each subject were controlled for the above ANCOVA and partial correlation analyses.

RESULTS

The demographic and clinical results of all participants are listed in **Table 1**. No significant difference was found in age, gender or education among the CN, MCI, and AD groups ($p \geq 0.183$ for all occasions). Significantly decreased MMSE scores were found in AD patients compared to the MCI ($p < 0.001$) and CN ($p < 0.001$) groups, and in the MCI group compared to the CN group ($p = 0.009$).

Functional parcellation of the precuneus based on the K-means clustering algorithm is illustrated in **Figure 1**. The precuneus was functionally divided into the dorsal anterior (DA_pcu), dorsal posterior (DP_pcu), and ventral (V_pcu) subregions. In order to show the variation of functional subregions of the precuneus among different subjects, we performed functional parcellations for each CN subject and calculated the overlap ratios between each individual parcellation and the group parcellation results. On average, the overlap ratios (mean ± SD) for DA_pcu, DP_pcu, and V_pcu were 73% ± 11.1%, 61.2% ± 15.1%, and 70.9% ± 14.0%, respectively. Moreover, we performed functional parcellations for the MCI and AD groups to show that the subregions did not vary substantially across groups (see **Supplementary Figure 1**).

Within the precuneus, maps of the FCS and FDG-SUVR both showed visually perceptible decreases in patients with MCI and AD, as shown in **Figure 2A**. The FCS of the whole precuneus and its subregions in the CN, MCI, and AD groups were displayed in **Figure 2B**. Specifically, the FCS of the whole precuneus showed a mild decrease in AD patients compared to CN subjects ($p = 0.047$). Looking into each subregion, we found that the FCS had significant decreases in V_pcu of AD patients ($p = 0.008$) and MCI patients ($p = 0.006$) compared to the CN subjects. Decreases in DP_pcu FCS were found in AD patients compared to the MCI ($p = 0.011$) and CN ($p = 0.073$, marginal difference) groups, and no changes were shown in the DA_pcu subregion. Glucose metabolism, estimated by FDG-SUVR, exhibited a similar pattern as FCS. As displayed in **Figure 2C**, significantly decreased SUVR of the entire precuneus was observed in the AD patients compared to the CN group ($p = 0.006$). In V_pcu, hypometabolism were found in the AD patients compared to both the CN ($p < 0.001$) and MCI ($p = 0.045$) groups, and in MCI patients compared to the CN group ($p = 0.059$, marginal difference). In DP_pcu, mild decreases were found in the AD patients compared to the CN subjects ($p = 0.038$) and MCI patients ($p = 0.073$, marginal difference). Finally, in DA_pcu, no significant changes were observed among the three subject groups. The quantitative values for both FCS and SUVR of all three groups are listed in **Supplementary Table 1**. Non-significant increases in the mean FCS and FDG-SUVR were observed in both DA_pcu and DP_pcu in the MCI group compared to the CN group.

We next investigated the associations between FCS and SUVR as well as between their reductions and cognitive decline in the whole and three subregions of the precuneus. As shown in **Figure 3**, V_pcu had the highest functional-metabolic correlation ($r = 0.707$, $p < 0.001$) within the precuneus. In addition, significant correlations between FCS and MMSE scores

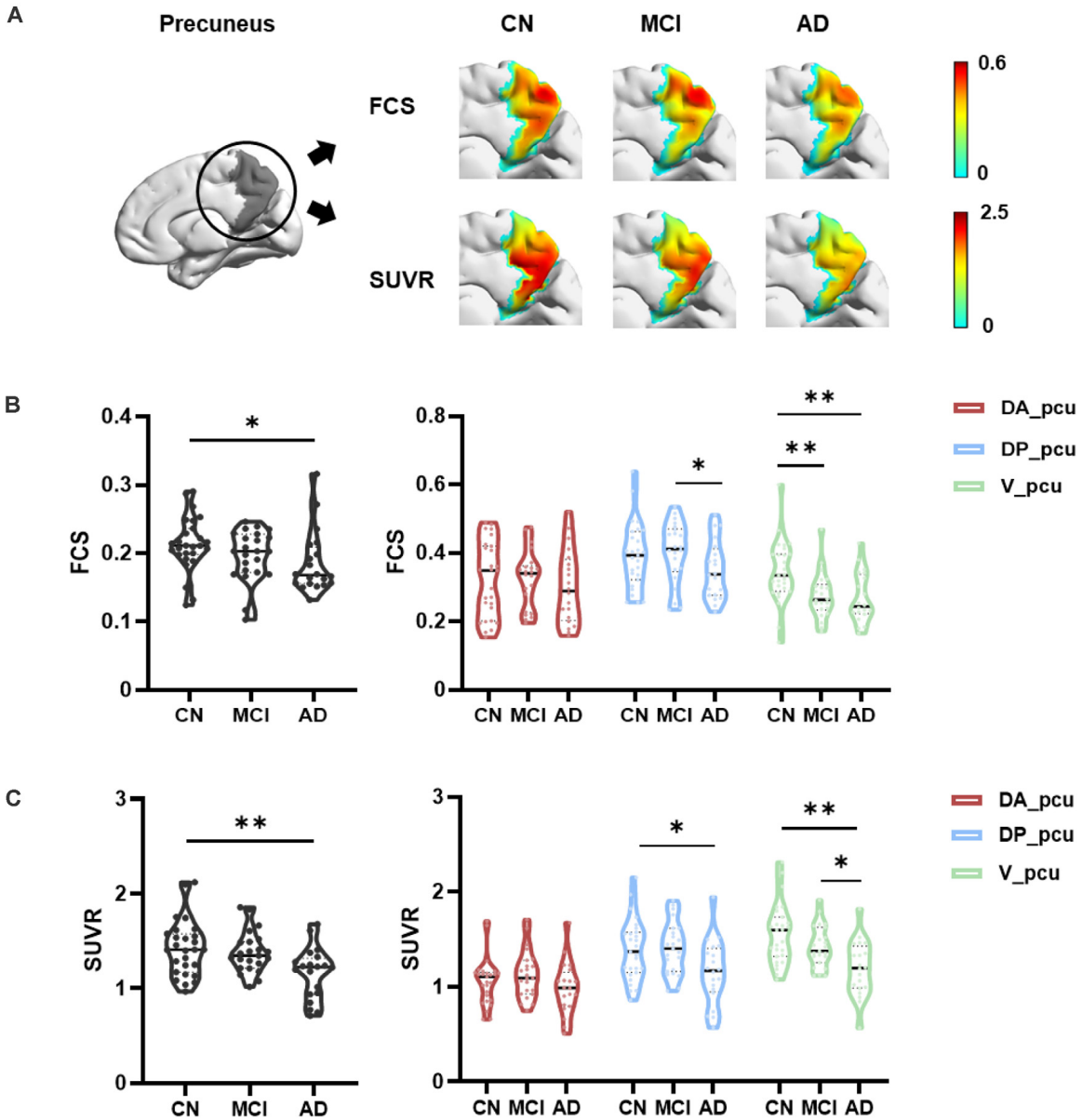

FIGURE 2 | Differences in the FCS and SUVR in the whole precuneus and its subregions between the CN, MCI, and AD groups. **(A)** Maps of both FCS ad SUVR within the precuneus decreased in patients. **(B)** For the whole precuneus, decreased FCS was observed in the AD patients compared to the CN group. For the subregions of the precuneus, decreased FCS was found in DP_pcu in AD patients compared to the MCI group, and in V_pcu in patients with AD and MCI compared to the CN group. No difference was observed in the FCS of DA_pcu among the three groups. **(C)** For the whole precuneus, decreased SUVR was observed in AD patients compared to the CN groups. For the subregions of the precuneus, decreased SUVR was found in DP_pcu of AD patients compared to the CN group, and in V_pcu of AD patients compared to both the MCI and CN groups. No difference in the SUVR of DA_pcu was observed among the three groups. Between-group differences were compared *via* ANCOVA with *post hoc* least significant difference tests and Bonferroni corrections. Age, gender, and education were considered as covariates. *$p < 0.05$, uncorrected; **$p < 0.05$, Bonferroni corrected. Abbreviations: FSC, functional connectivity strength; SUVR, standard uptake value ratio; CN, cognitively normal; MCI, mild cognitive impairment; AD, Alzheimer's Disease; V_pcu, ventral precuneus; DP_pcu, dorsal posterior precuneus; DA_pcu, dorsal anterior precuneus; ANCOVA, analysis of covariance.

(r = 0.498, p = 0.042) and between SUVR and MMSE scores (r = 0.566, p = 0.018) were found in V_pcu only, as displayed in **Figure 4** and **Table 2**. None of the other two subregions, or the whole precuneus, displayed significant correlations with cognitive declines.

As displayed in **Figure 5**, we observed that the significant difference in the FCS between DP_pcu and DA_pcu that existed in the CN and MCI groups disappeared in AD patients. Similarly, the significant difference in the glucose metabolism between DP_pcu and V_pcu that was in the

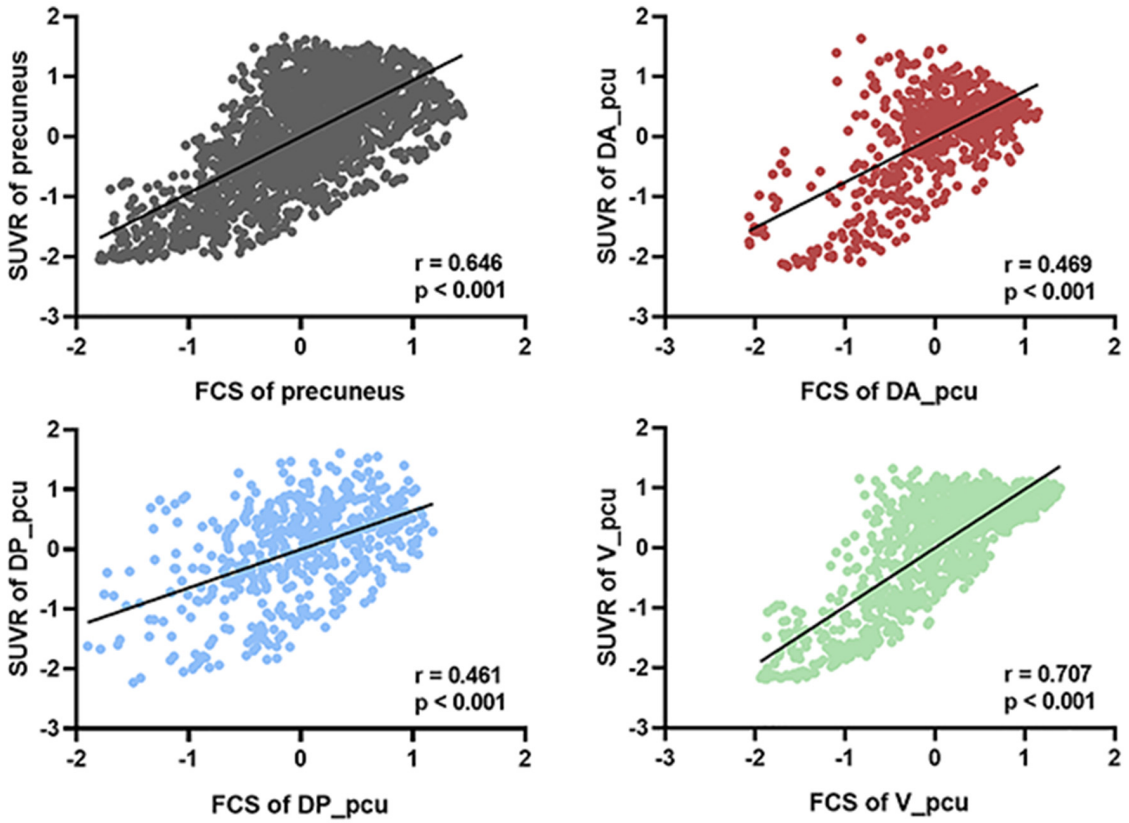

FIGURE 3 | Voxel-based correlations between FCS and SUVR in the whole precuneus and its subregions. V_pcu (green) had the highest functional-metabolic correlation compared to the precuneus and other subregions. For each voxel, standardized z-scores of both FCS and SUVR were averaged across all subjects (N = 70). Spearmen's correlation was performed between the two metrics across the voxels of the precuneus and each subregion. Abbreviations: FSC, functional connectivity strength; SUVR, standard uptake value ratio; V_pcu, ventral precuneus.

CN subjects gradually decayed in patient groups, with the overall ANOVA test yielding an insignificant main effect of subregion in the AD patients (p = 0.087). These observations indicated a progressive loss of both functional and metabolic distinctiveness among the three subregions affected by AD. Note that **Figures 2**, **5** are based on different methods of statistical analysis (i.e., ANCOVA with independent groups vs. ANOVA with repeated measures). In addition, **Figure 2** reflects the characteristics of selective vulnerability of the subregions, whereas **Figure 5** shows functional dedifferentiation within the precuneus in MCI and AD.

Finally, to investigate whether the results are dependent on the atlas used, we performed functional parcellation based on the precuneus defined by the Harvard-Oxford atlas (Desikan et al., 2006). As displayed in **Supplementary Figure 2A**, the precuneus was subdivided into four subregions, namely DA_pcu_HO, DP_pcu_HO, V_pcu_HO, and VP_pcu_HO. Among them, the first three subregions were similar as those defined by the AAL atlas. The additional VP_pcu_HO located at the posterior rim of the precuneus that was included by the HO atlas but not by the AAL atlas. Results of the statistical analysis are shown in **Supplementary Figure 2B**. The disruption patterns for both FCS and SUVR in DA_pcu_HO, DP_pcu_HO, and V_pcu_HO resemble those observed based on the AAL atlas. Specifically, V_pcu_HO was the earliest and most affected subregion. DP_pcu_HO was disrupted in AD patients whereas DA_pcu_HO did not exhibit significant changes. For VP_pcu_HO, a decrease in the SUVR in the AD group and no significant change in the FCS were observed. Overall, the functionally parcellated regions in our study could be consistently identified using different atlases, if the number of regions were appropriately selected. The main findings of the current study appear to be robust across different initial definitions of the precuneus.

DISCUSSION

In this study, a hybrid resting-state fMRI/FDG PET technique was employed to investigate the FCS and glucose metabolism in the precuneus and its subregions in groups of age- and education-matched healthy controls and patients with MCI and AD. Our results revealed a gradually disrupted pattern from the ventral precuneus in patients with MCI to dorsal precuneus in patients with AD. In particular, the ventral precuneus was the earliest affected subregion and its compromised FCS and

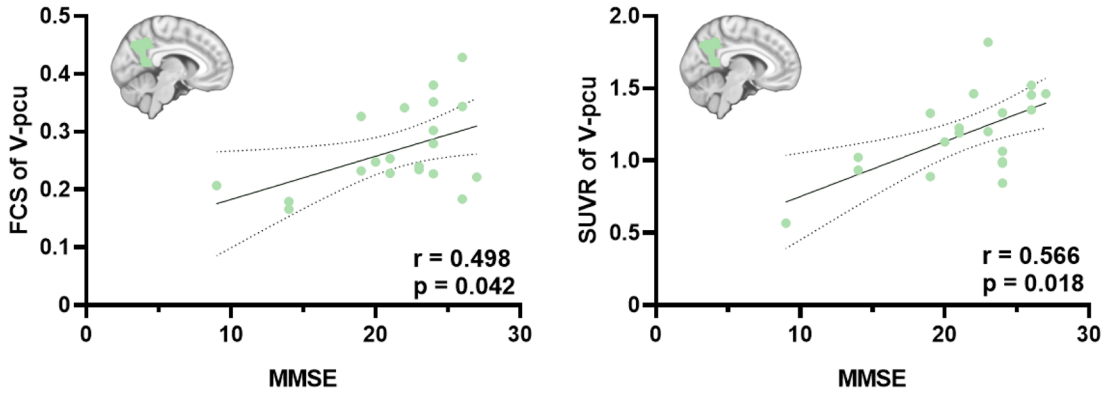

FIGURE 4 | Significant correlations between FCS and MMSE scores and between SUVR and MMSE scores in the V_pcu of AD patients. Partial Pearson's correlations were performed with age, gender and education were considered as covariates. Abbreviations: FSC, functional connectivity strength; SUVR, standard uptake value ratio; AD, Alzheimer's Disease; V_pcu, ventral precuneus; MMSE, Mini-Mental State Examination.

glucose metabolism were associated with cognitive decline of AD patients.

The precuneus has been considered as a typical cortical hub region that not only is involved in complex and specialized cognitive functions but also plays a pivotal role in the inter-regional mediation of the brain. It is preferentially attacked by amyloid plaques (Buckner et al., 2009) and has drawn extensive attentions in AD-related studies. Previous evidences and this study (**Figure 2**) consistently found that the precuneus suffered disrupted functional integrity and glucose metabolism in patients with AD. Specifically, abnormal functional integrity measured by significantly reduced local and global FC (Greicius et al., 2004; Drzezga et al., 2011; Damoiseaux et al., 2012; Dai et al., 2015) as well as the amplitude of low-frequency fluctuations (ALFF) and regional homogeneity (ReHo) of the BOLD signal (He et al., 2007; Hafkemeijer et al., 2012; Liu et al., 2014; Marchitelli et al., 2018) has been observed in patients with AD compared to CN subjects. In addition, as a reflection of synaptic dysfunction, glucose hypometabolism in the precuneus of AD patients has been repetitively reported by FDG PET studies (Del Sole et al., 2008; Ye et al., 2020). In patients with MCI, decreased functional activity (e.g., FC between nodes of the DMN, ReHo and ALFF of the precuneus) was reported in most fMRI studies (Hafkemeijer et al., 2012; Xue et al., 2019). This study observed a non-significant decrease of FCS in MCI compared to CN groups, which may be due to the different biomarker (i.e., FCS) applied. The FCS represents the average FC between a given voxel and all voxels of the region of interest (Liang et al., 2013; Dai et al., 2015). The averaging process may decrease the sensitivity but increase the robustness in the evaluation of functional changes compared to other functional metrics. In addition, hypometabolism in the precuneus has been reported in MCI patients with increased risks of AD, which was suggested as a predictor for AD conversion (Mosconi, 2005; Mosconi et al., 2008; Bailly et al., 2015; He et al., 2015; Kato et al., 2016; Baucknehet et al., 2018; Ma et al., 2018). In our data, a nonsignificant decreasing pattern of the FDG-SUVR from CN to MCI was observed in **Figure 2** and **Supplementary Table 1**. One possible reason behind this discrepancy may be a relatively older age (∼70 years) of our MCI group (Kato et al., 2016.) suggested that more severe hypometabolism in the precuneus and PCC regions can be observed in early onset-AD (onset <65 years) compared to late onset AD (onset >65 years). Going along with our study, Nobili et al. (2008) did not find significant hypometabolism in the parietal cortex including precuneus in a group of MCI patients with a mean age of 75 years. Another reason may be attributed to the heterogeneity of the MCI population. Patients with MCI may exhibit different FDG PET patterns and develop different types of dementia. For example, the FDG PET pattern of frontotemporal dementia (FTD) does not include significant hypometabolism in the precuneus (Kato et al., 2016). In a group of 45 patients with MCI, Cerami et al., 2015) reported that 14 of them did not exhibit cortical hypometabolism, and six of them (five with behavioral variant of FTD-like and 1 with semantic variant of primary progressive aphasia-like patterns) did not show hypometabolism in the precuneus. We did not exclusively recruit MCI patients with the amnestic subtype or positive amyloid deposition, which may result in the nonsignificant hypometabolism in the precuneus. Therefore, explanations of the MCI-related findings in our study should be restricted to the aspects of cognitive impairment and not be extended to prodromal AD.

Apart from its clinical significance to AD as a whole brain structure, the precuneus has been widely recognized to be composed of anatomically and functionally heterogeneous subareas which could be differentially impacted by AD

TABLE 2 | Associations of MMSE with FCS and SUVR in AD patients.

	Precuneus	DA_pcu	DP_pcu	V_pcu
FCS	r = 0.304	r = 0.338	r = 0.032	***r = 0.498***
	p = 0.236	p = 0.185	p = 0.903	***p = 0.042***
SUVR	r = 0.415	r = 0.056	r = 0.287	***r = 0.566***
	p = 0.098	p = 0.831	p = 0.264	***p = 0.018***

Partial Pearson's correlation analyses were performed with age, gender, and education as covariates. Abbreviations: FSC, functional connectivity strength; SUVR, standard uptake value ratio; AD, Alzheimer's Disease; V_pcu, ventral precuneus; DP_pcu, dorsal posterior precuneus; DA_pcu, dorsal anterior precuneus; MMSE, Mini-Mental State Examination.

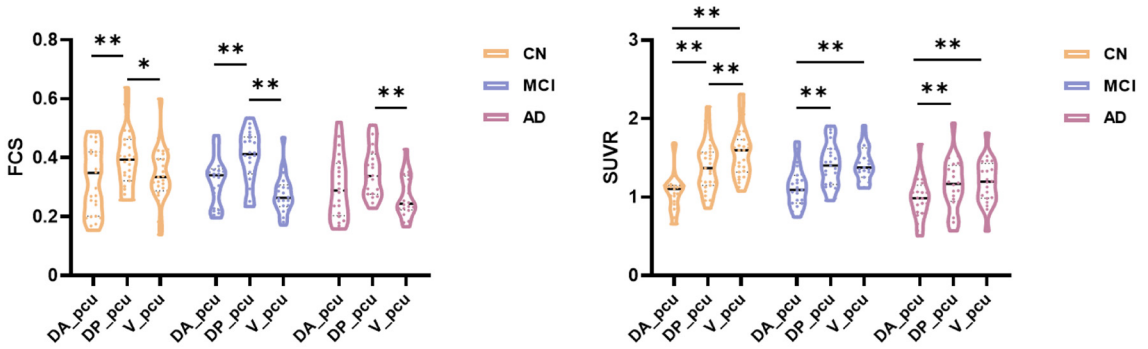

FIGURE 5 | Subregional dedifferentiation of the FCS and SUVR in MCI and AD. For FCS, the significant difference between DP_pcu and DA_pcu that existed in CN and MCI groups disappeared in the AD group. For SUVR, the significant difference between DP_pcu and V_pcu that existed in the CN subjects decayed in both MCI and AD patients. Additionally, the overall analysis of variance (ANOVA) test yielded an insignificant main effect of subregion for the SUVR in the AD patients ($p = 0.087$). Subregional differences were compared *via* ANOVA with *post hoc* paired *t*-tests and Bonferroni corrections. *$p < 0.05$, uncorrected; **$p < 0.05$, Bonferroni corrected. Abbreviations: FSC, functional connectivity strength; SUVR, standard uptake value ratio; CN, cognitively normal; MCI, mild cognitive impairment; AD, Alzheimer's Disease; V_pcu, ventral precuneus; DP_pcu, dorsal posterior precuneus; DA_pcu, dorsal anterior precuneus; ANOVA, analysis of variance.

(Khan et al., 2020). Originated from its cytoarchitecture (Cavanna and Trimble, 2006) and agreed by studies utilizing anatomical (Wang et al., 2019) and functional connectivities (Margulies et al., 2009; Ye et al., 2021) in both humans and macaques, three distinct subregions have been suggested, namely the dorsal-anterior, dorsal-posterior and ventral precuneus. Specifically, whereas DA_pcu and DP_pcu are majorly associated with sensorimotor and visual functions, V_pcu is involved in higher-order cognitive functions such as memory and self-related processing. Recently, finer sub-parcellation results (i.e., 4–6 parcels) have been proposed (Cauda et al., 2010; Zhang and Li, 2012; Zhang et al., 2014; Fan et al., 2016; Luo et al., 2020), which made delicate subdivisions of the precuneus remain an open question. In several occasions, however, these finer subregions were hieratically categorized into the ordinary three clusters (Zhang and Li, 2012; Xia et al., 2014; Luo et al., 2020) when analyzing the functional heterogeneity. Therefore, we went along with the three-subregion functional parcellation scheme generated by a K-means clustering algorithm based on the FC within the precuneus (Zhang and Li, 2012).

One of our major findings is that V_pcu was the earliest and most affected subregion by AD, compared to the whole and other subareas of the precuneus. From a functional perspective (**Figure 2A**), it was the only subregion which showed significantly decreased FCS in MCI compared to normal controls. Moreover, the FCS within V_pcu demonstrated a more sensitive biomarker (with more stringent p values) as compared to the whole precuneus in patients with AD. To the best of our knowledge, disrupted FCS within V_pcu (or any subregions of the precuneus), as a reflection of local intrinsic FC, has not been previously reported. Disrupted global FC between V_pcu and other brain regions has been consistently shown by studies investigating differential functional architecture of the subregions of the posteromedial cortex (PMC) affected by AD (Xia et al., 2014; Wu et al., 2016; Khan et al., 2020). Among them, Wu et al. (2016) reported that disruptions began in a transitional region between the posterior cingulate cortex (PCC) and precuneus, which has an overlap with the V_pcu in this study, in mild AD patients and then spread to other subregions of PMC as the disease became more severe. Our study extended this finding by showing that the disruption in the FCS of V_pcu could occur in the MCI stage. This observation may be partially due to the fact that local FC has less variability across subjects than global FC (Tomasi and Volkow, 2011) and thus is more sensitive to between-group effects. In future studies, it will be very interesting to explore the FC of precuneus subdivisions with other brain functional networks. For example, since the ventral precuneus has a considerable overlap and stronger connectivity with the DMN (Cauda et al., 2010; Zhang and Li, 2012), we speculated that the within-network disturbances of V_pcu would also reflect on its FC with further regions of the DMN. A preliminary comparison using our current data showed a significant decrease in the FC between V_pcu and DMN in patients with MCI ($p = 0.03$) and a trend of decrease in patients with AD. Further explorations with a larger sample size are in merit to investigate this. From a metabolic perspective (**Figure 2B**), significantly decreased glucose metabolism was observed in the V_pcu of AD patients compared to both MCI patients and normal controls. The precuneus and its surrounding areas are among the regions that bear the highest metabolic rates in healthy subjects (Cavanna and Trimble, 2006) and suffer excessive glucose hypometabolism relative to atrophy in AD patients (Chételat et al., 2008; Karow et al., 2010). Our results further demonstrated that such AD-related hypometabolism was not homogeneous in the precuneus, with impairments mostly occurred in V_pcu. By exploring the relationship between FCS and SUVR in subregions of the precuneus, we observed that V_pcu had the highest functional-metabolic correlation ($r = 0.707$, $p < 0.001$) within the precuneus (see **Figure 3**), suggesting a tight association between decreased FC and lower

neural activity in this subregion. Based on the connectivity degree-to-metabolism ratio, the ventral precuneus had even higher energy efficiency than cortical hubs (Tomasi et al., 2013). This connectivity-related high energy demand could render this subregion more vulnerable to Aβ deposition (Buckner et al., 2009; Drzezga et al., 2011; Khan et al., 2020) and might explain the sensitivity of V_pcu to neurodegeneration in patients with MCI and AD. In addition to the quantitative analysis applied in this study, metabolic connectivity (MC), a novel approach to measure interregional covariance of FDG PET (Lee et al., 2008; Shi et al., 2017, 2018), has received increasing attentions for differential diagnosis of dementing disorders (Shi et al., 2017; Titov et al., 2017). Specifically, reduced MCs in the precuneus and other regions have been reported in patients with prodromal AD (Morbelli et al., 2012), which has the potential to facilitate individual prediction of conversion from MCI to AD (Wang et al., 2020). Moreover, MC and FC may complement each other to reflect the coupling of energy utilization and neural synchronization in relative brain networks (Di and Biswal, 2012). In future work, MC can be applied to explore patterns of metabolic covariance in subregions of the precuneus and their disruptions with AD. Finally, the ventral precuneus participates in a spectrum of cognitive functions including self-reflective processing, such as self-awareness, and autobiographical/episodic memory retrieval, attention, language, emotion consciousness, etc. (Wang et al., 2019). As a result, disruptions in V_pcu were expected to be correlated with general cognitive decline in AD patients. Indeed, both decreased FCS and hypometabolism in V_pcu were better associated with the MMSE scores than the precuneus and its other subregions in AD patients (**Figure 4** and **Table 2**). Together, our observations demonstrated that V_pcu had a higher sensitivity in the detection of MCI patients from the healthy subjects and contributed to the cognitive-related neurodegeneration in AD patients.

The dorsal portion of the precuneus was generally less impaired than the ventral portion in this cross-sectional study, revealing a gradually degenerative pattern from ventral to dorsal precuneus. In patients with MCI, we observed non-significant increases in both FCS and glucose metabolism in the dorsal subregions (**Supplementary Table 1**), which may account for the absence of difference against the CN group. In line with this, previous work also showed increased connectivity and metabolism in patients with MCI, which claimed that additional neural resources might be in need to compensate for neurodegeneration and maintain cognitive performance, supporting the compensatory-recruitment hypothesis (Nobili et al., 2008; Hafkemeijer et al., 2012; Kato et al., 2016; Xue et al., 2019). In patients with AD, the FCS and glucose metabolism slightly decreased in DP_pcu and maintained relatively intact in DA_pcu (**Figure 2**). The DP_pcu locates in a bridge area between V_pcu and DA_pcu and may play a transitional role in the spread of AD-related disruptions across the precuneus. Functionally, it strongly interacts with adjacent vision-related areas (Zhang and Li, 2012; Zhang et al., 2014) and connects to several components of the DMN (Xia et al., 2014). The DA_pcu, however, primarily connects to adjacent sensorimotor-related areas. Likely due to its positioning at the superior end of the progressive FC shifts in the precuneus (Cauda et al., 2010) and its less involvements in cognitive-related functions (Zhang and Li, 2012), the DA_pcu stayed rather functionally and metabolically conserved in AD patients. Going along with our findings, Marchitelli et al. (2018) reported that both glucose metabolism and ReHo decreased in a combined area of V_pcu and DP_pcu but not DA_pcu in a group of patients with AD or amnestic MCI compared to control subjects. For the global FC of the DP_pcu and DA_pcu with other brain regions, however, previous studies did not reach a consensus and reported both decreased or unchanged results (Xia et al., 2014; Wu et al., 2016; Khan et al., 2020). This discrepancy among existing evidences, in our opinion, reflects the expanding of progressive disruptions from ventral to dorsal precuneus in different cohorts of AD patients at a later stage. Additionally, we reported that differences in the FCS and glucose metabolism between DP_pcu and DA_pcu and between DP_pcu and V_pcu, respectively, which existed in CN subjects, diminished in patient groups (**Figure 5**). This observation indicated a dedifferentiation among the subregions of the precuneus in patients with MCI and AD.

This study has limitations. We recruited a modest sample size. In addition, there is a lack of information about the Aβ and tau status of the individuals or their precise protein pathology in the precuneus and its subregions. Regarding the MCI group, we did not explicitly include the amnestic subtype or evaluate their APOE status. Therefore, cautions should be used in relating the MCI-related results of this study to prodromal AD. Future studies are needed to validate our results with larger samples of patients with preclinical and prodromal AD.

In conclusion, this study evidenced heterogeneous susceptibilities of precuneus subregions to both functional and metabolic disruptions in patients with MCI and AD. A disruption pattern from ventral to dorsal precuneus, with V_pcu and DA_pcu being the most and least affected subregion, respectively, was shown.

DATA AVAILABILITY STATEMENT

Anonymized data are available upon collaborative requests. Further inquiries can be directed to the corresponding authors.

ETHICS STATEMENT

The studies involving human participants were reviewed and approved by Institutional Review Board of Ruijin Hospital. The patients/participants provided their written informed consent to participate in this study.

AUTHOR CONTRIBUTIONS

YL, MZ, YZ, and BiaoL conceived and designed the study. MZ, BinyinL, GY, HM, XH, XL, JW, JL, and BiaoL recruited subjects and acquired the data. MZ, WS, ZG, JH, YZ, and YL analyzed the

data and interpreted the results. YZ, WS, MZ, and YL drafted the manuscript. All authors contributed to the article and approved the submitted version.

FUNDING

This work was supported by New Faculty Start-up Foundation of Shanghai Jiao Tong University (21X010500734), Key Program of Multidisciplinary Cross Research Foundation of Shanghai Jiao Tong University (YG2021QN40, YG2021ZD28), the National Natural Science Foundation of China (81871083), Shanghai Jiao Tong University Scientific and Technological Innovation Funds (2019QYA12), and Shanghai Municipal Key Clinical Specialty (shslczdzk03403).

SUPPLEMENTARY MATERIALS

The Supplementary Material for this article can be found online at: https://www.frontiersin.org/articles/10.3389/fnagi.2021.737002/full#supplementary-material.

REFERENCES

Bailly, M., Destrieux, C., Hommet, C., Mondon, K., Cottier, J. P., Beaufils, E., et al. (2015). Precuneus and cingulate cortex atrophy and hypometabolism in patients with Alzheimer's disease and mild cognitive impairment: MRI and (18)F-FDG PET quantitative analysis using FreeSurfer. *Biomed. Res. Int.* 2015:583931. doi: 10.1155/2015/583931

Bauckneht, M., Chincarini, A., Piva, R., Arnaldi, D., Girtler, N., Massa, F., et al. (2018). Metabolic correlates of reserve and resilience in MCI due to Alzheimer's disease (AD). *Alzheimers Res. Ther.* 10:35. doi: 10.1186/s13195-018-0366-y

Buckner, R. L., Sepulcre, J., Talukdar, T., Krienen, F. M., Liu, H., Hedden, T., et al. (2009). Cortical hubs revealed by intrinsic functional connectivity: mapping, assessment of stability, and relation to Alzheimer's disease. *J. Neurosci.* 29, 1860–1873. doi: 10.1523/JNEUROSCI.5062-08.2009

Cauda, F., Geminiani, G., D'Agata, F., Sacco, K., Duca, S., Bagshaw, A. P., et al. (2010). Functional connectivity of the posteromedial cortex. *PLoS One* 5:e13107. doi: 10.1371/journal.pone.0013107

Cavanna, A. E., and Trimble, M. R. (2006). The precuneus: a review of its functional anatomy and behavioural correlates. *Brain* 129, 564–583. doi: 10.1093/brain/awl004

Cecchin, D., Palombit, A., Castellaro, M., Silvestri, E., Bui, F., Barthel, H., et al. (2017). Brain PET and functional MRI: why simultaneously using hybrid PET/MR systems? *Q. J. Nucl. Med. Mol. Imaging* 61, 345–359. doi: 10.23736/S1824-4785.17.03008-4

Cerami, C., Della Rosa, P. A., Magnani, G., Santangelo, R., Marcone, A., Cappa, S. F., et al. (2015). Brain metabolic maps in mild cognitive impairment predict heterogeneity of progression to dementia. *Neuroimage Clin.* 7, 187–194. doi: 10.1016/j.nicl.2014.12.004

Chételat, G., Desgranges, B., Landeau, B., Mézenge, F., Poline, J. B., de la Sayette, V., et al. (2008). Direct voxel-based comparison between grey matter hypometabolism and atrophy in Alzheimer's disease. *Brain* 131, 60–71. doi: 10.1093/brain/awm288

Cox, R. W. (1996). AFNI: software for analysis and visualization of functional magnetic resonance neuroimages. *Comput. Biomed. Res.* 29, 162–173. doi: 10.1006/cbmr.1996.0014

Dai, Z., Yan, C., Li, K., Wang, Z., Wang, J., Cao, M., et al. (2015). Identifying and mapping connectivity patterns of brain network hubs in Alzheimer's disease. *Cereb. Cortex* 25, 3723–3742. doi: 10.1093/cercor/bhu246

Damoiseaux, J. S., Prater, K. E., Miller, B. L., and Greicius, M. D. (2012). Functional connectivity tracks clinical deterioration in Alzheimer's disease. *Neurobiol. Aging* 33, 828.e19–828.e30. doi: 10.1016/j.neurobiolaging.2011.06.024

Del Sole, A., Clerici, F., Chiti, A., Lecchi, M., Mariani, C., Maggiore, L., et al. (2008). Individual cerebral metabolic deficits in Alzheimer's disease and amnestic mild cognitive impairment: an FDG PET study. *Eur. J. Nucl. Med. Mol. Imaging* 35, 1357–1366. doi: 10.1007/s00259-008-0773-6

Desikan, R. S., Ségonne, F., Fischl, B., Quinn, B. T., Dickerson, B. C., Blacker, D., et al. (2006). An automated labeling system for subdividing the human cerebral cortex on MRI scans into gyral based regions of interest. *NeuroImage* 31, 968–980. doi: 10.1016/j.neuroimage.2006.01.021

Di, X., Biswal, B. B., and Alzheimer's Disease Neuroimaging Initiative. (2012). Metabolic brain covariant networks as revealed by FDG-PET with reference to resting-state fMRI networks. *Brain Connect.* 2, 275–283. doi: 10.1089/brain.2012.0086

Drzezga, A. (2018). The network degeneration hypothesis: spread of neurodegenerative patterns along neuronal brain networks. *J. Nucl. Med.* 59, 1645–1648. doi: 10.2967/jnumed.117.206300

Drzezga, A., Becker, J. A., Van Dijk, K. R., Sreenivasan, A., Talukdar, T., Sullivan, C., et al. (2011). Neuronal dysfunction and disconnection of cortical hubs in non-demented subjects with elevated amyloid burden. *Brain* 134, 1635–1646. doi: 10.1093/brain/awr066

Fan, L., Li, H., Zhuo, J., Zhang, Y., Wang, J., Chen, L., et al. (2016). The human brainnetome atlas: a new brain atlas based on connectional architecture. *Cereb. Cortex* 26, 3508–3526. doi: 10.1093/cercor/bhw157

Gonzalez-Escamilla, G., Lange, C., Teipel, S., Buchert, R., Grothe, M. J., and Alzheimer's Disease Neuroimaging, I. (2017). PETPVE12: an SPM toolbox for partial volume effects correction in brain PET—application to amyloid imaging with AV45-PET. *NeuroImage* 147, 669–677. doi: 10.1016/j.neuroimage.2016.12.077

Greicius, M. D., Srivastava, G., Reiss, A. L., and Menon, V. (2004). Default-mode network activity distinguishes Alzheimer's disease from healthy aging: evidence from functional MRI. *Proc. Natl. Acad. Sci. U S A* 101:4637. doi: 10.1073/pnas.0308627101

Hafkemeijer, A., van der Grond, J., and Rombouts, S. A. (2012). Imaging the default mode network in aging and dementia. *Biochim. Biophys. Acta* 1822, 431–441. doi: 10.1016/j.bbadis.2011.07.008

He, W., Liu, D., Radua, J., Li, G., Han, B., and Sun, Z. (2015). Meta-analytic comparison between PIB-PET and FDG-PET results in Alzheimer's disease and MCI. *Cell Biochem. Biophys.* 71, 17–26. doi: 10.1007/s12013-014-0138-7

He, Y., Wang, L., Zang, Y., Tian, L., Zhang, X., Li, K., et al. (2007). Regional coherence changes in the early stages of Alzheimer's disease: a combined structural and resting-state functional MRI study. *NeuroImage* 35, 488–500. doi: 10.1016/j.neuroimage.2006.11.042

Kahnt, T., Chang, L. J., Park, S. Q., Heinzle, J., and Haynes, J. D. (2012). Connectivity-based parcellation of the human orbitofrontal cortex. *J. Neurosci.* 32, 6240–6250. doi: 10.1523/JNEUROSCI.0257-12.2012

Kahnt, T., and Tobler, P. N. (2017). Dopamine modulates the functional organization of the orbitofrontal cortex. *J. Neurosci.* 37, 1493–1504. doi: 10.1523/JNEUROSCI.2827-16.2016

Kapogiannis, D., and Mattson, M. P. (2011). Disrupted energy metabolism and neuronal circuit dysfunction in cognitive impairment and Alzheimer's disease. *Lancet Neurol.* 10, 187–198. doi: 10.1016/S1474-4422(10)70277-5

Karow, D. S., McEvoy, L. K., Fennema-Notestine, C., Hagler, D. J., Jennings, R. G., Brewer, J. B., et al. (2010). Relative capability of MR imaging and FDG PET to depict changes associated with prodromal and early Alzheimer disease. *Radiology* 256, 932–942. doi: 10.1148/radiol.10091402

Kato, T., Inui, Y., Nakamura, A., and Ito, K. (2016). Brain fluorodeoxyglucose (FDG) PET in dementia. *Ageing Res. Rev.* 30, 73–84. doi: 10.1016/j.arr.2016.02.003

Khan, W., Amad, A., Giampietro, V., Werden, E., De Simoni, S., O'Muircheartaigh, J., et al. (2020). The heterogeneous functional architecture of the posteromedial cortex is associated with selective functional connectivity differences in Alzheimer's disease. *Hum. Brain Mapp.* 41, 1557–1572. doi: 10.1002/hbm.24894

Lee, D. S., Kang, H., Kim, H., Park, H., Oh, J. S., Lee, J. S., et al. (2008). Metabolic connectivity by interregional correlation analysis using statistical parametric mapping (SPM) and FDG brain PET; methodological development

and patterns of metabolic connectivity in adults. *Eur. J. Nucl. Med. Mol. Imaging* 35, 1681–1691. doi: 10.1007/s00259-008-0808-z

Liang, X., Zou, Q., He, Y., and Yang, Y. (2013). Coupling of functional connectivity and regional cerebral blood flow reveals a physiological basis for network hubs of the human brain. *Proc. Natl. Acad. Sci. U S A* 110, 1929–1934. doi: 10.1073/pnas.1214900110

Liu, Y., Yu, C., Zhang, X., Liu, J., Duan, Y., Alexander-Bloch, A. F., et al. (2014). Impaired long distance functional connectivity and weighted network architecture in Alzheimer's disease. *Cereb. Cortex* 24, 1422–1435. doi: 10.1093/cercor/bhs410

Luo, Z., Zeng, L.-L., Qin, J., Hou, C., Shen, H., and Hu, D. (2020). Functional parcellation of human brain precuneus using density-based clustering. *Cereb. Cortex* 30, 269–282. doi: 10.1093/cercor/bhz086

Ma, H. R., Sheng, L. Q., Pan, P. L., Wang, G. D., Luo, R., Shi, H. C., et al. (2018). Cerebral glucose metabolic prediction from amnestic mild cognitive impairment to Alzheimer's dementia: a meta-analysis. *Transl. Neurodegener.* 7:9. doi: 10.1186/s40035-018-0114-z

Marchitelli, R., Aiello, M., Cachia, A., Quarantelli, M., Cavaliere, C., Postiglione, A., et al. (2018). Simultaneous resting-state FDG-PET/fMRI in Alzheimer disease: relationship between glucose metabolism and intrinsic activity. *NeuroImage* 176, 246–258. doi: 10.1016/j.neuroimage.2018.04.048

Margulies, D. S., Vincent, J. L., Kelly, C., Lohmann, G., Uddin, L. Q., Biswal, B. B., et al. (2009). Precuneus shares intrinsic functional architecture in humans and monkeys. *Proc. Natl. Acad. Sci. U S A* 106, 20069–20074. doi: 10.1073/pnas.0905314106

Morbelli, S., Drzezga, A., Perneczky, R., Frisoni, G. B., Caroli, A., van Berckel, B. N. M., et al. (2012). Resting metabolic connectivity in prodromal Alzheimer's disease. A European Alzheimer disease consortium (EADC) project. *Neurobiol. Aging* 33, 2533–2550. doi: 10.1016/j.neurobiolaging.2012.01.005

Mosconi, L. (2005). Brain glucose metabolism in the early and specific diagnosis of Alzheimer's disease. FDG-PET studies in MCI and AD. *Eur. J. Nucl. Med. Mol. Imaging* 32, 486–510. doi: 10.1007/s00259-005-1762-7

Mosconi, L., Tsui, W. H., Herholz, K., Pupi, A., Drzezga, A., Lucignani, G., et al. (2008). Multicenter standardized 18F-FDG PET diagnosis of mild cognitive impairment, Alzheimer's disease, and other dementias. *J. Nucl. Med.* 49, 390–398. doi: 10.2967/jnumed.107.045385

Müller-Gärtner, H. W., Links, J. M., Prince, J. L., Bryan, R. N., McVeigh, E., Leal, J. P., et al. (1992). Measurement of radiotracer concentration in brain gray matter using positron emission tomography: MRI-based correction for partial volume effects. *J. Cereb. Blood Flow Metab.* 12, 571–583. doi: 10.1038/jcbfm.1992.81

Mutlu, J., Landeau, B., Gaubert, M., de La Sayette, V., Desgranges, B., and Chetelat, G. (2017). Distinct influence of specific versus global connectivity on the different Alzheimer's disease biomarkers. *Brain* 140, 3317–3328. doi: 10.1093/brain/awx279

Nobili, F., Salmaso, D., Morbelli, S., Girtler, N., Piccardo, A., Brugnolo, A., et al. (2008). Principal component analysis of FDG PET in amnestic MCI. *Eur. J. Nucl. Med. Mol. Imaging* 35, 2191–2202. doi: 10.1007/s00259-008-0869-z

Pascoal, T. A., Mathotaarachchi, S., Kang, M. S., Mohaddes, S., Shin, M., Park, A. Y., et al. (2019). Aβ-induced vulnerability propagates *via* the brain's default mode network. *Nat. Commun.* 10:2353. doi: 10.1038/s41467-019-10217-w

Shi, K., Savio, A., Grimmer, T., and Yakushev, I. (2018). Overlap between metabolic and other measures of brain connectivity: a multimodal imaging study. *J. Nucl. Med.* 59, 504–504. Available online at: https://jnm.snmjournals.org/content/59/supplement_1/504.

Shi, K., Schutte, M., Grimmer, T., Savio, A., Schultz, T., Diehl-schmid, J., et al. (2017). Structure-weighted metabolic connectivity for differential diagnosis of dementing disorders. *J. Nucl. Med.* 58, 290–290. Available online at: https://jnm.snmjournals.org/content/58/supplement_1/290.

Shokri-Kojori, E., Tomasi, D., Alipanahi, B., Wiers, C. E., Wang, G. J., and Volkow, N. D. (2019). Correspondence between cerebral glucose metabolism and BOLD reveals relative power and cost in human brain. *Nat. Commun.* 10:690. doi: 10.1038/s41467-019-08546-x

Titov, D., Diehl-Schmid, J., Shi, K., Perneczky, R., Zou, N., Grimmer, T., et al. (2017). Metabolic connectivity for differential diagnosis of dementing disorders. *J. Cereb. Blood Flow Metab.* 37, 252–262. doi: 10.1177/0271678X15622465

Tomasi, D., and Volkow, N. D. (2011). Functional connectivity hubs in the human brain. *NeuroImage* 57, 908–917. doi: 10.1016/j.neuroimage.2011.05.024

Tomasi, D., Wang, G.-J., and Volkow, N. D. (2013). Energetic cost of brain functional connectivity. *Proc. Natl. Acad. Sci. U S A* 110, 13642–13647. doi: 10.1073/pnas.1303346110

Tou, J. T., and Gonzalez, R. C. (1974). *Pattern Recognition Principles.* Cambridge, MA: Addison-Wesley Publishing Company.

Tzourio-Mazoyer, N., Landeau, B., Papathanassiou, D., Crivello, F., Etard, O., Delcroix, N., et al. (2002). Automated anatomical labeling of activations in SPM using a macroscopic anatomical parcellation of the MNI MRI single-subject brain. *NeuroImage* 15, 273–289. doi: 10.1006/nimg.2001.0978

Waites, A. B., Stanislavsky, A., Abbott, D. F., and Jackson, G. D. (2005). Effect of prior cognitive state on resting state networks measured with functional connectivity. *Hum. Brain Mapp.* 24, 59–68. doi: 10.1002/hbm.20069

Wang, J., Becker, B., Wang, L., Li, H., Zhao, X., and Jiang, T. (2019). Corresponding anatomical and coactivation architecture of the human precuneus showing similar connectivity patterns with macaques. *NeuroImage* 200, 562–574. doi: 10.1016/j.neuroimage.2019.07.001

Wang, M., Jiang, J., Yan, Z., Alberts, I., Ge, J., Zhang, H., et al. (2020). Individual brain metabolic connectome indicator based on Kullback-Leibler Divergence Similarity Estimation predicts progression from mild cognitive impairment to Alzheimer's dementia. *Eur. J. Nucl. Med. Mol. Imaging* 47, 2753–2764. doi: 10.1007/s00259-020-04814-x

Wu, Y., Zhang, Y., Liu, Y., Liu, J., Duan, Y., Wei, X., et al. (2016). Distinct changes in functional connectivity in posteromedial cortex subregions during the progress of Alzheimer's disease. *Front. Neuroanat.* 10:41. doi: 10.3389/fnana.2016.00041

Xia, M., Wang, Z., Dai, Z., Liang, X., Song, H., Shu, N., et al. (2014). Differentially disrupted functional connectivity in posteromedial cortical subregions in Alzheimer's disease. *J. Alzheimers Dis.* 39, 527–543. doi: 10.3233/JAD-131583

Xue, J., Guo, H., Gao, Y., Wang, X., Cui, H., Chen, Z., et al. (2019). Altered directed functional connectivity of the hippocampus in mild cognitive impairment and Alzheimer's disease: a resting-state fMRI study. *Front. Aging Neurosci.* 11:326. doi: 10.3389/fnagi.2019.00326

Ye, B. S., Lee, S., Yoo, H., Chung, S. J., Lee, Y. H., Choi, Y., et al. (2020). Distinguishing between dementia with Lewy bodies and Alzheimer's disease using metabolic patterns. *Neurobiol. Aging* 87, 11–17. doi: 10.1016/j.neurobiolaging.2019.10.020

Ye, Q., Zhang, Z., Sun, W., Fan, Q., and Li, Y. (2021). Disrupted functional connectivity of precuneus subregions in obsessive-compulsive disorder. *Neuroimage Clin.* 31:102720. doi: 10.1016/j.nicl.2021.102720

Zhang, Y., Fan, L., Zhang, Y., Wang, J., Zhu, M., Zhang, Y., et al. (2014). Connectivity-based parcellation of the human posteromedial cortex. *Cereb. Cortex* 24, 719–727. doi: 10.1093/cercor/bhs353

Zhang, S., and Li, C.-S. (2012). Functional connectivity mapping of the human precuneus by resting state fMRI. *NeuroImage* 59, 3548–3562. doi: 10.1016/j.neuroimage.2011.11.023

Conflict of Interest: The authors declare that the research was conducted in the absence of any commercial or financial relationships that could be construed as a potential conflict of interest.

Publisher's Note: All claims expressed in this article are solely those of the authors and do not necessarily represent those of their affiliated organizations, or those of the publisher, the editors and the reviewers. Any product that may be evaluated in this article, or claim that may be made by its manufacturer, is not guaranteed or endorsed by the publisher.

frontiers in Aging Neuroscience

ORIGINAL RESEARCH
published: 13 October 2021
doi: 10.3389/fnagi.2021.758053

Functional Abnormality Associated With Tau Deposition in Alzheimer's Disease – A Hybrid Positron Emission Tomography/MRI Study

Liping Fu[1], Zhi Zhou[2], Linwen Liu[3], Jinming Zhang[4], Hengge Xie[5], Xiaojun Zhang[2], Mingwei Zhu[5] and Ruimin Wang[4]**

[1] Department of Nuclear Medicine, China-Japan Friendship Hospital, Beijing, China, [2] Department of Neurology, China-Japan Friendship Hospital, Beijing, China, [3] Medical Research Center, Peking Union Medical College Hospital, Chinese Academy of Medical Sciences and Peking Union Medical College, Beijing, China, [4] Department of Nuclear Medicine, The First Medical Center, Chinese PLA General Hospital, Beijing, China, [5] Department of Neurology, The Second Medical Center, Chinese PLA General Hospital, Beijing, China

Objective: To investigate the characteristics of tau deposition and its impact on functional connectivity (FC) in Alzheimer's disease (AD).

Methods: Hybrid PET/MRI scans with [^{18}F]-THK5317 and neuropsychological assessments were undertaken in 26 participants with AD and 19 healthy controls (HC). The standardized uptake value ratio (SUVR) of [^{18}F]-THK5317 PET imaging was compared between the AD and HC groups. Significant clusters that revealed higher tau deposition in the AD group compared to the HC group were selected as regions of interest (ROI) for FC analysis. We evaluated the difference in the FC between the two groups for each ROI pair. The clinical and radiological characteristics were compared between the AD patients with negative FC and AD patients with positive FC for exploratory analysis.

Results: The bilateral inferior lateral temporal lobe, dorsal prefrontal cortex, precuneus, posterior cingulate cortex, hippocampus, and occipital lobe showed significantly higher [^{18}F]-THK5317 accumulation in AD patients. Decreased FC in regions with higher SUVR was observed in AD patients, and the FC strength was negatively correlated with regional SUVR. Patients with a positive FC exhibited older ages, better cognitive performances, and a lower SUVR than patients with a negative FC.

Conclusions: An impact of tau deposition was observed on FC at the individual level in AD patients. Our findings suggested that the combination of tau-PET and rs-fMRI might help predict AD progression.

Keywords: Alzheimer's disease, PET/MRI, tau, fMRI, functional connectivity

OPEN ACCESS

Edited by:
Ping Wu,
Fudan University, China

Reviewed by:
Chuantao Zuo,
Fudan University, China
Yong Ji,
Capital Medical University, China

****Correspondence:***
Liping Fu
flp39@163.com
Ruimin Wang
wrm@yeah.net

Received: *13 August 2021*
Accepted: *22 September 2021*
Published: *13 October 2021*

Citation:
Fu L, Zhou Z, Liu L, Zhang J, Xie H, Zhang X, Zhu M and Wang R (2021) Functional Abnormality Associated With Tau Deposition in Alzheimer's Disease – A Hybrid Positron Emission Tomography/MRI Study. Front. Aging Neurosci. 13:758053. doi: 10.3389/fnagi.2021.758053

INTRODUCTION

Abnormal deposition of amyloid-β (Aβ) and tau is the hallmark of pathology in Alzheimer's disease (AD). According to the pathological classification model, the accumulation of Aβ plaque (A) deposition occurs first, followed by phosphorylated tau (T) deposition and downstream neurodegenerative (N) events (Jack et al., 2018).

Tau protein plays an important role in promoting the stability of tubulin assemblies and maintaining the microarchitecture of neurons (Kametani and Hasegawa, 2018). Recent advances in molecular neuroimaging, including positron emission tomography (PET), have enabled the identification and quantification of pathological proteins *in vivo*. PET with tracers, including [^{18}F]-THK5317 and [^{18}F]-AV1451, is a well-established neuroimaging technique for measuring regional tau burden. Previous studies with tau-PET demonstrated that the spatial pattern of tau deposition was similar to the key features of the Braak histopathological stages illustrated by autopsy-based assessments (Schwarz et al., 2016). Compared with Aβ, the spread of tau pathology shows a strong relationship with the progression of AD (Kametani and Hasegawa, 2018).

The deposition of pathological proteins contributes to the cascade of functional and morphological changes in the brain. There are extensive reports indicating that tau causes direct toxic effects on neuronal activity and synaptic plasticity in AD, leading to disruption of functional connectivity (FC), which assesses the correlation between spontaneous activity fluctuations in remote brain regions (Busche et al., 2019). The combination of tau-PET and multi-modal MRI facilitates *in vivo* investigation. Recently, hybrid PET/MRI has become available in clinical practice, which provides the opportunity to combine PET and MRI in a single imaging session. Neuroimaging studies using resting state functional MRI (rs-fMRI) and tau-PET support the idea that tau disrupts FC in AD by showing that tau accumulation weakens FC.

Previous work primarily focused on FC disruption in known brain functional networks. Based on these observations, recent studies illustrated that highly connected nodes, which also are called hubs, displayed more tau pathology, and increases in tau burden were associated with decreases in FC at these same nodes (Cope et al., 2018; Yokoi et al., 2018; Franzmeier et al., 2019, 2020). These results provide evidence for the "network degeneration hypothesis," in which the spreading of pathological tau propagates *trans*-neuronally in a prion-like manner (Kametani and Hasegawa, 2018). However, these studies examined the alterations in FC and tau deposition separately. Therefore, the direct interaction of pathological tau deposition and regional FC and the influence on cognitive impairment remains unclear. In this study, using hybrid PET/MRI with [^{18}F]-THK5317, we investigated the characteristics of tau deposition and its impact on FC in AD patients at the individual level.

MATERIALS AND METHODS

Participants

Twenty-six AD and 19 HC subjects were recruited at the Chinese PLA General Hospital. The clinical diagnosis of AD was made based on the criteria for dementia cited in the International Classification of Diseases, 10th Revision (ICD-10) and the criteria for probable AD from the National Institute of Neurological and Communicative Disorders and the Stroke/Alzheimer Disease and Related Disorders Association (NINCDS-ADRDA) (McKhann et al., 2011). All participants were clinically assessed using the Clinical Dementia Rating (CDR) (Morris, 1993), which categorized the participants as HCs (CDR = 0) or patients in the early stages of AD (CDR>0.5). The inclusion criteria for AD included: (1) significant episodic memory problems reported by the patient, a relative, or caregiver; (2) impaired performance on a general cognition test [Mini-Mental State Examination (MMSE) score < 24] and in activities of daily living (ADL); (3) medial temporal lobe atrophy as assessed with the visual atrophy rating scale (Scheltens et al., 1992). Also, AD patients exhibited positive results obtained with an amyloid PET [(^{11}C)-PIB] scan. Participants were excluded if they presented one of the following criteria: (1) structural abnormalities that could result in dementia, including cortical infarction, tumors, or a subdural hematoma; (2) concurrent illnesses other than dementia that interfered with cognitive function at the time of the MRI examination; (3) metabolic conditions such as hypothyroidism, and vitamin B12 or folic acid deficiencies. The HCs had no history of neurological or psychiatric disorders, sensorimotor impairment, or cognitive complaints, no abnormal anatomical findings based on conventional brain MRI, and no evidence of cognitive deficits on neuropsychological tests. All participants exhibited right-hand dominance. Written informed consent was obtained from each participant, and this study was approved by the institutional review board of the Chinese PLA General Hospital. We conducted this study in compliance with the principles of the Declaration of Helsinki.

Positron Emission Tomography/MRI Scans

Forty minutes after the injection of approximately 370MBq (4.44–5.55 MBq/kg) of [^{18}F]-THK5317, each participant was positioned in a hybrid PET/MRI system (Biograph mMR, Siemens Healthineers, Erlangen, Germany) that consisted of a whole-body PET and a 3.0-T MRI. This hybrid scanner enables the acquisition of 127 transaxial planes over a 25.8 cm axial field of view, which allows the entire brain to be imaged in a one-bed position. The [^{18}F]-THK5317 PET scan started 40 min after the tracer was injected and lasted for 20 min. It was carried out simultaneously with the MRI scan, which included attenuation correction acquisition (ultra-short echo time (UTE) sequence, TE1/TE2 = 0.07/2.46 ms, TR = 11.94 ms, flip angle 10°, 192 slices, matrix size: 192 × 192 × 192, FOV = 300 mm × 300 mm, voxel size 1.6 mm × 1.6 mm × 1.6 mm, acquisition time 1:40 min/bed position), high-resolution sagittal 3D T1-weighted magnetization-prepared rapid gradient echo (MPRAGE) acquisition (TR = 1,900 ms, TE = 2.44 ms, inversion time = 900 ms, slice thickness = 1 mm, matrix = 256 × 256, FOV = 250 mm × 250 mm, voxel size 1.0 mm × 1.0 mm × 1.0 mm, acquisition time 8:54 min/bed position), a transverse T2-weighted turbo spin echo acquisition (TR = 4,500 ms, TE = 85 ms, flip angle 150°, 25 slices, slice thickness 4 mm, FOV = 220 mm × 220 mm, voxel size 0.7 mm × 0.7 mm × 4.0 mm, acquisition time 2:32 min/bed position) and single shot gradient echo-planner imaging with blood oxygenation level dependence (BOLD, TR = 2,000 ms, TE = 30 ms, slice thickness = 3.5 mm, slice = 43, Matrix = 64 × 64,

FOV = 224 mm × 224 mm, acquisition time 8:00 min/bed position). The 20 min (taken at 40–60 min) of PET data were converted into standardized uptake value (SUV) images for further analysis using an ordered subset expectation maximization algorithm with settings of iterate = 3, subset = 21, matrix = 336 × 336, and a Gaussian filter of 4 mm in full-width half-maximum (FWHM). All subjects underwent THK5317-PET and 3D-T1WI MRI scanning; 22 AD and 12 HC subjects had resting-state BOLD data that were acquired.

All participants underwent a 20-min [^{11}C]-PIB PET/MRI static scan, which was performed 40 min after injection (40–60 min) of 4.5 MBq/kg (McNamee et al., 2009). The [^{11}C]-PIB was synthesized from its corresponding precursors as described previously (Philippe et al., 2011), with a radiochemical purity of more than 95% and specific activity of 50 GBq/moL (1.48 Ci/moL). The [^{11}C]-PIB PET/MRI scan protocol was the same as the [^{18}F]-THK5317 PET/MRI scan.

Radiosynthesis of [^{18}F]-THK5317

[^{18}F]-THK5317 was prepared using ^{18}F- nucleophilic substitution of the tosylate in the precursor in the presence of K2CO3 and Kryptofix-222 using the automatic synthesis module (PET-MF-2V-IT-1, Beijing, China). After radiofluorination, the tetrahydropyranyl (THP) protecting group was removed using HCl (1 M) hydrolysis in the same reaction vessel, and the radiotracer was purified by semi-preparative HPLC. The identity of the radiotracer was confirmed using HPLC co-injection analysis. The radiochemical purity of [^{18}F]-THK5317 was greater than 95%, and its specific activities ranged from 90 to 123.5 GBq/μmol, which was corrected at the end of the synthesis.

Positron Emission Tomography Data Preprocessing

The MRI data were co-registered to the PET [(^{18}F)-THK5317 and (^{11}C)-PIB] data and spatially normalized to a customized template in Montreal Neurological Institute (MNI) space, which was constructed from the MRI T1W images acquired in this study. The transformative deformation fields were applied to the corresponding PET data, and then isotropic 2 mm spatial resolution-normalized PET data in MNI space were generated. The mean value of the cerebellar gray matter region was used to normalize the intensity values of the PET images, voxel-by-voxel. A 6 mm FWHM Gaussian kernel was used to smooth the normalized PET data. The cut-off value for PIB-PET was 1.4 (Tanaka et al., 2020).

Resting-State fMRI Data Preprocessing

The resting-state fMRI data were preprocessed using SPM12 software[1]. The first six volumes were discarded to allow for magnetization equilibrium and participants' adaption to the environment. The slice timing and rigid-body head movement during scans were corrected, so that all images were realigned to the first volume. The excessive motion was defined as a maximum displacement of 3 mm and a maximum angular motion of 3° in any direction. The structural images were co-registered to the first volume of the corresponding functional images, and then segmented into gray matter, white matter, and cerebrospinal fluid. All fMRI images were normalized to the MNI space following motion correction using a diffeomorphic non-linear registration algorithm (DARTEL) (Ashburner, 2007) and resampled to a 2-mm isotropic voxel. The normalized fMRI images were smoothed using a Gaussian kernel of 6 mm FWHM. The fMRI images were finally filtered with a temporal band-path of 0.01–0.1 Hz, and white matter and CSF signals were regressed out.

Statistics

Data were analyzed using SPSS, version 23.0 (IBM Corp., Chicago, IL, United States). Demographic and clinical variables were assessed for normality of distribution using Kolmogorov–Smirnov tests. Variables exhibiting a normal distribution were compared using the Student's *t*-test. Gender was analyzed using a Chi-square test. A *p*-value of <0.05 was considered significant.

A voxel-wise two-sample *t*-test was used to compare the difference of the [^{18}F]-THK5317 cortical-to-cerebellum standardized uptake value ratio (SUVR) between the AD and HC groups. The false discovery rate (FDR) for multiple comparisons was utilized to control the expected proportion of false-positive results among the suprathreshold voxels with a $p < 0.05$ and a cluster size larger than 800 mm3. Significant group differences ($p < 0.05$) were used as ROIs for rs-fMRI network construction.

Seven regions of interest (ROIs) were extracted from brain regions where tau deposition was significantly increased in the AD group compared to the HC group (details are presented in the "Results" section). An FC analysis was performed among the given ROIs, which was measured using Pearson's correlation coefficient. The correlation coefficient was derived between the mean time series of each pair of the seven ROIs, with each subject as the FC. A two-sample *t*-test was conducted to compare the FC difference between the two groups for each ROI pair. A significance level of an uncorrected $p < 0.05$ was obtained for the FC comparisons.

RESULTS

Demographic Characteristics

Table 1 lists the clinical and neuropsychological data. No significant differences were observed in age, gender, and education level. All AD participants had positive results from the PIB-PET scans. Also, the AD group exhibited significantly lower scores than the HC group for the MMSE.

Voxel-Based Morphometry Analysis of Tau Deposition

The results of the voxel-based morphometry (VBM) analysis of the SUVR maps are shown in **Table 2** and **Figure 1**. The AD group exhibited a significantly higher SUVR than the HC group in numerous cortical and subcortical areas, including the bilateral posterior cingulate cortex (PCC), ventromedial prefrontal cortex, temporal cortex, and parietal cortex (**Table 2** and **Figure 1**). No

[1]http://www.fil.ion.ucl.ac.uk/spm

TABLE 1 | Clinical and demographic characteristics of all subjects.

	HCs	AD patients	*p* value
N	19	26	–
Age (Y)	65.59 ± 8.05	70.68 ± 12.21	0.10
Gender (M/F)	9/8	17/12	0.29
Education (Y)	10.73 ± 4.99	11.23 ± 3.48	0.421
MMSE*	29.33 ± 0.18	20.27 ± 4.69	<0.001

**MMSE scores for AD patients vs. HCs were significantly different by a two-sample t-test, $p < 0.05$. Data are mean ± SD or numbers of subjects.*

TABLE 2 | Significant clusters of higher tau accumulation in Alzheimer's disease.

No	Cluster voxels	Lateralization	Regions	*T*	MNI coordinate		
					X	Y	Z
1	8,795	Left	Middle and inferior temporal cortex, Middle and inferior occipital cortex, Angular cortex, Precuneus cortex, Parahippocampal cortex	−7.827	−22	−74	44
2	10,995	Right	Temporal cortex, Middle and inferior occipital cortex, Angular cortex, Precuneus cortex, Parahippocampal cortex	−7.821	52	−60	−18
3	4,791	Left	Dorsal lateral prefrontal cortex	−7.015	−36	32	34
4	4,986	Right	Dorsal lateral prefrontal cortex	−8.390	22	16	60
5	105	Right	Parahippocampus	−4.661	20	−14	−16
6	479	Left	Caudate	−6.383	0	18	−4
7	4,401	Bilateral	Middle and posterior cingulate cortex	−8.087	8	−34	44

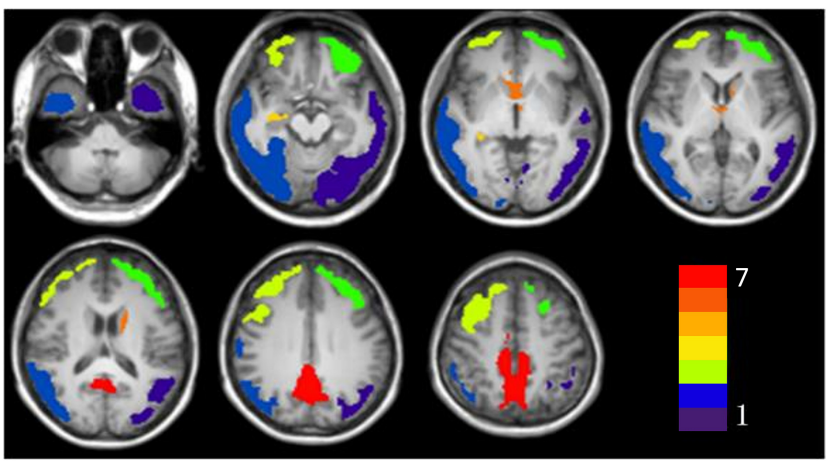

FIGURE 1 | The significant clusters of tau accumulation in Alzheimer's disease patients. The color bar indicates the different clusters (Cluster 1 to Cluster 7).

region was observed that had a significantly lower SUVR in the AD group compared to the HC group.

Functional Connectivity Analysis in Regions of Tau Deposition

Seven clusters were extracted from the VBM results and used as the ROIs in the FC analysis. The FC between each two ROIs was calculated as the correlation between their time series for all subjects. Compared with the HC group, the AD group showed a significantly decreased connectivity pattern between Clusters 1 and 2 (**Table 3**). We also found a negative correlation between the FC and SUVR between Clusters 1 and 2 (**Figure 2**).

Exploratory Analysis: Clinical and Radiological Characteristics of the Functional Connectivity-Positive and Functional Connectivity-Negative Alzheimer's Disease Subgroups

In the exploratory analysis, we observed that 12 subjects in the AD group showed a negative FC between Clusters 1 and 2. This

TABLE 3 | Group differences of the FC for each ROI pair between the AD and HC groups.

T *P*	Cluster 2	Cluster 3	Cluster 4	Cluster 5	Cluster 6	Cluster 7
Cluster 1	2.7241 *0.0096*	−1.5988 *0.1179*	1.0063 *0.3205*	1.3013 *0.2008*	−1.3574 *0.1825*	1.1228 *0.2684*
Cluster 2	–	0.5164 *0.6085*	−1.9831 *0.0544*	−0.8614 *0.3943*	−0.7879 *0.4355*	0.9712 *0.3374*
Cluster 3	–	–	1.0941 *0.2806*	0.3907 *0.6981*	0.4164 *0.6794*	0.1187 *0.9062*
Cluster 4	–	–	–	−0.6602 *0.5130*	0.1553 *0.8774*	−0.4688 *0.6418*
Cluster 5	–	–	–	–	0.4499 *0.6552*	−0.8712 *0.3890*
Cluster 6	–	–	–	–	–	−1.3901 *0.1724*

In each cell, the upper number is the T value, and the lower number is the p-value for each ROI pair.

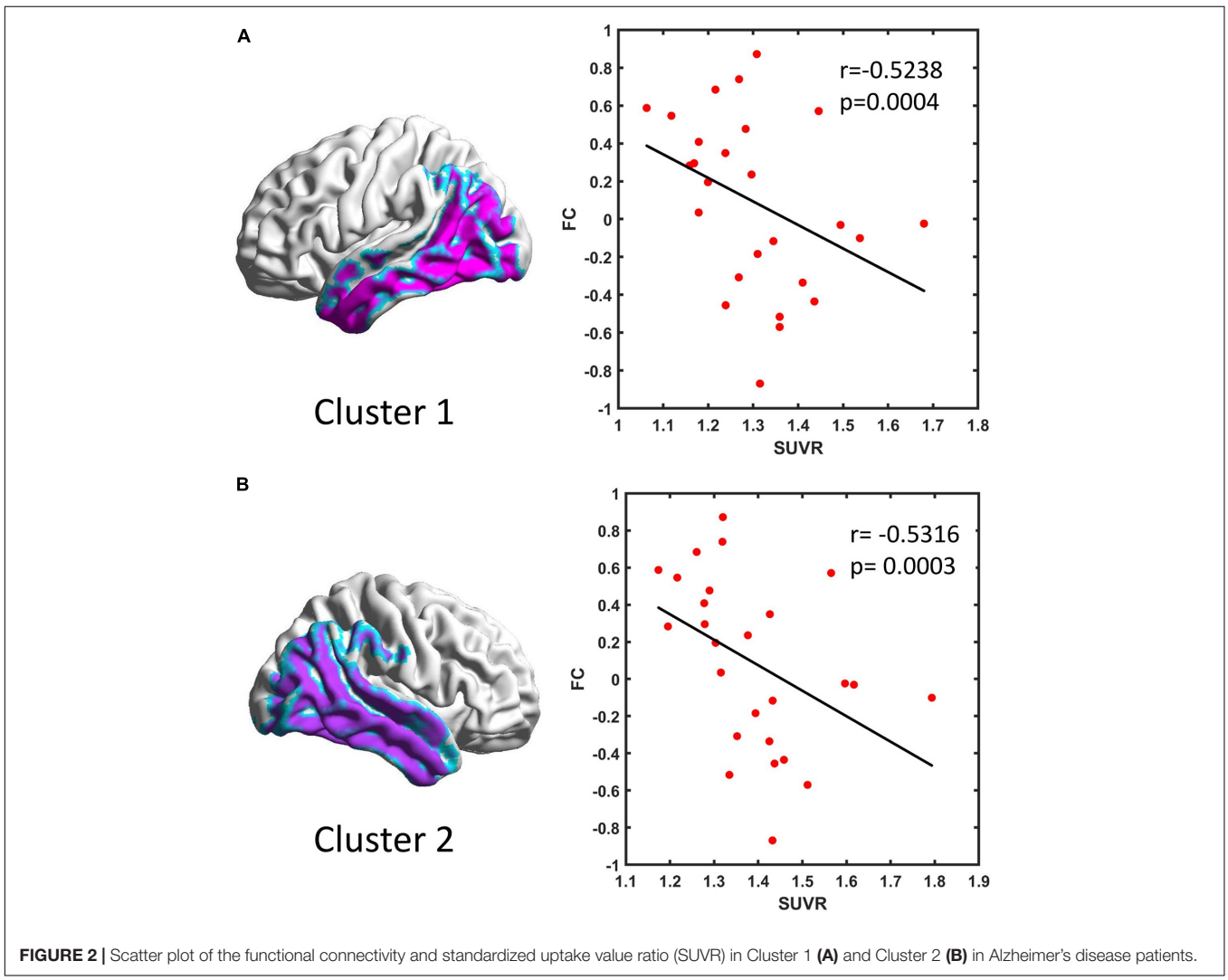

FIGURE 2 | Scatter plot of the functional connectivity and standardized uptake value ratio (SUVR) in Cluster 1 **(A)** and Cluster 2 **(B)** in Alzheimer's disease patients.

result indicated that the correlation of paired BOLD signals was negatively correlated, while the other 14 subjects in the AD group showed a positive FC between Clusters 1 and 2. However, all subjects in the HC group exhibited a positive FC between Clusters 1 and 2, which indicated that the correlation was positive or synergic (**Figure 3** and **Supplementary Material 1**).

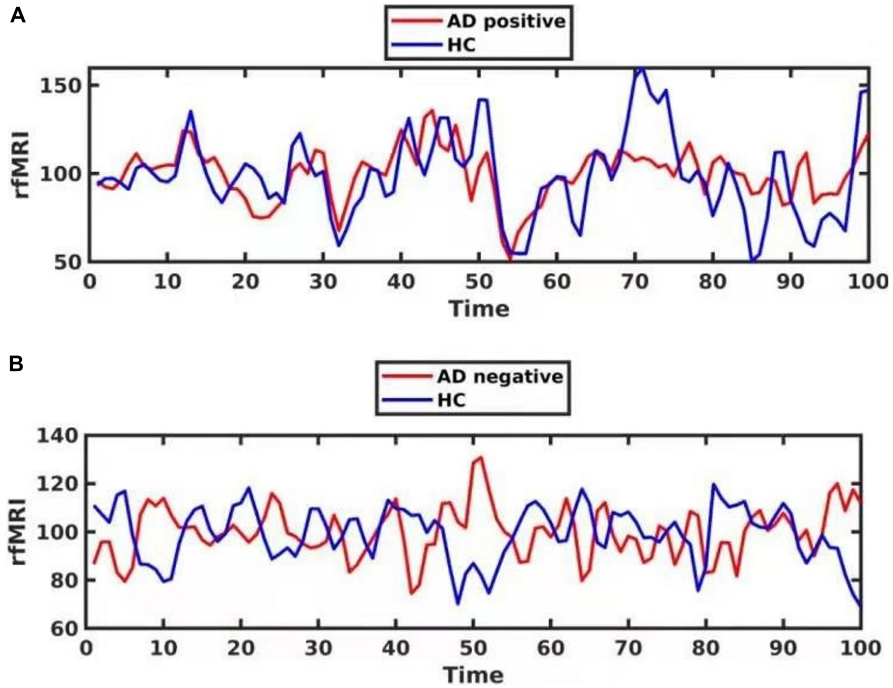

FIGURE 3 | The phase delay of the functional BOLD series for one Alzheimer's disease (AD) patient with positive functional connectivity (FC) [**(A)**, red] and another AD patient with negative FC [**(B)**, red]. The FC is between Cluster 1 and Cluster 2. The time series for one healthy control is shown in blue.

Based on the FC between Clusters 1 and 2, we divided the AD group into FC-positive and FC-negative subgroups. **Table 4** illustrates the clinical and radiological characteristics of these two AD subgroups. When compared to the FC-positive patients, the FC-negative patients were younger and exhibited lower MMSE scores. No significant difference of GMV in Clusters 1 and 2 was detected in the FC-negative and FC-positive subgroups. However, the FC-negative group had greater [^{18}F]-THK5317 binding in Clusters 1 and 2.

DISCUSSION

The main result of this cross-sectional study was the presence of higher tau deposition in the AD group in the bilateral inferior lateral temporal lobe, dorsal prefrontal cortex, precuneus, posterior cingulate cortex, hippocampus, and occipital lobe. FC analysis revealed decreased FC in regions with higher [^{18}F]-THK5317 signals. The FC strength was negatively correlated with the regional SUVR in patients with AD. Exploratory analysis revealed that patients with a positive FC were older and exhibited better cognitive performance than patients with a negative FC. In addition, tau accumulation was higher in patients with a negative FC than those with a positive FC. Taken together, these findings suggested that tau accumulation impacted the function and clinical performance of AD patients.

Pathological proteins, including tau, either directly or indirectly, interfere with cerebral function and morphology in AD. Previous studies have demonstrated disruptions of large-scale brain networks in AD, including the default-mode network (DMN) and other networks. However, little is known about alterations in FC patterns associated with high tau deposition. Consistent with previous studies, we demonstrated that regions of tau accumulation were located in important hubs of the posterior DMN, including the precuneus and angular cortex (Franzmeier et al., 2019). With respect to cognitive function, episodic memory is the most vulnerable cognitive subdomain in early AD and relies on the interaction between the DMN and the medial temporal lobe (Ward et al., 2015). Executive function also declined in concert with memory in the early stage of AD, implicating an interplay between the DMN and other relevant networks (La Corte et al., 2016). In AD, where tau accumulation predominates, the affected nodes become weakly connected, which reduces the local efficiency of information transfer.

Negative FC refers to a negative Pearson correlation coefficient for the spontaneous BOLD signal in two brain regions, indicating a negative correlation for the two regions. The origin and interpretation of a negative FC have been debated. Some studies have reported that a negative FC was an artifact induced by the global signal regression and excluded results that included a negative FC to avoid uncertainty (Weissenbacher et al., 2009). However, other studies found that a negative FC could exist without a global signal regression, and the characteristics of a negatively correlated network were not related to the global signal removal (Chang and Glover, 2009; Fox et al., 2009). Additional studies have revealed that a negative FC was associated with predominantly long-range

TABLE 4 | Demographic and radiological characteristics of the FC-positive and FC-negative groups in AD patients.

		FC-negative AD	FC-positive AD	*Z* score	*p* value
n		12	14		
Age*		66.08 ± 9.79	74.71 ± 12.32	−2.04	0.044
Gender (M/F)		4:8	7:7		0.46
MMSE*		17.00 ± 5.31	22.71 ± 2.84	−2.51	0.012
Cluster 1	GMV	5,687.31 ± 1,050.03	6,120.13 ± 920.18	−0.93	0.374
	SUVR*	1.40 ± 0.13	1.22 ± 0.95	−3.45	0.0005
Cluster 2	GMV	6,981.53 ± 1,250.72	7,570.47 ± 1,135.87	−1.18	0.237
	SUVR*	1.48 ± 0.13	1.31 ± 0.10	−3.55	0.0009

**Age, MMSE scores, and SUVR in cluster 1 and cluster 2 for FC-negative AD vs. FC-positive AD patients were significantly different based on a two-sample t-test, $p < 0.05$. Data are means ± SD or numbers of subjects.*

connections, which provides a possible explanation for the underlying neurobiological mechanism. Moreover, Chen et al. (2011) suggested that a negative FC might induce a phase delay in the synchronous signals along the shortest path in the brain functional networks. Because the mechanisms of negative FC still are not well understood (Chen et al., 2011), we compared the cognitive performance between the FC-positive and FC-negative AD subgroups. We observed that AD patients with a positive FC in the tau accumulation region performed better in the cognitive test. Also, the SUVR for [^{18}F]-THK5317 was higher in patients with a negative FC. It is worth mentioning that a negative FC was only found in the AD group. These findings support the biological mechanism of negative FC.

In this study, compared with the negative FC subgroup, the positive FC subgroup might be protective to compensate for the neuron injury caused by tau deposition and allows the cognitive performance to be maintained. This mechanism might lead to a period of hyperactivity until the neuronal loss overcomes the compensatory mechanism. However, whether the reserve capacity is related to the cognitive benefit in the presence of severe tau accumulation is controversial. Previous pathological studies suggested that the reserve capacity is related to decreased cognitive impairment in the presence of Aβ pathology but not tau pathology. However, a recent study using tau-PET found that a higher intelligence quotient was associated with an attenuated association between tau accumulation and cognitive decline (Halawa et al., 2019). Additional exploration of the cognitive reserve capacity will help identify individuals with a higher tolerance of tau pathologic burden in future studies, and help in the early diagnosis and intervention for AD patients.

If the network efficiency relates to the cognitive and clinical performance, then the FC alteration would predict the neurodegenerative process, particularly for the tau accumulation in hub regions. A negative FC might indicate a connectivity disruption in the temporal lobe and parietal cortex, which leads to an advanced stage of AD.

[^{18}F]-THK5117 has shown a high affinity for and selective binding to tau pathology (Harada et al., 2015; Lemoine et al., 2015). Its *S*-form enantiomer [also known as (^{18}F)-THK5317] has exhibited favorable pharmacokinetics (Jonasson et al., 2016). It was reported that, except for tau deposition in the neocortex, the monoamine oxidase-B (MAO-B) in the entire brain is correlated with retention of [^{18}F]-THK5317 (Harada et al., 2018). However, MAO-B is primarily localized in the inner mitochondrial membrane of astrocytes and linked to the presence of astrogliosis with the accumulation of misfolded proteins. In addition to tau deposition, the activation of microglia and astrogliosis also contributes to the development of AD (Leyns and Holtzman, 2017). Therefore, [^{18}F]-THK5317 retention in the AD neocortex is expected to indicate the distribution of tau pathology and reflect the presence of reactive astrocytes *in vivo*.

There are several limitations to this study. First, although all AD participants exhibited positive PIB-PET results, we did not include the influence of Aβ. Schultz et al. (2017) found that tau and Aβ both affect FC, and tau-FC associations were stronger and increased with Aβ levels (Schultz et al., 2017; Adams et al., 2019; Franzmeier et al., 2019). Second, in addition to tau, [^{18}F]-THK5317 retention has been reported to reflect reactive astrocytes (Shigemoto et al., 2018). Third, only the MMSE scores were used to evaluate the cognitive level of AD patients. More subdomain evaluations, such as memory, executive function, and others, are needed to assess the cognition of AD patients more accurately. Finally, the cross-sectional nature and small sample size limited our interpretation of causality. Additional longitudinal studies with larger sample sizes are needed to investigate whether tau deposits accurately predict atrophy and decreases in FC.

CONCLUSION

Therefore, the cortical regions, including the bilateral inferior lateral temporal lobe, dorsal prefrontal cortex, precuneus, posterior cingulate cortex, hippocampus, and occipital lobe, showed significantly higher [^{18}F]-THK5317 accumulation in patients with AD. Decreased FC in regions with higher SUVR was observed in AD patients, and the FC strength negatively correlated with regional SUVR. Patients with a positive FC exhibited older ages, better cognitive performances, and a lower SUVR than patients with a negative FC. The current results indicated that there was an impact of tau deposition on FC at the individual level in AD patients. Furthermore, our findings suggested that the combination of tau-PET and rs-fMRI might be useful to predict the progression of AD.

DATA AVAILABILITY STATEMENT

The original contributions presented in the study are included in the article/**Supplementary Material**, further inquiries can be directed to the corresponding author/s.

ETHICS STATEMENT

The studies involving human participants were reviewed and approved by the Chinese PLA General Hospital. The patients/participants provided their written informed consent to participate in this study.

AUTHOR CONTRIBUTIONS

LF contributed to the research concept and design, data analysis and interpretation, drafting of the manuscript, critical revision of the article, and final approval of the article. ZZ and LL contributed to data analysis and data interpretation. JZ and XZ contributed to radiosynthesis and data analysis. HX and MZ contributed to data collection and interpretation. RW contributed to the research concept and design. All authors contributed to the article and approved the submitted version.

FUNDING

This study was financially sponsored by the National Key Research and Development Program of China under grant (No. 2016YFC0103804), Beijing Municipal Natural Science Foundation (No. 7192192) and National Natural Science Foundation of China (Nos. 82071963 and 11975249).

ACKNOWLEDGMENTS

We would like to thank Dayi Yin and Jiajin Liu for technical support and PET/MRI data acquisition, as well as Jian Liu and Yungang Li for their help with the PET radiochemistry. We would also like to thank EditSprings (https://www.editsprings.com/) for their expert linguistic services.

SUPPLEMENTARY MATERIAL

The Supplementary Material for this article can be found online at: https://www.frontiersin.org/articles/10.3389/fnagi.2021.758053/full#supplementary-material

REFERENCES

Adams, J. N., Maass, A., Harrison, T. M., Baker, S. L., and Jagust, W. J. (2019). Cortical tau deposition follows patterns of entorhinal functional connectivity in aging. *Elife* 8:e49132. doi: 10.7554/eLife.49132.026

Ashburner, J. (2007). A fast diffeomorphic image registration algorithm. *Neuroimage* 38, 95–113. doi: 10.1016/j.neuroimage.2007.07.007

Busche, M. A., Wegmann, S., Dujardin, S., Commins, C., Schiantarelli, J., Klickstein, N., et al. (2019). Tau impairs neural circuits, dominating amyloid-beta effects, in Alzheimer models in vivo. *Nat. Neurosci.* 22, 57–64. doi: 10.1038/s41593-018-0289-8

Chang, C., and Glover, G. H. (2009). Effects of model-based physiological noise correction on default mode network anti-correlations and correlations. *Neuroimage* 47, 1448–1459. doi: 10.1016/j.neuroimage.2009.05.012

Chen, G., Chen, G., Xie, C., and Li, S. J. (2011). Negative functional connectivity and its dependence on the shortest path length of positive network in the resting-state human brain. *Brain Connect.* 1, 195–206. doi: 10.1089/brain.2011.0025

Cope, T. E., Rittman, T., Borchert, R. J., Jones, P. S., Vatansever, D., Allinson, K., et al. (2018). Tau burden and the functional connectome in Alzheimer's disease and progressive supranuclear palsy. *Brain* 141, 550–567. doi: 10.1093/brain/awx347

Fox, M. D., Zhang, D., Snyder, A. Z., and Raichle, M. E. (2009). The global signal and observed anticorrelated resting state brain networks. *J. Neurophysiol.* 101, 3270–3283. doi: 10.1152/jn.90777.2008

Franzmeier, N., Neitzel, J., Rubinski, A., Smith, R., Strandberg, O., Ossenkoppele, R., et al. (2020). Functional brain architecture is associated with the rate of tau accumulation in Alzheimer's disease. *Nat. Commun.* 11:347. doi: 10.1038/s41467-019-14159-1

Franzmeier, N., Rubinski, A., Neitzel, J., Kim, Y., Damm, A., Na, D. L., et al. (2019). Functional connectivity associated with tau levels in ageing. Alzheimer's, and small vessel disease. *Brain* 142, 1093–1107. doi: 10.1093/brain/awz026

Halawa, O. A., Gatchel, J. R., Amariglio, R. E., Rentz, D. M., Sperling, R. A., Johnson, K. A., et al. (2019). Inferior and medial temporal tau and cortical amyloid are associated with daily functional impairment in Alzheimer's disease. *Alzheimers Res. Ther.* 11:14. doi: 10.1186/s13195-019-0471-6

Harada, R., Ishiki, A., Kai, H., Sato, N., Furukawa, K., Furumoto, S., et al. (2018). Correlations of (18)F-THK5351 PET with postmortem burden of tau and astrogliosis in Alzheimer disease. *J. Nucl. Med.* 59, 671–674. doi: 10.2967/jnumed.117.197426

Harada, R., Okamura, N., Furumoto, S., Furukawa, K., Ishiki, A., Tomita, N., et al. (2015). [(18)F]THK-5117 PET for assessing neurofibrillary pathology in Alzheimer's disease. *Eur. J. Nucl. Med. Mol. Imaging* 42, 1052–1061. doi: 10.1007/s00259-015-3035-4

Jack, C. R. Jr., Bennett, D. A., Blennow, K., Carrillo, M. C., Dunn, B., et al. (2018). NIA-AA research framework: toward a biological definition of Alzheimer's disease. *Alzheimers Dement.* 14, 535–562. doi: 10.1016/j.jalz.2018.02.018

Jonasson, M., Wall, A., Chiotis, K., Saint-Aubert, L., Wilking, H., Sprycha, M., et al. (2016). Tracer kinetic analysis of (S)-^{18}8F-THK5117 as a PET tracer for assessing tau pathology. *J. Nucl. Med.* 57, 574–581. doi: 10.2967/jnumed.115.158519

Kametani, F., and Hasegawa, M. (2018). Reconsideration of amyloid hypothesis and tau hypothesis in Alzheimer's disease. *Front. Neurosci.* 12:25. doi: 10.3389/fnins.2018.00025

La Corte, V., Sperduti, M., Malherbe, C., Vialatte, F., Lion, S., Gallarda, T., et al. (2016). Cognitive decline and reorganization of functional connectivity in healthy aging: the pivotal role of the salience network in the prediction of age and cognitive performances. *Front. Aging Neurosci.* 8:204. doi: 10.3389/fnagi.2016.00204

Lemoine, L., Saint-Aubert, L., Marutle, A., Antoni, G., Eriksson, J. P., Ghetti, B., et al. (2015). Visualization of regional tau deposits using (3)H-THK5117 in Alzheimer brain tissue. *Acta Neuropathol. Commun.* 3:40. doi: 10.1186/s40478-015-0220-4

Leyns, C. E. G., and Holtzman, D. M. (2017). Glial contributions to neurodegeneration in tauopathies. *Mol. Neurodegener.* 12:50. doi: 10.1186/s13024-017-0192-x

McKhann, G. M., Knopman, D. S., Chertkow, H., Hyman, B. T., Jack, C. R., et al. (2011). The diagnosis of dementia due to Alzheimer's disease: recommendations from the national institute on Aging-Alzheimer's association workgroups on diagnostic guidelines for Alzheimer's disease. *Alzheimers Dement.* 7, 263–269. doi: 10.1016/j.jalz.2011.03.005

McNamee, R. L., Yee, S. H., Price, J. C., Klunk, W. E., Rosario, B., Weissfeld, L., et al. (2009). Consideration of optimal time window for pittsburgh compound B PET summed uptake measurements. *J. Nucl. Med.* 50, 348–355. doi: 10.2967/jnumed.108.057612

Morris, J. C. (1993). The clinical dementia rating (CDR): current version and scoring rules. *Neurology* 43, 2412–2414. doi: 10.1212/WNL.43.11.2412-a

Philippe, C., Haeusler, D., Mitterhauser, M., Ungersboeck, J., Viernstein, H., Dudczak, R., et al. (2011). Optimization of the radiosynthesis of the Alzheimer tracer 2-(4-N-[11C]methylaminophenyl)-6-hydroxybenzothiazole ([11C]PIB). *Appl. Radiat. Isot.* 69, 1212–1217. doi: 10.1016/j.apradiso.2011.04.010

Scheltens, P., Leys, D., Barkhof, F., Huglo, D., Weinstein, H. C., Vermersch, P., et al. (1992). Atrophy of medial temporal lobes on MRI in "probable" Alzheimer's disease and normal ageing: diagnostic value and neuropsychological correlates. *J. Neurol. Neurosurg. Psychiatry* 55, 967–972. doi: 10.1136/jnnp.55.10.967

Schultz, A. P., Chhatwal, J. P., Hedden, T., Mormino, E. C., Hanseeuw, B. J., Sepulcre, J., et al. (2017). Phases of hyperconnectivity and hypoconnectivity in the default mode and salience networks track with amyloid and tau in clinically normal individuals. *J. Neurosci.* 37, 4323–4331. doi: 10.1523/JNEUROSCI.3263-16.2017

Schwarz, A. J., Yu, P., Miller, B. B., Shcherbinin, S., Dickson, J., Navitsky, M., et al. (2016). Regional profiles of the candidate tau PET ligand 18F-AV-1451 recapitulate key features of Braak histopathological stages. *Brain* 139(Pt 5), 1539–1550. doi: 10.1093/brain/aww023

Shigemoto, Y., Sone, D., Imabayashi, E., Maikusa, N., Okamura, N., Furumoto, S., et al. (2018). Dissociation of tau deposits and brain atrophy in early Alzheimer's disease: a combined positron emission tomography/magnetic resonance imaging study. *Front. Aging Neurosci.* 10:223. doi: 10.3389/fnagi.2018.00223

Tanaka, T., Stephenson, M. C., Nai, Y. H., Khor, D., Saridin, F. N., Hilal, S., et al. (2020). Improved quantification of amyloid burden and associated biomarker cut-off points: results from the first amyloid Singaporean cohort with overlapping cerebrovascular disease. *Eur. J. Nucl. Med. Mol. Imaging* 47, 319–331. doi: 10.1007/s00259-019-04642-8

Ward, A. M., Mormino, E. C., Huijbers, W., Schultz, A. P., Hedden, T., and Sperling, R. A. (2015). Relationships between default-mode network connectivity, medial temporal lobe structure, and age-related memory deficits. *Neurobiol. Aging* 36, 265–272. doi: 10.1016/j.neurobiolaging.2014.06.028

Weissenbacher, A., Kasess, C., Gerstl, F., Lanzenberger, R., Moser, E., and Windischberger, C. (2009). Correlations and anticorrelations in resting-state functional connectivity MRI: a quantitative comparison of preprocessing strategies. *Neuroimage* 47, 1408–1416. doi: 10.1016/j.neuroimage.2009.05.005

Yokoi, T., Watanabe, H., Yamaguchi, H., Bagarinao, E., Masuda, M., and Imai, K. (2018). Involvement of the Precuneus/Posterior Cingulate Cortex is significant for the development of Alzheimer's disease: a PET (THK5351, PiB) and resting fMRI study. *Front. Aging Neurosci.* 10:304. doi: 10.3389/fnagi.2018.00304

Conflict of Interest: The authors declare that the research was conducted in the absence of any commercial or financial relationships that could be construed as a potential conflict of interest.

Publisher's Note: All claims expressed in this article are solely those of the authors and do not necessarily represent those of their affiliated organizations, or those of the publisher, the editors and the reviewers. Any product that may be evaluated in this article, or claim that may be made by its manufacturer, is not guaranteed or endorsed by the publisher.

frontiers in Aging Neuroscience

ORIGINAL RESEARCH
published: 18 October 2021
doi: 10.3389/fnagi.2021.707165

Application of Machine Learning and Weighted Gene Co-expression Network Algorithm to Explore the Hub Genes in the Aging Brain

Keping Chai[1†], Jiawei Liang[2†], Xiaolin Zhang[3], Panlong Cao[1], Shufang Chen[1], Huaqian Gu[1], Weiping Ye[1], Rong Liu[3], Wenjun Hu[2], Caixia Peng[4,5*], Gang Logan Liu[2*] and Daojiang Shen[1*]*

[1] Department of Pediatrics, Zhejiang Hospital, Hangzhou, China, [2] College of Life Science and Technology, Huazhong University of Science and Technology, Wuhan, China, [3] Key Laboratory of Ministry of Education for Neurological Disorders, Department of Pathophysiology, School of Basic Medicine, Tongji Medical College, Huazhong University of Science and Technology, Wuhan, China, [4] Key Laboratory for Molecular Diagnosis of Hubei Province, Tongji Medical College, The Central Hospital of Wuhan, Huazhong University of Science and Technology, Wuhan, China, [5] Central Laboratory, Tongji Medical College, The Central Hospital of Wuhan, Huazhong University of Science and Technology, Wuhan, China

OPEN ACCESS

Edited by:
Ping Wu,
Fudan University, China

Reviewed by:
Hudson Sousa Buck,
Universidade de São Paulo, Brazil
Liping Sun,
The First Affiliated Hospital of China Medical University, China

***Correspondence:**
Keping Chai
ckpzjyy@126.com
Caixia Peng
pengcaixia@zxhospital.com
Gang Logan Liu
loganliu@hust.edu.cn
Daojiang Shen
zjyysdj@126.com

[†] These authors have contributed equally to this work

Received: 09 May 2021
Accepted: 27 September 2021
Published: 18 October 2021

Citation:
Chai K, Liang J, Zhang X, Cao P, Chen S, Gu H, Ye W, Liu R, Hu W, Peng C, Liu GL and Shen D (2021) Application of Machine Learning and Weighted Gene Co-expression Network Algorithm to Explore the Hub Genes in the Aging Brain. Front. Aging Neurosci. 13:707165. doi: 10.3389/fnagi.2021.707165

Aging is a major risk factor contributing to neurodegeneration and dementia. However, it remains unclarified how aging promotes these diseases. Here, we use machine learning and weighted gene co-expression network (WGCNA) to explore the relationship between aging and gene expression in the human frontal cortex and reveal potential biomarkers and therapeutic targets of neurodegeneration and dementia related to aging. The transcriptional profiling data of the human frontal cortex from individuals ranging from 26 to 106 years old was obtained from the GEO database in NCBI. Self-Organizing Feature Map (SOM) was conducted to find the clusters in which gene expressions downregulate with aging. For WGCNA analysis, first, co-expressed genes were clustered into different modules, and modules of interest were identified through calculating the correlation coefficient between the module and phenotypic trait (age). Next, the overlapping genes between differentially expressed genes (DEG, between young and aged group) and genes in the module of interest were discovered. Random Forest classifier was performed to obtain the most significant genes in the overlapping genes. The disclosed significant genes were further identified through network analysis. Through WGCNA analysis, the greenyellow module is found to be highly negatively correlated with age, and functions mainly in long-term potentiation and calcium signaling pathways. Through step-by-step filtering of the module genes by overlapping with downregulated DEGs in aged group and Random Forest classifier analysis, we found that *MAPT*, *KLHDC3, RAP2A*, *RAP2B*, *ELAVL2,* and *SYN1* were co-expressed and highly correlated with aging.

Keywords: WGCNA (weighted gene co-expression network analyses), SOM (self-organization map), aging brain, random forest, machine learning

INTRODUCTION

The brain is highly sensitive to aging and lots of neurological diseases are aging-promoted processes. An important issue is how normal brain aging transitions to pathological aging, giving rise to neurodegenerative disorders (Wyss-Coray, 2016; Hou et al., 2019; Juan and Adlard, 2019). Despite this central role in disease pathogenesis and morbidity, the aging of the brain has not been well understood at a molecular level. Several hypotheses, such as DNA damage, loss of neural circuits and synapses, and mitochondrial dysfunction theories, were established (Lu et al., 2004; Yankner et al., 2008; Stern, 2012; Hou et al., 2019). Exploring molecular changes in the aging brain can provide a basis for a better understanding of neurodegenerative diseases and dementia.

SOM is a clustering and classification method based on neural network (Furukawa, 2009). Similar to other types of center point clustering algorithms such as K-means, SOM also finds a set of centroids (also called codebook vector), and then maps each object in the data set to the corresponding centroids according to the principle of most similarity. In neural network terms, each neuron corresponds to a center point. In our study, we performed SOM on gene expression matrix to cluster genes with highly similar expression patterns and find the pattern in which gene expression decreases with aging.

Weighted gene co-expression network analysis (WGCNA) is a biology algorithm used to describe the correlation of gene expression based on the microarray data (Langfelder and Horvath, 2008). WGCNA can be used for clustering genes with highly correlated expression, for relating the modules to phenotypes to get the most phenotypic trait-related module, and for summarizing these co-expressed gene clusters by identification of the module eigengene or hub genes. Random forest (RF) is a more advanced machine learning algorithm based on decision tree. Like other decision trees, random forests can be used for both regression and classification. In this study, we conducted RF classifier to classify the different age groups based on the gene expression matrix, then we selected the most significant genes for further analysis. Further Topological network analysis can identify the key players within modules, and thus facilitate the discovery of candidate biomarkers or therapeutic targets.

In this study, we performed machine learning and WGCNA analysis on publicly accessible transcriptome data obtained from human frontal cortex of individuals at different ages. We identified 17 co-expression modules. Through calculating the correlation coefficient between the module and age phenotype, we obtained a module of interest. Next, we disclosed the overlapping genes between differentially expressed genes (DEGs of aged group compared to young group) and genes in the module of interest. Using these overlapping genes, we conducted GO and Kyoto Encyclopedia of Genes and Genomes (KEGG) pathway enrichment analysis and further identify the central players within the module through network analysis. We concluded that *ELAVL2*, *RAP2A, RAP2B*, *KLHDC3*, and *CALM1* genes are significantly associated with aging, and may be novel biomarkers involved in neurodegeneration and dementia.

RESULTS

Self-Organizing Feature Map Construction and Cluster Identification

The expression matrix of GSE1572 was used as input dataset. In this dataset, after removing one abnormal sample, 30 samples were detected and used as SOM input features (**Figure 1A**). The expression data of each gene (in total more than 11,000 genes) in all samples was used as input data. We set the number of output neurons of the network to 100, and obtained the neural network after training (**Figure 1C** and **Supplementary Figure 1**). The weight matrix (30 × 100 size) corresponding to each feature was used as the input data of hierarchical clustering to cluster 100 neurons again. 100 neurons were clustered into six categories (**Figures 1B,C**). SOM clustering data showed that the gene expression of neuron 100, 99, and 89 gradually decreased with age. Next, we checked the expression levels of genes in these three clusters (**Figures 1B,D**). It was revealed that 240 genes, including *MAPT*, *MAP2*, *MAPK3*, *SYN2*, *RAP2A, RAP2B*, *KLHDC3,* and *CALM1*, gradually downregulated with aging.

Weight Gene Co-expression Network Construction and Module Identification

Before WGCNA, the genes detected in GSE1572 were filtered according to the filtering procedure described in "Materials and Methods" section, and 5,000 genes were obtained. Then the 30 samples' microarray data were read by R for Hierarchical clustering (**Supplementary Figure 2A**). Finally, 30 sets of data were obtained and matched to age (**Supplementary Figure 2B**). WGCNA was performed to identify gene co-expression networks associated with age. In the co-expression network, the degree of association between a module and other modules can be evaluated by the average connection degree and scale independence. Specifically, the closer the mean connectivity is to 0 and the closer the scale independence is to 1, the lower the correlation between modules. In the study, we set the threshold of scale independence to 0.9. We found that when the power value reaches 12, the scale independence can reach 0.9, and the mean connectivity is close to 0 (**Supplementary Figure 3**). Through the calculation of the correlation coefficient between genes, the genes were clustered according to the expression pattern theoretically, and the patterned genes are clustered into the same module. Seventeen co-expressed modules, ranging in size from 37 to 1,524 genes (assigning each module a color for reference), were identified (**Supplementary Table 1** and **Figure 2**).

Finding the Module of Interest, Functional Annotation, and Identification of the Overlapping Genes Between Differentially Expressed Genes in Young/Old Individuals and Genes in the Module of Interest Verified in Weighted Gene Co-expression Network Analysis

To identify modules most significantly associated with age, the Pearson's correlation coefficient between the module and age was

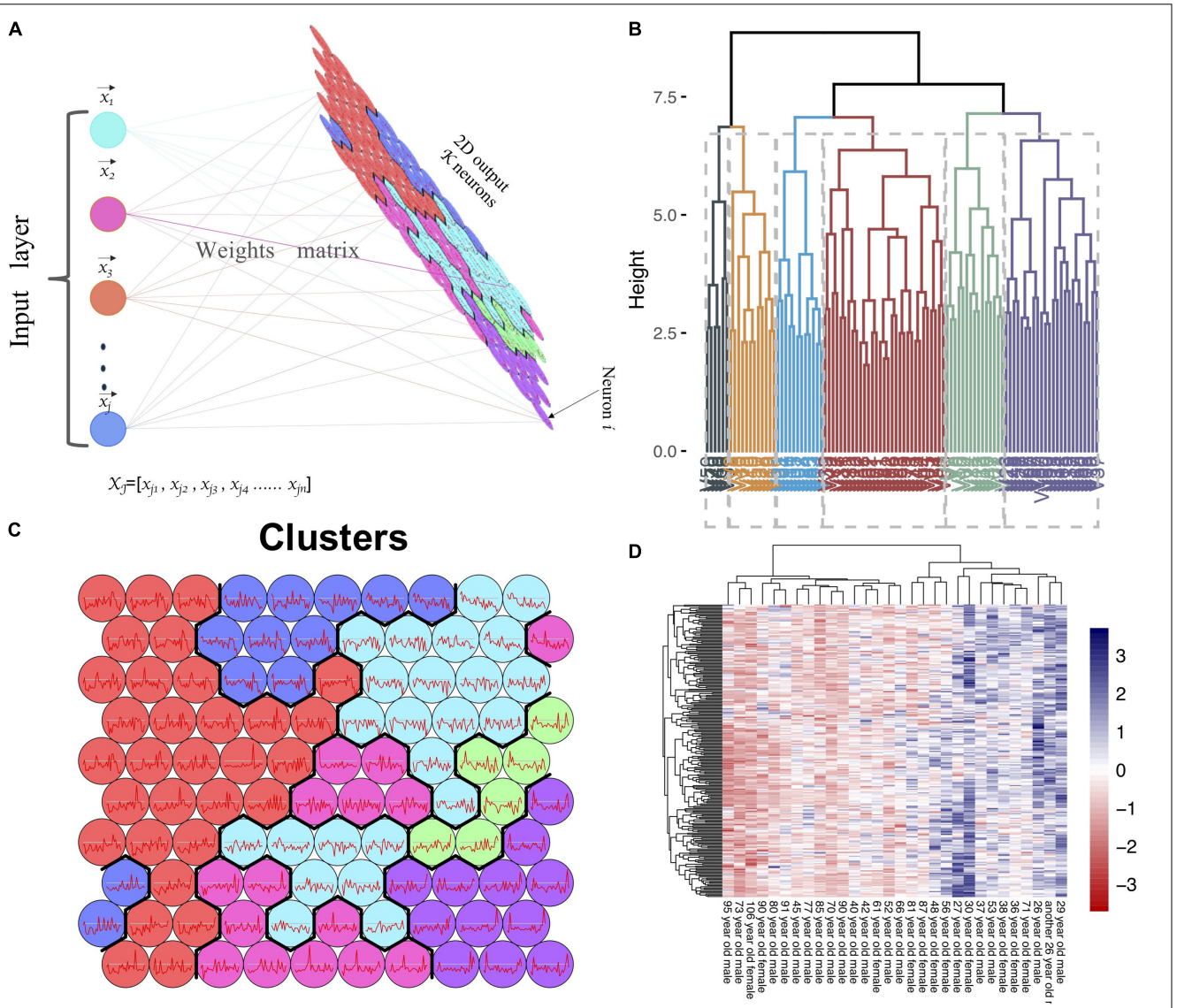

FIGURE 1 | SOM clustering of genes based on microarray data. **(A)** Flow chart of SOM clustering, x_{jn} refers to the gene j expression level in nth sample, neuron i refers to the i cluster. **(B)** Hierarchical clustering on SOM clustering results; each 100 sub-clusters were divided into six major clusters. **(C)** The expression trend of genes in each neuron in the samples (Neuron 1–100, from bottom to top, from left to right). **(D)** The heatmap of gene expression in neuron 89, 99, and 100.

calculated. The highest negative association in the module trait relationship was found between yellowgreen module and age score (cor = −0.83, $p < 0.001$, **Figure 2B**). Thus, yellowgreen module was selected as the module of interest in subsequent analyses. To confirm the correlation between module of interest and age, labeleHeatmap function was used to calculate the correlation values of module membership with gene significance (age) in the greenyellow module. The results showed significant correlation of module membership with gene significance in age (cor = 0.81, $p < 0.0001$) in greenyellow module (**Figure 2C**). To find the DEGs between young and aged individuals, the frontal cortical samples were grouped into individuals ≤42 and ≥73 years old and Limma packages were performed (see section "Materials and Methods" for age grouping criteria). About 4% of the genes analyzed were significantly changed (1.5-fold change or more, **Figure 3A**). Next, we performed overlap analysis between downregulated DEGs and genes in greenyellow module using the online veen tool; we found 45 genes in greenyellow module were also down-regulated DEGs (**Figures 3B–D**). These genes highly related to aging, and showed decreased expression during aging, suggesting that they might play important roles in age-related degeneration.

Identifying Hub Genes and Gene Functional Annotation

The above identified overlapping genes were subjected to GO functional and KEGG pathway enrichment analyses. Biological processes of overlapping genes were found to focus on

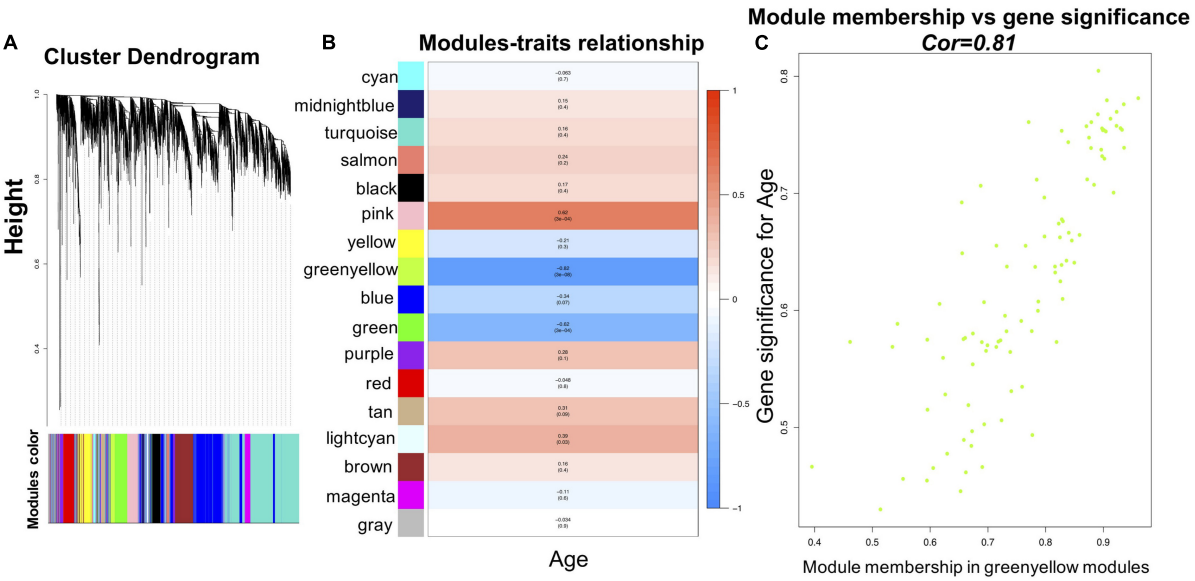

FIGURE 2 | WGCNA analysis of the microarray data. **(A)** Network analysis of gene expression in aging identifies distinct modules of co-expression data. **(B)** Pearson correlation coefficient between the age and module eigengene, numbers in brackets indicate the corresponding *p*-values. **(C)** Correlation between gene significance (GS) and module membership (MM) for the clinical trait of age of genes in yellowgreen module. Cor represents absolute correlation coefficient between MM and GS.

modulation of chemical synaptic transmission and regulation of trans-synaptic signaling. Cell components of overlapping genes were found to focus on postsynaptic density and axon part; molecule functions of overlapping genes were found to focus on primary active transmembrane transporter activity and P-P-bond-hydrolysis-driven transmembrane transporter activity (**Figure 4**). In KEGG pathway analysis, calcium signaling pathway (p = 1.1498E-06; **Table 1**) and MAPK signaling pathway (p = 0.000027; **Table 1**) were the most significant pathways involved in overlapping genes.

Identification of the Most Significant Genes and Network Construction

To identify the most important genes related to aging, the overlapping genes were further filtered by RF classification. Gene counts were input into RF classifier model, the unimportant genes, such as *ABI2*, *YWHAZ*, *MAPK9*, *RAN* and others were removed, and the 21 retained genes were used for the subsequent analysis (**Figure 5A**). To ascertain the significance of genes and analyze the network in the corresponding modules, the PPI maps were constructed via genemania and String (**Figures 5B,C**). Hub genes in the network, including *MAPT, PAK1, RAP2A, RAP2B, KLHDC3, TPPP,* and *ELAVL2,* were constructed. In the single-cell sequencing database Tubula, we found that the distribution of *KLHDC3* and *RAP2A* in brain cells is very similar, mainly in oligodendrocytes and neurons.

DISCUSSION

In this study, the dataset GSE1572 includes samples from individuals of varying age from 26 years old to 106 years old; such data from multiple samples based on age is a good candidate for SOM clustering and WGCNA analysis. First, we performed the SOM on the whole genome expression data. The SOM algorithm is usually used for data feature extraction, clustering, and classification (Furukawa, 2009). In this study, we used SOM to cluster genes in the expression matrix. In the clustering results of SOM, neurons 100, 89, and 99 are found to be related with aging. The genes in these neurons, such as *MAPT*, *MAP2*, *MAPK3*, *SYN2*, *RAP2A*, *RAP2B*, *KLHDC3,* and *CALM1*, were gradually down-regulated with age. Although SOM can identify some clusters of genes related to aging, this method has certain shortcomings, such as the large number of genes found, which makes it hard to screen key genes, and genes clusters having poor biological interpretation. In order to more accurately find the most relevant genes with aging, weight gene co-expression network was constructed, and we identified 17 co-expressed modules. The expression changes of genes in the same module in different samples are highly similar, indicating consistent effects and potential interaction of these gene-coded proteins in the same pathways during the aging process. Through Pearson's correlation coefficient between the module and age, we obtained the interest module. In order to identify the significant genes, we took the intersection of the genes in the greenyellow module and the differentially expressed genes which were downregulated in aged group, and obtained 45 genes. Furthermore, we found that these overlapping genes of greenyellow module and DEGs also exist in the gene cluster found in SOM, which further confirms that these genes may be related to aging. Further KEGG pathway and GO functional enrichment analyses indicated calcium signaling pathway, long-term potentiation, and MAPK signaling pathway as the most significant pathways in the module. In order to identify genes that

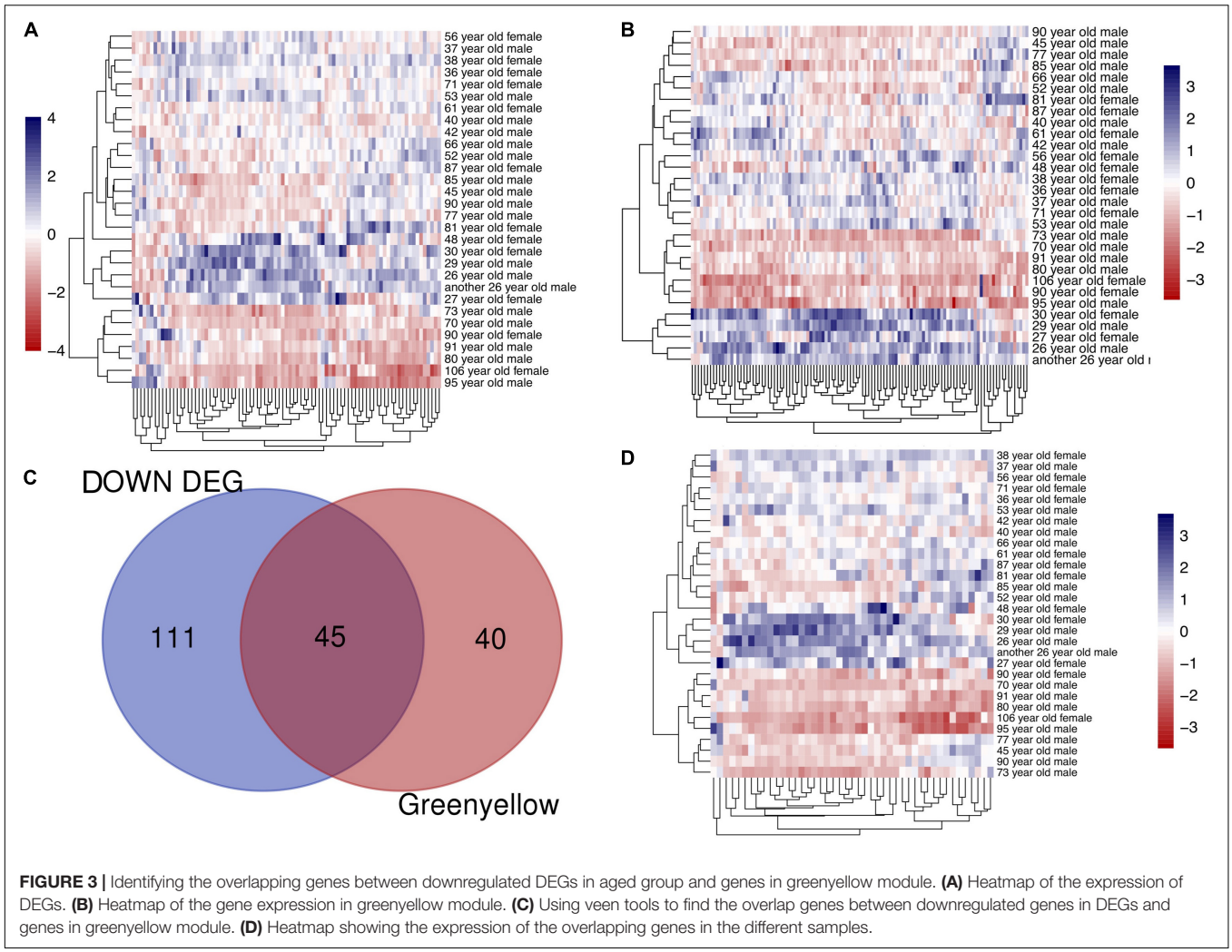

FIGURE 3 | Identifying the overlapping genes between downregulated DEGs in aged group and genes in greenyellow module. **(A)** Heatmap of the expression of DEGs. **(B)** Heatmap of the gene expression in greenyellow module. **(C)** Using veen tools to find the overlap genes between downregulated genes in DEGs and genes in greenyellow module. **(D)** Heatmap showing the expression of the overlapping genes in the different samples.

are most intensively related with aging, we further used one of the machine learning algorithms, Random Forest, and input the expression of the above 45 genes as feature values into the model for training, and finally screened out 21 key genes.

In another study by us (Liang et al., 2018; Chai et al., 2021), we took samples of different brain regions from different Braak stages (GSE131617) and found that microglia-mediated immune system activation plays a crucial role in the early stages of Alzheimer's disease. The samples we used in this study are only samples of the frontal cortex of different ages, and do not contain any clinical diagnosis and pathological changes, which is more conducive to discovering the changes in the brain during the aging process.

Analysis of hub genes showed that *SYN2* might play an important role in aging. In the Cell Component (CC) enrichment analyses, postsynaptic density and distal axon were identified as the most significant CC in the network. In the Biological Process (BP) enrichment analysis, synaptic vesicle localization was revealed to be a significant BP in the network. *SYN2* is a multigene family coding synaptic vesicle (SV) phosphoproteins implicated in the regulation of synaptic transmission and plasticity (Luk et al., 2012). In previous studies, it was shown that *SYN2* knockdown mice display emotional and spatial memory deficits that aggravated during aging (Corradi et al., 2008; Boido et al., 2010). In the co-expression network constructed in the present study, the expression of *SYN2* decreases with the increase of age. We suspected that the decreased expression of *SYN2* is either a result of synapse impairment/loss during aging, or an upstream factor that induces synaptic dysfunction.

In the co-expression network, *MAPT* and *MAP2* were identified as hub genes. *MAPT* encodes microtubule-associated protein tau, which promotes the stability and assembly of microtubules in axon of neurons (Dehmelt and Halpain, 2005; Irwin et al., 2013; Wang and Mandelkow, 2016; Saha and Sen, 2019; Vogels et al., 2019). This was in accordance with the fact that distal axon is a significant CC in the GO enrichment analysis. In age-related tauopathy, tau pathology has been considered as a significant marker in neurodegeneration. *MAP2* gene encodes dendritic marker MAP-2, which is also a microtubule-associated protein (Friedrich and Aszódi, 1991; Dehmelt and Halpain, 2005). Microtubule is a key player in neuronal activities and axoplasmic flow under physiological conditions. In our study, we

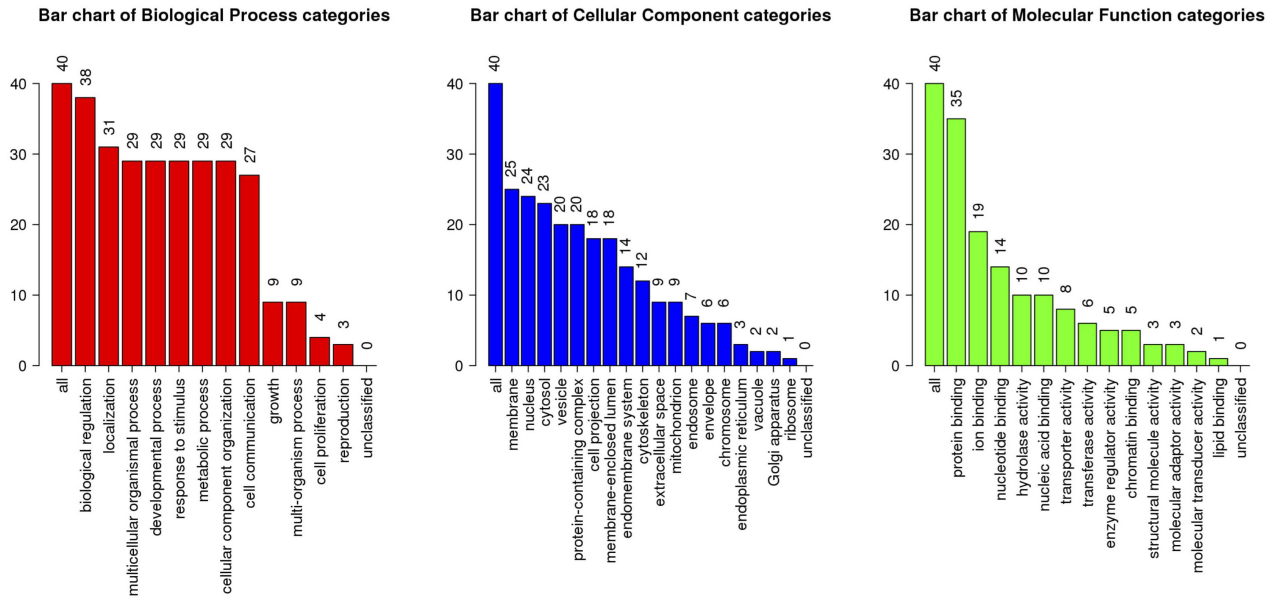

FIGURE 4 | GO enrichment analysis of the overlapping genes. X-axis shows the terms of GO pathway and Y-axis shows the number of genes.

found that with the increase of age, the expression of *MAPT* and MAP2 decreases, which may be a result of neurite degeneration during aging. However, genes that code other skeletal proteins such as tubulin were not identified as hub genes in aging. This result indicates that microtubule-associated proteins tau and MAP-2 may participate in aging-related pathogenesis through mechanisms other than cell skeletal stability.

Analysis of hub genes also showed that *RAP2A* and *RAP2B* were hub genes in the co-expression network. RAP2A and RAP2B belong to the small GTPase superfamily (Emery et al., 2017). Most studies about RAP2A and RAP2B focus on their functions in tumor (Zheng et al., 2017; Zhang et al., 2020). RAP2A is overexpressed in a multitude of human cancers and plays an important role in cytoskeleton rearrangement, arteriogenesis, and cell migration. In neurons, it was found that RAP2 stimulated dendritic pruning, reduced synaptic density, and caused removal of synaptic AMPA receptors, suggesting that RAP2 plays a role in regulating synaptic functions (Kawabe et al., 2010; Hu et al., 2019). In our study, we found that *RAP2A* and *RAP2B* were interacted and co-localized with *MAP2* in the co-expression network and string network. Therefore, RAP2A and RAP2B may have a similar function or cooperate with MAP2. We speculate that the main function of RAP2A in the brain is also involved in regulation of dendritic development and plasticity.

To our surprise, *KLDHC3* was found mainly co-expressed with *RAP2A* and *RAP2B* in the co-expression network. Its related pathways are Unfolded Protein Response (UPR) and metabolism of proteins, and a few studies report its function in the brain (Niculescu et al., 2015). In our study, *KLHDC3* and *RAP2A* are consistently distributed in different cells in the brain (**Figures 5D–F**), so we speculate they may also participate in similar functions in the brain. The decrease of the expression of *KLHDC3* with age may also play a role in the impairment of dendritic and synaptic plasticity during aging. Further studies needed to reveal the function of KLDHC3 in neurons.

At last, *ELAVL2* was characterized as a hub gene with *PAK1*, *MAPT*, *RAP2A*, and *RAP2B* in the same module. Some studies report that ELAVL2-regulated pathways are involved in normal human brain function and their disruption may play a role in neurodevelopmental disorders such as autism spectrum disorder (ASD) (Berto et al., 2016; Ohi et al., 2017; Kato et al., 2019). However, the function of ELAVL2 in the aging brain has not been reported yet. In our study, ELAVL2 was found to be co-localized with PAK1, and co-expressed and interacted with tau. Both tau and PAK1 are involved in axonal guidance and neuronal migration (Dehmelt and Halpain, 2005; Koth et al., 2014). Therefore, we speculate that ELAVL2 may play a consistent role with tau and PAK1 in neurons.

In summary, through machine learning and WGCNA on microarray data from human frontal cortex, we uncovered that *RAP2A, RAP2B, KLHDC3,* and *ELAVL2* may be associated

TABLE 1 | KEGG pathway analysis of the overlapping genes.

geneSet	Description	C	O	*P*-Value
hsa04020	Calcium signaling pathway	183	7	1.15E-06
hsa04014	Ras signaling pathway	232	7	5.62E-06
hsa04010	MAPK signaling pathway	295	7	2.71E-05
hsa04024	cAMP signaling pathway	199	6	2.99E-05
hsa04728	Dopaminergic synapse	131	5	5.00E-05
hsa04720	Long-term potentiation	67	4	5.49E-05
hsa05031	Amphetamine addiction	68	4	5.82E-05
hsa05161	Hepatitis B	144	5	7.86E-05
hsa04723	Retrograde endocannabinoid signaling	148	5	8.95E-05
hsa04012	ErbB signaling pathway	85	4	1.40E-04

with aging. The proteins encoded by these genes may play a coordinated role in the brain with the proteins tau, MAP-2, SYN, and CALM family in neurodegenerative diseases, which may be novel biomarkers of neurodegenerative diseases caused by aging.

MATERIALS AND METHODS

Data Acquisition and Preprocessing

The data used in this paper was obtained from the GEO database in NCBI[1] (Gene Expression Omnibus), and the data entry number is GSE1572 (Lu et al., 2004). The platform is Affymetrix Human Genome U95 Version 2 Array [HG_U95Av2]. Gene expression in the frontal cortex of 18 normal males and 12 normal females at 26–106 years old was detected. The normalized data was downloaded and the expression matrix was obtained, and data filtering was performed before WGCNA analysis. For data filtering, the standard deviation of the gene expression was calculated to obtain a list with decreasing standard deviations, the first 5,000 genes with large standard deviations were obtained, and the probe without corresponding annotation information were removed. There were about 11,000 genes in the dataset; after the data preprocessing, we kept 5,000 genes for further analysis.

[1]https://www.ncbi.nlm.nih.gov/geo/query/acc.cgi?acc=GSE1572

Finding Genes With Highly Similar Expression Pattern Through Self-Organizing Feature Map Algorithm

The SOM clustering was constructed by kohonen package based on R 3.4.2 (Furukawa, 2009). The 31 frontal cortical samples were treated as 31 input features. The expression counts of each gene in 31 samples are used as input data. Through inputting the data to SOM cluster model to cluster the genes, we can obtain the cluster to show which gene expression decreases with aging.

Construction of Weighted Gene Co-expression Network and Identification of Significant Modules

Data was processed using R 3.4.2 software. To ensure that the results of network construction are reliable, abnormal samples were removed. Then, the weighted gene co-expression network was constructed by WGCNA package based on R 3.4.2. First, the Pearson correlation coefficient was calculated to assess the similarity of the gene expression profiles. Second, the correlation coefficients between genes were weighted by a power function to obtain a scale-free network. A gene module is a cluster of densely interconnected genes in terms of co-expression. Then, hierarchical cluster was used to identify gene modules and different modules were

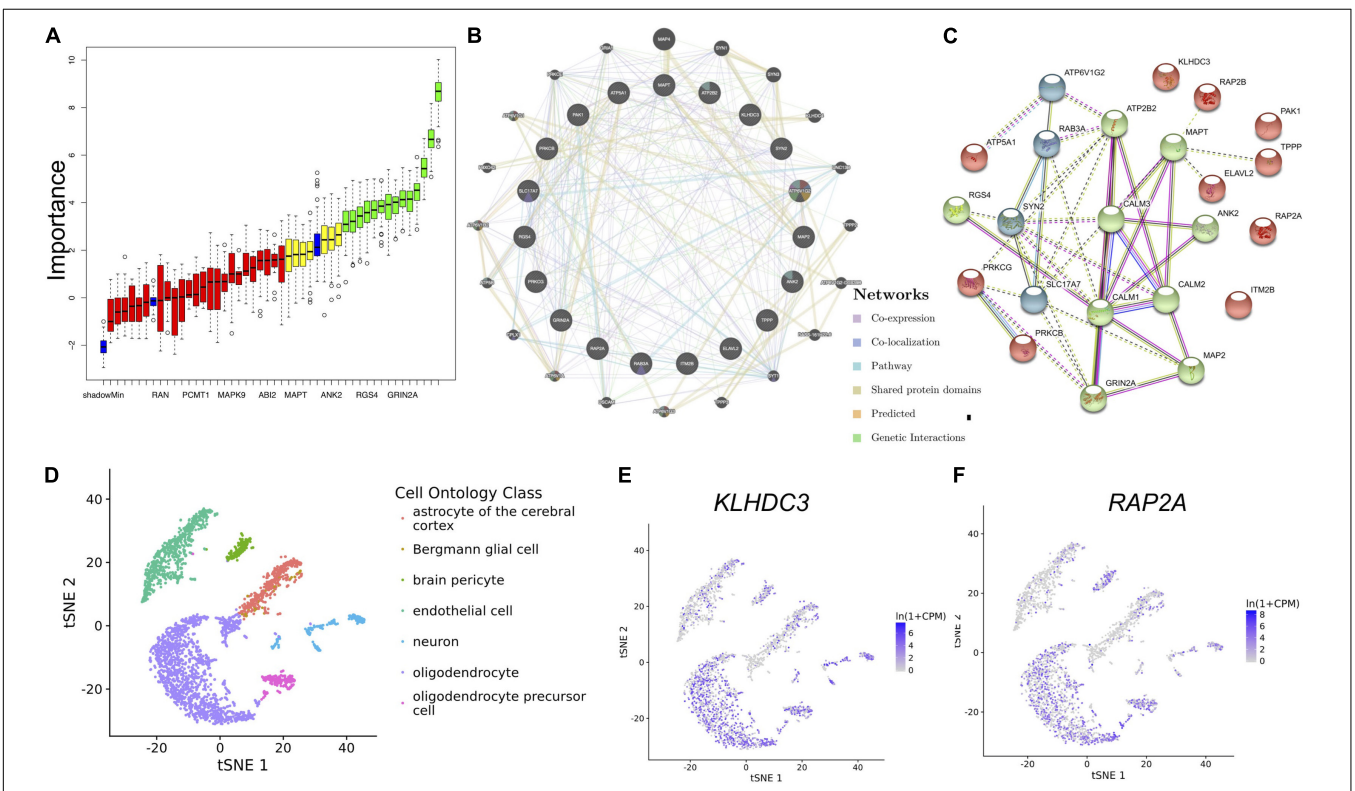

FIGURE 5 | Identifying the most important genes via RF and the cellular distribution of the important genes in the brain. **(A)** Random Forest algorithm result. The blue box plot corresponds to the minimum, average, and maximum Z scores of a color attribute. The red, yellow, and green boxes represent the Z scores of rejected, tentative, and confirmed genes, respectively. **(B)** The PPI network of important genes via genemalia. **(C)** The PPI network of important genes via String. **(D)** The scatterplot shows the distribution of different kinds of cells in TSNE. **(E,F)** KLHDC3 and RAP2A expression in different cell types.

represented by different colors. Dynamic treecut method was used to identify different modules, the adjacency matrix was converted to a topology overlay matrix (TOM), and modules were detected by cluster analysis during module selection.

Correlation Analysis of Gene Modules With Clinical Phenotype

To detect the associations of modules to clinical phenotype (age), first, the age data and gene expression data were correlated using the match function. Secondly, the associations of the module eigengene (ME) to the age were calculated by Pearson's correlation analysis. Modules showing significant association to age were obtained. At last, to further confirm the modules with significant correlation to age, the correlation coefficient between the module membership (gene expression level) with gene significance (GS, for assessing the association of genes with phenotypes) was calculated using the labeleHeatmap function, and the *p*-values were obtained.

Finding the Overlapping Genes Between the Differentially Expressed Genes (DEGs in Aged Compared to Young Group) and Genes in the Module of Interest Verified by Weighted Gene Co-expression Network Analysis

The frontal cortical samples were grouped into individuals ≤42 (young group) and ≥73 years (aged group) and Limma packages were performed to find the DEGs; the group of individuals ≤42 years old showed the most homogeneous pattern of gene expression, and the group ≥73 years old was also relatively homogeneous. Moreover, these two age groups were negatively correlated with each other. In contrast, the middle age group ranging in age from 45 to 71 exhibited much greater heterogeneity, with some cases resembling the young group and others resembling the aged group (Lu et al., 2004; Ritchie et al., 2015). Next, the overlapping genes between downregulated DEGs and genes in the module of interest were discovered by using online veen tools.[2]

Gene Ontology and Kyoto Encyclopedia of Genes and Genomes Pathway Enrichment Analyses, Identification of Hub Genes, and Protein-Protein Interaction Analysis

For the obtained overlapping genes, functional enrichment of Gene Ontology (GO) and KEGG pathways analyses were performed using GSAT (Zhang et al., 2005)[3] and GOplot packages based on R3.4.2. *P*-value < 0.05 was considered to be significant enrichment. These genes were also analyzed using cytoHubba in Cytoscape for identification of hub genes. The identified hub genes were further confirmed and analyzed using genemania (Warde-Farley et al., 2010).[4] String network was constructed by the online tools String.[5]

Application of Random Forest Algorithm to Find the Most Important Genes Related to Aging

The frontal cortical samples were grouped into individuals ≤42 (young) and ≥73 years (old). Through inputting the overlapping genes counts into random forest classifier model to predict which group the samples belong to, the most important overlapping genes for the most accurate model for grouping were identified.

Exploring the Cellular Distribution of the Identified Genes

By using the single cell RNA-seq database Tubula[6] (Tabula Muris Consortium et al., 2018), the cellular distribution of the identified important genes were further explored.

DATA AVAILABILITY STATEMENT

The datasets presented in this study can be found in online repositories. The names of the repository/repositories and accession number(s) can be found below: https://www.ncbi.nlm.nih.gov/geo/query/acc.cgi?acc=GSE1572.

AUTHOR CONTRIBUTIONS

KC contributed to the study design, performed the experiments, and contributed to the writing of the manuscript. JL contributed to the study design and the writing of the manuscript. XZ, PC, SC, WY, HG, RL, and WH conducted the experiments. CP, GL, and DS provided critical devices and contributed to the study design. All authors read and approved the final manuscript.

FUNDING

This work was supported by the National Natural Science Foundation of China (No. 31970964) and the Natural Science Foundation of Hubei Province, China (No. 2019CFB436).

ACKNOWLEDGMENTS

We acknowledge GEO database for providing their platforms and contributors for uploading their meaningful datasets.

SUPPLEMENTARY MATERIAL

The Supplementary Material for this article can be found online at: https://www.frontiersin.org/articles/10.3389/fnagi.2021.707165/full#supplementary-material

[2]http://bioinformatics.psb.ugent.be/webtools/Venn/

[3]http://www.webgestalt.org/option.php

[4]http://genemania.org

[5]http://string-db.org

[6]https://tabula-muris.ds.czbiohub.org

REFERENCES

Berto, S., Usui, N., Konopka, G., and Fogel, B. L. (2016). ELAVL2-regulated transcriptional and splicing networks in human neurons link neurodevelopment and autism. *Hum. Mol. Genet.* 25, 2451–2464. doi: 10.1093/hmg/ddw110

Boido, D., Farisello, P., Cesca, F., Ferrea, E., Valtorta, F., Benfenati, F., et al. (2010). Cortico-hippocampal hyperexcitability in synapsin I/II/III knockout mice: age-dependency and response to the antiepileptic drug levetiracetam. *Neuroscience* 171, 268–283. doi: 10.1016/j.neuroscience.2010.08.046

Chai, K., Liang, J., Zhang, X., Gu, H., Cao, P., Ye, W., et al. (2021). ARHGDIB Plays a Novel Role in the Braak Stages of Alzheimer's Diseases via the Immune Response Mediated by Microglia. *bioRxiv* [Preprint] doi: 10.21203/rs.3.rs-474315/v1

Corradi, A., Zanardi, A., Giacomini, C., Onofri, F., Valtorta, F., Zoli, M., et al. (2008). Synapsin-I- and synapsin-II-null mice display an increased age-dependent cognitive impairment. *J. Cell Sci.* 121, 3042–3051. doi: 10.1242/jcs.035063

Dehmelt, L., and Halpain, S. (2005). The MAP2/Tau family of microtubule-associated proteins. *Genome Biol.* 6:204. doi: 10.1186/gb-2004-6-1-204

Emery, A. C., Xu, W., Eiden, M. V., and Eiden, L. E. (2017). Guanine nucleotide exchange factor Epac2-dependent activation of the GTP-binding protein Rap2A mediates cAMP-dependent growth arrest in neuroendocrine cells. *J. Biol. Chem.* 292, 12220–12231. doi: 10.1074/jbc.M117.790329

Friedrich, P., and Aszódi, A. (1991). MAP2: a sensitive cross-linker and adjustable spacer in dendritic architecture. *FEBS Lett.* 295, 5–9. doi: 10.1016/0014-5793(91)81371-e

Furukawa, T. (2009). SOM of SOMs. *Neural. Netw.* 22, 463–478. doi: 10.1016/j.neunet.2009.01.012

Hou, Y., Dan, X., Babbar, M., Wei, Y., Hasselbalch, S. G., Croteau, D. L., et al. (2019). Ageing as a risk factor for neurodegenerative disease. *Nat. Rev. Neurol.* 15, 565–581. doi: 10.1038/s41582-019-0244-7

Hu, Y., Hong, X.-Y., Yang, X.-F., Ma, R.-H., Wang, X., Zhang, J.-F., et al. (2019). Inflammation-dependent ISG15 upregulation mediates MIA-induced dendrite damages and depression by disrupting NEDD4/Rap2A signaling. *Biochim. Biophys. Acta Mol. Basis Dis.* 1865, 1477–1489. doi: 10.1016/j.bbadis.2019.02.020

Irwin, D. J., Lee, V. M.-Y., and Trojanowski, J. Q. (2013). Parkinson's disease dementia: convergence of α-synuclein, tau and amyloid-β pathologies. *Nat. Rev. Neurosci.* 14, 626–636. doi: 10.1038/nrn3549

Juan, S. M. A., and Adlard, P. A. (2019). Ageing and cognition. *Subcell. Biochem.* 91, 107–122. doi: 10.1007/978-981-13-3681-2_5

Kato, Y., Iwamori, T., Ninomiya, Y., Kohda, T., Miyashita, J., Sato, M., et al. (2019). ELAVL2-directed RNA regulatory network drives the formation of quiescent primordial follicles. *EMBO Rep.* 20:e48251. doi: 10.15252/embr.201948251

Kawabe, H., Neeb, A., Dimova, K., Young, S. M., Takeda, M., Katsurabayashi, S., et al. (2010). Regulation of Rap2A by the ubiquitin ligase Nedd4-1 controls neurite development. *Neuron* 65, 358–372. doi: 10.1016/j.neuron.2010.01.007

Koth, A. P., Oliveira, B. R., Parfitt, G. M., Buonocore, J., de, Q., and Barros, D. M. (2014). Participation of group I p21-activated kinases in neuroplasticity. *J. Physiol. Paris* 108, 270–277. doi: 10.1016/j.jphysparis.2014.08.007

Langfelder, P., and Horvath, S. (2008). WGCNA: an R package for weighted correlation network analysis. *BMC Bioinformatics* 9:559. doi: 10.1186/1471-2105-9-559

Liang, J.-W., Fang, Z.-Y., Huang, Y., Liuyang, Z.-Y., Zhang, X.-L., Wang, J.-L., et al. (2018). Application of weighted gene co-expression network analysis to explore the key genes in Alzheimer's disease. *J. Alzheimers Dis.* 65, 1353–1364. doi: 10.3233/JAD-180400

Lu, T., Pan, Y., Kao, S.-Y., Li, C., Kohane, I., Chan, J., et al. (2004). Gene regulation and DNA damage in the ageing human brain. *Nature* 429, 883–891. doi: 10.1038/nature02661

Luk, K. C., Kehm, V., Carroll, J., Zhang, B., O'Brien, P., Trojanowski, J. Q., et al. (2012). Pathological -synuclein transmission initiates parkinson-like neurodegeneration in nontransgenic mice. *Science* 338, 949–953. doi: 10.1126/science.1227157

Niculescu, A. B., Levey, D. F., Phalen, P. L., Le-Niculescu, H., Dainton, H. D., Jain, N., et al. (2015). Understanding and predicting suicidality using a combined genomic and clinical risk assessment approach. *Mol. Psychiatry* 20, 1266–1285. doi: 10.1038/mp.2015.112

Ohi, K., Shimada, T., Yasuyama, T., Kimura, K., Uehara, T., and Kawasaki, Y. (2017). Spatial and temporal expression patterns of genes around nine neuroticism-associated loci. *Prog. Neuropsychopharmacol. Biol. Psychiatry* 77, 164–171. doi: 10.1016/j.pnpbp.2017.04.019

Ritchie, M. E., Phipson, B., Wu, D., Hu, Y., Law, C. W., Shi, W., et al. (2015). limma powers differential expression analyses for RNA-sequencing and microarray studies. *Nucleic Acids Res.* 43, e47. doi: 10.1093/nar/gkv007

Saha, P., and Sen, N. (2019). Tauopathy: a common mechanism for neurodegeneration and brain aging. *Mechan. Ageing Dev.* 178, 72–79. doi: 10.1016/j.mad.2019.01.007

Stern, Y. (2012). Cognitive reserve in ageing and Alzheimer's disease. *Lancet Neurol.* 11, 1006–1012. doi: 10.1016/S1474-4422(12)70191-6

Tabula Muris Consortium, Overall coordination, Logistical coordination, Organ collection and processing, Library preparation and sequencing, Computational data analysis, et al. (2018). Single-cell transcriptomics of 20 mouse organs creates a Tabula Muris. *Nature* 562, 367–372. doi: 10.1038/s41586-018-0590-4

Vogels, T., Murgoci, A.-N., and Hromádka, T. (2019). Intersection of pathological tau and microglia at the synapse. *Acta Neuropathol. Commun.* 7:109. doi: 10.1186/s40478-019-0754-y

Wang, Y., and Mandelkow, E. (2016). Tau in physiology and pathology. *Nat. Rev. Neurosci.* 17, 5–21. doi: 10.1038/nrn.2015.1

Warde-Farley, D., Donaldson, S. L., Comes, O., Zuberi, K., Badrawi, R., Chao, P., et al. (2010). The GeneMANIA prediction server: biological network integration for gene prioritization and predicting gene function. *Nucleic Acids Res.* 38, W214–W220. doi: 10.1093/nar/gkq537

Wyss-Coray, T. (2016). Ageing, neurodegeneration and brain rejuvenation. *Nature* 539, 180–186. doi: 10.1038/nature20411

Yankner, B. A., Lu, T., and Loerch, P. (2008). The aging brain. *Annu. Rev. Pathol. Mech. Dis.* 3, 41–66. doi: 10.1146/annurev.pathmechdis.2.010506.092044

Zhang, B., Kirov, S., and Snoddy, J. (2005). WebGestalt: an integrated system for exploring gene sets in various biological contexts. *Nucleic Acids Res.* 33, W741–W748. doi: 10.1093/nar/gki475

Zhang, J., Wei, Y., Min, J., Wang, Y., Yin, L., Cao, G., et al. (2020). Knockdown of RAP2A gene expression suppresses cisplatin resistance in gastric cancer cells. *Oncol. Lett.* 19, 350–358. doi: 10.3892/ol.2019.11086

Zheng, X., Zhao, W., Ji, P., Zhang, K., Jin, J., Feng, M., et al. (2017). High expression of Rap2A is associated with poor prognosis of patients with hepatocellular carcinoma. *Int. J. Clin. Exp. Pathol.* 10, 9607–9613.

Conflict of Interest: The authors declare that the research was conducted in the absence of any commercial or financial relationships that could be construed as a potential conflict of interest.

frontiers in Aging Neuroscience

SYSTEMATIC REVIEW
published: 20 October 2021
doi: 10.3389/fnagi.2021.755160

The Correlation Between Olfactory Test and Hippocampal Volume in Alzheimer's Disease and Mild Cognitive Impairment Patients: A Meta-Analysis

Ming-Wan Su[1†], *Jing-Nian Ni*[2†], *Tian-Yu Cao*[1], *Shuo-Shi Wang*[1], *Jing Shi*[2*] and *Jin-Zhou Tian*[2*]

[1] Dongzhimen Hospital, Beijing University of Chinese Medicine, Beijing, China, [2] Department of Neurology, Dongzhimen Hospital, Beijing University of Chinese Medicine, Beijing, China

OPEN ACCESS

Edited by:
Ping Wu,
Fudan University, China

Reviewed by:
Carlos Ayala Grosso,
Instituto Venezolano de Investigaciones Cientificas, IVIC, Venezuela
Liping Fu,
China-Japan Friendship Hospital, China

***Correspondence:**
Jing Shi
shijing87@hotmail.com
Jin-Zhou Tian
jztian@hotmail.com

[†] These authors have contributed equally to this work and share first authorship

Received: 08 August 2021
Accepted: 22 September 2021
Published: 20 October 2021

Citation:
Su M-W, Ni J-N, Cao T-Y, Wang S-S, Shi J and Tian J-Z (2021) The Correlation Between Olfactory Test and Hippocampal Volume in Alzheimer's Disease and Mild Cognitive Impairment Patients: A Meta-Analysis. Front. Aging Neurosci. 13:755160. doi: 10.3389/fnagi.2021.755160

Background: Previous studies have reported that olfactory identification deficits may be the earliest clinical features of Alzheimer's disease (AD). However, the association between odor identification and hippocampal atrophy remains unclear.

Objective: This meta-analysis quantified the correlation between odor identification test scores and hippocampal volume in AD.

Method: A search of the PUBMED, EMBASE, and WEB OF SCIENCE databases was conducted from January 2003 to June 2020 on studies with reported correlation coefficients between olfactory identification score and hippocampal volume in patients with amnestic AD or mild cognitive impairment (MCI). The quality of the studies was assessed using the Newcastle-Ottawa quality assessment scale (NOS). Pooled *r*-values were combined and computed in R studio.

Results: Seven of 627 original studies on AD/MCI using an olfactory identification test ($n = 902$) were included. A positive correlation was found between hippocampal volume and olfactory test scores ($r = 0.3392$, 95% CI: 0.2335–0.4370). Moderator analysis showed that AD and MCI patients were more profoundly correlated than normal controls (AD: $r = 0.3959$, 95% CI: 0.2605–0.5160; MCI: $r = 0.3691$, 95% CI: 0.1841–0.5288; NC: $r = 0.1305$, 95% CI: −0.0447–0.2980). Age difference and patient type were the main sources of heterogeneity in this analysis.

Conclusion: The correlation appears to be more predominant in the cognitive disorder group (including MCI and AD) than in the non-cognitive disorder group. Age is an independent factor that affects the severity of the correlation during disease progression. The mildness of the correlation suggests that olfactory tests may be more accurate when combined with other non-invasive examinations for early detection.

Systematic Review Registration: https://inplasy.com/, identifier INPLASY 202140088.

Keywords: olfactory deficits, hippocampus, mild cognitive impairment, Alzheimer's disease, meta-analysis

INTRODUCTION

Alzheimer's disease (AD) is an insidiously progressive neurodegenerative disease that primarily causes dementia. It is estimated that 44 million people live with this condition (Lane et al., 2018). Mild cognitive impairment (MCI) is a transitional stage between normal cognitive functioning and dementia (Albert et al., 2011). Approximately 15% to 20% of people aged $\geq$ 65 years have MCI and are susceptible to dementia, with a higher conversion rate (Roberts and Knopman, 2013). AD is characterized by memory decline, which is related to pre-mature atrophy of the hippocampus, entorhinal cortex, and other medial temporal lobe structures (Hatashita and Yamasaki, 2013). Alteration in olfactory function often coincides with clinical symptoms and may even precede it (Hawkes, 2003). Olfactory dysfunction (OD) typically occurs in the prodromal stage of AD and can progress to the disease. Since early detection is crucial to prevent and slow progression, OD has been considered as a potential clinical marker for AD prediction, severity, and progression (Servello et al., 2015; Zou et al., 2016b).

Olfactory structures, such as the entorhinal cortex, amygdala, hippocampus, caudate, and other medial temporal lobes have been discovered (Kovács et al., 1999; Karas et al., 2003) to contain classic pathological features, such as neurofibrillary tangles and amyloid-β plaques, which are also observed in olfactory regions in early stage AD and MCI patients, including the olfactory bulb and tract and anterior olfactory nucleus (Hyman et al., 1991). Studies have suggested that aggregation of Aβ and tau proteins occurs in the olfactory neuroepithelium. Nevertheless, the central olfactory structures play a more important role in olfactory dysfunction. Impaired odor identification during lifetime was found to be robustly related to increased density of tangles in the entorhinal cortex and CA1/subiculum region of the hippocampus, but unrelated to other cortical sites after death (Wilson et al., 2007).

Hippocampal atrophy and volumetric measurements are included among the biomarkers of neuronal injury in MCI and AD diagnosis (Albert et al., 2011). In recent years, the link between olfactory identification performance and hippocampal atrophy has been recognized in some cross-sectional and longitudinal studies (Murphy et al., 2003; Kjelvik et al., 2014; Marigliano et al., 2014; Hagemeier et al., 2016). These positive results suggest that olfactory deficits may be a potential biomarker of hippocampal function. The aim of this systematic review and meta-analysis was to examine whether olfactory deficits correlate quantitatively with hippocampal atrophy, and to provide a comprehensive overview of the circumstances under which this correlation may be prominent due to different moderation factors.

METHOD

Search Strategy

Our meta-analysis was prepared according to the PRISMA guidelines and checklist (http://www.prisma-statement.org/PRISMAStatement/Checklist) and was registered with insplay.com. (Systematic Registration Number: INPLASY202140088; doi: 10.37766/inplasy2021.4.0088) Two researchers (M-WS, S-SW) separately conducted an online search for papers from the PUBMED, EMBASE, and WEB OF SCIENCE databases from January 2003 to June 2020 using the MESH terms "Alzheimer's disease" and free words "olfactory" and "hippocampus OR hippocampal" (in the title/abstract). A complementary search of "Mild cognitive impairment" (free words in the title/abstract) substituting "Alzheimer's disease" was repeated. Among the results, we read through the abstract to include the studies that could potentially meet the criteria, then screened the full article for further verification, as well as relevant articles from the references in the full text for **Supplementary Material**.

Study Selection

Studies were included if they met the following criteria: (1) participants with clinical diagnosis of amnestic AD or MCI were involved, with or without a health control; (2) both olfactory testing and hippocampal volumetric counting from MRI images were conducted from both hemisphere; (3) the correlation coefficient could be extracted directly or through calculation from the raw data; (4) studies in English published in peer-reviewed journals from 2003 onwards; (5) study type was a cohort study, case-control or cross-sectional study. The results were filtered to include only those written in English and conducted on living humans.

Quality Assessment

The methodological quality of the included studies was assessed using the Newcastle-Ottawa Quality Assessment Scale (NOS) (Wells et al., 2013) by two independent researchers (M-WS and T-YC). Quality evaluation was applied to assess non-randomized studies. The NOS scale contains four domains including patient selection, comparability, and ascertainment of exposure or outcome of interest for case-control or cohort studies. The scale is assigned from 0 to 9 points, with studies scoring $\geq$ 7 points being considered high quality.

Data Extraction

The coefficient *r* between olfactory test scores and hippocampal volume (either calculated using the Pearson or Spearman method) were extracted in eligible studies, which could be either in total (left and right hippocampal volume) or bilaterally (left or right hippocampal volume). In some studies, the *r*-values were tabulated directly. For others in which these values were absent, SPSS 22.0 software (IBM, Inc., Chicago) was used to calculate the Pearson correlation coefficient if the raw data was obtainable.

However, the *r*-value usually does not follow a normal distribution. Since the variance strongly depends on the correlation, it usually cannot be directly synthesized. The bias from these sample correlations could be partially eliminated through correction of the Fisher estimator (Berry and Mielke, 2000). Thus, an *r* to *Z* transformation—Fisher's *z* transformation—was introduced. The correlation was converted to Fisher's *z*-scale to obtain a normal distribution.

In each study, the effect size was transformed into z through the equation $z' = 0.5\ [\ln(1 + r) - \ln(1 - r)]$. Then, the syntheses of z were performed in the meta-analysis.

Statistical Analysis

Meta-analysis was conducted in *R* language with "meta" package in R-studio Version 1.3.959 (https://rstudio.com/), where random and fixed effect models were applied according to the heterogeneity test. The I^2 statistic was calculated to assess the heterogeneity between studies. We attempted to fit a fixed effect model when the I^2-value is <50%. An I^2-value >50% or p-value < 0.05 suggests a rather heavy inconsistency and high heterogeneity, so we chose a sensitivity and subgroup analysis to render it and further discuss the potential sources.

Subgroups were divided into the following categories: (1) participants, patients/normal; (2) sides, left/right/both; and (3) age groups with a difference of 5 years.

RESULTS

Description of Included Studies

Our search strategy initially identified 627 citations (**Figure 1**). After removing 47 duplicates, 575 studies were excluded by viewing the abstract for the animal model ($n = 218$) or non-relevance ($n = 351$). Eleven papers met the inclusion criteria (Murphy et al., 2003; Devanand et al., 2008, 2010; Wang et al., 2010; Lojkowska et al., 2011; Kjelvik et al., 2014; Marigliano et al., 2014; Vasavada et al., 2015; Hagemeier et al., 2016; Wu et al., 2019; Yu et al., 2019), among which four studies were excluded by screening the full article for specific reasons: the correlation in one study (Devanand et al., 2008) cannot be calculated or extracted through proper methods due to incomplete records; another (Kjelvik et al., 2014) presented a coefficient in a linear regression model; and two studies demonstrated the hippocampal volume either in an fMRI activated form (Wang et al., 2010) or volume changes in a 24-month follow-up study (Lojkowska et al., 2011).

A total of seven studies were included in the meta-analysis (**Table 1**). Five of the seven studies were considered high-quality (**Table 2**). Follow-up research was performed in a pilot study (Marigliano et al., 2014) which contains a baseline TDI score, hippocampal volume, and 12-month follow-up data. We computed the Pearson correlation coefficient r from the baseline data, since the baseline participants were all clinically confirmed aMCI participants. A cohort study (Devanand et al., 2010) initially enrolled 1,092 participants, 571 of whom had undergone hippocampal volume measurement with olfactory data.

All seven studies yielded 22 effect sizes and 902 participants. The participants were clinically diagnosed with MCI/AD or normal controls. In four studies (Murphy et al., 2003; Hagemeier et al., 2016; Wu et al., 2019; Yu et al., 2019), the correlation coefficients were computed bilaterally according to hippocampal volume measurements on each side. In the three remaining studies (Devanand et al., 2010; Marigliano et al., 2014; Vasavada et al., 2015), r was calculated from the double-sided volume in total.

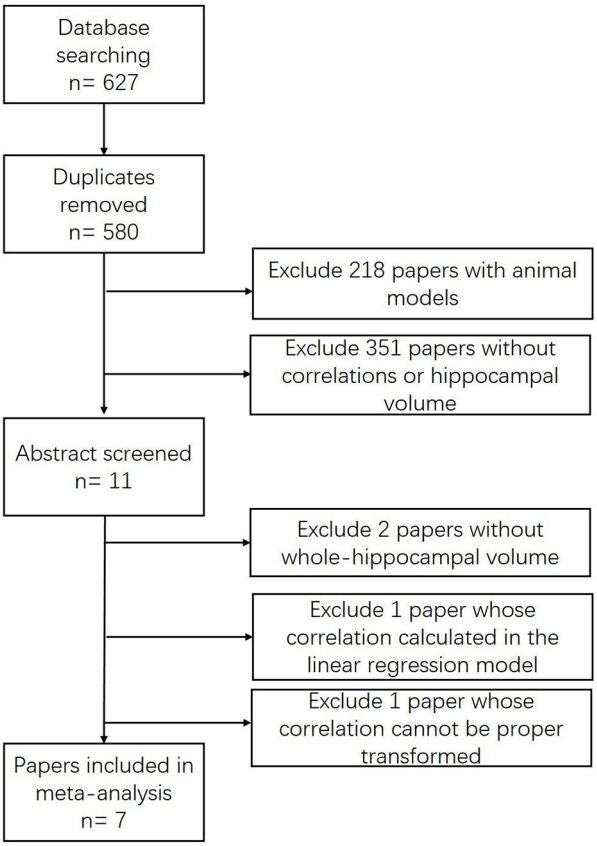

FIGURE 1 | Flow chart of study selection.

Association Between Olfactory Tests Score and Hippocampal Volumes

There was a positive correlation between olfactory test scores and hippocampal volume ($r = 0.3392$, 95% CI: 0.2335–0.4370, $p < 0.0001$) (**Figure 2**). Egger's regression test revealed an overall reporting bias ($p = 0.029$). A trim-and-fill funnel plot showed a weak positive correlation ($r = 0.2074$, 95% CI: 0.0876–0.3214, $p < 0.0001$). Further, an influential analysis identified that no outliers in the included studies could reverse the analytical results using the leave-one-out method (**Figure 3**). Moreover, there was moderate heterogeneity in the sample of all included studies ($I^2 = 57\%$, $p < 0.01$).

Moderator Effects

To investigate potential sources of heterogeneity, we performed a subgroup analysis with several moderator variables, including patient type, age, hemisphere, and olfactory tests. The following results revealed that patient type and age might be the two possible sources of heterogeneity.

A significant difference in the correlation between the AD, MCI, and NC groups was discovered. The moderator analysis for patient type was significant ($Q = 17.64$; $p = 0.0014$), suggesting that this variable may contribute to heterogeneity. Subgroups of AD ($r = 0.3959$, 95% CI: 0.2605–0.5160, $k = 6$), MCI ($r = 0.3691$,

TABLE 1 | Demographic data and relevant parameters.

References	Subject	*N*	Age	Sex (M/F)	Olfactory test	MMSE	Correlation *r*		Side(s)
Devanand et al., 2010	MCI	571	–	–	UPSIT	–	MCI + NC	0.16	Double
	NC								
Hagemeier et al., 2016	aMCI	19	73.6 ± 11	9/10	22.9 ± 8.6	–	AD	0.394	Right
	AD	42	76 ± 9	18/24	21.1 ± 7.9		aMCI	0.675	
	NC	19	69.4 ± 2.9	6/13	30.0 ± 6.7		NC	−0.185	
					UPSIT		AD	0.364	Left
							aMCI	0.438	
							NC	−0.132	
Vasavada et al., 2015	MCI	21	73.2 ± 9.0	10/11	24.2 ± 8.6	26.5 ± 1.9	AD + MCI + N	0.55	Double
	AD	16	71.9 ± 11.9	5/10	15.5 ± 8.4	18.9 ± 5.4	AD + MCI	0.33	
	NC	27	69.5 ± 10.4	12/15	34.0 ± 4.2	28.5 ± 1.5			
					UPSIT				
Wu et al., 2019	MCI	27	68.04 ± 7.58	13/14	CSIT	26 (25, 28)	AD	0.242	Right
	AD	37	66.86 ± 10.27	17/20		16.03 ± 4.04	MCI	0.231	
	NC	30	67.23 ± 6.71	11/19		29 (28, 30)	NC	0.167	
							TOTAL	0.512	
							AD	0.323	Left
							MCI	0.088	
							NC	0.326	
							TOTAL	0.512	
Yu et al., 2019	MCI	31	65.9 ± 7.9	14/17	UPSIT	–	MCI + NC	0.42	Right
	NC	9	66.44 ± 7.05	3/6			MCI + NC	0.55	Left
Marigliano et al., 2014	aMCI	18	68.05 ± 3.5	9/9	SSET	–		0.508	Double
Murphy et al., 2003	AD	13	73.08 ± 2.19	8/5	SDOIT	22.85 ± 1.04	AD	0.54	Right
	NC	22	72.45 ± 1.78	10/12		29.68 ± 0.12	NC	0.23	
							AD	0.85	Left
							NC	0.17	

M/F, Male/Female; MMSE, Mini-Mental State Examination; UPSIT, University of Pennsylvania Smell Identification Test; CSIT, Chinese smell identification test; SSET, Sniffin Sticks Extended Test; SDOIT, San Diego Odor Identification Test; MCI, mild cognitive impairment; NC, normal control; AD, Alzheimer's disease.

95% CI: 0.1841–0.5288, $k = 5$), and NC ($r = 0.1305$, 95% CI: −0.0447–0.2980, $k = 6$) were not significant in heterogeneity (AD: $I^2 = 27\%$, $p = 0.12$; MCI: $I^2 = 36\%$, $p = 0.18$; $I^2 = 0\%$, $p = 0.53$). The differences were not significant between AD and non-AD (MCI + NC) (AD: $r = 0.4222$, 95% CI: 0.2372–0.5776, $k = 6$; non-AD: $r = 0.2728$, 95% CI: 0.1494–0.3879, $k = 14$; $p = 0.1735$), AD and MCI ($p = 0.8072$), but significant in AD and NC ($p = 0.0154$) and AD. The correlation was significantly stronger in the patient group than in the control group ($p = 0.0121$) and in the AD group than in the MCI group, indicating a pathology-dependent penetrance (**Figure 4**).

The olfactory deficits were found to be most correlated in the age range of 70.6–75.6 years old ($r = 0.5113$, 95% CI: 0.3181–0.6637, $k = 7$) showing a low risk of heterogeneity ($I^2 = 46\%$, $p = 0.08$), and more predominantly than the 65.6–70.6 years group ($r = 0.2698$, 95%CI: 0.1376–0.3926, $k = 11$) and the 75.6–80.6 years group ($r = 0.2591$, 95% CI: 0.0809–0.4211, $k = 3$). The mean age of all the participants was 75.20 years (range from 66.86 to 80.6 years). For a mean age difference of 5 years, the moderator analysis was statistically significant ($Q = 17.14$, $p = 0.0002$).

The moderator analysis for hemisphere was not significant ($Q = 5.02$, $p = 0.0811$), suggesting that lateralization of odor memory might not contribute to the observed heterogeneity. Moreover, no obvious hemispheric dominance was found in olfaction (left: $r = 0.35$, 95% CI: 0.2318–0.4615, $I^2 = 53\%$, $p = 0.03$; right: $r = 0.31$, 95% CI: 0.1905–0.4268, $I^2 = 27\%$, $p = 0.20$). We further investigated the lateralization among patient groups and subgroup effects in the left hippocampus group. The hemispheric parameters in patients were not significant.

In all seven studies, odor identification scores were obtained using various methods: the University of Pennsylvania Smell Identification Test (UPSIT) in four studies (Vasavada et al., 2015; Hagemeier et al., 2016; Marin et al., 2018; Yu et al., 2019), the Chinese smell identification test (CIST) in Wu et al. (2019),

TABLE 2 | The Newcastle-Ottawa scale (NOS).

References	Selection				Comparability	Exposure			Scores
	Adequate definition of cases	Representativeness of the cases	Selection of controls	Definition of controls	Control for important factor	Ascertainment of exposure	Same method of ascertainment for cases and controls	Non-response rate	
Hagemeier et al., 2016	✵	✵	✵	✵	✵	✵	✵	–	7
Vasavada et al., 2015	✵	✵	–	✵	✵✵	✵	✵	–	7
Wu et al., 2019	✵	✵	✵	✵	✵✵	✵	✵	–	8
Yu et al., 2019	✵	✵	✵	✵	✵✵	✵	✵	–	8
Murphy et al., 2003	✵	✵	–	✵	✵	✵	✵	–	6
	Selection				**Comparability**	**Outcome**			
	Representativeness of the exposed cohort	Selection of the non-exposed cohort	Ascertainment of exposure	Demonstration that outcome of interest was not present at start of study	Comparability of cohorts on the basis of the design or analysis	Assessment of outcome	Enough follow-up of cohorts	Adequacy of follow-up of cohorts	
Devanand et al., 2010	✵	–	✵	–	✵✵	✵	✵	–	6
Marigliano et al., 2014	✵	–	✵	✵	✵	✵	✵	✵	7

A study can be awarded a maximum of one star for each numbered item within the selection and exposure categories. A maximum of two stars can be given for comparability.

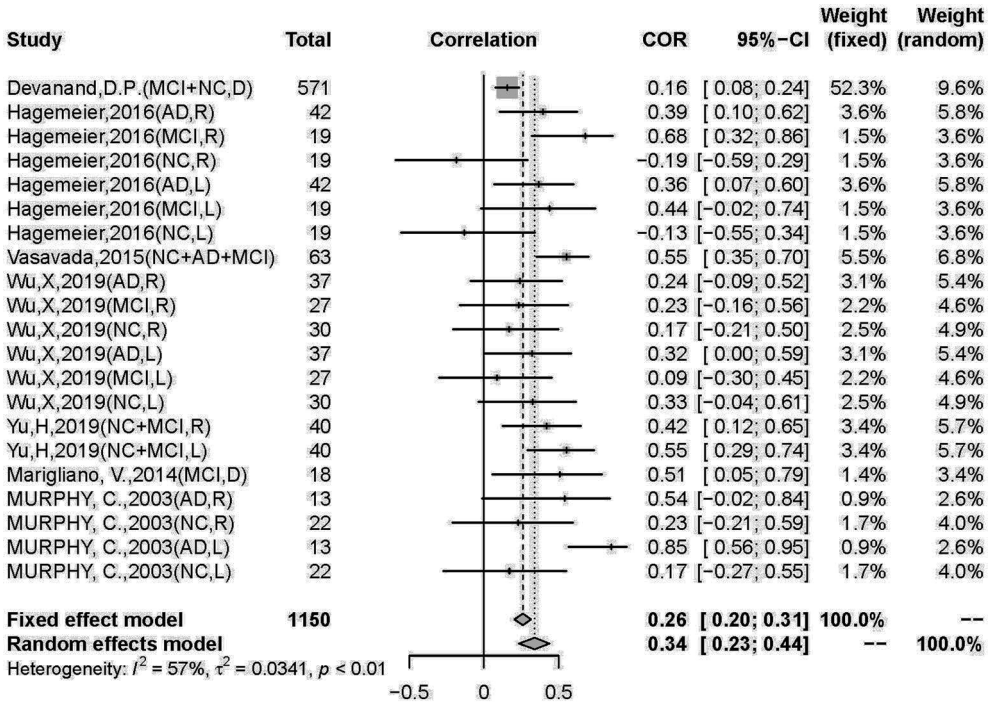

FIGURE 2 | Forest plot summarizing the overall correlation between odor identification score and hippocampal volume across all studies and their 95% interval for each study. (Random effects model selected. NC, normal control; AD, Alzheimer's disease; MCI, mild cognitive impairment; D, hippocampal volume measurement in double sides; R, hippocampal volume measurement in right side; L, hippocampal volume measurement in left side).

the Sniffin Sticks Extended Test (SSET) in Marigliano et al. (2014), and the San Diego Odor Identification Test (SDOIT) in Murphy et al. (2003). The subgroup analysis revealed that the difference between the types of olfactory identification tests was not significant ($Q = 3$, $p = 0.3916$).

Given the lack of demographic figures for gender information, the pooled *r*-value categorized by sex was unable to be detected. The subgroup analysis revealed that part of the heterogeneity was due to subject type and age.

DISCUSSION

Our meta-analysis explored the relationship between odor identification decline and hippocampal atrophy in AD and MCI patients with normal controls. The main result obtained from our meta-analysis showed a significant positive correlation ($r = 0.3392$, 95% CI: 0.2335–0.4370, $p < 0.0001$) between olfactory identification deficits and hippocampal atrophy. A prominent difference was noted in the MCI/AD group, with a stronger correlation than the control group ($p = 0.0121$). In addition, the association in the AD group was stronger than in the MCI group, suggesting that odor identification decline could be detected early in the MCI stage and followed the disease progression.

Moderate heterogeneity was detected, suggesting that the overall combination of associations might not be present across all contexts. This may be due to clinical heterogeneity in the variation in participants, and the diversity of participant numbers could considerably affect the precision of the statistical results. The moderator analysis showing patient types and age were the two main variables that might be most likely to account for heterogeneity. In addition, half of the sample size was due to one study alone whose *r*-value was nearly negligible ($r = 0.157$), but stronger relationships tended to be observed in smaller samples. Although no outliers were identified, the study of Devanand et al. (2010) has influenced the overall effect size to a greater extent for those with a heavier weight. Typically, sample sizes are reciprocal to the precision of the estimated effects (Sedgwick and Marston, 2015), and studies with larger sample sizes are given for more weight in analysis. Therefore, sample size is considered to affect heterogeneity, and thus studies with larger sample sizes are necessary for further validation. Additional unpublished papers and non-English results should also be involved to further reduce heterogeneity.

Patient type was an independent factor in OD. Olfactory identification deficits were more prominently correlated with hippocampal atrophy in the AD group than in the MCI group, both of which were consistently stronger than in the normal control group. Previous meta-analyses have validated similar results. Rahayel et al. (2012) conducted a meta-analysis and confirmed that AD has severe detrimental effects on olfactory function across the whole spectrum, but has a stronger effect on odor identification than odor detection. Olfactory identification was the most impaired among all domains in MCI (Roalf et al., 2017) and AD patients. Kotecha et al.

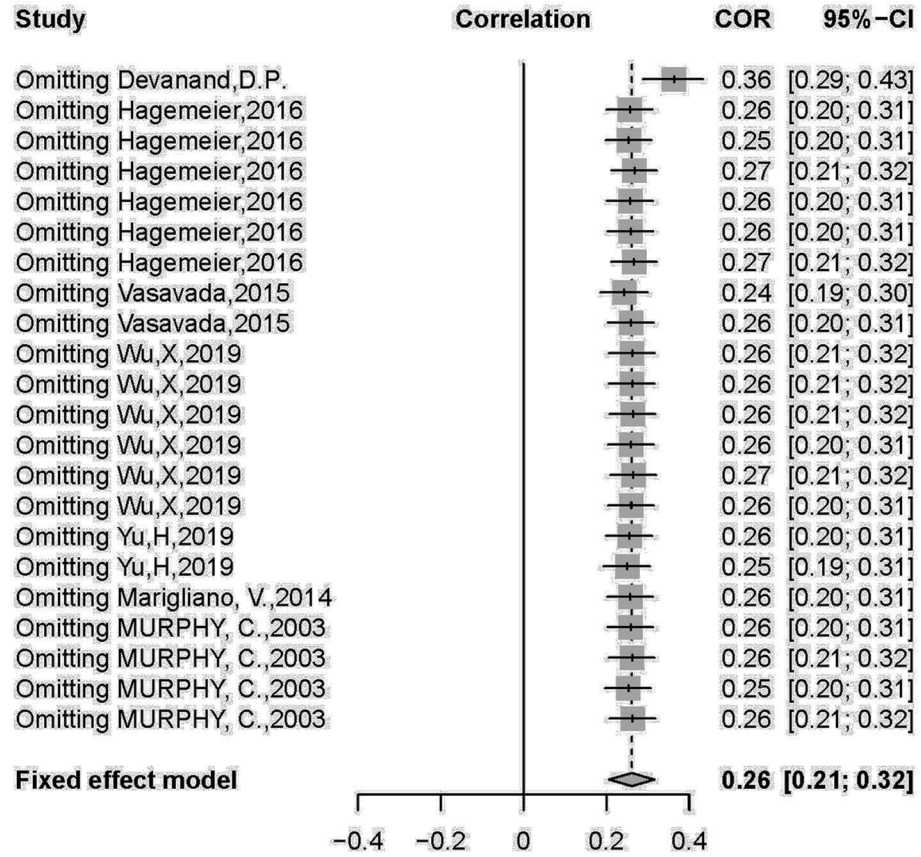

FIGURE 3 | Sensitive analysis in leave-one-out method.

(2018) systematically reviewed and concluded that olfaction progressively worsens from MCI to AD, which highlights the potential utility of olfactory identification tests as prognostic tools for AD (Sun et al., 2012). Jung et al. (2019) reported similar results, revealing that olfactory identification was more profoundly impaired in AD than in MCI; further, Roalf et al. (2017) concluded a more extensively impaired odor identification in MCI. The former result is compatible with our finding that the relationship in AD is higher than in MCI groups (MCI: $r = 0.3691$; AD: $r = 0.3959$; $p = 0.081$). This clear increase in odor identification deficits from cognitively normal to MCI and AD has been described in both clinical and epidemiological studies (Graves et al., 1999; Schubert et al., 2008; Devanand et al., 2015). In addition, this increase in correlation with disease progression might indicate that the olfactory cortex (hippocampus as the second olfactory cortex) is compromised through the pathophysiological continuum (Bathini et al., 2019) of sequential events of the pathology of the disease.

It is widely accepted that odor identification generally declines with normal aging, especially over age 70 (Doty et al., 1984). Significant age-related alterations have been observed in odor identification tests in various studies. In functional magnetic resonance imaging (fMRI), there is a decrease in the activation of olfactory-related regions in the elderly (Suzuki et al., 2001; Ferdon and Murphy, 2003). This was in line with a longitudinal study showing an inverse correlation of B-SIT scores before death and post-mortem density of neurofibrillary tangles in the entorhinal cortex, the CA1 subfield of the hippocampus. Our pooled correlation in age was predominant in patients between the ages of 70–75, showing a moderate association ($r = 0.5113$, 95% CI: 0.3181–0.6637). This result did not explain the progressive trend in olfactory impairment. Thus, we speculate that this is due to the discontinuity of the wide age interval. We re-analyzed a 2-year interval in patient and control groups separately, and discovered that the growth of correlation increases with age (66–68: $r = 0.2953$, 95% CI: 0.1030–0.4664; 70–72: $r = 0.2521$, 95% CI: 0.0060–0.4694; 72–74: $r = 0.4554$, 95% CI: 0.2434–0.6259; 74–76: $r = 0.4679$, 95% CI: 0.2999–0.6078; $Q = 15.18$, $p = 0.2317$). This indicates that aging could be an independent factor for odor identification deficits when the magnitude of the disease was ruled out. Thus, we inferred that age-dependent hippocampal volume decrement clouds affect olfactory function physiologically; on the other hand, this physiological function could be worsened under the pathological extension from MCI to AD.

Previous studies have suggested that odor memory is lateralized to the right hemisphere (Jones-Gotman and Zatorre,

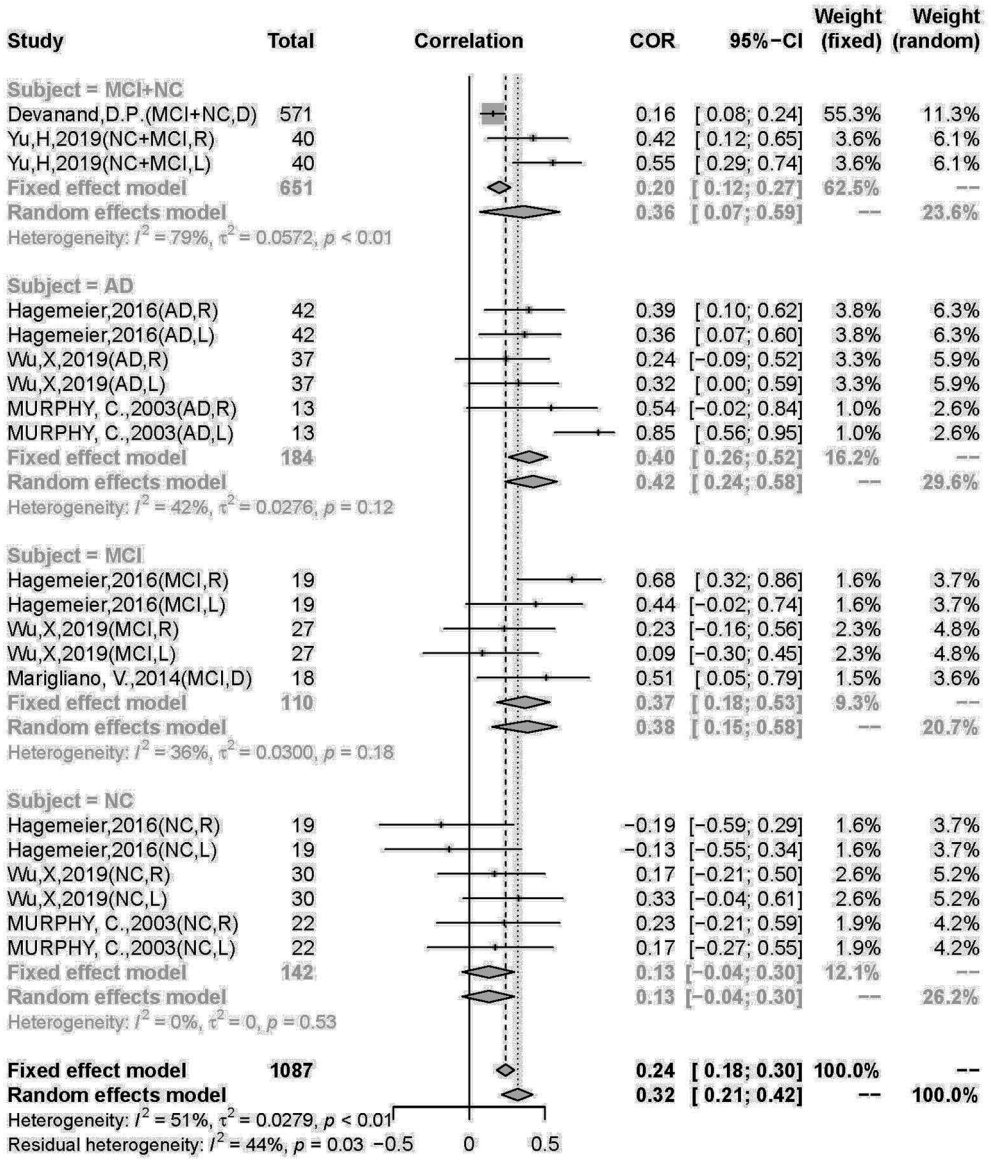

FIGURE 4 | Subgroup analysis in different subject in group of AD, MCI, NC.

1993; Olsson and Cain, 2003). The right hippocampus was found to be larger in the NC and MCI groups, while there was no significant difference in AD in Wolf et al.'s (2001) study. Zou et al. (2016a) concluded that the right hemisphere is predominant in odor hedonic judgment. In contrast, fMRI brain scans of brain activation are generally lateralized to the left hemisphere when received pleasant smell of odors, and unpleasant smells to the right (Henkin and Levy, 2001). However, the controversial hemispheric prominence generally did not include the hippocampus. Our analysis indicated that there were no significant hemispheric differences. One study (Murphy et al., 2003) reported a stronger correlation in the left hippocampus over the right ($r = 0.85$, $p < 0.001$), which made our heterogeneity in the hemispheric moderator on the left side significant. We would assume that the current, small numbered, and conflicting results require further observation.

It can be affirmed that our results in brain-behavior relationships are congruent with previous meta-analyses that have validated olfactory dysfunction in AD. However, the correlation between hippocampal atrophy and odor identification deficits is by far the first to be explored, which could be a key explanation for the hypothesis that it is generated from the pathology burden in the medial-temporal lobe. Consequently, olfactory deficits originate in central structures, suggesting that odor identification and recognition tests could be beneficial for the early detection of subclinical cases.

Several clinical studies have observed that OD and cognitive impairment share the same anatomical modifications of AD-signature cortex decrease (Lian et al., 2019), especially the olfactory cortex and the hippocampus (Al-Otaibi et al., 2020). In recent years, a link between olfactory deficits and AD has been consistently reported. It is commonly recognized that prior to cognitive symptoms (Price et al., 1991; Jellinger and Attems, 2005; Attems and Jellinger, 2006), AD pathology appears in the trans-entorhinal region, entorhinal cortex, hippocampus and successively in olfactory bulb (OB), olfactory tract, and other structures (Ohm and Braak, 1988; Kovács et al., 1999). However, the mechanisms underlying the relationship between odor identification (OI) and hippocampal pathology have not been fully elucidated. Evidence suggests that neuroinflammation occurs in Aβ burden structures (Hanzel et al., 2014). A decrease in hippocampal volume is associated with hippocampal-dependent dysfunction in learning and memory (Ziehn et al., 2010), which also correlates with microglial activation, synaptopathy/synaptic loss, and neurodegeneration (Mandolesi et al., 2010; Girard et al., 2014). Soluble Aβ accumulation in the OB is strongly correlated with early olfactory dysfunction in both AD patients and mouse models (Wesson et al., 2010). Further, a recently published meta-analysis by Tu et al. (2020) discovered a weak negative correlation between OI ability and cerebral Aβ PET ($r = -0.25$, $P = 0.008$) and CSF tau ($r = -0.17$, $p = 0.006$) levels. The specificity was speculated to be the marginal burden of pathological changes that implicate OI ability. The review concluded that the combination of OI tests and other biologic markers still preserves the predictive value of assessing cognitive decline and progression from MCI to AD. However, this may conversely explain the hypothesis that soluble toxic aggregates of both Aβ and tau can self-propagate and spread throughout the brain by prion-like mechanisms (Goedert et al., 2010; Bloom, 2014), and propagation of proteotoxicity along the olfactory nerve could likely affect olfactory-ERC-hippocampal circuits (Busche et al., 2008; Rey et al., 2018). Oligomeropathy (Forloni and Balducci, 2018), neuroinflammation, and the prion-like hypothesis may trigger olfactory dysfunction.

Our study has several limitations. First, there is inadequate inclusion of studies aiming at olfactory discrimination and detection threshold, along with studies reporting a correlation between OB and olfactory epithelium deficits and hippocampal atrophy. Odor discrimination and detection thresholds (Mesholam et al., 1998) were not adequately covered in our analysis. Second, according to the subgroup analysis, we could confirm that aging is one of the moderator factors; however, the linear regression could not be drawn from the present discontinuous data. Furthermore, heterogeneity in sample size preserves obvious differences in the statistical results, which could affect precision. Thus, meticulously designed studies with larger sample sizes are necessary for validation.

CONCLUSION

This meta-analysis quantified a positive correlation between olfactory identification deficits and hippocampal atrophy. The correlation appears to be more predominant in MCI and AD patients, suggesting that olfactory identification deficits appear in the early stages of the continuum. Age is an independent factor that affects the severity of the correlation during disease progression. The mildness of correlation suggests that olfactory tests may be more accurate in early detection when combined with other non-invasive examinations in AD.

DATA AVAILABILITY STATEMENT

The original contributions presented in the study are included in the article/**Supplementary Material**, further inquiries can be directed to the corresponding authors.

AUTHOR CONTRIBUTIONS

M-WS and J-NN wrote the manuscript. M-WS and T-YC performed the analysis. S-SW and M-WS helped to proofread the literature search. JS and J-ZT supervised the study. All authors contributed to the article and approved the submitted version.

FUNDING

This work was supported by the National Natural Science Foundation of China (Grant No. 82074362).

ACKNOWLEDGMENTS

We thank all the coauthors for their contribution for this study.

SUPPLEMENTARY MATERIAL

The Supplementary Material for this article can be found online at: https://www.frontiersin.org/articles/10.3389/fnagi.2021.755160/full#supplementary-material

REFERENCES

Albert, M. S., DeKosky, S. T., Dickson, D., Dubois, B., Feldman, H. H., Fox, N. C., et al. (2011). The diagnosis of mild cognitive impairment due to Alzheimer's disease: recommendations from the National Institute on Aging-Alzheimer's Association workgroups on diagnostic guidelines for Alzheimer's disease. *Alzheimers Dement.* 7, 270–279. doi: 10.1016/j.jalz.2011.03.008

Al-Otaibi, M., Lessard-Beaudoin, M., Castellano, C. A., Gris, D., Cunnane, S. C., and Graham, R. K. (2020). Volumetric MRI demonstrates atrophy of the olfactory cortex in AD. *Curr. Alzheimer Res.* 17, 904–915. doi: 10.2174/1567205017666201215120909

Attems, J., and Jellinger, K. A. (2006). Olfactory tau pathology in Alzheimer disease and mild cognitive impairment. *Clin. Neuropathol.* 25, 265–271.

Bathini, P., Brai, E., and Auber, L. A. (2019). Olfactory dysfunction in the pathophysiological continuum of dementia. *Ageing Res. Rev.* 55:100956. doi: 10.1016/j.arr.2019.100956

Berry, K. J., and Mielke, P. W. Jr. (2000). A Monte Carlo investigation of the Fisher Z transformation for normal and nonnormal distributions. *Psychol. Rep.* 87, 1101–1114. doi: 10.2466/pr0.2000.87.3f.1101

Bloom, G. S. (2014). Amyloid-β and tau: the trigger and bullet in Alzheimer disease pathogenesis. *JAMA Neurol.* 71, 505–508. doi: 10.1001/jamaneurol.2013.5847

Busche, M. A., Eichhoff, G., Adelsberger, H., Abramowski, D., Wiederhold, K. H., Haass, C., et al. (2008). Clusters of hyperactive neurons near amyloid plaques in a mouse model of Alzheimer's disease. *Science* 321, 1686–1689. doi: 10.1126/science.1162844

Devanand, D. P., Lee, S., Manly, J., Andrews, H., Schupf, N., Doty, R. L., et al. (2015). Olfactory deficits predict cognitive decline and Alzheimer dementia in an urban community. *Neurology* 84, 182–189. doi: 10.1212/WNL.0000000000001132

Devanand, D. P., Liu, X., Tabert, M. H., Pradhaban, G., Cuasay, K., Bell, K., et al. (2008). Combining early markers strongly predicts conversion from mild cognitive impairment to Alzheimer's disease. *Biol. Psychiatry* 64, 871–879. doi: 10.1016/j.biopsych.2008.06.020

Devanand, D. P., Tabert, M. H., Cuasay, K., Manly, J. J., Schupf, N., Brickman, A. M., et al. (2010). Olfactory identification deficits and MCI in a multi-ethnic elderly community sample. *Neurobiol. Aging* 31, 1593–1600. doi: 10.1016/j.neurobiolaging.2008.09.008

Doty, R. L., Shaman, P., Applebaum, S. L., Giberson, R., Siksorski, L., and Rosenberg, L. (1984). Smell identification ability: changes with age. *Science* 226, 1441–1443. doi: 10.1126/science.6505700

Ferdon, S., and Murphy, C. (2003). The cerebellum and olfaction in the aging brain: a functional magnetic resonance imaging study. *Neuroimage* 20, 12–21. doi: 10.1016/S1053-8119(03)00276-3

Forloni, G., and Balducci, C. (2018). Alzheimer's disease, oligomers, and inflammation. *J. Alzheimers Dis.* 62, 1261–1276. doi: 10.3233/JAD-170819

Girard, S. D., Jacquet, M., Baranger, K., Migliorati, M., Escoffier, G., Bernard, A., et al. (2014). Onset of hippocampus-dependent memory impairments in 5XFAD transgenic mouse model of Alzheimer's disease. *Hippocampus* 24, 762–772. doi: 10.1002/hipo.22267

Goedert, M., Clavaguera, F., and Tolnay, M. (2010). The propagation of prion-like protein inclusions in neurodegenerative diseases. *Trends Neurosci.* 33, 317–325. doi: 10.1016/j.tins.2010.04.003

Graves, A. B., Bowen, J. D., Rajaram, L., McCormick, W. C., McCurry, S. M., Schellenberg, G. D., et al. (1999). Impaired olfaction as a marker for cognitive decline: interaction with apolipoprotein E epsilon4 status. *Neurology* 53, 1480–1487. doi: 10.1212/WNL.53.7.1480

Hagemeier, J., Woodward, M. R., Rafique, U. A., Amrutkar, C. V., Bergsland, N., Dwyer, M. G., et al. (2016). Odor identification deficit in mild cognitive impairment and Alzheimer's disease is associated with hippocampal and deep gray matter atrophy. *Psychiatry Res. Neuroimag.* 255, 87–93. doi: 10.1016/j.pscychresns.2016.08.003

Hanzel, C. E., Pichet-Binette, A., Pimentel, L. S., Iulita, M. F., Allard, S., Ducatenzeiler, A., et al. (2014). Neuronal driven pre-plaque inflammation in a transgenic rat model of Alzheimer's disease. *Neurobiol. Aging* 35, 2249–2262. doi: 10.1016/j.neurobiolaging.2014.03.026

Hatashita, S., and Yamasaki, H. (2013). Diagnosed mild cognitive impairment due to Alzheimer's disease with PET biomarkers of beta amyloid and neuronal dysfunction. *PLoS ONE* 8:e66877. doi: 10.1371/journal.pone.0066877

Hawkes, C. (2003). Olfaction in neurodegenerative disorder. *Mov. Disord.* 18, 364–372. doi: 10.1002/mds.10379

Henkin, R. I., and Levy, L. M. (2001). Lateralization of brain activation to imagination and smell of odors using functional magnetic resonance imaging (fMRI): left hemispheric localization of pleasant and right hemispheric localization of unpleasant odors. *J. Comput. Assist. Tomogr.* 25, 493–514. doi: 10.1097/00004728-200107000-00001

Hyman, B. T., Arriagada, P. V., and Van Hoesen, G. W. (1991). Pathologic changes in the olfactory system in aging and Alzheimer's disease. *Ann. N. Y. Acad. Sci.* 640, 14–19. doi: 10.1111/j.1749-6632.1991.tb00184.x

Jellinger, K. A., and Attems, J. (2005). Alzheimer pathology in the olfactory bulb. *Neuropathol. Appl. Neurobiol.* 31, 203. doi: 10.1111/j.1365-2990.2004.00619.x

Jones-Gotman, M., and Zatorre, R. J. (1993). Odor recognition memory in humans: role of right temporal and orbitofrontal regions. *Brain Cogn.* 22, 182–198. doi: 10.1006/brcg.1993.1033

Jung, H. J., Shin, I. S., and Lee, J. E. (2019). Olfactory function in mild cognitive impairment and Alzheimer's disease: a meta-analysis. *Laryngoscope* 129, 362–369. doi: 10.1002/lary.27399

Karas, G. B., Burton, E. J., Rombouts, S. A., van Schijndel, R. A., O'Brien, J. T., Scheltens, P.h, et al. (2003). A comprehensive study of gray matter loss in patients with Alzheimer's disease using optimized voxel-based morphometry. *Neuroimage* 18, 895–907. doi: 10.1016/S1053-8119(03)00041-7

Kjelvik, G., Saltvedt, I., White, L. R., Stenumgård, P., Sletvold, O., Engedal, K., et al. (2014). The brain structural and cognitive basis of odor identification deficits in mild cognitive impairment and Alzheimer's disease. *BMC Neurol.* 14, 168. doi: 10.1186/s12883-014-0168-1

Kotecha, A. M., Corrêa, A. D. C., Fisher, K. M., and Rushworth, J. V. (2018). Olfactory dysfunction as a global biomarker for sniffing out Alzheimer's disease: a meta-analysis. *Biosensors (Basel)* 8:41. doi: 10.3390/bios8020041

Kovács, T., Cairns, N. J., and Lantos, P. L. (1999). Beta-amyloid deposition and neurofibrillary tangle formation in the olfactory bulb in ageing and Alzheimer's disease. *Neuropathol. Appl. Neurobiol.* 25, 481–491. doi: 10.1046/j.1365-2990.1999.00208.x

Lane, C. A., Hardy, J., and Schott, J. M. (2018). Alzheimer's disease. *Eur. J. Neurol.* 25, 59–70. doi: 10.1111/ene.13439

Lian, T. H., Zhu, W. L., Li, S. W., Liu, Y. O., Guo, P., Zuo, L. J., et al. (2019). Clinical, structural, and neuropathological features of olfactory dysfunction in patients with Alzheimer's disease. *J. Alzheimers Dis.* 70, 413–423. doi: 10.3233/JAD-181217

Lojkowska, W., Sawicka, B., Gugala, M., Sienkiewicz-Jarosz, H., Bochynska, A., Scinska, A., et al. (2011). Follow-up study of olfactory deficits, cognitive functions, and volume loss of medial temporal lobe structures in patients with mild cognitive impairment. *Curr. Alzheimer Res.* 8, 689–698. doi: 10.2174/156720511796717212

Mandolesi, G., Grasselli, G., Musumeci, G., and Centonze, D. (2010). Cognitive deficits in experimental autoimmune encephalomyelitis: neuroinflammation and synaptic degeneration. *Neurol. Sci.* 31, S255–S259. doi: 10.1007/s10072-010-0369-3

Marigliano, V., Gualdi, G., Servello, A., Marigliano, B., Volpe, L. D., Fioretti, A., et al. (2014). Olfactory deficit and hippocampal volume loss for early diagnosis of Alzheimer disease: a pilot study. *Alzheimer Dis. Assoc. Disord.* 28, 194–197. doi: 10.1097/WAD.0b013e31827bdb9f

Marin, C., Vilas, D., Langdon, C., Alobid, I., López-Chacón, M., Haehner, A., et al. (2018). Olfactory dysfunction in neurodegenerative diseases. *Curr. Allergy Asthma Rep.* 18:42. doi: 10.1007/s11882-018-0796-4

Mesholam, R. I., Moberg, P. J., Mahr, R. N., and Doty, R. L. (1998). Olfaction in neurodegenerative disease: a meta-analysis of olfactory functioning in Alzheimer's and Parkinson's diseases. *Arch. Neurol.* 55:8490. doi: 10.1001/archneur.55.1.84

Murphy, C., Jernigan, T. L., and Fennema-Notestine, C. (2003). Left hippocampal volume loss in Alzheimer's disease is reflected in performance on odor identification: a structural MRI study. *J. Int. Neuropsychol. Soc.* 9, 459–471. doi: 10.1017/S1355617703930116

Ohm, T. G., and Braak, H. (1988). The pigmented subpeduncular nucleus: a neuromelanin-containing nucleus in the human pontine tegmentum. Morphology and changes in Alzheimer's disease. *Acta Neuropathol.* 77, 26–32. doi: 10.1007/BF00688239

Olsson, M. J., and Cain, W. S. (2003). Implicit and explicit memory for odors: hemispheric differences. *Mem. Cognit.* 31, 44–50. doi: 10.3758/BF03196081

Price, J. L., Davis, P. B., Morris, J. C., and White, D. L. (1991). The distribution of tangles, plaques and related immunohistochemical markers in healthy aging and Alzheimer's disease. *Neurobiol. Aging* 12, 295–312. doi: 10.1016/0197-4580(91)90006-6

Rahayel, S., Frasnelli, J., and Joubert, S. (2012). The effect of Alzheimer's disease and Parkinson's disease on olfaction: a meta-analysis. *Behav. Brain Res.* 231, 60–74. doi: 10.1016/j.bbr.2012.02.047

Rey, N. L., Wesson, D. W., and Brundin, P. (2018). The olfactory bulb as the entry site for prion-like propagation in neurodegenerative diseases. *Neurobiol. Dis.* 109, 226–248. doi: 10.1016/j.nbd.2016.12.013

Roalf, D. R., Moberg, M. J., Turetsky, B. I., Brennan, L., Kabadi, S., Wolk, D. A., et al. (2017). A quantitative meta-analysis of olfactory dysfunction in mild cognitive impairment. *J. Neurol. Neurosurg. Psychiatry* 88, 226–232. doi: 10.1136/jnnp-2016-314638

Roberts, R., and Knopman, D. S. (2013). Classification and epidemiology of MCI. *Clin. Geriatr. Med.* 29, 753–772. doi: 10.1016/j.cger.2013.07.003

Schubert, C. R., Carmichael, L. L., Murphy, C., Klein, B. E., Klein, R., and Cruickshanks, K. J. (2008). Olfaction and the 5-year incidence of cognitive impairment in an epidemiological study of older adults. *J. Am. Geriatr. Soc.* 56, 1517–1521. doi: 10.1111/j.1532-5415.2008.01826.x

Sedgwick, P., and Marston, L. (2015). How to read a funnel plot in a meta-analysis. *BMJ* 351:h4718. doi: 10.1136/bmj.h4718

Servello, A., Fioretti, A., Gualdi, G., Di Biasi, C., Pittalis, A., Sollaku, S., et al. (2015). Olfactory dysfunction, olfactory bulb volume and Alzheimer's disease: is there a correlation? A pilot Study1. *J. Alzheimers Dis.* 48, 395–402. doi: 10.3233/JAD-150232

Sun, G. H., Raji, C. A., Maceachern, M. P., and Burke, J. F. (2012). Olfactory identification testing as a predictor of the development of Alzheimer's dementia: a systematic review. *Laryngoscope* 122, 1455–1462. doi: 10.1002/lary.23365

Suzuki, Y., Critchley, H. D., Suckling, J., Fukuda, R., Williams, S. C., Andrew, C., et al. (2001). Functional magnetic resonance imaging of odor identification: the effect of aging. *J. Gerontol. A Biol. Sci. Med. Sci.* 56, M756–M760. doi: 10.1093/gerona/56.12.M756

Tu, L., Lv, X., Fan, Z., Zhang, M., Wang, H., and Yu, X. (2020). Association of odor identification ability with amyloid-β and tau burden: a systematic review and meta-analysis. *Front. Neurosci.* 14:586330. doi: 10.3389/fnins.2020.586330

Vasavada, M. M., Wang, J., Eslinger, P. J., Gill, D. J., Sun, X., Karunanayaka, P., et al. (2015). Olfactory cortex degeneration in Alzheimer's disease and mild cognitive impairment. *J. Alzheimers Dis.* 45, 947–958. doi: 10.3233/JAD-141947

Wang, J., Eslinger, P. J., Doty, R. L., Zimmerman, E. K., Grunfeld, R., Sun, X., et al. (2010). Olfactory deficit detected by fMRI in early Alzheimer's disease. *Brain Res.* 1357, 184–194. doi: 10.1016/j.brainres.2010.08.018

Wells, G., Shea, B., O'Connell, D., Robertson, J., Peterson, J., Welch, V., et al. (2013). *The Newcastle-Ottawa Scale (NOS) for Assessing the Quality of Nonrandomised Studies in Meta-analyses*. Available online at: http://www3.med.unipmn.it/dispense_ebm/2009-2010/Corso%20Perfezionamento%20EBM_Faggiano/NOS_oxford.pdf (accessed May 9, 2021).

Wesson, D. W., Levy, E., Nixon, R. A., and Wilson, D. A. (2010). Olfactory dysfunction correlates with amyloid-beta burden in an Alzheimer's disease mouse model. *J. Neurosci.* 30, 505–514. doi: 10.1523/JNEUROSCI.4622-09.2010

Wilson, R. S., Arnold, S. E., Schneider, J. A., Tang, Y., and Bennett, D. A. (2007). The relationship between cerebral Alzheimer's disease pathology and odour identification in old age. *J. Neurol. Neurosurg. Psychiatry* 78, 30–35. doi: 10.1136/jnnp.2006.099721

Wolf, H., Grunwald, M., Kruggel, F., Riedel-Heller, S. G., Angerhöfer, S., Hojjatoleslami, A., et al. (2001). Hippocampal volume discriminates between normal cognition; questionable and mild dementia in the elderly. *Neurobiol. Aging* 22, 177–186. doi: 10.1016/S0197-4580(00)00238-4

Wu, X., Geng, Z., Zhou, S., Bai, T., Wei, L., Ji, G. J., et al. (2019). Brain structural correlates of odor identification in mild cognitive impairment and Alzheimer's disease revealed by magnetic resonance imaging and a Chinese olfactory identification test. *Front. Neurosci.* 13:842. doi: 10.3389/fnins.2019.00842

Yu, H. L., Chen, Z. J., Zhao, J. W., Duan, S. R., and Zhao, J. K. (2019). Olfactory impairment and hippocampal volume in a Chinese MCI clinical sample. *Alzheimer Dis. Assoc. Disord.* 33, 124–128. doi: 10.1097/WAD.0000000000000305

Ziehn, M. O., Avedisian, A. A., Tiwari-Woodruff, S., and Voskuhl, R. R. (2010). Hippocampal CA1 atrophy and synaptic loss during experimental autoimmune encephalomyelitis, EAE. *Lab. Invest.* 90, 774–786. doi: 10.1038/labinvest.2010.6

Zou, L. Q., van Hartevelt, T. J., Kringelbach, M. L., Cheung, E. F. C., and Chan, R. C. K. (2016a). The neural mechanism of hedonic processing and judgment of pleasant odors: an activation likelihood estimation meta-analysis. *Neuropsychology* 30, 970–979. doi: 10.1037/neu0000292

Zou, Y. M., Lu, D., Liu, L. P., Zhang, H. H., and Zhou, Y. Y. (2016b). Olfactory dysfunction in Alzheimer's disease. *Neuropsychiatr. Dis. Treat.* 12, 869–875. doi: 10.2147/NDT.S104886

Conflict of Interest: The authors declare that the research was conducted in the absence of any commercial or financial relationships that could be construed as a potential conflict of interest.

Publisher's Note: All claims expressed in this article are solely those of the authors and do not necessarily represent those of their affiliated organizations, or those of the publisher, the editors and the reviewers. Any product that may be evaluated in this article, or claim that may be made by its manufacturer, is not guaranteed or endorsed by the publisher.

frontiers in Aging Neuroscience

SYSTEMATIC REVIEW
published: 22 October 2021
doi: 10.3389/fnagi.2021.738971

Meta-Analysis of Neurochemical Changes Estimated via Magnetic Resonance Spectroscopy in Mild Cognitive Impairment and Alzheimer's Disease

Huanhuan Liu[1,2,3†], Dandan Zhang[4†], Huawei Lin[1,2,3†], Qi Zhang[3], Ling Zheng[3], Yuxin Zheng[3], Xiaolong Yin[1,2], Zuanfang Li[5,6], Shengxiang Liang[1,2,7] and Saie Huang[8*]*

[1] National-Local Joint Engineering Research Center of Rehabilitation Medicine Technology, Fujian University of Traditional Chinese Medicine, Fuzhou, China, [2] Rehabilitation Industry Institute, Fujian University of Traditional Chinese Medicine, Fuzhou, China, [3] College of Rehabilitation Medicine, Fujian University of Traditional Chinese Medicine, Fuzhou, China, [4] College of Traditional Chinese Medicine, Fujian University of Traditional Chinese Medicine, Fuzhou, China, [5] Academy of Integrative Medicine, Fujian University of Traditional Chinese Medicine, Fuzhou, China, [6] Fujian Key Laboratory of Integrative Medicine on Geriatrics, Fuzhou, China, [7] Traditional Chinese Medicine Rehabilitation Research Center of State Administration of Traditional Chinese Medicine, Fujian University of Traditional Chinese Medicine, Fuzhou, China, [8] Department of Neurological Rehabilitation, Fujian University of Traditional Chinese Medicine Subsidiary Rehabilitation Hospital, Fuzhou, China

OPEN ACCESS

Edited by:
Binbin Nie,
Institute of High Energy Physics, Chinese Academy of Sciences, China

Reviewed by:
Tianbin Song,
Capital Medical University, China
John McDaid,
NorthShore University HealthSystem, United States

***Correspondence:**
Shengxiang Liang
sxliang@fjtcm.edu.cn
Saie Huang
hse7411@163.com

[†] These authors have contributed equally to this work

Received: *09 July 2021*
Accepted: *26 August 2021*
Published: *22 October 2021*

Citation:
Liu H, Zhang D, Lin H, Zhang Q, Zheng L, Zheng Y, Yin X, Li Z, Liang S and Huang S (2021) Meta-Analysis of Neurochemical Changes Estimated via Magnetic Resonance Spectroscopy in Mild Cognitive Impairment and Alzheimer's Disease. Front. Aging Neurosci. 13:738971. doi: 10.3389/fnagi.2021.738971

The changes of neurochemicals in mild cognitive impairment (MCI) and Alzheimer's disease (AD) patients has been observed via magnetic resonance spectroscopy in several studies. However, whether it exists the consistent pattern of changes of neurochemicals in the encephalic region during the progression of MCI to AD were still not clear. The study performed meta-analysis to investigate the patterns of neurochemical changes in the encephalic region in the progress of AD. We searched the PubMed, Embase, Cochrane Library, and Web of Science databases, and finally included 63 studies comprising 1,086 MCI patients, 1,256 AD patients, and 1,907 healthy controls. It showed that during the progression from MCI to AD, N-acetyl aspartate (NAA) decreased continuously in the posterior cingulate (PC) (SMD: −0.42 [95% CI: −0.62 to −0.21], $z = -3.89$, $P < 0.05$), NAA/Cr (creatine) was consistently reduced in PC (SMD: −0.58 [95% CI: −0.86 to −0.30], $z = -4.06$, $P < 0.05$) and hippocampus (SMD: −0.65 [95% CI: −1.11 to −0.12], $z = -2.44$, $P < 0.05$), while myo-inositol (mI) (SMD: 0.44 [95% CI: 0.26–0.61], $z = 4.97$, $P < 0.05$) and mI/Cr (SMD: 0.43 [95% CI: 0.17–0.68], $z = 3.30$, $P < 0.05$) were raised in PC. Furthermore, these results were further verified by a sustained decrease in the NAA/mI of PC (SMD: −0.94 [95% CI: −1.24 to −0.65], $z = -6.26$, $P < 0.05$). Therefore, the levels of NAA and mI were associated with the cognitive decline and might be used as potentially biomarkers to predict the possible progression from MCI to AD.

Systematic Review Registration: https://www.crd.york.ac.uk/PROSPERO/, identifier: CRD42020200308.

Keywords: magnetic resonance spectroscopy, Alzheimer's disease, mild cognitive impairment, meta-analysis, myo-inositol, N-acetyl aspartate

INTRODUCTION

Alzheimer's disease (AD) is a neurodegenerative disease with age-related progressive cognitive impairment (Scheltens et al., 2016). According to Alzheimer's Disease International, the number of AD patients worldwide was about 50 million in 2018, which would be tripled by 2050 (Scheltens et al., 2021). Early detection and identification of the preclinical AD stage has been thought to be extremely important for slowing down the disease progression of AD. As the prodromal state of AD, there are about 31.5% of mild cognitive impairment (MCI) patients who will be converted to AD within 5 years (Ward et al., 2013). Therefore, exploring the potential biomarkers from MCI to AD is critical for early identification and developing evidence-based interventions of the condition.

The aggregation of amyloid-β (Aβ) in Aβ-pleated and the accumulation of tau in neurofibrillary tangles (NFT) is thought to be the key pathological features of AD (Holtzman et al., 2011). The cerebrospinal fluid (CSF) biomarkers Aβ 42, total tau, and phosphorylated tau are found to be sensitive and common biomarkers that can effectively reflect the typical pathological features of AD (Palmqvist et al., 2016; Sun et al., 2020). The main detection methods of these biomarkers are imaging examination such as ^{11}C-labeled Pittsburgh compound-B(PIB)-positron emission tomography (PET) or biological fluids examination, especially from CSF (Mattsson-Carlgren et al., 2020). However, the abnormalities of Aβ 42, T-tau, and P-tau may lag behind cognitive impairment (Jack et al., 2013). Moreover, some changes of biomarkers are found at a stage which the basic neuropathological examination has reached an advanced and irreversible state and needed to be tested and verified by autopsy and histopathology. As a result, it is urgent to identify sensitive and specific biomarkers and detection methods for facilitating early detection and effective treatment of AD.

With the advantages of non-invasiveness, higher sensitivity, and without any radiation, magnetic resonance spectroscopy (MRS) has been widely used to assess the changes of neurochemicals in specific brain tissues in MCI and AD. Increasing evidence suggests a link between the incidence and progression of AD and metabolic dysfunction. Studies have found that neurochemicals, including N-acetyl aspartate (NAA), choline (Cho), creatine (Cr), myo-inositol (mI), and glutamate and glutamine (Glx), have abnormal metabolic changes in the pathological process of AD. NAA is a specific metabolite of the nervous system, which is synthesized by aspartic acid and acetyl-CoA in neuronal mitochondria, and is highly expressed in neuronal mitochondria. It is widely considered as a specific indicator of neuronal activity. Studies have shown that the level of NAA is closely associated with cognitive dysfunction, especially memory impairment (Jessen et al., 2000). Moreover, the autopsy results showed that the level of NAA was decreased in AD patients. Cho signal is related to cell membrane phospholipid metabolism, which mainly reflects the damage of cholinergic neurons. When the cell membrane is destroyed, the level of Cho will show an increasing trend. In addition, Cho has a close relationship with learning, recall, and other cognitive abilities (Khomenko et al., 2019). The level of Cr *in vivo* is relatively stable, and is closely related to energy metabolism, maintaining ATP level in cells, but the content is reduced in the late stage of AD. Myo-inositol has a role in the second messenger cycle and is regarded as a marker of glial cells. Studies have found that mI level increased in the hippocampus in MCI but decreased in the late period of AD (Voevodskaya et al., 2016). Glx is a key amino acid in the brain and studies showed that a decrease of Glx and cognitive impairment always occurred simultaneously (Huang et al., 2017). Therefore, research on the changes of these neurochemicals in the brain may be helpful for the early diagnosis of MCI and AD.

In recent years, several studies have applied MRS to detect the metabolic changes of neurochemicals in the brain of MCI and AD patients to predict the progress of the condition. However, the results were various. The ratio of NAA/mI is often used to distinguish AD from normal people, and the sensitivity was as high as 83% (Kantarci et al., 2000). Interestingly, one study suggested that the NAA/mI in the posterior cingulate (PC) of MCI patients decreased (Mitolo et al., 2019), while another study found that the NAA/mI showed an increase trend in the same brain region (García et al., 2008). Previous studies have found that the ratio of NAA/Cr in the medial temporal lobe (MTL) is increased in AD patients, indicating neuron damage in the brain (Jessen et al., 2009). On the contrary, the level decreased markedly in the MTL region of AD patients in another study (Chao et al., 2005). To investigate whether there would be a consistent pattern of changes of neurochemicals in the encephalic region in the progress of AD, a meta-analysis was conducted. The goal was to identify the changes of abnormal neurochemicals in typical brain regions from MCI to AD.

METHODS

This meta-analysis and systematic review were reported according to the Preferred Reporting Items for Systematic Reviews and Meta-Analyses (PRISMA; Moher et al., 2009) and was registered at International Prospective Register of Systematic Reviews (https://www.crd.york.ac.uk/PROSPERO/) (number CRD42020200308).

Search Strategy

We searched PubMed, Web of Science, Embase, and Cochrane Library databases from database inception to June 1, 2020. The search strategy was [("Mild cognitive impairment" OR "Alzheimer's Disease") AND ("magnetic resonance spectroscopy" OR "MRS" OR "MR Spectroscopy")]. The search was limited to English language studies only. Regardless of the primary outcome or the type of study, we have considered all possible eligible studies for review.

Selection Criteria

Studies meeting the following criteria were included: (1) the proton MRS was performed to compare MCI patients, AD patients, and healthy controls. (2) NINCSD-ADRDA criteria were chosen as the diagnostic standard for AD, and criteria used for diagnosis of MCI were clearly reported. (3) At least one single metabolites ratio or concentration in a specific brain

TABLE 1 | Characteristics of included studies for the meta-analysis.

	References	Area	Field (Tesla)	Pulse	TR/TE (ms)	Subject total (HC/AD/MCI)	Metabolites				MMSE (mean ± SD)		
							Ratio		Concentration		HC	AD	MCI
#1	Ackl et al. (2005)	Hippocampus Parietal WM Parietal GM	1.5	PRESS	2,000/70	59 (22/18/19)	NAA/Cr ml/NAA	ml/Cr	/		29.4 ± 0.8	23.5 ± 4.4	29.2 ± 1.1
#2	Azevedo et al. (2008)	Temporal Parietal Occipital	1.5	PRESS	2,000/35	28 (15/13/–)	NAA/Cr Cho/Cr	ml/Cr	NAA Cho	Cr ml	26.53 ± 3.14	16.15 ± 4.02	/
#3	Bai et al. (2015)	Frontal Parietal	3	PRESS	8.2/3.7	30 (15/15/–)	GABA+/Cr	GM/(GM + WM)	/		29.20 ± 0.86	15.87 ± 5.03	/
#4	Block et al. (2002)	Hippocampus Temporal Occipital	1.5	/	2,400/20	56 (22/34/–)	NAA/tCr	Cho/tCr	/		28.6 ± 2.1	20.1 ± 4.5	/
#5	Catani et al. (2001)	PWM	1.5	PRESS	2,000/40	36 (11/14/11)	NAA/Cr Cho/Cr	ml/Cr	/		29.8 ± 0.4	20.3 ± 2.5	27 ± 2.5
#6	Catani et al. (2002)	PWM	1.5	PRESS	2,000/40	10 (10/10/–)	NAA/Cr Cho/Cr	ml/Cr	/		29 ± 0.5	20 ± 2	/
#7	Chantal et al. (2002)	MTLs PTCs FCs	1.5	PRESS	1,200/51	28 (14/14/–)	NAA/H_2O Cho/H_2O	Cr/H2O ml/H2O	//		29.3 ± 0.9	22.9 ± 4	/
#8	Chao et al. (2005)	MTL Frontal GM Parietal GM	1.5	PRESS	1,800/135	48 (24/24/–)	NAA/Cr		NAA		29 ± 0.8	17.4 ± 6.7	/
#9	Chao et al. (2010)	PC	1.5	STEAM	1,800/25	22 (9/–/13)	NAA/Cr NAA/ml	ml/Cr	/		29.6 ± 0.6	/	27 ± 2.2
#10	de Souza et al. (2011)	PC	1.5	PRESS	1,200 or 1,500/31	68 (33/25/10)	NAA/Cr Cho/Cr	ml/Cr ml/NAA	/		27.7 ± 2.09	20.45 ± 4.59	25.7 ± 2.49
#11	Delli et al. (2015)	Thalamus	3	PRESS	2,000/39	29 (13/16/–)	NAA/tCr tCho/tCr	tCr/H2O	/		28.3 ± 1.3	17.7 ± 4.5	/
#12	Ding et al. (2008)	PC	1.5	PRESS	1,500/35	40 (20/20/–)	NAA/Cr Cho/Cr	ml/Cr	/		28.3 ± 1.0	11.8 ± 3.8	/
#13	Ernst et al. (1997)	Frontal Temporo-parietal	1.5	PRESS	3,000/35	23 (11/12/–)	NAA/Cr Cho/Cr	ml/Cr	NAA Cr		/	/	/
#14	Fayed et al. (2011)	PC	1.5	PRESS	2,000/35	124 (26/30/68)	NAA/Cr Cho/Cr ml/Cr	Glu/Cr Glx/Cr	NAA Cho ml	Glu Glx	/	/	/
#15	Fayed et al. (2014)	PC	2.5	PRESS	2,000/36	295 (193/36/66)	NAA/Cr Cho/Cr ml/Cr	Glu/Cr Glx/Cr	NAA Cho ml	Glu Glx	/	/	/
#16	Fernández et al. (2005)	Temporo-parietal	1.5	PRESS	3,000/96	20 (10/10/–)	NAA/Cr ml/Cr	NAA/Cho ml/NAA	NAA Cho	ml Cr	34.2 ± 1.03	18.6 ± 4.8	/

(Continued)

TABLE 1 | Continued

	References	Area	Field (Tesla)	Pulse	TR/TE (ms)	Subject total (HC/AD/MCI)	Metabolites				MMSE (mean ± SD)		
							Ratio		Concentration		HC	AD	MCI
#17	Foy et al. (2011)	Hippocampus	1.5	PRESS	1,500/35	98 (39/38/21)	/		NAA Cho	Mi Cr + Pcr	28.8 ± 2.3	23 ± 4	27.1 ± 1.5
#18	Franczak et al. (2007)	Hippocampus	0.5	PRESS	1,500/41	10 (5/–/5)	NAA/Cr ml/Cr ml/NAA	Cho/Cr Glx/Cr Glx/NAA	NAA Cho ml	Cr Glx	≥29	/	≥24
#19	Frederick et al. (2004)	Temporal	1.5	PRESS	2,000/135	29 (14/15/–)	NAA/Cr ml/Cr	Cho/Cr ml/NAA	/		29.1 ± 0.9	17.1 ± 5.5	/
#20	García et al. (2008)	PC	1.5	PRESS	1,500/35 1,500/144	44 (34/–/10)	NAA/Cr ml/Cr	Cho/Cr	/		22.35 ± 1.54	/	22 ± 1.63
#21	Graff-Radford et al. (2014)	PC Occipital Frontal	1.5	PRESS	2,000/30	183 (148/35/–)	NAA/Cr ml/Cr NAA/Cho	NAA/ml Cho/Cr	/		/	/	/
#22	Griffith et al. (2010)	PC	3	PRESS	2,000/32	71 (42/–/29)	NAA/Cr ml/Cr	Cho/Cr	/		29.43 ± 1.04	/	28 ± 1.44
#23	Guo et al. (2016)	AC PC	3	PRESS	1,500/35	44 (16/15/13)	NAA/Cr ml/Cr	NAA/ ml Cho/Cr	/		29.5 ± 0.21	20.5 ± 2.42	26.1 ± 1.32
#24	Herminghaus et al. (2003)	Parietal GM Parietal WM Frontal WM Frontal GM Temporal	1.5	STEAM	2,000/68	75 (27/48/–)	tNAA/tCr TMA/tCr	Ins/Cr Glx/tCr	/		/	/	/
#25	Huang et al. (2017)	Hippocampus AC	1.5	PRESS	1,500/21	53 (15/17/21)	Glx/tCr GABA+/Cr	NAA/Cr	/		29.07 ± 0.96	16.47 ± 5.33	26.45 ± 2.28
#26	Jessen et al. (2005)	MTL	1.5	PRESS	2,700/120	56 (23/33/–)	NAA/Cr		NAA Cho	Cr	/	20.6 ± 4.5	/
#27	Jessen et al. (2000)	MTL Central region	1.5	PRESS	2,000/272	38 (18/20/–)	NAA/Cr	Cho/Cr	NAA/Cho	Cr	29.1 ± 0.9	19.1 ± 6.1	/
#28	Jessen et al. (2009)	MTL	1.5	/	2,000/272 2,000/30	213 (45/98/70)	NAA/Cr	ml/NAA	NAA Cho	Cr ml	28.9 ± 1	24.7 ± 3.7	26.9 ± 4
#31	Kantarci et al. (2000)	Temporal Occipital PC	1.5	PRESS	2,000/135 2,000/30	105 (63/21/21)	NAA/Cr ml/Cr	Cho/Cr	/		28.6 ± 1.3	18.4 ± 5.9	26.6 ± 2.8
#29	Kantarci et al. (2002)	PC	1.5	PRESS	2,000/30	107 (61/–/24)	NAA/Cr ml/Cr	NAA/ml	/		29	20	28
#30	Kantarci et al. (2007)	PC	1.5	PRESS	2,000/30	194 (85/60/49)	NAA/Cr ml/Cr	Cho/Cr	/		29	23	27
#32	Lazeyras et al. (1998)	CGM SGM WM	1.5	STEAM	1,500/20	29 (14/15/–)	/		Cho Cr	NAA ml	/	14-26	/

(Continued)

TABLE 1 | Continued

	References	Area	Field (Tesla)	Pulse	TR/TE (ms)	Subject total (HC/AD/MCI)	Metabolites				MMSE (mean ± SD)		
							Ratio		Concentration		HC	AD	MCI
#33	Li et al. (2010)	Frontal Temporal Parietal	1.5	/	1,500/30	68 (34/–/34)	NAA/Cr		NAA	Cr	/	/	/
#34	Lim et al. (2012)	AC PC	3	PRESS	2,000/9.177	78 (23/ 36 /19)	NAA/Cr	ml/Cr	/		27 ± 4.4	18.8 ± 5.3	25.1 ± 4.0
#35	Liu et al. (2013)	Hippocampus	1.5	PRESS	1,378/110	39 (18/–/21)	NAA/Cr ml/Cr Cho/Cr	NAA/Cho NAA/ml			26.17 ± 0.86	/	25.1 ± 2.5
#36	Liu et al. (2014)	PC Occipital WM Frontal WM Dorsal Thalamus Inferior precuneus	2.5	PRESS	1,500/35	57 (32/–/25)	NAA/Cr ml/Cr Cho/Cr	NAA/Cho NAA/ml	Cho Cr	NAA ml	28.08 ± 1.38	/	26.13 ± 1.78
#37	MacKay et al. (1996)	Anterior and posterior mesial cortex	2	/	3,000/30 3,000/80	32 (18/14/–)	NAA/Cr Cho/Cr	NAA/Cho	/		29 ± 0.8	14 ± 9	/
#38	Mandal et al. (2015)	Hippocampus Frontal	3	PRESS	2,500/120	64 (21/21/22) (Hippocampus) 66 (28/19/19) (Frontal)	/		GSH		28.7 ± 1.1 (Hippocampus) 29 ± 1.2 (Frontal)	18.4 ± 4.1 (Hippocampus) 18.4 ± 4.7 (Frontal)	25.5 ± 4.1 (Hippocampus) 27.4 ± 1.7 (Frontal)
#39	Marjańska et al. (2019)	PC Occipital	7	PRESS	5,000/8	49 (33/16/–)	/		NAA Cho Cr ml Glu GSH	Gln Asc Asp NAAG GABA slns	/	19 ± 2	/
#40	Metastasio et al. (2006)	PWM	1.5	PRESS	2,000/40	54 (29/–/25)	NAA/Cr Cho/Cr	ml/Cr	/		29.2 ± 0.9	/	26.96 ± 2.16
#41	Mitolo et al. (2019)	PC	1.5	PRESS	4,000/35	81 (18/25/38)	NAA/ml		/		/	/	/
#42	Modrego et al. (2011)	Parietal Occipital	1.5	PRESS	2,000/35	106 (35/–/71)	NAA/Cr Cho/Cr	ml/Cr NAA/ml	NAA		/	//	
#43	Oeltzschner et al. (2019)	AC PC	7	/	3,000/14 3,000/15	26 (13/–/13)	/		ml NAA GABA	Glu GSH NAAG	28.7 ± 1.2	/	27.5 ± 1.7
#44	Olson et al. (2008)	PC	1.5	/	3,000/20	71 (24/–/47)	NAA/Cr NAA/Cho Cho/Cr	ml/Cr NAA/ml Glx/Cr	Cho Cr NAA	ml Glx	29 ± 1.3	/	27.7 ± 1.9
#45	Parnetti et al. (1997)	Temporal GM Frontal WM	1.5	/	2,600/35	20 (7/13)	/		Cho Cr	NAA ml	>26	14.7 ± 5.4	/

(Continued)

TABLE 1 | Continued

	References	Area	Field (Tesla)	Pulse	TR/TE (ms)	Subject total (HC/AD/MCI)	Metabolites				MMSE (mean ± SD)		
							Ratio		Concentration		HC	AD	MCI
#46	Pilatus et al. (2009)	Parietal GM Parietal WM	1.5	PRESS	3,000/22	27 (12/–/15)	/		Cho Cr NAA	ml Glx	29.8 ± 0.39	/	26.4 ± 2.6
#47	Rami et al. (2007)	PC Temporal Temporo-parietal	1.5	PRESS	1,500/35	89 (27/35/27)	NAA/Cr Cho/Cr	ml/Cr	NAA Cr	Cho ml	27.5 ± 1	21.8 ± 3.8	25.1 ± 2.1
#48	Riese et al. (2015)	PC	2	PRESS	1,800/68	36 (21/–/15)	/		GABA Glx	NAA	29.7 ± 0.6	/	28.6 ± 1.2
#49	Schuff et al., 1998	Mesial cortex centrum semiovale	1.5	PRESS	3,000/80	50 (22/28/–)	/		NAA Cho	Cr	29.3 ± 1	19.1 ± 6.9	/
#50	Schuff et al. (2002)	MTL Frontal Parietal Hippocampus	1.5	PRESS	1,800/135	110 (54/56/–)	/		NAA		29.1 ± 0.8	19 ± 6.7	/
#51	Seo et al. (2012)	PC Hippocampus ERC Occipital WM	3	PRESS	2,000/40	24 (11/–/13)	NAA/Cr	Cho/Cr	/		28.5 ± 1.1	/	25.2 ± 2.3
#52	Shiino et al. (2012)	PC Hippocampus	1.5	PRESS	2,000/30	144 (45/99/–)	NAA/Cr Cho/Cr ml/Cr	Glx/Cr ml/NAA	NAA Glx Cho	ml Cr	29.1 ± 1.2	19.7 ± 3.4	/
#53	Siger et al. (2009)	Frontal Parietal	1.5	/	2,500/20	47 (16/17/14)	/		NAA	ml	29.5 ± 0.9	21.4 ± 5.4	27.6 ± 1.5
#54	Targosz-Gajniak et al. (2013)	PC Hippocampus Parietal	1.5	PRESS	1,500/35	76 (35/–/41)	NAA/Cr Cho/Cr ml/Cr	Glx/Cr NAA/Cho	/		/	/	/
#55	Wang et al. (2009)	Hippocampus PC	3	PRESS	1,700/30	48 (16/16/16)	NAA/Cr Cho/Cr	ml/Cr ml/NAA	/		28.13 ± 1.25	15.63 ± 7.25	26.5 ± 1.51
#56	Wang et al. (2012)	Hippocampus PC	3	PRESS	1,500/35	40 (56/47/32)	NAA/Cr Cho/Cr	ml/Cr NAA/ml	/		26.5 ± 3.5	13.8 ± 5.4	23.9 ± 3.8
#57	Watanabe et al. (2010)	Hippocampus Occipital PC ApPoDeepWM	1.5	PRESS	2,000/30	169 (52/70/47)	/		NAA ml	Cho Cr	29 ± 1.4	20.8 ± 3.6	27.2 ± 1.8
#58	Yang et al. (2012)	PC PWM Inferior precuneus Dorsal thalamus Lentiform nucleus	1.5	PRESS	1,500/35	29 (15/–/14)	NAA/Cr ml/Cr	Cho/Cr NAA/ml	NAA ml	Cho Cr	28.11 ± 1.23	/	25.79 ± 1.06
#59	Zeydan et al. (2017)	PC	3	LASER	2,300/2.98	46 (32/–/14)	Glu/ml		NAA ml Cho	Cr Glu	28	/	26

(Continued)

TABLE 1 | Continued

	References	Area	Field (Tesla)	Pulse	TR/TE (ms)	Subject total (HC/AD/MCI)	Metabolites		MMSE (mean ± SD)		
							Ratio	Concentration	HC	AD	MCI
#60	Zhang et al. (2009)	Hippocampus Temporo-parietal	1.5	/	2,000/25	40 (13/13/14)	NAA/Cr	ml/Cr /	/	/	/
#61	Zhu et al. (2006)	Parietal GM Parietal WM Front GM Front WM	1.5	/	/	36 (22/14/–)	NAA/Cr ml/Cr	NAA/ml NAA ml	29.7 ± 0.5	20 ± 6.7	/
#62	Zhu et al. (2015)	Hippocampus Basal ganglia Frontal	3	PRESS	1,500/30	62 (34/–/28)	NAA/Cr ml/Cr	Cho/Cr /	28.35 ± 1.3	7/±26	11 ± 1.17
#63	Zimny et al. (2011)	PC	1.5	PRESS	1,500/35	68 (15/30/23)	NAA/Cr ml/Cr Cho/Cr	ml/NAA ml/Cho /	29.8 ± 0.4	18 ± 5.4	27.4 ± 2.4

AC, anterior cingulate cortex; AD, Alzheimer's disease; ApPoDeepWM, anterior and posterior deep white matter; Asc, ascorbate; Asp, aspartate; CGM, cortical gray matter; Cho, choline; Cr, creatine; DT, dorsal thalamus; ERC, entorhinal cortex; GABA, γ-aminobutyric acid; Gln, glutamine; Glu, glutamine; Glx, glutamate + glutamine; GM, gray matter; GSH, glutathione; HC, healthy controls; Ins, inositol; LA, left anterior periventricular and deep white matter; LN, lentiform nucleus; LP, left posterior periventricular and deep white matter; MCI, mild cognitive impairment; mI, myo-inositol; MMSE, mini mental state examination; MTL, medial temporal lobe; NAA, N-acetyl aspartate; NAAG, N-acetylaspartylglutamate; PC, posterior cingulate cortex; PCr, phosphocreatine; PR, inferior precuneus; PRESS, point resolved spectroscopy sequence; PTC, parietotemporal cortices; PWM, paratrigonal white matter; RA, right anterior periventricular and deep white matter; RP, right posterior periventricular and deep white matter; SD, standard deviation; SGM, subcortical gray matter; sIns, scyllo-inositol; tCr, creatine and creatine phosphate; TE, echo time (ms); TMA, trimethylamines; TR, repetition time (ms),WM, white matter.

region was reported. (4) Specifications for spectrum acquisition were reported.

The exclusion criteria were as follows: (1) studies were published in languages other than English. (2) Original data could not be extracted, or the full text could not be obtained. (3) Duplicate or similar data published research. (4) The subjects were animals. (5) The subjects were taking drugs, had other significant medical conditions or substance abuse that could interfere with cognitive functioning.

Data Extraction

After applying the inclusion and exclusion criteria, we finally identified 63 articles and extracted the following characteristics for meta-analysis: the interested brain regions and the corresponding metabolites ratios and concentrations, the field strength, repetition time/echo time (TR/TE), and other characteristics which are shown in **Table 1**. Meanwhile, we also extracted standard deviations (SD) or standard error of mean (SEM) or median, as our main results.

Statistical Analyses

Stata 16.0 (Stata Corp) software was used to perform all statistical analysis. The sample size, mean value, and SD were used to generate the effective sizes, and when the mean ± SEM or median was provided, we converted it into mean ± SD for meta-analysis. Then, we calculated the standardized mean difference (SMD) and 95% CI and drew a forest map to compare the relationship between the metabolites' concentrations or metabolites' ratios between the healthy control group and AD patients, the healthy control group and MCI patients, and AD patients and MCI patients. We used the Q-test and I^2 index to evaluate heterogeneity. The statistical significance of the Q-test was set as $P < 0.1$, and heterogeneity was assessed by I^2 index, with 25, 50, and 75%, indicating that the heterogeneity was low, medium, and high (Higgins et al., 2003). For the statistical model, we first chose fixed effects model with the method of inverse-variance for analysis. If the heterogeneity of the results is greater, we used the random effect model with the method of Dersimonian and Laird for analysis. All statistical significances were set at $P < 0.05$ and $P < 0.1$ was regarded as a trend.

RESULTS

Description of Studies

We identified 4,436 articles from database searching and 2,812 remained after removal of duplicates. Then, 133 full-text articles were assessed for eligibility. Finally, according to the inclusion and exclusion criteria, 63 studies were included in the systematic review and meta-analysis (MacKay et al., 1996; Ernst et al., 1997; Parnetti et al., 1997; Lazeyras et al., 1998; Schuff et al., 1998, 2002; Jessen et al., 2000, 2005, 2009; Kantarci et al., 2000, 2002, 2007; Catani et al., 2001, 2002; Block et al., 2002; Chantal et al., 2002; Huang et al., 2002; Herminghaus et al., 2003; Frederick et al., 2004; Ackl et al., 2005; Chao et al., 2005, 2010; Fernández et al., 2005; Metastasio et al., 2006; Zhu et al., 2006, 2015; Franczak et al., 2007; Rami et al., 2007; Azevedo et al., 2008; Ding et al., 2008; García et al., 2008; Pilatus et al.,

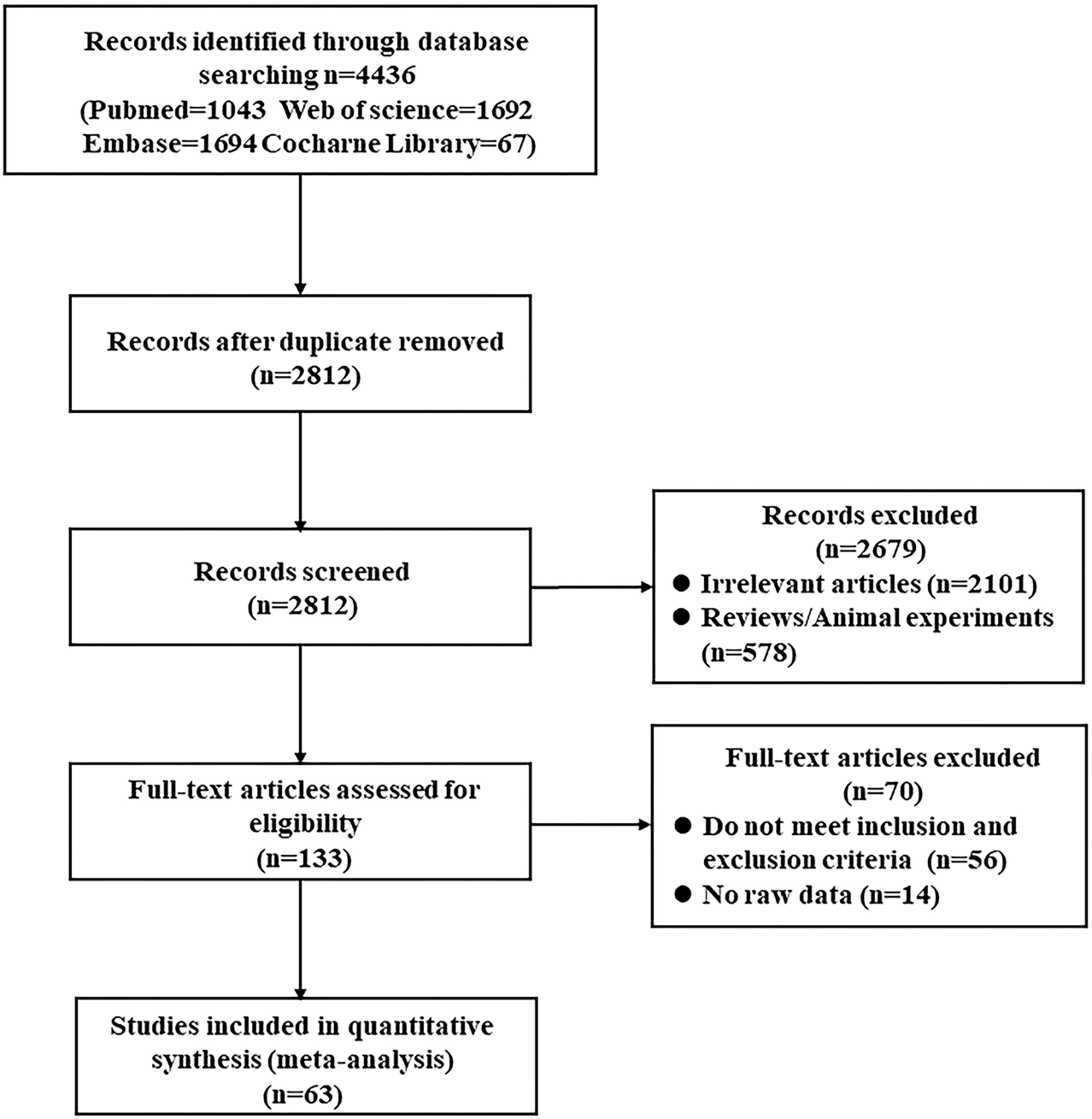

FIGURE 1 | Flowchart for study screening process.

2009; Siger et al., 2009; Wang et al., 2009, 2012; Zhang et al., 2009; Griffith et al., 2010; Li et al., 2010; Liu et al., 2010, 2013; Watanabe et al., 2010; de Souza et al., 2011; Fayed et al., 2011, 2014; Foy et al., 2011; Modrego et al., 2011; Zimny et al., 2011; Lim et al., 2012; Seo et al., 2012; Shiino et al., 2012; Yang et al., 2012; Targosz-Gajniak et al., 2013; Graff-Radford et al., 2014; Bai et al., 2015; Delli et al., 2015; Mandal et al., 2015; Riese et al., 2015; Guo et al., 2016; Zeydan et al., 2017; Marjańska et al., 2019; Mitolo et al., 2019; Oeltzschner et al., 2019; **Figure 1**).

The meta-analysis comprised of a total of 3,271 subjects, with 1,086 MCI patients, 1,256 AD patients, and 1,907 healthy controls. The following regions were investigated: hippocampus (including MTL), PC, temporal lobe, occipital regions, paratrigonal white matter area, temporo-parietal lobe, parietal lobe, frontal lobe (gray and white matter area), and

TABLE 2 | The Newcastle-Ottawa Scale (NOS) for the quality assessment of studies.

References	Selection				Comparability		Exposure				Total
	S1	S2	S3	S4	C1	C2	E1a	E1b	E2	E3	
Ackl et al. (2005)	*	–	–	*	*	*	–	–	*	–	5
Azevedo et al. (2008)	*	*	*	*	*	*	–	–	*	–	7
Bai et al. (2015)	*	–	–	*	*	*	–	–	*	–	5
Block et al. (2002)	*	–	–	*	*	*	–	–	*	–	5
Catani et al. (2001)	*	–	–	*	*	*	–	–	*	–	5
Catani et al. (2002)	*	–	–	*	*	*	–	–	*	–	5
Chantal et al. (2002)	*	–	–	*	*	*	–	–	*	–	5
Chao et al. (2005)	*	*	*	*	*	*	–	–	*	–	7
Chao et al. (2010)	*	*	*	*	*	–	–	–	*	–	6
de Souza et al. (2011)	*	*	–	*	*	*	–	–	*	–	6
Delli et al. (2015)	*	–	–	*	*	*	–	–	*	–	5
Ding et al. (2008)	*	–	–	*	*	*	–	–	*	–	5
Ernst et al. (1997)	*	–	–	*	*	*	–	–	*	–	5
Fayed et al. (2011)	*	–	–	*	*	*	–	–	*	*	6
Fayed et al. (2014)	*	–	–	*	*	*	–	–	*	–	5
Fernández et al. (2005)	*	*	–	*	*	*	–	–	*	–	6
Foy et al. (2011)	*	*	–	*	*	*	–	–	*	–	6
Franczak et al. (2007)	*	–	–	*	*	*	–	–	*	–	5
Frederick et al. (2004)	*	*	*	*	*	*	–	–	*	–	7
García et al. (2008)	*	–	*	*	*	*	–	–	*	*	7
Graff-Radford et al. (2014)	*	*	–	*	*	*	–	–	*	–	6
Griffith et al. (2010)	*	*	*	*	*	*	–	–	*	–	7
Guo et al. (2016)	*	*	–	*	*	*	–	–	*		6
Herminghaus et al. (2003)	*	*	–	*	*	*	–	–	*	–	6
Huang et al. (2017)	*	*	*	*	*	–	–	–	*	–	6
Jessen et al. (2000)	*	–	–	*	*	*	–	–	*		5
Jessen et al. (2005)	*	*	–	*	*	*	–	–	*	–	6
Jessen et al. (2009)	*	–	–	*	*	*	–	–	*	–	5
Kantarci et al. (2000)	*	–	–	*	*	*	–	–	*	–	5
Kantarci et al. (2002)	*	*	–	*	*	*	–	–	*	–	6
Kantarci et al. (2007)	*	*	–	*	*	*	–	–	*	*	7
Lazeyras et al. (1998)	*	–	–	*	*	*	–	–	*	–	5
Li et al. (2010)	*	–	–	*	*	*	–	–	*	–	5
Lim et al. (2012)	*	–	–	*	*	*	–	–	*	–	5
Liu et al. (2013)	*	–	–	*	*	*	–	–	*	–	5
Liu et al. (2014)	*	–	–	*	*	*	–	–	*	–	5

(Continued)

TABLE 2 | Continued

References	Selection				Comparability		Exposure				Total
	S1	S2	S3	S4	C1	C2	E1a	E1b	E2	E3	
MacKay et al. (1996)	*	*	–	*	*	*	–	–	*	–	6
Mandal et al. (2015)	*	*	*	*	*	*	–	–	*	–	7
Marjańska et al. (2019)	*	–	–	*	*	*	–	–	*	–	5
Metastasio et al. (2006)	*	–	–	*	*	*	–	–	*		5
Mitolo et al. (2019)	*	–	–	*	*	*	–	–	*	*	6
Modrego et al. (2011)	*	–	–	*	*	*	–	–	*	–	5
Oeltzschner et al. (2019)	*	*	*	*	*	*	–	–	*	–	7
Olson et al. (2008)	*	–	*	*	*	*	–	–	*	*	7
Parnetti et al. (1997)	*	*	*	*	*	–	–	–	*	–	6
Pilatus et al. (2009)	*	–	*	*	*	*	–	–	*	*	7
Rami et al. (2007)	*	*	–	*	*	*	–	–	*	–	6
Riese et al. (2015)	*	–	–	*	*	*	–	–	*	–	5
Schuff et al. (1998)	*	–	*	*	*	*	–	–	*	–	6
Schuff et al. (2002)	*	–	*	*	*	*	–	–	*	–	6
Seo et al. (2012)	*	–	–	*	*	*	–	–	*	–	5
Shiino et al. (2012)	*	*	–	*	*	*	–	–	*	–	6
Siger et al. (2009)	*	–	*	*	*	*	–	–	*	–	6
Targosz-Gajniak et al. (2013)	*	*	*	*	*	*	–	–	*	*	8
Wang et al. (2009)	*	–	*	*	*	*	–	–	*	–	6
Wang et al. (2012)	*	–	*	*	*	*	–	–	*	–	6
Watanabe et al. (2010)	*	*	–	*	*	*	–	–	*	–	6
Yang et al. (2012)	*	–	–	*	*	*	–	–	*	–	5
Zeydan et al. (2017)	*	*	–	*	*	*	–	–	*	–	6
Zhang et al. (2009)	*	–	–	*	*	*	–	–	*	–	5
Zhu et al. (2006)	*	–	*	*	*	*	–	–	*	–	6
Zhu et al. (2015)	*	–	–	*	*	*	–	–	*	–	5
Zimny et al. (2011)	*	–	–	*	*	*	–	–	*	–	5

**means that this study awarded one score on this question.*

anterior cingulate. The key characteristics of the studies are shown in **Table 1** among which 6 studies were classified as high quality and 57 studies were classified as medium quality (**Table 2**).

Meta-Analysis of Hippocampus

Nineteen studies (Jessen et al., 2000, 2005, 2009; Block et al., 2002; Schuff et al., 2002; Ackl et al., 2005; Chao et al., 2005; Franczak et al., 2007; Wang et al., 2009, 2012; Zhang et al., 2009; Watanabe et al., 2010; Foy et al., 2011; Seo et al., 2012; Shiino et al., 2012; Liu et al., 2013; Targosz-Gajniak et al., 2013; Zhu et al., 2015; Huang et al., 2017) investigated the ratios of metabolites in hippocampus from 358 MCI patients, 890 AD patients, and 787 healthy control subjects. Specifically, 12 studies (Ackl et al., 2005; Franczak et al., 2007; Wang et al., 2009, 2012; Zhang et al., 2009; Watanabe et al., 2010; Foy et al., 2011; Seo et al., 2012; Liu et al., 2013; Targosz-Gajniak et al., 2013; Zhu et al., 2015; Huang et al., 2017) performed a comparison of the changes between 358 MCI patients and 425 healthy control subjects, 14 studies (Jessen et al., 2000, 2005, 2009; Block et al., 2002; Schuff et al., 2002; Ackl et al., 2005; Chao et al., 2005; Wang et al., 2009, 2012; Zhang et al., 2009; Watanabe et al., 2010; Foy et al., 2011; Shiino et al., 2012; Huang et al., 2017) compared the differences in metabolites between 890 AD patients and 679 healthy control subjects, and 5 studies (Ackl et al., 2005; Wang et al., 2009, 2012; Zhang et al., 2009; Huang et al., 2017) were conducted to observe the differences of metabolites in 155 AD patients and 130 MCI patients. Moreover, there were another two articles (Modrego et al., 2011; Seo et al., 2012) longitudinally tracking the metabolite differences in the hippocampus between MCI-converter and MCI-stable patients.

Metabolite Ratios

We compared the ratios of five metabolites, extracting data from 243 MCI patients and 282 healthy control subjects in 10 studies (Ackl et al., 2005; Franczak et al., 2007; Wang et al., 2009, 2012; Zhang et al., 2009; Seo et al., 2012; Liu et al., 2013; Targosz-Gajniak et al., 2013; Zhu et al., 2015; Huang et al., 2017). The results showed that four metabolites' ratios (NAA/Cr, Cho/Cr, mI/Cr, and mI/NAA) were significantly different in MCI and healthy control subjects, but there was no significant difference in Glx/Cr (SMD: −0.76 [95% CI: −1.81 to 0.28], $z = -1.44$, $P > 0.1$, **Supplementary Table 1**). Among them, NAA/Cr (SMD: −0.65 [95% CI: −0.97 to −0.34], $z = -4.10$, $P < 0.05$, **Figures 2A**, **9**) and Cho/Cr (SMD: −0.20 [95% CI: −0.39 to −0.01], $z = -2.09$, $P < 0.05$, **Supplementary Figure 1A** and **Figure 9**) were significantly decreased in the hippocampus of MCI patients, while mI/Cr (SMD: 0.52 [95% CI: 0.20–0.83], $z = 3.24$, $P < 0.05$, **Supplementary Figure 1B** and **Figure 9**) and mI/NAA (SMD: 1.58 [95% CI: 0.71–2.45], $z = 3.55$, $P < 0.05$, **Supplementary Figure 1C** and **Figure 9**) were significantly increased.

In addition, 11 studies (Jessen et al., 2000, 2005, 2009; Block et al., 2002; Ackl et al., 2005; Chao et al., 2005; Wang et al., 2009, 2012; Zhang et al., 2009; Shiino et al., 2012; Huang et al., 2017) were combined to compare the ratios of NAA/Cr, Cho/Cr, mI/Cr, and mI/NAA in 600 AD patients and 428 healthy control subjects. The results showed that four metabolites' ratios (NAA/Cr, Cho/Cr, mI/Cr, and mI/NAA) were significantly different in AD and healthy control subjects. For the comparisons between AD and controls, NAA/Cr (SMD: −0.88 [95% CI: −1.25 to −0.51], $z = -4.59$, $P < 0.05$, **Figures 2B**, **9**) and Cho/Cr (SMD: −0.23 [95% CI: −0.39 to −0.06], $z = -2.67$, $P < 0.05$, **Supplementary Figure 2A** and **Figure 9**) were significantly decreased in the hippocampus of AD patients, while mI/Cr (SMD: 0.93 [95% CI: 0.76–1.11], $z = 10.40$, $P < 0.05$, **Supplementary Figure 2B** and **Figure 9**) and mI/NAA (SMD: 1.98 [95% CI: 0.81–3.15], $z = 3.31$, $P < 0.05$, **Supplementary Figure 2C** and **Figure 9**) showed a significant increase. Moreover, 4 studies of MTL were eligible for inclusion, comprising 199 AD patients and 134 healthy controls, all AD compared to controls NAA/Cr (SMD: −0.48 [95% CI: −0.93 to −0.03], $z = -2.07$, $P < 0.05$, **Supplementary Figure 3A** and **Figure 9**) were decreased.

Next, we performed a meta-analysis to compare the ratios of NAA/Cr, between 155 AD patients and 130 MCI patients (Ackl et al., 2005; Wang et al., 2009, 2012; Zhang et al., 2009; Huang et al., 2017). The results demonstrated significant difference. NAA/Cr (SMD: −0.62 [95% CI: −1.11 to −0.12], $z = -2.44$, $P < 0.05$, **Figures 2C**, **9**) in the MCI group were significantly higher than that in the AD patients. Four studies (Ackl et al., 2005; Wang et al., 2009, 2012; Zhang et al., 2009) investigated the mI/Cr from the hippocampus of 137 AD patients and 109 MCI patients, and the results showed that the mI/Cr ratio in the AD patients (SMD: 0.25 [95% CI: −0.01 to 0.50], $z = 1.92$, $P = 0.055$, **Supplementary Table 1**) were increased compared to the MCI patients.

Moreover, studies (Modrego et al., 2011; Seo et al., 2012) longitudinally tracked the metabolite differences in the hippocampus between MCI-converter and MCI-stable patients. Compared with MCI-stable patients, a downward trend in Cho/Cr (SMD: −0.47 [95%CI: −0.94 to 0.01], $z = -1.91$, $P = 0.06$, **Supplementary Table 1** and **Figure 9**) was observed in MCI-converter patients. Meanwhile, the analysis on NAA/Cr (SMD: −0.17 [95% CI: −0.65 to 0.30], $z = -0.72$, $P > 0.05$, **Supplementary Table 1** and **Figure 9**) revealed no significant difference between the two groups.

Above all, according to the results of meta-analysis of AD and MCI, the ratios of NAA/Cr and Cho/Cr are both decreased in AD and MCI patients. Notably, the decrease was more obvious in AD patients. In addition, mI/Cr and mI/NAA ratios were seen to increase faster in AD patients, compared to subjects who converted to MCI and cognitively normal elderly.

Metabolite Concentrations

Of the eligible studies, 4 studies (Franczak et al., 2007; Watanabe et al., 2010; Foy et al., 2011; Liu et al., 2013) investigated metabolite concentrations. These studies comprised 146 MCI patients and 171 healthy controls. The analysis showed that four metabolites' concentrations (NAA, Cr, Cho, and mI) were significantly different in MCI and healthy control subjects, and no significant difference in mI concentration (SMD: 0.23 [95% CI: −0.19 to 0.65], $z = 1.08$, $P > 0.1$, **Supplementary Table 1**). Among them, NAA (SMD: −1.01 [95% CI: −1.25 to −0.78], $z = -8.45$, $P < 0.05$, **Supplementary Figure 1D** and **Figure 9**),

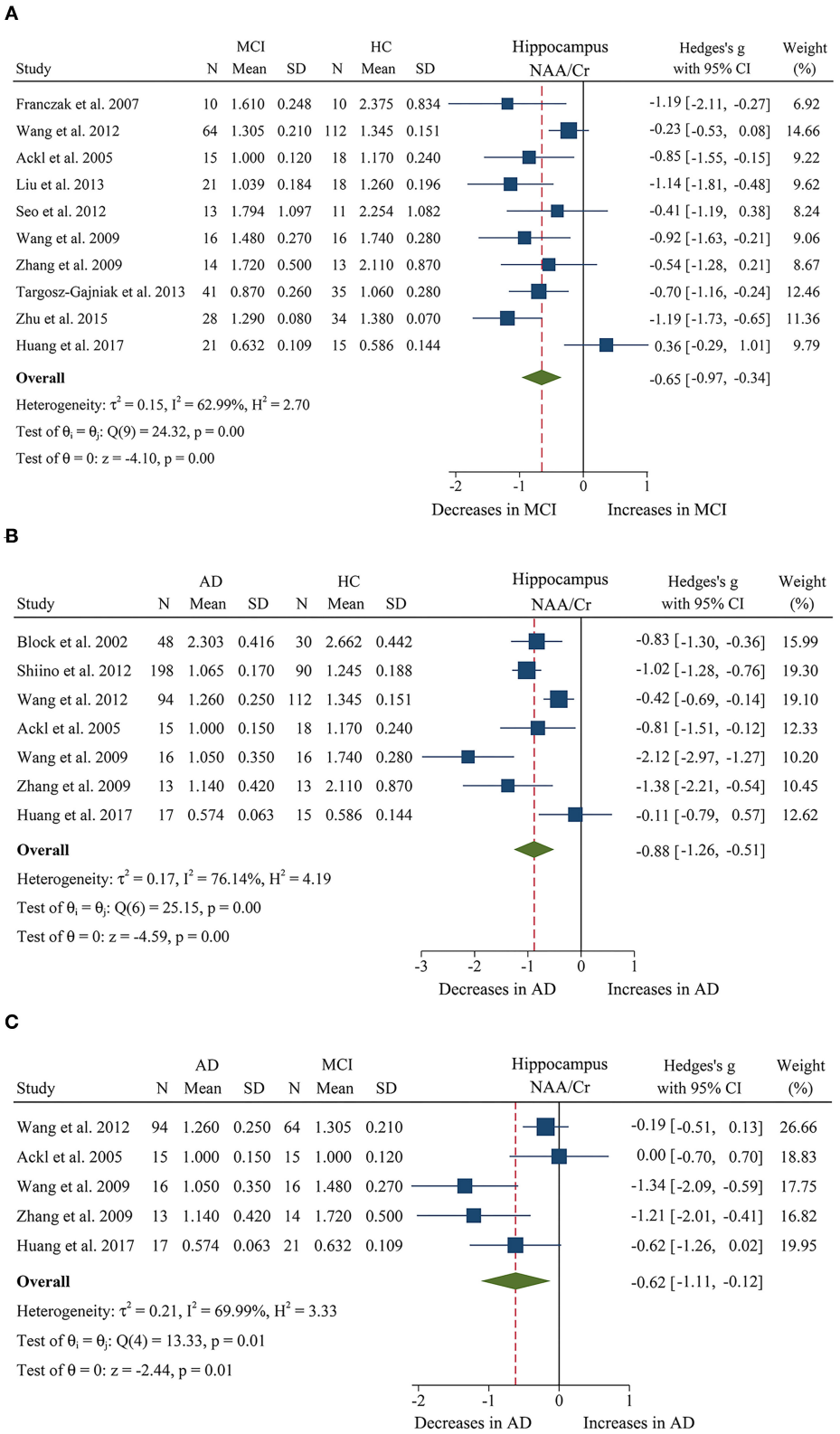

FIGURE 2 | Forest plots show the change of the ratio of NAA/Cr in the hippocampus between MCI, AD patients, and HC subjects. **(A)** Data include 525 individuals from 10 studies for meta-analysis of NAA/Cr levels between MCI and HC. **(B)** Data include 695 individuals from 7 studies for meta-analysis of NAA/Cr levels between AD and HC. **(C)** Data include 285 individuals from 5 studies for meta-analysis of NAA/Cr levels between AD and MCI.

Cr (SMD: −1.35 [95% CI: −2.50 to −0.20], $z = -2.30$, $P < 0.05$, **Supplementary Figure 1F** and **Figure 9**), and Cho (SMD: −0.55 [95% CI: −0.78 to −0.33], $z = -4.80$, $P < 0.05$, **Supplementary Figure 1E** and **Figure 9**) were low heterogeneity and remarkably decreased in the hippocampus of MCI patients.

Then, 4 studies (Schuff et al., 2002; Watanabe et al., 2010; Foy et al., 2011; Shiino et al., 2012) were extracted to compare the metabolite concentrations in 488 AD patients and 341 healthy control subjects. The analysis revealed that NAA, Cr, and Cho concentrations were significantly different in AD and healthy control subjects, while there was no difference of the concentration of mI between AD and healthy controls (SMD: 0.46 [95% CI: −0.11 to 1.03], $z = 1.57$, $P > 0.1$, **Supplementary Table 1**). For the comparisons between AD and controls, NAA (SMD: −1.17 [95% CI: −1.61 to −0.74], $z = -0.53$, $P < 0.05$, **Supplementary Figure 2D** and **Figure 9**), Cho (SMD: −0.58 [95% CI: −0.75 to −0.42], $z = -6.82$, $P < 0.05$, **Supplementary Figure 2E** and **Figure 9**), and Cr (SMD: −0.44 [95% CI: −0.71 to −0.16], $z = -3.12$, $P < 0.05$, **Supplementary Figure 2F** and **Figure 9**) concentrations were significantly decreased in the hippocampus of AD patients with statistically high heterogeneity. In addition, 4 studies (Jessen et al., 2000, 2005, 2009; Chao et al., 2005) of MTL were eligible for inclusion, comprising 288 AD patients and 221 healthy controls, all AD compared to controls NAA (SMD: −0.89 [95% CI: −1.08 to −0.7], $z = -9.40$, $P < 0.05$, **Supplementary Figure 3B** and **Figure 9**) were decreased.

In conclusion, based on the analysis of AD and MCI, 3 metabolites' concentrations (NAA, Cr, and Cho) were found to be lower in AD patients as compared to MCI patients and healthy control subjects.

Meta-Analysis of Posterior Cingulate

A total of 29 studies (Kantarci et al., 2000, 2002, 2007; Chao et al., 2005; Rami et al., 2007; García et al., 2008; Olson et al., 2008; Wang et al., 2009, 2012; Griffith et al., 2010; Watanabe et al., 2010; de Souza et al., 2011; Fayed et al., 2011, 2014; Zimny et al., 2011; Lim et al., 2012; Seo et al., 2012; Shiino et al., 2012; Yang et al., 2012; Targosz-Gajniak et al., 2013; Graff-Radford et al., 2014; Liu et al., 2014; Riese et al., 2015; Guo et al., 2016; Zeydan et al., 2017; Marjańska et al., 2019; Mitolo et al., 2019; Oeltzschner et al., 2019) investigated the ratio of metabolites in posterior cingulate with a sample size of 770 MCI patients, 585 AD patients, and 1,378 healthy controls. To be specific, 25 studies (Kantarci et al., 2000, 2002, 2007; Chao et al., 2005; Rami et al., 2007; García et al., 2008; Olson et al., 2008; Wang et al., 2009, 2012; Griffith et al., 2010; Watanabe et al., 2010; de Souza et al., 2011; Fayed et al., 2011, 2014; Zimny et al., 2011; Lim et al., 2012; Seo et al., 2012; Yang et al., 2012; Targosz-Gajniak et al., 2013; Liu et al., 2014; Riese et al., 2015; Guo et al., 2016; Zeydan et al., 2017; Mitolo et al., 2019; Oeltzschner et al., 2019) compared the differences in metabolites between 770 MCI patients and 1,132 healthy control subjects, 16 studies (Kantarci et al., 2007; Rami et al., 2007; Ding et al., 2008; Wang et al., 2009, 2012; Watanabe et al., 2010; de Souza et al., 2011; Fayed et al., 2011, 2014; Zimny et al., 2011; Lim et al., 2012; Shiino et al., 2012; Graff-Radford et al., 2014; Guo et al., 2016; Marjańska et al., 2019; Mitolo et al., 2019) compared the differences in metabolites between 610 AD patients and 822 healthy control subjects, and 12 studies (Kantarci et al., 2007; Rami et al., 2007; Wang et al., 2009, 2012; Watanabe et al., 2010; de Souza et al., 2011; Fayed et al., 2011, 2014; Zimny et al., 2011; Lim et al., 2012; Guo et al., 2016; Mitolo et al., 2019) made a comparison between 440 AD patients and 421 MCI patients. Moreover, there were another two studies (Kantarci et al., 2007; Seo et al., 2012) longitudinally tracking the metabolite differences between MCI-converter and MCI-stable patients.

Metabolite Ratios

We finally identified 21 studies (Kantarci et al., 2000, 2002, 2007; Rami et al., 2007; García et al., 2008; Olson et al., 2008; Wang et al., 2009, 2012; Chao et al., 2010; Griffith et al., 2010; de Souza et al., 2011; Fayed et al., 2011, 2014; Zimny et al., 2011; Lim et al., 2012; Seo et al., 2012; Yang et al., 2012; Targosz-Gajniak et al., 2013; Guo et al., 2016; Mitolo et al., 2019) with a total sample size of 1,695 (681 MCI patients and 1,014 healthy controls) comparing the metabolite ratio in the posterior cingulate. The results showed that NAA/Cr (SMD: −0.60 [95% CI: −0.85 to −0.35], $z = -4.74$, $P < 0.05$, **Figures 3A**, **9**) and NAA/mI (SMD: −1.01 [95% CI: −1.58 to −0.45], $z = -3.52$, $P < 0.05$, **Figures 4A**, **9**) were significantly decreased in MCI patients than in healthy controls, while mI/Cr (SMD: 0.44 [95% CI: 0.27–0.61], $z = 5.15$, $P < 0.05$, **Figures 5A**, **9**) and Glx/Cr (SMD: 0.28 [95% CI: 0.09–0.48], $z = 2.89$, $P < 0.05$, **Figures 6A**, **9**) were significantly increased. There was no significant difference in the ratio of mI/NAA (SMD: −0.02 [95% CI: −0.79 to 0.82], $z = 0.04$, $P > 0.1$, **Supplementary Table 1**). Besides, Cho/Cr (SMD: 0.34 [95% CI: −0.00 to 0.69], $z = 1.96$, $P > 0.05$, **Supplementary Table 1**) has an uptrend in the posterior cingulate of MCI patients. On the contrary, there was a downward trend in NAA/Cho (SMD: −0.35 [95% CI: −0.72 to 0.03], $z = -1.80$, $P > 0.05$, **Supplementary Table 1**).

Additionally, 14 studies (Kantarci et al., 2007; Rami et al., 2007; Ding et al., 2008; Wang et al., 2009, 2012; de Souza et al., 2011; Fayed et al., 2011, 2014; Zimny et al., 2011; Lim et al., 2012; Shiino et al., 2012; Graff-Radford et al., 2014; Guo et al., 2016; Mitolo et al., 2019) were analyzed to compare the metabolite ratios in 600 AD patients and 428 healthy control subjects. The results showed that five metabolites' ratios (NAA/Cr, mI/Cr, Cho/Cr, mI/NAA, NAA/mI, and Glx/Cr) were significantly different in AD and healthy control subjects. For the comparisons between AD and controls, NAA/Cr (SMD: −1.06 [95% CI: −1.46 to −0.67], $z = -5.27$, $P < 0.05$, **Figures 3B**, **9**) and NAA/mI (SMD: −1.73 [95% CI: −2.95 to −0.51], $z = -2.79$, $P < 0.05$, **Figures 4B**, **9**) were significantly decreased in the posterior cingulate of AD patients, while mI/Cr (SMD: 0.78 [95% CI: 0.57–1.00], $z = 7.19$, $P < 0.05$, **Figures 5B**, **9**), Glx/Cr (SMD: 0.01 [95% CI: −0.21 to 0.24], $z = 0.09$, $P < 0.05$, **Figure 6B**), mI/NAA (SMD:1.01 [95% CI: 0.75–1.26], $z = 7.64$, $P < 0.05$, **Supplementary Figure 4A** and **Figure 9**), and Cho/Cr (SMD:0.35 [95% CI: 0.11–0.59], $z = 2.85$, $P < 0.05$, **Supplementary Figure 4B** and **Figure 9**) were remarkably increased.

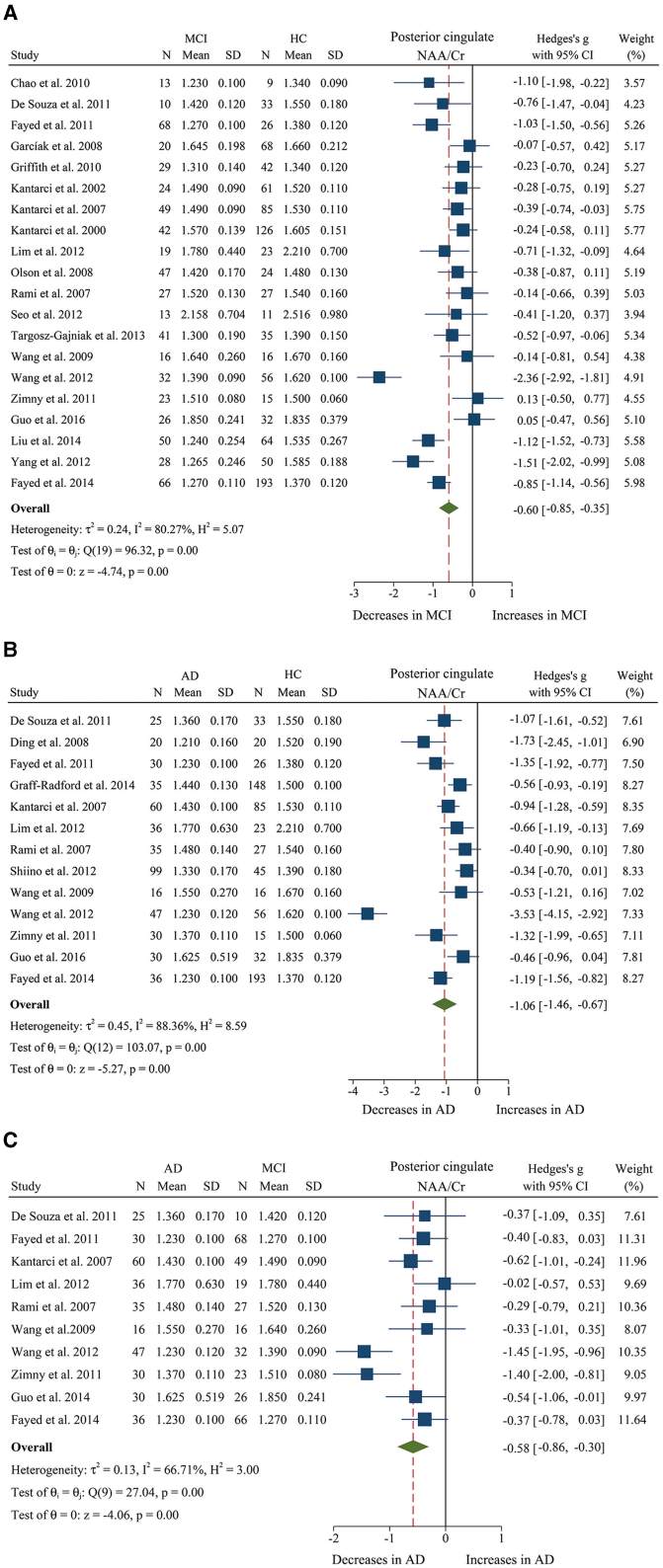

FIGURE 3 | Forest plots show the change of the ratio of NAA/Cr in the posterior cingulate between MCI, AD patients, and HC subjects. **(A)** Data include 1639 individuals from 20 studies for meta-analysis of NAA/Cr levels between MCI and HC. **(B)** Data include 1218 individuals from 13 studies for meta-analysis of NAA/Cr levels between AD and HC. **(C)** Data include 681 individuals from 5 studies for meta-analysis of NAA/Cr levels between AD and MCI.

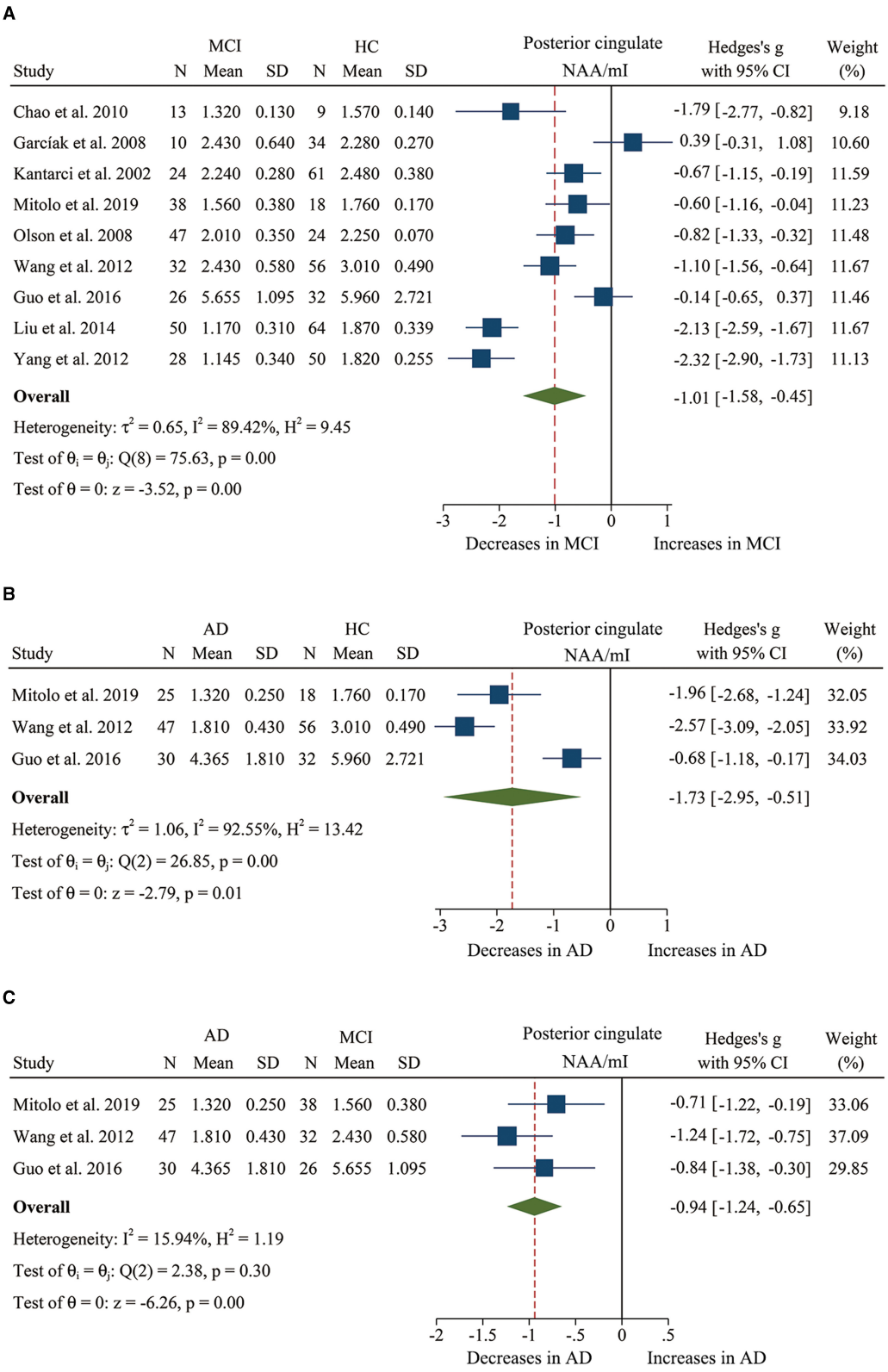

FIGURE 4 | Forest plots show the change of the ratio of NAA/mI in the posterior cingulate between MCI, AD patients, and HC subjects. **(A)** Data include 616 individuals from 9 studies for meta-analysis of NAA/mI levels between MCI and HC. **(B)** Data include 208 individuals from 3 studies for meta-analysis of NAA/mI levels between AD and HC. **(C)** Data include 198 individuals from 3 studies for meta-analysis of NAA/mI levels between AD and MCI.

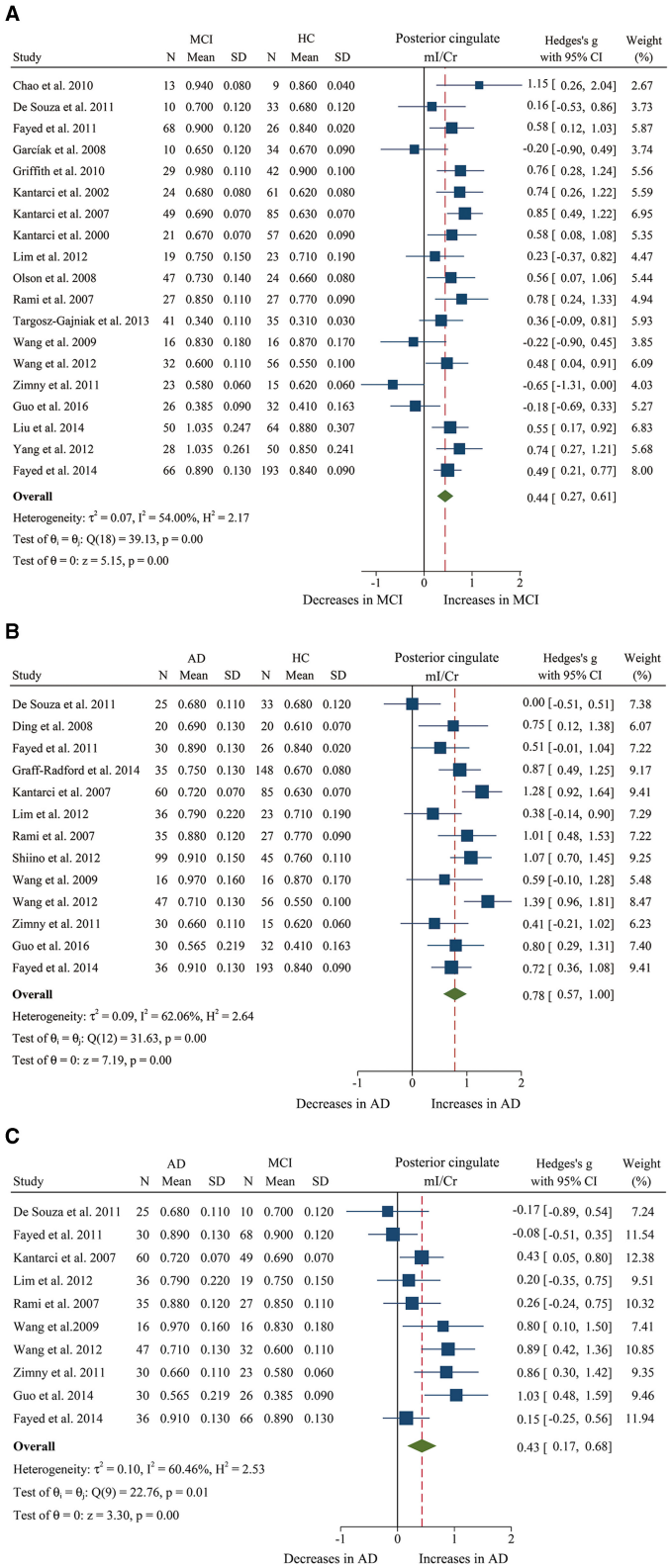

FIGURE 5 | Forest plots show the change of the ratio of mI/Cr in the posterior cingulate between MCI, AD patients, and HC subjects. **(A)** Data include 1481 individuals from 19 studies for meta-analysis of mI/Cr levels between MCI and HC. **(B)** Data include 1,218 individuals from 13 studies for meta-analysis of mI/Cr levels between AD and HC. **(C)** Data include 681 individuals from 5 studies for meta-analysis of mI/Cr levels between AD and MCI.

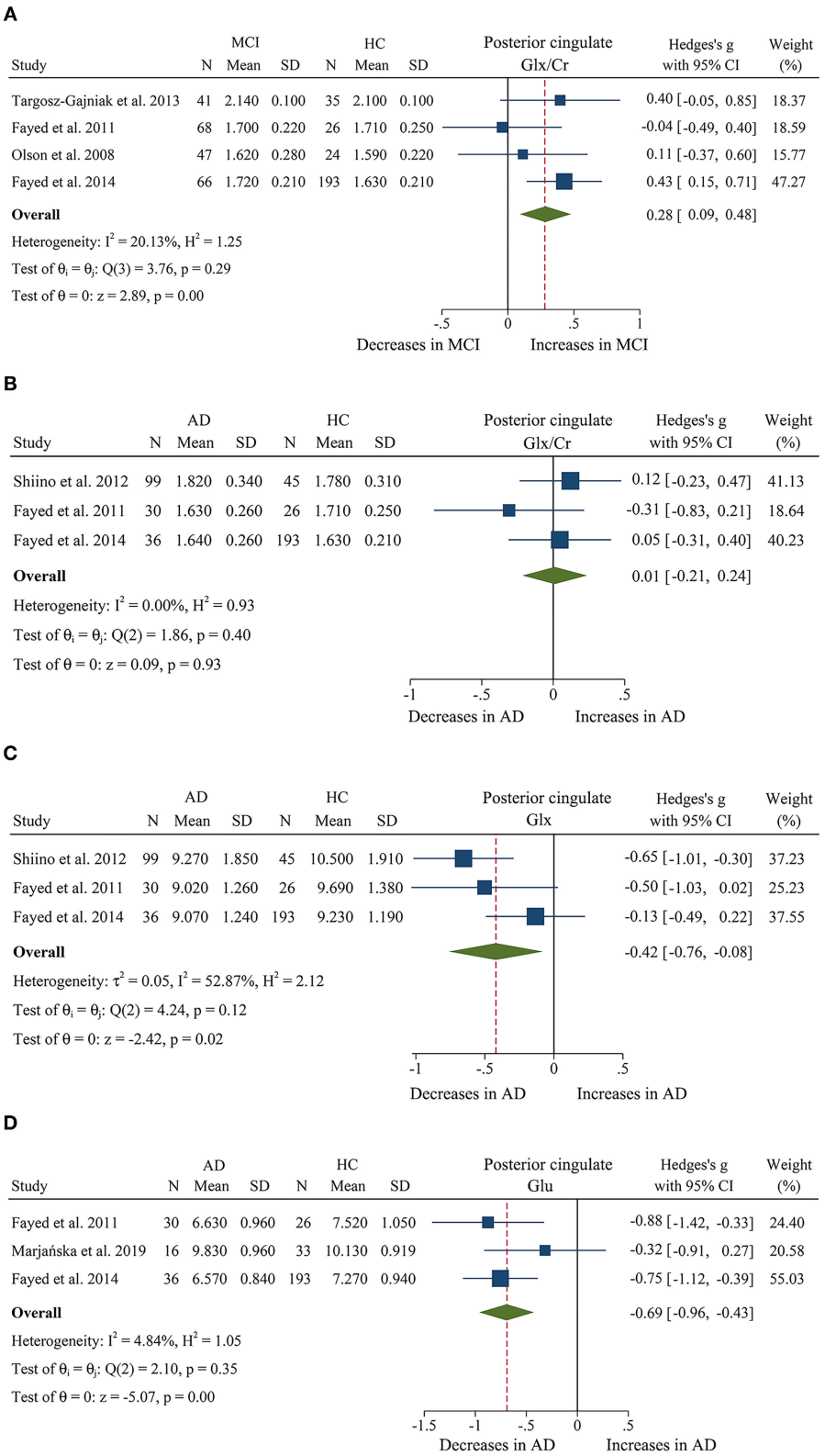

FIGURE 6 | Forest plots show the change of the levels of Glx/Cr, Glx, and Glu in the posterior cingulate between MCI, AD patients, and HC subjects. **(A)** Data include 500 individuals from 4 studies for meta-analysis of Glx/Cr levels between MCI and HC. **(B)** Data include 429 individuals from 3 studies for meta-analysis of Glx/Cr levels between AD and HC. **(C)** Data include 429 individuals from 3 studies for meta-analysis of Glx levels between AD and HC. **(D)** Data include 334 individuals from 3 studies for meta-analysis of Glu levels between AD and HC.

Next, we performed a meta-analysis to compare the ratios in the posterior cingulate, comprising 370 AD patients and 374 MCI patients (Kantarci et al., 2007; Rami et al., 2007; Wang et al., 2009, 2012; de Souza et al., 2011; Fayed et al., 2011, 2014; Zimny et al., 2011; Lim et al., 2012; Guo et al., 2016; Mitolo et al., 2019). The results demonstrated that NAA/Cr (SMD: −0.58 [95% CI: −0.86 to −0.30], $z = -4.06$, $P < 0.05$, **Figures 3C**, **9**) and NAA/mI (SMD: −0.94 [95% CI: −1.24 to −0.65], $z = -6.26$, $P < 0.05$, **Figures 4C**, **9**) were significantly higher in the MCI group than that in the AD patients. Meanwhile, the analysis revealed a remarkable increase in mI/Cr (SMD: 0.43 [95% CI: 0.17–0.68], $z = 3.03$, $P < 0.05$, **Figures 5C**, **9**) and mI/NAA (SMD: 0.92 [95% CI: 0.31–1.53], $z = 2.97$, $P < 0.05$, **Supplementary Figure 4C** and **Figure 9**) with a high heterogeneity.

Two studies were extracted to compare the ratios in 25 MCI-converter patients and 37 MCI-stable patients (Kantarci et al., 2007; Seo et al., 2012). The results revealed that there was no difference in NAA/Cr (SMD: 0.17 [95% CI: −0.33 to −0.67], $z = 0.68$, $P > 0.1$, **Supplementary Table 1**) and Cho/Cr (SMD: 0.11 [95% CI: −0.39 to 0.61], $z = -0.44$, $P > 0.1$, **Supplementary Table 1**).

Taken together, these results suggest that the ratios of NAA/Cr and NAA/mI were reduced in AD patients as compared to MCI patients and healthy controls. However, in the posterior cingulate, mI/NAA and Glx/Cr decreased remarkably compared to that of AD patients.

Metabolite Concentrations

We compared the concentrations of metabolites, extracting data from 10 studies with a sample size of 375 MCI patients and 502 healthy control subjects (Rami et al., 2007; Olson et al., 2008; Watanabe et al., 2010; Fayed et al., 2011, 2014; Yang et al., 2012; Liu et al., 2014; Riese et al., 2015; Zeydan et al., 2017; Oeltzschner et al., 2019). The analyses showed that NAA was significantly decreased in the posterior cingulate of MCI patients (SMD: −0.73 [95% CI: −0.88 to −0.59], $z = -9.92$, $P < 0.05$, **Figures 7A**, **9**), while mI was significantly increased (SMD: 0.54 [95% CI: 0.39–0.69], $z = 7.24$, $P < 0.05$, **Supplementary Figure 4D** and **Figure 9**). There was no significant difference in the concentrations of Cr (SMD: −0.17 [95% CI: −0.44 to 0.10], $z = -1.24$, $P > 0.1$), Cho (SMD: 0.12 [95% CI: −0.03 to 0.27], $z = 1.60$, $P > 0.1$), and Glx (SMD: −0.08 [95% CI: −0.62 to 0.46], $z = -0.46$, $P > 0.1$). Besides, three studies were included to investigate Glu concentration, and the analysis revealed a downward trend with a high heterogeneity (SMD: −0.44 [95% CI: −0.94 to 0.06], $z = -1.74$, $P = 0.08$).

Then, the metabolite concentrations were compared in 6 studies with 286 AD patients and 376 healthy controls (Rami et al., 2007; Watanabe et al., 2010; Fayed et al., 2011, 2014; Shiino et al., 2012; Marjańska et al., 2019). The results demonstrated that NAA (SMD: −0.94 [95% CI: −1.21 to −0.67], $z = -6.87$, $P < 0.05$, **Figures 7B**, **9**), Glu (SMD: −0.69 [95% CI: −0.96 to −0.43], $z = -5.07$, $P < 0.05$, **Figures 6D**, **9**), and Glx (SMD: −0.42 [95% CI: −0.76 to −0.08], $z = -2.42$, $P < 0.05$, **Figures 6C**, **9**) were significantly higher in healthy controls than that in the AD patients, while mI (SMD: 0.44 [95% CI: 0.26–0.61], $z = 4.97$, $P < 0.05$, **Supplementary Figure 4E** and **Figure 9**) was lower than that in the AD patients. Besides, 4 studies were included to investigate Cr concentration and the analysis revealed a downward trend with a high heterogeneity (SMD: −0.37 [95% CI: −0.80 to 0.05], $z = -1.71$, $P > 0.05$, **Supplementary Table 1** and **Figure 9**). Six studies (Rami et al., 2007; Watanabe et al., 2010; Fayed et al., 2011, 2014; Shiino et al., 2012; Marjańska et al., 2019) were included to investigate Cho concentration and the analysis manifested an upward trend with a medium heterogeneity (SMD: 0.23 [95% CI: −0.02 to 0.48], $z = 1.81$, $P > 0.05$, **Supplementary Table 1** and **Figure 9**).

Next, we compared the concentrations in the posterior cingulate, with 171 AD patients and 208 MCI patients (Rami et al., 2007; Watanabe et al., 2010; Fayed et al., 2011, 2014). The results demonstrated that NAA was significantly decreased in the AD patients (SMD: −0.42 [95% CI: −0.62 to −0.21], $z = -3.89$, $P < 0.05$, **Figures 7C**, **9**), while there was no difference in mI (SMD: −0.07 [95% CI: −0.28 to 0.13], $z = -0.69$, $P > 0.1$, **Supplementary Table 1**) and Cho (SMD: −0.05 [95% CI: −0.57 to 0.48], $z = -0.17$, $P > 0.1$, **Supplementary Table 1**).

Briefly, according to the results of meta-analysis of AD and MCI, the concentration of NAA was decreased in AD and MCI patients, especially in AD patients. In addition, mI concentration was seen to increase faster in AD patients, compared to subjects who converted to MCI and cognitively normal elderly.

Meta-Analysis of Temporal Lobe

There were 7 studies (Kantarci et al., 2000; Block et al., 2002; Herminghaus et al., 2003; Frederick et al., 2004; Rami et al., 2007; Azevedo et al., 2008; Li et al., 2010) investigating the ratio of metabolites in the temporal lobe and included 82 MCI patients, 157 AD patients, and 207 healthy controls. Of these studies, 3 (Kantarci et al., 2000; Rami et al., 2007; Li et al., 2010) compared the differences in metabolites between 82 MCI patients and 124 healthy control subjects, and 5 (Block et al., 2002; Herminghaus et al., 2003; Frederick et al., 2004; Rami et al., 2007; Azevedo et al., 2008) compared the differences between 157 AD patients and 110 healthy control subjects.

Metabolite Ratios

First, we performed a meta-analysis to compare the ratios of NAA/Cr in the temporal lobe, comprising 82 MCI patients and 124 healthy controls (Kantarci et al., 2000; Rami et al., 2007; Li et al., 2010). The analysis showed that there was no significant difference in NAA/Cr between the two groups (SMD: −0.12 [95% CI: −0.40 to 0.17], $z = -0.81$, $P > 0.1$, **Supplementary Table 1**).

When comparing AD with controls, 5 studies (Block et al., 2002; Herminghaus et al., 2003; Frederick et al., 2004; Rami et al., 2007; Azevedo et al., 2008) were included for meta-analysis. The results showed that the ratio of NAA/Cr was significantly different between the two groups, and there was a difference in the ratio of Cho/Cr and mI/Cr. The ratio of NAA/Cr (Block et al., 2002; Herminghaus et al., 2003; Frederick et al., 2004; Rami et al., 2007; Azevedo et al., 2008) was remarkably decreased in the AD patients with high heterogeneity (SMD: −0.68 [95% CI: −1.24 to −0.12], $z = -2.40$, $P < 0.05$, **Supplementary Figure 4F** and **Figure 9**). Meanwhile, Cho/Cr (Block et al., 2002; Frederick et al., 2004; Rami et al., 2007; Azevedo et al., 2008) has a downward trend in the temporal lobe of AD patients (SMD: −0.27 [95% CI: −0.57 to 0.01], $z = -1.87$, $P > 0.05$, **Supplementary Table 1**). On

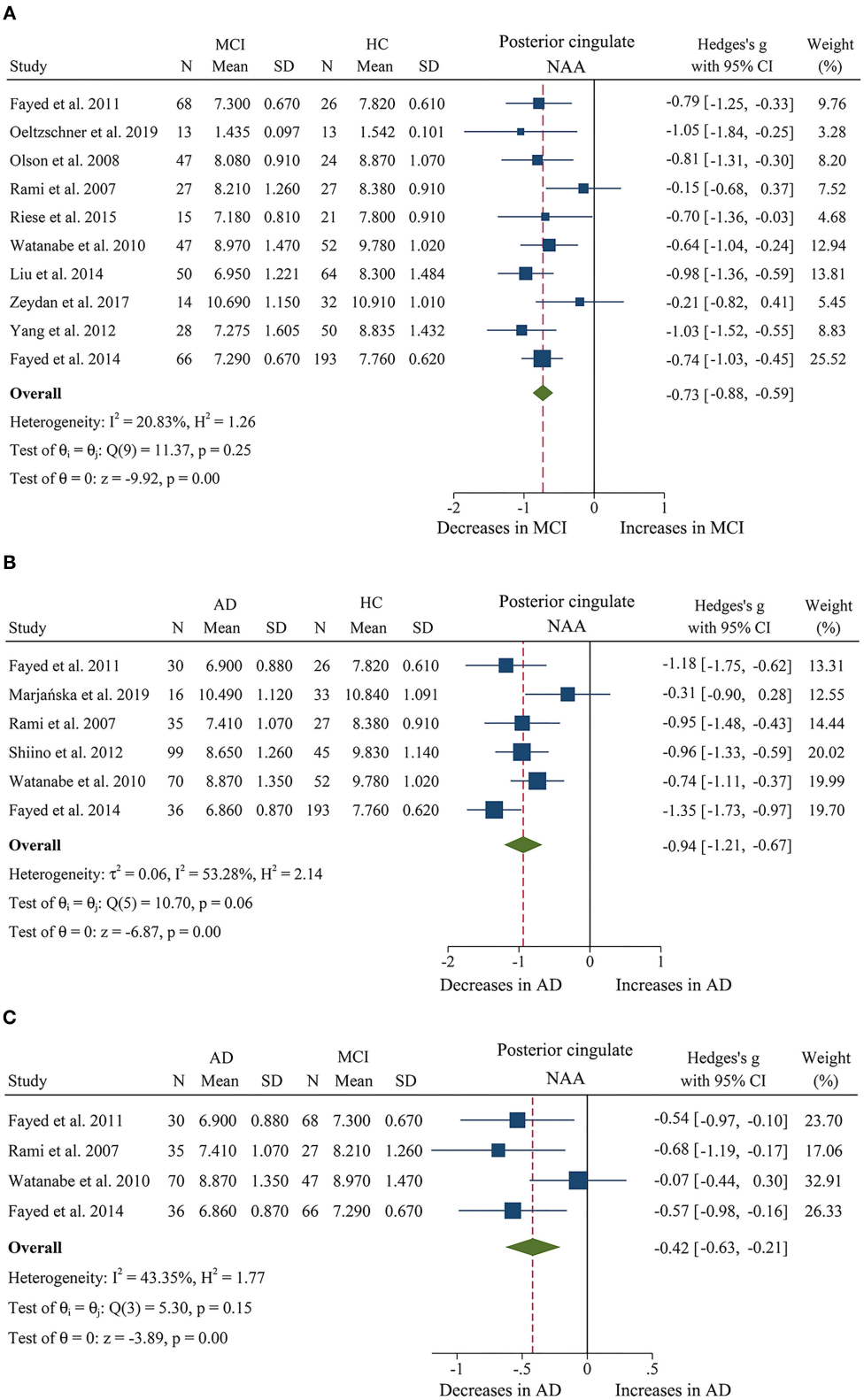

FIGURE 7 | Forest plots show the change of NAA in the posterior cingulate during the development from healthy people to AD. **(A)** Data include 877 individuals from 10 studies for meta-analysis of NAA levels between MCI and HC. **(B)** Data include 662 individuals from 6 studies for meta-analysis NAA levels between AD and HC. **(C)** Data include 379 individuals from 4 studies for meta-analysis NAA levels between AD and MCI.

the contrary, there was an uptrend in mI/Cr (SMD: 0.35 [95% CI: −0.01 to 0.71], $z = 1.91$, $P > 0.05$, **Supplementary Table 1**).

Meta-Analysis of the Parietal Lobe

Eight studies (Herminghaus et al., 2003; Ackl et al., 2005; Chao et al., 2005; Zhu et al., 2006; Siger et al., 2009; Li et al., 2010; Modrego et al., 2011; Targosz-Gajniak et al., 2013) with a total sample size of 639 (162 AD patients, 187 MCI patients, and 290 healthy controls) were included for meta-analysis to investigate the ratio of metabolites in the parietal lobe. Specifically, 3 studies (Herminghaus et al., 2003; Ackl et al., 2005; Zhu et al., 2006) compared the differences in metabolites between 80 AD patients and 71 healthy control subjects in parietal WM, and 5 studies (Herminghaus et al., 2003; Ackl et al., 2005; Chao et al., 2005; Zhu et al., 2006; Siger et al., 2009) compared the differences in metabolites between 162 AD patients and 151 healthy control subjects in parietal GM. Moreover, there were 2 studies (Modrego et al., 2005, 2011) longitudinally tracking the metabolite differences between MCI-converter and MCI-stable patients.

Metabolite Ratios

We finally identified 3 studies with a total sample size of 326 (187 MCI patients and 139 healthy controls) to compare the ratio of NAA/Cr in the parietal lobe. The analysis revealed that there was no significant difference observed between the two groups (SMD: 0.02 [95% CI: −0.20 to 0.24], $z = 0.16$, $P > 0.1$, **Supplementary Table 1**).

Next, 3 studies (Herminghaus et al., 2003; Ackl et al., 2005; Zhu et al., 2006) were included to compare the ratio of NAA/Cr in parietal WM, comprising 80 AD patients and 71 healthy controls. The analysis revealed a significant decrease in the AD patients with high significant heterogeneity (SMD: −1.16 [95% CI: −1.72 to −0.60], $z = -4.06$, $P < 0.05$, **Supplementary Figure 5A** and **Figure 9**) in parietal WM. A meta-analysis of 3 studies (Herminghaus et al., 2003; Ackl et al., 2005; Zhu et al., 2006) limited to the parietal GM lobe showed a remarkable decrease in NAA/Cr in the ADs patients (SMD: −1.10 [95% CI: −2.02 to −0.70], $z = -2.33$, $P < 0.05$, **Supplementary Figure 5B** and **Figure 9**).

When comparing the metabolite ratios between 56 MCI-converter patients and 68 MCI-stable patients in the parietal lobe (Modrego et al., 2005, 2011), there were significant differences in two ratios between the two groups. The results demonstrated that NAA/Cr (SMD: −0.88 [95% CI: −1.70 to −0.07], $z = -2.12$, $P < 0.05$, **Figures 8A**, **9**) was significantly higher than that in the MCI-converter patients, while the ratio of mI/Cr (SMD: 0.42 [95% CI: 0.06–0.78], $z = 2.30$, $P < 0.05$, **Figures 8B**, **9**) was lower than that in the MCI-converter patients. Besides, the results revealed that there was no difference in Cho/Cr (SMD: 0.15 [95% CI: −0.21 to 0.50], $z = 0.82$, $P > 0.1$, **Supplementary Table 1**) and NAA/mI (SMD: −0.08 [95% CI: −0.92 to 0.76], $z = -0.18$, $P > 0.1$, **Supplementary Table 1**) between the two groups.

Metabolite Concentrations

We compared the concentrations of metabolites, extracting data from 96 AD patients and 102 healthy control subjects in 3 studies (Chao et al., 2005; Zhu et al., 2006; Siger et al., 2009). The results showed that the concentrations of NAA were significantly decreased in the parietal GM of AD patients (SMD: −0.95 [95% CI: −1.24 to −0.66], $z = -6.36$, $P < 0.05$, **Supplementary Figure 5C** and **Figure 9**).

Meta-Analysis of the Occipital Lobe

There were 5 studies (Block et al., 2002; Azevedo et al., 2008; Watanabe et al., 2010; Graff-Radford et al., 2014; Marjańska et al., 2019) with a total sample size of 481 (195 AD patients and 286 healthy controls) included for meta-analysis to investigate the ratio of metabolites in the occipital lobe. Moreover, there were 3 more studies (Modrego et al., 2005, 2011; Seo et al., 2012) longitudinally tracking the metabolite differences between MCI-converter and MCI-stable patients.

Metabolite Ratios

Of the eligible studies, 3 (Block et al., 2002; Azevedo et al., 2008; Graff-Radford et al., 2014) reported data on metabolite ratios. These studies comprised 109 AD patients and 201 healthy controls. The results showed that there was a downward trend in NAA/Cr of AD patients (SMD: −0.22 [95% CI: −0.47 to 0.04], $z = -1.69$, $P > 0.05$, **Supplementary Table 1**), while there was no difference in Cho/Cr between the two groups (SMD: 0.22 [95% CI: −0.18 to 0.63], $z = 1.08$, $P > 0.1$, **Supplementary Table 1**).

Then, we identified 3 studies (Modrego et al., 2005, 2011; Seo et al., 2012) with a total sample size of 127 (63 MCI-converter and 74 MCI-stable patients) to compare the ratio in the occipital lobe The results demonstrated that NAA/Cr was significantly higher than that in the MCI-converter patients (SMD: −0.98 [95% CI: −1.98 to 0.02], $z = -1.93$, $P > 0.05$, **Supplementary Table 1**), while there were no differences in mI/Cr (SMD: −0.02 [95% CI: −0.37 to 0.34], $z = -0.09$, $P > 0.1$), Cho/Cr (SMD: −0.12 [95% CI: −0.45 to 0.22], $z = -0.67$, $P > 0.1$, **Supplementary Table 1**), and NAA/mI (SMD: −0.44 [95% CI: −1.44 to 0.56], $z = -0.87$, $P > 0.1$, **Supplementary Table 1**).

Metabolite Concentrations

Three studies (Azevedo et al., 2008; Watanabe et al., 2010; Marjańska et al., 2019) were extracted to compare the concentrations in 99 AD patients and 100 healthy controls. The results revealed that NAA concentrations were significantly decreased in the AD patients (SMD: −0.33 [95% CI: −0.62 to −0.05], $z = -2.29$, $P < 0.05$, **Supplementary Figure 6A** and **Figure 9**), while there were no differences in the concentrations of Cho (SMD: −0.11 [95% CI: −0.40 to 0.17], $z = -0.80$, $P > 0.1$, **Supplementary Table 1**), Cr (SMD: −0.21 [95% CI: −0.49 to 0.07], $z = -1.45$, $P > 0.1$, **Supplementary Table 1**), and mI (SMD: 1.09 [95%CI: −0.87 to 3.05], $z = 1.09$, $P > 0.1$, **Supplementary Table 1**).

Meta-Analysis of Anterior Cingulate

Three studies (Lim et al., 2012; Guo et al., 2016; Huang et al., 2017) investigated the anterior cingulate including 66 MCI patients, 83 patients with AD, and 70 healthy control subjects. Specifically, 3 studies (Lim et al., 2012; Guo et al., 2016; Huang et al., 2017) performed a comparison in the changes between 66 MCI patients and 70 healthy control subjects, 3 studies (Lim et al., 2012; Guo et al., 2016; Huang et al., 2017) performed

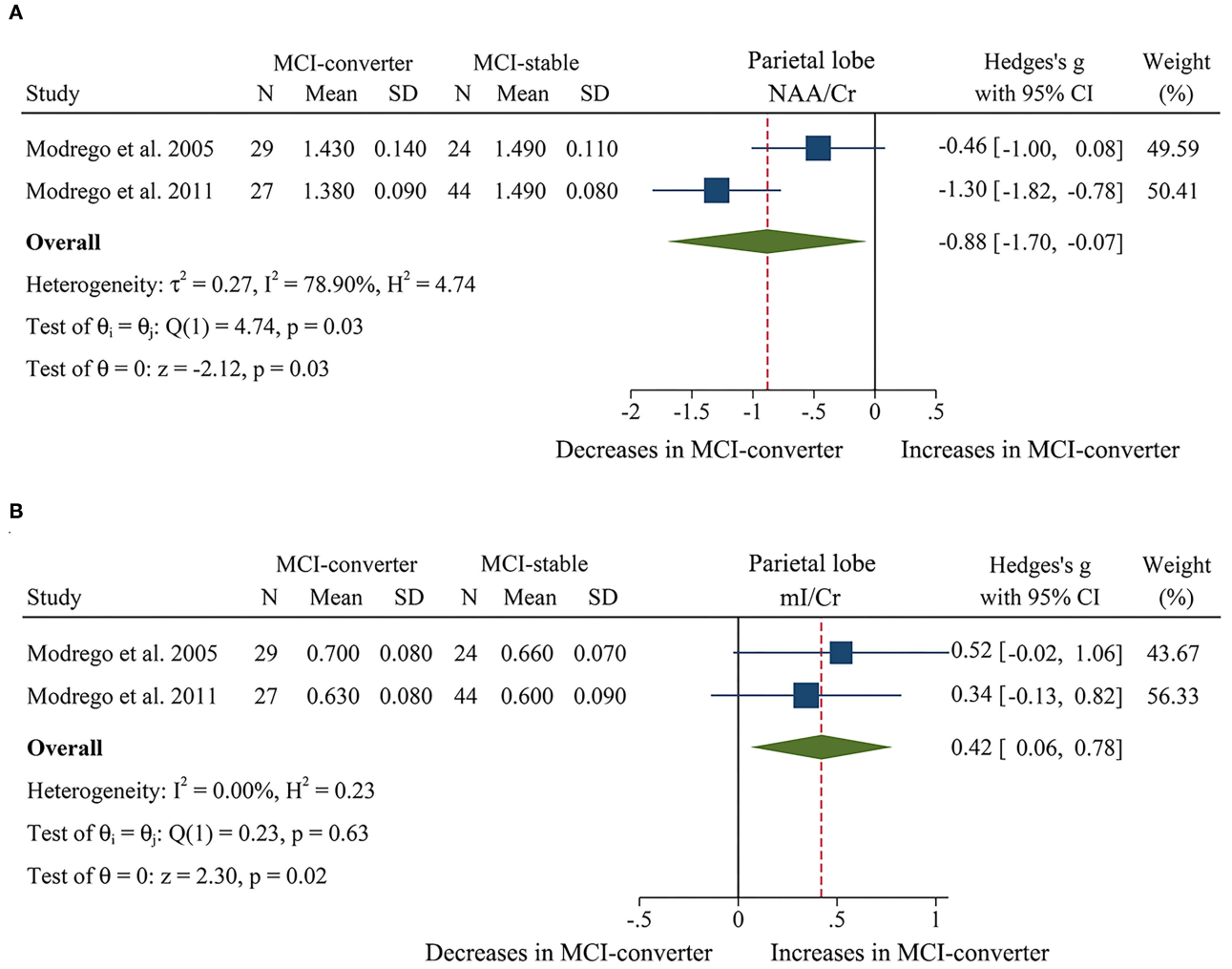

FIGURE 8 | Forest plots show the change of NAA/Cr and mI/Cr in parietal lobe between MCI-converter and MCI-stable patients. **(A)** Data include 124 individuals from 2 studies for meta-analysis of NAA/Cr levels between MCI-converter and MCI-stable patients. **(B)** Data include 124 individuals from 2 studies for meta-analysis mI/Cr levels between MCI-converter and MCI-stable patients.

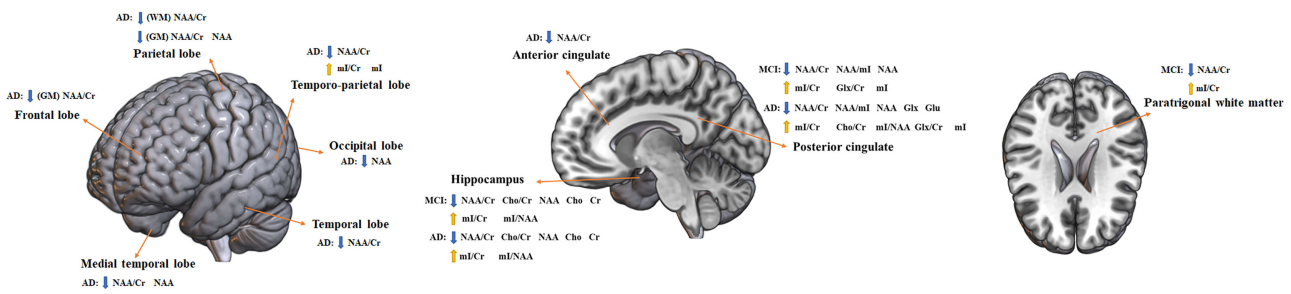

FIGURE 9 | Altered metabolites in MCI and AD brain structures. AD, Alzheimer's disease; MCI, mild cognitive impairment; WM, white matter; GM, gray matter; NAA, N-acetyl aspartate; Cr, creatine; mI, myo-inositol; Cho, choline; Glx, glutamate + glutamine; Glu, glutamine. Directions: down, decrease; up, increase.

a comparison in the changes between 83 AD patients and 70 healthy control subjects, and 3 studies (Lim et al., 2012; Guo et al., 2016; Huang et al., 2017) were conducted to observe the differences of metabolites in 83 AD patients and 66 MCI patients.

Metabolite Ratios

First, we identified 3 studies (Lim et al., 2012; Guo et al., 2016; Huang et al., 2017) with a total sample size of 136 (66 MCI patients and 70 healthy controls) to compare the ratio of NAA/Cr

in the anterior cingulate. The analysis showed that there was no difference between the two groups (SMD: −0.20 [95% CI: −0.68 to 0.29], $z = -0.80$, $P > 0.1$, **Supplementary Table 1**).

For the comparisons between 83 AD patients and 70 healthy controls (Lim et al., 2012; Guo et al., 2016; Huang et al., 2017), NAA/Cr was significantly decreased in the anterior cingulate of AD patients (SMD: −0.45 [95% CI: −0.77 to −0.13], $z = -2.75$, $P < 0.05$, **Supplementary Figure 6B** and **Figure 9**).

The comparison of 83 AD patients and 66 MCI patients in the ratio of NAA/Cr (Lim et al., 2012; Guo et al., 2016; Huang et al., 2017) revealed that there was no difference between the two groups (SMD: −0.25 [95% CI: −0.88 to 0.39], $z = -1.10$, $P > 0.1$, **Supplementary Table 1**).

Meta-Analysis of the Temporo-Parietal Lobe

Four studies (Ernst et al., 1997; Fernández et al., 2005; Rami et al., 2007; Zhang et al., 2009) investigated the temporo-parietal lobe including 80 AD patients and 71 healthy control subjects to compare the metabolites between the two groups.

Metabolite Ratios

We compared the ratios of metabolites, extracting data from 157 AD patients and 110 healthy control subjects in 4 studies (Ernst et al., 1997; Fernández et al., 2005; Rami et al., 2007; Zhang et al., 2009). The results showed that two metabolites' ratios (NAA/Cr, mI/Cr) were significantly different in AD and healthy control subjects. NAA/Cr was significantly decreased in the temporo-parietal lobe of AD patients (SMD: −0.72 [95% CI: −1.36 to −0.07], $z = -2.18$, $P < 0.05$, **Supplementary Figure 6C** and **Figure 9**), while mI/Cr were significantly increased (SMD: 1.43 [95% CI: 0.60–2.27], $z = 3.36$, $P < 0.05$, **Supplementary Figure 6D** and **Figure 9**).

Metabolite Concentrations

Three studies (Ernst et al., 1997; Fernández et al., 2005; Rami et al., 2007) were extracted to compare the concentrations in 67 AD patients and 58 healthy controls. Specifically, mI was significantly increased in AD patients (SMD: 1.37 [95% CI: 0.26–2.48], $z = 2.42$, $P < 0.05$, **Supplementary Figure 6E** and **Figure 9**). There were no differences in NAA (SMD: −0.17 [95% CI: −0.51 to 0.18], $z = -0.93$, $P > 0.1$, **Supplementary Table 1**), Cho (SMD: −0.10 [95% CI: −0.44 to 0.25], $z = -0.55$, $P > 0.1$, **Supplementary Table 1**), and Cr (SMD: 0.51 [95% CI: −0.61 to 1.62], $z = 0.89$, $P > 0.1$, **Supplementary Table 1**) concentrations between the two groups.

Meta-Analysis of the Frontal Region

Four studies (Parnetti et al., 1997; Chao et al., 2005; Zhu et al., 2006; Siger et al., 2009) with a total sample size of 218 (109 AD patients and 109 healthy controls) were included for meta-analysis to investigate the ratio of metabolites in the frontal region. Specifically, 3 studies (Parnetti et al., 1997; Zhu et al., 2006; Siger et al., 2009) compared the differences in metabolites between 61 AD patients and 61 healthy control subjects in the frontal WM, and 3 studies (Chao et al., 2005; Zhu et al., 2006; Siger et al., 2009) compared the differences in metabolites between 96 AD patients and 102 healthy control subjects in the frontal GM.

Metabolite Concentrations

We compared the concentrations of metabolites in the frontal WM, extracting data from 61 AD patients and 61 healthy control subjects in 3 studies (Parnetti et al., 1997; Zhu et al., 2006; Siger et al., 2009). The results showed that the concentration of mI has an upward trend in AD patients (SMD: 0.64 [95% CI: −0.06 to 1.34], $z = 1.80$, $P > 0.05$, **Supplementary Table 1**), and there was no significant difference in the concentrations of NAA between the two groups (SMD: −0.15 [95% CI: −0.50 to 0.21], $z = -0.80$, $P > 0.1$, **Supplementary Table 1**). Besides, 3 studies (Parnetti et al., 1997; Zhu et al., 2006; Siger et al., 2009) were included to investigate the concentration of NAA in the frontal GM and the analysis manifested a remarkable decrease with high heterogeneity (SMD: −0.37 [95% CI: −0.65 to −0.09], $z = -2.63$, $P < 0.05$, **Supplementary Figure 6F** and **Figure 9**).

Meta-Analysis of Paratrigonal White Matter

Three studies (Catani et al., 2001; Metastasio et al., 2006; Yang et al., 2012) reported data from paratrigonal white matter including 89 MCI patients and 177 healthy control subjects to compare the metabolites between the two groups.

Metabolite Ratios

We compared the ratios of metabolites, extracting data from 89 MCI patients and 177 healthy control subjects in 3 studies (Catani et al., 2001; Metastasio et al., 2006; Yang et al., 2012). The results showed that two metabolites' ratios (NAA/Cr, mI/Cr) were significantly different between the two groups, and there was no significant difference in the ratio of Cho/Cr (SMD: 0.00 [95% CI: −0.26 to 0.25], $z = -0.01$, $P > 0.1$, **Supplementary Table 1**). Among them, NAA/Cr (SMD: −0.76 [95% CI: −1.02 to −0.49], $z = -5.66$, $P < 0.05$, **Supplementary Figure 7A** and **Figure 9**) was significantly decreased in paratrigonal white matter of MCI patients, while mI/Cr (SMD: 1.02 [95% CI: 0.20–1.84], $z = 2.44$, $P < 0.05$, **Supplementary Figure 7B** and **Figure 9**) was significantly increased.

DISCUSSION

To investigate the changes of neurochemicals estimated by ^{1}H-MRS in brain regions with the progression of AD, we conducted a comprehensive meta-analysis including 63 studies with 3,271 subjects. The results showed that: (1) compared with MCI patients, the ratio of NAA/Cr in the hippocampus of AD patients decreased significantly; the ratios of NAA/Cr, NAA/mI, and the concentration of NAA in PC decreased significantly, whereas the ratios of mI/Cr and mI/NAA increased markedly. NAA and mI were considered as potential biomarkers for monitoring the progression from MCI to AD and early diagnosis of AD; (2) the metabolite difference of neurochemicals between MCI and AD was systematically analyzed and has found that the concentration of Glx in PC was different between MCI and AD patients, with an increase in AD but no changes in MCI groups. Therefore, Glx

was crucial in differentiating MCI from AD, and was regarded as a potential marker to predict AD.

Metabolic Changes of Neurochemicals During the Progression From MCI to AD

NAA is an important indicator of neuronal metabolism and plays a number of roles, which includes maintaining fluid balance in the brain, providing acetic acid salt for the synthesis of myelin in oligodendrocytes, and providing energy for the glutamylation of amino acid in neuronal mitochondria. Also, NAA is considered as a biomarker of neuronal function and density, as it can reflect the density and functional state of neurons and axons. Moreover, the concentration of NAA in the cortex can provide information about the growth of neurons. In addition, its concentration in white matter can reflect the development of axons. Due to NAA being located at the synaptic terminal, dendrites, and neuronal somata, its concentration may reflect the level of synapses and the ratio of NAA/Cr reflects the integrity of synapses (Onwordi et al., 2021). Our meta-analysis showed that during the pathological development from MCI to AD, the ratio of NAA/Cr in the hippocampus and PC, and the concentration of NAA in PC decreased dramatically. Meanwhile, the level of NAA/Cr in AD patients was decreased than that in the healthy subjects in the other brain lobes, such as the parietal lobe, the frontal lobe, the temporal lobe, and the temporo-parietal lobe. Previous studies showed that the hippocampus and PC were crucial brain regions that are differentially affected by neuropathological changes in AD patients (Silverman et al., 1997). Hippocampal atrophy is one of the pathological and radiological signs of AD, and the resting state functional magnetic resonance imaging and ^{18}F-deoxyglucose PET demonstrated that hippocampal dysfunction is closely related to the cognitive impairment in AD patients (Yan et al., 2020). The PC plays a crucial role in the default mode network of the brain, and previous studies demonstrated that the functional connections between the PC and the hippocampus have also been weakened during cognitive impairment (Huang et al., 2002). Studies have reported that the atrophy of the hippocampus was closely related to the loss of neurons and the number of neurons had a close connection with NAA (Shiino et al., 2012). The results of this meta-analysis suggested that with the pathological development of AD, the neurons in the hippocampus and the PC were gradually damaged. And the formation of Aβ and NFT in the brain of AD patients may lead to the decrease of NAA and the gradual loss of synapses, which is consistent with the progress of cognitive dysfunction in AD. Similarly, there are studies showing that the sensitivity and specificity of NAA/Cr of PC in predicting the conversion of MCI to AD were 82% and 72%, respectively (Fayed et al., 2008). Consequently, NAA may be considered as a biomarker for monitoring the progression of MCI to AD.

mI is a good indicator of the proliferation of glial cells, as it is mainly expressed in glial cells. Previous studies have reported the increased levels of mI and mI/Cr in the PC were found in MCI and AD patients (Yang et al., 2012), which was consistent with our research results. In this meta-analysis, the results showed that in the pathological development from MCI to AD, in addition to the decrease in the ratios of NAA/Cr and the concentration of NAA in PC, there was also an increase in the ratios of mI/Cr and mI/NAA; and, compared with the HC, the mI concentration in the PC of AD and MCI patients was significantly increased. Meanwhile, the level of mI in MCI and AD patients was significantly higher than that in the healthy subjects in the other brain regions, such as the temporo-parietal lobe and PWM. The increase in mI concentration may be caused by the activation of astrocytes or microglia, which is related to the neuroinflammation process, and has been considered as one of the core pathological features of AD. In addition, the increased mI may affect the phosphorylation of membrane proteins or cause changes in phospholipid metabolism, affecting the formation of Aβ, and thus leading to the deposition of amyloid plaques. In addition, the increased deposition of Aβ also induced the formation of nutritionally impaired synapses, and the astrocytes wrapped and phagocytosed the diseased synapses to remove the aberrations in the synapses. However, with the development of the disease, the deposition intensified, and this pathological change promoted the increase of inflammatory response, which would disrupt the normal form of synapses (Gomez-Arboledas et al., 2018). Studies have found that the change in the ratio of mI/Cr in PC was closely related to the early decline of cerebrospinal fluid Aβ42, and the decrease in the level of CSF Aβ42 can be detected 10–20 years before the onset of cognitive impairment (Bateman et al., 2012). Studies have found in the brain of Down's syndrome and other dementia patients, the ratio of mI/Cr was also significantly increased before significant manifestations of cognitive dysfunction (Voevodskaya et al., 2016). Therefore, these results suggested that the change in the level of mI may precede the onset of cognitive impairment, which had the potential to be applied to early diagnosis of AD.

Moreover, it is worth noting that this study showed that the concentration of Cr was significantly lower in the hippocampus of AD and MCI patients than that of healthy people, but there was no significant change in other brain regions such as PC. Interestingly, it is generally believed that the concentration of Cr is basically constant and uniformly distributed throughout the brain and is not changed with age or various diseases. Therefore, the level of Cr is often used as a reference value to indicate the level of other neurochemical substances. Some studies have also found that the concentration of Cr was relatively reduced in the late stage of AD as well as subcortical ischemic vascular dementia, which may be due to the fact that Cr existed in neurons and glial cells at the same time, and was affected by the density of brain tissue (Shiino et al., 2012).

Studies have regarded the ratio of mI/NAA a standard method to determine the severity of AD, as the sensitivity and specificity of the ratio of mI/NAA in the diagnosis for AD patients were 83 and 98%, respectively, and was consistent with the MMSE score (Shiino et al., 2012). This meta-analysis found that the ratio of mI/NAA increased during the progression from MCI to AD in PC, and the same result was also observed in the hippocampus. But since only 3 studies were included and a large heterogeneity was observed, this result should be interpreted cautiously. In addition, there was no meta-analysis results in the procession from MCI to AD in the hippocampus. Therefore, the change of mI/NAA is consistent in the progression from MCI to AD, but whether it can be used as markers in early diagnosis of AD is still questionable.

Different Metabolic Changes of Neurochemicals Between MCI and AD

The findings with respect to changes in the levels of Cho and Glx in MCI and AD were less consistent. As discussed above, the ratio of Cho/Cr was significantly higher in the PC of AD patients than that of HC, but there was a downward trend in MCI subjects. In addition, the concentration of Cho was found to be raised in the PC of AD patients compared with healthy controls, and no differences were seen in the MCI subjects. In contrast, the concentration of Cho was found to be reduced in the hippocampus of AD patients and MCI patients compared with healthy controls. It had been reported that a cholinergic lesion emerged as early as the MCI state and primarily in the presynaptic membrane, which may affect the long-term potentiation (Nordberg and Winblad, 1986). Cho plays an important role in the formation of cell membranes, and the change of concentration directly reflects the synthesis and degradation of membranes. Cho could be converted into acetylcholine (AchE) by choline acetyltransferase (ChAT) to play a neuroregulatory role, and the Cho signal may be closely related to the activity of ChAT (Klein, 2000). A clinical autopsy study found increased ChAT activity in the hippocampus of patients with MCI, which could explain that the decrease of Cho in the MCI stage is due to the increased activity of ChAT and the utilization of more choline substrates, thus resisting the damaging effect of cholinergic neurons (Ikonomovic et al., 2003). This compensatory activity may increase with the progression of the disease. Meanwhile, neuronal death will lead to an increase in membrane turnover, which will increase the ratio of Cho/Cr in AD patients. Recent investigations reported that the increase in the level of Cho in PC of AD patients may be the result of cell membrane rupture providing free Cho, which was in response to a decrease in the release of acetylcholine from cholinergic neurons in the brain of AD patients (Watanabe et al., 2010). In frontotemporal dementia and dementia with Lewy bodies, the increase in the ratio of Cho/Cr in the PC can also be detected. Interestingly, there was no significant change in the early stage of AD disease. In MCI patients, the concentration of Cho in PC remained basically the same with healthy controls, while the ratio of Cho/Cr had an upward trend, which may be due to the gradual aggravation of cholinergic neuron damage with the progression of the disease. Currently, cholinergic inhibitors such as donepezil, rivastigmine, and galanthamine are clinically used to treat AD. A meta-analysis showed that these drugs had modest but clinically significant overall benefits in stabilizing cognition, function, behavior, and overall clinical changes (Tan et al., 2014). Therefore, the change of Cho may reflect the severity of AD and was considered as a potential target for early detection and interventions.

In recent years, more research has focused on the change of Glx in patients with MCI and AD. Glx is a class of excitatory amino acid, including glutamate (Glu) and glutamine (Gln) (Bleich et al., 2003). In the brain, Glu and Gln are in dynamic equilibrium, and they can maintain and regulate synaptic information transmission through mutual transformation. In addition, Glu plays a crucial role in mitochondrial metabolism, neurotransmission of pyramidal cells, cerebral cortex function, and glutamate/GABA-glutamine cycle. And Glu-mediated synaptic transmission is critical for brain functions. However, excessive and continuous excitatory glutamatergic stimulation can lead to the death of neurons (Fayed et al., 2011). Interestingly, our results showed that compared with HC, the concentrations of Glx and Glu in PC of AD patients were lower, while the ratio of Glx/Cr was relatively higher, and the ratio of Glx/Cr in the PC of MCI patients was higher, while the concentration of Glu had a downward trend. In animal experiments, it was also found that the Glu/Cr was decreased in AD model mice (Liang et al., 2017). Studies have reported that the Aβ can induce several changes in nerve cells including the loss of neuronal viability and synaptic activity, leading to the reduction in glutamate levels. Meanwhile, the decrease of Glu content will affect the A-amino-3-hydroxy-5-methyl-4-isoxazolepropionic acid receptors (AMPARs), which play a key role in synaptic function and cognition. In addition, this decrease in AMPARs may be the reason for the loss of synaptic and the decrease of cognitive function in AD (Liu et al., 2010). Consequently, Glx/Cr and Glu may be seen as signs of cognitive deterioration in AD.

Limitations

Several limitations to the current meta-analysis should be pointed out. First, the number of longitudinal studies to investigate the changes of metabolites between MCI-converter and MCI-stable patients was limited, so the sample size for analysis was relatively small. Therefore, more longitudinal studies are required to observe and explain the metabolite changes during the progress of MCI to AD. In addition, a significant effect of heterogeneity was found in many studies, and we were temporarily unable to do any moderating analysis to detect systematic influence on heterogeneity. Additionally, the detection results of MRS are affected by multiple parameters such as TR, TE, and ROI. This meta-analysis did not unify these parameters, which may lead to heterogeneity and affect the results.

CONCLUSION

In conclusion, the main findings of our meta-analysis revealed robust metabolite changes in the PC and the hippocampus during the development from MCI to AD, especially the levels of NAA and mI show high accuracy in the discrimination between healthy controls, MCI, and AD, but were also able to predict the possible progression from MCI to AD.

DATA AVAILABILITY STATEMENT

The raw data supporting the conclusions of this article will be made available by the authors, without undue reservation.

AUTHOR CONTRIBUTIONS

SL, SH, and HLiu designed the study. SL and HLin revised the manuscript. HLiu, DZ, and HLin wrote the initial manuscript. HLiu, DZ, LZ, YZ, XY, and ZL collected the data and undertook

the statistical analysis. SL and QZ critically reviewed and modified the paper. All authors contributed to the article and approved the submitted version.

FUNDING

This work was supported by the grants from the National Natural Science Foundation of China (82004440), Fujian Provincial Health Technology Project (2019-1-65), and Scientific Research Foundation for the High-Level Talents funded by Fujian University of Traditional Chinese Medicine (X2019002-talents and X2019014-talents).

SUPPLEMENTARY MATERIAL

The Supplementary Material for this article can be found online at: https://www.frontiersin.org/articles/10.3389/fnagi.2021.738971/full#supplementary-material

REFERENCES

Ackl, N., Ising, M., Schreiber, Y. A., Atiya, M., Sonntag, A., and Auer, D. P. (2005). Hippocampal metabolic abnormalities in mild cognitive impairment and Alzheimer's disease. *Neurosci. Lett.* 384, 23–28. doi: 10.1016/j.neulet.2005.04.035

Azevedo, D., Tatsch, M., Hototian, S. R., Bazzarella, M. C., Castro, C. C., and Bottino, C. M. (2008). Proton spectroscopy in Alzheimer's disease and cognitive impairment no dementia: a community-based study. *Dement. Geriatr. Cogn. Disord.* 25, 491–500. doi: 10.1159/000128275

Bai, X., Edden, R. A., Gao, F., Wang, G., Wu, L., Zhao, B., et al. (2015). Decreased γ-aminobutyric acid levels in the parietal region of patients with Alzheimer's disease. *J. Magn. Reson. Imaging* 41, 1326–1331. doi: 10.1002/jmri.24665

Bateman, R. J., Xiong, C., Benzinger, T. L., Fagan, A. M., Goate, A., Fox, N. C., et al. (2012). Clinical and biomarker changes in dominantly inherited Alzheimer's disease. *New Engl. J. Med.* 367, 795–804. doi: 10.1056/NEJMoa1202753

Bleich, S., Römer, K., Wiltfang, J., and Kornhuber, J. (2003). Glutamate and the glutamate receptor system: a target for drug action. *Int. J. Geriatr. Psychiatry* 18, S33–S40. doi: 10.1002/gps.933

Block, W., Jessen, F., Traber, F., Flacke, S., Manka, C., Lamerichs, R., et al. (2002). Regional N-acetylaspartate reduction in the hippocampus detected with fast proton magnetic resonance spectroscopic imaging in patients with Alzheimer disease. *Archiv. Neurol.* 59, 828–834. doi: 10.1001/archneur.59.5.828

Catani, M., Cherubini, A., Howard, R., Tarducci, R., Pelliccioli, G. P., Piccirilli, M., et al. (2001). (1)H-MR spectroscopy differentiates mild cognitive impairment from normal brain aging. *Neuroreport* 12, 2315–2317. doi: 10.1097/00001756-200108080-00007

Catani, M., Mecocci, P., Tarducci, R., Howard, R., Pelliccioli, G. P., Mariani, E., et al. (2002). Proton magnetic resonance spectroscopy reveals similar white matter biochemical changes in patients with chronic hypertension and early Alzheimer's disease. *J. Am. Geriatr. Soc.* 50, 1707–1710. doi: 10.1046/j.1532-5415.2002.50465.x

Chantal, S., Labelle, M., Bouchard, R. W., Braun, C. M. J., and Boulanger, Y. (2002). Correlation of regional proton magnetic resonance spectroscopic metabolic changes with cognitive deficits in mild Alzheimer disease. *Archiv. Neurol.* 59, 955–962. doi: 10.1001/archneur.59.6.955

Chao, L. L., Mueller, S. G., Buckley, S. T., Peek, K., Raptentsetseng, S., Elman, J., et al. (2010). Evidence of neurodegeneration in brains of older adults who do not yet fulfill MCI criteria. *Neurobiol. Aging* 31, 368–377. doi: 10.1016/j.neurobiolaging.2008.05.004

Chao, L. L., Schuff, N., Kramer, J. H., Du, A. T., Capizzano, A. A., O'Neill, J., et al. (2005). Reduced medial temporal lobe N-acetylaspartate in cognitively impaired but nondemented patients. *Neurology* 64, 282–289. doi: 10.1212/01.WNL.0000149638.45635.FF

de Souza, A. S., de Oliveira-Souza, R., Moll, J., Tovar-Moll, F., Andreiuolo, P. A., and Bottino, C. M. C. (2011). Contribution of H-1 spectroscopy to a brief cognitive-functional test battery for the diagnosis of mild Alzheimer's disease. *Dement. Geriatr. Cogn. Disord.* 32, 351–361. doi: 10.1159/000334656

Delli, P. S., Franciotti, R., Taylor, J. P., Thomas, A., Tartaro, A., Onofrj, M., et al. (2015). Thalamic involvement in fluctuating cognition in dementia with Lewy bodies: magnetic resonance evidences. *Cereb. Cortex* 25, 3682–3689. doi: 10.1093/cercor/bhu220

Ding, B., Chen, K. M., Ling, H. W., Zhang, H., Chai, W. M., Li, X., et al. (2008). Diffusion tensor imaging correlates with proton magnetic resonance spectroscopy in posterior cingulate region of patients with Alzheimer's disease. *Dement. Geriatr. Cogn. Disord.* 25, 218–225. doi: 10.1159/000113948

Ernst, T., Chang, L., Melchor, R., and Mark, M. C. (1997). Frontotemporal dementia and early Alzheimer disease: differentiation with frontal lobe H-1 MR spectroscopy. *Radiology* 203, 829–836. doi: 10.1148/radiology.203.3.9169712

Fayed, N., Andrés, E., Viguera, L., Modrego, P. J., and Garcia-Campayo, J. (2014). Higher glutamate+glutamine and reduction of N-acetylaspartate in posterior cingulate according to age range in patients with cognitive impairment and/or pain. *Acad. Radiol.* 21, 1211–1217. doi: 10.1016/j.acra.2014.04.009

Fayed, N., Dávila, J., Oliveros, A., Castillo, J., and Medrano, J. J. (2008). Utility of different MR modalities in mild cognitive impairment and its use as a predictor of conversion to probable dementia. *Acad. Radiol.* 15, 1089–1098. doi: 10.1016/j.acra.2008.04.008

Fayed, N., Modrego, P. J., Rojas-Salinas, G., and Aguilar, K. (2011). Brain glutamate levels are decreased in Alzheimer's disease: a magnetic resonance spectroscopy study. *Am. J. Alzheimers Dis. Other Demen.* 26, 450–456. doi: 10.1177/1533317511421780

Fernández, A., García-Segura, J. M., Ortiz, T., Montoya, J., Maestú, F., Gil-Gregorio, P., et al. (2005). Proton magnetic resonance spectroscopy and magnetoencephalographic estimation of delta dipole density: a combination of techniques that may contribute to the diagnosis of Alzheimer's disease. *Dement. Geriatr. Cogn. Disord.* 20, 169–177. doi: 10.1159/000087094

Foy, C. M., Daly, E. M., Glover, A., O'Gorman, R., Simmons, A., Murphy, D. G., et al. (2011). Hippocampal proton MR spectroscopy in early Alzheimer's disease and mild cognitive impairment. *Brain Topogr.* 24, 316–322. doi: 10.1007/s10548-011-0170-5

Franczak, M., Prost, R. W., Antuono, P. G., Mark, L. P., Jones, J. L., and Ulmer, J. L. (2007). Proton magnetic resonance spectroscopy of the hippocampus in patients with mild cognitive impairment: a pilot study. *J. Comput. Assist. Tomogr.* 31, 666–670. doi: 10.1097/RCT.0b013e318031bc31

Frederick, B. D., Lyoo, I. K., Satlin, A., Ahn, K. H., Kim, M. J., Yurgelun-Todd, D. A., et al. (2004). *In vivo* proton magnetic resonance spectroscopy of the temporal lobe in Alzheimer's disease. *Prog. Neuropsychopharmacol. Biol. Psychiatry* 28, 1313–1322. doi: 10.1016/j.pnpbp.2004.08.013

García, S. J., Gavrila, D., Antúnez, C., Tormo, M. J., Salmerón, D., Carles, R., et al. (2008). Magnetic resonance spectroscopy performance for detection of dementia, Alzheimer's disease and mild cognitive impairment in a community-based survey. *Dement. Geriatr. Cogn. Disord.* 26, 15–25. doi: 10.1159/000140624

Gomez-Arboledas, A., Davila, J. C., Sanchez-Mejias, E., Navarro, V., Nuñez-Diaz, C., Sanchez-Varo, R., et al. (2018). Phagocytic clearance of presynaptic dystrophies by reactive astrocytes in Alzheimer's disease. *Glia* 66, 637–653. doi: 10.1002/glia.23270

Graff-Radford, J., Boeve, B. F., Murray, M. E., Ferman, T. J., Tosakulwong, N., Lesnick, T. G., et al. (2014). Regional proton magnetic resonance spectroscopy patterns in dementia with Lewy bodies. *Neurobiol. Aging* 35, 1483–1490. doi: 10.1016/j.neurobiolaging.2014.01.001

Griffith, H. R., Okonkwo, O. C., den Hollander, J. A., Belue, K., Copeland, J., Harrell, L. E., et al. (2010). Brain metabolic correlates of decision making in amnestic mild cognitive impairment. *Neuropsychol. Dev. Cogn. B Aging Neuropsychol. Cogn.* 17, 492–504. doi: 10.1080/13825581003646135

Guo, Z., Liu, X., Hou, H., Wei, F., Chen, X., Shen, Y., et al. (2016). (1)H-MRS asymmetry changes in the anterior and posterior cingulate gyrus in

patients with mild cognitive impairment and mild Alzheimer's disease. *Compr. Psychiatry* 69, 179–185. doi: 10.1016/j.comppsych.2016.06.001

Herminghaus, S., Frölich, L., Gorriz, C., Pilatus, U., Dierks, T., Wittsack, H. J., et al. (2003). Brain metabolism in Alzheimer disease and vascular dementia assessed by *in vivo* proton magnetic resonance spectroscopy. *Psychiatry Res.* 123, 183–190. doi: 10.1016/S0925-4927(03)00071-4

Higgins, J. P., Thompson, S. G., Deeks, J. J., and Altman, D. G. (2003). Measuring inconsistency in meta-analyses. *BMJ* 327, 557–560. doi: 10.1136/bmj.327.7414.557

Holtzman, D. M., Morris, J. C., and Goate, A. M. (2011). Alzheimer's disease: the challenge of the second century. *Sci. Transl. Med.* 3:77sr1. doi: 10.1126/scitranslmed.3002369

Huang, C., Wahlund, L. O., Svensson, L., Winblad, B., and Julin, P. (2002). Cingulate cortex hypoperfusion predicts Alzheimer's disease in mild cognitive impairment. *BMC Neurol.* 2:9. doi: 10.1186/1471-2377-2-9

Huang, D., Liu, D., Yin, J., Qian, T., Shrestha, S., and Ni, H. (2017). Glutamate-glutamine and GABA in brain of normal aged and patients with cognitive impairment. *Eur. Radiol.* 27, 2698–2705. doi: 10.1007/s00330-016-4669-8

Ikonomovic, M. D., Mufson, E. J., Wuu, J., Cochran, E. J., Bennett, D. A., and DeKosky, S. T. (2003). Cholinergic plasticity in hippocampus of individuals with mild cognitive impairment: correlation with Alzheimer's neuropathology. *J. Alzheimers Dis.* 5, 39–48. doi: 10.3233/JAD-2003-5106

Jack, C. J., Knopman, D. S., Jagust, W. J., Petersen, R. C., Weiner, M. W., Aisen, P. S., et al. (2013). Tracking pathophysiological processes in Alzheimer's disease: an updated hypothetical model of dynamic biomarkers. *Lancet Neurol.* 12, 207–216. doi: 10.1016/S1474-4422(12)70291-0

Jessen, F., Block, W., Träber, F., Keller, E., Flacke, S., Papassotiropoulos, A., et al. (2000). Proton MR spectroscopy detects a relative decrease of N-acetylaspartate in the medial temporal lobe of patients with AD. *Neurology* 55, 684–688. doi: 10.1212/WNL.55.5.684

Jessen, F., Gür, O., Block, W., Ende, G., Frölich, L., Hammen, T., et al. (2009). A multicenter (1)H-MRS study of the medial temporal lobe in AD and MCI. *Neurology* 72, 1735–1740. doi: 10.1212/WNL.0b013e3181a60a20

Jessen, F., Traeber, F., Freymann, N., Maier, W., Schild, H. H., Heun, R., et al. (2005). A comparative study of the different N-acetylaspartate measures of the medial temporal lobe in Alzheimer's disease. *Dement. Geriatr. Cogn. Disord.* 20, 178–183. doi: 10.1159/000087095

Kantarci, K., Jack, C. J., Xu, Y. C., Campeau, N. G., O'Brien, P. C., Smith, G. E., et al. (2000). Regional metabolic patterns in mild cognitive impairment and Alzheimer's disease: a 1H MRS study. *Neurology* 55, 210–217. doi: 10.1212/WNL.55.2.210

Kantarci, K., Weigand, S. D., Petersen, R. C., Boeve, B. F., Knopman, D. S., Gunter, J., et al. (2007). Longitudinal 1H MRS changes in mild cognitive impairment and Alzheimer's disease. *Neurobiol. Aging* 28, 1330–1339. doi: 10.1016/j.neurobiolaging.2006.06.018

Kantarci, K., Xu, Y., Shiung, M. M., O'Brien, P. C., Cha, R. H., Smith, G. E., et al. (2002). Comparative diagnostic utility of different MR modalities in mild cognitive impairment and Alzheimer's disease. *Dement. Geriatr. Cogn. Disord.* 14, 198–207. doi: 10.1159/000066021

Khomenko, Y. G., Kataeva, G. V., Bogdan, A. A., Chernysheva, E. M., and Susin, D. S. (2019). [Cerebral metabolism in patients with cognitive disorders: a combined MRS and PET study]. *Zh. Nevrol. Psikhiatr Im S S Korsakova* 119, 51–58. doi: 10.17116/jnevro201911901151

Klein, J. (2000). Membrane breakdown in acute and chronic neurodegeneration: focus on choline-containing phospholipids. *J. Neural Transm.* 107, 1027–1063. doi: 10.1007/s007020070051

Lazeyras, F., Charles, H. C., Tupler, L. A., Erickson, R., Boyko, O. B., and Krishnan, K. R. (1998). Metabolic brain mapping in Alzheimer's disease using proton magnetic resonance spectroscopy. *Psychiatry Res.* 82, 95–106. doi: 10.1016/S0925-4927(98)00010-9

Li, X., Shao, X., Wang, N., Wang, T., Chen, G., and Zhou, H. (2010). Correlation of auditory event-related potentials and magnetic resonance spectroscopy measures in mild cognitive impairment. *Brain Res.* 1346, 204–212. doi: 10.1016/j.brainres.2010.04.078

Liang, S., Huang, J., Liu, W., Jin, H., Li, L., Zhang, X., et al. (2017). Magnetic resonance spectroscopy analysis of neurochemical changes in the atrophic hippocampus of APP/PS1 transgenic mice. *Behav. Brain Res.* 335, 26–31. doi: 10.1016/j.bbr.2017.08.005

Lim, T. S., Hong, Y. H., Lee, H. Y., Choi, J. Y., Kim, H. S., and Moon, S. Y. (2012). Metabolite investigation in both anterior and posterior cingulate gyri in Alzheimer's disease spectrum using 3-tesla MR spectroscopy. *Dement. Geriatr. Cogn. Disord.* 33, 149–155. doi: 10.1159/000338177

Liu, S. J., Gasperini, R., Foa, L., and Small, D. H. (2010). Amyloid-beta decreases cell-surface AMPA receptors by increasing intracellular calcium and phosphorylation of GluR2. *J. Alzheimers Dis.* 21, 655–666. doi: 10.3233/JAD-2010-091654

Liu, Y., Cai, Z. L., Xue, S., Zhou, X., and Wu, F. (2013). Proxies of cognitive reserve and their effects on neuropsychological performance in patients with mild cognitive impairment. *J. Clin. Neurosci.* 20, 548–553. doi: 10.1016/j.jocn.2012.04.020

Liu, Y. Y., Yang, Z. X., Shen, Z. W., Xiao, Y. Y., Cheng, X. F., Chen, W., et al. (2014). Magnetic resonance spectroscopy study of amnestic mild cognitive impairment and vascular cognitive impairment with no dementia. *Am. J. Alzheimers Dis. Other Demen.* 29, 474–481. doi: 10.1177/1533317513495106

MacKay, S., Meyerhoff, D. J., Constans, J. M., Norman, D., Fein, G., and Weiner, M. W. (1996). Regional gray and white matter metabolite differences in subjects with AD, with subcortical ischemic vascular dementia, and elderly controls with 1H magnetic resonance spectroscopic imaging. *Arch. Neurol.* 53, 167–174. doi: 10.1001/archneur.1996.00550020079018

Mandal, P. K., Saharan, S., Tripathi, M., and Murari, G. (2015). Brain glutathione levels–a novel biomarker for mild cognitive impairment and Alzheimer's disease. *Biol. Psychiatry* 78, 702–710. doi: 10.1016/j.biopsych.2015.04.005

Marjańska, M., McCarten, J. R., Hodges, J. S., Hemmy, L. S., and Terpstra, M. (2019). Distinctive neurochemistry in Alzheimer's disease via 7 T *in vivo* magnetic resonance spectroscopy. *J. Alzheimers Dis.* 68, 559–569. doi: 10.3233/JAD-180861

Mattsson-Carlgren, N., Andersson, E., Janelidze, S., Ossenkoppele, R., Insel, P., Strandberg, O., et al. (2020). Aβ deposition is associated with increases in soluble and phosphorylated tau that precede a positive Tau PET in Alzheimer's disease. *Sci. Adv.* 6:eaaz2387. doi: 10.1126/sciadv.aaz2387

Metastasio, A., Rinaldi, P., Tarducci, R., Mariani, E., Feliziani, F. T., Cherubini, A., et al. (2006). Conversion of MCI to dementia: role of proton magnetic resonance spectroscopy. *Neurobiol. Aging.* 27, 926–932. doi: 10.1016/j.neurobiolaging.2005.05.002

Mitolo, M., Stanzani-Maserati, M., Capellari, S., Testa, C., Rucci, P., Poda, R., et al. (2019). Predicting conversion from mild cognitive impairment to Alzheimer's disease using brain (1)H-MRS and volumetric changes: a two- year retrospective follow-up study. *Neuroimage Clin.* 23:101843. doi: 10.1016/j.nicl.2019.101843

Modrego, P. J., Fayed, N., and Pina, M. A. (2005). Conversion from mild cognitive impairment to probable Alzheimer's disease predicted by brain magnetic resonance spectroscopy. *Am. J. Psychiatry* 162, 667–675. doi: 10.1176/appi.ajp.162.4.667

Modrego, P. J., Fayed, N., and Sarasa, M. (2011). Magnetic resonance spectroscopy in the prediction of early conversion from amnestic mild cognitive impairment to dementia: a prospective cohort study. *BMJ Open* 1:e000007. doi: 10.1136/bmjopen-2010-000007

Moher, D., Liberati, A., Tetzlaff, J., and Altman, D. G. (2009). Preferred reporting items for systematic reviews and meta-analyses: the PRISMA statement. *BMJ* 339:b2535. doi: 10.1136/bmj.b2535

Nordberg, A., and Winblad, B. (1986). Reduced number of [3H]nicotine and [3H]acetylcholine binding sites in the frontal cortex of Alzheimer brains. *Neurosci. Lett.* 72, 115–119. doi: 10.1016/0304-3940(86)90629-4

Oeltzschner, G., Wijtenburg, S. A., Mikkelsen, M., Edden, R., Barker, P. B., Joo, J. H., et al. (2019). Neurometabolites and associations with cognitive deficits in mild cognitive impairment: a magnetic resonance spectroscopy study at 7 tesla. *Neurobiol. Aging* 73, 211–218. doi: 10.1016/j.neurobiolaging.2018.09.027

Olson, B. L., Holshouser, B. A., Britt, W. R., Mueller, C., Baqai, W., Patra, S., et al. (2008). Longitudinal metabolic and cognitive changes in mild cognitive impairment patients. *Alzheimer Dis. Assoc. Disord.* 22, 269–277. doi: 10.1097/WAD.0b013e3181750a65

Onwordi, E. C., Whitehurst, T., Mansur, A., Statton, B., Berry, A., Quinlan, M., et al. (2021). The relationship between synaptic density marker SV2A, glutamate and N-acetyl aspartate levels in healthy volunteers and schizophrenia: a multimodal PET and magnetic resonance spectroscopy brain imaging study. *Transl. Psychiatry* 11:393. doi: 10.1038/s41398-021-01515-3

Palmqvist, S., Mattsson, N., and Hansson, O. (2016). Cerebrospinal fluid analysis detects cerebral amyloid-β accumulation earlier than positron emission tomography. *Brain Res.* 139(Pt 4), 1226–1236. doi: 10.1093/brain/aww015

Parnetti, L., Tarducci, R., Presciutti, O., Lowenthal, D. T., Pippi, M., Palumbo, B., et al. (1997). Proton magnetic resonance spectroscopy can differentiate Alzheimer's disease from normal aging. *Mech. Ageing Dev.* 97, 9–14. doi: 10.1016/S0047-6374(97)01877-0

Pilatus, U., Lais, C., Rochmont, A. M., Kratzsch, T., Frölich, L., Maurer, K., et al. (2009). Conversion to dementia in mild cognitive impairment is associated with decline of N-actylaspartate and creatine as revealed by magnetic resonance spectroscopy. *Psychiatry Res.* 173, 1–7. doi: 10.1016/j.pscychresns.2008.07.015

Rami, L., Gómez-Ansón, B., Bosch, B., Sánchez-Valle, R., Monte, G. C., Villar, A., et al. (2007). Cortical brain metabolism as measured by proton spectroscopy is related to memory performance in patients with amnestic mild cognitive impairment and Alzheimer's disease. *Dement. Geriatr. Cogn. Disord.* 24, 274–279. doi: 10.1159/000107487

Riese, F., Gietl, A., Zölch, N., Henning, A., O'Gorman, R., Kälin, A. M., et al. (2015). Posterior cingulate γ-aminobutyric acid and glutamate/glutamine are reduced in amnestic mild cognitive impairment and are unrelated to amyloid deposition and apolipoprotein E genotype. *Neurobiol. Aging* 36, 53–59. doi: 10.1016/j.neurobiolaging.2014.07.030

Scheltens, P., Blennow, K., Breteler, M. M., de Strooper, B., Frisoni, G. B., Salloway, S., et al. (2016). Alzheimer's disease. *Lancet Neurol.* 388, 505–517. doi: 10.1016/S0140-6736(15)01124-1

Scheltens, P., De Strooper, B., Kivipelto, M., Holstege, H., Chételat, G., Teunissen, C. E., et al. (2021). Alzheimer's disease. *Lancet Neurol.* 397, 1577–1590. doi: 10.1016/S0140-6736(20)32205-4

Schuff, N., Amend, D. L., Meyerhoff, D. J., Tanabe, J. L., Norman, D., Fein, G., et al. (1998). Alzheimer Disease: Quantitative H-1 Mr Spectroscopic Imaging of Frontoparietal Brain. *Radiology* 207, 91–102. doi: 10.1148/radiology.207.1.9530304

Schuff, N., Capizzano, A. A., Du, A. T., Amend, D. L., O'Neill, J., Norman, D., et al. (2002). Selective reduction of N-acetylaspartate in medial temporal and parietal lobes in AD. *Neurology* 58, 928–935. doi: 10.1212/WNL.58.6.928

Seo, S. W., Lee, J. H., Jang, S. M., Kim, S. T., Chin, J., Kim, G. H., et al. (2012). Neurochemical alterations of the entorhinal cortex in amnestic mild cognitive impairment (aMCI): a three-year follow-up study. *Arch. Gerontol. Geriatr.* 54, 192–196. doi: 10.1016/j.archger.2011.04.002

Shiino, A., Watanabe, T., Shirakashi, Y., Kotani, E., Yoshimura, M., Morikawa, S., et al. (2012). The profile of hippocampal metabolites differs between Alzheimer's disease and subcortical ischemic vascular dementia, as measured by proton magnetic resonance spectroscopy. *J. Cereb. Blood Flow Metab.* 32, 805–815. doi: 10.1038/jcbfm.2012.9

Siger, M., Schuff, N., Zhu, X., Miller, B. L., and Weiner, M. W. (2009). Regional myo-inositol concentration in mild cognitive impairment using 1H magnetic resonance spectroscopic imaging. *Alzheimer Dis. Assoc. Disord.* 23, 57–62. doi: 10.1097/WAD.0b013e3181875434

Silverman, W., Wisniewski, H. M., Bobinski, M., and Wegiel, J. (1997). Frequency of stages of Alzheimer-related lesions in different age categories. *Neurobiol. Aging* 18, 377–379; discussion 89-92. doi: 10.1016/S0197-4580(97)00051-1

Sun, X., Nie, B., Zhao, S., Ai, L., Chen, Q., Zhang, T., et al. (2020). Distinct relationships of amyloid-beta and tau deposition to cerebral glucose metabolic networks in Alzheimer's disease. *Neurosci. Lett.* 717:134699. doi: 10.1016/j.neulet.2019.134699

Tan, C. C., Yu, J. T., Wang, H. F., Tan, M. S., Meng, X. F., Wang, C., et al. (2014). Efficacy and safety of donepezil, galantamine, rivastigmine, and memantine for the treatment of Alzheimer's disease: a systematic review and meta-analysis. *J. Alzheimers Dis.* 41, 615–631. doi: 10.3233/JAD-132690

Targosz-Gajniak, M. G., Siuda, J. S., Wicher, M. M., Banasik, T. J., Bujak, M. A., Augusciak-Duma, A. M., et al. (2013). Magnetic resonance spectroscopy as a predictor of conversion of mild cognitive impairment to dementia. *J. Neurol. Sci.* 335, 58–63. doi: 10.1016/j.jns.2013.08.023

Voevodskaya, O., Sundgren, P. C., Strandberg, O., Zetterberg, H., Minthon, L., Blennow, K., et al. (2016). Myo-inositol changes precede amyloid pathology and relate to APOE genotype in Alzheimer disease. *Neurology* 86, 1754–1761. doi: 10.1212/WNL.0000000000002672

Wang, T., Xiao, S., Li, X., Ding, B., Ling, H., Chen, K., et al. (2012). Using proton magnetic resonance spectroscopy to identify mild cognitive impairment. *Int. Psychogeriatr.* 24, 19–27. doi: 10.1017/S1041610211000962

Wang, Z., Zhao, C., Yu, L., Zhou, W., and Li, K. (2009). Regional metabolic changes in the hippocampus and posterior cingulate area detected with 3-tesla magnetic resonance spectroscopy in patients with mild cognitive impairment and Alzheimer disease. *Acta Radiol.* 50, 312–319. doi: 10.1080/02841850802709219

Ward, A., Tardiff, S., Dye, C., and Arrighi, H. M. (2013). Rate of conversion from prodromal Alzheimer's disease to Alzheimer's dementia: a systematic review of the literature. *Dement. Geriatr. Cogn. Dis. Extra* 3, 320–332. doi: 10.1159/000354370

Watanabe, T., Shiino, A., and Akiguchi, I. (2010). Absolute quantification in proton magnetic resonance spectroscopy is useful to differentiate amnesic mild cognitive impairment from Alzheimer's disease and healthy aging. *Dement. Geriatr. Cogn. Disord.* 30, 71–77. doi: 10.1159/000318750

Yan, S., Zheng, C., Cui, B., Qi, Z., Zhao, Z., An, Y., et al. (2020). Multiparametric imaging hippocampal neurodegeneration and functional connectivity with simultaneous PET/MRI in Alzheimer's disease. *Eur. J. Nucl. Med. Mol. Imaging* 47, 2440–2452. doi: 10.1007/s00259-020-04752-8

Yang, Z. X., Huo, S. S., Cheng, X. F., Xu, Z. F., Cao, Z., Zeng, J. X., et al. (2012). Quantitative multivoxel proton MR spectroscopy study of brain metabolites in patients with amnestic mild cognitive impairment: a pilot study. *Neuroradiology* 54, 451–458. doi: 10.1007/s00234-011-0900-0

Zeydan, B., Deelchand, D. K., Tosakulwong, N., Lesnick, T. G., Kantarci, O. H., Machulda, M. M., et al. (2017). Decreased glutamate levels in patients with amnestic mild cognitive impairment: an sLASER proton MR spectroscopy and PiB-PET study. *J. Neuroimaging.* 27, 630–636. doi: 10.1111/jon.12454

Zhang, B., Li, M., Sun, Z. Z., Zhu, B., Yuan, L., Wang, Y., et al. (2009). Evaluation of functional MRI markers in mild cognitive impairment. *J. Clin. Neurosci.* 16, 635–641. doi: 10.1016/j.jocn.2008.07.080

Zhu, X., Cao, L., Hu, X., Dong, Y., Wang, H., Liu, F., et al. (2015). Brain metabolism assessed via proton magnetic resonance spectroscopy in patients with amnestic or vascular mild cognitive impairment. *Clin. Neurol. Neurosurg.* 130, 80–85. doi: 10.1016/j.clineuro.2014.12.005

Zhu, X., Schuff, N., Kornak, J., Soher, B., Yaffe, K., Kramer, J. H., et al. (2006). Effects of Alzheimer disease on fronto-parietal brain N-acetyl aspartate and myo-inositol using magnetic resonance spectroscopic imaging. *Alzheimer Dis. Assoc. Disord.* 20, 77–85. doi: 10.1097/01.wad.0000213809.12553.fc

Zimny, A., Szewczyk, P., Trypka, E., Wojtynska, R., Noga, L., Leszek, J., et al. (2011). Multimodal imaging in diagnosis of Alzheimer's disease and amnestic mild cognitive impairment: value of magnetic resonance spectroscopy, perfusion, and diffusion tensor imaging of the posterior cingulate region. *J. Alzheimers Dis.* 27, 591–601. doi: 10.3233/JAD-2011-110254

Conflict of Interest: The authors declare that the research was conducted in the absence of any commercial or financial relationships that could be construed as a potential conflict of interest.

Publisher's Note: All claims expressed in this article are solely those of the authors and do not necessarily represent those of their affiliated organizations, or those of the publisher, the editors and the reviewers. Any product that may be evaluated in this article, or claim that may be made by its manufacturer, is not guaranteed or endorsed by the publisher.

frontiers in Aging Neuroscience

ORIGINAL RESEARCH
published: 26 October 2021
doi: 10.3389/fnagi.2021.764872

Deep-Learning Radiomics for Discrimination Conversion of Alzheimer's Disease in Patients With Mild Cognitive Impairment: A Study Based on ^{18}F-FDG PET Imaging

Ping Zhou†, Rong Zeng†, Lun Yu, Yabo Feng, Chuxin Chen, Fang Li, Yang Liu, Yanhui Huang, Zhongxiong Huang and the Alzheimer's Disease Neuroimaging Initiative‡*

Department of PET-CT Center, Chenzhou No.1 People's Hospital, Chenzhou, China

Objectives: Alzheimer's disease (AD) is the most prevalent neurodegenerative disorder and the most common form of dementia in the older people. Some types of mild cognitive impairment (MCI) are the clinical precursors of AD, while other MCI forms tend to remain stable over time and do not progress to AD. To discriminate MCI patients at risk of AD from stable MCI, we propose a novel deep-learning radiomics (DLR) model based on ^{18}F-fluorodeoxyglucose positron emission tomography (^{18}F-FDG PET) images and combine DLR features with clinical parameters (DLR+C) to improve diagnostic performance.

Methods: ^{18}F-fluorodeoxyglucose positron emission tomography (PET) data from the Alzheimer's disease Neuroimaging Initiative database (ADNI) were collected, including 168 patients with MCI who converted to AD within 3 years and 187 patients with MCI without conversion within 3 years. These subjects were randomly partitioned into 90 % for the training/validation group and 10 % for the independent test group. The proposed DLR approach consists of three steps: base DL model pre-training, network features extraction, and integration of DLR+C, where a convolution network serves as a feature encoder, and a support vector machine (SVM) operated as the classifier. In comparative experiments, we compared our DLR+C method with four other methods: the standard uptake value ratio (SUVR) method, Radiomics-ROI method, Clinical method, and SUVR + Clinical method. To guarantee the robustness, 10-fold cross-validation was processed 100 times.

Results: Under the DLR model, our proposed DLR+C was advantageous and yielded the best classification performance in the diagnosis of conversion with the accuracy, sensitivity, and specificity of 90.62 ± 1.16, 87.50 ± 0.00, and 93.39 ± 2.19%, respectively. In contrast, the respective accuracy of the other four methods reached 68.38 ± 1.27, 73.31 ± 6.93, 81.09 ± 1.97, and 85.35 ± 0.72 %. These results suggested the DLR approach could be used successfully in the prediction of conversion to AD, and that our proposed DLR-combined clinical information was effective.

OPEN ACCESS

Edited by:
Ping Wu,
Fudan University, China

Reviewed by:
Jiehui Jiang,
Shanghai University, China
Woon-Man Kung,
Chinese Culture University, Taiwan

****Correspondence:***
Zhongxiong Huang
hzx1968@yeah.net

†These authors have contributed equally to this work and share first authorship

‡Data used in preparation of this article were obtained from the Alzheimer's Disease Neuroimaging Initiative (ADNI) database (adni.loni.usc.edu). As such, the investigators within the ADNI contributed to the design and implementation of ADNI and/or provided data but did not participate in analysis or writing of this report. A complete listing of ADNI investigators can be found at: http://adni.loni.usc.edu/wp-content/uploads/how_to_apply/ADNI_Acknowledgement_List.pdf

Received: *26 August 2021*
Accepted: *14 September 2021*
Published: *26 October 2021*

Citation:
Zhou P, Zeng R, Yu L, Feng Y, Chen C, Li F, Liu Y, Huang Y, Huang Z and the Alzheimer's Disease Neuroimaging Initiative (2021) Deep-Learning Radiomics for Discrimination Conversion of Alzheimer's Disease in Patients With Mild Cognitive Impairment: A Study Based on ^{18}F-FDG PET Imaging. Front. Aging Neurosci. 13:764872. doi: 10.3389/fnagi.2021.764872

Conclusions: This study showed DLR+C could provide a novel and valuable method for the computer-assisted diagnosis of conversion to AD from MCI. This DLR+C method provided a quantitative biomarker which could predict conversion to AD in MCI patients.

Keywords: deep learning radiomics, ^{18}F-fluorodeoxyglucose positron emission tomography, mild cognitive impairment, Alzheimer's disease, classification

INTRODUCTION

Alzheimer's disease (AD) is the most common type of dementia. Alzheimer's disease is an irreversible, progressive neurological brain disorder expected to increase significantly in the coming years due to aging and improvement in general health care (Ferri et al., 2006; 2020 Alzheimer's disease facts figures, 2020). Because mild memory decline and cognitive deficits appear before AD clinical manifestation (Braak and Braak, 1996; Delacourte et al., 1999), increasing attention has been focused on mild cognitive impairment (MCI). As a preclinical stage of AD, MCI is a board and heterogeneous phenotypic spectrum that has no evident cognitive behavioral symptoms, but can show subtle prodromal signs of dementia (Albert et al., 2011; McKhann et al., 2011). Because of its heterogeneous presentation (Schneider et al., 2009), MCI patients may remain stable, or develop AD or other forms of dementia (Bennett et al., 2003; Sanford, 2017). Therefore, it is crucial to exploit specific risks factors and biomarkers that can predict the progression to AD from MCI.

Currently, structural and functional neuroimaging modalities, such as magnetic resonance imaging (MRI) and positron emission tomography (PET), have been used to develop biomarkers for prediction conversion to AD in patients with MCI (Brooks and Loewenstein, 2010; Vos et al., 2012; Richard et al., 2013; Lange et al., 2015; Liu et al., 2017; Zhou et al., 2019). Numerous studies using ^{18}F-fluorodeoxyglucose positron emission tomography (^{18}F-FDG PET) have shown that there are metabolic alterations detected in MCI patients (Caroli et al., 2012; Pagani et al., 2017). Furthermore, FDG PET was found to be the only technique that can significantly improve the predictive value of demographic covariates regarding the development of AD. It further proved to be a better predictor of conversion than MRI (Shaffer et al., 2013). Specifically, FDG PET alone has shown accuracies in predicting the progression of MCI to AD ranging between 70 and 83% (Lange et al., 2015; Liu et al., 2017; Zhou et al., 2019; Wang et al., 2020). For example, Lange et al. (2015) performed voxel-based statistical testing by the statistical parametric mapping software (SPM8) and obtained an AUC of 0.728 with default settings. Zhou et al. (2019) applied radiomics analysis methods to extract radiomic features in MCI conversion-related regions of interest (ROIs), and the accuracy of prediction reached 0.733. Liu et al. (2017) analyzed FDG PET by using independent component analysis (ICA) and Cox models to extract independent sources of information from whole-brain data, and obtained an accuracy of 0.688 in the FDG PET single modality model.

The aforementioned methods retain some limitations, however. Radiomics based on ROI depend mostly on prior knowledge. The voxel-level analysis considered information across the whole brain, but modeling based on each voxel inevitably results in heavy computing workload. Further, although ICA eliminates the need for a priori knowledge of the effects on underlying brain anatomy and uses whole-brain data, instead of a region-of-interest approach, it requires hand-coding and tedious designing processes, which is analogous to the radiomics method and voxel-level analysis.

Deep-learning radiomics (DLR), a newly developing method, can provide quantitative and high-throughput features from medical images by supervised learning (Gillies et al., 2016; Wang et al., 2019a). This algorithm implemented via deep neural networks automatically embeds computational features to yield end-to-end models that facilitate discovery of relevant highly complex feature, avoiding hand-coding, and a priori knowledge. Wang et al. (2019a) applied this DLR method to shear wave elastography images and presented excellent performances in predicting the stages of liver fibrosis. Moreover, Zheng et al. (2020) used DLR to predict axillary lymph node status in early-stage breast cancer, and clinical parameter combined DLR (DLR+C) yielded the best diagnostic performance with an AUC of 0.902. This methodology has recently extended to other medical applications, such as neurodegenerative diseases (Lu et al., 2018b; Basaia et al., 2019; Spasov et al., 2019a). However, when applied to analyze medical images, there is a scarce-sample problem with DLR. Therefore, in this study we hypothesized that the DLR method might be effective in the diagnosis of conversion to AD in patients with MCI, and DLR+C might be able to provide more valuable information and improve identification of patients likely to convert to AD. We proposed a novel computer-aided diagnosis approach for the conversion to AD from MCI, based on DLR and evaluated the diagnostic performance of DLR features combined clinical information.

METHODS AND MATERIALS

The framework of this study, comprising six steps, is shown in **Figure 1**. First, we preprocessed the collected PET data, mainly including partial volume effects (PVE) correction, normalization, and smoothing. Then, several deep learning (DL) models were pre-trained to select the optimal Base DL model for DLR feature extraction. Subsequently, DLR+C were employed to classify MCI converters (MCI-c) and MCI non-converters (MCI-nc) using the Support vector machine (SVM). Simultaneously, we also designed a comparative experiment for analysis. The details are described in subsequent sections.

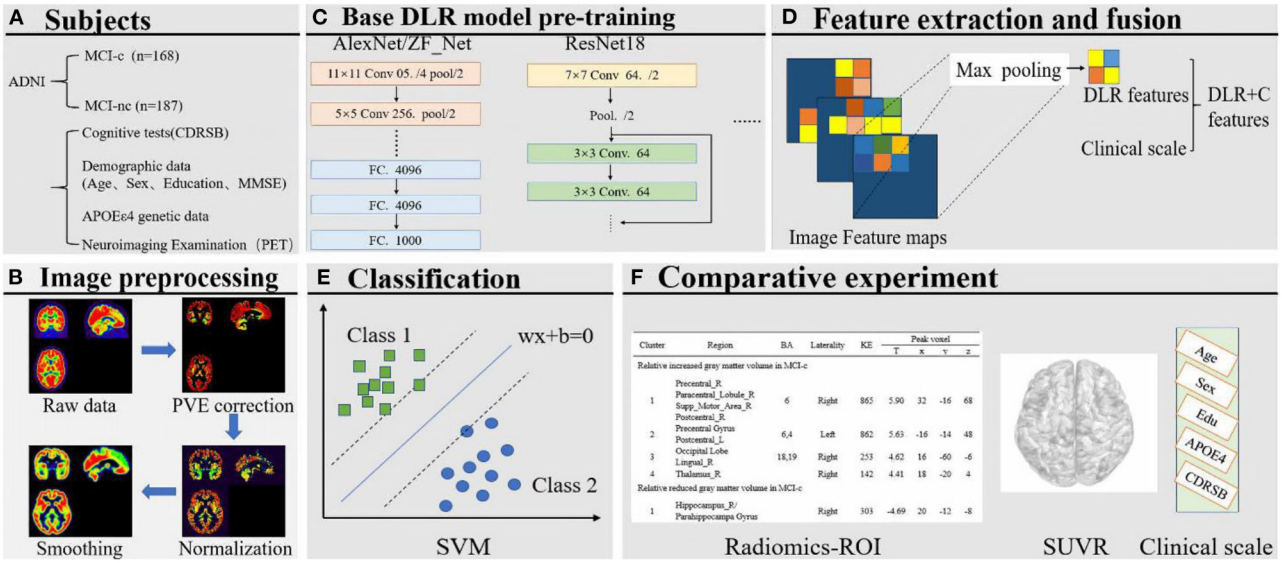

FIGURE 1 | (A) Collection of images and clinical scales. **(B)** Image preprocessing. **(C)** Base DL model pre-training. **(D)** Feature extraction and fusion. **(E)** Classification based on SVM. **(F)** Comparative experiment.

Subjects

The FDG-PET image data used in the preparation of this study were obtained from the Alzheimer's Disease Neuroimaging Initiative (ADNI) database (http://adni.loni.usc.edu/). Alzheimer's Disease Neuroimaging Initiative was launched in 2003 by the National Institute on Aging, the National Institute of Biomedical Imaging and Bioengineering, the Food and Drug Administration, private pharmaceutical companies, and non-profit organizations, as a $60 million, 5-year public–private partnership. The primary goal of ADNI has devoted to test whether serial MRI, PET, other biological markers, and clinical and neuropsychological assessment can be combined to measure the progression of mild MCI and early AD. Up-to-date information is provided on http://www.adni-info.org.

In this study, we collected 168 MCI-c and 187 MCI-nc PET Scan data from ADNI 1, ADNI 2, and ADNI GO cohorts in the ADNI database. Eligible participants with MCI underwent FDG-PET scanning and clinical cognitive evaluations at the baseline and were clinically followed-up during at least 36 months. Detailed eligibility criteria for these participants are as follows: (1) For MCI-nc, participants were evaluated for at least 3 years (including a 3 year time point) from the time of initial data collection. Scan data for MCI-nc were collected at baseline 3 and these participants did not convert to AD during the 3 years follow-up period. (2) For MCI-c, the evaluation time may be less than 3 years. Scan data for MCI-c were not all collected at the baseline. Participants with a bidirectional change of diagnosis (MCI to AD, and back to MCI) within the follow-up period were excluded.

All subjects were divided into two groups, a Training & Validation Group and an independent test group. Our Training & Validation Group contained 152 subjects with MCI-c, and 169 MCI-nc subjects. We used the FDG-PET scan data from this group to establish and test the validity of our predictive models. Our test group consisted of 16 MCI-c subjects and 18 MCI-nc subjects, and it was used to evaluate the diagnostic value of the predictive models. Demographic data including age, gender, sex, education, and neuropsychological cognitive assessment tests including the dementia rating scale (CDRSB), as well as the apolipoprotein E (APOE) ε4 genotyping characteristics of the dataset, are shown in **Table 1**.

FDG-PET Images Acquisition and Preprocessing

The PET acquisition process is detailed in the online information of the ADNI project. In 290 cases, dynamic 3D scans with six 5-min frames were acquired 30 min after injection of 185 ± 18.5 MBq FDG, and all frames were motion-corrected to the first frame and then summed to create a single image file. In the remaining cases ($n = 65$), patients were scanned for a static 30-min acquisition period.

Individual PET scan preprocessing (Ding et al., 2021; Dong et al., 2021) was performed by statistical parametric mapping (SPM12) software (Wellcome Department of Imaging Neuroscience, Institute of Neurology, London, United Kingdom) using Matlab2016b (Mathworks Inc., Sherborn, MA, USA). First, PET images were co-registered with their corresponding T1-weighted images and then corrected for PVE based on the Muller–Gartner algorithm, where PVE correction was applied to the images to minimize the PVE on PET measurements (Gonzalez-Escamilla et al., 2017). Thereafter, through linear and non-linear 3D transformations, the images were spatially normalized to a PET template in the Montreal Neurological Institute (MNI) brain space. The normalized PET images were then smoothed by a Gaussian filter of 8 mm full-width at half-maximum (FWHM) over a 3D space to blur the individual

TABLE 1 | Demographic and statistics of clinical assessments at time of data collection.

Groups	Gender (M/F)	Age (years)	EDU	MMSE	MoCA	APOEε4 positive rate	CDRSB
Training/Validation Groups							
MCI_c ($n = 152$)	86/66	74.2 ± 7.0	16.0 ± 2.7	26.5 ± 2.2	21.0 ± 2.9	65.1%	2.4 ± 1.0
MCI_nc ($n = 169$)	96/73	72.2 ± 7.4[b]	16.1 ± 2.6	28.1 ± 1.6[b]	23.9 ± 2.5[b]	34.9%	1.2 ± 0.7[b]
Test Groups ($n = 48$)							
MCI_c ($n = 16$)	9/7	71.4 ± 7.8	16.3 ± 2.5	26.3 ± 2.0	21.5 ± 2.1	75.0%	2.5 ± 1.1
MCI_nc ($n = 18$)	13/5[a]	71.3 ± 8.7	15.8 ± 2.8	27.7 ± 1.8[b]	23.2 ± 3.8	44.4%	0.9 ± 0.6[b]

All data except APOEε4 positive rate were presented as mean ± standard deviation. EDU, education; MMSE, Mini-mental State Examination; MoCA, Montreal Cognitive Assessment; CDRSB: clinical dementia rating sum of boxes.

[a,b]Group-level two-sample t test are conducted for Age, Education, MMSE, MoCA, and CDRSB; Group-level chi-square test are conducted for Gender.

anatomical variations and to increase the signal-to-noise ratio for subsequent analysis. Finally, individual PET images were intensity normalized to the global mean brain uptake and automatically parcellated into 90 ROIs defined by the automated anatomical labeling (AAL) atlas. The processed images had a spatial resolution of 91 × 109 × 91 with a voxel size of 2 × 2 × 2 mm^3. Lastly, each three-dimensional PET image was sliced and tiled into two-dimensional images, then being resized to 224 * 224 pixels for subsequent DL model pre-training.

Deep-Learning Radiomics Model

Figure 2 shows the pipeline of our proposed DLR method. The method is composed of three steps: (1) Base DL model pre-training, where we pre-trained several DL models and chose the optimal as the final DL model, to extract high-throughput DLR features of PET images; (2) Feature Fusion; and (3) Classification. Based on aforementioned DLR fusion features, SVM was used as the classifier to discriminate conversion to Alzheimer's disease in patients with MCI. Detailed technical demonstrations are described in the following sections.

Base DLR Model Pre-training

The Base DLR model acts as a feature encoder, which has a significant impact on classification. In this study, five convolutional neural networks (CNNs) namely AlexNet, ZF-Net, ResNet18, InceptionV3, and Xception, were introduced for pre-training to find the most suitable model for identifying conversion to AD from stable MCI patients.

In general, the complexity of the CNNs depends on two factors, namely "depth" and "width." The advantage of DL is that it can learn more representative features with the help of its neural network with numerous layers and broad width. But DL is flawed with highly dependence on data. Consequently, deeper networks do not necessarily reach better performance. This is mainly because the multi-layer back propagation of the error signal can easily lead to the gradient "dispersion" or the gradient "disappears" (He et al., 2016), based on the stochastic gradient descent when training. Especially for the sparse sample characteristics of medical images, the deeper network performs poorly, leading to overfitting. Considering above factors, to compare model performance, we introduced five CNNs, specifically AlexNet and ZF-Net with simple network structures, ResNet18, InceptionV3, and Xception with more network layers.

AlexNet, containing five convolutional layers and three fully-connected layers with learnable weights, competed in the ImageNet challenge in 2012 and achieved a top-five error of only 15.3% (Wang et al., 2019b; Rehman et al., 2020). There are several advanced techniques in AlexNet compared with traditional neural networks, including employing the rectified linear unit (ReLU) function and a pool operation. ZF-Net is based on AlexNet with only some changes in the convolutional kernel and step size, with no significant breakthrough in the network structure. Instead, based on the traditional CNN framework, the network structure of InceptionV3, Xception, and ResNet18 are more complex and deeper, and have their own unique network characteristics. The greatest advantage of the ResNet framework lies in adding identity mapping that is performed by the shortcut connections, the outputs of which are added to the outputs of the stacked layers (Chen et al., 2019). Therefore, the ResNet addressed the degradation problem and added neither extra parameters nor computational complexity. The advantage of Google's Inception structures is that there are good performance especially under strict constraints on memory and complexity of computational problems (Khosravi et al., 2018). For example, GoogLeNet (Szegedy et al., 2015) used five million parameters and the amount of parameters has significant reduction when compared with AlexNet (Krizhevsky et al., 2017). For this, Inception networks are always chose when a huge of data need to be processed at reasonable time and computational cost. And Inception V3 is one version of attempts to scale up deep networks, in which the fully connected layer of the auxiliary classifier is also-normalized based on Inception V2. In addition, Xception is an improved model based on Inception V3, whose main improvement is to use depth wise separable convolution to replace the Inception module.

There were two steps included in the entire training process, the forward computation and the backward propagation. Before modeling, the three-dimensional PET image of each subject was sliced and tiled into two-dimensional images, then being resized to 224 × 224 pixels and normalized. The pathology type was encoded to one hot, which was the label. Thereafter, in the training stage, data was fed into the network to update model parameters via backward propagation with the SGD algorithm,

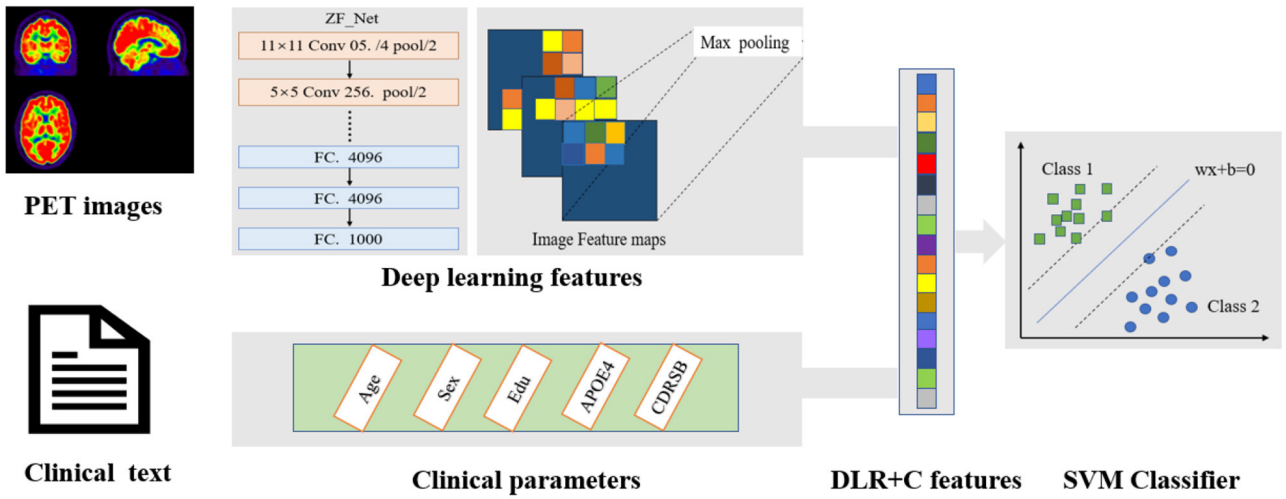

FIGURE 2 | The overall pipeline of DLR model. The pre-trained ZF-Net model acted as an feature encoder of the input images. Then the DLR features combined clinical parameters were classified by a SVM classifier.

a first-order gradient-based optimization algorithm that has been proven to be computationally efficient and appropriate for training deep neural networks. The outputs of the network were used as classification results, and the cross-entropy of the outputs was calculated as the loss function. More specifically, the output of the network for each individual PET image could be a binary value, in which one represented the highest probability of being MCI-c subjects, while zero represented highest probability of being MCI-nc subjects.

We employed several DL frameworks in this study. In the pre-training, we set the learning rate into 1e−2 and applied the SGD optimizer to update model parameters with a batch size of 8. The maximum number of iterations was set into 100. Note that we used Dropout and Early Stopping in this step to alleviate overfitting of our models, and we also adopted a learning rate decay strategy, setting the learning rate decay step to 10. Furthermore, a strategy called online data augmentation was used to prevent overfitting of small datasets, which meant horizontal flipping and Gaussian noise addition for input images in the training/validation group. Above all, pre-training of deep-learning models was processed on a GPU (graphics processing unit, GTX 1080 Ti acceleration of PyCharm 3.5).

DLR Features

Contrasting with hand-crafted and engineered features designed in previous medical experiences, DLR learned the high-throughput image features in a supervised manner, which could make full use of embedded information in PET images. After screening the optimal Base DL model, we replaced the FC layer with an SVM as classifier and fused the clinical information and network features to collaboratively make decisions.

Specifically, to obtain DLR features, the feature maps were first extracted from the last convolution layer of the convolution network, and they were transformed to raw values by taking the maximum values of each feature map with global max pooling. Afterwards, these extracted features, defined as DLR features, were combined with clinical parameters (CDRSD, Age, MMSE, etc.) as input data for future classification.

Classification

In this study, the enrolled subjects were randomly divided into one training/validation group and one independent test group at a ratio of 9:1, as shown in **Table 1**. The training group was then used to optimize the model parameters. We also randomly chose 10% of the training group to form a validation group to guide the choice of hyper parameters. We conducted training of several deep-learning models, including AlexNet, ZF-Net, ResNet18, InceptionV3, and Xception, and compared the classification performance for screening the optimum DLR. To evaluate classification performance, we repeatedly conducted 10-fold cross-validation in the training group. Subsequently, the extracted DLR features were combined with clinical scales, which were together named as DLR+C features serving as input. SVM served as a classifier to perform the classification. The training/validation group was used to train and validate the model, while the test group was used as an independent test dataset to verify the predictive performance of our proposed DLR+C approach. The model was trained and validated with 10-fold cross-validation 100 times. The linear kernel function was used to detect feature generalization ability and classification reliability.

The mean [± standard deviation (SD)] accuracy, sensitivity, and specificity were used to evaluate the results. The mathematical expression of the three parameters was as follows:

$$\begin{aligned} Accuracy &= \frac{Tn+Tp}{Tn+Tp+Fn+Fp} \\ Sensitivity &= \frac{Tp}{Tp+Fn} \\ Specificity &= \frac{Tn}{Tn+Fp} \end{aligned} \tag{1}$$

where *Tn*, *Tp*, *Fn*, and *Fp* denote true negatives, true positives, false negatives, and false positives, respectively.

Simultaneously, a receiver operating characteristic (ROC) curve was produced to intuitively compare the results of the different approaches, and the area under the curve (AUC) of the ROC was computed to quantitatively evaluate classification performance.

Comparative Experiment

To verify the superiority of the proposed DLR+C method in this research, we deployed the following four comparative experiments. They were all built with SVM classifiers, but with different input data. (1) Radiomics method: radiomic features of ROI in the brain (**Supplementary Material 1**, Zhou et al., 2019); (2) Standard uptake value ratio (SUVR) method: mean voxel uptake ratio of the whole brain according to AAL template; (3) Clinical method: Demographic data, neuropsychological cognitive assessment tests, as well as the APOE ε4 genotyping characteristics of all subjects. (4) SUVR + Clinical method.

Likewise, during the comparative experiments, the 10-fold cross-validation was performed in the training/validation group with 100 repetitions with the linear kernel. The test group was used to independently verify the generalization ability of the above model.

Decision Score

To more efficiently describe the discrimination ability of our proposed DLR+C method, we conducted a statistical analysis of the decision scores. A decision score could be output after the SVM model decision analysis to represent the class scores of MCI-nc or MCI-c. In the experiment, we calculated separately the decision scores of MCI-nc and MCI-c subjects of the test group. We used the scores to perform the *t*-test between MCI-nc and MCI-c to observe intergroup differences.

Statistical Analysis

Demographic and clinical characteristics were compared between groups using a two-sample *t*-test or the chi-square test. All statistical analyses were performed using SPSS Version 22.0 software (SPSS Inc., Chicago, IL, USA) and Matlab2016b (Mathworks Inc., Sherborn, MA, USA). All p-values < 0.05 were considered significant.

RESULTS

Base DLR Model Selection

To find the suitable Base DLR model for MCI-c vs. MCI-nc classification, the performances of AlexNet, ZF-Net, ResNet18, InceptionV3, and Xception in classifying MCI categories were compared. The classification performances on AlexNet, ZF-Net, ResNet18, InceptionV3, and Xception models are summarized in **Table 2**, including the classification accuracy, sensitivity, specificity, AUC, and execution time. Specially, the accuracy, sensitivity, specificity, AUC, and execution time of the ZF-Net were 74.12 ± 2.32, 70.63 ± 3.02, 77.22 ± 4.10%, 0.756, and 231.20 s, respectively. Finally, among these five models, the ZF-Net model proved to be the suitable model which not only had the best classification performance in the independent test group, but also had a shorter model training time. Therefore, ZF-Net was selected as the basic model to extract DLR features for further study. The ROC curves of the DLR pre-training models in the classification of MCI-c and MCI-nc were presented in **Figure 3A**.

Clinical Information Integration

When ZF-Net was selected as the Base DLR model with the best performance, clinical information was added to the diagnostic model. Consistently with the method described above, the model incorporating clinical information was called ZF-Net + C, where C represents clinical information. The method of adding clinical information was to directly fuse clinical information with the extracted DLR features from the last convolution layer of the convolution network. Thereafter, the fused features were fed into the SVM classifier. The ZF-Net + C, which integrated the deep features and clinical information offline, proved to be the best in terms of classification performance. Detailed results are summarized in **Table 3**.

Classification Performance

Table 3 lists the detailed results of five different methods including the SUVR method, Radiomics-ROI method, Clinical method, and DLR+C method in classification of MCI-c and MCI-nc subjects. Among five methods, the DLR+C method showed the best performance with accuracy of 90.62 ± 1.16%, sensibility of 87.50 ± 0.00%, and specificity of 93.39 ± 2.19% in the independent test group. The performance of the SUVR method, radiomics method, clinical method, and SUVR+Clinical method were all poorer than our proposed method, with accuracies of 68.38 ± 1.27, 73.31 ± 6.93, 81.09 ± 1.97, and 85.35 ± 0.72% in the independent test group, respectively.

Figure 3B presents the ROC curves of the five models in classification of MCI-c and MCI-nc. The average AUCs (±SD) of SUVR method, Clinical method, SUVR+Clinical method, and DLR+C method were 0.68 ± 0.01, 0.81 ± 0.02, 0.85 ± 0.01, and 0.90 ± 0.01, respectively, in the independent test group.

Decision Score

In our proposed DLR+C method, the performance of the output decision scores with the SVM linear kernel classification in the test group is shown in **Figure 4**. Decision scores of MCI-c were significantly higher than those of MCI-nc (linear: 0.82 ± 0.32 vs. 0.11 ± 0.19, $P < 0.001$). The results indicate that decision scores from the SVM output could effectively classify MCI-c and MCI-nc with significant differences, and could be used as a quantitative biomarker for classification between MCI-nc and MCI-c groups.

DISCUSSION

In this study, we proposed and applied a DLR+C method based on ^{18}F-FDG PET images to predict conversion to AD from stable MCI. Compared with other four traditional methods including Radiomics-ROI method, Clinical model or the voxel-level analysis, our proposed DLR+C model showed significant superiority in classification of MCI-nc and MCI-c subjects, demonstrating that the DLR+C model can be used for effectively

TABLE 2 | Performance of different classification approaches in mutiltasking classification.

Model	Accuracy (%)	Sensibility (%)	Specificity (%)	AUC	Execution time (s)
AlexNet	74.11 ± 2.88	73.12 ± 2.86	75.00 ± 4.48	0.746 ± 0.03	225.20 ± 72.59
ZF-Net	**74.12 ± 2.32**	**70.63 ± 3.02**	**77.22 ± 4.10**	**0.756 ± 0.04**	**231.20 ± 69.56**
InceptionV3	73.53 ± 4.60	69.37 ± 6.22	77.22 ± 6.65	0.733 ± 0.05	1090.00 ± 278.2
ResNet18	67.94 ± 2.92	68.75 ± 4.17	67.22 ± 3.15	0.680 ± 0.03	330.40 ± 55.71
Xception	69.71 ± 3.68	70.63 ± 4.22	68.89 ± 4.68	0.698 ± 0.04	665.50 ± 174.70

The methods are conducted with 10-fold cross-validation and their results are given as mean ± standard deviation.
Bold values indicate classification results of the optimal model ZFNet for Base DLR Model Selection.

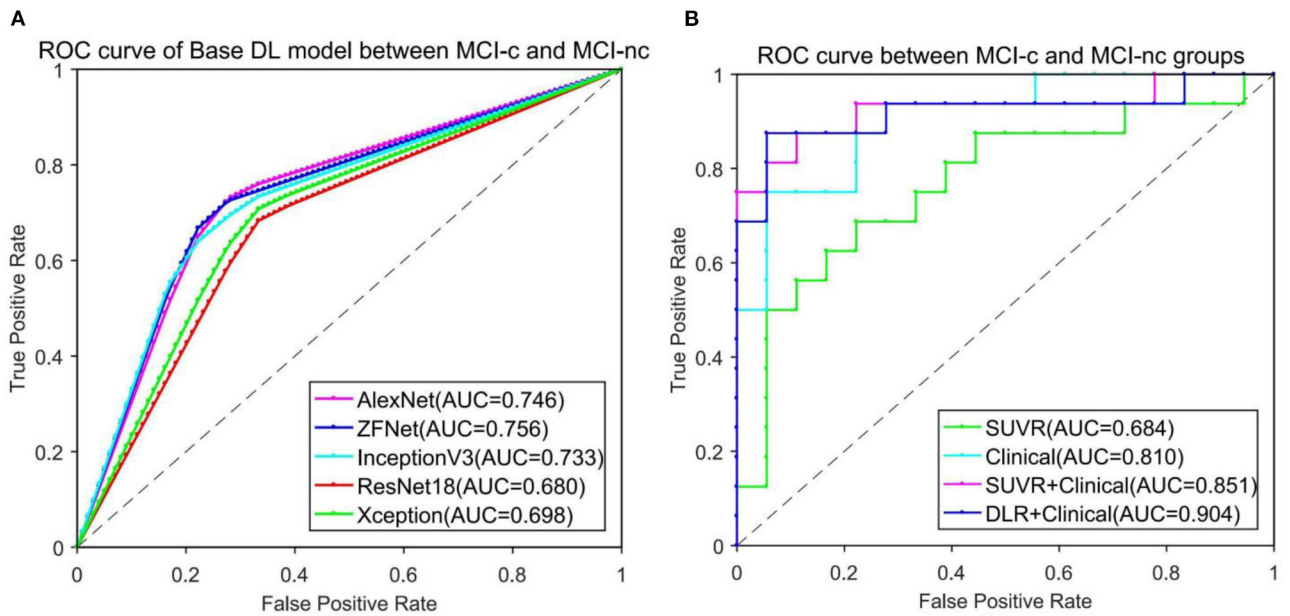

FIGURE 3 | ROC curve comparison in classification of MCI-c and MCI-nc. **(A)** ROC curve of five different Base DL pre-training models. **(B)** ROC curve of four different comparative experiments.

learning superior feature representation from small neuroimging data and avoid hand-coding and ROI segmentation based on a prior knowledge. Further, we validated that DLR+C had the potential to serve as a quantitative biomarker through the statistical analysis of decision scores. Overall, DLR+C might have possibility to provide clinicians with directions for the diagnosis of conversion to AD from stable MCI.

Base DLR Model Selection

As an emerging technique for image quantitative analysis, the DLR method represents a combination and development of DL and radiomics. The DLR method can automatically learn a large number of features including a neural network's hidden layers according to input images, and this process do not require object segmentation and hard-coded feature extraction (Lu et al., 2018b; Basaia et al., 2019; Spasov et al., 2019a; Roy et al., 2020; Yee et al., 2020; Pan et al., 2021). This has been successfully applied to oncology and cancer diagnosis at the present (Han et al., 2017; Deepak and Ameer, 2019; Jeyaraj and Samuel Nadar, 2019). In this study, DLR adopted CNN frameworks and was completely established on the analysis of 2D-slice FDG PET images.

To construct a DLR feature encoder, we compared the performance of several CNN models, including AlexNet, ZF-Net, ResNet18, InceptionV3, and Xception. As shown in **Table 2**, we observed that the results of ZF-Net were superior to those of other CNNs, showing the mean ± SD accuracy of 74.12 ± 2.32% in the independent test group. Further, in the process of training the model, with its simple network structure and fewer model parameters, the ZF-Net model exhibited a significantly shorter training time than other models, which was what we expected. Therefore, we chose ZF-Net as the final DLR model and feature encoder. The classification result was consistent with that of Yee et al. (2020) which used a 3D CNN with residual connections that took a 3D FDG-PET image as input and obtained an accuracy rate of 0.747. It was worth nothing that Yee et al. enrolled 871 MCI-nc and 362 MCI-c participants, but participants in our study were much fewer and also achieved the same performance. Besides, there are indeed advantages about

TABLE 3 | Performance of different classification approaches in mutiltasking classification.

Method	Accuracy (%)	Sensibility (%)	Specificity (%)	AUC
SUVR method	68.38 ± 1.27	68.06 ± 0.00	68.40±2.41	0.68 ± 0.01
Radiomics-ROI	73.31 ± 6.93	–	–	–
Clinical method	81.09 ± 1.97	75.69 ± 3.19	85.89±4.63	0.81 ± 0.02
SUVR+Clinical	85.35 ± 0.72	81.13 ± 0.88	89.11±1.09	0.85 ± 0.01
Our proposed DLR+C	**90.62 ± 1.16**	**87.50 ± 0.00**	**93.39±2.19**	**0.90 ± 0.01**

The methods are conducted with cross-validation and their results are given as mean ± standard deviation. DLR+C, Deep learning radiomics combined Clinical parameters; ROI, regions of interest.
Bold values represent the classification performance of the proposed DLR+C method.

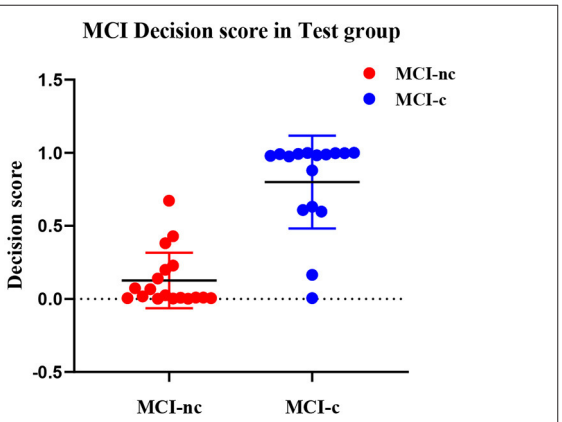

FIGURE 4 | The distribution of decision score of MCI-c and MCI-nc subjects.

the ResNet18, InceptionV3, and Xception networks. But their classification results were still poor when the execution time became longer, which was not what we expected. We speculated it might be due to too few subjects in our study which did not matched with deeper network structures and led to overfitting.

In addition, the above process about Base DLR model selection was also repeated when not resizing images after standard preprocessing. We found similar classification performance, but the later has heavier GPU load. Therefore, the results based on sliced and resized 224*224 images were taken as final.

Clinical Integration and Classification Performance

One issue is that a data scarcity problem remains when DLR is applied in medical databases (Dluhoš et al., 2017). Insufficient inputs proved incapable of training effective network parameters, and thus the optimal model becomes elusive. Considering this, we proposed the DLR+C method, providing complementary information to improve the diagnosis of conversion to AD.

According to the classification results of **Table 3**, our proposed DLR+C method obtained the mean accuracy of 90.62% and outperformed the result of the Base DL model. Hence, the ^{18}F-FDG PET images after integrating with standard cognitive tests (CDRSB), demographic information (age, gender, education, and MMSE), and APOEε4 genetic status indeed represented more valuable information and thus improved the diagnostic performance. Further, as discussed in the study of Moradi et al. (2015), the diagnostic labeling and number of ADNI subjects vary across studies, thus impeding direct comparison. Hence, to validate the superiority of our DLR+C method, we designed comparative experiments at three levels in turn: the voxel-based, radiomics, and the clinical. As shown in **Table 3**, the voxel-level analysis, SUVR method, performed the poorest with a mean accuracy of 68.38%. The Clinical method obtained a mean accuracy of 81.09%, and the SUVR+Clinical method had an accuracy of 85.35%. These results were consistent with previously relevant publications, where data were collected from the ADNI database (Young et al., 2013; Liu et al., 2017; Spasov et al., 2019b), and thus verified the validity and reliability of our experiments. Young et al. (2013) used the voxel-based method and obtained 69.9% accuracy, 55.3% sensitivity, 77.1% specificity by SVM classifiers. Moreover, the results of our clinical method were coherent with those in Spasov et al. (2019b) and Liu et al. (2017), where clinical data were provided with demographic information, cognitive tests, and APOEε4 status. Spasov et al. (2019b) achieved 81% accuracy, 83% sensitivity, 81% specificity; Liu et al. (2017) achieved 81.62% accuracy, 77.78% sensitivity, and 86.11% specificity. Nonetheless, it is deserving to clarify that the outcome of our proposed DLR+C method is optimal. In summary, the above results sufficiently illustrated the superiority of our DLR+C method. DLR avoided the need for prior knowledge and hard-coded feature extraction, while clinical parameters provided more complementary and valuable information.

Decision Score

To better demonstrate the discriminability of the proposed DLR+C method, we conducted a statistical analysis of decision values. As the distribution of decision scores in **Figure 4**, there were significant differences of decision scores between MCI-c and MCI-nc groups. Thus, it could be used as a quantitative biomarker for classification between the MCI-nc and MCI-c groups.

LIMITATIONS

Although the DLR+C method enhanced the performance of discrimination of conversion to AD in patients with MCI,

some limitations must be addressed. First, we need more available data to verify the generalizability and robustness of the proposed method. In this study, a small number of subjects were collected only from the ADNI database. Although the final DLR+C model performed excellent diagnostic performance, there is still potential to improve the representation of our Base DL model, where the accuracy only reached 74.12% in the independent test group and did not exceed those of Pan et al. (2021) and Lu et al. (2018a). Therefore, it is possible to improve the performance of our DLR+C method when comprehensive and homogeneous databases are developed and become available. Secondly, in this study, the DLR+C method was focused on the single image modality of ^{18}F-FDG PET. Whether multi-modalities of ^{18}F-FDG PET combined MRI can improve the classification performance of DLR+C method is to be explored in a further study. Third, the proposed method can provide a prediction whether MCI subjects would convert to AD, but it cannot decide when the conversion occurs in the future. To enroll longitudinal data to determine the severity of MCI-c subjects may well be of interest in our following studies.

CONCLUSION

We developed a DLR+C method for the ^{18}F-FDG PET modality in an effort to perform the diagnosis of MCI-c and MCI-nc subjects. This study demonstrates that the proposed DLR+C method can improve the diagnostic performance and provide a quantitative biomarker for predicting conversion to AD in MCI patients. Future, the DLR+C model holds potential to become a practical method for the computer-assisted diagnosis of conversion to AD. Prospective multi-modalities research is expected to apply our proposed DLR+C method and acquire more reliable evidence in predicting the conversion of MCI to AD.

DATA AVAILABILITY STATEMENT

The original contributions presented in the study are included in the article/**Supplementary Material**, further inquiries can be directed to the corresponding author/s.

ETHICS STATEMENT

Ethical review and approval was not required for the study on human participants in accordance with the local legislation and institutional requirements. The patients/participants provided their written informed consent to participate in this study. Written informed consent was obtained from the individual(s) for the publication of any potentially identifiable images or data included in this article.

AUTHOR CONTRIBUTIONS

PZ, RZ, and ZH conceived and designed the experiments, analyzed and interpreted the data, and wrote the manuscript. LY, FL, and CC performed the experiments and wrote the manuscript. CC, YF, YL, and YH analyzed and interpreted the data and wrote the manuscript. The Alzheimer's Disease Neuroimaging Initiative contributed reagents, materials, and data. All authors contributed to the article and approved the submitted version.

FUNDING

This program is sponsored by scientific development projects from ChenZhou Municipal Science and Technology Bureau (No.yfzx201906). Data collection and dissemination for this project were funded by the Alzheimer's Disease Neuroimaging Initiative (ADNI): the National Institutes of Health (grant number U01 Hindawi Template version: Apr19 14 AG024904), and the Department of Defense (award numberW81XWH-12-2-0012). ADNI is funded by the National Institute of Aging and the National Institute of Biomedical Imaging and Bioengineering as well as through generous contributions from the following organizations: AbbVie, Alzheimer's Association, Alzheimer's Drug Discovery Foundation, Araclon Biotech, BioClinica Inc., Biogen, Bristol-Myers Squibb Company, CereSpir Inc., Eisai Inc., Elan Pharmaceuticals Inc., Eli Lilly and Company, EuroImmun, F. Hoffmann-La Roche Ltd. and its affiliated company Genentech Inc., Fujirebio, GE Healthcare, IXICO Ltd., Janssen Alzheimer Immunotherapy Research & Development LLC., Johnson & Johnson Pharmaceutical Research &Development LLC., Lumosity, Lundbeck, Merck & Co. Inc., Meso Scale Diagnostics LLC., NeuroRx Research, Neurotrack Technologies, Novartis Pharmaceuticals Corporation, Pfizer Inc., Piramal Imaging, Servier, Takeda Pharmaceutical Company, and Transition Therapeutics. The Canadian Institutes of Health Research are providing funds to support ADNI clinical sites in Canada. Private sector contributions are facilitated by the Foundation for the National Institutes of Health (www.fnih.org). The grantee organization is the Northern California Institute for Research and Education, and the study is coordinated by the Alzheimer's Disease Cooperative Study at the University of California, San Diego, CA, USA. ADNI data are disseminated by the Laboratory for Neuro Imaging at the University of Southern California, CA, USA.

SUPPLEMENTARY MATERIAL

The Supplementary Material for this article can be found online at: https://www.frontiersin.org/articles/10.3389/fnagi.2021.764872/full#supplementary-material

REFERENCES

2020 Alzheimer's disease facts and figures (2020). *Alzheimers Dement*. 16, 391–460. doi: 10.1002/alz.12068

Albert, M. S., DeKosky, S. T., Dickson, D., Dubois, B., Feldman, H. H., Fox, N. C., et al. (2011). The diagnosis of mild cognitive impairment due to Alzheimer's disease: recommendations from the National Institute on Aging-Alzheimer's Association workgroups on diagnostic guidelines for Alzheimer's disease. *Alzheimers Dement*. 7, 270–279. doi: 10.1016/j.jalz.2011.03.008

Basaia, S., Agosta, F., Wagner, L., Canu, E., Magnani, G., Santangelo, R., et al. (2019). Automated classification of Alzheimer's disease and mild cognitive impairment using a single MRI and deep neural networks. *NeuroImage Clin*. 21, 101645. doi: 10.1016/j.nicl.2018.101645

Bennett, D. A., Wilson, R. S., Schneider, J. A., Evans, D. A., Mendes de Leon, C. F., Arnold, S. E., et al. (2003). Education modifies the relation of AD pathology to level of cognitive function in older persons. *Neurology* 60, 1909–1915. doi: 10.1212/01.WNL.0000069923.64550.9F

Braak, H., and Braak, E. (1996). Development of Alzheimer-related neurofibrillary changes in the neocortex inversely recapitulates cortical myelogenesis. *Acta Neuropathol*. 92, 197–201. doi: 10.1007/s004010050508

Brooks, L. G., and Loewenstein, D. A. (2010). Assessing the progression of mild cognitive impairment to Alzheimer's disease: current trends and future directions. *Alzheimer's Res. Ther.* 2, 28. doi: 10.1186/alzrt52

Caroli, A., Prestia, A., Chen, K., Ayutyanont, N., Landau, S. M., Madison, C. M., et al. (2012). Summary metrics to assess Alzheimer disease-related hypometabolic pattern with 18F-FDG PET: head-to-head comparison. *J. Nucl. Med*. 53, 592–600. doi: 10.2967/jnumed.111.094946

Chen, K. J., Chen, K. L., Wang, Q., He, Z. Y., Hu, J., and He, J. L. (2019). Short-term load forecasting with deep residual networks. *IEEE Trans. Smart Grid* 10, 3943–3952. doi: 10.1109/TSG.2018.2844307

Deepak, S., and Ameer, P. M. (2019). Brain tumor classification using deep CNN features via transfer learning. *Comput. Biol. Med*. 111, 103345. doi: 10.1016/j.compbiomed.2019.103345

Delacourte, A., David, J. P., Sergeant, N., Buée, L., Wattez, A., Vermersch, P., et al. (1999). The biochemical pathway of neurofibrillary degeneration in aging and Alzheimer's disease. *Neurology* 52, 1158–1165. doi: 10.1212/WNL.52.6.1158

Ding, C., Zhang, Q., and Wang, L. (2021). Coupling relationship between glucose and oxygen metabolisms to differentiate preclinical Alzheimer' s disease and normal individuals. *Hum. Brain Mapp.* 2021, 1–12. doi: 10.1002/hbm.25599

Dluhoš, P., Schwarz, D., Cahn, W., van Haren, N., and Kahn, R., Španiel, F., et al. (2017). Multi-center machine learning in imaging psychiatry: a meta-model approach. *Neuroimage* 155, 10–24. https://doi.org/10.1016/j.neuroimage.2017.03.027

Dong, Q., Li, T., Jiang, X., Wang, X., Han, Y., and Jiang, J. (2021). Glucose metabolism in the right middle temporal gyrus could be a potential biomarker for subjective cognitive decline : a study of a Han population. *Alz. Res. Therapy* 13, 74. doi: 10.1186/s13195-021-00811-w

Ferri, C. P., Prince, M., Brayne, C., Brodaty, H., Fratiglioni, L., Ganguli, M., et al. (2006). Global prevalence of dementia: a Delphi consensus study. *Tijdschr. Verpleeghuisgeneeskd*. 31, 46–46. doi: 10.1007/bf03075138

Gillies, R. J., Kinahan, P. E., and Hricak, H. (2016). Radiomics: images are more than pictures, they are data. *Radiology* 278, 563–577. doi: 10.1148/radiol.2015151169

Gonzalez-Escamilla, G., Lange, C., Teipel, S., Buchert, R., and Grothe, M. J. (2017). PETPVE12: an SPM toolbox for partial volume effects correction in brain PET – application to amyloid imaging with AV45-PET. *Neuroimage* 147, 669–677. doi: 10.1016/j.neuroimage.2016.12.077

Han, Z., Wei, B., Zheng, Y., Yin, Y., Li, K., and Li, S. (2017). Breast cancer multi-classification from histopathological images with structured deep learning model. *Sci. Rep*. 7, 1–10. doi: 10.1038/s41598-017-04075-z

He, K., Zhang, X., Ren, S., and Sun, J. (2016). Deep residual learning for image recognition. *Proc. IEEE Comput. Soc. Conf. Comput. Vis. Pattern Recognit*. 2016, 770–778. doi: 10.1109/CVPR.2016.90

Jeyaraj, P. R., and Samuel Nadar, E. R. (2019). Computer-assisted medical image classification for early diagnosis of oral cancer employing deep learning algorithm. *J. Cancer Res. Clin. Oncol.* 145, 829–837. doi: 10.1007/s00432-018-02834-7

Khosravi, P., Kazemi, E., and Imielinski, M. (2018). EBioMedicine deep convolutional neural networks enable discrimination of heterogeneous digital pathology images. *EBioMedicine* 27, 317–328. doi: 10.1016/j.ebiom.2017.12.026

Krizhevsky, A., Sutskever, I., and Hinton, G. E. (2017). ImageNet classification with deep convolutional neural networks. *Commun. ACM* 60, 84–90. doi: 10.1145/3065386

Lange, C., Suppa, P., Frings, L., Brenner, W., Spies, L., and Buchert, R. (2015). Optimization of statistical single subject analysis of brain FDG PET for the prognosis of mild cognitive impairment-to-Alzheimer's disease conversion. *J. Alzheimers Dis*. 49, 945–959. doi: 10.3233/JAD-150814

Liu, K., Chen, K., Yao, L., and Guo, X. (2017). Prediction of mild cognitive impairment conversion using a combination of independent component analysis and the cox model. *Front. Hum. Neurosci*. 11, 33. doi: 10.3389/fnhum.2017.00033

Lu, D., Popuri, K., Ding, G. W., Balachandar, R., and Beg, M. F. (2018a). Multiscale deep neural network based analysis of FDG-PET images for the early diagnosis of Alzheimer's disease. *Med. Image Anal*. 46, 26–34. doi: 10.1016/j.media.2018.02.002

Lu, D., Popuri, K., Ding, G. W., Balachandar, R., Beg, M. F., Weiner, M., et al. (2018b). Multimodal and multiscale deep neural networks for the early diagnosis of Alzheimer's disease using structural MR and FDG-PET images. *Sci. Rep*. 8, 1–13. doi: 10.1038/s41598-018-22871-z

McKhann, G. M., Knopman, D. S., Chertkow, H., Hyman, B. T., Jack, C. R., Kawas, C. H., et al. (2011). The diagnosis of dementia due to Alzheimer's disease: recommendations from the National Institute on Aging-Alzheimer's Association workgroups on diagnostic guidelines for Alzheimer's disease. *Alzheimer's Dement*. 7, 263–269. doi: 10.1016/j.jalz.2011.03.005

Moradi, E., Pepe, A., Gaser, C., Huttunen, H., and Tohka, J. (2015). Machine learning framework for early MRI-based Alzheimer's conversion prediction in MCI subjects. *Neuroimage* 104, 398–412. doi: 10.1016/j.neuroimage.2014.10.002

Pagani, M., Nobili, F., Morbelli, S., Arnaldi, D., and Giuliani, A., Öberg, J., et al. (2017). Early identification of MCI converting to AD: a FDG PET study. *Eur. J. Nucl. Med. Mol. Imaging* 44, 2042–2052. doi: 10.1007/s00259-017-3761-x

Pan, X., Phan, T-L., Adel, M., Fossati, C., Gaidon, T., Wojak, J., et al. (2021). Multi-view separable pyramid network for AD prediction at MCI stage by 18F-FDG brain PET imaging. *IEEE Trans. Med. Imaging* 40, 81–92. doi: 10.1109/TMI.2020.3022591

Rehman, A., Naz, S., Razzak, M. I., Akram, F., and Imran, M. (2020). A deep learning-based framework for automatic brain tumors classification using transfer learning. *Circuits Syst. Signal Process*. 39, 757–775. doi: 10.1007/s00034-019-01246-3

Richard, E., Schmand, B. A., Eikelenboom, P., and Van Gool, W. A. (2013). MRI and cerebrospinal fluid biomarkers for predicting progression to Alzheimer's disease in patients with mild cognitive impairment: a diagnostic accuracy study. *BMJ Open* 3, e002541. doi: 10.1136/bmjopen-2012-002541

Roy, S. S., Sikaria, R., and Susan, A. (2020). A deep learning based CNN approach on MRI for Alzheimer's disease detection. *Intell. Decis. Technol*. 13, 495–505. doi: 10.3233/idt-190005

Sanford, A. M. (2017). Mild cognitive impairment. *Clin. Geriatr. Med*. 33, 325–337. doi: 10.1016/j.cger.2017.02.005

Schneider, J. A., Arvanitakis, Z., Leurgans, S. E., and Bennett, D. A. (2009). The neuropathology of probable Alzheimer disease and mild cognitive impairment. *Ann. Neurol*. 66, 200–208. doi: 10.1002/ana.21706

Shaffer, J. L., Petrella, J. R., Sheldon, F. C., Choudhury, K. R., Calhoun, V. D., Edward Coleman, R., et al. (2013). Predicting cognitive decline in subjects at risk for Alzheimer disease by using combined cerebrospinal fluid, MR imaging, and PET biomarkers. *Radiology* 266, 583–591. doi: 10.1148/radiol.12120010

Spasov, S., Passamonti, L., Duggento, A., Liò, P., and Toschi, N. (2019a). A parameter-efficient deep learning approach to predict conversion from mild cognitive impairment to Alzheimer's disease. *Neuroimage* 189, 276–287. doi: 10.1016/j.neuroimage.2019.01.031

Spasov, S., Passamonti, L., Duggento, A., Liò, P., and Toschi, N. (2019b). A parameter-efficient deep learning approach to predict conversion from mild cognitive impairment to Alzheimer's disease. *Neuroimage* 189, 276–287. doi: 10.1016/j.neuroimage.2019.1.031

Szegedy, C., Liu, W., Jia, Y., Sermanet, P., Reed, S., Anguelov, D., et al. (2015). "Going deeper with convolutions," in *2015 IEEE Conference on*

Computer Vision and Pattern Recognition (CVPR) (Boston, MA), 1–9. doi: 10.1109/CVPR.2015.7298594

Vos, S., van Rossum, I., Burns, L., Knol, D., Scheltens, P., Soininen, H., et al. (2012). Test sequence of CSF and MRI biomarkers for prediction of AD in subjects with MCI. *Neurobiol. Aging* 33, 2272–2281. doi: 10.1016/j.neurobiolaging.2011.12.017

Wang, K., Lu, X., Zhou, H., Gao, Y., Zheng, J., Tong, M., et al. (2019a). Deep learning radiomics of shear wave elastography significantly improved diagnostic performance for assessing liver fibrosis in chronic hepatitis B: a prospective multicentre study. *Gut* 68, 729–741. doi: 10.1136/gutjnl-2018-316204

Wang, M., Jiang, J. H., Yan, Z. Z., Alberts, I., Ge, J. J., Zhang, H. W., et al. (2020). Individual brain metabolic connectome indicator based on Kullback-Leibler Divergence Similarity Estimation predicts progression from mild cognitive impairment to Alzheimer's dementia. *Eur. J. Nucl. Med. Mol. Imaging* 47, 2753–2764. doi: 10.1007/s00259-020-04814-x

Wang, S. H., Xie, S., Chen, X., Guttery, D. S., Tang, C., Sun, J., et al. (2019b). Alcoholism identification based on an Alexnet transfer learning model. *Front. Psychiatry* 10, 205. doi: 10.3389/fpsyt.2019.00205

Yee, E., Popuri, K., and Beg, M. F. (2020). Quantifying brain metabolism from FDG-PET images into a probability of Alzheimer's dementia score. *Hum. Brain Mapp*. 41, 5–16. doi: 10.1002/hbm.24783

Young, J., Modat, M., Cardoso, M. J., Mendelson, A., Cash, D., and Ourselin, S. (2013). Accurate multimodal probabilistic prediction of conversion to Alzheimer's disease in patients with mild cognitive impairment. *NeuroImage Clin*. 2, 735–745. doi: 10.1016/j.nicl.2013.05.004

Zheng, X., Yao, Z., Huang, Y., Yu, Y., Wang, Y., Liu, Y., et al. (2020). Deep learning radiomics can predict axillary lymph node status in early-stage breast cancer. *Nat. Commun*. 11, 1–9. doi: 10.1038/s41467-020-15027-z

Zhou, H., Jiang, J., Lu, J., Wang, M., Zhang, H., and Zuo, C. (2019). Dual-model radiomic biomarkers predict development of mild cognitive impairment progression to Alzheimer's disease. *Front. Neurosci*. 13, 1045. doi: 10.3389/fnins.2018.01045

Conflict of Interest: The authors declare that the research was conducted in the absence of any commercial or financial relationships that could be construed as a potential conflict of interest.

Publisher's Note: All claims expressed in this article are solely those of the authors and do not necessarily represent those of their affiliated organizations, or those of the publisher, the editors and the reviewers. Any product that may be evaluated in this article, or claim that may be made by its manufacturer, is not guaranteed or endorsed by the publisher.

frontiers in Aging Neuroscience

ORIGINAL RESEARCH
published: 23 November 2021
doi: 10.3389/fnagi.2021.765432

Diffusion Tensor Imaging Study of Olfactory Identification Deficit in Patients With Mild Cognitive Impairment

Yongjia Shao[1†], Zijian Wang[2†], Bin Ji[1†], Hang Qi[1], Shangci Hao[1], Gang Li[3], Yue Zhang[3] and Qian Xi[1]**

[1] Department of Radiology, Shanghai East Hospital, Tongji University School of Medicine, Shanghai, China, [2] School of Computer Science and Technology, Donghua University, Shanghai, China, [3] Department of Neurology, Shanghai East Hospital, Tongji University School of Medicine, Shanghai, China

OPEN ACCESS

Edited by:
Ping Wu,
Fudan University, China

Reviewed by:
Kenji Toba,
Tokyo Metropolitan Institute of Gerontology, Japan
Yuxin Li,
Fudan University, China
Jerzy Walecki,
Medical University of Warsaw, Poland

***Correspondence:**
Yue Zhang
dyuezhang@126.com
Qian Xi
96125007@sina.com

[†] These authors have contributed equally to this work and share first authorship

Received: 27 August 2021
Accepted: 01 November 2021
Published: 23 November 2021

Citation:
Shao Y, Wang Z, Ji B, Qi H, Hao S, Li G, Zhang Y and Xi Q (2021) Diffusion Tensor Imaging Study of Olfactory Identification Deficit in Patients With Mild Cognitive Impairment. Front. Aging Neurosci. 13:765432. doi: 10.3389/fnagi.2021.765432

Objective: To explore the relationship between white matter changes and olfactory ability among patients with mild cognitive impairment (MCI) and to develop a tool to predict the development of Alzheimer's disease among patients with MCI.

Methods: The Montreal Cognitive Assessment (MoCA) was used for cognitive assessments, and the 70% isopropanol test paper was used to evaluate olfactory function. Tract-based spatial statistics, based on the diffusion tensor imaging technology, were used to obtain relevant parameters, and behavioral and imaging results were compared between patients with MCI (n = 36) and healthy older adults (n = 32).

Results: The olfactory ability of MCI patients was lower overall, which was positively correlated with the MoCA score. Fractional anisotropy (FA) changes significantly of all parameters. Lower FA regions were mainly located in the corpus callosum, the orbitofrontal gyrus, and the left occipital lobe. The olfactory score was significantly correlated with the FA value of the orbitofrontal gyrus. Fibrous connections in several brain regions, such as the entorhinal cortex, were stronger in patients with MCI.

Conclusion: The olfactory ability of MCI patients in our group was positively correlated with the neuropsychological scale results. Impairment in olfactory function was superior to memory deficits for predicting cognitive decline among cognitively intact participants. The fibrous connections in several brain regions, such as the entorhinal cortex, were higher in patients with MCI, which suggested that there may be a compensatory mechanism in the olfactory pathway in MCI patients. The decline in olfactory function may be a significant and useful indicator of neuropathological changes in MCI patients and an effective marker for the development of cognitive decline and dementia.

Keywords: diffusion tensor imaging, tract-based spatial statistics, mild cognitive impairment, Alzheimer's disease, olfactory dysfunction

INTRODUCTION

Alzheimer's disease (AD), which is characterized by latent and progressive cognitive decline, is the most common etiology for dementia and is recognized as an urgent concern that has significant implications for both individuals and society (Lane et al., 2018). Mild cognitive impairment (MCI), which is considered a transitional state between normal aging and dementia, has a conversion range of 8–15% per year (Shu et al., 2021). In line with recommendations form the National Institute on Aging-Alzheimers's Association workgroups, we use the term "MCI due to AD" to refer to the symptomatic predementia phase of AD, which suggests that MCI is a critical stage for preventive treatment for dementia (Albert et al., 2011). Therefore, there is significant interest in developing a sensitive, specific, and non-invasive method for the early prediction of MCI before progression to AD. At present, neuropsychological tests and neuroimaging technology, such as positron emission tomography (PET), cerebrospinal fluid (CSF) measurements, and magnetic resonance imaging (MRI), are commonly used for early diagnosis of MCI (Jung et al., 2019). However, neuropsychological tests are subjective and are easily affected by factors, such as subject's mood, mental status, and educational background. Furthermore, the high cost of PET and the invasive nature of obtaining CSF limit their utility. Neuroimaging methods have proliferated in recent years; among them, diffusion-tensor imaging (DTI) is a non-invasive neuroimaging modality used to evaluate the structure of white matter in the brain, which is currently the only way to map white matter fiber architecture in brain tissue. Fractional anisotropy (FA), mean diffusivity (MD), radial diffusivity (DR), and axial diffusivity (DA; Georgiopoulos et al., 2017) are the most commonly used DTI metrics. Among these, FA and MD are most frequently reported. In DTI, the displacement of water molecules is used to measure white matter tract integrity. FA assesses the degree of directionality of water diffusion, whereas MD measures the mean water diffusion rate.

The olfactory center of the brain is composed of the primary (POC) and secondary olfactory cortices (SOC). The POC plays an important role in olfactory detection and has a complex structure that mainly comprises the entorhinal cortex (EC), amygdala, and piriform cortex (Kjelvik et al., 2020). The SOC is involved in olfactory recognition and mainly includes the hippocampus, hypothalamus, orbitofrontal gyrus, striatum, and corpus callosum. Among them, the orbitofrontal gyrus is the highest olfactory center, that determines the pleasure and familiarity of odors (Zhao et al., 2016). The olfactory pathway not only overlaps with hippocampus, the typical lesion site of AD, but also is involved in early pathological changes of AD (Marin et al., 2018). In line with a recent study, AD-related pathological alterations first resulted in synaptic neurodegeneration and then neuronal loss, it found no significant neuronal loss in the EC was detectable in cognitively normal subjects, by contrast, there was a very severe neuronal loss in the EC even in very mild AD cases (Li et al., 2021). The results highlighted the EC maybe helpful for predicting the pre-symptomatic and very mild stages of AD, therefore, olfactory function assessment provides the possibility for early recognition of cognitive dysfunction. Numerous recent studies applied neuroimaging modality to identify a clinical marker for predicting the preclinical AD, a study verified a strong correlation between olfactory impairment and white matter damage (Woodward et al., 2017). Some have also found, compared with cognitively normal controls (NC), patients with MCI were shown to have lower FA and higher MD in the hippocampus, EC, medial temporal lobe, and corpus callosum (Knight et al., 2019), which overlap with several of the olfactory functional areas described above. In addition, one study reported patients with more severe cognitive dysfunction had worse olfactory function (Yoo et al., 2018). All of these findings suggest that olfactory identification (OI) is a significant factor for predicting the risk of MCI-to-AD transition (Devanand, 2016). However, further research is needed to identify a visual indicator for predicting the development of AD in MCI patients with OI impairment.

In this prospective study, DTI and tract-based-spatial-statistics (TBSS) were used to conduct a cross-sectional analysis of white matter microstructural changes in MCI patients and NC to explore the relationship between white matter changes and olfactory ability in patients with MCI and to develop a reliable method for improving diagnoses and reducing underdiagnoses of MCI and dementia.

MATERIALS AND METHODS

Study Participants

Sixty-eight subjects (36 MCI and 32 NC) were recruited from the Shanghai Jinguang community from March 2017 to December 2019. All patients were recruited by the Neurology Department of Shanghai East Hospital (Southern Branch) after they underwent neuropsychological tests. The study was reviewed and approved by the Ethics Review Committee of Shanghai East Hospital, and written informed consent was obtained from all participants.

The Mini-Mental State Examination (MMSE) is the most widely used screening scale owing to its speed and ease of administration. However, its sensitivity in identifying patients with MCI, AD and healthy people is relatively low (Albert et al., 2011). While, the Montreal Cognitive Assessment (MoCA) covers a wider range of cognitive domains, including attention and concentration, executive function, memory, language, visual-spatial structure skills, abstract thinking, computation and orientation, therefore, it has superior sensitivity and specificity to the MMSE in predicting cognitive decline (Lu et al., 2011).

Inclusion criteria for MCI patients were the following: (1) a subjective complaint of mild cognitive decline by the patient, preferably confirmed by an insider; (2) minimal effect of working and living independently and handling complex tasks; (3) objective evidence of memory loss, with an MMSE score $\leq$27 and $\geq$24; (4) absence of dementia, with a MoCA score $\leq$24 (illiterate group $\leq$13 points, primary school group $\leq$19 points, middle school and above group $\leq$24 points), based on MoCA for detecting MCI in Chinese older adults (Lu et al., 2011).

Inclusion criteria for NC were the following: (1) independent behavioral ability, no cognitive or memory impairment, no

depression, and no organic nervous system diseases; and (2) a MoCA score >24 (Lu et al., 2011).

Exclusion criteria were the following: (1) history of nervous system tumor, craniocerebral surgery, stroke, or brain trauma; (2) serious medical diseases, such as organ dysfunction, autoimmune diseases, blood system diseases, anemia, and tumor; (3) unable to cooperate with examination because of a mental disorder, speech confusion, or severe hearing impairment; and (4) other neurodegenerative diseases causing cognitive impairment, such as bipolar disorder, mania, schizophrenia, epilepsy, PD, and multiple sclerosis.

Olfactory Identification Test

The most commonly used odor identification test is the University of Pennsylvania Smell Identification Test (UPSIT), however, it takes too long to administer by using 40 scents. Furthermore, too much odor identification can be affected by differences in region, culture, and individual experiences, so it is complicated to use as a screening test for the elderly (Kim et al., 2020, 2021). The "Sniffin' Sticks" Test (SST) is another widely used odor test, but its applicability is limited because of the high cost and the regional-cultural differentiation of odor recognition (Demir et al., 2021). Therefore, all of our subjects underwent the Alcohol Sniff Test, which is a simple, rapid, and reliable measure of olfaction, it takes less than 5 min to administer, has good test-retest reliability and can be used cross-culturally, which is easy to use in the elderly (Davidson et al., 1998). In a quiet, ventilated, and private environment, subjects kept their eyes and mouth closed while the researcher placed a soft ruler under the subject's nose with the proximal end of the ruler perpendicular to the tip of the nose. The isopropyl alcohol (70 g/100 ml) test paper was placed under the subject's nose at the 30 cm mark of the soft ruler. The subject was then instructed to take a deep breath while the researcher simultaneously moved the test paper in 1 cm increments up the ruler with each breath until the subject could smell an isopropyl alcohol odor. The test was repeated four times, and the average distance was calculated. The score was based on the distance from the tip of the nose to the test paper, which indicated anosmia (average distance <10 cm), hyposmia (10 cm ≤average distance ≤15 cm), or normal smell (average distance >15 cm) (Ashwin et al., 2014).

Magnetic Resonance Imaging

All participants underwent a DTI scan on an M750w 3.0T GE Signa MRI system (GE Healthcare, American) with a 32-channel head and neck coil. During scanning, all subjects lay in a supine position with their head positioned in the center of the coil, and earplugs were placed in their ears to reduce scanner noise. Participants were asked to minimize head movements as much as possible. T1-weighted three-dimensional (3D-T1), axial T2-weighted, and fluid-attenuated inversion recovery images constituted the structural imaging, which was used to exclude abnormalities other than atrophy or white matter degeneration. 3D-T1 images were acquired using a fast-spoiled gradient recalled echo sequence [repetition time (TR) = 8.5 ms, echo time [TE] = 3.2 ms, field of view [FOV] = 256 × 256 mm, slice thickness = 1 mm]. In addition, diffusion-weighted imaging (DWI) and DTI were acquired simultaneously. The DWI sequence parameters were: TR = 13700 ms, TE = 85 ms, FOV = 224 × 224 mm, slice thickness = 2 mm. The DTI sequence parameters were: TR = 13701 ms, TE = 114 ms, FOV = 224 × 224 mm, slice thickness = 2 mm, diffusion coefficient b = 1000 s/mm^2, 64 diffusion-sensitive gradients, one $b = 0$ s/mm^2, and 70 continuous slices in each gradient direction.

Imaging Processing

3D-T1 images were reviewed by two experienced radiologists to check for any morphological abnormalities. The regions of interest (ROIs) were determined jointly by neurologists and radiologists who had no knowledge of patient information, including the hippocampus, the corpus callosum, the orbitofrontal gyrus and the left inferior occipital gyrus. Post-processing of DTI data was performed using the Functional Magnetic Resonance Imaging of the Brain (FMRIB) Software Library version 5.0[1], which contains TBSS and FMRIB's diffusion toolbox (FDT). Original DTI images were corrected for head movement and eddy current distortions, which was followed by brain extraction to eliminate non-brain tissue and brain mask generation to ensure inclusion of the ventral surface of the forebrain using the Brain Extraction Tool (BET). Subsequently, commonly used DTI metrics were estimated, derived and calculated using FDT, such as FA, MD, DA, and DR, which applies a diffusion tensor model to describe fibrous structural characteristics that indicate white matter microdamage (Tae et al., 2018). Then, we used the abnormal area based on the whole-brain TBSS analysis results as the seed region to perform probabilistic diffusion tractography with a probability of over 90%, and the specific process mainly includes tracer modeling, image registration and tracer analysis.

[1]https://fsl.fmrib.ox.ac.uk/fsl/fslwiki

TABLE 1 | Demographic information of participants.

Group	MCI (n = 36)		NC (n = 32)		Test	
	Mean	SD	Mean	SD	t	p
Age (year)	67.794	6.3331	68.810	5.5463	−0.6050	0.548
Education background (year)	9.2060	2.4093	9.1430	2.0071	0.1000	0.921
OI score	10.118	3.8672	17.143	2.3084	−7.5220	<0.001
MoCA score	17.412	6.2091	27.000	1.4491	−6.9380	<0.001
	N	Female (%)	N	Female (%)	F	X^2
Sex ratio	36.000	58.300	32.000	42.900	1.0000	0.1710

TABLE 2 | Comparison of behavioral score between MCI patients and NCs.

	MCI (n = 36)	NC (n = 32)	P
OI score	10.12 ± 3.87	17.14 ± 2.31	<0.010
MoCA score	17.41 ± 6.21	27.00 ± 1.45	<0.010

TABLE 3 | Correlation between MoCA score and OI score.

		MoCA score	OI score
MoCA score	*r*	1.000	0.682
	p	–	<0.001
OI score	*r*	0.682	1.000
	p	<0.001	–

Statistical Analysis

Statistical calculations were performed with the Statistical Package for the Social Sciences version 23.0 IBM. Means ± standard deviations (SD) were used to express measurement data, which were assessed for normality test prior to statistical analysis, and then the two independent sample *t*-tests were carried out according to the normality test result; whereas chi-squared tests were used for enumeration data. The FSL-Randomize function was used to extract the average values of FA, DA, DR, and MD of the whole brain in the experimental and control group, and then statistical tests were performed on the average values of above DTI metrics, and inter- and intra-group statistical analyses of DTI data for ROIs were performed. In addition, correlation analyses were conducted between the behavioral indicators and olfactory test values, as well as between the behavioral and the imaging indicators. At the same time, we make the receiver operating characteristic (ROC) curve to reveal the correlation between sensitivity and specificity.

RESULTS

Clinical Characteristics of the Study Cohort

Results showed that there were no significant differences in sex ratio, age, or educational background between the groups ($p > 0.05$, **Table 1**). However, OI and MoCA scores were significantly different between the experimental and control groups ($p < 0.05$, **Table 1**).

Correlational Analysis of Behavioral Indicators

Patients with MCI had significantly poorer performance on the OI test than the NC, and there were significant differences in the OI and MoCA scores between the MCI and NC groups ($p < 0.01$, **Table 2**). After MoCA score was converted into ranked information, the Pearson correlation test showed that the olfactory function of patients with MCI was poorer than NC, and neuropsychological test results were positively correlated with the olfactory test value ($r = 0.682$, $p < 0.01$; **Table 3** and **Figure 1**). In addition, we found that the value of the olfaction test had high specificity for predicting MCI (area under the curve = 0.951; **Figure 2**).

Correlational Analysis of Imaging Indicators

Compared with the NC group, the MCI group showed significantly higher DR and lower FA ($p < 0.05$; **Table 4**).

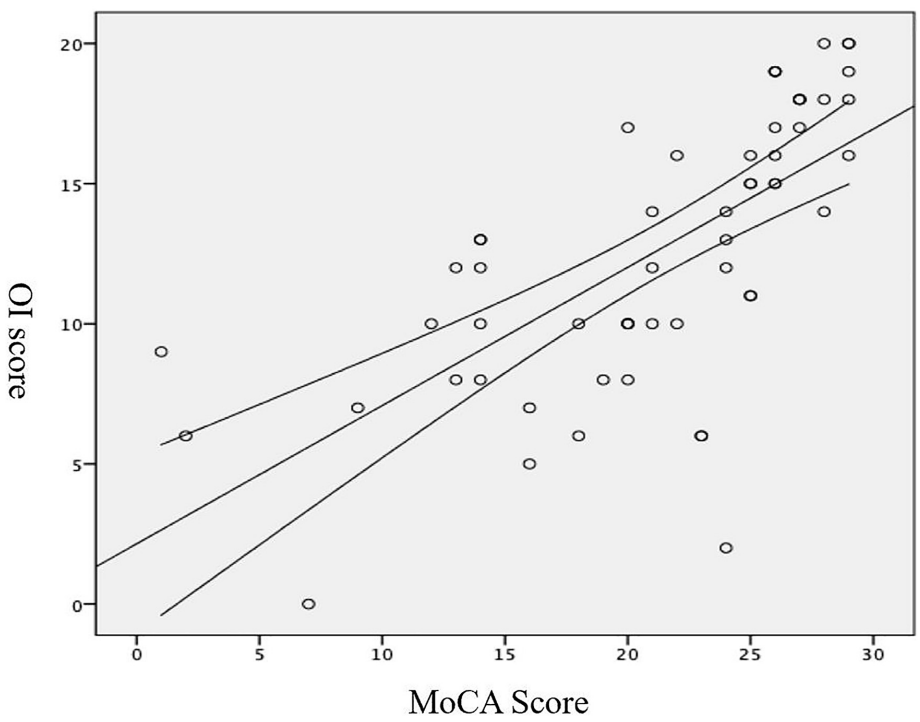

FIGURE 1 | Correlation between the MoCA and OI scores.

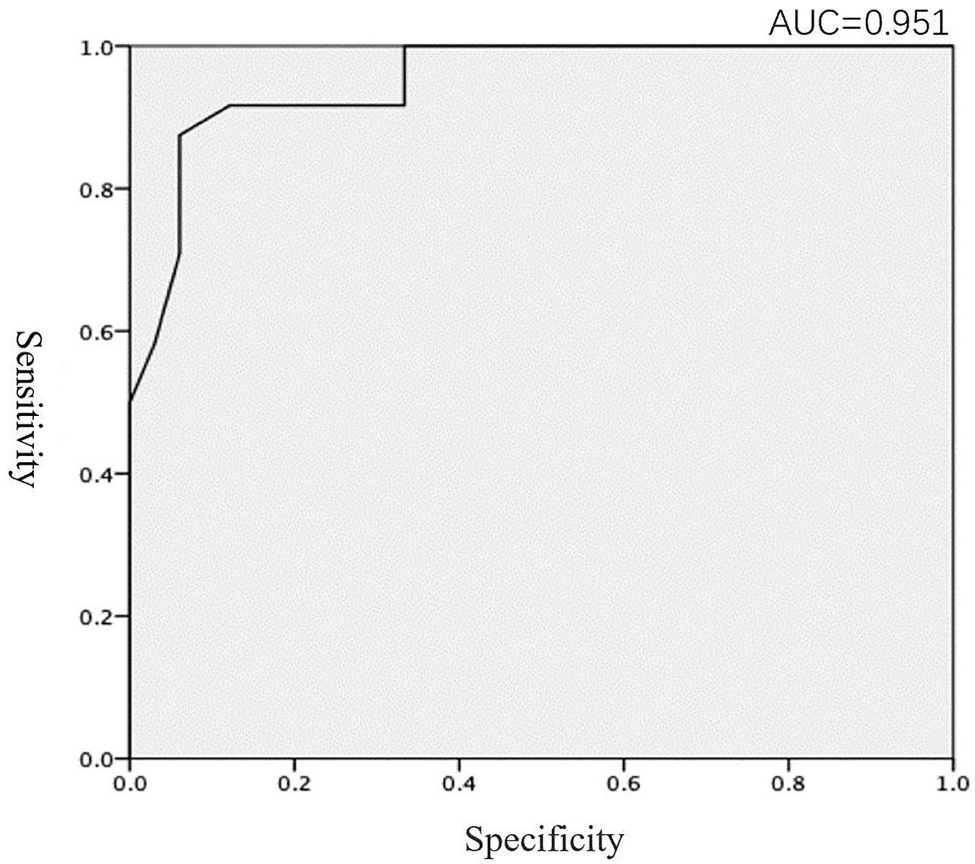

FIGURE 2 | ROC curve of the MoCA and OI scores.

Whole-brain TBSS analysis showed that the areas of lower FA (active area) were primarily localized to areas around the corpus callosum, orbitofrontal gyrus, and left inferior occipital gyrus. However, there was no significant FA difference around the hippocampus (**Figure 3**).

Compared with the NC group, the fiber tracking connection area (red area) in the MCI group was significantly lower (**Figure 4**). In the MCI group, a large number of fibers reached the cerebellum (Cerebelum_3_L), insula (Supp_Motor_Area_R), and intraorbital superior frontal gyrus (Frontal_Mid_2_R) (**Figure 5A** blue underline). In the NC group, numerous fibers reached the parahippocampal gyrus (ParaHippocampal_L), cerebellum (Cerebelum_6_R), and fusiform gyrus (Fusiform_R) (**Figure 5B** red underline). Notably, several connection areas were observed in the MCI group, which were not observed in the NC group, such as the intraorbital superior frontal gyrus (Frontal_Mid_2_R), inferior frontal gyrus of island cap (Frontal_Inf_Tri_R), and olfactory cortex (Olfactory_L) (**Figure 5A** orange underline). Compared with the NC group, the number and range of fibers reaching the parahippocampal gyrus in the MCI group were significantly lower (**Figures 4**, **5**).

In the present study, the main functional areas (hippocampus, bilateral medial temporal lobe, and parahippocampal gyrus) that are responsible for olfactory and cognitive functions were weaker in MCI patients, especially the parahippocampal gyrus and bilateral medial temporal lobe (**Figures 4**, **5**).

TABLE 4 | Whole-brain DTI analyses.

	MCI	NC	*t*	*p*
FA	0.67200 ± 0.02800	0.69100 ± 0.01600	−2.814	0.007
MD	0.00069 ± 0.00003	0.00068 ± 0.00002	1.1230	0.268
DA	0.00130 ± 0.00003	0.00130 ± 0.00004	−1.139	0.261
DR	0.00037 ± 0.00004	0.00035 ± 0.00002	2.1110	0.040

Correlations Between Behavioral and Imaging Indicators

The mean FAs of the orbitofrontal gyrus, hippocampus, inferior occipital gyrus, and parahippocampal gyrus were extracted from the ROIs of all subjects, and Pearson correlation analyses were performed between the MoCA, OI scores and the FA values. Compared with the NC group, the OI score was significantly correlated with the FA value of the orbitofrontal gyrus in the MCI group, followed by the inferior occipital gyrus, and there were significant differences ($p < 0.05$; **Table 5**). However, in our cohort of MCI group, there were no significant differences between the MoCA score and the FA values.

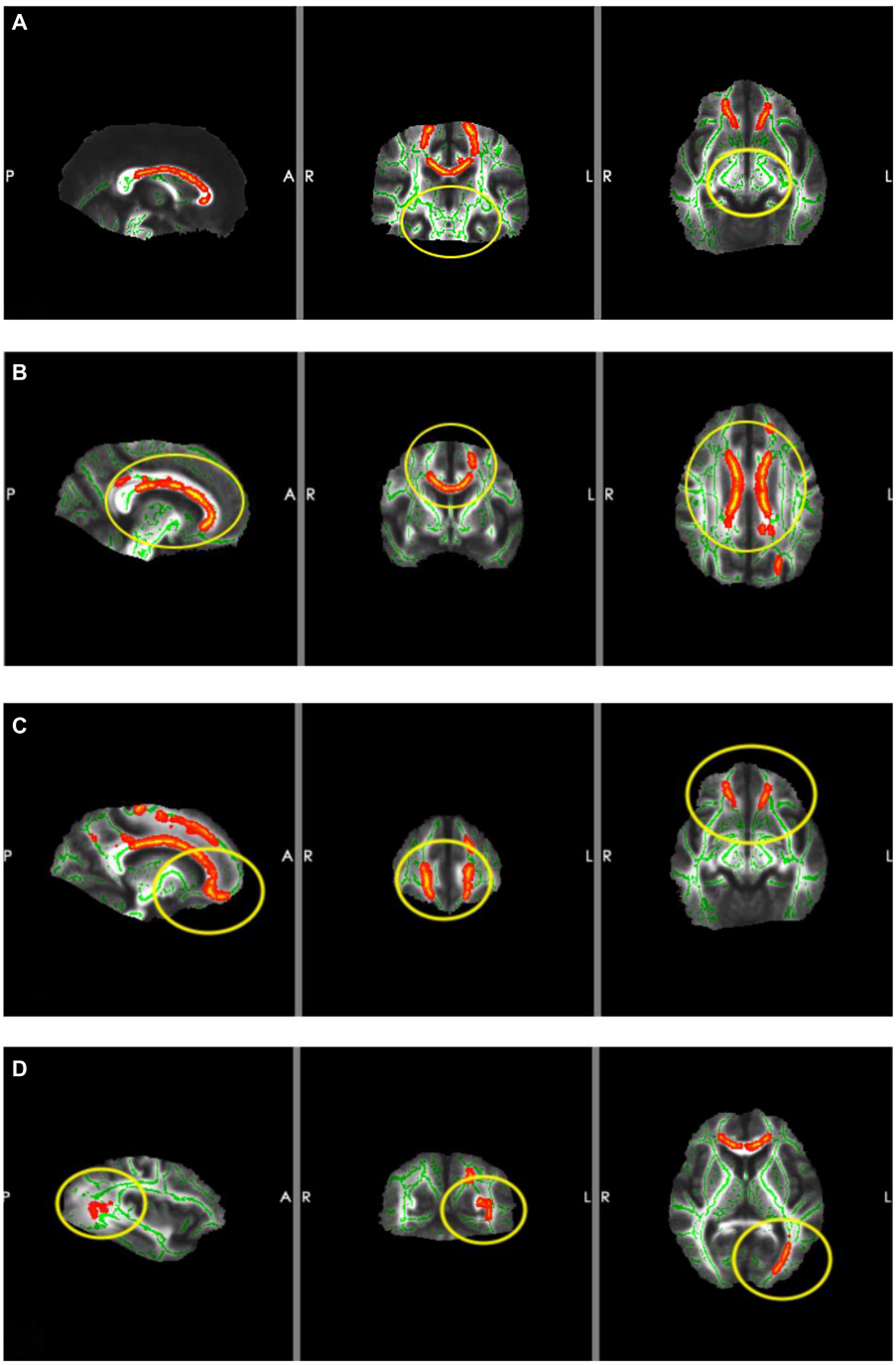

FIGURE 3 | Results of TBSS. The red areas are the areas of lower FA (active area) and the yellow circles are the ROIs. **(A)** ROI located around the hippocampus (there were no significant changes in FA). **(B)** ROI located around the corpus callosum (FA was lower in MCI patients). **(C)** ROI located around the orbitofrontal gyrus (FA was lower in MCI patients). **(D)** ROI located around the left inferior occipital gyrus (FA was lower in MCI patients).

DISCUSSION

In line with our *a priori* hypothesis, we found that the olfactory ability of MCI patients was impaired overall and was positively correlated with the MoCA score. Using receiver operating characteristic (ROC) analysis, we revealed that the olfactory test value had high specificity for predicting MCI. Impaired olfactory function was associated with lower general cognitive performance, which was associated with a higher prevalence of MCI. This result suggests that OI is an important marker of cerebral neuropathological changes (Devanand et al., 2015; Palta et al., 2018). Indeed, a meta-analysis reported that olfactory

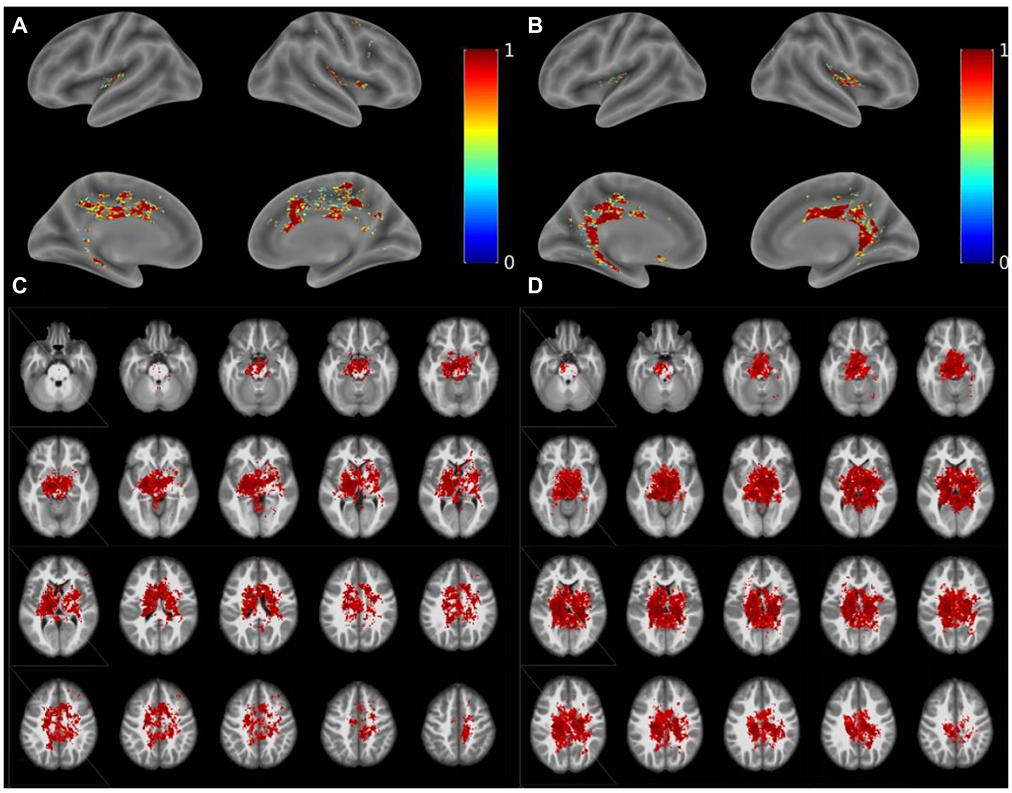

FIGURE 4 | Results of diffusion tractography. **(A,C)** Diffusion tractography results of the MCI group. **(B,D)** Diffusion tractography results of the NC group.

function is vulnerable to pathological changes in patients with AD and MCI and that olfactory function is impaired in patients with AD more profoundly than in those with MCI (Jung et al., 2019), which indicates that OI may also be a marker of MCI-to-AD transition risk (Wu et al., 2019).

It is well established that the orbitofrontal gyrus serves as the higher olfactory center. The corpus callosum, which serves as a communication channel between the bilateral cerebral hemispheres, connects the frontal lobes of the bilateral cerebral hemispheres. The frontal lobe is the higher brain area and is responsible for a variety of activities, which include smell and emotion. This explains why abnormalities in the structure of the corpus callosum cause damage to nerve pathways projecting to the frontal lobe, which result in changes in sense of smell and episodic memory. Therefore, structural abnormalities of the corpus callosum should also be regarded as a crucial factor that causes olfactory function impairment. Several studies have confirmed that early pathological changes in AD occur in the primary olfactory cortex (Conti et al., 2013; Roberts et al., 2016), which is consistent with our study. Our TBSS results showed that the areas of disruption in the MCI group were located primarily in the corpus callosum, orbitofrontal gyrus, and left occipital lobe. However, the area around the hippocampus was not significantly different between the groups; moreover, there were fewer fibrous connections between brain regions related to olfaction, memory, and cognition. These findings suggested that, in MCI patients, the microstructure of the orbitofrontal gyrus and corpus callosum was damaged, whereas changes in hippocampal microstructure were not significant. This indicated that white matter damage in regions underlying olfactory function was obvious in MCI patients, whereas white matter damage in areas involved in memory and cognition was not apparent. Taken together, these findings suggest that decline in olfactory function occurs earlier than does cognitive function impairment. The olfactory system was highly connected with entorhinal–hippocampal–cortical and amygdala–parasympathetic clusters, which is in line with previous literature (Ubeda-Bañon et al., 2020). Furthermore, results from a pilot study suggested that the reduction in the size of the hippocampus is associated with a loss of OI ability, rather than the loss of memory in relation to early AD (Kjelvik et al., 2014). However, another study reported that olfactory impairment was associated with white matter lesions that were independent of hippocampal atrophy (Heinrich et al., 2018). Our TBSS results of the MCI group indicated that there were no significant alterations in the area around the hippocampus, which is involved in cognitive and memory functions; thus, indicating that changes in hippocampal microstructure in MCI patients were not significant. This further confirms that impairment in olfactory function is superior to memory deficits for predicting cognitive decline.

As shown in a previous investigation, olfactory changes can appear earlier than typical dementia symptoms and inflict

A

Contrast Name	Region Label	Extent	t-value	MNI Coordinates x	y	z
Positive	Cerebelum_3_L	139986	1.000	-3	-40	-14
	Frontal_Mid_2_R	140	1.000	35	8	36
	Frontal_Mid_2_R	55	1.000	28	10	45
	Cerebelum_4_5_R	134	0.957	19	-38	-27
	Fusiform_R	51	0.957	29	-62	-5
	Lingual_R	43	0.957	12	-70	-3
	Lingual_R	20	0.957	23	-57	-3
	Olfactory_L	145	0.957	-2	25	-3
	Precuneus_R	23	0.957	10	-40	5
	Precuneus_L	67	0.957	1	-50	38
	Frontal_Sup_2_R	111	0.957	16	18	49
	Supp_Motor_Area_R	216	0.957	4	16	52
	Vermis_9	43	0.913	-1	-54	-30
	Fusiform_R	24	0.913	22	-32	-18
	Lingual_R	50	0.913	21	-71	-12
	Frontal_Mid_2_R	50	0.913	24	47	3
	Frontal_Inf_Tri_R	84	0.913	47	40	4
	Calcarine_R	46	0.913	29	-68	7
	Cingulate_Ant_R	56	0.913	14	41	19
	Frontal_Sup_Medial_R	25	0.913	4	54	20
	Frontal_Mid_2_R	39	0.913	42	46	22
	Frontal_Sup_Medial_R	61	0.913	7	60	29
	Frontal_Sup_2_R	27	0.913	24	35	30
	Frontal_Mid_2_R	213	0.913	34	38	33
	Frontal_Sup_2_R	28	0.913	17	42	33
	Frontal_Sup_2_R	20	0.913	24	31	38
(A)	Frontal_Sup_2_R	59	0.913	25	23	40

B

Contrast Name	Region Label	Extent	t-value	MNI Coordinates x	y	z
Positive	ParaHippocampal_L	179823	1.000	-18	-22	-18
	Temporal_Sup_R	63	1.000	48	-39	17
	Cerebelum_6_R	171	0.955	20	-69	-19
	Fusiform_R	21	0.955	28	-49	-15
	Fusiform_R	79	0.955	33	-57	-10
	Lingual_L	35	0.955	-19	-55	-7
	Lingual_L	21	0.955	-26	-69	-4
	Insula_R	26	0.955	38	13	2
	Temporal_Sup_R	29	0.955	44	-26	5
	Calcarine_R	22	0.955	7	-74	15
	Cingulate_Ant_L	59	0.955	-3	24	24
	Precuneus_R	28	0.955	12	-59	28
	Cuneus_R	31	0.955	20	-83	41
	Cingulate_Mid_R	75	0.955	17	-35	48
	Fusiform_L	73	0.909	-30	-72	-14
	Insula_L	21	0.909	-35	6	-6
	Precuneus_L	22	0.909	1	-66	28
	Occipital_Mid_R	24	0.909	32	-69	30
(B)	Precuneus_L	61	0.909	0	-70	33

FIGURE 5 | Statistic map of the fiber probability tracking. **(A)** Statistic map of the fiber probability tracking in the MCI group. Blue underline is on behalf of the areas which a large number of fibers mainly reached in the MCI group. Orange underline is on behalf of some areas which can be observed in the MCI group, but can't be observed in the NC group. **(B)** Statistic map of the fiber probability tracking in the NCI group. Red underline is on behalf of the areas which a large number of fibers mainly reached in the NC group.

greater cognitive impairment (Josefsson et al., 2017); however, the underlying mechanism and pathology remain unclear. Therefore, we speculate that olfaction impairment is a foremost outcome of the pathological changes in these areas, which suggests that changes in olfactory ability lead to pathological changes in these areas, which cause alterations in cognitive function. In addition,

TABLE 5 | Correlation between behavioral indicators and FA values of the ROIs.

	Orbitofrontal gyrus		Hippocampus		Inferior occipital gyrus		Parahippocampal gyrus	
	p	*r*	*p*	*r*	*p*	*r*	*p*	*r*
OI score	<0.001	0.5360	0.049	0.2920	0.001	0.4470	0.415	−0.123
MoCA score	0.050	0.2910	0.720	0.0540	0.101	0.2450	0.134	−0.273

our findings indicated that fibrous connections in several brain regions, such as the entorhinal cortex, were higher in patients with MCI, which is suggestive of a compensatory mechanism of the olfactory pathway. Thus, we speculate that olfactory training may be useful for improving cognition and may contribute to the prevention of various neurodegenerative diseases. In our traditional perception, the olfactory decline observed in aging may seem irreversible, but emerging evidence suggested that olfactory function may be trained, and olfactory training even has positive effects on cognitive function (Birte-Antina et al., 2018). Indeed, if olfactory training can lead to cognitive benefits, what are the mechanisms? One study found that olfactory training led to increased thickness not only in key olfactory structures but also in fronto-temporal areas outside of the olfactory cortex (Al Ain et al., 2019). A similar study showed that functional brain activity changes in a fronto-parietal network associated with higher cognitive abilities under odor identification training (Fournel et al., 2017). Above findings suggested that intensive olfactory training can improve olfactory function and that this improvement is associated with changes in the structure of olfactory processing areas of the brain. It indicated that olfactory training may give a positive future for improvement of cognition.

Based on the principle of TBSS (Smith et al., 2006), abnormal areas detected in TBSS analyses are those areas that have a significantly lower FA value, which indicates that nerve fibers in these areas have reduced integrity and a limited ability for water molecules to diffuse in the same direction. In our study, we found that the orbitofrontal gyrus had a significantly lower FA value in MCI patients compared with NCs, which also correlated with the olfactory score. However, our imaging findings revealed no correlation between the MoCA score and FA value. One study reported that the MoCA score positively correlated with the FA value of the corpus callosum (Mascalchi et al., 2019). We speculate that the reason for this discrepancy is the susceptibility of the experimental results to bias due to our small sample size.

Most previous studies of AD and MCI patients assessed whole-brain white matter, which included both superficial and deep white matter. Recently, one study evaluated only the superficial white matter and found that microstructural changes in superficial white matter are related to clinical symptoms of AD (Bigham et al., 2020). Therefore, we suggest that microstructural changes in the hippocampus may be detected by exploring the superficial white matter. However, further research investigating superficial white matter is needed to ascertain the precise mechanisms of OI dysfunction.

This study has several limitations. Firstly, we used a relatively small sample size, which may have prevented the detection of biological associations. Nevertheless, we were still able to reveal significant differences. Studying a larger group of patients will likely allow further details to be uncovered. Secondly, because the study used a cross-sectional design, we could not infer whether the changes were due to progression to AD. Thirdly, we used the MoCA to diagnose MCI, because there is currently no specific diagnostic tool based on pathological or molecular imaging assessments. However, the MoCA is only to be a screening tool, it is inaccurate especially in cases who refuse to answer survey questions of the MoCA. Hence, in this community cohort, the predictive accuracy of the MoCA for cognitive decline was moderate, which suggested that the MoCA may need to be combined with other measures to improve predictive power.

Studies on MCI are still limited for preventing progression to dementia. The most valuable finding of our study is that the decline in olfactory function may occur earlier than impairment of cognitive function, which suggests that OI is a significant and useful indicator of neuropathological changes and an effective marker for the development of cognitive decline and dementia.

CONCLUSION

In summary, the impairment of olfactory function was superior to memory deficits for predicting cognitive decline in cognitively intact participants. We revealed that olfactory function tests are a useful screening tool for cognitive decline in older adults. Moreover, this tool can be used to screen for cognitive decline before the onset of other clinical symptoms of dementia, which will help to reduce delayed and underdiagnoses of MCI and dementia. Taken together, more attention should be given to those with olfactory disorders, because of the associated higher risk of cognitive decline.

PERMISSION TO REUSE AND COPYRIGHT

DATA AVAILABILITY STATEMENT

The original contributions presented in the study are included in the article/supplementary material, further inquiries can be directed to the corresponding author/s.

ETHICS STATEMENT

The studies involving human participants were reviewed and approved by the Ethics Review Committee of Shanghai East Hospital. The patients/participants provided their written informed consent to participate in this study. Written informed consent was obtained from the individual(s) for the publication of any potentially identifiable images or data included in this article.

AUTHOR CONTRIBUTIONS

YS, BJ, HQ, SH, and YZ helped to collect the behavioral and imaging data. YS wrote the first draft of the manuscript. ZW and BJ helped in MRI data analysis. YZ, QX and GL supervised the initial drafting, and critically revised the manuscript. QX analyzed the article and critically revised the manuscript. All authors read and approved the final manuscript and contributed to the article conception.

FUNDING

This project was supported by the National Natural Science Foundation of China (Grant No. 81301200), and the Science and Technology Commission of Shanghai Municipality (Grant Nos. 19411951400 and 20Y11911700).

ACKNOWLEDGMENTS

We thank all the participants for their cooperation during this study.

REFERENCES

Al Ain, S., Poupon, D., Hetu, S., Mercier, N., Steffener, J., and Frasnelli, J. (2019). Smell training improves olfactory function and alters brain structure. *Neuroimage* 189, 45–54. doi: 10.1016/j.neuroimage.2019.01.008

Albert, M. S., DeKosky, S. T., Dickson, D., Dubois, B., Feldman, H. H., Fox, N. C., et al. (2011). The diagnosis of mild cognitive impairment due to Alzheimer's disease: recommendations from the National Institute on Aging-Alzheimer's Association workgroups on diagnostic guidelines for Alzheimer's disease. *Alzheimers Dement.* 7, 270–279. doi: 10.1016/j.jalz.2011.03.008

Ashwin, C., Chapman, E., Howells, J., Rhydderch, D., Walker, I., and Baron-Cohen, S. (2014). Enhanced olfactory sensitivity in autism spectrum conditions. *Mol. Autism* 5:53. doi: 10.1186/2040-2392-5-53

Bigham, B., Zamanpour, S. A., Zemorshidi, F., Boroumand, F., and Zare, H. (2020). Alzheimer's disease neuroimaging initiative. Identification of superficial white matter abnormalities in Alzheimer's disease and mild cognitive impairment using diffusion tensor imaging. *J. Alzheimers Dis. Rep.* 4, 49–59. doi: 10.3233/ADR-190149

Birte-Antina, W., Ilona, C., Antje, H., and Thomas, H. (2018). Olfactory training with older people. *Int. J. Geriatr. Psychiatry* 33, 212–220. doi: 10.1002/gps.4725

Conti, M. Z., Vicini-Chilovi, B., Riva, M., Zanetti, M., Liberini, P., Padovani, A., et al. (2013). Odor identification deficit predicts clinical conversion from mild cognitive impairment to dementia due to Alzheimer's disease. *Arch. Clin. Neuropsychol.* 28, 391–399. doi: 10.1093/arclin/act032

Davidson, T. M., Freed, C., Healy, M. P., and Murphy, C. (1998). Rapid clinical evaluation of anosmia in children: the alcohol sniff test. *Ann. N. Y. Acad. Sci.* 855, 787–792. doi: 10.1111/j.1749-6632.1998.tb10659.x

Demir, S., Sizer, B., Gul, A., and Topcu, I. (2021). Culturally modified olfactory test adapted to East-Turkey: a comparison with Sniffin' Sticks. *Int. J. Clin. Pract.* 75:e14458. doi: 10.1111/ijcp.14458

Devanand, D. P. (2016). Olfactory identification deficits, cognitive decline, and dementia in older adults. *Am. J. Geriatr. Psychiatry* 24, 1151–1157. doi: 10.1016/j.jagp.2016.08.010

Devanand, D. P., Lee, S., Manly, J., Andrews, H., Schupf, N., Doty, R. L., et al. (2015). Olfactory deficits predict cognitive decline and Alzheimer dementia in an urban community. *Neurology* 84, 182–189. doi: 10.1212/WNL.0000000000001132

Fournel, A., Sezille, C., Licon, C. C., Sinding, C., Gerber, J., Ferdenzi, C., et al. (2017). Learning to name smells increases activity in heteromodal semantic areas. *Hum. Brain Mapp.* 38, 5958–5969. doi: 10.1002/hbm.23801

Georgiopoulos, C., Warntjes, M., Dizdar, N., Zachrisson, H., Engström, M., Haller, S., et al. (2017). Olfactory impairment in Parkinson's disease studied with diffusion tensor and magnetization transfer imaging. *J. Parkinsons Dis.* 7, 301–311. doi: 10.3233/JPD-161060

Heinrich, J., Vidal, J. S., Simon, A., Rigaud, A. S., Hanon, O., Epelbaum, J., et al. (2018). Relationships between lower olfaction and brain white matter lesions in elderly subjects with mild cognitive impairment. *J. Alzheimers Dis.* 61, 1133–1141. doi: 10.3233/JAD-170378

Josefsson, M., Larsson, M., Nordin, S., Adolfsson, R., and Olofsson, J. (2017). APOE-ε4 effects on longitudinal decline in olfactory and non-olfactory cognitive abilities in middle-aged and old adults. *Sci. Rep.* 7:1286. doi: 10.1038/s41598-017-01508-7

Jung, H. J., Shin, I. S., and Lee, J. E. (2019). Olfactory function in mild cognitive impairment and Alzheimer's disease: a meta-analysis. *Laryngoscope* 129, 362–369. doi: 10.1002/lary.27399

Kim, S. M., Kim, H. R., Min, H. J., Kim, K. S., Ga, H., Lee, S. H., et al. (2020). Impaired odor identification of culturally familiar odorants associated with dementia in South Korean older adults. *Int. J. Environ. Res. Public Health* 17:8441. doi: 10.3390/ijerph17228441

Kim, S. M., Kim, H. R., Min, H. J., Kim, K. S., Jin, J. C., and Han, D. H. (2021). A novel olfactory threshold test for screening cognitive decline among elderly people. *PLoS One* 16:e0254357. doi: 10.1371/journal.pone.0254357

Kjelvik, G., Evensmoen, H. R., Hummel, T., Engedal, K., Selbæk, G., Saltvedt, I., et al. (2020). The human brain representation of odor identification in amnestic mild cognitive impairment and Alzheimer's dementia of mild degree. *Front. Neurol.* 11:607566. doi: 10.3389/fneur.2020.607566

Kjelvik, G., Saltvedt, I., White, L. R., Stenumgård, P., Sletvold, O., Engedal, K., et al. (2014). The brain structural and cognitive basis of odor identification deficits in mild cognitive impairment and Alzheimer's disease. *BMC Neurol.* 14:168. doi: 10.1186/s12883-014-0168-1

Knight, M. J., Wearn, A., Coulthard, E., and Kauppinen, R. A. (2019). T2 relaxometry and diffusion tensor indices of the hippocampus and entorhinal cortex improve sensitivity and specificity of MRI to detect amnestic mild cognitive impairment and Alzheimer's disease dementia. *J. Magn. Reson. Imaging* 49, 445–455. doi: 10.1002/jmri.26195

Lane, C. A., Hardy, J., and Schott, J. M. (2018). Alzheimer's disease. *Eur. J. Neurol.* 25, 59–70. doi: 10.1111/ene.13439

Li, Q., Wang, J., Liu, J., Wang, Y., and Li, K. (2021). Magnetic resonance imaging measurement of entorhinal cortex in the diagnosis and differential diagnosis of mild cognitive impairment and Alzheimer's disease. *Brain Sci.* 11:1129. doi: 10.3390/brainsci11091129

Lu, J., Li, D., Li, F., Zhou, A., Wang, F., Zuo, X., et al. (2011). Montreal cognitive assessment in detecting cognitive impairment in chinese elderly individuals: a population-based study. *J. Geriatr. Psychiatry Neurol.* 24, 184–190. doi: 10.1177/0891988711422528

Marin, C., Vilas, D., Langdon, C., Alobid, I., López-Chacón, M., Haehner, A., et al. (2018). Olfactory dysfunction in neurodegenerative diseases. *Curr. Allergy Asthma Rep.* 18:42. doi: 10.1007/s11882-018-0796-4

Mascalchi, M., Salvadori, E., Toschi, N., Giannelli, M., Orsolini, S., Ciulli, S., et al. (2019). DTI-derived indexes of brain WM correlate with cognitive performance in vascular MCI and small-vessel disease. A TBSS study. *Brain Imaging Behav.* 13, 594–602. doi: 10.1007/s11682-018-9873-5

Palta, P., Chen, H., Deal, J. A., Sharrett, A. R., Gross, A., Knopman, D., et al. (2018). Olfactory function and neurocognitive outcomes in old age: the atherosclerosis risk in communities neurocognitive study. *Alzheimers Dement.* 14, 1015–1021. doi: 10.1016/j.jalz.2018.02.019

Roberts, R. O., Christianson, T. J., Kremers, W. K., Mielke, M. M., Machulda, M. M., Vassilaki, M., et al. (2016). Association between olfactory dysfunction and amnestic mild cognitive impairment and Alzheimer disease dementia. *JAMA Neurol.* 73, 93–101. doi: 10.1001/jamaneurol.2015.2952

Shu, H., Gu, L., Yang, P., Lucas, M. V., Gao, L., Zhang, H., et al. (2021). Disturbed temporal dynamics of episodic retrieval activity with preserved spatial activity pattern in amnestic mild cognitive impairment: a simultaneous EEG-fMRI study. *Neuroimage Clin.* 30:102572. doi: 10.1016/j.nicl.2021.102572

Smith, S. M., Jenkinson, M., Johansen-Berg, H., Rueckert, D., Nichols, T. E., Mackay, C. E., et al. (2006). Tract-based spatial statistics: voxelwise analysis of multi-subject diffusion data. *Neuroimage* 31, 1487–1505. doi: 10.1016/j.neuroimage.2006.02.024

Tae, W. S., Ham, B. J., Pyun, S. B., Kang, S. H., and Kim, B. J. (2018). Current clinical applications of diffusion-tensor imaging in neurological disorders. *J. Clin. Neurol.* 14, 129–140. doi: 10.3988/jcn.2018.14.2.129

Ubeda-Bañon, I., Saiz-Sanchez, D., Flores-Cuadrado, A., Rioja-Corroto, E., Gonzalez-Rodriguez, M., Villar-Conde, S., et al. (2020). The human olfactory system in two proteinopathies: Alzheimer's and Parkinson's diseases. *Transl. Neurodegener.* 9:22. doi: 10.1186/s40035-020-00200-7

Woodward, M. R., Dwyer, M. G., Bergsland, N., Hagemeier, J., Zivadinov, R., Benedict, R. H., et al. (2017). Olfactory identification deficit predicts white matter tract impairment in Alzheimer's disease. *Psychiatry Res. Neuroimaging* 266, 90–95. doi: 10.1016/j.pscychresns.2017.06.004

Wu, X., Geng, Z., Zhou, S., Bai, T., Wei, L., and Ji, G. (2019). Brain structural correlates of odor identification in mild cognitive impairment and Alzheimer's disease revealed by magnetic resonance imaging and a chinese olfactory identification test. *Front. Neurosci.* 13:842. doi: 10.3389/fnins.2019.00842

Yoo, H. S., Jeon, S., Chung, S. J., Yun, M., Lee, P. H., Sohn, Y. H., et al. (2018). Olfactory dysfunction in Alzheimer's disease- and lewy body-related cognitive impairment. *Alzheimers Dement.* 14, 1243–1252. doi: 10.1016/j.jalz.2018.05.010

Zhao, F., Wang, X., Zariwala, H. A., Uslaner, J. M., Houghton, A. K., Evelhoch, J. L., et al. (2016). FMRI study of olfaction in the olfactory bulb and high olfactory structures of rats: insight into their roles in habituation. *Neuroimage* 127, 445–455. doi: 10.1016/j.neuroimage.2015.10.080

Conflict of Interest: The authors declare that the research was conducted in the absence of any commercial or financial relationships that could be construed as a potential conflict of interest.

Publisher's Note: All claims expressed in this article are solely those of the authors and do not necessarily represent those of their affiliated organizations, or those of the publisher, the editors and the reviewers. Any product that may be evaluated in this article, or claim that may be made by its manufacturer, is not guaranteed or endorsed by the publisher.

frontiers in Aging Neuroscience

ORIGINAL RESEARCH
published: 30 November 2021
doi: 10.3389/fnagi.2021.757808

Evolution of Brain Morphology in Spontaneously Hypertensive and Wistar-Kyoto Rats From Early Adulthood to Aging: A Longitudinal Magnetic Resonance Imaging Study

*Yingying Yang[1,2], Quan Zhang[3], Jialiang Ren[4], Qingfeng Zhu[5], Lixin Wang[5], Yongzhi Zhang[1] and Zuojun Geng[5]**

[1] Graduate School, Hebei Medical University, Shijiazhuang, China, [2] Department of Imaging, The First Hospital of Qinhuangdao, Qinhuangdao, China, [3] Tianjin Key Laboratory of Functional Imaging, Department of Radiology, Tianjin Medical University General Hospital, Tianjin, China, [4] GE Healthcare China, Beijing, China, [5] Department of Medical Imaging, The Second Hospital of Hebei Medical University, Shijiazhuang, China

The influence of hypertension and aging alone on brain structure has been described extensively. Our understanding of the interaction of hypertension with aging to brain morphology is still limited. We aimed to detect the synergistic effects of hypertension and aging on brain morphology and to describe the evolution patterns of cerebral atrophy from spatial and temporal perspectives. In 8 spontaneously hypertensive rats (SHRs) and 5 Wistar-Kyoto rats, high-resolution magnetic resonance imaging scans were longitudinally acquired at 10, 24, 52, and 80 weeks. We analyzed the tissue volumes of gray matter, white matter, cerebral spinal fluid, and total intracranial volume (TIV), and then evaluated gray matter volume in detail using voxel-based morphometry (VBM) and region of interest-based methods. There were interactive effects on hypertension and aging in tissue volumes of gray matter, white matter, and TIV, of which gray matter atrophy was most pronounced, especially in elderly SHRs. We identified the vulnerable gray matter volume with combined effects of hypertension and aging in the septal region, bilateral caudate putamen, hippocampus, primary somatosensory cortex, cerebellum, periaqueductal gray, right accumbens nucleus, and thalamus. We automatically extracted the septal region, anterior cingulate cortex, primary somatosensory cortex, caudate putamen, hippocampus, and accumbens nucleus and revealed an inverted-U trajectory of volume change in SHRs, with volume increase at the early phase and decline at the late phase. Hypertension interacts with aging to affect brain volume changes such as severe atrophy in elderly SHRs.

Keywords: hypertension, aging, magnetic resonance imaging, voxel-based morphometry, brain atrophy, spontaneously hypertensive rat

OPEN ACCESS

Edited by:
Binbin Nie, Institute of High Energy Physics, Chinese Academy of Sciences (CAS), China

Reviewed by:
Weilin Liu, Fujian University of Traditional Chinese Medicine, China
Shengxiang Liang, Fujian University of Traditional Chinese Medicine, China

****Correspondence:***
Zuojun Geng
1980756261@qq.com

Received: *12 August 2021*
Accepted: *08 November 2021*
Published: *30 November 2021*

Citation:
Yang Y, Zhang Q, Ren J, Zhu Q, Wang L, Zhang Y and Geng Z (2021) Evolution of Brain Morphology in Spontaneously Hypertensive and Wistar-Kyoto Rats From Early Adulthood to Aging: A Longitudinal Magnetic Resonance Imaging Study. Front. Aging Neurosci. 13:757808. doi: 10.3389/fnagi.2021.757808

HIGHLIGHTS

- Hypertension and aging have interactive effects on brain morphology.
- Longitudinal changes in gray matter volume are not uniform across space and time.
- Spontaneously hypertensive rats show an inverted-U trajectory of gray matter volume.
- MRI is a powerful tool for analyzing the dynamic evolution of whole brain morphology.

INTRODUCTION

Hypertension was defined as 130 mmHg systolic or 80 mmHg diastolic blood pressure or greater according to the 2017 set of hypertension guidelines released by the American College of Cardiology and American Heart Association (Whelton et al., 2018). As the risk of hypertension increases with advancing age, its prevalence will increase dramatically with global aging. Additionally, an increasing number of younger individuals suffer from hypertension due to unhealthy lifestyles (Erdos et al., 2011; Mills et al., 2020). It has been well established that hypertension is an important risk factor for neuropathology. Multiple studies have demonstrated changes in cerebral functional integrity in hypertensive populations (Naumczyk et al., 2017; Feng et al., 2020), and brain structural deformities have also been observed, including hippocampal volume reductions and cortical atrophy (Korf et al., 2004; Gianaros et al., 2006). It is worth noting that brain atrophy also occurs in normal elderly individuals (Raz et al., 2005). However, the combined influence of hypertension and aging on brain morphology is not entirely clear. Previous clinical studies have shown that temporal and occipital regions appear most vulnerable due to the interactive effects of hypertension and age (Strassburger et al., 1997). Moreover, hypertension and aging may have strong interrelationship effects on brain damage, which is associated with cognitive decline (Kern et al., 2017).

It is difficult to investigate brain abnormalities in hypertensive populations while avoiding interferences from various environmental risk factors or treatment interventions. Furthermore, such clinical studies are typically cross-sectional, and only a few have attempted to longitudinally evaluate brain changes over a short age span (Gilsanz et al., 2017). Animal models provide convenience for exploring the impacts of hypertension on brain aging over the lifespan. Spontaneously hypertensive rats (SHRs), introduced by Okamoto and Aoki (1963), are the most extensively used animal model for essential hypertension. SHRs are normotensive at birth and progressively develop hypertension without any intervention. SHRs are commonly used to evaluate hypertensive brain damage and potential treatments (Chan et al., 2018; Shi et al., 2020). Postmortem histology analysis has revealed enlarged cerebral ventricles and reduced regional brain volumes in adult SHRs. Animal magnetic resonance imaging (MRI) is not only a powerful tool for whole-brain investigation but also a useful addition for noninvasively describing brain dynamic evolution. Brain atrophy is already present in SHRs at 7–9 weeks (Koundal et al., 2019). Although some aspects of cerebral damage in SHRs have been investigated, these results can differ since they are affected by aging (Li et al., 2016). Animal model experiments have shown that hypertension and aging induce an increase in ischemic susceptibility in aged SHRs (Lee et al., 2011). Research on cerebral blood volume with the combined effects of hypertension and aging suggests that a decrease in cerebral blood volume correlates with age but not hypertension, whereas a reduction in vasodilatory capacity is due to hypertension in SHRs based on near-infrared spectroscopy findings (Shaul et al., 2014). All these studies have added to our understanding about SHR brain aging; however, we could not accurately answer where and how hypertension exacerbates the brain morphological changes that accompany aging. Whether hypertension and aging affect only certain sensitive brain regions or a broader area remains unclear. SHR brain morphological trajectories with aging have never been depicted, and could present the evolution of brain atrophy as either on-going and progressive or relatively static. Hence, it is urgently needed to longitudinally characterize the spatial and temporal brain structural changes with brain aging in SHRs.

In the current study, we aimed to longitudinally assess brain morphology in SHRs and Wistar-Kyoto (WKY) rats from early adulthood to aging using *in vivo* MRI and to describe the evolution patterns of cerebral atrophy from spatial and temporal perspectives. We plan to delineate the combined effects of chronic hypertension on brain volume in the context of aging. We hypothesize that the combined effects of hypertension and aging would exacerbate cerebral atrophy. Cerebral morphological alterations are age dependent, and obvious brain atrophy may occur in aged SHRs. We intend to assess overall tissue volume changes in gray matter (GM), white matter (WM), and cerebral spinal fluid (CSF), and then evaluate regional GM morphological abnormalities in detail using voxel-based morphometry (VBM) and region of interest (ROI)-based methods. Quantitative analysis of brain volume alterations in SHRs over the life span will be necessary to understand the cumulative effects of hypertension on brain aging. These MRI markers of longitudinal changes in brain structure provide more comprehensive information about the evolution underlying the pathogenesis of chronic hypertension with brain aging.

MATERIALS AND METHODS

Experimental Animals

Thirteen male SHRs and 10 WKY rats aged 8 weeks were purchased from Beijing Vital River Laboratory Animal Technology Company Limited. Five died in each of the two groups by the age of 80 weeks throughout their natural life cycle, so a total of 8 SHRs and 5 WKY rats were studied. All rats housed in an air-conditioned room (constant temperature 22–24°C, relative humidity 50–60%), at a light/dark cycle of 12 h. They were maintained on a standard pellet diet and tap water *ad libitum*. At the age of 20 weeks, blood pressure was measured by non-invasive blood pressure system. Body weight was recorded every week from 8 to 80 weeks. This study was approved by the Experimental Animal Ethics Committee of Hebei Medical University.

Magnetic Resonance Imaging Scanning Protocol

MRI experiments were performed on two identical 7.0 T Bruker scanners (Pharma Scan 70/16 US) at the different sites. All rats were scanned 4 times repeatedly: at 10, 24, and 52 weeks at one place and subsequently 80 weeks at the other. Rats were initially anesthetized with 3% isoflurane in an induction chamber and then administered an intramuscular injection of 0.015 mg/kg dexmedetomidine into the back of the right thigh. Rats were placed in a prone position with a mixture of pure

oxygen and isoflurane during MRI acquisition. The isoflurane level was adjusted between 0.5 and 1.2% to maintain breathing rate at 50–60 breath/min during scanning. A noninvasive pulse oximeter was attached to the left hind paw to ensure that oxygen saturation was above 96% during scanning. Body temperature was maintained at 37°C using a water circulation heating system. Whole brain T2-weighted MRI was acquired in coronal plane using a rapid acquisition with relaxation enhancement (RARE) sequence. Scan parameters: TR = 10,700 ms, effective TE = 36 ms, RARE factor = 8, FOV = 35 × 35 mm^2, matrix size = 256 × 256, special resolution = 0.137 × 0.137 mm^2, slice number = 90, slice thickness = 0.3 mm, number of averages = 4, and scan time = 22 min 50 s.

Data Processing

We performed MRI data processing using the SPM12 toolbox in MATLAB (2013b). A whole brain population-specific template set for SHRs created by our team was used for image registration. First, all the T2-weighted images were multiplied by a factor of 10 to approximate the size of a human brain, which enabled the usage of data processing algorithms developed for humans. Second, these resized images were reoriented manually according to the template space. Third, the images were normalized and segmented based on our customized template set using the unified segmentation approach. In detail, the voxel values of the tissue maps were modulated by the Jacobian determinants of nonlinear components to account for the expansion or contraction in brain regions. Finally, the modulated GM volume images were smoothed by a 4 mm full width at half maximum Gaussian kernel for VBM. Individual GM, WM, and CSF volumes were calculated by multiplying total voxel numbers by mean volume values from modulated volume images. The total intracranial volume (TIV) was defined as the sum volume of GM, WM, and CSF. We also calculated the volume index of GM/TIV, WM/TIV, and CSF/TIV by dividing brain tissue volume by TIV in each rat. We automatically extracted certain ROIs from the modulation GM volume maps according to our template set, including the septal region, anterior cingulate cortex, primary somatosensory cortex, caudate putamen, hippocampus, and accumbens nucleus. The volume of each ROI was computed by multiplying the mean volume by the number of total voxels.

Statistical Analysis

A flexible factorial design was performed within SPM12 for VBM analysis. We excluded voxels in which the volume value was below 0.2 in the smoothed GM volume images to ensure sufficient test effects. Voxel-level familywise error (FWE, $P < 0.05$) corrected for multiple comparisons with a minimal cluster size of 200 voxels was performed. Then, the mean value of each cluster was extracted to explore the *post hoc* analysis between groups at each time point using a *t*-test.

ROI-based volume changes over age between groups were evaluated with repeated-measures analysis of variance using SPSS (version 22.0), with group being the between-subject factor and age being the within-subject factor. Significant differences were examined using two sample *t*-tests on the volume at each time point to determine differences between groups and using paired *t*-tests in each group to determine the trend of volume changing with age. We correlated the TIV with the body weight in SHRs and WKY rats using Pearson's correlative analysis. The threshold of statistical significance was $P < 0.05$.

RESULTS

Brain Tissue Volume

Figure 1 shows the brain volume and volume index changes in SHRs and WKY rats aged 10, 24, 52, and 80 weeks. There were interactions of group and age in the tissue volume of GM, WM, and TIV, and these tissue volumes were smaller in the SHRs than in WKY rats. Overall, the GM, WM, and TIV volumes exhibited continuous increases from 10 to 52 weeks but declined at different rates from 52 to 80 weeks in both groups. Compared with other tissues, GM volume demonstrated a steeper decline, especially in elderly SHRs. The temporal trajectories of the volume index showed that GM/TIV continuously declined and WM/TIV gradually increased in both groups. In addition, neither the CSF volume nor the CSF/TIV volume index differed between the two groups. Body weight was higher in the SHRs than in the WKY rats at 52 weeks old, while no difference was found at the other 3 time points. We observed a positive correlation between TIV and body weight in both groups: the correlation coefficients were 0.896 and 0.839 in SHRs and WKY rats, respectively. **Table 1** shows the absolute volumes of GM, WM, CSF, and TIV in SHRs and WKY rats at 10, 24, 52, and 80 weeks old.

Voxel-Based Gray Matter Volume

The significant voxels were superimposed on the T2-weighted MRI template (FWE, $P < 0.05$; cluster extent > 200 voxels), which presented 13 clusters with interactions of group and age on the volume changes in SHRs and WKY rats (**Figure 2**). All these brain regions are summarized in **Table 2**. We performed a *post hoc* test by extracting the mean volume values from each cluster. Temporal trajectories of volume changes show obvious heterogeneity, differing across regions (**Figure 3**). In addition, elderly SHRs exhibit severe GM atrophy.

Region of Interest-Based Gray Matter Volume

We calculated the volume of the septal region, anterior cingulate cortex, primary somatosensory cortex, caudate putamen, hippocampus, and accumbens nucleus. There was no bilateral difference in caudate putamen volume in the two groups at all-time points, so the caudate putamen volume was represented as the average of both sides. The volume of other regions significantly differs between hemispheres at certain time points, so we analyzed the other regions on both sides. **Table 3** presents regional GM volume in SHRs and WKY rats at different ages. Except for the hippocampus, the volume of other selected ROIs has interactions of group and age. **Figure 4** demonstrates the GM volume longitudinal changes in both groups at 4 time points. Temporal trajectories of GM volume changes show obvious

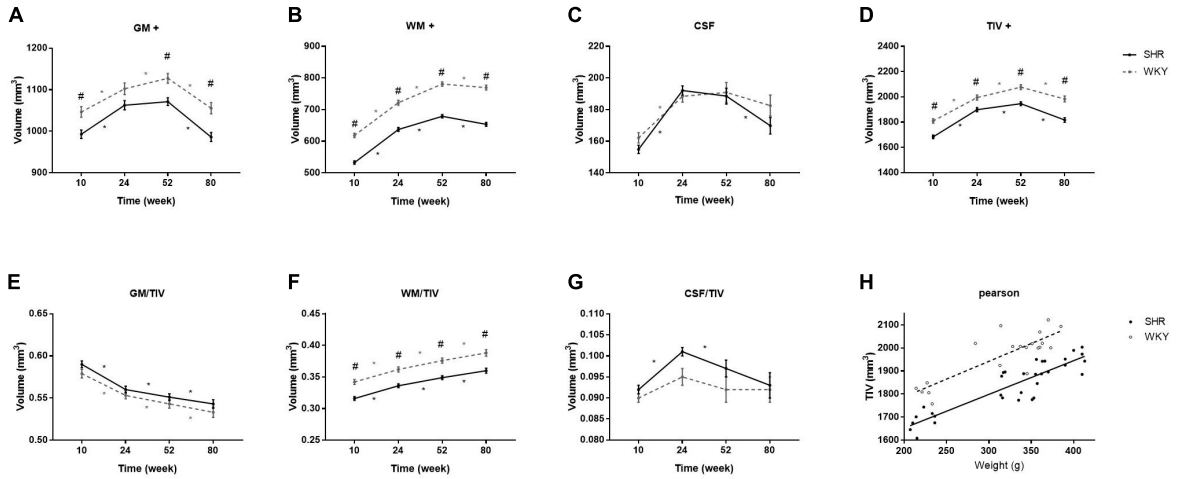

FIGURE 1 | Comparisons of brain volume **(A–D)** and volume index **(E–G)** changes in SHRs and WKY rats at 10, 24, 52, and 80 weeks old. + indicates significant interactions of group and age. # Indicates a significant volume difference between SHRs and age-matched WKY rats, and * indicates a significant trend determined by paired *t*-tests in each group. Positive correlation between TIV and body weight in both groups **(H)**.

TABLE 1 | Brain volume of the gray matter (GM), white matter (WM), cerebrospinal fluid (CSF), and total intracranial volume (TIV) in spontaneously hypertensive rats (SHRs) and Wistar-Kyoto (WKY) rats at 10, 24, 52, and 80 weeks old.

Tissue	Group	10 weeks	24 weeks	52 weeks	80 weeks
GM (mm^3)	SHR	993.0 ± 10.2	1062.9 ± 11.0	1071.4 ± 9.3	986.2 ± 10.9
	WKY	1046.6 ± 12.8	1102.4 ± 13.9	1127.7 ± 11.7	1055.7 ± 13.7
WM (mm^3)	SHR	532.6 ± 5.4	637.4 ± 6.2	679.0 ± 5.6	653.4 ± 6.1
	WKY	618.4 ± 6.8	721.7 ± 7.8	780.8 ± 7.1	769.6 ± 7.7
CSF (mm^3)	SHR	154.9 ± 2.6	192.1 ± 2.9	188.5 ± 5.0	169.8 ± 5.2
	WKY	162.2 ± 3.3	188.4 ± 3.7	190.9 ± 6.3	182.6 ± 6.6
TIV (mm^3)	SHR	1683.5 ± 13.9	1899.0 ± 15.9	1946.1 ± 15.4	1817.1 ± 18.3
	WKY	1809.4 ± 17.6	1994.5 ± 20.1	2077.0 ± 19.5	1983.3 ± 23.1

heterogeneity between the two groups. The trajectories of the volume changing with age show an inverted-U shape in SHRs, increasing at the early phase and declining at the late phase. Furthermore, unbalanced regional volume atrophy was more pronounced in the SHRs. The rate of GM atrophy was fastest in the right primary somatosensory cortex barrel field in elderly SHRs.

DISCUSSION

To the best of our knowledge, this is the first longitudinal study combining hypertension with aging to detect the evolution of brain morphology in rats. Using high-resolution structural MRI, our study demonstrates a spatial and temporal pattern of brain volume alterations in SHRs and WKY rats from early adulthood to aging. The major strength of the current study lies in the longitudinal evaluation of the long-term changes in brain morphology. Our study produced two main findings. First, there are interactive effects of hypertension and aging on brain morphology: chronic hypertension makes cerebral atrophy more evident. Second, longitudinal changes in GM volume are not uniform, with different shrinkage magnitudes occurring across space and time.

Brain Tissue Volume

The association of brain shrinkage with the interactions of hypertension and aging suggests that the effects of hypertension are not only cumulative but also progressive. In other words, the negative effects of chronic hypertension on cerebral atrophy become more evident with aging. Changes in brain tissue volume are not uniform. The volumes of GM, WM, and TIV were smaller in SHRs than in WKY rats. SHRs and WKY rats expressed similar brain tissue atrophy patterns but to different degrees. From 24 to 52 weeks, the GM volume in SHRs was relatively stable, while the GM volume in WKY rats continued to increase. Histopathological studies have previously reported GM volume loss in SHRs. It should be noted that *ex vivo* studies with brain fixation, extraction, and dehydration may result in ventricle collapse and anatomical shrinkage. An *in vivo* MRI study found that GM volume had no interaction effects between hypertension and aging in SHRs (Koundal et al., 2019). This controversy may be related to the age of the rats. Our study included elderly rats with chronic hypertension, while theirs was only based on early

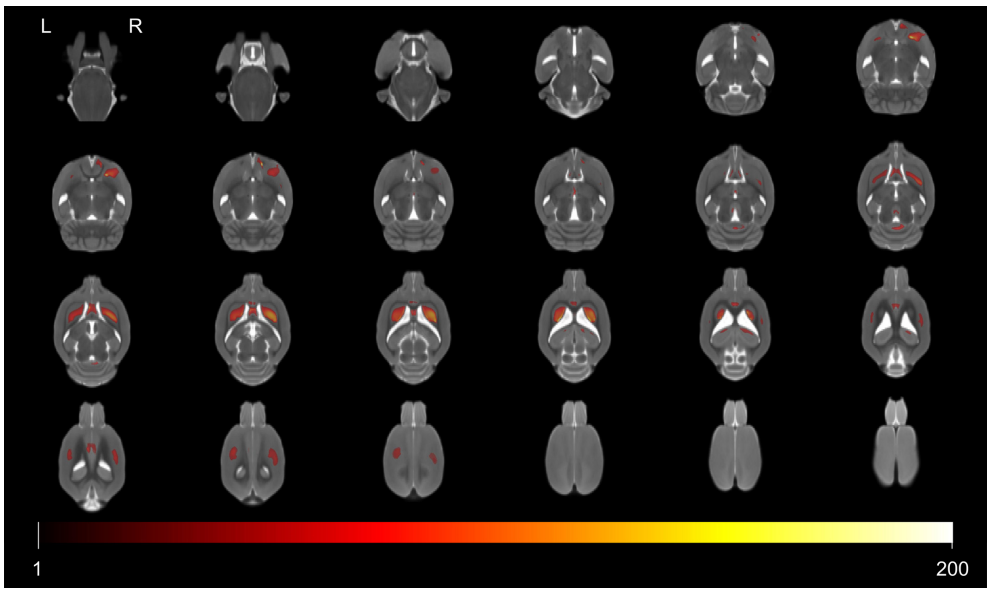

FIGURE 2 | Colored voxels superimposed on the T2-weighted MRI template represent clusters with the interactions of group and age on gray matter volume (FWE, *P*-value < 0.05; threshold of 200 voxels). All 13 clusters included the septal region, bilateral caudate putamen, hippocampus, primary somatosensory cortex, cerebellum, periaqueductal gray, right accumbens nucleus, and thalamus. Note that L and R represent the left and right sides of the brain, respectively.

hypertensive rats. A clinical study revealed that cerebral perfusion increased with increasing blood pressure at low baseline but decreased at high baseline (Glodzik et al., 2019). Accordingly, we speculate that GM loss may be related to brain hypoperfusion caused by chronic hypertension.

We found that the volume index of GM/TIV gradually decreased, whereas the WM/TIV increased from 10 to 80 weeks in both groups. One preclinical study on hypertension and white matter disruption in inducible hypertensive rats reported that hypertension fails to disrupt white matter integrity in young or aged rats, which is consistent with our findings (Holland et al., 2015). Regional brain changes in aging adults with hypertension have confirmed white matter injury (Sabisz et al., 2019). We hypothesized that the opposite conclusion might be due to the lower proportion of white matter in rats. It is worth noting that the CSF volume shows nonsynchronous changes at the late phase, when it is reduced in SHRs and stable in WKY rats. These results do not seem to support the speculation that cerebral atrophy is compensated by an enlargement of the ventricles. Previous work confirmed that the CSF production rate and intracranial pressure are normal in SHRs. Perhaps we can explain the ventricle enlargement from the blood brain barrier permeability perspective. One study reported no evidence for blood brain barrier leakage in SHRs (Naessens et al., 2018); however, the opposing view was reported in aged SHRs (Wang et al., 2018). We believe that it is vital to explore the impacts of chronic hypertension on cerebral circulation (Cipolla et al., 2018). The body weight was higher in SHRs than in WKY rats at 52 weeks old, while there was no difference between groups at other time points. Linear regression analyses between body weight and TIV revealed that the correlation coefficients were similar between the two groups, and TIV in SHRs was consistently lower than that in WKY rats. Thus, we hypothesized that the smaller TIV in SHRs might be unrelated to their higher body weight.

TABLE 2 | Voxel-based morphometry analysis revealed some GM regions with interactions of group and age in SHRs and WKY rats.

Brain regions	Coordinates			Voxels	Peak F-score
	X	Y	Z		
Septal region	−4	−48	16	4,960	140.7
Caudate putamen L	−30	−35	−6	8,430	209.3
Caudate putamen R	31	−33	−7	9,483	204.1
Hippocampus L	−24	−30	−29	226	55.2
Hippocampus R	17	−32	−26	769	77.0
S1FL L	−36	−23	6	2,815	69.3
S1BF R, S1FL R	45	−26	0	3,333	66.0
Cerebellum	9	−37	−93	877	94.2
Periaqueductal gray	−4	−45	−62	239	91.1
Caudate putamen L	−32	−73	3	334	71.8
Caudate putamen R	29	−70	4	5,819	271.1
Accumbens nucleus R	18	−67	24	1,619	209.1
Thalamus R	0	−55	−32	321	92.4

The names of these regions, the atlas coordinate of the peak point, the number of voxels, and the maximum F-score in the cluster are summarized in (Familywise error, P < 0.05; threshold of 200 voxels).
L, left; R, right; S1FL, Primary somatosensory cortex forelimb region; S1BF, Primary somatosensory cortex barrel field.

Voxel-Based Gray Matter Volume

In order to detect vulnerable GM volume alterations with interactive effects of hypertension and aging, we performed VBM

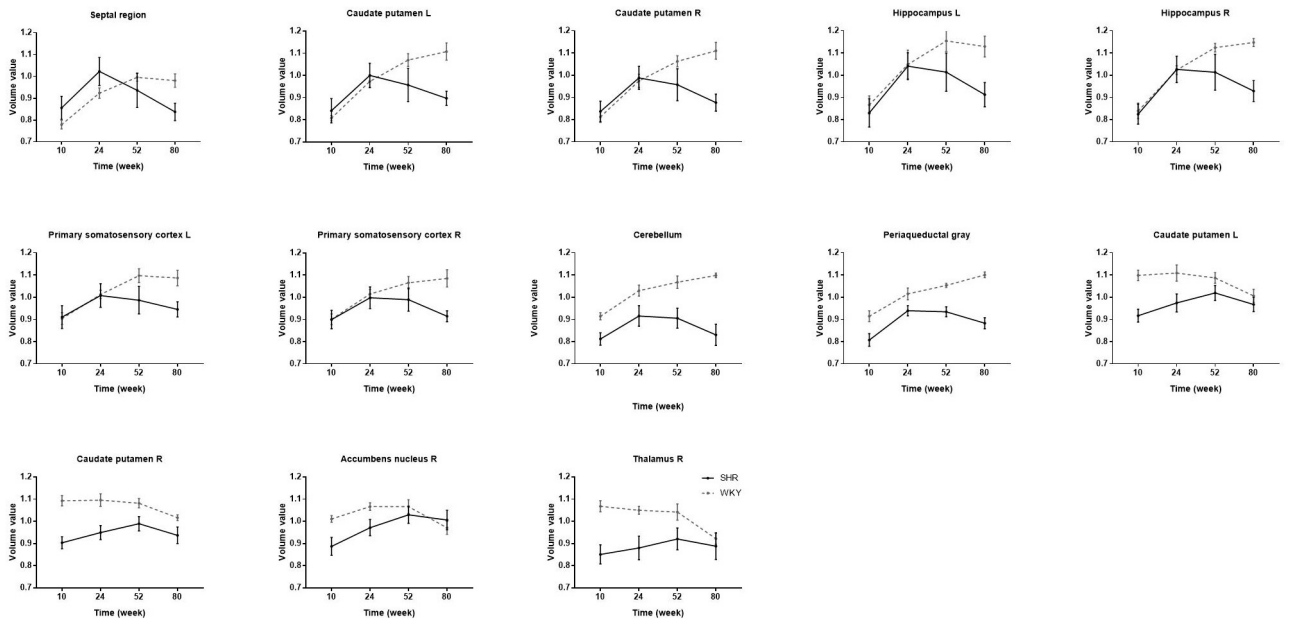

FIGURE 3 | The volume changes in each cluster with interactions of group and age in SHRs and WKY rats aged 10, 24, 52, and 80 weeks. Temporal trajectories of each cluster morphology show obvious heterogeneity, which is different across regions. Compared with WKY rats, elderly SHRs exhibit severe gray matter atrophy. As early as 24 weeks of age, gray matter volume begins to atrophy significantly in the septal region, bilateral caudate putamen, and hippocampus.

TABLE 3 | Volume (mm^3) of selected regions of interest of SHRs and WKY rats at different time points.

Region of interest	Group	10 weeks	24 weeks	52 weeks	80 weeks
Septal region	SHR	8.0 ± 0.1	9.2 ± 0.1	8.7 ± 0.2	7.5 ± 0.1
	WKY	7.6 ± 0.2	8.8 ± 0.1	9.3 ± 0.2	8.7 ± 0.1
Caudate putamen	SHR	36.1 ± 1.5	39.5 ± 1.4	39.4 ± 1.5	37.2 ± 1.3
	WKY	38.1 ± 0.8	41.2 ± 0.7	42.2 ± 0.6	41.7 ± 0.8
Hippocampus L	SHR	42.7 ± 0.4	47.6 ± 0.5	49.2 ± 0.5	45.6 ± 0.6
	WKY	44.9 ± 0.5	49.8 ± 0.7	52.0 ± 0.6	48.7 ± 0.7
Hippocampus R	SHR	43.5 ± 0.4	47.6 ± 0.5	49.5 ± 0.5	46.0 ± 0.5
	WKY	45.0 ± 0.6	49.5 ± 0.6	51.7 ± 0.7	49.1 ± 0.6
Accumbens nucleus L	SHR	4.9 ± 0.1	5.4 ± 0.1	5.5 ± 0.0	4.9 ± 0.1
	WKY	5.4 ± 0.1	5.7 ± 0.1	5.8 ± 0.0	5.4 ± 0.1
Accumbens nucleus R	SHR	5.2 ± 0.1	5.6 ± 0.1	5.8 ± 0.1	5.5 ± 0.1
	WKY	5.9 ± 0.1	6.1 ± 0.1	6.2 ± 0.1	5.8 ± 0.1

There was no bilateral difference in caudate putamen volume in the two groups at all-time points, so the caudate putamen volume was represented as the average of both sides.

analysis. We found that the interactive regions included certain cortical and subcortical regions such as the septal region, bilateral caudate putamen, hippocampus, primary somatosensory cortex, cerebellum, periaqueductal gray, right accumbens nucleus, and thalamus. *Post hoc* analysis revealed the patterns of GM volume changes. As early as 24 weeks of age, gray matter volume begins to atrophy obviously in certain brain regions, such as the septal region, bilateral caudate putamen, and hippocampus. These findings seem to contradict prior studies in aging SHRs showing that hippocampal volumes were similar in SHRs and WKY rats (Naessens et al., 2020). These conflicting results might be explained by the method of MRI data analysis and the rats' age, since our studies used VBM analysis in rats with longer life span, while prior studies used manually drawn ROI-based methods in 10-month-old SHRs. Our study is generally consistent with previous clinical MRI studies that indicated that hypertension exacerbates the volume reductions accompanying advanced age (Strassburger et al., 1997). Our studies have shown that rats with chronic hypertension are much more prone to GM atrophy with aging in some specific brain regions.

Region of Interest-Based Gray Matter Volume

The spatial heterogeneity of GM volume was detected using VBM analysis, while the temporal heterogeneity was explored using the

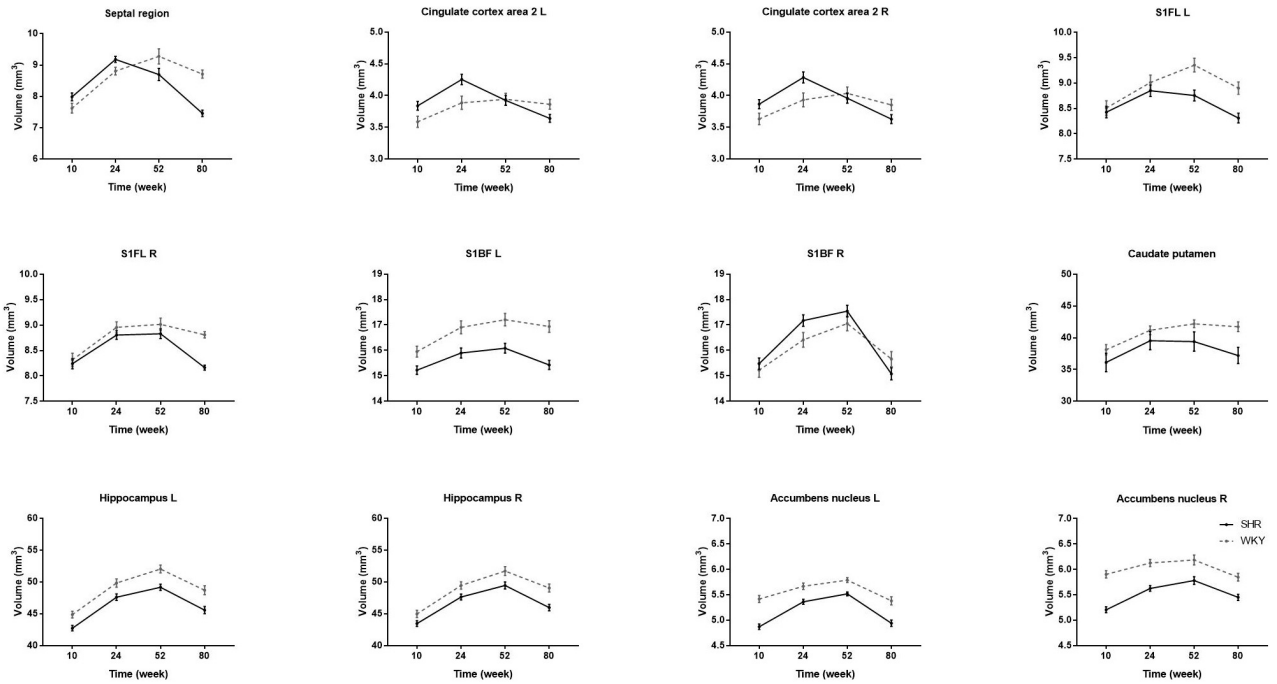

FIGURE 4 | Comparisons of longitudinal changes in each ROI volume in SHRs and WKY rats at 10, 24, 52, and 80 weeks old. The caudate putamen volume is the average volume of both sides because there was no significant bilateral difference in the two groups at any time point. Temporal trajectories of gray matter volume show obvious heterogeneity between the two groups. The trajectories of the volume change show an inverted-U shape in SHRs, increasing at the early phase and declining at the late phase. Compared with WKY rats, regional unbalanced volume atrophy is more pronounced in SHRs. The rate of gray matter atrophy is fastest in the right primary somatosensory cortex barrel field in elderly SHRs.

ROI-based method. We used a longitudinal design to examine the evolution patterns of the GM volume over aging in rats with and without hypertension. Although longitudinal designs impede interindividual variation, one limitation is the shorter time windows (Elliott, 2020). We only selected 4 representative time points to obtain the trends in GM volume with age. We chose the septal region, anterior cingulate cortex, primary somatosensory cortex, caudate putamen, hippocampus, and accumbens nucleus as ROIs. We found that anterior cingulate cortex area 2, overlapping within the cluster of septal region, had the combined effects of hypertension and aging. Previous animal studies have also reported that anterior cingulate cortex damage is involved in hypertension-associated brain atrophy (Gianaros et al., 2006; Lai et al., 2021). We found that all the above ROIs had interactions, except for the bilateral hippocampus. We speculate that there should be hypertension-aging interactions in certain hippocampal subregions, but these interactions were offset by the relatively large volume of the hippocampus. A previous study observed an age-dependent neural reduction in the hippocampal CA1 area (Li et al., 2016). Our data suggested an inverted-U trajectory of GM volume change in SHR lifespan, with volume increase at the early phase and decline at the late phase. Therefore, the GM volume can rise, plateau, or decrease according to different time phases. One study showed that hippocampal volume increased with age in a normal aging rat strain (Alexander et al., 2020); however, another study found that hippocampal volume was similar in SHRs and WKY rats (Naessens et al., 2020). The difference between these results can be explained by our trajectory. Clinical studies reported that reduced hippocampal volume was correlated with hypertension duration and poorer cognitive aging (Triantafyllou et al., 2020; Van Etten et al., 2020). These results support our view that elderly SHRs experienced pronounced shrinkage. Moreover, the rate of GM atrophy was fastest in the right primary somatosensory cortex barrel field in elderly SHRs. We speculate that the right primary somatosensory cortex barrel field may be more sensitive to chronic hypoperfusion. Our results laterally support the neurovascular pathological theory with biphasic responses in cerebral blood flow and neurovascular coupling (Li et al., 2021).

Magnetic Resonance Imaging Data Analysis

Structural MRI is a valid tool that can be used to noninvasively investigate alterations in the rat brain. We comprehensively assessed the spatial temporal course of GM volume change patterns using VBM and ROI-based methods. VBM analyzes the GM volume at the voxel level. A key advantage of VBM is that it allows for detecting whole brain volume automatically and objectively, while the disadvantage is that its accuracy might be impeded by registration errors. To minimize this problem, we used a custom template set for image registration. We checked the registration step by step and did not find any misregistration. Space smoothing can reduce image noise and enhance the

statistical effect. We chose a 4 mm Gaussian smoothing kernel. A previous study confirmed that smoothing kernels did not significantly influence whole brain volume test-retest reliability in rats (Jing et al., 2018). Alternatively, we quantified regional GM volumes using automatic ROI-based analysis. Automatic ROI extraction omits manual drawing to improve the reliability of the results. Quantitative ROI-based analysis is beneficial for multicenter and cross-species comparisons.

Animal Models

One benefit of animal models lies in the capability for within-subject longitudinal designs in the disease course. Many animal experiments on hypertensive brain damage have been performed in acute conditions (Meissner et al., 2017; Menard et al., 2018). The acute effects of hypertension on brain have been recognized for a long time (Iyonaga et al., 2019), while the long-term impacts of chronic hypertension on brain impairment remain incompletely understood. Only a few experiments have evaluated the influence of chronic hypertension (Willeman et al., 2019). SHRs are the most widely used animal model for human essential hypertension. SHRs are normotensive at birth and progressively develop hypertension without any intervening procedure. We chose scanning MRI at 10, 24, 52, and 80 weeks according to the features of SHRs. Blood pressure increases prominently at 3–10 weeks and remains stable for at least 20 weeks in SHRs. Animal models enable longitudinal design for analysis of chronic hypertension across the life cycle.

Limitations

Several potential limitations should be noted. First, the MRI scanner at the last time point was not the same as before, although it was an identical type. To minimize the bias, we tried to keep the scanning protocol consistent. Second, the present work is based on male rats with a modest sample size. Strict-corrected statistical thresholds were restricted to minimize the risk of false positives. This is an issue of concern for higher blood pressure in male SHRs than in females (Amaral and Michelin, 2011). Few studies have explored sex differences in SHRs (Pietranera et al., 2016), and previous research investigations were mostly conducted in males. Further studies with larger sample sizes and longer follow-up periods are needed. Third, a longitudinal neuroimaging study of rats requires repeated anesthesia. A low dose of isoflurane in combination with dexmedetomidine is a viable option for longitudinal imaging in rats (Brynildsen et al., 2017). Fourth, as a longitudinal study covering natural aging rats, various comorbidities were inescapable, such as heart failure, atherosclerosis, and Alzheimer's disease (Suzuki et al., 2015; Dinh et al., 2017; Chang et al., 2020). Since this phenomenon is common among elderly people, it may not prevent the clinical translation of our results. Finally, our present study primarily focused on evaluating brain morphology, and it would be interesting to compare the correlation of these volume results with cognition and behavioral function. Moreover, a recent clinical study confirmed that early onset hypertension was related to midlife cognitive function (Suvila et al., 2021). Future pathological- or molecular-level studies should expound the complex mechanisms of chronic hypertension related to brain aging.

CONCLUSION

In conclusion, the current study presented a neuroimaging approach to longitudinally characterize brain morphology in SHRs and WKY rats from early adulthood to aging. There are interactive effects of hypertension and aging on brain volume alterations, and GM shrinkage is heterogeneous across space and time. Our results provide evidence supporting the notion that chronic hypertension accelerates brain aging. We hope that the longitudinal neuroimaging characteristics of aging SHRs may constitute a useful paradigm to explore the intricate pathological mechanisms of hypertension and aging.

DATA AVAILABILITY STATEMENT

The datasets presented in this article are not readily available because the data also form part of an ongoing study. Requests to access the datasets should be directed to YY.

ETHICS STATEMENT

The animal study was reviewed and approved by the Laboratory Animal Ethical and Welfare Committee Hebei Medical University.

AUTHOR CONTRIBUTIONS

ZG, QZa, QZu, and YY conceived and designed the research. YY and YZ performed the experiment. YY and JR analyzed the data. YY and ZG wrote the manuscript. QZa, QZu, and LW participated in the discussion and provided the comments. All authors contributed to the article and approved the submitted version.

FUNDING

This research was supported by the National Natural Science Foundation of China (8177070094).

ACKNOWLEDGMENTS

We would like to thank Guorong Wu for the help updating the xjView software.

SUPPLEMENTARY MATERIAL

The Supplementary Material for this article can be found online at: https://www.frontiersin.org/articles/10.3389/fnagi.2021.757808/full#supplementary-material

REFERENCES

Alexander, G. E., Lin, L., Yoshimaru, E. S., Bharadwaj, P. K., Bergfield, K. L., Hoang, L. T., et al. (2020). Age-Related Regional Network Covariance of Magnetic Resonance Imaging Gray Matter in the Rat. *Front. Aging Neurosci.* 12:267. doi: 10.3389/fnagi.2020.00267

Amaral, S. L., and Michelin, L. C. (2011). Effect of gender on training-induced vascular remodeling in SHR. *Braz. J. Med. Biol. Res.* 44, 814–826. doi: 10.1590/s0100-879x2011007500055

Brynildsen, J. K., Hsu, L. M., Ross, T. J., Stein, E. A., Yang, Y., and Lu, H. (2017). Physiological characterization of a robust survival rodent fMRI method. *Magn. Reson. Imaging* 35, 54–60. doi: 10.1016/j.mri.2016.08.010

Chan, S. L., Bishop, N., Li, Z., and Cipolla, M. J. (2018). Inhibition of PAI (Plasminogen Activator Inhibitor)-1 Improves Brain Collateral Perfusion and Injury After Acute Ischemic Stroke in Aged Hypertensive Rats. *Stroke* 49, 1969–1976. doi: 10.1161/STROKEAHA.118.022056

Chang, Y. M., Ashok Kumar, K., Ju, D. T., Ho, T. J., Mahalakshmi, B., Lin, W. T., et al. (2020). Dipeptide IF prevents the effects of hypertension-induced Alzheimer's disease on long-term memory in the cortex of spontaneously hypertensive rats. *Environ. Toxicol.* 35, 570–581. doi: 10.1002/tox.22892

Cipolla, M. J., Liebeskind, D. S., and Chan, S. L. (2018). The importance of comorbidities in ischemic stroke: Impact of hypertension on the cerebral circulation. *J. Cereb. Blood Flow Metab.* 38, 2129–2149. doi: 10.1177/0271678X18800589

Dinh, Q. N., Chrissobolis, S., Diep, H., Chan, C. T., Ferens, D., Drummond, G. R., et al. (2017). Advanced atherosclerosis is associated with inflammation, vascular dysfunction and oxidative stress, but not hypertension. *Pharmacol. Res.* 116, 70–76. doi: 10.1016/j.phrs.2016.12.032

Elliott, M. L. (2020). MRI-based biomarkers of accelerated aging and dementia risk in midlife: how close are we? *Ageing Res. Rev.* 61:101075. doi: 10.1016/j.arr.2020.101075

Erdos, B., Kirichenko, N., Whidden, M., Basgut, B., Woods, M., Cudykier, I., et al. (2011). Effect of age on high-fat diet-induced hypertension. *Am. J. Physiol. Heart Circ. Physiol.* 301, H164–H172. doi: 10.1152/ajpheart.01289.2010

Feng, R., Rolls, E. T., Cheng, W., and Feng, J. (2020). Hypertension is associated with reduced hippocampal connectivity and impaired memory. *EBioMedicine* 61:103082. doi: 10.1016/j.ebiom.2020.103082

Gianaros, P. J., Greer, P. J., Ryan, C. M., and Jennings, J. R. (2006). Higher blood pressure predicts lower regional grey matter volume: Consequences on short-term information processing. *Neuroimage* 31, 754–765. doi: 10.1016/j.neuroimage.2006.01.003

Gilsanz, P., Mayeda, E. R., Glymour, M. M., Quesenberry, C. P., Mungas, D. M., DeCarli, C., et al. (2017). Female sex, early-onset hypertension, and risk of dementia. *Neurology* 89, 1886–1893. doi: 10.1212/WNL.0000000000004602

Glodzik, L., Rusinek, H., Tsui, W., Pirraglia, E., Kim, H. J., Deshpande, A., et al. (2019). Different Relationship Between Systolic Blood Pressure and Cerebral Perfusion in Subjects With and Without Hypertension. *Hypertension* 73, 197–205. doi: 10.1161/HYPERTENSIONAHA.118.11233

Holland, P. R., Pannozzo, M. A., Bastin, M. E., McNeilly, A. D., Ferguson, K. J., Caughey, S., et al. (2015). Hypertension fails to disrupt white matter integrity in young or aged Fisher (F44) Cyp1a1Ren2 transgenic rats. *J. Cereb. Blood Flow Metab.* 35, 188–192. doi: 10.1038/jcbfm.2014.201

Iyonaga, T., Shinohara, K., Mastuura, T., Hirooka, Y., and Tsutsui, H. (2019). Brain perivascular macrophages contribute to the development of hypertension in stroke-prone spontaneously hypertensive rats *via* sympathetic activation. *Hypertens Res.* 43, 99–110. doi: 10.1038/s41440-019-0333-4

Jing, B., Liu, B., Li, H., Lei, J., Wang, Z., Yang, Y., et al. (2018). Within-subject test-retest reliability of the atlas-based cortical volume measurement in the rat brain: A voxel-based morphometry study. *J. Neurosci, Methods* 307, 46–52. doi: 10.1016/j.jneumeth.2018.06.022

Kern, K. C., Wright, C. B., Bergfield, K. L., Fitzhugh, M. C., Chen, K., Moeller, J. R., et al. (2017). Blood Pressure Control in Aging Predicts Cerebral Atrophy Related to Small-Vessel White Matter Lesions. *Front. Aging Neurosci.* 9:132. doi: 10.3389/fnagi.2017.00132

Korf, E. S., White, L. R., Scheltens, P., and Launer, L. J. (2004). Midlife blood pressure and the risk of hippocampal atrophy: the Honolulu Asia Aging Study. *Hypertension* 44, 29–34. doi: 10.1161/01.HYP.0000132475.32317.bb

Koundal, S., Liu, X., Sanggaard, S., Mortensen, K., Wardlaw, J., Nedergaard, M., et al. (2019). Brain Morphometry and Longitudinal Relaxation Time of Spontaneously Hypertensive Rats (SHRs) in Early and Intermediate Stages of Hypertension Investigated by 3D VFA-SPGR MRI. *Neuroscience* 404, 14–26. doi: 10.1016/j.neuroscience.2019.01.030

Lai, A. Y., Joo, I. L., Trivedi, A. U., Dorr, A., Hill, M. E., Stefanovic, B., et al. (2021). Cerebrovascular damage after midlife transient hypertension in non-transgenic and Alzheimer's disease rats. *Brain Res.* 1758:147369. doi: 10.1016/j.brainres.2021.147369

Lee, T. H., Liu, H. L., Yang, S. T., Yang, J. T., Yeh, M. Y., and Lin, J. R. (2011). Effects of aging and hypertension on cerebral ischemic susceptibility: Evidenced by MR diffusion–perfusion study in rat. *Exp. Neurol.* 227, 314–321. doi: 10.1016/j.expneurol.2010.12.003

Li, Y., Li, R., Liu, M., Nie, Z., Muir, E. R., and Duong, T. Q. (2021). MRI study of cerebral blood flow, vascular reactivity, and vascular coupling in systemic hypertension. *Brain Res.* 1753, 147224. doi: 10.1016/j.brainres.2020.147224

Li, Y., Liu, J., Gao, D., Wei, J., Yuan, H., Niu, X., et al. (2016). Age-related changes in hypertensive brain damage in the hippocampi of spontaneously hypertensive rats. *Mol. Med. Rep.* 13, 2552–2560. doi: 10.3892/mmr.2016.4853

Meissner, A., Minnerup, J., Soria, G., and Planas, A. M. (2017). Structural and functional brain alterations in a murine model of Angiotensin II-induced hypertension. *J. Neurochem.* 140, 509–521. doi: 10.1111/jnc.13905

Menard, B., Chazalviel, L., Roussel, S., Bernaudin, M., and Touzani, O. (2018). Two-kidney one-clip is a pertinent approach to integrate arterial hypertension in animal models of stroke: Serial magnetic resonance imaging studies of brain lesions before and during cerebral ischemia. *J. Cereb. Blood Flow Metab.* 38, 1769–1780. doi: 10.1177/0271678X17715813

Mills, K. T., Stefanescu, A., and He, J. (2020). The global epidemiology of hypertension. *Nat. Rev. Nephrol.* 16, 223–237. doi: 10.1038/s41581-019-0244-2

Naessens, D. M. P., Coolen, B. F., de Vos, J., VanBavel, E., Strijkers, G. J., and Bakker, E. (2020). Altered brain fluid management in a rat model of arterial hypertension. *Fluids Barriers CNS.* 17:41. doi: 10.1186/s12987-020-00203-6

Naessens, D. M. P., de Vos, J., VanBavel, E., and Bakker, E. (2018). Blood-brain and blood-cerebrospinal fluid barrier permeability in spontaneously hypertensive rats. *Fluids Barriers CNS.* 15:26. doi: 10.1186/s12987-018-0112-7

Naumczyk, P., Sabisz, A., Witkowska, M., Graff, B., Jodzio, K., Gąsecki, D., et al. (2017). Compensatory functional reorganization may precede hypertension-related brain damage and cognitive decline. *J. Hypertens* 35, 1252–1262. doi: 10.1097/HJH.0000000000001293

Okamoto, K., and Aoki, K. (1963). Development of a strain of spontaneously hypertensive rats. *JPN Circ. J.* 27, 282–293. doi: 10.1253/jcj.27.282

Pietranera, L., Correa, J., Brocca, M. E., Roig, P., Lima, A., Di Giorgio, N., et al. (2016). Selective Oestrogen Receptor Agonists Rescued Hippocampus Parameters in Male Spontaneously Hypertensive Rats. *J. Neuroendocrinol.* 28:145. doi: 10.1111/jne.12415

Raz, N., Lindenberger, U., Rodrigue, K. M., Kennedy, K. M., Head, D., Williamson, A., et al. (2005). Regional brain changes in aging healthy adults: general trends, individual differences and modifiers. *Cereb. Cortex* 15, 1676–1689. doi: 10.1093/cercor/bhi044

Sabisz, A., Naumczyk, P., Marcinkowska, A., Graff, B., Gasecki, D., Glinska, A., et al. (2019). Aging and Hypertension - Independent or Intertwined White Matter Impairing Factors? Insights From the Quantitative Diffusion Tensor Imaging. *Front. Aging Neurosci.* 11:35. doi: 10.3389/fnagi.2019.00035

Shaul, M. E., Hallacoglu, B., Sassaroli, A., Shukitt-Hale, B., Fantini, S., Rosenberg, I. H., et al. (2014). Cerebral blood volume and vasodilation are independently diminished by aging and hypertension: a near infrared spectroscopy study. *J. Alzheimers Dis.* 42, S189–S198. doi: 10.3233/JAD-132504

Shi, H. K., Guo, H. C., Liu, H. Y., Zhang, Z. L., Hu, M. Y., Zhang, Y., et al. (2020). Cannabinoid type 2 receptor agonist JWH133 decreases blood pressure of spontaneously hypertensive rats through relieving inflammation in the rostral ventrolateral medulla of the brain. *J. Hypertens* 38, 886–895. doi: 10.1097/HJH.0000000000002342

Strassburger, T. L., Lee, H. C., Daly, E. M., Szczepanik, J., Krasuski, J. S., Mentis, M. J., et al. (1997). Interactive effects of age and hypertension on volumes of brain structures. *Stroke* 28, 1410–1417. doi: 10.1161/01.str.28.7.1410

Suvila, K., Lima, J. A. C., Yano, Y., Tan, Z. S., Cheng, S., and Niiranen, T. J. (2021). Early-but Not Late-Onset Hypertension Is Related to Midlife Cognitive

Function. *Hypertension* 77, 972–979. doi: 10.1161/HYPERTENSIONAHA.120.16556

Suzuki, H., Sumiyoshi, A., Matsumoto, Y., Duffy, B. A., Yoshikawa, T., Lythgoe, M. F., et al. (2015). Structural abnormality of the hippocampus associated with depressive symptoms in heart failure rats. *Neuroimage* 105, 84–92. doi: 10.1016/j.neuroimage.2014.10.040

Triantafyllou, A., Ferreira, J. P., Kobayashi, M., Micard, E., Xie, Y., Kearney-Schwartz, A., et al. (2020). Longer Duration of Hypertension and MRI Microvascular Brain Alterations Are Associated with Lower Hippocampal Volumes in Older Individuals with Hypertension. *J. Alzheimers Dis.* 74, 227–235. doi: 10.3233/JAD-190842

Van Etten, E. J., Bharadwaj, P. K., Nguyen, L. A., Hishaw, G. A., Trouard, T. P., and Alexander, G. E. (2020). Right hippocampal volume mediation of subjective memory complaints differs by hypertension status in healthy aging. *Neurobiol. Aging* 94, 271–280. doi: 10.1016/j.neurobiolaging.2020.06.012

Wang, Y., Zhang, R., Tao, C., Xu, Z., Chen, W., Wang, C., et al. (2018). Blood-Brain Barrier Disruption and Perivascular Beta-Amyloid Accumulation in the Brain of Aged Rats with Spontaneous Hypertension: Evaluation with Dynamic Contrast-Enhanced Magnetic Resonance Imaging. *Korean J. Radiol.* 19, 498–507. doi: 10.3348/kjr.2018.19.3.498

Whelton, P. K., Carey, R. M., Aronow, W. S., Casey, D. E., Collins, K. J., Dennison Himmelfarb, C., et al. (2018). 2017 ACC/AHA/AAPA/ABC/ACPM/AGS/APhA/ASH/ASPC/NMA/PCNA Guideline for the Prevention, Detection, Evaluation, and Management of High Blood Pressure in Adults: A Report of the American College of Cardiology/American Heart Association Task Force on Clinical Practice Guidelines. *Hypertension* 71, 13–115 e. doi: 10.1161/HYP.0000000000000065

Willeman, M. N., Chawla, M. K., Zempare, M. A., Biwer, L. A., Hoang, L. T., Uprety, A. R., et al. (2019). Gradual hypertension induction in middle-aged Cyp1a1-Ren2 transgenic rats produces significant impairments in spatial learning. *Physiol. Rep.* 7:e14010. doi: 10.14814/phy2.14010

Conflict of Interest: JR was employed by company GE Healthcare China.

The remaining authors declare that the research was conducted in the absence of any commercial or financial relationships that could be construed as a potential conflict of interest.

Publisher's Note: All claims expressed in this article are solely those of the authors and do not necessarily represent those of their affiliated organizations, or those of the publisher, the editors and the reviewers. Any product that may be evaluated in this article, or claim that may be made by its manufacturer, is not guaranteed or endorsed by the publisher.

frontiers in Aging Neuroscience

ORIGINAL RESEARCH
published: 06 December 2021
doi: 10.3389/fnagi.2021.774607

A Comparative Study of Structural and Metabolic Brain Networks in Patients With Mild Cognitive Impairment

Cuibai Wei[1,2†], Shuting Gong[1,3†], Qi Zou[1,4†], Wei Zhang[5†], Xuechun Kang[1,3], Xinliang Lu[1,3], Yufei Chen[1], Yuting Yang[1,3], Wei Wang[1], Longfei Jia[1], Jihui Lyu[6] and Baoci Shan[5] for Alzheimer's Disease Neuroimaging Initiative (ADNI)[‡]*

[1] Innovation Center for Neurological Disorders and Department of Neurology, Xuanwu Hospital, Capital Medical University, National Clinical Research Center for Geriatric Diseases, Beijing, China, [2] Center of Alzheimer's Disease, Beijing Institute for Brain Disorders, Beijing Key Laboratory of Geriatric Cognitive Disorders, Neurodegenerative Laboratory of Ministry of Education of the People's Republic of China, Beijing, China, [3] School of Biological Science and Medical Engineering, Beihang University, Beijing, China, [4] College of Integrated Traditional Chinese and Western Medicine, Changchun University of Chinese Medicine, Changchun, China, [5] Institute of High Energy Physics, Chinese Academy of Sciences, Neurodegenerative Laboratory of Ministry of Education of the People's Republic of China, Beijing, China, [6] Center for Cognitive Disorders, Beijing Geriatric Hospital, Beijing, China

Background: Changes in the metabolic and structural brain networks in mild cognitive impairment (MCI) have been widely researched. However, few studies have compared the differences in the topological properties of the metabolic and structural brain networks in patients with MCI.

Methods: We analyzedmagnetic resonance imaging (MRI) and fluoro-deoxyglucose positron emission tomography (FDG-PET) data of 137 patients with MCI and 80 healthy controls (HCs). The HC group data comes from the Alzheimer's Disease Neuroimaging Initiative (ADNI) database. The permutation test was used to compare the network parameters (characteristic path length, clustering coefficient, local efficiency, and global efficiency) between the two groups. Partial Pearson's correlation analysis was used to calculate the correlations of the changes in gray matter volume and glucose intake in the key brain regions in MCI with the Alzheimer's Disease Assessment Scale-Cognitive (ADAS-cog) sub-item scores.

Results: Significant changes in the brain network parameters (longer characteristic path length, larger clustering coefficient, and lower local efficiency and global efficiency) were greater in the structural network than in the metabolic network (longer characteristic path length) in MCI patients than in HCs. We obtained the key brain regions (left globus pallidus, right calcarine fissure and its surrounding cortex, left lingual gyrus) by scanning the hubs. The volume of gray matter atrophy in the left globus pallidus was significantly positively correlated with comprehension of spoken language (p = 0.024) and word-finding difficulty in spontaneous speech item scores (p = 0.007) in the ADAS-cog. Glucose intake in the three key brain regions was significantly negatively correlated with remembering test instructions items in ADAS-cog (p = 0.020, p = 0.014, and p = 0.008, respectively).

OPEN ACCESS

Edited by:
Ping Wu,
Fudan University, China

Reviewed by:
Dantao Peng,
China-Japan Friendship Hospital, China
Yuping Ning,
Guangzhou Medical University, China

***Correspondence:**
Cuibai Wei
chuibainews@126.com

[†] These authors have contributed equally to this work

[‡] Data used in this study were obtained from the Alzheimer's Disease Neuroimaging Initiative (ADNI) database (adni.loni.usc.edu). The investigators of the ADNI contributed to the design and implementation of ADNI and/or provided data but did not participate in the analysis or writing of this report. A complete listing of ADNI investigators can be found at http://adni.loni.usc.edu/wp-content/uploads/how_to_apply/ADNI_Acknowledgement_List.pdf.

Specialty section:
This article was submitted to Alzheimer's Disease and Related Dementias, a section of the journal Frontiers in Aging Neuroscience

Received: *12 September 2021*
Accepted: *08 November 2021*
Published: *06 December 2021*

Citation:
Wei C, Gong S, Zou Q, Zhang W, Kang X, Lu X, Chen Y, Yang Y, Wang W, Jia L, Lyu J and Shan B (2021) A Comparative Study of Structural and Metabolic Brain Networks in Patients With Mild Cognitive Impairment. Front. Aging Neurosci. 13:774607. doi: 10.3389/fnagi.2021.774607

Conclusion: Structural brain networks showed more changes than metabolic brain networks in patients with MCI. Some brain regions with significant changes in betweenness centrality in both structural and metabolic networks were associated with MCI.

Keywords: mild cognitive impairment, brain network, structure, metabolism, brain regions

INTRODUCTION

Alzheimer's disease (AD) is a common neurodegenerative disorder, which is the leading cause of dementia (Alzheimer's Association, 2016). Mild cognitive impairment (MCI) is an intermediate state between normal aging and dementia (Yao et al., 2010; Liu et al., 2012), and approximately 10–15% patients with MCI progress to AD every year (Petersen et al., 1997; Davatzikos et al., 2011). Therefore, the pathological mechanisms underlying MCI should be explored. Additionally, effective interventions in the MCI phase may considerably reduce the incidence of AD.

Magnetic resonance imaging (MRI) and 18F-labeledfluoro-deoxyglucose positron emission tomography (FDG-PET) are common neuroimaging modalities, whichrespectively reflect the glucose metabolism in different brain regions and analyze the characteristic features of brain atrophy such as whole brain volume, localized brain areas, cortical thickness, and curvature in a reliable manner (Son et al., 2015; Hojjati et al., 2019). Currently, MRI and PET findings, such as hippocampal gray matter atrophy and hypometabolism in the posterior cingulate cortex and temporoparietal cortex, pertaining to individual brain regions have been shown to serve as *in vivo* imaging markers for the diagnosis of AD (Mutlu et al., 2016). However, the function of the brain is not determined only by a single brain region, but by a series of interactions among brain regions (Mutlu et al., 2016). The emergence of brain networks has provided a new method for understanding the connections among cerebral regions contributing to the potential findings of AD that can help in diagnosis, predicting disease progression, and exploring pathogenesis.

The current focus is on research regarding AD from the perspective of brain networks. Brain networks provide biomarkers to distinguish between normal cognition and MCI. The importance of nodal graph measurements as markers in the early diagnosis of AD has been demonstrated (Xu et al., 2020). The right Crus II of the cerebellar hemisphere and fusiform gyrus could be the potential diagnostic biomarkers for MCI (Zhang et al., 2020). Moreover, brain networks can predict the progression of MCI to AD because of their close relationship with the course of the disease in the AD continuum (Sun et al., 2018; Zheng et al., 2019). The emergence of brain networks has also provided a new perspective for explaining the pathogenesis of AD. He et al. (2008) established the first structural brain network model of AD in 2008 and found that the cortical network and regional centrality of patients with AD were destroyed, which proved that the pathological changes in AD were associated with the destruction of large-scale brain networks (He et al., 2008). Similar to the results pertaining to brain networks, the topological properties of brain network building have been reported to be damaged, as evident from MRI, FDG-PET, and resting state-functional MRI (rs-fMRI) data (Yao et al., 2010; Sanabria-Diaz et al., 2013; Sun et al., 2014). The degree of variations in specific network parameters [e.g., small-world properties, characteristic path length (L), clustering coefficient (C), local efficiency (E_{loc}), and global efficiency (E_{glob})] of patients with MCI lies between that of healthy individuals and patients with AD, representing a continuity from aging to AD.However, to describe the complex pathological mechanisms underlying AD, the information provided by the network built by these single imaging modes is limited.

In contrast to the shortage of single imaging modes, studies assessing the multiple modes of brain network can easily clarify the pathological status by comparing the differences and internal relationships among two or more modal information. A previous study comparing brain networks based on rs-fMRI and diffusion tensor imaging (DTI) data reported that there was no one-to-one relationship between functional and structural connection strengths of different brain regions in MCI networks (Sun et al., 2014). The asynchrony in the damage between the two brain networks was shown in Palesi's research, in which the functional network changed in MCI, the early state of AD, before the destruction of the structural network. rs-fMRI-based functional connectivity is significantly altered in AD and MCI, whereas DTI-based structural connectivity is shifted significantly only in AD (Palesi et al., 2016). However, another study using MCI data showed conflicting results (Filippi et al., 2020), which may be due to the difference in DTI reconstruction methods. At present, studies that analyze the difference between metabolic networks and structural modes in MCI use data collected from DTI and fMRI scans. Little is known about the associations between MRI and FDG-PET networks in the MCI stage.

In this study, it is hypothesized that the shape of structural brain network damaged differ from the metabolic network under AD pathology, but that the damage in two brain networks was related. We compared the topological properties of different modes in MCI and observed the differences in topological parameters of structural and metabolic networks between patients with MCI and healthy controls (HCs). The key brain regions of networks were determined by screening important hub nodes with significant changes in betweenness centrality in both the structural and metabolic networks. Finally, we analyzed the potential correlation between key brain regions and cognitive function. Our research will help in understanding the metabolic mechanisms associated with the structural disconnection during MCI, and show the brain areas that may be affected by the pathogenesis of AD in the brain network.

MATERIALS AND METHODS

Participants

We recruited 137 patients diagnosed with MCI from 25 hospitals in China and 80 healthy subjects from the Alzheimer's Disease Neuroimaging Initiative (ADNI) database[1] to serve as HCs. The ADNI was launched in 2003 as a public-private partnership led by principal investigator Michael W. Weiner, MD. The primary goal of ADNI has been to assess whether serial MRI, PET, other biological markers, and clinical and neuropsychological assessment can be combined to assess the progression of MCI to early AD.

Patients included in the study were hospitalized or out-patients with MCI aged 50–85 years. Referring to the 2011 clinical MCI diagnostic criteria by the National Institute of Aging and Alzheimer's Disease Association (NIA-AA), patients were diagnosed according to a comprehensive assessment including clinical history, neurological examination, and neuropsychological tests. Inclusion criteria were patients who were right-handed, who were hospitalized or out-patients aged between 50 and 85 years, with diagnosis of probable MCI according to established criteria (McKhann et al., 2011), with Mini-Mental State Examination (MMSE) scores of 20–26 (including 20 and 26),Clinical Dementia Rating (CDR)score of 0.5, and who could professionally communicate in Chinese (non-illiterate). Exclusion criteria included patients with a diagnosis of dementia, focal or diffuse brain damage, severe leukoencephalopathy, Fazekas scores $\geq$ 3, consciousness disorders, severe aphasia or physical disability that could interfere with neuropsychological examination, history of alcoholism, and history of drug addiction. Participants of the ADNI were included in this study if they met the following criteria: age between 50 and 80 years, non-depression, non-MCI, and non-dementia, with an MMSE score of 24–30 and CDR score near zero. All participants (or their caregivers) provided written informed consent prior to study inclusion.

Neuropsychological Assessment

All patients underwent neuropsychological evaluations, including MMSE (Tombaugh and McIntyre, 1992) and Alzheimer's Disease Assessment Scale-Cognitive (ADAS-cog) 11 (Rosen et al., 1984). MMSE is the favored assessment method for dementia screening and is performed by professional neuropsychologists. It allows the assessment of seven cognitive domains, including time and site orientation, comprehension, language, immediate and delayed memory, attention, visual space, and calculation, with a maximum score of 30. ADAS-cog is one of the most widely used cognitive assessment tools for AD. It contains the following sub-items: word recall task, naming objects and fingers, following commands, constructional praxis, ideational praxis, orientation, word-recognition task, recall of test instructions, comprehension of spoken language, word-finding difficulty in spontaneous speech, and spoken language ability. Our study calculated the correlations of the changes in volume of gray matter atrophy and glucose metabolism in key brain regions in MCI with the ADAS-cog sub-item scores.

Magnetic Resonance Imaging Scanning

The dataset in the experiment is standard T1- weighted MR images using volumetric 3D Magnetization Prepared-Rapid Gradient Echo (MPRAGE) imaging. The MCI data comes from 25 research centers in China, using 3T scanners from Siemens, GE and Philips. FOV = 256 mm $\times$ 256 mm, layer thickness = 1 mm, layers = 170, TE = 3 ms, TR = 1,900 ms, TI = 900 ms and flip angle = 9 degree. The HCs data comes from the ADNI database, also scanned by 3T scanners from Siemens, GE and Philips with the same MPRAGE protocol. FOV = 240 mm $\times$ 256 mm, layer thickness = 1 mm, layers = 170, TE = 3 ms, TR = 2,300 ms, TI = 900 ms and flip angle = 9 degree.Further scanning details of ADNI are available in[1].

Fluoro-Deoxyglucose Positron Emission Tomography Scanning

Whole brain FDG-PET imaging was performed in this study. The HCs data were obtained from the ADNI database, and the MCI data were obtained from 25 research centers in China. All participants fasted for 4–6 h before the injection of the 18F-FDG PET tracer. Each patient was injected with 0.1 mCi/kg FDG tracer, and scanning began 60 min after tracer injection. The PET scanning time was 15 min (axial FOV = 30 cm, acquisition matrix = 128 $\times$ 128, layer thickness = 2.5 mm, layers = 80).

Image Pre-processing

Statistical Parametric Mapping software (SPM12; Wellcome Department of Cognitive Neurology, London, United Kingdom) and its toolboxes, computational anatomy toolbox (CAT12) and PET partial volume effects 12 (PETPVE12), were used to preprocess MRI and FDG-PET scans. The specific steps are as follows: First, the PET images were co-registered with the original MRI space of the corresponding individual. Second, a voxel-based correction method was used for partial volume correction of the co-registered PET images using PETPVE12. The MR image wasincorporated into the standard Montreal Neurological Institute space and modulated using the Jacobian determinant. Third, the MRI image was segmented, and the deformation field, aligned with the specific template, was obtained using Diffeomorphic Anatomical Registration Through Exponentiated Lie Algebra (DARTEL). The corrected PET images were spatially normalized using the deformation fields obtained at the segmentation step of MRI. Next, in the PET images, the standardized uptake value ratio (SUVR) was generated using the average standardized uptake value of the cerebellar gray matter as the benchmark. Finally, the resulting gray matter images and glucose metabolism images were smoothed using an 8 mm isotropic Gaussian kernel.

Construction of Brain Networks

A brain network is composed of defined nodes and edges that connect nodes. In this study, an undirected weighted similarity network is established, and the weight of edges represents the

[1]http://adni.loni.usc.edu/

correlation of glucose metabolism or gray matter volume between nodes. The gray matter volume determined using MRI and SUVR from FDG-PET images of the 137 cases in the MCI group and 80 cases in the HC group was used to construct the structural and metabolic brain networks. Using the MATLAB (Mathworks Inc., Natick, MA, United States) script, theAnatomical Automatic Labeling (AAL) template was used to divide brain regions into 90 brain regions (Desikan et al., 2006).

The partial Pearson correlation was used to calculate the correlation coefficient between the parameters of each node and the edge of the connecting nodes, considering the effect of age and sex on the edge of the network.

Calculation of Network Metrics

In this study, the sparsity method was used to threshold the network. Within the range of 5–50%, the network topology parameters under different sparsity thresholds were calculated with 5% step size, and parameters were compared between groups. We chose a network sparsity of 30% to show the network results. Under this sparsity, the network attributes were relatively stable, and the number of nodes in the four brain networks was approximately 90. The figures of correlation matrix of 90 × 90 ROIs for each group have been provided in **Supplementary Material**. The betweenness centrality of the nodes was considered in the networks. The betweenness centrality of a node i (BC_i) is defined as the number of shortest paths between any two nodes that run through the node i. Hub nodes in this study were defined as nodes in which the betweenness centrality was twice the average betweenness centrality of the network. The nodes in which betweenness centrality changed significantly in both structural and metabolic brain networks were defined as key brain regions associated with the pathology of MCI. For the definition of small world, L, C, E_{loc}, and E_{glob}, see **Supplementary Material**.

Statistical Analysis

The permutation test was used to test the statistical significance of group differences in the network parameters. In our study, we obtained a new reference distribution after repeatedly rearranging the observed network data obtained from the HC and MCI groups, calculated the differences between the new groups, and repeated this process 1,000 times. Repeated differences were also recorded. If the differences in the observed networks were contained without 95% of the supposed differences, we accepted that there were significant differences between the two groups.

We also performed a partial correlation analysis to investigate the correlations of mean glucose intake and gray matter volume in key brain regions with individuals' ADAS-cog scores, adjusted for age and sex with a Bonferroni-adjusted p value of 0.016.

RESULTS

Participants

As shown in **Table 1**, the mean age of patients in the MCI group was 66.5 ± 7.7 years, and of individuals in the HC group was 67.3 ± 4.0 years ($p = 0.441$). The sex ratio (M/F) in the MCI group was 61/76 and in the HC group was 35/45 ($p = 0.912$).

TABLE 1 | Comparison of the structural and metabolic brain networks in patients with MCI and HCs.

	MCI (n = 137)	HC (n = 80)	p value
Age (years)	66.5 ± 7.7	67.3 ± 4.0	0.441
Gender (M/F)	61/76	35/45	0.912
MMSE	24.23 ± 1.69	29.16 ± 1.08	0

Age and MMSE scoreare described in terms of mean ± standard deviation.
P < 0.05 indicates that the difference is significant.
MCI, mild cognitive impairment; HC, healthy controls.

Structural and Metabolic Brain Networks in Mild Cognitive Impairment and Healthy Control

Structural Brain Network Relative to Metabolic Brain Network in Mild Cognitive Impairment

In this study, 30% sparsity was selected to compare the relevant parameters of brain networks, and the weighted matrix constructed under this sparsity is shown in the **Supplementary Material**. Both the structural and metabolic brain networks in patients with MCI had small-world attributes, and the small-world attribute (σ) of the structural brain network was relatively stronger (σ of the structural brain network = 8.002, σ of the metabolic brain network = 4.375). Using the permutation test, we compared the L, C, E_{loc}, and E_{glob} of the two networks. As shown in **Table 2**, the L of the MCI structural brain network was significantly smaller than that of the metabolic brain network ($p < 0.0001$), while the E_{loc}, and E_{glob} of the structural brain network were significantly larger than those of the metabolic brain network ($p < 0.0001$).

Mild Cognitive Impairment Relative to Healthy Control in Structural Brain Network

The structural brain networks of both patients with MCI and HCs had small-world properties, and the small-world parameters were almost the same at 30% sparsity (σ of the structural brain network in patients with MCI = 8.002, σ of the structural brain network in HCs = 7.954). We also compared the L, C, E_{loc}, and E_{glob} of the two networks using the permutation test. As shown in **Table 2**, the L ($p = 0.001$) and C ($p < 0.0001$) of the MCI structural brain network were significantly larger than those of the HC structural brain network, while the E_{glob} and E_{loc} of the MCI structural brain network were significantly smaller than that of the HC structural brain network ($p < 0.0001$).

Mild Cognitive Impairment Relative to Healthy Control in Metabolic Brain Network

At 30% sparsity, the metabolic brain networks of patients with MCI and HCs had small-world attributes, and the small-world parameters of the MCI metabolic brain network were smaller than the HC metabolic brain network (σ of the metabolic brain network in patients with MCI = 4.375, σ of the metabolic brain network in HC = 5.500). Using the permutation test, we compared the L, C, E_{loc}, and E_{glob} of the two networks.

TABLE 2 | Comparison of the structural and metabolic brain networks in patients with MCI and HCs.

Network parameters	MCI structural brain network vs. MCI metabolic brain network			MCI structural brain network vs. HC structural brain network			MCI metabolic brain network vs. HC metabolic brain network		
	MCI structural network	MCI metabolic network	*p* value	MCI	HC	*p* value	MCI	HC	*p* value
Characteristic path length	2.429	3.211	<0.0001	2.429	2.276	0.01	3.211	2.832	0.047
Clustering coefficient	0.735	0.539	<0.0001	0.735	0.692	<0.0001	0.539	0.597	0.073
Local efficiency	0.510	0.403	<0.0001	0.510	0.535	<0.0001	0.403	0.437	0.123
Global efficiency	0.510	0.404	<0.001	0.510	0.536	<0.0001	0.404	0.437	0.131

The permutation test was used for all comparisons and a value of $p < 0.05$ indicated that the difference was significant.
MCI, mild cognitive impairment; HC, healthy controls.

TABLE 3 | Structural and metabolic brain network hub nodes in MCI and HC groups.

Hub nodes			BC_i in structural networks			BC_i in metabolic networks		
			MCI	HC	*p* value	MCI	HC	*p* value
Common hub of three networks	MCI structural brain network and HC and MCI metabolic brain networks	INS.L	0.048	0.023	0.154	0.034	0.056	0.907
Common hub of two networks	HC and MCI structural brain networks	LING.L	0.035	0.081	0.018*	0.011	0.022	0.031▲
		MTG.R	0.036	0.047	0.427	0.011	0.011	0.367
		MOG.L	0.128	0.045	0.002*	0.011	0.011	0.382
	MCI structural and metabolic brain networks	PUT.R	0.034	0.023	0.018*	0.034	0.012	0.104
	HC metabolic and MCI structural brain networks	LING.R	0.035	0.012	0.019*	0.011	0.045	1.000
Unique hub	MCI structural brain network	STG.L	0.056	0.012	0.092	0.011	0.023	0.929
		STG.R	0.037	0.011	0.107	0.012	0.011	0.229
		MTG.L	0.036	0.011	0.179	0.011	0.012	0.514
	HC structural brain network	HIP.R	0.012	0.057	0*	0.011	0.011	0.217
		MFG.L	0.017	0.050	0.006*	0.015	0.011	0.851
	MCI metabolic brain network	ORBinf.L	0.012	0.011	0*	0.037	0.023	0.116
		OLF.R	0.012	0.011	0*	0.034	0.024	0.390
		PAL.L	0.012	0.011	0*	0.034	0.011	0.014▲
	HC metabolic brain network	CAL.R	0.012	0.023	0.011*	0.011	0.034	0.015▲
		ORBsup.L	0.012	0.023	0.183	0.014	0.030	0.014▲

The table summarizes all the hub nodes of the structural and metabolic brain networks in the MCI and HC groups.
**Significant difference between the structural networks in the HC and MCI groups ($p < 0.05$), ▲Significant difference between the metabolic networks in the HC and MCI groups ($p < 0.05$).*
MCI, mild cognitive impairment; HC, healthy controls; INS.L, left insula; LING.L, left lingual gyrus; MTG.R, right middle temporal gyrus; MOG.L, left middle occipital gyrus; PET.R, right putamen; LING.R, right lingual gyrus; STG.L, left superior temporal gyrus; STG.R, right superior temporal gyrus; MTG.L, left middle temporal gyrus; HIP.R, right hippocampus; MFG.L, left middle frontal gyrus; ORBinf.L, left orbital inferior frontal gyrus; OLF.R, right olfactory cortex; PAL.L, left globus pallidus; CAL.R, right calcarine fissure and surrounding cortex; ORBsup.L, left orbital superior frontal gyrus.

Table 2 shows that the L of the MCI metabolic brain network was significantly larger than that of the HC metabolic brain network ($p = 0.047$), but there was no significant difference in C, E_{loc}, and E_{glob}.

Screening the Key Areas of Brain Function in Patients With Mild Cognitive Impairment and Hub Analysis

The node information for all the hubs in the four networks is shown in **Table 3**. The betweenness centralities of 10 hubs were significantly different between the HC structural brain network and the MCI structural brain network. These brain regions were located in the frontal lobe, occipital lobe, marginal lobe, and gray matter nucleus (**Figure 1**). The betweenness centralities of the right putamen, right lingual gyrus, left middle occipital gyrus, left orbital inferior frontal gyrus, right olfactory cortex, and left globus pallidus increased significantly in the MCI structural brain network than in the HC structural brain network, and the increase ranged from 1.018 to 3.035 times. The subsequences from high to low in increased betweenness centrality were the right lingual gyrus, left middle occipital gyrus, right putamen, left inferior frontal gyrus, right olfactory cortex, and globus pallidus, among which the increases in the left inferior frontal gyrus, right olfactory cortex, and globus pallidus in the left orbital region were the same and the smallest. The betweenness centrality of the left

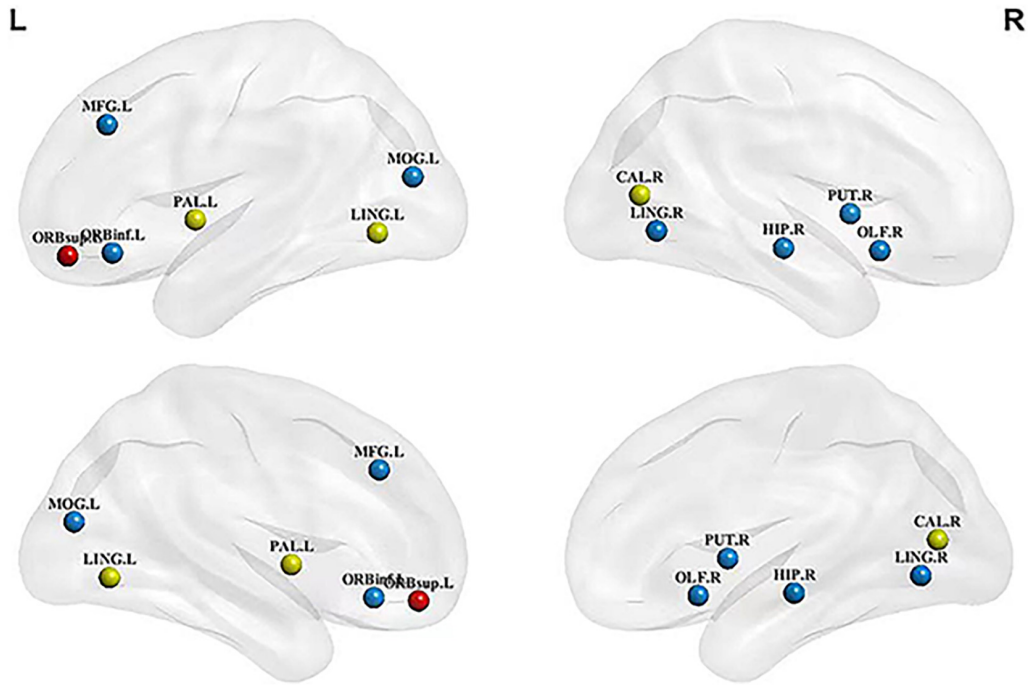

FIGURE 1 | Hubs with significant changes in structural and metabolic networks in MCI and HC groups. The blue sphere represents the hub that is significant only in the structural brain network, red sphere represents the hub that is significant only in the metabolic brain network, and yellow sphere represents the hub that is significant in both networks. There are the key brain regions related to MCI pathology. MCI, mild cognitive impairment; HC, healthy control;LING.L, left lingual gyrus; LING.R, right lingual gyrus; MFG.L, left middle frontal gyrus; ORBinf.L, left orbital inferior frontal gyrus; ORBsup.L, left orbital superior frontal gyrus; PAL.L, left globus pallidus; MOG.L, left middle occipital gyrus; CAL.R, right calcarine fissure and surrounding cortex; HIP.R, right hippocampus; PET.R, right putamen; OLF.R, right olfactory cortex.

lingual gyrus, right hippocampus, left middle frontal gyrus, right talus fissure, and surrounding cortex decreased significantly, with a range of 0.203 to 0.511 times. The subsequences from high to low in decreased betweenness centrality were the right hippocampus, left middle frontal gyrus, left lingual gyrus, and right calcarine fissure and its surrounding cortex.

Compared with the HC metabolic brain network, four hubs were significantly altered in the MCI metabolic brain network. These brain regions were distributed in the frontal and occipital lobes (**Figure 1**). Among them, the betweenness centrality of the left globus pallidus was significantly increased (2.947 times that of the HC group). The betweenness centralities of the left lingual gyrus, right calcarine fissure and its surrounding cortex, and left superior frontal gyrus of the orbital region were significantly decreased, with a range of 0.330 to 0.500 times. The subsequences from high to low in decreased betweenness centrality were the right calcarine fissure and its surrounding cortex, left superior frontal gyrus, and left lingual gyrus.

The key brain regions screened from all hub nodes were shown in the left lingual gyrus, left globus, right calcarine fissure, and its surrounding cortex. The betweenness centralities of patients in the MCI group showed significant changes in brain networks obtained from both MRI and FDG-PET scans (**Figure 2**). The betweenness centralities of the left globus pallidus in both structural and metabolic brain networks were increased in the MCI group (1.018 times and 2.947 times of the HC group, respectively), while those of the right calcarine and its surrounding cortex and left lingual gyrus in both structural and metabolic brain networks was decreased in the MCI group (0.511 times and 0.330 times of the HC group in the right calcarine and 0.434 times and 0.500 times of the HC group in the left lingual gyrus, respectively).

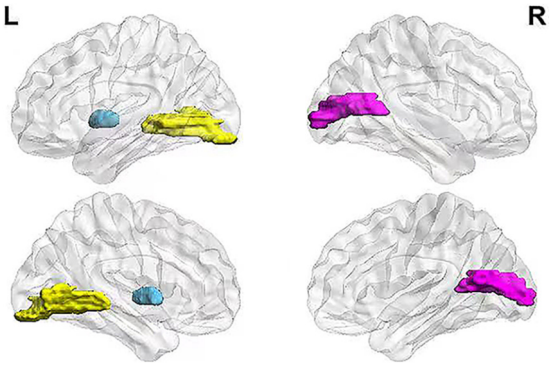

FIGURE 2 | Key brain regions related to MCI pathology. The figure shows the selected key brain regions associated with MCI pathology. The blue area represents the left globus pallidus, yellow area represents the left lingual gyrus, and pink area represents the right calcarine fissure and its surrounding cortex. MCI, mild cognitive impairment.

Correlation Analysis Between Key Brain Regions and Cognitive Function in Mild Cognitive Impairment

Partial correlations between key brain regions and cognitive scores are shown in **Figure 3**. The volume of gray matter atrophy in the left globus pallidus was positively correlated with the comprehension of spoken language (p = 0.024, corrected for multiple comparisons) and word-finding difficulty in spontaneous speech item scores (p = 0.007, corrected for multiple comparisons) in the ADAS-cog, but was not significantly correlated with other sub-items and total score items. The three key brain regions were the left glossal gyrus, left globus pallidus, and right talus cleft and its surrounding cortex, and their mean glucose intakes were significantly negatively correlated with the instruction items of the remembering test in the ADAS-cog (p = 0.020, p = 0.014, and p = 0.008, respectively, corrected for multiple comparisons). The mean glucose intake of the left globus pallidus was significantly positively correlated with the ideational praxis in ADAS-cog, with a low correlation coefficient.

DISCUSSION

This study reported that the changes in network topology parameters or hub levels of the structural brain network are more than those in the metabolic brain network in MCI. To the best of our knowledge, this is the first study to present the differences among multimodal brain networks constructed using MRI and FDG-PET data of patients with MCI. The right calcarine, left lingual, and left globus pallidus were identified as the key brain regions associated with cognitive function.

Our research showed that the topological properties of structural and metabolic brain networks differed between patients with MCI and HCs. Similar results have been reported by few single-mode brain network studies that collected data from MRI, electroencephalogram, and fMRI of patients with MCI (Stam et al., 2007; Sanz-Arigita et al., 2010; Phillips et al., 2015). The contrasting changes in the parameter intensity of two brain networks between patients with MCI and HCs were highlighted in this research. The structural brain network showed stronger small-world attribute, shorter L, higher C, lower E_{loc}, and E_{glob} than metabolic brain networks. A longer L reflects a decrease in remote connection capability, and a higher C reflects the strengthening of local connections (Yao et al., 2010). These results suggest that structural and metabolic brain networks are distinct in their internal structures and information transmission modes.

Based on the comparison of the number of changing parameters and hubs, we found differences in the topological properties of brain networks between MRI and FDG-PET in MCI. This research showed that there were four topological parameters in the structural brain networks and only one in the metabolic brain network. The L, C, E_{loc}, and E_{glob} of the structural brain network differed between the MCI group and the HC group, while only L was significantly greater in the metabolic brain network of HCs than of patients with MCI. These findings show that damage to the structural brain network may be larger than that to the metabolic brain network in the MCI disease phase. This finding is similar to that of a previous study, which was based on different construct networks obtained using DTI data and metabolic networks obtained using fMRI data. The study showed that in the structural network, patients with MCI showed lower E_{loc} and C than HCs, while no significant parameter changes were observed in the functional brain network (Filippi et al., 2020). Although the used data were different for constructing the structural and metabolic network connections, two studies showed consist results that the damage in the parameters of the structural brain network was greater than that in the parameters of the metabolic brain network in patients with MCI. In addition, a comparison of the number of hubs in the two brain networks showed that the severity of harm in the structural network is greater than in the metabolic network. As an important reflection of the high betweenness centrality of nodes in the brain network, a hub point was used to reflect the critical position of nodes in brain networks, which could be a more focused representation of changes in brain networks. In our survey, ten hubs showed significant changes in the structural brain network, while only four showed significant changes in the metabolic brain network. Our research demonstrated that structural network changes were more than the metabolic network changes at the hub level in MCI. The possible reasons for the inequality between the two networks could be the damage to the structural brain network anterior to the metabolic network. This possibility shows a certain degree of coincidence with the hypothesis proposed in a previous study, in which the patterns of functional connectivity in the brain were proposed to be determined by, but not limited to, structure (Palesi et al., 2016). In our research, the shorter side length and C of the L in the MCI structural brain network reflected a decrease in distant connection ability and an increase in local connection. We believe that this is an automatic compensation mechanism within the brain structure network. After the structural network is damaged, the internal topological properties are adjusted to retain the relatively stable parameters in the metabolic network. However, the accuracy of this conclusion needs to be verified through multi-mode brain network studies.

We obtained the key brain regions through scanning of the hubs, and the betweenness centrality of the hubs varied significantly between the MCI and HC groups in both structural and metabolic brain networks. In this study, we identified the left lingual gyrus, right talus cleft and its surrounding cortex, and left globus pallidus as the three key brain regions. The left lingual gyrus and the right talus cleft and its surrounding cortex were significantly reduced in the two brain networks, while the left globus pallidus was significantly increased and played a certain compensatory role in the flow of network information. We also investigated the association of the three key brain regions with cognitive function evaluated using ADAS-cog. We found that the volume of gray matter atrophy in the left globus pallidus was significantly positively correlated with comprehension of spoken language and word-finding difficulty in spontaneous speech item scores in ADAS-cog, while the glucose intake in the three key brain regions remained significantly negatively correlated with

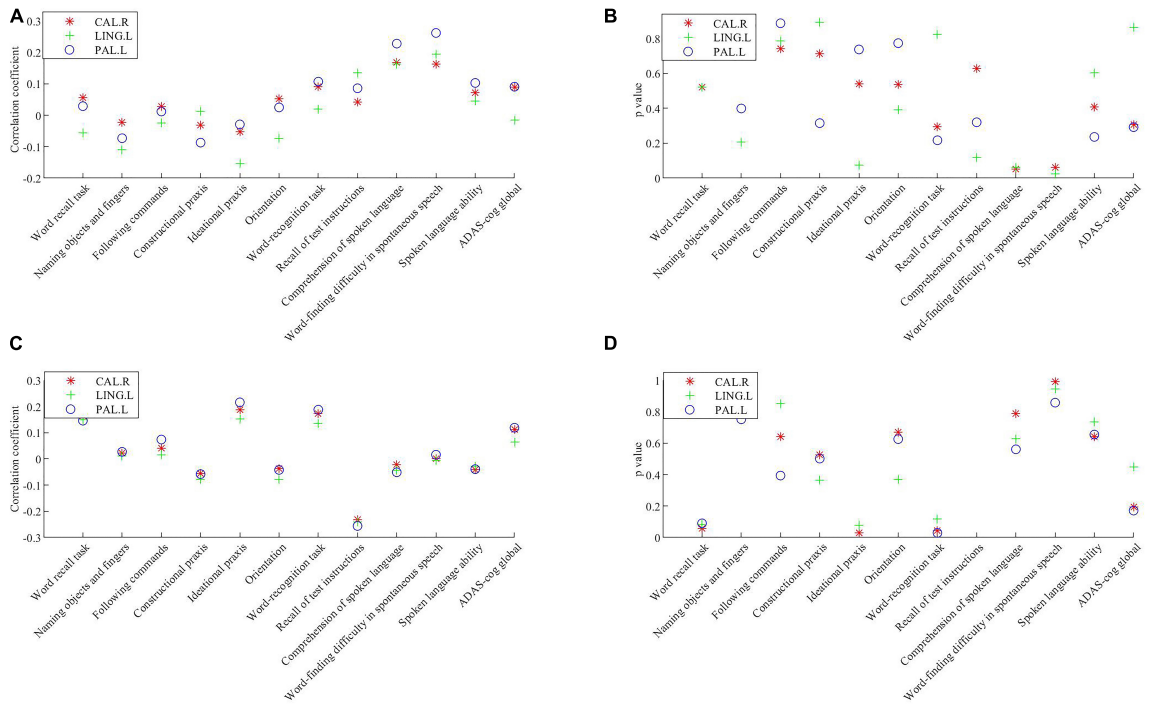

FIGURE 3 | Correlations between the volume of the gray matter atrophy/the mean glucose intake in key brain regions and cognitive scores. **(A)** Correlation coefficient between the volume of gray matter atrophy in key brain regions and cognitive scores. **(B)** *P* value of the correlations between the volume of gray matter atrophyin key brain regions and cognitive scores. **(C)** Correlation coefficient between the mean glucose intake in key brain regions and cognitive scores. **(D)** *P* value of the correlations between the mean glucose intake in key brain regions and cognitive scores. Significance was determined with a Bonferroni adjusted *p* value of 0.016. CAL.R, right calcarine fissure and surrounding cortex; LING.L, left lingual gyrus; PAL.L, left globus pallidus; ADAS-cog, Alzheimer's Disease Assessment Scale-Cognitive.

remembering test instructions items in ADAS-cog, indicating that these three key brain regions were involved in cognitive function. In previous studies, the three key brain regions have been reported to be associated with cognition. Schmidt et al. (2007) used fMRI to explore the brain mechanisms of viewpoint change in 3D spatial visual memory tasks and found that the left lingual gyrus plays a special role in the coding of spatial scene memory and center. Zhang et al. (2001) applied the echo plane technique for fMRI of blood oxygen-level dependence of the human visual cortex under two contrasting conditions of stimulation and rest and found that the lesions of the talar fiscus, which is located above the lingual gyrus and the hippocampus, may cause displacement of the visual cortex in patients with AD. The lesions of the globus pallidus may be caused by indirect dementia and cognitive dysfunction (Kim et al., 2008).

The correlation analyses performed in this study showed that the globus pallidus was related to two ADAS-cog sub-items in the structural network presented by the volume of gray matter atrophy, but only one sub-item in the metabolic network was constructed according to the value of glucose intake. In addition, both the left lingual gyrus and the right talus cleft and its surrounding cortex in the structural network were significantly correlated with one sub-item, but no significant correlation with any of the sub-items in the metabolic network was evident. We consider that the different correlations between the same brain region and sub-items in different modal images may be due to their varying roles in structural or metabolic brain networks. Interestingly, there was a significant positive correlation between glucose intake in the left globus pallidus and ideational praxis in the ADAS-cog. A possible reason could be the functional adaptation or compensation of pathology-induced injury in the course of disease change, and related mechanisms need to be discussed in future studies.

Our study is the first to report the differences in topological properties of two brain networks obtained using MRI and FDG-PET data in MCI, but has some limitations. This was a cross-sectional study. Longitudinal studies are necessary to assess the changes in brain networks during the course of the disease. The topological properties of brain networks depend on the construction methods of the networks. However, there is no consensus on the research methods for networks. In addition, all networks built in this study were group networks; therefore, the analysis of individual networks should be considered at a later stage. The HC group of this study was obtained from the ADNI database, and the results of this study should be further verified by expanding and diversifying the sample at a later stage.Moreover, in the light of the limitations of multiple comparisons, our findings should be regarded as preliminary.

In this study, we constructed cluster networks through MRI and PDG-PET images of MCI and HC groups respectively,

and compared the differences in the number of topological parameter changesas well as the differences in the number of central nodes between structural and metabolic networks. In addition, we found that the betweenness centrality of the right calcarine fissure and its surrounding cortex, left lingual gyrus, and left globus pallidusdiffered significantly between HCs and patients with MCI in both structural and metabolic networks, and both structural and metabolic brain networks were related to cognition. Our results indicate that the structural network changeslarger than the metabolic network during MCI stage, which helps us better understand the network changes during the pathogenesis of AD.Our findings highlight the important role of the construction of a multimodal brain networkin identifying key brain regions of MCI and provide insights into the use of hubs to describe the transmission of in the brain.

DATA AVAILABILITY STATEMENT

The original contributions presented in the study are included in the article/**Supplementary Material**, further inquiries can be directed to the corresponding author/s.

ETHICS STATEMENT

The studies involving human participants were reviewed and approved by Ethics Committee of Xuan Wu Hospital (No. 2017-058). The patients/participants provided their written informed consent to participate in this study.

AUTHOR CONTRIBUTIONS

XL, YC, YY, and WW collected the patients' clinical data. WZ and XK completed the data statistics. CW, SG, QZ, and WZ drafted the manuscript. CW designed the research project and revised the manuscript with BS. LJ and JL participated in the case diagnosis. All authors read and approved the final manuscript.

FUNDING

This study was supported by the National Key R&D Program of China (No. 2017YFC1310103), Beijing Municipal Administration of Hospitals Clinical Medicine Development of Special Funding Support (No. ZYLX201837; ZYLX201834), and Beijing Municipal Natural Science Foundation (No. 7192192).

ACKNOWLEDGMENTS

We would like to thank all the participants and their guardians for their cooperation and contribution to this research.

SUPPLEMENTARY MATERIAL

The Supplementary Material for this article can be found online at: https://www.frontiersin.org/articles/10.3389/fnagi.2021.774607/full#supplementary-material

REFERENCES

Alzheimer's Association (2016). 2016 Alzheimer's disease facts and figures. *Alzheimers Dement.*12, 459–509. doi: 10.1016/j.jalz.2016.03.001

Davatzikos, C., Bhatt, P., Shaw, L. M., Batmanghelich, K. N., and Trojanowski, J. Q. (2011). Prediction of MCI to AD conversion, via MRI, CSF biomarkers, and pattern classification. *Neurobiol. Aging*32, 2322.e19–27. doi: 10.1016/j.neurobiolaging.2010.05.023

Desikan, R. S., Ségonne, F., Fischl, B., Quinn, B. T., Dickerson, B. C., Blacker, D., et al. (2006). An automated labeling system for subdividing the human cerebral cortex on MRI scans into gyral based regions of interest. *Neuroimage*31, 968–980. doi: 10.1097/01.wnr.0000220135.16844.b6

Filippi, M., Basaia, S., Canu, E., Imperiale, F., Magnani, G., Falautano, M., et al. (2020). Changes in functional and structural brain connectome along the Alzheimer's disease continuum. *Mol. Psychiatry*25, 230–239. doi: 10.1038/s41380-018-0067-8

He, Y., Chen, Z., and Evans, A. (2008). Structural insights into aberrant topological patterns of large-scale cortical networks in Alzheimer's disease. *J. Neurosci.*28, 4756–4766. doi: 10.1523/JNEUROSCI.0141-08.2008

Hojjati, S. H., Ebrahimzadeh, A., and Babajani-Ferem, A. (2019). Identification of the Early Stage of Alzheimer's Disease Using Structural MRI and Resting-State fMRI. *Front. Neurol.*10:904. doi: 10.3389/fneur.2019.00904

Kim, S. H., Park, K. H., Sung, Y. H., Lee, Y. B., Park, H. M., and Shin, D. J. (2008). Dementia mimicking a sudden cognitive and behavioral change induced by left globus pallidus infarction: review of two cases. *J. Neurol. Sci.*272, 178–182. doi: 10.1016/j.jns.2008.04.031

Liu, Z., Zhang, Y., Yan, H., Bai, L., Dai, R., Wei, W., et al. (2012). Altered topological patterns of brain networks in mild cognitive impairment and Alzheimer's disease: a resting-state fMRI study. *Psychiatry Res.*202, 118–125. doi: 10.1016/j.pscychresns.2012.03.002

McKhann, G. M., Knopman, D. S., Chertkow, H., Hyman, B. T., Jack, C. R., KawasCH., et al. (2011). The diagnosis of dementia due to Alzheimer's disease: recommendations from the National Institute on Aging-Alzheimer's Association workgroups on diagnostic guidelines for Alzheimer's disease. *Alzheimers Dement.*7, 263–269. doi: 10.1016/j.jalz.2011.03.005

Mutlu, J., Landeau, B., Tomadesso, C., de Flores, R., Mézenge, F., de La Sayette, V., et al. (2016). Connectivity Disruption, Atrophy, and Hypometabolism within Posterior Cingulate Networks in Alzheimer's Disease. *Front. Neurosci.*10:582. doi: 10.3389/fnins.2016.00582

Palesi, F., Castellazzi, G., Casiraghi, L., Sinforiani, E., Vitali, P., and Gandini Wheeler-Kingshott, C. A. (2016). Exploring Patterns of Alteration in Alzheimer's Disease Brain Networks: a Combined Structural and Functional Connectomics Analysis. *Front. Neurosci.*10:380. doi: 10.3389/fnins.2016.00380

Petersen, R. C., Smith, G. E., Waring, S. C., Ivnik, R. J., Kokmen, E., and Tangelos, E. G. (1997). Aging, memory, and mild cognitive impairment. *Int. Psychogeriatr.*9, 65–69. doi: 10.1017/S1041610297004717

Phillips, D. J., McGlaughlin, A., Ruth, D., Jager, L. R., Soldan, A., and Alzheimer's Disease Neuroimaging Initiative (2015). Graph theoretic analysis of structural connectivity across the spectrum of Alzheimer's disease: the importance of graph creation methods. *Neuroimage Clin.*7, 377–390. doi: 10.1016/j.nicl.2015.01.007

Rosen, W. G., Mohs, R. C., and Davis, K. L. (1984). A new rating scale for Alzheimer's disease. *Am. J. Psychiatry*141, 1356–1364. doi: 10.1176/ajp.141.11.1356

Sanabria-Diaz, G., Martínez-Montes, E., Melie-Garcia, L., and Alzheimer's Disease Neuroimaging Initiative (2013). Glucose metabolism during resting state reveals abnormal brain networks organization in the Alzheimer's disease and mild cognitive impairment. *PLoS One*8:e68860. doi: 10.1371/journal.pone.0068860

Sanz-Arigita, E. J., Schoonheim, M. M., Damoiseaux, J. S., Rombouts, S. A., Maris, E., Barkhof, F., et al. (2010). Loss of 'small-world' networks in Alzheimer's disease: graph analysis of FMRI resting-state functional connectivity. *PLoS One*5:e13788. doi: 10.1371/journal.pone.0013788

Schmidt, D., Krause, B. J., Weiss, P. H., Fink, G. R., Shah, N. J., Amorim, M. A., et al. (2007). Visuospatial working memory and changes of the point of view in 3D space. *Neuroimage*36, 955–968. doi: 10.1016/j.neuroimage.2007.03.050

Son, S. J., Kim, J., Seo, J., Lee, J. M., Park, H., and Alzheimer's Disease Neuroimaging Initiative [ADNI] (2015). Connectivity analysis of normal and mild cognitive impairment patients based on FDG and PiB-PET images. *Neurosci. Res*.98, 50–58. doi: 10.1016/j.neures.2015.04.002

Stam, C. J., Jones, B. F., Nolte, G., Breakspear, M., and Scheltens, P. (2007). Small-world networks and functional connectivity in Alzheimer's disease. *Cereb. Cortex*17, 92–99. doi: 10.1093/cercor/bhj127

Sun, Y., Bi, Q. H., Wang, X. N., Hu, X., Li, H., Li, X., et al. (2018). Prediction of Conversion From Amnestic Mild Cognitive Impairment to Alzheimer's Disease Based on the Brain Structural Connectome. *Front. Neurol.*9:1178. doi: 10.3389/fneur.2018.01178

Sun, Y., Yin, Q., Fang, R., Yan, X., Wang, Y., Bezerianos, A., et al. (2014). Disrupted functional brain connectivity and its association to structural connectivity in amnestic mild cognitive impairment and Alzheimer's disease. *PLoS One*9:e96505. doi: 10.1371/journal.pone.0096505

Tombaugh, T. N., and McIntyre, N. J. (1992). The mini-mental state examination: a comprehensive review. *J. Am. Geriatr. Soc.*40, 922–935. doi: 10.1111/j.1532-5415.1992.tb01992.x

Xu, X., Li, W., Mei, J., Tao, M., Wang, X., Zhao, Q., et al. (2020). Feature Selection and Combination of Information in the Functional Brain Connectome for Discrimination of Mild Cognitive Impairment and Analyses of Altered Brain Patterns. *Front. Aging Neurosci.*12:28. doi: 10.3389/fnagi.2020.00028

Yao, Z., Zhang, Y., Lin, L., Zhou, Y., Xu, C., Jiang, T., et al. (2010). Alzheimer's Disease Neuroimaging Initiative. Abnormal cortical networks in mild cognitive impairment and Alzheimer's disease. *PLoS Comput. Biol.*6:e1001006. doi: 10.1371/journal.pcbi.1001006

Zhang, L., Ni, H., Yu, Z., Wang, J., Qin, J., Hou, F., et al. (2020). Investigation on the Alteration of Brain Functional Network and Its Role in the Identification of Mild Cognitive Impairment. *Front. Neurosci.*14:558434. doi: 10.3389/fnins.2020.558434

Zhang, S., Liu, L., Wu, J., Wu, J., Zhao, H., Qian, Z., et al. (2001). A preliminary study of human visual cortex and clinical application by functional magnetic resonance imaging. *Chin. J. Radiol.* 35, 44–47. doi: 10.3760/j.issn:1005-1201.2001.07.011

Zheng, W., Yao, Z., Li, Y., Zhang, Y., Hu, B., Wu, D., et al. (2019). Brain connectivity based prediction of Alzheimer's disease in patients with mild cognitive impairment based on multi-modal images. *Front. Hum. Neurosci.*13:399. doi: 10.3389/fnhum.2019.00399

Conflict of Interest: The authors declare that the research was conducted in the absence of any commercial or financial relationships that could be construed as a potential conflict of interest.

frontiers in Aging Neuroscience

ORIGINAL RESEARCH
published: 26 January 2022
doi: 10.3389/fnagi.2021.789099

Radiomic Features of the Hippocampus for Diagnosing Early-Onset and Late-Onset Alzheimer's Disease

Yang Du[1,2†], Shaowei Zhang[1,2†], Yuan Fang[1], Qi Qiu[1], Lu Zhao[1], Wenjing Wei[1], Yingying Tang[3] and Xia Li[1,2]**

[1]Department of Geriatric Psychiatry, Shanghai Mental Health Center, Shanghai Jiao Tong University School of Medicine, Shanghai, China, [2]Alzheimer's Disease and Related Disorders Center, Shanghai Jiao Tong University, Shanghai, China, [3]Shanghai Key Laboratory of Psychotic Disorders, Shanghai Mental Health Center, Shanghai Jiao Tong University School of Medicine, Shanghai, China

OPEN ACCESS

Edited by:
Ping Wu,
Fudan University, China

Reviewed by:
Nacim Betrouni,
INSERM U1171 Troubles Cognitifs Dégénératifs et Vasculaires, France
Niharika Gajawelli,
Children's Hospital of Los Angeles, United States

***Correspondence:**
Yingying Tang
yytang0522@gmail.com
Xia Li
lixia11111@sjtu.edu.cn

†These authors have contributed equally to this work

Specialty section:
This article was submitted to Alzheimer's Disease and Related Dementias, a section of the journal Frontiers in Aging Neuroscience

Received: 04 October 2021
Accepted: 28 December 2021
Published: 26 January 2022

Citation:
Du Y, Zhang S, Fang Y, Qiu Q, Zhao L, Wei W, Tang Y and Li X (2022) Radiomic Features of the Hippocampus for Diagnosing Early-Onset and Late-Onset Alzheimer's Disease. Front. Aging Neurosci. 13:789099. doi: 10.3389/fnagi.2021.789099

Background: Late-onset Alzheimer's disease (LOAD) and early-onset Alzheimer's disease (EOAD) are different subtypes of AD. This study aimed to build and validate radiomics models of the hippocampus for EOAD and young controls (YCs), LOAD and old controls (OCs), as well as EOAD and LOAD.

Methods: Thirty-six EOAD patients, 36 LOAD patients, 36 YCs, and 36 OCs from the Alzheimer's Disease Neuroimaging Initiative (ADNI) database were enrolled and allocated to training and test sets of the EOAD-YC groups, LOAD-OC groups, and EOAD-LOAD groups. Independent external validation sets including 15 EOAD patients, 15 LOAD patients, 15 YCs, and 15 OCs from Shanghai Mental Health Center were constructed, respectively. Bilateral hippocampal segmentation and feature extraction were performed for each subject, and the least absolute shrinkage and selection operator (LASSO) method was used to select radiomic features. Support vector machine (SVM) models were constructed based on the identified features to distinguish EOAD from YC subjects, LOAD from OC subjects, and EOAD from LOAD subjects. The areas under the receiver operating characteristic curves (AUCs) were used to evaluate the performance of the models.

Results: Three, three, and four features were selected for EOAD and YC subjects, LOAD and OC subjects, and EOAD and LOAD subjects, respectively. The AUC and accuracy of the SVM model were 0.90 and 0.77 in the test set and 0.91 and 0.87 in the validation set for EOAD and YC subjects, respectively; for LOAD and OC subjects, the AUC and accuracy were 0.94 and 0.86 in the test set and 0.92 and 0.78 in the validation set, respectively. For the SVM model of EOAD and LOAD subjects, the AUC was 0.87 and the accuracy was 0.79 in the test set; additionally, the AUC was 0.86 and the accuracy was 0.77 in the validation set.

Conclusion: The findings of this study provide insights into the potential of hippocampal radiomic features as biomarkers to diagnose EOAD and LOAD. This study is the first to show that SVM classification analysis based on hippocampal radiomic features is a valuable method for clinical applications in EOAD.

Keywords: early-onset Alzheimer's disease, late-onset Alzheimer's disease, hippocampus, radiomics, support vector machine

INTRODUCTION

Alzheimer's disease (AD), characterized by progressive cognitive dysfunction, is a common neurodegenerative disorder that significantly affects the quality of life of patients (DeTure and Dickson, 2019). AD is clinically classified into early-onset AD (EOAD) and late-onset AD (LOAD) based on the age of symptom onset (Tellechea et al., 2018). A recent study has suggested considerable differences between EOAD and LOAD in etiological and clinical heterogeneity (Ayodele et al., 2021). Compared with LOAD patients, EOAD patients exhibit more aggressive disease progression and an atypical presentation of preserved memory function but focal cortical symptoms such as language, visuospatial, and executive dysfunction (Cacace et al., 2016).

Consistent with the differences in clinical characteristics, EOAD and LOAD patients also exhibit distinctions in neuroimaging findings. Previous structural imaging studies have shown that compared with LOAD patients, EOAD patients present with less atrophy in the hippocampus but more severe atrophy in the neocortex, particularly the parietal and precuneus and posterior cingulate cortices (Moller et al., 2013; Cavedo et al., 2014; Joubert et al., 2016). Furthermore, some resting-state functional magnetic resonance imaging (fMRI) studies have indicated that patients with EOAD exhibit functional disruption between the hippocampus and middle frontal cortex, while LOAD patients show more widely disrupted hippocampal functional connectivity (Park et al., 2017; Li et al., 2018). These findings indicate that AD is a heterogeneous disorder with significant differences between EOAD and LOAD. Therefore, the hippocampus is likely to exert a specific effect on the pathologies of the two subtypes of AD and function as a useful biomarker in the differential diagnosis of EOAD and LOAD.

Radiomics, an emerging imaging analysis method, can objectively and quantitatively describe phenotypic information using advanced imaging features (Gillies et al., 2016). Radiomic features refer to histogram-based features, including skewness and kurtosis, and texture-based features, such as the gray-level cooccurrence matrix (GLCM) and the gray-level run-length matrix (GLRLM), which provide microstructural information unique from that indicated by volumetric measures (Mayerhoefer et al., 2020). Currently, radiomics has been widely applied to MRI and positron emission tomography (PET) as imaging biomarkers of AD (Cai et al., 2020). Recent MRI-based radiomics studies have shown that textural features of the hippocampus are valid to distinguish AD patients from healthy controls (Chaddad et al., 2018; Feng et al., 2018, 2019; Luk et al., 2018; Li et al., 2020). Several studies have suggested that hippocampal texture is superior to volume changes as a predictor of AD (Beheshti et al., 2017; Shu et al., 2021). However, most of the above studies have concentrated on the textural features of the hippocampus in patients with LOAD, and several studies included both EOAD and LOAD patients as a whole AD group, missing an opportunity to identify differences between the two subtypes of AD. No evidence exists regarding the extraction and modeling of radiomic features between EOAD and healthy subjects or between EOAD and LOAD patients.

In this study, we are the first to investigate and validate hippocampus-based radiomic features for diagnosing EOAD patients and young healthy subjects. Additionally, we sought to ascertain hippocampal texture as a good biomarker in patients with LOAD and old healthy subjects. Furthermore, this study is the first to explore and validate hippocampal radiomic features and construct classification models for distinguishing between patients with EOAD and LOAD.

METHODS

Study Participants

The training and test data used in this study were obtained from the Alzheimer's Disease Neuroimaging Initiative (ADNI) database[1]. The ADNI was launched in 2003 as a public-private partnership led by the National Institute on Aging (NIA), the Food and Drug Administration (FDA), and National Institute of Biomedical Imaging and Bioengineering (NIBIB). The ADNI aims to aid researchers and clinicians in developing new treatments and monitoring their effectiveness as well as to lessen the time and cost of clinical trials. Up-to-date information can be found at www.adni-info.org. The use of the ADNI data was approved by the institutional review board at each site, and all the participants provided their written consent.

A total of 144 ADNI participants were included in this study 36 EOAD, 36 LOAD, 36 young control (YC), and 36 old control (OC) participants from the ADNI1, ADNI2/GO, and ADNI3 databases. Scans were collected at either screening or baseline visits. First, 36 patients diagnosed with AD onset before the age of 65 years (EOAD) who were enrolled in the ADNI database were eligible for this study. Next, we included 36 patients who were 65 years or older at disease onset (LOAD) and who were 1:1 matched to the EOAD patients by the Clinical Dementia Rating (CDR) Scale. Accordingly, we selected two control groups for each patient group. The controls were matched 1:1 to AD patients for age and sex, thus obtaining a YC group for EOAD (n = 36; YC) and an OC group for LOAD

[1]http://adni.loni.usc.edu

(n = 36; OC). Furthermore, demographic information, medical history, baseline symptoms, and assessment scale scores were included. The MRI and clinical data were downloaded in June 2021.

Independent external validation data were acquired from the Memory Clinic of Shanghai Mental Health Center (SMHC) between July 2017 and May 2021, and normal control subjects were recruited from the community. A total of 60 participants including 15 EOAD, 15 LOAD, 15 YCs, and 15 OCs were enrolled in this study. Similarly, 15 LOAD patients were also 1:1 matched to the EOAD patients using the CDR Scale, and the controls were matched to AD patients for age and sex. EOAD and LOAD patients were diagnosed by two experienced geriatric psychiatrists. The exclusion criteria included the following: (1) other psychiatric disorders comorbidities; (2) a history of major physical illness, cardiovascular disease, or neurological disorder; (3) substance abuse or dependence; (4) pregnancy. Neuropsychological tests and brain imaging scans were performed in all subjects. The retrospective study was approved by the ethics committee of the Shanghai Mental Health Centre of Shanghai Jiao Tong University School of Medicine, and all the participants provided written informed consent after they were given a description of this study.

Image Acquisition

Regarding ADNI data, T1-weighted structural imaging was collected using a 3D MPRAGE (magnetization prepared rapid gradient-echo imaging) sequence with slightly different MR parameters among participants. The MR images acquired using Siemens scanner were scanned with the parameters as follows: repetition *time* (TR) = 2,300 ms, matrix = 240 × 256 × 176, slice thickness = 1.2 mm, and those parameters in General Electric scanner were as follows: TR = 7 ms, matrix = 256 × 256 × 166, slice thickness = 1.2 mm and those parameters in Philips scanner were as follows: TR = 6.8 ms, matrix = 256 × 256 × 170, slice thickness = 1.2 mm, respectively. More detailed information about the image acquisition procedures is available on the ADNI website[2]. Additionally, the MR data of Shanghai Mental Health Center were acquired using a Siemens Magnetom Verio 3.0 T scanner, and high-resolution T1-weighted structural images with 176 sagittal slices were collected using a MPRAGE sequence (TR = 2,530 ms, TE = 3.5 ms, flip angle = 9°, FOV = 256 mm × 256 mm, voxel size = 1.0 × 1.0 × 1.2 mm^3).

Imaging Preprocessing

Standardized preprocessing was necessary to improve discrimination between textural features and was performed using Statistical Parametric Mapping (SPM12) software[3] implemented in MATLAB R2017a (The MathWorks, Natick, MA, USA). Firstly, each T1-weighted Digital Imaging and Communications in Medicine (DICOM) image was converted to Neuroimaging Informatics Technology Initiative (NIFTI) data. Secondly, correction for bias field inhomogeneities and intensity normalization of images were performed in the VBM12 toolbox. The corrected images were normalized to the Montreal Neurological Institute (MNI) standard T1 template (standard space 181 × 217 × 181 with a resolution of 1 mm × 1 mm × 1 mm) using DARTEL normalization. Then, the obtained images were spatially normalized to ensure that a given voxel corresponded to the same anatomical position in different subjects. Finally, we resliced those images to the standard MNI space with a resolution of 1 mm × 1 mm × 1 mm.

Segmentation

Segmentation of the hippocampus was required to describe the texture characteristics of the region of interest (ROI). First, the bilateral hippocampus from the Anatomical Automatic Labeling (AAL) template provided by the MNI was chosen as the ROI mask. Then, the open-source software 3D-slicer[4] was applied for medical image visualization and segmentation (Fedorov et al., 2012). Specifically, the viewer window of 3D-Slicer was used to select image "layers", including "background" image and "label" image. Then, the standardized preprocessing image of each subject was loaded as the "background" image, and the left and right hippocampus mask was loaded as the"label" image, respectively. Next, two expert radiologists worked together to check the segmentation of the hippocampus for each subject and manually modified the unsatisfied image in the "Segment Editor" window of 3D slicer after reaching a consensus. In fact, a previous study has shown that the dice similarity coefficient (DSC) between the manual segmentation and atlas-based methods in brain structure segmentation are 0.79 (Ourselin et al., 2013). In our study, the combination of atlas-based segmentation and manual inspections could assure the segmentation quality and improve the time consumption.

Feature Extraction

First, we loaded the standardized 3D T1-MPRAGE data for the EOAD, LOAD, YC, and OC subjects into 3D-slicer software, and then we imported the segmented left and right hippocampus. Massive features were selected using the "pyradiomics" package of the software[5], including the histogram-based matrix (HISTO), GLCM, gray-level dependence matrix (GLDM), gray-level size zone matrix (GLSZM), GLRLM, and neighboring gray-tone difference matrix (NGTDM) in the "feature classes" window.

HISTO is a statistical description of discrete units, while the GLCM using second-order statistics reflects the spatial relationship of pixel gray-level values in the image (Dhruv et al., 2019). The GLDM is also based on the gray-level relationship to acquire the first-order statistics of local property values, and the GLRLM estimates the spatial relationships between groups of pixels with similar gray-level values (Araujo et al., 2018). The GLSZM can be used to compute different pixel distances, whereas the NGTDM measures the total differences in the gray level of a pixel (Thibault et al., 2014).

Feature Selection

Before feature selection, preprocessing was required for accurate and valid selection. First, we checked the extracted data and replaced the abnormal values that deviated more than three

[2]http://adni.loni.usc.edu/methods/documents/
[3]http://www.fil.ion.ucl.ac.uk/spm/software/spm12/
[4]https://www.slicer.org/
[5]http://www.jetbrains.com/pycharm/

standard deviations from the mean by the mean. Considering that deleting the abnormal values may cause loss of information and the lack of processing may affect the model construction, combined with the normal distribution of the data, we decided to replace outliers with the mean. Next, the subjects from ADNI data were randomly divided into training and test datasets at proportions of 0.7 and 0.3 for EOAD-YC groups, LOAD-OC groups, and EOAD-LOAD groups, respectively. Then, every extracted feature was standardized by the function of sklearn.preprocessing.scale based on Python programming to achieve Z-score normalization to remove the dimensional constraint.

We used Python programming to accomplish feature selection. First, t-test and Mann-Whitney U test were used to select the features with significant differences ($p < 0.05$). Next, correlation analysis was performed to further reduce the dimensionality. If the correlation coefficient of two feature columns exceeded 0.8, we removed one of them randomly. Finally, the least absolute shrinkage and selection operator (LASSO) regression analysis method with 10-fold cross validation was applied to determine the most valid features in the training data, and the corresponding lambda value was selected with minimum mean-squared error (MSE) values. The mechanism of LASSO, combining the penalty function and linear regression, makes some regression coefficients become zero and achieve dimension reduction (Tibshirani, 2013).

Classification Analysis

Support vector machine (SVM) algorithms were used to construct radiomic models for EOAD and YCs, LOAD and OCs, and EOAD and LOAD. SVM is one of the most popular and mature machine learning algorithms based on the neuroimaging literature (Orru et al., 2012). The SVM model employs a radial basis function kernel using LIBSVM[6] to implement nonlinear mapping from the input space to the feature space (Chang and Lin, 2011). Accordingly, the SVM models were used to construct the prediction models of the EOAD-YC groups, LOAD-OC groups, and EOAD-LOAD groups based on the selected prediction features in training sets, and then the test sets were used to calculate the predictive efficiency based on the predictive models, respectively (Nalepa and Kawulok, 2019). Then, all subjects from the data from Shanghai Mental Health Center were used as independent external validation sets to verify the reliability and robustness of the corresponding models. Additionally, receiver operating characteristic (ROC) curves and the corresponding areas under the curve (AUCs) were used to evaluate the diagnostic capabilities of the radiomic features.

Statistical Analysis

Statistical analyses were performed using SPSS software 22.0 (IBM Corporation, Armonk, NY). The demographic information of the participants was collected as numbers or means ± SD for categorical and continuous variables. The comparisons between the EOAD and OC (EOAD-OC), LOAD and YC (LOAD-YC), and EOAD and LOAD (EOAD-LOAD) subjects were performed using χ^2 test for categorical variables and Student's t-test for continuous variables (two-tailed) to evaluate the differences between groups. A $p < 0.05$ was considered statistically significant.

[6]http://www.csie.ntu.edu.tw/∼cjlin/libsvm/index.html

RESULTS

Demographic and Clinical Characteristics

The demographic and clinical characteristics of the four groups are presented in **Table 1**. No difference was found in age or sex between the EOAD patients and YCs (EOAD-YC) or between the LOAD patients and OCs (LOAD-OC) in the ADNI and SMHC data. The Mini-Mental State Examination (MMSE) scores were significantly different in the EOAD-YC and LOAD-OC groups ($p < 0.001$). No significant differences were found in the clinical dementia rating (CDR) scores and MMSE scores between the EOAD and LOAD patients (EOAD-LOAD).

Feature Selection Results

A total of 214 features were extracted from the bilateral hippocampus. After t-test and Mann-Whitney U test, 99, 102, and 37 features were preserved in the EOAD-YC, LOAD-OC, and EOAD-LOAD groups, respectively. After correlation analysis, 51, 73, and 24 (**Figure 1**) features remained. Finally, the LASSO regression model identified three, four, and four features for the EOAD-YC, LOAD-OC, and EOAD-LOAD groups (**Table 2**). Meanwhile, the values of the coefficients and the corresponding lambda values, and the MSE values and the corresponding lambda values for the EOAD-YC, LOAD-OC, and EOAD-LOAD groups are shown in **Figure 2**.

Classification Analysis Results

The accuracy (ACC), sensitivity (SEN), specificity (SPE), and AUC were used to evaluate the classification performance. **Figure 3** and **Table 3** show the final classification performance on the test set and validation set. In the analysis between the EOAD patients and YCs, the ACC, SEN, SPE, and AUC were 0.77, 0.91, 0.64, and 0.90 in the test set and 0.87, 0.87, 0.87, and 0.91 in the validation set, respectively (**Figure 3A**). By contrast, in the LOAD patients and OCs, the ACC, SEN, SPE, and AUC were 0.86, 0.87, 0.86, and 0.94 in the test set and 0.78, 0.85, 0.70, and 0.92 in the validation set, respectively (**Figure 3B**). Finally, in the analysis between the EOAD and LOAD patients, the ACC, SEN, SPE, and AUC were 0.79, 0.67, 0.93, and 0.87 in the test set and 0.77, 0.60, 0.93, and 0.86 in the validation set, respectively (**Figure 3C**). Similar classification performance was found in the test and validation datasets, indicating that our models may have relatively good robustness.

DISCUSSION

The present study aimed to explore hippocampal radiomic features to distinguish between patients with EOAD and LOAD and healthy controls. Our findings show that the hippocampal radiomic-based classification model can discriminate patients with EOAD from YC subjects and distinguish LOAD patients from OC participants. Additionally,

TABLE 1 | Demographic, clinical parameters for EOAD, LOAD, YC, and OC subjects.

	EOAD	YC	*p*	LOAD	OC	*p*	*P* (EOAD vs. LOAD)
ADNI data							
N	36	36		36	36		1
Age, y	59.80 ± 2.8	60.40 ± 2.4	0.31	72.45 ± 2.8	72.08 ± 1.4	0.48	<0.001
Gender, F(%)	18 (50%)	18 (50%)	1	19 (53%)	19 (53%)	1	0.81
CDR	0.8	-	-	0.8	-	-	1
MMSE	23.0 ± 1.6	29.0 ± 0.9	<0.001	22.5 ± 3.0	29.2 ± 0.4	<0.001	0.63
SMHC data							
N	15	15		15	15		1
Age, y	58.15 ± 5.4	59.85 ± 4.2	0.34	74.05 ± 5.8	73.51 ± 3.6	0.76	<0.001
Gender, F(%)	9 (60%)	9 (60%)	1	8 (53%)	8 (53%)	1	0.71
CDR	0.75	-	-	0.75	-	-	1
MMSE	22.1 ± 1.1	29.1 ± 0.7	<0.001	21.7 ± 1.8	28.3 ± 0.6	<0.001	0.47

Values presented as mean ± standard deviation. EOAD, early-onset Alzheimer's disease; LOAD, late-onset Alzheimer's disease; YC, young control; OC, old control; CDR, Clinical Dementia Rating Scale; MMSE, Mini-Mental State Examination.

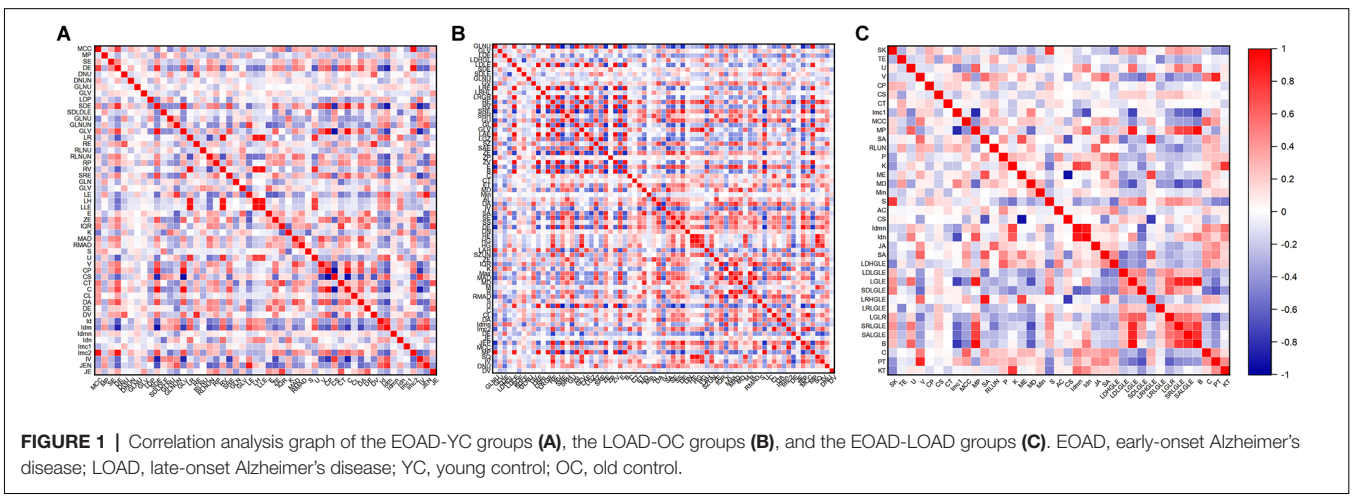

FIGURE 1 | Correlation analysis graph of the EOAD-YC groups **(A)**, the LOAD-OC groups **(B)**, and the EOAD-LOAD groups **(C)**. EOAD, early-onset Alzheimer's disease; LOAD, late-onset Alzheimer's disease; YC, young control; OC, old control.

TABLE 2 | The preserved radiomic features after the feature selection.

Type of features	EOAD-YC	LOAD-OC	EOAD-LOAD
Histogram	Kurtosis	Kurtosis Skewness	Kurtosis
GLCM	IMC1	IDMN	IDMN
GLDM		Dependence Entropy	Small Dependence Low Gray Level Emphasis
GLRLM			Long Run Low Gray Level Emphasis
NGTDM	Coarseness		

GLCM, Gray-Level Co-Occurrence Matrix; GLDM, Gray Level Dependence Matrix; GLRLM, Gray-Level Run-Length Matrix; NGTDM, Neighbouring Gray Tone Difference Matrix; IMC1, Informational Measure of Correlation (IMC) 1; IDMN, Inverse difference moment normalized.

hippocampal texture was identified as a useful biomarker for LOAD and EOAD patients. Additionally, results from other datasets verified the generalizability and robustness of the models.

To our knowledge, this study is the first to construct a classification model of hippocampal radiomic features for EOAD patients and healthy subjects. This model reveals relatively good accuracy and sensitivity with a successful diagnostic value. Although EOAD patients account for 5–10% of reported AD cases (Lambert et al., 2014), this AD subtype is valuable to understand the underlying mechanism. Currently, studies on patients with EOAD have focused particularly on structural magnetic resonance imaging (sMRI; Yang et al., 2019). A quantitative analysis of the hippocampal volume in EOAD patients suggested that hippocampal atrophy has limited usefulness as a diagnostic biomarker for these patients (Falgas et al., 2019). Radiomic features, different from volumetric features, have captured considerable information and have shown great promise for personalized clinical applications (Avanzo et al., 2017). Our results show that the radiomic features of the hippocampus can be defined as a useful biomarker to identify EOAD patients and healthy controls, with great promise for personalized clinical application.

Our findings indicate that the hippocampal radiomic model presented excellent diagnostic value with good sensitivity and specificity to distinguish LOAD patients from OCs. Consistent with our results, radiomic analysis has been used to identify hippocampal features to distinguish LOAD patients from healthy control subjects. Chaddad et al. (2018) employed random forest (RF) models to identify hippocampal textural features to

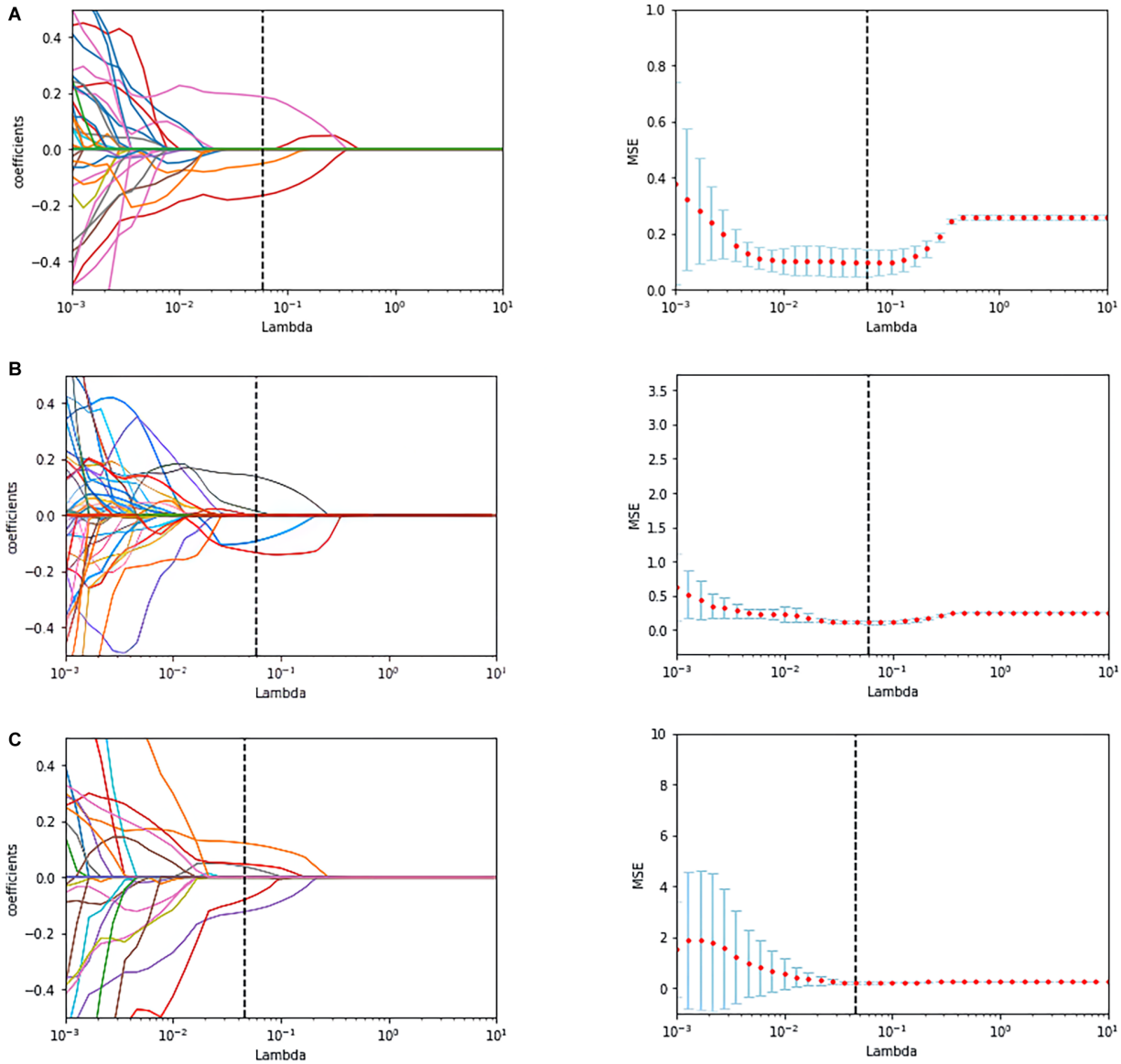

FIGURE 2 | The coefficients-lambda graph and the MSE-lambda graph **(A)** in the EOAD-YC groups, the LOAD-OC groups **(B)**, and the EOAD-LOAD groups **(C)**. MSE, mean-squared error.

differentiate LOAD patients from normal controls (NCs) with an AUC of 0.84. Feng et al. (2018) demonstrated hippocampal radiomic features that distinguish LOAD patients from NCs with a classification accuracy of 0.87 *via* the SVM model. Luk et al. (2018) calculated a logistic regression model to classify LOAD patients and NCs, and the AUC was 0.93. Liu et al. (2018) achieved an AUC of 0.90 for classifying LOAD patients and NCs based on convolutional neural networks (CNNs). Furthermore, recent evidence suggests that hippocampal texture is significantly superior to hippocampal volumetry in the early detection of AD (Sorensen et al., 2016; Luk et al., 2018). Taken together, our findings support the significance of hippocampal textural features as promising neuroimaging biomarkers of AD.

Another important finding in this study worth noting is the relatively satisfying classification model of hippocampal radiomic features between EOAD and LOAD patients. This model has demonstrated relatively high specificity and accuracy with moderate diagnostic value. Notably, no radiomic analysis has investigated the radiomic features of brain regions to distinguish EOAD patients from LOAD patients directly. More recent attention has focused on neuroimaging analysis methods, including voxel-based morphometry (VBM), fMRI, diffusion tensor imaging (DTI), and multimodal MRI, to detect structural and functional changes in AD (Herdick et al., 2020). A recent structural MRI study revealed that compared with healthy controls, EOAD and LOAD patients exhibit a similar pattern of hippocampal atrophy (Eckerstrom et al., 2018). Therefore, it

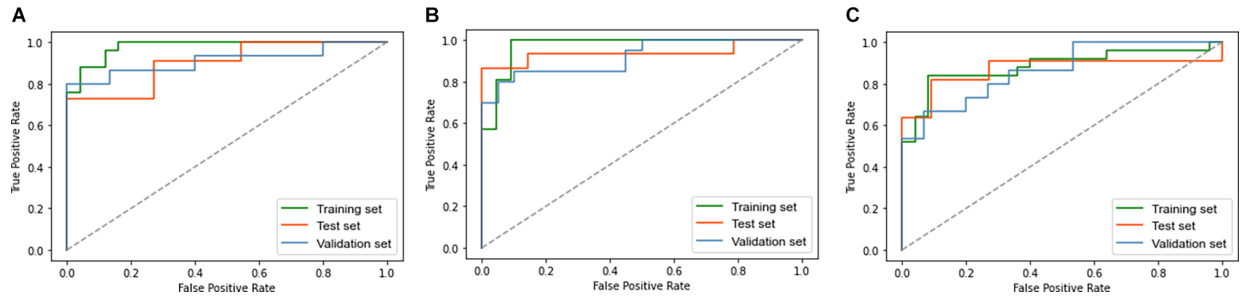

FIGURE 3 | The ROC curve of the EOAD-YC groups in the training and test and validation sets **(A)**. The ROC curve of the LOAD-OC groups in the training and test and validation sets **(B)**. The ROC curve of the EOAD-LOAD groups in training and test and validation sets **(C)**. ROC, receiver operating characteristic.

TABLE 3 | Classification performance on test and validation datasets.

		Accuracy	Sensitivity	Specificity	AUC
EOAD-YC	Training set	0.90	0.94	0.88	0.95
	Test set	0.77	0.91	0.64	0.90
	Validation set	0.87	0.87	0.87	0.91
LOAD-OC	Training set	0.91	0.96	0.82	0.97
	Test set	0.86	0.87	0.86	0.94
	Validation set	0.78	0.85	0.70	0.92
EOAD-LOAD	Training set	0.86	0.84	0.88	0.88
	Test set	0.79	0.67	0.93	0.87
	Validation set	0.77	0.60	0.93	0.86

AUC, areas under the curve.

may be a challenge to distinguish between EOAD and LOAD relying on structural MRI. Radiomic analysis can extract and model many medical image features, and promises to increase precision in diagnosis and provide decision support for precision medicine (Lambin et al., 2017). Thus, radiomic studies of EOAD deserve higher priority. Our findings support the hypothesis that hippocampal radiomic features are valuable to distinguish the two types of AD.

Furthermore, in this study, three radiomic features were selected for the EOAD-YC groups—namely, kurtosis, coarseness, and informational measure of correlation 1 (IMC1). Kurtosis measures the degree of histogram sharpness, coarseness reflects the spatial rate of changes in gray-level intensities, and IMC1 captures the spatial relationships of pairs of pixels (Guiot et al., 2022). Concerning the LOAD-OC groups, kurtosis, skewness, inverse difference moment normalized (IDMN), and dependence entropy were filtered. Kurtosis and skewness are the parameters of the histogram, and skewness describes the degree of histogram asymmetry. IDMN describes texture homogeneity, whereas dependence entropy reflects the complexity in gray distribution (Salvatore et al., 2021). Additionally, four radiomic features—kurtosis, IDMN, small dependence low gray-level emphasis (SDLGLE), and long-run low gray-level emphasis (LRLGLE) were selected for the EOAD-LOAD groups. The first two features were consistent with the LOAD-OC groups. SDLGLE and LRLGLE are the parameters of GLDM and GLRLM, respectively. SDLGLE measures the joint distribution of small dependence with lower gray-level values, while LRLGLE evaluates the joint distribution of long run lengths with lower gray-level values (van Griethuysen et al., 2017). In summary, our results indicate differences and similarities in radiomic features among the EOAD-YC, LOAD-OC, and EOAD-LOAD groups.

This study has some limitations. First, owing to the relatively low prevalence rates for EOAD (Zhu et al., 2015), the limited sample size may affect the performance of the radiomic models. Second, the hippocampus is a heterogeneous structure encompassing different subregions, each of which may have distinct textural features (Blanken et al., 2017). Further studies regarding the radiomic features of hippocampal subregions are warranted. Finally, more longitudinal studies are needed combining texture with cerebrospinal fluid (CSF) and genomic and metabolic markers to achieve an accurate screening, diagnostic, and monitoring tool for clinical applications (Li et al., 2019).

CONCLUSION

In conclusion, we found that hippocampal radiomic features can be used to distinguish patients with EOAD and LOAD from YCs and OCs. Furthermore, this study reports the moderately successful diagnostic classification of EOAD vs. LOAD based on hippocampal radiomic features. Generally, our findings support the possibility that hippocampal textural features may serve as potential neuroimaging biomarkers of AD, providing a useful tool for decision support in precision medicine.

DATA AVAILABILITY STATEMENT

The datasets presented in this study can be found in online repositories. The names of the repository/repositories and accession number(s) can be found below: http://adni.loni.usc.edu. The datasets from Shanghai Mental Health Center generated for this study are available on request to the corresponding author.

ETHICS STATEMENT

The studies involving human participants were reviewed and approved by Shanghai Mental Health Center. The patients/participants provided their written informed consent to participate in this study. The use of the ADNI data was approved

by the institutional review board at each site. Written informed consent was obtained from the individual(s) for the publication of any potentially identifiable images or data included in this article.

AUTHOR CONTRIBUTIONS

XL, YT, and YD conceived the study. YD, SZ, YF, QQ, LZ, and WW acquired and analyzed the data. YD and SZ drafted the manuscript. All authors contributed to the article and approved the submitted version.

FUNDING

This study was supported by grants of the National Key Research and Development Program of China (2017YFC1310500) and Shanghai Fifth Round of Public Health Three-year Action Plan (GMV-9.2).

REFERENCES

Araujo, A. S., Conci, A., Moran, M., and Resmini, R. (2018). "Comparing the use of sum and difference histograms and gray levels occurrence matrix for texture descriptors," in *2018 International Joint Conference on Neural Networks (IJCNN)*, (Rio de Janeiro, Brazil), 1–8. doi: 10.1109/IJCNN.2018.8489705

Avanzo, M., Stancanello, J., and El Naqa, I. (2017). Beyond imaging: the promise of radiomics. *Phys. Med.* 38, 122–139. doi: 10.1016/j.ejmp.2017.05.071

Ayodele, T., Rogaeva, E., Kurup, J. T., Beecham, G., and Reitz, C. (2021). Early-onset Alzheimer's disease: what is missing in research? *Curr. Neurol. Neurosci. Rep.* 21:4. doi: 10.1007/s11910-020-01090-y

Beheshti, I., Maikusa, N., Daneshmand, M., Matsuda, H., Demirel, H., and Anbarjafari, G. (2017). Classification of Alzheimer's disease and prediction of mild cognitive impairment conversion using histogram-based analysis of patient-specific anatomical brain connectivity Networks. *J. Alzheimers Dis.* 60, 295–304. doi: 10.3233/JAD-161080

Blanken, A. E., Hurtz, S., Zarow, C., Biado, K., Honarpisheh, H., Somme, J., et al. (2017). Associations between hippocampal morphometry and neuropathologic markers of Alzheimer's disease using 7 T MRI. *Neuroimage Clin.* 15, 56–61. doi: 10.1016/j.nicl.2017.04.020

Cacace, R., Sleegers, K., and Van Broeckhoven, C. (2016). Molecular genetics of early-onset Alzheimer's disease revisited. *Alzheimers Dement.* 12, 733–748. doi: 10.1016/j.jalz.2016.01.012

Cai, J. H., He, Y., Zhong, X. L., Lei, H., Wang, F., Luo, G. H., et al. (2020). Magnetic resonance texture analysis in Alzheimer's disease. *Acad. Radiol.* 27, 1774–1783. doi: 10.1016/j.acra.2020.01.006

Cavedo, E., Pievani, M., Boccardi, M., Galluzzi, S., Bocchetta, M., Bonetti, M., et al. (2014). Medial temporal atrophy in early and late-onset Alzheimer's disease. *Neurobiol. Aging* 35, 2004–2012. doi: 10.1016/j.neurobiolaging.2014.03.009

Chaddad, A., Niazi, T., and Ieee, . (2018). *Radiomics Analysis of Subcortical Brain Regions Related to Alzheimer Disease.* New York: IEEE

Chang, C.-C., and Lin, C.-J. (2011). Libsvm: a library for support vector machines. *ACM Trans. Intell. Systems Technol.* 2:27. doi: 10.1145/1961189.1961199

DeTure, M. A., and Dickson, D. W. (2019). The neuropathological diagnosis of Alzheimer's disease. *Mol. Neurodegener.* 14:32. doi: 10.1186/s13024-019-0333-5

Dhruv, B., Mittal, N., and Modi, M. (2019). Study of Haralick's and GLCM texture analysis on 3D medical images. *Int. J. Neurosci.* 129, 350–362. doi: 10.1080/00207454.2018.1536052

Eckerstrom, C., Klasson, N., Olsson, E., Selnes, P., Rolstad, S., and Wallin, A. (2018). Similar pattern of atrophy in early- and late-onset Alzheimer's disease. *Alzheimers Dement. (Amst)* 10, 253–259. doi: 10.1016/j.dadm.2018.02.001

Falgas, N., Sanchez-Valle, R., Bargallo, N., Balasa, M., Fernandez-Villullas, G., Bosch, B., et al. (2019). Hippocampal atrophy has limited usefulness as a diagnostic biomarker on the early onset Alzheimer's disease patients: a comparison between visual and quantitative assessment. *Neuroimage Clin.* 23:101927. doi: 10.1016/j.nicl.2019.101927

Fedorov, A., Beichel, R., Kalpathy-Cramer, J., Finet, J., Fillion-Robin, J. C., Pujol, S., et al. (2012). 3D slicer as an image computing platform for the quantitative imaging network. *Magn. Reson. Imaging* 30, 1323–1341. doi: 10.1016/j.mri.2012.05.001

Feng, Q., Song, Q., Wang, M., Pang, P., Liao, Z., Jiang, H., et al. (2019). Hippocampus radiomic biomarkers for the diagnosis of amnestic mild cognitive impairment: a machine learning method. *Front. Aging Neurosci.* 11:323. doi: 10.3389/fnagi.2019.00323

Feng, F., Wang, P., Zhao, K., Zhou, B., Yao, H., Meng, Q., et al. (2018). Radiomic features of hippocampal subregions in Alzheimer's disease and amnestic mild cognitive impairment. *Front. Aging Neurosci.* 10:290. doi: 10.3389/fnagi.2018.00290

Gillies, R. J., Kinahan, P. E., and Hricak, H. (2016). Radiomics: images are more than pictures, they are data. *Radiology* 278, 563–577. doi: 10.1148/radiol.2015151169

Guiot, J., Vaidyanathan, A., Deprez, L., Zerka, F., Danthine, D., Frix, A. N., et al. (2022). A review in radiomics: making personalized medicine a reality *via* routine imaging. *Med. Res. Rev.* 42, 426–440. doi: 10.1002/med.21846

Herdick, M., Dyrba, M., Fritz, H. J., Altenstein, S., Ballarini, T., Brosseron, F., et al. (2020). Multimodal MRI analysis of basal forebrain structure and function across the Alzheimer's disease spectrum. *Neuroimage Clin.* 28:102495. doi: 10.1016/j.nicl.2020.102495

Joubert, S., Gour, N., Guedj, E., Didic, M., Gueriot, C., Koric, L., et al. (2016). Early-onset and late-onset Alzheimer's disease are associated with distinct patterns of memory impairment. *Cortex* 74, 217–232. doi: 10.1016/j.cortex.2015.10.014

Lambert, M. A., Bickel, H., Prince, M., Fratiglioni, L., Von Strauss, E., Frydecka, D., et al. (2014). Estimating the burden of early onset dementia; systematic review of disease prevalence. *Eur. J. Neurol.* 21, 563–569. doi: 10.1111/ene.12325

Lambin, P., Leijenaar, R. T. H., Deist, T. M., Peerlings, J., de Jong, E. E. C., van Timmeren, J., et al. (2017). Radiomics: the bridge between medical imaging and personalized medicine. *Nat. Rev. Clin. Oncol.* 14, 749–762. doi: 10.1038/nrclinonc.2017.141

Li, K. C., Luo, X., Zeng, Q. Z., Xu, X. J., Huang, P. Y., Shen, Z. J., et al. (2018). Distinct patterns of interhemispheric connectivity in patients with early- and late-onset Alzheimer's disease. *Front. Aging Neurosci.* 10:261. doi: 10.3389/fnagi.2018.00261

Li, W., Qiu, Q., Sun, L., Li, X., and Xiao, S. (2019). Short-term adverse effects of the apolipoprotein E epsilon4 allele over language function and executive function in healthy older adults. *Neuropsychiatr. Dis. Treat.* 15, 1855–1861. doi: 10.2147/NDT.S183064

Li, T. R., Wu, Y., Jiang, J. J., Lin, H., Han, C. L., Jiang, J. H., et al. (2020). Radiomics analysis of magnetic resonance imaging facilitates the identification of preclinical Alzheimer's disease: an exploratory study. *Front. Cell Dev. Biol.* 8:605734. doi: 10.3389/fcell.2020.605734

Liu, M., Cheng, D., Wang, K., and Wang, Y. (2018). Multi-modality cascaded convolutional neural networks for Alzheimer's disease diagnosis. *Neuroinformatics* 16, 295–308. doi: 10.1007/s12021-018-9370-4

Luk, C. C., Ishaque, A., Khan, M., Ta, D., Chenji, S., Yang, Y. H., et al. (2018). Alzheimer's disease: 3-dimensional MRI texture for prediction of conversion from mild cognitive impairment. *Alzheimers Dement. (Amst)* 10, 755–763. doi: 10.1016/j.dadm.2018.09.002

Mayerhoefer, M. E., Materka, A., Langs, G., Haggstrom, I., Szczypinski, P., Gibbs, P., et al. (2020). Introduction to radiomics. *J. Nucl. Med.* 61, 488–495. doi: 10.2967/jnumed.118.222893

Moller, C., Vrenken, H., Jiskoot, L., Versteeg, A., Barkhof, F., Scheltens, P., et al. (2013). Different patterns of gray matter atrophy in early- and late-onset Alzheimer's disease. *Neurobiol. Aging* 34, 2014–2022. doi: 10.1016/j.neurobiolaging.2013.02.013

Nalepa, J., and Kawulok, M. (2019). Selecting training sets for support vector machines: a review. *Artif. Intell. Rev.* 52, 857–900. doi: 10.1007/s10462-017-9611-1

Orru, G., Pettersson-Yeo, W., Marquand, A. F., Sartori, G., and Mechelli, A. (2012). Using support vector machine to identify imaging biomarkers of

neurological and psychiatric disease: a critical review. *Neurosci. Biobehav. Rev.* 36, 1140–1152. doi: 10.1016/j.neubiorev.2012.01.004

Ourselin, S., Achterberg, H. C., Poot, D. H. J., van der Lijn, F., Vernooij, M. W., Ikram, M. A., et al. (2013). Local appearance features for robust MRI brain structure segmentation across scanning protocols. *Med. Image Process.* 8669:866905. doi: 10.1117/12.2006038

Park, K. H., Noh, Y., Choi, E. J., Kim, H., Chun, S., and Son, Y. D. (2017). Functional connectivity of the hippocampus in early- and vs. late-onset Alzheimer's disease. *J. Clin. Neurol.* 13, 387–393. doi: 10.3988/jcn.2017.13.4.387

Salvatore, C., Castiglioni, I., and Cerasa, A. (2021). Radiomics approach in the neurodegenerative brain. *Aging Clin. Exp. Res.* 33, 1709–1711. doi: 10.1007/s40520-019-01299-z

Shu, Z. Y., Mao, D. W., Xu, Y. Y., Shao, Y., Pang, P. P., and Gong, X. Y. (2021). Prediction of the progression from mild cognitive impairment to Alzheimer's disease using a radiomics-integrated model. *Ther. Adv. Neurol. Disord.* 14:17562864211029551. doi: 10.1177/17562864211029551

Sorensen, L., Igel, C., Liv Hansen, N., Osler, M., Lauritzen, M., Rostrup, E., et al. (2016). Early detection of Alzheimer's disease using MRI hippocampal texture. *Hum. Brain Mapp.* 37, 1148–1161. doi: 10.1002/hbm.23091

Tellechea, P., Pujol, N., Esteve-Belloch, P., Echeveste, B., Garcia-Eulate, M. R., Arbizu, J., et al. (2018). Early- and late-onset Alzheimer disease: are they the same entity? *Neurologia (Engl Ed)* 33, 244–253. doi: 10.1016/j.nrl.2015.08.002

Thibault, G., Angulo, J., and Meyer, F. (2014). Advanced statistical matrices for texture characterization: application to Cell classification. *IEEE Trans. Biomed. Eng.* 61, 630–637. doi: 10.1109/TBME.2013.2284600

Tibshirani, R. J. (2013). The lasso problem and uniqueness. *Electron. J. Statist.* 7, 1456–1490. doi: 10.1214/13-EJS815

van Griethuysen, J. J. M., Fedorov, A., Parmar, C., Hosny, A., Aucoin, N., Narayan, V., et al. (2017). Computational radiomics system to decode the radiographic phenotype. *Cancer. Res.* 77, e104–e107. doi: 10.1158/0008-5472.CAN-17-0339

Yang, H., Xu, H., Li, Q., Jin, Y., Jiang, W., Wang, J., et al. (2019). Study of brain morphology change in Alzheimer's disease and amnestic mild cognitive impairment compared with normal controls. *Gen. Psychiatr.* 32:e100005. doi: 10.1136/gpsych-2018-100005

Zhu, X. C., Tan, L., Wang, H. F., Jiang, T., Cao, L., Wang, C., et al. (2015). Rate of early onset Alzheimer's disease: a systematic review and meta-analysis. *Ann. Trans. Med.* 3:38. doi: 10.3978/j.issn.2305-5839.2015.01.19

Conflict of Interest: The authors declare that the research was conducted in the absence of any commercial or financial relationships that could be construed as a potential conflict of interest.

Publisher's Note: All claims expressed in this article are solely those of the authors and do not necessarily represent those of their affiliated organizations, or those of the publisher, the editors and the reviewers. Any product that may be evaluated in this article, or claim that may be made by its manufacturer, is not guaranteed or endorsed by the publisher.

frontiers in Aging Neuroscience

ORIGINAL RESEARCH
published: 10 February 2022
doi: 10.3389/fnagi.2022.809767

Gender-Related Differences in Regional Cerebral Glucose Metabolism in Normal Aging Brain

Bei Feng[1†], Jiang Cao[1,2†], YaPing Yu[1], HaiYan Yang[3], YangHongYan Jiang[1], Ying Liu[1], Rong Wang[1], and Qian Zhao[1]*

[1]*Department of Nuclear Medicine, General Hospital of Ningxia Medical University, Yinchuan, China,* [2]*Department of Nuclear Medicine, Xi'an Central Hospital, Xi'an, China,* [3]*Obstetrics and Gynecology Center Functional Examination Department, General Hospital of Ningxia Medical University, Yinchuan, China*

OPEN ACCESS

Edited by:
Behrooz Hooshyar Yousefi, University of Marburg, Germany

Reviewed by:
Youngkyoo Jung, University of California, Davis, United States
Chuantao Zuo, Fudan University, China

****Correspondence:***
Qian Zhao
cecilia_hh@126.com

†These authors have contributed equally to this work and share first authorship

Specialty section:
This article was submitted to Neurocognitive Aging and Behavior, a section of the journal Frontiers in Aging Neuroscience

Received: *05 November 2021*
Accepted: *12 January 2022*
Published: *10 February 2022*

Citation:
Feng B, Cao J, Yu Y, Yang H, Jiang Y, Liu Y, Wang R and Zhao Q (2022) Gender-Related Differences in Regional Cerebral Glucose Metabolism in Normal Aging Brain. Front. Aging Neurosci. 14:809767. doi: 10.3389/fnagi.2022.809767

Objectives: This study was aimed to investigate the gender-related differences of regional cerebral glucose metabolism in healthy people along the age using 18F-FDG PET/CT.

Methods: We recruited 344 healthy volunteers, including 217 males and 127 females (age range: 40–89 years old). All subjects underwent fluorine-18 fluorodeoxyglucose(18F-FDG) positron emission tomography (PET). All the data were divided into four groups for every 10 years old. Each participant was carefully screened from PET, MR, and other examinations in order to exclude the abnormalities, such as neurodegenerative or psychiatric disorders, alcohol/abuse, cerebral vascular disorders, metabolic diseases like diabetes mellitus and hyperthyroidism, and other systemic malignancies. The 40–50 years old group was set as the baseline group. Statistical parametric mapping (SPM) analysis was employed to illustrate the differences among groups.

Results: Compared to the baseline group, whether in a cohort or different gender groups, the decrease of brain glucose metabolism was shown in the bilateral frontal lobe, anterior cingulate gyrus, and the bilateral temporal lobe. In males, the regions of decreased metabolism were bilateral frontal lobe, caudate nucleus, and cingulate gyrus, whereas that of females were left occipital lobe, cerebellum, and the thalamus. However, the overall decrease of brain metabolism in men and women began from the age of 60s, an aggravated decrease from 70s was only observed in males.

Conclusion: (1) An obviously decreased brain metabolism was found from 60 years old, especially in the bilateral frontal lobe, bilateral temporal lobe, and inferior cingulate gyrus; (2) We found specific brain metabolic differences between genders, including the caudate nucleus region in males and the occipital lobe region in females; and (3) The aging trend is different between genders.

Keywords: aging brain, gender differences, 18F-FDG, PET, SPM

INTRODUCTION

Aging can lead to changes in brain function and structure, such as cognitive decline, which indicates dementia, disease, and death (Uchida et al., 2019). A study shows that brain aging may be the initial stage of neurodegeneration (Loewenstein et al., 2004). Another study shows that the pathological changes of familial AD in the brain seem to develop 25 years before clinical symptom onset (Florez, 2012). A robust feature of human biology is that women live longer than men in almost all countries (Austad and Bartke, 2015). In order to detect the preclinical stage of patients of different genders, it is necessary to catch a subtle abnormality that deviates from the healthy state. In other words, it is important to know the healthy brain morphology and activity beforehand, especially between different genders.

Positron emission tomography (Positron Emission Tomography, PET) brain imaging is a functional neuroimaging method that can noninvasively reflect glucose metabolism *in vivo*. Because the change of function is earlier than the structure, PET imaging is more and more widely used in detecting the changes in brain function, such as aging. An early study using FDG-PET showed higher global cerebral glucose metabolic rates in females than in males (Andreason et al., 1994). The latest longitudinal study, which was performed decade-long, showed that functional and morphological changes were affected by gender differences (Thompson et al., 2020). Besides the gender-related differences in brain aging, researches are also focused on the aging speed of the reginal cerebrum. A previous study suggested that some age-related changes in brain structure and metabolism were not linear with age, and showed unequally accelerated changes in the elder people (Brickman et al., 2003).

However, the study on gender-related differences in regional cerebral glucose metabolism in the aging brain has been rarely reported. In this study, we examined the cerebral glucose metabolism using FDG PET/CT in healthy subjects of different genders, and discussed the metabolic differences between sexes and the age-related brain aging.

MATERIALS AND METHODS

Subjects

From November 2014 to December 2018, 344 examinees (age range: 40–89 years) underwent a routine FDG positron emission tomography (FDG PET) in General Hospital of Ningxia Medical University, including 217 males and 127 females. The inclusion criteria were as follows: healthy subjects, age between 40 and 89 years, right-handed, and with complete clinical data. The exclusion criteria were that each participant was carefully screened from PET, MR, and other examinations to exclude the abnormalities, such as neurodegenerative or psychiatric disorders, alcohol abuse, cerebral vascular disorders, metabolic disease like diabetes mellitus and hyperthyroidism, and other systemic diseases. The institutional review board approved the current study. Informed consent was obtained from the subjects after explaining the procedure, risk, and purpose/benefit of the FDG PET study.

PET Image Analysis

All subjects were asked to fast at least 6 h before scanning. Each of them was injected intravenously with 370 megabecquerel (MBq) of FDG and rested supine with their eyes closed in a quiet, dimly lit room. Imaging was performed with a positron emission tomography scanner (General Electric Company, GE Discovery VCT 64 system). Scanning began 45 min after the injection of FDG. When subjects were positioned in the scanner, a molded headrest and a head restraining Velcro band were applied to firmly secure their heads in order to reduce motion artifact. Whole-body PET images were acquired from the head to upper thighs in the 2-dimensional mode. After finishing the whole-body scan, the brain scan commenced with 4 min 3-dimensional emission scan. The attenuation correction was performed with a uniform attenuation coefficient (μ = 0.096 cm^{-1}). In-plane and axial resolution of the scanner was 4.2 and 5.6 mm full width at half maximum (FWHM), respectively.

SPM Analysis of F-18 FDG Brain PET

In this study, a voxel-by-voxel group analysis was done using SPM8 (Statistical Parametric Mapping 8) running on MATLAB R2014a. The raw data were initially converted from the DICOM to the ANALYZE format using MRIcro (available at www.mricro.com) and transferred to SPM8. MRIcro allows efficient viewing and creation of analyze format headers for exporting brain images to other platforms with common personal computers. After transferring to SPM8, the data were then normalized into the standard PET template provided in SPM8 by using a 12-parameter affine transformation, followed by nonlinear transformations and bilinear interpolation. Dimensions of the resulting voxels were $2 \times 2 \times 2$ mm^3. Standardized data were then smoothed by a Gaussian filter (full width of half maximum, FWHM = 16 mm). Male and female subjects were analyzed, respectively, with their ages as the covariance to check the relationship between age and brain metabolism. In addition, male subjects were compared with female subjects with age as the nuisance variable to analyze the sex-related differences in brain metabolism. The statistical parametric map SPM was initially obtained at a height threshold T to meet $P = 0.05$ (corrected with familywise error), and then an extent threshold k was set as 100 voxels. The Talairach Daemon database was used to convert the coordinates of these statistically significant areas into corresponding anatomical locations in the Talairach atlas. Results were listed with the Talairach coordinates of the representative peak voxels, as well as their individual k value, t score, and Brodmann area (BA). The k value represents the number of significant voxels in the particular cluster.

RESULTS

Subject Characteristics

Table 1 shows the clinical data of healthy subjects. Subjects were divided into four groups by every 10 years old. Each group was compared with reference group (40–50 years old group). We

TABLE 1 | Descriptive statistics of the subjects in this study.

Age groups (Years old)	Total (N)	Male (N, %)	Female (N, %)	Age Mean ± Standard
40–49	172	109 (63.4%)	63 (36.6%)	44.65 ± 2.83
50–59	103	72 (69.9%)	31 (30.1%)	53.06 ± 2.87
60–69	44	23 (52.3%)	21 (47.7%)	63.16 ± 3.13
70–89	25	13 (52.0%)	12 (48.0%)	75.25 ± 4.81
Total	344	217 (63.1%)	127 (36.9%)	59.03 ± 3.41

merged the age of 70 and 89 into one group due to the small sample.

Changing Pattern of Brain Metabolism Over Ages in Cohort

The age-related glucose metabolism differences in cohort were listed in **Tables 2**, **3** and **Figure 1**.

Changing Pattern of Brain Metabolism Over Ages in Different Gender Groups

The age-related glucose metabolism differences between males and females were listed in **Tables 4–7** and **Figures 2**, **3**. No decrease or increase metabolic changes were found before the age of 60s in both groups.

Changing Tendency of Brain Metabolism With Age in Cohort and Different Gender Groups

We found that the overall decrease of brain metabolism in men and women were all began from the age of 60s. Interestingly, the trend of decrease was not the same between men and women, i.e., men showed aggravated decrease from the 70s (**Table 8**, **Figures 4, 5**).

DISCUSSION

In the past, there were many reports using PET about brain metabolism in neurological, psychiatric, and tumor patients, but little is known about the changes in brain metabolism in aging people of different sexes. Some studies have shown that decreased brain metabolism and brain atrophy mostly occur after the age of 40 (Chance, 2006; Shen et al., 2012). This is the reason why we set the subjects in this experiment as healthy people aged 40 and 89 years old. We investigated the changes in brain metabolism with age in healthy people of different genders. The main finding of our study was as follows: (1) an obviously decreased brain metabolism was found from 60 years old, especially in the bilateral frontal lobe, bilateral temporal lobe, inferior cingulate gyrus; (2) we found specific brain metabolic differences between genders, including the caudate nucleus region in males and the occipital lobe region in females; and (3) the aging trend is different between genders. We discussed and compared the results with other researches as follows.

Consistent Brain Metabolic Changes Among Cohort, Males and Females

An obviously decreased brain metabolism was found in 60-year-olds, especially in the bilateral frontal lobe (BA10, 11, 25, 47), anterior cingulate gyrus (BA32), and the bilateral temporal lobe (BA22, 30, 38). Meanwhile, the areas of increased brain metabolism were the lenticular nucleus and thalamus.

These findings were consistent with previous studies showing that cerebral metabolic activity decreases gradually with normal aging and primarily affects frontal lobes bilaterally (Beheshti and Kim, 2014). The frontal cortex is the most advanced brain region, which is mainly involved in advanced activities such as body movement and language and is also the brain area most affected by age. Brodmann area 10 (BA 10), is the largest frontal brain region that has been shown to be involved in a wide variety of functions including risk and decision making, odor evaluation, reward and conflict, pain, and working memory (Peng et al., 2018). Recent functional studies have demonstrated that left BA47 has been observed to participate not only in language but also in other domains such as working memory and deductive reasoning, while right BA47 was related with affective prosody as reported (Ardila et al., 2017).

The Anterior Cingulate Cortex (ACC) is an anatomically distinct subregion of the ventromedial frontal cortex consisting of the cingulate sulcus and gyrus that lie dorsal to the corpus callosum and ventral to the superior frontal gyrus. It encompasses Broadmann area 24 and adjacent regions (Gasquoine, 2013). Neuropsychological follow-up of bilateral cingulotomy psychosurgical cases suggests a role for ACC in cognition, specifically executive functioning (Yarkoni, 2009).

Besides frontal lobes and ACC, temporal lobes were involved in many aging-related diseases. We found the decrease of temporal lobes was obvious. Only primates have temporal lobes, which are largest in man, accommodating 17% of the cerebral cortex and including areas with auditory, olfactory, vestibular, visual, and linguistic functions (Kiernan, 2012). A study suggested a series of changes across a wide range of proteins in the human temporal lobe that may relate to aging and age-related neurodegenerative disorders (Xu et al., 2016).

Substrates of memory list learning performance reportedly reside in the anterior part of the brain including the cingulate cortex, frontal cortex, and temporal cortex (Nobili et al., 2007). The frontal aging hypothesis (Tisserand and Jolles, 2003) suggests that hypometabolism in anterior regions including the anterior cingulate gyrus and the frontal lobe is related to executive function and attentional performance, which may decline even in the healthy elderly. Our results, coupled with past studies, support the frontal aging hypothesis.

Not only decreased metabolism was observed, increased regions were also seen along with aging. An increased metabolism was found in the gray matter of the cerebellum and thalamus (Bonte et al., 2017). The results were paralleled with our results. Biswal et al. (2010) using a large sample of over 1,000 subjects have shown reduced resting-state activity in aging mainly in the default model network and increased activity in the visual, motor, and the subcortical regions. The difference from our results was probably due to the sample size and population.

Why do some brain areas increase during aging? We guess the reason is "network". Given the different rates of declines or relative preservations of different brain regions in aging, and large-scale brain networks working in synchrony during

both task execution and resting-state (Biswal et al., 2010), it is likely that the regions that are working together affect each other during the aging process. Specifically, a region that declines faster may influence another region during functional interactions on an everyday basis. For example, the bilateral anterior temporal positively influenced the medial parietal, but negatively influenced the basal ganglia. It is consistent with the direction of the spread of age effects (Di et al., 2019). Therefore, would cause the other region to decline or show a compensatory increase of functional activity.

In addition, the thalamus, with its cortical, subcortical, and cerebellar connections, is a critical node in networks supporting cognitive functions known to decline in normal aging, including component processes of memory and executive functions of attention and information processing (Fama and Sullivan, 2015).

Inconsistent Brain Metabolic Changes Among Cohort, Males, and Females

In our study, the metabolism of the cerebellum decreased obviously in females, but not in males. The cerebellum is an

TABLE 2 | Brain regions with decreased metabolism in cohort.

Age group (Years old)	Brain regions	*T* value	K_E value	Total K_E	Talairach coordinates			Brodmann
					x	*y*	*z*	
50–59	None	None	None	None	-	None	-	None
	Left superior temporal gyrus	6.88	786	2,304	−46	16	−10	38
	Right thalamus	5.87	104		2	−22	6	-
60–69	Right superior temporal gyrus	5.60	762		52	16	−8	38
	Right parahippocampal gyrus	5.06	58		16	−36	−6	30
	Right cerebellum	5.05	265		54	−64	−26	-
	Right anterior cingulate gyrus	10.12	1,718	4,933	2	44	12	32
	Right inferior frontal gyrus	9.00	1,714		48	18	−10	47
	Left inferior frontal gyrus	8.18	922		−44	16	−8	47
70∼89	Left caudate nucleus	7.97	105		−10	12	4	-
	Right thalamus	7.60	287		6	−24	6	-
	Left medial frontal gyrus	5.43	40		−2	10	−20	25

Voxel height threshold T = 5.01; P = 0.05 with familywise error correction; cluster extent threshold k = 100 voxels.

TABLE 3 | Brain regions with increased metabolism in cohort.

Age group (Years old)	Brain regions	*T* value	K_E value	Total K_E	Talairach coordinates			Brodmann
					x	*y*	*z*	
50–59	None	None	None	None	-	None	-	None
	Right lenticular nucleus	6.95	429	1,056	18	−12	−2	-
	Left thalamus	6.35	334		−18	−14	2	-
60–69	Right suboccipital gyrus	5.91	257		38	−72	−4	19
	Right insular lobe	5.58	21		34	24	20	13
	Right lenticular nucleus	10.39	1,364	3,152	18	−12	0	-
	Left thalamus	9.73	730		−16	−12	2	-
	Right suboccipital gyrus	7.38	582		38	−72	−4	19
70–89	Left medial frontal gyrus	5.57	18		−16	48	−6	10
	Right middle frontal gyrus	5.49	296		34	46	−4	11
	Left temporal lobe	5.43	22		−48	−42	−10	37

Voxel height threshold T = 5.01; P = 0.05 with familywise error correction; cluster extent threshold k = 100 voxels.

TABLE 4 | Brain regions with decreased metabolism in males.

Age group (Years old)	Brain regions	*T* value	K_E value	Total K_E	Talairach coordinates			Brodmann
					x	*y*	*z*	
50–59	None	None	None	None	-	None	-	None
	Right inferior frontal gyrus	5.60	290	719	50	18	−6	47
	Left inferior frontal gyrus	5.56	333		−46	18	−4	47
60–69	Left caudate nucleus	5.33	40		−10	8	8	-
	Left superior frontal gyrus	5.19	26		−24	66	6	-
	Left thalamus	5.11	13	-	−10	−28	12	-
	Right anterior cingulate gyrus	8.49	2,310	5,027	2	46	6	32
	Left caudate nucleus	7.46	173	-	−12	6	10	-
	Left superior temporal gyrus	7.04	1,097	-	−46	−16	8	22
70–89	Right superior temporal gyrus	6.75	1,056		48	48	8	22
	Right caudate nucleus	6.70	109		14	14	8	-
	Right thalamus	6.41	281		8	8	8	-

Voxel height threshold T = 5.01; P = 0.05 with familywise error correction; cluster extent threshold k = 100 voxels.

TABLE 5 | Brain regions with increased metabolism in males.

Age group (Years old)	Brain regions	*T* value	K_E value	Total K_E	Talairach coordinates			Brodmann
					x	*y*	*z*	
50–59	None	None	None	None	-	None	-	None
	Right cingulate gyrus	5.88	47	455	18	−8	48	24
	Right lenticular nucleus	5.73	189		18	−12	−2	-
	Left thalamus	5.62	151		−20	−20	2	-
	Right lenticular nucleus	6.81	434	972	18	−12	2	-
	Left thalamus	6.18	287		−18	−14	4	-
70–89	Left anterior cingulate gyrus	5.51	94		−16	46	−8	32
	Right paracenter lobule	5.08	52		22	−44	52	5
	Right claustroid nucleus	5.04	55		26	16	−6	-

Voxel height threshold T = 5.01; P = 0.05 with familywise error correction; cluster extent threshold k = 100 voxels.

TABLE 6 | Brain regions with decreased metabolism in females.

Age group (Years old)	Brain regions	*T* value	K_E value	Total K_E	Talairach coordinates			Brodmann
					x	*y*	*z*	
50–59	None	None	None	None	-	None	-	None
	Left fusiform gyrus	5.71	438	725	−28	−90	−26	18
	Right cerebellum	5.51	257		52	−68	−24	-
60–69	Right thalamus	5.10	30		2	−24	4	-
	Left cerebellum	5.87	173	1,331	−48	−52	−30	-
	Right medial frontal gyrus	5.64	218		2	46	14	10
	Right cerebellum	5.62	307		28	−30	−26	-
70–89	Right inferior frontal gyrus	5.59	273		48	18	−8	47
	Left inferior frontal gyrus	5.17	79		−44	16	−10	47

Voxel height threshold T = 5.01; P = 0.05 with familywise error correction; cluster extent threshold k = 100 voxels.

TABLE 7 | Brain regions with increased metabolism in females.

Age group (Years old)	Brain regions	*T* value	K_E value	Total K_E	Talairach coordinates			Brodmann
					x	*y*	*z*	
50–59	None	None	None	None	-	None	-	None
	Right lenticular nucleus	6.13	324	669	18	−14	−2	-
	Right suboccipital gyrus	6.09	132		40	−74	−6	19
	Right suboccipital gyrus	6.09	132		40	−74	−6	19
60–69	Left thalamus	5.81	148		−18	−14	2	-
	Right insular lobe	5.08	8		32	26	20	13
	Right lenticular nucleus	9.49	937	2,033	18	−12	−2	-
	Left thalamus	9.28	556		−18	−16	0	-
	Right suboccipital gyrus	7.40	194		38	−72	−4	19
70–89	Right middle frontal gyrus	5.68	147		32	48	−2	10
	Left insular lobe	5.66	15		32	26	20	13
	Left inferior frontal gyrus	5.60	35		−30	32	8	47
	Left lenticular nucleus	5.46	52		−22	16	6	-
	Right middle temporal gyrus	5.09	52		52	−48	0	22

Voxel height threshold T = 5.01; P = 0.05 with familywise error correction; cluster extent threshold k = 100 voxels.

TABLE 8 | Changing of whole brain voxels in cohort and different gender groups.

	Age groups	Relatively decreased metabolism in total voxels			Relatively increased metabolism in total voxels		
		Whole brain	Left brain	Right brain	Whole brain	Left brain	Right brain
Cohort	60–69	2,304	1,114	1,190	1,056	348	708
	70–89	4,933	1,194	3,739	3,152	892	2,260
Male	60–69	719	413	306	455	203	252
	70–89	5,027	1,270	3,757	972	414	558
Female	60–69	725	438	287	669	148	521
	70–89	1,331	280	1,051	2,033	703	1,330

important, but an understudied region in aging research. The cerebellum plays a role in both motor and cognitive behavior (Ferrucci and Priori, 2014). Atrophy of the cerebellar vermis has been reported to occur with human aging and the age-related loss of Purkinje cells affects most severely the anterior superior vermis in parallel with the ethanol-induced Purkinje cell loss.

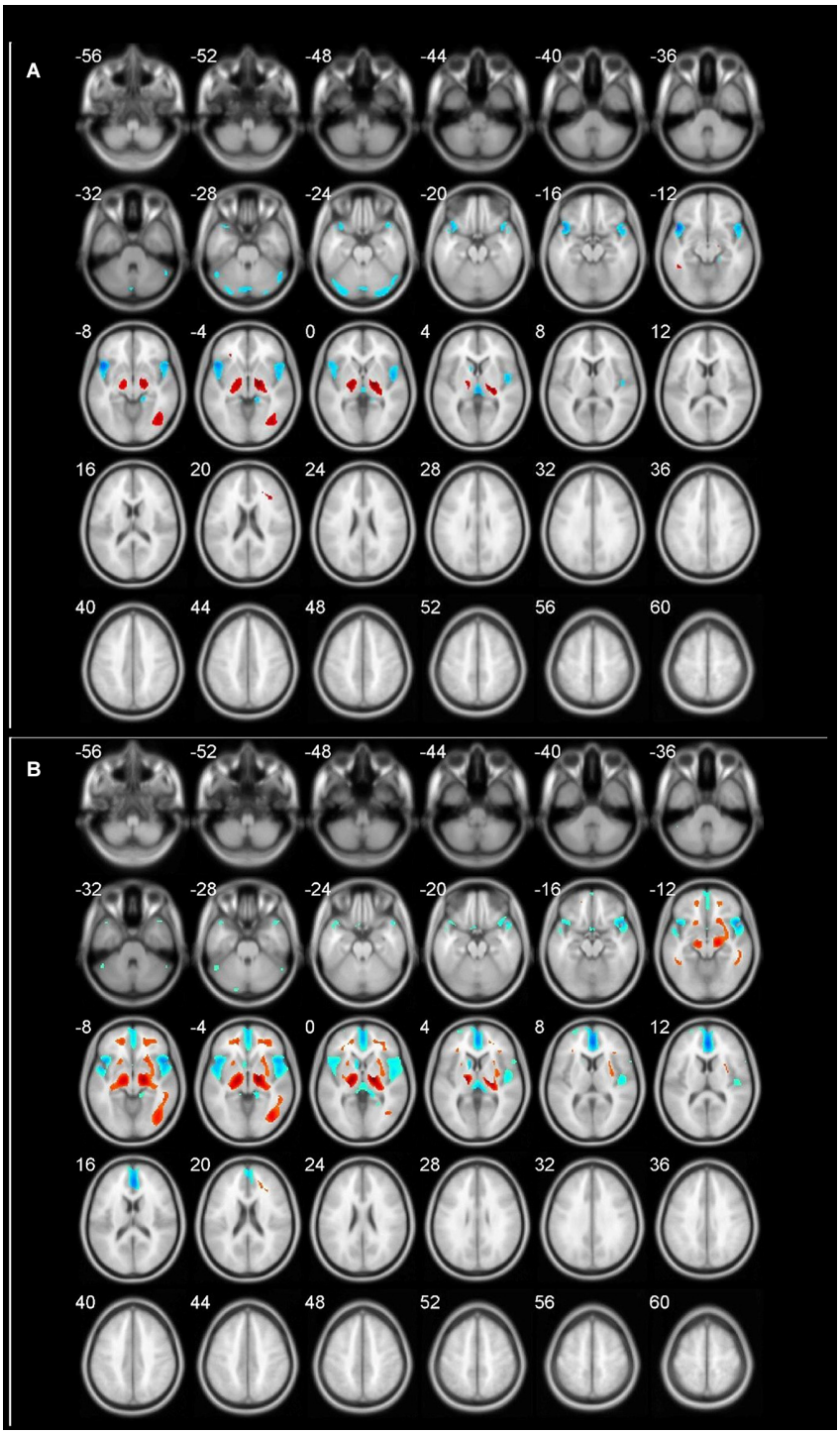

FIGURE 1 | Different brain regions in cohort (blue indicates decrease; red indicates increase). **(A)** 60–69 age group; **(B)** 70–89 age group.

In this study, the decrease of bilateral frontal lobe metabolism began in the 60-year-old group in men and the 70-year-old group in women. Some scholars believed that this might be caused by a higher alcohol intake in men than women (Rando et al., 2011).

The fusiform gyrus (FG; BA 18) commonly belongs to a part of the temporal lobe and is considered as a key structure for functionally-specialized computations of high-level vision such as face perception, object recognition, and reading (Weiner and Zilles, 2016). In this study, we found the FG showed

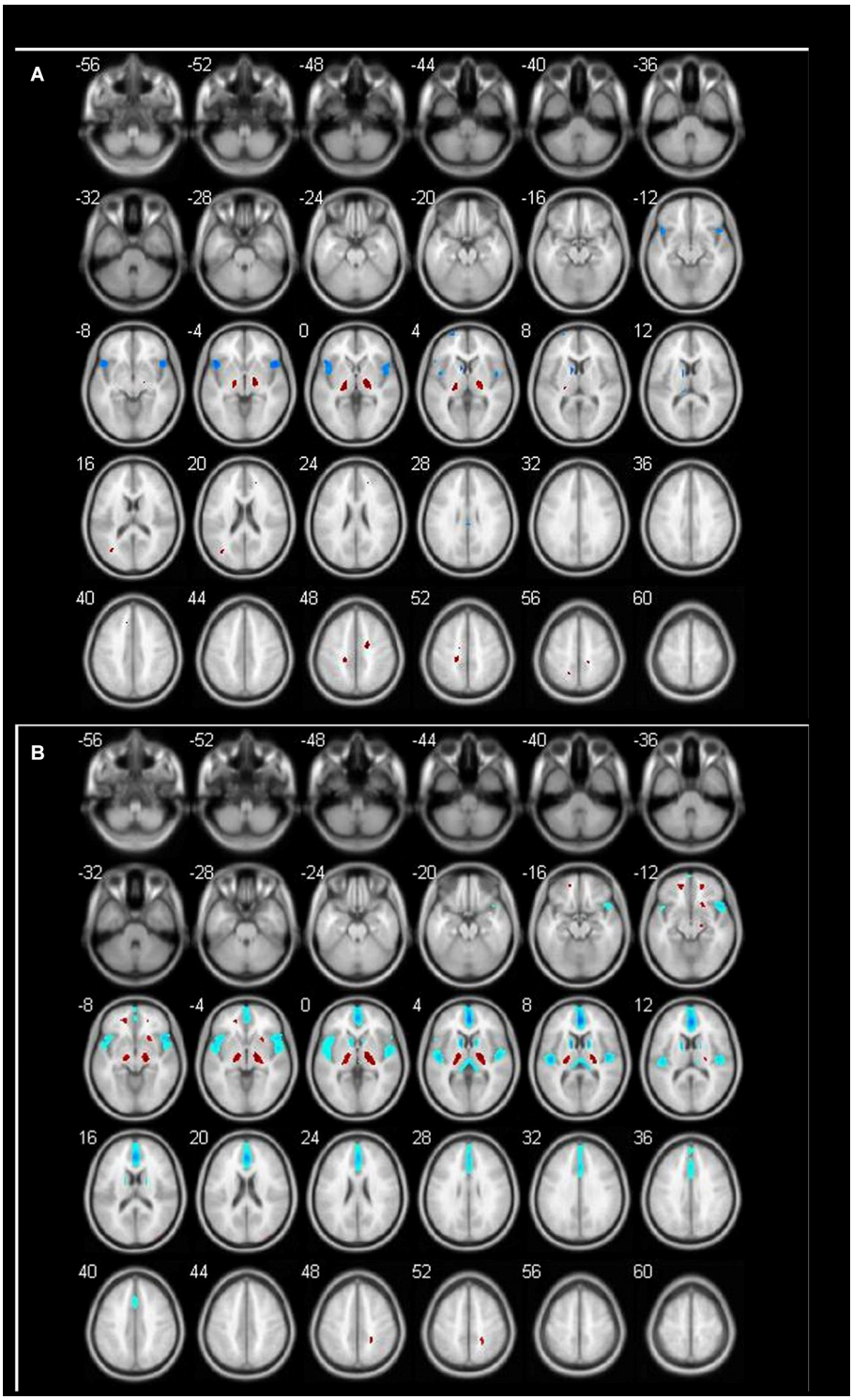

FIGURE 2 | Different brain regions in male groups (blue indicates decrease; red indicates increase). **(A)** Male 60–69 age group; **(B)** male 70–89 age group.

a significant decrease along with aging. It is the brain area in 60-year-old women with the most significant decrease in metabolism.

In addition, we found that there was a significant decrease in metabolism in the anterior cingulate gyrus in the male 70-year-old group. A study showed increasing age correlated with

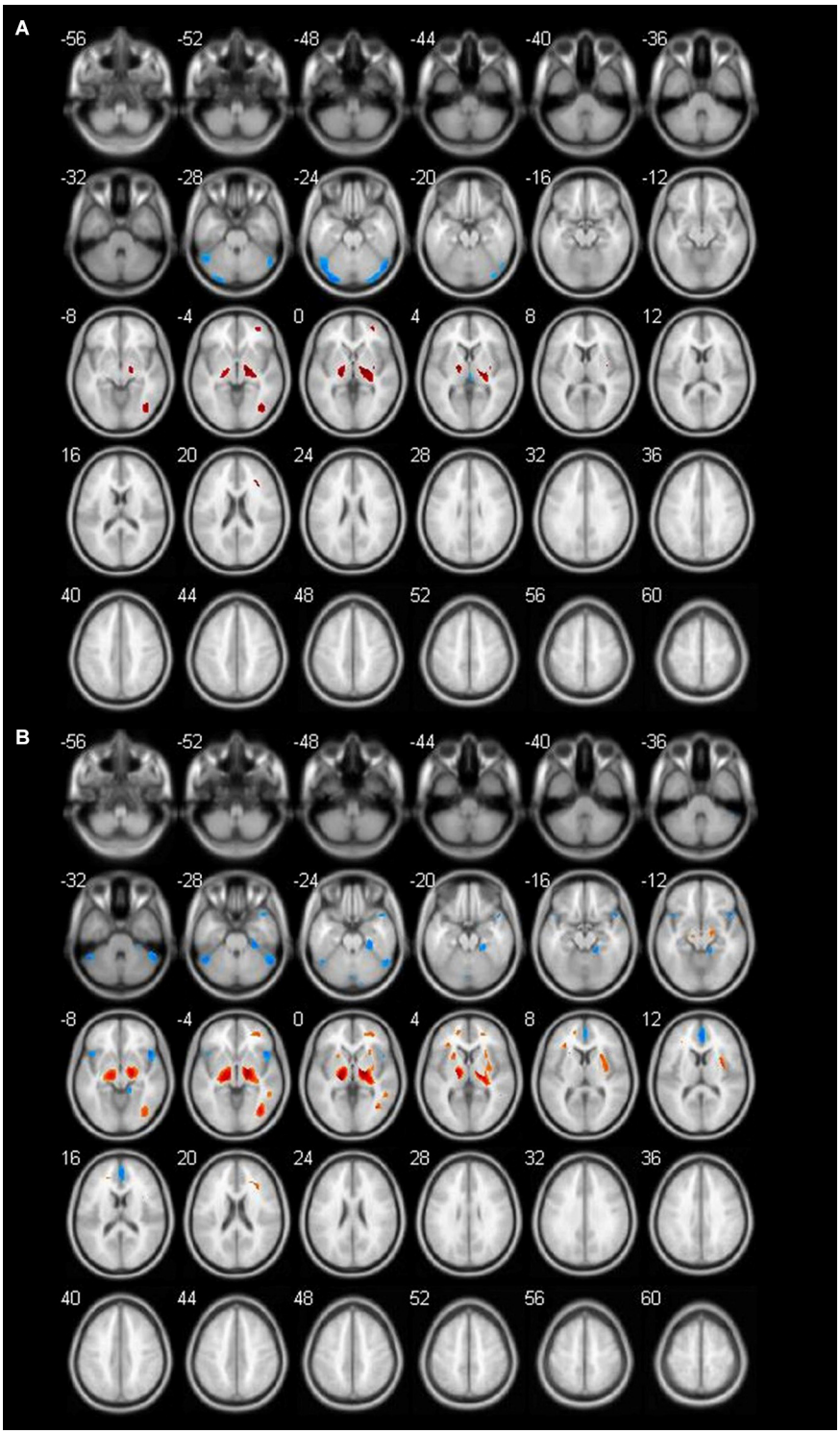

FIGURE 3 | Different brain regions in female groups (blue indicates decrease; red indicates increase). **(A)** Female 60–69 age group; **(B)** female 70–89 age group.

significant and extended reduction of brain metabolism in the medial frontal cortex and anterior cingulate gyrus in males (Jaatinen and Rintala, 2008). This result was as same as our results. Another study of 130 healthy people aged 21–90 found that glucose metabolism in the anterior cingulate gyrus decreased with age (Moeller et al., 1996). Some studies indicated that

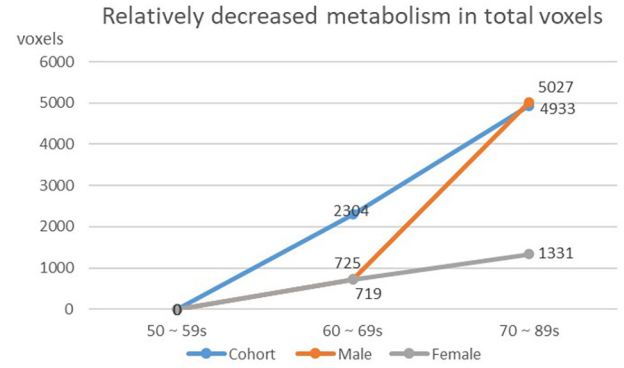

FIGURE 4 | Decreasing of whole brain voxels in cohort and different gender groups.

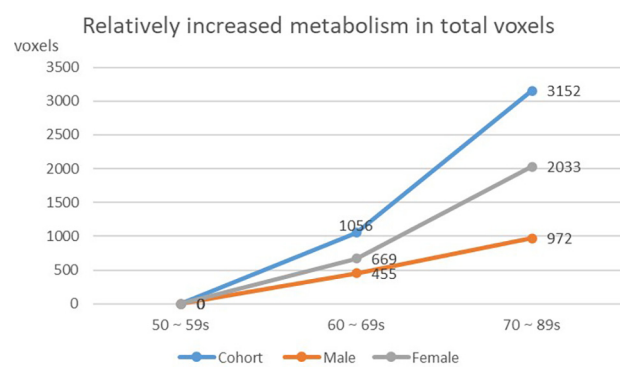

FIGURE 5 | Increasing of whole brain voxels in cohort and different gender groups.

there was an age-related metabolic decrease in the anterior cingulate gyrus accompanied by a decline in cognitive function (Pardo et al., 2007).

Another effect of aging is that bilateral thalamic glucose metabolism increases with aging in males but not in females (Murphy et al., 1996). A study shows that the metabolism of males in the left thalamus increased with aging, though the cause of this increase is unclear (Kawachi et al., 2002). The results were paralleled with our results.

Metabolic Differences Between Males and Females

In the second part, we discussed inconsistent brain metabolic changes among cohort, male and female. In fact, there were metabolic differences between males and females even in the same age group and made sense. We found specific brain metabolic differences in different genders. In the male group, the brain metabolism decreased to varying degrees in the caudate nucleus region in both the 60-year-old group and the 70-year-old group, while in the female group, the specific decreased brain area appeared in the occipital lobe region in the 60-year-old group.

The age-associated increased FDG uptake regions were clearly different in male and female subjects (Kim et al., 2009). Indeed, it is often said that men outperform women in tasks of visuospatial processing and women outperform men in tasks of speech processing (Strelnikov et al., 2009). The previous studies have recognized that males perform better in the visual-spatial domain, whereas females perform better in the verbal domain of cognitive tasks (Hsieh et al., 2012). A more recent functional MRI (fMRI) study also provides evidences of more prominent brain activation in the occipital cortex in males during visual-spatial cognitive tasks (Bell et al., 2006).

Trend of Metabolic Changes With Aging

There were some differences in the change trend of brain metabolism between men and women in the previous literature (Baxter et al., 1987; Fujimoto et al., 2008).

In our study, we found that the brain aging of men begins at the age of 60 and shows more after the age of 70, while the brain aging of women begins at the age of 60, and the degree of brain aging at the age of 70 is less than that at the age of 60. These data suggest that women may age slower than men. It has been pointed out that this situation may be related to hormone levels (Marrocco and McEwen, 2016). Studies have shown that estrogen has a certain correlation with emotional control, the protective effects of cerebral vessels and neurons (Murphy et al., 1998). Using estrogen replacement therapy can reduce the risk of AD in women (Sherwin, 2002).

There were also some limitations of our study. The main limitation was the sample size. The aging of the human brain is variational, in our study the data was collected from the age of 40 years old, however the change of brain metabolism was unknown before 40 years old. Further research of big sample size was needed including age before 40 and after 80.

CONCLUSION

The conclusions of our study were as follows: (1) an obviously decreased brain metabolism was found from 60 years old, especially in the bilateral frontal lobe, bilateral temporal lobe, and inferior cingulate gyrus; (2) we found specific brain metabolic differences between genders, including the caudate nucleus region in male and the occipital lobe region in female; and (3) the aging trend is different between genders.

DATA AVAILABILITY STATEMENT

The original contributions presented in the study are included in the article, further inquiries can be directed to the corresponding author.

ETHICS STATEMENT

Ethical review and approval was not required for the study on human participants in accordance with the local legislation and institutional requirements. The patients/participants

provided their written informed consent to participate in this study.

AUTHOR CONTRIBUTIONS

BF and JC initiated the idea for this article and prepared the final copy of the manuscript. JC is responsible for making pictures and tables. YY, HY, YJ, RW, and YL took responsibility for collecting patient's data. QZ took responsibility for reviewing this article. All authors contributed to the article and approved the submitted version.

FUNDING

This study was funded by the Natural Science Foundation of Ningxia Hui Autonomous Region (No. 2018AAC03136) and Ningxia Innovation and Entrepreneurship Program for returned overseas students (No. 2021-5).

REFERENCES

Andreason, P. J., Zametkin, A. J., Guo, A. C., Baldwin, P., and Cohen, R. M. (1994). Gender-related differences in regional cerebral glucose metabolism in normal volunteers. *Psychiatry Res.* 51, 175–183. doi: 10.1016/0165-1781(94)90037-x

Ardila, A., Bernal, B., and Rosselli, M. (2017). Should Broca's area include Brodmann area 47? *Psicothema* 29, 73–77. doi: 10.7334/psicothema2016.11

Austad, S. N., and Bartke, A. (2015). Sex differences in longevity and in responses to anti-aging interventions: a mini-review. *Gerontology* 62, 40–46. doi: 10.1159/000381472

Baxter, L. R., Jr., Mazziotta, J. C., Phelps, M. E., Selin, C. E., Guze, B. H., and Fairbanks, L. (1987). Cerebral glucose metabolic rates in normal human females versus normal males. *Psychiatry Res.* 21, 237–245. doi: 10.1016/0165-1781(87)90028-x

Beheshti, M., and Kim, C. K. (2014). FDG PET/CT: normal variations and benign findings - translation to PET/MRI. *PET Clin.* 9, xiii–xiv. doi: 10.1016/j.cpet.2014.02.001

Bell, E. C., Willson, M. C., Wilman, A. H., Dave, S., and Silverstone, P. H. (2006). Males and females differ in brain activation during cognitive tasks. *Neuroimage* 30, 529–538. doi: 10.1016/j.neuroimage.2005.09.049

Biswal, B. B., Mennes, M., Zuo, X. N., Gohel, S., Kelly, C., Smith, S. M., et al. (2010). Toward discovery science of human brain function. *Proc. Natl. Acad. Sci. U S A* 107, 4734–4739. doi: 10.1073/pnas.0911855107

Bonte, S., Vandemaele, P., Verleden, S., Audenaert, K., Deblaere, K., Goethals, I., et al. (2017). Healthy brain ageing assessed with 18F-FDG PET and age-dependent recovery factors after partial volume effect correction. *Eur. J. Nucl. Med. Mol. Imaging* 44, 838–849. doi: 10.1007/s00259-016-3569-0

Brickman, A. M., Buchsbaum, M. S., Shihabuddin, L., Hazlett, E. A., Borod, J. C., and Mohs, R. C. (2003). Striatal size, glucose metabolic rate and verbal learning in normal aging. *Brain Res. Cogn. Brain Res.* 17, 106–116. doi: 10.1016/s0926-6410(03)00085-5

Chance, S. A. (2006). Subtle changes in the ageing human brain. *Nutr. Health* 18, 217–224. doi: 10.1016/s0926-6410(03)00085-5

Di, X., Wölfer, M., Amend, M., Wehrl, H., Ionescu, T. M., Pichler, B. J., et al. (2019). Interregional causal influences of brain metabolic activity reveal the spread of aging effects during normal aging. *Hum. Brain Mapp.* 40, 4657–4668. doi: 10.1002/hbm.24728

Fama, R., and Sullivan, E. V. (2015). Thalamic structures and associated cognitive functions: relations with age and aging. *Neurosci. Biobehav. Rev.* 54, 29–37. doi: 10.1016/j.neubiorev.2015.03.008

Ferrucci, R., and Priori, A. (2014). Transcranial cerebellar direct current stimulation (tcDCS): motor control, cognition, learning and emotions. *Neuroimage* 85, 918–923. doi: 10.1016/j.neuroimage.2013.04.122

Florez, J. C. (2012). Clinical and biomarker changes in Alzheimer's disease. *N. Engl. J. Med.* 367:2051. doi: 10.1056/NEJMc1211767

Fujimoto, T., Matsumoto, T., Fujita, S., Takeuchi, K., Nakamura, K., Mitsuyama, Y., et al. (2008). Changes in glucose metabolism due to aging and gender-related differences in the healthy human brain. *Psychiatry Res.* 164, 58–72. doi: 10.1016/j.pscychresns.2006.12.014

Gasquoine, P. G. (2013). Localization of function in anterior cingulate cortex: from psychosurgery to functional neuroimaging. *Neurosci. Biobehav. Rev.* 37, 340–348. doi: 10.1016/j.neubiorev.2013.01.002

Hsieh, T. C., Lin, W. Y., Ding, H. J., Sun, S. S., Wu, Y. C., Yen, K. Y., et al. (2012). Sex- and age-related differences in brain FDG metabolism of healthy adults: an SPM analysis. *J. Neuroimaging* 22, 21–27. doi: 10.1111/j.1552-6569.2010.00543.x

Jaatinen, P., and Rintala, J. (2008). Mechanisms of ethanol-induced degeneration in the developing, mature and aging cerebellum. *Cerebellum* 7, 332–347. doi: 10.1007/s12311-008-0034-z

Kawachi, T., Ishii, K., Sakamoto, S., Matsui, M., Mori, T., and Sasaki, M. (2002). Gender differences in cerebral glucose metabolism: a PET study. *J. Neurol. Sci.* 199, 79–83. doi: 10.1016/s0022-510x(02)00112-0

Kiernan, J. A. (2012). Anatomy of the temporal lobe. *Epilepsy Res. Treat.* 2012:176157. doi: 10.1155/2012/176157

Kim, I. J., Kim, S. J., and Kim, Y. K. (2009). Age- and sex-associated changes in cerebral glucose metabolism in normal healthy subjects: statistical parametric mapping analysis of F-18 fluorodeoxyglucose brain positron emission tomography. *Acta Radiol.* 50, 1169–1174. doi: 10.3109/02841850903258058

Loewenstein, D. A., Acevedo, A., Czaja, S. J., and Duara, R. (2004). Cognitive rehabilitation of mildly impaired Alzheimer disease patients on cholinesterase inhibitors. *Am. J. Geriatr. Psychiatry* 12, 395–402. doi: 10.1176/appi.ajgp.12.4.395

Marrocco, J., and McEwen, B. S. (2016). Sex in the brain: hormones and sex differences. *Dialogues Clin. Neurosci.* 18, 373–383. doi: 10.31887/DCNS.2016.18.4/jmarrocco

Moeller, J. R., Ishikawa, T., Dhawan, V., Spetsieris, P., Mandel, F., Alexander, G. E., et al. (1996). The metabolic topography of normal aging. *J. Cereb. Blood Flow Metab.* 16, 385–398. doi: 10.1097/00004647-199605000-00005

Murphy, D. D., Cole, N. B., Greenberger, V., and Segal, M. (1998). Estradiol increases dendritic spine density by reducing GABA neurotransmission in hippocampal neurons. *J. Neurosci.* 18, 2550–2559. doi: 10.1523/JNEUROSCI.18-07-02550.1998

Murphy, D. G., DeCarli, C., McIntosh, A. R., Daly, E., Mentis, M. J., Pietrini, P., et al. (1996). Sex differences in human brain morphometry and metabolism: an *in vivo* quantitative magnetic resonance imaging and positron emission tomography study on the effect of aging. *Arch. Gen. Psychiatry* 53, 585–594. doi: 10.1001/archpsyc.1996.01830070031007

Nobili, F., Koulibaly, P. M., Rodriguez, G., Benoit, M., Girtler, N., Robert, P. H., et al. (2007). 99mTc-HMPAO and 99mTc-ECD brain uptake correlates of verbal memory in Alzheimer's disease. *Q. J. Nucl. Med. Mol. Imaging* 51, 357–363.

Pardo, J. V., Lee, J. T., Sheikh, S. A., Surerus-Johnson, C., Shah, H., Munch, K. R., et al. (2007). Where the brain grows old: decline in anterior cingulate and medial prefrontal function with normal aging. *Neuroimage* 35, 1231–1237. doi: 10.1016/j.neuroimage.2006.12.044

Peng, K., Steele, S. C., Becerra, L., and Borsook, D. (2018). Brodmann area 10: Collating, integrating and high level processing of nociception and pain. *Prog. Neurobiol.* 161, 1–22. doi: 10.1016/j.pneurobio.2017.11.004

Rando, K., Hong, K. I., Bhagwagar, Z., Li, C. S., Bergquist, K., Guarnaccia, J., et al. (2011). Association of frontal and posterior cortical gray matter volume with time to alcohol relapse: a prospective study. *Am. J. Psychiatry* 168, 183–192. doi: 10.1176/appi.ajp.2010.10020233

Shen, X., Liu, H., Hu, Z., Hu, H., and Shi, P. (2012). The relationship between cerebral glucose metabolism and age: report of a large brain PET data set. *PLoS One* 7:e51517. doi: 10.1371/journal.pone.0051517

Sherwin, B. B. (2002). Estrogen and cognitive aging in women. *Trends Pharmacol. Sci.* 23, 527–534. doi: 10.1016/s0165-6147(02)02093-x

Strelnikov, K., Rouger, J., Lagleyre, S., Fraysse, B., Deguine, O., and Barone, P. (2009). Improvement in speech-reading ability by auditory training: evidence from gender differences in normally hearing, deaf and cochlear implanted subjects. *Neuropsychologia* 47, 972–979. doi: 10.1016/j.neuropsychologia.2008.10.017

Thompson, P. M., Jahanshad, N., Ching, C. R. K., Salminen, L. E., Thomopoulos, S. I., Bright, J., et al. (2020). ENIGMA and global neuroscience: a decade of large-scale studies of the brain in health and disease across more than 40 countries. *Transl. Psychiatry* 10:100. doi: 10.1038/s41398-020-0705-1

Tisserand, D. J., and Jolles, J. (2003). On the involvement of prefrontal networks in cognitive ageing. *Cortex* 39, 1107–1128. doi: 10.1016/s0010-9452(08)70880-3

Uchida, Y., Sugiura, S., Nishita, Y., Saji, N., Sone, M., and Ueda, H. (2019). Age-related hearing loss and cognitive decline - the potential mechanisms linking the two. *Auris Nasus Larynx* 46, 1–9. doi: 10.1016/j.anl.2018.08.010

Weiner, K. S., and Zilles, K. (2016). The anatomical and functional specialization of the fusiform gyrus. *Neuropsychologia* 83, 48–62. doi: 10.1016/j.neuropsychologia.2015.06.033

Xu, B., Xiong, F., Tian, R., Zhan, S., Gao, Y., Qiu, W., et al. (2016). Temporal lobe in human aging: a quantitative protein profiling study of samples from Chinese human brain bank. *Exp. Gerontol.* 73, 31–41. doi: 10.1016/j.exger.2015.11.016

Yarkoni, T. (2009). Big correlations in little studies: inflated fMRI correlations reflect low statistical power-commentary on Vul. *Perspect. Psychol. Sci.* 4, 294–298. doi: 10.1111/j.1745-6924.2009.01127.x

Conflict of Interest: The authors declare that the research was conducted in the absence of any commercial or financial relationships that could be construed as a potential conflict of interest.

Publisher's Note: All claims expressed in this article are solely those of the authors and do not necessarily represent those of their affiliated organizations, or those of the publisher, the editors and the reviewers. Any product that may be evaluated in this article, or claim that may be made by its manufacturer, is not guaranteed or endorsed by the publisher.

frontiers in Aging Neuroscience

ORIGINAL RESEARCH
published: 03 March 2022
doi: 10.3389/fnagi.2022.806828

Machine Learning for Detecting Parkinson's Disease by Resting-State Functional Magnetic Resonance Imaging: A Multicenter Radiomics Analysis

*Dafa Shi[1], Haoran Zhang[1], Guangsong Wang[1], Siyuan Wang[1], Xiang Yao[1], Yanfei Li[1], Qiu Guo[1], Shuang Zheng[2] and Ke Ren[1,3]**

[1] Department of Radiology, Xiang'an Hospital of Xiamen University, School of Medicine, Xiamen University, Xiamen, China, [2] School of Medicine, Xiamen University, Xiamen, China, [3] Xiamen Key Laboratory for Endocrine-Related Cancer Precision Medicine, Xiang'an Hospital of Xiamen University, School of Medicine, Xiamen University, Xiamen, China

OPEN ACCESS

Edited by:
Ping Wu,
Fudan University, China

Reviewed by:
Zhengshi Yang,
Cleveland Clinic, United States
Ting Xue,
Inner Mongolia University of Science and Technology, China

***Correspondence:**
Ke Ren
renke815@sina.com

Specialty section:
This article was submitted to Parkinson's Disease and Aging-related Movement Disorders, a section of the journal Frontiers in Aging Neuroscience

Received: *01 November 2021*
Accepted: *19 January 2022*
Published: *03 March 2022*

Citation:
Shi D, Zhang H, Wang G, Wang S, Yao X, Li Y, Guo Q, Zheng S and Ren K (2022) Machine Learning for Detecting Parkinson's Disease by Resting-State Functional Magnetic Resonance Imaging: A Multicenter Radiomics Analysis. Front. Aging Neurosci. 14:806828. doi: 10.3389/fnagi.2022.806828

Parkinson's disease (PD) is one of the most common progressive degenerative diseases, and its diagnosis is challenging on clinical grounds. Clinically, effective and quantifiable biomarkers to detect PD are urgently needed. In our study, we analyzed data from two centers, the primary set was used to train the model, and the independent external validation set was used to validate our model. We applied amplitude of low-frequency fluctuation (ALFF)-based radiomics method to extract radiomics features (including first- and high-order features). Subsequently, *t*-test and least absolute shrinkage and selection operator (LASSO) were harnessed for feature selection and data dimensionality reduction, and grid search method and nested 10-fold cross-validation were applied to determine the optimal hyper-parameter λ of LASSO and evaluate the performance of the model, in which a support vector machine was used to construct the classification model to classify patients with PD and healthy controls (HCs). We found that our model achieved good performance [accuracy = 81.45% and area under the curve (AUC) = 0.850] in the primary set and good generalization in the external validation set (accuracy = 67.44% and AUC = 0.667). Most of the discriminative features were high-order radiomics features, and the identified brain regions were mainly located in the sensorimotor network and lateral parietal cortex. Our study indicated that our proposed method can effectively classify patients with PD and HCs, ALFF-based radiomics features that might be potential biomarkers of PD, and provided further support for the pathological mechanism of PD, that is, PD may be related to abnormal brain activity in the sensorimotor network and lateral parietal cortex.

Keywords: Parkinson's disease, amplitude of low-frequency fluctuation, radiomics, support vector machine, machine learning, biomarker, sensorimotor network

INTRODUCTION

Parkinson's disease (PD) is the second most common progressive neurodegenerative disease, affecting 1% of the population over 60 years (Lin et al., 2020; Ren et al., 2021), and it is becoming more and more prevalent and associated with increased mortality (Shu et al., 2021). The clinical symptoms of PD are heterogeneous, presenting a variety of motor symptoms (e.g., static tremor, bradykinesia, or rigidity) and non-motor symptoms (e.g., sensory and autonomic dysfunction, cognitive deficits, or disorders of mood) (Kim et al., 2017; Amoroso et al., 2018; Lin et al., 2020; Sheng et al., 2021). The diagnosis of PD is mainly based on clinical manifestations, imaging scans, and related biochemical examinations, which remain clinically challenging (Badea et al., 2017; Heim et al., 2017). However, accurate diagnosis of PD is essential for effective treatment and favorable prognosis. Moreover, even the main neural and pathophysiological mechanisms of PD are the degeneration of the nigrostriatal dopaminergic system; it cannot fully explain the heterogeneity of symptoms (Tuovinen et al., 2018; Sheng et al., 2021). The exact mechanism of PD is still not well understood (Tuovinen et al., 2018; Cao et al., 2020; Lin et al., 2020; Sheng et al., 2021). Therefore, quantifiable biomarkers are urgently needed for a more comprehensive understanding of the physiological mechanism of PD and improving the diagnosis accuracy.

Resting-state functional magnetic resonance imaging (rs-fMRI), as one of the most commonly used non-invasive techniques in neuroimaging, has been widely used in the diagnosis (Heim et al., 2017; Rubbert et al., 2019; Pang et al., 2021; Shi et al., 2021a), monitoring of treatment effects (Morgan et al., 2017; Ge et al., 2020), clinical score prediction (Hou et al., 2016), and conversion prediction (Hojjati et al., 2018) in neuropsychiatric diseases. The amplitude of low-frequency fluctuations (ALFF) is one of the most commonly used measurements of rs-fMRI. It can detect the amplitude of spontaneous, low-frequency oscillations of blood oxygen level-dependent signals to reflect the regularity and physiological state of neuron autonomous activity in different brain regions (Qian et al., 2020). This approach provides a reliable and sensitive measurement to characterize the spontaneous neural activity and has been widely used in PD (Cao et al., 2020; Tian et al., 2020; Pang et al., 2021; Shi et al., 2021b).

Radiomics is a data mining method proposed by Lambin et al. (2012), which can extract high-throughput features from medical images to characterize the characteristics of the lesions (Lambin et al., 2012; Aerts et al., 2014). Subsequently, the machine learning methods are performed for data mining. Recently, rs-fMRI-based radiomics has been applied to explore neurological disease biomarkers for disease diagnosis and underlying mechanisms (Sun et al., 2018; Mo et al., 2019; Wang Y. et al., 2020; Zhao et al., 2020), including PD (Cao et al., 2020; Shi et al., 2021b). However, the sample sizes of the above studies are limited and come from a single center, and the extracted features are the intensity histogram-based features.

In this study, we aimed to use data from two centers (one for model training and the other one for external validation of the model), and ALFF-based multi-order radiomics (including first- and high-order features) to identify potential neuroimaging biomarkers for distinguishing patients with PD from healthy controls (HCs) and explore the underlying mechanisms of PD. To the best of our knowledge, our study is the first to apply multi-order radiomics to identify PD biomarkers.

MATERIALS AND METHODS

Participants

The data for this study were obtained from two independent public available databases. The primary set included 59 patients with PD and 41 age- and sex-matched HCs (Hu et al., 2015).[1] The independent external validation set included 27 patients with PD and 16 HCs from the NEUROCON dataset, which were available at Functional Connectomes Project/International Neuroimaging Data-Sharing Initiative (FCP/INDI) (Badea et al., 2017).[2] Clinical measurements were obtained, which included the Mini-Mental State Examination (MMSE) and the 17-item Hamilton Depression Rating Scale (HDRS-17) for the primary set and the Hoehn and Yahr staging scale (H&Y) and Unified Parkinson's Disease Rating Scale (UPDRS, on/off medication) motor score for the external validation set. Demographic and clinical information of participants are listed in **Table 1**. Ethical approval was obtained by each institution, and all participants provided written informed consent.

Data Acquisition

Primary Set

All subjects underwent structural and functional MRI scanning on a 3-T Siemens Verio scanner. Data acquisition parameters can be found in previous studies (Hu et al., 2015; Shi et al., 2021b). The structural images were acquired with high-resolution three-dimensional T1-weighted sequences [slices = 128, repetition time (TR)/echo time (TE) = 2,530/3.43 ms, field of view (FOV) = 256 × 256 mm, slice thickness/gap = 1.33/0.5 mm, matrix = 256 × 192, voxel size = 1 × 1.33 × 1.83 mm^3, and flip angle (FA) = 7]. Rs-fMRI images were acquired with a gradient-recalled echo-planar imaging (GRE-EPI) pulse sequences (140 volumes, slices = 31, TR/TE = 2,000/30 ms, FOV = 220 × 220 mm, slice thickness/gap = 3.5/0.6 mm, matrix = 64 × 64, voxel size = 3.4 × 3.4 × 4.1 mm^3, and FA = 90°).

External Validation Set

All subjects underwent structural and functional MRI scanning on a 1.5-T Siemens Avanto scanner. Data acquisition parameters can be found in the previous study (Badea et al., 2017) and online (see text footnote 2). The structural images were acquired with T1-weighted magnetization prepared rapid acquisition gradient-echo sequences (TR/TE = 1,940/3.08 ms and voxel size = 0.97 × 0.97 × 1 mm^3). Rs-fMRI images were acquired with EPI sequences (137 volumes, slices = 27, TR/TE = 3,480/50 ms, voxel size = 3.8 × 3.8 × 5 mm^3, and FA = 90°).

[1] http://dx.doi.org/10.6084/m9.figshare.1433996

[2] http://fcon_1000.projects.nitrc.org/indi/retro/parkinsons.html

TABLE 1 | Demographic and clinical data of the two datasets.

	Primary set			External validation set		
	PD	**HC**	***P*-value**	**PD**	**HC**	***P*-value**
Age (years)[a]	56.46 ± 9.16 (32–71)	56.37 ± 5.01 (47–70)	0.95	68.70 ± 10.55 (45–86)	67.62 ± 11.89 (46–82)	0.76
Sex (M/F)[b]	35/24	20/21	0.32	16/11	5/11	0.12
Education (years)	11.31 ± 3.43 (2–19)	11.29 ± 4.58 (2–22)	0.99	–	–	–
MMSE[c]	29 (28–30) (24–30)	30 (29–30) (24–30)	0.017	–	–	–
HDRS-17[c]	9 (5–17) (0–28)	2 (1–3) (0–10)	<0.001			
H&Y	–	–	–	2 (2–2) (1.0–2.5)		–
UPDRS motor score (off)	–	–	–	28.33 ± 9.27 (10–43)	–	–
UPDRS motor score (on)	–	–	–	9.22 ± 5.27 (0–19)	–	–

Data are presented as the mean ± SD (range) for normally distributed data or median (interquartile range) (range) for non-normally distributed data.
[a]The P-value was calculated using t-test.
[b]The P-value was calculated using the chi-square test.
[c]The P-value was calculated using the Mann-Whitney test.
Abbreviations: MMSE, Mini-mental State Examination; HDRS-17, 17-item Hamilton Depression Rating Scale; H&Y, Hoehn and Yahr staging scale; UPDRS, Unified Parkinson's Disease Rating Scale; M, male; F, female.

Data Preprocessing and Amplitude of Low-Frequency Fluctuation Calculation

In this study, the data preprocessing was performed using the toolbox for Data Processing and Analysis of Brain Imaging (DPABI) (Yan et al., 2016).[3] The primary set has completed the data preprocessing and ALFF calculation, and the processing flow is detailed in the previous study (Hu et al., 2015). A similar procedure as described above was used for processing the external validation set data. In brief, the preprocessing procedures included the following: removal of the first six time points (20.88 s); slice timing and spatial realignment (subjects with head motion >2.5 mm or >2.5° were excluded); segmentation of 3D T1-weighted anatomical images by new segment and registration by the Diffeomorphic Anatomical Registration Through Exponentiated Lie Algebra (DARTEL); spatial normalization by DARTEL and resampling ($3 \times 3 \times 3$ mm^3); smooth with a 6-mm full-width-half-maximum Gaussian kernel; band-pass filter (0.01–0.10 Hz); linear drift, nuisance signal (white matter, cerebrospinal fluid, and global signal), and 24 head motion parameters were removed. Subsequently, we obtained the mean ALFF maps by DPABI's default algorithm.

Feature Extraction

The mean ALFF maps were segmented into 246 regions of interest (ROIs) using the Brainnetome 246 atlas (**Supplementary Material**). In this study, a total of 432 multi-order radiomics features were extracted from each ROI, including first-order intensity histogram-based features (15 features), texture features (33 features), and features of wavelet transformation in eight directions [$(15 + 33) \times 8 = 384$ features]. In our study, the intensity histogram-based features are first-order features, which are used to characterize the gray level intensity in the image, using first-order statistics, calculated from the histogram of all voxels in the image. The texture features and wavelet features are high-order features. The texture features were able to quantify the spatial heterogeneity of the intensity level in the image. For wavelet features, wavelet filters are applied to the original images to convert original images to versions that focus on the information at different scales. Wavelet decomposition with all possible combinations of high (H)- or low (L)-pass filters in each of the three dimensions (LLL, LLH, LHL, LHH, HLL, HLH, HHL, and HHH) is applied. In this study, the first-order and texture features of eight directions were calculated. The definitions and detailed descriptions of the features can also be found in previous studies (Aerts et al., 2014; Feng et al., 2018; Zhao et al., 2020; Cui et al., 2021; Peng et al., 2021) and are listed in the **Supplementary Material**. The whole feature extraction process is illustrated in **Figures 1A,B**.

Feature Selection, Model Construction, and Evaluation

In our study, we used the primary set for hyper-parameter optimization, feature selection, and model training and used the independent external validation set for external validation of the model. For feature selection, *t*-test and least absolute shrinkage and selection operator (LASSO) were applied, and the support vector machine (SVM) model with a linear kernel and default parameter value (i.e., $C = 1$) was chose as the classifier. The performance of the model was evaluated with receiver operating

[3]http://rfmri.org/DPABI

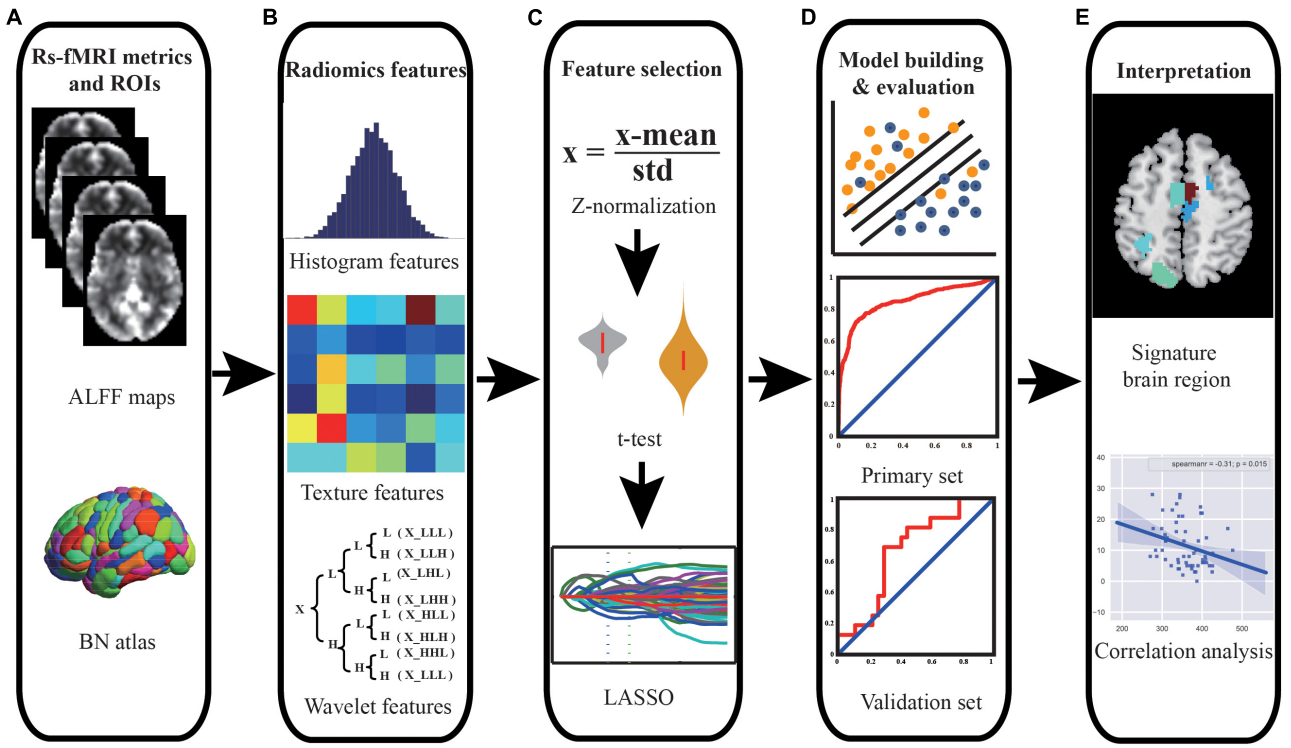

FIGURE 1 | Schematic outline of the whole study analysis procedure. **(A)** ALFF maps and brain segmentation with Brainnetome 246 atlas. **(B)** Intensity histogram-, texture-, and wavelet transformation-based features were extracted from ALFF images. **(C)** Feature selection was performed using *t*-test and LASSO to select significant features and reduce dimensionality. **(D)** SVM model was constructed, and ROC curve analysis was employed to quantify the performance of the classifier in the primary set and independent external validation set. **(E)** The discriminative features were identified, and correlation analyses were performed to explain the underlying pathological mechanism of PD. Abbreviations: ALFF, amplitude of low-frequency fluctuation; BN, Brainnetome; LASSO, least absolute shrinkage and selection operator; SVM, support vector machine; ROC, receiver operating characteristic; PD, Parkinson's disease.

characteristic (ROC) curve analysis. In addition, the independent external dataset was applied for validating the generalization of our model. The whole procedure is illustrated in **Figures 1C,D**, **2**.

First, we performed *Z*-score standardization on the features to reduce the influence of the different units imposed by the units of each feature and improve the performance of the model. The normalization of the primary and validation set were performed, respectively. Subsequently, we applied the *t*-test ($P < 0.05$) to select the features with significant differences between the patients with PD and HCs. Then, LASSO logistic regression was utilized to further reduce the dimensionality of the data. For LASSO logistic regression, the regularization parameter λ controls the number of model features and affects the performance of the model. So, the grid search method was optimized to determine the optimal hyper-parameter λ. According to the previous study (Chen X. et al., 2017; Zhao et al., 2018), the value of λ in our study was set to (0.05, 0.10, . . ., 0.60). The nested 10-fold cross-validation method (Ding et al., 2015, 2017; Zhao et al., 2018; Wottschel et al., 2019; Tu et al., 2020; Zhou B. et al., 2020) was performed to determine the optimal hyper-parameter λ of LASSO and evaluate the performance of the model. The outer 10-fold cross-validation was applied to estimate the performance of the model, and the inner 10-fold cross-validation was performed to determine the optimal hyper-parameter (optimal λ), in which the λ with the highest accuracy was selected as the optimal λ value.

To avoid the category information leakage, *t*-test and LASSO were carried out in a training set of inner 10-fold cross-validation, not for all subjects. Specifically, in each fold of the inner 10-fold cross-validation procedure, we had conducted the above *t*-test and LASSO on all subjects except one fold that was taken out. In other words, *t*-test and LASSO were only performed in the training set in the inner training set; no statistical tests were performed on the independent hold-out test data (inner and outer test set). Thus, analyses were unbiased in the sense that the training features were selected independently of test subjects. The whole procedure of nested 10-fold cross-validation was illustrated in **Figure 2**. To obtain unbiased estimates of classification error, we repeated the nested 10-fold cross-validation framework 20 times (Oh et al., 2019; Lin et al., 2020).

For model construction, we used an SVM to construct the model, where the SVM model adopted linear kernel function and default parameters (i.e., $C = 1$). The 10-fold cross-validation method (repeated 20 times) was applied to evaluate the

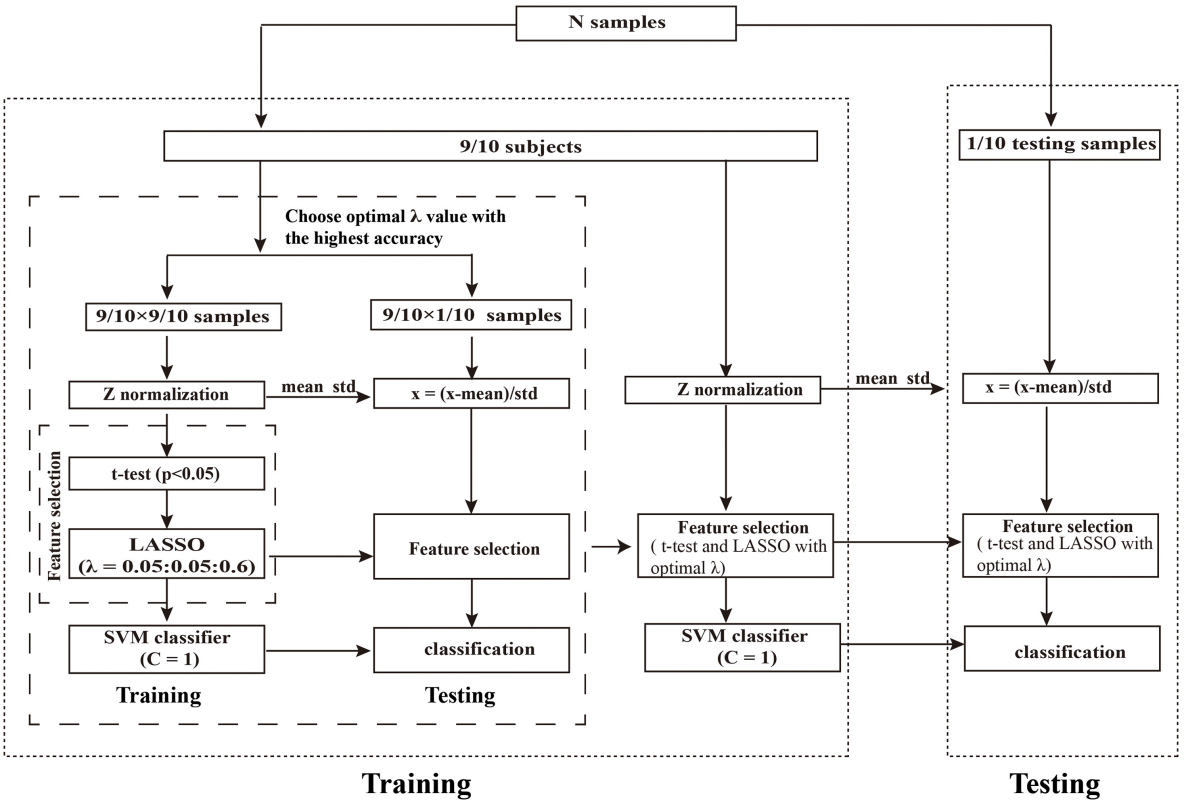

FIGURE 2 | Schematic overview of the nested 10-fold cross-validation classification framework. We determined the optimal λ by grid-search from the set of (0.05, 0.10,. . .,0.60) with 10-fold cross-validation. The λ with the highest classification accuracy was selected as the optimal λ. Abbreviations: LASSO, least absolute shrinkage and selection operator; SVM, support vector machine.

performance of the SVM model. The mean accuracy, area under the curve (AUC), sensitivity, specificity, precision, F1 score, and balance accuracy across all folds (10-folds) and all repetitions (20 times) (Chen et al., 2016; Chen X. et al., 2017; Zhao et al., 2018) were employed to quantify the performance of the classifier. The accuracy, sensitivity, specificity, precision, F1 score, and balance accuracy were defined as follows:

$$\text{Accuracy} = (\text{TP} + \text{TN})/(\text{TP} + \text{TN} + \text{FP} + \text{FN})$$

$$\text{Sensitivity} = \text{TP}/(\text{TP} + \text{FN})$$

$$\text{Specificity} = \text{TN}/(\text{TN} + \text{FP})$$

$$\text{Precision} = \text{TP}/(\text{TP} + \text{FP})$$

$$\text{Recall} = \text{TP}/(\text{TP} + \text{FN})$$

$$\text{F1 score} = 2 \times \text{Precision} \times \text{Recall}/(\text{Precision} + \text{Recall})$$

$$\text{Balance Accuracy} = 0.5 \times (\text{Sensitivity} + \text{Specificity})$$

where TP represents the number of positive samples correctly classified; TN represents the number of negative samples correctly classified; FP represents the number of negative samples incorrectly classified; FN represents the number of positive samples incorrectly classified.

To obtain the final model, all the participants in the primary set were used to train the model with the optimal λ value (Shen et al., 2019; Zhao et al., 2020). Due to the different data of each fold, the optimal hyper-parameter might be different. We chose the λ with the highest frequency selected in all folds as the optimal hyper-parameter. In addition, to evaluate the generalization of the model, the independent external validation set was conducted to validate the performance of our model, where the model parameters (linear kernel function, $C = 1$) and selected features were the same as our final model. The accuracy, AUC, sensitivity, specificity, precision, F1 score, and balance accuracy were calculated to quantify the performance of the classifier in the external validation set.

To test the significance of model performances (AUC and accuracy), permutation tests were performed (Tang et al., 2017; Shen et al., 2019; Tian et al., 2020). Specifically, we shuffled the class labels (PD or HC) 1,000 times without replacement and performed the above-mentioned feature selection and model construction analysis process each time to obtain the permutated accuracies and AUCs. The *P*-value was defined as follows:

$$\text{P} = (1 + \text{N}_{\text{GP}})/(1 + \text{N})$$

where N_{GP} represents the number of permutations that obtained greater accuracy or AUC than the actual value, and N was the

TABLE 2 | Classifier performances in the primary and external validation sets.

	Accuracy	AUC	Sensitivity	Specificity	Precision	F1 score	Balance accuracy	*P*-value (accuracy)	*P*-value (AUC)
Primary set	81.45%	0.850	86.86%	73.66%	82.59%	83.68%	80.26%	0.001	0.001
Validation set	67.44%	0.667	70.37%	62.50%	76.00%	73.08%	66.44%	0.035	0.030

Abbreviation: AUC, area under the curve.

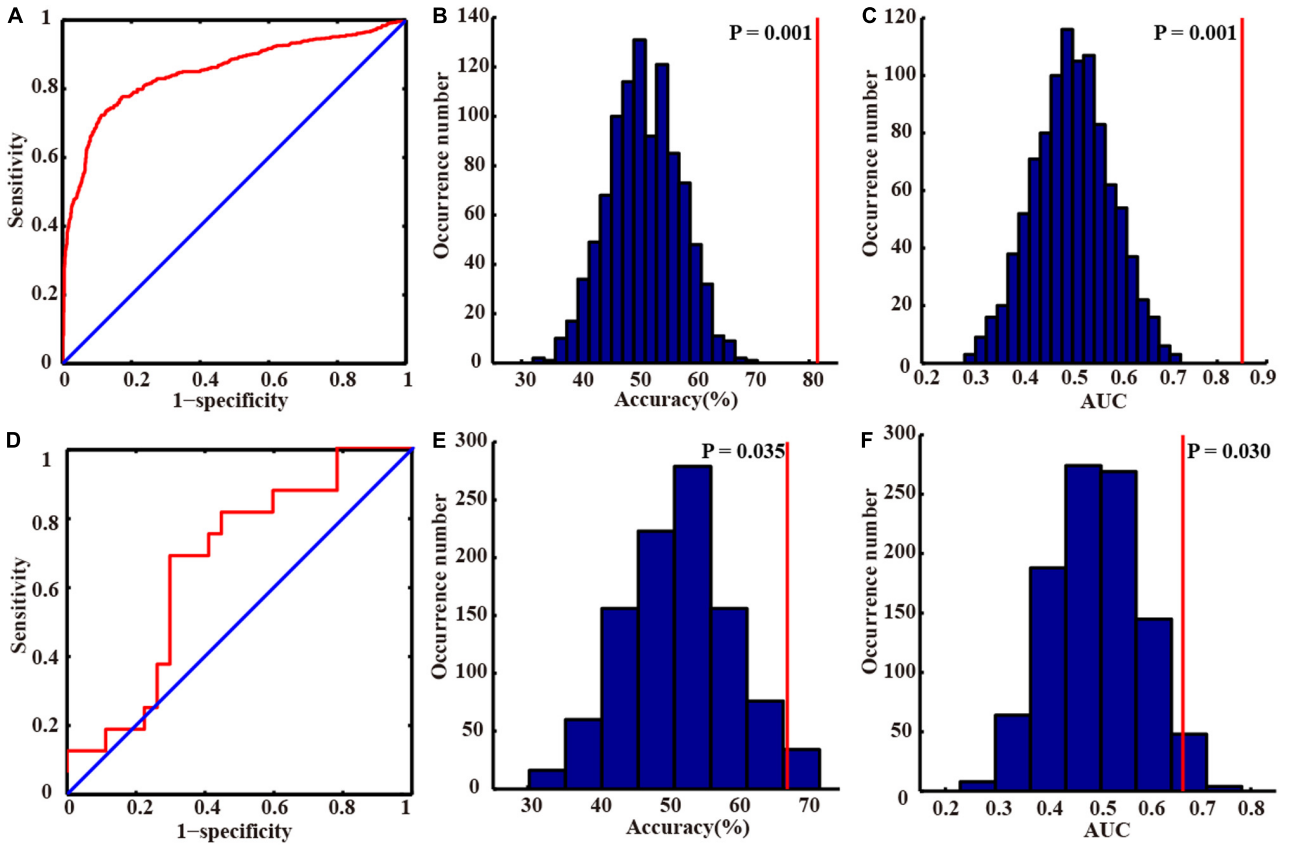

FIGURE 3 | Classification performances in the primary and independent external validation sets. The receiver operating characteristic curves of the primary **(A)** and independent external validation sets **(D)**. The distributions of the permutated accuracy values of the primary **(B)** and validation set **(E)**. The distributions of the permutated AUC values of the primary **(C)** and validation set **(F)**. The red line indicates the values obtained using the real labels. Abbreviation: AUC, area under the curve.

times of permutation. In this study, the value of N is 1,000. We performed this analysis on the primary and external validation set, respectively.

Identification of Discriminative Features

Since we implemented 10-fold cross-validation to evaluate the performance of our model, the training sets were different in each fold, and the selected features were also different. We sorted the selected feature frequencies and selected features in the top 10 discriminative regions as discriminative features (Zhou B. et al., 2020; **Figure 1E**). In each fold, we could also obtain feature weights. We calculated the mean weight of discriminative features across all folds. The greater the absolute value of the feature weight, the greater the contribution to the model.

Relationship Between the Discriminative Features and Clinical Measurements

Spearman's correlation coefficients were calculated to assess the association between the discriminative features and clinical measurements of patients with PD in the primary and external validation set (**Figure 1E**). $P < 0.05$ was considered statistically significant.

RESULTS

Demographic and Clinical Information

The demographic and clinical characteristics of the participants in the primary and external validation set are summarized in **Table 1**. There were no significant differences in age, sex,

and education duration between patients with PD and HCs ($P > 0.05$). The MMSE and HDRS-17 of patients with PD were significantly lower/higher than that of HCs in the primary set ($Z = -2.39$, $P = 0.017$; $Z = -7.07$, $P < 0.001$, respectively).

Classification Performance

In our study, we applied the grid search method to determine the optimal hyper-parameter λ of nested 10-fold cross-validation in the primary set. The mean accuracy was 81.45%, and AUC was 0.850 in the primary set. We chose the λ with the highest frequency selected in all folds as the optimal λ (λ = 0.45, **Supplementary Figure 1**) and constructed the final model. In the external validation set, our model also achieved great model generalization (accuracy = 67.44% and AUC = 0.667). The permutation test showed that the AUCs and accuracies were significantly higher than chance ($P < 0.05$). More detailed results are shown in **Table 2** and **Figure 3**.

Discriminative Features

To determine which features contributed the most to the classification of patients with PD, we reported discriminative features and the feature weights. The features of the top 10 discriminative regions were selected as discriminative features in this study (**Table 3** and **Figure 4**). The discriminative regions (including 17 features) included the bilateral superior frontal gyrus [SFG, SFG_R_7_4, and SFG_L(R)_7_5], precentral gyrus [PrG, PrG_L(R)_6_4], right paracentral lobule (PCL, PCL_R_2_2), precuneus (PCun, PCun_R_4_3), left inferior temporal gyrus (ITG, ITG_L_7_3), and superior parietal lobule (SPL, SPL_L_5_2, and SPL_L_5_3). The brain regions were mainly located in the frontal lobe, especially SFG.

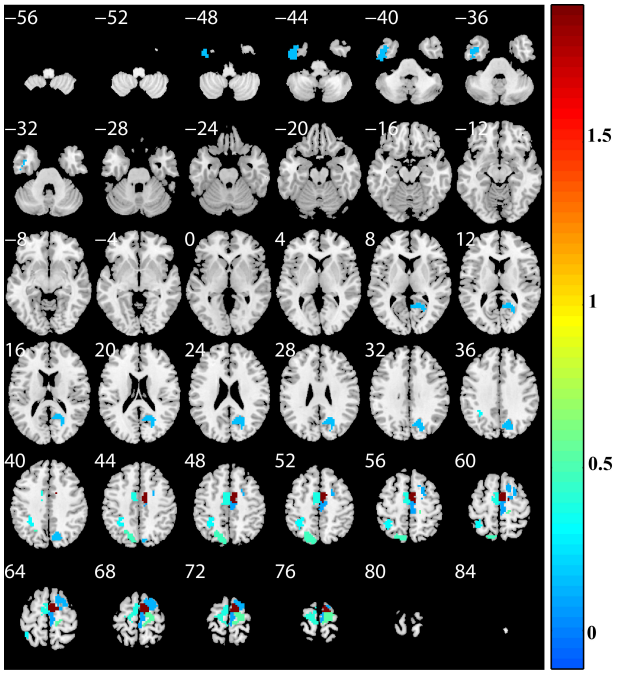

FIGURE 4 | Discriminative brain regions. The discriminative regions included the bilateral superior frontal gyrus, precentral gyrus, right paracentral lobule, precuneus, left inferior temporal gyrus, and superior parietal lobule. The color bar value represents the absolute value of the weight value of the brain regions.

TABLE 3 | Discriminative features for patients with PD classification.

Lobe	Gyrus regions	Anatomical and modified cyto-architectonic descriptions	Feature	Weight
Frontal lobe	PrG_L_6_4	Area 4 (trunk region)	Minimum	0.2093
Frontal lobe	PrG_R_6_4	Area 4 (trunk region)	Minimum	−0.0612
Temporal lobe	ITG_L_7_3	Rostral area 20	Mean-HHL	−0.1392
Frontal lobe	SFG_L_7_5	Medial area 6	Median-HLL	−0.3554
Parietal lobe	SPL_L_5_3	Lateral area 5	Minimum-LLL	−0.3194
Frontal lobe	SFG_R_7_5	Medial area 6	Minimum-HLL	−0.3867
Frontal lobe	SFG_R_7_5	Medial area 6	Range-HLL	0.2307
Parietal lobe	PCun_R_4_3	Dorsomedial parietooccipital sulcus	Entropy-HHH	−0.1593
Frontal lobe	PrG_R_6_4	Area 4 (trunk region)	CT-HLL	0.3091
Frontal lobe	SFG_R_7_5	Medial area 6	Contrast-LHH	−0.4821
Frontal lobe	PrG_R_6_4	Area 4 (trunk region)	Correlation-HLL	0.1678
Parietal lobe	SPL_L_5_2	Caudal area 7	Homogenetity 2-HHH	0.4561
Frontal lobe	PCL_R_2_2	Area 4 (lower limb region)	IMC1-HHH	−0.0929
Frontal lobe	SFG_R_7_4	Dorsolateral area 6	SRE-HLH	−0.1312
Frontal lobe	SFG_R_7_5	Medial area 6	GLN-HHL	0.2744
Frontal lobe	PrG_L_6_4	Area 4 (trunk region)	GLN-HHH	0.1876
Frontal lobe	SFG_R_7_5	Medial area 6	RLN-HHH	−0.4933

Abbreviations: PD, Parkinson's disease; PrG, precentral gyrus; ITG, inferior temporal gyrus; SFG, superior frontal gyrus; SPL, superior parietal lobule; PCun, precuneus; SPL, superior parietal lobule; PCL, paracentral lobule; CT, cluster tendency; IMC, informational measure of correlation; SRE, short-run emphasis; GLN, gray level non-uniformity; RLN, run-length non-uniformity; L, left; R, right.

Correlations Between the Discriminative Features and Clinical Measurements

The results of correlation analyses are shown in **Figure 5**. In primary set, SFG_R_7_5-GLN-HHL was negatively correlated with HDRS-17 (Spearman's correlation $r = -0.31$ and $P = 0.015$). In addition, in external validation set, we found positive correlations between SFG_R_7_4-SRE-LHL and UPDRS motor score (on medication) and UPDRS motor score (off medication) (Spearman's correlation $r = 0.43$, $P = 0.024$; Spearman's correlation $r = 0.39$, $P = 0.043$).

DISCUSSION

In our study, we selected brain region ROIs and extracted radiomics features based on Brainnetome 246 atlas, including intensity histogram-, texture-, and wavelet transformation-based features, and applied an SVM classifier to construct a model to classify patients with PD and HCs. We found that the classification accuracy of the model was 81.45%, and the AUC

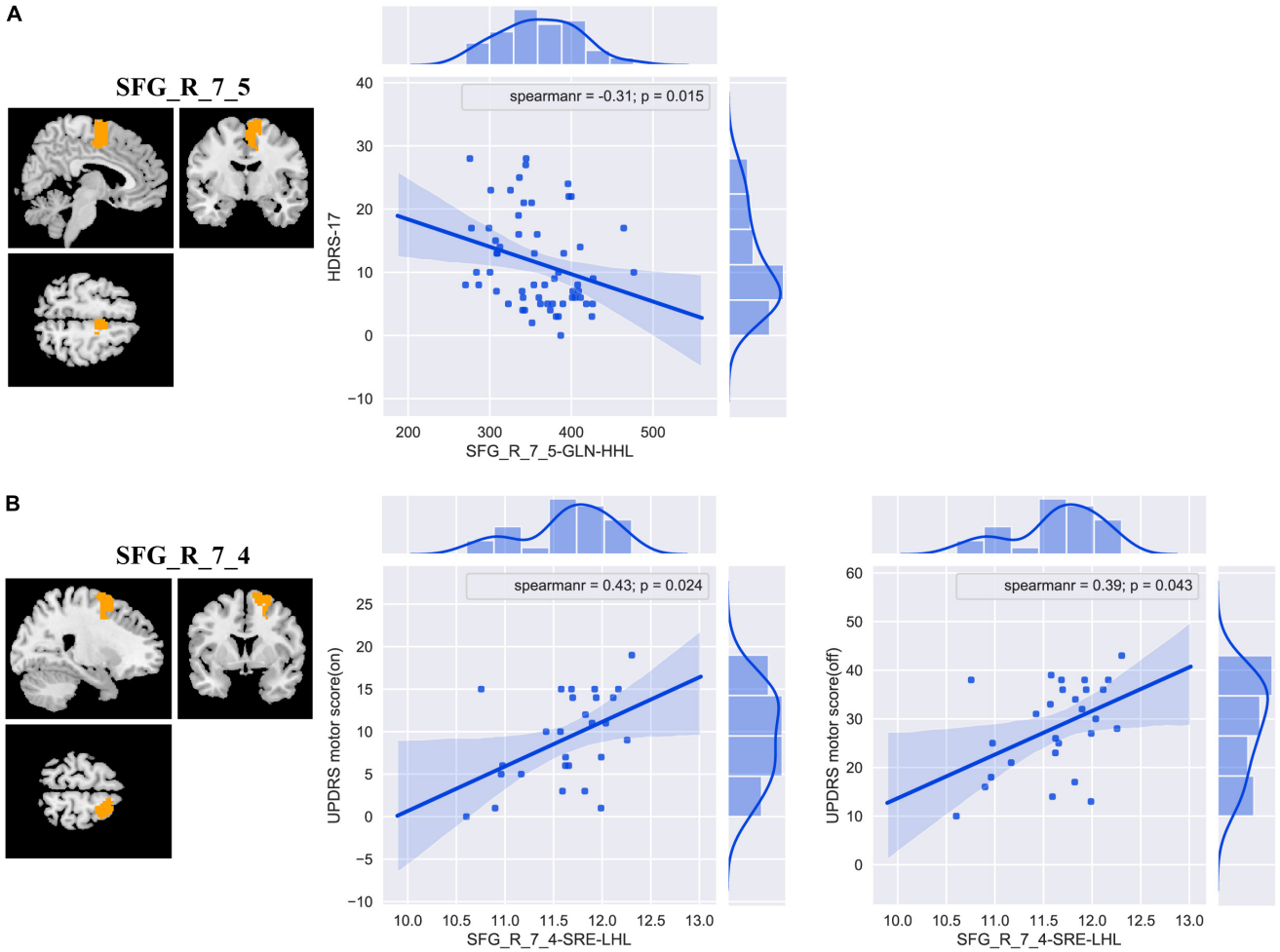

FIGURE 5 | The correlation analyses between the discriminative features and clinical measurements in patients with PD in the primary **(A)** and external validation **(B)** set. Abbreviations: SFG, superior frontal gyrus; HDRS-17, 17-item Hamilton Depression Rating Scale; UPDRS, Unified Parkinson's Disease Rating Scale; GLN, gray level non-uniformity; SRE, short-run emphasis; PD, Parkinson's disease.

was 0.850 in the primary set. In the independent external validation set, our model has good generalization ability with an accuracy of 67.44% and an AUC of 0.667. More importantly, we are the first to apply multi-order (including first- and high-order features) radiomics to identify PD biomarkers, and our study demonstrated that radiomics features may be potential biomarkers of PD.

Previous studies have confirmed the value of rs-fMRI in neuropsychiatric diseases (Szewczyk-Krolikowski et al., 2014; Hu et al., 2015; O'Callaghan et al., 2016). Recently, with the development of machine learning technologies, more and more studies have used machine learning methods to explore the classification, prognosis prediction, and physiological mechanism of neuropsychiatric diseases, including PD (Cao et al., 2020; Lin et al., 2020; Pang et al., 2021; Shu et al., 2021; Talai et al., 2021; Zhang et al., 2021). The ROI-based feature extraction is the most commonly used feature extraction method (Wang L. et al., 2020; Zhao et al., 2020; Shi et al., 2021b; Talai et al., 2021), and it is a useful method to reduce the data dimensionality (Wang L. et al., 2020). Functionally defined parcelation and high spatial resolution segmentation might be able to detect a more significant difference, and the anatomical boundary might not match the functional boundary that has been reported in previous literature (Rosenberg et al., 2016; Chen et al., 2018). Therefore, we chose Brainnetome 246 atlas to segment brain region ROIs in our study. The previous ROI-based feature extraction methods mostly only extracted intensity histogram-based features (Peng et al., 2017; Cao et al., 2020; Jin et al., 2020; Tian et al., 2020; Zhou B. et al., 2020). In recent years, the value of high-order features (texture and wavelet features) had been confirmed and widely used in various studies (Feng et al., 2018; Mo et al., 2019; Zhao et al., 2020; Shu et al., 2021). To the best of our knowledge, the application of multi-order radiomics (including first- and high-order features) on PD has not been reported. We found that our method achieved perfect classification performance (accuracy = 81.45% and AUC = 0.850) and also obtained great performance in the independent external validation set (accuracy = 67.44% and AUC = 0.667), indicating

that our model had good generalization (Zhao et al., 2020). In addition, our study indicates that the features that significantly contributed to the classification were mainly high-order features (wavelet features). Additionally, only two of the 17 discriminative features identified by this study were first-order features, the remaining 15 features were high-order features, and the brain region identified by both the two features based on first-order features was also identified by high-order features. Those results confirmed the value of high-order radiomics features, which may be a better characterization of lesions than first-order radiomics features and more suitable as potential biomarkers for PD (Feng et al., 2018; Mo et al., 2019; Zhao et al., 2020). Those findings are consistent with the previous results mentioned earlier.

Radiomics can extract high-throughput features from medical images (Lambin et al., 2012; Aerts et al., 2014; Feng et al., 2018; Sun et al., 2018; Zhao et al., 2020), and the dimension of features is much higher than the sample size, which may easily make the model fall into a "curse of dimension" and model overfitting. Especially, we extracted not only first-order features but also high-order features. In addition, many features may be uninformative, irrelevant, or redundant; therefore, feature selection and data dimensionality reduction were performed before our SVM model construction. First, we performed the *t*-test ($P < 0.05$) to identify the significant features between the patients with PD and HCs. Subsequently, LASSO logistic regression was performed to choose the most important features for classification. The *t*-test is a filter method to reduce the data dimensionality. It can simply and quickly remove features with no or less information and has been widely used in machine learning (Lanka et al., 2020a; Tu et al., 2020; Wang Y. et al., 2020). It is a built-in algorithm of many software, such as BrainNetClass (Zhou Z. et al., 2020), MALINI (Lanka et al., 2020b), and MANIA (Grotegerd et al., 2014), and it is recommended as the first step in data dimensionality reduction (Lanka et al., 2020b). LASSO is very suitable for high-dimensional data processing (Chen X. et al., 2017; Zhao et al., 2018; Wang Y. et al., 2020; Shu et al., 2021). It can select the most important features, compress unimportant feature coefficients to zero, and eliminate multicollinearity between features to achieve the purpose of data dimensionality reduction and feature selection (Chen et al., 2016; Chen X. et al., 2017; Zhao et al., 2018; Huang et al., 2020; Wang Y. et al., 2020; Shu et al., 2021). We used the grid search method ($\lambda = 0.05, 0.10...0.60$) and nested 10-fold cross-validation to determine the optimal lasso hyper-parameter λ and evaluate the performance of the model. The outer 10-fold cross-validation was applied to estimate the performance of the model, and the inner 10-fold cross-validation was performed to determine the optimal hyper-parameter (optimal λ). In our study, in each fold of 10-fold cross-validation, the mean number of remaining features after LASSO analysis was 16. LASSO analysis greatly reduced the number of features, and most of the features appeared repeatedly in multiple folds. Those confirmed the effectiveness of LASSO and the stability of the features that we identified (Feng et al., 2018; Mo et al., 2019; Zhao et al., 2020; Shu et al., 2021). Those are consistent with the above-mentioned previous results.

Support vector machine is one of the most commonly used machine models, especially in neuroimaging studies in which the sample size is relatively limited (Hong et al., 2017; Tian et al., 2020; Shu et al., 2021; Talai et al., 2021; Zhang et al., 2021). SVM incorporates several advantageous properties to reduce overfitting and deliver good generalization performance despite a small sample size (Hong et al., 2017; Mo et al., 2019). The SVM classifier was selected to construct the model in our study. The results demonstrated that our method achieved perfect classification performance and also obtained great generalization performance in the external validation set (**Table 2** and **Figure 3**).

We found that, in addition, the discriminative regions included bilateral SFG, PrG, right PCL, precuneus, left ITG, and SPL. The features of bilateral SFG and PrG served as the most important features in classification, and the features of SFG were correlated with clinical measurements [HDRS-17 and UPDRS motor score (on/off medication)]. The SFG and PrG are important components of the sensorimotor network, which plays a central role in the preparation and execution of motor functions. Multiple previous studies have reported the sensorimotor network dysfunction in patients with PD (Tuovinen et al., 2018; Rubbert et al., 2019; Cao et al., 2020; Chen et al., 2021; De Micco et al., 2021; Wang et al., 2021). Abnormal brain activation of SFG and PrG was also revealed in previous studies (Lin et al., 2017; Peng et al., 2017; Cao et al., 2020; Guo et al., 2020; Tian et al., 2020; Pang et al., 2021). Our study found that the SFG features were correlated with UPDRS motor score and HDRS, indicating the association between SFG and PD symptoms. Many studies indicated that the lateral parietal cortex (including SPL) plays an important role in PD with movement dysfunction (Tian et al., 2020), and the precuneus is located in SPL and involved in visuospatial processing, episodic memory, self-reflection, and consciousness (Guo et al., 2020). Abnormal spontaneous brain activities in right PCL (Chen B. et al., 2017; Guo et al., 2020; Sheng et al., 2021; Suo et al., 2021), left ITG (Jiang et al., 2016; Chen B. et al., 2017; Guo et al., 2020; Tian et al., 2020), and STG (Chen B. et al., 2017; Lin et al., 2017) in patients with PD had also been reported. Those are consistent with the previous results. Our results indicated that our method could effectively identify the brain spontaneous abnormal activities of patients with PD and could be used as a potential biomarker for PD and provided further support for the pathological mechanism of PD, that is, PD may be related to abnormal brain activity in the sensorimotor network and lateral parietal cortex.

Several issues need to be addressed in this study. First, although the sample size of our study is relatively larger than that of some machine learning studies (Hou et al., 2016; Tang et al., 2017) and our data come from two centers, the sample size is still relatively limited. Therefore, future study with more participants and multiple centers will improve the generalizability of our findings. Second, although the field strength of the MRI scanners and data acquisition parameters of the two datasets are different, we analyzed the data of the two centers separately. One was used to train the model; the other one was used to validate the performance of the model. Both the two datasets had good classification performance, which further indicated the good classification performance and generalization of our model. Third, it has been reported that combining multimodal data and clinical data can improve the performance of the

machine learning model (Shi et al., 2021a; Talai et al., 2021), but the primary set in this study only contained ALFF data. A subsequent study should incorporate other modal MRI data, metrics, and clinical data to construct and evaluate the model. Fourth, previous studies (Lin et al., 2017; Pang et al., 2021) have reported that patients with PD have structural and functional abnormalities in the cerebellum, but the Brainnetome 246 atlas we used in this study did not include the cerebellum.

CONCLUSION

This study uses the ALFF-based radiomics method to extract multi-order features and uses an SVM to construct the model to classify patients with PD and HCs. Good model performances were achieved in both primary and independent external validation sets, most of the discriminative features were high-order features and moderately related to PD symptom scores, and the identified brain regions were mainly located in the sensorimotor network and lateral parietal cortex. Our results indicated that our proposed method can effectively classify patients with PD and HCs, in which ALFF-based radiomics features might be potential biomarkers of PD, and provided further support for the pathological mechanism of PD, that is, PD may be related to abnormal brain activity in the sensorimotor network, thalamus, and lateral parietal cortex.

DATA AVAILABILITY STATEMENT

Data used in this study were obtained from two independent publicly available databases: primary set downloaded from http://dx.doi.org/10.6084/m9.figshare.1433996 and external validation set downloaded from http://fcon_1000.projects.nitrc.org/indi/retro/parkinsons.html. Further inquiries can be directed to the corresponding author.

ETHICS STATEMENT

The studies involving human participants were reviewed and approved by Medical Research Ethical Committee of Nanjing Brain Hospital and National Institute for Research and Development in Informatics, Bucharest, Romania. The patients/participants provided their written informed consent to participate in this study.

AUTHOR CONTRIBUTIONS

DS conducted the experiment, performed the data processing and analysis, and wrote and edited the manuscript. HZ and GW collected the data, performed the data processing and analysis, and edited the manuscript. SW, XY, YL, QG, and SZ collected the data and performed the data processing and analysis. KR supervised the whole study. All authors contributed to this study and approved the submitted version.

FUNDING

This study was supported by the Scientific Research Foundation for Advanced Talents, Xiang'an Hospital of Xiamen University (No. PM201809170011).

ACKNOWLEDGMENTS

We thank the data authors for providing access to the data used in our study.

SUPPLEMENTARY MATERIAL

The Supplementary Material for this article can be found online at: https://www.frontiersin.org/articles/10.3389/fnagi.2022.806828/full#supplementary-material

REFERENCES

Aerts, H. J., Velazquez, E. R., Leijenaar, R. T., Parmar, C., Grossmann, P., Carvalho, S., et al. (2014). Decoding tumour phenotype by noninvasive imaging using a quantitative radiomics approach. *Nat. Commun.* 5:4006. doi: 10.1038/ncomms5006

Amoroso, N., La Rocca, M., Monaco, A., Bellotti, R., and Tangaro, S. (2018). Complex networks reveal early MRI markers of Parkinson's disease. *Med. Image Anal.* 48, 12–24. doi: 10.1016/j.media.2018.05.004

Badea, L., Onu, M., Wu, T., Roceanu, A., and Bajenaru, O. (2017). Exploring the reproducibility of functional connectivity alterations in Parkinson's disease. *PLoS One* 12:e0188196. doi: 10.1371/journal.pone.0188196

Cao, X., Wang, X., Xue, C., Zhang, S., Huang, Q., and Liu, W. (2020). A radiomics approach to predicting Parkinson's disease by incorporating whole-brain functional activity and gray matter structure. *Front. Neurosci.* 14:751. doi: 10.3389/fnins.2020.00751

Chen, B., Wang, S., Sun, W., Shang, X., Liu, H., Liu, G., et al. (2017). Functional and structural changes in gray matter of Parkinson's disease patients with mild cognitive impairment. *Eur. J. Radiol.* 93, 16–23. doi: 10.1016/j.ejrad.2017.05.018

Chen, L., Bedard, P., Hallett, M., and Horovitz, S. G. (2021). Dynamics of top-down control and motor networks in Parkinson's disease. *Mov. Disord.* 36, 916–926. doi: 10.1002/mds.28461

Chen, X., Liao, X., Dai, Z., Lin, Q., Wang, Z., Li, K., et al. (2018). Topological analyses of functional connectomics: a crucial role of global signal removal, brain parcellation, and null models. *Hum. Brain Mapp.* 39, 4545–4564. doi: 10.1002/hbm.24305

Chen, X., Zhang, H., Gao, Y., Wee, C. Y., Li, G., Shen, D., et al. (2016). High-order resting-state functional connectivity network for MCI classification. *Hum. Brain Mapp.* 37, 3282–3296. doi: 10.1002/hbm.23240

Chen, X., Zhang, H., Zhang, L., Shen, C., Lee, S. W., and Shen, D. (2017). Extraction of dynamic functional connectivity from brain grey matter and white matter for MCI classification. *Hum. Brain Mapp.* 38, 5019–5034. doi: 10.1002/hbm.23711

Cui, L. B., Zhang, Y. J., Lu, H. L., Liu, L., Zhang, H. J., Fu, Y. F., et al. (2021). Thalamus radiomics-based disease identification and prediction of early treatment response for schizophrenia. *Front. Neurosci.* 15:682777. doi: 10.3389/fnins.2021.682777

De Micco, R., Agosta, F., Basaia, S., Siciliano, M., Cividini, C., Tedeschi, G., et al. (2021). Functional connectomics and disease progression in drug-naive

Parkinson's disease patients. *Mov. Disord.* 36, 1603–1616. doi: 10.1002/mds.28541

Ding, X., Yang, Y., Stein, E. A., and Ross, T. J. (2015). Multivariate classification of smokers and nonsmokers using SVM-RFE on structural MRI images. *Hum. Brain Mapp.* 36, 4869–4879. doi: 10.1002/hbm.22956

Ding, X., Yang, Y., Stein, E. A., and Ross, T. J. (2017). Combining multiple resting-state fMRI features during classification: optimized frameworks and their application to nicotine addiction. *Front. Hum. Neurosci.* 11:362. doi: 10.3389/fnhum.2017.00362

Feng, F., Wang, P., Zhao, K., Zhou, B., Yao, H., Meng, Q., et al. (2018). Radiomic features of hippocampal subregions in Alzheimer's disease and amnestic mild cognitive impairment. *Front. Aging Neurosci.* 10:290. doi: 10.3389/fnagi.2018.00290

Ge, R., Downar, J., Blumberger, D. M., Daskalakis, Z. J., and Vila-Rodriguez, F. (2020). Functional connectivity of the anterior cingulate cortex predicts treatment outcome for rTMS in treatment-resistant depression at 3-month follow-up. *Brain Stimul.* 13, 206–214. doi: 10.1016/j.brs.2019.10.012

Grotegerd, D., Redlich, R., Almeida, J. R., Riemenschneider, M., Kugel, H., Arolt, V., et al. (2014). MANIA-a pattern classification toolbox for neuroimaging data. *Neuroinformatics* 12, 471–486. doi: 10.1007/s12021-014-9223-8

Guo, M., Ren, Y., Yu, H., Yang, H., Cao, C., Li, Y., et al. (2020). Alterations in degree centrality and functional connectivity in Parkinson's disease patients with freezing of gait: a resting-state functional magnetic resonance imaging study. *Front. Neurosci.* 14:582079. doi: 10.3389/fnins.2020.582079

Heim, B., Krismer, F., De Marzi, R., and Seppi, K. (2017). Magnetic resonance imaging for the diagnosis of Parkinson's disease. *J. Neural Transm. (Vienna)* 124, 915–964. doi: 10.1007/s00702-017-1717-8

Hojjati, S. H., Ebrahimzadeh, A., Khazaee, A., Babajani-Feremi, A., and Alzheimer's Disease Neuroimaging Initiative (2018). Predicting conversion from MCI to AD by integrating rs-fMRI and structural MRI. *Comput. Biol. Med.* 102, 30–39. doi: 10.1016/j.compbiomed.2018.09.004

Hong, S. J., Bernhardt, B. C., Caldairou, B., Hall, J. A., Guiot, M. C., Schrader, D., et al. (2017). Multimodal MRI profiling of focal cortical dysplasia type II. *Neurology* 88, 734–742. doi: 10.1212/WNL.0000000000003632

Hou, Y., Luo, C., Yang, J., Ou, R., Song, W., Wei, Q., et al. (2016). Prediction of individual clinical scores in patients with Parkinson's disease using resting-state functional magnetic resonance imaging. *J. Neurol. Sci.* 366, 27–32. doi: 10.1016/j.jns.2016.04.030

Hu, X., Song, X., Li, E., Liu, J., Yuan, Y., Liu, W., et al. (2015). Altered resting-state brain activity and connectivity in depressed Parkinson's disease. *PLoS One* 10:e0131133. doi: 10.1371/journal.pone.0131133

Huang, K., Lin, Y., Yang, L., Wang, Y., Cai, S., Pang, L., et al. (2020). A multipredictor model to predict the conversion of mild cognitive impairment to Alzheimer's disease by using a predictive nomogram. *Neuropsychopharmacology* 45, 358–366. doi: 10.1038/s41386-019-0551-0

Jiang, S., Wang, M., Zhang, L., Yuan, Y., Tong, Q., Ding, J., et al. (2016). Regional homogeneity alterations differentiate between tremor dominant and postural instability gait difficulty subtypes of Parkinson's disease. *J. Neural Transm. (Vienna)* 123, 219–229. doi: 10.1007/s00702-015-1490-5

Jin, D., Wang, P., Zalesky, A., Liu, B., Song, C., Wang, D., et al. (2020). GrabAD: generalizability and reproducibility of altered brain activity and diagnostic classification in Alzheimer's Disease. *Hum. Brain Mapp.* 41, 3379–3391. doi: 10.1002/hbm.25023

Kim, J., Criaud, M., Cho, S. S., Diez-Cirarda, M., Mihaescu, A., Coakeley, S., et al. (2017). Abnormal intrinsic brain functional network dynamics in Parkinson's disease. *Brain* 140, 2955–2967. doi: 10.1093/brain/awx233

Lambin, P., Rios-Velazquez, E., Leijenaar, R., Carvalho, S., van Stiphout, R. G., Granton, P., et al. (2012). Radiomics: extracting more information from medical images using advanced feature analysis. *Eur. J. Cancer* 48, 441–446. doi: 10.1016/j.ejca.2011.11.036

Lanka, P., Rangaprakash, D., Dretsch, M. N., Katz, J. S., Denney, T. S. Jr., and Deshpande, G. (2020a). Supervised machine learning for diagnostic classification from large-scale neuroimaging datasets. *Brain Imaging Behav.* 14, 2378–2416. doi: 10.1007/s11682-019-00191-8

Lanka, P., Rangaprakash, D., Gotoor, S. S. R., Dretsch, M. N., Katz, J. S., Denney, T. S. Jr., et al. (2020b). MALINI (Machine Learning in NeuroImaging): a MATLAB toolbox for aiding clinical diagnostics using resting-state fMRI data. *Data Brief* 29:105213. doi: 10.1016/j.dib.2020.105213

Lin, H., Cai, X., Zhang, D., Liu, J., Na, P., and Li, W. (2020). Functional connectivity markers of depression in advanced Parkinson's disease. *Neuroimage Clin.* 25:102130. doi: 10.1016/j.nicl.2019.102130

Lin, W. C., Chou, K. H., Lee, P. L., Tsai, N. W., Chen, H. L., Hsu, A. L., et al. (2017). Parkinson's disease: diagnostic utility of volumetric imaging. *Neuroradiology* 59, 367–377. doi: 10.1007/s00234-017-1808-0

Mo, J., Liu, Z., Sun, K., Ma, Y., Hu, W., Zhang, C., et al. (2019). Automated detection of hippocampal sclerosis using clinically empirical and radiomics features. *Epilepsia* 60, 2519–2529. doi: 10.1111/epi.16392

Morgan, V. L., Englot, D. J., Rogers, B. P., Landman, B. A., Cakir, A., Abou-Khalil, B. W., et al. (2017). Magnetic resonance imaging connectivity for the prediction of seizure outcome in temporal lobe epilepsy. *Epilepsia* 58, 1251–1260. doi: 10.1111/epi.13762

O'Callaghan, C., Hornberger, M., Balsters, J. H., Halliday, G. M., Lewis, S. J., and Shine, J. M. (2016). Cerebellar atrophy in Parkinson's disease and its implication for network connectivity. *Brain* 139, 845–855. doi: 10.1093/brain/awv399

Oh, K., Kim, W., Shen, G., Piao, Y., Kang, N. I., Oh, I. S., et al. (2019). Classification of schizophrenia and normal controls using 3D convolutional neural network and outcome visualization. *Schizophr. Res.* 212, 186–195. doi: 10.1016/j.schres.2019.07.034

Pang, H., Yu, Z., Yu, H., Cao, J., Li, Y., Guo, M., et al. (2021). Use of machine learning method on automatic classification of motor subtype of Parkinson's disease based on multilevel indices of rs-fMRI. *Parkinsonism Relat. Disord.* 90, 65–72. doi: 10.1016/j.parkreldis.2021.08.003

Peng, B., Wang, S., Zhou, Z., Liu, Y., Tong, B., Zhang, T., et al. (2017). A multilevel-ROI-features-based machine learning method for detection of morphometric biomarkers in Parkinson's disease. *Neurosci. Lett.* 651, 88–94. doi: 10.1016/j.neulet.2017.04.034

Peng, S., Chen, L., Tao, J., Liu, J., Zhu, W., Liu, H., et al. (2021). Radiomics analysis of multi-phase DCE-MRI in predicting tumor response to neoadjuvant therapy in breast cancer. *Diagnostics (Basel)* 11:2086. doi: 10.3390/diagnostics11112086

Qian, H., Qin, D., Qi, S., Teng, Y., Li, C., Yao, Y., et al. (2020). Less is better: single-digit brain functional connections predict T2DM and T2DM-induced cognitive impairment. *Front. Neurosci.* 14:588684. doi: 10.3389/fnins.2020.588684

Ren, Q., Wang, Y., Leng, S., Nan, X., Zhang, B., Shuai, X., et al. (2021). Substantia nigra radiomics feature extraction of Parkinson's disease based on magnitude images of susceptibility-weighted imaging. *Front. Neurosci.* 15:646617. doi: 10.3389/fnins.2021.646617

Rosenberg, M. D., Finn, E. S., Scheinost, D., Papademetris, X., Shen, X., Constable, R. T., et al. (2016). A neuromarker of sustained attention from whole-brain functional connectivity. *Nat. Neurosci.* 19, 165–171. doi: 10.1038/nn.4179

Rubbert, C., Mathys, C., Jockwitz, C., Hartmann, C. J., Eickhoff, S. B., Hoffstaedter, F., et al. (2019). Machine-learning identifies Parkinson's disease patients based on resting-state between-network functional connectivity. *Br. J. Radiol.* 92:20180886. doi: 10.1259/bjr.20180886

Shen, W., Tu, Y., Gollub, R. L., Ortiz, A., Napadow, V., Yu, S., et al. (2019). Visual network alterations in brain functional connectivity in chronic low back pain: a resting state functional connectivity and machine learning study. *Neuroimage Clin.* 22:101775. doi: 10.1016/j.nicl.2019.101775

Sheng, W., Guo, T., Zhou, C., Wu, J., Gao, T., Pu, J., et al. (2021). Altered cortical cholinergic network in Parkinson's disease at different stage: a resting-state fMRI study. *Front. Aging Neurosci.* 13:723948. doi: 10.3389/fnagi.2021.723948

Shi, D., Li, Y., Zhang, H., Yao, X., Wang, S., Wang, G., et al. (2021a). Machine learning of schizophrenia detection with structural and functional neuroimaging. *Dis. Markers* 2021:9963824. doi: 10.1155/2021/9963824

Shi, D., Zhang, H., Wang, S., Wang, G., and Ren, K. (2021b). Application of functional magnetic resonance imaging in the diagnosis of Parkinson's disease: a histogram analysis. *Front. Aging Neurosci.* 13:624731. doi: 10.3389/fnagi.2021.624731

Shu, Z. Y., Cui, S. J., Wu, X., Xu, Y., Huang, P., Pang, P. P., et al. (2021). Predicting the progression of Parkinson's disease using conventional MRI and machine learning: an application of radiomic biomarkers in whole-brain white matter. *Magn. Reson. Med.* 85, 1611–1624. doi: 10.1002/mrm.28522

Sun, H., Chen, Y., Huang, Q., Lui, S., Huang, X., Shi, Y., et al. (2018). Psychoradiologic utility of MR imaging for diagnosis of attention deficit hyperactivity disorder: a radiomics analysis. *Radiology* 287, 620–630. doi: 10.1148/radiol.2017170226

Suo, X., Lei, D., Li, N., Li, W., Kemp, G. J., Sweeney, J. A., et al. (2021). Disrupted morphological grey matter networks in early-stage Parkinson's disease. *Brain Struct. Funct.* 226, 1389–1403. doi: 10.1007/s00429-020-02200-9

Szewczyk-Krolikowski, K., Menke, R. A., Rolinski, M., Duff, E., Salimi-Khorshidi, G., Filippini, N., et al. (2014). Functional connectivity in the basal ganglia network differentiates PD patients from controls. *Neurology* 83, 208–214. doi: 10.1212/WNL.0000000000000592

Talai, A. S., Sedlacik, J., Boelmans, K., and Forkert, N. D. (2021). Utility of Multi-Modal MRI for differentiating of Parkinson's disease and progressive Supranuclear palsy using machine learning. *Front. Neurol.* 12:648548. doi: 10.3389/fneur.2021.648548

Tang, Z., Liu, Z., Li, R., Yang, X., Cui, X., Wang, S., et al. (2017). Identifying the white matter impairments among ART-naive HIV patients: a multivariate pattern analysis of DTI data. *Eur. Radiol.* 27, 4153–4162. doi: 10.1007/s00330-017-4820-1

Tian, Z. Y., Qian, L., Fang, L., Peng, X. H., Zhu, X. H., Wu, M., et al. (2020). Frequency-specific changes of resting brain activity in Parkinson's disease: a machine learning approach. *Neuroscience* 436, 170–183. doi: 10.1016/j.neuroscience.2020.01.049

Tu, Y., Zeng, F., Lan, L., Li, Z., Maleki, N., Liu, B., et al. (2020). An fMRI-based neural marker for migraine without aura. *Neurology* 94, e741–e751. doi: 10.1212/WNL.0000000000008962

Tuovinen, N., Seppi, K., de Pasquale, F., Muller, C., Nocker, M., Schocke, M., et al. (2018). The reorganization of functional architecture in the early-stages of Parkinson's disease. *Parkinsonism Relat. Disord.* 50, 61–68. doi: 10.1016/j.parkreldis.2018.02.013

Wang, L., Liu, Y., Zeng, X., Cheng, H., Wang, Z., and Wang, Q. (2020). Region-of-Interest based sparse feature learning method for Alzheimer's disease identification. *Comput. Methods Programs Biomed.* 187:105290. doi: 10.1016/j.cmpb.2019.105290

Wang, S., Zhang, Y., Lei, J., and Guo, S. (2021). Investigation of sensorimotor dysfunction in Parkinson disease by resting-state fMRI. *Neurosci. Lett.* 742:135512. doi: 10.1016/j.neulet.2020.135512

Wang, Y., Sun, K., Liu, Z., Chen, G., Jia, Y., Zhong, S., et al. (2020). Classification of unmedicated bipolar disorder using whole-brain functional activity and connectivity: a radiomics analysis. *Cereb. Cortex* 30, 1117–1128. doi: 10.1093/cercor/bhz152

Wottschel, V., Chard, D. T., Enzinger, C., Filippi, M., Frederiksen, J. L., Gasperini, C., et al. (2019). SVM recursive feature elimination analyses of structural brain MRI predicts near-term relapses in patients with clinically isolated syndromes suggestive of multiple sclerosis. *Neuroimage Clin.* 24:102011. doi: 10.1016/j.nicl.2019.102011

Yan, C. G., Wang, X. D., Zuo, X. N., and Zang, Y. F. (2016). DPABI: data processing & analysis for (Resting-State) brain imaging. *Neuroinformatics* 14, 339–351. doi: 10.1007/s12021-016-9299-4

Zhang, J., Gao, Y., He, X., Feng, S., Hu, J., Zhang, Q., et al. (2021). Identifying Parkinson's disease with mild cognitive impairment by using combined MR imaging and electroencephalogram. *Eur. Radiol.* 31, 7386–7394. doi: 10.1007/s00330-020-07575-1

Zhao, F., Zhang, H., Rekik, I., An, Z., and Shen, D. (2018). Diagnosis of autism spectrum disorders using multi-level high-order functional networks derived from resting-state functional MRI. *Front. Hum. Neurosci.* 12:184. doi: 10.3389/fnhum.2018.00184

Zhao, K., Ding, Y., Han, Y., Fan, Y., Alexander-Bloch, A. F., Han, T., et al. (2020). Independent and reproducible hippocampal radiomic biomarkers for multisite Alzheimer's disease: diagnosis, longitudinal progress and biological basis. *Sci. Bull.* 65, 1103–1113. doi: 10.1016/j.scib.2020.04.003

Zhou, B., An, D., Xiao, F., Niu, R., Li, W., Li, W., et al. (2020). Machine learning for detecting mesial temporal lobe epilepsy by structural and functional neuroimaging. *Front. Med.* 14, 630–641. doi: 10.1007/s11684-019-0718-4

Zhou, Z., Chen, X., Zhang, Y., Hu, D., Qiao, L., Yu, R., et al. (2020). A toolbox for brain network construction and classification (BrainNetClass). *Hum. Brain Mapp.* 41, 2808–2826. doi: 10.1002/hbm.24979

Conflict of Interest: The authors declare that the research was conducted in the absence of any commercial or financial relationships that could be construed as a potential conflict of interest.

Publisher's Note: All claims expressed in this article are solely those of the authors and do not necessarily represent those of their affiliated organizations, or those of the publisher, the editors and the reviewers. Any product that may be evaluated in this article, or claim that may be made by its manufacturer, is not guaranteed or endorsed by the publisher.

frontiers in Aging Neuroscience

ORIGINAL RESEARCH
published: 15 March 2022
doi: 10.3389/fnagi.2022.792778

Combined Application of Quantitative Susceptibility Mapping and Diffusion Kurtosis Imaging Techniques to Investigate the Effect of Iron Deposition on Microstructural Changes in the Brain in Parkinson's Disease

Lin Yang[1,2], Yan Cheng[2], Yongyan Sun[3], Yinghua Xuan[4], Jianping Niu[5], Jitian Guan[2], Yunjie Rong[6], Yanlong Jia[2], Zerui Zhuang[7], Gen Yan[1] and Renhua Wu[2,8]**

[1] Department of Radiology, The Second Affiliated Hospital of Xiamen Medical College, Xiamen, China, [2] Department of Radiology, The Second Affiliated Hospital, Medical College of Shantou University, Shantou, China, [3] Department of Pharmacy, Guangdong Second Provincial General Hospital, Zhuhai Hospital, Zhuhai, China, [4] Department of Basic Medicine, Xiamen Medical College, Xiamen, China, [5] Department of Neurology, The Second Affiliated Hospital of Xiamen Medical College, Xiamen, China, [6] Department of Ultrasound, Foshan Women and Children's Hospital Affiliated to Southern Medical University, Foshan, China, [7] Department of Neurosurgery, Sun Yat-sen Memorial Hospital, Sun Yat-sen University, Guangzhou, China, [8] Guangdong Provincial Key Laboratory for Breast Cancer Diagnosis and Treatment, Cancer Hospital of Shantou University Medical College, Shantou, China

OPEN ACCESS

Edited by:
Binbin Nie,
Institute of High Energy Physics (CAS), China

Reviewed by:
Xiaojun Xu,
Zhejiang University, China
Gang Xiao,
Hanshan Normal University, China

***Correspondence:**
Gen Yan
gyan@stu.edu.cn
Renhua Wu
rhwu@stu.edu.cn

Specialty section:
This article was submitted to Parkinson's Disease and Aging-related Movement Disorders, a section of the journal Frontiers in Aging Neuroscience

Received: 11 October 2021
Accepted: 23 February 2022
Published: 15 March 2022

Citation:
Yang L, Cheng Y, Sun Y, Xuan Y, Niu J, Guan J, Rong Y, Jia Y, Zhuang Z, Yan G and Wu R (2022) Combined Application of Quantitative Susceptibility Mapping and Diffusion Kurtosis Imaging Techniques to Investigate the Effect of Iron Deposition on Microstructural Changes in the Brain in Parkinson's Disease. Front. Aging Neurosci. 14:792778. doi: 10.3389/fnagi.2022.792778

Objectives: Brain iron deposition and microstructural changes in brain tissue are associated with Parkinson's disease (PD). However, the correlation between these factors in Parkinson's disease has been little studied. This study aimed to use quantitative susceptibility mapping combined with diffusion kurtosis imaging to investigate the effects of iron deposition on microstructural tissue alterations in the brain.

Methods: Quantitative susceptibility mapping and diffusion kurtosis imaging were performed on 24 patients with early PD, 13 patients with advanced PD, and 25 healthy controls. The mean values of magnetic susceptibility and diffusion kurtosis were calculated for the bilateral substantia nigra, red nucleus, putamen, globus pallidus, and caudate nucleus, and compared between the groups. Correlation analyses between the diffusion kurtosis of each nucleus and its magnetic susceptibility parameters in PD patients and healthy controls were performed.

Results: The study found a significant increase in iron deposition in the substantia nigra, red nucleus, putamen and globus pallidus, bilaterally, in patients with PD. Mean kurtosis values were increased in the substantia nigra but decreased in the globus pallidus; axial kurtosis values were decreased in both the substantia nigra and red nucleus; radial kurtosis values were increased in the substantia nigra but showed an opposite trend in the globus pallidus and caudate nucleus. In the substantia nigra of patients with PD, magnetic susceptibility was positively correlated with mean and radial kurtosis values,

and negatively correlated with axial kurtosis. None of these correlations were significantly different in the control group. In the putamen, magnetic susceptibility was positively correlated with mean, axial, and radial kurtosis only in patients with advanced-stage PD.

Conclusion: Our study provides new evidence for brain iron content and microstructural alterations in patients with PD. Iron deposition may be a common mechanism for microstructural alterations in the substantia nigra and putamen of patients with PD. Tracking the dynamic changes in iron content and microstructure throughout the course of PD will help us to better understand the dynamics of iron metabolism and microstructural alterations in the pathogenesis of PD and to develop new approaches to monitor and treat PD.

Keywords: Parkinson's disease (PD), quantitative susceptibility mapping (QSM), diffusion kurtosis imaging (DKI), iron content, microstructure

INTRODUCTION

Parkinson's disease (PD) is characterized clinically by rest tremor, bradykinesia, rigidity, and postural instability. The main pathological change in PD is dopaminergic neuron degenerative death in the nigrostriatal system due to iron deposition (Dexter et al., 1987; Jin et al., 2011; Kalia and Lang, 2015; Xu et al., 2021). The link between excessive iron deposition and the pathophysiology of PD has been shown in recent studies that revealed that ferrous iron promotes both oxidative stress and α-synuclein aggregation (Wolozin and Golts, 2002; Barnham et al., 2004). Several studies have demonstrated that a variety of microstructural changes occur in the brains of patients with PD (Taylor et al., 2018). In addition to the loss of dopaminergic neurons, there is an accumulation of Lewy bodies (LBs) and Lewy neurites (LNs) (Covell et al., 2017; Ghosh et al., 2017), neuroinflammation (Kumar et al., 2012), and glial cell proliferation (Batassini et al., 2015). Non-invasive understanding of pathological changes by imaging is important for early detection of the disease and guidance of effective treatment. Although iron deposition can lead to microstructural changes in the gray matter nuclei, studies investigating associations between brain iron deposition and microstructural changes in the brain in PD are rare and the associations have not been evaluated using imaging techniques. Quantitative susceptibility mapping (QSM) is a new post-processing technique that provides a robust magnetization measurement that correlates significantly with brain iron content, enabling quantitative tissue magnetization measurement (He et al., 2015; Du et al., 2016). This approach detects magnetic tissue properties more sensitively than traditional quantitative-based iron imaging techniques (R2, R2*, and R2') and has been used to identify several human brain substructures that are partially indistinguishable when using Gradient Echo (GRE)-based comparisons (Wieler et al., 2015; Guan et al., 2017b).

Diffusion kurtosis imaging (DKI) is a state-of-the-art method for quantifying non-Gaussian water diffusion (Jensen et al., 2005; Coutu et al., 2014; Filli et al., 2014). An alternative, diffusion tensor imaging, does not consider the isotropic nature of gray matter structure (Pierpaoli and Basser, 1996). Therefore, DKI is better suited for quantifying subtle pathological changes in gray matter than diffusion tensor imaging (Jensen and Helpern, 2010). By measuring direction-specific kurtosis, DKI reflects the complexity of neural tissue in normal, developmental, and pathological states. Mean kurtosis (MK), axial kurtosis (Ka), and radial kurtosis (Kr) are direction-specific kurtosis parameters. It has been suggested that Kr decrease is associated with demyelination, Ka changes reflect axonal degeneration (Cheung et al., 2009), and increases in MK may indicate injury-related microglial proliferation and increased axonal bead granulation (Weber et al., 2015).

Magnetic susceptibility (MS) (Li et al., 2018; Uchida et al., 2019, 2020) and diffusion kurtosis parameters (Wang et al., 2011; Kamagata et al., 2017; Guan et al., 2019) have been shown in past studies to reflect brain iron deposition levels and brain tissue microstructural changes, respectively, in patients with PD. The substantia nigra (SN), red nucleus (RN), and striatum are the main nuclei involved in PD. We hypothesized that there may be a correlation between excessive iron deposition in these regions of the brain and alterations in apparent diffusion kurtosis in patients with PD. To our knowledge, few previous reports have combined QSM and DKI in the evaluation of PD. Herein, we aimed to jointly apply QSM and DKI techniques to investigate microstructural changes in the gray matter nuclei, due to iron deposition, and identify the specific features of observed changes. Enhancing our understanding of correlations between the findings of magnetic susceptibility and diffusion kurtosis may improve our knowledge of pathological changes in PD and their effects on disease activity and contribute to early detection and treatment.

MATERIALS AND METHODS

Subjects

All examinations in this study were performed with the written consent of each participant, and the study was approved by the Ethics Department of the Second Affiliated Hospital of Xiamen Medical College. All processes were conducted in accordance with the principles of the Declaration of Helsinki.

In the study, we prospectively assessed 37 patients with PD who attended the Department of Neurology at the hospital between January 2019 and December 2020. All patients were diagnosed with PD by a movement disorder neurologist (Dr. Niu, with more than 30 years of experience), underwent MRI, and met British Parkinson's Disease Association Brain Bank criteria. The following exclusion criteria were applied: atypical or secondary PD, history of other neurological disease e.g., severe head trauma or stroke, poor image quality, or general MRI scan contraindications. All patients were older than 50 years, right-handed, and underwent a thorough neurological examination. Patients and their families provided detailed information on the onset, course, and evolution of PD. Hoehn-Yahr (HandY) stage and Unified Parkinson's Disease Rating Scale (UPDRS) were used to assess disease severity and motor function (Greffard et al., 2006).

Patients were further categorized into early-stage PD (ESPD) (HandY stage $\leq$ 2.5; 12 men, 12 women; mean age, 63.0 $\pm$ 7.4 years) and advanced stage PD (ASPD) (HandY stage $\geq$ 3; 8 men, 5 women; mean age, 71.1 $\pm$ 7.5 years) groups. PD duration was defined as the time difference between first motor symptom development and the study examination date. The mental status of all patients was assessed using the Mini-mental State Examination (MMSE) and the Montreal Cognitive Assessment (MoCA) scores (Folstein et al., 1975).

Since both methods have unique characteristics, we conducted two PD tests for each patient (Pinto et al., 2019). Clinical evaluation and MRI imaging were performed at least 12 h after discontinuation of all anti-PD medications. Twenty-five age- and sex-matched healthy control (HC) participants (10 men, 15 women; mean age, 67.0 $\pm$ 9.3 years) were recruited from a medical examination center. HC participants met the following inclusion criteria: no history of neuropsychiatric or neurodegenerative disease; no white matter damage, such as epilepsy, multiple sclerosis, tumors, trauma, cranial arteritis, or encephalitis; no history of alcohol dependence or other psychoactive substance abuse; and MMSE score $>$ 28 points.

Imaging Protocol

All participants underwent MRI examinations on a 3 T scanner (Discovery MR750, GE Healthcare, Milwaukee, WI, United States) equipped with an eight-channel phased array receiver coil. Participants were instructed to relax and avoid any motion during the test. Noise-proof earplugs and foam pads were applied to minimize acoustic scanner noise and motion artifacts, respectively. Auto shimming was employed at the start of each scan to ensure uniformity of the static magnetic field. Before QSM and DKI imaging, routine images, including T1-weighted imaging, T2-weighted imaging, fluid-attenuated inversion recovery (FLAIR) images, and diffusion-weighted imaging (DWI), were acquired. They were used to confirm the absence of structural abnormalities, and to exclude secondary Parkinson's syndrome caused by severe vascular disease, multisystem atrophy, trauma, or encephalitis.

Diffusion kurtosis imaging images were obtained using a single-shot spin-echo echo-planar imaging (SE-EPI) sequence with the following parameters: repetition time (TR) = 3,000 ms; echo time (TE) = 60 ms; slice thickness/gap = 5/1.5 mm; field of view (FOV) = 240 $\times$ 240 mm; matrix size = 128 $\times$ 128; number of excitations (NEX) = 1; *b*-values = 0, 1,000 (30 directions), and 2,000 (30 directions) s/mm^2; number of slices = 15; total scan time = 3 min 2 s. QSM source images, including magnitude and phase images, were obtained using a three-dimensional multi-echo fast spoiled gradient recalled echo (FSPGR) sequence with the following parameters: TR = 23.7 ms; TE = 3.4/5.8/8.1/10.5/12.8/15.2/17.5/19.9 ms; flip angle = 12°; slice thickness/gap = 1/0 mm; FOV = 256 $\times$ 256 mm; matrix size = 256 $\times$ 256; NEX = 1; number of slices = 140; total acquisition time = 5 min 1 s. Two experienced neuroradiologists provided diagnostic support. All sequences were acquired in the axial plane parallel to the anterior commissure-posterior commissure (AC-PC) line. All images were carefully reviewed after scanning to ensure image quality, and poor image quality due to motion artifacts prompted rescanning.

Image Analyses and Region-of-Interest Selection

Raw DKI and QSM data were transferred to the Advantage Workstation 4.6 (GE Healthcare) and post-processed by the FuncTool software. Specifically, DKI parameter maps, including MK, Ka, and Kr, were calculated by using the following equation (Jensen et al., 2005):

$$\ln\left[S_{(n,b)}/S_0\right] = -b\sum_{i=1}^{3}\sum_{j=1}^{3} n_i n_j D_{ij} + \frac{1}{6}b^2 D^{-2}\sum_{i=1}^{3}\sum_{j=1}^{3}\sum_{k=1}^{3}\sum_{l=1}^{3} n_i n_j n_k n_l W_{ijkl}$$

$S_{(n,b)}$ denotes the diffusion encoding direction n and the diffusion signal intensity of the diffusion-weighted *b*-value, S_0 denotes the diffusion signal intensity of b_0, and D_{ij} and W_{ijkl} represent the components of the diffusion tensor and the diffusion kurtosis tensor, respectively. We have also used this DKI analysis method in our earlier studies (Zheng et al., 2017; Yang et al., 2021). Multi-echo QSM data were processed by Laplacian-based phase unwrapping, and V-SHARP background field removal (Li et al., 2014b), and improved the sparse linear equation and least squares (iLSQR) method (Li et al., 2015b) to generate MS maps, based on the images of the last three echoes.

Regions of interest (ROIs) were delineated three times manually by two independent, double-blinded neuroradiologists with B0 images as references, and values were recorded each time to reduce offset errors (**Supplementary Figure 1**). The average of the six time delineation for the ROI values was taken as the final value. Each nucleus side was recorded as a separate sample. The mean parametric values of the bilateral SN, RN, globus pallidus (GP), putamen, and caudate nuclei were used for further analysis. The intraclass correlation coefficient (ICC) was used to assess the agreement between the two neuroradiologists for the MS, MK, Ka, and Kr measurements

(Landis and Koch, 1977). Usually, ICC values > 0.75 are considered good correlation. To minimize deviation due to partial volume effects, the following criteria were applied: (1) choose the clear boundary and the largest display area of each nucleus to outline the ROI, and carefully avoid blood vessels and cerebrospinal fluid; (2) when delineating the nucleus boundary, move one pixel inward to ensure that the ROI is within the range of the nucleus.

Statistical Analyses

All data were analyzed using SPSS Statistics Package, version 19.0 (IBM Corporation, New York, NY, United States). The Kolmogorov–Smirnov test was used to confirm the normal distribution of data. One-way analysis of variance (ANOVA) or unpaired *t*-tests were used to compare demographic information and clinical characteristics among the groups. Average MS values and corresponding 95% confidence intervals of QSM imaging data were calculated for each region, along with MK, Ka, and Kr values from DKI. One-way ANOVA followed by false discovery rate (FDR) correction, as described by the Benjamini–Hochberg method, were used to compare the differences in MS, MK, Ka, and Kr values using the R software package (R for Windows v. 4.0.3)[1] in patients with different stages of PD to HCs. For intergroup comparisons of non-normally distributed data, the non-parametric Kruskal–Wallis test was used. Pearson correlation analyses were used to investigate the relationship between the MS of the nucleus and the MK, Ka, and Kr values in patients with PD and HCs. Nuclei with good correlations in prior assessments were further divided to investigate correlations with different PD stages. We performed an FDR correction for multiple correlation tests. Finally, the associations between the QSM and DKI parameters and disease severity in the SN were examined using the Pearson correlation test, with adjustments for age and sex effects. For all analyses, values of $P < 0.05$ were considered significant.

RESULTS

Demographics and Neuropsychiatric Assessment

The demographic and clinical characteristics of the participants are shown in **Table 1**. Although the proportion of males with PD was higher than that of females, consistent with the epidemiological characteristics of PD, no significant sex differences were observed among the groups. Further, no significant between-group differences regarding age, or MMSE, MoCA, or UPDRS Part I and Part IV scores were observed. The disease duration of patients with ASPD was significantly longer than that of ESPD ($p < 0.001$). Meanwhile, the UPDRS-total, UPDRS-II, UPDRS-III scores, and the HandY stage of patients with ASPD were significantly greater than those of ESPD ($p < 0.05$).

[1]https://cran.r-project.org

Group Differences Assessed via Quantitative Susceptibility Mapping and Diffusion Kurtosis Imaging

The results of the ICC analysis of the QSM and DKI parameter values for the left and right ROIs of HCs and patients with PD are shown in **Supplementary Table 1**. The results showed that the ICC values for both the HC and PD groups were >0.75, so the consistency of measurement was reliable enough to continue with the subsequent statistical analysis. MS and DKI values of deep gray matter nuclei in HCs and patients with PD are presented in **Figure 1** and **Supplementary Table 2**. We found that the MS of the SN in the healthy group was significantly lower than that of the ESPD and ASPD groups ($p = 0.003$ and $p < 0.001$, respectively), indicating that the SNs of patients with PD have greater paramagnetism, and thus, greater iron deposition levels than healthy people. We also found that MK and Kr values in the SN in the PD group were higher than that of the control group, while the Ka of the control group was higher than that of the PD group. The MS of the RN was elevated in patients with different stages of PD compared to HCs ($p = 0.004$ and 0.001, respectively), while Ka in the ESPD group decreased more than in the HCs ($p < 0.001$). Although the MS value of the putamen in patients with ASPD was significantly higher than that of the HCs ($p < 0.001$), diffusion kurtosis did not change significantly. Compared with the HCs, the MS of the GP of ESPD and ASPD patients increased ($p < 0.001$ and $p < 0.001$, respectively), while MK ($p = 0.004$ and 0.02, respectively) and Kr ($p < 0.001$ and $p < 0.001$, respectively) decreased. No significant differences in Ka were found in this experiment. A slight decrease in the Kr of the caudate nucleus in ESPD, compared to HCs, was observed ($p = 0.02$).

Associations Between Diffusion Kurtosis Imaging and Magnetic Susceptibility Parameters in the Nuclei of Patients With Parkinson's Disease

Figure 2 shows the correlation between the diffusion kurtosis metrics and MS in different brain regions of patients with PD. **Figure 3** shows this relationship in the SN and putamen at different stages of disease progression. In the gray matter nuclei of patients with PD, MS, and DKI kurtosis values correlated only in the SN and putamen. Further analysis showed that a correlation between MS and DKI was only observed in the SN in ESPD. In ASPD, there was a correlation between MS and DKI in both the SN and putamen.

Associations Between Diffusion Kurtosis Imaging and Magnetic Susceptibility Parameters in the Nuclei of Healthy Controls

Supplementary Figure 2 shows the correlation between diffusion kurtosis metrics and MS in different nuclei of the HCs. Our results showed that in HCs, only the Ka of the caudate nucleus was positively correlated with MS. There was no significant

TABLE 1 | Demographics of patients with Parkinson's disease and healthy controls.

Variable	Normal (*N* = 25)	ESPD (*N* = 24)	ASPD (N = 13)	*p*-Value
Male sex, *N* (%)	10.0 (42.7)	12.0 (50.0)	8.0 (61.5)	0.443[a]
Age, years [Mean (SD)]	67.0 (9.3)	63.0 (7.4)	71.1 (7.5)	0.128[b]
Disease duration, years [Mean (SD)]	–	3.5 (5.7)	9.0 (7.3)	**<0.001[c]**
MMSE, [Mean (SD)]		22.4 (5.9)	18.9 (6.0)	0.225[c]
MoCA, [Mean (SD)]		18.4 (6.6)	16.0 (7.5)	0.460[c]
Hoehn-Yahr stage, Mean (SD)	–	1.6 (0.5)	3.7 (0.8)	**<0.001[c]**
UPDRS score, Mean (SD)	–			
Total	–	29.4 (12.0)	44.6 (12.7)	**0.010[c]**
Part I	–	2.1 (1.7)	2.1 (2.0)	0.798[c]
Part II	–	8.8 (4.8)	15.0 (5.3)	**0.010[c]**
Part III	–	17.7 (7.8)	25.8 (5.9)	**0.019[c]**
Part IV[d]	–	1.9 (1.8)	1.8 (2.1)	0.904[c]

ESPD, early-stage Parkinson's disease; ASPD, advanced-stage Parkinson's disease; SD, standard deviation; UPDRS, unified Parkinson's disease rating scale; MMSE, mini-mental state examination; MoCA, montreal cognitive assessment. Bold values indicate statistically significant differences.
[a]According to Pearson chi-square test.
[b]According to One-Way ANOVA.
[c]According to Unpaired t-test.
[d]Provided for patients using levodopa.

correlation between QSM and DKI parameters in the SN, RN, putamen, and GP of HCs.

Quantitative Susceptibility Mapping and Diffusion Kurtosis Imaging Correlations With Clinical Indices in the Substantia Nigra

The results of our regression analysis are summarized in **Supplementary Figure 3**. Magnetic susceptibilities and diffusion kurtosis parameters within the SN correlated with the motor and cognitive scores of patients with PD. In the SN of patients with PD, there was a positive correlation between Ka and MMSE (p = 0.0305), a positive correlation between Kr and UPDRS III (p = 0.0355), and a negative correlation between MK and MMSE and MoCA (p = 0.0069 and 0.0233, respectively). MS was positively correlated with HandY staging and UPDRS III (p = 0.0268 and 0.0036, respectively), and negatively correlated with MMSE and MoCA scores (p = 0.0381 and 0.0399, respectively). The remaining identified correlations were not statistically significant.

Maps of Quantitative Susceptibility Mapping and Diffusion Kurtosis Imaging at the Midbrain Level

Maps of diffusion kurtosis and MS at the midbrain level were successfully constructed. **Figure 4** includes representative DKI and QSM maps of the HC and PD groups, where MS demonstrates an increasing signal, which was especially pronounced in the SN of patients with PD. MK and Kr signals in the SN gradually increase throughout disease progression, and the diffusion range correspondingly increases, while Ka decreases. In contrast, only the MS signal increased in the RN, and there was no obvious change in diffusion signal or range.

DISCUSSION

We used DKI to identify microstructural changes in brain tissue associated with brain iron deposition in patients with PD. We found, for the first time, that microstructural alterations in the SN and putamen have unique characteristics and may be associated with brain iron deposition. In addition, we found that in ESPD, changes in kurtosis correlated with paramagnetism exclusively in the SN. We performed an etiological analysis of these interesting results, which are described below.

Substantia Nigra

QSM data, shown in **Figure 1D**, are consistent with previously reported findings, which revealed increased MS values in the SN of patients with PD (Du et al., 2018; Bergsland et al., 2019). MS increases are considered indirect indicators of iron deposition. Abnormal distribution of MS is consistent with LB and LN regions previously identified in the SN of patients with symptomatic PD, corresponding to Braak's stage III (Braak et al., 2003). Further, patients with PD show abnormalities in DKI parameters (MK, Ka, and Kr), and these differences become more pronounced with disease progression. Patients with PD had elevated MK and Kr values compared to HCs, which is consistent with some (Khairnar et al., 2015; Zhang et al., 2015), but not all, prior reports (Guan et al., 2019). Reported changes in diffusion kurtosis parameter values for PD vary considerably. A major reason for this may be that prior studies did not consider iron deposition levels.

Mean kurtosis elevation in the SN may be due to a combination of several factors. First, following dopaminergic neuronal injury and apoptosis (Zhang et al., 2014), damaged axons may activate major histocompatibility complex class II-positive microglia with phagocytic and trophic functions, leading to elevated tissue structural complexity and kurtosis values (Imamura et al., 2003). Second, loss of dopaminergic neurons in

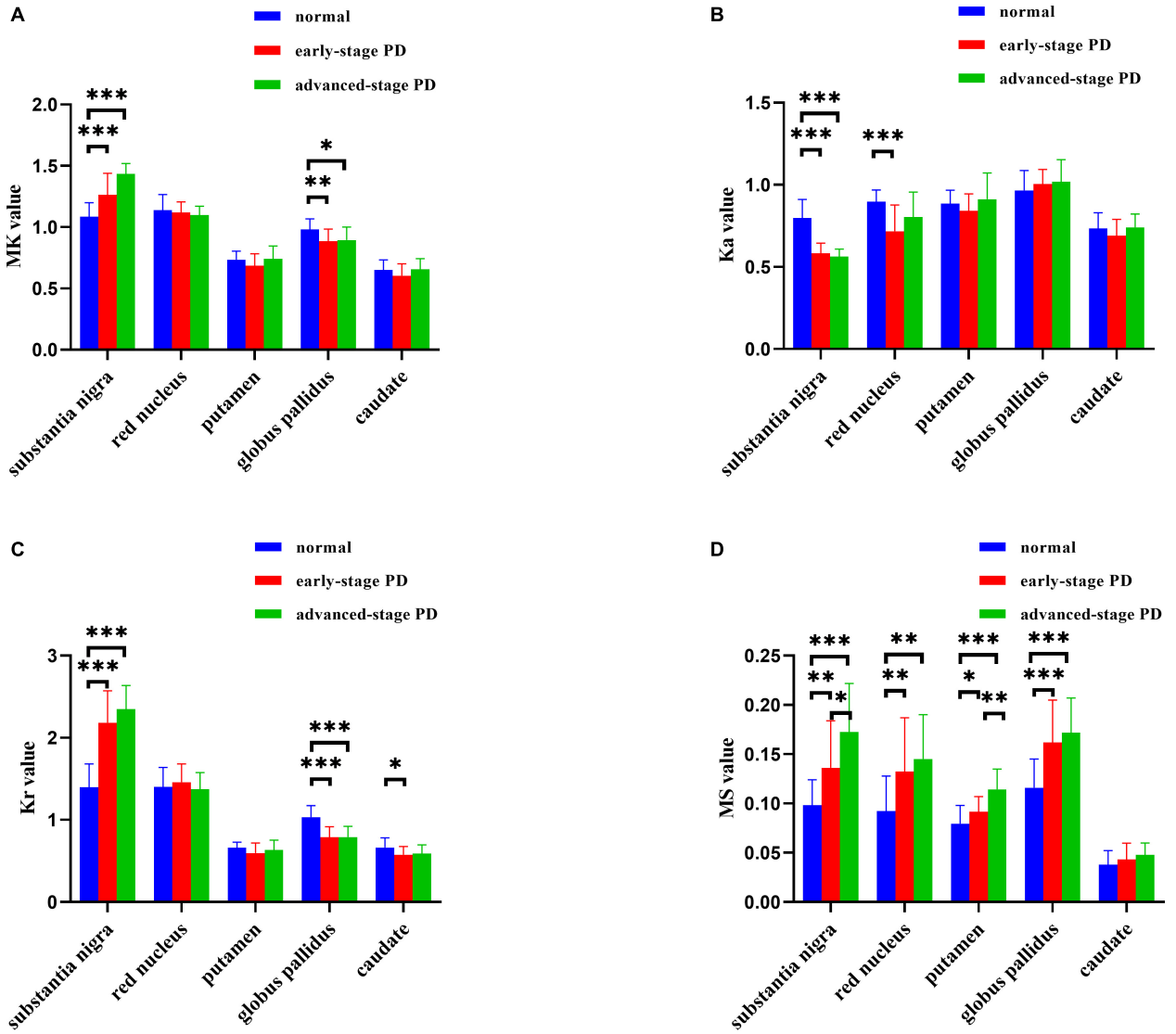

FIGURE 1 | (A–D) Histograms depicting intergroup comparisons of imaging parameters in the substantia nigra, red nucleus, globus pallidus, putamen, and caudate nucleus (FDR-corrected). Error bars represent standard errors of the mean (*$P < 0.05$; **$P < 0.01$; ***$P < 0.001$). MK, mean kurtosis; Ka, axial kurtosis; Kr, radial kurtosis; MS, magnetic susceptibility. The normal group is shown in blue, the early-stage PD group is shown in red, and the advanced-stage PD group is shown in green.

the pars compacta of the SN enhances diffuse heterogeneity due to nigrostriatal pathway deafferentation (Giannelli et al., 2012). Third, LB and LN accumulation in the cytosol of neuronal cells and axons reduces the free diffusion of water, which increases MK (Giannelli et al., 2012).

As iron accumulates, microglia activate to release reactive oxygen species, causing neurotoxicity, and eventually, fluid accumulation in the myelin sheath, causing edema. Because myelin travels directionally, water molecules within myelin do not diffuse freely in each direction, elevating Kr (McGeer and McGeer, 2004; Block et al., 2007).

Axial kurtosis decreases in the SN, which is revealed via DKI in patients with PD and may be due to axonal atrophy in the SN. First, in initial LN accumulation phases in axons, axonal transport (especially reverse axonal transport) is inhibited, which manifests as structural changes of axonal atrophy (Perlson et al., 2010; Millecamps and Julien, 2013). Recently, an *in vivo* high-resolution positron emission tomography study revealed that synaptic density was significantly reduced in the SN, RN, and locus coeruleus in PD (Matuskey et al., 2020). Second, α-synuclein can inhibit axonal branching and growth (Koch et al., 2015).

As shown in **Figure 2A**, MS was positively correlated with MK and Kr, and negatively correlated with Ka in the SN of patients with PD. In addition, staging analysis correlations revealed that among all gray matter ROIs in patients with PD, correlations between QSM and DKI parameters at an early stage were only observed in the SN, and the association was consistent

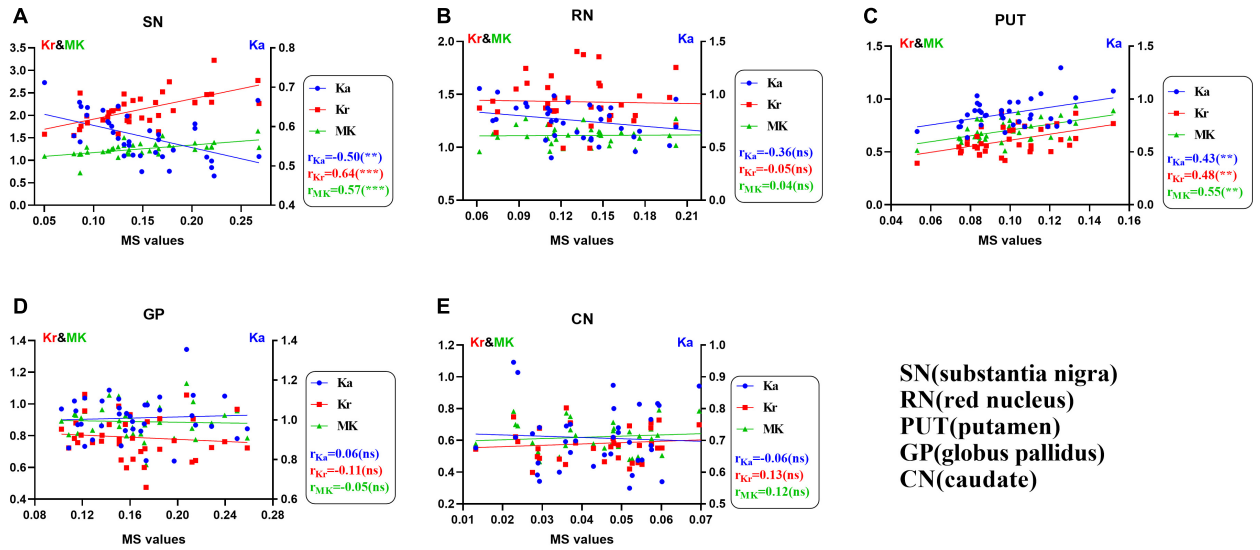

FIGURE 2 | (A–E) Univariate correlations of diffusion kurtosis parameters with magnetic susceptibility values in patients with Parkinson's disease in five nuclei of interest (**P < 0.01; ***P < 0.001; ns, no statistical significance). False discovery rate correction was used for multiple correlations. MK (green, triangles), mean kurtosis; Ka (blue, circles), axial kurtosis; Kr (red, squares), radial kurtosis; MS, magnetic susceptibility.

with that of the overall analysis (**Figure 3**). The correlations in **Figures 2A**, **3A,B** are consistent with SN parameter trends throughout disease progression, shown in **Figures 1**, **4**. The mechanistic basis of disease progression remains increased levels of iron deposition (Braak et al., 2003).

Our data showed that in the SN of patients with PD, MS correlated positively with HandY staging, and, most significantly, UPDRS III scores, and negatively with cognitive test (MMSE and MoCA) scores, which is consistent with a prior report (He et al., 2015; Langkammer et al., 2016; Guan et al., 2017a,c; Du et al., 2018). It has been demonstrated that iron levels in both the hippocampus and thalamus are higher in patients with PD dementia than in PD and healthy groups (Li et al., 2018). We suggest that the relationship between MS and cognitive scores in **Supplementary Figures 3C,D** may be a manifestation of iron overload in the SN during progression of brain histopathological stages to the hippocampus (Braak's stages 5–6) in patients with PD, rather than an indicator that the SN is associated with cognition (Braak et al., 2003).

An interesting phenomenon was observed in the SN of patients with PD, in which Ka was positively correlated with MMSE scores; Kr was positively correlated with UPDRS III scores, and MK was negatively correlated with MMSE and MoCA scores. We hypothesize that some specific microstructural alterations may be associated with clinical symptoms. The presence of a relationship between neuropsychological symptoms and imaging indicators should be investigated at more sites in future studies. Therefore, QSM and DKI parameter abnormalities are clinically significant and likely reflect PD symptom severity.

Red Nucleus

The RN is composed of dense cells and small myelinated axons with a complex microstructure (Onodera and Hicks, 2009). The ventrolateral magnocellular portion of the RN is directly involved in motor control (Kennedy et al., 1986; Mewes and Cheney, 1994; Rodriguez-Oroz et al., 2008). The RN also contains high levels of iron and may be affected by oxidative stress (Martin et al., 2008). **Figure 1D** shows that RN MS values in both the ESPD and ASPD groups were higher than that of the HCs. This finding was different from that which was reported by Du et al. (2018) an inconsistency that may have been due to differing machine types or scanning parameters. Our results validate the claim of Haacke et al. (2005) that the RN is one of the tissues with a high iron concentration in the brain. Although the Ka of the RN of the PD group (**Figure 1B**) was lower than that of the HCs, only the difference between ESPD and HC was significant. We suspect that similar atrophic pathological changes occur in the RN and SN, which result in decreased microstructural complexity or heterogeneity in areas of maximal diffusion (Matuskey et al., 2020). In the RN, a multiple comparison correction for multiple correlation revealed no correlation between MS and MK, Ka, or Kr, either in the PD or HC groups (**Figure 2B** and **Supplementary Figure 2B**). This may mean that the damage associated with iron deposition in the RN is relatively mild compared to the SN and putamen and did not cause significant microstructure changes in the PD group.

Striatum

Throughout neuronal degeneration, the number of major histocompatibility complex class II-positive microglia increased in both the SN and putamen (Imamura et al., 2003). A prospective study revealed MK elevation in the bilateral SN, putamen, GP, and caudate nucleus in patients with PD (Wang et al., 2011). In the putamen (**Figure 1**), only MS differences were observed in patients with PD versus HCs. However, positive correlations between MS and all three kurtosis indicators, especially, in

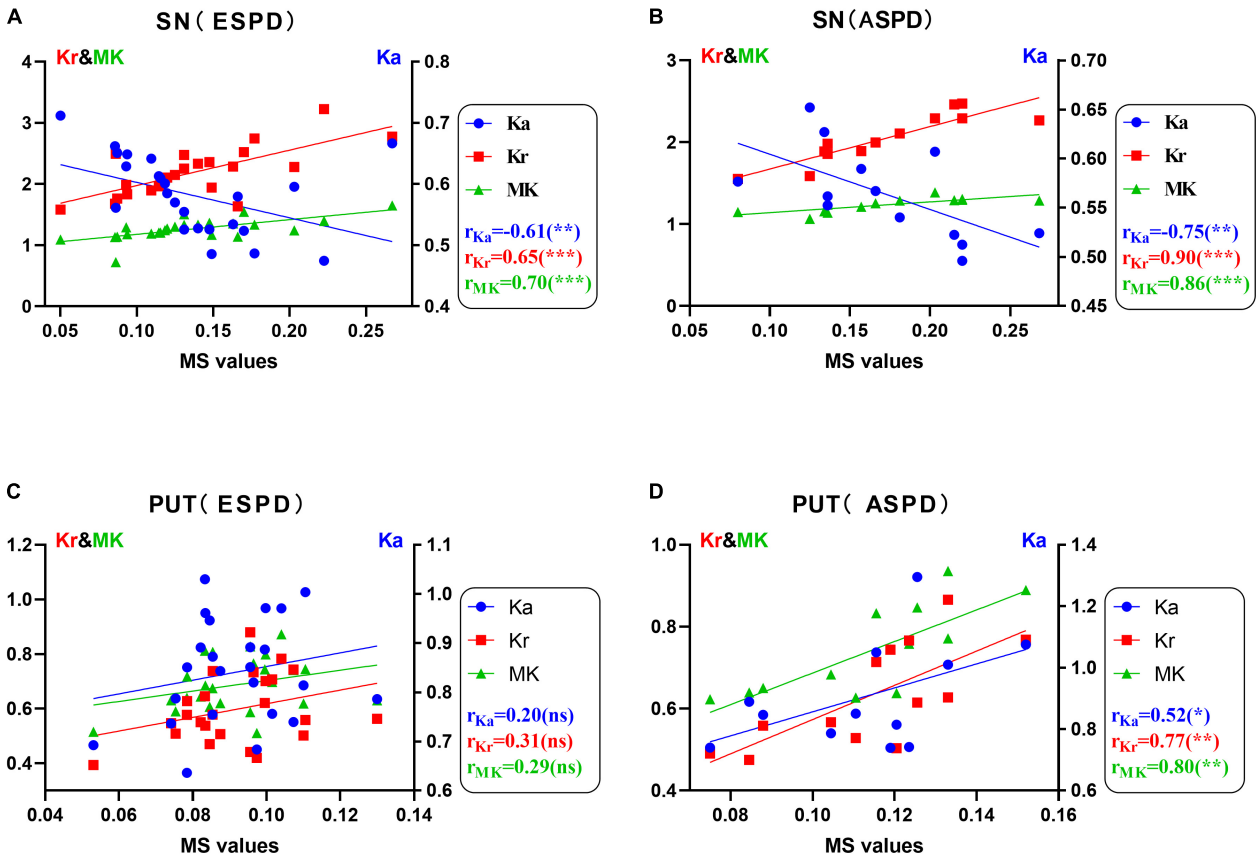

FIGURE 3 | (A–D) Correlations between diffusion kurtosis parameters and magnetic susceptibility in the substantia nigra and putamen determined via univariate analysis in patients with different stages of Parkinson's disease (*$P < 0.05$; **$P < 0.01$; ***$P < 0.001$; ns, no statistical significance). False discovery rate correction was used for multiple correlations. MK (green, triangles), mean kurtosis; Ka (blue, circles), axial kurtosis; Kr (red, squares), radial kurtosis; MS, magnetic susceptibility; ESPD, early-stage Parkinson's disease; ASPD, advanced-stage Parkinson's disease.

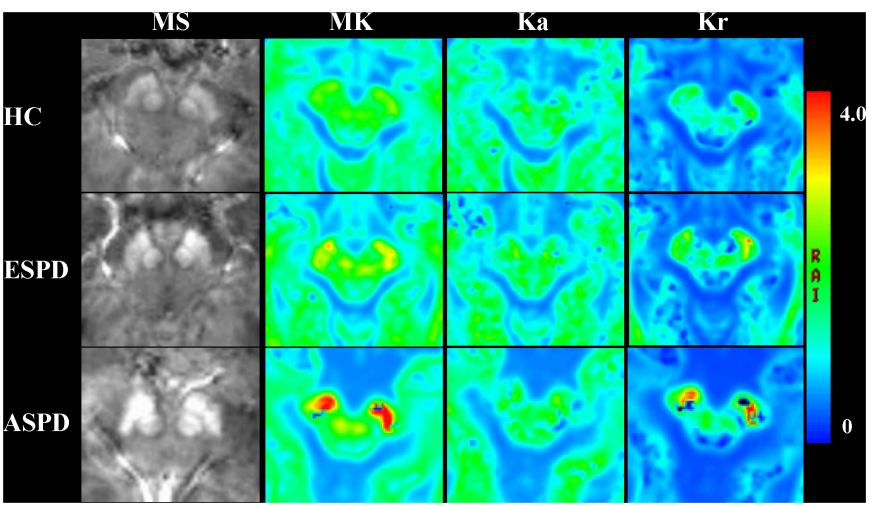

FIGURE 4 | Comparison of magnetic susceptibility and diffusion kurtosis imaging parameter mapping at the midbrain level in healthy participants and patients with Parkinson's disease. MK, mean kurtosis; Ka, axial kurtosis; Kr, radial kurtosis; MS, magnetic susceptibility; ESPD, early-stage Parkinson's disease; ASPD, advanced-stage Parkinson's disease.

the ASPD group were observed (**Figures 2**, **3**). However, no correlations were observed between MS and MK, Ka, and Kr in the putamen of the HC group (**Supplementary Figure 2C**). This may further indicate the characteristic nature of the correlations in the putamen of the PD group. We hypothesize that since iron accumulation in PD is progressive, iron levels in the putamen had not accumulated sufficiently to cause microstructural differences between the groups. Pathological changes in the putamen correspond to Braak's stage IV with low levels of iron deposition in the putamen in ESPD. Observed correlations were due to the characteristics of the ASPD group (Braak et al., 2003).

Autopsy results of GP iron levels are controversial. Our results and those of Chen et al. (1993) revealed increased levels of iron deposition, but levels reported by Riederer et al. (1989) were normal, and Dexter et al. (1991) observed a decrease. Differences may be due to the use of different procedures and quantification methods or measuring levels in the internal versus external GP (Griffiths et al., 1999). Changes in MK are associated with changes in myelin, axon, and neuronal density. Most current studies suggest that increased MK reflects glial cell proliferation or an increased density of myelin to cell ratio (Steven et al., 2014), and decreased MK may reflect histological changes in neuronal cell bodies or synapses, or mild demyelination changes (Gong et al., 2013). An interesting phenomenon was found in our results: PD compared to HCs showed opposite performances of MK for both SN and GP although MS was elevated for both (**Figure 1**). First, this may reflect a difference in pathological alterations because major histocompatibility complex class II - positive microglia proliferation occurs predominantly in the SN (Imamura et al., 2003). Second, this may be because of the different protein alterations in the SN and GP. Several amide proton transfer imaging studies have validated this possibility in terms of molecular imaging (Li et al., 2014a, 2015a, 2017). The team suggests that the main reason for the opposite signaling changes is that the SN is dominated by a reduction in dopaminergic neurons and dopamine production (Braak et al., 2003), whereas the GP is dominated by the deposition of cytoplasmic proteins and peptides (Tong et al., 2010). Finally, it is possible that axonal disintegration and cell loss play a dominant role in microstructural changes in the GP, and thus a decrease in MK. For example, two studies found a negative correlation between the MK of GP and age (Lätt et al., 2013; Gong et al., 2014). After multiple comparison correction of multiple correlations within each gray matter nucleus in the HC group, only correlations between MS and Ka in the caudate nucleus were found (**Supplementary Figure 2E**). We suggest that this may be due to systematic errors such as the small size of the caudate nucleus and the insufficient number of healthy controls included in this study. We will continue to increase the sample size in future studies to reduce the occurrence of such errors.

Study Limitations

The study has some limitations. First, iron in the SN initially accumulates in the dorsal pars compacta; however, in the present study, the entire SN was assessed, which reduced sensitivity. Second, according to Braak's stage, iron deposition initially occurs in the dorsal IX/X motor nucleus and/or intermediate reticular zone, and gradually accumulates in the coeruleus–subcoeruleus complex. By Braak's stage III, a lesion forms in the SN, by which time clinical motor symptoms are already present. The present study assessed the correlation between iron deposition and tissue microstructure in the major gray matter nuclei. The association should be comprehensively studied in the future, considering all voxels from the medulla oblongata to the neocortex. Finally, most of the patients with PD included in the study were clinically symptomatic, with disease that was more severe than Braak stage III. It is not clear whether brain iron deposition in patients with PD with pre-Braak stage III disease will have a different kurtosis index profile. To address this problem, a study with a greater sample size, with preclinical patients with PD, is needed.

CONCLUSION

In recent years, many efforts have been made to examine brain iron levels and their effects on patients with PD. Our study provides new insights into iron overload and associated microstructural alterations from a neuroimaging perspective, which has the potential to integrate previous findings. Tracking the dynamic changes in iron content and microstructure throughout the course of PD will help us to better understand the dynamics of iron metabolism and microstructural alterations in the pathogenesis of PD and to develop new approaches to monitor and treat PD. First, we found that iron deposition in the SN and putamen may have an impact on changes in brain microstructure in patients with PD. Increased SN iron deposition was positively correlated with MK and Kr, and negatively correlated with Ka. Increased iron deposition in the putamen was positively correlated with MK, Ka, and Kr. This was especially true for the SN in which correlations were observable during early-stage PD. In addition, magnetic sensitivity was significantly higher in patients with PD, especially in the SN, RN, putamen, and GP. Finally, we confirmed that iron deposition in the SN affects brain microstructure, and, potentially, motor function in PD.

DATA AVAILABILITY STATEMENT

The original contributions presented in the study are included in the article/**Supplementary Material**, further inquiries can be directed to the corresponding authors.

ETHICS STATEMENT

The studies involving human participants were reviewed and approved by the Ethics Department of the Second Affiliated Hospital of Xiamen Medical College. The patients/participants provided their written informed consent to participate in this study.

AUTHOR CONTRIBUTIONS

LY, YC, YS, and YX: conceptualization, organization, and execution of research projects. JN, JG, YR, YJ, and ZZ: design, execution, and review of statistical analyses. LY, GY, and RW: wrote and reviewed the manuscript. All authors contributed to this article and approved the final submitted version.

FUNDING

This research was supported by the Natural Science Foundation of China (grant numbers 82020108016 and 31870981), the 2020 LKSF Cross-Disciplinary Research Grants (grant number 2020LKSFBME06), the 2020 Li Ka Shing Foundation Cross-Disciplinary Research Grant (grant number 2020LKSFG05D), the Grant for Key Disciplinary Project of Clinical Medicine under the Guangdong High-Level University Development Program (grant number 002-18120302), the Joint Funds for the Health and Education of Fujian Province, China (grant number 2019-WJ-31), and the Institute of Respiratory Diseases, Xiamen Medical College (grant number HXJB-06, 15).

ACKNOWLEDGMENTS

We thank Pu-Ye Wu from GE Healthcare for help in solving some MR technical problems and related consultation. We wish to thank all volunteers and researchers who contributed to the study's success.

SUPPLEMENTARY MATERIAL

The Supplementary Material for this article can be found online at: https://www.frontiersin.org/articles/10.3389/fnagi.2022.792778/full#supplementary-material

REFERENCES

Barnham, K. J., Masters, C. L., and Bush, A. I. (2004). Neurodegenerative diseases and oxidative stress. *Nat. Rev. Drug Discov.* 3, 205–214. doi: 10.1038/nrd1330

Batassini, C., Broetto, N., Tortorelli, L. S., Borsoi, M., Zanotto, C., Galland, F., et al. (2015). Striatal Injury with 6-OHDA Transiently Increases Cerebrospinal GFAP and S100B. *Neural. Plast.* 2015:387028. doi: 10.1155/2015/387028

Bergsland, N., Zivadinov, R., Schweser, F., Hagemeier, J., Lichter, D., and Guttuso, T. Jr. (2019). Ventral posterior substantia nigra iron increases over 3 years in Parkinson's disease. *Mov. Disord* 34, 1006–1013. doi: 10.1002/mds.27730

Block, M. L., Zecca, L., and Hong, J. S. (2007). Microglia-mediated neurotoxicity: uncovering the molecular mechanisms. *Nat. Rev. Neurosci.* 8, 57–69. doi: 10.1038/nrn2038

Braak, H., Del Tredici, K., Rüb, U., de Vos, R. A., Jansen Steur, E. N., and Braak, E. (2003). Staging of brain pathology related to sporadic Parkinson's disease. *Neurobiol. Aging* 24, 197–211. doi: 10.1016/s0197-4580(02)00065-9

Chen, J. C., Hardy, P. A., Kucharczyk, W., Clauberg, M., Joshi, J. G., Vourlas, A., et al. (1993). MR of human postmortem brain tissue: correlative study between T2 and assays of iron and ferritin in Parkinson and Huntington disease. *AJNR Am. J. Neuroradiol.* 14, 275–281.

Cheung, M. M., Hui, E. S., Chan, K. C., Helpern, J. A., Qi, L., and Wu, E. X. (2009). Does diffusion kurtosis imaging lead to better neural tissue characterization? A rodent brain maturation study. *Neuroimage* 45, 386–392. doi: 10.1016/j.neuroimage.2008.12.018

Coutu, J. P., Chen, J. J., Rosas, H. D., and Salat, D. H. (2014). Non-Gaussian water diffusion in aging white matter. *Neurobiol. Aging* 35, 1412–1421. doi: 10.1016/j.neurobiolaging.2013.12.001

Covell, D. J., Robinson, J. L., Akhtar, R. S., Grossman, M., Weintraub, D., Bucklin, H. M., et al. (2017). Novel conformation-selective alpha-synuclein antibodies raised against different in vitro fibril forms show distinct patterns of Lewy pathology in Parkinson's disease. *Neuropathol. Appl. Neurobiol.* 43, 604–620. doi: 10.1111/nan.12402

Dexter, D. T., Carayon, A., Javoy-Agid, F., Agid, Y., Wells, F. R., Daniel, S. E., et al. (1991). Alterations in the levels of iron, ferritin and other trace metals in Parkinson's disease and other neurodegenerative diseases affecting the basal ganglia. *Brain* 114(Pt 4), 1953–1975. doi: 10.1093/brain/114.4.1953

Dexter, D. T., Wells, F. R., Agid, F., Agid, Y., Lees, A. J., Jenner, P., et al. (1987). Increased nigral iron content in postmortem parkinsonian brain. *Lancet* 2, 1219–1220. doi: 10.1016/s0140-6736(87)91361-4

Du, G., Lewis, M. M., Sica, C., He, L., Connor, J. R., Kong, L., et al. (2018). Distinct progression pattern of susceptibility MRI in the substantia nigra of Parkinson's patients. *Mov. Disord.* 33, 1423–1431. doi: 10.1002/mds.27318

Du, G., Liu, T., Lewis, M. M., Kong, L., Wang, Y., Connor, J., et al. (2016). Quantitative susceptibility mapping of the midbrain in Parkinson's disease. *Mov. Disord.* 31, 317–324. doi: 10.1002/mds.26417

Filli, L., Wurnig, M., Nanz, D., Luechinger, R., Kenkel, D., and Boss, A. (2014). Whole-body diffusion kurtosis imaging: initial experience on non-Gaussian diffusion in various organs. *Invest. Radiol.* 49, 773–778. doi: 10.1097/rli.0000000000000082

Folstein, M. F., Folstein, S. E., and McHugh, P. R. (1975). Mini-mental state". A practical method for grading the cognitive state of patients for the clinician. *J. Psychiatr. Res.* 12, 189–198. doi: 10.1016/0022-3956(75)90026-6

Ghosh, D., Mehra, S., Sahay, S., Singh, P. K., and Maji, S. K. (2017). α-synuclein aggregation and its modulation. *Int. J. Biol. Macromol.* 100, 37–54. doi: 10.1016/j.ijbiomac.2016.10.021

Giannelli, M., Toschi, N., Passamonti, L., Mascalchi, M., Diciotti, S., and Tessa, C. (2012). Diffusion kurtosis and diffusion-tensor MR imaging in Parkinson disease. *Radiology* 265, 645–646. doi: 10.1148/radiol.12121036

Gong, N. J., Wong, C. S., Chan, C. C., Leung, L. M., and Chu, Y. C. (2013). Correlations between microstructural alterations and severity of cognitive deficiency in Alzheimer's disease and mild cognitive impairment: a diffusional kurtosis imaging study. *Magn. Reson. Imag.* 31, 688–694. doi: 10.1016/j.mri.2012.10.027

Gong, N. J., Wong, C. S., Chan, C. C., Leung, L. M., and Chu, Y. C. (2014). Aging in deep gray matter and white matter revealed by diffusional kurtosis imaging. *Neurobiol. Aging* 35, 2203–2216. doi: 10.1016/j.neurobiolaging.2014.03.011

Greffard, S., Verny, M., Bonnet, A. M., Beinis, J. Y., Gallinari, C., Meaume, S., et al. (2006). Motor score of the Unified Parkinson Disease Rating Scale as a good predictor of Lewy body-associated neuronal loss in the substantia nigra. *Arch. Neurol.* 63, 584–588. doi: 10.1001/archneur.63.4.584

Griffiths, P. D., Dobson, B. R., Jones, G. R., and Clarke, D. T. (1999). Iron in the basal ganglia in Parkinson's disease. An in vitro study using extended X-ray absorption fine structure and cryo-electron microscopy. *Brain* 122(Pt 4), 667–673. doi: 10.1093/brain/122.4.667

Guan, J., Ma, X., Geng, Y., Qi, D., Shen, Y., Shen, Z., et al. (2019). Diffusion Kurtosis Imaging for Detection of Early Brain Changes in Parkinson's Disease. *Front. Neurol.* 10:1285. doi: 10.3389/fneur.2019.01285

Guan, X., Xu, X., and Zhang, M. (2017a). Region-Specific Iron Measured by MRI as a Biomarker for Parkinson's Disease. *Neurosci. Bull.* 33, 561–567. doi: 10.1007/s12264-017-0138-x

Guan, X., Xuan, M., Gu, Q., Huang, P., Liu, C., Wang, N., et al. (2017b). Regionally progressive accumulation of iron in Parkinson's disease as measured by quantitative susceptibility mapping. *NMR Biomed.* 30:4. doi: 10.1002/nbm.3489

Guan, X., Xuan, M., Gu, Q., Xu, X., Huang, P., Wang, N., et al. (2017c). Influence of regional iron on the motor impairments of Parkinson's disease: a quantitative susceptibility mapping study. *J. Magn. Reson. Imag.* 45, 1335–1342. doi: 10.1002/jmri.25434

Haacke, E. M., Cheng, N. Y., House, M. J., Liu, Q., Neelavalli, J., Ogg, R. J., et al. (2005). Imaging iron stores in the brain using magnetic resonance imaging. *Magn. Reson. Imag.* 23, 1–25. doi: 10.1016/j.mri.2004.10.001

He, N., Ling, H., Ding, B., Huang, J., Zhang, Y., Zhang, Z., et al. (2015). Region-specific disturbed iron distribution in early idiopathic Parkinson's disease measured by quantitative susceptibility mapping. *Hum. Brain Mapp.* 36, 4407–4420. doi: 10.1002/hbm.22928

Imamura, K., Hishikawa, N., Sawada, M., Nagatsu, T., Yoshida, M., and Hashizume, Y. (2003). Distribution of major histocompatibility complex class II-positive microglia and cytokine profile of Parkinson's disease brains. *Acta Neuropathol.* 106, 518–526. doi: 10.1007/s00401-003-0766-2

Jensen, J. H., and Helpern, J. A. (2010). MRI quantification of non-Gaussian water diffusion by kurtosis analysis. *NMR Biomed.* 23, 698–710. doi: 10.1002/nbm.1518

Jensen, J. H., Helpern, J. A., Ramani, A., Lu, H., and Kaczynski, K. (2005). Diffusional kurtosis imaging: the quantification of non-gaussian water diffusion by means of magnetic resonance imaging. *Magn. Reson. Med.* 53, 1432–1440. doi: 10.1002/mrm.20508

Jin, L., Wang, J., Zhao, L., Jin, H., Fei, G., Zhang, Y., et al. (2011). Decreased serum ceruloplasmin levels characteristically aggravate nigral iron deposition in Parkinson's disease. *Brain* 134(Pt 1), 50–58. doi: 10.1093/brain/awq319

Kalia, L. V., and Lang, A. E. (2015). Parkinson's disease. *Lancet* 386, 896–912. doi: 10.1016/s0140-6736(14)61393-3

Kamagata, K., Zalesky, A., Hatano, T., Ueda, R., Di Biase, M. A., Okuzumi, A., et al. (2017). Gray Matter Abnormalities in Idiopathic Parkinson's Disease: evaluation by Diffusional Kurtosis Imaging and Neurite Orientation Dispersion and Density Imaging. *Hum. Brain Mapp.* 38, 3704–3722. doi: 10.1002/hbm.23628

Kennedy, P. R., Gibson, A. R., and Houk, J. C. (1986). Functional and anatomic differentiation between parvicellular and magnocellular regions of red nucleus in the monkey. *Brain Res.* 364, 124–136. doi: 10.1016/0006-8993(86)90993-5

Khairnar, A., Latta, P., Drazanova, E., Ruda-Kucerova, J., Szabó, N., Arab, A., et al. (2015). Diffusion Kurtosis Imaging Detects Microstructural Alterations in Brain of α-Synuclein Overexpressing Transgenic Mouse Model of Parkinson's Disease: a Pilot Study. *Neurotox Res.* 28, 281–289. doi: 10.1007/s12640-015-9537-9

Koch, J. C., Bitow, F., Haack, J., d'Hedouville, Z., Zhang, J. N., Tönges, L., et al. (2015). Alpha-Synuclein affects neurite morphology, autophagy, vesicle transport and axonal degeneration in CNS neurons. *Cell Death Dis.* 6:e1811. doi: 10.1038/cddis.2015.169

Kumar, H., Lim, H. W., More, S. V., Kim, B. W., Koppula, S., Kim, I. S., et al. (2012). The role of free radicals in the aging brain and Parkinson's Disease: convergence and parallelism. *Int. J. Mol. Sci.* 13, 10478–10504. doi: 10.3390/ijms130810478

Landis, J. R., and Koch, G. G. (1977). The measurement of observer agreement for categorical data. *Biometrics* 33, 159–174.

Langkammer, C., Pirpamer, L., Seiler, S., Deistung, A., Schweser, F., Franthal, S., et al. (2016). Quantitative Susceptibility Mapping in Parkinson's Disease. *PLoS One* 11:e0162460. doi: 10.1371/journal.pone.0162460

Lätt, J., Nilsson, M., Wirestam, R., Ståhlberg, F., Karlsson, N., Johansson, M., et al. (2013). Regional values of diffusional kurtosis estimates in the healthy brain. *J. Magn. Reson. Imag.* 37, 610–618. doi: 10.1002/jmri.23857

Li, C., Chen, M., Zhao, X., Wang, R., Chen, H., Su, W., et al. (2017). Chemical Exchange Saturation Transfer MRI Signal Loss of the Substantia Nigra as an Imaging Biomarker to Evaluate the Diagnosis and Severity of Parkinson's Disease. *Front. Neurosci.* 11:489. doi: 10.3389/fnins.2017.00489

Li, C., Peng, S., Wang, R., Chen, H., Su, W., Zhao, X., et al. (2014a). Chemical exchange saturation transfer MR imaging of Parkinson's disease at 3 Tesla. *Eur. Radiol.* 24, 2631–2639. doi: 10.1007/s00330-014-3241-7

Li, C., Wang, R., Chen, H., Su, W., Li, S., Zhao, X., et al. (2015a). Chemical Exchange Saturation Transfer MR Imaging is Superior to Diffusion-Tensor Imaging in the Diagnosis and Severity Evaluation of Parkinson's Disease: a Study on Substantia Nigra and Striatum. *Front. Aging Neurosci.* 7:198. doi: 10.3389/fnagi.2015.00198

Li, D. T. H., Hui, E. S., Chan, Q., Yao, N., Chua, S. E., McAlonan, G. M., et al. (2018). Quantitative susceptibility mapping as an indicator of subcortical and limbic iron abnormality in Parkinson's disease with dementia. *Neuroimage Clin.* 20, 365–373. doi: 10.1016/j.nicl.2018.07.028

Li, W., Avram, A. V., Wu, B., Xiao, X., and Liu, C. (2014b). Integrated Laplacian-based phase unwrapping and background phase removal for quantitative susceptibility mapping. *NMR Biomed.* 27, 219–227. doi: 10.1002/nbm.3056

Li, W., Wang, N., Yu, F., Han, H., Cao, W., Romero, R., et al. (2015b). A method for estimating and removing streaking artifacts in quantitative susceptibility mapping. *Neuroimage* 108, 111–122. doi: 10.1016/j.neuroimage.2014.12.043

Martin, W. R., Wieler, M., and Gee, M. (2008). Midbrain iron content in early Parkinson disease: a potential biomarker of disease status. *Neurology* 70(16 Pt 2), 1411–1417. doi: 10.1212/01.wnl.0000286384.31050.b5

Matuskey, D., Tinaz, S., Wilcox, K. C., Naganawa, M., Toyonaga, T., Dias, M., et al. (2020). Synaptic Changes in Parkinson Disease Assessed with in vivo Imaging. *Ann. Neurol.* 87, 329–338. doi: 10.1002/ana.25682

McGeer, P. L., and McGeer, E. G. (2004). Inflammation and neurodegeneration in Parkinson's disease. *Parkinsonism Relat. Disord.* 10(Suppl. 1), S3–S7. doi: 10.1016/j.parkreldis.2004.01.005

Mewes, K., and Cheney, P. D. (1994). Primate rubromotoneuronal cells: parametric relations and contribution to wrist movement. *J. Neurophysiol.* 72, 14–30. doi: 10.1152/jn.1994.72.1.14

Millecamps, S., and Julien, J. P. (2013). Axonal transport deficits and neurodegenerative diseases. *Nat. Rev. Neurosci.* 14:161–176. doi: 10.1038/nrn3380

Onodera, S., and Hicks, T. P. (2009). A comparative neuroanatomical study of the red nucleus of the cat, macaque and human. *PLoS One* 4:e6623. doi: 10.1371/journal.pone.0006623

Perlson, E., Maday, S., Fu, M. M., Moughamian, A. J., and Holzbaur, E. L. (2010). Retrograde axonal transport: pathways to cell death? *Trends Neurosci.* 33, 335–344. doi: 10.1016/j.tins.2010.03.006

Pierpaoli, C., and Basser, P. J. (1996). Toward a quantitative assessment of diffusion anisotropy. *Magn. Reson. Med.* 36, 893–906. doi: 10.1002/mrm.1910360612

Pinto, T. C. C., Machado, L., Bulgacov, T. M., Rodrigues-Júnior, A. L., Costa, M. L. G., Ximenes, R. C. C., et al. (2019). Is the Montreal Cognitive Assessment (MoCA) screening superior to the Mini-Mental State Examination (MMSE) in the detection of mild cognitive impairment (MCI) and Alzheimer's Disease (AD) in the elderly? *Int. Psychogeriatr.* 31, 491–504. doi: 10.1017/s1041610218001370

Riederer, P., Sofic, E., Rausch, W. D., Schmidt, B., Reynolds, G. P., Jellinger, K., et al. (1989). Transition metals, ferritin, glutathione, and ascorbic acid in parkinsonian brains. *J. Neurochem.* 52, 515–520. doi: 10.1111/j.1471-4159.1989.tb09150.x

Rodriguez-Oroz, M. C., Rodriguez, M., Leiva, C., Rodriguez-Palmero, M., Nieto, J., Garcia-Garcia, D., et al. (2008). Neuronal activity of the red nucleus in Parkinson's disease. *Mov. Disord.* 23, 908–911. doi: 10.1002/mds.22000

Steven, A. J., Zhuo, J., and Melhem, E. R. (2014). Diffusion kurtosis imaging: an emerging technique for evaluating the microstructural environment of the brain. *AJR Am. J. Roentgenol.* 202, W26–W33. doi: 10.2214/ajr.13.11365

Taylor, K. I., Sambataro, F., Boess, F., Bertolino, A., and Dukart, J. (2018). Progressive Decline in Gray and White Matter Integrity in de novo Parkinson's Disease: an Analysis of Longitudinal Parkinson Progression Markers Initiative Diffusion Tensor Imaging Data. *Front. Aging Neurosci.* 10:318. doi: 10.3389/fnagi.2018.00318

Tong, J., Wong, H., Guttman, M., Ang, L. C., Forno, L. S., Shimadzu, M., et al. (2010). Brain alpha-synuclein accumulation in multiple system atrophy, Parkinson's disease and progressive supranuclear palsy: a comparative investigation. *Brain* 133(Pt 1), 172–188. doi: 10.1093/brain/awp282

Uchida, Y., Kan, H., Sakurai, K., Arai, N., Kato, D., Kawashima, S., et al. (2019). Voxel-based quantitative susceptibility mapping in Parkinson's disease with mild cognitive impairment. *Mov. Disord* 34, 1164–1173. doi: 10.1002/mds.27717

Uchida, Y., Kan, H., Sakurai, K., Inui, S., Kobayashi, S., Akagawa, Y., et al. (2020). Magnetic Susceptibility Associates With Dopaminergic Deficits and Cognition in Parkinson's Disease. *Mov. Disord* 35, 1396–1405. doi: 10.1002/mds.28077

Wang, J. J., Lin, W. Y., Lu, C. S., Weng, Y. H., Ng, S. H., Wang, C. H., et al. (2011). Parkinson disease: diagnostic utility of diffusion kurtosis imaging. *Radiology* 261, 210–217. doi: 10.1148/radiol.11102277

Weber, R. A., Hui, E. S., Jensen, J. H., Nie, X., Falangola, M. F., Helpern, J. A., et al. (2015). Diffusional kurtosis and diffusion tensor imaging reveal different time-sensitive stroke-induced microstructural changes. *Stroke* 46, 545–550. doi: 10.1161/strokeaha.114.006782

Wieler, M., Gee, M., and Martin, W. R. (2015). Longitudinal midbrain changes in early Parkinson's disease: iron content estimated from R2*/MRI. *Parkinsonism Relat. Disord.* 21, 179–183. doi: 10.1016/j.parkreldis.2014.11.017

Wolozin, B., and Golts, N. (2002). Iron and Parkinson's disease. *Neuroscientist* 8, 22–32. doi: 10.1177/107385840200800107

Xu, J., Xiao, C., Song, W., Cui, X., Pan, M., Wang, Q., et al. (2021). Elevated Heme Oxygenase-1 Correlates With Increased Brain Iron Deposition Measured by Quantitative Susceptibility Mapping and Decreased Hemoglobin in Patients With Parkinson's Disease. *Front. Aging Neurosci.* 13:656626. doi: 10.3389/fnagi.2021.656626

Yang, Z., Rong, Y., Cao, Z., Wu, Y., Zhao, X., Xie, Q., et al. (2021). Microstructural and Cerebral Blood Flow Abnormalities in Subjective Cognitive Decline Plus: diffusional Kurtosis Imaging and Three-Dimensional Arterial Spin Labeling Study. *Front. Aging Neurosci.* 13:625843. doi: 10.3389/fnagi.2021.625843

Zhang, G., Zhang, Y., Zhang, C., Wang, Y., Ma, G., Nie, K., et al. (2015). Diffusion Kurtosis Imaging of Substantia Nigra Is a Sensitive Method for Early Diagnosis and Disease Evaluation in Parkinson's Disease. *Parkinsons Dis.* 2015:207624. doi: 10.1155/2015/207624

Zhang, W., Yan, Z. F., Gao, J. H., Sun, L., Huang, X. Y., Liu, Z., et al. (2014). Role and mechanism of microglial activation in iron-induced selective and progressive dopaminergic neurodegeneration. *Mol. Neurobiol.* 49, 1153–1165. doi: 10.1007/s12035-013-8586-4

Zheng, W., Wu, C., Huang, L., and Wu, R. (2017). Diffusion Kurtosis Imaging of Microstructural Alterations in the Brains of Paediatric Patients with Congenital Sensorineural Hearing Loss. *Sci. Rep.* 7:1543. doi: 10.1038/s41598-017-01263-9

Conflict of Interest: The authors declare that the research was conducted in the absence of any commercial or financial relationships that could be construed as a potential conflict of interest.

Publisher's Note: All claims expressed in this article are solely those of the authors and do not necessarily represent those of their affiliated organizations, or those of the publisher, the editors and the reviewers. Any product that may be evaluated in this article, or claim that may be made by its manufacturer, is not guaranteed or endorsed by the publisher.

frontiers in Aging Neuroscience

ORIGINAL RESEARCH
published: 17 March 2022
doi: 10.3389/fnagi.2022.836568

Computed Tomography Density and β-Amyloid Deposition of Intraorbital Optic Nerve May Assist in Diagnosing Mild Cognitive Impairment and Alzheimer's Disease: A ^{18}F-Flutemetamol Positron Emission Tomography/Computed Tomography Study

Han Wu[1,2†], Zhe Lei[1,2†], Yinghui Ou[1,2†], Xin Shi[1], Qian Xu[1], Keqing Shi[1], Jing Ding[3], Qianhua Zhao[4], Xiuzhe Wang[5], Xiaolong Cai[5], Xueyuan Liu[6], Jingjing Lou[2] and Xingdang Liu[1,2]**

[1] Department of Nuclear Medicine, Huashan Hospital, Fudan University, Shanghai, China, [2] Department of Nuclear Medicine, Pudong Hospital, Fudan University, Shanghai, China, [3] Department of Neurology, Zhongshan Hospital, Fudan University, Shanghai, China, [4] Department of Neurology, Huashan Hospital, Fudan University, Shanghai, China, [5] Department of Neurology, Shanghai Sixth People's Hospital Affiliated to Shanghai Jiao Tong University, Shanghai, China, [6] Department of Neurology, Tenth People's Hospital affiliated to Tongji University, Shanghai, China

Objective: The aim was to study whether the computed tomography (CT) density and β-amyloid (Aβ) level of intraorbital optic nerve could assist in diagnosing mild cognitive impairment (MCI) and Alzheimer's disease (AD).

Methods: A total of sixty subjects were recruited in our study, including nine normal control (NC) subjects (i.e., 4 men and 5 women), twenty four MCI subjects (i.e., 11 men and 13 women), and twenty seven AD subjects (i.e., 14 men and 13 women). All subjects conducted ^{18}F-flutemetamol amyloid positron emission tomography (PET)/CT imaging. Blinded to the clinical information of the subjects, two physicians independently measured and calculated the standardized uptake value ratio (SUVR) of the bilateral occipital cortex, SUVR of the bilateral intraorbital optic nerve, and CT density of the bilateral intraorbital optic nerve by using GE AW 4.5 Workstation.

Results: Between AD and NC groups, the differences of the bilateral intraorbital optic nerve SUVR were statistically significant; between AD and MCI groups, the differences of the left intraorbital optic nerve SUVR were statistically significant. Between any two of the three groups, the differences in the bilateral intraorbital optic nerve density were statistically significant. The bilateral occipital SUVR was positively correlated with the bilateral intraorbital optic nerve SUVR and negatively correlated with the bilateral intraorbital optic nerve density. Bilateral intraorbital optic nerve SUVR was negatively

OPEN ACCESS

Edited by:
Binbin Nie,
Institute of High Energy Physics (CAS), China

Reviewed by:
Lihua Sun,
Turku PET Centre, Finland
Jun Zhao,
Tongji University, China

***Correspondence:**
Jingjing Lou
1436150464@qq.com
Xingdang Liu
xingdliu@fudan.edu.cn

† These authors have contributed equally to this work

Specialty section:
This article was submitted to Alzheimer's Disease and Related Dementias, a section of the journal Frontiers in Aging Neuroscience

Received: *15 December 2021*
Accepted: *26 January 2022*
Published: *17 March 2022*

Citation:
Wu H, Lei Z, Ou Y, Shi X, Xu Q, Shi K, Ding J, Zhao Q, Wang X, Cai X, Liu X, Lou J and Liu X (2022) Computed Tomography Density and β-Amyloid Deposition of Intraorbital Optic Nerve May Assist in Diagnosing Mild Cognitive Impairment and Alzheimer's Disease: A ^{18}F-Flutemetamol Positron Emission Tomography/Computed Tomography Study. Front. Aging Neurosci. 14:836568. doi: 10.3389/fnagi.2022.836568

correlated with the bilateral intraorbital optic nerve density. The area under the receiver operating characteristic (ROC) curve of multiple logistic regression was 0.9167 (for MCI vs. NC) and 0.8951 (for AD vs. MCI). The Montreal Cognitive Assessment (MoCA) and Mini-Mental State Examination (MMSE) scores were positively associated with the intraorbital optic nerve density and were negatively associated with the intraorbital optic nerve SUVR. The regression equation of MoCA was y = 16.37-0.9734 × x_1 + 0.5642 × x_2-3.127 × x_3 + 0.0275 × x_4; the R^2 was 0.848. The regression equation of MMSE was y = 19.57-1.633 × x_1 + 0.4397 × x_2-1.713 × x_3 + 0.0424 × x_4; the R^2 was 0.827.

Conclusion: The CT density and Aβ deposition of the intraorbital optic nerve were associated with Aβ deposition of the occipital cortex and the severity of cognitive impairment. The intraorbital optic nerve CT density and intraorbital optic nerve Aβ deposition could assist in diagnosing MCI and AD.

Keywords: intraorbital optic nerve, mild cognitive impairment, Alzheimer's disease, computed tomography, positron emission tomography, ^{18}F-flutemetamol, β-Amyloid

INTRODUCTION

Alzheimer's disease (AD) is the most common form of dementia among older adults that affects wide areas of the cerebral cortex and the hippocampus. From a diagnostic perspective, AD is increasingly viewed along a continuum from preclinical AD, through mild cognitive impairment (MCI), to AD dementia (Jack et al., 2011). β-amyloid (Aβ) plaques and neurofibrillary tangles were the characteristic pathologic lesions in the AD brain (Holtzman et al., 2011). Positron emission tomography (PET)/computed tomography (CT) imaging of Aβ in the brain was expected to be useful for improving the accuracy in the diagnosis of AD. However, there is still no effective methods to accurately diagnose MCI and AD; a study showed that Aβ may not be a cause of AD but a consequence of the progression of cognitive impairment (Thomas et al., 2020). Therefore, the application of brain amyloid PET alone may not be sufficient to diagnose MCI and AD, especially in the early stages. It has been demonstrated in a previous study that several patients with AD developed visual anomalies, which were correlated with abnormalities in the optic nerves, such as widespread axonal degeneration and reduction in the thickness of the nerve fiber layer (Hinton et al., 1986). Studies in the past decades reveal that the visual system might be affected by AD, including the optic nerve; the detection of degenerative changes in the optic nerve by medical imaging might be a potential method of diagnosing MCI and AD.

As a part of the central nervous system, the optic nerve travels posteriorly in the orbit, enters the middle cranial fossa *via* the optic canal, connects to the optic cross, and ends at the lateral geniculate body *via* the optic tract to conduct visual impulses. The optic nerve is divided into four parts, namely, the intraocular segment, the intraorbital segment, the intratubular segment, and the intracranial segment; the intraorbital optic nerve was the longest of the four (∼25–30 mm) (Miller, 1996). The fibers of the optic nerve originate from the retinal ganglion cells (RGC). A study showed that there was a functional abnormality of the outer retina concerning the foveal and parafoveal area of the central retina even in the mild stages of AD without visual impairment (Moschos et al., 2012). Previous studies showed that the visual pathway was affected in patients with AD. A study about the retinal nerve fiber layer demonstrated that ocular degeneration in patients with AD and MCI results in decreased thickness of the retinal nerve fiber layer and reduced macular volume in patients with AD and MCI (Gao et al., 2015). Another study about AD transgenic mice showed evidence of molecular, functional, and morphological degenerative changes in the inner retina (Gupta et al., 2016). In another study comparing the optic nerve in patients with AD and normal controls (NCs), a reduction in the number of optic nerve fibers in patients with AD was found (Syed et al., 2005). The previous studies have inspired us that structural and functional optic nerve degeneration should be associated with the ipsilateral occipital visual cortex degeneration in patients with MCI and AD.

Brain amyloid PET/CT was one of the most common and effective modern neuroimaging tools for the diagnosis of MCI and AD (Sevigny et al., 2016). Several fluorine-18-labeled (^{18}F) PET tracers, including ^{18}F-flutemetamol, have become available for clinical practice and have been incorporated as amyloid pathology biomarkers in the revised research criteria for AD (McKhann et al., 2011). The Aβ deposition in PET images of the AD brain has been demonstrated by many previous studies (Zwan et al., 2017; Cho et al., 2020; Hwang et al., 2021). However, few studies have been conducted on the structural and functional degeneration of the optic nerve in patients with MCI and AD. In Aβ PET brain studies, the standardized uptake value ratio (SUVR) is an effective method that measured the SUV ratio of different brain regions for the semiquantitative analysis (Matsuda et al., 2020); SUVR can reflect the degree of uptake of the radioactive tracers and, consequently, reflect the deposition of Aβ. The Hounsfield unit (HU) was a relatively quantitative measurement of radio density used by radiologists in the interpretation of CT images (Levine et al., 2018); the absorption/attenuation coefficient of

radiation within a tissue was used during CT reconstruction to produce a grayscale image. In addition, CT has the advantage of wider availability and significantly lower cost than other neuroimaging methods, such as functional MRI (fMRI), and is still an important tool in clinical practice of neurological diseases in both high-income areas and low- and middle-income areas (Papanicolas et al., 2018; Dieleman et al., 2020). Therefore, the exploration of CT density of the optic nerve could help improve the diagnosis of MCI and AD in low- and middle-income areas and make early treatment available to a wider range of patients with dementia.

To the best of our knowledge, there was no study aimed at Aβ deposition and CT density of the intraorbital optic nerve in patients with MCI and AD. The aim of our research was to study whether CT density and Aβ deposition of the intraorbital optic nerve in ^{18}F-flutemetamol PET/CT images could assist in diagnosing MCI and AD. We made a hypothesis that CT density and Aβ deposition of the intraorbital optic nerve would be expected to correlate with the Aβ deposition of the occipital visual cortex and the severity of cognitive impairment.

MATERIALS AND METHODS

Ethics

The study received ethical approval from the Committee for Medical and Health Research Ethics of Huashan Hospital affiliated to Fudan University, Shanghai, China. The clinical registration number is ChiCTR2000035791. The written informed consent was signed by each subject in accordance with the Declaration of Helsinki prior to inclusion in the study. All procedures were conducted in accordance with the institutional regulations and ethical guidelines.

Participants

Sixty subjects were recruited in this study, including nine NC subjects (i.e., 4 men and 5 women), twenty four MCI subjects (i.e., 11 men and 13 women), and twenty seven AD subjects (i.e., 14 men and 13 women). The NC subjects were recruited from two major communities in Shanghai city; it is necessary to note here that recruiting normal subjects (especially elderly citizens) was a challenge in China due to the lack of scientific education; most of the elderly citizens were so scared of ionizing radiation that they were reluctant to participate in this research. Subjects with MCI and AD were recruited from the outpatient neurology clinics of Huashan Hospital affiliated to Fudan University, Zhongshan Hospital affiliated to Fudan University, and Shanghai Sixth People's Hospital affiliated to Shanghai Jiao Tong University. The clinical criteria of the National Institute on Aging-Alzheimer's Association (NIA-AA) workgroups (Jack et al., 2011) were used for the diagnosis of subjects with MCI and AD. All the sixty subjects were tested at inclusion by a standardized neuropsychological battery of tests including the Mini-Mental State Examination (MMSE) and the Montreal Cognitive Assessment (MoCA) for the estimation of cognitive impairment (Folstein et al., 1975; Nasreddine et al., 2005). Subjects were excluded if they had disturbance of myopia, consciousness, delirium, psychosis, severe aphasia, major sensorimotor impairment, and structural brain lesions. All patients regarded themselves as right-handed.

^{18}F-Flutemetamol Positron Emission Tomography/Computed Tomography Studies

^{18}F-flutemetamol PET/CT studies were performed in the Nuclear Medicine Department of Pudong Hospital affiliated to Fudan University, Shanghai, China. All the subjects had an intravenous line while they rested in a quiet and dimly lit room 20 min prior to and 70 min post injection of 200 MBq of ^{18}F-flutemetamol (Vizamyl®). A normalized PET/CT (Neusoft NeuWise Pro PET/CT) scan was started according to the imaging acquisition guidelines of the Vizamyl®,[1]which recommends a PET scan start time of 60–120 min after Vizamyl® injection. For all participants, all appropriate corrections, including scatter and time-of-flight, were applied with a low-dose CT. Images were reconstructed using the OSEM method (consisting of 16 subsets and 4 iterations) (Nelissen et al., 2009; Vandenberghe et al., 2010). Filtered back-projection reconstruction was used with a slice thickness of 2–4 mm and matrix size of 128 × 128 mm with the pixel size of 2 mm. A full-width half-maximum postsmoothing filter was applied of not more than 5 mm. The duration of the scan lasted 30 min (Nelissen et al., 2009; Vandenberghe et al., 2010). The clinical status was checked before and after the scanning in each participant. Patients were observed for adverse events from the administration of the tracer and were immediately after the PET scan.

Image Processing and Analysis

Positron emission tomography and CT images were measured by two certified nuclear medicine physicians using the GE AW 4.5 Workstation after passing a subsequent training. The two physicians were blinded to clinical information and independently measured the images using the GE AW 4.5 software according to the training instructions. For PET images, the two physicians independently measured the cortex SUV_{max} of the bilateral cerebellum and the occipital lobe, and the SUV_{max} of the bilateral intraorbital optic nerve and the SUV_{max} values measured by two physicians were averaged. For CT images, two physicians independently measured the mean CT density (HU) of the bilateral intraorbital optic nerve, and the CT density values measured by two physicians were averaged. One side of the cerebellum cortex was used as the ipsilateral reference region to compute the SUVR of the ipsilateral occipital lobe and the intraorbital optic nerve; for instance, the left cerebellum cortex was used as the reference region for left hemispheric measures. Consequently, the left and right SUVR of the bilateral occipital cortex and the intraorbital optic nerve were computed.

Statistical Analysis

Quantitative variables were described with mean ± SD. Qualitative variables were expressed as absolute and relative

[1]https://www.accessdata.fda.gov/drugsatfda_docs/label/2017/203137s008lbl.pdf

frequencies. The Kruskal-Wallis test was used for the comparison of age, education, duration of cognitive impairment, MMSE score, and MoCA score of different groups. The Mann-Whitney *U*-test was used for the comparison of SUVR and CT density between each of the two groups of subjects in NC, MCI, and AD groups; the Bonferroni correction method was used to avoid potential bias due to the small sample size of the NC group; differences were statistically significant if the *p*-value is < 0.017 (corrected: 0.05/3) (Curtin and Schulz, 1998). Simple linear regression was used with the entire sample for the comparison between the occipital cortex SUVR and the intraorbital optic nerve SUVR, between the occipital cortex SUVR and the intraorbital optic nerve CT density, and between the intraorbital optic nerve SUVR and CT density. Multiple logistic regression was used to analyze whether the intraorbital optic nerve SUVR and CT density could assist in distinguishing MCI from NC and AD from MCI. Multiple linear regression was used to explore whether the intraorbital optic nerve SUVR and CT density could predict the MoCA and MMSE scores. Differences were statistically significant if the *p*-value was < 0.05. Analyses were conducted using the IBM SPSS version 26.0 software (SPSS, Chicago, IL, United States).

RESULTS

Clinical Characteristics of Study Subjects

Characteristics of the subjects are shown in **Table 1**. The Kruskal-Wallis test was used for the comparison of age, education, duration of cognitive impairment, MMSE score, and MoCA score of different groups. There was no significant difference in terms of age and duration of disease (between MCI and AD groups). There was a significant difference in terms of MoCA and MMSE scores.

The Occipital Standardized Uptake Value Ratio, the Intraorbital Optic Nerve Standardized Uptake Value Ratio, and the Intraorbital Optic Nerve Density of Three Groups

We measured and calculated the SUVR of the bilateral occipital lobe and the intraorbital optic nerve and measured the mean CT density (HU) of the bilateral intraorbital optic nerve. The values of the abovementioned three groups are shown in **Table 2** and **Figure 1**, and the representative images of subjects with NC, MCI, and AD are shown in **Figure 2**.

Comparison of the Occipital Standardized Uptake Value Ratio, the Intraorbital Optic Nerve Standardized Uptake Value Ratio, and the Intraorbital Optic Nerve Density Between Each of the Two Groups

The Mann-Whitney *U*-test was used for the comparison of occipital SUVR, the intraorbital optic nerve SUVR, and the intraorbital optic nerve CT density between each of the two groups of subjects in NC, MCI, and AD

TABLE 1 | Clinical characteristics of study subjects.

	Normal control	MCI	AD	*p*-value
	Mean ± *SD*	**Mean ± *SD***	**Mean ± *SD***	
Subjects	9	24	27	N/A
Age (years)	60.50 ± 8.90	66.58 ± 8.30	69.00 ± 4.38	0.10
Duration of disease (years)	N/A	2.25 ± 0.89	2.71 ± 1.81	0.64
MoCA (score)	27.50 ± 1.50	21.15 ± 3.55	14.50 ± 2.75	**0.02**
MMSE (score)	28.35 ± 1.06	23.95 ± 3.80	18.00 ± 3.48	**0.03**

MCI, mild cognitive impairment; AD, Alzheimer's Disease; MoCA, Montreal Cognitive Assessment; MMSE, Mini-Mental State Examination. p-value below 0.05 were in bold.

TABLE 2 | The occipital standardized uptake value ratio (SUVR), the intraorbital optic nerve SUVR, and the intraorbital optic nerve density of three groups.

	Normal control	MCI	AD
	Mean ± SD	*Mean ± SD*	*Mean ± SD*
Left occipital lobe SUVR	1.25 ±0.05	1.34 ± 0.20	1.51 ± 0.22
Right occipital lobe SUVR	1.18 ± 0.09	1.41 ± 0.21	1.51 ± 0.22
Left intraorbital optic nerve SUVR	0.72 ± 0.10	0.79 ±0.15	0.92 ±0.15
Right intraorbital optic nerve SUVR	0.67 ± 0.14	0.81 ± 0.16	0.87 ± 0.14
Left intraorbital optic nerve density (HU)	20.29 ± 4.34	11.23 ± 6.80	2.79 ± 3.45
Right intraorbital optic nerve density (HU)	24.9 ± 6.62	13.1 ± 9.01	3.24 ± 3.68

MCI, mild cognitive impairment; AD, Alzheimer's Disease; SUVR, standard uptake value ratio; HU, Hounsfield Unit.

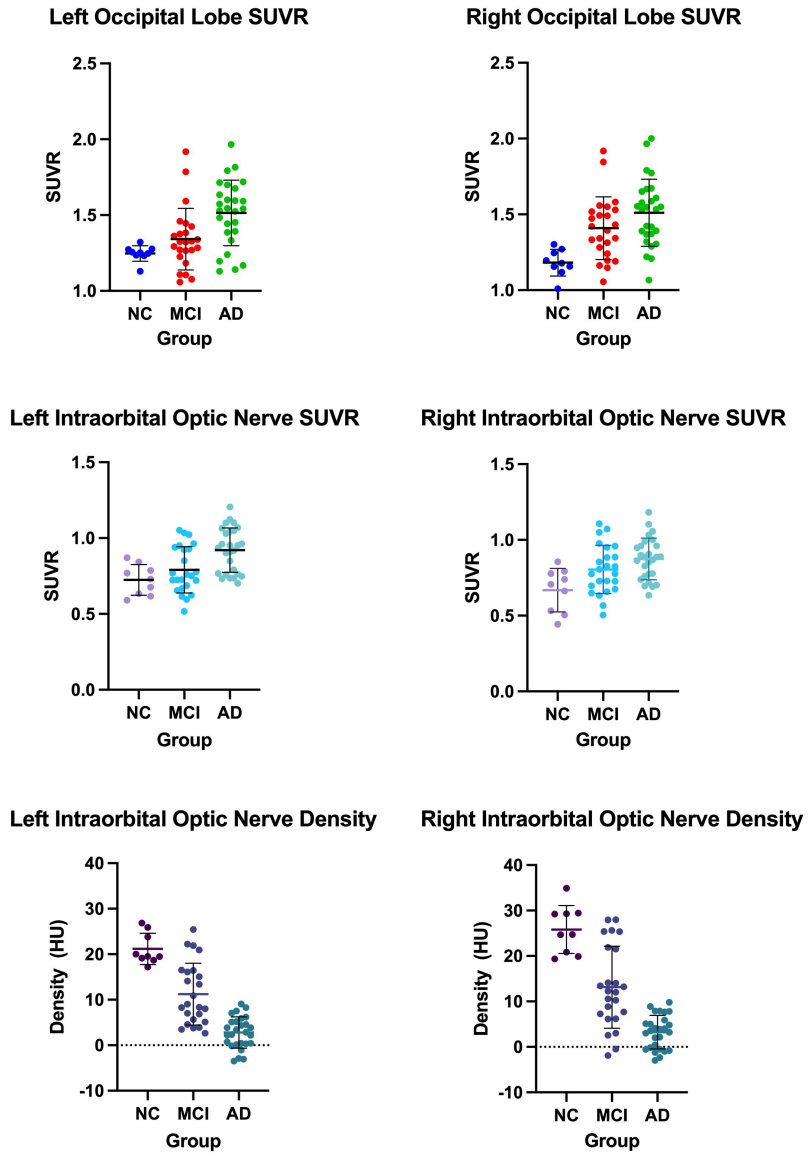

FIGURE 1 | The occipital standardized uptake value ratio (SUVR), the intraorbital optic nerve SUVR, and the intraorbital optic nerve density of three groups.

groups. The *p*-values of the Mann-Whitney *U*-test were corrected by the Bonferroni correction between each of the two groups of occipital SUVR, the intraorbital optic nerve SUVR, and the intraorbital optic nerve density, and differences were statistically significant of the *p*-value < 0.017 (corrected: 0.05/3).

Between AD and NC groups, the differences of the bilateral intraorbital optic nerve SUVR were statistically significant. Between AD and MCI groups, the differences of the left intraorbital optic nerve SUVR were statistically significant. Between any two of the three groups, the differences of the bilateral intraorbital optic nerve density were statistically significant. The results are shown in **Table 3**.

Simple Linear Regression Between the Occipital Standardized Uptake Value Ratio and the Intraorbital Optic Nerve Standardized Uptake Value Ratio, Between the Occipital Standardized Uptake Value Ratio and the Intraorbital Optic Nerve Density, and Between the Intraorbital Optic Nerve Standardized Uptake Value Ratio and the Intraorbital Optic Nerve Density

Simple linear regression was used with the entire sample between occipital SUVR and intraorbital optic nerve SUVR, between

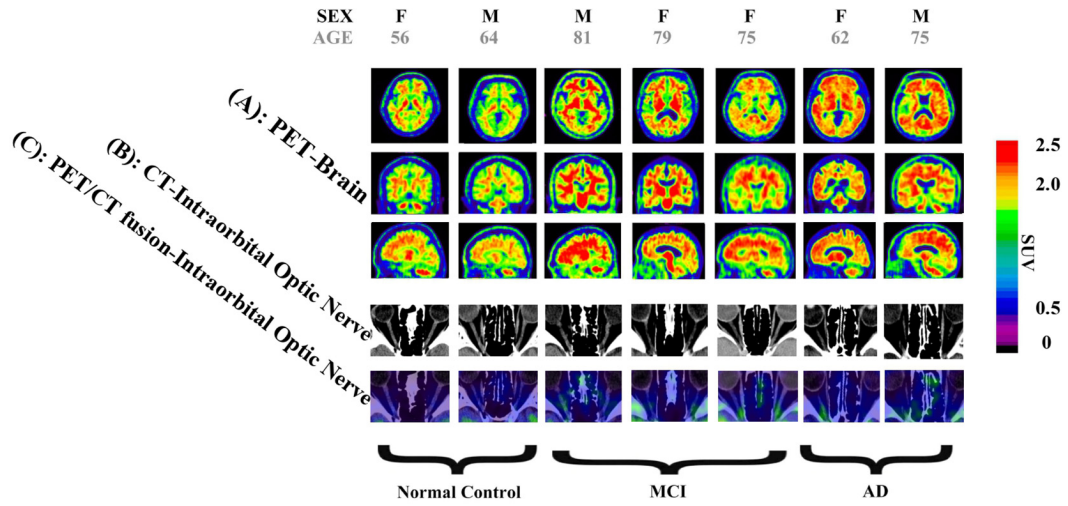

FIGURE 2 | Images of two normal controls (NCs), three subjects with mild cognitive impairment (MCI), and two subjects with Alzheimer's disease (AD). (A) Brain positron emission tomography (PET) images, showed that: (1) Among images of NC subjects, there is more ^{18}F-flutemetamol radioactivity in the white matter than in the gray matter of bilateral occipital lobes, creating clear gray/white matter contrast. (2) Some areas of the gray matter ^{18}F-flutemetamol radioactivity of bilateral occipital lobes are as intense as that in the adjacent white matter among MCI subjects. (3) The gray matter ^{18}F-flutemetamol radioactivity of bilateral occipital lobes are as intense as that in the adjacent white matter among AD subjects. (B) CT images of bilateral intraorbital optic nerves showed that the CT density of the bilateral intraorbital optic nerves of NC, MCI, and AD subjects was gradually decreased. (C) PET/CT fusion images of the bilateral intraorbital optic nerves showed that: (1) among images of NC subjects, almost no significant ^{18}F-flutemetamol radioactivity was observed on the bilateral intraorbital optic nerves; (2) among images of MCI subjects, slight ^{18}F-flutemetamol radioactivity was detected on the bilateral intraorbital optic nerves; and (3) among images of AD subjects, ^{18}F-flutemetamol radioactivity was detected on the bilateral intraorbital optic nerves.

TABLE 3 | The *p*-value of the occipital SUVR, the intraorbital optic nerve SUVR, and the intraorbital optic nerve density between each of the two groups.

	MCI vs. NC	AD vs. NC	AD vs. MCI
	p-value	*p*-value	*p*-value
Left occipital lobe SUVR	0.072	**0.002**	**0.002**
Right occipital lobe SUVR	**0.001**	**0.001**	0.023
Left intraorbital optic nerve SUVR	0.116	**0.001**	**0.003**
Right intraorbital optic nerve SUVR	0.079	**0.002**	0.031
Left intraorbital optic nerve Density	**0.004**	**0.001**	**0.001**
Right intraorbital optic nerve Density	**0.001**	**0.001**	**0.001**

MCI, mild cognitive impairment; AD, Alzheimer's Disease; NC, normal control; SUVR, standard uptake value ratio.p-values below 0.017 (corrected: 0.05/3) were in bold.

occipital SUVR and intraorbital optic nerve density, and between intraorbital optic nerve SUVR and intraorbital optic nerve density. The results are shown in **Table 4** and **Figure 3**.

In the analysis between occipital SUVR and intraorbital optic nerve SUVR and between occipital SUVR and intraorbital optic nerve density, the occipital SUVR was set as the dependent variable (y). Bilateral occipital SUVR (y) was positively associated with the bilateral intraorbital optic nerve SUVR (x); the regression equation was $y = 0.5768 \times x + 0.9211$ (left) and $y = 0.6056 \times x + 0.9264$ (right), respectively. Bilateral occipital SUVR (y) was negatively associated with the bilateral intraorbital optic nerve density (x), and the regression equation was $y = -0.0092 \times x + 1.486$ (left) and $y = -0.0078 \times x + 1.501$ (right), respectively.

In the analysis between the intraorbital optic nerve SUVR and intraorbital optic nerve density, the intraorbital optic nerve SUVR was set as the dependent variable (y). Bilateral intraorbital optic nerve SUVR (y) was negatively associated with the bilateral intraorbital optic nerve density (x); the regression equation was $y = -0.0103 \times x + 0.929$ (left) and $y = -0.0060 \times x + 0.878$ (right), respectively.

Multiple Logistic Regression of the Intraorbital Optic Nerve Standardized Uptake Value Ratio and Computed Tomography Density

Multiple logistic regression was used to analyze whether the intraorbital optic nerve SUVR and CT density could assist in distinguishing MCI from NC and AD from MCI. The groups (i.e., NC, MCI, and AD) of the subjects were set as the dependent variable (y); the left and right intraorbital optic nerve SUVR and

TABLE 4 | Results of simple linear regression.

	Slope	*p*-value	Equation	R^2
Occipital SUVR vs. Intraorbital optic nerve SUVR (Left)	0.5768	0.0007	$y = 0.5768*x + 0.9211$	0.1804
Occipital SUVR vs. Intraorbital optic nerve SUVR (Right)	0.6056	0.0006	$y = 0.6056*x + 0.9264$	0.1933
Occipital SUVR vs. Intraorbital optic nerve density (Left)	-0.0092	0.008	$y = -0.0092*x + 1.486$	0.1152
Occipital SUVR vs. Intraorbital optic nerve density (Right)	-0.0078	0.007	$y = -0.0078*x + 1.501$	0.1188
Intraorbital optic nerve SUVR vs. Intraorbital optic nerve density (Left)	-0.0103	0.001	$y = -0.0103*x + 0.929$	0.2623
Intraorbital optic nerve SUVR vs. Intraorbital optic nerve density (Right)	-0.0060	0.003	$y = -0.0060*x + 0.878$	0.1427

SUVR, standard uptake value ratio.

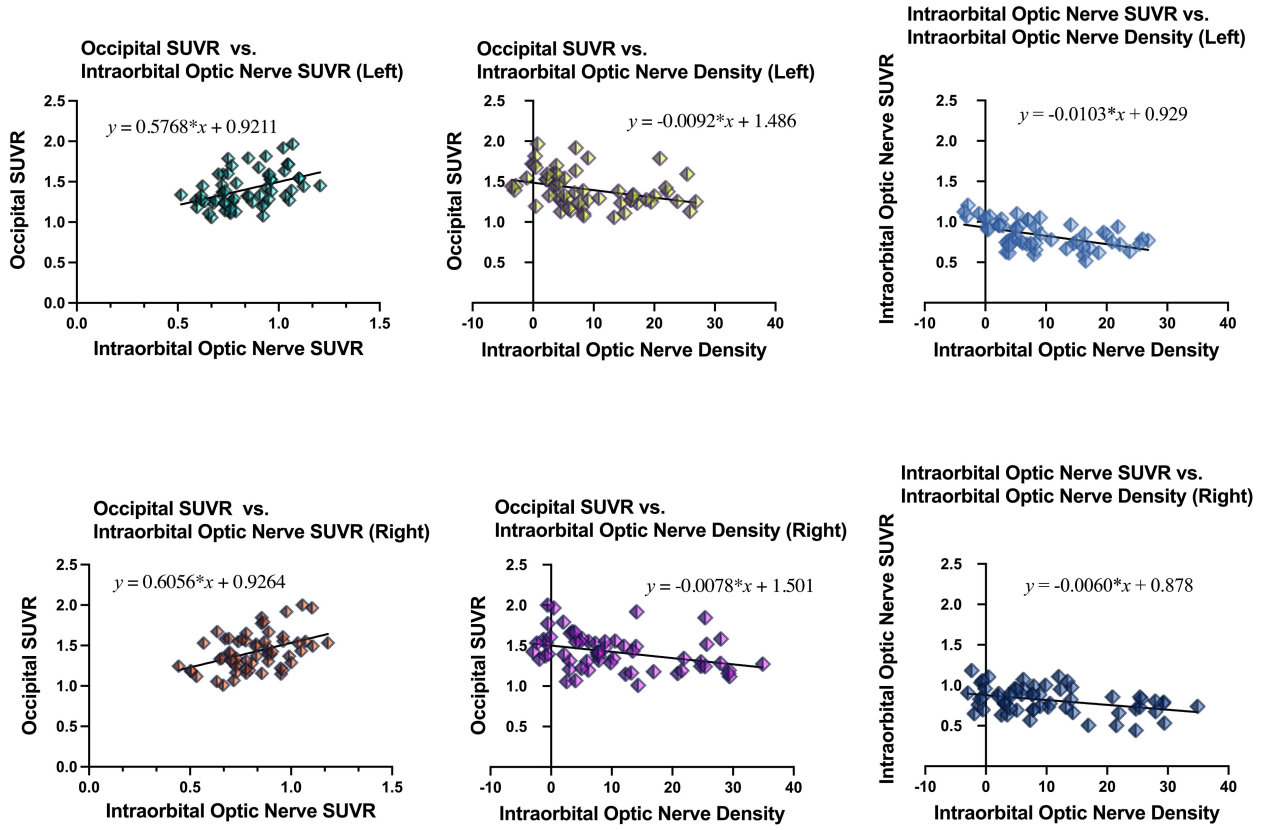

FIGURE 3 | Results of simple linear regression between the occipital SUVR and the intraorbital optic nerve SUVR, between the occipital SUVR and the intraorbital optic nerve density, and between the intraorbital optic nerve SUVR and the intraorbital optic nerve density.

CT density were set as the independent variables (x_1–x_4, refer to **Table 5**). The fitting equation of MCI vs. NC was $\ln[P(y = 1)/P(y = 0)] = 1.431\text{-}6.737 \times x_1\text{-}0.2980 \times x_2 + 12.68 \times x_3 + 0.01946 \times x_4$; the fitting equation of AD vs. MCI was $\ln[P(y = 1)/P(y = 0)] = 0.1679 + 4.15 \times x_1\text{-}0.2833 \times x_2\text{-}0.9103 \times x_3\text{-}0.1721 \times x_4$.

The area under the curve (AUC) of the receiver operating characteristic (ROC) of multiple logistic regression was 0.9167 (for MCI vs. NC) and 0.8951 (for AD vs. MCI), respectively, and the *p*-values of AUC were 0.0003 (for MCI vs. NC) and 0.0001 (for AD vs. MCI), respectively. The results are shown in **Tables 5, 6** and **Figure 4**.

Multiple Linear Regression Between Neuropsychological Tests Scores and the Intraorbital Optic Nerve Standardized Uptake Value Ratio and the Intraorbital Optic Nerve Density

Multiple linear regression was used to explore whether the intraorbital optic nerve SUVR and CT density could predict the MoCA and MMSE scores. The MoCA and MMSE scores were set as the dependent variable (y), and the left and right intraorbital optic nerve SUVR and CT density were set as the independent variables (x_1–x_4, refer to **Table 7**). The MoCA and MMSE scores were positively associated with the intraorbital optic nerve

TABLE 5 | Results of multiple logistic regression.

	MCI vs. NC	AD vs. MCI
β0 (Intercept)	1.431	0.1679
β1 (Left Intraorbital optic nerve SUVR, x_1)	-6.737	4.15
β2 (Left intraorbital optic nerve density, x_2)	-0.2980	-0.2833
β3 (Right intraorbital optic nerve SUVR, x_3)	12.68	-0.9103
β4 (Right intraorbital optic nerve density, x_4)	0.01946	-0.1721
Fitting equation	$\ln[P(y = 1)/P(y = 0)] = 1.431 - 6.737^*x_1 - 0.2980^*x_2 + 12.68^*x_3 + 0.01946^*x_4$	$\ln[P(y = 1)/P(y = 0)] = 0.1679 + 4.15^*x_1 - 0.2833^*x_2 - 0.9103^*x_3 - 0.1721^*x_4$

MCI, mild cognitive impairment; AD, Alzheimer's Disease; NC, normal control; SUVR, standard uptake value ratio.

TABLE 6 | Results from receiver operating characteristic (ROC) analysis of multiple logistic regression.

	MCI vs. NC	AD vs. MCI
Area under the ROC curve (AUC)	0.9167	0.8951
p-value of AUC	0.0003	0.0001
Cut off	0.7209	0.5505
Sensitivity (%)	79.17	81.48
Specificity (%)	88.89	83.33

MCI, mild cognitive impairment; AD, Alzheimer's Disease; NC, normal control.

density and negatively associated with the intraorbital optic nerve SUVR. The regression equation of MoCA was $y = 16.37 - 0.9734 \times x_1 + 0.5642 \times x_2 - 3.127 \times x_3 + 0.0275 \times x_4$; the R^2 was 0.848. The regression equation of MMSE was $y = 19.57 - 1.633 \times x_1 + 0.4397 \times x_2 - 1.713 \times x_3 + 0.0424 \times x_4$; the R^2 was 0.827. The actual vs. predicted plots are shown in **Figure 5**.

DISCUSSION

The AD-related degeneration of the optic nerve is characterized by irreversible structural and functional changes. Some studies have reported the loss of large diameter axons (Hinton et al., 1986), while others have suggested that optic nerve axons are lost in small size (Syed et al., 2005). In another case-control study comparing the optic nerve in patients with AD and NCs, it was found that there was a reduction in the number of optic nerve fibers in patients with AD, with a threefold greater odds ratio for a larger optic cup-to-disc ratio in patients with AD (Danesh-Meyer et al., 2006). These above studies aimed at the intraocular segment of the optic nerve, but we focused on structural and functional changes of the intraorbital optic nerve in this study.

In our study, the comparison of the occipital SUVR between each of the two groups showed that the differences were statistically significant, except for the left occipital SUVR between MCI and NC ($p = 0.218$) and the right occipital SUVR between AD and MCI ($p = 0.068$). We initially thought that the comparisons between each of the two groups of the occipital SUVR would be statistically significant. Considering that the sample size was not large enough might be the possible reason why the results were different than expected; especially, the sample size of the NC group was small due to the difficulty in recruiting normal subjects. A previous study using ^{18}F-flutemetamol PET showed that the differences of both the left and right occipital SUVR between subjects with MCI and AD were statistically significant with high efficacy (bao et al., 2021).

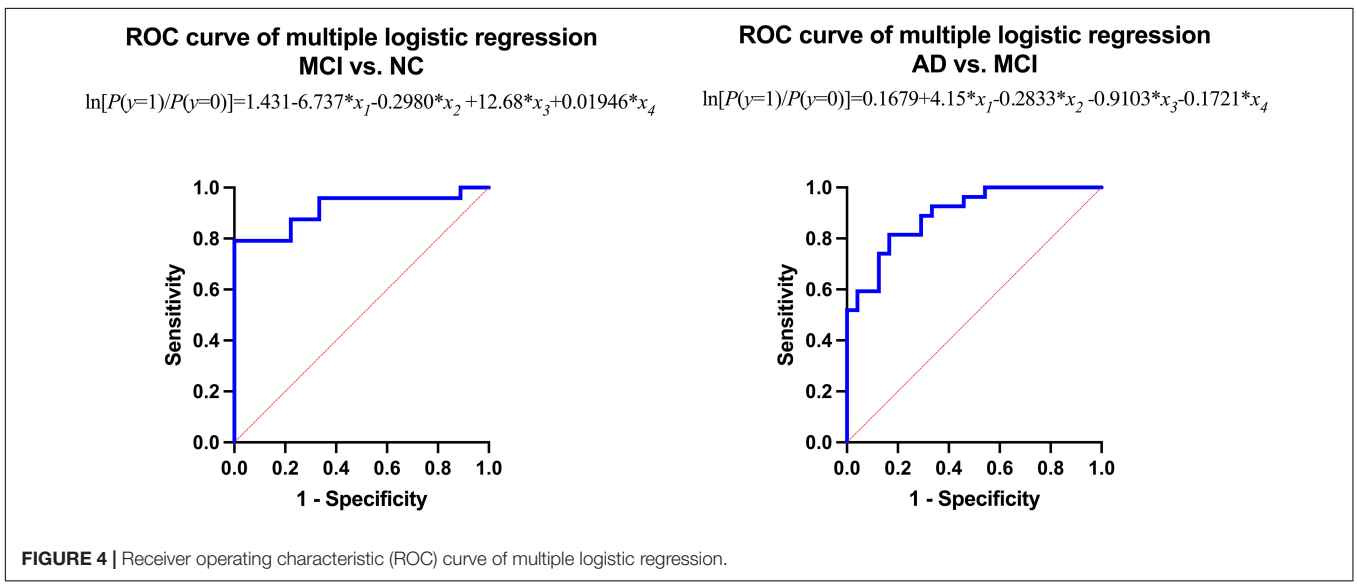

FIGURE 4 | Receiver operating characteristic (ROC) curve of multiple logistic regression.

TABLE 7 | Results of multiple linear regression.

	MoCA	MMSE
β0 (Intercept)	16.37	19.57
β1 (Left intraorbital optic nerve SUVR, x_1)	−0.9734	−1.633
β2 (Left intraorbital optic nerve density, x_2)	0.5642	0.4397
β3 (Right intraorbital optic nerve SUVR, x_3)	−3.127	−1.713
β4 (Right intraorbital optic nerve density, x_4)	0.0275	0.0424
Fitting equation	$y = 16.37-0.9734*x_1 + 0.5642*x_2-3.127*x_3 + 0.0275*x_4$	$y = 19.57-1.633*x_1 + 0.4397*x_2-1.713*x_3 +0.0424*x_4$
R^2	0.848	0.827

MoCA, Montreal Cognitive Assessment; MMSE, Mini-Mental State Examination; SUVR, standard uptake value ratio.

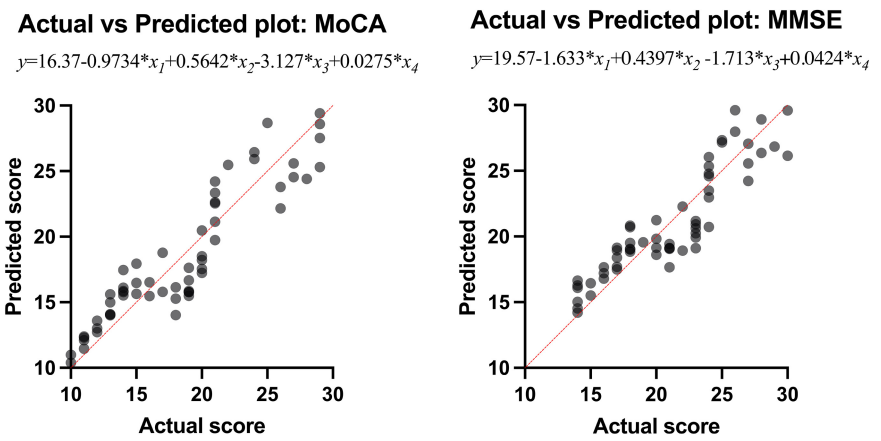

FIGURE 5 | The actual vs. predicted plots of multiple linear regression.

To our surprise, the differences of bilateral intraorbital optic nerve SUVR between MCI and NC groups were not statistically significant, while the differences were statistically significant between AD and NC groups. It means that there was significant amyloid deposition in bilateral intraorbital optic nerves of patients with AD, not of patients with MCI. This finding was consistent with a recent study that indicated that amyloid deposition might be the result rather than the cause of neurodegeneration (Thomas et al., 2020). In addition, the differences of the intraorbital optic nerve SUVR between AD and MCI groups were statistically significant on the left only, consistent with the results of the occipital SUVR between AD and MCI groups (also statistically significant on the left only). This might imply that the deposition of amyloid in the intraorbital optic nerve was consistent with that of the occipital lobe in patients with AD; whether the deposition of amyloid in the intraorbital optic nerve was associated with other cerebral regions needs further research to demonstrate.

The differences of the bilateral intraorbital optic nerve density were statistically significant between any two of the three groups. This might indicate that bilateral intraorbital optic nerve degeneration begins at the MCI stage, and CT density reflects the degree of optic nerve degeneration. A study showed that there was a difference between optic nerve volumes of subjects with AD and control subjects, but there was no correlation between the optic nerve volume and cerebral volume in patients with AD (Kusbeci et al., 2015). This meant that degenerative changes in the optic nerve possibly tend to develop independently rather than in parallel with degenerative changes in the brain. A previous study about the human visual pathway demonstrated that the spread of neurodegeneration may be independent of the neurotransmission machinery (You et al., 2019). If this hypothesis could be confirmed by more studies in the future, visual degeneration might become an independent marker to diagnose cognitive impairment and dementia.

In this study, the results of simple linear regression showed that the bilateral occipital SUVR was positively associated with the bilateral intraorbital optic nerve SUVR, the bilateral occipital SUVR was negatively associated with the bilateral intraorbital optic nerve density, and the bilateral intraorbital optic nerve SUVR was negatively associated with the bilateral intraorbital optic nerve density. Similar to the visual cortex, it was no surprise that the occipital SUVR was associated with the structural and functional degenerative changes of the optic nerve, as well as the embryological ties of the neuroretina and brain structures stated in a study (Coppola et al., 2015). The negative association between the occipital SUVR and intraorbital optic nerve density was an exciting finding to us, as the CT density of the optic nerve was much easier to measure compared with the measurement of cerebral amyloid deposition. Also, the CT scan is more accessible than fMRI and PET brain scan, especially in low- and middle-income countries and areas. According to the above results, the

lower intraorbital optic nerve density was corresponded to the higher occipital SUVR and intraorbital optic nerve SUVR and indicated a higher level of amyloid deposition in the intraorbital optic nerve and in the brain. However, the intraorbital optic nerve density should not only be associated with cerebral amyloid deposition and cognitive impairment. Many physiological or pathological factors may influence intraorbital optic nerve density, such as age, nutritional status, daily light hours, and daily sleep duration (Woon et al., 1995; Chapman et al., 2012; Mentek et al., 2018). Further studies with larger sample size are needed to study the relationship between the optic nerve density and other influencing variables.

The results of multiple logistic regression showed that the intraorbital optic nerve SUVR and CT density could assist in distinguishing MCI from NC and AD from MCI. The fitting equation of MCI vs. NC was $\ln[P(y=1)/P(y=0)] = 1.431\text{-}6.737 \times x_1\text{-}0.2980 \times x_2 + 12.68 \times x_3 + 0.01946 \times x_4$; the fitting equation of AD vs. MCI was $\ln[P(y=1)/P(y=0)] = 0.1679 + 4.15 \times x_1\text{-}0.2833 \times x_2\text{-}0.9103 \times x_3\text{-}0.1721 \times x_4$. In the fitting equations, x_1–x_4 represent the left intraorbital optic nerve SUVR, the left intraorbital optic nerve density, the right intraorbital optic nerve SUVR, and the right intraorbital optic nerve density, respectively. The ROC analysis of multiple logistic regression showed that the AUC was 0.9167 (for MCI vs. NC) and 0.8951 (for AD vs. MCI), which suggested that the efficiency and efficacy in distinguishing MCI from NC and AD from MCI were relatively high.

The results of multiple linear regression showed that the intraorbital optic nerve SUVR and CT density were associated with MoCA and MMSE scores, demonstrating that the Aβ deposition and CT density of intraorbital optic nerve were correlated with the severity of cognitive impairment. A study showed that postmenopausal women who had large cup-to-disc ratio without glaucoma or ocular hypertension exhibited lower global cognitive function (Vajaranant et al., 2019). Another study showed that the decrease of the coronal optic nerve sheath diameter was associated with postoperative cognitive decline (Zhang et al., 2021). These studies demonstrated that multiple structural degeneration of the optic nerve was associated with cognitive impairment. The regression equation of MoCA was $y = 16.37\text{-}0.9734 \times x_1 + 0.5642 \times x_2\text{-}3.127 \times x_3 + 0.0275 \times x_4$; the R^2 was 0.848. The regression equation of MMSE was $y = 19.57\text{-}1.633 \times x_1 + 0.4397 \times x_2\text{-}1.713 \times x_3 + 0.0424 \times x_4$; the R^2 was 0.827. The regression equations and their R^2 indicated that the intraorbital optic nerve SUVR and CT density could predict MoCA and MMSE scores with a relatively high ability. **Figure 5** showed that the scatters of the predicted MoCA and MMSE scores were mostly around the red straight line and demonstrated that the regression models with intraorbital optic nerve SUVR and CT density could predict MoCA and MMSE scores and further predict the severity of cognitive impairment. This means that a high likelihood of cognitive impairment should be noted if a decreased intraorbital optic nerve density was found on cranial CT images, and further examination like brain amyloid PET should be conducted to confirm the cognitive impairment.

In this study, we examined the relationship between occipital SUVR and intraorbital optic nerve SUVR and its CT density, demonstrated the assisting ability of the optic nerve SUVR and CT density in diagnosing MCI and AD, and found intraorbital optic nerve SUVR and its CT density could help predict MoCA and MMSE scores and further predict the severity of cognitive impairment. We have made our efforts to fill the gap in the structural and functional changes of the optic nerve and the association between the optic nerve and the cerebral visual cortex. In addition, the potential application of intraorbital optic nerve CT density could reduce the cost of diagnosis of MCI and AD. Compared with traditional imaging methods for diagnosing MCI and AD such as fMRI and PET, CT was less expensive and more accessible, especially in low- and middle-income areas. Therefore, this might enable early diagnosis of AD to reach more people and expand the coverage of precise treatment of patients with AD.

There were several limitations in our study. First, the sample size was not large enough, especially, the sample size of the NC group was small due to the difficulty in recruiting normal subjects; studies with larger samples covering a wider age range are needed in the future to confirm the results of this study. Second, further and deeper studies (especially animal experiments based on the cellular and molecular mechanisms) aimed at the association between occipital Aβ deposition and intraorbital optic nerve density are strongly needed to clearly demonstrate and clarify the mechanisms.

CONCLUSION

The CT density and Aβ deposition of the intraorbital optic nerve were associated with Aβ deposition of in occipital cortex and the severity of cognitive impairment. The intraorbital optic nerve CT density and intraorbital optic nerve Aβ deposition could assist in diagnosing MCI and AD.

DATA AVAILABILITY STATEMENT

All data in this study are clinical data. According to the requirements of the ethics committee of Huashan Hospital, Zhongshan Hospital, and Shanghai Sixth People's Hospital, data is only to be made available via a request to the authors, and after requesting approval from the authors' local ethics committee. Requests to access the datasets should be directed to JL and XdL (1436150464@qq.com, xingdliu@fudan.edu.cn).

ETHICS STATEMENT

The studies involving human participants were reviewed and approved by the Committee for Medical and Health Research Ethics of Huashan Hospital affiliated to Fudan University, Shanghai, China. The patients/participants provided their written informed consent to participate in this study.

AUTHOR CONTRIBUTIONS

HW recruited the subjects and wrote this manuscript. ZL and YO processed the data and assisted in writing the manuscript.

XS, QX, and KS injected the subjects with the tracer and acquired the images. JD, QZ, XW, XC, and XyL helped to recruit subjects. JL helped design the research. XdL designed the research and provided funding. All authors contributed to the article and approved the submitted version.

FUNDING

This work was supported by the Shanghai Science and Technology Commission Project: Molecular imaging study on mild cognitive impairment (No. 17411950102), the National Key Research and Development Plan Digital Diagnosis and Treatment Equipment Research and Development Project: Research and Practice of PET-CT Comprehensive Evaluation System and Training System (No. 2017YFC0113300), the Pudong New Area Clinical Characteristic Discipline Project (No. PWYts2021-01), and the Pudong Hospital, Fudan University, College Project (No. YJYJRC202108/YJYJRC202101).

ACKNOWLEDGMENTS

We thank Liwei Wu (wu.lw@neusoft.com) and Jun Yang (yangjun_neu@neusoft.com) of the Neusoft Research of Intelligent Healthcare Technology, Co., Ltd., for their guidance during the image acquisition and processing.

REFERENCES

Bao, Y. W., Chau, A. C. M., Chiu, P. K., Shea, Y. F., Kwan, J. S. K., Chan, F. H. W., et al. (2021). Heterogeneity of Amyloid B inding in Cognitively Impaired Patients Consecutively Recruited from a Memory Clinic: Evaluating the Utility of Quantitative 18F-Flutemetamol Pet-Ct in Discrimination of Mild Cognitive Impairment from Alzheimer's Disease and Other Dementias. *J. Alzheimers. Dis.* 79, 819–832.

Chapman, G. B., Tarboush, R., and Connaughton, V. P. (2012). The effects of rearing light level and duration differences on the optic nerve, brain, and associated structures in developing zebrafish larvae: a light and transmission electron microscope study. *Anat Rec.*295, 515–531. doi: 10.1002/ar.22403

Cho, S. H., Choe, Y. S., Kim, Y. J., Lee, B., Kim, H. J., Jang, H., et al. (2020). Concordance in detecting amyloid positivity between (18)F-florbetaben and (18)F-flutemetamol amyloid PET using quantitative and qualitative assessments. *Sci. Rep.* 10:5461.

Coppola, G., Di Renzo, A., Ziccardi, L., Martelli, F., Fadda, A., Manni, G., et al. (2015). Optical Coherence Tomography in Alzheimer's Disease: A Meta-Analysis. *PLoS One.* 10:e0134750. doi: 10.1371/journal.pone.0134750

Curtin, F., and Schulz, P. (1998). Multiple correlations and Bonferroni's correction. *Biol. Psychiat.* 44, 775–777. doi: 10.1016/s0006-3223(98)00043-2

Danesh-Meyer, H. V., Birch, H., Ku, J. Y., Carroll, S., and Gamble, G. (2006). Reduction of optic nerve fibers in patients with Alzheimer disease identified by laser imaging. *Neurology.* 67, 1852–1854. doi: 10.1212/01.wnl.0000244490.07925.8b

Dieleman, J. L., Cao, J., Chapin, A., Chen, C., Li, Z., Liu, A., et al. (2020). US Health Care Spending by Payer and Health Condition, 1996-2016. *Jama* 323, 863–884. doi: 10.1001/jama.2020.0734

Folstein, M. F., Folstein, S. E., and McHugh, P. R. (1975). "Mini-mental state". A practical method for grading the cognitive state of patients for the clinician. *J. Psychiatr Res.* 12, 189–198.

Gao, L., Liu, Y., Li, X., Bai, Q., and Liu, P. (2015). Abnormal retinal nerve fiber layer thickness and macula lutea in patients with mild cognitive impairment and Alzheimer's disease. *Arch. Gerontol. Geriatr.* 60, 162–167. doi: 10.1016/j.archger.2014.10.011

Gupta, V. K., Chitranshi, N., Gupta, V. B., Golzan, M., Dheer, Y., Wall, R. V., et al. (2016). Amyloid β accumulation and inner retinal degenerative changes in Alzheimer's disease transgenic mouse. *Neurosci. Lett.* 623, 52–56. doi: 10.1016/j.neulet.2016.04.059

Hinton, D. R., Sadun, A. A., Blanks, J. C., and Miller, C. A. (1986). Optic-nerve degeneration in Alzheimer's disease. *N. Engl. J. Med.* 315, 485–487. doi: 10.1056/NEJM198608213150804

Holtzman, D. M., Morris, J. C., and Goate, A. M. (2011). Alzheimer's disease: the challenge of the second century. *Sci. Transl. Med.* 3:77sr1. doi: 10.1126/scitranslmed.3002369

Hwang, J., Kim, C. M., Kim, J. E., Oh, M., Oh, J. S., Yoon, Y. W., et al. (2021). Clinical Implications of Amyloid-Beta Accumulation in Occipital Lobes in Alzheimer's Continuum. *Brain Sci.* 11, 1232. doi: 10.3390/brainsci11091232

Jack, C. R. Jr., Albert, M. S., Knopman, D. S., McKhann, G. M., Sperling, R. A., Carrillo, M. C., et al. (2011). Introduction to the recommendations from the National Institute on Aging-Alzheimer's Association workgroups on diagnostic guidelines for Alzheimer's disease. *Alzheimers Dement.* 7, 257–262. doi: 10.1016/j.jalz.2011.03.004

Kusbeci, T., Kusbeci, O. Y., Mas, N. G., Karabekir, H. S., Yavas, G., and Yucel, A. (2015). Stereological Evaluation of the Optic Nerve Volume in Alzheimer Disease. *J. Craniofac. Surg.* 26, 1683–1686. doi: 10.1097/SCS.0000000000001853

Levine, Z. H., Peskin, A. P., Holmgren, A. D., and Garboczi, E. J. (2018). Preliminary X-ray CT investigation to link Hounsfield unit measurements with the International System of Units (SI). *PLoS One.* 13:e0208820. doi: 10.1371/journal.pone.0208820

Matsuda, H., Ito, K., Ishii, K., Shimosegawa, E., Okazawa, H., Mishina, M., et al. (2020). Quantitative Evaluation of (18)F-Flutemetamol PET in Patients With Cognitive Impairment and Suspected Alzheimer's Disease: A Multicenter Study. *Front Neurol.* 11:578753. doi: 10.3389/fneur.2020.578753

McKhann, G. M., Knopman, D. S., Chertkow, H., Hyman, B. T., Jack, C. R. Jr., Kawas, C. H., et al. (2011). The diagnosis of dementia due to Alzheimer's disease: recommendations from the National Institute on Aging-Alzheimer's Association workgroups on diagnostic guidelines for Alzheimer's disease. *Alzheimers Dement.* 7, 263–269. doi: 10.1016/j.jalz.2011.03.005

Mentek, M., Aptel, F., Godin-Ribuot, D., Tamisier, R., Pepin, J. L., and Chiquet, C. (2018). Diseases of the retina and the optic nerve associated with obstructive sleep apnea. *Sleep Med. Rev.* 38, 113–130. doi: 10.1016/j.smrv.2017.05.003

Miller, N. R. (1996). The optic nerve. *Curr. Opin. Neurol.* 9, 5–15. doi: 10.5005/jp/books/10069_2

Moschos, M., Markopoulos, I., Chatziralli, I., Rouvas, A. G., Papageorgiou, S., Ladas, I., et al. (2012). Structural and Functional Impairment of the Retina and Optic Nerve in Alzheimer's Disease. *Curr. Alzheimer Res.* 9, 782–788. doi: 10.2174/156720512802455340

Nasreddine, Z. S., Phillips, N. A., Bédirian, V., Charbonneau, S., Whitehead, V., Collin, I., et al. (2005). The Montreal Cognitive Assessment, MoCA: a brief screening tool for mild cognitive impairment. *J. Am. Geriatr. Soc.* 53, 695–699. doi: 10.1111/j.1532-5415.2005.53221.x

Nelissen, N., Van Laere, K., Thurfjell, L., Owenius, R., Vandenbulcke, M., Koole, M., et al. (2009). Phase 1 study of the Pittsburgh compound B derivative 18F-flutemetamol in healthy volunteers and patients with probable Alzheimer disease. *J. Nucl. Med.* 50, 1251–1259. doi: 10.2967/jnumed.109.063305

Papanicolas, I., Woskie, L. R., and Jha, A. K. (2018). Health Care Spending in the United States and Other High-Income Countries. *Jama.* 319, 1024–1039.

Sevigny, J., Suhy, J., Chiao, P., Chen, T., Klein, G., Purcell, D., et al. (2016). Amyloid PET Screening for Enrichment of Early-Stage Alzheimer Disease Clinical Trials: Experience in a Phase 1b Clinical Trial. *Alzheimer Dis. Assoc. Disord.* 30, 1–7. doi: 10.1097/WAD.0000000000000144

Syed, A. B., Armstrong, R. A., and Smith, C. U. (2005). A quantitative analysis of optic nerve axons in elderly control subjects and patients with Alzheimer's disease. *Folia Neuropathol.* 43, 1–6.

Thomas, K. R., Bangen, K. J., Weigand, A. J., Edmonds, E. C., Wong, C. G., Cooper, S., et al. (2020). Objective subtle cognitive difficulties predict future

amyloid accumulation and neurodegeneration. *Neurology*. 94, e397–e406. doi: 10.1212/WNL.0000000000008838

Vajaranant, T. S., Hallak, J., Espeland, M. A., Pasquale, L. R., Klein, B. E., Meuer, S. M., et al. (2019). An Association Between Large Optic Nerve Cupping and Cognitive Function. *Am. J. Ophthalmol.* 206, 40–47. doi: 10.1016/j.ajo.2019.05.019

Vandenberghe, R., Van Laere, K., Ivanoiu, A., Salmon, E., Bastin, C., Triau, E., et al. (2010). 18F-flutemetamol amyloid imaging in Alzheimer disease and mild cognitive impairment: a phase 2 trial. *Ann. Neurol.* 68, 319–329. doi: 10.1002/ana.22068

Woon, C., Tang, R. A., and Pardo, G. (1995). Nutrition and optic nerve disease. *Semin Ophthalmol.* 10, 195–202.

You, Y., Joseph, C., Wang, C., Gupta, V., Liu, S., Yiannikas, C., et al. (2019). Demyelination precedes axonal loss in the transneuronal spread of human neurodegenerative disease. *Brain.* 142, 426–442. doi: 10.1093/brain/awy338

Zhang, L. M., Li, Y., Zhang, Y. T., Zhang, B. X., Wang, J. Z., and Zhang, D. X. (2021). Decrease of Coronal Optic Nerve Sheath Diameter is Associated With Postoperative Cognitive Decline in Patients Undergoing Carotid Endarterectomy. *J. Cardiothorac. Vasc. Anesth.* 35, 2355–2362. doi: 10.1053/j.jvca.2020.11.006

Zwan, M. D., Bouwman, F. H., Konijnenberg, E., van der Flier, W. M., Lammertsma, A. A., Verhey, F. R., et al. (2017). Diagnostic impact of [(18)F]flutemetamol PET in early-onset dementia. *Alzheimers Res. Ther.* 9, 2. doi: 10.1186/s13195-016-0228-4

Conflict of Interest: The authors declare that the research was conducted in the absence of any commercial or financial relationships that could be construed as a potential conflict of interest.

JZ declared a shared parent affiliation with XL at the time of review.

Publisher's Note: All claims expressed in this article are solely those of the authors and do not necessarily represent those of their affiliated organizations, or those of the publisher, the editors and the reviewers. Any product that may be evaluated in this article, or claim that may be made by its manufacturer, is not guaranteed or endorsed by the publisher.

frontiers | Frontiers in Aging Neuroscience

ORIGINAL RESEARCH
published: 01 April 2022
doi: 10.3389/fnagi.2022.799545

Altered Interhemispheric Functional Connectivity Associated With Early Verbal Fluency Decline After Deep Brain Stimulation in Parkinson's Disease

Bei Luo[1†], Wenwen Dong[1†], Lei Chang[1], Chang Qiu[1], Yue Lu[1], Dongming Liu[2], Chen Xue[3], Li Zhang[4], Weiguo Liu[5], Wenbin Zhang[1] and Jun Yan[4*]*

[1] Department of Functional Neurosurgery, The Affiliated Brain Hospital of Nanjing Medical University, Nanjing, China, [2] Department of Neurosurgery, The Affiliated Brain Hospital of Nanjing Medical University, Nanjing, China, [3] Department of Radiology, The Affiliated Brain Hospital of Nanjing Medical University, Nanjing, China, [4] Department of Geriatric Neurology, The Affiliated Brain Hospital of Nanjing Medical University, Nanjing, China, [5] Department of Neurology, The Affiliated Brain Hospital of Nanjing Medical University, Nanjing, China

OPEN ACCESS

Edited by:
Ping Wu,
Fudan University, China

Reviewed by:
Lihua Qiu,
Second People's Hospital of Yibin, China
Feng-Tao Liu,
Fudan University, China

***Correspondence:**
Wenbin Zhang
wenbinzhang@njmu.edu.cn
Jun Yan
2519002414@qq.com

[†] These authors have contributed equally to this work and share first authorship

Specialty section:
This article was submitted to Parkinson's Disease and Aging-related Movement Disorders, a section of the journal Frontiers in Aging Neuroscience

Received: 21 October 2021
Accepted: 08 February 2022
Published: 01 April 2022

Citation:
Luo B, Dong W, Chang L, Qiu C, Lu Y, Liu D, Xue C, Zhang L, Liu W, Zhang W and Yan J (2022) Altered Interhemispheric Functional Connectivity Associated With Early Verbal Fluency Decline After Deep Brain Stimulation in Parkinson's Disease. Front. Aging Neurosci. 14:799545. doi: 10.3389/fnagi.2022.799545

Background: Patients with Parkinson's disease (PD) experience a decline in verbal fluency (VF) immediately after undergoing deep brain stimulation (DBS) of the subthalamic nucleus (STN). This phenomenon is thought to be related to surgical microlesions.

Purpose: We investigated the alterations in interhemispheric functional connectivity after STN-DBS in PD patients. We also evaluated the correlation between these changes and decreased VF scores.

Method: Overall, 30 patients with PD were enrolled in the study. Resting-state functional magnetic resonance imaging scans were performed twice, once before and once after DBS, in PD patients. Voxel-mirrored homotopic connectivity (VMHC) was applied in order to evaluate the synchronicity of functional connectivity between the hemispheres.

Result: After undergoing STN-DBS, PD patients demonstrated reduced VMHC value in the posterior cerebellum lobe, angular gyrus, precuneus/posterior cingulate gyrus (PCC), supramarginal gyrus, superior frontal gyrus (SFG) (medial and dorsolateral) and middle frontal gyrus (MFG). In addition, we observed a significant positive correlation between the altered VMHC value in the SFG and MFG and the change of phonemic VF scores.

Conclusion: PD patients demonstrated an interhemispheric coordination disorder in the prefrontal cortex, cerebellum, supramarginal gyrus and DMN after undergoing STN-DBS. The positive correlation between reduced VMHC value in the SFG and MFG and the changes of VF scores provides a novel understanding with regard to the decline of VF after DBS.

Keywords: Parkinson's disease, deep brain stimulation, verbal fluency, voxel-mirrored homotopic connectivity, resting state functional magnetic resonance

INTRODUCTION

Deep brain stimulation (DBS), a widely accepted and effective treatment for mid-to-late-stage Parkinson's disease (PD), improves the motor symptoms and the quality of life of patients, and reduces complications that are caused by anti-Parkinsonian drugs (Deuschl et al., 2006; Benabid et al., 2009). However, after the deep brain electrodes are implanted into the subthalamic nucleus (STN), PD patients often experience adverse neuropsychological reactions. Although the overall cognitive level of patients after chronic STN-DBS is relatively safe (Witt et al., 2008), a decline in verbal fluency (VF) decline is a common postoperative cognitive side effect (Mikos et al., 2011; Lefaucheur et al., 2012; Borden et al., 2014; Le Goff et al., 2015; Costentin et al., 2019). The specific mechanism behind this side effect remains unclear. Multiple studies have discovered that PD patients demonstrate an immediate decline in VF performance after undergoing DBS surgery, while PD patients who suffered from STN-DBS did not demonstrate any significant change in VF scores under "switched-on" and "switched-off" stimulus conditions (Morrison et al., 2004; Witt et al., 2004). To date, evidence suggests that a decline in language fluency after DBS is more likely related to surgical microlesions than to stimulating-induced reactions.

Advanced cognitive processes require participation of both hemispheres (Sauerwein and Lassonde, 1994). The corpus callosum is thought to contain major interhemispheric pathways (Sauerwein and Lassonde, 1994). Previous studies have demonstrated that people with disconnection or atrophy of the corpus callosum tend to have sensory, motor, and cognitive processing deficits (Dimond, 1979; Sauerwein and Lassonde, 1994; Yaldizli et al., 2014), which illustrates the importance of coordinating between the hemispheres for implementation of high-level complex tasks. One study discovered that atrophy of the corpus callosum affects the performance of VF tasks, highlighting the importance the integrity of the corpus callosum for cognitive information processing related to VF (Pozzilli et al., 1991). Given the importance of inter-hemispheric coordination for VF tasks, we hypothesized that decreased VF in PD patients after DBS may be associated with a deficiency in inter-hemispheric interaction.

Functional magnetic resonance (fMRI), particularly functional connectivity, is an important tool to study the basis of neurological and psychiatric disorders. The resting-state fMRI is able to capture the pattern of fluctuation of blood oxygen levels in resting-state, which has better operability and repeatability, compared to task-state fMRI (Smitha et al., 2019). Functional homotopy is an essential feature of the inner functional structure of the brain, and refers to a high degree of synchronization of spontaneous activity in the corresponding positions of the hemisphere (Zuo et al., 2010; Luo et al., 2015). The homotopic resting-state function connectivity (RSFC) is a good indicator of interhemispheric coordination, and reflects the degree of integration of brain functions, which may be detected through the voxel-mirrored homotopic connectivity (VMHC) method (Hu et al., 2015; Luo et al., 2015). Alterations of homotopic RSFC were discovered in normal aging, as well as neurological and mental illness (Zuo et al., 2010; Guo et al., 2014; Cao et al., 2020; Gan et al., 2020). The VMHC approach has been widely utilized to study neural mechanisms of PD, and has become an important tool to identify changes in inter-hemispheric functional communication (Hu et al., 2015; Li et al., 2018; Gan et al., 2020; Jin et al., 2021).

Herein, we hypothesized that a decline in VF performance after DBS in PD patients may be associated with dysfunction of functional coordination between the hemispheres. Therefore, we analyzed resting-state fMRI data prior to and after STN-DBS surgery among PD patients using the VMHC method to determine changes in homotopic RSFC. Furthermore, we evaluated the correlation between VMHC values of significantly different brain regions before and after DBS and VF scores.

MATERIALS AND METHODS

Participants

The data used in this study is from PD patients who were treated with functional neurosurgery at the Brain Hospital affiliated with Nanjing Medical University. Overall, 37 patients with PD were recruited, all of whom met United Kingdom Parkinson's Disease Society Brain Bank clinical diagnostic criteria. DBS surgery was carried out on all recruited PD patients after evaluating indications for DBS surgery. The exclusion criteria were as follows: (1) previous neurological disorders and psychiatric history, (2) a history of suffering from non-PD diseases affecting the nervous system (i.e., brain trauma), (3) having taken drugs that affect brain function for six months (i.e., antipsychotics), and (4) contraindications to magnetic resonance examination. All participants were right-handed. This study was granted approval by the Ethics Committee of Brain Hospital affiliated with Nanjing Medical University. All subjects signed written informed consent prior to the start of the experiment.

Clinical Assessments

The VF test mainly assess spontaneous verbal motor ability, which can be divided into semantic fluency and phonemic fluency. The semantic fluency test asks participants to name as many animals as they can think of in 1 min. Due to the different educational backgrounds of the participants, we chose a Chinese version of the test in order to evaluate phonemic fluency of all subjects. For detailed description, please refer to previous literature (Quan et al., 2015), which has been used in the phonemic fluency test of Chinese people (Liao et al., 2019; Yang et al., 2020). The testing process consists of three phases, including a 30-s baseline, a 60-s task, and a 30-s break after the task. During the task, three Chinese characters (白, 天, and 大, representing white, day and big, respectively) were shown to the testers and each character lasted for 20 s. Next, participants were asked to verbally generate as many phrases or four-character idioms as possible, starting with each given character. The total number of correct animals or words that each participant could say was scored. Patients with PD were evaluated four times using the VF test, including three days before DBS, one day after DBS, one month after DBS, and six months after DBS. At the same

time, we also assessed the overall cognitive level of all participants using Montreal Cognitive Assessment (MoCA). In addition, MRI data for PD patients was collected three days before DBS and one day after DBS, which were included in the PD-Pre-DBS and PD-Post-DBS group, respectively. All scales and MRI data were collected after the patient had stopped taking anti-Parkinsonian drugs for more than 12 h, and lacked electrical stimulation. The details of the VF and MoCA assessment were provided in **Supplementary Table**.

Surgery

Deep brain stimulation (DBS) surgery was carried out by a single neurosurgeon via a unified surgical procedure in this study. Bilateral STN was chosen as an implant target in all patients. Prior to implanting the stimulation electrode, the STN nucleus single-cell discharge was monitored through the use of OMEGA electrophysiological instrument and the recording electrode. Furthermore, the DBS electrodes (model L301, PINS, Pins Medical Co, China) were implanted after the location was determined. The electrode implantation was completely in accordance with the preoperative target plan, and the electrode position was not adjusted during or after surgery. We did not observe any significant surgical complications on postoperative cranial imaging. The specific position of electrode implantation was shown in the **Supplementary Material**.

Image Acquisition

The MRI data were acquired with 1.5 Tesla GE Medical Systems scanner (produced by GE Medical System, Milwaukee, WI) equipped with an eight-channel head coil. Structural images were acquired through the use of 3D magnetization-prepared rapid gradient-echo sequence (MPRAGE) with the following parameters: repetition time (TR) of 11.864 ms, echo time (TE) of 4.932 ms, flip angle (FA) of 20°, number of slices = 112, matrix size = 256 × 256, field of view (FOV) = 152 × 152mm^2, thickness of 1.4mm, and voxel size of 0.59 × 0.59 × 1.4 mm^3. Functional images were acquired through the use of a gradient-recalled echo-planar imaging sequence (GRE-EPI) with the following parameters: TR of 2000ms, TE of 40 ms, FA of 90°, FOV = 240 × 240 mm^2, matrix size = 64 × 64, number of slices = 28, thickness of 3.0mm with no gap, spatial resolution = 3.75 × 3.75 × 3mm^3, and number of total volumes = 128. During the MRI scans, all participants were instructed to close their eyes, stay relaxed and awake, and not think about anything in particular.

Data Preprocessing

Resting-state fMRI data preprocessing was carried out by the Data Processing Assistant for resting-State fMRI (DPABI_V4.3[1]) on the MATLAB 2013b platform.[2] The steps of data preprocessing are briefly described as follows. The first five points were discarded and the remaining 123 images underwent slice-time and motion corrections. Seven PD patients were excluded for exhibiting head movements greater than 3mm or 3 degrees. The individual T1 structure image was co-registered with an average EPI image and segmented into either gray matter or white matter using a new segment and DARTEL segmentation algorithm. Next, the structural images were spatially normalized to the Montreal Neurological Institute (MNI) standard template space, and the transformation information obtained were applied to EPI images. The generated image was then resampled to 3 × 3 × 3mm^3 and spatially smoothed with a 6 mm full width half maximum Gaussian kernel. The resulting EPI data were linearly trend removed and temporally filtered (0.01–0.10Hz). Next, the nuisance signals were regressed out, including 24 motion parameters, global signals, white matter signals, and cerebrospinal fluid signals using a general linear mode.

Voxel-Mirrored Homotopic Connectivity Analysis

The VMHC value represents the Pearson correlation coefficient between each voxel's residual time series, as well as corresponding residual time series in another hemisphere, as described in previous studies (Zuo et al., 2010). First, the normalized T1 images of all participants were averaged in order to generate mean normalized T1 image. The left and right mirror versions of this image were averaged to the group-specific symmetrical T1 template. Then, the normalized T1 image was registered into a specific symmetric template. The transformation information was applied to normalized functional image. The VMHC computation was performed using the DPABI_V4.3 software. Then, Fisher Z transform was performed on correlation values in order to improve normality. The resulting value represents the VMHC value.

Statistical Analysis

Statistical analysis of demographic and clinical characteristics for PD patients was carried out using SPSS Statistics 22.0 (IBM, Armonk, NY, United States) using repeated measures analysis of variance and following *post hoc t*-test, as appropriate. The paired *t*-test was utilized to identify VMHC differences between the PD-Pre-DBS and the PD-Post-DBS groups with mean framewise displacement (FD) as covariates. All of the above results were corrected by multiple comparisons of the family wise error rate with a voxel $p < 0.001$ and cluster $p < 0.05$ using SPM12 (London, United Kingdom[3]).

Correlation Analysis

The brain regions with statistically significant differences between PD patients before and after surgery were defined as regions of interest (ROIs). For each PD patient before DBS surgery, the REST software.[4] was utilized to calculate mean VMHC values for each ROI. The Pearson correlation analysis with SPSS 22.0 software helped calculate the correlation between VMHC values of each ROI, as well as preoperative VF score. In addition, we investigated whether alterations in inter-hemispheric functional connections induced by surgical microlesions correlated with decreased VF scores.

[1]http://rfmri.org/dpabi

[2]https://www.mathworks.com/products/matlab

[3]https://www.fil.ion.ucl.ac.uk/spm/software/spm12/

[4]http://www.restfmri.net/

RESULTS

Demographic and Clinical Characteristics

Overall, 30 PD patients were included in this study. The demographics of all participants are presented in **Table 1**. We discovered that MoCA and VF scores of PD patients immediately decreased after surgery, and MoCA scores returned to preoperative levels one month after surgery. However, VF scores were found to still be significantly lower than before.

Voxel-Mirrored Homotopic Connectivity Findings

Compared to the PD-Pre-DBS group, the PD-Post-DBS group demonstrated decreased VMHC values in the posterior cerebellum lobe, midbrain, angular gyrus, precuneus/posterior cingulate gyrus (PCC), supramarginal gyrus, superior frontal gyrus (SFG) (medial and dorsolateral) and middle frontal gyrus (MFG). We did not find any increased VMHC value in the PD-Post-DBS group, compared to the PD-Pre-DBS group (see **Figure 1** and **Table 2**).

Correlation Analysis

A correlation analysis demonstrated that significant positive correlations were discovered between phonemic VF scores and the VMHC value of the precuneus/PCC (see **Figure 2B**), SFG and MFG before DBS (see **Figure 2C**). A significant positive correlation was also seen between semantic VF scores and VMHC value of SFG and MFG (see **Figure 2A**). Additionally, altered VMHC value in SFG and MFG demonstrated a significant positive correlation with a change in phonemic VF scores (see **Figure 2D**).

TABLE 1 | Demographic and clinical data of all subjects.

	PD (*n* = 30) Mean ± SD	*P*-value
Age (years)	62.27 ± 8.73	-
Sex (male/female)	15/15	-
Education (year)	8.1 ± 3.38	-
Disease duration (year)	8.37 ± 2.86	-
LEDD (mg/d)	787.2 ± 181.89	-
MoCA score		
Before DBS	24.70 ± 2.60	0.003[a]*
The first day after DBS	22.37 ± 4.18	
One month after DBS	24.17 ± 2.93	-
Six months after DBS	24.13 ± 2.81	-
Semantic VF		
Before DBS	20.20 ± 4.34	< 0.001[a]*
The first day after DBS	14.07 ± 3.95	-
One month after DBS	16.30 ± 3.87	-
Six months after DBS	16.23 ± 4.06	-
Phonemic VF		
Before DBS	10.10 ± 2.06	< 0.001[a]*
The first day after DBS	7.37 ± 1.73	
One month after DBS	8.73 ± 2.08	-
Six months after DBS	8.87 ± 1.68	-

PD, Parkinson's disease; LEDD, levodopa equivalent daily dose; MoCA, Montreal Cognitive Assessment; VF, verbal fluency; DBS, deep brain stimulation; Mean ± SD, mean ± standard deviation.
[a]Repeated measures variance analysis.
**P < 0.05.*

DISCUSSION

Herein, VMHC was utilized, for the first time and to the best of our knowledge, to study homotopic RSFC changes among PD patients immediately after DBS surgery. Strong and weak homotopic RSFC were interpreted as a tendency to coordinate processing or independent processing in allelic brain regions, respectively (Baldo et al., 2001). In the past, many functional imaging studies have discovered impaired interhemispheric coordination among PD patients (Hu et al., 2015; Zhu et al., 2016; Li et al., 2018; Gan et al., 2021). The focus of this study was to explore changes in functional coordination of homotopic brain regions post-DBS. Our main findings included that PD patients had decreased interhemispheric RSFC in the prefrontal cortex, cerebellum, supramarginal gyrus and default mode network (DMN)-related brain regions. Furthermore, we observed significant positive correlations between the VMHC values of SFG and MFG before DBS and phonemic VF scores in PD patients. The VMHC changes of SFG and MFC induced by DBS surgery were found to be positively correlated with decreased phonemic VF. DBS is able to cause a temporary decline in overall cognitive function among PD patients after surgery. However, in the long run, there was no significant influence on the overall cognitive function. The VF performance of PD patients decreased significantly immediately after DBS, and improved one month later. In the long term, VF performance declined compared to before the surgery, which is consistent with results in previous literature (Lefaucheur et al., 2012; Borden et al., 2014; Le Goff et al., 2015; Costentin et al., 2019).

Our results demonstrated that altered VMHC values were discovered in the prefrontal cortex, including in the SFG and MFG, and in the PD-Pre-DBS group compared to the PD-Post-DBS group. The integrity of executive function or higher cognitive tasks depends on integrity of the structure and function of the frontal lobe (Yuan and Raz, 2014). In addition, increased frontal lobe activity was consistently observed in the resting state fMRI studies of normal adults performing tasks (Yuan and Raz, 2014). The prefrontal lobe is a key area for word comprehension and production (Costafreda et al., 2006). The semantic and phonemic fluency was found to be impaired to varying degrees after partial frontal lobe damage (Baldo and Shimamura, 1998; Thompson-Schill et al., 1998). In addition, impaired VF is considered to be a marker of frontal lobe dysfunction (Baldo and Shimamura, 1998; Baldo et al., 2001). The left side of the brain is the dominant hemisphere and, therefore, the VF is more sensitive to damage to the left prefrontal lobe (Janowsky et al., 1989). However, one study found that VF performance was significantly decreased, regardless of left or right frontal lobe damage (Baldo and Shimamura, 1998). FMRI studies have generally found that the VF task is associated with activation of the frontal and parietal

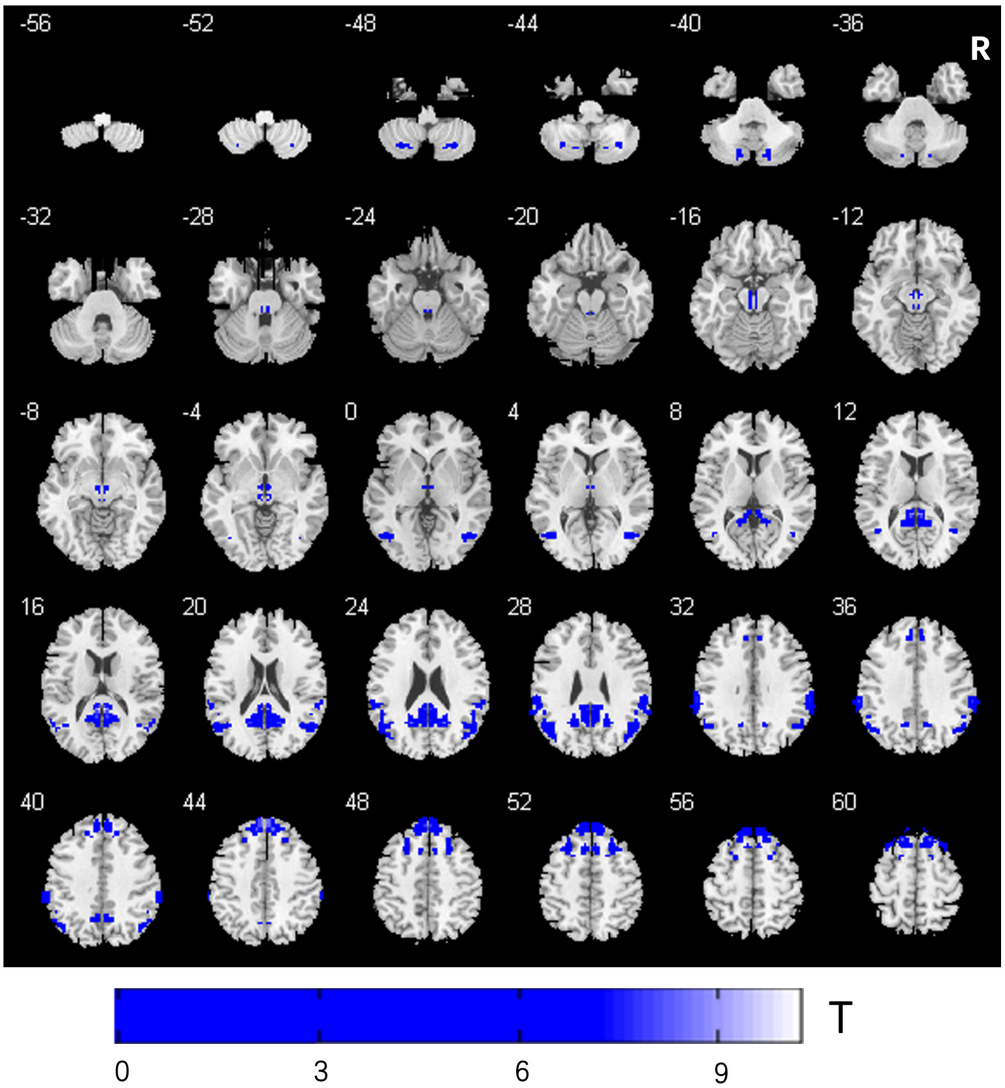

FIGURE 1 | Comparison of VMHC between the PD-Pre-DBS group and PD-Post-DBS group. PD, Parkinson's disease; DBS, deep brain stimulation; PD-Pre-DBS, three days before DBS, PD-Post-DBS, one day after DBS; VMHC, voxel-mirrored homotopic connectivity; L, left; R, right; Regions showing decreased VMHC in blue; Family wise error correction (voxel $p < 0.001$, cluster $p < 0.05$).

TABLE 2 | VMHC differences between the PD-Pre-DBS and PD-Post-DBS group.

	Brain region (AAL)	Cluster size	Peak MNI coordinate			Peak intensity
PD-Pre-DBS > PD-Post-DBS						
Cluster 1	Cerebelum_Crus2_R	46	± 18	−75	−39	5.1415
Cluster 2	Midbrain	45	± 3	−15	−9	6.3615
Cluster 3	Angular_R	205	± 45	−66	0	5.3717
Cluster 4	Precuneus_R Cingulum_Post_R	270	± 3	−42	15	9.0389
Cluster 5	SupraMarginal_R	127	± 63	−33	36	6.5664
Cluster 6	Superior Frontal Gyrus (Medial + dorsolateral) Frontal_Mid_R	332	± 3	48	42	7.6007

PD, Parkinson's disease; DBS, deep brain stimulation; PD-Pre-DBS, three days before DBS, PD-Post-DBS, one day after DBS; VMHC, voxel-mirrored homotopic connectivity; AAL, anatomical automatic labeling; MNI, Montreal Neurological Institute; Family wise error correction (voxel $p < 0.001$, cluster $p < 0.05$).

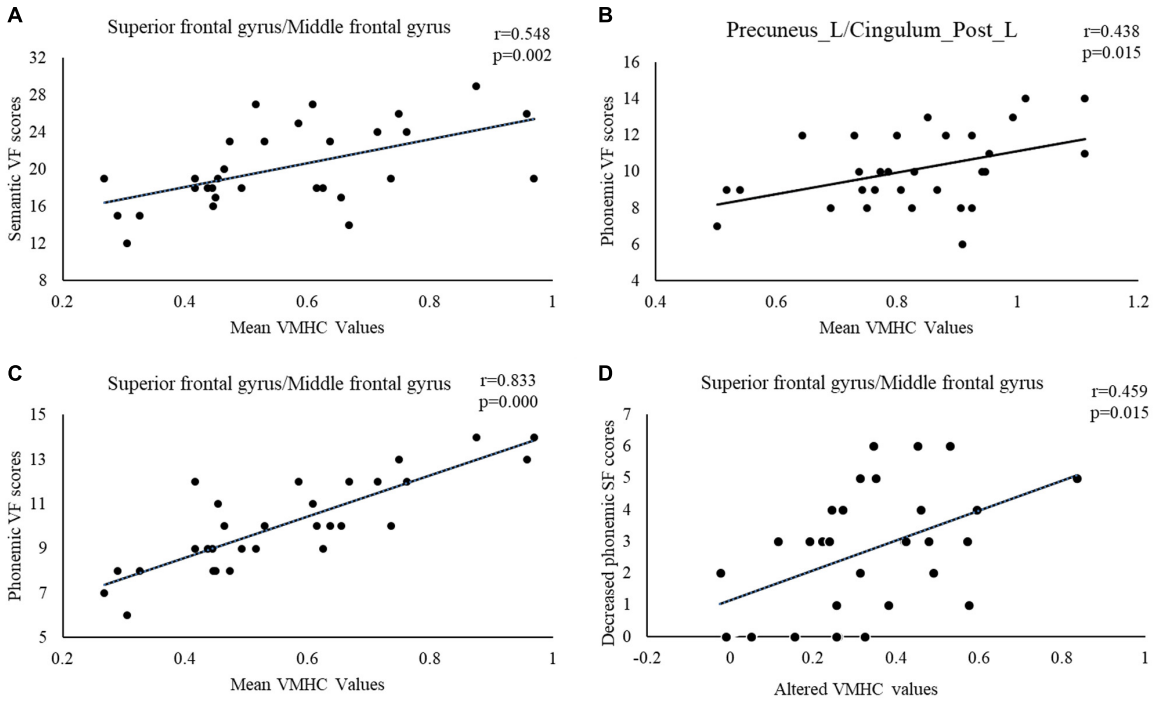

FIGURE 2 | The correlations between VF scores and mean VMHC values in brain regions with statistically significant differences between PD patients before and after surgery. Relationships between: **(A)** Semantic VF and mean VMHC value of superior frontal gyrus and middle frontal gyrus, **(B)** Phonemic VF and mean VMHC value of precuneus/posterior cingulate gyrus, **(C)** Phonemic VF and mean VMHC value of superior frontal gyrus and middle frontal gyrus, and **(D)** Decreased phonemic VF and altered VMHC value in the superior frontal gyrus and middle frontal gyrus. VMHC, voxel-mirrored homotopic connectivity; VF, verbal fluency.

lobes (Vitali et al., 2005; Birn et al., 2010). The decline in VF among patients with PD occurs at initial stages of this illness and is one of the common cognitive changes among PD patients (Henry and Crawford, 2004; Dubois et al., 2007). Pereira et al. (2009) discovered that gray matter density in the frontal lobe, temporal lobe and cerebellum were significantly correlated with semantic fluency scores. The VF performance in PD patients decreased immediately after deep brain electrode implantation. We hypothesized that decreased postoperative VF performance is likely related to decreased homotopic RSFC between the bilateral frontal lobes. Our study discovered that altered VMHC value of SFG and MFG was correlated with changes in phonemic VF scores, which further confirms our speculation.

We also discovered that PD patients had decreased VMHC values in the posterior lobe of the cerebellum after DBS. It is commonly believed that the cerebellum is associated with coordinating voluntary movement, regulating muscle tension and body balance. Research has shown that the cerebellum plays an increasingly important role in the processing of higher cognitive functions, including language, emotion and memory (Hubrich-Ungureanu et al., 2002; De Smet et al., 2013; Starowicz-Filip et al., 2017). A large number of fMRI studies have demonstrated that the right cerebellum was significantly activated during semantic and sentence processing and VF tasks (Hubrich-Ungureanu et al., 2002; Starowicz-Filip et al., 2017; Geva et al., 2021). Hubrich-Ungureanu et al. (2002) applied fMRI in order to check the activation of brain activity in left-handed and right-handed normal volunteers, while carrying out silent VF tasks. When the right-hand volunteers performed a language task, the left fronto-parietal cortex and right cerebellar hemisphere were found to be visibly activated, while the left-hand volunteers were discovered to be visibly activated in the right fronto-parieto-temporal cortex and left cerebellar hemisphere. The volunteers performed VF tasks in a silent state in order to ensure that the brain areas that were activated were due to speech production rather than vocal action. Alexander et al. (2012) discovered that patients with localized lesions of the right cerebellum had lower VF manifestations compared to those with localized lesions of the left cerebellum. These studies have proven the importance of the cerebellum in VF task execution. Therefore, we suggest that interhemispheric coordination disorders of the bilateral cerebellum may be involved in decreased performance of speech fluency, immediately after surgery.

Another important finding in our study was the decrease of VMHC value in the angular gyrus and precuneus/PCC. These brain regions were key brain areas of the DMN, which was associated with cognitive dysfunction among many diseases, including PD and Alzheimer's disease (AD) (Ding et al., 2014; Liao et al., 2018; Wolters et al., 2019). Liao et al. (2018) demonstrated that the inter-hemispheric RSFC of DMN among AD patients was significantly reduced and that the VMHC peak value of the precuneus was significantly positively correlated

with the MoCA score. Therefore, we speculated that the overall cognitive decline of postoperative patients may be related to dysfunction of interhemispheric functional coordination in the DMN brain regions. Additionally, we also observed a reduced interhemispheric synchrony between supramarginal gyrus. The gray matter density of the bilateral supramarginal gyrus is known to be positively correlated with vocabulary knowledge among monolinguals (Lee et al., 2007; Grogan et al., 2012). Bilinguals, relative to monolinguals, have a higher gray matter density in the supramarginal gyrus, and the gray matter density was shown to be positively correlated with vocabulary knowledge (Lee et al., 2007; Grogan et al., 2012). Behaviorally, both vocabulary and VF tasks involve verbal output, and the vocabulary in the sample are significantly correlated with both semantic fluency and phonological production (Lee et al., 2007). It can be concluded from the above studies that VF performance may be related to the density of gray matter in the supramarginal gyrus. Therefore, we hypothesized that the postoperatively homotopic coordination disorder in the supramarginal gyrus observed may be related to the impairment of postoperative speech fluency.

There were several limitations to this study. First, VMHC has methodological limitations, and it is not possible to determine which side of the brain is damaged in order to cause changes in the VMHC. Furthermore, the brain structure is asymmetrical, and we try to resolve this problem using a symmetrical template. Second, although anti-Parkinsonian drugs were discontinued for 12 h, it was still difficult to avoid the long-term effects of drugs on brain function. Third, Given the metal electrodes implanted in the subjects' brains, 1.5T MRI instead of 3.0T MRI scanner was used in this study. With the development of technology, the development of higher field strength compatible electrodes will further promote the study of deep brain stimulation mechanisms. In addition, in order to reduce patients' head movement or discomfort caused by long collection time, the collection time of fMRI was only 128 time points. The short collection time was a disadvantage of the design of this study. In the following study, we will extend the collection time to avoid that the short collection time may affect the results of this study. Finally, the sample size of our study remains small, and more samples need to be included in the future in order to further verify our results.

CONCLUSION

Overall, we found that PD patients showed decreased interhemispheric RSFC in the prefrontal cortex, cerebellum, supramarginal gyrus, and DMN-related brain regions after STN-DBS. This result indicates a disorder of hemispheric coordination after DBS. Furthermore, the positive correlation between altered VMHC value of SFG and MFG and the changed phonemic VF scores observed suggests a potential clinical implication of VMHC measure for decreased postoperative VF in PD patients. All findings provide novel insights into the pathogenesis of VF decline after DBS from an interhemispheric perspective.

DATA AVAILABILITY STATEMENT

The original contributions presented in the study are included in the article/**Supplementary Material**, further inquiries can be directed to the corresponding authors.

ETHICS STATEMENT

The studies involving human participants were reviewed and approved by the Ethics Committee of Brain Hospital Affiliated with Nanjing Medical University. The patients/participants provided their written informed consent to participate in this study.

AUTHOR CONTRIBUTIONS

BL, WD, and CQ designed and wrote this manuscript. LC and YL collected the data. CX and DL were responsible for data processing and analysis. LZ and WL contributed to the design of the study. WZ and JY edited and revised the manuscript. All authors contributed to and approved the final manuscript.

FUNDING

This study was supported by the grant from subtopic of the 13th Five-Year National Key Research and Development Plan (No. 2016YFC0105901NNZ), Special Funds of the Jiangsu Provincial Key Research and Development Projects (No. BE2019612), Jiangsu Provincial Cadre Health Research Projects (No. BJ17006), and Nanjing Health Science and Technology Development Special Fund Project (No. ZKX20031).

SUPPLEMENTARY MATERIAL

The Supplementary Material for this article can be found online at: https://www.frontiersin.org/articles/10.3389/fnagi.2022.799545/full#supplementary-material

REFERENCES

Alexander, M. P., Gillingham, S., Schweizer, T., and Stuss, D. T. (2012). Cognitive impairments due to focal cerebellar injuries in adults. *Cortex* 48, 980–990. doi: 10.1016/j.cortex.2011.03.012

Baldo, J. V., and Shimamura, A. P. (1998). Letter and category fluency in patients with frontal lobe lesions. *Neuropsychology* 12, 259–267. doi: 10.1037//0894-4105.12.2.259

Baldo, J. V., Shimamura, A. P., Delis, D. C., Kramer, J., and Kaplan, E. (2001). Verbal and design fluency in patients with frontal lobe lesions. *J. Int. Neuropsychol. Soc* 7, 586–596. doi: 10.1017/s1355617701755063

Benabid, A. L., Chabardes, S., Mitrofanis, J., and Pollak, P. (2009). Deep brain stimulation of the subthalamic nucleus for the treatment of Parkinson's disease. *Lancet Neurol.* 8, 67–81. doi: 10.1016/s1474-4422(08)70291-6

Birn, R. M., Kenworthy, L., Case, L., Caravella, R., Jones, T. B., Bandettini, P. A., et al. (2010). Neural systems supporting lexical search guided by letter and

semantic category cues: a self-paced overt response fMRI study of verbal fluency. *Neuroimage* 49, 1099–1107. doi: 10.1016/j.neuroimage.2009.07.036

Borden, A., Wallon, D., Lefaucheur, R., Derrey, S., Fetter, D., Verin, M., et al. (2014). Does early verbal fluency decline after STN implantation predict long-term cognitive outcome after STN-DBS in Parkinson's disease? *J. Neurol. Sci.* 346, 299–302. doi: 10.1016/j.jns.2014.07.063

Cao, X., Wang, X., Xue, C., Zhang, S., Huang, Q., and Liu, W. (2020). A radiomics approach to predicting Parkinson's disease by incorporating whole-brain functional activity and gray matter structure. *Front. Neurosci.* 14:751. doi: 10.3389/fnins.2020.00751

Costafreda, S. G., Fu, C. H., Lee, L., Everitt, B., Brammer, M. J., and David, A. S. (2006). A systematic review and quantitative appraisal of fMRI studies of verbal fluency: role of the left inferior frontal gyrus. *Hum. Brain. Mapp.* 27, 799–810. doi: 10.1002/hbm.20221

Costentin, G., Derrey, S., Gérardin, E., Cruypeninck, Y., Pressat-Laffouilhere, T., Anouar, Y., et al. (2019). White matter tracts lesions and decline of verbal fluency after deep brain stimulation in Parkinson's disease. *Hum. Brain Mapp.* 40, 2561–2570. doi: 10.1002/hbm.24544

De Smet, H. J., Paquier, P., Verhoeven, J., and Mariën, P. (2013). The cerebellum: its role in language and related cognitive and affective functions. *Brain Lang.* 127, 334–342. doi: 10.1016/j.bandl.2012.11.001

Deuschl, G., Schade-Brittinger, C., Krack, P., Volkmann, J., Schäfer, H., Bötzel, K., et al. (2006). A randomized trial of deep-brain stimulation for Parkinson's disease. *N. Engl. J. Med.* 355, 896–908. doi: 10.1056/NEJMoa060281

Dimond, S. J. (1979). Performance by split-brain humans on lateralized vigilance tasks. *Cortex* 15, 43–50. doi: 10.1016/s0010-9452(79)80005-2

Ding, X., Li, C. Y., Wang, Q. S., Du, F. Z., Ke, Z. W., Peng, F., et al. (2014). Patterns in default-mode network connectivity for determining outcomes in cognitive function in acute stroke patients. *Neuroscience* 277, 637–646. doi: 10.1016/j.neuroscience.2014.07.060

Dubois, B., Burn, D., Goetz, C., Aarsland, D., Brown, R. G., Broe, G. A., et al. (2007). Diagnostic procedures for Parkinson's disease dementia: recommendations from the movement disorder society task force. *Mov. Disord.* 22, 2314–2324. doi: 10.1002/mds.21844

Gan, C., Wang, L., Ji, M., Ma, K., Sun, H., Zhang, K., et al. (2021). Abnormal interhemispheric resting state functional connectivity in Parkinson's disease patients with impulse control disorders. *NPJ Parkinsons Dis.* 7:60. doi: 10.1038/s41531-021-00205-7

Gan, C., Wang, M., Si, Q., Yuan, Y., Zhi, Y., Wang, L., et al. (2020). Altered interhemispheric synchrony in Parkinson's disease patients with levodopa-induced dyskinesias. *NPJ Parkinsons Dis.* 6:14. doi: 10.1038/s41531-020-0116-2

Geva, S., Schneider, L. M., Roberts, S., Green, D. W., and Price, C. J. (2021). The effect of focal damage to the right medial posterior cerebellum on word and sentence comprehension and production. *Front. Hum. Neurosci.* 15:664650. doi: 10.3389/fnhum.2021.664650

Grogan, A., Parker Jones, O., Ali, N., Crinion, J., Orabona, S., Mechias, M. L., et al. (2012). Structural correlates for lexical efficiency and number of languages in non-native speakers of english. *Neuropsychologia* 50, 1347–1352. doi: 10.1016/j.neuropsychologia.2012.02.019

Guo, W., Xiao, C., Liu, G., Wooderson, S. C., Zhang, Z., Zhang, J., et al. (2014). Decreased resting-state interhemispheric coordination in first-episode, drug-naive paranoid schizophrenia. *Prog. Neuropsychopharmacol. Biol. Psychiatry* 48, 14–19. doi: 10.1016/j.pnpbp.2013.09.012

Henry, J. D., and Crawford, J. R. (2004). Verbal fluency deficits in Parkinson's disease: a meta-analysis. *J. Int. Neuropsychol. Soc.* 10, 608–622. doi: 10.1017/s1355617704104141

Hu, X., Zhang, J., Jiang, X., Zhou, C., Wei, L., Yin, X., et al. (2015). Decreased interhemispheric functional connectivity in subtypes of Parkinson's disease. *J. Neurol.* 262, 760–767. doi: 10.1007/s00415-014-7627-x

Hubrich-Ungureanu, P., Kaemmerer, N., Henn, F. A., and Braus, D. F. (2002). Lateralized organization of the cerebellum in a silent verbal fluency task: a functional magnetic resonance imaging study in healthy volunteers. *Neurosci. Lett.* 319, 91–94. doi: 10.1016/s0304-3940(01)02566-6

Janowsky, J. S., Shimamura, A. P., Kritchevsky, M., and Squire, L. R. (1989). Cognitive impairment following frontal lobe damage and its relevance to human amnesia. *Behav. Neurosci.* 103, 548–560. doi: 10.1037//0735-7044.103.3.548

Jin, C., Qi, S., Teng, Y., Li, C., Yao, Y., Ruan, X., et al. (2021). Integrating structural and functional interhemispheric brain connectivity of gait freezing in Parkinson's disease. *Front. Neurol.* 12:609866. doi: 10.3389/fneur.2021.609866

Le Goff, F., Derrey, S., Lefaucheur, R., Borden, A., Fetter, D., Jan, M., et al. (2015). Decline in verbal fluency after subthalamic nucleus deep brain stimulation in Parkinson's disease: a microlesion effect of the electrode trajectory? *J. Parkinsons Dis.* 5, 95–104. doi: 10.3233/jpd-140443

Lee, H., Devlin, J. T., Shakeshaft, C., Stewart, L. H., Brennan, A., Glensman, J., et al. (2007). Anatomical traces of vocabulary acquisition in the adolescent brain. *J. Neurosci.* 27, 1184–1189. doi: 10.1523/jneurosci.4442-06.2007

Lefaucheur, R., Derrey, S., Martinaud, O., Wallon, D., Chastan, N., Gérardin, E., et al. (2012). Early verbal fluency decline after STN implantation: is it a cognitive microlesion effect? *J. Neurol. Sci.* 321, 96–99. doi: 10.1016/j.jns.2012.07.033

Li, J., Yuan, Y., Wang, M., Zhang, J., Zhang, L., Jiang, S., et al. (2018). Decreased interhemispheric homotopic connectivity in Parkinson's disease patients with freezing of gait: a resting state fMRI study. *Parkinsonism Relat. Disord.* 52, 30–36. doi: 10.1016/j.parkreldis.2018.03.015

Liao, J., Li, T., Dong, W., Wang, J., Tian, J., Liu, J., et al. (2019). Reduced prefrontal-temporal cortical activation during verbal fluency task in obsessive-compulsive disorder: a multi-channel near-infrared spectroscopy study. *J. Psychiatr. Res.* 109, 33–40. doi: 10.1016/j.jpsychires.2018.11.006

Liao, Z. L., Tan, Y. F., Qiu, Y. J., Zhu, J. P., Chen, Y., Lin, S. S., et al. (2018). Interhemispheric functional connectivity for Alzheimer's disease and amnestic mild cognitive impairment based on the triple network model. *J. Zhejiang Univ. Sci. B* 19, 924–934. doi: 10.1631/jzus.B1800381

Luo, C., Guo, X., Song, W., Zhao, B., Cao, B., Yang, J., et al. (2015). Decreased resting-state interhemispheric functional connectivity in Parkinson's disease. *Biomed. Res. Int.* 2015:692684. doi: 10.1155/2015/692684

Mikos, A., Bowers, D., Noecker, A. M., McIntyre, C. C., Won, M., Chaturvedi, A., et al. (2011). Patient-specific analysis of the relationship between the volume of tissue activated during DBS and verbal fluency. *Neuroimage* 54, S238–S246. doi: 10.1016/j.neuroimage.2010.03.068

Morrison, C. E., Borod, J. C., Perrine, K., Beric, A., Brin, M. F., Rezai, A., et al. (2004). Neuropsychological functioning following bilateral subthalamic nucleus stimulation in Parkinson's disease. *Arch. Clin. Neuropsychol.* 19, 165–181. doi: 10.1016/s0887-6177(03)00004-0

Pereira, J. B., Junqué, C., Martí, M. J., Ramirez-Ruiz, B., Bartrés-Faz, D., and Tolosa, E. (2009). Structural brain correlates of verbal fluency in Parkinson's disease. *Neuroreport* 20, 741–744. doi: 10.1097/WNR.0b013e328329370b

Pozzilli, C., Bastianello, S., Padovani, A., Passafiume, D., Millefiorini, E., Bozzao, L., et al. (1991). Anterior corpus callosum atrophy and verbal fluency in multiple sclerosis. *Cortex* 27, 441–445. doi: 10.1016/s0010-9452(13)80039-1

Quan, W., Wu, T., Li, Z., Wang, Y., Dong, W., and Lv, B. (2015). Reduced prefrontal activation during a verbal fluency task in Chinese-speaking patients with schizophrenia as measured by near-infrared spectroscopy. *Prog. Neuropsychopharmacol. Biol. Psychiatry* 58, 51–58. doi: 10.1016/j.pnpbp.2014.12.005

Sauerwein, H. C., and Lassonde, M. (1994). Cognitive and sensori-motor functioning in the absence of the corpus callosum: neuropsychological studies in callosal agenesis and callosotomized patients. *Behav. Brain Res.* 64, 229–240. doi: 10.1016/0166-4328(94)90135-x

Smitha, K. A., Arun, K. M., Rajesh, P. G., Thomas, B., Radhakrishnan, A., Sarma, P. S., et al. (2019). Resting fMRI as an alternative for task-based fMRI for language lateralization in temporal lobe epilepsy patients: a study using independent component analysis. *Neuroradiology* 61, 803–810. doi: 10.1007/s00234-019-02209-w

Starowicz-Filip, A., Chrobak, A. A., Moskała, M., Krzyżewski, R. M., Kwinta, B., Kwiatkowski, S., et al. (2017). The role of the cerebellum in the regulation of language functions. *Psychiatr. Pol.* 51, 661–671. doi: 10.12740/pp/68547

Thompson-Schill, S. L., Swick, D., Farah, M. J., D'Esposito, M., Kan, I. P., and Knight, R. T. (1998). Verb generation in patients with focal frontal lesions: a neuropsychological test of neuroimaging findings. *Proc. Natl. Acad. Sci. U S A* 95, 15855–15860. doi: 10.1073/pnas.95.26.15855

Vitali, P., Abutalebi, J., Tettamanti, M., Rowe, J., Scifo, P., Fazio, F., et al. (2005). Generating animal and tool names: an fMRI study of effective connectivity. *Brain Lang.* 93, 32–45. doi: 10.1016/j.bandl.2004.08.005

Witt, K., Daniels, C., Reiff, J., Krack, P., Volkmann, J., Pinsker, M. O., et al. (2008). Neuropsychological and psychiatric changes after deep brain stimulation for Parkinson's disease: a randomised, multicentre study. *Lancet. Neurol.* 7, 605–614. doi: 10.1016/s1474-4422(08)70114-5

Witt, K., Pulkowski, U., Herzog, J., Lorenz, D., Hamel, W., Deuschl, G., et al. (2004). Deep brain stimulation of the subthalamic nucleus improves cognitive flexibility but impairs response inhibition in Parkinso'n disease. *Arch. Neurol.* 61, 697–700. doi: 10.1001/archneur.61.5.697

Wolters, A. F., van de Weijer, S. C. F., Leentjens, A. F. G., Duits, A. A., Jacobs, H. I. L., and Kuijf, M. L. (2019). Resting-state fMRI in Parkinson's disease patients with cognitive impairment: a meta-analysis. *Parkinsonism Relat. Disord.* 62, 16–27. doi: 10.1016/j.parkreldis.2018.12.016

Yaldizli, Ö, Penner, I. K., Frontzek, K., Naegelin, Y., Amann, M., Papadopoulou, A., et al. (2014). The relationship between total and regional corpus callosum atrophy, cognitive impairment and fatigue in multiple sclerosis patients. *Mult. Scler.* 20, 356–364. doi: 10.1177/1352458513496880

Yang, J., Ji, X., Quan, W., Liu, Y., Wei, B., and Wu, T. (2020). Classification of schizophrenia by functional connectivity strength using functional near infrared spectroscopy. *Front. Neuroinform.* 14:40. doi: 10.3389/fninf.2020.00040

Yuan, P., and Raz, N. (2014). Prefrontal cortex and executive functions in healthy adults: a meta-analysis of structural neuroimaging studies. *Neurosci. Biobehav. Rev.* 42, 180–192. doi: 10.1016/j.neubiorev.2014.02.005

Zhu, Y., Song, X., Xu, M., Hu, X., Li, E., Liu, J., et al. (2016). Impaired interhemispheric synchrony in Parkinson's disease with depression. *Sci. Rep.* 6:27477. doi: 10.1038/srep27477

Zuo, X. N., Kelly, C., Di Martino, A., Mennes, M., Margulies, D. S., Bangaru, S., et al. (2010). Growing together and growing apart: regional and sex differences in the lifespan developmental trajectories of functional homotopy. *J. Neurosci.* 30, 15034–15043. doi: 10.1523/jneurosci.2612-10.2010

Conflict of Interest: The authors declare that the research was conducted in the absence of any commercial or financial relationships that could be construed as a potential conflict of interest.

Publisher's Note: All claims expressed in this article are solely those of the authors and do not necessarily represent those of their affiliated organizations, or those of the publisher, the editors and the reviewers. Any product that may be evaluated in this article, or claim that may be made by its manufacturer, is not guaranteed or endorsed by the publisher.

frontiers | Frontiers in Aging Neuroscience

ORIGINAL RESEARCH
published: 05 April 2022
doi: 10.3389/fnagi.2022.785495

Identifying Mild Alzheimer's Disease With First 30-Min ^{11}C-PiB PET Scan

*Chushu Shen[1], Zhenguo Wang[1], Hongzhao Chen[1], Yan Bai[2], Xiaochen Li[2], Dong Liang[1], Xin Liu[1], Hairong Zheng[1], Meiyun Wang[2], Yongfeng Yang[1], Haifeng Wang[1] and Tao Sun[1]**

[1] Paul C. Lauterbur Research Center for Biomedical Imaging, Shenzhen Institute of Advanced Technology, Chinese Academy of Science, Shenzhen, China, [2] Henan Provincial People's Hospital and the People's Hospital of Zhengzhou, University of Zhengzhou, Zhengzhou, China

Introduction: ^{11}C-labeled Pittsburgh compound B (^{11}C-PiB) PET imaging can provide information for the diagnosis of Alzheimer's disease (AD) by quantifying the binding of PiB to β-amyloid deposition in the brain. Quantification index, such as standardized uptake value ratio (SUVR) and distribution volume ratio (DVR), has been exploited to effectively distinguish between healthy and subjects with AD. However, these measures require a long wait/scan time, as well as the selection of an optimal reference region. In this study, we propose an alternate measure named amyloid quantification index (AQI), which can be obtained with the first 30-min scan without the selection of the reference region.

Methods: ^{11}C-labeled Pittsburgh compound B PET scan data were obtained from the public dataset "OASIS-3". A total of 60 mild subjects with AD and 60 healthy controls were included, with 50 used for training and 10 used for testing in each group. The proposed measure AQI combines information of clearance rate and mid-phase PIB retention in featured brain regions from the first 30-min scan. For each subject in the training set, AQI, SUVR, and DVR were calculated and used for classification by the logistic regression classifier. The receiver operating characteristic (ROC) analysis was performed to evaluate the performance of these measures. Accuracy, sensitivity, and specificity were reported. The Kruskal–Wallis test and effect size were also performed and evaluated for all measures. Then, the performance of three measures was further validated on the testing set using the same method. The correlations between these measures and clinical MMSE and CDR-SOB scores were analyzed.

Results: The Kruskal–Wallis test suggested that AQI, SUVR, and DVR can all differentiate between the healthy and subjects with mild AD ($p < 0.001$). For the training set, ROC analysis showed that AQI achieved the best classification performance with an accuracy rate of 0.93, higher than 0.88 for SUVR and 0.89 for DVR. The effect size of AQI, SUVR, and DVR were 2.35, 2.12, and 2.06, respectively, indicating that AQI was the most effective among these measures. For the testing set, all three measures achieved less superior performance, while AQI still performed the best with the highest accuracy of 0.85. Some false-negative cases with below-threshold SUVR and DVR values were correctly identified using AQI. All three measures showed significant and comparable correlations with clinical scores ($p < 0.01$).

OPEN ACCESS

Edited by:
Behrooz Hooshyar Yousefi, University of Marburg, Germany

Reviewed by:
Yi Su, Banner Alzheimer's Institute, United States
David Brooks, Imperial College London, United Kingdom

***Correspondence:**
Tao Sun
tao.sun@siat.ac.cn

Specialty section:
This article was submitted to Alzheimer's Disease and Related Dementias, a section of the journal Frontiers in Aging Neuroscience

Received: *29 September 2021*
Accepted: *23 February 2022*
Published: *05 April 2022*

Citation:
Shen C, Wang Z, Chen H, Bai Y, Li X, Liang D, Liu X, Zheng H, Wang M, Yang Y, Wang H and Sun T (2022) Identifying Mild Alzheimer's Disease With First 30-Min ^{11}C-PiB PET Scan. Front. Aging Neurosci. 14:785495. doi: 10.3389/fnagi.2022.785495

Conclusion: Amyloid quantification index combines early-phase kinetic information and a certain degree of β-amyloid deposition, and can provide a better differentiating performance using the data from the first 30-min dynamic scan. Moreover, it was shown that clinically indistinguishable AD cases regarding PiB retention potentially can be correctly identified.

Keywords: Alzheimer's disease, ^{11}C-PiB PET, β-amyloid, imaging protocol, dynamic imaging

INTRODUCTION

Alzheimer's disease (AD) is an irreversible neurodegenerative disease that is characterized by dementia symptoms such as memory loss and cognitive impairment (Winblad et al., 2016). Currently, the diagnosis of AD is mainly based on clinical symptoms, while the presence of pathologically relevant biomarkers, including amyloid plaques and neurofibrillary tangles, could help to confirm the results and enable early detection (Jellinger, 1998). With radiotracers specific to β-amyloid plaques, PET imaging provides a useful tool for quantifying β-amyloid deposition in the brain regions. In 2019, the IDEAS (Imaging Dementia-Evidence for Amyloid Scanning) study involving 18,295 patients with mild cognitive impairment (MCI) or dementia and 946 dementia experts proved that implementing amyloid PET scanning would lead to higher diagnostic certainty, changing patient management and leading to improved outcomes (Rabinovici et al., 2019). ^{11}C-labeled Pittsburgh compound B (PiB) is a radiotracer that performs *in vivo* imaging of amyloid deposition (Klunk et al., 2004). Previous studies suggested that a significant difference in PiB retention was observed in areas known to contain amyloid deposition, such as frontal, parietal cortex, and striatum (Klunk et al., 2004; Forsberg et al., 2010; Tryputsen et al., 2015). PiB PET imaging has been successfully used in discriminating AD, MCI, and healthy subjects (Lowe et al., 2009) as well as predicting MCI progression (Forsberg et al., 2008).

The most widely used quantification measures for ^{11}C-PiB imaging are standardized uptake value ratio (SUVR) and distribution volume ratio (DVR). SUVR measures the ratio of SUV in target and reference regions over a late-scan period. The value of SUVR reflects the degree of PiB retention and thus the amyloid deposition in the region of interest (ROI) at the equilibrium stage of tracer distribution. This semi-quantitative method works effectively in assisting AD diagnosis, although it was known to suffer from non-specific tracer binding (Liu et al., 2021). DVR is the ratio of distribution volume from a receptor-containing region (target region) to a non-receptor region (reference region), which can be obtained by Reference Logan Graphical analysis (Logan et al., 1996). In PiB imaging, the DVR value reflects the equilibrium distribution of PiB and is significantly higher for subjects with AD in regions with β-amyloid deposition than normal. Apart from DVR and SUVR, relative tracer flow (R1) has also been reported to provide information for differentiating subjects with AD and HC (Peretti et al., 2019b; Ponto et al., 2019). It is defined as the ratio of tracer influx rate in the target region to that in the reference region, which measures the transport of tracer from plasma to tissue at the initial scan. Both DVR and R1 can be derived by fitting the simplified reference tissue model (SRTM) to the dynamic PET data (Lammertsma and Hume, 1996). Previous studies reported that R1 generated by the SRTM2 model is highly correlated with regional cerebral blood flow (Meyer et al., 2011) as well as FDG SUVR (Peretti et al., 2019c), and thus can serve as a biomarker of neuronal activity and neurodegeneration.

Although these measures have been proved useful for AD diagnosis, there are some issues with the current workflow. For example, the total scan and wait time for SUVR/DVR would add up to at least 1 h as they measure the tracer uptake at the late equilibrium state. While R1 can be estimated using early-stage PET data, it serves as a potential surrogate for FDG SUVR and is not directly correlated to amyloid quantification (Meyer et al., 2011; Peretti et al., 2019b). Moreover, all the three methods involve selecting a reference region without specific binding. The most frequently used reference region, the cerebellum, however, has been reported to have higher PiB retention in subjects with higher cortical β-amyloid deposition, which could in turn blur the significant results of β-amyloid deposition in target regions (Price et al., 2005).

In this study, we proposed an alternate measure for AD identification based on dynamic PiB PET data. The aim is to achieve comparable or even better discriminative performance on mild AD identification with a short scan time and not using the reference region for calculation. The proposed measure, amyloid quantification index (AQI), requires only the first 30-min scan which reflects both clearance rate from tissue at the early stage and PiB retention before equilibrium. Its performance in differentiating mild AD and HC subjects was assessed and compared with those of SUVR and DVR. Limitations and future work were discussed at the end of this paper.

MATERIALS AND METHODS

Participants and Cognitive Assessments

A total of 60 mild AD subjects and 60 healthy controls (HCs) from the OASIS-3 dataset (LaMontagne et al., 2019) were included. AD scans were selected as those confirmed by two clinical diagnoses before and after the scan time. Both the clinical diagnoses for AD and non-AD dementia were made based on the National Alzheimer Coordinating Center Uniform Data Set (UDS) (Morris et al., 2006) assessments. Patients with non-AD dementia were excluded. Sixty-four PiB scans satisfied these criteria. Four scans were deserted due to the problem of missing necessary scan data. Among the remaining 60 scans,

TABLE 1 | Demographic information of 120 subjects by group.

	AD group	HC group
No. of subjects	60	60
Age (yr)	76.2 ± 7.2	66.5 ± 8.1
Sex (M/F)	45/15	22/38
ApoE 4 positive (%)	36/60	19/60
MMSE	25.7 ± 2.9	29.4 ± 1.0
CDR-SOB	3.2 ± 2.1	0

MMSE, Mini-Mental State Examination; ApoE, apolipoprotein E; CDR-SOB, Clinical Dementia Rating Scale Sum of Boxes.

50 were included in the training set and 10 were included in the testing set. HC scans were selected in the order of serial number, excluding subjects with AD and those with other diseases. In this study, AD_001 indicates the 1st AD subject while HC_001 indicates the 1st HC subject. Demographics of all subjects can be found in **Table 1**. Clinical and neuropsychological assessments were performed on all subjects prior to scans. Each subject received a clinical dementia rating (CDR) score, with a CDR of 0 indicating normal cognitive function and 0.5 or 1 indicating cognitive impairment. Confirmed subjects with AD were clinically diagnosed as "AD dementia". As participants reaching CDR = 2 were no longer eligible for the study, here only mild and very mild AD cases were included ($0.5 \leq$ CDR ≤ 1 or $0.5 \leq$ CDR-SOB ≤ 9) (LaMontagne et al., 2019). To obtain more accurate assessment results we use CDR-SOB (O'Bryant et al., 2008) to evaluate the degree of dementia for each subject, with the score being 0 for HCs and ranging from 0.5 to 9.0 for patients with AD (Sendi et al., 2021). General cognitive status was also evaluated for each subject through the Mini-Mental State Examination (MMSE), with scores ranging from 0 (severe impairment) to 30 (no impairment) (Tombaugh and McIntyre, 1992).

Imaging and Post-processing

^{11}C-labeled Pittsburgh compound B (PiB) PET imaging was performed on each subject. Subjects were given 6–20 mCi ^{11}C-labeled PiB intravenously. Dynamic scans (60 mins;12 x 10 s, 3 × 60 s, 11 × 5 min) were conducted on one of the three Siemens PET scanners: ECAT HR+ 962 PET, Biograph 40 PET/CT, and BioGraph mMR PET-MR. PET imaging analysis was performed as follows (LaMontagne et al., 2019). Reconstructed images were first smoothed to achieve a spatial resolution of 8 mm. Motion correction was applied to each set of dynamic images with an extensive frame-by-frame registration procedure. No partial volume or entropy corrections were applied. Brain parcellation was performed for each subject by registering PET images to the corresponding T1-weighted MR images, which had been segmented using FreeSurfer 5.3 (http://surfer.nmr.mgh.harvard.edu). Reference region-based Logan graphical analysis was implemented on each segmented region to calculate DVR (Logan et al., 1996). Regional SUVR was estimated for all the regions. Both DVR and SUVR used 30–60 min post-injection as the time window with the cerebellar cortex as the reference region.

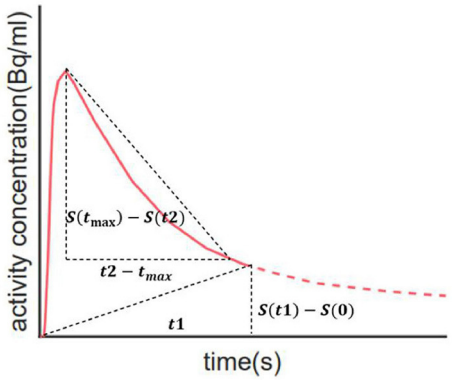

FIGURE 1 | Illustration of how index AQI was calculated. The two oblique dashed lines represent the two slopes that reflect clearance rate and PiB retention respectively. Calculation of AQI only requires 30-min scan, as indicated by the solid red line.

Use Short Scan Data

The first 30-min dynamic data in 100 subjects of the training set were used to exploit optimal features which can effectively distinguish between AD and HC subjects. The mean uptake over time for each brain region was quantified as time-activity curves (TACs). Linear interpolation was performed on TACs to obtain a fine sampling time for all scans.

According to the kinetics of PiB (Rodell et al., 2013), each TAC was split into three phases: flow-in phase, peak uptake, and clearance from tissue. The flow-in phase denotes the initial clearance of PiB by tissue, the rate of which is determined by cerebral blood flow and vascular permeability. The peak uptake phase describes the time when maximal tracer uptake was reached, generally within 4 min from the start (Gjedde et al., 2013). The clearance phase denotes the clearance of tracer from tissue after reaching the peak value, the rate of which can reflect amyloid load in the ROI. Compared with HCs, the AD group usually features greater PiB retention together with a lower clearance rate (Engler et al., 2006; Peretti et al., 2019a). Therefore, it is assumed that the combination of these two characteristics would work effectively in discriminating between diseased and healthy subjects. Based on this assumption, we proposed AQI. For each ROI, we calculated the descending slope from peak to a time point t1 afterward as well as the slope between the start point and a later time point t2 on the corresponding TAC (**Figure 1**). The first slope reflects the clearance rate whereas the second measures the PiB retention in mid-stage scans. Then these two slopes were linearly combined to yield the index AQI_roi in each ROI:

$$\text{AQI\_roi} = a \times \frac{S(t1) - S(0)}{t1} - (1 - a) \times \frac{S(t_{\max}) - S(t2)}{t2 - t_{\max}} \quad (1)$$

Here t is the middle time point of each dynamic frame and t_{max} denotes the frame where peak uptake value occurs. S(t) represents the activity concentration (Bq/ml) of PiB as a function of t. S(0) is the average activity concentration of the first frame (0–10 s).

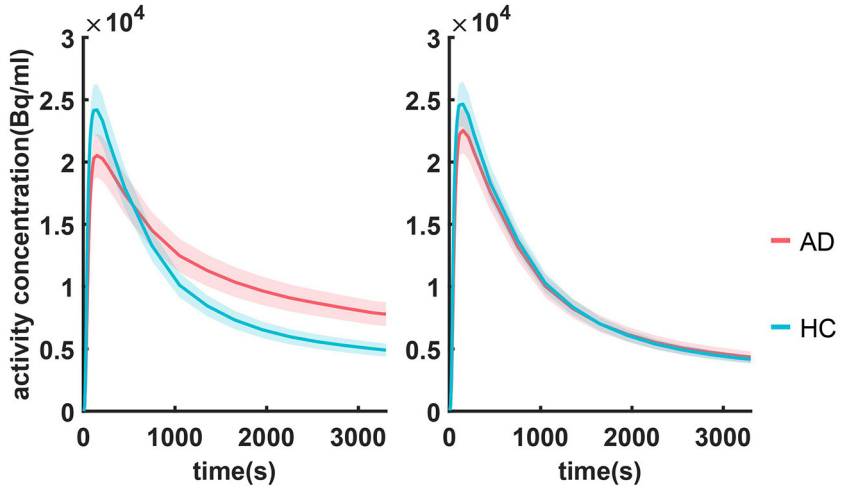

FIGURE 2 | Summarized TACs for all 120 subjects in **(A)** caudal anterior cingulate cortex and **(B)** cerebellar cortex. The solid lines indicate that the mean value in each group and the shadowed areas indicate 95% confidence interval.

Normalization was performed using injected dose for each scan. The optimal values for t1 and t2 and the coefficient "a" were determined by maximizing the classification accuracy. Then, a 10-fold cross-validation procedure using logistic regression classifier was applied to evaluate the performance of AQI_roi on differentiating subjects in the training set. The parameters that had the best compromise between accuracy and scan time were chosen to be the optimal value.

Selection of Optimal Brain Regions

Conventional analysis of quantification methods is based on single or several regions known to contain amyloid deposition without investigating optimal regions. In this study, we identified featured brain regions for AQI using lasso regression analysis (Tibshirani, 1996). Lasso regression could perform variable selection as well as generalized linear regression by finding a set of coefficients β such that the sum of Mean Squared Error (MSE), and the regularization term can be minimized. Here the optimal regularization strength was empirically chosen as the largest value such that MSE is within one standard error of the minimum MSE. Predictors with relatively large coefficients were considered featured brain regions, the AQI_roi of which were linearly combined to distinguish between the AD and HC groups.

Statistical Analysis

Statistical analysis was performed using MATLAB Statistics and Machine Learning Toolbox (version R2018b). The discriminatory performance of index AQI was compared with those of SUVR and DVR. Here the value of SUVR and DVR were calculated as the average values in anterior cingulate, frontal cortex, parietal cortex, and precuneus, which have been reported to accompany higher amyloid binding in subjects with AD than in HC (Klunk et al., 2004; Tryputsen et al., 2015). AQI was calculated linearly by combining the AQI_roi in featured brain regions, the coefficients of which were determined by linear regression. To test the performance of each measure, a 10-fold cross-validation was implemented by randomly partitioning the training subjects into 10 subsets, each containing five AD and five HC subjects. A logistic regression classifier was trained using nine subsets as training data and validated on the remaining subset. The process was repeated 10 times. Then, ROC analysis was performed to compare the classification results of these 10 iterations with true labels, and the sensitivity, specificity, accuracy, area under the curve (AUC), and optimal threshold were reported. To further validate the performance of the three methods, we used an additional 10 AD and 10 HC scans as the testing set. For each subject., AQI, SUVR, and DVR were calculated, as previously mentioned, for training sets. The logistic regression classifier that was trained with the previous 100 subjects was then applied to the testing set. Results of the ROC analysis and the above evaluation metrics were reported and compared. Moreover, the correlations between the three measures (SUVR/DVR/AQI) and clinical scores (MMSE/CDR-SOB) were analyzed using linear regression. The correlation coefficient and *p*-value were reported for each pair of variables.

RESULTS

Summarized TACs in Sampled Regions for all Subjects

Summarized TACs for all 120 subjects in the caudal anterior cingulate cortex and cerebellar cortex are shown in **Figure 2**. Compared with HC, subjects with mild AD feature lower clearance rate and greater PiB retention in the caudal anterior cingulate cortex, whereas in the cerebellar cortex TACs for these two groups are similar due to the lack of specific binding. The difference in the dynamic uptake of certain brain regions allows AD and HC subjects to be separated.

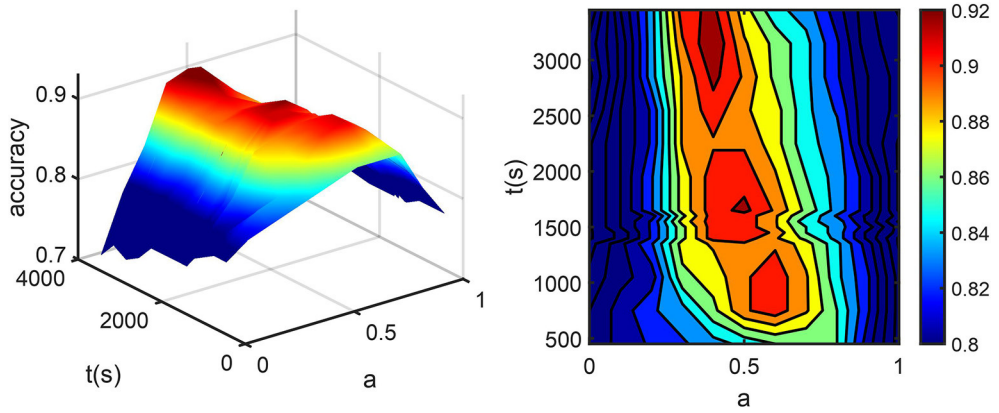

FIGURE 3 | (A) The percentage of correctly classified subjects (accuracy) vs. t2 and a. **(B)** accuracy was projected into the a-t plane. Here t1 is fixed at 1,650 s for the convenience of display. The dark red part in the center corresponds to sets of parameters with maximum accuracy, among which the one with minimum scan time was chosen.

Optimal Parameters for Index AQI

Optimal coefficients and time points in Eq. (1) were found by grid search, where the searching intervals were t1 ∈[0, 3300s], t2∈[300, 3,300 s] with a step size of 50 s and a∈[0, 1] with a step size of 0.1. AQI_roi in the caudal anterior cingulate cortex was then calculated for all training subjects with each set of parameters and used for classifying the AD and HC groups. **Figure 3** shows how the parameter selection was performed. The optimal parameters were a = 0.5, t1 = t2 = 1,650 s, resulting in a maximum classification accuracy of 0.92. With these optimized parameters, equation (1) became:

$$\text{AQI\_roi} = 0.5 \times \frac{S(1650) - S(0)}{1650} - 0.5 \times \frac{S(1650) - S(t_{\max})}{1650 - t_{\max}} \quad (2)$$

where t_{max} was different for each subject, ranging from 80 to 240 s. Each AQI_roi value was normalized using an injected dose. As a result, one would only need scan data of the first 1,650 s (<30 min). All data after this time point were not necessary for computing AQI.

Selection of Featured Brain Regions

The contribution of AQI_roi in different brain regions was evaluated using lasso regression. The selected brain regions were caudal anterior cingulate cortex (β = 2.5214) and caudate(β = 0.1976), with the value of coefficient β reflecting their contribution for differentiating AD and HC subjects. An overall AQI was calculated for each subject by linearly combining AQI_roi in the caudal anterior cingulate cortex and caudate:

$$\text{AQI}_{\text{overall}} = 3.6092 \times X1 + 0.2750 \times X2 + 0.5378 \quad (3)$$

where $X1$ and $X2$ denote the z-score normalized value of AQI_roi in the caudal anterior cingulate cortex and caudate, respectively. The discriminative accuracy of $AQI_{overall}$ on the 100 training subjects was 0.93.

Performance Comparison

Performance Evaluation on Training Set

The discriminating performance of SUVR, DVR, and AQI on the 100 training subjects were evaluated and compared using the 10-fold cross-validation. ROC analysis suggested that AQI performed the best in discriminating AD and HC subjects among all three methods. **Figure 4** shows the ROC curves for the three methods plotted as the false positive rate against the true positive rate at different classification thresholds. We conclude that AQI performed better than SUVR and DVR, as its curve was above the other two with the highest AUC value of 0.9444. AUC, sensitivity, specificity, accuracy, and optimal threshold for each method are reported in **Table 2**. All three methods performed well on identifying HC subjects, with the specificity being 0.96 (SUVR), 0.98 (DVR), and 0.96 (AQI) respectively. While SUVR and DVR had an increased error rate for classifying AD subjects, AQI achieved superior performance with a sensitivity of 0.90 over 0.80. The overall accuracy for SUVR, DVR, and AQI was 0.88,0.89, and 0.93, respectively.

Figure 5 shows the boxplots of these three measures for the AD and HC groups. AD subjects had PiB retention in cortical regions and thus had higher values for SUVR and DVR. The median and quantiles of AD were higher than those of HCs for all three measures. AQI measured the difference between PiB retention and the tracer cleaning rate from the brains, which was also more significant in the AD group. The Kruskal–Wallis tests suggested that all three measures could discriminate HC and AD subjects ($p < 0.001$), while AQI had the least degree of overlap on two boxplots. Indeed, Cohen's effect size for SUVR, DVR, and AQI were 2.12, 2.06, and 2.35 respectively, which further proved that AQI was the most effective in discriminating these two groups.

Performance Validation on Testing Set

The performances of the three measures on the testing set were evaluated using the threshold derived from the training dataset. In **Figure 6**, the ROC curve of AQI was still above those of

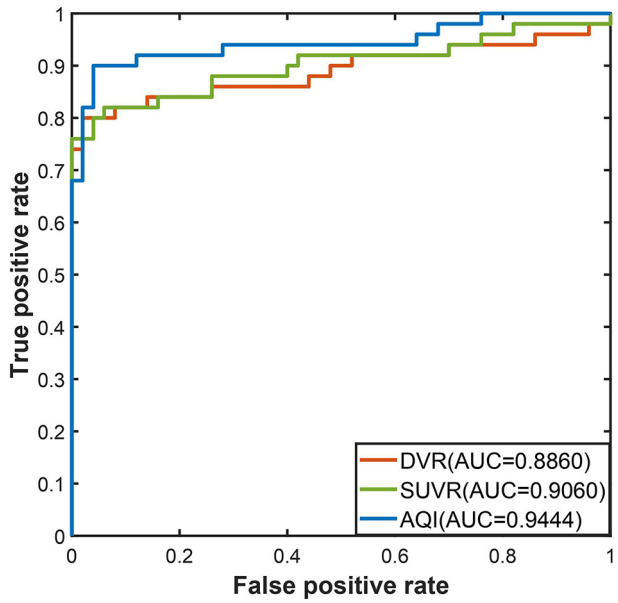

FIGURE 4 | ROC curves for three methods in the training set.

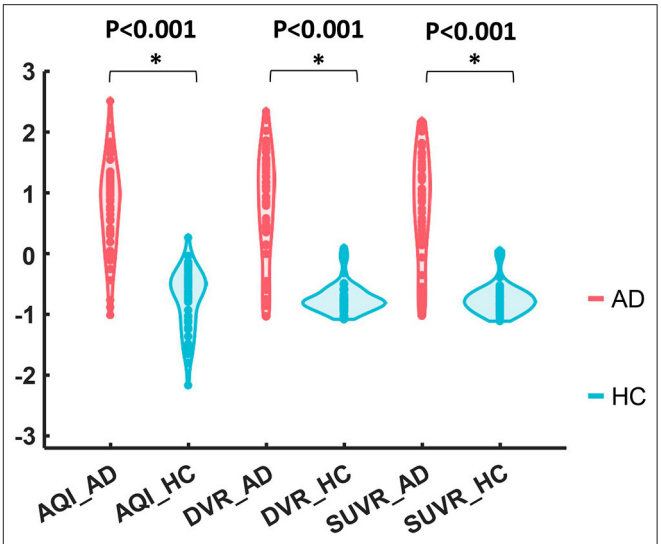

FIGURE 5 | Boxplots of DVR, SUVR, and AQI for AD and HC. For each method, the corresponding data were Z-score normalized to have mean 0 and standard deviation 1 for visual comparison.

TABLE 2 | The classification performance of SUVR, DVR, and AQI on training set.

Methods	SUVR	DVR	AQI
AUC	0.9060	0.8860	0.9444
sensitivity	0.8000	0.8000	0.9000
specificity	0.9600	0.9800	0.9600
accuracy	0.8800	0.8900	0.9300
optimal threshold	1.4510	1.2795	0.0114

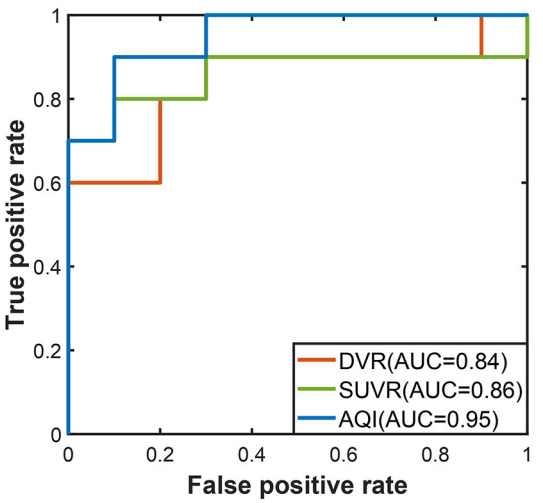

FIGURE 6 | ROC curves for three methods in the testing set.

SUVR and DVR, with the highest value of 0.95. The evaluation metrics in **Table 3** indicated that all three methods achieved a sensitivity of 0.8, and that AQI performed better than the other two measures in terms of specificity and overall accuracy. Compared with the training set, all three measures achieved less superior performance on the testing set, although AQI still performed the best among these measures.

SUVR Images of Selected Samples

To further investigate AD subjects that were misclassified as HC regarding SUVR and DVR, we analyzed SUVR images and TACs of these cases. SUVR images of AD_038, AD_001, AD_040, and AD_005 are shown in **Figure 7**. All four scans were correctly identified as AD by AQI, while AD_038 and AD_040 were misclassified as HC subjects according to the SUVR and DVR value under the classification threshold. TACs showed that these misclassified AD subjects did not have significant PiB retention or dynamic uptake at the equilibrium stage (see **Figure 8**), which explained why measures of SUVR and DVR failed to separate them from the HC subjects. This decreased PiB retention is probably due to the lack of fibrillar β-amyloid deposition, as the clearance rate during the clearance period is still more typical of AD subjects (**Figure 8**). Therefore, by measuring AQI, which considers both retention and clearance rate, these seemingly asymptomatic scans can still be correctly identified.

Correlation With MMSE and CDR-SOB Scores

Figure 9 shows the correlation between measures and scores of clinical tests (CDR and MMSE). Pearson's correlation coefficients and the significance level were reported for each pair of variables (see **Figure 9**). For all three measures, their values were proportional to CDR-SOB and inversely proportional to MMSE, with the absolute value of coefficient *r* ranging from 0.60 to 0.66.

TABLE 3 | The classification performance of SUVR, DVR, and AQI on testing set.

Methods	SUVR	DVR	AQI
AUC	0.8600	0.8400	0.9500
sensitivity	0.8000	0.8000	0.9000
specificity	0.8000	0.8000	0.8000
accuracy	0.8000	0.8000	0.8500
optimal threshold	1.4510	1.2795	0.0114

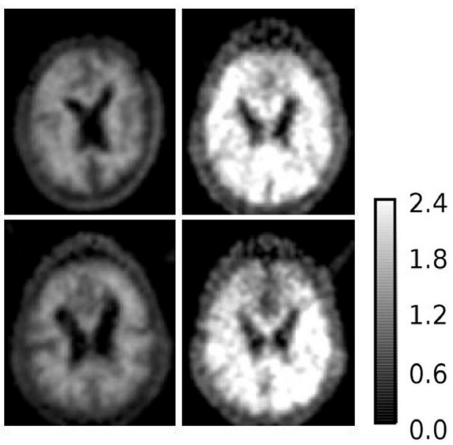

FIGURE 7 | SUVR images of example AD subjects (1) upper left: AD_038 (SUVR = 1.1207); (2) upper right: AD_001 (SUVR = 2.0235); (3) lower left: AD_040 (SUVR = 1.1699); (4) lower right: AD_005 (SUVR = 1.5531). AD_038 and AD_040 were misclassified as HC subjects by SUVR and DVR. AD_001 and AD_005 were correctly classified AD subjects by all three measures.

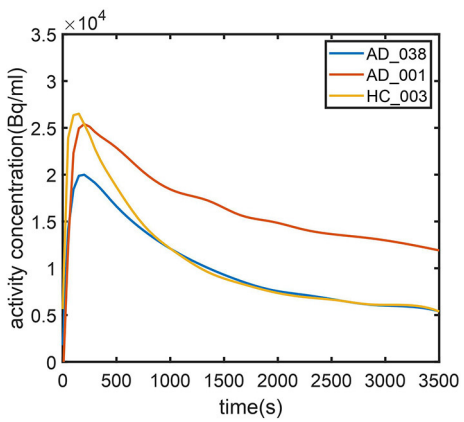

FIGURE 8 | Time–activity curves for (1) typical AD subject (AD_001, blue line) (2) atypical AD subject (AD_038, red line) (3) typical HC subject (HC_003, green line). AD_038 was not identified by SUVR (**Figure 6**) but was correctly classified by AQI.

All of these associations between measures and clinical scores attained statistical significance with $p<0.01$. AQI did not have a significantly higher correlation with the clinical scores than SUVR/ DVR did.

DISCUSSION

Amyloid quantification index is a semi-quantitative measure for PiB PET imaging, which is calculated by linearly combining the information corresponding to clearance rate and mid-phase PiB retention. In this study, AQI was shown to effectively distinguish mild AD and HC subjects for 120 scans from a public dataset. AQI achieved an overall accuracy rate of 0.93, which was higher than SUVR and DVR, in the 100 subjects in the training set. The AUC and sensitivity of AQI were also higher than those of SUVR and DVR, while the specificity was comparable. Moreover, the effective size of AQI was 2.35, larger than 2.12 and 2.06, for SUVR and DVR, respectively. Compared with the training set, all three measures achieved less superior performance on the 20 subjects in the testing set, while AQI still performed best among these measures, with the highest accuracy of 0.85.

The AQI can be obtained with the first 30-min scan, which enables a scan protocol with significantly reduced scan/wait time. This could, in turn, improve the scan efficiency, hence reducing the overall cost of a large-scale study. In terms of image quality, a shorter scan has the further advantage of reducing the possibility of motion artifacts (Sureshbabu and Mawlawi, 2005; Dinges et al., 2013). Moreover, the proposed method does not require the selection of a reference region. Using the cerebellar cortex as a reference region could introduce errors as it is not fully devoid of specific binding. A post-mortem study suggested that the widely used reference regions, the cerebellum and the brain stem, were involved in β-amyloidosis when AD progressed into late stages (Thal et al., 2002). Therefore, the SUVR and DVR in target regions could be offset by the increased binding in the reference region.

Unlike SUVR and DVR, which focus on the PiB retention at late scans, AQI accounts for the information of the early-kinetics and mid-phase retention. The underlying concept is in line with several previous studies, which aimed at deriving diagnostic information from early- or mid-stage PiB scans. Blomquist et al. (2008) reported that some patients with AD could not be distinguished regarding PiB retention as they showed equally low PiB uptake ratio in cortical areas as healthy controls, while they still had decreased K1 (influx rate constant), typical of other AD subjects. Therefore, early-phase dynamics can provide extra information when differentiating AD and HC subjects. Sato et al. (2012) showed that the microkinetic parameter k3, estimated from a 28-min scan, could differentiate AD and HC subjects. Jia et al. (2011) reported that the PiB radioactivity clearance rate differed significantly in patients with AD and HCs in the cortex, subcortical nucleus, and pons, with the rate in the AD group being much smaller. Although the actual quantification methods for utilizing early-phase data were different, these researches suggested the importance of exploiting early-phase information.

The AQI combines retention with early kinetics, which enables correctly identifying indistinguishable AD cases regarding PiB retention. For AD_038 and AD_040, which are devoid of enhanced PiB retention in cortical regions, further *in vitro* analysis is needed to confirm whether amyloid deposition is truly absent or is not bound by PiB. One possible explanation

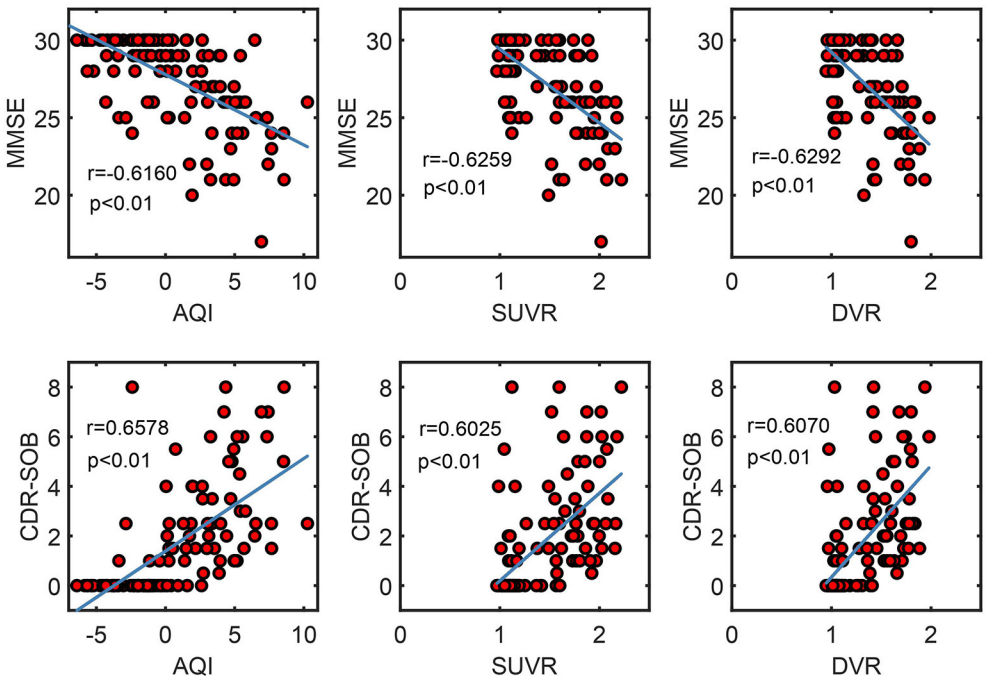

FIGURE 9 | Scatter plots show the correlation between measures (AQI/SUVR/DVR) and clinical scores (MMSE/CDR-SOB). Pearson correlation coefficient r and the corresponding *p*-value were reported for each pair of variables.

is that these subjects are at an early stage or genetically mutated, and thus lack the obvious fibrillar β-amyloid deposition. Previous studies suggested that PiB may be unable to detect AD variants characterized by diffuse β-amyloid plaques as it binds specifically to fibrillar β-amyloid deposition (Bacskai et al., 2007; Ikonomovic et al., 2008). Cairns et al. (2009) reported an ^{11}C-PiB-negative AD patient with substantial amounts of diffuse no-fibrillar β-amyloid plaques, as confirmed by the autopsy. Although the PiB scan was performed 2.5 years before the autopsy, the scarcity of fibrillar β-amyloid plaques was unlikely to be identified by PiB–PET imaging even at the time of the autopsy (Cairns et al., 2009). Tomiyama et al. (2008) reported that AD patients with an amyloid precursor protein mutation would have enhanced the formation of β-amyloid oligomers but no fibrilization and displayed very low signal on PiB PET imaging. The above findings suggested that PiB retention was not completely reliable for AD identification as it may overlook certain AD cases. In our study, the false negative AD cases still display symbolic pathological changes in terms of PiB dynamics and thus can be correctly identified using AQI (**Figure 8**). Moreover, one HC subject without significant PiB retention was misclassified as AD by AQI. This subject was later diagnosed as having uncertain dementia, which suggested that AQI may have detected early-stage symptoms of AD based on abnormal PiB kinetics. Another possibility would be that the ground truth used in this study may be inaccurate as even clinical AD diagnosis can be inaccurate since AD can only be definitely diagnosed neuropathologically at autopsy. If this is true, some of the correctly classified AD subjects, e.g., **Figure 7**, can actually be because of cognitive impairment due to non-AD causes. Whether this is valid or not is subject to further neuropathological support.

There are several limitations of this study. One limitation is that the current results were based on subjects from a single source of dataset and thus may not apply to others. One conclusion of this article is that by exploiting both clearance rate and PiB retention, the performance of differentiating mild AD and HC subjects is superior to using PiB retention alone, while the actual performance may vary across datasets acquired at different centers with various models of scanners. Although, it can be difficult to obtain full dynamic scans to test the proposed method, as most of the centers currently execute a late-scan protocol. A second limitation is that during subject selection those patients with non-AD dementia were excluded, while the clinical situation can be more complicated as diseases such as frontotemporal dementia and Lewy body dementia are likely to interfere with the diagnosis of AD. Future work is needed to test whether AQI will be affected by other types of dementia. The third limitation is that a more appropriate normalization method requires to be investigated as we found that normalization simply by dose only achieved comparable results to ones even without normalization. The last limitation is that the logistic regression classifier used for classifying subjects in this study is probably not the best choice. Other machine learning techniques, e.g., support vector machines, could be used to further improve the performance. However, the main goal of this work is to propose and validate a measure with short scan time and acceptable accuracy in differentiating mild AD and HC subjects.

In the future, AQI can be tested on differentiating MCI from AD and HC and predicting MCI progression. AQI can be

applied in combination with MRI imaging, which may provide stronger evidence and achieve greater accuracy than using either of the imaging modality alone (Patel et al., 2020). Another possibility is to explore whether AQI can be applied to PET data obtained with other amyloid imaging agents, such as ^{18}F-Florbetapir. It is expected ^{18}F-Florbetapir and PiB share similar kinetics, which could enable AQI to simplify the ^{18}F-Florbetapir scan protocol.

DATA AVAILABILITY STATEMENT

Data were provided by OASIS-3 dataset, which is publicly available via the website: https://www.oasis-brains.org/ (principal investigators: T. Benzinger, D. Marcus, and J. Morris; NIH P50AG00561, P30NS09857781, P01AG026276, P01AG003991, R01AG043434, UL1TR000448, and R01EB009352).

ETHICS STATEMENT

The studies involving human participants were reviewed and approved by Washington University School of Medicine. The patients/participants provided their written informed consent to participate in this study.

AUTHOR CONTRIBUTIONS

TS and CS: conception and design. TS, YY, DL, XL, HZ, and MW: administrative support. CS and TS: provision of study materials or patients. CS, TS, ZW, and HC: collection and assembly of data. TS, YY, HW, ZW, HC, YB, and XL: data analysis and interpretation. All authors: manuscript writing and final approval of manuscript.

FUNDING

This work is supported by the Scientific Instrument Innovation Team of the Chinese Academy of Sciences (GJJSTD20180002), the Key Laboratory for Magnetic Resonance and Multimodality Imaging of Guangdong Province (2020B1212060051), the Chinese Academy of Sciences Engineering Laboratory for Medical Imaging Technology and Equipment (KFJ-PTXM-012), the National Natural Science Foundation of China (Nos. 81729003 and 61871373), the Pearl River Talent Recruitment Program of Guangdong Province (No. 2019QN01Y986), the Shenzhen Science and Technology Program (JCYJ20210324115810030), and the Shenzhen Peacock Plan Team Program (KQTD20180413181834876).

REFERENCES

Bacskai, B. J., Frosch, M. P., Freeman, S. H., Raymond, S. B., Augustinack, J. C., Johnson, K. A., et al. (2007). Molecular imaging with pittsburgh compound b confirmed at autopsy: a case report. *Arch. Neurol.* 64, 431–434. doi: 10.1001/archneur.64.3.431

Blomquist, G., Engler, H., Nordberg, A., Ringheim, A., Wall, A., Forsberg, A., et al. (2008). Unidirectional influx and net accumulation of PIB. *The open neuroimaging journal* 2, 114–125. doi: 10.2174/1874440000802010114

Cairns, N. J., Ikonomovic, M. D., Benzinger, T., Storandt, M., Fagan, A. M., Shah, A. R., et al. (2009). Absence of Pittsburgh compound B detection of cerebral amyloid beta in a patient with clinical, cognitive, and cerebrospinal fluid markers of Alzheimer disease: a case report. *Arch. Neurol.* 66, 1557–1562. doi: 10.1001/archneurol.2009.279

Dinges, J., Nekolla, S. G., and Bundschuh, R. A. (2013). Motion artifacts in oncological and cardiac PET imaging. *PET Clin.* 8, 1–9. doi: 10.1016/j.cpet.2012.10.001

Engler, H., Forsberg, A., Almkvist, O., Blomquist, G., Larsson, E., Savitcheva, I., et al. (2006). Two-year follow-up of amyloid deposition in patients with Alzheimer's disease. *Brain.* 129, 2856–2866. doi: 10.1093/brain/awl178

Forsberg, A., Almkvist, O., Engler, H., Wall, A., Långström, B., and Nordberg, A. (2010). High PIB retention in Alzheimer's disease is an early event with complex relationship with CSF biomarkers and functional parameters. *Curr. Alzheimer Res.* 7, 56–66. doi: 10.2174/156720510790274446

Forsberg, A., Engler, H., Almkvist, O., Blomquist, G., Hagman, G., Wall, A., et al. (2008). PET imaging of amyloid deposition in patients with mild cognitive impairment. *Neurobiol. Aging.* 29, 1456–1465. doi: 10.1016/j.neurobiolaging.2007.03.029

Gjedde, A., Aanerud, J., Braendgaard, H., and Rodell, A. (2013). Blood-brain transfer of Pittsburgh compound B in humans. *Front. Aging Neurosci.* 5. doi: 10.3389/fnagi.2013.00070

Ikonomovic, M. D., Klunk, W. E., Abrahamson, E. E., Mathis, C. A., Price, J. C., Tsopelas, N. D., et al. (2008). Post-mortem correlates of in vivo PiB-PET amyloid imaging in a typical case of Alzheimer's disease. *Brain.* 131, 1630–1645. doi: 10.1093/brain/awn016

Jellinger, K. A. (1998). The neuropathological diagnosis of Alzheimer disease. *J. Neural. Transm. Suppl.* 53, 97–118. doi: 10.1007/978-3-7091-6467-9_9

Jia, J., Sun, B., Guo, Z., Zhang, J., Tian, J., Tang, H., et al. (2011). Positron emission tomography with Pittsburgh compound B in diagnosis of early stage Alzheimer's disease. *Cell Biochem. Biophys.* 59, 57–62. doi: 10.1007/s12013-010-9111-2

Klunk, W. E., Engler, H., Nordberg, A., Wang, Y., Blomqvist, G., Holt, D. P., et al. (2004). Imaging brain amyloid in Alzheimer's disease with Pittsburgh Compound-B. *Ann. Neurol.* 55, 306–319. doi: 10.1002/ana.20009

Lammertsma, A. A., and Hume, S. P. (1996). Simplified reference tissue model for PET receptor studies. *Neuroimage.* 4, 153–158. doi: 10.1006/nimg.1996.0066

LaMontagne, P. J., Benzinger, T. L., Morris, J. C., Keefe, S., Hornbeck, R., Xiong, C., et al. (2019). OASIS-3: longitudinal neuroimaging, clinical, and cognitive dataset for normal aging and Alzheimer disease. *medRxiv.* 2019.2012.2013.19014902. doi: 10.1101/2019.12.13.19014902

Liu, H., Nai, Y.-H., Saridin, F., Tanaka, T., O.', Doherty, J., Hilal, S., et al. (2021). Improved amyloid burden quantification with nonspecific estimates using deep learning. *Eur. J. Nucl. Med.* 48, 1842–1853. doi: 10.1007/s00259-020-05131-z

Logan, J., Fowler, J. S., Volkow, N. D., Wang, G. J., Ding, Y. S., and Alexoff, D. L. (1996). Distribution volume ratios without blood sampling from graphical analysis of PET data. *J. Cereb. Blood Flow Metab.* 16, 834–840. doi: 10.1097/00004647-199609000-00008

Lowe, V. J., Kemp, B. J., Jack, C. R., Senjem, M., Weigand, S., Shiung, M., et al. (2009). Comparison of 18F-FDG and PiB PET in cognitive impairment. *J. Nucl. Med.* 50, 878–886. doi: 10.2967/jnumed.108.058529

Meyer, P. T., Hellwig, S., Amtage, F., Rottenburger, C., Sahm, U., Reuland, P., et al. (2011). Dual-biomarker imaging of regional cerebral amyloid load and neuronal activity in dementia with PET and ^{11}C-labeled pittsburgh compound B. *J. Nuclear Med.* 52, 393–400. doi: 10.2967/jnumed.110.083683

Morris, J. C., Weintraub, S., Chui, H. C., Cummings, J., DeCarli, C., Ferris, S., et al. (2006). The uniform data set (UDS): clinical and cognitive variables and descriptive data from alzheimer disease centers. *Alzheimer Dis Assoc Disord.* 20:210–6. doi: 10.1097/01.wad.0000213865.09806.92

O'Bryant, S. E., Waring, S. C., Cullum, C. M., Hall, J., Lacritz, L., Massman, P. J., et al. (2008). a*Arch. Neurol.* 65, 1091–1095. doi: 10.1001/archneur.65.8.1091

Patel, K. P., Wymer, D. T., Bhatia, V. K., Duara, R., and Rajadhyaksha, C. D. (2020). Multimodality imaging of dementia: clinical importance and role of integrated anatomic and molecular imaging. *RadioGraphics.* 40, 200–222. doi: 10.1148/rg.2020190070

Peretti, D. E., Reesink, F. E., Doorduin, J., De Jong, B. M., De Deyn, P. P., Dierckx, R., et al. (2019a). Optimization of the k2′ parameter estimation for the pharmacokinetic modeling of dynamic PIB PET scans using SRTM2. *Front. Phys.* 7. doi: 10.3389/fphy.2019.00212

Peretti, D. E., Vállez García, D., Reesink, F. E., Doorduin, J., De Jong, B. M., De Deyn, P. P., et al. (2019b). Diagnostic performance of regional cerebral blood flow images derived from dynamic PIB scans in Alzheimer's disease. *EJNMMI Res.* 9, 59. doi: 10.1186/s13550-019-0528-3

Peretti, D. E., Vállez García, D., Reesink, F. E., Van Der Goot, T., De Deyn, P. P., De Jong, B. M., et al. (2019c). Relative cerebral flow from dynamic PIB scans as an alternative for FDG scans in Alzheimer's disease PET studies. *PLoS ONE.* 14, e0211000. doi: 10.1371/journal.pone.0211000

Ponto, L. L. B., Moser, D. J., Menda, Y., Harlynn, E. L., Devries, S. D., Oleson, J. J., et al. (2019). Early phase PIB-PET as a surrogate for global and regional cerebral blood flow measures. *J. Neuroimag.* 29, 85–96. doi: 10.1111/jon.12582

Price, J. C., Klunk, W. E., Lopresti, B. J., Lu, X., Hoge, J. A., Ziolko, S. K., et al. (2005). Kinetic modeling of amyloid binding in humans using PET imaging and Pittsburgh Compound-B. *J. Cereb. Blood Flow Metab.* 25, 1528–1547. doi: 10.1038/sj.jcbfm.9600146

Rabinovici, G. D., Gatsonis, C., Apgar, C., Chaudhary, K., Gareen, I., Hanna, L., et al. (2019). Association of amyloid positron emission tomography with subsequent change in clinical management among medicare beneficiaries with mild cognitive impairment or dementia. *JAMA* 321, 1286–1294. doi: 10.1001/jama.2019.2000

Rodell, A., Aanerud, J., Braendgaard, H., and Gjedde, A. (2013). Washout allometric reference method (WARM) for parametric analysis of [11C]PIB in human brains. *Front. Aging Neurosci.* 5. doi: 10.3389/fnagi.2013.00045

Sato, K., Fukushi, K., Shinotoh, H., Shimada, H., Tanaka, N., Hirano, S., et al. (2012). A short-scan method for k3 estimation with moderately reversible PET ligands: Application of irreversible model to early-phase PET data. *NeuroImage.* 59, 3149–3158. doi: 10.1016/j.neuroimage.2011.10.087

Sendi, M. S. E., Zendehrouh, E., Miller, R. L., Fu, Z., Du, Y., Liu, J., et al. (2021). Alzheimer's disease projection from normal to mild dementia reflected in functional network connectivity: a longitudinal study. *Front. Neural Circuits.* 14. doi: 10.3389/fncir.2020.593263

Sureshbabu, W., and Mawlawi, O. (2005). PET/CT Imaging Artifacts. *J. Nucl. Med. Technol.* 33, 156–161.

Thal, D. R., Rüb, U., Orantes, M., and Braak, H. (2002). Phases of A beta-deposition in the human brain and its relevance for the development of AD. *Neurology.* 58, 1791–1800. doi: 10.1212/WNL.58.12.1791

Tibshirani, R. (1996). Regression shrinkage and selection via the lasso. *J R Stat Soc Series B.* 58, 267–288. doi: 10.1111/j.2517-6161.1996.tb02080.x

Tombaugh, T. N., and McIntyre, N. J. (1992). The Mini-Mental State Examination: A Comprehensive Review. *J. Am. Geriatr. Soc.* 40, 922–935. doi: 10.1111/j.1532-5415.1992.tb01992.x

Tomiyama, T., Nagata, T., Shimada, H., Teraoka, R., Fukushima, A., Kanemitsu, H., et al. (2008). A new amyloid beta variant favoring oligomerization in Alzheimer's-type dementia. *Ann. Neurol.* 63, 377–387. doi: 10.1002/ana.21321

Tryputsen, V., Dibernardo, A., Samtani, M., Novak, G. P., Narayan, V. A., and Raghavan, N. (2015). Optimizing regions-of-interest composites for capturing treatment effects on brain amyloid in clinical trials. *J. Alzheimers Dis.* 43, 809–821. doi: 10.3233/JAD-131979

Winblad, B., Amouyel, P., Andrieu, S., Ballard, C., Brayne, C., Brodaty, H., et al. (2016). Defeating Alzheimer's disease and other dementias: a priority for European science and society. *Lancet Neurol.* 15, 455–532. doi: 10.1016/S1474-4422(16)00062-4

Conflict of Interest: The authors declare that the research was conducted in the absence of any commercial or financial relationships that could be construed as a potential conflict of interest.

Publisher's Note: All claims expressed in this article are solely those of the authors and do not necessarily represent those of their affiliated organizations, or those of the publisher, the editors and the reviewers. Any product that may be evaluated in this article, or claim that may be made by its manufacturer, is not guaranteed or endorsed by the publisher.

frontiers | Frontiers in Aging Neuroscience

SYSTEMATIC REVIEW
published: 21 April 2022
doi: 10.3389/fnagi.2022.841696

Diagnostic Performance of Generative Adversarial Network-Based Deep Learning Methods for Alzheimer's Disease: A Systematic Review and Meta-Analysis

Changxing Qu[1,2†], Yinxi Zou[1,3†], Yingqiao Ma[1†], Qin Chen[4], Jiawei Luo[5], Huiyong Fan[6], Zhiyun Jia[1], Qiyong Gong[1,7] and Taolin Chen[1,8,9*]*

[1] Huaxi MR Research Center (HMRRC), Department of Radiology, West China Hospital, Sichuan University, Chengdu, China, [2] State Key Laboratory of Oral Diseases, National Clinical Research Center for Oral Diseases, West China School of Stomatology, Sichuan University, Chengdu, China, [3] West China School of Medicine, Sichuan University, Chengdu, China, [4] Department of Neurology, West China Hospital, Sichuan University, Chengdu, China, [5] West China Biomedical Big Data Center, West China Clinical Medical College of Sichuan University, Chengdu, China, [6] College of Education Science, Bohai University, Jinzhou, China, [7] Department of Radiology, West China Xiamen Hospital of Sichuan University, Xiamen, China, [8] Research Unit of Psychoradiology, Chinese Academy of Medical Sciences, Chengdu, China, [9] Functional and Molecular Imaging Key Laboratory of Sichuan Province, Department of Radiology, West China Hospital of Sichuan University, Chengdu, China

OPEN ACCESS

Edited by:
Wei Cheng,
Fudan University, China

Reviewed by:
Yi Su,
Banner Alzheimer's Institute, United States
Jiyang Jiang,
University of New South Wales, Australia

***Correspondence:**
Taolin Chen
tlchen@scu.edu.cn
Qiyong Gong
qiyonggong@hmrrc.org.cn

[†]These authors share first authorship

Specialty section:
This article was submitted to Alzheimer's Disease and Related Dementias, a section of the journal Frontiers in Aging Neuroscience

Received: *22 December 2021*
Accepted: *03 March 2022*
Published: *21 April 2022*

Citation:
Qu C, Zou Y, Ma Y, Chen Q, Luo J, Fan H, Jia Z, Gong Q and Chen T (2022) Diagnostic Performance of Generative Adversarial Network-Based Deep Learning Methods for Alzheimer's Disease: A Systematic Review and Meta-Analysis. Front. Aging Neurosci. 14:841696. doi: 10.3389/fnagi.2022.841696

Alzheimer's disease (AD) is the most common form of dementia. Currently, only symptomatic management is available, and early diagnosis and intervention are crucial for AD treatment. As a recent deep learning strategy, generative adversarial networks (GANs) are expected to benefit AD diagnosis, but their performance remains to be verified. This study provided a systematic review on the application of the GAN-based deep learning method in the diagnosis of AD and conducted a meta-analysis to evaluate its diagnostic performance. A search of the following electronic databases was performed by two researchers independently in August 2021: MEDLINE (PubMed), Cochrane Library, EMBASE, and Web of Science. The Quality Assessment of Diagnostic Accuracy Studies-2 (QUADAS-2) tool was applied to assess the quality of the included studies. The accuracy of the model applied in the diagnosis of AD was determined by calculating odds ratios (ORs) with 95% confidence intervals (CIs). A bivariate random-effects model was used to calculate the pooled sensitivity and specificity with their 95% CIs. Fourteen studies were included, 11 of which were included in the meta-analysis. The overall quality of the included studies was high according to the QUADAS-2 assessment. For the AD vs. cognitively normal (CN) classification, the GAN-based deep learning method exhibited better performance than the non-GAN method, with significantly higher accuracy (OR 1.425, 95% CI: 1.150–1.766, P = 0.001), pooled sensitivity (0.88 vs. 0.83), pooled specificity (0.93 vs. 0.89), and area under the curve (AUC) of the summary receiver operating characteristic curve (SROC) (0.96 vs. 0.93). For the progressing MCI (pMCI) vs. stable MCI (sMCI) classification, the GAN method

exhibited no significant increase in the accuracy (OR 1.149, 95% CI: 0.878–1.505, P = 0.310) or the pooled sensitivity (0.66 vs. 0.66). The pooled specificity and AUC of the SROC in the GAN group were slightly higher than those in the non-GAN group (0.81 vs. 0.78 and 0.81 vs. 0.80, respectively). The present results suggested that the GAN-based deep learning method performed well in the task of AD vs. CN classification. However, the diagnostic performance of GAN in the task of pMCI vs. sMCI classification needs to be improved.

Systematic Review Registration: [PROSPERO], Identifier: [CRD42021275294].

Keywords: generative adversarial networks (GANs), Alzheimer's disease, mild cognitive impairment (MCI), diagnosis, psychoradiology, systematic review, meta-analysis

INTRODUCTION

Alzheimer's disease (AD) is the most common form of dementia and is characterized by a progressive decline in memory and other cognitive functions. Notably, the pathophysiological processes of AD begin decades before clinical symptoms appear (Sperling et al., 2011; Atri, 2019; Matsuda et al., 2019); thus, early diagnosis and intervention are particularly important in AD management (Martí-Juan et al., 2020; Ansart et al., 2021). Mild cognitive impairment (MCI) is the prodromal stage, with symptoms occurring up to decades before dementia onset (Petersen, 2004; Misra et al., 2009). Approximately 10–15% of patients with MCI may progress to AD (pMCI) each year (Petersen et al., 2001), while the remaining patients may remain stable in the MCI stage (sMCI) (Li et al., 2016; Spasov et al., 2019). Studies examining the difference between AD and cognitively normal groups and between patients with pMCI and sMCI might facilitate the prediction of disease progression and help to provide the time window for administering potential disease-modifying therapy.

Neuroimaging biomarkers have been widely used in studies of AD to explain the underlying pathophysiological processes (McKhann et al., 2011; Chetelat, 2018). According to the National Institute on Aging and the Alzheimer's Association (NIA-AA) research framework, biomarkers for the AD continuum were classified as AT(N) for amyloid, tau and neurodegeneration (Jack et al., 2016). A indicates amyloid-beta (Aβ) protein deposition, as reflected on amyloid positron emission tomography (PET) images (Jack et al., 2008). T indicates tau protein accumulation, as reflected by tau PET imaging (Cho et al., 2016). N indicates biomarkers of neurodegeneration or injury, including a reduction in glucose metabolism in the temporoparietal region, as reflected by fluorodeoxyglucose positron emission tomography (FDG-PET) imaging, and hippocampal atrophy observed using structural magnetic resonance imaging (MRI) (Jagust et al., 2007; Jack, 2011; Arbizu et al., 2018). The development of diagnostic methods based on these neuroimaging biomarkers is important to improve the diagnosis of AD, especially in the prodromal stage (Chetelat, 2018).

Artificial intelligence (AI) has been increasingly important in clinical diagnosis for the past few years. Psychoradiology with AI are emerging research directions for brain disorders (Lui et al., 2016). As one of the most important AI techniques, deep learning performs well in image processing for image detection, classification, and segmentation (Lee et al., 2017; Suzuki, 2017). It has been applied in some studies to achieve an accurate diagnosis of AD based on features extracted from AD-related images. Multiple deep learning models are being applied for the early detection and prediction of AD, such as convolutional neural networks (CNNs) (Zhou J. et al., 2021), autoencoders (AEs) (Ju et al., 2019), and deep belief networks (DBNs) (Shen et al., 2019; Lin E. et al., 2021).

The generative adversarial network (GAN) is a recent model first proposed by Goodfellow et al. (2014). It is a generative model mainly used for image processing based on the adversarial training of two components: the generative network (G) and the discriminative network (D). Fake images generated by this model, which highly resemble the real images, might exercise the same function as real images in disease diagnosis. In recent years, GAN has shown application value in diagnosing AD by providing image processing support, including quality improvement for low-dose PET images or 1.5-T MRIs (Wang et al., 2018; Ouyang et al., 2019; Zhou X. et al., 2021), predicting brain images at a future time point (Wegmayr et al., 2019; Zhao et al., 2021), data augmentation for network training (Islam and Zhang, 2020; Sajjad et al., 2021), and interconversion of PET and MRI data (Gao et al., 2021; Lin W. et al., 2021). With the GAN-based deep-learning classification framework, a more accurate diagnosis of AD is promising and may be achieved.

Some recent reviews reported the application of GAN in AD predictions and image classification. Logan et al. (2021) reported the application value of GAN in improving image quality and converting the modality. However, only two studies were included, and the results for the AD diagnosis were not reported. Lin E. et al. (2021) reported the application of GAN in a mouse model of AD with genomic data. Both studies were not comprehensive and did not include any data analysis for the AD diagnosis. To our knowledge, a gap exists in the meta-analysis for GAN application in the diagnosis of AD. This study systemically reviewed studies examining the application of GAN-based deep learning methods in the diagnosis of AD and subsequently performed a meta-analysis evaluating their diagnostic performance to fill this gap.

MATERIALS AND METHODS

This study was conducted according to the Preferred Reporting Items for a Systematic Review and Meta-analysis of Diagnostic Test Accuracy Studies (PRISMA-DTA) statement (McInnes et al., 2018).

Protocol and Registration

This study was registered on PROSPERO with the registration number CRD42021275294.

Focused Question

The focused question of this study is what is the performance of GAN in the diagnosis of AD?

Patients, Intervention, Comparison, Outcome and Study Design Criteria

This study followed the Patients, Intervention, Comparison, Outcome and Study design (PICOS) criteria:

Patients (P): patients with AD or MCI.

Intervention (I): GAN-based deep learning methods for the diagnosis of AD. Specifically, the task of AD diagnosis referred to the AD vs. CN classification and pMCI vs. sMCI classification.

Comparison (C): the deep learning methods without GAN.

Outcome (O): the performance for the diagnosis of AD, including accuracy, sensitivity, specificity, and the area under the curve (AUC) of the summary receiver operating characteristic curve (SROC).

Study design (S): studies using neuroimaging data.

Literature Search

A search of the following electronic databases was performed by two researchers (CQ and YZ) independently in August 2021: MEDLINE (PubMed), Cochrane Library, EMBASE, and Web of Science. The database coverage was up to August 2021. In addition, a manual search was conducted of references of the initially included articles and relevant reviews. The detailed search strategy is displayed in **Supplementary Material**.

Inclusion and Exclusion Criteria

The inclusion and exclusion criteria followed the PICOS criteria.

Inclusion criteria: (1) participants who were clinically diagnosed with AD or MCI; (2) the application of GAN in the deep learning models; (3) report of the performance for diagnosis; and (4) diagnosis based on neuroimaging data (PET, MRI, etc.).

Exclusion criteria: (1) participants diagnosed with other brain disorders, such as brain tumors; (2) report of an assessment of generated image quality only, such as the peak signal to noise ratio (PSNR) and structural similarity (SSIM); (3) diagnosis based on other subjects rather than images; (4) conference abstracts (published abstracts of papers participating in academic conferences without the full text), editorials, letters, or review articles.

Article Screening

Two researchers (CQ and YZ) independently performed the screen according to the PICOS criteria. The initial screen was performed by reading titles and abstracts. The full text was then read for further screening. A consensus was finally reached through negotiation in cases of any divergence between the two researchers.

Data Extraction

A self-developed data extraction form was used by two researchers (CQ and YZ) independently. The following data were collected: author, year, country, data, participants, structure of the model, type of GAN, function of GAN, classification task, and performance.

Quality Assessment

The quality of the included studies was assessed by two researchers independently with the Quality Assessment of Diagnostic Accuracy Studies-2 (QUADAS-2) tool. Assessment domains were as follows: risk of bias (patient selection, index test, reference standard, and flow and timing) and applicability concerns (patient selection, index test, and reference standard).

Data Analysis

Stata 15 and MetaDiSc 1.4 software were used to analyze the data. For the accuracy analysis, researchers calculated the odds ratio (OR) with a 95% confidence interval (CI). Cochran's Q-test and Higgins inconsistency index (I^2)-test were performed to test heterogeneity. A fixed-effects model was used when non-significant heterogeneity was observed ($P > 0.05$ and $I^2 < 50\%$); otherwise ($P < 0.05$ or $I^2 > 50\%$), a random-effects model was applied.

The true positive (TP), false negative (FN), false-positive (FP), and true negative (TN) were calculated, and 2×2 tables were plotted based on the performance for diagnosis (accuracy, sensitivity, specificity, and other parameters) reported. Based on the data calculated above, researchers adopted a bivariate random-effects model to calculate the pooled sensitivity and specificity with their 95% CIs. An SROC curve was constructed, and the AUC was calculated. The Spearman correlation coefficient was obtained, and a value greater than 0.5 with $P < 0.05$ indicated the presence of threshold effects. Heterogeneity was assessed using the same method described for accuracy. The narrative analysis was adopted for the studies excluded from the meta-analysis.

According to the pooled sensitivity and specificity of neuroimaging biomarkers for diagnosis reported in some meta-analyses and rules for evaluating the AUC of classification models (Bloudek et al., 2011; Morris et al., 2016), we proposed that a method with great potential for clinical application should meet the following criteria: the pooled sensitivity or specificity was greater than 0.90 and the AUC was greater than 0.90.

RESULTS

Study Selection

In total, 364 articles were obtained by performing electronic and manual searches. Two hundred two articles were excluded during the initial screen, and 21 articles were selected after reading the full text. Eventually, 14 articles were included in this study. Researchers conducted a meta-analysis on 11 of these studies. The study selection process is displayed in **Figure 1**.

Characteristics of the Included Studies

A detailed description of the study characteristics is provided in **Table 1** and **Figure 2**. Regarding the publication year, all the included articles were published between 2018 and 2021, and more than half of them (8/14) were published in 2021 (**Figure 2A**; Baydargil et al., 2021; Gao et al., 2021; Han et al., 2021; Kang et al., 2021; Lin W. et al., 2021; Sajjad et al., 2021; Zhao et al., 2021; Zhou X. et al., 2021). Regarding the data source, neuroimaging data analyzed in 13 studies were mainly from the Alzheimer's Disease Neuroimaging Initiative (ADNI) (Pan et al., 2018; Yan et al., 2018; Wegmayr et al., 2019; Islam and Zhang, 2020; Kim et al., 2020; Shin et al., 2020; Baydargil et al., 2021; Gao et al., 2021; Kang et al., 2021; Lin W. et al., 2021; Sajjad et al., 2021; Zhao et al., 2021; Zhou X. et al., 2021), and some data were from the Open Access Series of Imaging Studies (OASIS) (Han et al., 2021; Zhao et al., 2021), the Australian Imaging, Biomarker and Lifestyle Flagship Study of Aging (AIBL) and the National Alzheimer's Coordinating Center (NACC) databases (**Figure 2B**; Zhou X. et al., 2021). Two studies established a test set from the collection of clinical data (Wegmayr et al., 2019; Kim et al., 2020). Regarding the data modality, 36 percent (5/14) of studies used data from two modalities (**Figure 2C**; Pan et al., 2018; Yan et al., 2018; Shin et al., 2020; Gao et al., 2021; Lin W. et al., 2021). One study used MRI and other clinical data (age, sex, education level, and other parameters) (Zhao et al., 2021). A deep convolutional GAN (DCGAN) was applied in 3 studies (Islam and Zhang, 2020; Kang et al., 2021; Sajjad et al., 2021), and conditional GAN (CGAN) was applied in 2 studies (**Figure 2E**; Yan et al., 2018; Shin et al., 2020). The type of GAN in the remaining studies varied. For the diagnostic task, 11 studies focused on the AD vs. CN classification (Pan et al., 2018; Islam and Zhang, 2020; Kim et al., 2020; Shin et al., 2020; Baydargil et al., 2021; Gao et al., 2021; Han et al., 2021; Kang et al., 2021; Lin W. et al., 2021; Sajjad et al., 2021; Zhou X. et al., 2021), and 7 studies were devoted to the pMCI vs. sMCI classification (**Figure 2D**; Pan et al., 2018; Yan et al., 2018; Wegmayr et al., 2019; Gao et al., 2021; Kang et al., 2021; Lin W. et al., 2021; Zhao et al., 2021). For the assessment of the diagnostic performance, accuracy was reported in all studies, while sensitivity and specificity were reported in 6 studies examining the AD vs. CN classification (Pan et al., 2018; Kim et al., 2020; Gao et al., 2021; Kang et al., 2021; Lin W. et al., 2021; Zhou X. et al., 2021) and 4 studies examining the pMCI vs. sMCI classification (Pan et al., 2018; Gao et al., 2021; Kang et al., 2021; Lin W. et al., 2021).

Regarding the function of image processing, one study applied GAN to generate higher-quality MRI data. Two studies stimulated the process of brain aging observed in MRI images (Wegmayr et al., 2019; Zhao et al., 2021). Two studies used GAN to augment imaging data and improve the training effects of the classifiers (Islam and Zhang, 2020; Sajjad et al., 2021). Five studies achieved conversion between PET and MRI data to provide supplementary data (Pan et al., 2018; Yan et al., 2018; Shin et al., 2020; Gao et al., 2021; Lin W. et al., 2021).

Generative Adversarial Networks

GAN is composed of a G and a D. The goal of the GAN is to generate the image most similar to the real image through G-D competitions. As a random vector input, G generates a fake image. The goal of G is to make it as close as possible to the real image. As the generated and corresponding real image input, D provides a probability for the generated image being real (1 indicates real and 0 indicates fake). The goal of D is to identify fake images as accurately as possible. With the continuous adversarial training on G and D, the similarity between the image generated by G and the real image is maximized, and concurrently, the accuracy of D in identifying fake images is maximized. When G and D reach a Nash equilibrium state through training (the probability output by D is 1/2 each time), the model reaches the optimum. At this time, GAN outputs an image closest to the real image.

Except for the function of image processing, GANs have high structural flexibility. This property allows any differential function to be applied in G and D construction and cooperates with other recognized deep learning networks (such as CNN) to constitute the deep generative model. Yan et al. (2018) and Zhao et al. (2021) built the G based on U-net, and Yan et al. (2018) and Lin W. et al. (2021) established the Markovian-based D (PatchGAN). Additionally, the GAN framework embraces all types of loss functions and constraints, which provides individualized methods according to different tasks. The modified GAN was applied in the included studies and contributed to an improved diagnosis of AD. Some improvements in the structure of GAN and their contributions are shown in **Figure 3**. For the generator, Baydargil et al. (2021) proposed a parallel structure, with CNN extracting local features and DCN extracting global features. The generator produces images that are close to the real images using comprehensive features. Gao et al. (2021) and Han et al. (2021) added the self-attention module to focus the attention of the algorithm on specific regions instead of focusing indiscriminately on the whole image, reducing redundant information extraction. For the discriminator, Gao et al. (2021) added the task-induced mechanism. The task-induced discriminator focused not only on the quality of the generated images but also on whether AD pathological information was retained. In addition, the results of the downstream classification task were fed back to the generator and discriminator during training in the study by Zhou X. et al. (2021). This training may ensure the classification performance of the generated images.

TABLE 1 | Characteristics of the included studies.

Authors	Year	Country	Data		Participants					Structure of the model	Type of GAN	Function of GAN	Task of classification	Performance						
			Source	Modality	AD	MCI	pMCI	sMCI	CN					Accuracy	Sensitivity	Specificity	F1-score	Recall	Precision	AUC
Pan et al. (2018)	2018	China	ADNI[a]	MRI+PET	358	–	205	465	429	Two-stage: GAN+ LM3IL[b]	cycleGAN	Modality conversion	AD vs. CN; pMCI vs. sMCI	0.92; 0.79	0.90; 0.55	0.94; 0.83	0.91; 0.41	–	–	0.96; 0.76
Islam and Zhang (2020)	2020	United States	ADNI	PET	98	–	–	–	105	Two-stage: GAN+CNN[c]	DCGAN[d]	Data augmentation	AD vs. CN	0.71	–	–	–	–	–	–
Kim et al. (2020)	2020	Korea	ADNI; clinical	PET	139	–	–	–	347	Two-stage: GAN+SVM[e]	BEGAN[f]	Feature extraction	AD vs. CN	0.94	0.92	0.97	–	–	–	0.98
Wegmayr et al. (2019)	2019	Switzerland	ADNI; clinical	MRI	–	–	89	116	–	Two-stage: GAN+CNN	WGAN[g]	Aging simulation	pMCI vs. sMCI	0.73	–	–	0.71	0.75	0.68	–
Yan et al. (2018)	2018	United Kingdom	ADNI	MRI+PET	–	–	58	50	–	Two-stage: GAN+ Resnet	cGAN[h]	Modality conversion	pMCI vs. sMCI	0.82	–	–	–	–	–	0.81
Baydargil et al. (2021)	2021	Korea	ADNI	PET	25	–	–	–	148	GAN only	GAN	Anomaly detection	AD vs. CN	–	–	–	–	–	–	0.75
Gao et al. (2021)	2021	China	ADNI	MRI+PET	352	–	234	342	427	Two-stage: GAN+ DCN[i]	TPA-GAN[j]	Modality conversion	AD vs. CN; pMCI vs. sMCI	0.93; 0.75	0.92; 0.71	0.94; 0.78	0.92; 0.70	–	–	0.96; 0.78
Han et al. (2021)	2021	Japan	OASIS[k]	MRI	96	152	–	–	576	GAN only	SAGAN[l]	Anomaly detection	AD vs. CN	–	–	–	–	–	–	0.89
Kang et al. (2021)	2021	China	ADNI	MRI	187	–	138	181	229	Ensemble learning: discriminator of GAN+VGG16+ ResNet50	DCGAN	Transfer learning	AD vs. CN; pMCI vs. sMCI	0.90; 0.63	0.94; 0.58	0.84; 0.64	–	–	–	0.90; 0.62
Lin W. et al. (2021)	2021	China	ADNI	MRI+PET	362	–	183	233	308	Two-stage: GAN+CNN	revGAN[m]	Modality conversion	AD vs. CN; pMCI vs. sMCI	0.89; 0.71	0.90; 0.74	0.88; 0.68	–	–	–	0.88; 0.74
Sajjad et al. (2021)	2021	Pakistan	ADNI	PET	30	–	–	–	42	Two-stage: GAN+VGG16	DCGAN	Data augmentation	AD vs. CN	0.83	–	–	0.88	0.86	0.91	–
Zhou X. et al. (2021)	2021	United States	ADNI; AIBL[n]; NACC[o]	MRI	411	–	–	–	678	Two-stage: GAN+FCN[p]	GAN	Quality improvement	AD vs. CN	0.82	0.74	0.89	0.79	–	–	–
Shin et al. (2020)	2020	Korea	ADNI	MRI+PET	162	675	–	–	428	GAN only	cGAN	Modality conversion; classification	AD vs. CN	0.85	–	–	–	0.84	0.84	–
Zhao et al. (2021)	2021	China	ADNI; OASIS	MRI+other information	151	341	–	–	113	Two-stage: GAN+DenseNet	mi-GAN[q]	Aging simulation	pMCI vs. sMCI	0.78	–	–	0.74	0.71	0.78	–

[a]Alzheimer's Disease Neuroimaging Initiative; [b]andmark-based Multimodal Multi-Instance Learning; [c]Convolutional Neural Network; [d]Deep Convolutional Generative Adversarial Network; [e] Support Vector Machine; [f]Boundary Equilibrium Generative Adversarial Network; [g]Wasserstein Generative Adversarial Network; [h]Conditional Generative Adversarial Network; [i]Dense Convolution Network; [j]Task-induced Pyramid and Attention Generative Adversarial Network; [k]Open Access Series of Imaging Studies; [l]Self Attention Generative Adversarial Network; [m]Reversible Generative Adversarial Network; [n]Australian Imaging, Biomarker and Lifestyle Flagship Study of Aging; [o]National Alzheimer's Coordinating Center; [p]Fully Convolutional Network; [q]Multi-information Generative Adversarial Network.

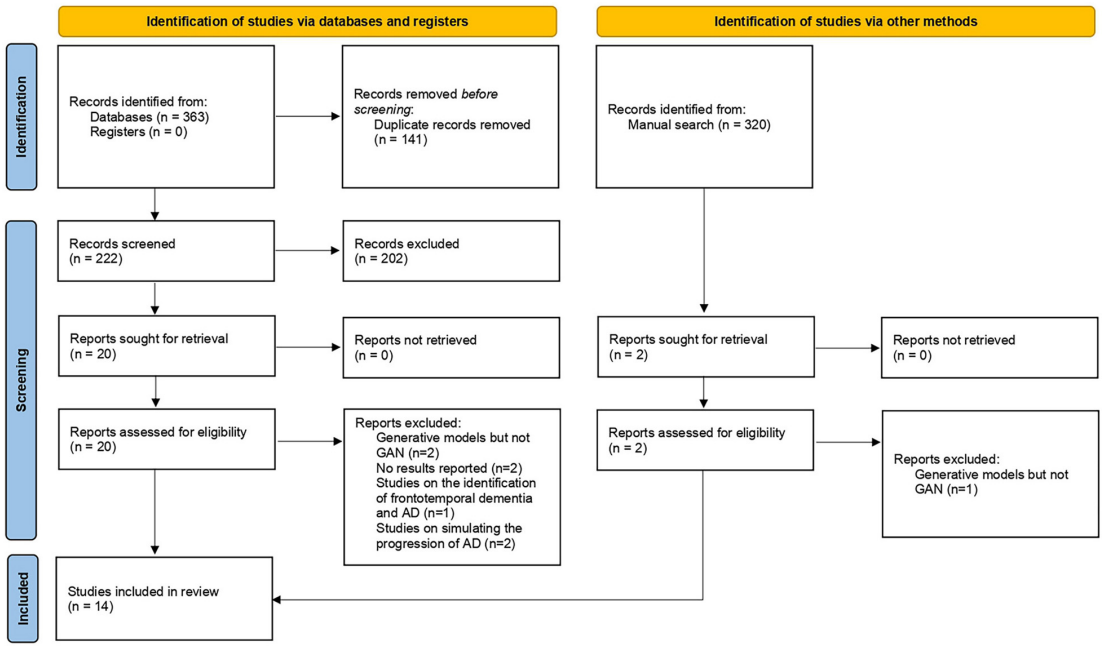

FIGURE 1 | Flowchart of the study selection process (PRISMA flow chart).

Quality Assessment

The quality assessment is described in detail in **Figure 2F**. Two studies had high concerns regarding the applicability (Baydargil et al., 2021; Han et al., 2021). In these studies, GAN was developed for anomaly detection, which is a screen for AD, while diagnosis is the main focus of our study. Applicability concerns of reference standard were low in the study by Han et al. (2021) because they clearly indicate that the diagnostic criteria for AD were the clinical dementia rating (CDR). In addition, the risk of bias in flow and timing was low in this study, as the authors ensured that the interval between CDR and MRI acquisition was as short as possible (Han et al., 2021).

Diagnostic Performance of Generative Adversarial Network-Based Deep Learning Methods

The Task of Alzheimer's Disease vs. Cognitively Normal Classification

Eleven studies focused on the application of GAN to the task of AD vs. CN classification (Pan et al., 2018; Islam and Zhang, 2020; Kim et al., 2020; Shin et al., 2020; Baydargil et al., 2021; Gao et al., 2021; Han et al., 2021; Kang et al., 2021; Lin W. et al., 2021; Sajjad et al., 2021; Zhou X. et al., 2021). Meta-analyses were performed on 6 studies reporting the accuracy, sensitivity, and specificity (Pan et al., 2018; Kim et al., 2020; Gao et al., 2021; Kang et al., 2021; Lin W. et al., 2021; Zhou X. et al., 2021). The results of the meta-analyses are shown in **Table 2**. For the accuracy assessment, the pooled OR was 1.425 (95% CI: 1.150–1.766; P = 0.001). Heterogeneity among the studies was not significant (I^2 = 37.4, P = 0.157), and the fixed-effects model was applied. This result revealed that GAN-based deep learning methods efficiently increased the accuracy of the task of AD vs. CN classification (**Figure 4**).

In the group with GAN, the pooled sensitivity was 0.88 (95% CI: 0.82–0.93), the pooled specificity was 0.93 (95% CI: 0.90–0.95), and the AUC of the SROC was 0.96 (95% CI: 0.94–0.97). Significant heterogeneity was observed in both sensitivity (I^2 = 87.27, P = 0) and specificity (I^2 = 61.30, P = 0.02). These values were much higher than those in the group without GAN (**Figures 5**, **6**). Threshold effects were absent in both groups according to Spearman's correlation coefficients (−0.029, P = 0.957; 0.257, P = 0.623). Generally, GAN-based deep learning methods were superior to the method without GAN and had great potential for clinical application based on the criteria described above.

The advantage of GAN was also observed in studies not included in the meta-analysis. Baydargil et al. (2021) reported that the AUC for the GAN-based method was 0.7, which was significantly higher than that of other methods. Han et al. (2021) reported the medical anomaly detection GAN (MAGAN) with an AUC of 0.89. Three studies showed higher accuracy of GAN-based methods (0.71, 0.85, and 0.83) (Islam and Zhang, 2020; Shin et al., 2020; Sajjad et al., 2021).

The Task of Progressing MCI vs. Stable MCI Classification

Seven studies focused on the application of GAN to the task of pMCI vs. sMCI classification (Pan et al., 2018; Yan et al., 2018; Wegmayr et al., 2019; Gao et al., 2021; Kang et al., 2021; Lin W. et al., 2021; Zhao et al., 2021). A meta-analysis was performed on 5 studies reporting the accuracy (Pan et al., 2018; Yan et al., 2018;

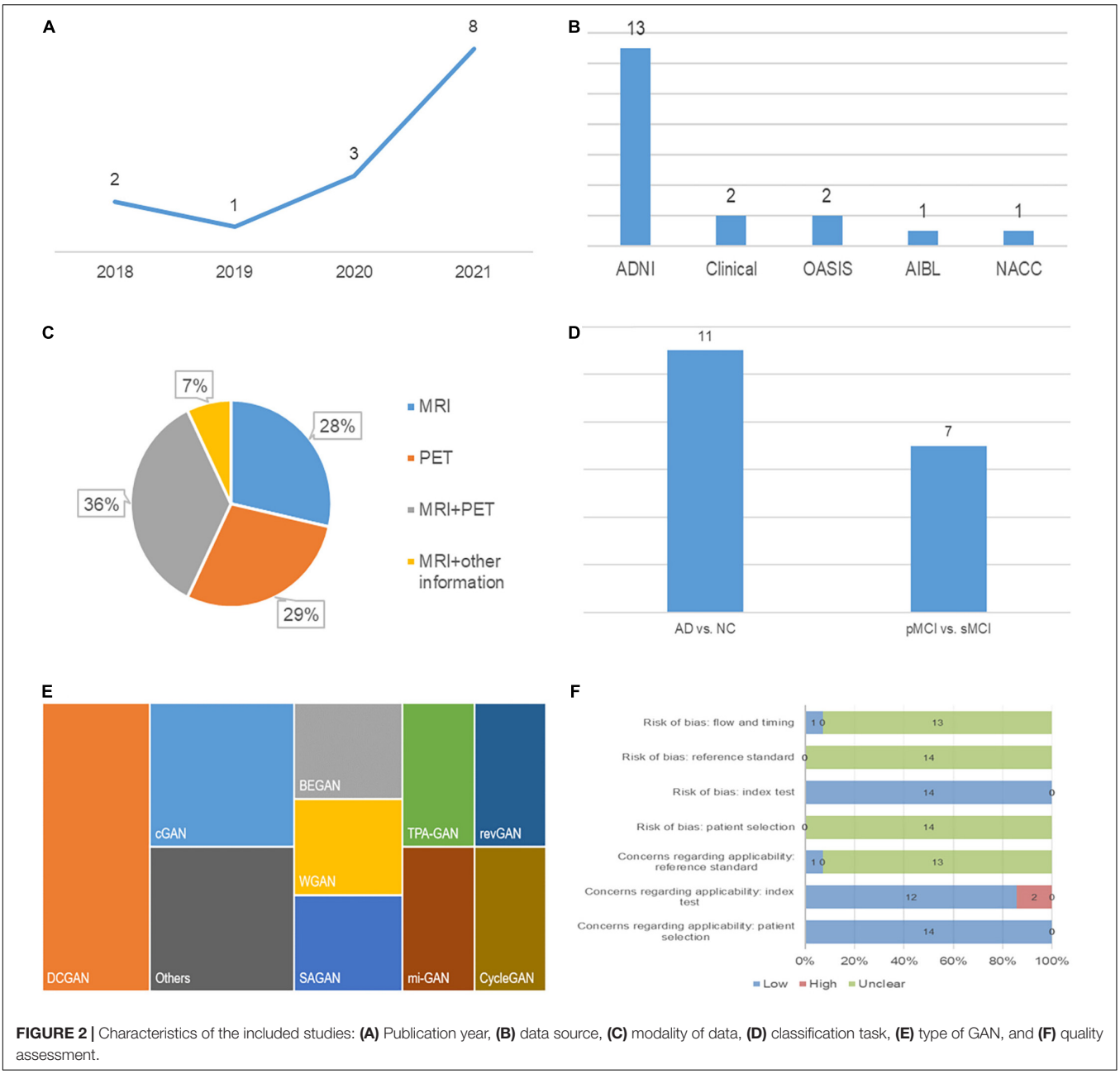

FIGURE 2 | Characteristics of the included studies: **(A)** Publication year, **(B)** data source, **(C)** modality of data, **(D)** classification task, **(E)** type of GAN, and **(F)** quality assessment.

Gao et al., 2021; Kang et al., 2021; Lin W. et al., 2021), and another was performed on 3 studies reporting sensitivity and specificity (Pan et al., 2018; Gao et al., 2021; Lin W. et al., 2021). For accuracy, the pooled OR was 1.149 (95% CI: 0.878–1.505; P = 0.310). Heterogeneity among the studies was not significant (I^2 = 0, P = 0.884), and the fixed-effects model was applied (**Figure 7**).

In the group with GAN, the pooled sensitivity was 0.66 (95% CI: 0.57–0.75), the pooled specificity was 0.81 (95% CI: 0.76–0.85), and the AUC of the SROC was 0.81 (95% CI: 0.72–0.89) (**Figure 8**). Low heterogeneity was observed in both sensitivity (I^2 = 33.50, P = 0.22) and specificity (I^2 = 25.10, P = 0.26). The specificity and AUC of the SROC were slightly higher than those in the group without GAN (**Figure 9**). Threshold effects were strong on both groups according to Spearman's correlation coefficients. Overall, in the task of pMCI vs. sMCI classification, the differences between the group with GAN and the group without GAN were not significant.

DISCUSSION

In this study, we analyzed the performance of GAN in diagnosing AD. GAN-based deep learning methods significantly increased the accuracy, sensitivity, and specificity in the task of AD vs. CN

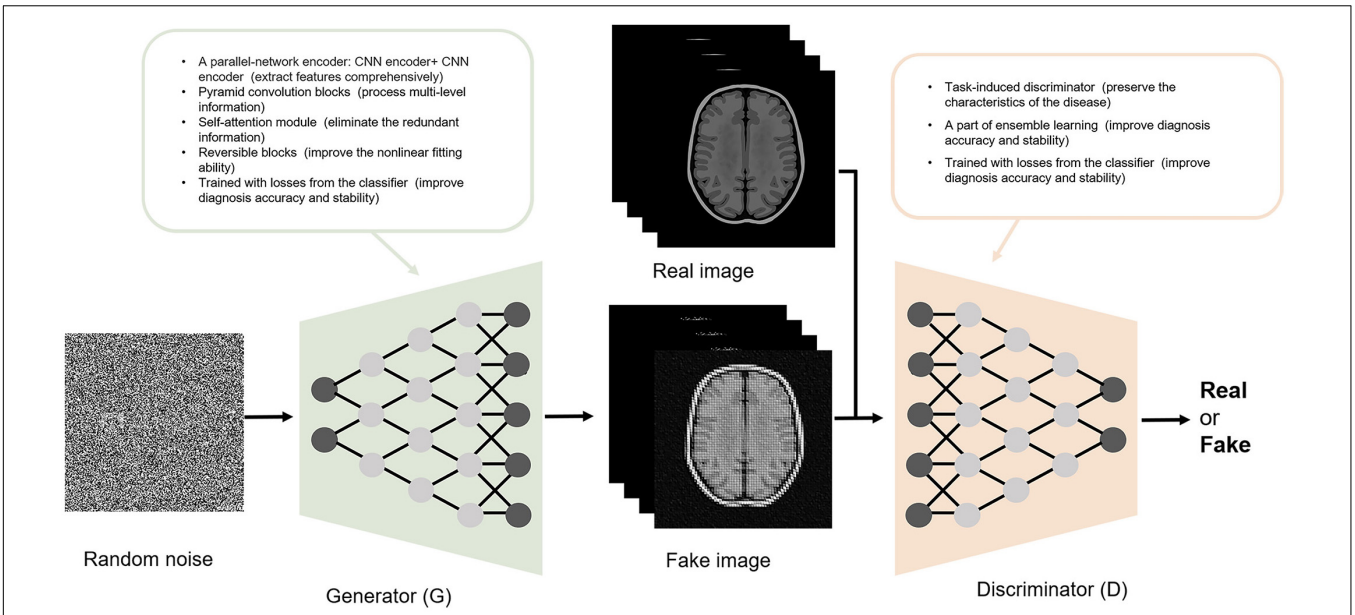

FIGURE 3 | The structure of the GAN and some improvements reported in the included studies.

classification. However, their diagnostic performance in the task of pMCI vs. sMCI classification was not remarkable.

Performance of Generative Adversarial Network-Based Deep Learning Methods in the Task of Alzheimer's Disease vs. Cognitively Normal Classification

Developments in disease-modifying therapy for AD have slowly progressed, with a failure rate of 99.6% in clinical trials (Cummings et al., 2014; Marinescu et al., 2019). Based on this information, identifying patients with early AD has become a focus in current studies (Chong and Sahadevan, 2005; Davis et al., 2018). Effective discrimination between AD and CN might help identify patients with AD in a timely manner and implement targeted interventions to delay disease progression.

Our study showed that GAN-based deep learning methods with different data modalities and different structures of the model all showed good performance in the task of AD vs. CN classification.

Regarding the data modality, some studies used MRI data, while others used PET data. Zhou X. et al. (2021) developed a GAN model to generate 3-T MRI scans from 1.5-T scans. Then, researchers trained a fully convolutional network (FCN) using generated 3-T MRI as inputs to complete the task of AD vs. CN classification. The classification efficiency was ensured by the concurrent training of the GAN and FCN. In that study, the FCN trained on the generated 3-T MRI data performed better than that trained on 1.5-T MRI data, with higher accuracy (0.84 vs. 0.82), sensitivity (0.74 vs. 0.67), and specificity (0.9037 vs. 0.8989). Sajjad et al. (2021) trained a VGG16 classifier on DCGAN-amplified PET data. Good performance of this classifier was reported in the task of AD vs. CN classification (accuracy: 0.83; recall: 0.86; precision: 0.91; F1-score: 0.88). Islam and Zhang (2020) reported an accuracy of 71.45% when using GAN-augmented PET data in the AD vs. CN classification, a 10% increase compared to the classifier trained on data without GAN augmentation.

Regarding the structure of the model, some researchers constructed anomaly detection models based on GAN to identify patients with AD. Baydargil et al. (2021) established a deep-learning model based on adversarial training for diagnosing AD. The G was an encoder-decoder network with the encoder a parallel feature extractor consisting of CNN and DCN, which were used for extracting local and global features from the real PET images, respectively. The G reconstructed a PET image based on these feature vectors and then input it to the encoder-type D for AD diagnosis. This study finally reported that the AUC of this method was 0.75. Han et al. (2021) proposed a medical anomaly detection GAN (MADGAN) using multiple adjacent brain MRI slice reconstruction to detect patients with AD by considering that AD is composed of the accumulation of subtle anomalies (AUC = 0.89).

Moreover, some researchers trained the classifier based on features extracted or images processed using GAN to complete the task of pMCI vs. sMCI classification. Kim et al. (2020) extracted features of two brain PET slices with the encoder-decoder D in GAN and trained an SVM classifier on these features to achieve accurate classification of AD and CN. Compared with the 2D-CNN model, the SVM classifier exhibited a 12.77% increase in accuracy, a 6.82% increase in sensitivity, and a 19.37% increase in specificity. Shin et al. (2020) constructed an end-to-end network based on the GAN model, with G for MRI-PET conversion and D for AD classification. The structure of this network is different from the conventional two-step structure, which

TABLE 2 | The results of meta-analyses of the diagnosis of AD.

Task	Method	OR[a] of accuracy	SEN[b]	SPE[c]	AUC[d] of the SROC[e]	Spearman correlation coefficient
AD vs. NC	w/[f] GAN	1.425* (1.150–1.766)	0.88 (0.82–0.93)	0.93 (0.90–0.95)	0.96 (0.94–0.97)	−0.029
	w/o[g] GAN		0.83 (0.76–0.88)	0.89 (0.86–0.92)	0.93 (0.90–0.95)	0.257
pMCI vs. sMCI	w/ GAN	1.149 (0.878–1.505)	0.66 (0.57, 0.75)	0.81 (0.76, 0.85)	0.81 (0.72–0.89)	1.000*
	w/o GAN		0.66 (0.57, 0.75)	0.78 (0.74, 0.82)	0.80 (0.74–0.87)	1.000*

**Statistically significant, $p \leq 0.05$. [a]Odds ratio; [b]sensitivity; [c]specificity; [d]area under the curve; [e]summary receiver operating characteristic curve; [f] with; [g]without.*

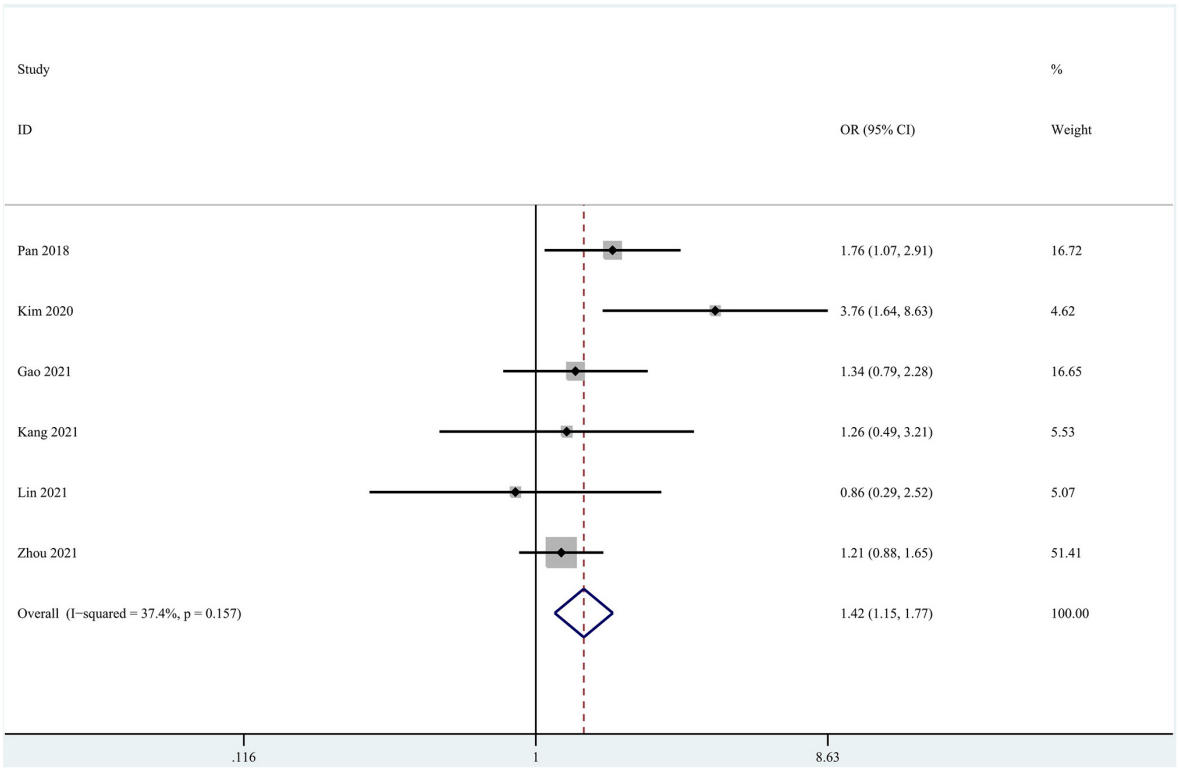

FIGURE 4 | Forest plot of the accuracy in the task of AD vs. CN classification.

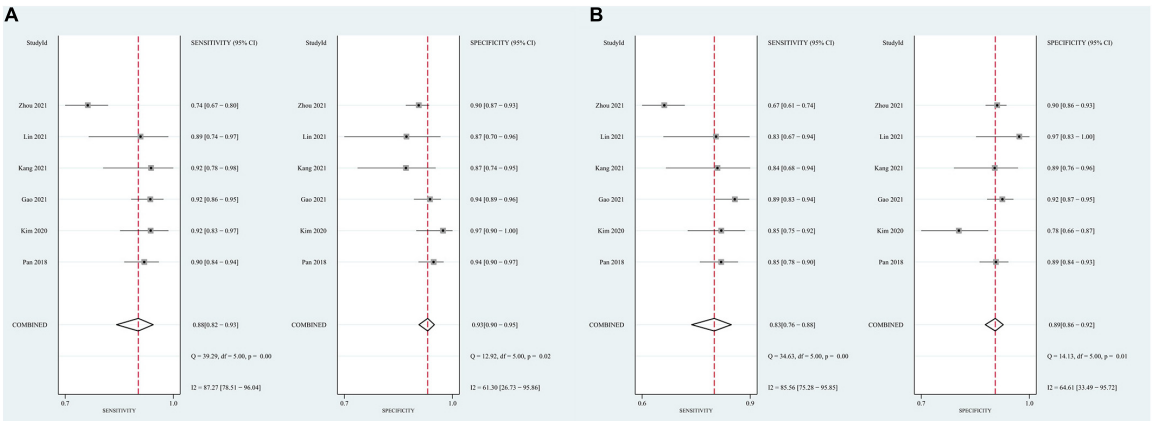

FIGURE 5 | Forest plots showing the pooled sensitivity and specificity in the task of AD vs. CN classification. **(A)** The pooled sensitivity and specificity in the GAN group; **(B)** the pooled sensitivity and specificity in the non-GAN group.

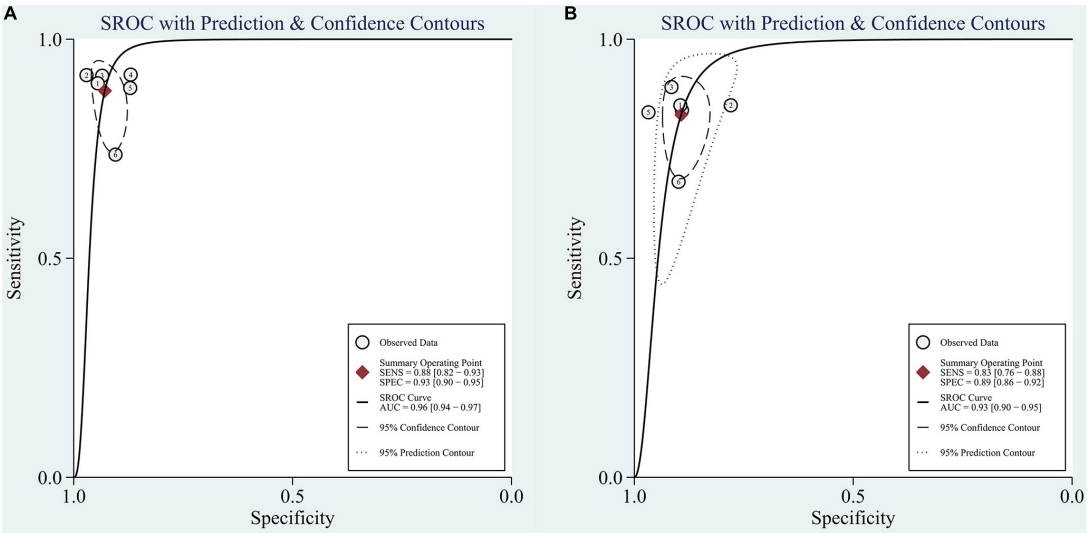

FIGURE 6 | SROC curve for the task of AD vs. CN classification: **(A)** SROC curve for the GAN group and **(B)** SROC curve for the non-GAN group.

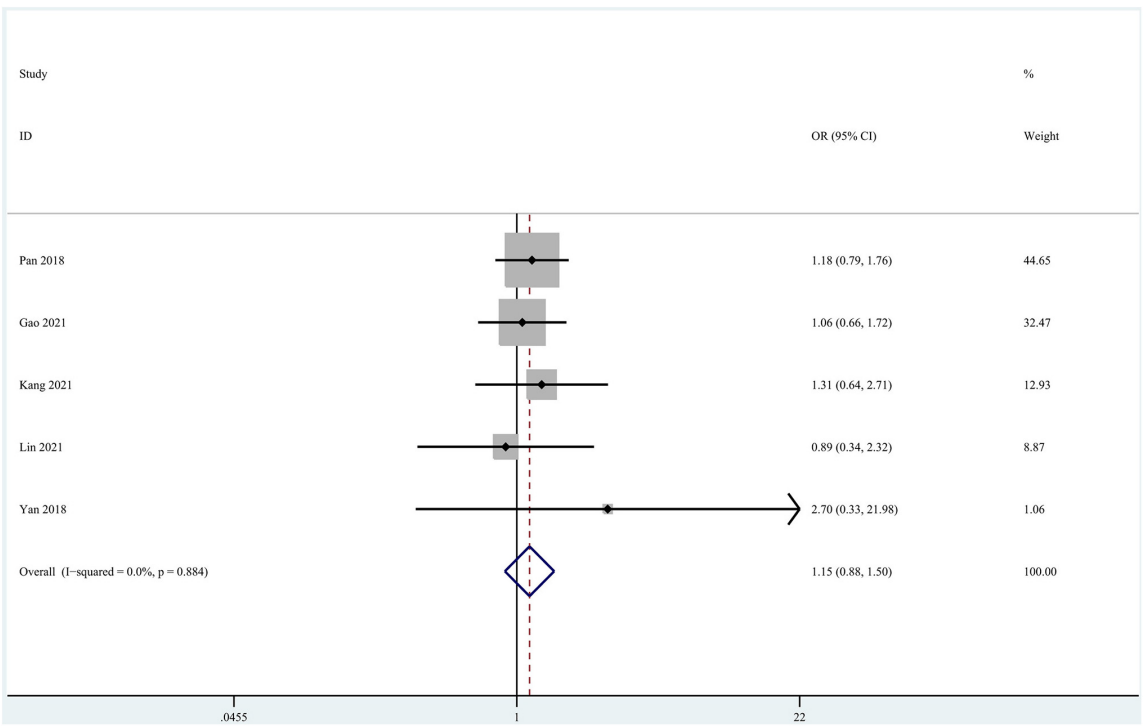

FIGURE 7 | Forest plot of the accuracy in the pMCI vs. sMCI classification task.

starts from PET data generation based on MRI data to AD diagnosis with the generated PET data, leading to 0.85 accuracy and 0.84 precision and recall in the task of AD vs. CN classification.

All included studies used data of AD patients through clinical diagnosis rather than neuropathological examination. Although neuropathological diagnosis at autopsy serves as the gold standard for diagnosing AD (Hyman et al., 2012), data of AD diagnosed through it are sparse and difficult to obtain. Researchers may consider that small data sizes could limit the adequate training of deep learning networks and chose to use data of clinically diagnosed AD from large publicly available databases, such as ADNI, OASIS, AIBL, and so on. However, clinical diagnosis may be less accurate

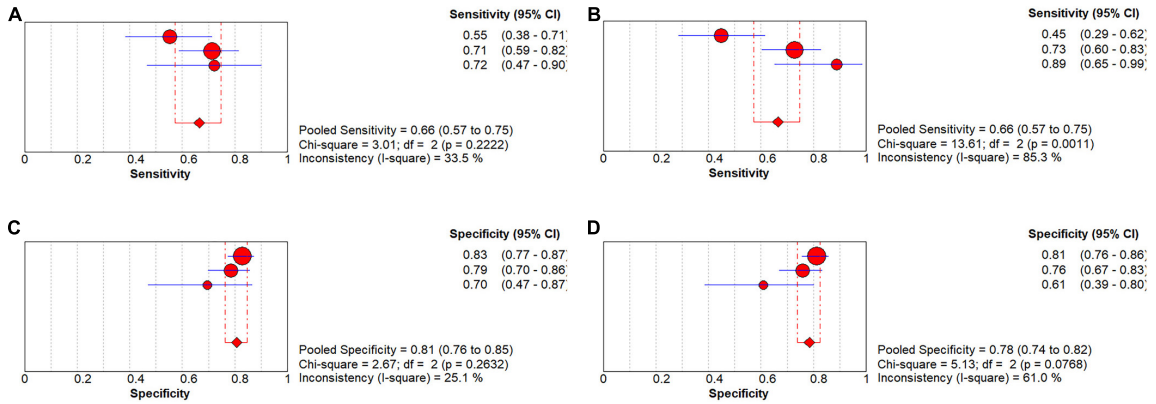

FIGURE 8 | Forest plots showing the pooled sensitivity and specificity in the task of pMCI vs. sMCI classification. **(A)** The pooled sensitivity in the GAN group and **(B)** the non-GAN group. **(C)** The pooled specificity in the GAN group and **(D)** the non-GAN group.

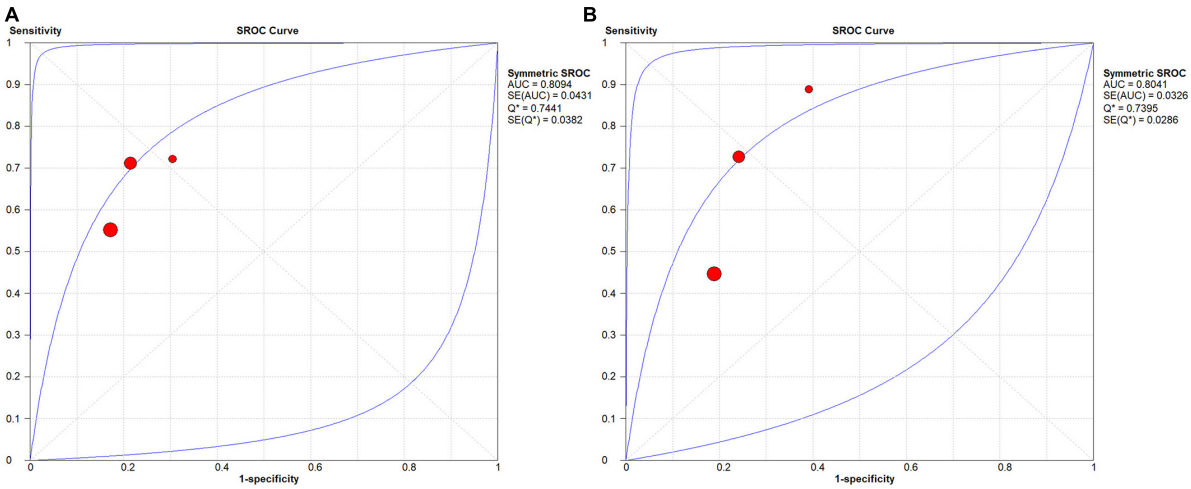

FIGURE 9 | SROC curves for the task of pMCI vs. sMCI classification: **(A)** SROC curve for the GAN group and **(B)** SROC curve for the non-GAN group.

compared to neuropathological examination currently. One study reported that sensitivity for AD clinical diagnosis based on the NINCDS-ADRDA guidelines ranged from 70.9 to 87.3% and specificity ranged from 44.3 to 70.8% compared to the golden standard (Beach et al., 2012). This could affect the evaluation of the diagnostic performance of GAN-based deep learning methods.

Performance of Generative Adversarial Network-Based Deep Learning Methods in the Task of Progressing MCI vs. Stable MCI Classification

MCI is a transition between CN and AD (Petersen, 2004). Patients with MCI who progress to AD are classified as having pMCI, while those who maintain stable disease conditions and even return to normal are classified as having sMCI (Petersen et al., 2001; Li et al., 2016). Efficient discrimination between pMCI and sMCI groups is beneficial for the early identification of patients at high risk of developing AD and helps further detect the high-risk factors responsible for disease progression. Using this approach, corresponding interventions might be scheduled, in turn delaying disease progression and decreasing the occurrence of AD.

In our study, GAN-based deep learning methods showed no remarkable classification performance in the task of pMCI vs. sMCI classification compared to the task of AD vs. CN classification. This difference is mainly attributed to the subtle pathological differences between patients with pMCI and sMCI (Kang et al., 2021). Compared to CN patients, significant hippocampal atrophy has been observed in both patients with pMCI and sMCI (Zeng et al., 2021). In this setting, the result is generally negative if the deep learning model only uses the whole hippocampal volume as the input feature in the task of pMCI vs. sMCI classification. A recent cohort study revealed that the volume of the bilateral subiculum and molecular layer in patients with pMCI was smaller than that in patients with sMCI, along with more rapid atrophy (Zeng et al., 2021). The

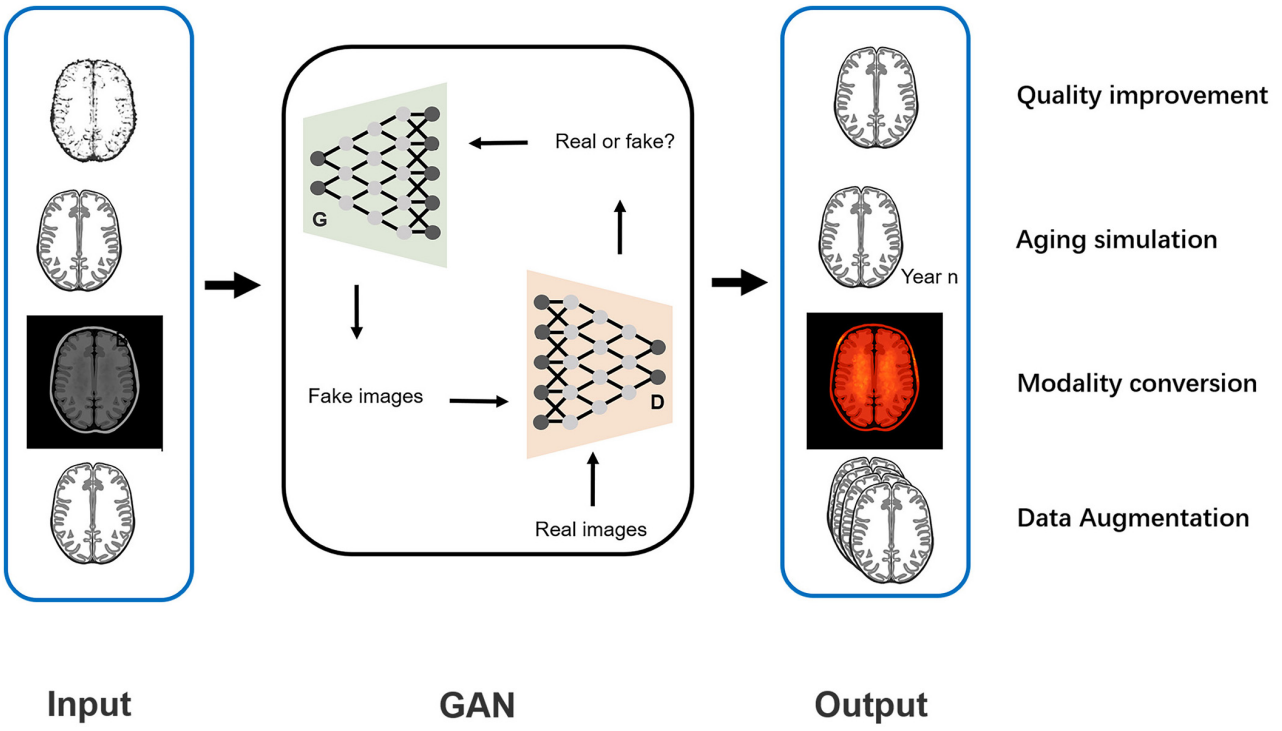

FIGURE 10 | Schematic diagram of the function of image processing using GAN.

volume of the hippocampal subregion is the main source of the difference between these two types. However, the volume of these subregions is very small, especially in 2D images. The difference in volume is difficult to capture using the deep learning method due to the floor effect and might provide an interpretation of the lack of remarkable performance in the task of pMCI vs. sMCI classification.

The included studies have attempted to overcome this limitation and achieve better performance in the task of pMCI vs. sMCI classification.

Some studies applied multimodal data to improve the performance. Lin W. et al. (2021) first developed a GAN with reversible blocks to achieve PET-MRI conversion. Then, they trained a 3D-CNN classifier (4 layers) by generating images of the hippocampus using these 2 modalities (PET and MRI) to complete the tasks of AD vs. CN and pMCI vs. sMCI classification. In this study, the hippocampus was set as the region of interest (ROI), which decreased unnecessary calculations and contributed to 89.05% accuracy in the AD vs. CN classification and 71.23% accuracy in the pMCI vs. sMCI classification. Gao et al. (2021) proposed a DCN classifier trained on MRI data and the corresponding PET data by GAN conversion. Pathwise transfer blocks were adopted to allow information communication across two paths of PET and MRI data. This approach enabled the classifier to make full use of complementary information of these images and improve the classification performance. Researchers performed a comparative analysis with the method without GAN and found that the GAN-based model exhibited better performance in both AD vs. CN and pMCI vs. sMCI classification tasks. Pan et al. (2018) and Yan et al. (2018) also used GAN to perform MRI-PET data conversion to compensate for insufficient training due to missing PET data. With classifiers trained on MRI data and the generated PET data, Yan et al. (2018) obtained a 7% increase in classification accuracy compared to the classifier trained on PET data with traditional augmentation. Pan et al. (2018) also reported better performance in both AD vs. CN and pMCI vs. sMCI classification tasks.

Some researchers applied the ensemble learning strategy to increase the accuracy and stability in the pMCI vs. sMCI classification task. Kang et al. (2021) devised a multimodal ensemble learning model for AD diagnosis based on three classifiers (GAN-D, VGG16, and ResNet50) trained on 11 MRI slices with the best diagnostic performance selected by the VGG16 classifier. The introduction of multiple slices and the multimodal classifier increased the accuracy and stability of the ensemble learning model in classification. Their result showed a 5.8% increase in accuracy of the ensemble learning model in the AD vs. CN classification compared to the single VGG16 classifier. Meanwhile, the three classifiers were separately analyzed, and the GAN-D was reported to be superior to VGG16 and ResNet50 classifiers in both AD vs. CN and pMCI vs. sMCI classification tasks, indicating the advantage of GAN to some extent. The differences in pathological changes between patients with pMCI and sMCI increases with aging. Based on this information, some studies simulated the process of aging observed in MRI data to predict disease progression. Zhao et al. (2021) constructed

a 3D patch-based multi-information GAN (MI-GAN) model to generate aging-related MRI images based on baseline MRI image data and related clinical information. Then, they trained a 3D Multi-Classification Model on these aging images to perform the pMCI vs. sMCI classification. The results showed 78.45% accuracy, a 3.01% increase compared to the deep neural networks and ensemble learning models. Wegmayr et al. (2019) also simulated the aging process of patients (as evidenced by MRI data) using time as the variable and then established a pMCI-sMCI classifier trained on aging images to identify patients at high risk of developing AD. The authors found that the classifier trained on aging images displayed a higher accuracy (0.73 vs. 0.70) and F1-score (0.71 vs. 0.61) than the classifier trained on baseline images.

The Function of Generative Adversarial Network in the Diagnostic Model

The excellent performance of GAN-based deep learning methods in diagnosing AD is attributed to the powerful functions of image processing by GAN and the model structure. In most of the included studies, the diagnostic model included 2 stage: the first was image processing by GAN and the second was the classifier established with other algorithms (primarily CNN) and training on images processed in stage one. Stage 1, instead of stage 2, is recognized as the critical stage for good performance in diagnosing AD (Sabuncu and Konukoglu, 2015). Therefore, the function of GAN determines the final effects of the entire diagnostic model. In the GAN, D provides a self-adaptive loss function based on different tasks and data, which is known as GAN-loss for G. The GAN-loss function might become powerful with the discriminative ability of D strengthening during training. This powerful loss function might promote image processing by G. In contrast, in other generative models, the image processing ability is limited, as their training is confined to the loss function preset. GAN, therefore, might provide images of higher quality for the diagnostic model and increase the diagnostic performance.

Specifically, the GAN provided image processing from four aspects in the included studies: quality improvement, aging simulation, data augmentation, and modality conversion (shown in **Figure 10**). The next section provides a description of the four functions and their effects on the AD diagnosis.

Quality Improvement

A GAN generates MRI data at high magnetic field strength from data collected at a low strength. Zhou X. et al. (2021) constructed a diagnostic model for AD based on 3-T MRI data generated by GAN, whose image quality was significantly higher than that of 1.5-T MRI scans based on SNR, BRISQUE, and NIQE metrics. The clear presentation of the diagnostic features by improving quality is the cause for the excellent performance of this deep learning method in disease diagnosis. Hippocampal atrophy on MRI is considered as potential neuroimaging markers for neurodegeneration in patients with AD. It might be presented much more clearly with a more accurate segmentation boundary in 3-T MRI than in 1.5-T MRI (Ho et al., 2010). A study also reported a much more widespread pattern of significant atrophy in the temporal lobe when scanned at 3-T vs. 1.5-T in the AD vs. CN classification. Due to the quality improvement function of GAN, the classifier easily obtained more accurate diagnostic features and detected differences between the AD and CN cohorts in these target areas, contributing to better classification performance.

Moreover, the increase in the quality of low-dose PET images obtained using GAN was reported in some studies. Wang et al. (2018) obtained full-dose PET images from low-dose images using the CGAN with a 3D U-net-like generator. The skip connections strategy was applied to combine hierarchical features. The authors obtained imaging data from healthy subjects and patients with MCI with the highest PSNR and the lowest NMSE compared to the methods based on the sparse representation and CNN. Additionally, the difference in the SUV between the PET images generated using GAN and the real full-dose PET images was the smallest. Ouyang et al. (2019) added an amyloid status classifier to GAN to ensure the preservation of pathological features in the generated image, which was superior to the CNN-based method, with a 1.87 dB PSNR, 2.04% SSIM, and 24.75% RMSE. The reductions in glucose metabolism in the parietal lobe, posterior cingulate, and temporal regions observed using FDG-PET are known as potential biomarkers reflecting the pathophysiological process of neuronal degeneration and injury in patients with AD (Zhang et al., 2011). High-dose PET images contain less noise than low-dose images, preserving more details of these diagnostic regions and more disease features that could be used in the classification. This finding also supports the good diagnostic performance of GAN-based deep learning methods.

Aging Simulation

In some studies, GAN was applied to predict disease progression by simulating cerebral aging with time as the variable. Zhao et al. (2021) generated aging MRI data based on baseline MRI scans and other clinical information. The generated images at year 1 and year 4 were highly similar to the real images (SSIM: 0.945 ± 0.038, 0.943 ± 0.028). Wegmayr et al. (2019) also built a model to simulate cerebral aging based on WGAN. These generated aging images had the same role as real images in the pMCI vs. sMCI classification (accuracy: 0.73, F1-score: 0.71). Some longitudinal pathological changes were observed using the aging simulation. In patients with pMCI, atrophy of the temporal lobe may extend forward to the parietal lobe, frontal lobe, lateral occipital cortex, and subsequent anterior cingulate cortex during the aging process (McDonald et al., 2009). Meanwhile, losses in the hippocampal and whole-brain volumes along with increasing ventricular volume have been reported (Jack et al., 2005; Hu et al., 2014). The larger differences between patients with pMCI and sMCI observed in the aging images compared to those observed in baseline images were shown, and the classifier performed better in the classification. The aging simulation function of GAN contributes to excellent performance in the task of pMCI vs. sMCI classification.

Data Augmentation

Large datasets with labels are commonly the basis of the construction and training of deep learning frameworks, especially

for supervised learning. However, the medical images are labeled largely based on the subjective experience and professional level of experts and might be affected by the image quality. Notably, labeling images from patients with different stages of AD is more challenging. Sparse labeled medical images might limit the application of deep learning in the diagnosis of AD (Tajbakhsh et al., 2020). The GAN can compensate for data insufficiency during the development of AD-related deep learning frameworks through the augmentation of PET and MRI data. Sajjad et al. (2021) performed augmentation on PET data with the DCGAN model. They reported high levels of PSNR (0.82, 0.73) and SSIM (25.66, 22.85) in generated images for patients with AD and MCI. Additionally, the corresponding classifier exhibited good performance in the task of AD vs. CN classification with an accuracy of 0.78. Islam and Zhang (2020) reported mean PSNR and SSIM values of 32.83 and 77.48, respectively, on the generated PET image data. The accuracy of the classifier based on these augmented data was 71.45% in the AD vs. CN classification, which was evidently higher than the value of 10% obtained using the classifier without data augmentation.

Modality Conversion

The type of data is also a vital factor contributing to diagnostic performance. In our study, 36% (5/14) of the included studies used multimodal data (PET and MRI) for analysis. PET data commonly provide metabolic information that is helpful in determining the diagnosis. For example, the reduction in glucose metabolism in the bilateral parietal lobes (involving the posterior cingulate gyrus and the precuneus) detected using 18F-FDG-PET and the Aβ protein and Tau protein deposition detected in the corresponding PET images are regarded as one of the most potential biomarkers for AD (Panegyres et al., 2009; Clark et al., 2012; Mallik et al., 2017; Xia and Dickerson, 2017). MRI data, especially sMRI, mainly provide structural information for diagnosis. Cerebral neurodegenerative structural changes in sMRI, such as a reduction in hippocampal volume and atrophy of some specific cerebral regions (parahippocampal gyrus, amygdala, temporal gyrus, upper parietal lobe, and posterior cingulate gyrus), have been detected in patients with AD (Reitz et al., 2011). The combination of PET and MRI data provides complementary features for AD diagnosis and obtains more promising results than data obtained with a single modality (Mirzaei et al., 2016; Liu et al., 2018). This superiority might be more prominent between two cohorts with small differences, such as patients with pMCI and sMCI. Deep learning methods based on multimodal data have become increasingly popular in diagnosing AD. A GAN can provide **Supplementary Data** for multimodality studies, as it facilitates the conversion between PET and MRI data. Lin W. et al. (2021) achieved PET and MRI data conversion using a GAN model with reversible blocks. The addition of these blocks improved the non-linear fitting ability of the model and provided images of higher quality. The authors showed high similarity between the generated images of the hippocampal region (as the ROI) and the ground truth (PSNR: 29.34, SSIM: 0.8034 on PET and PSNR: 29.81, SSIM: 0.9389 on MRI). Gao et al. (2021) proposed a GAN model with two pyramid convolution blocks and a self-attention mechanism to achieve MRI-PET data conversion. They also applied the task-induced mechanism in D to preserve important pathological information. The result revealed a high SSIM (0.915 ± 0.04) and PSNR (29.0 ± 2.99) of the generated PET image.

Researchers have also focused on biomarkers detected using different MRI modalities, including sMRI, functional magnetic resonance imaging (fMRI), and diffusion tensor imaging (DTI). For sMRI, alterations in anatomy reflected by T1-weighted MRI, such as atrophy of the hippocampus and rates of brain atrophy, have been extensively investigated (Jack, 2011). In addition, T2 heterogeneity is a potential biomarker reflecting changes in the integrity of brain microstructure and predicting cognitive decline (Wearn et al., 2020). Changes in the microstructure and integrity of white matter are observed on DTI (Sundgren et al., 2004). One study showed that a decrease in fractional anisotropy is detected in multiple posterior white matter regions in patients with AD (Medina et al., 2006). For fMRI, changes in the functional connectivity of different brain regions also have the potential for AD diagnosis (Forouzannezhad et al., 2019). All included studies used T1-weighted MRI data, without GAN based on multimodal MRI data. Except for the potential biomarkers reflected by T1-weighted MRI, those reflected by other MRI modalities are emerging. Although some studies reported the excellent diagnostic performance of multimodal MRI deep learning methods (Hojjati et al., 2018; Marzban et al., 2020), we propose that caution must be exercised in the development of this type of method until these emerging biomarkers are confirmed further.

Some risk factors for AD have been identified, such as the presence of apolipoprotein E (APOE) ε4ε4, depression, diabetes, hypertension, older age, female sex, and lower Mini-Mental State Examination (MMSE) scores (Li et al., 2016; Hersi et al., 2017). Therefore, clinical information may also be considered an important part of multimodal studies. Zhao et al. (2021) considered the function of this information, such as baseline age, sex, education level, and APOE ε4 allele, in the aging simulation process to generate more realistic aging images and obtain accurate predictions for AD progression.

In contrast to the two-stage structure, networks in some studies were established based only on the GAN structure. Baydargil et al. (2021) and Han et al. (2021) only applied a GAN without any other classifiers in anomaly detection for AD, as the D of GAN is actually a classifier. In their study, the G of GAN was run to reconstruct images of subjects based on features learned from images of CN individuals, while the D of GAN was operated to identify patients with AD based on the difference between the reconstructed images and the images of CN individuals. The advantage of this structure over the two-stage structure is that the result of the classification will be fed back to G, ensuring that the generated images have a good classification effect, not simply high quality based on PSNR and SSIM metrics.

Some studies have considered both the two-stage structure and the feedback from the classifier. Zhou X. et al. (2021) applied a GAN to obtain 3-T MRI data from 1.5-T MRI data and further used the generated 3-T imaging data to train an FCN classifier for AD classification. The G of GAN obtained feedback from the FCN and subsequently generate images with good classification

effects. They found that the entire diagnostic model exhibited better diagnostic performance.

However, GANs still have some disadvantages when used in practical applications. First, concurrent training of G and D without making a certain network more powerful is a substantial challenge (Sorin et al., 2020). Second, the function of GAN is difficult to interpret. It operates as a black box with visible input and output sides and invisible functions of G and D. The internal logic is difficult to clearly explain.

Our study showed the potential of GAN-based deep learning methods for diagnosing AD and MCI. The following criteria were applied to ensure the diagnosis if possible for the use of this method in clinical practice in the future: (1) diagnoses of other possible brain disorders were excluded; (2) at least one type of neuroimaging data was available, such as sMRI and PET; and (3) the conclusive diagnosis should be based on a combination of the results from GAN methods with those from neuropsychological tests, history analysis, and other clinical diagnoses.

Limitations and Future Research Directions

Limitations: (1) All included studies used data of AD patients through clinical diagnosis rather than neuropathological examination. Currently, there is still a certain gap between their diagnostic accuracy (Beach et al., 2012). Therefore, the diagnostic performance of GAN methods should be validated further on AD patients diagnosed through neuropathology, even though it is not easy to achieve this goal in the near future. (2) The number of studies included in the meta-analysis of the task of pMCI vs. sMCI classification is relatively small. (3) Due to the limited number of studies, this study only investigated the tasks of AD vs. CN and pMCI vs. sMCI classification. The classification performance of GAN-based deep learning methods must be explored in other tasks, such as the AD vs. MCI vs. CN classification. (3) The lack of subgroup analysis based on the type of data and the method of image processing by GAN is also a limitation of the study.

Some suggestions are provided for future research. First, studies on the task of pMCI vs. sMCI classification and other tasks are needed to further explore the performance of GAN-based deep learning methods. Second, researchers should conduct studies to analyze the roles of the type of data, the type of GAN, and the method of image processing in the diagnostic model. Third, GAN application in other fields (non-medical imaging) may also be considered, such as AD molecular data (Park et al., 2020). Data insufficiency in bioinformatics may be resolved with data augmentation by GAN (Lan et al., 2020). Fourth, using data from patients definitively diagnosed with AD through a neuropathological examination at autopsy rather than a clinical diagnosis would result in methods with more clinical application value.

CONCLUSION

This systematic review and meta-analysis reported the good performance of GAN-based deep learning methods in the task of AD vs. CN classification. This good performance is largely attributed to its powerful functions in image processing, including quality improvement, aging simulation, data augmentation, and modality conversion. However, their diagnostic performance in the task of pMCI vs. sMCI classification was not remarkable. Studies using large datasets must be conducted to further explore these methods.

DATA AVAILABILITY STATEMENT

The original contributions presented in the study are included in the article/**Supplementary Material**, further inquiries can be directed to the corresponding author/s.

AUTHOR CONTRIBUTIONS

CQ, YZ, and TC: conceptualization, methodology, and writing original draft preparation. CQ and YM: software and formal analysis. YZ, QC, YM, HF, and JL: validation. CQ, YZ, YM, QC, JL, ZJ, TC, and QG: writing—review and editing. TC and QG: supervision and funding acquisition. All authors contributed to the article and approved the submitted version.

FUNDING

This research was funded by the National Natural Science Foundation of China (Grant Nos. 81820108018 and 81401398), the National Key Research and Development Project (Grant No. 2018YFC1704605), the Sichuan Science and Technology Program (Grant No. 2019YJ0049), the Sichuan Provincial Health and Family Planning Commission (Grant No. 19PJ080), the National College Students' Innovation and Entrepreneurship Training Program (Grant No. C2021116624), and the Chinese Postdoctoral Science Foundation (Grant No. 2013M530401).

SUPPLEMENTARY MATERIAL

The Supplementary Material for this article can be found online at: https://www.frontiersin.org/articles/10.3389/fnagi.2022.841696/full#supplementary-material

REFERENCES

Ansart, M., Epelbaum, S., Bassignana, G., Bône, A., Bottani, S., Cattai, T., et al. (2021). Predicting the progression of mild cognitive impairment using machine learning: a systematic, quantitative and critical review. *Med. Image Anal.* 67:101848. doi: 10.1016/j.media.2020.101848

Arbizu, J., Festari, C., Altomare, D., Walker, Z., Bouwman, F., Rivolta, J., et al. (2018). Clinical utility of FDG-PET for the clinical diagnosis in MCI.

Eur. J. Nuclear Med. Mol. Imaging 45, 1497–1508. doi: 10.1007/s00259-018-4039-7

Atri, A. (2019). The Alzheimer's disease clinical spectrum diagnosis and management. *Med. Clin. North Am.* 103, 263–293. doi: 10.1016/j.mcna.2018.10.009

Baydargil, H. B., Park, J.-S., and Kang, D.-Y. (2021). Anomaly analysis of Alzheimer's disease in PET images using an unsupervised adversarial deep learning model. *Appl. Sci.* 11:2187. doi: 10.3390/app11052187

Beach, T. G., Monsell, S. E., Phillips, L. E., and Kukull, W. (2012). Accuracy of the clinical diagnosis of Alzheimer disease at National Institute on Aging Alzheimer Disease Centers, 2005-2010. *J. Neuropathol. Exp. Neurol.* 71, 266–273. doi: 10.1097/NEN.0b013e31824b211b

Bloudek, L. M., Spackman, D. E., Blankenburg, M., and Sullivan, S. D. (2011). Review and meta-analysis of biomarkers and diagnostic imaging in Alzheimer's disease. *J. Alzheimers Dis.* 26, 627–645. doi: 10.3233/jad-2011-110458

Chetelat, G. (2018). Multimodal neuroimaging in Alzheimer's disease: early diagnosis, physiopathological mechanisms, and impact of lifestyle. *J. Alzheimers Dis.* 64, S199–S211. doi: 10.3233/jad-179920

Cho, H., Choi, J. Y., Hwang, M. S., Lee, J. H., Kim, Y. J., Lee, H. M., et al. (2016). Tau PET in Alzheimer disease and mild cognitive impairment. *Neurology* 87, 375–383. doi: 10.1212/wnl.0000000000002892

Chong, M. S., and Sahadevan, S. (2005). Preclinical Alzheimer's disease: diagnosis and prediction of progression. *Lancet Neurol.* 4, 576–579. doi: 10.1016/s1474-4422(05)70168-x

Clark, C. M., Pontecorvo, M. J., Beach, T. G., Bedell, B. J., Coleman, R. E., Doraiswamy, P. M., et al. (2012). Cerebral PET with florbetapir compared with neuropathology at autopsy for detection of neuritic amyloid-β plaques: a prospective cohort study. *Lancet Neurol.* 11, 669–678. doi: 10.1016/s1474-4422(12)70142-4

Cummings, J. L., Morstorf, T., and Zhong, K. (2014). Alzheimer's disease drug-development pipeline: few candidates, frequent failures. *Alzheimers Res. Ther.* 6:37. doi: 10.1186/alzrt269

Davis, M., Connell, T. O., Johnson, S., Cline, S., Merikle, E., Martenyi, F., et al. (2018). Estimating Alzheimer's disease progression rates from normal cognition through mild cognitive impairment and stages of dementia. *Curr. Alzheimer Res.* 15, 777–788. doi: 10.2174/1567205015666180119092427

Forouzannezhad, P., Abbaspour, A., Fang, C., Cabrerizo, M., Loewenstein, D., Duara, R., et al. (2019). A survey on applications and analysis methods of functional magnetic resonance imaging for Alzheimer's disease. *J. Neurosci. Methods* 317, 121–140. doi: 10.1016/j.jneumeth.2018.12.012

Gao, X., Shi, F., Shen, D., and Liu, M. (2021). Task-induced pyramid and attention GAN for multimodal brain image imputation and classification in Alzheimers disease. *IEEE J. biomed. Health Inform.* 26, 36–43. doi: 10.1109/jbhi.2021.3097721

Goodfellow, I. J., Pouget-Abadie, J., Mirza, M., Xu, B., Warde-Farley, D., Ozair, S., et al. (2014). Generative adversarial networks. *Adv. Neural Inform. Process. Syst.* 3, 2672–2680.

Han, C., Rundo, L., Murao, K., Noguchi, T., Shimahara, Y., Milacski, Z. Á, et al. (2021). MADGAN: unsupervised medical anomaly detection GAN using multiple adjacent brain MRI slice reconstruction. *BMC Bioinformatics* 22(Suppl. 2):31. doi: 10.1186/s12859-020-03936-1

Hersi, M., Irvine, B., Gupta, P., Gomes, J., Birkett, N., and Krewski, D. (2017). Risk factors associated with the onset and progression of Alzheimer's disease: a systematic review of the evidence. *Neurotoxicology* 61, 143–187. doi: 10.1016/j.neuro.2017.03.006

Ho, A. J., Hua, X., Lee, S., Leow, A. D., Yanovsky, I., Gutman, B., et al. (2010). Comparing 3 T and 1.5 T MRI for tracking Alzheimer's disease progression with tensor-based morphometry. *Hum. Brain Mapp.* 31, 499–514. doi: 10.1002/hbm.20882

Hojjati, S. H., Ebrahimzadeh, A., Khazaee, A., Babajani-Feremi, A., and Alzheimer's Disease Neuroimaging Initiative (2018). Predicting conversion from MCI to AD by integrating rs-fMRI and structural MRI. *Comput. Biol. Med.* 102, 30–39. doi: 10.1016/j.compbiomed.2018.09.004

Hu, Z., Wu, L., Jia, J., and Han, Y. (2014). Advances in longitudinal studies of amnestic mild cognitive impairment and Alzheimer's disease based on multi-modal MRI techniques. *Neurosci. Bull.* 30, 198–206. doi: 10.1007/s12264-013-1407-y

Hyman, B. T., Phelps, C. H., Beach, T. G., Bigio, E. H., Cairns, N. J., Carrillo, M. C., et al. (2012). National Institute on Aging-Alzheimer's association guidelines for the neuropathologic assessment of Alzheimer's disease. *Alzheimers Dement.* 8, 1–13. doi: 10.1016/j.jalz.2011.10.007

Islam, J., and Zhang, Y. (2020). GAN-based synthetic brain PET image generation. *Brain Inform.* 7:3. doi: 10.1186/s40708-020-00104-2

Jack, C. R. Jr. (2011). Alliance for aging research AD biomarkers work group: structural MRI. *Neurobiol. Aging* 32, S48–S57. doi: 10.1016/j.neurobiolaging.2011.09.011

Jack, C. R. Jr., Bennett, D. A., Blennow, K., Carrillo, M. C., Feldman, H. H., Frisoni, G. B., et al. (2016). A/T/N: an unbiased descriptive classification scheme for Alzheimer disease biomarkers. *Neurology* 87, 539–547. doi: 10.1212/wnl.0000000000002923

Jack, C. R. Jr., Lowe, V. J., Senjem, M. L., Weigand, S. D., Kemp, B. J., Shiung, M. M., et al. (2008). 11C PiB and structural MRI provide complementary information in imaging of Alzheimer's disease and amnestic mild cognitive impairment. *Brain* 131(Pt 3), 665–680. doi: 10.1093/brain/awm336

Jack, C. R. Jr., Shiung, M. M., Weigand, S. D., O'Brien, P. C., Gunter, J. L., Boeve, B. F., et al. (2005). Brain atrophy rates predict subsequent clinical conversion in normal elderly and amnestic MCI. *Neurology* 65, 1227–1231. doi: 10.1212/01.wnl.0000180958.22678.91

Jagust, W., Reed, B., Mungas, D., Ellis, W., and DeCarli, C. (2007). What does fluorodeoxyglucose PET imaging add to a clinical diagnosis of dementia? *Neurology* 69, 871–877. doi: 10.1212/01.wnl.0000269790.05105.16

Ju, R., Hu, C., Zhou, P., and Li, Q. (2019). Early diagnosis of Alzheimer's disease based on resting-state brain networks and deep learning. *IEEE Trans. Comput. Biol. Bioinform.* 16, 244–257. doi: 10.1109/tcbb.2017.2776910

Kang, W., Lin, L., Zhang, B., Shen, X., and Wu, S. (2021). Multi-model and multi-slice ensemble learning architecture based on 2D convolutional neural networks for Alzheimer's disease diagnosis. *Comput. Biol. Med.* 136:104678. doi: 10.1016/j.compbiomed.2021.104678

Kim, H. W., Lee, H. E., Lee, S., Oh, K. T., Yun, M., and Yoo, S. K. (2020). Slice-selective learning for Alzheimer's disease classification using a generative adversarial network: a feasibility study of external validation. *Eur. J. Nuclear Med. Mol. Imaging* 47, 2197–2206. doi: 10.1007/s00259-019-04676-y

Lan, L., You, L., Zhang, Z., Fan, Z., Zhao, W., Zeng, N., et al. (2020). Generative adversarial networks and its applications in biomedical informatics. *Front. Public Health* 8:164. doi: 10.3389/fpubh.2020.00164

Lee, J. G., Jun, S., Cho, Y. W., Lee, H., Kim, G. B., Seo, J. B., et al. (2017). Deep learning in medical imaging: general overview. *Korean J. Radiol.* 18, 570–584. doi: 10.3348/kjr.2017.18.4.570

Li, J. Q., Tan, L., Wang, H. F., Tan, M. S., Tan, L., Xu, W., et al. (2016). Risk factors for predicting progression from mild cognitive impairment to Alzheimer's disease: a systematic review and meta-analysis of cohort studies. *J. Neurol. Neurosurg. Psychiatry* 87, 476–484. doi: 10.1136/jnnp-2014-310095

Lin, E., Lin, C. H., and Lane, H. Y. (2021). Deep learning with neuroimaging and genomics in Alzheimer's disease. *Int. J. Mol. Sci.* 22:7911. doi: 10.3390/ijms22157911

Lin, W., Lin, W., Chen, G., Zhang, H., Gao, Q., Huang, Y., et al. (2021). Bidirectional mapping of brain MRI and PET with 3D reversible GAN for the diagnosis of Alzheimer's disease. *Front. Neurosci.* 15:646013. doi: 10.3389/fnins.2021.646013

Liu, X., Chen, K., Wu, T., Weidman, D., Lure, F., and Li, J. (2018). Use of multimodality imaging and artificial intelligence for diagnosis and prognosis of early stages of Alzheimer's disease. *Transl. Res.* 194, 56–67. doi: 10.1016/j.trsl.2018.01.001

Logan, R., Williams, B. G., Ferreira da Silva, M., Indani, A., Schcolnicov, N., Ganguly, A., et al. (2021). Deep convolutional neural networks with ensemble learning and generative adversarial networks for Alzheimer's disease image data classification. *Front. Aging Neurosci.* 13:720226. doi: 10.3389/fnagi.2021.720226

Lui, S., Zhou, X. J., Sweeney, J. A., and Gong, Q. (2016). Psychoradiology: the frontier of neuroimaging in psychiatry. *Radiology* 281, 357–372. doi: 10.1148/radiol.2016152149

Mallik, A., Drzezga, A., and Minoshima, S. (2017). Clinical amyloid imaging. *Semin. Nucl. Med.* 47, 31–43. doi: 10.1053/j.semnuclmed.2016.09.005

Marinescu, R. V., Oxtoby, N. P., Young, A. L., Bron, E. E., Toga, A. W., Weiner, M. W., et al. (2019). TADPOLE challenge: accurate Alzheimer's disease prediction through crowdsourced forecasting of future data. *Predict. Intell. Med.* 11843, 1–10. doi: 10.1007/978-3-030-32281-6_1

Martí-Juan, G., Sanroma-Guell, G., and Piella, G. (2020). A survey on machine and statistical learning for longitudinal analysis of neuroimaging data in Alzheimer's disease. *Comput. Methods Programs Biomed.* 189:105348. doi: 10.1016/j.cmpb.2020.105348

Marzban, E. N., Eldeib, A. M., Yassine, I. A., Kadah, Y. M., and Alzheimer's Disease Neurodegenerative Initiative (2020). Alzheimer's disease diagnosis from diffusion tensor images using convolutional neural networks. *PLoS One* 15:e0230409. doi: 10.1371/journal.pone.0230409

Matsuda, H., Shigemoto, Y., and Sato, N. (2019). Neuroimaging of Alzheimer's disease: focus on amyloid and tau PET. *Jpn. J. Radiol.* 37, 735–749. doi: 10.1007/s11604-019-00867-7

McDonald, C. R., McEvoy, L. K., Gharapetian, L., Fennema-Notestine, C., Hagler, D. J. Jr., Holland, D., et al. (2009). Regional rates of neocortical atrophy from normal aging to early Alzheimer disease. *Neurology* 73, 457–465. doi: 10.1212/WNL.0b013e3181b16431

McInnes, M. D. F., Moher, D., Thombs, B. D., McGrath, T. A., Bossuyt, P. M., Clifford, T., et al. (2018). Preferred reporting items for a systematic review and meta-analysis of diagnostic test accuracy studies: the PRISMA-DTA statement. *JAMA* 319, 388–396. doi: 10.1001/jama.2017.19163

McKhann, G. M., Knopman, D. S., Chertkow, H., Hyman, B. T., Jack, C. R. Jr., Kawas, C. H., et al. (2011). The diagnosis of dementia due to Alzheimer's disease: recommendations from the National Institute on Aging-Alzheimer's Association workgroups on diagnostic guidelines for Alzheimer's disease. *Alzheimers Dement.* 7, 263–269. doi: 10.1016/j.jalz.2011.03.005

Medina, D., DeToledo-Morrell, L., Urresta, F., Gabrieli, J. D. E., Moseley, M., Fleischman, D., et al. (2006). White matter changes in mild cognitive impairment and AD: a diffusion tensor imaging study. *Neurobiol. Aging* 27, 663–672. doi: 10.1016/j.neurobiolaging.2005.03.026

Mirzaei, G., Adeli, A., and Adeli, H. (2016). Imaging and machine learning techniques for diagnosis of Alzheimer's disease. *Rev. Neurosci.* 27, 857–870. doi: 10.1515/revneuro-2016-0029

Misra, C., Fan, Y., and Davatzikos, C. (2009). Baseline and longitudinal patterns of brain atrophy in MCI patients, and their use in prediction of short-term conversion to AD: results from ADNI. *Neuroimage* 44, 1415–1422. doi: 10.1016/j.neuroimage.2008.10.031

Morris, E., Chalkidou, A., Hammers, A., Peacock, J., Summers, J., and Keevil, S. (2016). Diagnostic accuracy of F-18 amyloid PET tracers for the diagnosis of Alzheimer's disease: a systematic review and meta-analysis. *Eur. J. Nuclear Med. Mol. Imaging* 43, 374–385. doi: 10.1007/s00259-015-3228-x

Ouyang, J., Chen, K. T., Gong, E., Pauly, J., and Zaharchuk, G. (2019). Ultra-low-dose PET reconstruction using generative adversarial network with feature matching and task-specific perceptual loss. *Med. Phys.* 46, 3555–3564. doi: 10.1002/mp.13626

Pan, Y., Liu, M., Lian, C., Zhou, T., Xia, Y., and Shen, D. (2018). Synthesizing missing PET from MRI with cycle-consistent generative adversarial networks for Alzheimer's disease diagnosis. *Med. Image Comput. Comput. Assist. Interv.* 11072, 455–463. doi: 10.1007/978-3-030-00931-1_52

Panegyres, P. K., Rogers, J. M., McCarthy, M., Campbell, A., and Wu, J. S. (2009). Fluorodeoxyglucose-positron emission tomography in the differential diagnosis of early-onset dementia: a prospective, community-based study. *BMC Neurol.* 9:41. doi: 10.1186/1471-2377-9-41

Park, J., Kim, H., Kim, J., and Cheon, M. (2020). A practical application of generative adversarial networks for RNA-seq analysis to predict the molecular progress of Alzheimer's disease. *PLoS Comput. Biol.* 16:e1008099. doi: 10.1371/journal.pcbi.1008099

Petersen, R. C. (2004). Mild cognitive impairment as a diagnostic entity. *J. Intern. Med.* 256, 183–194. doi: 10.1111/j.1365-2796.2004.01388.x

Petersen, R. C., Doody, R., Kurz, A., Mohs, R. C., Morris, J. C., Rabins, P. V., et al. (2001). Current concepts in mild cognitive impairment. *Arch. Neurol.* 58, 1985–1992. doi: 10.1001/archneur.58.12.1985

Reitz, C., Brayne, C., and Mayeux, R. (2011). Epidemiology of Alzheimer disease. *Nat. Rev. Neurol.* 7, 137–152. doi: 10.1038/nrneurol.2011.2

Sabuncu, M. R., and Konukoglu, E. (2015). Clinical prediction from structural brain MRI scans: a large-scale empirical study. *Neuroinformatics* 13, 31–46. doi: 10.1007/s12021-014-9238-1

Sajjad, M., Ramzan, F., Khan, M. U. G., Rehman, A., Kolivand, M., Fati, S. M., et al. (2021). Deep convolutional generative adversarial network for Alzheimer's disease classification using positron emission tomography (PET) and synthetic data augmentation. *Microsc. Res. Tech.* 84, 3023–3034. doi: 10.1002/jemt.23861

Shen, T., Jiang, J., Lu, J., Wang, M., Zuo, C., Yu, Z., et al. (2019). Predicting Alzheimer disease from mild cognitive impairment with a deep belief network based on 18F-FDG-PET images. *Mol. Imaging* 18:1536012119877285. doi: 10.1177/1536012119877285

Shin, H.-C., Ihsani, A., Xu, Z., Mandava, S., Sreenivas, S. T., Forster, C., et al. (2020). "GANDALF: generative adversarial networks with discriminator-adaptive loss fine-tuning for Alzheimer's disease diagnosis from MRI," in *Proceedings of the Conference on Medical Image Computing and Computer Assisted Intervention*, Lima.

Sorin, V., Barash, Y., Konen, E., and Klang, E. (2020). Creating artificial images for radiology applications using generative adversarial networks (GANs) – a systematic review. *Acad. Radiol.* 27, 1175–1185. doi: 10.1016/j.acra.2019.12.024

Spasov, S., Passamonti, L., Duggento, A., Liò, P., and Toschi, N. (2019). A parameter-efficient deep learning approach to predict conversion from mild cognitive impairment to Alzheimer's disease. *Neuroimage* 189, 276–287. doi: 10.1016/j.neuroimage.2019.01.031

Sperling, R. A., Aisen, P. S., Beckett, L. A., Bennett, D. A., Craft, S., Fagan, A. M., et al. (2011). Toward defining the preclinical stages of Alzheimer's disease: recommendations from the National Institute on Aging-Alzheimer's association workgroups on diagnostic guidelines for Alzheimer's disease. *Alzheimers Dement.* 7, 280–292. doi: 10.1016/j.jalz.2011.03.003

Sundgren, P. C., Dong, Q., Gomez-Hassan, D., Mukherji, S. K., Maly, P., and Welsh, R. (2004). Diffusion tensor imaging of the brain: review of clinical applications. *Neuroradiology* 46, 339–350. doi: 10.1007/s00234-003-1114-x

Suzuki, K. (2017). Overview of deep learning in medical imaging. *Radiol. Phys. Technol.* 10, 257–273. doi: 10.1007/s12194-017-0406-5

Tajbakhsh, N., Jeyaseelan, L., Li, Q., Chiang, J. N., Wu, Z., and Ding, X. (2020). Embracing imperfect datasets: a review of deep learning solutions for medical image segmentation. *Med. Image Anal.* 63:101693. doi: 10.1016/j.media.2020.101693

Wang, Y., Yu, B., Wang, L., Zu, C., Lalush, D. S., Lin, W., et al. (2018). 3D conditional generative adversarial networks for high-quality PET image estimation at low dose. *Neuroimage* 174, 550–562. doi: 10.1016/j.neuroimage.2018.03.045

Wearn, A. R., Nurdal, V., Saunders-Jennings, E., Knight, M. J., Isotalus, H. K., Dillon, S., et al. (2020). T2 heterogeneity: a novel marker of microstructural integrity associated with cognitive decline in people with mild cognitive impairment. *Alzheimers Res. Ther.* 12:105. doi: 10.1186/s13195-020-00672-9

Wegmayr, V., Horold, M., and Buhmann, J. M. (2019). "Generative aging of brain MRI for early prediction of MCI-AD conversion," in *Proceedings of the 2019 IEEE 16th International Symposium on Biomedical Imaging (ISBI 2019)* (Venice: IEEE), 1042–1046.

Xia, C., and Dickerson, B. C. (2017). Multimodal PET imaging of amyloid and tau pathology in Alzheimer disease and non-Alzheimer disease dementias. *PET Clin.* 12, 351–359. doi: 10.1016/j.cpet.2017.02.005

Yan, Y., Lee, H., Somer, E., and Grau, V. (2018). "Generation of amyloid PET images via conditional adversarial training for predicting progression to Alzheimer's disease," in *PRedictive Intelligence in MEdicine*, eds I. Rekik, G. Unal, E. Adeli, and S. H. Park (Cham: Springer International Publishing), 26–33. doi: 10.1007/978-3-030-00320-3_4

Zeng, Q., Li, K., Luo, X., Wang, S., Xu, X., Li, Z., et al. (2021). Distinct atrophy pattern of hippocampal subfields in patients with progressive and stable mild cognitive impairment: a longitudinal MRI study. *J. Alzheimers Dis.* 79, 237–247. doi: 10.3233/jad-200775

Zhang, D., Wang, Y., Zhou, L., Yuan, H., and Shen, D. (2011). Multimodal classification of Alzheimer's disease and mild cognitive impairment. *Neuroimage* 55, 856–867. doi: 10.1016/j.neuroimage.2011.01.008

Zhao, Y., Ma, B., Jiang, P., Zeng, D., Wang, X., and Li, S. (2021). Prediction of Alzheimer's disease progression with multi-information generative adversarial network. *IEEE J. Biomed. Health Inform.* 25, 711–719. doi: 10.1109/jbhi.2020.3006925

Zhou, J., Hu, L., Jiang, Y., and Liu, L. (2021). A correlation analysis between SNPs and ROIs of Alzheimer's disease based on deep learning. *Biomed. Res. Int.* 2021:8890513. doi: 10.1155/2021/8890513

Zhou, X., Qiu, S., Joshi, P. S., Xue, C., Killiany, R. J., Mian, A. Z., et al. (2021). Enhancing magnetic resonance imaging-driven Alzheimer's disease classification performance using generative adversarial learning. *Alzheimers Res. Ther.* 13:60. doi: 10.1186/s13195-021-00797-5

Conflict of Interest: The authors declare that the research was conducted in the absence of any commercial or financial relationships that could be construed as a potential conflict of interest.

frontiers | Frontiers in Aging Neuroscience

ORIGINAL RESEARCH
published: 27 April 2022
doi: 10.3389/fnagi.2022.787516

Modeling the Properties of White Matter Tracts Using Diffusion Tensor Imaging to Characterize Patterns of Injury in Aging and Neurodegenerative Disease

*Chun Yen Kok[1], Christine Lock[2], Ting Yao Ang[2] and Nicole C. Keong[1,2]**

[1] Duke-National University of Singapore (NUS) Medical School, Singapore, Singapore, [2] Department of Neurosurgery, National Neuroscience Institute, Singapore, Singapore

OPEN ACCESS

Edited by:
Ping Wu,
Fudan University, China

Reviewed by:
Eric Schmidt,
Université de Toulouse, France
Ian Brian Malone,
University College London, United Kingdom

***Correspondence:**
Nicole C. Keong
nchkeong@cantab.net

Specialty section:
This article was submitted to Neurocognitive Aging and Behavior, a section of the journal Frontiers in Aging Neuroscience

Received: *30 September 2021*
Accepted: *15 March 2022*
Published: *27 April 2022*

Citation:
Kok CY, Lock C, Ang TY and Keong NC (2022) Modeling the Properties of White Matter Tracts Using Diffusion Tensor Imaging to Characterize Patterns of Injury in Aging and Neurodegenerative Disease. Front. Aging Neurosci. 14:787516. doi: 10.3389/fnagi.2022.787516

Diffusion tensor imaging (DTI) is a relatively novel magnetic resonance-based imaging methodology that can provide valuable insight into the microstructure of white matter tracts of the brain. In this paper, we evaluated the reliability and reproducibility of deriving a semi-automated pseudo-atlas DTI tractography method vs. standard atlas-based analysis alternatives, for use in clinical cohorts with neurodegeneration and ventriculomegaly. We showed that the semi-automated pseudo-atlas DTI tractography method was reliable and reproducible across different cohorts, generating 97.7% of all tracts. However, DTI metrics obtained from both methods were significantly different across the majority of cohorts and white matter tracts ($p < 0.001$). Despite this, we showed that both methods produced patterns of white matter injury that are consistent with findings reported in the literature and with DTI profiles generated from these methodologies. Scatter plots comparing DTI metrics obtained from each methodology showed that the pseudo-atlas method produced metrics that implied a more preserved neural structure compared to its counterpart. When comparing DTI metrics against a measure of ventriculomegaly (i.e., Evans' Index), we showed that the standard atlas-based method was able to detect decreasing white matter integrity with increasing ventriculomegaly, while in contrast, metrics obtained using the pseudo-atlas method were sensitive for stretch or compression in the posterior limb of the internal capsule. Additionally, both methods were able to show an increase in white matter disruption with increasing ventriculomegaly, with the pseudo-atlas method showing less variability and more specificity to changes in white matter tracts near to the ventricles. In this study, we found that there was no true gold-standard for DTI methodologies or atlases. Whilst there was no congruence between absolute values from DTI metrics, differing DTI methodologies were still valid but must be appreciated to be variably sensitive to different changes within white matter injury occurring concurrently. By combining

both atlas and pseudo-atlas based methodologies with DTI profiles, it was possible to navigate past such challenges to describe white matter injury changes in the context of confounders, such as neurodegenerative disease and ventricular enlargement, with transparency and consistency.

Keywords: diffusion tensor imaging (DTI), white matter, region of interest (ROI), tractography, Alzheimer's disease, ventriculomegaly

INTRODUCTION

Diffusion tensor imaging (DTI) is a relatively novel magnetic resonance-based imaging methodology that maps the water diffusion properties within the brain (Mori and Zhang, 2006). Since water generally diffuses along intact white matter tracts of the brain, the diffusion properties can therefore provide information about the microarchitecture of specific white matter tracts in the brain. DTI metrics that can be obtained consist of fractional anisotropy (FA), mean diffusivity (MD), axial diffusivity (L1) and radial diffusivity (L2 and 3).

DTI has been used to investigate patterns of white matter changes at a microstructural level in various cohorts, such as normal pressure hydrocephalus (NPH), optic nerve decompression and in the developing human brain (Lebel et al., 2008; Paul et al., 2014; Keong et al., 2017). Diffusion tensor metrics have been shown to be reliable biomarkers for Alzheimer's disease progression (Acosta-Cabronero et al., 2012), and are also sensitive to changes in white matter injury and compression in patients with NPH after surgical intervention (Scheel et al., 2012; Keong et al., 2017).

However, DTI acquisition, processing, and analysis is a complex multi-step process that is subject to many variables which may affect the results and interpretation thereof (Mukherjee et al., 2008; Soares et al., 2013; Christidi et al., 2016). The post-processing and analysis of DTI metrics is non-trivial and dependent on the availability of software and infrastructure. Quantitative DTI metrics can be obtained by various methods including tract-based spatial statistics (TBSS) which is a voxel-based morphometry-like approach; or the manual placement of 2D region of interest (ROI); atlas-registration based parcellations using a pre-defined white matter atlas to describe tracts of interest (Smith et al., 2006; Mukherjee et al., 2008; Oishi et al., 2009; Soares et al., 2013). or per-image automated tractography approaches, such as TRACULA (Yendiki et al., 2011). ROI analyses are time consuming, influenced by inter-rater variability, and subject to variations along a tract. The Alzheimer's Disease Neuroimaging Initiative (ADNI) group have previously published (Nir et al., 2013) on the use of both (i) white matter tract atlas ROIs, i.e., registration of images from a DTI atlas to each subject's distortion corrected FA image, before applying an atlas of white matter labels and superimposing these atlas ROIs into the same coordinate space as subject results for analysis and (ii) TBSS tract atlas ROIs as per (Smith et al., 2006). Per-image automated DTI tractography approaches are an attractive method for disease specific cohorts but are dependent on accurate registration and may be confounded by anatomical differences attributed to neurodegenerative diseases like Alzheimer's disease and the distortions of white matter tracts secondary to the presence of significant ventriculomegaly, such as in NPH (Mukherjee et al., 2008; Zalesky, 2011; Scheel et al., 2012; Acosta-Cabronero and Nestor, 2014).

In this paper, we evaluated the reliability and reproducibility of differing automated DTI tractography methods to produce diffusion metrics of various white matter tracts in the presence of known confounders such as atrophy in aging, neurodegeneration and significant ventriculomegaly. We firstly aimed to develop a cohort-specific pseudo atlas-based semi-automated tractography method that was comparable to an atlas-based DTI analysis currently utilized by the ADNI group; as we interrogated ADNI datasets for this study, we have therefore defined the latter method as the "gold-standard" approach for reference. We found that the diffusion metrics generated from the former were significantly different from those generated by the latter.

We hypothesized that the results from differing DTI methodologies could be subject to the impact of different algorithmic modifications. To test our hypotheses, we designed the following experiments to optimize the application of DTI methodologies to describe white matter injury patterns in the presence of confounders such as neurodegenerative disease and degree of ventriculomegaly:

1. We developed a cohort-specific pseudo atlas-based semi-automated tractography to generate white matter tracts of interest and compared it to that of the "gold standard" atlas-based DTI analysis currently utilized by ADNI, in order to assess the reproducibility and reliability of the novel methodology.
2. We performed initial comparisons on this pilot to examine the agreement of DTI metrics obtained from white matter tracts generated by both methodologies.
   a. Due to the poor agreement of the metrics, we proceeded to test the differing DTI methodologies under different processing algorithms to assess how these impacted the agreement of the metrics generated.
3. We performed testing using a known model of white matter at-risk of injury. This ROI model allowed us to test for white matter distortion patterns in three cohorts of patients with different levels of confounders, namely varying degrees of neurodegeneration and atrophy along the spectrum from cognitively normal to Alzheimer's disease.
4. In addition, we performed testing to examine the effect of increasing ventriculomegaly on this ROI model of white matter at-risk. We performed independent quantification

of ventricular size by measuring the Evans' index (EI) and concurrently examined changes in DTI metrics in the context of increasing ventriculomegaly for the ROI model of white matter tracts at risk.

5. Finally, we performed a further layer of analysis to confirm the diffusivity changes in this study by generating morphological patterns of DTI metrics for independent interpretation. We utilized DTI profiles, radar graphs of all DTI metrics (FA, MD, L1, L2, and 3), in order to illustrate differences between DTI methodologies and across cohorts. The concept and utility of DTI profiles has been previously described by our group in describing patterns of white matter injury across clinical cohorts (Lock et al., 2018).

MATERIALS AND METHODS

Data used in the preparation of this article were obtained from the ADNI database.[1] ADNI DTI metrics used for comparison were the UCLA DTI ROI summary measures for ADNIGO and ADNI2.

Subjects

The ADNI study recruited patients between the ages of 55 and 90 from 57 sites in the United States and Canada. For this study, we retrospectively selected subjects who had screening/baseline MRI scans with diffusion-weighted images (DWI) from the ADNI image data archive. The selected scans included 51 cognitively normal (CN) subjects (mean age 72.47 ± 6.13 years; 45.1% male), 48 patients with Alzheimer's disease (AD) (75.00 ± 8.67 years; 58.3% male) and 70 patients with early mild cognitive impairment (EMCI) (72.71 ± 8.29 years; 61.4% male). These cohorts were selected because we wanted to interrogate the methodologies in patients with varying degrees of cognitive impairment and atrophy.

Open-Source Software Used

3D slicer is an open source quantitative imaging network tool we used to derive ventricular morphological indices and to conduct 3D volumetric segmentation (Fedorov et al., 2012). ***MRIcroGL*** is an open source software developed by Neuroimaging Tools and Resources Collaboratory (NITRC) used in this study to convert DICOM images to NIfTI format [(Nitrc) N.T.R.C, 2014]. ***ExploreDTI*** is a graphical toolbox written in MATLAB that was used in this project for DTI and white matter tractography (Leemans et al., 2009).

MRI Acquisition and Post-processing

MRI scans were performed on 3T GE Medical Systems scanners across participating ADNI sites. Diffusion scans were acquired with 256 × 256 matrix; voxel size 2.7 mm × 2.7 mm × 2.7 mm; 41 DWI (b = 1,000 s/mm2) and 5 b0 images. More information on the MRI protocol is available at http://adni.loni.usc.edu/methods/documents/mri-protocols/.

[1] adni.loni.usc.edu

Pre-processing was required to convert each patient's set of unsorted DICOM format axial DWI images where two-dimensional DICOM image slices were converted into a single 3D NIfTI file with ***MRIcroGL***. During this step, 1 subject in the CN cohort was excluded due to a failure to convert it from DICOM to NIfTI format.

DTI files were generated using ***ExploreDTI***. Thereafter, they were corrected for subject motion and eddy current induced geometric distortion. Whole brain tractography was then performed.

White Matter Tracts

Utilizing the known ROI model of white matter at-risk, we chose to analyze 8 unique white matter tracts. Bilaterally, we analyzed a total of 14 white matter tracts, and they were as follows: Body of the corpus callosum (bCC), Genu of the corpus callosum (gCC), Inferior fronto-occipital Fasciculus (IFO), Inferior Longitudinal Fasciculus (ILF), Anterior Thalamic Radiation (ATR), Posterior Thalamic Radiation (PTR), Posterior Limb of the Internal Capsule (PLIC), and Uncinate Fasciculus (UF) (Hofer and Frahm, 2006; Wakana et al., 2007; Oishi et al., 2010; Borden et al., 2015; Keong et al., 2017). The bCC and gCC are midline structures while the rest are found bilaterally. Therefore, with 48 DWI in the AD cohort and 50 DWI in the CN cohort, this amounted to a total of 672 and 700 white matter tracts in the AD and CN cohort, respectively.

Methods of Automated Diffusion Tensor Imaging Tractography

In this paper, two methods of automated tractography were compared. The first method was a cohort-specific pseudo atlas-based semi-automated tractography method (termed **Method 1**) where a randomly selected image in each cohort is used as a template for white matter tract generation in the remaining images. The second method was an automated atlas-based ROI analysis (termed **Method 2**) where a standardized lab-based atlas was used as the template. These two methods were tested on the AD and CN cohorts. We followed this up by implementing additional algorithmic modifications to assess if they affected the results of the methodologies.

We implemented two modifications to the processing algorithms. The first was to try an alternative standardized atlas as a template in Method 2 (using the alternative atlas template is termed **Method 3**). The second was to optimize the alignment to the ACPC plane prior to performing the DTI analysis by following protocol adapted from the Human Connectome Project (HCP) pre-processing pipelines (Glasser et al., 2013). This was done by co-registration of the DWI to the MNI template (standardized template from 152 subject scans) and the corresponding T1-weighted image. This allowed all images in the dataset to be oriented and aligned to the same space such that the anterior and posterior commissures (ACPC) were aligned along a horizontal plane. By ensuring that all images in the dataset were standardized in terms of position and orientation, we sought to improve the fit of both atlases (and the pseudo-atlas) as applied to the images in the dataset.

Once we compared and found the technical considerations to have improved the tractography, we subsequently applied the refined methodology to all available cohorts to complete our DTI analysis, with the exception of the EMCI cohort, where only the ACPC alignment was enacted. This was because earlier results from AD and CN cohorts already showed that ACPC alignment improved the tract analysis success rate but did not fully eliminate the large differences between methodologies, so we proceeded to refine our analysis by only using ACPC aligned EMCI scans.

Method 1: Automated Atlas Based Tractography

We randomly chose a representative subject in each cohort and set its FA map as a "pseudo-atlas." To ensure that it was suitable as a template, the image was subject to visual inspection as a quality check and compared to other images to ensure that there were no obvious defects and distortions. Using ExploreDTI, specific white matter tracts of the pseudo-atlas were generated from user-determined regions of interests (ROIs). The type of ROI placed enforced different conditions within the area enclosed by the ROI. Placing an AND ROI generated tracts that passed through this area. Placing a NOT ROI excluded fibers that passed through this area. **Table 1** Shows the types of ROIs and their respective locations which were used to isolate the corresponding white matter tracts.

With the pseudo-atlas and ROIs as input, the software applied similar ROIs to the remaining images in the cohort using a deterministic streamline method (Lebel et al., 2008). White matter tracts were then automatically reconstructed via the automatically generated ROIs in the remaining images of the cohort. Where the ROIs extruded to an image failed to generate any tracts, this resulted in missing data.

Methods 2 and 3: Automated Atlas-Based Region of Interest Analysis

A widely used standardized DTI template with its associated white matter tracts was used as an atlas. The white matter tracts in the atlas were generated from ROIs determined by the template creator. The atlas template was warped, and the associated ROIs transformed and applied to each image in the dataset. The diffusion metrics were then automatically generated from the resulting white matter tracts defined by the ROIs. The problem of missing data as in Method 1 was also found to occur using this method but was not as significant as in Method 1.

Method 2 utilized the ICBM-DTI-81 atlas from the ICBM DTI workgroup (Oishi et al., 2008). This atlas template was created by averaging hand segmentation of diffusion tensor maps from 81 subjects with a mean age of 39 with 42 males and 39 females.

Method 3 utilized the JHU white matter tractography atlas from the Laboratory of Brain Anatomical MRI, Johns Hopkins University (Oishi et al., 2009). This atlas was based on averaging results from running deterministic tractography on 28 normal subjects with a mean age of 29 with 17 males and 11 females.

The atlas used in Method 2 contained all 8 unique white matter tracts we wanted to investigate whereas the atlas used in

TABLE 1 | ROI constraints used to isolate white matter tracts in the pseudo-atlas for Method 1.

Tract	ROI constraints
gCC	- Sagittal AND: Define anterior 1/6 of the length of the corpus callosum. - Parasagittal NOT: Slices lateral to corticospinal tract bilaterally, defining entire slice.
bCC	- Splenium of corpus callosum consists of the posterior 1/4 of the length of corpus callosum. - Sagittal AND: Define remaining length of the corpus callosum excluding the genu and splenium—from 1/6 to 3/4 length of corpus callosum. - Axial NOT: Slice just beneath the bCC, defining entire slice.
ATR	- Coronal AND: Slice chosen in the middle of the gCC, defining anterior limb of internal capsule. - Coronal AND: Slice at the anterior edge of pons, defining entire thalamus. - Sagittal NOT: Defining entire central slice. - Coronal NOT: Slice at the posterior thalamic edge, defining entire slice.
IFO	- Coronal AND: Slice at the anterior edge of gCC, defining entire slice. - Coronal AND: Slice at the halfway mark of parieto-occipital sulcus, defining the occipital lobe. - Sagittal NOT: Define entire central slice.
ILF	- Coronal AND: Slice at the posterior edge of cingulum, defining occipital lobe. - Coronal AND: Most posterior coronal slice in which the temporal lobe is not connected to the frontal lobe (as seen on axial view), defining the anterior temporal lobe. - Coronal NOT: Same slice as above, defining the rest of the brain except anterior temporal lobe. - Sagittal NOT: Defining entire central slice.
PLIC	- Axial AND: Slice where PLIC is visibly the largest, defining the PLIC. - Axial AND: Slice at the inferior slice where the PLIC is still visible, defining the PLIC. - Axial NOT: Slice at the condensed portion of the corticospinal tract in the brain stem, defining entire slice.
PTR	- Coronal AND: Slice at the posterior edge of the cingulum, defining anterior-posterior directing, periventricular white matter tracts. - Parasagittal AND: Slice at the lateral edge of thalamus, defining entire thalamus. - Coronal NOT: Slice at the anterior edge of thalamus, defining entire slice. - Axial NOT: slice at the inferior edge of thalamus, defining entire slice.
UF	- Axial AND: Slice where condensed cephalic-caudal directed fibers are distinct in the temporal lobe, defining temporal lobe. - Coronal AND: Slice anterior to the condensed cephalic-caudal directed fibers, defining inferior frontal lobe. - Coronal AND: Same slice as above, defining temporal lobe - Coronal NOT: Slice posterior to the condensed cephalic-caudal directed fibers, defining entire slice.

gCC, genu of the corpus callosum; bCC, body of the corpus callosum; ATR, anterior thalamic radiation; IFO, inferior fronto-occipital fasciculus; ILF, inferior longitudinal fasciculus; PLIC, posterior limb of the internal capsule; PTR, posterior thalamic radiation; UF, uncinate fasciculus.

Method 3 only identified 5 of the 8 tracts we required: gCC, ATR, IFO, ILF, and UF.

Characterizing Ventriculomegaly—Evans' Index

The Evans' index (EI) is commonly used to characterize the degree of ventriculomegaly from a patient's MRI or CT scan (Yamada et al., 2016). It is defined as the ratio of the maximum width of the frontal horns of the lateral ventricles to the maximum internal width of the cranial vault as seen on the axial view (Yamada et al., 2016). 3D Slicer was used to re-align T1 scans to the ACPC for consistency and derive the EI (Soon et al., 2021).

Statistical Analysis

Diffusion metrics FA and MD from both left and right tracts were averaged for the purposes of the analysis. Paired *t*-tests were used to test for differences between the different methodologies. Linear correlation was used to investigate the association between diffusion metrics and ventriculomegaly measured by the Evans' index. Scatter plots of FA and MD obtained from both methodologies for all tracts across the AD, EMCI, and CN cohorts were plotted to show the agreement of metrics and the variance within each methodology. All statistical analyses were performed using R statistical software (version 4.0.4) (R Development Core Team, 2010). A p-value of < 0.05 was considered to be statistically significant.

Diffusion Tensor Imaging Profiles

DTI profiles are presented as radar graphs of means of all DTI metrics (FA, MD, L1, L2, and 3), in order to provide a simplistic illustration of differences between the various methods, as well as differences across the spectrum of disease for AD. We have previously demonstrated the utility of DTI profiles to describe and compare disease processes in white matter tracts across different cohorts (Keong et al., 2017; Lock et al., 2018). White matter tract profiles were also generated using Tract Analysis Profiles to illustrate how DTI metrics vary **along** each white matter tract (Yeatman et al., 2012).

RESULTS

Reproducibility and Reliability of Methodologies

Method 1 generated 96.3% (647/672) of all white matter tracts in the AD cohort and 96.9% (678/700) in the CN cohort. Method 1 was unable to generate 25 tracts in the AD cohort and 22 tracts in the CN cohort. This is in contrast to Method 2 which was able to generate 99.6% (669/672) and 100% (700/700) tracts in the AD and CN cohorts, respectively. This amounts to 3 missing tracts in the AD cohort. After the implementation of the ACPC alignment, the reliability and reproducibility of Method 1 improved with 98.7% (663/672) and 98.9% (692/700) success rate in the AD and CN cohort, respectively. There were 9 missing tracts in the former and 8 in the latter. Method 2 generated 100% of tracts in both AD and CN cohorts. Implementation of Methods 1 and 2 on the ACPC aligned-EMCI cohort likewise showed high success rates of 96.2% (916/952) and 99.9% (951/952), respectively.

Comparison of Diffusion Tensor Imaging Metrics Across Methodologies

Tables 2, **3** show the results of the paired *t*-tests conducted on the DTI metrics obtained from the two methodologies across all 8 white matter tracts. **Table 2** compares the FA and MD obtained using Method 1 with those using Methods 2 and 3 applied on non-ACPC aligned images in the AD and CN cohorts, respectively. **Table 3** also compares Methods 1 with 2 and 3 but applied on scans that have undergone the ACPC alignment and include scans from the EMCI cohort.

Non-ACPC aligned Method 1 was not well correlated to Methods 2 and 3 (**Table 2**). FA and MD from Method 1 were significantly different ($p < 0.001$) from Methods 2 and 3 for all tracts in AD and CN cohorts, except for PTR MD in CN. After ACPC alignment and co-registration, Method 1 was significantly different ($p < 0.001$) from Methods 2 and 3 for all tracts in AD, CN, and EMCI cohorts, except for PTR MD in AD and CN (**Table 3**).

Figure 1 compares the FA of ACPC aligned images and non-ACPC aligned images obtained using Methods 2 and 3 against Method 1 in the 8 white matter tracts across CN and AD cohorts. **Figure 2** compares the MD of ACPC aligned images and non-ACPC aligned images obtained using Methods 2 and 3 against Method 1. **Figure 3** compares both the FA and MD of ACPC aligned images using Methods 2 and 3 against Method 1 in the EMCI cohort. Non-ACPC aligned images in the EMCI cohort were not compared here because the results were similar to AD and CN images. The findings here seem to generally agree with those from the paired *t*-tests.

FA and MD scatter plots demonstrated poor agreement between Method 1 vs. 2 and Method 1 vs. 3 across all tracts in AD and CN (**Figures 1**, **2**). This was not improved even with ACPC alignment and co-registration of images. These trends are also present with the addition of a cohort with an intermediate severity of disease process (i.e., EMCI).

Across the paired *t*-tests in **Tables 2**, **3** and scatter plots in **Figures 1**–**3**, FA and MD obtained using Methods 1, 2, and 3 show poor agreement and consistency across the CN, AD, and EMCI cohorts. This is evidenced by the low linear correlation coefficients and relatively large mean differences in the metrics obtained across all tracts and cohorts as well as the scatterplots showing a large deviation from the 45-degree diagonal line. This demonstrates that the type of standard atlases used in Method 2 (i.e., an alternative atlas was also tested using Method 3) did not meaningfully improve the agreement. Additionally, comparing across the AD and CN cohorts also showed no changes in agreements. Implementing the ACPC alignment across all scans improved the agreements across all tracts only marginally. Notably, the inter-methodological differences were greater than the differences due to the application of technical considerations. This confirmed the fact that there were external confounding factors impacting the methodologies which rendered them incomparable.

White Matter Pattern Changes in Cognitively Normal vs. Early Mild Cognitive Impairment vs. Alzheimer's Disease Cohorts

Despite the lack of agreement, Methods 1, 2, and 3 showed general trends that illustrate and reaffirm the presence of different white matter pattern changes when comparing across the AD, EMCI, and CN cohorts with varying degrees of neurodegeneration. **Figures 1–3** show that there was greater variability for white matter structures adjacent or near to the ventricles such as the bCC and gCC as well as multidirectional tracts like the PLIC and UF. The difference, however, is that Method 1 reports white matter tracts having generally higher FA and lower MD values, implying a more preserved neural structure, compared to the other two methods for each cohort tested.

Effect on White Matter Pattern Changes With Increasing Ventriculomegaly

Figure 4 shows the scatter plots of FA and MD obtained from both Methods 1 and 2 plotted against the Evans' index (EI) for all 8 white matter tracts across all 3 cohorts of AD, EMCI, and CN combined. Only the ACPC aligned images are used in this analysis due to its superior reliability and reproducibility as previously shown. From the figures, we observed differing patterns of correlation with EI when using Method 1 compared to Method 2. From metrics obtained using Method 2, as EI increased (implying increasing ventriculomegaly) there was a

TABLE 2 | Comparison of FA and MD derived by Method 1 against Methods 2 and 3 (non-ACPC aligned and co-registered) across white matter tracts in the **(A)** Alzheimer's disease cohort and **(B)** cognitively normal cohort.

(A) AD cohort

		Linear correlation		Significance of correlation		Mean difference		Paired *t*-test significance	
Tract		**1 vs. 2**	**1 vs. 3**	**1 vs. 2**	**1 vs. 3**	**1 vs. 2**	**1 vs. 3**	**1 vs. 2**	**1 vs. 3**
bCC	FA	0.150		0.308		–0.099		<0.001	
	MD	0.514		<0.001		0.0004		<0.001	
gCC	FA	0.226	0.494	0.127	<0.001	–0.144	–0.237	<0.001	<0.001
	MD	0.511	0.557	<0.001	<0.001	0.0003	0.0004	<0.001	<0.001
ATR	FA	0.416	0.378	0.004	0.009	–0.136	–0.136	<0.001	<0.001
	MD	0.502	0.281	<0.001	0.056	0.0005	0.0005	<0.001	<0.001
IFO	FA	0.469	0.474	<0.001	<0.001	–0.213	–0.208	<0.001	<0.001
	MD	0.421	0.406	0.003	0.005	0.0002	0.0002	<0.001	<0.001
ILF	FA	0.291	0.091	0.047	0.542	–0.236	–0.230	<0.001	<0.001
	MD	0.124	0.138	0.408	0.355	0.0002	0.0002	<0.001	<0.001
PLIC	FA	0.145		0.330		–0.086		<0.001	
	MD	0.054		0.716		0.0002		<0.001	
PTR	FA	0.352		0.015		–0.100		<0.001	
	MD	0.298		0.042		0.0001		<0.001	
UF	FA	–0.045	0.237	0.762	0.109	–0.202	–0.207	<0.001	<0.001
	MD	0.263	0.396	0.074	0.006	0.0008	0.0005	<0.001	<0.001

(B) CN cohort

		Linear correlation		Significance of correlation		Mean difference		Paired *t*-test significance	
Tract		**1 vs. 2**	**1 vs. 3**	**1 vs. 2**	**1 vs. 3**	**1 vs. 2**	**1 vs. 3**	**1 vs. 2**	**1 vs. 3**
bCC	FA	0.415		0.003		–0.066		<0.001	
	MD	0.502		<0.001		0.0003		<0.001	
gCC	FA	0.354	0.602	0.012	<0.001	–0.124	–0.234	<0.001	<0.001
	MD	0.520	0.459	<0.001	<0.001	0.0002	0.0003	<0.001	<0.001
ATR	FA	0.340	0.301	0.017	0.036	–0.127	–0.128	<0.001	<0.001
	MD	0.481	0.545	<0.001	<0.001	0.0004	0.0004	<0.001	<0.001
IFO	FA	0.547	0.505	<0.001	<0.001	–0.217	–0.213	<0.001	<0.001
	MD	0.607	0.554	<0.001	<0.001	0.0001	0.0001	<0.001	<0.001
ILF	FA	0.427	0.290	0.002	0.041	–0.235	–0.227	<0.001	<0.001
	MD	0.571	0.532	<0.001	<0.001	0.0001	0.0001	<0.001	<0.001
PLIC	FA	–0.022		0.879		–0.058		<0.001	
	MD	0.182		0.205		0.0001		<0.001	
PTR	FA	0.174		0.232		–0.086		<0.001	
	MD	0.479		<0.001		0.0000		0.296	
UF	FA	–0.086	0.445	0.554	0.001	–0.205	–0.206	<0.001	<0.001
	MD	0.154	0.389	0.286	0.005	0.0005	0.0004	<0.001	<0.001

A negative mean difference indicates that FA/MD derived by Method 1 is higher than that of Methods 2 or 3. All mean difference of MD is in mm^2/s.

TABLE 3 | Comparison of FA and MD derived by Method 1 against Methods 2 and 3 (ACPC aligned and co-registered) across white matter tracts in the **(A)** Alzheimer's disease cohort, **(B)** cognitively normal cohort, and **(C)** early mild cognitive impairment cohort.

(A) AD cohort

		Linear correlation		Significance of correlation		Mean difference		Paired *t*-test significance	
Tract		**1 vs. 2**	**1 vs. 3**	**1 vs. 2**	**1 vs. 3**	**1 vs. 2**	**1 vs. 3**	**1 vs. 2**	**1 vs. 3**
bCC	FA	0.271		0.062		–0.073		<0.001	
	MD	0.506		<0.001		0.0004		<0.001	
gCC	FA	0.204	0.509	0.163	<0.001	–0.127	–0.244	<0.001	<0.001
	MD	0.686	0.561	<0.001	<0.001	0.0003	0.0004	<0.001	<0.001
ATR	FA	0.325	0.422	0.024	0.003	–0.131	–0.133	<0.001	<0.001
	MD	0.715	0.775	<0.001	<0.001	0.0005	0.0005	<0.001	<0.001
IFO	FA	0.550	0.537	<0.001	<0.001	–0.212	–0.215	<0.001	<0.001
	MD	0.307	0.323	0.034	0.025	0.0002	0.0002	<0.001	<0.001
ILF	FA	0.122	0.173	0.408	0.241	–0.235	–0.233	<0.001	<0.001
	MD	0.302	0.311	0.037	0.032	0.0002	0.0002	<0.001	<0.001
PLIC	FA	0.104		0.484		–0.074		<0.001	
	MD	0.312		0.031		0.0002		<0.001	
PTR	FA	0.337		0.019		–0.086		<0.001	
	MD	0.406		0.004		0.0000		0.060	
UF	FA	0.115	0.446	0.436	0.001	–0.202	–0.210	<0.001	<0.001
	MD	0.281	0.392	0.053	0.006	0.0009	0.0005	<0.001	<0.001

(B) CN cohort

		Linear correlation		Significance of correlation		Mean difference		Paired *t*-test significance	
Tract		**1 vs. 2**	**1 vs. 3**	**1 vs. 2**	**1 vs. 3**	**1 vs. 2**	**1 vs. 3**	**1 vs. 2**	**1 vs. 3**
bCC	FA	0.302		0.033		–0.055		<0.001	
	MD	0.503		<0.001		0.0004		<0.001	
gCC	FA	0.268	0.426	0.062	0.002	–0.109	–0.245	<0.001	<0.001
	MD	0.556	0.510	<0.001	<0.001	0.0002	0.0003	<0.001	<0.001
ATR	FA	0.488	0.473	<0.001	<0.001	–0.116	–0.120	<0.001	<0.001
	MD	0.688	0.672	<0.001	<0.001	0.0004	0.0004	<0.001	<0.001
IFO	FA	0.548	0.424	<0.001	0.002	–0.213	–0.215	<0.001	<0.001
	MD	0.730	0.683	<0.001	<0.001	0.0001	0.0002	<0.001	<0.001
ILF	FA	0.331	0.317	0.019	0.025	–0.234	–0.233	<0.001	<0.001
	MD	0.583	0.618	<0.001	<0.001	0.0001	0.0001	<0.001	<0.001
PLIC	FA	–0.191		0.184		–0.047		<0.001	
	MD	0.181		0.208		0.0001		<0.001	
PTR	FA	0.114		0.429		–0.069		<0.001	
	MD	0.437		0.002		0.0000		0.449	
UF	FA	–0.088	0.479	0.545	<0.001	–0.199	–0.209	<0.001	<0.001
	MD	0.123	0.422	0.394	0.002	0.0005	0.0004	<0.001	<0.001

(C) EMCI cohort

		Linear correlation		Significance of correlation		Mean difference		Paired *t*-test significance	
Tract		**1 vs. 2**	**1 vs. 3**	**1 vs. 2**	**1 vs. 3**	**1 vs. 2**	**1 vs. 3**	**1 vs. 2**	**1 vs. 3**
bCC	FA	0.334		0.006		–0.048		<0.001	
	MD	0.436		<0.001		0.0004		<0.001	
gCC	FA	0.414	0.553	<0.001	<0.001	–0.106	–0.245	<0.001	<0.001
	MD	0.420	0.440	<0.001	<0.001	0.0002	0.0003	<0.001	<0.001
ATR	FA	0.460	0.483	<0.001	<0.001	–0.127	–0.129	<0.001	<0.001
	MD	0.227	0.535	0.069	<0.001	0.0005	0.0005	<0.001	<0.001
IFO	FA	0.628	0.597	<0.001	<0.001	–0.208	–0.209	<0.001	<0.001
	MD	0.572	0.523	<0.001	<0.001	0.0002	0.0002	<0.001	<0.001
ILF	FA	0.502	0.558	<0.001	<0.001	–0.231	–0.230	<0.001	<0.001
	MD	0.531	0.564	<0.001	<0.001	0.0001	0.0001	<0.001	<0.001
PLIC	FA	0.114		0.361		–0.275		<0.001	
	MD	0.360		0.003		0.0001		<0.001	
PTR	FA	0.438		<0.001		–0.063		<0.001	
	MD	0.570		<0.001		0.0000		0.008	
UF	FA	0.161	0.562	0.197	<0.001	–0.193	–0.205	<0.001	<0.001
	MD	0.398	0.580	0.001	<0.001	0.0006	0.0004	<0.001	<0.001

A negative mean difference indicates that FA/MD derived by Method 1 is higher than that of Methods 2 or 3. All mean difference of MD is in mm^2/s.

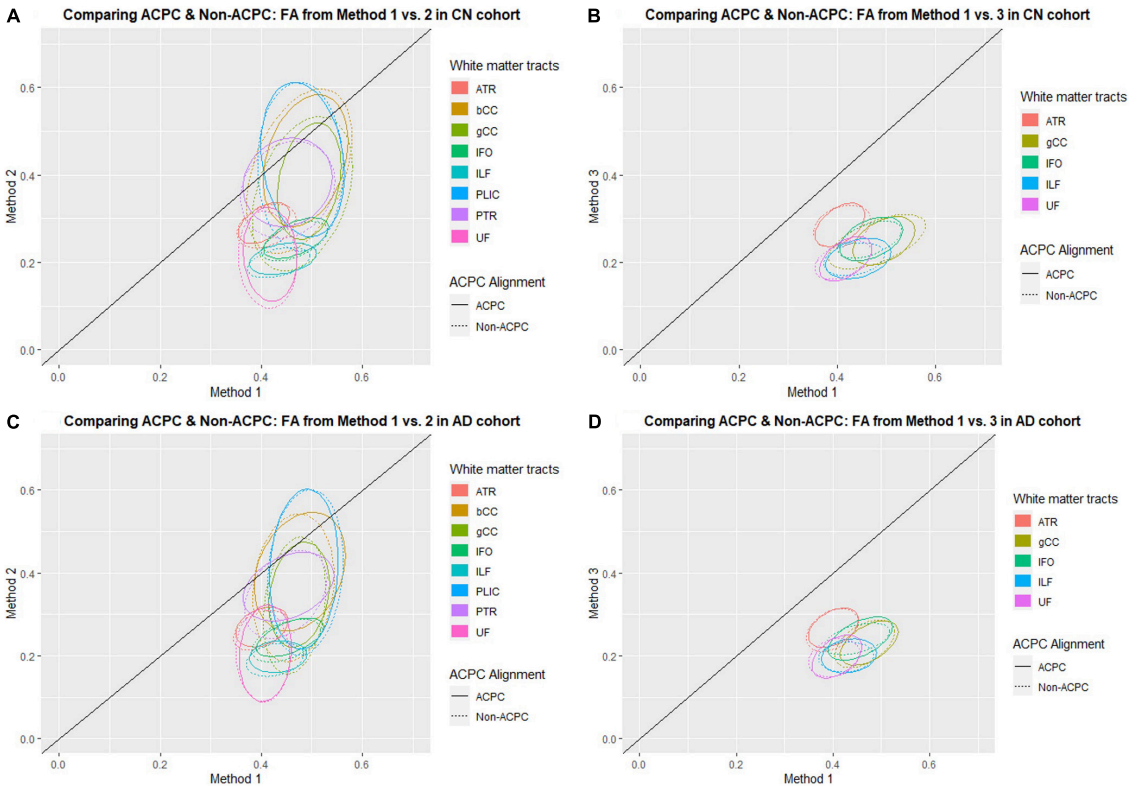

FIGURE 1 | Distribution of scatter plots of FA obtained using Methods 2 and 3 against Method 1, comparing non-ACPC aligned and co-registered with ACPC aligned white matter tracts across cognitively normal (CN) and Alzheimer's Disease (AD) cohorts. The ellipses assume a multivariate normal distribution with the mean at the center and area of the ellipse representing 95% confidence level. gCC, genu of the corpus callosum; bCC, body of the corpus callosum; ATR, anterior thalamic radiation; IFO, inferior fronto-occipital fasciculus; ILF, inferior longitudinal fasciculus; PLIC, posterior limb of the internal capsule; PTR, posterior thalamic radiation; UF, uncinate fasciculus. **(A)** Comparing ACPC and Non-ACPC: FA from Method 1 vs. 2 in CN cohort. **(B)** Comparing ACPC and Non-ACPC: FA from Method 1 vs. 3 in CN cohort. **(C)** Comparing ACPC and Non-ACPC: FA from Method 1 vs. 2 in AD cohort. **(D)** Comparing ACPC and Non-ACPC: FA from Method 1 vs. 3 in AD cohort.

significant decrease in FA which is consistent with decreased white matter integrity. By contrast, metrics obtained using Method 1, showed that with increasing EI, there was a significant increase in FA seen in the PLIC which is consistent with patterns of stretch or compression. Both methods showed significant increases in MD with increasing EI, suggesting an increase in global, multi-directional white matter disruption. Method 1, however, showed less variability and was more specific to changes in white matter tracts near to the ventricles.

Correlation to Diffusion Tensor Imaging Profiles of White Matter Tracts

DTI profiles for the gCC and the UF tracts were selected to illustrate differences between the methods and between cohorts. **Figure 5** shows that the difference in DTI metrics generated by Methods 1, 2, and 3 can be distinguished with DTI profiles. Method 1 consistently produced the lowest MD, L1 and L2, and 3 values, compared to Methods 2 and 3. Profiles for DTI metrics before and after ACPC alignment were nearly visually indistinguishable for Methods 1 and 2. Failure to correct for ACPC alignment did not influence the results as much as the variation produced by the different methods. DTI profiles demonstrated cohort differences between AD, CN, and EMCI, across the spectrum of disease, but inter-methodological differences were larger than inter-cohort differences (**Figure 6A**). Likewise, change in DTI morphology in the AD cohort after 12 months was not as pronounced as inter-methodological differences (**Figure 6B**). White matter tract profiles in **Figure 7** show the variability of DTI metrics along different white matter tracts.

DISCUSSION

In this paper, we demonstrated that it was possible to reliably develop and refine an SOP for a pseudo atlas-based semi-automated tractography DTI analysis method in the presence of confounders comprising aging, neurodegenerative disease, and ventricular enlargement. However, the absolute values of the DTI metrics generated by this novel methodology did not align well with those generated by standardized atlas-based DTI analyses, despite implementing a differential of algorithmic modifications. Regardless, we managed to show that the inter-methodological differences between DTI metrics obtained from Method 1 and 2 were greater than the effects of implementing the algorithmic

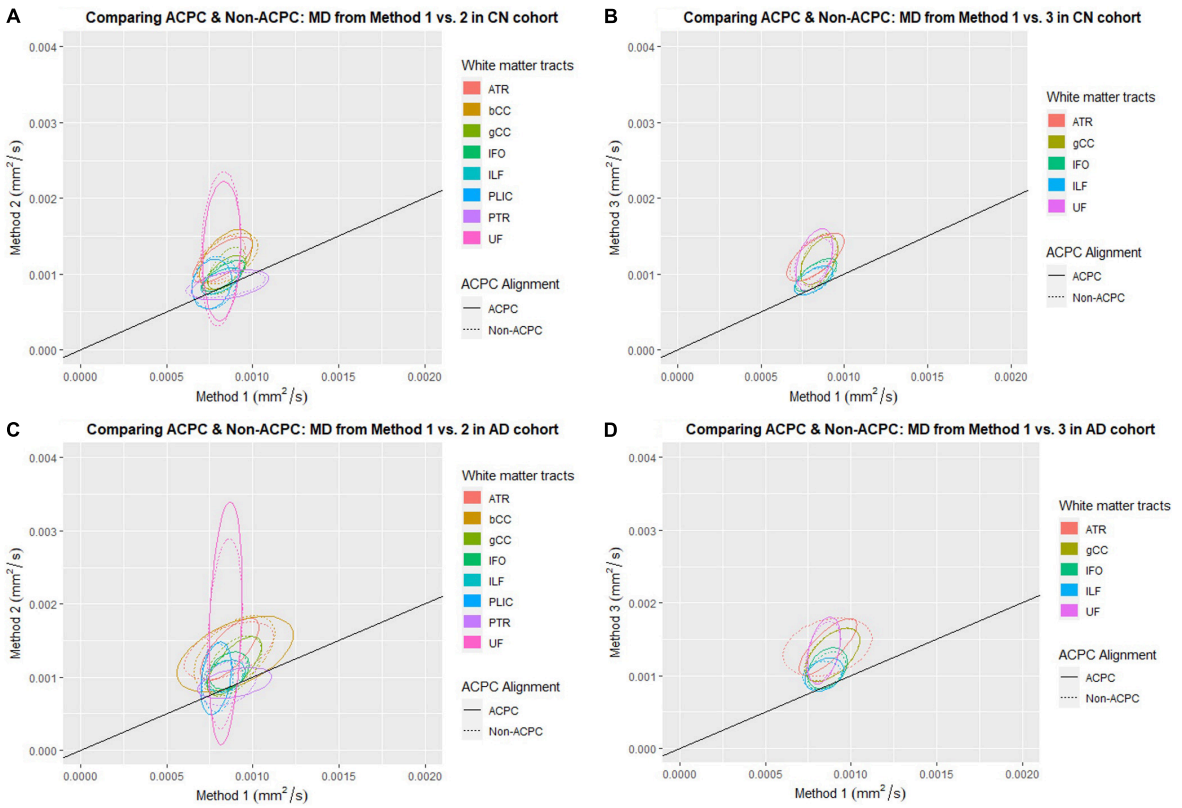

FIGURE 2 | Distribution of scatter plots of MD obtained using Methods 2 and 3 against Method 1, comparing non-ACPC aligned and co-registered with ACPC aligned white matter tracts across cognitively normal (CN) and Alzheimer's Disease (AD) cohorts. The ellipses assume a multivariate normal distribution with the mean at the center and area of the ellipse representing 95% confidence level. gCC, genu of the corpus callosum; bCC, body of the corpus callosum; ATR, anterior thalamic radiation; IFO, inferior fronto-occipital fasciculus; ILF, inferior longitudinal fasciculus; PLIC, posterior limb of the internal capsule; PTR, posterior thalamic radiation; UF, uncinate fasciculus. **(A)** Comparing ACPC and Non-ACPC: MD from Method 1 vs. 2 in CN cohort. **(B)** Comparing ACPC and Non-ACPC: MD from Method 1 vs. 3 in CN cohort. **(C)** Comparing ACPC and Non-ACPC: MD from Method 1 vs. 2 in AD cohort. **(D)** Comparing ACPC and Non-ACPC: MD from Method 1 vs. 3 in AD cohort.

modifications. Whilst this suggests that DTI output metrics from differing methodologies cannot be directly compared for statistical analysis, we also showed that DTI methodologies were differentially impacted upon by confounders affecting structural brain or ventricular changes. In the presence of such considerations, we found that there was no true "gold-standard" but rather, the differing methodologies were sensitive to differing significant findings on a spectrum from contiguous to non-contiguous changes, in ways that were both complementary to each other and consistent with differences between such cohorts as reported in published literature. Nevertheless, by creating the DTI profiles from metrics generated by the methodologies, we showed that, despite differing DTI values, the morphology of DTI changes was consistent across DTI analysis methods.

A Cohort-Specific Pseudo Atlas-Based Semi-Automated Tractography Method vs. Standardized Atlas-Based Diffusion Tensor Imaging Analysis

In our study, we found that a novel pseudo atlas-based semi-automated tractography DTI analysis method (Method 1) was reliable and reproducible. This was evidenced by the high success rate of generating white matter tracts across both AD and CN sub cohorts. Upon implementing the ACPC alignment (one modification to the algorithm), the number of missing tracts decreased from 25 to 9 tracts in the AD cohort and 22–8 tracts in the CN cohorts. This showed that the intracohort variability in image orientation could be a main contributor to the missing tracts and that this refinement improved the reliability and reproducibility of the methodology.

Surprisingly, we could not show that the actual DTI metrics generated from the pseudo atlas-based semi-automated tractography DTI analysis method (Method 1) were exactly comparable to the standardized atlas-based DTI analysis (Methods 2). This was despite implementing the both modifications to the algorithm including an alternative published and verified atlas (Method 3) and applying the ACPC alignment. From observing the scatter plots in **Figures 1–3** we noted that this disagreement can be attributed to Method 1 reporting white matter tracts as having generally higher FA and lower MD values compared to those obtained via Methods 2 and 3 across AD, CN, and EMCI cohorts. However, as this finding was consistent across the varying spectrums of disease and aging,

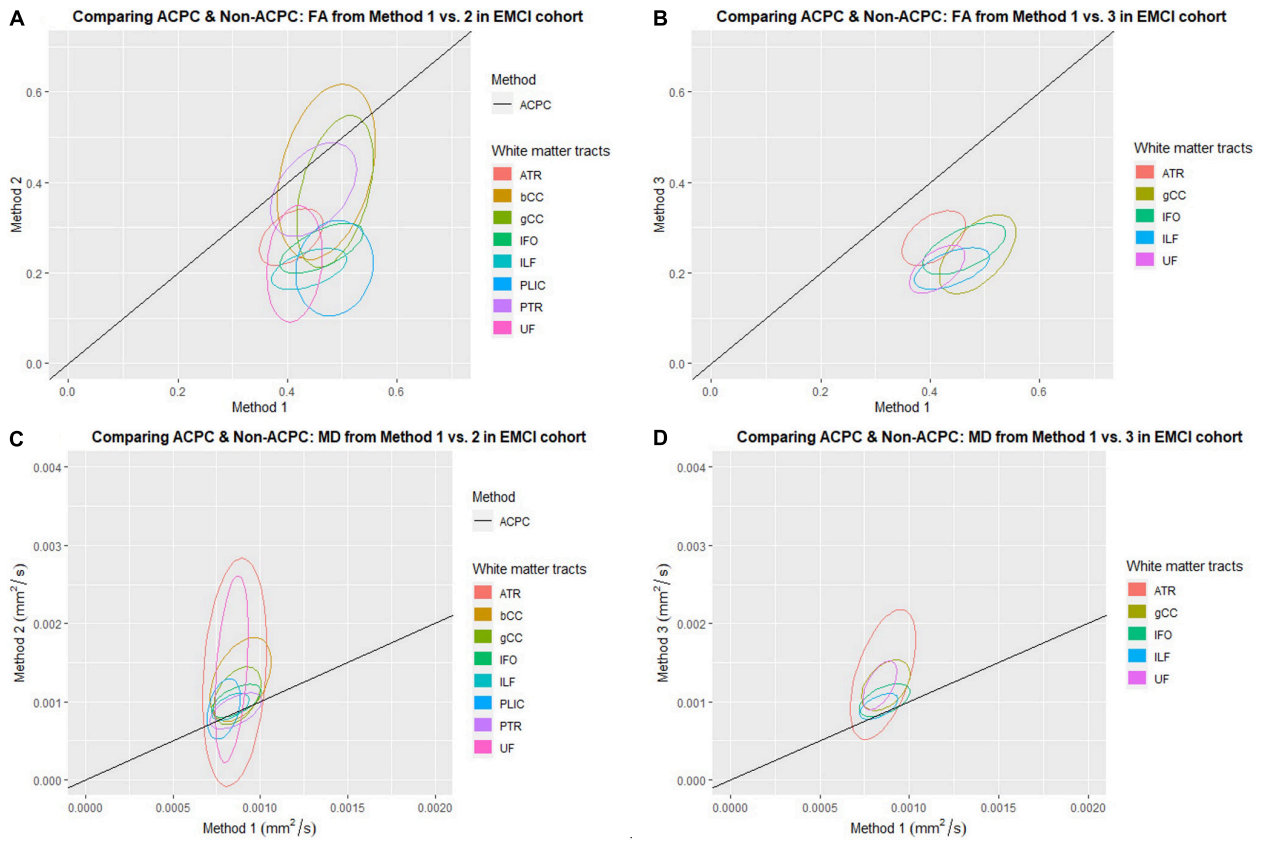

FIGURE 3 | Distribution of scatter plots of FA and MD obtained using Methods 2 and 3 against Method 1 (ACPC aligned and co-registered) across white matter tracts in the early mild cognitive impairment (EMCI) cohort. The ellipses assume a multivariate normal distribution with the mean at the center and area of the ellipse representing 95% confidence level. gCC, genu of the corpus callosum; bCC, body of the corpus callosum; ATR, anterior thalamic radiation; IFO, inferior fronto-occipital fasciculus; ILF, inferior longitudinal fasciculus; PLIC, posterior limb of the internal capsule; PTR, posterior thalamic radiation; UF, uncinate fasciculus. **(A)** Comparing ACPC and Non-ACPC: FA from Method 1 vs. 2 in EMCI cohort. **(B)** Comparing ACPC and Non-ACPC: FA from Method 1 vs. 3 in EMCI cohort. **(C)** Comparing ACPC and Non-ACPC: MD from Method 1 vs. 2 in EMCI cohort. **(D)** Comparing ACPC and Non-ACPC: MD from Method 1 vs. 3 in EMCI cohort.

i.e., in AD (neurodegenerative), EMCI (mild neurodegenerative) and CN (aging) cohorts, it suggests that a cohort-specific white matter template (the pseudo-atlas) as employed in Method 1 was more sensitive to generating white matter tracts in the presence of confounders compared to Methods 2 and 3. This showed that while Method 1 was internally consistent across cohorts, DTI output measures may not be directly comparable to DTI measures from Methods 2 and 3 for purposes of statistical analysis.

The Effect of Ventriculomegaly on the Degree of Patterns of White Matter Change

From **Figure 4**, we noted that with increasing EI, signifying an increasing degree of ventriculomegaly, Method 1 showed that PLIC had a significant increase in FA, Method 2 showed a significant decrease in FA across all tracts and both Methods 1 and 2 showed significant increases in MD across all tracts. An increase in FA is consistent with tracts under stretch or compression while a decrease in FA is consistent with decreased white matter integrity. Conversely, a rise in MD across all tracts suggested an increase in global, multidirectional white matter disruption. These patterns of white matter injury in the setting of ventriculomegaly are consistent with findings reported in the literature (Keong et al., 2017). Whilst the FA changes in PLIC reflected in Methods 1 and 2 appear to be contradictory, such conflict is consistent with DTI findings of previous work in hydrocephalus where it was shown that FA can increase and decrease within the same context, depending on the reversibility of white matter injury (Assaf et al., 2006; Hattori et al., 2011; Kanno et al., 2011; Ben-Sira et al., 2015; Keong et al., 2017; Tan et al., 2018). This represents an important fallacy of interpreting DTI changes based solely on global measures, such as FA or MD alone. In particular, FA is highly dependent upon relative changes in diffusivity measures; it can be driven to higher or lower values based on predominant changes in axial diffusivity over radial diffusivity and vice versa. In this study, we found that the different patterns that were reflected in both methods could be interpreted as complementary to each other. For example, Method 2 may have detected the reduced white matter integrity and hence decreased FA, whereas Method 1 detected the compressive mechanism of injury and hence increased FA. Method 1, however, showed less variability and was more specific to changes in white matter tracts nearer to the ventricles (i.e., bCC, gCC), when compared to Method 2. These known DTI

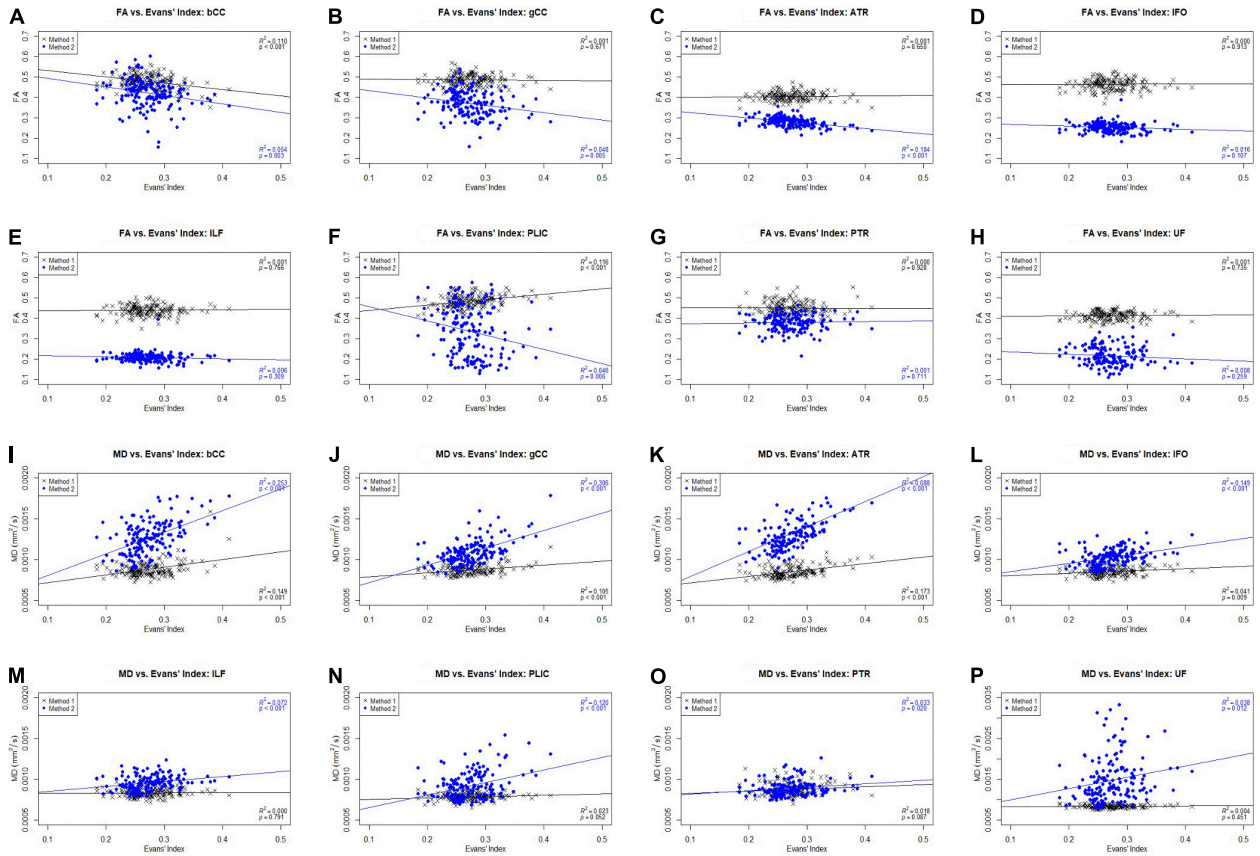

FIGURE 4 | Scatter plots of FA and MD against Evans' index (EI) across white matter tracts for CN, AD, and EMCI cohorts combined. gCC, genu of the corpus callosum; bCC, body of the corpus callosum; ATR, anterior thalamic radiation; IFO, inferior fronto-occipital fasciculus; ILF, inferior longitudinal fasciculus; PLIC, posterior limb of the internal capsule; PTR, posterior thalamic radiation; UF, uncinate fasciculus. **(A)** FA vs. Evans' Index: bCC. **(B)** FA vs. Evans' Index: gCC. **(C)** FA vs. Evans' Index: ATR. **(D)** FA vs. Evans' Index: IFO. **(E)** FA vs. Evans' Index: ILF. **(F)** FA vs. Evans' Index: PLIC. **(G)** FA vs. Evans' Index: PTR. **(H)** FA vs. Evans' Index: UF. **(I)** MD vs. Evans' Index: bCC. **(J)** MD vs. Evans' Index: gCC. **(K)** MD vs. Evans' Index: ATR. **(L)** MD vs. Evans' Index: IFO. **(M)** MD vs. Evans' Index: ILF. **(N)** MD vs. Evans' Index: PLIC. **(O)** MD vs. Evans' Index: PTR. **(P)** MD vs. Evans' Index: UF.

conflicts impacting upon the transparency and consistency of interpretation of DTI results across literature would benefit from the application of a more standardized common taxonomy; this is an approach we have proposed elsewhere (Keong et al., 2017, manuscript in submission).

Correlation to Diffusion Tensor Imaging Profiles

The DTI profiles in **Figures 5**, **6** align with the above findings. We showed that Method 1 reports more preserved white matter profiles in comparison to Methods 2 and 3 across AD, CN and EMCI cohorts. This supports the suggestion that a cohort-specific template (the pseudo-atlas) was more sensitive to demonstrating white matter integrity in the presence of confounders due to aging and neurodegenerative disease. Additionally, we found evidence that ACPC alignment did not significantly affect the morphology of DTI profiles generated and that inter-methodological differences were indeed larger than inter-cohort differences. These cohorts include the spectrum of Alzheimer's disease, from CN to EMCI and finally to AD. Inter-methodological differences were similar to or greater than changes in DTI profiles in the AD cohort after 12 months.

Despite the variability of DTI values along the tracts (**Figure 7**) as well as between methodologies (as seen in DTI profiles), the morphology of the DTI profile still remains consistent across cohorts and aligns well with published literature. This lack of comparability in DTI analysis methodologies and variability, ultimately supports the use of DTI profiles in the analysis of DTI metrics.

Strengths and Weakness of Differing Diffusion Tensor Imaging Methodologies

As we have previously discussed, the success rate in generating white matter tracts is marginally higher (after the ACPC alignment) for Method 2 compared to Method 1. This is likely because our use of a single subject pseudo atlas restricted the automated tractography, rendering it more selective in its ability to generate the white matter tracts. This can be seen as an advantage to Method 1 as its selectiveness may reduce the likelihood of generating spurious tracts and thus erroneous data. The use of Method 2 incorporated the use of validated

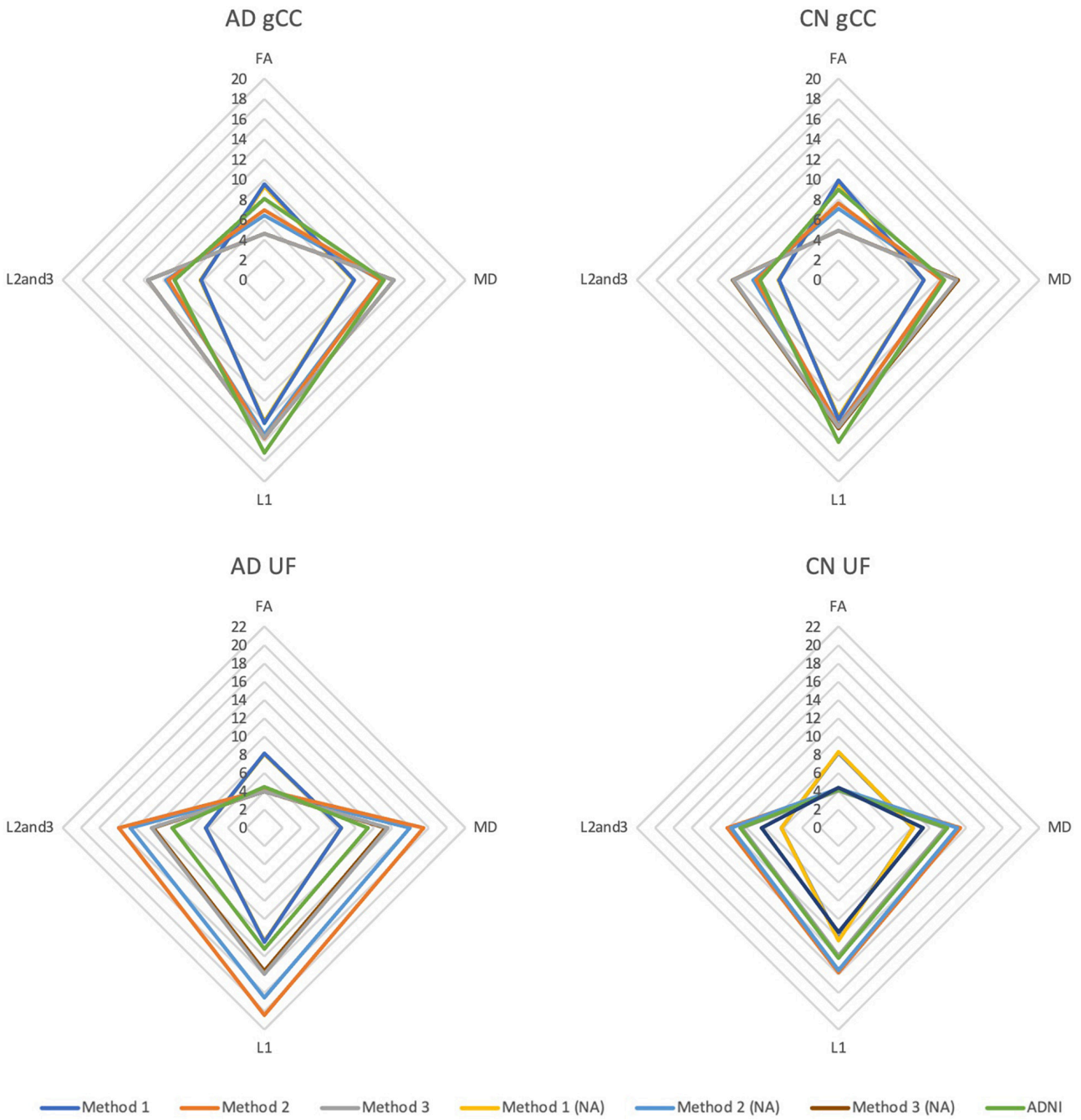

FIGURE 5 | DTI radar graph profiles for comparison of methods with and without ACPC alignment and co-registration in Alzheimer's disease (AD) and cognitively normal (CN) cohorts. DTI metrics from the ADNI data archive are included for reference. FA values are presented as x20 for illustration; MD, L1, L2, and 3 values are presented as $\times 10^4$. gCC, genu of the corpus callosum; UF, uncinate fasciculus; NA, no ACPC alignment.

atlases which have been derived from group-averaging from a sample cohort. This may also be perceived as providing this option with a technical advantage over Method 1, which used a single subject selected from the dataset to generate the pseudo-atlas. However, as we have discovered, the use of a pseudo-atlas may equally be argued to be advantageous as it promotes a template that is more representative of the cohorts compared to the standardized atlases used in Methods 2 and 3. Our study has shown that this resulted in Method 1 (the pseudo-atlas) being more sensitive than standardized atlas-based DTI analyses, in characterizing changes in the model of white matter at-risk due to pathophysiological processes of distortion and disease.

In terms of processing, Method 1 required a much longer time to produce the DTI data compared to Methods 2 or 3. This was for two main reasons. The first was that the white

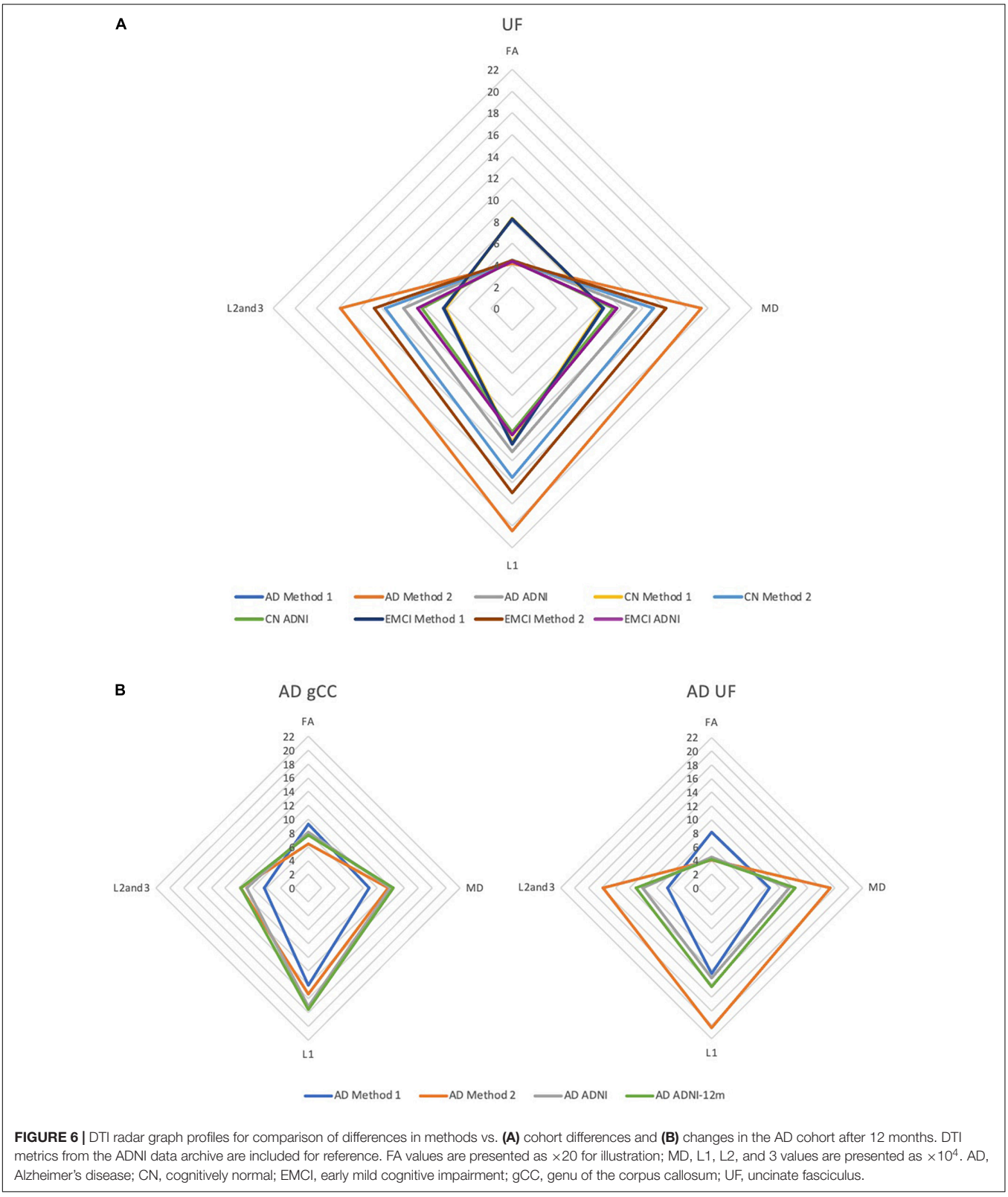

FIGURE 6 | DTI radar graph profiles for comparison of differences in methods vs. **(A)** cohort differences and **(B)** changes in the AD cohort after 12 months. DTI metrics from the ADNI data archive are included for reference. FA values are presented as ×20 for illustration; MD, L1, L2, and 3 values are presented as $\times 10^4$. AD, Alzheimer's disease; CN, cognitively normal; EMCI, early mild cognitive impairment; gCC, genu of the corpus callosum; UF, uncinate fasciculus.

matter tracts had to be manually generated in the pseudo-atlas template prior to performing the tractography. This process could be lengthy and required individuals with a working knowledge of neuroanatomy to perform. Additionally, there could be inherent subjectivity when it came to generating the tracts because it was difficult to determine if there were

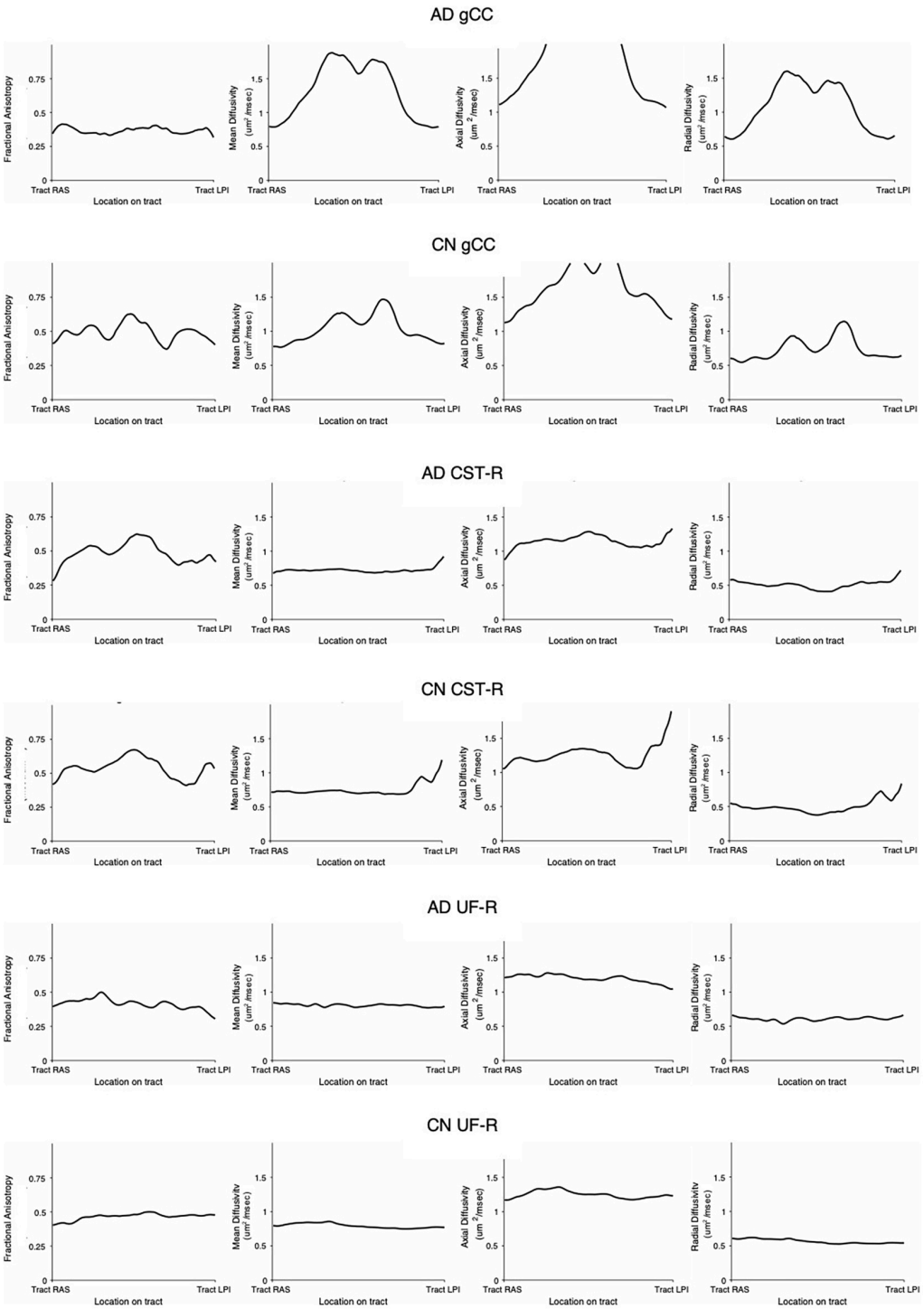

FIGURE 7 | White matter tract profiles demonstrating variability along tracts. AD, Alzheimer's disease; CN, cognitively normal; gCC, genu of the corpus callosum; CST-R, corticospinal tract (right); UF-R, uncinate fasciculus (right).

missing "strands" of white matter or conversely, if spurious "strands" were being generated. Secondly, the tractography itself of Method 1 also required a long time, which required approximately 3 h to generate a single tract from a single DWI. In contrast, Methods 2 and 3 did not require manual generation of the white matter tracts as it utilized readily available atlases compiled and verified by other groups. In terms of processing speed, Method 2 was about 50 times faster than

Method 1, requiring 3 h to generate a single tract from a cohort of 50 DWIs.

Study Limitations

DTI has a low specificity and is generally due to its low signal to noise ratio (Ranzenberger and Snyder, 2022). As a result, the imaging quality may be poor, and artifacts become a problem. Additionally, the DTI metrics are highly dependent on the size of the voxel during analysis. A single voxel may contain multi-directional structures which can result in inaccurate DTI measurements. Ideally, a single voxel should be small enough that it encompasses a single white matter bundle, taking a point measurement of DTI metrics. Therefore, the inter-methodological differences found in our paper could be in part be attributed to its low signal to noise ratio.

In this study, we only considered two disease cohorts (AD and EMCI) and healthy controls (CN). The full ADNI dataset included other cohorts along the disease spectrum, such as the late mild cognitive impairment (LMCI) and significant memory concern (SMC) cohorts. With further analysis it may have been possible that one of the three methods chosen would have emerged as the predominantly reliable and reproducible method of DTI analysis, with findings entirely consistent with literature. In addition, despite widespread use of ROI methodologies in literature, manual specifications and semi-automated tractography may be considered less reliable than fully automated white matter analytical approaches. Nevertheless, due to their ubiquity, results from this study would be easily translated to other settings involving DTI analysis at the clinical-research interface.

In Method 1, a randomly selected image from each study cohort was used as an atlas. This may have potentially introduced bias as we could not be certain that the selected images were adequately representative of the entire cohort. However, the selected images were inspected for abnormal or outrightly distinctive features that could render them significantly different from other images within the cohort. Future work might include creating a more representative atlas by generating a grouped average of multiple images from the cohort.

We also recognize that previous studies that have utilized a representative cohort-specific subject-based approach to DTI analysis have explored and demonstrated its limitations. For example, Keihaninejad et al. (2012) compared different methods of registration schemes for the use of TBSS for DTI analysis (Standard, Most-Representative-Subject, Study-Specific-Template, and Group-wise) in terms of their performance in reducing misalignment within the context of Alzheimer's disease and large deformations due to atrophy. They found that the approaches studied all showed false-positive error in evaluation of specificity, likely due to variations in levels of white matter atrophy and ventricular size. However, it was possible to improve the performance of aligning DTI data using a group-wise average atlas approach (Keihaninejad et al., 2012). The degree of confounders such as white matter atrophy and ventriculomegaly can be highly variable between patients; it could therefore be equally argued that, in certain cohorts such as ours, the use of a Most-Representative Subject approach may still be more advantageous, since we would expect the white matter pattern changes to affect similar "at-risk" locations within the same disease process but group-wise averaging may introduce further unintended distortions to the template of the "at-risk atlas" of disease. Nevertheless, our study showed that even in the absence of confounders such as atrophy and ventriculomegaly as in the CN cohort, and despite implementation of the algorithmic modifications. There is still a poor agreement between methodologies, which supports our conclusion that no true "gold-standard" DTI methodology exists without limitations for all possible disease datasets of interest.

It is also important to note that the use of Evans' Index as a marker for ventriculomegaly is imperfect because it is dependent on the inter-rater reliability at measuring the maximal width of the frontal horns and the internal diameter of the skull. These measurements are also highly dependent on the chosen slice and location at which the markers are placed. In addition, the orientation of each image has a large influence on the slices and thus the measurements. Although this effect is mitigated by alignment of the commissures, such technical considerations should be addressed and optimized by each rater, prior to its application as a biomarker for ventricular enlargement across a range of datasets.

Future Work

We plan to expand our analyses using both DTI methodologies, to include other cohorts of interest along the spectrum of AD and other neurodegenerative diseases. We also aim to use other anatomical segmentation methods to examine macro-structural features of white matter, such as its volume and thickness, as well as to create topological maps of adjacent surfaces, in order to augment the interpretation of the morphology of white matter changes, as described by DTI profiles. In the context of ventriculomegaly, we plan to utilize complementary biomarkers for both 2-dimensional and 3-directional measures in specific groups that possess significant ventriculomegaly such as cohorts with NPH. Finally, we aim to further expand the concept of DTI profiles as an invaluable tool toward boosting our capacity to compare the interpretation of DTI findings across methodologies which are not directly comparable using conventional statistical methods.

CONCLUSION

In this study, we found that there was no true gold-standard for DTI methodologies or atlases. It was possible to create a pseudo-atlas that was cohort-specific for immediate study use. Whilst there was no congruence between absolute values from DTI metrics, differing DTI methodologies were still valid but must be appreciated to be variably sensitive to different changes within white matter injury occurring concurrently. When such changes were found to exist in the same dataset, the use of differing methods were complementary in elucidating the characterization of such DTI changes. We found that,

despite such algorithmic modifications, the use of DTI profiles, a methodology of distilling the complexity of DTI changes to their most simplistic, graphical forms, confirmed the morphology of white matter injury as described by DTI metrics, remained consistent. By combining both atlas and pseudo-atlas based methodologies with DTI profiles, it was possible to navigate past such challenges to describe white matter injury changes in the context of confounders, such as neurodegenerative disease and ventricular enlargement, with transparency and consistency.

DATA AVAILABILITY STATEMENT

The data will be made available but is subject to approval from the ADNI (Alzheimer's Disease Neuroimaging Initiative) as they own the scans that the data were derived from.

ETHICS STATEMENT

Data used in preparation of this article were obtained from the ADNI database (adni.loni.usc.edu). Written informed consent was obtained from all ADNI subjects, and participating sites in the ADNI study received approval from their respective governing Institutional Review Boards.

AUTHOR CONTRIBUTIONS

CK, NK, and CL conceptualized and designed the study methodology, wrote the manuscript, and contributed to the analysis and interpretation of study data. CK, NK, CL, and TA contributed to data collection and validation. All authors contributed to the article and approved the submitted version.

FUNDING

NK was supported by a National Medical Research Council Clinician Scientist Award (MOH-CSAINV18nov-0005).

ACKNOWLEDGMENTS

We would like to thank Assistant Prof. Seyed Ehsan Saffari for providing advice on the statistical analyses for this manuscript. Data used in preparation of this article were obtained from the Alzheimer's Disease Neuroimaging Initiative (ADNI) database (adni.loni.usc.edu). As such, the investigators within the ADNI contributed to the design and implementation of ADNI and/or provided data but did not participate in analysis or writing of this report. A complete listing of ADNI investigators can be found at: http://adni.loni.usc.edu/wp-content/uploads/how_to_apply/ADNI_Acknowledgement_List.pdf. Data collection and sharing for this project was funded by the Alzheimer's Disease Neuroimaging Initiative (ADNI) (National Institutes of Health Grant U01 AG024904) and DOD ADNI (Department of Defense award number W81XWH-12-2-0012). ADNI is funded by the National Institute on Aging, the National Institute of Biomedical Imaging and Bioengineering, and through generous contributions from the following: AbbVie, Alzheimer's Association; Alzheimer's Drug Discovery Foundation; Araclon Biotech; BioClinica, Inc.; Biogen; Bristol-Myers Squibb Company; CereSpir, Inc.; Cogstate; Eisai Inc.; Elan Pharmaceuticals, Inc.; Eli Lilly and Company; EuroImmun; F. Hoffmann-La Roche Ltd., and its affiliated company Genentech, Inc.; Fujirebio; GE Healthcare; IXICO Ltd.; Janssen Alzheimer Immunotherapy Research & Development, LLC.; Johnson & Johnson Pharmaceutical Research & Development LLC.; Lumosity; Lundbeck; Merck & Co., Inc.; Meso Scale Diagnostics, LLC.; NeuroRx Research; Neurotrack Technologies; Novartis Pharmaceuticals Corporation; Pfizer Inc.; Piramal Imaging; Servier; Takeda Pharmaceutical Company; and Transition Therapeutics. The Canadian Institutes of Health Research is providing funds to support ADNI clinical sites in Canada. Private sector contributions are facilitated by the Foundation for the National Institutes of Health (www.fnih.org). The grantee organization is the Northern California Institute for Research and Education, and the study is coordinated by the Alzheimer's Therapeutic Research Institute at the University of Southern California. ADNI data are disseminated by the Laboratory for Neuro Imaging at the University of Southern California.

REFERENCES

Acosta-Cabronero, J., Alley, S., Williams, G. B., Pengas, G., and Nestor, P. J. (2012). Diffusion tensor metrics as biomarkers in Alzheimer's disease. *PLoS One* 7:e49072. doi: 10.1371/journal.pone.0049072

Acosta-Cabronero, J., and Nestor, P. J. (2014). Diffusion tensor imaging in Alzheimer's disease: insights into the limbic-diencephalic network and methodological considerations. *Front. Aging Neurosci.* 6:266. doi: 10.3389/fnagi.2014.00266

Assaf, Y., Ben-Sira, L., Constantini, S., Chang, L. C., and Beni-Adani, L. (2006). Diffusion tensor imaging in hydrocephalus: initial experience. *AJNR Am. J. Neuroradiol.* 27, 1717–1724.

Ben-Sira, L., Goder, N., Bassan, H., Lifshits, S., Assaf, Y., and Constantini, S. (2015). Clinical benefits of diffusion tensor imaging in hydrocephalus. *J. Neurosurg. Pediatr.* 16, 195–202. doi: 10.3171/2014.10.PEDS13668

Borden, N. M., Forseen, S. E., and Stefan, C. (2015). *Imaging Anatomy of the Human Brain : A Comprehensive Atlas Including Adjacent Structures*. New York, NY: Springer Publishing Company.

Christidi, F., Karavasilis, E., Samiotis, K., Bisdas, S., and Papanikolaou, N. (2016). Fiber tracking: a qualitative and quantitative comparison between four different software tools on the reconstruction of major white matter tracts. *Eur. J. Radiol. Open* 3, 153–161. doi: 10.1016/j.ejro.2016.06.002

Fedorov, A., Beichel, R., Kalpathy-Cramer, J., Finet, J., Fillion-Robin, J. C., Pujol, S., et al. (2012). 3D slicer as an image computing platform for the quantitative imaging network. *Magn. Reson. Imaging* 30, 1323–1341. doi: 10.1016/j.mri.2012.05.001

Glasser, M. F., Sotiropoulos, S. N., Wilson, J. A., Coalson, T. S., Fischl, B., Andersson, J. L., et al. (2013). The minimal preprocessing pipelines for the human connectome project. *Neuroimage* 80, 105–124. doi: 10.1016/j.neuroimage.2013.04.127

Hattori, T., Yuasa, T., Aoki, S., Sato, R., Sawaura, H., Mori, T., et al. (2011). Altered microstructure in corticospinal tract in idiopathic normal pressure

hydrocephalus: comparison with Alzheimer disease and Parkinson disease with dementia. *AJNR Am. J. Neuroradiol.* 32, 1681–1687. doi: 10.3174/ajnr.A2570

Hofer, S., and Frahm, J. (2006). Topography of the human corpus callosum revisited–comprehensive fiber tractography using diffusion tensor magnetic resonance imaging. *Neuroimage* 32, 989–994. doi: 10.1016/j.neuroimage.2006.05.044

Kanno, S., Abe, N., Saito, M., Takagi, M., Nishio, Y., Hayashi, A., et al. (2011). White matter involvement in idiopathic normal pressure hydrocephalus: a voxel-based diffusion tensor imaging study. *J. Neurol.* 258, 1949–1957. doi: 10.1007/s00415-011-6038-5

Keihaninejad, S., Ryan, N. S., Malone, I. B., Modat, M., Cash, D., Ridgway, G. R., et al. (2012). The importance of group-wise registration in tract based spatial statistics study of neurodegeneration: a simulation study in Alzheimer's disease. *PLoS One* 7:e45996. doi: 10.1371/journal.pone.0045996

Keong, N. C., Pena, A., Price, S. J., Czosnyka, M., Czosnyka, Z., Devito, E. E., et al. (2017). Diffusion tensor imaging profiles reveal specific neural tract distortion in normal pressure hydrocephalus. *PLoS One* 12:e0181624. doi: 10.1371/journal.pone.0181624

Lebel, C., Walker, L., Leemans, A., Phillips, L., and Beaulieu, C. (2008). Microstructural maturation of the human brain from childhood to adulthood. *Neuroimage* 40, 1044–1055. doi: 10.1016/j.neuroimage.2007.12.053

Leemans, A. J., Jeurissen, B., Sijbers, J., and Jones, D. K. (2009). "ExploreDTI: a graphical toolbox for processing, analyzing, and visualizing diffusion MR data," in *in: Proceedings of the 17th Annual Meeting of International Society of Magnetic Resonance Medicine*, (Hawaii), 3537.

Lock, C., Kwok, J., Kumar, S., Ahmad-Annuar, A., Narayanan, V., Ng, A. S. L., et al. (2018). DTI profiles for rapid description of cohorts at the clinical-research interface. *Front. Med. (Lausanne)* 5:357. doi: 10.3389/fmed.2018.00357

Mori, S., and Zhang, J. (2006). Principles of diffusion tensor imaging and its applications to basic neuroscience research. *Neuron* 51, 527–539. doi: 10.1016/j.neuron.2006.08.012

Mukherjee, P., Chung, S. W., Berman, J. I., Hess, C. P., and Henry, R. G. (2008). Diffusion tensor MR imaging and fiber tractography: technical considerations. *AJNR Am. J. Neuroradiol.* 29, 843–852. doi: 10.3174/ajnr.A1052

Nir, T. M., Jahanshad, N., Villalon-Reina, J. E., Toga, A. W., Jack, C. R., Weiner, M. W., et al. (2013). Effectiveness of regional DTI measures in distinguishing Alzheimer's disease. MCI, and normal aging. *Neuroimage Clin.* 3, 180–195. doi: 10.1016/j.nicl.2013.07.006

(Nitrc) N.T.R.C (2014). *MRIcroGL*. Available Online at (https://www.nitrc.org/projects/mricrogl/) (accessed March 2, 2021).

Oishi, F., Van Zijl, P. C. M., Mori, S., and Andreia, V. (2010). *MRI Atlas of Human White Matter*. Cambridge, MS: Academic Press.

Oishi, K., Faria, A., Jiang, H., Li, X., Akhter, K., Zhang, J., et al. (2009). Atlas-based whole brain white matter analysis using large deformation diffeomorphic metric mapping: application to normal elderly and Alzheimer's disease participants. *Neuroimage* 46, 486–499. doi: 10.1016/j.neuroimage.2009.01.002

Oishi, K., Zilles, K., Amunts, K., Faria, A., Jiang, H., Li, X., et al. (2008). Human brain white matter atlas: identification and assignment of common anatomical structures in superficial white matter. *Neuroimage* 43, 447–457. doi: 10.1016/j.neuroimage.2008.07.009

Paul, D. A., Gaffin-Cahn, E., Hintz, E. B., Adeclat, G. J., Zhu, T., Williams, Z. R., et al. (2014). White matter changes linked to visual recovery after nerve decompression. *Sci. Transl. Med.* 6:266ra173. doi: 10.1126/scitranslmed.3010798

R Development Core Team. (2010). *R: A language and Environment for Statistical Computing". 4.0*, 4 Edn. Vienna: R Foundation for Statistical Computing.

Ranzenberger, L. R., and Snyder, T. (2022). *Diffusion Tensor Imaging*. Treasure Island, FL: StatPearls Publishing.

Scheel, M., Diekhoff, T., Sprung, C., and Hoffmann, K. T. (2012). Diffusion tensor imaging in hydrocephalus–findings before and after shunt surgery. *Acta Neurochir. (Wien)* 154, 1699–1706. doi: 10.1007/s00701-012-1377-2

Smith, S. M., Jenkinson, M., Johansen-Berg, H., Rueckert, D., Nichols, T. E., Mackay, C. E., et al. (2006). Tract-based spatial statistics: voxelwise analysis of multi-subject diffusion data. *Neuroimage* 31, 1487–1505.

Soares, J. M., Marques, P., Alves, V., and Sousa, N. (2013). A hitchhiker's guide to diffusion tensor imaging. *Front. Neurosci.* 7:31. doi: 10.3389/fnins.2013.00031

Soon, S. X. Y., Kumar, A. A., Tan, A. J. L., Lo, Y. T., Lock, C., Kumar, S., et al. (2021). The impact of multimorbidity burden, frailty risk scoring, and 3-directional morphological indices vs. testing for csf responsiveness in normal pressure hydrocephalus. *Front Neurosci.* 15:751145. doi: 10.3389/fnins.2021.751145

Tan, K., Meiri, A., Mowrey, W. B., Abbott, R., Goodrich, J. T., Sandler, A. L., et al. (2018). Diffusion tensor imaging and ventricle volume quantification in patients with chronic shunt-treated hydrocephalus: a matched case-control study. *J. Neurosurg.* 129, 1611–1622. doi: 10.3171/2017.6.JNS162784

Wakana, S., Caprihan, A., Panzenboeck, M. M., Fallon, J. H., Perry, M., Gollub, R. L., et al. (2007). Reproducibility of quantitative tractography methods applied to cerebral white matter. *Neuroimage* 36, 630–644. doi: 10.1016/j.neuroimage.2007.02.049

Yamada, S., Ishikawa, M., and Yamamoto, K. (2016). Comparison of CSF distribution between idiopathic normal pressure hydrocephalus and Alzheimer Disease. *AJNR Am. J. Neuroradiol.* 37, 1249–1255. doi: 10.3174/ajnr.A4695

Yeatman, J. D., Dougherty, R. F., Myall, N. J., Wandell, B. A., and Feldman, H. M. (2012). Tract profiles of white matter properties: automating fiber-tract quantification. *PLoS One* 7:e49790. doi: 10.3389/fnins.2013.00031

Yendiki, A., Panneck, P., Srinivasan, P., Stevens, A., Zollei, L., Augustinack, J., et al. (2011). Automated probabilistic reconstruction of white-matter pathways in health and disease using an atlas of the underlying anatomy. *Front. Neuroinform.* 5:23. doi: 10.3389/fninf.2011.00023

Zalesky, A. (2011). Moderating registration misalignment in voxelwise comparisons of DTI data: a performance evaluation of skeleton projection. *Magn. Reson. Imaging* 29, 111–125. doi: 10.1016/j.mri.2010.06.027

Conflict of Interest: The authors declare that the research was conducted in the absence of any commercial or financial relationships that could be construed as a potential conflict of interest.

frontiers | Frontiers in Aging Neuroscience

ORIGINAL RESEARCH
published: 06 May 2022
doi: 10.3389/fnagi.2022.781883

Pallidal Structural Changes Related to Levodopa-induced Dyskinesia in Parkinson's Disease

Jinyoung Youn[1,2†], *Mansu Kim*[3†], *Suyeon Park*[4], *Ji Sun Kim*[1,2], *Hyunjin Park*[5,6*] and *Jin Whan Cho*[1,2*]

[1] Department of Neurology, Samsung Medical Center, Sungkyunkwan University School of Medicine, Seoul, South Korea, [2] Neuroscience Center, Samsung Medical Center, Seoul, South Korea, [3] Department of Artificial Intelligence, Catholic University of Korea, Bucheon, South Korea, [4] Department of Biostatistics, Soonchunhyang University Seoul Hospital, Soonchunhyang University College of Medicine, Seoul, South Korea, [5] Center for Neuroscience Imaging Research, Institute for Basic Science, Suwon, South Korea, [6] School of Electronic and Electrical Engineering, Sungkyunkwan University, Suwon, South Korea

Background: Despite the clinical impact of levodopa-induced dyskinesia (LID) in Parkinson's disease (PD), the mechanism, especially the role of basal ganglia (BG), is not fully elucidated yet. We investigated the BG structural changes related to LID in PD using a surface-based shape analysis technique.

Methods: We recruited patients with PD who developed LID within 3 years (LID group, 28 patients) and who did not develop it after 7 years (non-LID group, 35 patients) from levodopa treatment for the extreme case-control study. BG structure volumes were measured using volumetry analysis and the surface-based morphometry feature (i.e., Jacobian) from the subcortical surface vertices. We compared the volume and Jacobian of meshes in the regions between the two groups. We also performed a correlation analysis between local atrophy and the severity of LID. Additionally, we evaluated structural connectivity profiles from globus pallidus interna and externa (GPi and GPe) to other brain structures based on the group comparison.

Results: The demographic and clinical data showed no significant difference except for disease duration, treatment duration, parkinsonism severity, and levodopa equivalent dose. The LID group had more local atrophies of vertices in the right GPi than the non-LID group, despite no difference in volumes. Furthermore, the LID group demonstrated significantly reduced structural connectivity between left GPi and thalamus.

Conclusion: This is the first demonstration of distinct shape alterations of basal ganglia structures, especially GPi, related to LID in PD. Considering both direct and indirect BG pathways share the connection between GPi and thalamus, the BG pathway plays a crucial role in the development of LID.

Keywords: dyskinesia, levodopa-induced dyskinesia, basal ganglia, globus pallidus, pallidum, Parkinson's disease

OPEN ACCESS

Edited by:
Behrooz Hooshyar Yousefi, University of Marburg, Germany

Reviewed by:
Aristide Merola, The Ohio State University, United States
Atsushi Nambu, National Institute for Physiological Sciences (NIPS), Japan

***Correspondence:**
Jin Whan Cho
jinwhan.cho@samsung.com
Hyunjin Park
hyunjinp@skku.edu

[†] These authors have contributed equally to this work

Specialty section:
This article was submitted to Parkinson's Disease and Aging-related Movement Disorders, a section of the journal Frontiers in Aging Neuroscience

Received: *23 September 2021*
Accepted: *28 March 2022*
Published: *06 May 2022*

Citation:
Youn J, Kim M, Park S, Kim JS, Park H and Cho JW (2022) Pallidal Structural Changes Related to Levodopa-induced Dyskinesia in Parkinson's Disease. Front. Aging Neurosci. 14:781883. doi: 10.3389/fnagi.2022.781883

INTRODUCTION

Considering Parkinson's disease (PD) is a neurodegenerative disorder with progressive dopaminergic degeneration, the administration of levodopa, a dopamine precursor, is the most effective treatment for PD. However, chronic levodopa medication could cause disabling motor complications, especially levodopa-induced dyskinesia (LID), which affects the quality of life of

patients with PD. Additionally, almost half of patients could develop dyskinesias after 5 years of treatment, and the majority of patients after 10 years (Manson et al., 2012).

Although the mechanism of LID development is not completely understood, presynaptic dopaminergic denervation and chronic pulsatile stimulation of dopamine receptors have been considered to be associated with its development (Calabresi et al., 2010). However, the time of onset and LID severity are highly heterogeneous among patients (Hely et al., 2005). These variable presentations could be explained by the different involvement of relevant brain structures associated with LID. Studies reported that morphological changes were strong biomarkers with wide applications in various neurodegenerative diseases (Ment et al., 2009; Turcano et al., 2018). LID development could be delayed with medication and LID severity could be effectively controlled with deep brain stimulation (Follett, 2004), thus it is important to find the brain structure changes with LID in patients with PD. However, the morphological substrate of LID in patients with PD remains underexplored.

Surface shape analysis is a sensitive and quantitative technique to detect structural changes in the subcortical nuclei in patients with PD (Lee et al., 2014; Menke et al., 2014). Therefore, the present study aimed to explore the structural changes in the basal ganglia, connected to LID development in patients with PD, using a volumetry, surface-based shape analysis technique, and connectivity analysis.

METHODS

Subjects and Study Design

This study was approved by the Institutional Review Board of the Samsung Medical Center, Seoul, Korea (IRB #2012-10-102-017), and each patient provided informed consent to participate. All methods were carried out in accordance with the relevant guidelines and regulations.

For this extreme case-control study design (Salim et al., 2014), we enrolled patients with PD who developed LID within 3 years (LID group) and who did not develop it after 7 years from starting levodopa treatment (non-LID group) at the Movement Disorders Clinic, Samsung Medical Center, Seoul, from March 2013 to December 2016. PD was diagnosed according to the UK Brain Bank Criteria for the diagnosis of PD (Hughes et al., 1992). Subjects with any of the following were also excluded: (1) structural brain lesions, including stroke, tumor, trauma, or white matter changes (age-related white matter change score $\geq$ 2 on brain MRI) (Wahlund et al., 2001); (2) other known neurodegenerative diseases or psychiatric disorders requiring medications; (3) other diseases, including symptomatic neuropathy, or musculoskeletal problems, that affected parkinsonism.

For clinical assessments, the Unified Parkinson's Disease Rating Scale (UPDRS) part 3, H&Y stage, Unified Dyskinesia Rating Scale (UDysRS), and the Korean version of the Montreal Cognitive Assessment (K-MoCA) were evaluated in all the recruited subjects with PD (Lee et al., 2008). UPDRS part 3 score was divided into 4 sub-scores for tremor, bradykinesia, rigidity, and axial symptom (Diederich et al., 2003). Levodopa equivalent dose (LED) was calculated based on previous literature (Tomlinson et al., 2010). Total LED was divided into 3 groups, which were the levodopa and catechol-O-methyltransferase (COMT) inhibitor, dopamine agonist, and others.

MRI Acquisition

We collected T1-weighted MRI (T1-MRI) and diffusion-weighted MRI (dMRI) data using a 3-T MRI scanner (Philips 3-T Achieva, Best, the Netherland). The T1-MRI was acquired with the following acquisition parameters: sagittal slice thickness, 1 mm; contiguous slices with 50% overlap; no gap; repetition time (TR), 9.9 ms; echo time (TE), 4.6 ms; flip angle, 8°; matrix size of 240 × 240 pixels, which was reconstructed to 480 × 480 over a field of view (FOV) of 240 mm. The dMRI was acquired with the following acquisition parameters: TR/TE = 5,900/88 ms, 2 mm^3 isotropic resolution; 72 contiguous slices, two-fold acceleration, axial–oblique aligned along the anterior-posterior commissure, and diffusion-weighting along 64 gradient directions with a b-value of 1,000 s/mm^2.

Volumetric and Shape Analysis

The brain morphometry was evaluated on the left and the right caudate nucleus, putamen, globus pallidus, and thalamus in terms of volume and Jacobian determinant. The volume of each structure was computed using FreeSurfer (version 6; Athinoula A. Martinos Center at the Massachusetts General Hospital, Harvard Medical School, MA, USA) (Fischl, 2012). We normalized the volume by dividing the calculated volume by the intracranial volume. The Jacobian determinant was used to measure the ratio of surface dilation between a given subject and the template in the region. The Jacobian determinant was computed according to the protocol set by the ENIGMA consortium (Gutman et al., 2012, 2013). Briefly, we obtained the subject-specific segmentation of the subcortical structures and then applied the "Medial Demons" framework to register subcortical shapes onto the pre-specified template (Roshchupkin et al., 2016). The meshes for the eight basal ganglia structures of each subject were defined on the template space. Finally, we computed the natural logarithm of the Jacobian determinant (referred to as *Jacobian* hereafter) that represented the ratio of surface dilation between the given subjects with respect to the template.

Connectivity Analysis

Additionally, based on the initial results of basal ganglia structures between two groups in the present study (**Figure 1**), we chose globus pallidus and compared the structural connectivity profiles of globus pallidus to other brain structures between LID and non-LID groups. The structural connectivity was computed using the probabilistic tractography algorithm implemented in FSL (probtrackX) (Behrens et al., 2007). Briefly, we performed pre-processing steps using FSL software, which were as follows: intensity normalization, distortion correction, eddy current correction, and head motion correction. Then, we estimated the fiber orientation for each voxel from dMRI with the multi-shell-spherical deconvolution toolbox (bedpostx) (Behrens et al., 2007;

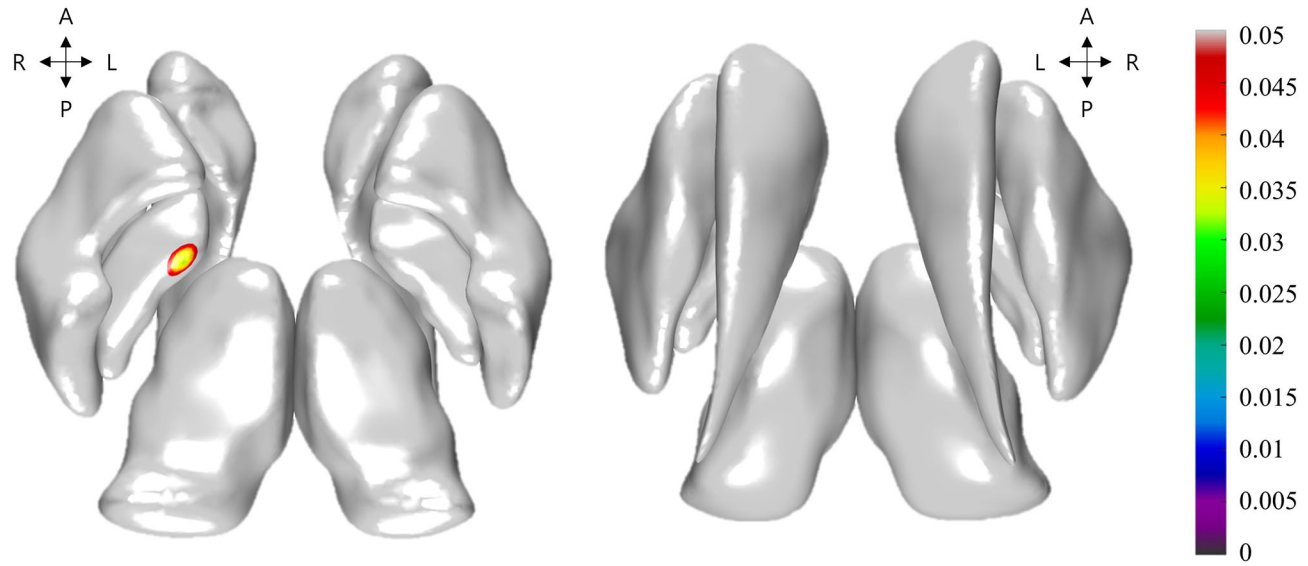

FIGURE 1 | Illustration of the group-wise differences of Jacobian between levodopa-induced dyskinesia (LID) group and non-LID group. Non-gray color regions denote the vertices with significantly different Jacobian. The color bar shows the corrected *p*-values for the statistical test. The left and right subfigures denoted the top axial view and bottom axial view, respectively.

Jbabdi et al., 2012). We estimated fiber streamlines for every voxel using probtrackX and mapped them onto the brain regions. The 83 brain regions were defined based on the Desikan-Killany atlas and we manually divided the globus palladium regions into two sub-regions (e.g., globus pallidus interna and externa), yielding a total of 85 brain regions. Finally, we computed and compared the structural connectivity profiles of left and right globus pallidus interna and externa (GPi and GPe) between the LID and non-LID groups.

Statistical Analysis

The demographic and clinical variables were compared between LID and non-LID groups using an unpaired Student's *t*-test or the Mann-Whitney U test for continuous and ordinal variables, while Pearson's chi-square test or Fisher's exact test were used to determine categorical variables. We rejected the null hypotheses of no difference if *p*-values were <0.05. These statistical analyses were conducted using commercially available software (PASW for Windows, version 18; SPSS, Chicago, IL, USA). For the volume and structural connectivity profile analysis, we performed two-sample student's *t*-tests for identifying the group difference between LID and non-LID groups, and the Bonferroni correction was conducted for correcting the multiple comparisons issue.

Group-wise differences of the *Jacobian* in the basal ganglia structures between the LID group and non-LID groups were assessed with non-parametric permutation tests adjusted for age, disease duration, treatment duration for levodopa medication, LED for levodopa and COMT inhibitor, and dopamine agonist, and UPDRS part 3 sub-scores (Nichols and Holmes, 2001). We performed the permutation tests by randomly assigning LID and non-LID groups 10,000 times. If the real difference of *Jacobian* did not belong to the 95% of the null distribution derived from the permutations, it was deemed significant and the multiple comparisons were corrected by false discovery rate (FDR) correction (p <0.05) (Boca and Leek, 2018). The correlation analysis was performed to detect potential links between the *Jacobian* of basal ganglia structures and the UDysRS score. These statistical analyses were performed with MATLAB (The MathWorks Inc., Natick, MA, USA) (MATLAB and Statistics Toolbox Release, 2020).

RESULTS

Demographic and Clinical Features of LID and Non-LID Groups

We enrolled 63 non-demented right-handed subjects, among which 28 patients were in the LID group and 35 patients were in the non-LID group. **Table 1** presented the demographic and clinical data of each group. There were no significant differences in demographic data between the two groups. In terms of clinical data, the non-LID group demonstrated significantly longer disease duration, higher tremor, and lower bradykinesia sub-score than the LID group. For medication, the LID group took more medication (total LED and LED for levodopa and COMT inhibitor) than the non-LID group.

Comparison of Basal Ganglia Structures Between LID and Non-LID Groups

The volumes of basal ganglia structures were illustrated in **Table 2**. There was no difference in the volume of basal ganglia structures between the two groups. However, the LID group had significant local atrophy in the right GPi (32 vertices with mean corrected $p = 0.041 \pm 0.006$ in mean $\pm$ *SD*) than the non-LID

TABLE 1 | Demographic information of PD with and without LID.

	Early-LID group	Non-LID group	*p*-value
Number of subjects	28	35	–
Onset age (years)	52.3 ± 9.2	53.1 ± 6.2	0.661
Disease duration (years)	6.4 ± 2.4	11.4 ± 3.2	<0.001
Treatment duration for antiparkinsonian medication (month)	64.9 ± 30.1	117.9 ± 38.4	<0.001
Treatment duration for levodopa medication (month)	56.3 ± 28.9	85.2 ± 57.5	0.078
Sex (Male/Female)	12/16	17/18	0.800
Symptom-dominant side, right/left	14/14	19/16	0.803
UPDRS part 3			
Tremor	2.6 ± 2.8	3.8 ± 2.4	0.024
Bradykinesia	14.4 ± 5.1	7.6 ± 8.3	0.002
Rigidity	5.8 ± 2.5	4.9 ± 3.2	0.085
Axial symptoms	7.8 ± 2.9	7.8 ± 3.7	0.838
Total score	30.6 ± 9.0	24.2 ± 12.7	0.009
HY stage	2.3 ± 0.6	2.2 ± 0.6	0.689
K-MoCA	26.1 ± 3.3	25.8 ± 2.6	0.509
UDysRS	19.8 ± 13.7	0	<0.001
Levodopa equiva lent dose			
Levodopa + COMT inhibitor (mg/day)	631.1 ± 246.6	419.5 ± 252.3	0.001
Dopamine agonist (mg/day)	166.5 ± 86.4	207.6 ± 149.7	0.469
Others (mg/day)	112.5 ± 131.7	107.4 ± 102.7	0.699
Total dose (mg/day)	910.2 ± 337.5	734.5 ± 305.3	0.009

UPDRS, Unified Parkinson's Disease Rating Scale; H&Y, Hoehn and Yahr score; K-MoCA, Korean-Montreal Cognitive Assessment; UDysRS, Unified Dyskinesia Rating Scale; LED, levodopa equivalent doses.

TABLE 2 | Group-wise differences in the volumetric features of eight subcortical regions.

	Volume (mm^3)		*p*-value
	LID group	Non-LID group	
Left thalamus	7136.2 ± 797.8	7068.0 ± 932.5	0.761
Right thalamus	6742.9 ± 671.5	6706.4 ± 838.1	0.852
Left caudate	3272.0 ± 564.8	3227.9 ± 431.8	0.728
Right caudate	3331.1 ± 459.2	3367.0 ± 470.8	0.761
Left putamen	4518.7 ± 518.9	4432.2 ± 499.1	0.503
Right putamen	4481.2 ± 455.8	4420.7 ± 504.3	0.619
Left pallidum	1919.0 ± 223.3	1961.5 ± 250.7	0.478
Right pallidum	1875.7 ± 232.3	1906.9 ± 261.2	0.617

group (i.e., −0.223 ± 0.164 of Jacobian for LID group; −0.178 ± 0.131 of Jacobian for the non-LID group), as shown in **Figure 1**.

Correlation of the Basal Ganglia Local Atrophy With UDysRS Score

For correlation analysis, we controlled age, disease duration, treatment duration for levodopa medication, LED (levodopa and COMT inhibitor, and dopamine agonist), and UPDRS part 3 sub-scores. There were no basal ganglia areas showing local atrophy significantly correlated with the UDysRS score (**Supplementary Figure**).

Comparison of Connectivity From Globus Pallidus to Other Brain Regions

Based on the results of local atrophy in basal ganglia structures, we compared the structural connectivity profiles of globus pallidus to other brain structures. The LID group demonstrated significantly reduced connectivity between left GPi and left thalamus compared to the non-LID group (0.000002 for the LID group and 0.00068 for the non-LID group, corrected $p = 0.017$) (**Supplementary Table**).

DISCUSSION

This is the first study to the best of our knowledge to explore the distinct shape alterations of basal ganglia structures in patients with PD having with and without LID. We found the local atrophy in right GPi and reduced connectivity between left GPi and thalamus in the LID group compared to the non-LID group. Based on our results, we suggest GPi as a key brain structure related to LID. The present study revealed discrepant results from shape and connectivity analyses, local atrophy in the right pallidum, and reduced connectivity in the left pallidum. In our study, there was no difference in the symptom-dominant side between the two groups. Previous studies using imaging analysis also demonstrated asymmetric results (Herz et al., 2014; Cerasa et al., 2015; Farre et al., 2015), and there is still no consensus about the laterality in LID development.

Previous studies focusing on LID-related anatomical abnormalities showed structural alterations mainly in the

cortical structures (Cerasa et al., 2011, 2013). Cortical thickness analysis and voxel-based morphometry revealed increased cortical thickness and gray matter volume in the frontal cortex in patients with LID compared to those without LID. Basal ganglia are structures directly involved in PD, and also with wide efferent and afferent connections with the frontal lobe. Therefore, there would be changes in basal ganglia structures between the aforementioned cortical changes and nigral degeneration in PD. However, unlike the anatomical changes in the cortical structures, those in the basal ganglia were not fully investigated. A previous study with the PD rat model revealed the hypertrophy of medial GPi and substantia nigra reticulata with levodopa treatment unlike our results (Tomiyama et al., 2004). However, this study focused on the structural changes related to levodopa treatment, not LID, and did not compare between PD models with and without LID.

Additionally, various hypotheses, including pre-synaptic and post-synaptic changes in the basal ganglia, are suggested for LID in PD (Iravani and Jenner, 2011; Phillips et al., 2016), but the main mechanism underlying LID is pulsatile stimulation of the striatal postsynaptic receptors. In patients with PD, dopaminergic modulation of the striatal activity and compensatory mechanism are already impaired; therefore, exogenous administration of repeated doses of levodopa induces molecular and neurophysiological changes (Calabresi et al., 1993), and abnormal firing pattern of the basal ganglia neuron (DeLong, 1990). However, it is difficult to evaluate the changes in subcortical nuclei, including basal ganglia structures. Previous studies used volumetric techniques and failed to find a decrease in the volume or density in the subcortical nuclei even between patients with PD and normal control (Messina et al., 2011). Similarly, we also performed the volumetric analysis of basal ganglia structures and could not find any significant differences in basal ganglia volumes. Surface-based morphometry can provide novel information that cannot be obtained with conventional volumetry and voxel-based analysis (Veldsman, 2017). We adopted the determinant of Jacobian as it provides a compact summary of the surface shape at the regional level compared to using the vertex meshes directly (Veldsman, 2017). Thus, surface-based morphometry could be well-suited to quantify the complex local shape of basal ganglia and we could demonstrate local atrophy of the GPi in patients with PD who developed LID using surface-based morphometry.

Local shape atrophies in the GPi of the LID group might reflect the complex and integrated impairment in these networks. It is underpinned by reduced connectivity between the GPi and thalamus in the LID group compared to the non-LID group. The connection between GPi and the thalamus is a common pathway involved in both direct and indirect pathways, thus the imbalance in GPi between two pathways could be related to LID (Barroso-Chinea and Bezard, 2010). Additionally, these output nuclei of basal ganglia also project connections mainly to the frontal lobe, where the structural difference was reported in a previous study among patients with PD who developed LID (Cerasa et al., 2011, 2013). Therefore, based on our results and previous studies, the output nuclei of basal ganglia (GPi and thalamus) play a crucial role in the development of LID in patients with PD, and these areas could be effective targets for the management of LID. Deep brain stimulation in the GPi has direct suppression effects on LID in patients with PD (Follett, 2004), and fibroblast transplantation at GPi also improved LID in the primate model (Singh et al., 2015).

However, it is difficult to explain the laterality of GPi in shape and connectivity analysis. We used multi-model imaging analysis, and the difference in methodology could have also affected our results. The local atrophy of right GPi was from shape analysis with T1-MRI while reduced connectivity between left GPi and thalamus from tractography with dMRI. However, both imaging analyses demonstrated that changes in GPi were related to LID in patients with PD, thus we suggested the importance of GPi in LID development in patients with PD.

In our study, there were significant differences, including age, disease duration, UPDRS part 3 score, and LED between LID and non-LID groups. Various clinical variables, including early age at onset, non-tremor dominant subtype, and levodopa dose, were already reported as risk factors for LID in patients with PD (Tran et al., 2018; Lee et al., 2019). In accordance with previous studies, LID groups showed earlier age at onset, less tremor sub-score of UPDRS part 3, and higher levodopa dose in our study. As well as the clinical factors associated with LID, the disease itself and even medications that could cause structural changes in patients with PD. To overcome the possible confounding factors, we controlled these variables, including age, disease duration, treatment duration, medications, and motor subtypes, in the imaging analysis. Therefore, if we control fewer clinical variables in imaging analysis, we might find more brain areas related to LID. Additionally, LID is usually present in patients with advanced PD and these patients could show a wide clinical spectrum. In the present study, we tried to eliminate possible confounding effects from other symptoms, because various brain structures could reflect all of these symptoms, as well as LID.

Our study has several strengths. To maximize the shape differences between the patient with and without LID, we used the extreme case-control study design: the earliest development of LID for the LID group and the longest-surviving control from LID for the non-LID group. This is a research design that is one of the most used methods to efficiently estimate a model with less sample size and costs. Although the duration of the disease was shorter in the LID group, the pallidal atrophy was more severe in the LID group. This method improves the efficiency as compared to the standard study design. Besides, we used shape analysis, which offers an intuitive and powerful means of quantifying anatomy in the context of brain imaging. However, this study also has some limitations. The cross-sectional study design made the assessment of time-related changes difficult. A longitudinal design will be necessary to confirm these shape alterations as the dynamic components of LID development. Although there are several advantages of computing fiber tractography based on probabilistic tractography, it may lead to the false-positive fiber bundle estimation due to its high sensitivity in low FA voxels. Hence, this analysis should be further confirmed with different tractography algorithms with independent replications to reduce false discoveries. In addition,

we enrolled a small-sized sample; however, even with the sample size, we were able to identify the basal ganglia structures associated with LID, using the extreme case-control study design. Lastly, early-LID and non-LID groups in our study showed different clinical characteristics, thus it is impossible to compare the two groups directly. PD is a heterogeneous disorder with a wide clinical spectrum and the progression rate could vary depending on the subtypes of PD. We adjusted as many clinical variables as possible, including disease duration, treatment duration medication, and UPDRS part 3 sub-scores, to minimize the possible confounding effect from subtypes associated with different progressions.

In conclusion, our study demonstrated that local atrophy of GPi and reduced connectivity with the thalamus were related to LID in patients with PD. This is the first study to demonstrate distinct shape alterations of basal ganglia structures related to LID and our results emphasized the role of basal ganglia pathways in the development of LID.

DATA AVAILABILITY STATEMENT

The data analyzed in this study is subject to the following licenses/restrictions: the data that support the findings of this study are available on request from the corresponding authors (JC or HP). The data are not publicly available due to research participant privacy/consent. Requests to access these datasets should be directed to JC, jinwhan.cho@samsung.com.

ETHICS STATEMENT

The studies involving human participants were reviewed and approved by the Institutional Review Board of the Samsung Medical Center, Seoul, Korea (IRB #2012-10-102-017). The patients/participants provided their written informed consent to participate in this study.

AUTHOR CONTRIBUTIONS

JY, JK, MK, HP, and JC contributed to the concept and design. JY, JK, and JC contributed to data acquisition. MK, SP, and HP contributed to the data analysis. JY, SP, JK, and MK contributed to the interpretation of data. JY, MK, SP, HP, and JC contributed to substantive revision. All authors contributed to the article and approved the submitted version.

FUNDING

This study was supported by the Institute for Basic Science (Grant Number IBS-R015-D1), National Research Foundation of Korea (NRF-2020M3E5D2A01084892 and NRF-2020R1A6A3A03038525), Ministry of Science and ICT (IITP-2020-2018-0-01798), IITP grant funded by the AI Graduate School Support Program (2019-0-00421), ICT Creative Consilience program (IITP-2020-0-01821), and the Artificial Intelligence Innovation Hub program (2021-0-02068).

SUPPLEMENTARY MATERIAL

The Supplementary Material for this article can be found online at: https://www.frontiersin.org/articles/10.3389/fnagi.2022.781883/full#supplementary-material

REFERENCES

Barroso-Chinea, P., and Bezard, E. (2010). Basal Ganglia circuits underlying the pathophysiology of levodopa-induced dyskinesia. *Front. Neuroanat.* 4, 131. doi: 10.3389/fnana.2010.00131

Behrens, T. E., Berg, H. J., Jbabdi, S., Rushworth, M. F., and Woolrich, M. W. (2007). Probabilistic diffusion tractography with multiple fibre orientations: what can we gain? *Neuroimage* 34, 144–155. doi: 10.1016/j.neuroimage.2006.09.018

Boca, S. M., and Leek, J. T. (2018). A direct approach to estimating false discovery rates conditional on covariates. *PeerJ* 6, e6035. doi: 10.7717/peerj.6035

Calabresi, P., Di Filippo, M., Ghiglieri, V., Tambasco, N., and Picconi, B. (2010). Levodopa-induced dyskinesias in patients with Parkinson's disease: filling the bench-to-bedside gap. *Lancet Neurol.* 9, 1106–1117. doi: 10.1016/S1474-4422(10)70218-0

Calabresi, P., Mercuri, N. B., Sancesario, G., and Bernardi, G. (1993). Electrophysiology of dopamine-denervated striatal neurons. Implications for Parkinson's disease. *Brain* 116, 433–452.

Cerasa, A., Koch, G., Donzuso, G., Mangone, G., Morelli, M., Brusa, L., et al. (2015). A network centred on the inferior frontal cortex is critically involved in levodopa-induced dyskinesias. *Brain* 138, 414–427. doi: 10.1093/brain/awu329

Cerasa, A., Messina, D., Pugliese, P., Morelli, M., Lanza, P., Salsone, M., et al. (2011). Increased prefrontal volume in PD with levodopa-induced dyskinesias: a voxel-based morphometry study. *Mov. Disord.* 26, 807–812. doi: 10.1002/mds.23660

Cerasa, A., Morelli, M., Augimeri, A., Salsone, M., Novellino, F., Gioia, M. C., et al. (2013). Prefrontal thickening in PD with levodopa-induced dyskinesias: new evidence from cortical thickness measurement. *Parkinsonism Relat. Disord.* 19, 123–125. doi: 10.1016/j.parkreldis.2012.06.003

DeLong, M. R. (1990). Primate models of movement disorders of basal ganglia origin. *Trends Neurosci.* 13, 281–285. doi: 10.1016/0166-2236(90)90110-v

Diederich, N. J., Moore, C. G., Leurgans, S. E., Chmura, T. A., and Goetz, C. G. (2003). Parkinson disease with old-age onset: a comparative study with subjects with middle-age onset. *Arch. Neurol.* 60, 529–533. doi: 10.1001/archneur.60.4.529

Farre, D., Munoz, A., Moreno, E., Reyes-Resina, I., Canet-Pons, J., Dopeso-Reyes, I. G., et al. (2015). Stronger dopamine D1 receptor-mediated neurotransmission in dyskinesia. *Mol. Neurobiol.* 52, 1408–1420. doi: 10.1007/s12035-014-8936-x

Fischl, B. (2012). FreeSurfer. *Neuroimage* 62, 774–781. doi: 10.1016/j.neuroimage.2012.01.021

Follett, K. A. (2004). Comparison of pallidal and subthalamic deep brain stimulation for the treatment of levodopa-induced dyskinesias. *Neurosurg. Focus* 17, E3. doi: 10.3171/foc.2004.17.1.3

Gutman, B. A., Madsen, S. K., Toga, A. W., and Thompson, P. M. (2013). "A family of fast spherical registration algorithms for cortical shapes," in *Multimodal Brain Image Analysis*, eds L. Shen, T. Liu, P. T. Yap, H. Huang, D. Shen, and C. F. Westin (Cham: Springer), 246–257.

Gutman, B. A., Wang, Y., Rajagopalan, P., Toga, A. W., and Thompson, P. M. (2012). "Shape matching with medial curves and 1-D group-wise registration," in *2012 9th IEEE International Symposium on Biomedical Imaging* (Barcelona), 716–719.

Hely, M. A., Morris, J. G., Reid, W. G., and Trafficante, R. (2005). Sydney Multicenter Study of Parkinson's disease: non-L-dopa-responsive problems dominate at 15 years. *Mov. Disord.* 20, 190–199. doi: 10.1002/mds.20324

Herz, D. M., Haagensen, B. N., Christensen, M. S., Madsen, K. H., Rowe, J. B., Lokkegaard, A., et al. (2014). The acute brain response to levodopa heralds dyskinesias in Parkinson disease. *Ann. Neurol.* 75, 829–836. doi: 10.1002/ana.24138

Hughes, A. J., Daniel, S. E., Kilford, L., and Lees, A. J. (1992). Accuracy of clinical diagnosis of idiopathic Parkinson's disease: a clinico-pathological study of 100 cases. *J. Neurol. Neurosurg. Psychiatry* 55, 181–184.

Iravani, M. M., and Jenner, P. (2011). Mechanisms underlying the onset and expression of levodopa-induced dyskinesia and their pharmacological manipulation. *J. Neural Transm.* 118, 1661–1690. doi: 10.1007/s00702-011-0698-2

Jbabdi, S., Sotiropoulos, S. N., Savio, A. M., Grana, M., and Behrens, T. E. (2012). Model-based analysis of multishell diffusion MR data for tractography: how to get over fitting problems. *Magn. Reson. Med.* 68, 1846–1855. doi: 10.1002/mrm.24204

Lee, H. M., Kwon, K. Y., Kim, M. J., Jang, J. W., Suh, S. I., Koh, S. B., et al. (2014). Subcortical grey matter changes in untreated, early stage Parkinson's disease without dementia. *Parkinsonism Relat. Disord.* 20, 622–626. doi: 10.1016/j.parkreldis.2014.03.009

Lee, J. W., Song, Y. S., Kim, H., Ku, B. D., and Lee, W. W. (2019). Alteration of tremor dominant and postural instability gait difficulty subtypes during the progression of Parkinson's disease: analysis of the PPMI Cohort. *Front. Neurol.* 10, 471. doi: 10.3389/fneur.2019.00471

Lee, J. Y., Dong Woo, L., Cho, S. J., Na, D. L., Hong Jin, J., Kim, S. K., et al. (2008). Brief screening for mild cognitive impairment in elderly outpatient clinic: validation of the Korean version of the Montreal Cognitive Assessment. *J. Geriatr. Psychiatry Neurol.* 21, 104–110. doi: 10.1177/0891988708316855

Manson, A., Stirpe, P., and Schrag, A. (2012). Levodopa-induced-dyskinesias clinical features, incidence, risk factors, management and impact on quality of life. *J. Parkinsons. Dis.* 2, 189–198. doi: 10.3233/JPD-2012-12010 3

MATLAB and Statistics Toolbox Release. (2020). *The MathWorks, Inc*. Natick, MA.

Menke, R. A., Szewczyk-Krolikowski, K., Jbabdi, S., Jenkinson, M., Talbot, K., Mackay, C. E., et al. (2014). Comprehensive morphometry of subcortical grey matter structures in early-stage Parkinson's disease. *Hum. Brain Mapp.* 35, 1681–1690. doi: 10.1002/hbm.22282

Ment, L. R., Hirtz, D., and Huppi, P. S. (2009). Imaging biomarkers of outcome in the developing preterm brain. *Lancet Neurol.* 8, 1042–1055. doi: 10.1016/S1474-4422(09)70257-1

Messina, D., Cerasa, A., Condino, F., Arabia, G., Novellino, F., Nicoletti, G., et al. (2011). Patterns of brain atrophy in Parkinson's disease, progressive supranuclear palsy and multiple system atrophy. *Parkinsonism Relat. Disord.* 17, 172–176. doi: 10.1016/j.parkreldis.2010.12.010

Nichols, T. E., and Holmes, A. P. (2001). Nonparametric permutation tests for functional neuroimaging: a primer with examples. *Hum. Brain Mapp* 15, 1–25. doi: 10.1002/hbm.1058

Phillips, J. R., Eissa, A. M., Hewedi, D. H., Jahanshahi, M., El-Gamal, M., Keri, S., et al. (2016). Neural substrates and potential treatments for levodopa-induced dyskinesias in Parkinson's disease. *Rev. Neurosci.* 27, 729–738. doi: 10.1515/revneuro-2016-0009

Roshchupkin, G. V., Gutman, B. A., Vernooij, M. W., Jahanshad, N., Martin, N. G., Hofman, A., et al. (2016). Heritability of the shape of subcortical brain structures in the general population. *Nat. Commun.* 7, 13738. doi: 10.1038/ncomms13738

Salim, A., Ma, X., Fall, K., Andren, O., and Reilly, M. (2014). Analysis of incidence and prognosis from 'extreme' case-control designs. *Stat. Med.* 33, 5388–5398. doi: 10.1002/sim.6245

Singh, A., Gutekunst, C. A., Uthayathas, S., Finberg, J. P., Mewes, K., Gross, R. E., et al. (2015). Effects of fibroblast transplantation into the internal pallidum on levodopa-induced dyskinesias in parkinsonian non-human primates. *Neurosci. Bull.* 31, 705–713. doi: 10.1007/s12264-015-1559-z

Tomiyama, M., Mori, F., Kimura, T., Ichinohe, N., Wakabayashi, K., Matsunaga, M., et al. (2004). Hypertrophy of medial globus pallidus and substantia nigra reticulata in 6-hydroxydopamine-lesioned rats treated with L-DOPA: implication for L-DOPA-induced dyskinesia in Parkinson's disease. *Neuropathology* 24, 290–295. doi: 10.1111/j.1440-1789.2004.00559.x

Tomlinson, C. L., Stowe, R., Patel, S., Rick, C., Gray, R., and Clarke, C. E. (2010). Systematic review of levodopa dose equivalency reporting in Parkinson's disease. *Mov. Disord.* 25, 2649–2653. doi: 10.1002/mds.23429

Tran, T. N., Vo, T. N. N., Frei, K., and Truong, D. D. (2018). Levodopa-induced dyskinesia: clinical features, incidence, and risk factors. *J. Neural. Transm.* 125, 1109–1117. doi: 10.1007/s00702-018-1900-6

Turcano, P., Mielke, M. M., Bower, J. H., Parisi, J. E., Cutsforth-Gregory, J. K., Ahlskog, J. E., et al. (2018). Levodopa-induced dyskinesia in Parkinson disease: a population-based cohort study. *Neurology* 91, e2238–e2243. doi: 10.1212/WNL.0000000000006643

Veldsman, M. (2017). Brain atrophy estimated from structural magnetic resonance imaging as a marker of large-scale network-based neurodegeneration in aging and stroke. *Geriatrics* 2, 34. doi: 10.3390/geriatrics2040034

Wahlund, L. O., Barkhof, F., Fazekas, F., Bronge, L., Augustin, M., Sjogren, M., et al. (2001). A new rating scale for age-related white matter changes applicable to MRI and CT. *Stroke* 32, 1318–1322. doi: 10.1161/01.str.32.6.1318

Conflict of Interest: JY received speaker's honoraria from SK chemicals, and research support from Medtronic and Boston Scientific.

The remaining authors declare that the research was conducted in the absence of any commercial or financial relationships that could be construed as a potential conflict of interest.

Publisher's Note: All claims expressed in this article are solely those of the authors and do not necessarily represent those of their affiliated organizations, or those of the publisher, the editors and the reviewers. Any product that may be evaluated in this article, or claim that may be made by its manufacturer, is not guaranteed or endorsed by the publisher.

frontiers | Frontiers in Aging Neuroscience

ORIGINAL RESEARCH
published: 17 May 2022
doi: 10.3389/fnagi.2022.838161

Concurrent Structural and Functional Patterns in Patients With Amnestic Mild Cognitive Impairment

*Li Liu[1], Tenglong Wang[2], Xiangdong Du[3], Xiaobin Zhang[3], Chuang Xue[1], Yu Ma[3] and Dong Wang[3]**

[1] Affiliated Mental Health Center, Hangzhou Seventh People's Hospital, Zhejiang University School of Medicine, Hangzhou, China, [2] School of Humanities and Management, Graduate School of Wannan Medical College, Wuhu, China, [3] Department of Geriatric Psychiatry, Suzhou Mental Health Center, Suzhou Guangji Hospital, The Affiliated Guangji Hospital of Soochow University, Suzhou, China

Amnestic mild cognitive impairment (aMCI) is a clinical subtype of MCI, which is known to have a high risk of developing Alzheimer's disease (AD). Although neuroimaging studies have reported brain abnormalities in patients with aMCI, concurrent structural and functional patterns in patients with aMCI were still unclear. In this study, we combined voxel-based morphometry (VBM), amplitude of low-frequency fluctuations (ALFFs), regional homogeneity (Reho), and resting-state functional connectivity (RSFC) approaches to explore concurrent structural and functional alterations in patients with aMCI. We found that, compared with healthy controls (HCs), both ALFF and Reho were decreased in the right superior frontal gyrus (SFG_R) and right middle frontal gyrus (MFG_R) of patients with aMCI, and both gray matter volume (GMV) and Reho were decreased in the left inferior frontal gyrus (IFG_L) of patients with aMCI. Furthermore, we took these overlapping clusters from VBM, ALFF, and Reho analyses as seed regions to analyze RSFC. We found that, compared with HCs, patients with aMCI had decreased RSFC between SFG_R and the right temporal lobe (subgyral) (TL_R), the MFG_R seed and left superior temporal gyrus (STG_L), left inferior parietal lobule (IPL_L), and right anterior cingulate cortex (ACC_R), the IFG_L seed and left precentral gyrus (PRG_L), left cingulate gyrus (CG_L), and IPL_L. These findings highlighted shared imaging features in structural and functional magnetic resonance imaging (MRI), suggesting that SFG_R, MFG_R, and IFG_L may play a major role in the pathophysiology of aMCI, which might be useful to better understand the underlying neural mechanisms of aMCI and AD.

Keywords: amnestic mild cognitive impairment, voxel-based morphometry, amplitude of low-frequency fluctuations, regional homogeneity, resting-state functional connectivity

OPEN ACCESS

Edited by:
Binbin Nie,
Institute of High Energy Physics (CAS), China

Reviewed by:
Carmen Jiménez-Mesa,
University of Granada, Spain
Haiqing Song,
Capital Medical University, China

***Correspondence:**
Dong Wang
xiangya511@163.com

Specialty section:
This article was submitted to Alzheimer's Disease and Related Dementias, a section of the journal Frontiers in Aging Neuroscience

Received: *17 December 2021*
Accepted: *01 April 2022*
Published: *17 May 2022*

Citation:
Liu L, Wang T, Du X, Zhang X, Xue C, Ma Y and Wang D (2022) Concurrent Structural and Functional Patterns in Patients With Amnestic Mild Cognitive Impairment. Front. Aging Neurosci. 14:838161. doi: 10.3389/fnagi.2022.838161

INTRODUCTION

Mild cognitive impairment (MCI) is an early but abnormal state of cognitive impairment, which is considered a transitional period between normal aging and early Alzheimer's disease (AD) (Petersen, 2010), usually characterized by cognitive decline, and without dementia (Petersen et al., 2009). According to the difference in the impaired cognitive domain, there are two major types of MCI: amnestic MCI (aMCI) and non-amnestic MCI (naMCI) (Petersen et al., 2014). aMCI is characterized by memory deficits and, to a large extent, often leads to AD. Actually, people with

aMCI have a high risk of developing AD, and about 10–15% of patients with aMCI will progress to AD, while the annual rate in the normal population is 1–2% (Petersen et al., 2001). AD has become a social problem in recent decades due to its heavy financial burden and poor effective treatment. However, the pathophysiology of AD and aMCI remains unclear.

Neuroimaging studies may provide valuable information to predict the incidence and development of aMCI and have great potential to provide the pathological process that leads to cognitive decline. Recently, numerous studies have reported damage to structural or functional changes in the brain of patients with aMCI. Structural magnetic resonance imaging (sMRI) studies have shown the changes of gray matter (GM) atrophy in many regions such as in the amygdala, hippocampus (HP), medial temporal lobe, and thalamus in aMCI (Nickl-Jockschat et al., 2012; Zhang J. et al., 2021). Resting-state functional MRI (rs-fMRI) is a supplement to sMRI, which can describe functional changes in the whole brain (Zhang et al., 2020). The impairment of functional brain activity occurred mainly in the default mode network (DMN), executive control network (ECN), and salience network (SN) in aMCI (Li et al., 2020; Fu et al., 2021; Xue et al., 2021a). Liu et al. (2021) suggested that the impairment of functional brain activity occurred mainly in the DMN and language network in MCI. However, the results of these structural and functional MRI studies were inconsistent and difficult to replicate. Therefore, the combination of functional and structural analysis may provide new insights into an understanding of the changes in the brain of patients with aMCI.

In recent years, several studies have used combined structural and functional MRI in patients with aMCI. Some studies focused on specific predefined brain networks or regions (such as the DMN, SN, or HP) (Bharath et al., 2017; Wang et al., 2020; Xue et al., 2021b), or focused on specific band oscillations (Zhao et al., 2015) to investigate the difference between patients with aMCI and the other groups. Some studies have used machine learning methods to investigate structural and functional patterns between patients with aMCI and the other groups (Wee et al., 2012; Yan et al., 2019). However, the results of these studies were inconsistent due to small samples or inconsistent parameters. Especially, these studies also did not describe concurrent structural and functional connectivity patterns in aMCI. Therefore, in this study, we aimed to combine voxel-based morphometry (VBM), amplitude of low-frequency fluctuations (ALFFs), regional homogeneity (Reho), and seed-based resting-state functional connectivity (RSFC) to explore possible concurrent structural and functional changes in patients with aMCI. We hypothesized that patients with aMCI have concurrent functional and structural brain regions and that these regions may play an important role in aMCI.

MATERIALS AND METHODS

Participants

The study was conducted under the ethical approval of the Ethics Committee of Suzhou Guangji Hospital, and all individuals gave written informed consent prior to participation. A total of 232 subjects were recruited in this study from July 2019 to March 2021, including 122 patients with aMCI and 110 healthy controls (HCs). Patients with aMCI were screened to meet the Peterson MCI criteria (Petersen et al., 1999): (1) had a memory complaint; (2) Mini-Mental State Examination (MMSE) scores between 24 and 30; (3) objective memory loss adjusted for education and age; (4) a Clinical Dementia Rating (CDR) of 0.5; (5) normal or near-normal performance in cognitive function without significant levels of impairment in other cognitive domains; (6) the absence of dementia according to Diagnostic and Statistical Manual of Mental Disorders, 4th edition, revised (DSM-IV); and (7) essentially preserved activities of daily living. HCs were enrolled as described in the structured interview for DSM-IV non-patient edition to confirm the lifelong absence of psychiatric and neurological illness. Exclusion criteria applied to all subjects were as follows: mental and neurological diseases, history of stroke, substance abuse, several medical conditions that cause cognitive impairment, such as syphilis, thyroid dysfunction, severe anemia, and HIV.

Magnetic Resonance Imaging Data Acquisition

All data were acquired with the GE Discovery MR750W 3.0 T System (General Electric Discovery silent, United States) at the Suzhou Guangji Hospital. Functional imaging data (echo-planar imaging, EPI sequence) were obtained with the following parameters: repetition time = 2000 ms; echo time = 30 ms; flip angle = 90°; field of view (FOV) = 224 mm × 224 mm; acquisition matrix = 64 × 64; 36 slices; 200 volumes; voxel size = 3.5 × 3.5 × 3.5; and slice thickness = 3.6 mm. Structural imaging data were collected (3D T1-weighted SFPGR sequence) with the following parameters: repetition time = 7.7 ms; echo time = 3.1 ms; FOV = 256 mm × 256 mm; and voxel size = 1 mm × 1 mm × 1 mm. The scan time lasts for 400 s. All subjects were asked to keep their eyes closed and remain awake during the scan.

Data Analysis

Clinical Data Analysis

Demographic and clinical variables were analyzed with SPSS25.0 (IBM, IL, United States). Data with non-normality were log-transformed into a normal distribution. Two-sample *t*-tests were used to compare differences in age, education, and MMSE scores between the two groups. χ^2-test was used to compare gender differences between the two groups. $p < 0.05$ was statistically significant.

Structural Magnetic Resonance Imaging Analysis

Voxel-based morphometry data were processed with the VBM8 tool of the SPM8 software package[1] on the MATLAB R2012a platform (The MathWorks, Natick, MA, United States). First, T1 images were visually inspected for anomalies by orienting them to place the anterior commissure at the origin of the Montreal Neurological Institute (MNI) 3D coordinate system. Then, the images were normalized to template space and segmented into

[1]https://www.fil.ion.ucl.ac.uk/spm/

GM, white matter (WM), and cerebrospinal fluid (CSF) using SPM8 standard unified segmentation. The next step was spatial normalization of the segmented GM and WM images using the DARTEL algorithm (Ashburner, 2007). Finally, the normalized GM images were smoothed by a Gaussian kernel with full width at half maximum (FWHM) of 8 mm. A voxel-wise analysis with two-sample *t*-tests was conducted to detect an abnormality in gray matter volume (GMV) between the aMCI group and HC group with age, sex, years of education, and total intracranial volume (TIV) as covariates. Correction for multiple comparisons was performed with $p < 0.01$ [false discovery rate (FDR) correction for multiple comparisons].

Resting-State Functional MRI Analysis

The rs-fMRI data preprocessing was carried out with SPM8 and DPABI V4.3.[2] The data were processed as follows: (1) The first 10 volumes were discarded to reduce scan noise and magnetic field instability. (2) Slice timing and head motion in the rs-fMRI images were corrected. (3) Coregistered, segmentation, and regression of the nuisance signals of the WM signal, CSF signal, and head motion parameters. (4) The data were normalized to the MNI space and resampled to a voxel size of 3 mm × 3 mm × 3 mm. (5) Frames with a displacement (FD) greater than 0.5 mm were removed. (6) Detrended, bandpass filtering from 0.01 to 0.08 Hz was carried out in Reho analysis, and smoothing with an 8-mm FWHM Gaussian kernel was carried out in the ALFF analysis.

Amplitude of Low-Frequency Fluctuation and Regional Homogeneity Analyses

We compared the Reho and ALFF differences between aMCI and the HC group in SPM8 and DPABI V4.3. The detailed Reho measurement was described in our previous research (Liu et al., 2021). Briefly, individual Reho maps were performed by calculating Kendall's coefficient concordance (KCC) of the time series of a given voxel with its neighboring 26 voxels (Zang et al., 2004). Then, the data were smoothed with an 8-mm FWHM Gaussian kernel to generate Reho maps for each subject in each group. Fast Fourier transform (FFT) was used to transform the filtered time series to the frequency domain to obtain the power spectrum. Then, the square root was calculated at each frequency of the power spectrum and the root mean square at 0.01–0.08 Hz was obtained for each voxel as ALFF values. Subsequently, similar to Reho analysis, the ALFF value of each voxel was divided by the global mean ALFF value within the whole-brain mask (Yang et al., 2007). The significance of group differences was set at $p < 0.01$ using the FDR correction for multiple comparisons, accompanied with age, gender, and years of education as covariates.

Seed-Based Resting-State Functional Connectivity Analysis

To further characterize the nature of RSFC alterations in aMCI, whole-brain analyses restricted to overlapping brain regions that were repeatedly reported in previous findings were conducted. These important clusters that showed an significant brain region overlap during VBM, ALFF, and Reho analyses were selected as the seed regions of interest (ROIs). In this study, we selected the peak coordinates of the left inferior frontal gyrus (IFG_L), right superior frontal gyrus (SFG_R), and right middle frontal gyrus (MFG_R) to create spherical regions with a radius of 5 mm as ROIs. Then, we extracted the average time series of each ROI and calculated the Pearson correlation between the time series of whole-brain voxels and each ROI to generate the FC maps for each subject. Subsequently, the *z*-map was obtained using Fisher's *z* transformation to improve normality. Finally, we compared the global connectivity difference of the three ROIs between the two groups using two-sample *t*-tests. The significance of group differences was set at $p < 0.01$ using the FDR correction with age, gender, and years of education as covariates.

[2]http://www.restfmri.net/forum/DPARSF

RESULTS

Baseline Characteristics

A total of 232 subjects were recruited in this study. A total of 17 subjects were excluded due to excessive movement and direction during the scan. Finally, 114 patients with aMCI and 101 HCs were included in the next sMRI and rs-fMRI analysis. Demographic and clinical data are shown in **Table 1**. There were no significant differences between patients with aMCI and the HC group in terms of gender ($\chi^2 = 0.50$, $p = 0.49$), age ($F = 0.78$, $p = 0.44$), and education ($F = 1.21$, $p = 0.23$). Additionally, compared with the HC group, patients with aMCI had significantly lower MMSE scores ($F = -33.85$, $p < 0.001$).

Voxel-Based Morphometry, Amplitude of Low-Frequency Fluctuation, and Regional Homogeneity Differences Between Amnestic Mild Cognitive Impairment and Healthy Control

Voxel-Based Morphometry Results

Compared with the HC group, patients with aMCI showed significantly decreased GMV in the right cerebellum posterior

TABLE 1 | Demographic and clinical characteristics of patients with aMCI and HC.

	aMCI	HC	F/χ^2 values	*p*-Values
Number	114	101		
Female/male	68/46	65/36	0.50	0.49[a]
Age (years)	72.35 ± 5.23	71.69 ± 4.95	0.78	0.44[b]
Formal education (years)	10.78 ± 3.71	10.24 ± 2.73	1.21	0.23[b]
MMSE score	24.11 ± 1.01	28.31 ± 0.97	−33.85	<0.001[b]
CDR score	0.5	0		

aMCI, amnesic mild cognitive impairment; HC, healthy control; MMSE, Mini-Mental State Examination; CDR, Clinical Dementia Rating; values are mean ± standard deviation (SD).

[a]The value of p was obtained by using the χ^2 test.

[b]The p-value was obtained using two-sample t-tests.

lobe (CPL_R), right posterior cingulate cortex (PCC_R), right middle temporal gyrus (MTG_R), bilateral HP, and bilateral parahippocampal gyrus (PHG), left fusiform gyrus (FG_L), IFG_L, right superior temporal gyrus (STG_R), and right cingulate gyrus (CG_R) ($p < 0.01$, FDR corrected). Additionally, compared with the HC group, patients with aMCI showed no significantly increased volumes in any brain region (**Table 2** and **Figure 1**).

Amplitude of Low-Frequency Fluctuation Results

Compared with the HC group, patients with aMCI showed decreased ALFF values in the left thalamus (THA_L), left anterior cingulate cortex (ACC_L), left precentral gyrus (PRG_L), SFG_R, and MFG_R ($p < 0.01$, FDR corrected). Additionally, compared with the HC group, patients with aMCI showed no significantly increased ALFF values in any brain region (**Table 2** and **Figure 2**).

Regional Homogeneity Results

Compared with the HC group, patients with aMCI showed decreased Reho values in PCC_L, the bilateral inferior frontal gyrus (IFG), SFG_R, and MFG_R ($p < 0.01$, FDR corrected). Additionally, compared with the HC group, patients with aMCI showed no significantly increased Reho values in any brain region (**Table 2** and **Figure 3**).

Resting-State Functional Connectivity Differences Between Amnestic Mild Cognitive Impairment and Healthy Control

Right Superior Frontal Gyrus Resting-State Functional Connectivity Results

Comparing the ALFF and Reho results, only one shared cluster showed alterations in both ALFF and Reho in patients with aMCI. Considering that the size of this cluster was very large, including two key brain regions (SFG_R and MFG_R) associated with aMCI, we chose the peak coordinates of SFG_R and MFG_R as the two ROIs for the following RSFC analysis.

Using SFG_R as the ROI, the RSFC analysis revealed that FC values of the right temporal lobe (subgyral) (TL_R) were reduced in patients with aMCI than in the HC group. Additionally, compared with the HC group, patients with aMCI showed no significantly increased RSFC between SFG_R and any other brain region (**Table 3**).

Right Middle Frontal Gyrus Resting-State Functional Connectivity Results

Using MFG_R as the ROI, the RSFC analysis displayed that FC values of the left superior temporal gyrus (STG_L), left

TABLE 2 | The VBM, ALFF, and Reho comparisons between patients with aMCI and HCs.

Contrast	Brain regions	Voxels	Brodmann areas	Peak MNI (*X*, *Y*, *Z*)			*Z* score
VBM comparison between aMCI and HC							
aMCI < HC	R cerebellum posterior lobe	697	NA	25.5	−70.5	−39	−4.39
	R posterior cingulate cortex	6470	18/19/30/31	7.5	−60	22.5	−5.42
	R cerebellum posterior lobe	163	NA	4.5	−64.5	−36	−4.60
	R middle temporal gyrus	220	20/21	48	0	−22.5	−5.51
	R parahippocampal gyrus/hippocampus	370	35/36	21	−31.5	−12	−4.42
	L parahippocampal gyrus/hippocampus	938	28/34/35	−31.5	−18	−13.5	−4.75
	L fusiform gyrus	224	37	−40.5	−60	−13.5	−5.72
	L inferior frontal gyrus	**102**	**47**	**−46.5**	**21**	**−1.5**	**−4.40**
	R superior temporal gyrus	161	22	52.5	−18	−3	−4.14
	R cingulate gyrus	346	5/7/31	1.5	−33	43.5	−4.56
	R cingulate gyrus	141	19/24	9	−24	37.5	−4.81
aMCI > HC	No brain region above the threshold						
ALFF comparison between aMCI and HC							
aMCI < HC	L thalamus	268	NA	−15	−21	0	−4.86
	L anterior cingulate cortex	979	24	−9	21	24	−5.53
	L precentral gyrus	190	9/44	−42	0	27	−4.18
	R superior/middle frontal gyrus	**511**	**6/40**	**24**	**12**	**42**	**−5.03**
aMCI > HC	No brain region above the threshold						
Reho comparison between aMCI and HC							
aMCI < HC	L posterior cingulate cortex	1162	24/23	−3	−30	24	−5.65
	R inferior frontal gyrus	140	NA	42	27	15	−5.74
	R superior/middle frontal gyrus	**1337**	**6/40**	**24**	**12**	**42**	**−5.86**
	L inferior frontal gyrus	**166**	6/44	**−39**	**3**	**27**	**−5.00**
aMCI > HC	No brain region above the threshold						

aMCI, amnesic mild cognitive impairment; HC, healthy control; L, left; R, right; NA, not applicable; MNI, Montreal Neurological Institute; X, Y, Z, indicate the coordinates according to the MNI; VBM, voxel-based morphometry; ALFFs, amplitude of low-frequency fluctuations; Reho, regional homogeneity.
A threshold of p < 0.01, false discovery rate (FDR) correction, only clusters with k = 100 or larger are mentioned.
Bold terms and values indicating overlapping brain region.

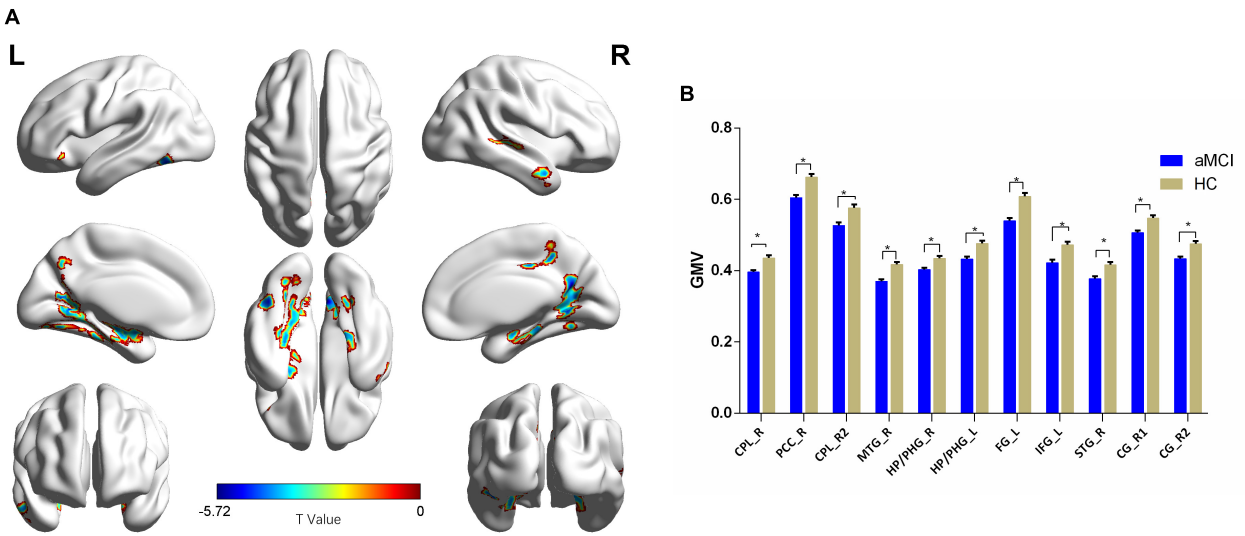

FIGURE 1 | The VBM comparison between patients with aMCI and the HC group. **(A)** Significant clusters obtained from two-sample *t*-tests, the color bar represents the range of *t*-values; **(B)** brain regions showing decreased gray matter volume (GMV) in patients with aMCI. The error bars represent the standard error of the mean (SEM) and asterisks show significant differences between the groups; a threshold of $p < 0.01$, false discovery rate (FDR) correction, only clusters with $k = 100$ or large are mentioned. CPL, cerebellum posterior lobe; PCC, posterior cingulate cortex; MTG, middle temporal gyrus; HP, hippocampus; PHG, parahippocampal gyrus; FG, fusiform gyrus; IFG, inferior frontal gyrus; STG, superior temporal gyrus; CG, cingulate gyrus; aMCI, amnesic mild cognitive impairment; HC, healthy control; VBM, voxel-based morphometry; L, left; R, right. *$p < 0.01$.

inferior parietal lobule (IPL_L), and right anterior cingulate cortex (ACC_R) were reduced in patients with aMCI than in the HC group. Additionally, compared with the HC group, aMCI patients showed no significant differences of RSFC between MFG_R and any other brain region (**Table 3**).

Left Inferior Frontal Gyrus Resting-State Functional Connectivity Results

In comparison of the VBM and ALFF/Reho results, only IFG_L shared the GMV and Reho alterations in patients with aMCI. Therefore, we selected the peak coordinate of IFG_L as the ROI for the RSFC analysis.

Using IFG_L as the ROI, the RSFC analysis found that FC values of PRG_L, the left cingulate gyrus (CG_L), and IPL_L were reduced in patients with aMCI than in the HC group. Additionally, compared with the HC group, patients with aMCI had no significantly increased RSFC between IFG_L and any other brain region (**Table 3**).

DISCUSSION

In this study, large samples and multi-modal data methods were used to explore the structural and resting-state functional neuroimaging changes in patients with aMCI, and to seek for concurrent patterns of brain functional and structural changes in patients with aMCI. We found that both ALFF and Reho were decreased in the SFG_R and MFG_R of patients with aMCI, and both GMV and Reho were decreased in the IFG_L of patients with aMCI. Furthermore, we used the overlapping clusters derived from VBM, ALFF, and Reho analyses as ROIs for the RSFC analysis, which can provide reasonable and persuasive results. And, this finding showed that RSFC between the SFG_R seed and TL_R (subgyral) was decreased; RSFC between the MFG_R seed and STG_L, IPL_L, and ACC_R was decreased; and RSFC between the IFG_L seed and PRG_L, CG_L, and IPL_L was also decreased in patients with aMCI. These important results support the involvement of SFG_R, MFG_R, and IFG_L in the pathophysiology of aMCI.

Altered Resting-State Functional Connectivity Patterns of Right Superior Frontal Gyrus in Patients With Amnestic Mild Cognitive Impairment

Amplitude of low-frequency fluctuations reflects the intensity of spontaneous brain activity (Yang et al., 2007), and Reho reflects the synchronization of spontaneous brain activity (Zang et al., 2004). In patients with aMCI, Zhang Z. et al. (2021) observed decreased Reho in the superior frontal gyrus (SFG) and middle frontal gyrus. Wang et al. (2021) observed decreased ALFF in SFG. Our study showed that the SFG_R of patients with aMCI had both decreased ALFF and Reho values, which is consistent with previous studies. Therefore, we speculated that the weakened spontaneous neuronal activity of SFG_R might help to distinguish aMCI from HC. SFG is mainly located in the upper part of the prefrontal cortex and includes multiple subregions (Li et al., 2013). SFG is a core region of the dorsolateral prefrontal cortex (DLPFC) (Koenigs and Grafman, 2009), and it plays a key role in ECN, which is associated with executive dysfunction. Evidence shows that episodic memory, executive function, language, and visuospatial function were the major

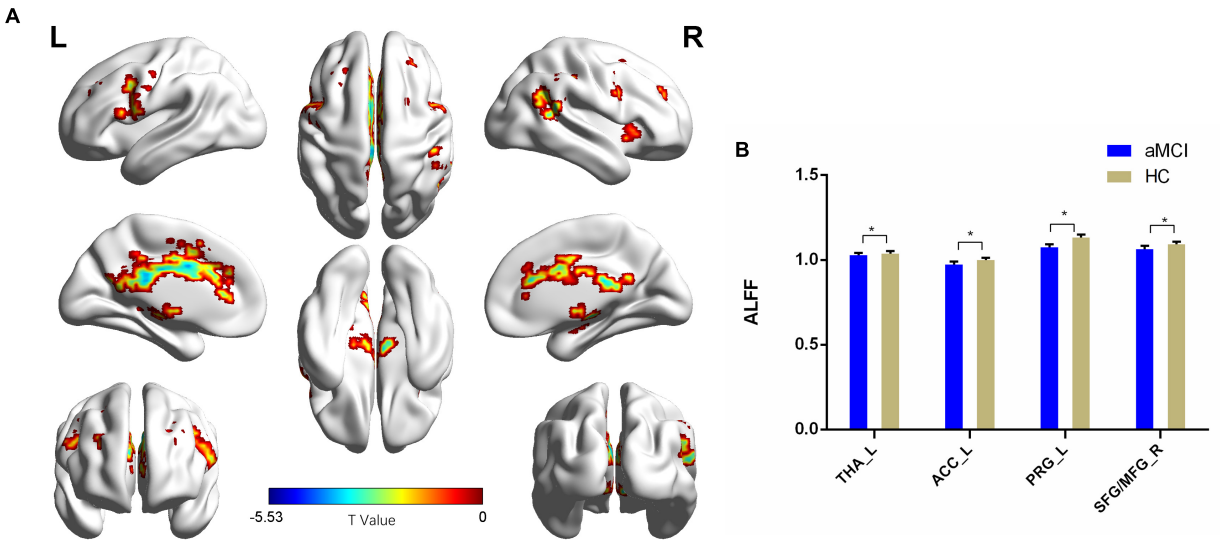

FIGURE 2 | The ALFF comparison between patients with aMCI and the HC group. **(A)** Significant clusters obtained from two-sample *t*-tests, the color bar represents the range of *t*-values; **(B)** brain regions showing decreased ALFF in patients with aMCI. The error bars represent the SEM and asterisks show significant differences between the groups; a threshold of $p < 0.01$, FDR correction, only clusters with $k = 100$ or large are mentioned. THA, thalamus; ACC, anterior cingulate cortex; PRG, precentral gyrus; SFG, superior frontal gyrus; MFG, middle frontal gyrus; aMCI, amnesic-mild cognitive impairment; HC, healthy control; ALFFs, amplitude of low-frequency fluctuations; L, left; R, right. $^*p < 0.01$.

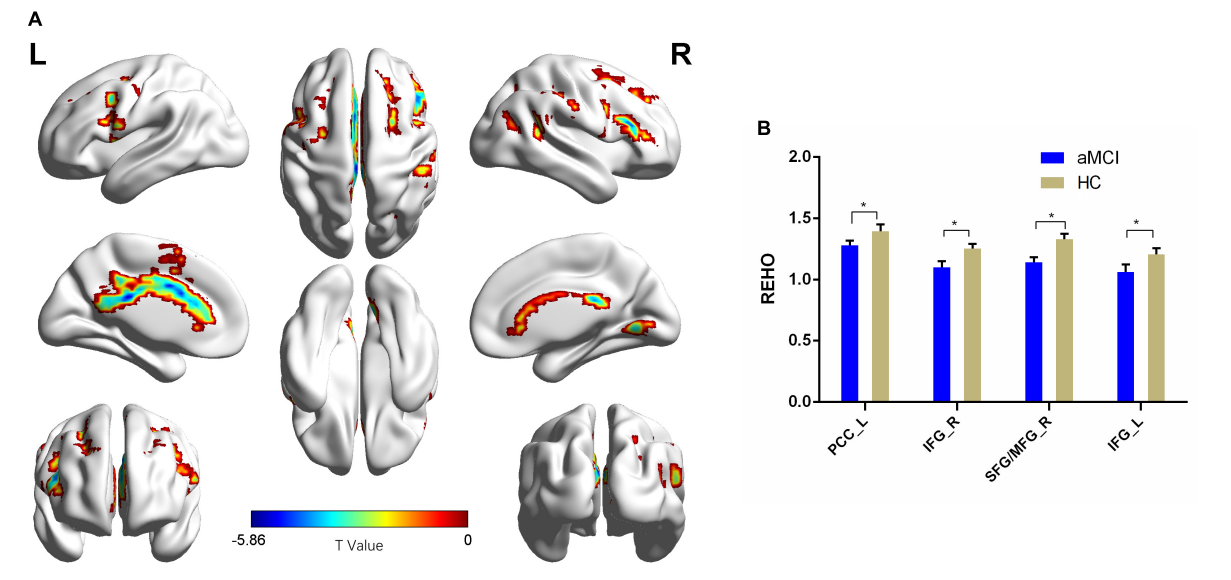

FIGURE 3 | The Reho comparison between patients with aMCI and the HC group. **(A)** Significant clusters obtained from two-sample *t*-tests, the color bar represents the range of *t*-values; **(B)** brain regions showing decreased Reho in patients with aMCI. The error bars represent the SEM and asterisks show significant differences between the groups; a threshold of $p < 0.01$, FDR correction, only clusters with $k = 100$ or large are mentioned. PCC, posterior cingulate cortex; IFG, inferior frontal gyrus; SFG, superior frontal gyrus; MFG, middle frontal gyrus; aMCI, amnesic-mild cognitive impairment; HC, healthy control; Reho, regional homogeneity; L, left; R, right. $^*p < 0.01$.

impaired cognitive domains in multi-domain patients with aMCI (Winblad et al., 2004), suggesting that SFG_R may participate in executive dysfunction in patients with aMCI.

To further explore the correlation between SFG_R and other brain regions in patients with aMCI, SFG_R was chosen as the ROI for the RSFC analysis. In this study, we found that, compared with HCs, decreased RSFC in the aMCI group was mainly in TL_R.

The temporal lobe is located below the lateral sulcus of the brain, associated with hearing, memory, and emotion (Li et al., 2021). Xie et al. (2015) reported a decrease in functional connectivity in the TL in patients with aMCI. Additionally, they

TABLE 3 | Regions showing seed-based functional connectivity differences between the two groups.

Seed	Brain regions	Voxels	Peak MNI (*X*, *Y*, *Z*)			*Z* score
R superior frontal gyrus						
aMCI < HC	R temporal lobe (subgyral)	61	42	−27	−12	−5.06
aMCI > HC	No brain regions above the threshold					
R middle frontal gyrus						
aMCI < HC	L superior temporal gyrus	132	−54	−3	9	−4.59
	L inferior parietal lobule	117	−39	−39	30	−4.47
	R anterior cingulate cortex	151	12	30	18	−4.86
aMCI > HC	No brain regions above the threshold					
L inferior frontal gyrus						
aMCI < HC	L precentral gyrus	35	−42	0	30	−4.47
	L cingulate gyrus	104	−3	12	45	−6.36
	L inferior parietal lobule	46	−42	−63	39	−4.14
aMCI > HC	No brain regions above the threshold					

aMCI, amnesic mild cognitive impairment; HC, healthy control; L, left; R, right; MNI, Montreal Neurological Institute; X, Y, Z, indicate the coordinates according to the MNI. A threshold of $p < 0.01$, FDR correction, only clusters with $k = 35$ or larger are mentioned.

found that the medial TL was impaired in the early stages of AD. Along with disease progression, the damage might extend to other regions, eventually leading to cognitive impairments. According to our results, RSFC alteration was mainly found in the TL, which was consistent with the study conducted by Xie et al. (2015). Based on the abovementioned results, we inferred that abnormal functional connectivity of the TL may lead to cognition dysfunction in patients with aMCI, and the TL may be an effective biomarker in monitoring the progression of AD.

Altered Resting-State Functional Connectivity Patterns of Right Middle Frontal Gyrus in Patients With Amnestic Mild Cognitive Impairment

The middle frontal gyrus is located mainly in the lateral prefrontal cortex, a core region of the DLPFC (Koenigs and Grafman, 2009), and it plays a key role in the ECN. It has been reported to be associated with episodic memory and emotional processing (Carballedo et al., 2011; Rajah et al., 2011). In this study, we found that the MFG_R of patients with aMCI had both decreased ALFF and Reho, which was consistent with previous studies (Wang et al., 2021; Zhang Z. et al., 2021). Based on the abovementioned findings, abnormal spontaneous activity of MFG_R may be related to executive dysfunction and episodic memory in the aMCI group.

To further explore the correlation between MFG_R and other brain regions in patients with aMCI, MFG_R was used as the ROI for the RSFC analysis. In this study, we found that, compared with HCs, decreased RSFC in the aMCI group was mainly in the STG_L, IPL_L, and ACC_R, which were functionally associated with the DMN, ECN, and auditory network.

The anterior cingulate cortex is related to cognition, emotional processing, and executive function (Fillinger et al., 2018; Jung et al., 2019). The inferior parietal lobule (IPL) is associated with episodic memory, semantic processing, and spatial cognitive function (Wang et al., 2017). Both the anterior cingulate cortex (ACC) and IPL belong to the DMN (Buckner et al., 2008; Raichle, 2015). The DMN is an important network, which is closely involved in episodic memory processing and emotion regulation in patients with cognitive decline (Raichle, 2015; Xie et al., 2016). It plays a crucial role in the progression of AD (Greicius et al., 2004). Consistent with our findings, numerous studies reported a typical disruption of the DMN in patients with AD and aMCI (Li et al., 2020; Ma et al., 2020). Actually, the deposition of β-amyloid proteins occurs in the DMN and might reduce the connection with other brain regions (Wang et al., 2013). Hence, an abnormal RSFC between the middle frontal gyrus and DMN may be related to altered cognition in patients with aMCI, which provides valuable insights into identifying high-risk groups for AD. Additionally, STG is an important region of the language network, involved in language and episodic memory (Yi et al., 2019; Liu et al., 2021). In this study, decreased RSFC in the STG_L may reflect an intimate relationship between STG_L and language dysfunction in patients with aMCI.

Altered Resting-State Functional Connectivity Patterns of Left Inferior Frontal Gyrus in Patients With Amnestic Mild Cognitive Impairment

In this study, we found that the IFG_L of patients with aMCI had concurrent structural and functional changes, which suggested that IFG_L might be a better indicator for predicting cognitive deficits in aMCI (Gilmore et al., 2021). IFG_L was related to language/semantic processing. Xue et al. (2021b) found negative associations between IFG_L and cognitive domains in patients with aMCI, such as executive function and working memory. Therefore, we inferred that alterations in the IFG_L might be associated with executive function and the language network.

To further explore the correlation between IFG_L and the other brain regions in patients with aMCI, IFG_L was selected as the ROI for the RSFC analysis. We found that, compared to HC, decreased RSFC in the aMCI group was mainly in PRG_L, CG_L, and IPL_L, which were functionally associated with the sensorimotor network (SMN), DMN, and limbic system.

Precentral gyrus is involved in motor and executive functions, and it plays a central role in the SMN (Chenji et al., 2016; Feng et al., 2018). The SMN is mainly composed of visual, auditory, and sensory-motor cortex. Studies reported that changes in sensory and motor function may be earlier than cognitive symptoms in AD and may increase the risk of AD (Albers et al., 2015). These findings suggested that the SMN may be a predictor of conversion to AD. Additionally, Wang et al. (2015) proposed that the functional connectivity of the SMN was firstly impaired in AD and then extended to other key regions in AD, suggesting that the SMN may coordinate with other networks, and lead to clinical symptoms of patients with AD and MCI. In these data, decreased RSFC in the PRG implicated in the SMN could explain the impairment of the sensory-motor function and executive function in aMCI. As a core region of the limbic system, CG is mainly involved in the regulation of emotional state (Heimer and Hoesen, 2006). Yang et al. (2015) reported that emotional stimuli were thought to enhance episodic memory through the production of automatic attention and the old/new parietal effect. Based on this finding, we speculate that CG may affect episodic memory through emotion regulation. In addition, CG was found to play an important role in the whole-brain language network (Battistella et al., 2019). Therefore, decreased CG RSFC may be involved in multiple cognitive domains, including language and episodic memory impairments in aMCI.

Limitations

Although these findings have been of great value, there are still several limitations. First, the present study was a cross-sectional, single-center design with a small sample size and may not have sufficient power. In the future, longitudinal and multicenter studies with large sample sizes are required to explore the relationship between structural and functional findings. Second, there was no detection of biology-related data and genetic information. Third, further patient recruitment in the prodromal and more severe stages of AD is warranted to understand the structural–functional association in the preclinical AD spectrum. Fourth, fMRI and VBM analyses using SPM in this study might give rise to the observation of false-positive functional and structural changes (Eklund et al., 2016; Gorriz et al., 2019). The data still need to be interpreted with caution.

CONCLUSION

In summary, using combined structural and functional MRI analyses, we found the shared brain region alterations in patients with aMCI. SFG_R, MFG_R, and IFG_L were detected as the primary regions that may be involved in various cognitive deficits in patients with aMCI, from both structural and functional perspectives. Our results suggested that these damaged brain areas might play a major role in the aMCI stage of AD, which may help to better understand complicated neurobiology mechanisms and provide crucial insights into imaging methods for early diagnosis, intervention, and more effective prevention for MCI and AD.

DATA AVAILABILITY STATEMENT

The raw data supporting the conclusions of this article will be made available by the authors, without undue reservation.

ETHICS STATEMENT

The studies involving human participants were reviewed and approved by the Ethics Committee of Suzhou Guangji Hospital. The patients/participants provided their written informed consent to participate in this study.

AUTHOR CONTRIBUTIONS

LL wrote the first draft of the manuscript. TW and YM were responsible for data collection. DW was responsible for study design, data analysis, and subsequent editing. CX, XZ, and XD made critical revisions to this manuscript. All authors contributed to the article and approved the submitted version.

FUNDING

This work was supported by the Natural Science Foundation of Jiangsu Province of China (BK20211081), the Youth Science and Technology Project of Suzhou (KJXW2019048), Key Science and Technology Project of Suzhou (SS202071), Geriatric Health Research Project of Jiangsu Province of China (LR2021046), and Key Clinical Discipline and Geriatric Psychiatry Project of Suzhou (SZXK202116).

ACKNOWLEDGMENTS

We are deeply grateful to all participants for participating in this study.

REFERENCES

Albers, M. W., Gilmore, G. C., Kaye, J., Murphy, C., Wingfield, A., Bennett, D. A., et al. (2015). At the interface of sensory and motor dysfunctions and Alzheimer's disease. *Alzheimers Dement.* 11, 70–98. doi: 10.1016/j.jalz.2014.04.514

Ashburner, J. (2007). A fast diffeomorphic image registration algorithm. *Neuroimage* 38, 95–113. doi: 10.1016/j.neuroimage.2007.07.007

Battistella, G., Henry, M., Gesierich, B., Wilson, S. M., Borghesani, V., Shwe, W., et al. (2019). Differential intrinsic functional connectivity changes in semantic variant primary progressive aphasia. *Neuroimage Clin.* 22:101797. doi: 10.1016/j.nicl.2019.101797

Bharath, S., Joshi, H., John, J. P., Balachandar, R., Sadanand, S., Saini, J., et al. (2017). A multimodal structural and functional neuroimaging study of amnestic mild cognitive impairment. *Am. J. Geriatr.* 25, 158–169. doi: 10.1016/j.jagp.2016.05.001

Buckner, R. L., Andrews-Hanna, J. R., and Schacter, D. L. (2008). The brain's default network: anatomy, function, and relevance to disease. *Ann. N. Y. Acad. Sci.* 1124, 1–38. doi: 10.1196/annals.1440.011

Carballedo, A., Scheuerecker, J., Meisenzahl, E., Schoepf, V., Bokde, A., Möller, H.-J., et al. (2011). Functional connectivity of emotional processing in depression. *J. Affect. Disord.* 134, 272–279. doi: 10.1016/j.jad.2011.06.021

Chenji, S., Jha, S., Lee, D., Brown, M., Seres, P., Mah, D., et al. (2016). Investigating default mode and sensorimotor network connectivity in amyotrophic lateral sclerosis. *PLoS One* 11:e0157443. doi: 10.1371/journal.pone.0157443

Eklund, A., Nichols, T. E., and Knutsson, H. (2016). Cluster failure: Why fMRI inferences for spatial extent have inflated false-positive rates. *Proc. Natl. Acad. Sci. U. S. A.* 113, 7900–7905. doi: 10.1073/pnas.1602413113

Feng, W., Wang, D., Tang, L., Cheng, Y., Wang, G., Hu, G., et al. (2018). Effects of different cognitive trainings on amnestic mild cognitive impairment in the elderly: a one-year longitudinal functional magnetic resonance imaging (MRI) study. *Med. Sci. Monit.* 24, 5517–5527. doi: 10.12659/msm.908315

Fillinger, C., Yalcin, I., Barrot, M., and Veinante, P. (2018). Efferents of anterior cingulate areas 24a and 24b and midcingulate areas 24a' and 24b' in the mouse. *Brain Struct. Funct.* 223, 1747–1778. doi: 10.1007/s00429-017-1585-x

Fu, Z., Zhao, M., He, Y., Wang, X., and Li, S. (2021). Divergent connectivity changes in gray matter structural covariance networks in subjective cognitive decline, amnestic mild cognitive impairment, and Alzheimer's Disease. *Front. Aging Neurosci.* 13:686598. doi: 10.3389/fnagi.2021.686598

Gilmore, N., Yücel, M. A., Li, X., Boas, D. A., and Kiran, S. (2021). Investigating language and domain-general processing in neurotypicals and individuals with aphasia - a functional near-infrared spectroscopy pilot study. *Front. Hum. Neurosci.* 15:728151. doi: 10.3389/fnhum.2021.728151

Gorriz, J. M., Group, S., and Neuroscience, C. (2019). Statistical agnostic mapping: a framework in neuroimaging based on concentration inequalities. *Informat. Fusion* 66, 198–212. doi: 10.1016/j.inffus.2020.09.008

Greicius, M. D., Srivastava, G., Reiss, A. L., and Menon, V. (2004). Default-mode network activity distinguishes Alzheimer's disease from healthy aging: evidence from functional MRI. *Proc. Natl. Acad. Sci. U. S. A.* 101, 4637–4642. doi: 10.1073/pnas.0308627101

Heimer, L., and Hoesen, G. W. V. (2006). The limbic lobe and its output channels: implications for emotional functions and adaptive behavior. *Neurosci. Biobehav. Rev.* 30, 126–147. doi: 10.1016/j.neubiorev.2005.06.006

Jung, F., Kazemifar, S., Bartha, R., and Rajakumar, N. (2019). Semiautomated assessment of the anterior cingulate cortex in Alzheimer's Disease. *J. Neuroimaging* 29, 376–382. doi: 10.1111/jon.12598

Koenigs, M., and Grafman, J. (2009). The functional neuroanatomy of depression: distinct roles for ventromedial and dorsolateral prefrontal cortex. *Behav. Brain Res.* 201, 239–243. doi: 10.1016/j.bbr.2009.03.004

Li, T., Liao, Z., Mao, Y., Hu, J., Le, D., Pei, Y., et al. (2021). Temporal dynamic changes of intrinsic brain activity in Alzheimer's disease and mild cognitive impairment patients: a resting-state functional magnetic resonance imaging study. *Ann. Transl. Med.* 9:63. doi: 10.21037/atm-20-7214

Li, W., Qin, W., Liu, H., Fan, L., Wang, J., Jiang, T., et al. (2013). Subregions of the human superior frontal gyrus and their connections. *Neuroimage* 78, 46–58. doi: 10.1016/j.neuroimage.2013.04.011

Li, X., Wang, F., Liu, X., Cao, D., Cai, L., Jiang, X., et al. (2020). Changes in brain function networks in patients with amnestic mild cognitive impairment: a resting-state fMRI Study. *Front. Neurol.* 11:554032. doi: 10.3389/fneur.2020.554032

Liu, L., Jiang, H., Wang, D., and Zhao, X.-F. (2021). A study of regional homogeneity of resting-state Functional Magnetic Resonance Imaging in mild cognitive impairment. *Behav. Brain Res.* 402:113103. doi: 10.1016/j.bbr.2020.113103

Ma, X., Zhuo, Z., Wei, L., Ma, Z., Li, Z., Li, H., et al. (2020). Altered temporal organization of brief spontaneous brain activities in patients with Alzheimer's Disease. *Neuroscience* 425, 1–11. doi: 10.1016/j.neuroscience.2019.11.025

Nickl-Jockschat, T., Kleiman, A., Schulz, J. B., Schneider, F., Laird, A. R., Fox, P. T., et al. (2012). Neuroanatomic changes and their association with cognitive decline in mild cognitive impairment: a meta-analysis. *Brain Struct. Funct.* 217, 115–125. doi: 10.1007/s00429-011-0333-x

Petersen, R. C. (2010). Mild cognitive impairment as a diagnostic entity. *J. Internal Med.* 256, 183–194. doi: 10.1111/j.1365-2796.2004.01388.x

Petersen, R. C., Caracciolo, B., Brayne, C., Gauthier, S., Jelic, V., and Fratiglioni, L. (2014). Mild cognitive impairment: a concept in evolution. *J. Internal Med.* 275, 214–228. doi: 10.1111/joim.12190

Petersen, R. C., Doody, R., Kurz, A., Mohs, R. C., Morris, J. C., Rabins, P. V., et al. (2001). Current concepts in mild cognitive impairment. *Arch. Neurol.* 58, 1985–1992. doi: 10.1001/archneur.58.12.1985

Petersen, R. C., Roberts, R. O., Knopman, D. S., Boeve, B. F., Geda, Y. E., Ivnik, R. J., et al. (2009). Mild cognitive impairment: ten years later. *Arch. Neurol.* 66, 1447–1455. doi: 10.1001/archneurol.2009.266

Petersen, R. C., Smith, G. E., Waring, S. C., Ivnik, R. J., Tangalos, E. G., and Kokmen, E. (1999). Mild cognitive impairment: clinical characterization and outcome. *Arch. Neurol.* 56, 303–308. doi: 10.1001/archneur.56.3.303

Raichle, M. E. (2015). The brain's default mode network. *Ann. Rev. Neurosci.* 38, 433–447. doi: 10.1146/annurev-neuro-071013-014030

Rajah, M. N., Languay, R., and Grady, C. L. (2011). Age-related changes in right middle frontal gyrus volume correlate with altered episodic retrieval activity. *J. Neurosci.* 31, 17941–17954. doi: 10.1523/jneurosci.1690-11.2011

Wang, J., Xie, S., Guo, X., Becker, B., Fox, P. T., Eickhoff, S. B., et al. (2017). Correspondent functional topography of the human left inferior parietal lobule at rest and under task revealed using resting-state fmri and coactivation based parcellation. *Hum. Brain Mapp.* 38, 1659–1675. doi: 10.1002/hbm.23488

Wang, L., Brier, M. R., Snyder, A. Z., Thomas, J. B., Fagan, A. M., Xiong, C., et al. (2013). Cerebrospinal fluid Aβ42, phosphorylated Tau181, and resting-state functional connectivity. *JAMA Neurol.* 70, 1242–1248. doi: 10.1001/jamaneurol.2013.3253

Wang, P., Zhou, B., Yao, H., Xie, S., Feng, F., Zhang, Z., et al. (2020). Aberrant hippocampal functional connectivity is associated with fornix white matter integrity in alzheimer's disease and mild cognitive impairment. *J. Alzheimers Dis.* 75, 1153–1168. doi: 10.3233/jad-200066

Wang, P., Zhou, B., Yao, H., Zhan, Y., Zhang, Z., Cui, Y., et al. (2015). Aberrant intra- and inter-network connectivity architectures in Alzheimer's disease and mild cognitive impairment. *Sci. Rep.* 5:14824. doi: 10.1038/srep14824

Wang, S., Rao, J., Yue, Y., Xue, C., Hu, G., Qi, W., et al. (2021). Altered frequency-dependent brain activation and white matter integrity associated with cognition in characterizing preclinical Alzheimer's disease stages. *Front. Hum. Neurosci.* 15:625232. doi: 10.3389/fnhum.2021.625232

Wee, C.-Y., Yap, P.-T., Zhang, D., Denny, K., Browndyke, J. N., Potter, G. G., et al. (2012). Identification of MCI individuals using structural and functional connectivity networks. *Neuroimage* 59, 2045–2056. doi: 10.1016/j.neuroimage.2011.10.015

Winblad, B., Palmer, K., Kivipelto, M., Jelic, V., Fratiglioni, L., Wahlund, L.-O., et al. (2004). Mild cognitive impairment–beyond controversies, towards a consensus: report of the International Working Group on Mild Cognitive Impairment. *J. Internal Med.* 256, 240–246. doi: 10.1111/j.1365-2796.2004.01380.x

Xie, C., Bai, F., Yuan, B., Yu, H., Shi, Y., Yuan, Y., et al. (2015). Joint effects of gray matter atrophy and altered functional connectivity on cognitive deficits in amnestic mild cognitive impairment patients. *Psychol. Med.* 45, 1799–1810. doi: 10.1017/s0033291714002876

Xie, X., Bratec, S. M., Schmid, G., Meng, C., Doll, A., Wohlschläger, A., et al. (2016). How do you make me feel better? Social cognitive emotion regulation and the default mode network. *Neuroimage* 134, 270–280. doi: 10.1016/j.neuroimage.2016.04.015

Xue, C., Qi, W., Yuan, Q., Hu, G., Ge, H., Rao, J., et al. (2021a). Disrupted dynamic functional connectivity in distinguishing subjective cognitive decline and amnestic mild cognitive impairment based on the triple-network model. *Front. Aging Neurosci.* 13:711009. doi: 10.3389/fnagi.2021.711009

Xue, C., Sun, H., Yue, Y., Wang, S., Qi, W., Hu, G., et al. (2021b). Structural and functional disruption of salience network in distinguishing subjective cognitive decline and amnestic mild cognitive impairment. *ACS Chem. Neurosci.* 12, 1384–1394. doi: 10.1021/acschemneuro.1c00051

Yan, T., Wang, Y., Weng, Z., Du, W., Liu, T., Chen, D., et al. (2019). Early-stage identification and pathological development of Alzheimer's disease using multimodal MRI. *J. Alzheimers Dis.* 68, 1013–1027. doi: 10.3233/jad-181049

Yang, H., Long, X.-Y., Yang, Y., Yan, H., Zhu, C.-Z., Zhou, X.-P., et al. (2007). Amplitude of low frequency fluctuation within visual areas revealed by resting-state functional MRI. *Neuroimage* 36, 144–152. doi: 10.1016/j.neuroimage.2007.01.054

Yang, L., Zhao, X., Wang, L., Yu, L., Song, M., and Wang, X. (2015). Emotional face recognition deficit in amnestic patients with mild cognitive impairment: behavioral and electrophysiological evidence. *Neuropsychiatr. Dis. Treat.* 11, 1973–1987. doi: 10.2147/NDT.85169

Yi, H. G., Leonard, M. K., and Chang, E. F. (2019). The encoding of speech sounds in the superior temporal gyrus. *Neuron* 102, 1096–1110. doi: 10.1016/j.neuron.2019.04.023

Zang, Y., Jiang, T., Lu, Y., He, Y., and Tian, L. (2004). Regional homogeneity approach to fMRI data analysis. *Neuroimage* 22, 394–400. doi: 10.1016/j.neuroimage.2003.12.030

Zhang, J., Liu, Y., Lan, K., Huang, X., He, Y., Yang, F., et al. (2021). Gray matter atrophy in amnestic mild cognitive impairment: a voxel-based meta-analysis. *Front. Aging Neurosci.* 13:627919. doi: 10.3389/fnagi.2021.627919

Zhang, Y.-D., Dong, Z., Wang, S.-H., Yu, X., Yao, X., Zhou, Q., et al. (2020). Advances in multimodal data fusion in neuroimaging: overview, challenges, and novel orientation. *Int. J. Inform. Fusion* 64, 149–187. doi: 10.1016/j.inffus.2020.07.006

Zhang, Z., Cui, L., Huang, Y., Chen, Y., Li, Y., and Guo, Q. (2021). Changes of regional neural activity homogeneity in preclinical Alzheimer's Disease: compensation and dysfunction. *Front. Neurosci.* 15:646414. doi: 10.3389/fnins.2021.646414

Zhao, Z.-L., Fan, F.-M., Lu, J., Li, H.-J., Jia, L.-F., Han, Y., et al. (2015). Changes of gray matter volume and amplitude of low-frequency oscillations in amnestic MCI: an integrative multi-modal MRI study. *Acta Radiol.* 56, 614–621. doi: 10.1177/0284185114533329

Conflict of Interest: The authors declare that the research was conducted in the absence of any commercial or financial relationships that could be construed as a potential conflict of interest.

Publisher's Note: All claims expressed in this article are solely those of the authors and do not necessarily represent those of their affiliated organizations, or those of the publisher, the editors and the reviewers. Any product that may be evaluated in this article, or claim that may be made by its manufacturer, is not guaranteed or endorsed by the publisher.

frontiers | Frontiers in Aging Neuroscience

ORIGINAL RESEARCH
published: 06 June 2022
doi: 10.3389/fnagi.2022.788567

Spatial Distribution and Hierarchical Clustering of β-Amyloid and Glucose Metabolism in Alzheimer's Disease

Da-An Zhou[1†], Kai Xu[2†], Xiaobin Zhao[3], Qian Chen[3], Feng Sang[4], Di Fan[3], Li Su[5], Zhanjun Zhang[4], Lin Ai[3] and Yaojing Chen[4]**

[1] Department of Rehabilitation, The Third Affiliated Hospital of Jinzhou Medical University, Jinzhou, China, [2] School of Artificial Intelligence, Beijing Normal University, Beijing, China, [3] Department of Nuclear Medicine, Beijing Tiantan Hospital, Capital Medical University, Beijing, China, [4] State Key Laboratory of Cognitive Neuroscience and Learning, Beijing Normal University, Beijing, China, [5] Department of Psychiatry, University of Cambridge, Cambridge, United Kingdom

Increased amyloid burden and decreased glucose metabolism are important characteristics of Alzheimer's disease (AD), but their spatial distribution and hierarchical clustering organization are still poorly understood. In this study, we explored the distribution and clustering organization of amyloid and glucose metabolism based on ^{18}F-florbetapir and ^{18}F-fluorodeoxyglucose PET data from 68 AD patients and 20 cognitively normal individuals. We found that: (i) cortical regions with highest florbetapir binding were the regions with high glucose metabolism; (ii) the percentage changes of amyloid deposition were greatest in the frontal and temporal areas, and the hypometabolism was greatest in the parietal and temporal areas; (iii) brain areas can be divided into three hierarchical clusters by amyloid and into five clusters by metabolism using a hierarchical clustering approach, indicating that adjacent regions are more likely to be grouped into one sub-network; and (iv) there was a significant positive correlation in any pair of amyloid-amyloid and metabolism-metabolism sub-networks, and a significant negative correlation in amyloid-metabolism sub-networks. This may suggest that the influence forms and brain regions of AD on different pathological markers may not be synchronous, but they are closely related.

Keywords: Alzheimer's Disease, glucose metabolism, hierarchical organization, spatial distribution, β-amyloid

OPEN ACCESS

Edited by:
Ping Wu,
Fudan University, China

Reviewed by:
Mitsuru Shinohara,
National Center for Geriatrics and Gerontology (NCGG), Japan
Roger Gutiérrez-Juárez,
National Autonomous University of Mexico, Mexico
Isabel Arrieta-Cruz,
National Institute of Geriatrics, Mexico

***Correspondence:**
Lin Ai
ailin@bjtth.org
Yaojing Chen
luckychen1989@gmail.com

[†]These authors have contributed equally to this work

Specialty section:
This article was submitted to Alzheimer's Disease and Related Dementias, a section of the journal Frontiers in Aging Neuroscience

Received: *02 October 2021*
Accepted: *09 May 2022*
Published: *06 June 2022*

Citation:
Zhou D-A, Xu K, Zhao X, Chen Q, Sang F, Fan D, Su L, Zhang Z, Ai L and Chen Y (2022) Spatial Distribution and Hierarchical Clustering of β-Amyloid and Glucose Metabolism in Alzheimer's Disease. Front. Aging Neurosci. 14:788567. doi: 10.3389/fnagi.2022.788567

INTRODUCTION

Alzheimer's disease (AD) is a progressive neurodegenerative disease that usually has a slow progression and long course. The typical pathological feature of AD is extracellular β-amyloid protein (Aβ) deposition, which starts a decade or more before the onset of illness and appears to be a trigger of the pathological cascade of events leading to AD dementia. Observations suggest that Aβ deposition has reached a peak 10–12 years before the onset of AD symptoms, it is hypothesized that Aβ initiates tangle formation and neuronal cell death (Hardy and Allsop, 1991;

Klunk et al., 2006). Recently, biomarkers have been emphasized in the diagnosis of AD. The National Institute on Aging and Alzheimer's Association (NIA-AA) Research Framework state that Aβ changes, pathologic tau, and neurodegeneration (ATN) comprise the diagnostic standard of AD and highlight the importance of neuroimaging and fluid biomarkers for the accurate diagnosis of AD (Jack et al., 2018).

β-amyloid deposition accumulates early as disease progresses, and varies among brain regions, including deposition in some key regions which mediate cognition (Grimmer et al., 2009). The brain regions susceptible to Aβ accumulation comprise large areas of the medial and lateral association cortex in amyloid-positive individuals without dementia (Palmqvist et al., 2017). The posterior cingulate and the frontal and parietal cortices are most commonly regions affected early in AD and in mild cognitive impairment (MCI) due to AD (Kemppainen et al., 2006, 2007), which is consistent with other studies including post-mortem evaluations (Klunk et al., 2004; Driscoll et al., 2012). The presence of Aβ deposition in different brain regions at different stages may be associated with inconsistencies in the effects of Aβ on spatial areas of the brain, which may reflect regional differences in susceptibility to AD pathology. More recently, Aβ deposition in the cerebral cortex has been shown to have a hierarchical organization in elderly cognitively normal individuals, with four Aβ clusters based on spatial features (Sepulcre et al., 2017). It is uncertain if this hierarchical clustering organization of cognitively normal elderly is present in symptomatic AD patients and whether it reflects the spatial distribution of AD pathological changes.

β-amyloid is a critical hallmark in AD diagnosis whereas ^{18}F-fluorodeoxyglucose (^{18}F-FDG) positron emission tomography (PET) is a strong predictor of progression from MCI to AD dementia (Landau et al., 2010). In AD dementia patients Aβ deposition is widespread but is present in many individual who have not cognitive symptoms and it has a weak association with cognitive decline (Klunk et al., 2004). Reduced glucose metabolism is used as an indicator of synaptic dysfunction and neurodegeneration caused by Aβ. Patients with AD typically show temporal and parietal hypometabolism on FDG PET imaging in patients with AD (Ossenkoppele et al., 2012), where gray matter atrophy is common. Some studies have attempted to correlate metabolic function with the presence of Aβ deposition. However, the spatial distribution of hypometabolism and Aβ deposition is different in both AD patients and normal older adults (La Joie et al., 2012). A few multimodal imaging studies using FDG-PET and amyloid PET approached the question of whether local amyloid plaque deposition is correlated with local levels of glucose metabolism. These studies showed that the correlation was discordant, and changed with disease stages (Li et al., 2008; Cohen et al., 2009; Altmann et al., 2015). The spatial distribution relationship between the Aβ deposition and metabolism in AD, if any, remains uncertain. Studies have shown that Aβ tends to be deposited in core brain regions with higher structural and functional connections (Daianu et al., 2015) which may also be areas with high glucose metabolism.

The purpose of the present study was to examine the spatial distribution and extent of Aβ deposits and glucose metabolism and verify whether regions with high Aβ deposition are regions with high glucose metabolism by using florbetapir (^{18}F-AV-45) and FDG PET. Additionally, we attempted to characterize a hierarchical structure of amyloid burden and metabolism organization that contains meaningful information about regional covariance patterns in AD patients. We further explored the relationship between regional Aβ deposition and glucose metabolism in AD patients.

MATERIALS AND METHODS

Participants

Participants were selected from the Beijing Aging Brain Rejuvenation Initiative (BABRI) study, an ongoing longitudinal study examining the brain and cognitive decline in an elderly, community-dwelling sample (Li et al., 2013). All enrolled participants were Han Chinese, right-handed. Sixty-eight patients with AD dementia and 20 cognitive normal controls were included in the current study. All participants received a standard dementia screening that included medical history, physical and neurological examinations, brain CT or MRI and neuropsychological testing. All the AD patients were firstly diagnosed with AD when they were screened for cognitive problems from the BABRI cohort and were later referred to Beijing Tiantan Hospital, Capital Medical University. All enrolled participants (1) had no history of coronary disease, nephritis, tumors, neurological or psychiatric disorders, or addiction; (2) had no conditions known to affect cerebral function, including alcoholism, current depression, Parkinson's disease, or epilepsy; and (3) had no large vessel diseases such as cortical or subcortical infarcts or watershed infarcts. Dementia was diagnosed based on criteria modified from DSM-5 and further evaluated by brain CT or MRI. The diagnosis of AD was made according to the criteria of the National Institute of Neurological and Communicative Disorders and Stroke and the Alzheimer's Disease and Related Disorders Association (McKhann et al., 1984). Nine patients were CDR stage 0.5, 26 stage 1, 30 stage 2, and 3 stage 3. All patients were amyloid positive determined by visual read of florbetapir PET imaging by two experienced readers (XZ and LA). Control participants were amyloid negative determined by visual read of florbetapir PET scanning and denied any significant neuropsychiatric disease or memory trouble, were not taking any psychoactive medicines, and had a Mini Mental State Examination (MMSE) score of 26 or more and CDR = 0. The Ethics Committee and Institutional Review Board of Beijing Normal University approved this study (ICBIR_A_0041_002.02). For those AD patients who were unable to give informed consent, written, informed consent was obtained from their legal guardian.

Positron Emission Tomography Image Acquisition and Data Analysis

All participants underwent a florbetapir PET scan and a ^{18}F-FDG PET scan on a Discovery TM PET/CT Elite scanner (General Electric) at the Beijing Tiantan Hospital, Capital Medical University (Beijing, China). The florbetapir PET session

that consisted of intravenous injection of 10 mCi of tracer followed by an uptake phase of 50 min. At 50 min patients were positioned in the scanner. FDG-PET scans were required to fast for 6 h before the injection of 185 ± 8 MBq of ^{18}F-FDG. After approximately 60 min, an emission acquisition was performed. Native-slice thickness was 3.27 mm, with field of view 700/153. Florbetapir and FDG PET scans were acquired on different days, but within 1 week of each other. Florbetapir PET images were visually read by two experienced nuclear medicine physicians who were blind to the clinical data, and only Aβ-positive patients and Aβ-negative controls were included.

Positron emission tomography data were preprocessed using Statistical Parametric Mapping software version 12 (SPM12), and spatial normalization to Montreal Neurological Institute (MNI) templates was performed for all patients. We later analyzed the images using automatically detected regions of interest (ROI) from the LPBA40 template, an established set of 56 cortical and subcortical brain regions (LONI Probabilistic Brain Atlas, LPBA40) (Shattuck et al., 2008). Here, we analyzed all cortical regions (25 for each hemisphere) and calculated standard uptake value ratios (SUVRs) in each of the regions for both PET tracers, comparing them to the cerebellar gray reference.

Statistical Analysis

Independent two-sample *t*-tests were used to assess between-group differences in age and MMSE score. The chi-square test was used to compare gender ratio difference.

(1) Percentage change calculation of Aβ deposition and glucose metabolism. AD have Aβ deposition and glucose hypometabolism in various brain regions, we used the relative change ratio of AD to normal controls to measure the degree of influence of AD on each brain region.

$$Percentage\ change\ (i) = \frac{M_{\mathrm{i}}(\mathrm{AD}) - M_{\mathrm{i}}(HC)}{M_{\mathrm{i}}(\mathrm{HC})} \times 100$$

Here, M_{i}(AD) is considered to be the mean SUVR of brain i for AD group, and $M_{\mathrm{i}}(HC)$ means SUVR of brain i for controls.

(2) Hierarchical clustering analysis of brain amyloid load and metabolism. To determine whether the 50 cortical amyloid load or glucose metabolism can be classified into different categories, we performed the following hierarchical clustering analysis. The data vectors (florbetapir and FDG SUVR) for all regions used as input for cluster analysis. First, we treated each brain area as a cluster and calculated the Euclidean distance between every cluster pair, that is, the similarity between the brain areas. Next, we identified the two closest classes between the classes, grouped them together, and then recalculated the similarity between the generated class and the old classes. Finally, we repeated the above steps until all the clusters were grouped into one cluster together and the algorithm ended. When calculating the distance between clusters, the distance between the two sets of areas furthest from each other was taken as the distance between the two sets. In this way, we can divide all the brain areas into certain clusters by setting a certain distance after the algorithm is finished. The calculation process used the clustering function in MATLAB.

(3) Amyloid deposition and glucose metabolism correlations. For each Aβ or FDG hierarchical cluster, mean SUVR values were obtained by averaging the signals across all regions within each hierarchical clustering category. Pearson correlation coefficients between each pair of all Aβ and FDG categories were further computed to produce a symmetric correlation matrix for all patients, controlling for age, gender, and disease duration.

RESULTS

Characteristics of the study participants are given in **Table 1**. At the time of scan, patients with AD were on average 64.94 ± 8.14 years old. Forty-one percent of the patients were male and 88% had a Clinical Dementia Rating (CDR) score greater than one. There were no significant differences in chronic diseases like hypertension, type 2 diabetes mellitus and hyperlipidemia between these two groups.

Amyloid Load and Glucose Metabolism Distribution in Alzheimer's Disease

Figure 1 shows average patterns of cortical florbetapir and FDG SUVR images of AD patients and cognitively normal elderly people. The highest amyloid load of regional florbetapir SUVR in AD patients was in cingulate gyrus, precuneus, lingual gyrus, followed by parietal and frontal areas, then by occipital and temporal regions. Many areas with high amyloid deposition are also areas with high glucose metabolism in AD patients, such as the cingulate gyrus, precuneus, lingual gyrus (**Figure 2**). To verify that areas with high amyloid load and metabolism in AD patients are indeed high and not unique to AD patients, we collected florbetapir and FDG-PET data from 20 cognitively normal elderly people. The results showed that both AD patients and normal elderly people had similar high and low metabolic consumption regions, such as the cingulate gyrus, precuneus, lingual gyrus, and cuneus with high glucose metabolism, while the hippocampal, parahippocampal gyrus, and inferior temporal gyrus had low glucose metabolism (**Figure 1**). Areas with high amyloid deposition are confirmed to be regions of the brain with high metabolic activity.

β-amyloid deposition and glucose hypometabolism gradually spread to various areas of the brain in AD, and we calculated

TABLE 1 | Sample characteristics.

Characteristics	Alzheimer's disease (*n* = 68)	Healthy controls (*n* = 20)	*p*-value
Age (50–85 years)	64.94 ± 8.14	62.73 ± 9.62	0.301
Sex, M/F	28/40	9/11	0.801
CDR, 0/0.5/1/2/3	0/9/26/30/3	20/0/0/0/0	–
MMSE	12.31 ± 6.73	27.95 ± 1.36	<0.0001
AD duration (years)	2.69 ± 1.67	–	–
Hypertension, yes/no	15/53	4/16	0.844
Type 2 diabetes mellitus, yes/no	13/55	3/17	0.675
Hyperlipidemia, yes/no	18/50	7/13	0.457

M, male; F, female; CDR, Clinical Dementia Rating; AD, Alzheimer's disease; MMSE, Mini-Mental State Examination.

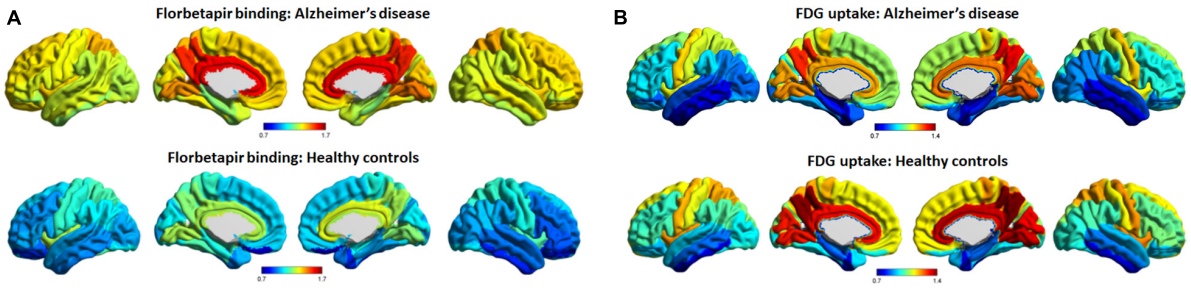

FIGURE 1 | Average patterns of cortical florbetapir binding and FDG uptake (cerebellar reference). The spatial average patterns of cortical regional florbetapir binding **(A)** and FDG uptake **(B)** in AD patients and healthy controls. Color bars represent standard uptake value ratios. AD, Alzheimer's disease; FDG, fluorodeoxyglucose.

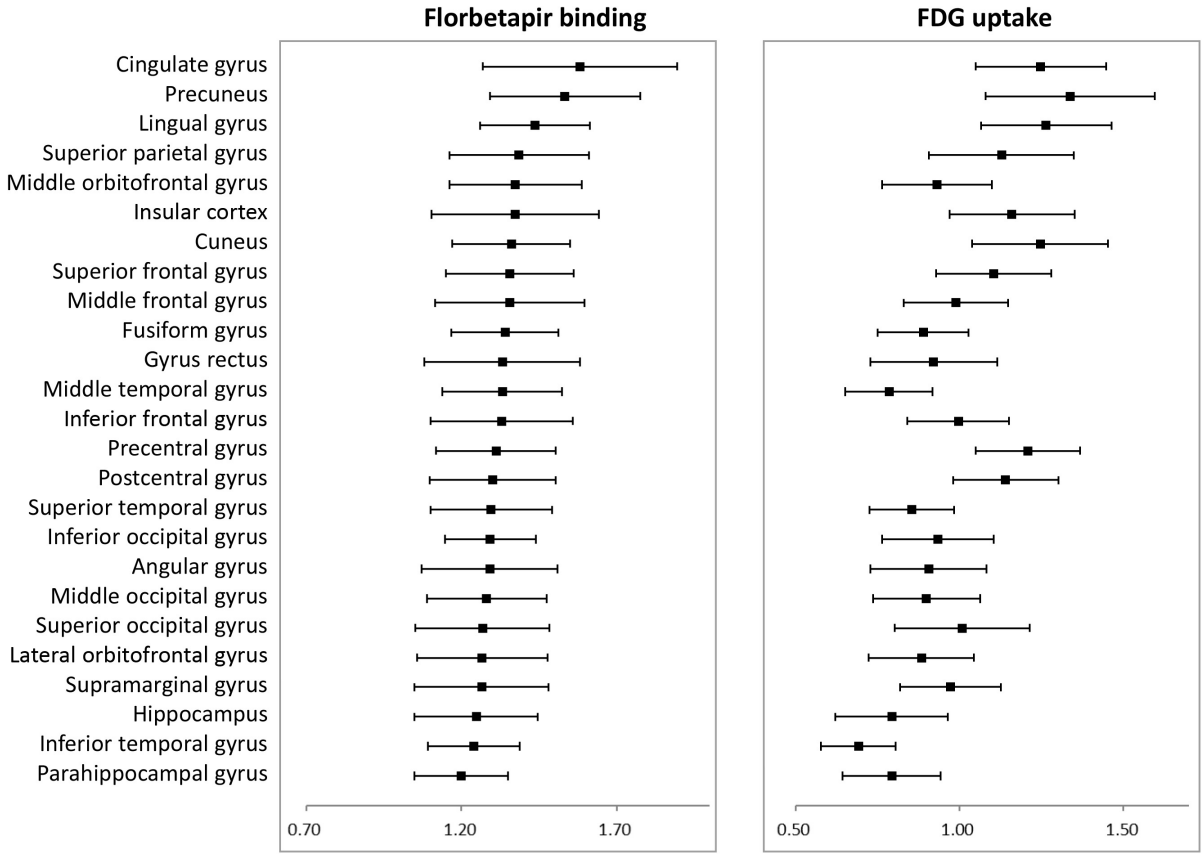

FIGURE 2 | Average florbetapir binding and FDG uptake in 25 cortical areas in AD patients where error bars represent standard deviations. AD, Alzheimer's disease; FDG, fluorodeoxyglucose.

the percentage change to determine which areas were affected more severely in AD. Amyloid deposition in all cortical regions was significant higher in patients than in controls and percentage changes were highest in frontal and temporal lobes, with many areas exceeding 30%. Although the hippocampus and parahippocampal gyrus are early accumulated, the frontal and other temporal regions have a greater Aβ accumulation for the entire AD process. Metabolism was significant lower in patients in most areas, especially the parietal and temporal areas. For example, angular gyrus and precuneus are the areas with highest rate of change in patients, i.e., the areas with the most severe metabolic decline (**Figure 3**).

Hierarchical Clustering of Cortical β-Amyloid Deposition and Glucose Metabolism in Alzheimer's Disease

Hierarchical clustering was used to construct the clusters of the brain amyloid load based on the regional Aβ and FDG data in AD patients. As shown in **Figure 4**, we set the distance to 2.2

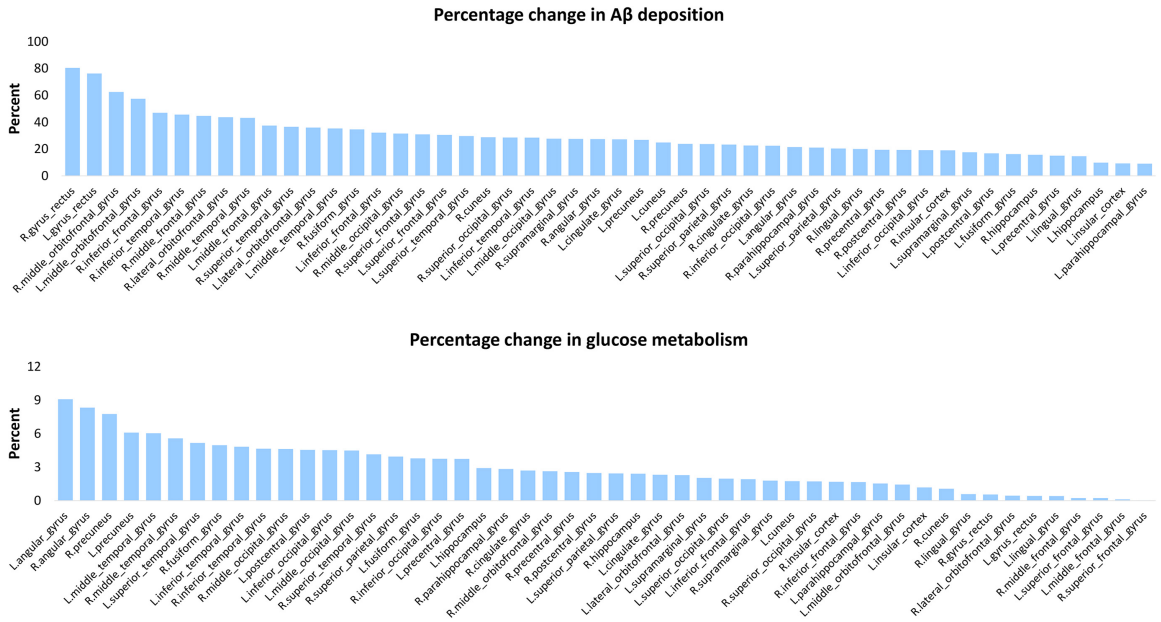

FIGURE 3 | Percentage change of Aβ deposition and glucose metabolism for each cortical area. This chart displays the percentage increase of Aβ deposition (top panel) percentage decrease and of glucose metabolism (bottom panel) of AD vs. controls in 50 cortical areas.

and divided the all areas into three clusters for Aβ deposition and five clusters for metabolism. Among the three categories of Aβ deposition, category 1 mainly included the medial temporal lobe regions such as hippocampus and parahippocampal, category 2 mainly included the cingulate gyrus and precuneus, and category 3 included a wide range of cortical regions (**Supplementary Table 1**). The average deposition of amyloid in the three categories was calculated, and it was found that the deposition of category 1 was the lowest and that of category 2 was the highest (**Figure 4A**). Unlike the Aβ categories, the five categories of FDG showed more regionalization, where adjacent brain regions were clustered into one category. Among the five categories of FDG, category 1 mainly included the temporal lobe region, category 2 mainly included the lateral frontal, parietal lobe and occipital regions, category 3 mainly included the superior parietal gyrus and superior occipital gyrus, category 4 mainly included the cingulate gyrus, superior frontal gyrus, precentral and postcentral gyrus, and category 5 mainly included the precuneus, cuneus and lingual gyrus (**Supplementary Table 1**). The average glucose metabolism increased from category 1 to category 5 (**Figure 4B**).

Amyloid Deposition and Glucose Metabolism Correlations

Correlation analysis (adjusted for gender, age, and disease duration) were used to assess the relationship between Aβ deposition and glucose metabolism in each hierarchical clustering category pair in patients with AD. Metabolism was significantly positively correlated between any two of the five FDG categories; florbetapir burden was significantly positively correlated between any two of the three Aβ categories. The correlation analysis between Aβ and FDG categories showed that the florbetapir burden of each Aβ category was negatively correlated with the metabolism of multiple FDG categories, that is, the metabolism of multiple FDG categories decreased with the increase of Aβ (**Figure 5**). It should be noted here that the previously mentioned "amyloid load and glucose metabolism distribution in AD" results indicated that areas with high Aβ deposition tend to be areas with high metabolism, compared with areas with low Aβ deposition. In this part, amyloid-metabolism correlation measures the relationship between the change rules of the two, that is, the degree of dependency and affinity.

DISCUSSION

This study examined the spatial distribution and hierarchical structure of amyloid burden and metabolism organization in AD patients. Several clear findings about the relationship between Aβ and energy metabolism are presented here. First of all, from the spatial distribution view, cortical regions with highest florbetapir binding like cingulate gyrus, precuneus, lingual gyrus, frontal and parietal areas, were also the regions with high glucose metabolism. This is consistent with several previous studies which described the topographic patterns of AD, MCI and HC groups (Klunk et al., 2004; Kemppainen et al., 2007; Rowe et al., 2007). Previous studies have shown that the cingulate gyrus and precuneus are the hub regions for structural and functional brain networks, which are central in brain communication and neural integration (van den Heuvel and Sporns, 2013). Frequent and massive information operations require high energy consumption. The posterior cingulate, precuneus and retrosplenial cortices together show the highest level of glucose use of any area of the cerebral cortex in humans

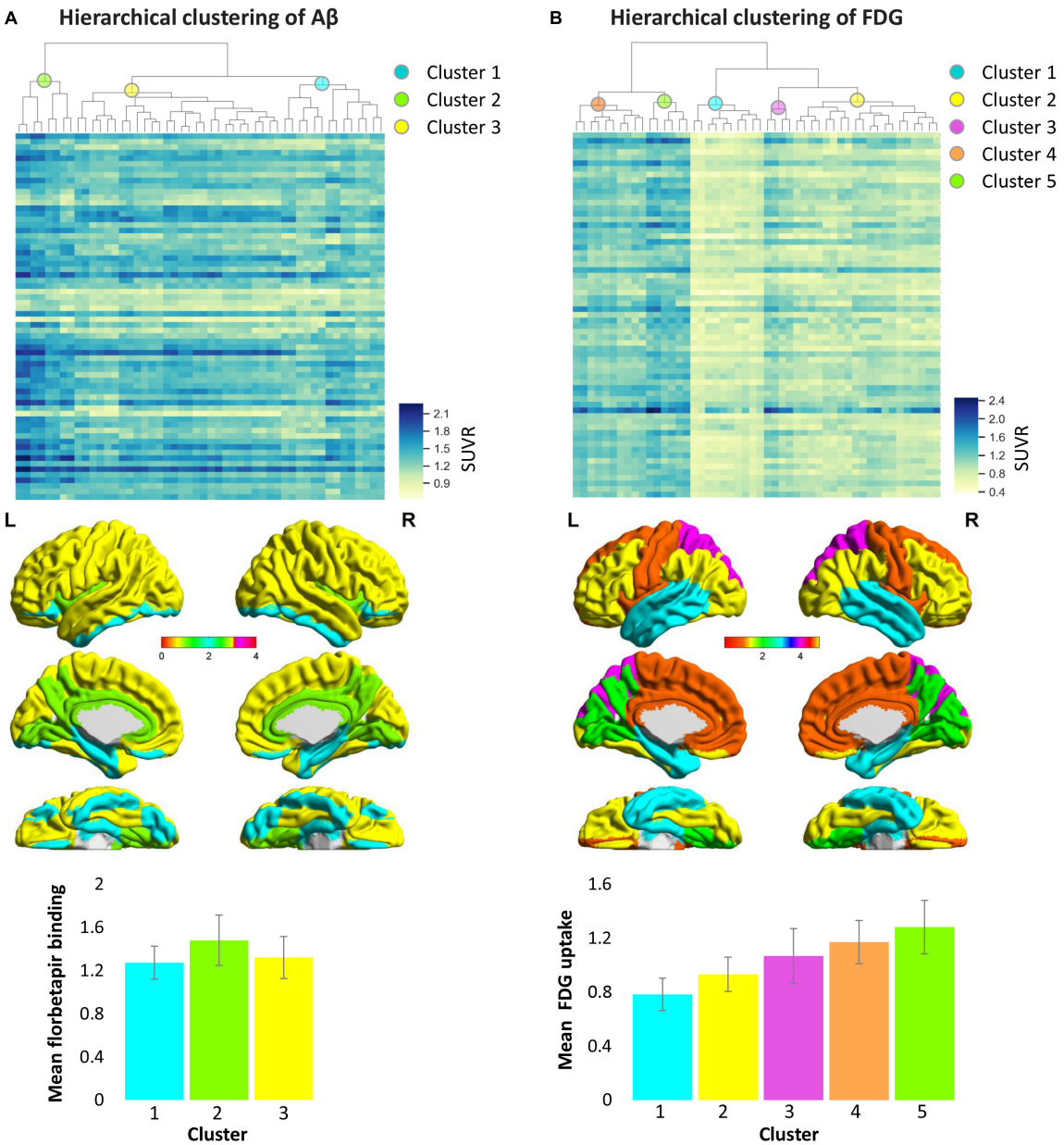

FIGURE 4 | Hierarchical clustering of cortical Aβ deposition **(A)** and glucose metabolism **(B)** patterns in AD patients. Columns of heat maps correspond to the Aβ and FDG values of each cortical area, and rows correspond to samples. Color bars marked on the right indicates SUVR value, blue, highest; yellow, lowest. The dendrograms on the top show the classification results, which indicate the three categories from Aβ data and five categories from FDG data represented by the different colored spheres. The bar chart below shows the average SUVR values of each category in patients with Alzheimer's disease. The colors in the bar chart correspond to categories in the brain maps. AD, Alzheimer's disease; FDG, fluorodeoxyglucose; SUVR, standardized uptake value ratio.

(Gusnard and Raichle, 2001). These hub regions carry a large burden in everyday cognitive activities, making themselves prime targets for toxic metabolites accumulation like Aβ.

In terms of the magnitude of the change in Aβ deposition and glucose hypometabolism, some very interesting phenomena were found. Briefly speaking, the brain regions that changed the most in florbetapir binding and FDG uptake were not those regions with the highest absolute levels in those indicators. The percentage changes of amyloid deposition were greatest in the gyrus rectus and middle orbitofrontal gyrus, and the hypometabolism was greatest in the angular gyrus. The indicators of cingulate gyrus and precuneus ranked top by absolute magnitude, but they did not change the most from HC to AD. This is not surprising because these brain regions have already existed high deposition in the early stage of the disease (shown in **Figure 1**), and as the deposition of Aβ has a platform, it will not continue to quickly accumulate after a certain amount of accumulation. As a result, the final variability of these regions

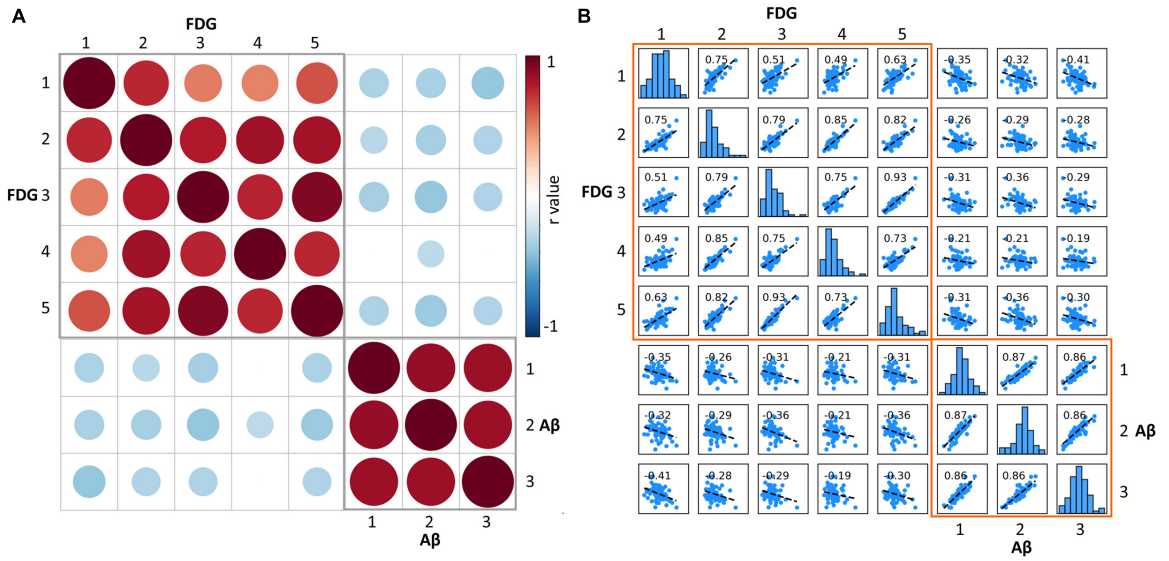

FIGURE 5 | (A) Matrix of Pearson correlation coefficients between amyloid deposition and glucose metabolism for each category. The red circle represents significant positive correlation, the blue circle represents significant negative correlation, and the empty grid represents insignificant correlation. The size of the circle represents the size of the correlation coefficient. **(B)** Scatterplot matrix shows the correlation of each Aβ-FDG category pair. The diagonal-bar graph represents the SUVR value distribution of each category. FDG, fluorodeoxyglucose; SUVR, standardized uptake value ratio.

between AD and HC might probably not be as big as we thought. In contrast, the major indicators for determining the progression from mild to severe disease phase will be frontal and other temporal regions.

From the perspective of regional clustering, although the number of clustering of the two indicators was different, with three categories in florbetapir binding and five categories in FDG uptake, they were not that distinct. For example, Aβ cluster 1 and FDG cluster 1 are basically overlapped, mainly including the temporal lobe region such as hippocampus and parahippocampal, Pearson correlation coefficients between amyloid deposition and glucose metabolism of these two clusters was significant ($r = -0.35$). Another example, FDG cluster 5 is totally part of Aβ cluster 2 in anatomical location ($r = -0.36$). The similarity of location distribution and subsequent correlation analysis of different data clustering implies the internal relationship between these two indicators. Further, we also found Aβ deposit exerts a negative influence on energy metabolism not only in local areas, but also contralaterally distant brain areas. The underlying reason may include the following aspects. Aβ deposition appears to follow distinct pathways, spreading progressively through interconnected brain regions, rather than emerging from stochastic aggregation of Aβ in different brain areas over time (Heilbronner et al., 2013; Eisele and Duyckaerts, 2016; Condello and Stöhr, 2017). The distant brain areas with hypometabolism may be affected by propagated Aβ, the majority of which may be monomers or oligomers of Aβ. Oligmeric Aβ is reported to exert more toxic effects on neurons than fibrillar Aβ (Sun et al., 2015).

Decades before the onset of AD dementia, abnormal accumulation of insoluble amyloid proteins are detectable in the temporal lobe and association cortex (Villain et al., 2012; Grothe et al., 2017). It has been shown in vivo that Aβ deposits follow some degree of spatial specificity. In our study, we tried to describe the hierarchical spatial organization of Aβ pathology. With our hierarchical clustering analysis of amyloid PET data, we identified that the pattern of distribution of Aβ deposition in AD patients resembled the proposed Braak stages (Braak and Braak, 1991). The brain regions in the first cluster was closely linked with the amyloid pathology at the early stage, with areas of major changes being the fusiform, hippocampus, parahippocampal, rectus, lateral orbitofrontal, inferior temporal, and inferior occipital areas. The second cluster had almost closed spatial distribution with the amyloid pathology at the mid-stage, including cingulate gyrus, insular, lingual gyrus, and precuneus. The third cluster contained the majority of cortical areas, which correspond with amyloid pathology at late stage. The clustering results may suggest that some brain areas share similar pathological mechanisms, so that these areas are threatened by disease at the same stage.

This study helps us to comprehensively examine the pathological mechanism of AD from A multi-dimensional perspective, and researches about the pathological mechanism of Aβ from the perspective of energy metabolism are still not sufficient. Only a few multimodal imaging studies using FDG-PET and amyloid-PET approached the question of whether local amyloid plaque deposition is correlated with local levels of glucose metabolism. These studies showed that the correlation could be complex and changed with disease stages (Landau et al., 2012; Altmann et al., 2015). Some suggested that the amyloid deposition in MCI patients is associated with higher metabolism as a compensatory response (Cohen et al., 2009;

Oh et al., 2014). However, negative correlations were observed between amyloid deposition and metabolism in AD patients (Landau et al., 2012; Grothe and Teipel, 2016), which is consistent with our observations. A mechanistic view linking accumulation of Aβ to the hypometabolism, however, has been lacking so far. The possible explanation underlying the association between Aβ and glucose metabolism may include insulin resistance (Neth and Craft, 2017; Kellar and Craft, 2020), mitochondrial dysfunction (involving TCA cycle and oxidative phosphorylation system), reactive oxygen species, apoptosis, inflammatory factors, excitotoxicity, glycation end products, hyper-activation of some protein kinases and so on (Devi et al., 2006; Chen and Zhong, 2013). Accumulating evidence suggests that mitochondrial dysfunction may play a fundamental role among these above pathways. Several *in vitro* studies posit that neurodegenerative disorders are associated with changes in mitochondrial dynamics and can be induced by Aβ that progressively accumulates within this organelle, acting as a direct toxin (Ferreira et al., 2010). Accumulation of the Aβ precursor protein, at mitochondrial membrane can cause mitochondrial dysfunction by blocking the translocation of other intra-mitochondrial molecules/proteins and disrupting the electron-transport chain (Sun et al., 2015). The Aβ localized in mitochondria can bind to two pro-apoptotic factors including Aβ-binding alcohol dehydrogenase and cyclophilin D, consequently increasing neurodegenerative cell death (Lustbader et al., 2004; Moura et al., 2010). Aβ induces activation of glutamate N-methyl-D-aspartate receptors and/or excessive release of calcium from endoplasmic reticulum that may underlie mitochondrial calcium dyshomeostasis thereby disturbing organelle functioning like energy conversion, and ultimately, damaging neurons (Ferreira et al., 2010).

There are limitations of our study. First, it is very important in the future to validate continuity and change in the AD progression by longitudinal studies in cohorts including MCI. Interrogation of a longitudinal dataset is also warranted to verify the hierarchical clustering results from our cross-sectional analyses. AD in this sample has likely been present longer than recorded, given the difficulty of identifying and documenting early cognitive changes. It remains unclear if apolipoprotein E gene is implicated in the AD-related effects of Aβ load patterns and this should be addressed in future studies.

In summary, we demonstrated that cortical regions with more Aβ accumulation were the regions with high glucose metabolism. The hierarchical clustering provides evidence that Aβ accumulation and glucose metabolism are region-specific and regions in the same cluster may be specifically affected in AD. Amyloid in each hierarchical category is significantly negatively correlated with metabolism in multiple categories supporting the hypothesis that Aβ deposition is an early event of the pathological process and relates to neurodegenerative changes of multiple brain regions.

DATA AVAILABILITY STATEMENT

The raw data supporting the conclusions of this article will be made available by the authors, without undue reservation.

ETHICS STATEMENT

The studies involving human participants were reviewed and approved by the Ethics Committee and Institutional Review Board of Beijing Normal University. The patients/participants provided their written informed consent to participate in this study.

AUTHOR CONTRIBUTIONS

YC had full access to all of the data in the study and took responsibility for the integrity of the data and accuracy of the data analysis. YC and LA conceived the original idea for the study, supervised the conception, and revised and drafted the manuscript. YC, D-AZ, KX, XZ, QC, FS, DF, ZZ, and LA recruited the study population and conducted the neuropsychological tests. YC, FS, and LS analyzed the data. All authors read and approved the final manuscript.

FUNDING

This work was supported by Funds for International Cooperation and Exchange of the National Natural Science Foundation of China (grant number 81820108034), National Natural Science Foundation of China (grant numbers 31700997, 82071205, 8213000253, and 81771143), State Key Program of National Natural Science of China (grant number 81430100), and Beijing Natural Science Foundation (grant number 7192054).

SUPPLEMENTARY MATERIAL

The Supplementary Material for this article can be found online at: https://www.frontiersin.org/articles/10.3389/fnagi.2022.788567/full#supplementary-material

REFERENCES

Altmann, A., Ng, B., Landau, S. M., Jagust, W. J., and Greicius, M. D. (2015). Regional brain hypometabolism is unrelated to regional amyloid plaque burden. *Brain* 138, 3734–3746. doi: 10.1093/brain/awv278

Braak, H., and Braak, E. (1991). Neuropathological stageing of alzheimer-related changes. *Acta Neuropathol.* 82, 239–259. doi: 10.1007/BF00308809

Chen, Z., and Zhong, C. (2013). Decoding Alzheimer's disease from perturbed cerebral glucose metabolism: implications for diagnostic and therapeutic strategies. *Progr. Neurobiol.* 108:21. doi: 10.1016/j.pneurobio.2013.06.004

Cohen, A. D., Price, J. C., Weissfeld, L. A., James, J., Rosario, B. L., Bi, W., et al. (2009). Basal cerebral metabolism may modulate the cognitive effects of abeta in mild cognitive impairment: an example of brain reserve. *J. Neurosci.* 29, 14770–14778. doi: 10.1523/JNEUROSCI.3669-09.2009

Condello, C., and Stöhr, J. (2017). Aβ propagation and strains: implications for the phenotypic diversity in Alzheimer's disease. *Neurobiol. Dis.* 2017:109. doi: 10.1016/j.nbd.2017.03.014

Daianu, M., Jahanshad, N., Nir, T. M., Jack, C. R., Weiner, M. W., Bernstein, M. A., et al. (2015). Rich club analysis in the Alzheimer's disease connectome reveals a relatively undisturbed structural core network. *Hum. Brain Mapp.* 36, 3087–3103. doi: 10.1002/hbm.22830

Devi, L., Prabhu, B. M., Galati, D. F., Avadhani, N. G., and Anandatheerthavarada, H. K. (2006). Accumulation of amyloid precursor protein in the mitochondrial import channels of human Alzheimer's disease brain is associated with mitochondrial dysfunction. *J. Neurosci. Offi. J. Soc. Neurosci.* 26, 9057–9068. doi: 10.1523/JNEUROSCI.1469-06.2006

Driscoll, I., Troncoso, J. C., Rudow, G., Sojkova, J., Pletnikova, O., Zhou, Y., et al. (2012). Correspondence between in vivo (11)C-PiB-PET amyloid imaging and postmortem, region-matched assessment of plaques. *Acta Neuropathol.* 124, 823–831. doi: 10.1007/s00401-012-1025-1

Eisele, Y. S., and Duyckaerts, C. (2016). Propagation of Aß pathology: hypotheses, discoveries, and yet unresolved questions from experimental and human brain studies. *Acta Neuropathol.* 131:5.

Ferreira, I. L., Resende, R., Ferreiro, E., Rego, A. C., and Pereira, C. F. (2010). Multiple defects in energy metabolism in Alzheimer's disease. *Curr. Drug Targets* 11, 1193–1206. doi: 10.2174/1389450111007011193

Grimmer, T., Henriksen, G., Wester, H. J., Förstl, H., Klunk, W. E., Mathis, C. A., et al. (2009). Clinical severity of Alzheimer's disease is associated with PIB uptake in PET. *Neurobiol. Aging* 30, 1902–1909. doi: 10.1016/j.neurobiolaging.2008.01.016

Grothe, M. J., Barthel, H., Sepulcre, J., Dyrba, M., Sabri, O., Teipel, S. J., et al. (2017). In vivo staging of regional amyloid deposition. *Neurology* 89, 2031–2038.

Grothe, M. J., and Teipel, S. J. (2016). Spatial patterns of atrophy, hypometabolism, and amyloid deposition in Alzheimer's disease correspond to dissociable functional brain networks. *Hum. Brain Mapp.* 37, 35–53. doi: 10.1002/hbm.23018

Gusnard, D. A., and Raichle, M. E. (2001). Searching for a baseline: functional imaging and the resting human brain. *Nat. Rev. Neurosci.* 2, 685–694. doi: 10.1038/35094500

Hardy, J., and Allsop, D. (1991). Amyloid deposition as the central event in the aetiology of Alzheimer's disease. *Trends Pharmacol. Sci.* 12, 383–388. doi: 10.1016/0165-6147(91)90609-v

Heilbronner, G., Eisele, Y. S., Langer, F., Kaeser, S. A., Novotny, R., Nagarathinam, A., et al. (2013). Seeded strain-like transmission of β-amyloid morphotypes in APP transgenic mice. *Embo. Rep.* 14, 1017–1022. doi: 10.1038/embor.2013.137

Jack, C. R. Jr., Bennett, D. A., Blennow, K., Carrillo, M. C., Dunn, B., Haeberlein, S. B., et al. (2018). NIA-AA research framework: toward a biological definition of Alzheimer's disease. *Alzheimers Dement* 14, 535–562. doi: 10.1016/j.jalz.2018.02.018

Kellar, D., and Craft, S. (2020). Brain insulin resistance in Alzheimer's disease and related disorders: mechanisms and therapeutic approaches. *Lancet Neurol.* 19, 758–766. doi: 10.1016/S1474-4422(20)30231-3

Kemppainen, N. M., Aalto, S., Wilson, I. A., Någren, K., Helin, S., Brück, A., et al. (2006). Voxel-based analysis of PET amyloid ligand [11C]PIB uptake in Alzheimer disease. *Neurology* 67, 1575–1580. doi: 10.1212/01.wnl.0000240117.55680.0a

Kemppainen, N. M., Aalto, S., Wilson, I. A., Någren, K., Helin, S., Brück, A., et al. (2007). PET amyloid ligand [11C]PIB uptake is increased in mild cognitive impairment. *Neurology* 68, 1603–1606. doi: 10.1212/01.wnl.0000260969.94695.56

Klunk, W. E., Engler, H., Nordberg, A., Wang, Y., Blomqvist, G., Holt, D. P., et al. (2004). Imaging brain amyloid in Alzheimer's disease with pittsburgh compound-B. *Ann. Neurol.* 55, 306–319. doi: 10.1002/ana.20009

Klunk, W. E., Mathis, C. A., Price, J. C., Lopresti, B. J., and Dekosky, S. T. (2006). Two-year follow-up of amyloid deposition in patients with Alzheimer's disease. *Brain* 129, 2805–2807.

La Joie, R., Perrotin, A., Barre, L., Hommet, C., Mezenge, F., Ibazizene, M., et al. (2012). Region-specific hierarchy between atrophy, hypometabolism, and beta-amyloid (a beta) load in Alzheimer's disease dementia. *J. Neurosci.* 32, 16265–16273. doi: 10.1523/JNEUROSCI.2170-12.2012

Landau, S. M., Harvey, D., Madison, C. M., Reiman, E. M., Foster, N. L., Aisen, P. S., et al. (2010). Comparing predictors of conversion and decline in mild cognitive impairment. *Neurology* 75, 230–238. doi: 10.1212/WNL.0b013e3181e8e8b8

Landau, S. M., Mintun, M. A., Joshi, A. D., Koeppe, R. A., Petersen, R. C., Aisen, P. S., et al. (2012). Amyloid deposition, hypometabolism, and longitudinal cognitive decline. *Ann. Neurol.* 72, 578–586. doi: 10.1002/ana.23650

Li, X., Ma, C., Zhang, J., Liang, Y., Chen, Y., Chen, K., et al. (2013). Prevalence of and potential risk factors for mild cognitive impairment in community-dwelling residents of beijing. *J. Am. Geriatr. Soc.* 61, 2111–2119. doi: 10.1111/jgs.12552

Li, Y., Rinne, J. O., Mosconi, L., Pirraglia, E., Rusinek, H., Desanti, S., et al. (2008). Regional analysis of FDG and PIB-PET images in normal aging, mild cognitive impairment, and Alzheimer's disease. *Eur. J. Nucl. Med. Mol. Imaging* 35, 2169–2181. doi: 10.1007/s00259-008-0833-y

Lustbader, J. W., Cirilli, M., Lin, C., Xu, H. W., Takuma, K., Wang, N., et al. (2004). ABAD directly links Abeta to mitochondrial toxicity in Alzheimer's disease. *Science* 304, 448–452. doi: 10.1126/science.1091230

McKhann, G., Drachman, D., Folstein, M., Katzman, R., Price, D., and Stadlan, E. M. (1984). Clinical diagnosis of Alzheimer's disease: report of the NINCDS-ADRDA work group under the auspices of department of health and human services task force on Alzheimer's disease. *Neurology* 34, 939–944. doi: 10.1212/wnl.34.7.939

Moura, M. B. D., Santos, L. S. D., and Houten, B. V. (2010). Mitochondrial dysfunction in neurodegenerative diseases and cancer. *Environ. Mol. Mutagenesis* 51, 391–405.

Neth, B. J., and Craft, S. (2017). Insulin resistance and Alzheimer's disease: bioenergetic linkages. *Front. Aging Neurosci.* 2017:9. doi: 10.3389/fnagi.2017.00345

Oh, H., Habeck, C., Madison, C., and Jagust, W. (2014). Covarying alterations in Aβ deposition, glucose metabolism, and gray matter volume in cognitively normal elderly. *Hum. Brain Mapp.* 35, 297–308. doi: 10.1002/hbm.22173

Ossenkoppele, R., Zwan, M. D., Tolboom, N., Van Assema, D. M., Adriaanse, S. F., Kloet, R. W., et al. (2012). Amyloid burden and metabolic function in early-onset Alzheimer's disease: parietal lobe involvement. *Brain* 135, 2115–2125.

Palmqvist, S., Scholl, M., Strandberg, O., Mattsson, N., Stomrud, E., Zetterberg, H., et al. (2017). Earliest accumulation of beta-amyloid occurs within the default-mode network and concurrently affects brain connectivity. *Nat. Commun.* 8:1214. doi: 10.1038/s41467-017-01150-x

Rowe, C. C., Ng, S., Ackermann, U., Gong, S. J., Pike, K., Savage, G., et al. (2007). Imaging beta-amyloid burden in aging and dementia. *Neurology* 68, 1718–1725.

Sepulcre, J., Grothe, M. J., Sabuncu, M., Chhatwal, J., Schultz, A. P., Hanseeuw, B., et al. (2017). Hierarchical organization of tau and amyloid deposits in the cerebral cortex. *JAMA Neurol.* 74, 813–820. doi: 10.1001/jamaneurol.2017.0263

Shattuck, D. W., Mirza, M., Adisetiyo, V., Hojatkashani, C., Salamon, G., Narr, K. L., et al. (2008). Construction of a 3D probabilistic atlas of human cortical structures. *Neuroimage* 39:1064. doi: 10.1016/j.neuroimage.2007.09.031

Sun, X., Chen, W. D., and Wang, Y. D. (2015). β-amyloid: the key peptide in the pathogenesis of Alzheimer's disease. *Front. Pharmacol.* 6:221.

van den Heuvel, M. P., and Sporns, O. (2013). Network hubs in the human brain. *Trends Cogn. Sci.* 17, 683–696.

Villain, N., Chetelat, G., Grassiot, B., Bourgeat, P., Jones, G., Ellis, K. A., et al. (2012). Regional dynamics of amyloid-beta deposition in healthy elderly, mild cognitive impairment and Alzheimer's disease: a voxelwise PiB-PET longitudinal study. *Brain* 135, 2126–2139. doi: 10.1093/brain/aws125

Conflict of Interest: The authors declare that the research was conducted in the absence of any commercial or financial relationships that could be construed as a potential conflict of interest.

Advantages of publishing in Frontiers

OPEN ACCESS
Articles are free to read for greatest visibility and readership

FAST PUBLICATION
Around 90 days from submission to decision

HIGH QUALITY PEER-REVIEW
Rigorous, collaborative, and constructive peer-review

TRANSPARENT PEER-REVIEW
Editors and reviewers acknowledged by name on published articles

Frontiers
Avenue du Tribunal-Fédéral 34
1005 Lausanne | Switzerland

Visit us: www.frontiersin.org
Contact us: frontiersin.org/about/contact

REPRODUCIBILITY OF RESEARCH
Support open data and methods to enhance research reproducibility

DIGITAL PUBLISHING
Articles designed for optimal readership across devices

FOLLOW US
@frontiersin

IMPACT METRICS
Advanced article metrics track visibility across digital media

EXTENSIVE PROMOTION
Marketing and promotion of impactful research

LOOP RESEARCH NETWORK
Our network increases your article's readership